

# **Thermoelectric Energy Conversion**

**Woodhead Publishing Series in Electronic  
and Optical Materials**

# **Thermoelectric Energy Conversion**

**Theories and Mechanisms, Materials,  
Devices, and Applications**

*Editor-in-Chief*

***Ryoji Funahashi***

*Section Editors*

***Lidong Chen***

***Emmanuel Guilmeau***

***Qiang Li***

***Gao Min***

***Yuzuru Miyazaki***



**ELSEVIER**

**WP**

WOODHEAD  
PUBLISHING

An imprint of Elsevier

Woodhead Publishing is an imprint of Elsevier  
The Officers' Mess Business Centre, Royston Road, Duxford, CB22 4QH, United Kingdom  
50 Hampshire Street, 5th Floor, Cambridge, MA 02139, United States  
The Boulevard, Langford Lane, Kidlington, OX5 1GB, United Kingdom

© 2021 Elsevier Ltd. All rights reserved.

No part of this publication may be reproduced or transmitted in any form or by any means, electronic or mechanical, including photocopying, recording, or any information storage and retrieval system, without permission in writing from the publisher. Details on how to seek permission, further information about the Publisher's permissions policies and our arrangements with organizations such as the Copyright Clearance Center and the Copyright Licensing Agency, can be found at our website: [www.elsevier.com/permissions](http://www.elsevier.com/permissions).

This book and the individual contributions contained in it are protected under copyright by the Publisher (other than as may be noted herein).

#### Notices

Knowledge and best practice in this field are constantly changing. As new research and experience broaden our understanding, changes in research methods, professional practices, or medical treatment may become necessary.

Practitioners and researchers must always rely on their own experience and knowledge in evaluating and using any information, methods, compounds, or experiments described herein. In using such information or methods they should be mindful of their own safety and the safety of others, including parties for whom they have a professional responsibility.

To the fullest extent of the law, neither the Publisher nor the authors, contributors, or editors, assume any liability for any injury and/or damage to persons or property as a matter of products liability, negligence or otherwise, or from any use or operation of any methods, products, instructions, or ideas contained in the material herein.

#### Library of Congress Cataloging-in-Publication Data

A catalog record for this book is available from the Library of Congress

#### British Library Cataloguing-in-Publication Data

A catalogue record for this book is available from the British Library

ISBN: 978-0-12-818535-3 (print)

ISBN: 978-0-12-819916-9 (online)

For information on all Woodhead publications  
visit our website at <https://www.elsevier.com/books-and-journals>

*Publisher:* Matthew Deans  
*Acquisitions Editor:* Kayla Dos Santos  
*Editorial Project Manager:* John Leonard  
*Production Project Manager:* Vignesh Tamil  
*Cover Designer:* Greg Harris

Typeset by SPi Global, India



Working together  
to grow libraries in  
developing countries

[www.elsevier.com](http://www.elsevier.com) • [www.bookaid.org](http://www.bookaid.org)

# Contributors

**Feridoon Azough** School of Materials, University of Manchester, Manchester, United Kingdom

**Shengqiang Bai** The State Key Laboratory of High Performance Ceramics and Superfine Microstructure, Shanghai Institute of Ceramics, Chinese Academy of Sciences, Shanghai; Center of Materials Science and Optoelectronics Engineering, University of Chinese Academy of Sciences, Beijing, China

**Slavko Bernik** Jožef Stefan Institute, Department for Nanostructured Materials, Ljubljana, Slovenia

**Kanishka Biswas** New Chemistry Unit; School of Advanced Materials; International Centre of Materials Science, Jawaharlal Nehru Centre for Advanced Scientific Research (JNCASR), Bangalore, India

**Jan-Willem G. Bos** Institute of Chemical Sciences and Centre for Advanced Energy Storage and Recovery, School of Engineering and Physical Sciences, Heriot-Watt University, Edinburgh, Scotland

**Harsh Chandra** Department of Mechanical Engineering, The University of Tokyo, Tokyo, Japan

**Lidong Chen** The State Key Laboratory of High Performance Ceramics and Superfine Microstructure, Shanghai Institute of Ceramics, Chinese Academy of Sciences, Shanghai; Center of Materials Science and Optoelectronics Engineering, University of Chinese Academy of Sciences, Beijing, China

**Raju Chetty** Global Zero Emission Research Center, National Institute of Advanced Industrial Science and Technology (AIST), Tsukuba, Ibaraki, Japan

**Doug Crane** DTP Thermoelectrics, Altadena, CA, United States

**Ramzy Daou** Normandie Université, ENSICAEN, UNICAEN, CNRS, CRISMAT, Caen, France

**Kasey P. Devlin** Chemistry Department, University of California, Davis, CA, United States

**Moinak Dutta** New Chemistry Unit, Jawaharlal Nehru Centre for Advanced Scientific Research (JNCASR), Bangalore, India

**Dursun Ekren** School of Materials, University of Manchester, Manchester, United Kingdom

**Robert Freer** School of Materials, University of Manchester, Manchester, United Kingdom

**Ryoji Funahashi** National Institute of Advanced Industrial Science & Technology, Osaka, Japan

**Tanmoy Ghosh** New Chemistry Unit, Jawaharlal Nehru Centre for Advanced Scientific Research (JNCASR), Bangalore, India

**Emmanuel Guilmeau** Normandie Université, ENSICAEN, UNICAEN, CNRS, CRISMAT, Caen, France

**Hirokuni Hachiuma** Manufacturing Engineering Development Center, Production Division, Komatsu Ltd., Osaka, Japan

**Noriaki Hamada** Center for Spintronics Research Network, Osaka University, Osaka; Faculty of Science and Technology, Tokyo University of Science, Chiba, Japan

**Euripides Hatzikraniotis** Department of Physics, Aristotle University of Thessaloniki, Thessaloniki, Greece

**Sylvie Hébert** Normandie Université, ENSICAEN, UNICAEN, CNRS, CRISMAT, Caen, France

**Naomi Hirayama** Next Generation TATARA Co-Creation Centre, Shimane University, Shimane, Japan

**Tsutomu Iida** Department of Materials Science & Technology, Tokyo University of Science, Tokyo, Japan

**Hitomi Ikenishi** National Institute of Advanced Industrial Science & Technology, Osaka, Japan

**Satoaki Ikeuchi** ADVANCE RIKO, Inc., Yokohama, Japan

**Ryo Inoue** Department of Mechanical Engineering, Tokyo University of Science, Tokyo, Japan

**Kashif Irshad** Center of Research Excellence in Renewable Energy (CoRE-RE), King Fahd University of Petroleum & Minerals, Dhahran, Saudi Arabia

**Takao Ishida** Global Zero Emission Research Center, National Institute of Advanced Industrial Science and Technology, Tsukuba, Ibaraki, Japan

**Priyanka Jood** Global Zero Emission Research Center, National Institute of Advanced Industrial Science and Technology (AIST), Tsukuba, Ibaraki, Japan

**Mercouri G. Kanatzidis** Department of Chemistry, Northwestern University, Evanston; Materials Science Division, Argonne National Laboratory, Argonne, IL, United States

**Susan M. Kauzlarich** Chemistry Department, University of California, Davis, CA, United States

**Kazuhiro Kiriha** Nanomaterials Research Institute, National Institute of Advanced Industrial Science and Technology, Tsukuba, Ibaraki, Japan

**Yasuo Kogo** Department of Materials Science & Technology, Tokyo University of Science, Tokyo, Japan

**Theodora Kyrtatsi** Department of Mechanical and Manufacturing Engineering, University of Cyprus, Nicosia, Cyprus

**Jing-Feng Li** State Key Laboratory of New Ceramics and Fine Processing, School of Materials Science and Engineering, Tsinghua University, Beijing, PR China

**Yuxuan Liao** Department of Mechanical Engineering, The University of Tokyo, Tokyo, Japan

**Sajjad Mahmoudinezhad** Department of Energy Technology, Aalborg University, Aalborg, Denmark

**Antoine Maignan** Normandie Université, ENSICAEN, UNICAEN, CNRS, CRISMAT, Caen, France

**Yoko Matsumura** National Institute of Advanced Industrial Science & Technology, Osaka, Japan

**Masashi Mikami** National Institute of Advanced Industrial Science and Technology, AIST, Nagoya, Japan

**Yuzuru Miyazaki** Department of Applied Physics, Graduate School of Engineering, Tohoku University, Sendai, Japan

**Masakazu Mukaida** Nanomaterials Research Institute, National Institute of Advanced Industrial Science and Technology, Tsukuba, Ibaraki, Japan

**Hiroyo Murakami** National Institute of Advanced Industrial Science & Technology, Osaka, Japan

**Kanae Nakagawa** Fujitsu Laboratories LTD., Kawasaki, Japan  
Current affiliation: Sony LSI Design Inc., Atsugi-shi, Japan

**Yoichi Nishino** Department of Physical Science and Engineering, Nagoya Institute of Technology, Nagoya, Japan

**Yoshiyuki Nonoguchi** Division of Materials Science, Nara Institute of Science and Technology, Ikoma, Japan

**Michihiro Ohta** Global Zero Emission Research Center, National Institute of Advanced Industrial Science and Technology (AIST), Tsukuba, Ibaraki, Japan

**Yu Pan** State Key Laboratory of New Ceramics and Fine Processing, School of Materials Science and Engineering, Tsinghua University, Beijing, PR China;  
Max Planck Institute for Chemical Physics of Solids, Dresden, Germany

**Florent Pawula** Normandie Université, ENSICAEN, UNICAEN, CNRS, CRISMAT, Caen, France

**Christopher J. Perez** Chemistry Department, University of California, Davis, CA, United States

**Georgios S. Polymeris** Institute of Nanoscience and Nanotechnology, NCSR “Demokritos”, Athens, Greece

**Anthony V Powell** Department of Chemistry, University of Reading, Reading, United Kingdom

**Alireza Rezaniakolaei** Department of Energy Technology, Aalborg University, Aalborg, Denmark

**James R Salvador** Chemical and Materials Systems Laboratory, GM Global Research and Development Center, Warren, MI, United States

**Daishi Shiojiri** Department of Materials Science & Technology, Tokyo University of Science, Tokyo, Japan

**Junichiro Shiomi** Department of Mechanical Engineering, The University of Tokyo, Tokyo, Japan

**Koichiro Suekuni** Department of Applied Science for Electronics and Materials, Interdisciplinary Graduate School of Engineering Sciences, Kyushu University, Fukuoka, Japan

**Takashi Suzuki** Fujitsu Laboratories LTD., Kawasaki, Japan  
Current affiliation: KYOCERA Corporation, Yokohama-shi, Japan

**Toshiro Takabatake** Department of Quantum Matter, Graduate School of Advanced Sciences of Matter, Hiroshima University, Higashi-Hiroshima, Japan

**Ichiro Terasaki** Department of Physics, Nagoya University, Nagoya, Japan

**Ctirad Uher** University of Michigan, Ann Arbor, MI, United States

**Tomoyuki Urata** National Institute of Advanced Industrial Science & Technology, Osaka, Japan

**Hong Wang** Frontier Institute of Science and Technology, Xi'an Jiaotong University, Xi'an, PR China

**Hsin Wang** Oak Ridge National Laboratory, Oak Ridge, TN, United States

**Takanobu Watanabe** Waseda University, Tokyo, Japan

**Qingshuo Wei** Nanomaterials Research Institute, National Institute of Advanced Industrial Science and Technology, Tsukuba, Ibaraki, Japan

**Choongho Yu** Department of Mechanical Engineering, Texas A&M University, College Station, TX, United States

**Qihao Zhang** The State Key Laboratory of High Performance Ceramics and Superfine Microstructure, Shanghai Institute of Ceramics, Chinese Academy of Sciences, Shanghai, China

# About the editors

## Ryoji Funahashi (editor-in-chief)

Dr. Ryoji Funahashi is a prime senior researcher at National Institute of Advanced Industrial Science and Technology, Kansai. He received his BS and MS degrees at Faculty of Science from Nagoya University and PhD at Graduate School of Engineering from Nagoya University in 1998. Prior to his PhD work on a thesis entitled, “Recrystallization mechanism and superconducting property of Bi-based superconducting oxide,” he took a researching position in Osaka National Research Institute in 1992 (National Institute of Advanced Industrial Science and Technology, Kansai from 2001), where the main topic of his works was processing of Bi-Sr-Ca-Cu-O superconducting materials. He switched his research to thermoelectric oxides in 1999, and reported on the thermoelectric p-type layered cobaltites in a number of articles originated from his group in 2000. In 2002–2007, he explored new thermoelectric oxides as a member of JST CREST team lead by Prof. Kunihito Koumoto, Nagoya University. He also focused on the development of thermoelectric modules from 2002 and demonstrated thermoelectric generation using oxide thermoelectric modules in a Startup Support Program by NEDO. In May 2010, he established a start-up company (TES Newenergy) for producing and selling thermoelectric systems. He chaired the 32nd International Conference on Thermoelectrics (ICT 2013), which gathered about 700 people, at Kobe in 2013. He was given an excellent paper award from Journal of Japan Applied Physics and Thermoelectric Society of Japan in 2001. He edited several books and special issues of academic journals. He serves as a board member of the International Thermoelectric Society and the Thermoelectric Society of Japan.

## Section editors

### *Lidong Chen*

Lidong Chen is a professor of Shanghai Institute of Ceramics, Chinese Academy of Sciences (SICCAS). He received his BS degree in Materials Science and Engineering from Hunan University in 1982 and doctor degree in Materials Science from Tohoku University in 1990. After being chief engineer and postdoctoral appointment, at Riken Cooperation and Japan National Aerospace Laboratory, respectively, he worked at the Institute for Materials Research, Tohoku University, as research associate and associate professor. He joined SICCAS as professor in 2001. His research activity has majorly been focused on the design, synthesis, and characterization of novel

thermoelectric materials, as well as the integration of thermoelectric devices. He developed a series of high-performance TE materials such as filled skutterudites, half-Heusler, and copper chalcogenide. He also made contributions to the development of the design/integration technology of thermoelectric devices. His recent discovery is the deformable inorganic semiconductors,  $\alpha$ -Ag<sub>2</sub>S and InSe, which show metal-like ductility at room temperature while possessing tunable semiconducting properties. He has published more than 400 authored or coauthored papers on thermoelectrics and ceramics. He serves as a board member of the International Thermoelectric Society and the Coeditor-in-chief of *npj Computational Materials*.

### ***Emmanuel Guilmeau***

Emmanuel Guilmeau received his PhD in Materials Chemistry (oxide superconductors) from the University of Caen Normandy (France) at CRISMAT laboratory in 2003. He then worked at the National Institute of Advanced Industrial Science and Technology (AIST, Osaka, Japan, 2003/2004) and the LCIS laboratory at University of Liège (Belgium, 2004/2005) as a postdoctoral fellow where he focused his work on the study of oxide thermoelectrics. In 2005, he returned to CRISMAT as a CNRS researcher, and was promoted as CNRS director of research in 2017. His research interests include oxide and sulfide thermoelectrics, solid-state chemistry, processing of materials (mechanical-alloying, SPS), and transport property measurements. Emmanuel Guilmeau has published more than 160 peer-reviewed articles, 2 patents, and 3 book chapters. He has been invited to 40 national/international conferences and coorganized several international conferences.

### ***Qiang Li***

Dr. Qiang Li received his PhD in physics from Iowa State University in 1991, worked on single vortex motion and pinning in Josephson junctions at US Department of Energy (DOE) Ames Lab. He then joined the Condensed Matter Physics and Materials Science Department at DOE's Brookhaven National Laboratory (BNL) in New York, where he is the head of Advanced Energy Materials Group. His research interests range from basic physics and material sciences of superconductors, thermoelectrics, and topological quantum materials to their applications in energy and quantum information technology. At BNL, he leads DOE's BES program on chiral and superconducting materials, and has led several DOE's projects on high-temperature superconductors for grid scale energy storage, wind power generation, and next-generation electrical machine. In 2011, he was named a New York State Leader in Superconductivity at New York State Superconductor Technology Summit. He also led the BNL's effort in several DOE EERE funded programs on vehicle waste heat recovery by thermoelectrics over a decade. He is a fellow of American Physical Society, a recipient of R&D 100 award, and Brookhaven Science and Technology Award for the discovery of chiral magnetic effect. In the autumn semester of 2020, he joined the Department of Physics and Astronomy at Stony Brook University as a SUNY Empire Innovation Professor, and continued to hold a joint scientist appointment at BNL to lead the Advanced Energy Materials Group.

**Gao Min**

Gao Min is a professor of Energy Materials, Group Leader of Magnetics and Materials at School of Engineering, Cardiff University, UK. He obtained BSc in Semiconductor Physics from Xidian University, Xian, China in 1982 and PhD under supervision of Professor David Michael Rowe at Cardiff University in 1996. He was a research scientist at Kunming Institute of Physics, China (1985–93) and visiting scientist at MIT in 2005. Gao Min has been working at the forefront of thermoelectric research for decades and created many radical concepts and approaches, including the use of the Peltier modules as generators, electron energy filtering by potential barriers of grain boundaries, integrated thermoelectric microcooler, thermoelectric structure-property diagram, ring-structured thermoelectric module, module design theory for a given thermal input, thermoelectric preheating combustion system, complete thermoelectric characterisation based on dual I–V curves, thermoelectric impedance spectroscope and thermal interface measurement using an infrared microscope.

**Yuzuru Miyazaki**

Dr. Yuzuru Miyazaki is currently a professor at Department of Applied Physics, Tohoku University, Japan. After receiving his BS and MS degrees in Materials Science, he joined a research division of Honda R&D Co. Ltd. In 1994, he obtained a PhD degree in Materials Science (Design and superconducting properties of novel oxycarbonate superconductors) and moved to Department of Applied Physics in Tohoku University as a Research Associate. He was awarded a JSPS postdoctoral fellowship to study abroad and worked for 2 years at the School of Chemistry in University of Birmingham, UK, under the supervision of Professor Peter P. Edwards, FRS. He was promoted to an associate professor in 2004 and a full professor in 2012, both at Department of Applied Physics in Tohoku University. His research is based on the deep understanding of the crystal structure of a target material. He devoted himself to explore novel superconductors, thermoelectric materials, and cathode materials for secondary batteries. Up to now, he has discovered more than 30 novel compounds, including oxycarbonate cuprate  $\text{Sr}_2\text{CuO}_2\text{CO}_3$ , infinite-layered cuprate  $(\text{Sr},\text{Ca})\text{CuO}_2$ , incommensurate spin-chain cuprate  $(\text{Ca},\text{Ln})_{0.82}\text{CuO}_2$ , and misfit-layered cobaltates in Ca-Co-O and Ca-Co-Cu-O systems. He is a member of American Chemical Society, International Thermoelectric Society, Thermoelectric Society of Japan (TSJ), Japan Society of Applied Physics, and so on. In 2018, he was awarded with the Academic Award by TSJ for the development of new thermoelectric materials through a precise material design based on detailed crystal structure analyses.

# Preface

I would like to begin by extending my deepest condolences and sympathies to those who have succumbed to the novel coronavirus, COVID-19, and to those who are suffering from its ravaging effects.

Almost from the earliest days of 2020, various aspects of our daily lives have been upended by the viral outbreak. Hundreds of thousands have died from, tens of millions have been infected by, or have been forced into quarantine because of COVID-19. Even now, more than 6 months since its onset, the crisis shows no sign of coming to an end.

It is my view that humanity has drawn certain crucial lessons from the current pandemic. I have heard, for instance, that air quality has improved in many locations due to the partial shutdown in global economic activity. While the validity of this statement must be examined critically, it appears that the flip side of such a welcome phenomenon is a flailing economy with devastating secondary consequences for ordinary people's lives. At the same time, several news outlets have reported on a dangerous link between global warming and viral plagues, by which I refer to the thawing of the permafrost in Siberia that led to the discovery of an ancient virus estimated to be hundreds of millions of years old. It goes without saying that such a virus may have the potential to wreak havoc on humans and other creatures alike. Ultimately, environmental protection must be pursued quickly but steadily, and to do so requires innovative scientific and technological methods.

Thermoelectric conversion as applied to areas as diverse as high-efficiency and high-precision temperature regulation, utilization of waste heat from automobiles and factories, and the use of body and ambient heat for IoT (Internet of things) power generation is expected to play a crucial role in meeting the environmental and energy challenges of today and tomorrow, as well as in creating safe living environments and in forging new industries.

The present book is a handbook on thermoelectric conversion technology based on the Peltier and Seebeck effects. By going through this book, the reader will be able to gain a view of the works done by the world's leading researchers in a broad array of fields ranging from the fundamental sciences to device technology and applications.



Ryoji Funahashi  
Osaka, Japan

# Acknowledgments

I wish to express my gratitude to the contributing authors for dedicating their valuable time to writing sections of this book. Your research accomplishments are bright flames of knowledge illuminating a still largely uncharted field that will burn ever brighter in the years to come. I would also thank Ms Kayla Dos Santos of Elsevier for first introducing me to this project and for presenting me with this rare and exciting opportunity. I still remember the rush I felt during our first discussion at that conference in Phoenix. I am grateful to my coeditors Prof. Lidong Chen, Prof. Gao Min, Dr. Emmanuel Guilmeau, Dr. Qiang Li, and Prof. Yuzuru Miyazaki for agreeing to take time out of their busy schedules to assist me in planning this book and reviewing the manuscripts. It was an immense pleasure to work on this book with friends whom I have been in amicable competition over my many years as a researcher. Thanks also go to everyone at Elsevier who helped bring this book to publication. Finally, I wish to thank Mr. John Leonard of Elsevier for his patience and encouragement when progress was slow owing to my lack of editorial experience. It was his continuous support that allowed this book to see the light of day. Thank you from the bottom of my heart, and I look forward to meeting you someday over a glass of nice cold beer cooled by a thermoelectric refrigerator.

A handwritten signature in blue ink, appearing to read "Ryoji Funahashi".

Ryoji Funahashi  
Osaka, Japan

# Introduction

The book is divided into four sections. **Section 1: Theory and Mechanism** gives an in-depth treatment of the fundamental aspects of the thermoelectric effect with a focus on electrons and phonons. A detailed analysis of hitherto-identified thermoelectric materials contained in this section will serve as a useful guide in enabling performance improvements.

**Section 2: Materials**, which forms the bulk of the book, discusses in detail the physical properties, synthesis techniques, and microstructures of a wide array of thermoelectric materials. The wealth of topics covered—ranging from inorganic materials through organic materials to nanocarbon materials, and thermoelectric properties that arise in both low and high temperature spectra—will allow readers to gain exposure to the latest ideas and advances taking place in this field.

**Sections 3: Devices and Modules** and **4: Applications** deal with material that the editors were determined to include from the outset of this project. Section 3 gives an account of research and development activities on modules and devices. Here, segment modules and nanowire-based micromodules are described. Also described is modular measurement technology, which is an industrial application of thermoelectric conversion and is widely seen as a driver of future market growth. There is no doubt that this technology will play a pivotal role in achieving international standardization. Section 4 explores the frontiers of applied research and development with an eye toward commercialization. This section not only showcases the latest thermoelectric conversion technologies underlying thermoelectric cooling, automotive applications, solar-thermal utilization, and IoT power generation, but also presents a deep analysis of findings from recent studies that are sure to offer clues to future trends and opportunities in the market for thermoelectric energy conversion.

This text has been edited with the hope that it will benefit not only experienced researchers active in the field of thermoelectric conversion, but also a range of audiences that might include novice researchers taking their first steps into this field, students interested in learning the subject matter for the first time, developers exploring new business opportunities in a corporate setting, and policymakers responsible for crafting energy-related legislation. It is my hope that the reader's professional opportunities and intellectual horizons will broaden as a result of gaining insight into some of the world's most cutting-edge research and researchers.

# Thermoelectric properties beyond the standard

## Boltzmann model in oxides: A focus on the ruthenates

1.1

Florent Pawula, Ramzy Daou, Sylvie Hébert, and Antoine Maignan  
Normandie Université, ENSICAEN, UNICAEN, CNRS, CRISMAT, Caen, France

### 1.1.1 Introduction

Research on “thermoelectric oxides” emerged after 1997, following the discovery of a large thermopower in  $\text{Na}_x\text{CoO}_2$ , an oxide exhibiting “bad metal” properties [1]. This material remains emblematic of this field of research, as it is still one of the best p-type thermoelectric oxides [2], and the original and unique physical properties associated with its peculiar crystallographic structure are at the origin of this larger ZT, compared to other p-type oxides. These properties have moreover stimulated intense research on the development of new models to describe thermoelectric properties in the presence of strong electronic correlations [3–6]. It is interesting to note that this crystallographic structure leads to very rich properties in the field of energy, as it is analogous to other cobaltates already used in the field of batteries, i.e., the well-known  $\text{Li}_x\text{CoO}_2$ .

The layered cobaltates  $\text{Na}_x\text{CoO}_2$  ( $x \sim 0.7$ ) and cobalt misfits are still the best p-type thermoelectric oxides, with ZT values of more than 0.5 at 973 K. The unique and original properties of these cobalt oxides come from the crystallographic structure, which can be described as a layered material made of  $\text{CoO}_2$  layers of edge-shared octahedra, separated by  $\text{Na}^+$  layers or rock-salt-type layers. The properties for these triangular Co layers have led to the development of different models, which include the peculiar band structure associated with this crystallographic structure [7], the presence of strong electronic correlations for this Co doping [4], the low spin states of  $\text{Co}^{3+}$  and  $\text{Co}^{4+}$  stabilized by this structure, and the role of the disorder potential induced on the  $\text{CoO}_2$  layer by the  $\text{Na}^+$  network or by the NaCl-type layer [8]. Among the intriguing properties, the combination of a bad metal resistivity in these p-type oxides together with a large Seebeck coefficient S has shown that the entropy of carriers, associated with their spin and orbital states, can strongly contribute to the thermopower, even at room temperature [6].

Following the first reports on  $\text{Na}_x\text{CoO}_2$ , the search for an efficient n-type oxide has become a major issue. Promising values of ZT were reported in 1996 in Al-doped  $\text{ZnO}$  by Ohtaki et al. [9], even before the first reports on  $\text{Na}_x\text{CoO}_2$ . Different families have been investigated since then, such as electron-doped manganese oxides (from the

colossally magnetoresistive manganite family),  $\text{SrTiO}_3$  perovskites, and  $\text{In}_2\text{O}_3$  bixbyites or  $\text{ZnO}$  [10–13]. For all these oxides, contrary to the case of  $\text{Na}_x\text{CoO}_2$  and related p-type oxides, the Seebeck coefficient can be described using a degenerate semiconductor model, with  $S$  calculated from the Boltzmann theory [14–16]. For all these oxides, the major issue is the too large thermal conductivity, and the research on how to reduce thermal conductivity has been the most active in this field in the last 20 years. Several approaches have been followed, such as the reduction of the grain size and increase of grain boundaries scattering, or the preparation of composites with graphene [17, 18].

A strong difference is thus observed between the properties of p-type and n-type oxides, with the n-type oxide properties being generally described by the Boltzmann transport equation and the p-type oxides being more sensitive to electronic correlations or peculiar band structures [19, 20]. We show here first the peculiarities of these p-type oxides, and then focus on the ruthenates for which a combination of electronic correlations and spin-orbit coupling generates a dominant role of the entropy on the thermopower.

### 1.1.2 Thermoelectric properties of p-type oxides

The thermopower  $S$  can be described as the sum of two terms as in the formula

$$S = -\frac{S^{(2)}/S^{(1)} + \mu/e}{T}$$

The first term is related to the transport functions with  $S^{(1)}$  and  $S^{(2)}$  integrals depending on the velocity and energy flux operators, and the second term represents the entropy of the system, with  $\mu$  being the chemical potential [21]. Depending on the temperature, the first term can dominate in a large range of temperatures, but at very high temperatures (very high with respect to bandwidth), the entropy term can dominate [5, 21]. In transition metal oxides, the carriers can often be associated with spins, and therefore spin and orbital degrees of freedom can contribute to entropy. The presence of strong electronic correlations by reducing the bandwidth can induce a major role of the spin and orbital degrees of freedom. The entropy term has been evidenced in doped manganites [22]. When extrapolating the Seebeck coefficient experiments to very high temperatures, all the curves converge to a unique value of  $-20\mu\text{VK}^{-1}$ , independent of  $x$  in  $\text{La}_{1-x}\text{Ca}_x\text{MnO}_3$  (for  $x < 0.9$ ). In the case of oxides with localized p-type carriers such as  $\text{Pr}_{1-x}\text{Ca}_x\text{CrO}_3$ , this entropy term can be directly measured, even at relatively low temperature. An increase of  $S$  by  $70\mu\text{VK}^{-1}$  has been measured at  $T$  larger than 250 K [23], and has been quantitatively accounted for by the configurational entropy of  $\text{Cr}^{3+}$  and  $\text{Cr}^{4+}$ , with  $3d^3$  and  $3d^2$  filling of the  $t_{2g}$  orbitals. In the case of the “112” cobaltates, the thermopower is also increased, and this family is an interesting playground to observe the role of the different spin states of cobalt on the thermopower, as the spin and orbital entropy directly depends on the spin states [24, 25]. The strong

impact of entropy has also been evidenced in vanadates, close to the Mott insulator regime and at relatively low temperatures, above 200 K [26].

In the case of metallic oxides, the transport term should play a major role. Original band structures such as the pudding-mold band model [19] have been proposed for  $\text{Na}_x\text{CoO}_2$ , and the apparent Fermi liquid (AFL) model has been established to explain the transport properties of delafossites [20, 27]. However, in the case of misfits, the role of entropy has been evidenced, even at room temperature. All the Seebeck coefficient curves present an almost constant value of  $S$ , from room temperature to high temperature, which can be interpreted taking into account the spin and orbital terms associated with low spin states  $\text{Co}^{3+}$  and  $\text{Co}^{4+}$  [2, 4, 28], with the specific orbital splitting induced by this geometry [7, 29, 30]. At high  $T$ , this entropy term can be associated to an atomic-like description of these oxides, but the entropy term can also be observed at low  $T$ , i.e., when magnetic exchanges start to play a role. For example, in paramagnetic misfits, the increase of magnetic susceptibility as  $T$  decreases induces a large magneto-thermopower at low  $T$ . As the magnetic field increases, the alignment of paramagnetic spins strongly reduces magnetic entropy, leading to a  $-50\%$  decrease of the Seebeck coefficient in  $\text{BiCaCoO}$  misfits at 5 K and 9  $T$  [31, 32]. The spins and magnetism are thus an interesting tool to optimize the properties in these materials.

### 1.1.3 A focus on the ruthenates

One fascinating family of oxides is the ruthenates, as exemplified by the emblematic  $\text{SrRuO}_3$  perovskite, known to exhibit a bad metal behavior. For these oxides, the Hund coupling  $J$  can play a major role, and can induce by itself electronic correlations. In the case of one electron per site, it has been shown [33] that the Hund coupling decreases the correlations, inducing a metallic behavior and, on the contrary, in the case of half-filling the correlations are increased by  $J$ , inducing an insulating state. In the other cases, the Hund coupling has a “two faces” role on the correlations, as Janus, the two-faced Roman god, which has the effect of inducing a bad metal behavior.

In the presence of spin-orbit coupling (SOC) and electronic correlations, the thermopower presents characteristics very close to the ones of correlated oxides such as misfit cobaltates. As shown in Fig. 1.1.1, the thermopower of  $\text{SrRuO}_3$  presents a rapid increase at low  $T$ , followed by a plateau at room temperature, reaching  $\sim 30\text{--}35 \mu\text{VK}^{-1}$  at 300 K. This value is relatively constant up to 800 K. The thermopower is very stable against doping, as previously shown in Ref. [34], where several substitutions have been performed in  $\text{SrRuO}_3$ , to shift the formal valency from 4 to both below and above 4. Even if magnetism and resistivity are affected by these substitutions, thermopower is almost unaffected, with a similar shape for all the investigated levels of doping, and the room temperature Seebeck values remain in a narrow range of between 20 and  $35 \mu\text{VK}^{-1}$ .

The limited dependency of  $S$  on doping is very surprising considering the strong doping dependency in the Heikes formula usually considered to describe the Seebeck

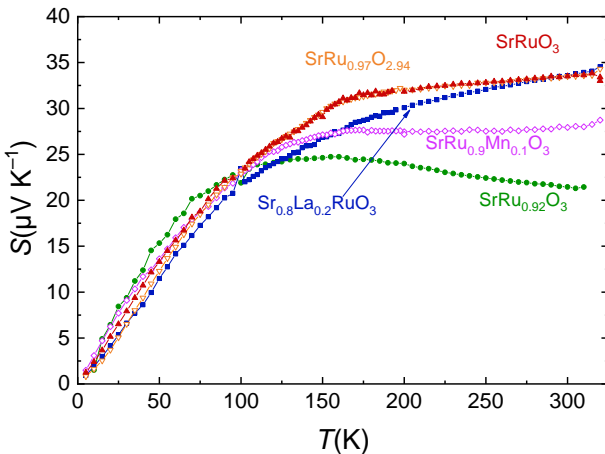


**Fig. 1.1.1**  $T$ -dependent Seebeck coefficient of  $\text{SrRuO}_3$ .

From Y. Klein, S. Hébert, A. Maignan, S. Kolesnik, T. Maxwell, B. Dabrowski, Phys. Rev. B 73 (2006) 052412.

coefficient in these correlated oxides. One straightforward explanation [34] suggested that the thermopower would be dominated by the spin entropy term only. Indeed, by considering ruthenium as  $\text{Ru}^{3+}/\text{Ru}^{4+}$  or  $\text{Ru}^{4+}/\text{Ru}^{5+}$ , the part of the Seebeck coefficient arising from the spin entropy term only can be defined as

$$S_{\text{entropy}} = -\frac{k_B}{|e|} \ln(\beta) = -\frac{k_B}{|e|} \ln \left( \frac{2S_n + 1}{2S_{n+1} + 1} \right),$$

with  $S_n$  and  $S_{n+1}$  being the spins of  $\text{M}^{n+}$  and  $\text{M}^{(n+1)+}$ , respectively. This results in  $S_{\text{entropy}} = 35 \mu\text{VK}^{-1}$  for  $\text{Ru}^{3+}/\text{Ru}^{4+}$  and  $S_{\text{entropy}} = 25 \mu\text{VK}^{-1}$  for  $\text{Ru}^{4+}/\text{Ru}^{5+}$ ; the two values very close to the experimental ones, with indeed smaller  $S$  values in the case of formal ruthenium valency larger than 4 than below 4. Thus, the doping and the orbital dependency from the Heikes formula appeared to be quenched.

In the case of layered  $\text{Sr}_2\text{RuO}_4$ , thermopower exhibits very similar values, close to  $30 \mu\text{VK}^{-1}$  at room temperature for the in-plane component.  $\text{Sr}_2\text{RuO}_4$  is one of the ruthenates that has been the most extensively investigated, as a hallmark of a metallic Hund's paramagnet, combining bad metal behavior with strong antiferromagnetic fluctuations, together with superconductivity appearing below 1.5 K. The thermopower of  $\text{Sr}_2\text{RuO}_4$  has been recently theoretically investigated, taking into account the transport part and the spin and orbital entropy parts [35] within the dynamical mean field theory. In the case of Ru with a 4+ formal valency, the Heikes formula becomes [35]

$$S = \frac{k_B}{2e} \ln \left( \frac{2S_{n+1} + 1}{2S_{n-1} + 1} \right) \simeq 30 \mu\text{VK}^{-1}$$

where the orbital term no longer appears. This value of  $30 \mu\text{VK}^{-1}$  corresponds reasonably well with the one measured at room temperature. The unexpected result is that when calculating the entropy of  $\text{Sr}_2\text{RuO}_4$ , the orbital entropy is shown to be quenched up to very high  $T$ ,  $\sim 1250\text{K}$ , while the spin part is released from  $\sim 250\text{K}$ . The exact calculation of the thermopower shows that for its in-plane component, the Seebeck coefficient is close to the one of  $\text{SrRuO}_3$ , with values reaching  $\sim 30 \mu\text{VK}^{-1}$ . This calculation shows that, at least for  $\text{Sr}_2\text{RuO}_4$ , the entropy plays a major role on  $S$ , and that the orbital part is frozen in the experimentally available temperature range.

Following the experimental results obtained on  $\text{SrRuO}_3$  and the theoretical calculation of  $S$  in  $\text{Sr}_2\text{RuO}_4$ , different families of ruthenates have been investigated. The motivation was to investigate the role of spin and orbital entropy on the Seebeck coefficient in ruthenates exhibiting different ground states, from ferromagnetic, as in  $\text{SrRuO}_3$  to paramagnetic or with Pauli magnetism, and different transport mechanisms. The influence of the Ru coordination has also been investigated, from corner-shared to edge-shared  $\text{RuO}_6$  octahedra.

In the quadruple perovskites  $\text{ACu}_3\text{Ru}_4\text{O}_{12}$ , the copper atoms are in a quasi square planar  $\text{CuO}_4$  coordination, and the presence of Jahn-Teller  $d^9 \text{Cu}^{2+}$  on the A-site induces strong distortion. The  $\text{RuO}_6$  corner-shared octahedra can be heavily distorted depending on the nature of A cations (Fig. 1.1.2), on the A cation size, and on the doping induced by the A cation. From A cation changing from  $\text{Na}^+$  to  $\text{La}^{3+}$ , the formal valence of ruthenium changes from  $\text{Ru}^{4.25+}$  to  $\text{Ru}^{3.75+}$ .

Quadruple perovskites with  $A = \text{Na}, \text{Ca}, \text{Ca}_{0.5}\text{La}_{0.5}$ , and  $\text{La}$  present a Pauli-like paramagnetic behavior [36, 37] and references therein, with very small susceptibility values, 1000 times smaller than the one of  $\text{SrRuO}_3$ . Their resistivity follows a bad metal behavior with  $\rho \sim \rho_0 + AT^2$ , no signs of saturation up to 900 K, and remain in the range of  $\text{m}\Omega\text{cm}$  up to 900 K (Fig. 1.1.3A) [38]. The  $\gamma$  Sommerfeld coefficients extracted from specific heat experiments are found to increase from  $\text{Na}^+$  to  $\text{La}^{3+}$ , from 75 to  $136 \text{mJ f.u.mol}^{-1} \text{K}^{-2}$  [39]. Together with the  $\gamma$  increase, the resistivity (and the A parameter) increases, following the Kadowaki-Woods ratio, as shown in Fig. 1.1.3.

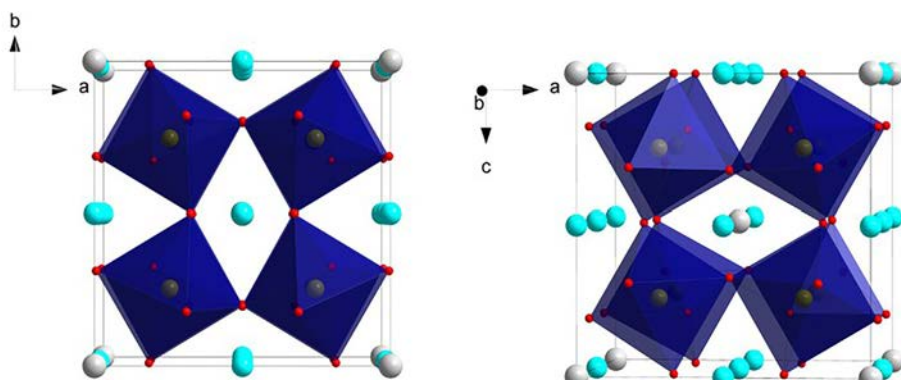


**Fig. 1.1.2** Octahedra distortion in  $\text{AA}'_3\text{Ru}_4\text{O}_{12}$  quadruple perovskites.

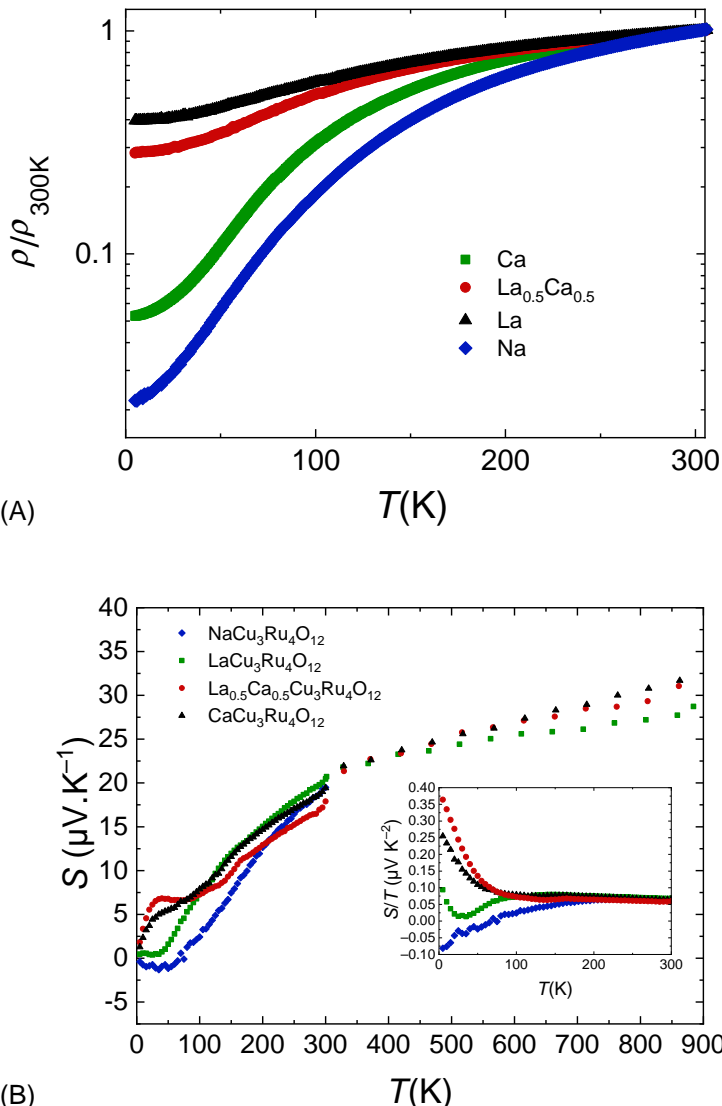


**Fig. 1.1.3** (A)  $T$ -dependent electrical resistivity  $\rho$  normalized at  $\rho_{300K}$  for  $\text{Ca}_{1-x}\text{La}_x\text{Cu}_3\text{Ru}_4\text{O}_{12}$  [ $x=0$  (Ca), 0.5 (La/Ca), 1 (La)]. The  $\rho(T)$  of  $\text{NaCu}_3\text{Ru}_4\text{O}_{12}$  is also given. (B)  $T$ -dependent Seebeck coefficient  $S$  for the four  $AA'\text{Cu}_3\text{Ru}_4\text{O}_{12}$  quadruple perovskites series. Inset:  $S/T$  as a function of  $T$ .

(A and B) From S. Hébert, R. Daou, A. Maignan, Phys. Rev. B 91 (2015) 045106.

For the four quadruple perovskites, the Kadowaki-Woods ratio is of the order of a few  $\mu\Omega\text{cm mol}^2 \text{K}^2 \text{J}^{-2}$  suggesting the existence of electronic correlations.

In these Pauli metallic ruthenates, the Seebeck coefficient curves show a positive value of  $S$ , continuously increasing from low temperatures to 900 K, and separated into

two domains. Above  $\sim 250$ – $300$  K, the curves are almost superimposed, and exhibit a linear behavior typical of a metal, and reaching  $\sim 35 \mu\text{V K}^{-1}$  at  $900$  K, while they exhibit small differences at lower temperatures (Fig. 1.1.3B). This is clearly observed when  $S/T$  is plotted as a function of  $T$  at low temperatures, as shown in the inset of Fig. 1.1.3B.

The results presented in Fig. 1.1.3B confirm that the Seebeck coefficient depends on the band structure of these quadruple ruthenates at low  $T$ , the band structure being modified by the doping and the distortion of the octahedra. On the other hand, as for ruthenium perovskites, the high temperature data are much less sensitive to the band structure. Even in these (less correlated) Pauli metals, the Seebeck coefficient is dominated by its entropic part.

This investigation has been extended to other families of ruthenates, with  $\text{RuO}_6$  edge-sharing octahedra instead of corner-sharing octahedra. In ruthenium hollandites, the crystallographic structure is composed of double chains of edge-sharing octahedra forming channels (Fig. 1.1.4). The hollandite structure is rather versatile as it can host different cations inside the channels, such as  $\text{Ba}^{2+}$ ,  $\text{Sr}^{2+}$ ,  $\text{Pb}^{2+}$ ,  $\text{K}^+$ , etc. The  $\text{Ba}_x\text{Ru}_8\text{O}_{16}$  or  $\text{KRu}_4\text{O}_8$  hollandites are metallic, with a Pauli-like behavior. The electronic properties of  $\text{Ba}_x\text{Ru}_8\text{O}_{16}$  have been extensively studied due to the high sensitivity to disorder of this quasi-1D oxide. The resistivity is metallic along the tunnel up to  $300$  K, while a semiconductor to metal transition appears at  $210$  K in the perpendicular direction. Interestingly, in  $\text{KRu}_4\text{O}_8$ , the Seebeck coefficient measured on a single crystal (with the gradient of temperature applied along  $c$ , i.e., along the tunnel) shows a complex behavior at low  $T$ , with a sign change at low  $T$ , and an unexplained  $T^2$  dependence, but at high temperatures,  $S$  reaches a value close to  $30 \mu\text{V K}^{-1}$ , very close to the one observed in perovskites and quadruple perovskites [40].

In these hollandites, a mixed occupation of the Ru site has been reported [41], and new hollandites with a mixed Ru/Cr composition have been synthesized following the  $\text{A}_{1.5}\text{Ru}_{6.1}\text{Cr}_{1.9}\text{O}_{16}$  formula ( $\text{A} = \text{Sr}$  or  $\text{Ba}$ ) [42]. The larger  $\text{Ba}^{2+}$  cation induces a modification of the channel, with a more regular channel in this hollandite (Fig. 1.1.4). These two new hollandites enable direct investigation of (i) the localization effect induced by the Cr substitution and (ii) the modification of the transport and/or magnetic properties depending on the  $\text{A}$  cation, and their relationship with the Seebeck coefficient.

The Ru hollandites exhibit a Pauli-type magnetism, while in the Ru/Cr hollandites, a larger susceptibility is observed, with a transition at  $22$  K (for  $\text{Ba}_{1.5}\text{Ru}_{6.1}\text{Cr}_{1.9}\text{O}_{16}$ ) associated with a cluster glass state. The magnetism is more complex in  $\text{Sr}_{1.5}\text{Ru}_{6.1}\text{Cr}_{1.9}\text{O}_{16}$ , with stronger ferromagnetic interactions appearing below  $188$  K, and a transition to a cluster glass state below  $38$  K. In these disordered magnetic states, resistivity remains in the  $\Omega\text{cm}$  range, with a tendency to localization ( $d\rho/dT < 0$  in the whole  $T$  range), the larger resistivity being observed for  $\text{Ba}_{1.5}\text{Ru}_{6.1}\text{Cr}_{1.9}\text{O}_{16}$ . Above  $\sim 200$  K, the two resistivity curves are almost superimposed, and  $\rho$  tends to  $18 \text{m}\Omega\text{cm}$  at  $700$  K (Fig. 1.1.5A). As shown in the insets of Fig. 1.1.5A, the transport in these cluster glass oxides can be described by a variable range hopping (VRH) model with

$$\rho(T) \sim \rho_0 e^{\left(\frac{T_0}{T}\right)^{1/4}}$$

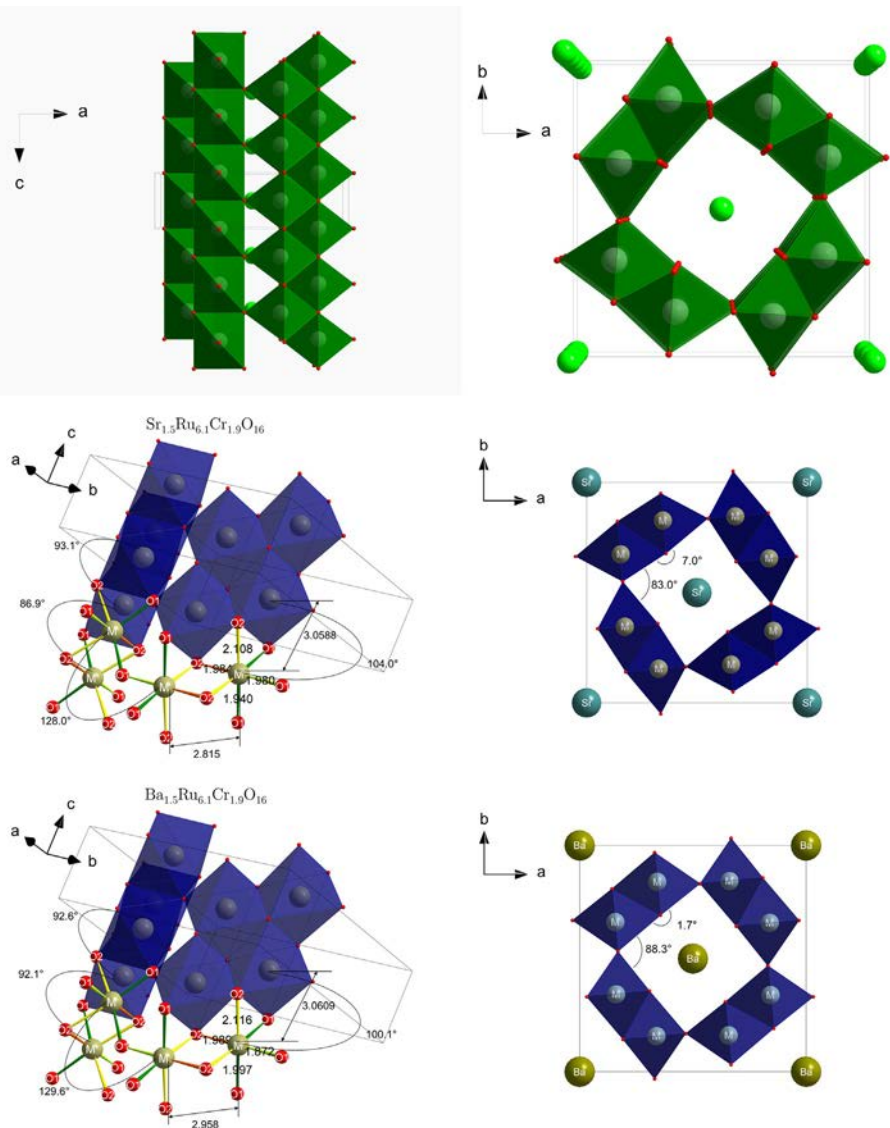


**Fig. 1.1.4** Crystallographic structure of hollandites and angular distortion of the channel of  $(\text{Ba}, \text{Sr})_{1.5}\text{Ru}_{6.1}\text{Cr}_{1.9}\text{O}_{16}$  hollandites.

From F. Pawula, S. Hébert, D. Pelloquin, A. Maignan, J. Mater. Chem. C 7 (1) (2019) 86.

and  $T_0 = 6000\text{ K}$  for  $\text{Ba}_{1.5}\text{Ru}_{6.1}\text{Cr}_{1.9}\text{O}_{16}$  and  $3160\text{ K}$  for  $\text{Sr}_{1.5}\text{Ru}_{6.1}\text{Cr}_{1.9}\text{O}_{16}$ . This VRH transport is associated with a large and negative magnetoresistance reaching  $-20\%$  at low  $T$  in  $\text{Ba}_{1.5}\text{Ru}_{6.1}\text{Cr}_{1.9}\text{O}_{16}$ .

The thermopower of these two hollandites is presented in Fig. 1.1.5B. The two curves follow a very similar behavior, with  $S$  increasing in the whole  $T$  range, and increasing up to  $\sim 29\text{ }\mu\text{VK}^{-1}$  at  $765\text{ K}$ . The larger values are obtained for the more resistive

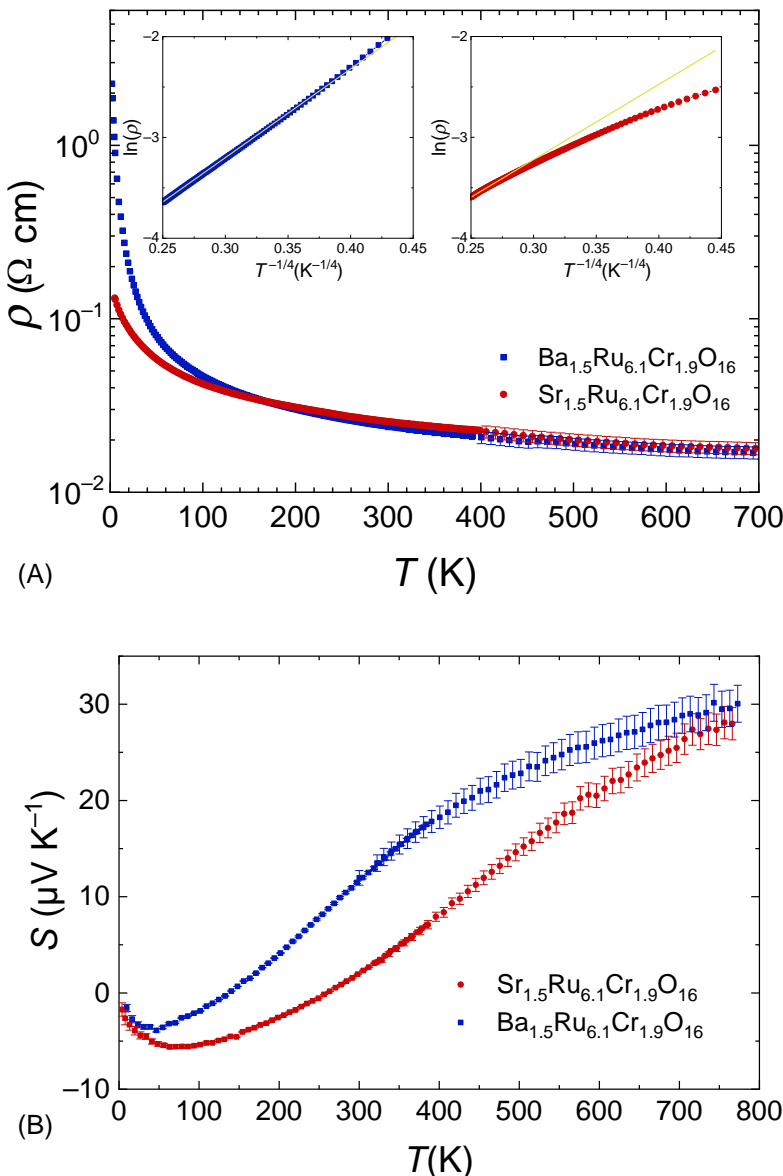


**Fig. 1.1.5** (A)  $T$ -dependent resistivities of  $\text{Ba}_{1.5}\text{Ru}_{6.1}\text{Cr}_{1.9}\text{O}_{16}$  (blue) and  $\text{Sr}_{1.5}\text{Ru}_{6.1}\text{Cr}_{1.9}\text{O}_{16}$  (red). Insets: VRH plots. (B)  $T$ -dependent Seebeck coefficient of  $\text{Ba}_{1.5}\text{Ru}_{6.1}\text{Cr}_{1.9}\text{O}_{16}$  (blue) and  $\text{Sr}_{1.5}\text{Ru}_{6.1}\text{Cr}_{1.9}\text{O}_{16}$  (red).

From F. Pawula, S. Hébert, D. Pelloquin, A. Maignan, J. Mater. Chem. C 7 (1) (2019) 86.

hollandite, as classically expected. The values are positive except at low  $T$ , where a sign change is observed below 300K for  $\text{Sr}_{1.5}\text{Ru}_{6.1}\text{Cr}_{1.9}\text{O}_{16}$  and below 150K for  $\text{Ba}_{1.5}\text{Ru}_{6.1}\text{Cr}_{1.9}\text{O}_{16}$ . The same sign change was observed, but at much higher  $T$  in the  $\text{KRu}_4\text{O}_8$  hollandite. For these hollandites, it is thus clear that the transport term plays a role on the thermopower, in a large temperature range, up to  $\sim 600\text{K}$ ; but above

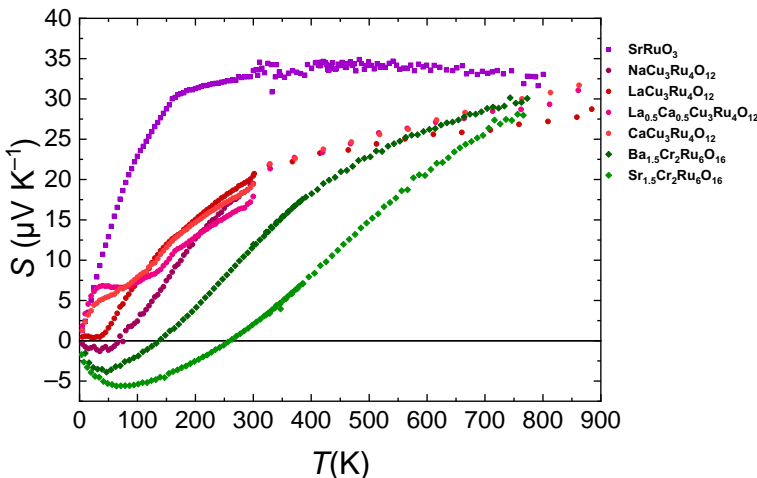


**Fig. 1.1.6**  $T$ -dependent Seebeck coefficient of all presented oxoruthenates.

600 K, the values are very close for the three different hollandites. This means that even in the presence of 25% of Cr on the RuO<sub>6</sub> octahedra site, the Ru entropy plays a major role on the Seebeck coefficient.

**Fig. 1.1.6** summarizes all the data presented here. Different families of ruthenium oxides with completely different electronic and magnetic properties have been investigated, from Pauli magnetism, to cluster-glass disordered state, and to ferromagnetism, together with a metallic behavior or a more localized one in the case of hollandites. For all these ruthenates, the high temperature value of the Seebeck coefficient remains almost unchanged. In these ruthenates, depending on the transport term, and thus on the bandwidth, the entropic term can be observed even from 200 K for SrRuO<sub>3</sub> to above 600–700 K for hollandites or quadruple perovskites. This figure clearly shows the peculiarity of these oxides with Ru<sup>4+</sup>, and the ability of these oxides with Ru<sup>4+</sup> to generate an “atomic-like” description of its Seebeck coefficient, with moreover a dominant role of the spin entropy.

## 1.1.4 Conclusion

The discovery of a large Seebeck coefficient in Na<sub>x</sub>CoO<sub>2</sub> has generated a great deal of enthusiasm for thermoelectric oxides, due to the ability of oxides (at least some of them) to work in oxidizing conditions, and up to high temperatures. The best n-type oxides are electron-doped perovskites, bixbyites, or ZnO wurtzite, while the best p-type oxides are still Na<sub>x</sub>CoO<sub>2</sub> and related misfit cobalt oxides. The CoO<sub>2</sub> layered family is thus a unique family where the large ZT values come from a combination of fascinating physics (electronic correlations being at the origin of Seebeck enhancement), together with a crystallographic structure prone to reducing phonon

propagation. A combination of spin-orbit coupling and electronic correlations also favors entropy-dominated thermoelectric properties as observed in different families of ruthenium oxides, the entropy being dominated by its spin contribution. Even if the band structure and thus transport and magnetic properties are very different at low  $T$ , the high temperature properties are dominated by the spin entropy in these ruthenates.

In oxides, the strong interplay between carriers, spins, and lattice is known to induce very interesting properties such as colossal magnetoresistance, multiferroïsm, or large magnetocaloric effect. Recently, the spin Seebeck effect has been investigated in insulating oxides such as yttrium iron garnet  $\text{Y}_3\text{Fe}_5\text{O}_{12}$  (YIG), where a voltage can be generated in platinum electrodes by an inverse spin Hall effect when a thermal gradient is applied on the YIG [43]. As shown in this review, the spin is actually a very interesting parameter on the thermopower by itself, as at high temperatures, it will set the spin entropy term, while at low  $T$ , magnetism can induce a strong magnetic field dependence of the thermopower as exemplified in misfits, where the alignment of paramagnetic spins strongly reduces the magnetic entropy and thus the Seebeck coefficient.

Still the ZT of these p-type oxides is limited by the too small carrier mobility. The sulfides have thus been extensively investigated by many international groups due to their larger carrier mobility compared to the one of oxides, and large power factors and ZT are indeed achieved in these materials [44–46]. Recently, a large magnetothermopower has also been evidenced in sulfides, in the thiospinel  $\text{CuCrTiS}_4$  [47] with variable range hopping transport mechanism, and large magnetothermopower effects are therefore not restricted to oxides. Thus, spin and magnetic interactions should also be considered for the optimization of thermoelectric properties of sulfides.

## References

- [1] I. Terasaki, Y. Sasago, K. Uchinokura, Phys. Rev. B 56 (1997) R12685.
- [2] S. Hébert, D. Berthebaud, R. Daou, Y. Bréard, D. Pelloquin, E. Guilmeau, F. Gascoin, O. Lebedev, A. Maignan, J. Phys. Condens. Matter 28 (2016) 013001.
- [3] J.-P. Doumerc, J. Solid State Chem. 110 (1994) 419.
- [4] W. Koshiba, K. Tsutsui, S. Maekawa, Phys. Rev. B 62 (2000) 6869.
- [5] M.R. Peterson, B.S. Shastry, J.O. Haerter, Phys. Rev. B 76 (2007) 165118.
- [6] M.R. Peterson, B.S. Shastry, Phys. Rev. B 82 (2010) 195105.
- [7] D.J. Singh, Phys. Rev. B 61 (2000) 13397.
- [8] C.A. Marianetti, G. Kotliar, Phys. Rev. Lett. 98 (2007) 176405.
- [9] M. Ohtaki, T. Tsubota, K. Eguchi, H. Arai, J. Appl. Phys. 79 (1996) 1816.
- [10] M. Ohtaki, H. Koga, T. Tokunaga, K. Eguchi, H. Arai, J. Solid State Chem. 120 (1995) 105.
- [11] H. Muta, K. Kurosaki, S. Yamanaka, J. Alloys Compd. 350 (1) (2003) 292.
- [12] D. Bérardan, E. Guilmeau, A. Maignan, B. Raveau, Solid State Commun. 146 (1) (2008) 97.
- [13] M. Ohtaki, K. Araki, K. Yamoto, J. Electron. Mater. 38 (7) (2009) 1234.
- [14] G.J. Snyder, E.S. Toberer, Nat. Mater. 7 (2008) 105.
- [15] S. Hébert, A. Maignan, in: D.W. Bruce, D. O'Hare, R.I. Walton (Eds.), *Functional Oxides*, John Wiley & Sons Ltd, 2010.

- [16] J. Hejtmanek, Z. Jirak, M. Marysko, C. Martin, A. Maignan, M. Hervieu, B. Raveau, *Phys. Rev. B* 60 (1999) 14057.
- [17] L. Bocher, M.H. Aguirre, D. Logvinovich, A. Shkabko, R. Robert, M. Truttman, A. Weidenkaff, *Inorg. Chem.* 47 (2008) 8077.
- [18] Y. Lin, C. Norman, D. Srivastava, F. Azough, L. Wang, M. Robbins, K. Simpson, R. Freer, I.A. Kinloch, *Appl. Mater. Interfaces* 7 (29) (2015) 15898.
- [19] K. Kuroki, A.R. Ryotaro, *J. Phys. Soc. Jpn.* 76 (2007) 083707.
- [20] S. Kremer, R. Frésard, *Ann. Phys.* 524 (2012) 21.
- [21] P.M. Chaikin, G. Beni, *Phys. Rev. B* 13 (1976) 647.
- [22] T.T.M. Palstra, A.P. Ramirez, S.-W. Cheong, B.R. Zegarski, P. Schiffer, J. Zaanen, *Phys. Rev. B* 56 (1997) 5104.
- [23] S. Pal, S. Hébert, C. Yaicle, C. Martin, A. Maignan, *Eur. Phys. J. B.* 53 (2006) 5.
- [24] A. Maignan, V. Caigaert, B. Raveau, D. Khomskii, G. Sawatzky, *Phys. Rev. Lett.* 93 (2004) 026401.
- [25] A.A. Taskin, A.N. Lavrov, Y. Ando, *Phys. Rev. B* 73 (2006) 121101.
- [26] M. Uchida, K. Oishi, M. Matsuo, W. Koshiba, Y. Onose, M. Mori, J. Fujioka, S. Miyasaka, S. Maekawa, Y. Tokura, *Phys. Rev. B* 83 (2011) 165127.
- [27] R. Daou, R. Frésard, V. Eyert, S. Hébert, A. Maignan, *Sci. Technol. Adv. Mater.* 18 (2017) 919.
- [28] M. Pollet, J.-P. Doumerc, E. Guilmeau, D. Grebille, J.-F. Fagnard, R. Cloots, *J. Appl. Phys.* 101 (2007) 083108.
- [29] H.-J. Lin, Y.Y. Chin, Z. Hu, G.J. Shu, F.C. Chou, H. Ohta, K. Yoshimura, S. Hébert, A. Maignan, A. Tanaka, L.H. Tjeng, C.T. Chen, *Phys. Rev. B* 81 (2010) 115138.
- [30] S. Landron, M.-B. Lepetit, *Phys. Rev. B* 77 (2008) 125106.
- [31] A. Maignan, S. Hébert, M. Hervieu, C. Michel, D. Pelloquin, D. Khomskii, *J. Phys. Condens. Matter* 15 (2003) 2711.
- [32] P. Limelette, S. Hébert, V. Hardy, R. Frésard, C. Simon, A. Maignan, *Phys. Rev. Lett.* 97 (2006) 046601.
- [33] L. de' Medici, J. Mravlje, A. Georges, *Phys. Rev. Lett.* 107 (2011) 256401.
- [34] Y. Klein, S. Hébert, A. Maignan, S. Kolesnik, T. Maxwell, B. Dabrowski, *Phys. Rev. B* 73 (2006) 052412.
- [35] J. Mravlje, A. Georges, *Phys. Rev. Lett.* 117 (2016) 036401.
- [36] W. Kobayashi, I. Terasaki, J. Takeya, I. Tsukada, Y. Ando, *J. Phys. Soc. Jpn.* 73 (9) (2004) 2373.
- [37] S. Hébert, R. Daou, A. Maignan, *Phys. Rev. B* 91 (2015) 045106.
- [38] S. Tanaka, N. Shimazui, H. Takatsu, S. Tonezawa, Y. Maeno, *J. Phys. Soc. Jpn.* 78 (2009) 024706.
- [39] S. Tanaka, H. Takatsu, Y. Maeno, *Phys. Rev. B* 80 (2009) 035113.
- [40] W. Kobayashi, *Phys. Rev. B* 79 (2009) 155116.
- [41] M.C. Cadée, G.C. Verschoor, *Acta Crystallogr. B* 34 (1978) 3554.
- [42] F. Pawula, S. Hébert, D. Pelloquin, A. Maignan, *J. Mater. Chem. C* 7 (1) (2019) 86.
- [43] K. Uchida, H. Adachi, T. Ota, H. Nakayama, A. Maekawa, E. Saitoh, *Appl. Phys. Lett.* 97 (2010) 172505.
- [44] E.J. Skoug, J.D. Cain, D.T. Morelli, *Appl. Phys. Lett.* 98 (2011) 261911.
- [45] C. Bourgès, Y. Bouyrie, A.R. Supka, R. Al Rahal Al Orabi, P. Lemoine, O.I. Lebedev, M. Ohta, K. Suekuni, V. Nassif, V. Hardy, R. Daou, Y. Miyazaki, M. Fornari, E. Guilmeau, *J. Am. Chem. Soc.* 140 (2018) 2186.
- [46] Y. Shi, C. Sturm, H. Kleinke, *J. Solid State Chem.* 270 (2019) 273.
- [47] D. Berthebaud, O.I. Lebedev, A. Maignan, S. Hébert, *J. Appl. Phys.* 124 (2018) 063905.

# Electron correlation

1.2

Ichiro Terasaki

Department of Physics, Nagoya University, Nagoya, Japan

## 1.2.1 Introduction

Since an electron is a negatively-charged elementary particle, it interacts with other electrons through the Coulomb repulsion. As a result, the electrons move in such a correlated way that they should separate from each other as far away as possible. This behavior is often referred to as electron correlation, which has been known as a long-standing difficult many-body problem. Fortunately, the electron correlation can be neglected in most semiconductors and metals, in which the one-electron picture, i.e., the band theory, works well.

In some classes of materials, on the contrary, such as transition-metal oxides, rare-earth intermetallic compounds, and charge-transfer organic salts, small transfer energies or narrow bands cannot screen the Coulomb repulsion among the conduction electrons. Such electron systems are called “strongly correlated electrons,” which have been a fertile source for magnetic materials [1]. A most fascinating feature in those systems is that there are plenty of chances to exceed theoretical limits based on band calculations.

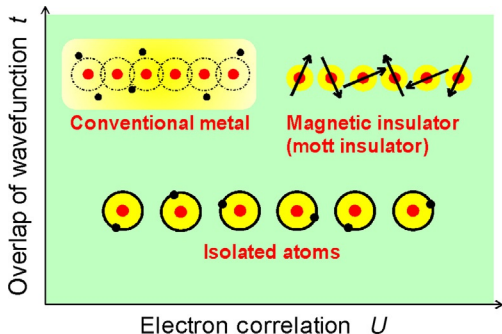
In this section, the author will give an overview on the physics of strongly correlated electrons, and discuss why and how the correlation effects improve the thermoelectric performance. The electron correlation has been a playground for magnetic and charge ordered phenomena, because it generates large excess entropy. Here, we see that the large entropy can lead to large thermopower in the absence of ordering phenomena, and can thereby enhance the thermoelectric performance. As typical examples, the thermoelectric properties of the layered cobalt oxides and heavy-fermion compounds will be presented.

## 1.2.2 Hubbard model and Mott insulator

Fig. 1.2.1 shows a schematic diagram of various electronic states in the transfer energy  $t$  and the electron-electron repulsion  $U$  on the same sites. At the bottom of this diagram, an array of isolated hydrogen atoms is displayed, in which electronic states are exactly solved and labeled for each atom as 1s, 2s, 2p, 3s, 3p, 3d, etc. In this array, each electron is tightly bound in the corresponding atom, and never meets other electrons in the different atoms so that the electron-electron repulsion does not work.

Next, we imaginatively apply pressure to put the atoms in the array closer to each other, until the wave function of an electron overlaps with the neighboring one. In such a situation, the electrons acquire a finite probability to hop from one atom to another

**Fig. 1.2.1** Schematic representation of various electronic states with overlap of wave function  $t$  and electron correlation  $U$ . The bottom picture represents a set of isolated atoms where  $t=0$ . The top left figure represents a conventional metal where electrons are itinerant ( $t \neq 0$ ,  $U=0$ ), while the top right figure represents a magnetic insulator ( $|t| \ll U$ ).



and gain kinetic energy by delocalizing in the whole array. This is what we expect in a conventional metal, in which the conduction electrons are spread in the whole system as the Bloch wave. However, in this state, an inconvenient event may happen: two electrons can exist at the same place at the same time, so that the Coulomb repulsion energy can diverge infinitely.

If the degree of the Coulomb repulsion on the same atom can be parameterized as  $U$ , we expect that all the electrons cannot hop to the neighboring atom in the large limit of  $U$  as in the case of the isolated atom array. But in this case, the spin degree of freedom survives and tends to order antiferromagnetically. This state, what we call the Mott insulator, emphasizes the particle nature of the electron, and acts as a magnetic insulator. The Hubbard model mimics the abovementioned behavior in the quantum field theory in solids. Here we will skip the concrete expression for the Hubbard Hamiltonian [2], but just note that it has explored many nontrivial ground states in terms of the two physical parameters  $t$  and  $U$  together with carrier concentration per atom. A nontrivial problem is what happens if  $t \sim U$ , where unexpected properties emerge from many-body effects of interacting electrons.

### 1.2.3 Thermopower enhanced by electron correlation

Let us recall the physical meaning of thermopower. Just for the sake of simplicity, we consider a one-dimensional system. According to the Boltzmann equation, the electric current density  $j$  and the thermal current density  $j_q$  can be written as a linear combination of electric field  $E$  and temperature gradient  $dT/dx$  given by.

$$j = \sigma E + \sigma S (-dT/dx) \quad (1)$$

$$j_q = \sigma TSE + \kappa (-dT/dx) \quad (2)$$

where  $\sigma$ ,  $S$ , and  $\kappa$  are the electrical conductivity, thermopower, and thermal conductivity, respectively. In the absence of a temperature gradient, only electrons can carry

heat, which is known as the Peltier effect. Putting  $dT/dx=0$  into Eqs. (1) and (2), we get the Peltier effect as

$$j_q/T = Sj \quad (3)$$

Eq. (3) is important in the sense that the entropy current density  $j_q/T$  is proportional to the electrical current density  $j$ . If the two scattering times included in  $j$  and  $j_q$  are identical, the proportional constant  $S$  has the meaning of entropy per charge. If the Gibbs-Duhem equation is employed, the entropy per carrier is associated with the temperature derivative of chemical potential:  $qS = -d\mu/dT$ . This is proved to be valid even in the presence of a strong correlation, being known as the Kelvin formula [3]. In order to find large  $S$  in solids, therefore, we have to find a large entropy carried by conduction electrons.

In relation to this, it is important that the Mott insulators hold a large, excess entropy at high temperatures. In a conventional metal, all the electrons degenerate to form the Fermi surface at the Fermi energy  $E_F$ , where the entropy is dominated by a small number of electrons in a thin skin of  $k_B T$  near  $E_F$ . Thus, the entropy per electron is reduced by a factor of  $k_B T/E_F$  and decreases with decreasing temperature. On the other hand, the spin degree of freedom of up and down exists in each atom in a Mott insulator (see the right top of Fig. 1.2.1), and there remains macroscopically large entropy of the order of  $k_B \ln 2$  per atom. Even if they have antiferromagnetic interaction with each other, a significant amount of entropy survives above the magnetic transition. We should further note that the magnetic interaction between spins does not always mean a magnetically ordered state. In spin liquid materials, no long-range order is realized at the lowest temperatures achievable, which is due to geometrical frustration [4]. A most interesting and important issue is what happens in metallic states near the Mott insulating state. We expect that the magnetism and/or localized magnetic moments intrinsically affect the transport properties from which novel electronic states emerge with peculiar physical properties. Typical examples are high-temperature superconducting copper oxides and colossally large magnetoresistive manganese oxides.

Fig. 1.2.2 schematically shows the electronic states between weak and strong correlations. For the sake of simplicity, we consider a simple solid consisting of a single

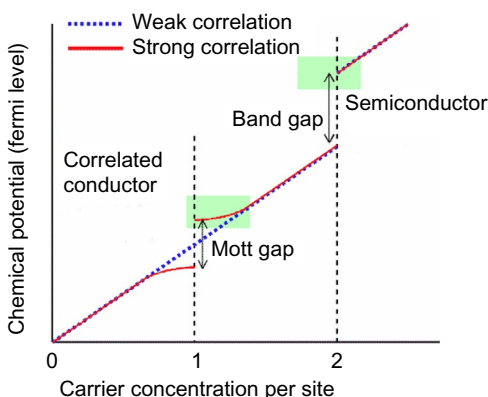


**Fig. 1.2.2** Schematic representation of the chemical potential plotted as a function of carrier concentration per site. The dotted line is a simplified curve for an uncorrelated (weakly correlated) electron system, while the solid curve corresponds to a strongly correlated electron system. We assume that the electronic states adiabatically transit from weakly correlated to strongly correlated ones.

atom with a single orbit. We further neglect the singularity at the Brillouin zone edges. As is seen, the chemical potential (equivalent to  $E_F$  in the weak correlation case) monotonically increases with carrier concentration per atom ( $n$ ). As  $n$  increases from zero, the chemical potential continuously increases, passing through  $n=1$ . By slowly increasing the degree of electron correlation  $U$ , the electrons in the system begin to feel the Coulomb repulsion from other electrons. Above a certain value of  $U_c$ , the system eventually has a gap in the chemical potential at  $n=1$ . Note that the  $n=1$  state is identical to that discussed in Fig. 1.2.1, in which the double occupancy at the same site is inevitable when an electron moves from one to another. The  $n=1$  state is thus special in the sense that the electron correlation affects most dramatically, and is referred to as “half-filled.” When  $n$  approaches 2, another gap opens, because all the orbitals are occupied. This is indeed a conventional bandgap in semiconductors and insulators.

If  $U$  increases from zero slowly enough, all the electronic states concomitantly (adiabatically) change with one to one correspondence. Since the electronic states near  $n=1$  change from gapless to gapped, the corresponding electronic states are degenerate near the gap edge as shown in Fig. 1.2.2. In addition, the electronic states near  $n=0$  (and 2) unlikely change with  $U$ , because electrons (holes) are unlikely to meet other electrons (holes) in such low concentrations. Consequently, the chemical potential of the Mott insulator is schematically drawn as a function of  $n$  as shown in Fig. 1.2.2 irrespective of the detailed structure of a material.

Accordingly, if a material is near the Mott gap ( $n \sim 1$ ), many of the electronic states are degenerate, which comes from the large entropy of  $k_B \ln 2$  previously discussed. Thus, the doped Mott insulator can carry a large degenerate state, with electric charge, the thermopower of which is expected to be enhanced by the spin degrees of freedom.

## 1.2.4 Layered cobalt oxides and heavy-fermion compounds

Layered cobalt oxides have been known as good thermoelectric oxides that show reasonably high values of dimensionless figure of merit at high temperatures. The crystal structure of  $\text{Na}_x\text{CoO}_2$  is schematically drawn in Fig. 1.2.3. This cobalt oxide includes a  $\text{CdI}_2$ -type  $\text{CoO}_2$  layer, in which a Co ion is surrounded with six octahedrally coordinated O ions, and the Co-O octahedral share the edges to form a two-dimensional hexagonal lattice. The author and his coworkers found good thermoelectric properties in  $\text{Na}_x\text{CoO}_2$ , [5] and have pursued a possibility of oxide thermoelectrics [6]. In this compound, the highly disordered Na layer and the  $\text{CoO}_2$  layer alternately stack along the c-axis. While the Na layer is responsible for low lattice thermal conductivity, the  $\text{CoO}_2$  layer gives rise to a high power factor through the strong correlation described below. Other layered cobalt oxides have been synthesized and identified after the discovery of the thermoelectric properties in  $\text{Na}_x\text{CoO}_2$ , and have been found to consist of the  $\text{CoO}_2$  layer and  $\text{NaCl}$ -type block layer. Since the regular  $\text{NaCl}$  layer shows a four-fold symmetry, it induces a lattice misfit at the interface of the hexagonal  $\text{CoO}_2$  layer. This lattice misfit effectively works to lower lattice thermal conductivity [7].

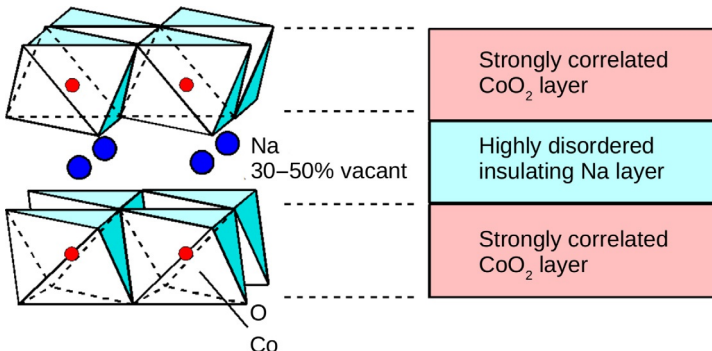


**Fig. 1.2.3** Crystal structure of  $\text{Na}_x\text{CoO}_2$  (left) and schematic representation of the corresponding functional layer structure (right).

Koshibae et al. [8] have pointed out that the entropy per charge can be large in the limit of ionic model in which all the valence electrons are localized in the cobalt ions owing to the strong correlation. In this picture, the conducting  $\text{CoO}_2$  layer is regarded as a mixture of  $\text{Co}^{3+}$  and  $\text{Co}^{4+}$  ions, and the electric conduction occurs by moving one hole in the  $\text{Co}^{4+}$  ion to a neighboring  $\text{Co}^{3+}$  ion. This hopping process is as if the  $\text{Co}^{4+}$  and  $\text{Co}^{3+}$  ions exchanged their positions. From the magnetic measurement, we know that the  $\text{Co}^{3+}$  and  $\text{Co}^{4+}$  ions are in the low spin state. Here the  $\text{Co}^{3+}$  ion with the  $e_g^0 t_{2g}^6$  configuration holds zero entropy, while the  $\text{Co}^{4+}$  ion with  $e_g^0 t_{2g}^5$  holds a large entropy of  $k_B \ln 6$ . Thus, the entropy per charge will be around  $k_B \ln 6/e \sim 150 \mu\text{V/K}$ , which almost equals the thermopower of  $\text{Na}_x\text{CoO}_2$  at high temperatures.

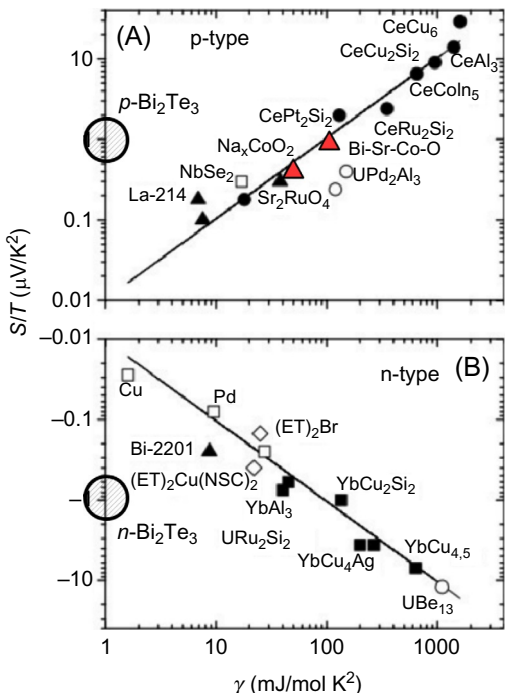
On the other hand, Kuroki and Arita [9] have proposed that the large thermopower in  $\text{Na}_x\text{CoO}_2$  comes from its peculiar band structures. According to their theory, when the valence band top is flat in a substantial range in the Brillouin zone, the electron–hole symmetry is seriously broken near  $E_F$  to let the thermopower enhance. Note that the electronic states near the Fermi level is quite symmetric between electrons and holes in conventional metals, and thus the contributions to the thermopower are canceled out. Although they did not assume a strong correlation directly, they have explained the magnetism and superconductivity in  $\text{Na}_x\text{CoO}_2$  and the related compounds using the same theoretical model with spin fluctuation. In fact, the layered cobalt oxides show metallic conduction and  $T$ -linear specific heat at low temperatures, which are a hallmark of itinerant electrons.

Heavy-fermion intermetallic compounds belong to another class of strongly correlated electron systems [10]. They consist of more than two kinds of different metallic elements, one of which is responsible for localized moments of 4f or 5f electrons, such as Ce, Yb, and U. The other elements supply conduction electrons, which interact the f electrons via the Kondo effect to screen the localized moments. As a result, at sufficiently low temperature (below the Kondo temperature), the localized f electrons become itinerant to travel coherently with the conduction electrons. This can be regarded as the coherent state between the conduction electrons and the spin fluctuation of the f electrons, where the conduction electrons travel as slowly as the spin

fluctuation does. From the aspect of specific heat, the entropy of f electrons originating from the spin fluctuation merges into the whole entropy of the conduction electrons. Such slowly moving conduction electrons with largely enhanced specific heat can be identified to electrons with a heavy effective mass enhanced by the f electrons, hence the name “heavy fermion.”

According to the Kelvin formula, the thermopower can be compared with the entropy of the electron or the electronic specific heat. Of course, thermopower should be evaluated as the entropy per carrier, but if we restrict ourselves to discussion of metals, we can associate the thermopower with the electronic specific heat coefficient. Behnia et al. [11] have clearly shown the validity of this relationship in various metals as shown in Fig. 1.2.4. In this figure, the temperature slope of the thermopower at low temperatures ( $S/T$ ) is plotted against the electronic specific heat coefficient ( $\gamma$ ) for various metals. In the left side, weakly correlated metals such as Cu are plotted. In going from the left to right, the effective mass increases systematically, and  $S/T$  roughly scales with  $\gamma$ . In the rightest side, typical heavy-fermion compounds CeCu<sub>6</sub> and UBe<sub>13</sub> are located, and they have a 1000 times enhanced effective mass and a 1000 times enhanced  $S/T$ . From this figure one can conclude that the electron correlation is beneficial to enhance the thermopower to improve the thermoelectric figure of merit. However, this relationship is only valid in metals. In semiconductors, the carrier concentration is much smaller and simultaneously the specific heat is much smaller, while the entropy per charge is larger owing to the smaller Fermi energy.

**Fig. 1.2.4** The temperature slope of the thermopower ( $S/T$ ) for various metals plotted as a function of electronic specific heat coefficient ( $\gamma$ ): (A) p-type materials and (B) n-type materials. The data for the layered cobalt oxides are highlighted, and the data for conventional thermoelectric material Bi<sub>2</sub>Te<sub>3</sub> are added. The original figure is taken from Behnia et al.



The data for the thermoelectric semiconductor  $\text{Bi}_2\text{Te}_3$  are also plotted, which lie seriously away from the linear relationship of  $S/T$  to  $\gamma$ .

An interesting point is that the data of the layered cobalt oxides are also of the same tendency, as shown in Fig. 1.2.4A. This indicates that the enhanced thermopower of the layered cobalt oxides can be compared with those of the heavy-fermion compounds, although there is no distinction between conduction electrons and localized moment in these oxides. The layered cobalt oxides initially hold a macroscopically large entropy in the  $\text{Co}^{4+}$  ion, but no phase transition takes place down to 4 K, perhaps owing to the two-dimensional electronic states. As is well known, a purely two-dimensional system cannot show thermodynamic phase transition, and many layered materials do not show magnetic/electric phase transitions. We think that the layered cobalt oxides are also such materials, and the entropy of the  $\text{Co}^{4+}$  ions cannot be released by phase transitions, and are attached with conduction electrons to form a heavy-fermion-like state. In this case, the microscopic origin to enhance the effective mass completely differs from the Kondo interaction in the case of heavy-fermion compounds, but thermodynamic quantities look similar.

## 1.2.5 Concluding remarks

We have briefly reviewed the thermopower of strongly correlated materials, which is substantially enhanced by the electron-electron interaction or equivalently magnetism. In conventional thermoelectrics, the thermopower is predominantly determined by the carrier concentration and the number of the valleys of conduction/valence bands. Thus once the material is fixed, there is no other room for improvement in enhancing the thermopower other than tuning of carrier concentration. In strongly correlated materials, however, the magnetism can be used as yet another control parameter. Since it couples with the external magnetic field, the thermopower can be tuned by the magnetic field and other external parameters [12], through which a new type of thermoelectric device can be designed.

## References

- [1] For example, see E. Morosan, D. Natelson, A.H. Nevidomskyy, Q. Si, *Adv. Mater.* 24 (2012) 4896, <https://doi.org/10.1002/adma.201202018>.
- [2] H. Terasaki, *J. Phys. Condens. Matter* 10 (1998) 4353, <https://doi.org/10.1088/0953-8984/10/20/004>.
- [3] M.R. Peterson, B.S. Shastry, *Phys. Rev. B* 82 (2010) 195105, <https://doi.org/10.1103/PhysRevB.82.195105>.
- [4] L. Balents, *Nature* 464 (2010) 199, <https://doi.org/10.1038/nature08917>.
- [5] I. Terasaki, Y. Sasago, K. Uchinokura, *Phys. Rev. B* 56 (1997) 12685(R), <https://doi.org/10.1103/PhysRevB.56.R12685>.
- [6] I. Terasaki, *J. Appl. Phys.* 110 (2011), <https://doi.org/10.1063/1.3626459>.
- [7] K. Koumoto, I. Terasaki, R. Funahashi, *MRS Bull.* 31 (2006) 206, <https://doi.org/10.1557/mrs2006.46>.

- [8] W. Koshibae, K. Tsutsui, S. Maekawa, Phys. Rev. B 62 (2000) 6869, <https://doi.org/10.1103/PhysRevB.62.6869>.
- [9] K. Kuroki, R. Arita, J. Phys. Soc. Jpn. 76 (2007) 083707, <https://doi.org/10.1143/jpsj.76.083707>.
- [10] G.R. Stewart, Rev. Mod. Phys. 56 (1984) 755, <https://doi.org/10.1103/RevModPhys.56.755>.
- [11] K. Behnia, D. Jaccard, J. Flouquet, J. Phys. Condens. Matter 16 (2004) 5187, <https://doi.org/10.1088/0953-8984/16/28/037>.
- [12] H. Takahashi, S. Ishiwata, R. Okazaki, Y. Yasui, I. Terasaki, Phys. Rev. B 98 (2018) 024405, <https://doi.org/10.1103/PhysRevB.98.024405>.

# Thermal transport by phonons in thermoelectrics

1.3

*Yuxuan Liao, Harsh Chandra, and Junichiro Shiomi*

Department of Mechanical Engineering, The University of Tokyo, Tokyo, Japan

## 1.3.1 Introduction

### 1.3.1.1 Importance of phonon transport to thermoelectrics

Thermoelectric materials are capable of directly converting heat into electricity by the Seebeck effect. They are applicable to a wide range of industrial applications, such as energy harvesting to power sensors for Internet of Things (IoT), waste heat utilization in automobiles or industrial furnaces, solar thermal power generation, charging of mobile devices in remote areas, and cogeneration such as topping power generation [1–4]. The benefits of using thermoelectric devices include long service life, silent operation, and environment-friendliness [5, 6]. The performance of the material is gauged by the dimensionless figure of merit,  $ZT = (S^2\sigma/(\kappa_e + \kappa_{ph}))T$ , where  $S$ ,  $\sigma$ ,  $\kappa_e$ ,  $\kappa_{ph}$ , and  $T$  are the Seebeck coefficient, electrical conductivity, electron and lattice thermal conductivity, and absolute temperature, respectively. Apparently, a good thermoelectric material simultaneously demands a large power factor ( $S^2\sigma$ ) and low electron and lattice thermal conductivity ( $\kappa_e + \kappa_{ph}$ ), which is dominated by the transport of electrons and phonons (lattice vibrations), respectively. For semiconductor thermoelectrics, one of the most effective ways to enhance their performance ( $ZT$ ) is to use appropriate nanostructures, which are smaller than the phonon mean free path (MFP) but much larger than the electron MFP, to significantly reduce lattice thermal conductivity without dramatically sacrificing electrical properties ( $S^2\sigma$ ). Due to the importance of phonon transport in semiconductor nanostructures for the enhancement of  $ZT$  of thermoelectric materials, the basic concepts, numerical and experimental method in terms of phonon transport, and several examples related to phonon engineering with nanostructures are introduced, aiming at achieving the ultimate scalable thermoelectric materials. Thereafter, thermal conductivity is referred to as lattice thermal conductivity, accordingly in this chapter.

### 1.3.1.2 Thermal conductivity and phonons

Thermal conductivity ( $\kappa$ ) is the physical property that characterizes the ability of a material to transport heat, and it is defined by the temperature gradient in the materials and the relevant heat flux that flows through it, as expressed by Fourier's law [7–10]:

$$Q = -\kappa\nabla T \quad (1.3.1)$$

where  $Q$  is the heat flux and  $T$  is the temperature.

From a microscopic point of view, lattice  $\kappa$  of crystal semiconductor materials is governed by atomistic elastic waves, which can be quantized as quasiparticles, and thus referred to as phonons. The character of phonons can be specified by their vibration frequencies  $\omega$  and wave vectors  $\mathbf{q}$  defined by their wavelength  $\lambda$  as

$$\mathbf{q} = \frac{2\pi}{\lambda} \mathbf{q}_0 \quad (1.3.2)$$

where  $\mathbf{q}_0$  is defined as the unit vector of  $\mathbf{q}$  and specifies the direction of the wave vectors.

The most familiar case of phonons is sound waves (or sound phonons) that propagate at the sound velocity  $v_s$  with the relation being

$$\omega = v_s |\mathbf{q}| \quad (1.3.3)$$

The relationship between  $\omega$  and  $\mathbf{q}$  is referred to as the dispersion relation of phonons. The dispersion relation of the sound phonons is linear, with the slope corresponding to the sound velocity. However, as the wavelength of phonons becomes shorter, the dispersion relation starts to deviate from that of the sound, the slope of the dispersion relation curve becomes

$$\mathbf{v}_g = \frac{\partial \omega}{\partial \mathbf{q}} \quad (1.3.4)$$

where  $\mathbf{v}_g$  is the group velocity. The group velocity tends to the sound velocity when  $\mathbf{q} \rightarrow \mathbf{0}$ .

One of the simplest examples to illustrate the properties of phonons is the one-dimensional (1D) atom chain with a fixed force constant between the atoms (**Fig. 1.3.1A**). When  $M=m$ , the periodicity (or the lattice constant) of the system is  $a$ , and the dispersion relation has one acoustic branch, with the maximum group

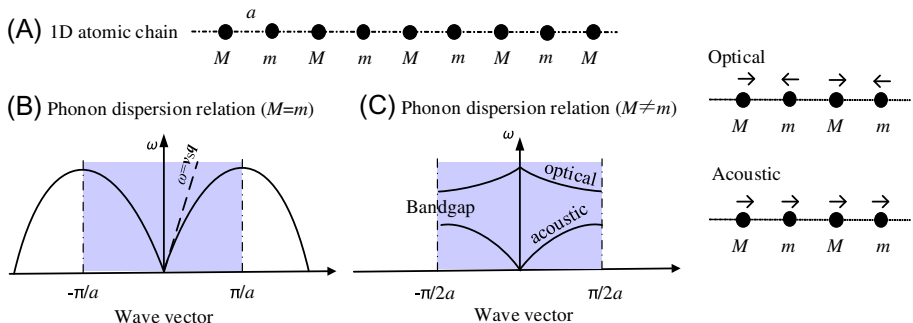


**Fig. 1.3.1** Dispersion relations of 1D atom chain: (A) Atoms with the lattice constant of  $a$  and periodic mass of  $m$  and  $M$ , (B) dispersion relations for  $M=m$ , (C) dispersion relations for  $M \neq m$ .

velocity being the sound velocity (Fig. 1.3.1B). Since solid materials are constructed by atoms, they are complete discrete sets; thus, the wavelength of phonon  $\lambda$  should be an integer ( $N$ ) multiple of  $2a$ , i.e.,  $2Na$ . Therefore, the allowed  $q$  is given by the equation

$$q = \frac{\pi}{Na} \quad (1.3.5)$$

Eq. (1.3.5) defines the  $q$ -space for phonons. The shortest wavelength is  $2a$ , which gives  $q$  within  $(-\pi/a, \pi/a)$  referred to as the first Brillouin zone (BZ), as shown by the purple regime in Fig. 1.3.1B. BZs are periodically placed in the system. When  $M \neq m$ , the periodicity of the system is  $2a$ . Phonon dispersions are folded with bandgaps (Fig. 1.3.1C). For a given  $q$  point, there are acoustic and optical branches. The atom displacement of acoustic phonons is in-phase, that is one atom moving to the right, and its neighbor atom to the right, while the atom displacement of optical phonons is out of phase, that is one atom moving to the left (right), and its neighbor atom to the right (left) (Fig. 1.3.1C). These concepts in the 1D atomic chain can be extended into 3D materials in a similar way [11].

### 1.3.1.3 The phonon Boltzmann transport equation

In view of quantum mechanics, phonons with mode  $(\mathbf{q}, \omega)$  can be approximated as quasiparticles with quantized energy  $E_{\mathbf{q}, \omega}$ :

$$E_{\mathbf{q}, \omega} = n_{\mathbf{q}, \omega} \hbar \omega_{\mathbf{q}, \omega} \quad (1.3.6)$$

where  $\hbar$  is Planck's constant divided by  $2\pi$  and  $n_{\mathbf{q}, \omega}$  is the number of phonons for mode  $(\mathbf{q}, \omega)$  that follow the Bose-Einstein distribution.

The quantized energy  $E_{\mathbf{q}, \omega}$  that is carried by these phonons is transported at the velocity of phonon group velocity; thus, the heat current  $S_{\mathbf{q}, \omega}$  can be defined as

$$S_{\mathbf{q}, \omega} = n_{\mathbf{q}, \omega} \hbar \omega_{\mathbf{q}} v_g \quad (1.3.7)$$

Transport of phonons in the material obeys the law of conservation of energy as

$$\frac{\partial E_{\mathbf{q}, \omega}}{\partial t} + \nabla \cdot S_{\mathbf{q}, \omega} = \left( \frac{\partial E_{\mathbf{q}, \omega}}{\partial t} \right)_{coll} \quad (1.3.8)$$

The term on the right-hand side of Eq. (1.3.8) is the source or collision term, in which phonons are produced or destroyed during the collision process. Using Eqs. (1.3.6), (1.3.7), the law of conservation of energy of particle phonons, Eq. (1.3.8), can be further rewritten as the phonon Boltzmann transport equation as

$$\frac{\partial n_{\mathbf{q}, \omega}}{\partial t} + v_g(\mathbf{q}, \omega) \nabla \cdot n_{\mathbf{q}, \omega} = \left( \frac{\partial n_{\mathbf{q}, \omega}}{\partial t} \right)_{coll} \quad (1.3.9)$$

With linear approximations of the collision term, Eq. (1.3.9) can be simplified as

$$\frac{\partial n_{\mathbf{q},\omega}}{\partial t} + v_g(\mathbf{q}, \omega) \nabla \cdot n_{\mathbf{q},\omega} = \frac{n_{\mathbf{q},\omega} - n_0}{\tau_{\mathbf{q},\omega}} \quad (1.3.10)$$

where  $n_0$  is the phonon population distribution in local thermal equilibrium condition and  $n_{\mathbf{q},\omega}$  is a perturbation from  $n_0$  due to the phonon scattering process. The phonon relaxation time  $\tau_{\mathbf{q},\omega}$  specifies the time for phonons with the population distribution of  $n_{\mathbf{q},\omega}$  returning to that of  $n_0$ .

In steady state, Eq. (1.3.10) can be written in terms of net heat current  $S_{\text{net}}$  and heat capacity  $c_{\mathbf{q},\omega}$  as

$$S_{\text{net}} = \hbar \omega_q v_g(\mathbf{q}, \omega) (n_{\mathbf{q},\omega} - n_0) = c_{\mathbf{q},\omega} v_g^2 \tau_{\mathbf{q},\omega} \nabla \cdot T \quad (1.3.11)$$

Comparing with Eq. (1.3.1), we have  $\kappa$  for phonon mode  $(\mathbf{q}, \omega)$  as

$$\kappa_{\mathbf{q},\omega} = \frac{1}{3} c_{\mathbf{q},\omega} v_g^2 \tau_{\mathbf{q},\omega} \quad (1.3.12)$$

The total  $\kappa$  then can be expressed as the summation of all phonon modes as

$$\kappa = \frac{1}{3} \sum_{\mathbf{q},\omega} c_{\mathbf{q},\omega} v_g^2 \tau_{\mathbf{q},\omega} = \frac{1}{3} \sum_{\mathbf{q},\omega} c_{\mathbf{q},\omega} v_g \Lambda_{\mathbf{q},\omega} \quad (1.3.13)$$

where  $\Lambda$  is the MFP of phonons. The term 1/3 comes from the average of group velocity in three axis directions. Eq. (1.3.13) corresponds to as the phonon kinetic gas model. It has been demonstrated that the phonon kinetic gas model can be applied to various kinds of crystal materials.

#### 1.3.1.4 Scattering mechanisms of phonons

Phonon relaxation time and MFP can be limited by various kinds of scattering processes. Typical examples are intrinsic scatterings such as three-phonon scattering, Akhiezer damping, etc., and extrinsic scatterings such as surface and interface scatterings, etc. Assuming that the scattering process is independent of each other, the total relaxation time  $\tau_T(\mathbf{q}, \omega)$  of phonon mode  $(\mathbf{q}, \omega)$  can be expressed using Matthiessen's rule:

$$\tau_T^{-1}(\mathbf{q}, \omega) = \sum_i \tau_i^{-1}(\mathbf{q}, \omega) \quad (1.3.14)$$

where  $\tau_i(\mathbf{q}, \omega)$  is the relaxation time of phonons due to the  $i$ th scattering mechanism.  $\tau_i^{-1}(\mathbf{q}, \omega)$  is inverse relaxation time, which characterizes the phonon scattering rate.

In what follows, we give an introduction to the typical kinds of scatterings in nano-structured materials.

**Three-phonon scattering:** Because of anharmonic interaction that comes from the cubic interatomic force constant, a phonon has the probability to scatter into two new phonons, or to be scattered by another phonon to produce a new phonon (i.e., the three-phonon scattering process). During the scattering process, energy and momentum of phonons are conserved:

$$\begin{cases} \hbar\omega + \hbar\omega_1 = \hbar\omega_2 \\ \mathbf{q} + \mathbf{q}_1 = \mathbf{q}_2 \\ \mathbf{q} + \mathbf{q}_1 = \mathbf{q}_2 + \mathbf{G} \end{cases} \quad (1.3.15)$$

here,  $\mathbf{G}$  is the reciprocal lattice vectors. The three-phonon scattering rate is proportional to the number of pairs of phonons that satisfy Eq. (1.3.15). The three-phonon scattering process can be classified as the normal (N-) and (U-) Umklapp processes corresponding to the second and third equations in Eq. (1.3.15), respectively. Since  $\mathbf{G}$  in the U-process is almost opposite to the directions of  $\mathbf{q}$  and  $\mathbf{q}_1$ , which effectively change the directions of heat current, the U-process is regarded as the main cause of thermal resistance in bulk crystal semiconductor materials.

**Four-phonon scattering:** The physical origin of four-phonon scattering comes from the fourth order of interatomic force constants. The four-phonon scattering process also satisfies the energy and momentum conservation equation similar to Eq. (1.3.15). Since the interatomic force constant in terms of four-phonon scattering is much smaller than that of three-phonon scattering, it can be neglected for most of the materials. However, for materials with large bandgaps, the number of pairs of phonons that satisfy the energy and momentum conservation in three-phonon scattering can be much smaller than that in the four-phonon scattering; therefore, the effect of four-phonon scattering cannot be neglected despite the small interatomic force constant.

**Akhiezer damping:** Three-phonon scattering dominates the intrinsic phonon scattering process for above-THz phonons. However, for sound phonons with sub-THz frequencies at high temperatures, the relaxation process is governed by the Akhiezer mechanism, which is referred to as the coupling of the strain of sound waves and thermal phonons [12]. Since the original work of Akhiezer, the mechanism of Akhiezer was found to be important for the absorption of sound waves, as well as for energy dissipation in mechanical nanoresonators. Recently, the work of Liao et al. has shown that Akhiezer damping plays an important role in coherent heat conduction for low-dimensional materials [13].

**Surface scattering:** Surface scattering of phonons can be specular, diffusive, or partial specular and diffusive, which can be characterized by the specularity parameter  $p$  ranging from 0 to 1. The value of  $p$  depends on the relation of the characteristic lengths of roughness and the wavelengths of phonons, as expressed by the Ziman formula [14]. When the characteristic length is comparable to the MFP of phonons that dominate  $\kappa$ , the scattering is diffusive ( $p=0$ ), relaxation time is limited by  $\tau^{-1}(\mathbf{q},\omega) = v_g(\mathbf{q},\omega)/L$ , where  $L$  is the geometry length of the structure in the system, and the corresponding  $\kappa$  is referred to as the Casimir limit. In specular scattering ( $p=1$ ), the phase of phonons is preserved, which is essential for coherent phonon transport.

**Interface scattering:** Interface scattering is characterized by the transmittance  $t$  ranging from 0 to 1, which specifies the transmission probability of a phonon transmitting the interface. The scattering on the surface of the interface can also be specular, diffusive, or partially specular and diffusive.

Other scattering mechanisms such as impurity scattering and electron-phonon scattering can be found in various textbooks [11, 14].

## 1.3.2 Advances in computational methods

### 1.3.2.1 Lattice dynamics

The motion of atoms in crystal materials can be approximated by a system of coupled harmonic oscillators, the vibration modes  $(\mathbf{q}, \omega)$  of which can be obtained by solving the equation of motions in Newton's form (harmonic lattice dynamics). Consider a system of coupled harmonic oscillators, in which atom  $b$  with mass  $m_b$  along the  $\alpha$  direction in the  $l$ -th unit cell with atom  $b'$  along the  $\beta$  direction in the  $l'$ -th unit cell is linked by the harmonic force constant  $\Phi_{lb,l'b'}^{\alpha,\beta}$ , which can be obtained either from derivations of first principles or empirical interatomic potentials. The equation of motion for mode  $(\mathbf{q}, \omega)$  in frequency space then can be written as

$$\begin{cases} \omega_{qs}^2 e_{qs} = \mathbf{D}_q \cdot e_{qs} \\ \mathbf{D}_q = \sum_{l'b'l'b'} \frac{1}{\sqrt{m_b m_{b'}}} \Phi_{lb,l'b'}^{\alpha,\beta} \exp[(i\mathbf{q} \cdot (r_{l'b'} - r_{lb})] \end{cases} \quad (1.3.16)$$

where  $e(\mathbf{q}, s)$  is the eigenvector and  $r_{lb}$  is the equilibrium position of atom  $b$  in the  $l$ -th unit cell.  $\mathbf{D}_q$  is the dynamic matrix, which can be diagonalized, and the eigenvalue of the diagonalized dynamic matrix corresponds to the square of the eigenfrequencies. The relation of  $\omega$  and  $\mathbf{q}$  solved from Eq. (1.3.16) is the rigorous dispersion relation for crystal materials.

Anharmonic properties such as the three-phonon scattering rate are related to the third-order interatomic potential. For materials like silicon, where the single-phonon relaxation approximation is valid, phonon relaxation time can be evaluated by Fermi's golden rules from the perturbation theory [11, 15, 16]:

$$\begin{aligned} \tau_{ph}^{-1}(k) &= \frac{2\pi}{N_k} \sum_{k_1 j_1, k_2 j_2} \frac{|V_3(kj, k_1 j_1, k_2 j_2)|^2}{\omega \omega_1 \omega_2} \\ &\times \left[ (n_1 - n_2) \delta(\omega + \omega_1 - \omega_2) + \frac{1}{2} (n_1 + n_2 + 1) \delta(\omega - \omega_1 - \omega_2) \right] \end{aligned} \quad (1.3.17)$$

where  $n$  and  $N_k$  are the Bose-Einstein distribution and the number of  $k$ -points, respectively.  $V_3$  is the anharmonic scattering magnitude. The delta functions in Eq. (1.3.17) ensure energy conservation.

### 1.3.2.2 Molecular dynamics

In contrast to lattice dynamics, which solves the equation of motion in wave vector and frequency space, molecular dynamics (MD) simulates the motions of  $N$  atoms in real coordinate and time space, as expressed by Hamilton's equation of motion:

$$\dot{\mathbf{x}}_i = \nabla_{\mathbf{p}_i} H, \dot{\mathbf{p}}_i = -\nabla_{x_i} H, i = 1, \dots, N \quad (1.3.18)$$

where  $\mathbf{x}_i$  and  $\mathbf{p}_i$  are the position and momentum of atom  $i$ , respectively. The over dots on  $x_i$  and  $p_i$  represents the differential over time.  $H$  is the Hamiltonian of the system, which reads

$$H(x_1, \dots, x_N, p_1, \dots, p_N) = \sum_{i=1}^N \frac{\mathbf{p}_i^2}{2m_i} + V(x_1, \dots, x_N) \quad (1.3.19)$$

where the first and second terms are the kinetic and interatomic potential energies, respectively.

Hamilton's equation of motion can be solved numerically by discretization with appropriate initial and boundary conditions. The solutions in real coordinate and time space obtained by MD can be transferred into frequency and wave vector space by using the Fourier transformation. Moreover, MD can provide time-dependent velocity and position of all particles in a thermodynamic system with the timescale varying from picoseconds to microseconds. The limitation is that MD usually not works well at low temperatures, where the thermal equilibrium takes a considerably long time.

### 1.3.2.3 Atomistic Green's function

When phonons encounter an interface at the grain boundaries, they have the probability to transmit at the interface, which is characterized by the transmittance parameter,  $\Xi$ . By definition,  $1 - \Xi$  gives the probability of phonons that is reflected by the interface. The transmittance is usually frequency dependent and can be approximated by the empirical model if the interface is thin enough and that the material on both side of the interface is the same, which is the case for most thermoelectrics [17–19]:

$$\Xi(\omega) = \frac{1}{\gamma\omega/\omega_{\max} + 1} \quad (1.3.20)$$

where  $\omega_{\max}$  is the maximum frequency of phonons in the material and  $\gamma$  is the fitting parameter.

The fitting parameter  $\gamma$  can be obtained by using Atomistic Green's function (AGF) method with empirical- or first-principles-based atomistic force constants. Nevertheless, the application of AGF is not limited in the special case expressed by Eq. (1.3.20), it can be applied to evaluate  $\Xi(\omega)$  for various kinds of interfaces. Phonon scattering

process at the interface naturally affects thermal transport, the relation of  $\Xi(\omega)$ , and the heat current for ballistic transport is expressed by the Landauer formula:

$$J = \frac{\Delta T}{2\pi} \int \hbar\omega \frac{df_B}{dT} \Xi(\omega) d\omega \quad (1.3.21)$$

where  $J$  is the heat current;  $f_B$  is the Bose-Einstein distribution;  $\Delta T$  is the temperature drop between the left (hot) and right side (cold) when phonons pass through the interface.

Thermal boundary conductance ( $TBC$ ) of phonons across the interface is given by  $J/(\Delta T A)$ :

$$TBC = \frac{1}{2\pi A} \int \hbar\omega \frac{df_B}{dT} \Xi(\omega) d\omega \quad (1.3.22)$$

where  $A$  is the cross-sectional area of the interface.

For a harmonic system, where thermal conductivity is dominated by elastic interface scatterings, the  $TBC$  gives the thermal conductivity as

$$\kappa = TBC \times L \quad (1.3.23)$$

where  $L$  is the length of the system.

### 1.3.2.4 Monte Carlo ray tracing for phonons

In analogy to the Monte Carlo ray-tracing method for photons, the Monte Carlo ray tracing (MCRT) for phonons is used to evaluate boundary and interface scatterings of phonons in terms of specularity  $p$  and transmittance parameter  $t$ . Numerically, when a phonon meets the boundary, the treatment of the specularity in MCRT is to generate a random number,  $p_0$  within (0,1) with the selected rule as:

- (1) if  $p_0 < p$ , the scattering of the boundary is specular, the reflected angle is equal to the incident angle.
- (2) if  $p_0 > p$ , the scattering of the boundary is diffusive, the reflected angle is randomly determined.

The numerical treatment of transmittance is similar when the phonon meets the interface. Detailed explanations of MCRT for phonons can be found in the works of Hori et al. [20].

## 1.3.3 Advances in experimental measurements

### 1.3.3.1 Inelastic neutron scattering for phonon dispersion and scattering rate

Phonon dispersion relations and scattering rate, or relaxation time can be directly measured by using thermal neutrons, which provide valuable information for phonon transport [21]. The first reason is that the wavelength of these uncharged thermal

neutrons is of the order of interatomic spacing of solid and liquid, and thus they can penetrate deeply into the material and interference in solids if the Bragg law is satisfied; the second reason is that the energy of thermal neutrons is on the same order of phonons, so when the neutron is scattered by phonons, the change in the energy is a large proportion of its initial energy; therefore, measurement of the energy change can provide accurate information of the energy of phonons [21].

The mechanism is that the energy and momentum of the phonons, incident and scattered thermal neutrons follows the energy and momentum conservation law, which is expressed as

$$E - E' - \hbar\omega_{ph} = 0 \quad (1.3.24)$$

$$\mathbf{k} - \mathbf{k}' - \mathbf{q} - \mathbf{G} = 0 \quad (1.3.25)$$

where  $E$  and  $E'$  are the energy of incident and scattered neutrons, respectively;  $\mathbf{k}$  and  $\mathbf{k}'$  are the corresponding wave vector of the incident and scattered neutrons, and  $\hbar\omega_{ph}$  and  $\hbar\mathbf{q}$  are the energy and momentum of phonons;  $\mathbf{G}$  is the reciprocal lattice vector.

The energy  $E$  and  $E'$ , and momentum  $\mathbf{k}$  and  $\mathbf{k}'$  for thermal neutrons are measurable parameters; therefore, Eqs. (1.3.24), (1.3.25) indicate that the energy or frequency of phonons can be obtained by the energy and momentum transfer of thermal neutrons:

$$E - E' = \hbar\omega_{ph} \quad (1.3.26)$$

$$\mathbf{k} - \mathbf{k}' = \mathbf{q} + \mathbf{G} \quad (1.3.27)$$

Eqs. (1.3.26), (1.3.27) are fundamental for phonon dispersion relation measurement in inelastic neutron scatterings experiment.  $\mathbf{q} = \mathbf{0}$  corresponds to elastic scattering. The scattering rate of phonons, which is the inverse of phonon relaxation time, can be obtained by the linewidth of the measured dispersion relations if it is larger than the instrumental resolution of neutron scattering equipment.

### 1.3.3.2 Time-domain thermal reflectance for thermal conductivity measurement

The technique for the measurement of thermal conductivity of bulk solid materials is well developed since the 19th century. However, when the length scale of the structures is reduced to the nanoscale, the measurement of thermal conductivity becomes extremely challenging. The time-domain thermoreflectance (TDTR) [22] technique is a recent well-established method for thermal conductivity measurements of nano-structured materials such as superlattice and phononic materials. Here, we take our TDTR setup as an example to illustrate the setups (Fig. 1.3.2).

The femtosecond pulsed-laser light beam generated by the Ti:Sapphire pulsed laser (power: 4 W; wavelength: 800 nm; repetition frequency: 80.21 MHz; pulse width 140 fs) first goes through an optical isolator to eliminate the fluctuation, then it was separated into a probe light (red curve in Fig. 1.3.2) and a pump light (blue curve in Fig. 1.3.2) when it passes through a polarized beam splitter (PBS), which is an

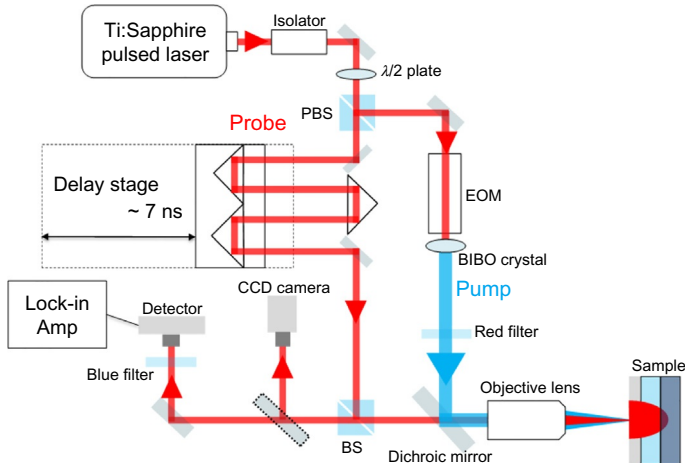


**Fig. 1.3.2** Schematic diagram of the time-domain thermal reflectance (TDTR) device for thermal conductivity measurements.

optical element that separates light according to the polarization. The pump light beam reaches and heats the surface of the sample after its wavelength is modulated from 800 to 400 nm by the nonlinear crystal Bismuth Triborate (BIBO) and the laser shape is corrected by the objective lens. The diameter of the pump light beam can be set by adjusting the position of this lens.

The probe light transmitted through PBS is expanded in diameter by four times by a beam expander, and then enters a delay stage, which was used to suppress the fluctuation of the probe light diameter due to the optical path length fluctuation. After that, the diameter of the light is reduced to 1/4 by a beam compressor. Then it was reflected by the BS and, finally, it also reaches the sample by passing through the objective lens.

The probe light that is reflected on the sample surface is detected as an electrical signal by a photon detector and processed by a lock-in amplifier. The lock-in amplifier is a narrow band-pass filter that extracts minute alternating current signals  $V_{in}$  and  $V_{out}$  of the order of  $\mu\text{V}$ . This makes it possible to detect minute signals due to thermoreflectance with a high SN ratio –  $V_{in}/V_{out}$ , from which the thermal conductivity can be obtained by the typical fitting process in TDTR.

### 1.3.3.3 **3 $\omega$ method for thermal conductivity measurement**

The 3 $\omega$  method based on the transient AC hot wire is an inexpensive and versatile robust tool for measuring thermophysical properties like thermal conductivity and heat capacity of thin films with thickness  $d_f$  (Fig. 1.3.3A) ranging from 0.01 to 1  $\mu\text{m}$ , which has been proved to be validated for a wide variety of materials such as a-SiO<sub>2</sub> [23, 24], suspended wire [25], superlattices [26], and nanotubes [27].

The idea of the AC method is that a radial heat flow with a frequency of  $\omega$  is driven by Joule heating of a narrow metal line (width:  $b$ , electric resistance:  $R_0$ ) patterned on the sample surface (Fig. 1.3.3A). The narrow metal line, usually made by metals like Pt,

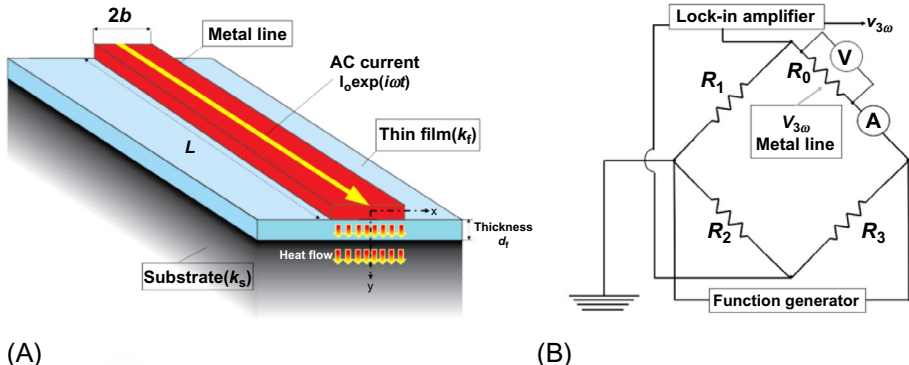


**Fig. 1.3.3** (A) Schematic diagram of the  $3\omega$  method used for thermal conductivity measurement and (B) the balanced bridge circuit.

serves both as heater and thermometer. Since the resistance of the heater is proportional to temperature, the resistance induced in the line gets modulated at  $2\omega$ . Finally, the current at  $\omega$  mixes with heater resistance at  $2\omega$  leading to a voltage signal at  $3\omega$ . Consequently, this voltage drop along the wire thus contains a third harmonic  $3\omega$  oscillations that can be used to measure temperature oscillations and therefore the thermal response of the dielectric film and substrate. Hence the name “ $3\omega$  method.” [20] The  $3\omega$  voltage component,  $V_{3\omega}$  is related to the temperature oscillation  $\Delta T$  as

$$\Delta T = \frac{2dTR_0}{dR} \frac{V_{3\omega}}{V} \quad (1.3.28)$$

where  $V$  is the applied voltage and  $dT/dR$  is the temperature dependence of  $R_0$ .

After subtracting the  $\omega$  voltage using a balanced bridge circuit (Fig. 1.3.3B),  $V_{3\omega}$  is determined by measuring the nonequilibrium voltage  $v_{3\omega}$  using a lock-in amplifier. The conversion from  $v_{3\omega}$  to  $V_{3\omega}$  is given by

$$V_{3\omega} = \frac{(R_0 + R_1) \cdot (R_2 + R_3)}{R_1 \cdot (R_2 + R_3)} v_{3\omega} \quad (1.3.29)$$

where  $R_i$  ( $i = 1, 2, 3$ ) is the resistance of the bridge circuit as shown in Fig. 1.3.3B.

To determine thermal conductivity, the  $3\omega$  voltage is measured as a function of heater frequency. The  $3\omega$  voltage can be decomposed into in-phase and out-of-phase components each as a function of heater frequency, and the slope of in-phase voltage can be used to estimate the accurate value of thermal conductivity. Using the  $3\omega$  voltage measured at two frequencies  $f_1$  and  $f_2$ , the thermal conductivity  $\kappa$  is calculated:

$$\kappa = \frac{V_{3\omega} \ln(f_2/f_1)}{4\pi l R_0^2 (V_{3\omega,1} - V_{3\omega,2})} \frac{dR_0}{dT} \quad (1.3.30)$$

where  $V_{3\omega,1}$  and  $V_{3\omega,2}$  are the in-phase  $3\omega$  voltage at frequency  $f_1$  and frequency  $f_2$ , respectively.

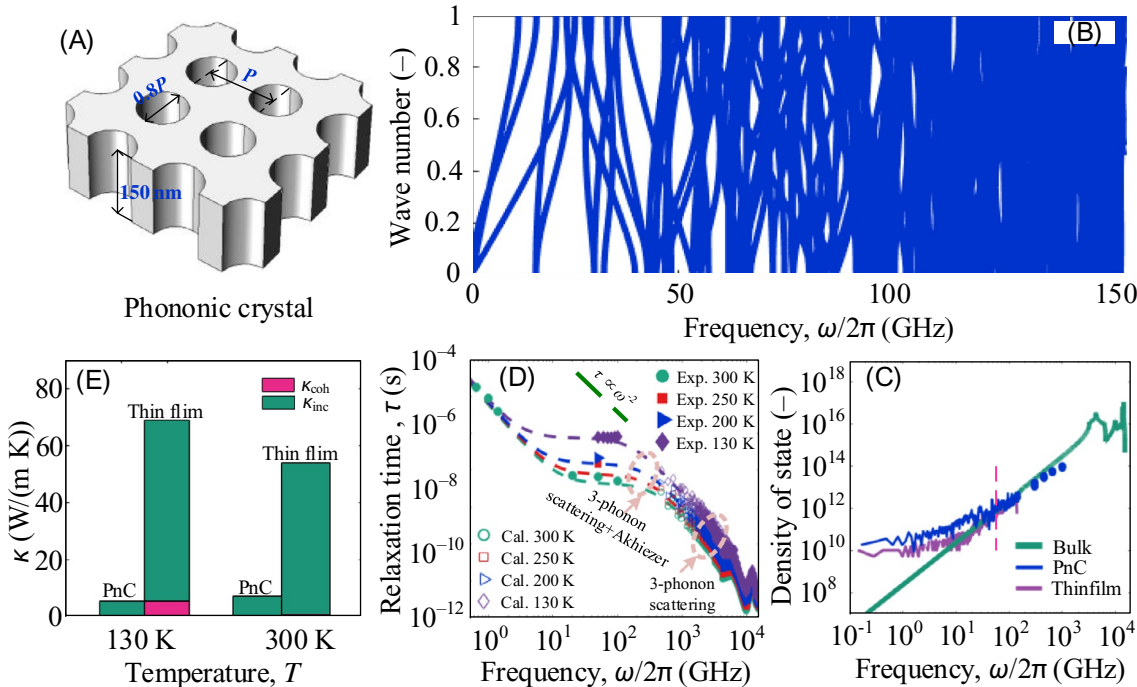


**Fig. 1.3.4** (A) Schematic representation of two-dimensional Si PnC with a periodicity ( $P$ ) of 100 nm. (B) Phonon dispersion relation of PnC along G-X. (C) Phonon density of states of thin films and PnC, and a comparison with that of bulk Si. (D) Phonon relaxation time of bulk Si from 130 to 300 K, and a comparison with experimental data for longitudinal acoustic (LA) modes, which are taken from Refs. [28–31] (E) Comparison of the contributions of  $\kappa$  from coherent ( $\kappa_{\text{coh}}$ ) and incoherent ( $\kappa_{\text{inc}}$ ) phonons in thin films and PnCs at 130 K and 300 K. The figures are obtained from the works of Y. Liao, T. Shiga, M. Kashiwagi, J. Shiomi, Akhiezer mechanism limits coherent heat conduction in phononic crystals, Phys. Rev. B 98 (13) (2018) 134307.

## 1.3.4 Engineering phonon transport by nanostructures

In the past decades, rapid development of nanotechnology has enabled to make the length scale of microstructures in nanodevices comparable to the mean free path and even the wavelength of phonons that dominate the thermal conductivity of the material at room temperature, which makes it possible to achieve significant thermal conductivity reduction to enhance  $ZT$  of semiconductor thermoelectrics through diffusive scattering or the coherent effect of phonons. In the following, we give examples to show how to use nanostructures to manipulate phonon transport in Si. We emphasize the importance of using the wave nature of phonons and its applications in the field of thermoelectrics, with the aim to explore the ultimate thermoelectrics. The bulk Si phonon properties in [Sections 1.3.4.1–1.3.4.3](#) were calculated by first-principles lattice dynamics; interface structure optimization and phonon transmittance in [Sections 1.3.4.2 and 1.3.4.3](#) were calculated by molecular dynamics and atomistic Green's function, respectively; boundary and interface scatterings of phonons in [Sections 1.3.4.1–1.3.4.3](#) were done by the Monte Carlo ray-tracing method. Thermal conductivity in [Sections 1.3.4.2 and 1.3.4.3](#) was measured by TDTR or  $3\omega$  method, respectively. Phonon dispersion relation measurements by inelastic neutron or X-ray scattering can be found in the works of Tubino et al. [32] and Uchiyama et al. [33].

### 1.3.4.1 Phonon coherent effect

When incident phonons propagate in specifically designed periodic structures, they can interfere with the phase-preserved reflected waves, which are created by specular scattering of phonons at each surface or interface, analogous to the interference effect of light in photonic crystals. Thus, such periodic structures are referred to as phononic crystals (PnCs), as shown by [Fig. 1.3.4A](#). The coherent effect makes phonons follow the dispersion relations of PnCs with folded branches and bandgaps ([Fig. 1.3.4B](#)), which results in reductions of group velocity, and hence reductions of thermal conductivity. Since a period of PnCs can exceed tens of nanometers, which is much larger than the mean free path of electrons, PnCs are able to significantly reduce thermal conductivity without largely sacrificing electrical properties, which hold the key importance for enhancing  $ZT$  of thermoelectric materials.,

However, the recent work of Liao et al. [7] has shown that the promising prospect of controlling phonons by using the coherent effect in PnCs can be extremely challenging to achieve above 130K [\[13\]](#). The work has shown that low-frequency coherent phonons in low-dimensional materials like PnCs have extremely large density of states due to their low-dimensional nature ([Fig. 1.3.4C](#)); therefore, the relaxation time of these phonons should be carefully treated. Otherwise, their contributions to thermal conductivity would be significantly overestimated when only considering three-phonon scattering. By comparing calculation with experimental data, it is shown that the relaxation process of these low-frequency phonons follows the Akhiezer mechanism rather than the three-phonon scattering within a temperature range of 130–300K, which significantly reduces the relaxation time of these coherent phonons (here, we

show the case for bulk Si in Fig. 1.3.4D as the example). Because of Akhiezer mechanism,  $\kappa_{coh}$  of thin films becomes intrinsically small when comparing with the incoherent counterpart  $\kappa_{inc}$  even when there is no roughness (Fig. 1.3.4E), which indicates that there is no space to manipulate  $\kappa_{coh}$  and thus  $\kappa$  of the PnC when we make periodic holes on the thin film. The work provides new insight into coherent phonon transport in PnCs.

### 1.3.4.2 Interface softening

Up to date, extremely high  $ZT$  values ( $>1$ ) have been achieved based on crystal compounds such as  $\text{Bi}_2\text{Te}_3$  [34],  $\text{PbTe}$  [35], and  $\text{SnSe}$  [36]. However, the actual application of these high- $ZT$  thermoelectric materials is still limited because of accompanying bottlenecks such as their high costs with heavy and toxic elements and challenges due to device integrations, which calls for the fabrication of thermoelectric materials based on standard semiconductors with a sufficient figure of merit ( $ZT$ ) at room temperature. Si is a nontoxic element with the highest abundance, high thermal stability and mechanical strength, and high  $S^2\sigma$ , and its compatibility with the existing and matured Si technology would reduce the process cost for module integration [37–41], and hence comes on the top of the list. Up to date, high room temperature  $ZT$  (0.4–0.6) of Si-based thermoelectric materials have only been reported for “holey” Si thin film [42] or a rough nanowire [41], the length scale of which being in nanometers extremely limits their applications in actual devices. Moreover, attempts of scaling up nanowire, for instance, to a nanowire network so far have failed because  $\sigma$  is reduced by several orders of magnitude to reach the above-mentioned levels of  $ZT$  even with the large Seebeck coefficient and low thermal conductivity [43]. Therefore, the next nontrivial and discontinuous step is to realize similar  $ZT$  with a scalable material.

Here, we introduce the works of Kashiwagi and Liao et al., which have realized nanostructured silicon materials with  $ZT$  larger than 0.3 at room temperature by a scalable process consisting of metal-assisted chemical etching and plasma-activated sintering [44]. The material structure is highly complex being composed of randomly distributed nanograins, nanopores, and metal nanoprecipitates with hierarchical sizes (Fig. 1.3.5A), which significantly reduces thermal conductivity to the level that is comparable to that of amorphous Si (1.86 W/mK) without appreciably sacrificing electrical conductivity (Fig. 1.3.5B). It is further identified by detailed experimental and theoretical investigations that the key contribution to the reduction comes from the softening of grain boundaries, which not only largely reduces the elastic modulus of the nanocomposite (Fig. 1.3.5C) but also significantly limits the phonon TBC to as low as  $40 \text{ MW m}^{-2} \text{ K}^{-1}$  such that the phonon MFP is extremely shorter than that of single-crystal Si (Fig. 1.3.5D). The developed high-performance silicon nanocomposite is expected to greatly enhance the application of thermoelectrics by lowering the material and process costs.

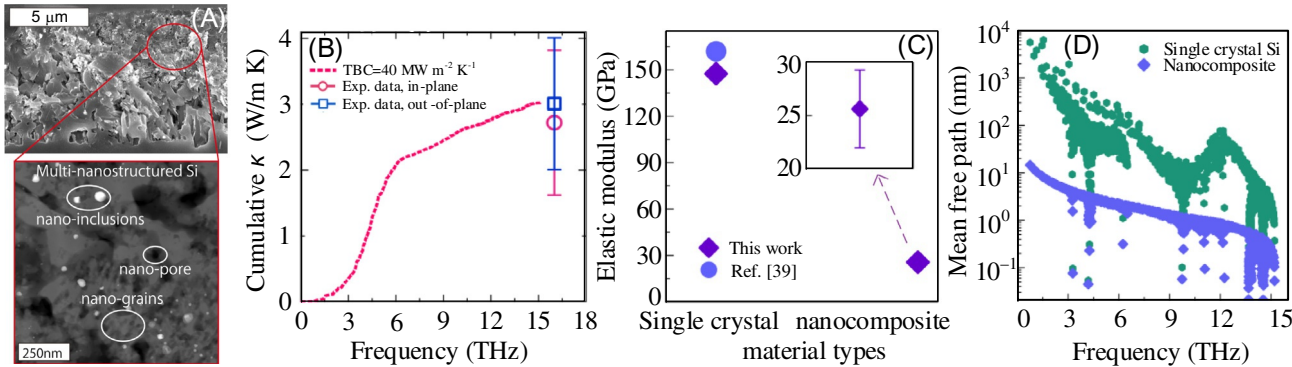


**Fig. 1.3.5** (A) Scanning electron microscope (SEM) images of nanostructures of the nanocomposite. (B) Measured in-plane and out-of-plane thermal conductivity of the nanocomposite at 300K. The *dashed red line* is the calculated cumulative thermal conductivity as a function frequency with a TBC of  $40 \text{ MW m}^{-2} \text{ K}^{-1}$ . (C) Measured elastic modulus of the nanocomposite and a comparison with that of single-crystal Si. The *blue circle dot* is experimental data taken from the works of Bellet et al. [45]. (D) Phonon mean free path of the nanocomposite and a comparison with that of single-crystal Si.

The figures are obtained from the works of M. Kashiwagi, Y. Liao, S. Ju, A. Miura, S. Konishi, T. Shiga, T. Kodama, J. Shiomi, Scalable multi-nanostructured silicon for room-temperature thermoelectrics, ACS Appl. Energy Mater. 2 (10) (2019) 7083–7091.

### 1.3.4.3 Phonon confinement

As discussed in [Section 1.3.4.2](#), the bottleneck for the application of Si-based thermoelectric materials at room temperature is to scale them up to bulk scale and to maintain the high  $ZT$  comparable to that of “holey” Si thin film [\[42\]](#) and a rough nanowire [\[41\]](#). Interface softening is one of the ways to achieve the goal, the other way to realize it is using phonon confinement in nanostructured materials, as indicated in the works of Oyake et al. [\[43\]](#). They found that the thermal conductivity of Si nanocrystalline (SiNC) with a grain size of 3–5 nm, which are separated by ultrathin  $\text{SiO}_2$  layers ( $\sim 0.3$  nm) ([Fig. 1.3.6A](#)), can even be largely below the amorphous limit in a wide temperature range from 50 to 300 K ([Fig. 1.3.6B](#)). To explain the ultralow thermal conductivity of the SiNC, the frequency-dependent phonon transmittance across an ultrathin  $\text{SiO}_2$  interface layer is calculated by AGF ([Fig. 1.3.6C](#)), which reproduced the measured data without any fitting parameters. The underlying mechanism is that the ultrathin  $\text{SiO}_2$  layers ( $\sim 0.3$  nm) existing at the interfaces of the grains significantly reduce phonon transmittance ([Fig. 1.3.6C](#)), which lead to extremely effective grain boundary scattering, resulting in significant strong classical confinement of phonon propagation such that the relaxation time is equivalent to or even below that of the minimum thermal conductivity scenario ([Fig. 1.3.6D](#)). This result demonstrates the controllability of thermal conductivity of dense crystal materials far beyond the Casimir and amorphous limits.

## 1.3.5 Summary and outlook

This chapter stresses the importance of phonon transport in nanostructured semiconductor thermoelectric materials. First, the chapter provides the basics in terms of the transport of phonons, including the concept of phonons, the phonon Boltzmann transport equation, and various kinds of scattering mechanisms, which are of crucial importance for the investigation of thermal transport in nanostructured materials. Then, the fundamentals of well-established numerical tools such as lattice dynamics, molecular dynamic, atomistic Green’s function, and Monte Carlo ray tracing, and experimental methods such as inelastic neutron scattering, time-domain thermal reflectance, and  $3\omega$  method are introduced. Experimental measurements usually provide macroscopic information such as temperature-dependent heat capacity, thermal conductivity, and thermal boundary conductance, while numerical methods are able to capture microscopic properties such as frequency-dependent thermal spectra, phonon mean free path, and transmission functions, which offer an understanding of the phonon transport mechanism. Recently, there is a trend to measure microscopic properties such as phonon mean free path, relaxation time in nanostructures via methods such as time-domain thermal reflectance and inelastic neutron and x-ray scatterings. We expect that such a trend would become more and more popular in the future of the phonon field despite that these measurements are quite challenging.

Finally, examples are given to illustrate the recent progress of manipulating thermal conductivity with nanostructures using the introduced numerical and

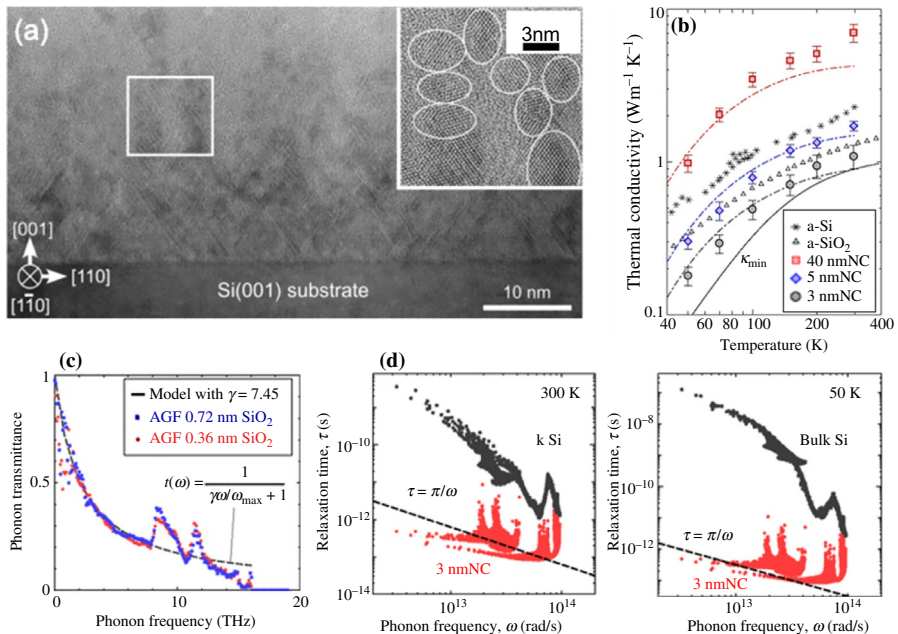


**Fig. 1.3.6** (A) Transmission electron microscopy (TEM) image of the SiNC. (B) Temperature-dependent thermal conductivity of SiNC structures compared with amorphous Si and SiO<sub>2</sub>. The black solid line represents the minimum thermal conductivity ( $\kappa_{\min}$ ) model. Dotted lines show  $\kappa$  calculated by phonon gas model with inputs from anharmonic lattice dynamics and AGF calculations. (C) Phonon transmittance of the SiO<sub>2</sub> layer; (D) summarizes relaxation times of bulk Si (black x marks) and SiNC with a grain size of 3 nm (red dots) at 300 and 50 K. The dashed line represents  $\kappa_{\min}$  ( $\tau = \pi/\omega$ ).

The figures are obtained from the works of T. Oyake, L. Feng, T. Shiga, M. Isogawa, Y. Nakamura, J. Shiomi, Ultimate confinement of phonon propagation in silicon nanocrystalline structure, Phys. Rev. Lett. 120 (4) (2018).

experimental methods, with the question of “What are the ultimate thermoelectric materials at room temperature?” We emphasize that the realization of scalable room temperature high ZT thermoelectrics with standard semiconductors may hold the key. The attractive approach of using phonon coherence is quite challenging at room temperature because of Akhiezer damping; however, mechanisms such as interface softening [44] and phonon confinement [17] in nanostructures can be the practical way of achieving the ultimate scalable thermoelectric materials.

## Acknowledgment

The authors acknowledge the members of Thermal Energy Engineering Lab and the collaborators who contributed to the studies reviewed in this paper, particularly Dr. Makoto Kashiwagi and Dr. Takafumi Oyake who are the first authors of some of the studies. The studies were partially supported by CREST “Scientific Innovation for Energy Harvesting Technology”

(Grant No. JPMJCR16Q5) and Grant-in-Aid for Scientific Research (B) (Grant No. JP16H04274) and Fellowship (Grant No. JP18J14024) from JSPS KAKENHI, Japan. This work was also supported by JSPS Fellowship (26-9110), a Grant-in-Aid for Scientific Research A (Grant No. 16H02078) and a Grant-in-Aid for Exploratory Research (Grant No. 15K13276).

## References

- [1] M. Hamid Elsheikh, D.A. Shnawah, M.F.M. Sabri, S.B.M. Said, M. Haji Hassan, M.B. Ali Bashir, M. Mohamad, A review on thermoelectric renewable energy: principle parameters that affect their performance, *Renew. Sust. Energ. Rev.* 30 (2014) 337–355.
- [2] D. Zhao, G. Tan, A review of thermoelectric cooling: materials, modeling and applications, *Appl. Therm. Eng.* 66 (1) (2014) 15–24.
- [3] S.B. Riffat, X. Ma, Thermoelectrics: a review of present and potential applications, *Appl. Therm. Eng.* 23 (8) (2003) 913–935.
- [4] B. Orr, A. Akbarzadeh, M. Mochizuki, R. Singh, A review of car waste heat recovery systems utilising thermoelectric generators and heat pipes, *Appl. Therm. Eng.* 101 (2016) 490–495.
- [5] L.E. Bell, Cooling, heating, generating power, and recovering waste heat with thermoelectric systems, *Science* 321 (5895) (2008) 1457–1461.
- [6] F.J. DiSalvo, Thermoelectric cooling and power generation, *Science* 285 (5428) (1999) 703–706.
- [7] T.L. Bergman, F.P. Incropera, D.P. DeWitt, A.S. Lavine, *Fundamentals of Heat and Mass Transfer*, John Wiley & Sons, 2011.
- [8] F. Incropera, D. DeWitt, *Introduction to Heat Transfer*, John Wiley and Sons Inc, 1985.
- [9] F.P. Incropera, A.S. Lavine, T.L. Bergman, D.P. DeWitt, *Fundamentals of Heat and Mass Transfer*, Wiley, 2007.
- [10] J.R. Howell, M.P. Menguc, R. Siegel, *Thermal Radiation Heat Transfer*, CRC Press, 2015.
- [11] G.P. Srivastava, *The Physics of Phonons*, CRC Press, 1990.
- [12] H.J. Maris, Ultrasonic attenuation in dirty dielectric crystals, *Phys. Rev.* 175 (3) (1968) 1077–1081.
- [13] Y. Liao, T. Shiga, M. Kashiwagi, J. Shiomi, Akhiezer mechanism limits coherent heat conduction in phononic crystals, *Phys. Rev. B* 98 (13) (2018) 134307.
- [14] J.M. Ziman, *Electrons and Phonons: The Theory of Transport Phenomena in Solids*, Oxford University Press, 2001.
- [15] A. Debernardi, S. Baroni, E. Molinari, Anharmonic phonon lifetimes in semiconductors from density-functional perturbation theory, *Phys. Rev. Lett.* 75 (9) (1995) 1819–1822.
- [16] T. Shiga, D. Aketo, L. Feng, J. Shiomi, Harmonic phonon theory for calculating thermal conductivity spectrum from first-principles dispersion relations, *Appl. Phys. Lett.* 108 (20) (2016) 201903.
- [17] T. Oyake, L. Feng, T. Shiga, M. Isogawa, Y. Nakamura, J. Shiomi, Ultimate confinement of phonon propagation in silicon nanocrystalline structure, *Phys. Rev. Lett.* 120 (4) (2018) 045901.
- [18] Z. Wang, J.E. Alaniz, W. Jang, J.E. Garay, C. Dames, Thermal conductivity of nanocrystalline silicon: importance of grain size and frequency-dependent mean free paths, *Nano Lett.* 11 (6) (2011) 2206–2213.
- [19] C. Hua, A.J. Minnich, Importance of frequency-dependent grain boundary scattering in nanocrystalline silicon and silicon–germanium thermoelectrics, *Semicond. Sci. Technol.* 29 (12) (2014) 124004.

- [20] T. Hori, J. Shiomi, C. Dames, Effective phonon mean free path in polycrystalline nanostructures, *Appl. Phys. Lett.* 106 (17) (2015) 5.
- [21] G.L. Squires, *Introduction to the Theory of Thermal Neutron Scattering*, Cambridge University Press, 2012.
- [22] D.G. Cahill, Analysis of heat flow in layered structures for time-domain thermoreflectance, *Review of Scientific Instruments* 75 (12) (2004) 5119–5122.
- [23] D.G. Cahill, Thermal conductivity measurement from 30 to 750 K: the  $3\omega$  method, *Review of Scientific Instruments* 61 (2) (1990) 802–808.
- [24] S.M. Lee, D.G. Cahill, Heat transport in thin dielectric films, *Journal of Applied Physics* 81 (6) (1997) 2590–2595.
- [25] L. Lu, W. Yi, D. Zhang,  $3\omega$  method for specific heat and thermal conductivity measurements, *Rev. Sci. Instrum.* 72 (7) (2001) 2996–3003.
- [26] B. Yang, W. Liu, J. Liu, K. Wang, G. Chen, Measurements of anisotropic thermoelectric properties in superlattices, *Appl. Phys. Lett.* 81 (19) (2002) 3588–3590.
- [27] T.Y. Choi, D. Poulikakos, J. Tharian, U. Sennhauser, Measurement of thermal conductivity of individual multiwalled carbon nanotubes by the  $3\omega$  method, *Appl. Phys. Lett.* 87 (1) (2005) 013108.
- [28] B.C. Daly, K. Kang, Y. Wang, D.G. Cahill, Picosecond ultrasonic measurements of attenuation of longitudinal acoustic phonons in silicon, *Phys. Rev. B* 80 (17) (2009) 174112.
- [29] J.Y. Duquesne, B. Perrin, Ultrasonic attenuation in a quasicrystal studied by picosecond acoustics as a function of temperature and frequency, *Phys. Rev. B* 68 (13) (2003) 134205.
- [30] H.Y. Hao, H.J. Maris, Dispersion of the long-wavelength phonons in Ge, Si, GaAs, quartz, and sapphire, *Phys. Rev. B* 63 (22) (2001) 224301.
- [31] M. Pomerantz, Temperature dependence of microwave phonon attenuation, *Phys. Rev.* 139 (2A) (1965). A501 –.
- [32] R. Tubino, L. Piseri, G. Zerbi, Lattice dynamics and spectroscopic properties by a valence force potential of diamondlike crystals: C, Si, Ge, and Sn, *J. Chem. Phys.* 56 (3) (1972) 1022–1039.
- [33] H. Uchiyama, Y. Oshima, R. Patterson, S. Iwamoto, J. Shiomi, K. Shimamura, Phonon lifetime observation in epitaxial ScN film with inelastic X-ray scattering spectroscopy, *Phys. Rev. Lett.* 120 (23) (2018) 235901.
- [34] B. Poudel, Q. Hao, Y. Ma, Y. Lan, A. Minnich, B. Yu, X. Yan, D. Wang, A. Muto, D. Vashaee, X. Chen, J. Liu, M.S. Dresselhaus, G. Chen, Z. Ren, High-thermoelectric performance of nanostructured bismuth antimony telluride bulk alloys, *Science* 320 (5876) (2008) 634–638.
- [35] K. Biswas, J. He, I.D. Blum, C.-I. Wu, T.P. Hogan, D.N. Seidman, V.P. Dravid, M.G. Kanatzidis, High-performance bulk thermoelectrics with all-scale hierarchical architectures, *Nature* 489 (2012) 414.
- [36] L.-D. Zhao, S.-H. Lo, Y. Zhang, H. Sun, G. Tan, C. Wolverton, V.P. Dravid, M.G. Kanatzidis, Ultralow thermal conductivity and high thermoelectric figure of merit in SnSe crystals, *Nature* 508 (2014) 373.
- [37] J. Shiomi, Research update: phonon engineering of nanocrystalline silicon thermoelectrics, *APL Mater.* 4 (10) (2016) 104504.
- [38] G. Schiering, Silicon nanostructures for thermoelectric devices: a review of the current state of the art, *Phys. Status Solidi (a)* 211 (6) (2014) 1235–1249.
- [39] G. Schiering, J. Stoetzel, R. Chavez, V. Kessler, J. Hall, R. Schmechel, T. Schneider, N. Petermann, H. Wiggers, S. Angst, D.E. Wolf, B. Stoib, A. Greppmair, M. Stutzmann, M.S. Brandt, Silicon-based nanocomposites for thermoelectric application, *Phys. Status Solidi (a)* 213 (3) (2016) 497–514.

- 
- [40] A.I. Boukai, Y. Bunimovich, J. Tahir-Kheli, J.-K. Yu, W.A. Goddard III, J.R. Heath, Silicon nanowires as efficient thermoelectric materials, *Nature* 451 (7175) (2008) 168–171.
  - [41] A.I. Hochbaum, R. Chen, R.D. Delgado, W. Liang, E.C. Garnett, M. Najarian, A. Majumdar, P. Yang, Enhanced thermoelectric performance of rough silicon nanowires, *Nature* 451 (7175) (2008) 163–U5.
  - [42] J. Tang, H.-T. Wang, D.H. Lee, M. Fardy, Z. Huo, T.P. Russell, P. Yang, Holey silicon as an efficient thermoelectric material, *Nano Lett.* 10 (10) (2010) 4279–4283.
  - [43] A.J. Lohn, E. Coleman, G.S. Tompa, N.P. Kobayashi, Assessment on thermoelectric power factor in silicon nanowire networks, *Phys. Status Solidi (a)* 209 (1) (2012) 171–175.
  - [44] M. Kashiwagi, Y. Liao, S. Ju, A. Miura, S. Konishi, T. Shiga, T. Kodama, J. Shiomi, Scalable multi-nanostructured silicon for room-temperature Thermoelectrics, *ACS Appl. Energy Mater.* 2 (10) (2019) 7083–7091.
  - [45] D. Bellet, P. Lamagnere, A. Vincent, Y. Brechet, Nanoindentation investigation of the Young's modulus of porous silicon, *J. Appl. Phys.* 80 (7) (1996) 3772–3776.

# Bismuth telluride

2.1

Yu Pan<sup>a,b</sup> and Jing-Feng Li<sup>a</sup>

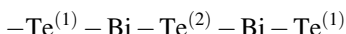
<sup>a</sup>State Key Laboratory of New Ceramics and Fine Processing, School of Materials Science and Engineering, Tsinghua University, Beijing, PR China, <sup>b</sup>Max Planck Institute for Chemical Physics of Solids, Dresden, Germany

## 2.1.1 Overview of bismuth telluride

$\text{Bi}_2\text{Te}_3$  and its alloys with  $\text{Sb}_2\text{Te}_3$  (for p-type) and  $\text{Bi}_2\text{Se}_3$  (for n-type) are the best thermoelectric materials with the highest figure of merit near room temperature. The excellent thermoelectric performance originates from both high power factor and relatively low lattice thermal conductivity. Since 1960,  $(\text{Bi},\text{Sb})_2\text{Te}_3$  and  $\text{Bi}_2(\text{Te},\text{Se})_3$  alloys have dominated the Peltier cooling applications and have been widely applied in temperature control of precise electronic devices [1]. In recent years, researchers have tried to apply  $(\text{Bi},\text{Sb})_2\text{Te}_3$  and  $\text{Bi}_2(\text{Te},\text{Se})_3$  alloys in power generation via waste heat recovery by shifting the maximum  $ZT$  values to elevated temperatures.

### 2.1.1.1 Crystal structure of $\text{Bi}_2\text{Te}_3$

$\text{Bi}_2\text{Te}_3$  crystallizes in the rhombohedra structure with a  $R\bar{3}m$  space group, which can also be recognized by a hexagonal cell ( $a=b=0.4385\text{ nm}$ ,  $c=3.0497\text{ nm}$ ) shown in Fig. 2.1.1. The hexagonal cell is formed by the stacking of layers perpendicular to the  $c$ -axis, as the following sequence:



where the superscripts refer to different Te sites due to two types of bonding. Te<sup>(2)</sup> and Bi layers are held together by strong ionic-covalent bonds, while the Te<sup>(1)</sup>-Te<sup>(1)</sup> is weak van der Waals bonding [2]. The lamellar structure along with the weak bonding of Te<sup>(1)</sup>-Te<sup>(1)</sup> between the quintuples leads to easy cleavage of  $\text{Bi}_2\text{Te}_3$  in the in-plane direction (perpendicular to the  $c$ -axis). In addition to the mechanical anisotropy, its thermoelectric transport properties also possess a strong anisotropy [3–6]. Generally, the in-plane direction has higher electrical conductivity and thermal conductivity than the cross-plane direction (parallel to the  $c$ -axis). The differences in a single crystal can be as large as  $\sim 4$  and  $\sim 2$  times for electrical and thermal conductivity, respectively [6]. This is the reason why higher performance is almost achieved in the in-plane direction.

### 2.1.1.2 Band structure of $\text{Bi}_2\text{Te}_3$

$\text{Bi}_2\text{Te}_3$  has a complex electronic band structure, which has been studied extensively as both thermoelectric and topological materials. With heavy elements, strong spin-orbit

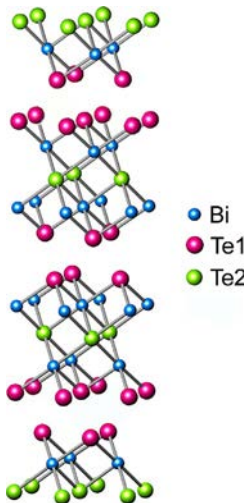


**Fig. 2.1.1** Crystal structure of  $\text{Bi}_2\text{Te}_3$ . The fundamental building block along  $c$ -axis is quintuple layers in the sequence of  $\text{Te}^{(1)}\text{-}\text{Bi}\text{-}\text{Te}^{(2)}\text{-}\text{Bi}\text{-}\text{Te}^{(1)}$ .

coupling exists in  $\text{Bi}_2\text{Te}_3$ , making the band extreme move off the high symmetry points in the Brillouin zone (Fig. 2.1.2A) [7]. This results in a small bandgap and high valley degeneracy. Optical absorption indicates the indirect gap of  $\text{Bi}_2\text{Te}_3$  is  $0.14\text{ eV}$ , which is quite narrow and it decreases with the temperature at a rate of  $0.95 \times 10^{-4}\text{ eV K}^{-1}$ . Through alloying with  $\text{Sb}_2\text{Te}_3$  or  $\text{Bi}_2\text{Se}_3$ , the bandgap increases and becomes almost unchanged after  $\text{Bi}_2\text{Se}_3$  reaches 33% (Fig. 2.1.2B) [8, 9].

Benefiting from the multi-valley nature and small effective mass,  $\text{Bi}_2\text{Te}_3$  shows exceptional electronic properties. Both the conduction and valence band extremes of  $\text{Bi}_2\text{Te}_3$  are sixfold degenerate [11, 12], as demonstrated by galvanomagnetic [13, 14] and de Haas-van Alphen measurements [15, 16]. The shapes of the Fermi surfaces are dependent on the carrier concentration and become much more complex with higher Fermi energy as other degenerate pocket appears for both conduction and valence band (Fig. 2.1.2C) [10]. This is also the case for  $\text{Sb}_2\text{Te}_3$ , while the Fermi surfaces of  $\text{Bi}_2\text{Se}_3$  are relatively simpler. From this point of view, tuning the Fermi level plays a significant role in enhancing the electrical transport properties.

### 2.1.1.3 Major physical parameters of $\text{Bi}_2\text{Te}_3$

Table 2.1.1 summarizes the major physical properties of  $\text{Bi}_2\text{Te}_3$ . Typical effective mass obtained from Pisarenko plot based on the effective mass model is  $\sim 1.0 m_e$  for  $\text{Bi}_{0.5}\text{Sb}_{1.5}\text{Te}_3$  [19] and  $0.8 m_e$  for  $\text{Bi}_{2.7}\text{Se}_{0.3}$  [20], respectively. Deviation in different publications could be due to the large errors of Hall measurements as well as the Seebeck coefficient. With a relatively low sound velocity and large Grüneisen parameter, the thermal conductivity of  $\text{Bi}_2\text{Te}_3$  is relatively low. Overall,  $\text{Bi}_2\text{Te}_3$  shows

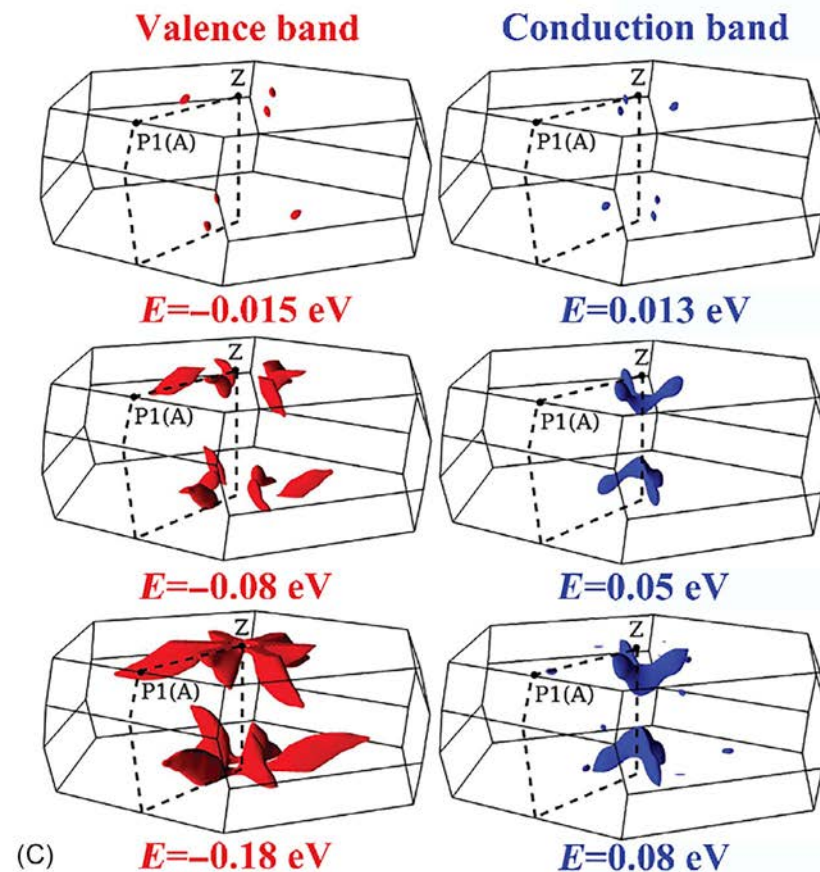
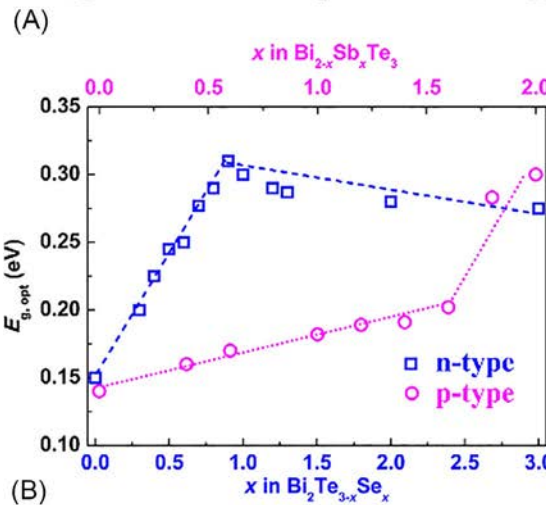
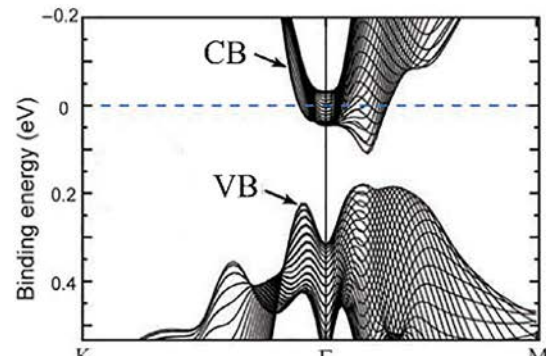


**Fig. 2.1.2** (A) Band structure of  $\text{Bi}_2\text{Te}_3$  [7], (B) optical bandgap of  $\text{Bi}_2\text{Te}_3$  alloyed with  $\text{Sb}_2\text{Te}_3$  and  $\text{Bi}_2\text{Se}_3$  [8, 9], and (C) Fermi surfaces grow with increasing Fermi energy and new pockets show up at higher Fermi energy [10].

Figures are modified from Y.L. Chen, J.G. Analytis, J.-H. Chu, Z.K. Liu, S.-K. Mo, X.L. Qi, H.J. Zhang, D.H. Lu, X. Dai, Z. Fang, S.C. Zhang, I.R. Fisher, Z. Hussain, Z.-X. Shen, Science 325 (2009) 178; R. Sew, L.R. Testardi, J. Phys. Chem. Solids 23 (1962) 1219; I.G. Austin, A. Sheard, J. Electron. Control 3 (1957) 236–237; I.T. Witting, T.C. Chasapis, F. Ricci, M. Peters, N.A. Heinz, G. Hautier, G.J. Snyder, Adv. Electron. Mater. 5 (2019) 1800904.

**Table 2.1.1** Major physical and thermoelectric properties of Bi<sub>2</sub>Te<sub>3</sub>.

Parameters	Values
Melting point	858 K [17]
Density	7.856 [18]
Bandgap at room temperature	0.14 eV [9]
Effective mass at 300K	1.0 m <sub>e</sub> (Bi <sub>0.5</sub> Sb <sub>1.5</sub> Te <sub>3</sub> ) [19] 0.8 m <sub>e</sub> (Bi <sub>2</sub> Te <sub>2.7</sub> Se <sub>0.3</sub> ) [20]
Sound velocity	2147 m/s ( <i>a</i> -axis), 2070 m/s ( <i>c</i> -axis) [21]
Grüneisen constant	1.5 (Bi <sub>2</sub> Te <sub>3</sub> ), 2.3(Sb <sub>2</sub> Te <sub>3</sub> ), 1.4(Bi <sub>2</sub> Se <sub>3</sub> ) [22]

metallic behavior and bipolar effect easily happens at elevated temperature due to the small bandgap.

## 2.1.2 Fine-grained Bi<sub>2</sub>Te<sub>3</sub> alloys

Conventional Bi<sub>2</sub>Te<sub>3</sub> materials are often fabricated by zone-melting and Bridgman methods, where the unidirectionally solidified ingot presents good thermoelectric performance with *ZT* values around 1 at room temperature [23, 24]. However, the mechanical strength is relatively poor due to easy cleavage and coarse grains. With the requirement of both good thermoelectric and mechanical properties, some researches have focused on the fine-grained polycrystalline Bi<sub>2</sub>Te<sub>3</sub>-based materials. Among the multiple powder metallurgy technologies, ball milling and mechanical alloying combined with subsequent spark plasma sintering or hot pressing, have been often used to synthesize fine-grained Bi<sub>2</sub>Te<sub>3</sub>-based alloys [25–27]. More and more attention had been paid to the application of advanced powder processing technologies after 2008 when Poudel et al. reported a peak *ZT* of 1.4 in nanocrystalline BiSbTe bulk in *Science* [28]. Since then, fine-grained thermoelectric materials have been intensively investigated for *ZT* enhancement via reducing thermal conductivity as well as for mechanical strength improvement.

In addition to the influence of thermal conductivity and mechanical strength, another special effect of grain refinement on Bi<sub>2</sub>Te<sub>3</sub> and its alloys should be noted: it changes the concentration of charged point defects, e.g., antisite defects and anion vacancies [29]. This is significant since they are closely related to the charge carrier concentration, which can strongly affect the thermoelectric transport properties.

In this section, the role of grain refinement will be discussed. As listed above, the effects of grain refinement mainly reflect on three parts: firstly, reducing thermal conductivity; secondly, changing point defects; and thirdly, improving the mechanical strength. The discussion in this part is a basis of the next section where different strategies for *ZT* enhancement in fine-grained bulks will be illustrated.

### 2.1.2.1 Decreased thermal conductivity by grain refinement

Until Poudel et al.'s work [28], the  $ZT$  values of traditional  $\text{Bi}_2\text{Te}_3$  and its alloys obtained from zone melting have remained around 1 for decades. The large enhancement of  $ZT$  originates from a significant reduction in thermal conductivity due to strong phonon scattering introduced by the nanostructures. As a simple, cost-effective, and time-efficient method, ball milling can produce (sub)micro- or even nanoscale powders. Through fast hot pressing the nanopowders obtained from ball milling, nano-grained bulk with great amounts of interfaces are produced. Compared to single or coarse grain structure, those interfaces play a significant role in impeding phonons' transport leading to a large reduction of thermal conductivity [30]. Furthermore, the bipolar effect is also suppressed in the nano-grained bulks compared to the zone melting-made ingots. Poudel et al. attributed the reason to the nanostructure-induced interfacial potential that scatters more minority carriers [28]. Such  $ZT$  enhancement by introducing nanostructures has also been achieved in many other materials as well [31–34].

Since then, not only nanocrystals but also other nanoscopic structures like 1-D point defects and 2-D dislocations have been widely employed to construct a hierarchical structure for the reduction of thermal conductivity [35–37]. This structure engineering has also promoted the development of other advanced powder processing technologies for thermoelectric materials. For one example, melt spinning is demonstrated to be effective in reducing the thermal conductivity and improving the  $ZT$  values of  $(\text{Bi},\text{Sb})_2\text{Te}_3$  alloys [38]. In addition to the powder processing technologies, subsequent hot pressing and spark plasma sintering should also be highlighted in the reduction of thermal conductivity. As a fast-sintering technique, spark plasma sintering can maintain the nanoscale of the powders. In recent years, more and more modified methods based on conventional powder processing technologies have been developed to construct unique micro- and nanostructures, for example, liquid phase sintering to form dense dislocations at the grain boundaries [39]. In general, many nanostructuring strategies have been demonstrated to be effective in decreasing the thermal conductivity and hence improve  $ZT$  values, especially in p-type  $(\text{Bi},\text{Sb})_2\text{Te}_3$  alloys.

### 2.1.2.2 Point defect chemistry in $\text{Bi}_2\text{Te}_3$ and its alloys

The studies of point defect chemistry in bismuth telluride can be dated back to 1950s by Satterthwaite and Ure [17], and Brebrick [40]. They have revealed a region of existence bounded by a solidus line at high temperatures. Intrinsic point defects are produced to the deviation of the melting point composition from the stoichiometric  $\text{Bi}_2\text{Te}_3$  [17]. As shown in Fig. 2.1.3, at the melting point, the composition is bismuth rich with the atomic ratio of 40.065%, whereas that of Te is less than 60% (while 59.935% instead) [17]. In this way, inherent defects are produced and they are electrically active which can influence the thermoelectric properties.

Due to the small difference of electronegativity and ionic radius between Bi and Te, excess Bi would induce antisite defects  $\text{Bi}_{\text{Te}}^{1-}$  [18, 41]. Since Bi has one less electron

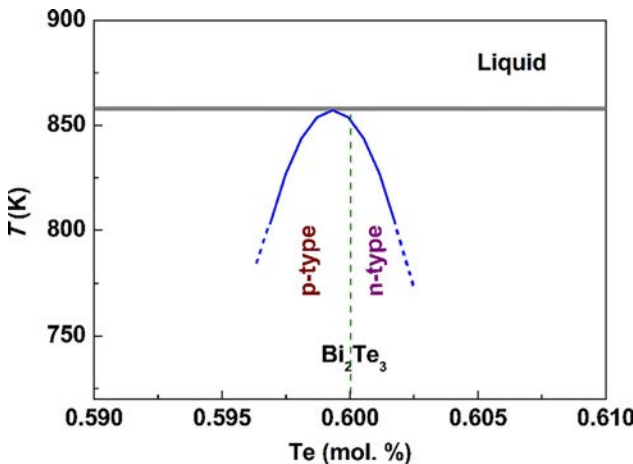


**Fig. 2.1.3** Phase diagram of Bi-Te system. It illustrates that the composition near the melting point is deviated from the stoichiometric  $\text{Bi}_2\text{Te}_3$ .

Figures are modified from C.B. Satterthwaite, R.W. Ure, Phys. Rev. 108 (1957) 1164–1170.

than Te, each negatively charged antisite defect  $\text{Bi}_{\text{Te}}^{1-}$  produces a hole in the valence band. This is why  $\text{Bi}_2\text{Te}_3$  is naturally p-type for the ingots made by slowly cooling methods. Only under Te-rich conditions, n-type behavior shows up because of the positively charged  $\text{Te}_{\text{Bi}}^{1+}$  antisite defects. For  $\text{Sb}_2\text{Te}_3$ , it is always of p-type because of the lower formation energy of the accepter antisite defect  $\text{Sb}_{\text{Te}}^{1-}$  [41]. However,  $\text{Bi}_2\text{Se}_3$  is different as the difference between Bi and Se is large and Se easily evaporates during fabrication.  $\text{Bi}_2\text{Se}_3$  shows n-type transport behavior, since the dominated Se vacancies can contribute two electrons.

The situation in fine-grained polycrystals is more complicated than the ingots. The defect concentrations can be greatly changed by both processing conditions and composition [42]. Two main effects change the point defect concentration in fine-grained polycrystals. One is donor-like effect introduced by strong mechanical deformation [43]. Another is the plenty of grain boundaries [44].

During the process to make fine-grained polycrystals, for instance, grinding, ball milling, mechanical alloying, hot-extrusion, etc. strong mechanical deformation is introduced, leading to a donor-like effect:

$$2V_{\text{Bi}}''' + 3V_{\text{Te}}^{\bullet\bullet} + \text{Bi}'_{\text{Te}} = V_{\text{Bi}}''' + \text{Bi}^{\times}_{\text{Bi}} + 4V_{\text{Te}}^{\bullet\bullet} + 6e'$$

It is clear that more electrons are produced by donor-like effect, making the fine-grained materials more n-type [43, 45–47]. This is why zone-melting-processed  $\text{Bi}_2\text{Te}_3$  ingots are p-type while powder-processed fine-grained sintered materials are in contrast n-type. Due to the different formation energy of point defects between Bi, Sb, Te, and Se, it is possible to tune the carrier concentration in ternary compounds  $(\text{Bi}, \text{Sb})_2\text{Te}_3$  or  $\text{Bi}_2(\text{Te}, \text{Se})_3$  by varying the composition [20, 48–50]. For example, by replacing Bi with Sb, more accepter antisite defects are formed, resulting in an

increase of the hole concentration in  $(\text{Bi},\text{Sb})_2\text{Te}_3$  alloys. In this scenery, the optimal composition corresponding to the optimized charge carrier concentration can be different between the ingots and the fine-grained sintered materials. More details will be discussed by experimental examples in [Section 2.1.3.1](#).

Large amounts of grain boundaries in fine-grained polycrystals can also influence the defect concentration so as the carrier concentration. Since the Te dangling bonds at the grain boundaries are recognized as cation vacancies [44], this is profound to affect the electron concentration in n-type  $\text{Bi}_2(\text{Te},\text{Se})_3$ . From this point of view, it provides opportunities for manipulation of Fermi level through controlling the grain microstructure. For example, it is found that the carrier concentration of n-type  $\text{Bi}_2(\text{Te},\text{Se})_3$  decreases by adding inert SiC particles like a second phase as they reduce the grain size [51].

### **2.1.2.3 Improved mechanical strength of fine-grained sintered materials**

In addition to the high  $ZT$  values, the nano-grained bulk materials are much more isotropic compared to layer structured zone-melting-processed ingots. Hence they do not suffer from the cleavage problem, which guarantee easier device fabrication and system integration and a potentially longer device lifetime. Taking the materials fabricated by ball milling [52] and melt spinning [53] combined with spark plasma sintering as examples, [Fig. 2.1.4](#) compared the mechanical strength of fine-grained polycrystals to zone melting made ingots. It is clearly illustrated that the fine-grained sintered samples have much better mechanical strength than zone melting ingots, including modified small punch (MSP) strength, Vickers hardness as well as the fracture toughness. In addition, the parallel strip cracks of the ingots declare its cleavage nature which polycrystalline materials hardly suffer from. Moreover, further improvement of the mechanical strength is easier to achieve in powder-processed materials. For example,  $\text{Bi}_2\text{Te}_3$ -based materials containing SiC nanoparticles as a second phase have further enhanced mechanical properties. This will be discussed in [Section 2.1.4](#).

## **2.1.3 Thermoelectric performance enhancement in $(\text{Bi},\text{Sb})_2\text{Te}_3$ and $\text{Bi}_2(\text{Te},\text{Se})_3$**

As the state-of-the-art thermoelectric materials,  $(\text{Bi},\text{Sb})_2\text{Te}_3$  and  $\text{Bi}_2(\text{Te},\text{Se})_3$  show high  $ZT$  values at room temperature and have been used in industry for decades in solid-state cooling. Widespread implementation of thermoelectric materials is limited by the low energy conversion efficiency.  $ZT$  enhancement has been an everlasting research topic and researchers have made tremendous efforts in materials design. Early works have determined the optimal Bi/Sb and Te/Se ratios as  $\sim 0.5/1.5$  and  $2.7/0.3$  for p-type  $(\text{Bi},\text{Sb})_2\text{Te}_3$  and n-type  $\text{Bi}_2(\text{Te},\text{Se})_3$  alloys, respectively [1]. Thereafter most of the studies have been focused on developing different fabrication strategies to enhance the thermoelectric performance of  $\text{Bi}_{0.5}\text{Sb}_{1.5}\text{Te}_3$  and  $\text{Bi}_2\text{Te}_{2.7}\text{Se}_{0.3}$  alloys. For instance, defect chemistry manipulation [20, 54], carrier concentration

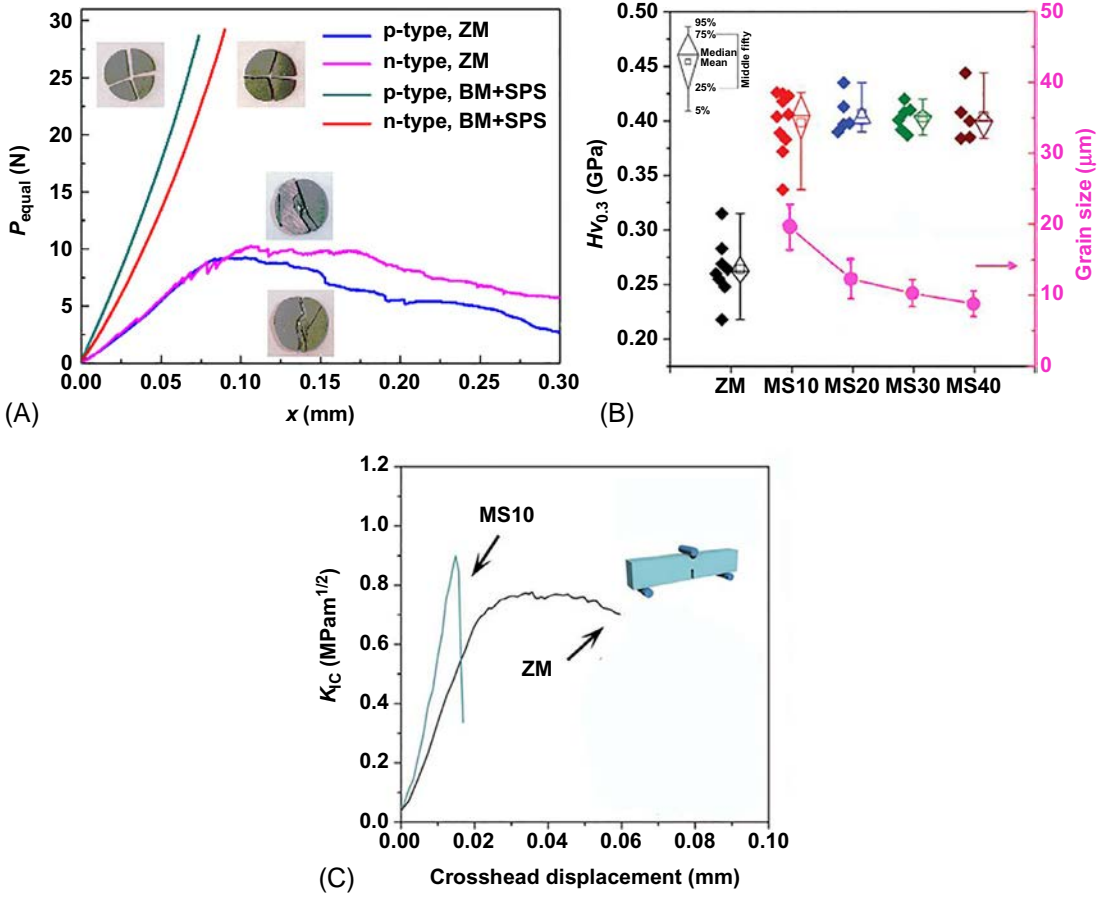


**Fig. 2.1.4** Mechanical properties of zone melting made ingots and fine-grained sintered materials. (A) MSP load-deflection curves of zone melting made ingots and ball milling combined spark plasma sintering polycrystalline, inset images show the samples' fracture feature [52]. (B) Vickers Hardness along with grain size and (C) fracture toughness of zone melting made ingots and melt spinning combined spark plasma sintering polycrystalline [53]. Figures are reproduced with permission from Y. Pan, T.-R. Wei, Q. Cao, J.-F. Li, Mater. Sci. Eng. B 197 (2015) 75–81; Y. Zheng, Q. Zhang, X. Su, H. Xie, S. Shu, T. Chen, G. Tan, Y. Yan, X. Tang, C. Uher, G. J. Snyder, Adv. Energy Mater. 5 (2015) 1401391.

optimization [55, 56], band convergence [19], microstructure engineering [28, 39, 57–60], etc. [61]

Generally, it is much easier for p-type  $(\text{Bi},\text{Sb})_2\text{Te}_3$  to achieve high performance in fine-grained polycrystals. Pan et al. have compared the thermoelectric properties of zone-melting ingots and fine-grained sintered materials for both p-type  $\text{Bi}_{0.5}\text{Sb}_{1.5}\text{Te}_3$  and n-type  $\text{Bi}_2\text{Te}_{2.7}\text{Se}_{0.3}$  [52]. In addition to the reduction of thermal conductivity due to grain refinement, it is found that the electrical transport properties (both mobility and charge carrier concentration) of n-type  $\text{Bi}_2\text{Te}_{2.7}\text{Se}_{0.3}$  are strongly dependent on the microstructure, while p-type is less influenced [52]. In this case, enhancing the thermoelectric performance of p-type materials can be realized by focusing on further decreasing the thermal conductivity, while more aspects including the Fermi level, mobility, reproducibility, etc. should be taken into consideration when dealing with n-type  $\text{Bi}_2(\text{Te},\text{Se})_3$ . In this section, representative examples of how to enhance the thermoelectric performance of fine-grained ternary  $(\text{Bi},\text{Sb})_2\text{Te}_3$  and  $\text{Bi}_2(\text{Te},\text{Se})_3$ -based bulks since 2000 will be summarized, with an emphasis on the works by our group.

### 2.1.3.1 Composition optimization of n-type $\text{Bi}_2(\text{Te},\text{Se})_3$

The optimal composition of fine-grained polycrystals can be different from that of ingots since the defect concentrations are sensitive to the preparation process. Optimal carrier concentrations are  $\sim 2$  and  $\sim 4 \times 10^{19} \text{ cm}^{-3}$  for p-type  $(\text{Bi},\text{Sb})_2\text{Te}_3$  and n-type  $\text{Bi}_2(\text{Te},\text{Se})_3$ , respectively. The donor-like effect introduced by strong mechanical deformation produces more electrons, which can deviate the carrier concentration (particularly in n-type alloys) from the optimal range. Through manipulating the defect chemistry via changing the Bi/Sb or Te/Se ratio, it is possible to control the carrier concentration and thus thermoelectric performance.

Hole concentration hardly changes from the optimal range in p-type  $\text{Bi}_{0.5}\text{Sb}_{1.5}\text{Te}_3$ , while electron concentration increases obviously in n-type  $\text{Bi}_2\text{Te}_{2.7}\text{Se}_{0.3}$ . The increase of the electron concentration (with a value of  $\sim 6 \times 10^{19} \text{ cm}^{-3}$ ) from the optimal range ( $\sim 4 \times 10^{19} \text{ cm}^{-3}$ ) can be attributed to the donor-like effect. As shown in Fig. 2.1.5A and B, the hole concentrations of p-type  $\text{Bi}_{0.5}\text{Sb}_{1.5}\text{Te}_3$  are still in the optimal concentration range of  $2 \times 10^{19} \text{ cm}^{-3}$  [49], however, the electron concentration of n-type  $\text{Bi}_2\text{Te}_{2.7}\text{Se}_{0.3}$  increases to  $\sim 6 \times 10^{19} \text{ cm}^{-3}$  [20]. Therefore, the optimal composition of p-type is unchanged as  $\text{Bi}_{0.5}\text{Sb}_{1.5}\text{Te}_3$  while it is no longer  $\text{Bi}_2\text{Te}_{2.7}\text{Se}_{0.3}$  for n-type. To shift the electron carrier concentration to the optimal range, the donor-like effect should be suppressed, which can be realized by increasing the Se amount in  $\text{Bi}_2(\text{Te},\text{Se})_3$ . Noteworthy, higher Se content tends to make the material more n-type in zone melting ingots, while it is not the case in fine-grained polycrystals where the donor-like effect is dominant. It is shown that the electron concentration goes back to the optimal range at the composition near  $\text{Bi}_2\text{Te}_{2.2}\text{Se}_{0.8}$ . As such, defect manipulation is more effective in n-type  $\text{Bi}_2(\text{Te},\text{Se})_3$  polycrystalline samples than p-type.

In addition to the carrier concentration, alloying different amounts of  $\text{Bi}_2\text{Se}_3$  in  $\text{Bi}_2\text{Te}_3$  also affects the mobility as well as the lattice thermal conductivity. Theoretically, Se will firstly enter  $\text{Te}^{(2)}$  sites due to stronger electronegativity, and  $\text{Bi}_2\text{Te}_2\text{Se}_1$

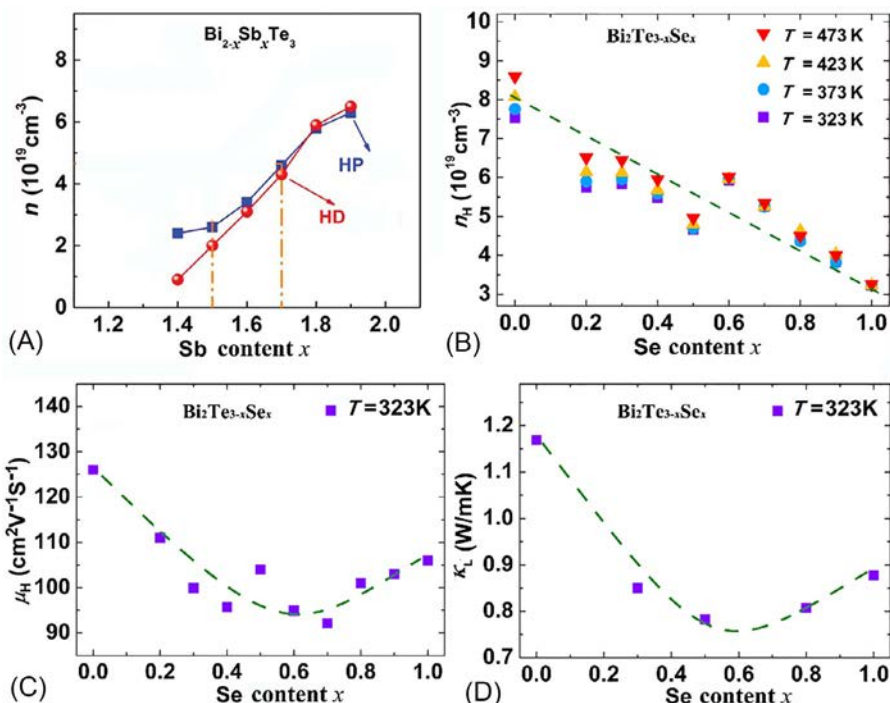


**Fig. 2.1.5** (A) Sb content dependence of carrier concentration in p-type  $(\text{Bi},\text{Sb})_2\text{Te}_3$  [49], Se content dependence of (B) carrier concentration, (C) Hall mobility, and (D) lattice thermal conductivity in n-type  $\text{Bi}_2(\text{Te},\text{Se})_3$  [20].

Figures are modified from L. Hu, T. Zhu, X. Liu, X. Zhao, *Adv. Funct. Mater.* 24 (2014) 5211–5218; Y. Pan, T.-R. Wei, C.-F. Wu, J.-F. Li, J. Mater. Chem. C 3 (2015) 10583.

can be recognized as an ordered structure with all the  $\text{Te}^{(2)}$  sites replaced by Se [62]. In consequence, lowest mobility and lattice thermal conductivity should lie in the middle around  $\text{Bi}_2\text{Te}_{2.5}\text{Se}_{0.5}$ . As shown in Fig. 2.1.5C and D, minimum mobility and lattice thermal conductivity are obtained at the composition around  $\text{Bi}_2\text{Te}_{2.4}\text{Se}_{0.6}$ , where the Se amount is slightly higher than  $\text{Bi}_2\text{Te}_{2.5}\text{Se}_{0.5}$  since not all the Se will enter  $\text{Te}^{(2)}$  sites in practical. Comprehensively, the best thermoelectric performance of fine-grained polycrystalline  $\text{Bi}_2(\text{Te},\text{Se})_3$  is obtained at the composition with the Se amount of  $x \sim 0.6\text{--}0.8$  [20, 49, 63].

### 2.1.3.2 Doping mechanism in $(\text{Bi},\text{Sb})_2\text{Te}_3$ and $\text{Bi}_2(\text{Te},\text{Se})_3$

Best thermoelectric performance requires precise control of the Fermi level. As discussed in Section 2.1.3.1, the optimal charge carrier concentration is around  $2\text{--}4 \times 10^{19} \text{ cm}^{-3}$  and can be usually controlled by self-doping via intrinsic defects. Alternatively, the charge carrier density can also be adjusted by extrinsic doping using

substitution atoms with one more electron (donors) or one fewer electrons (acceptors). However, the introduction of extrinsic dopants usually decreases the mobility of the host materials, which should be taken into consideration when tuning the Fermi level. Generally, halogens are ideal donors and Pb, Sn are ideal acceptors [6, 64–69]. Interestingly, Cu can be a dopant for both p-type  $(\text{Bi},\text{Sb})_2\text{Te}_3$  and n-type  $\text{Bi}_2(\text{Te},\text{Se})_3$ , which has been widely studied [44, 56, 70–73]. In p-type  $(\text{Bi},\text{Sb})_2\text{Te}_3$ , Cu dopants increase the concentration of holes by taking the cation sites, while they go to the interstitial sites in n-type  $\text{Bi}_2(\text{Te},\text{Se})_3$  producing electrons. This can be due to the different tetragonal sizes in p- and n-type alloys, which is larger in n-type than in p-type. Hao et al. have studied the thermoelectric properties of Cd-, Ag-, Cu-doped  $\text{Bi}_{0.5}\text{Sb}_{1.5}\text{Te}_3$  alloys [55]. Xu et al. have studied the effect of In doping in  $(\text{Bi},\text{Sb})_2\text{Te}_3$  alloys [74]. Benefiting from the large suppression of bipolar effect and the reduction of thermal conductivity by doping, the maximum  $ZT_{\max}$  has been shifted to higher temperatures which can be potentially used for power generation.

According to the effective mass model, a higher carrier concentration is required for maximum  $ZT$  values at higher temperatures. In contrast to the conventional doping effect, Pan et al. have reported a self-tuning carrier concentration behavior in Cu-doped  $\text{Bi}_2\text{Te}_{2.2}\text{Se}_{0.8}$ -SiC composite [51]. Due to the increasing solubility of Cu with increasing temperatures in the composites, the carrier concentration increases with temperature, as shown in Fig. 2.1.6A. Notably, this is different from bipolar effect as the upturning temperature is even lower than the undoped sample with lower carrier concentration. Because of the self-tuning charge carrier concentration, stable thermoelectric performance with a  $ZT$  plateau of  $\sim 0.85$  between 473 and 573 K is achieved, as illustrated in Fig. 2.1.6B. Instead of a single  $ZT$  peak, this  $ZT$  plateau is promising in practical device applications. Taking advantages of the high  $ZT$  of zone melting ingots at low temperatures and the present  $ZT$  plateau at high temperatures, a segmented leg can be designed with a maximum calculated device  $ZT$  over 0.9 in the whole temperature range from 300 to 573 K (Fig. 2.1.6C) [51]. By extending the use of the segmented leg to higher temperatures, the overall efficiency is increased to 9.2%, which rivals that of mid-temperature materials, making  $\text{Bi}_2\text{Te}_3$  alloys competitive for waste-heat power generation applications [51].

How to shift the maximum  $ZT$  values to higher temperatures in  $\text{Bi}_2\text{Te}_3$  alloys and apply  $\text{Bi}_2\text{Te}_3$ -based thermoelectric materials in waste-heat recovery are receiving more and more attention. Since two-thirds of the primary energy is lost as waste heat (low-temperature region at 100–300°C constitutes over 50%), there is a high demand for stable thermoelectric performance in the low-temperature range up to 300°C. Better understanding of the doping mechanisms is of great significance for the realization of high  $ZT$  values at high temperatures in  $\text{Bi}_2\text{Te}_3$  alloys.

### 2.1.3.3 Band convergence in $\text{Bi}_{0.5}\text{Sb}_{1.5}\text{Te}_3$

Volotsky et al. have described a band structure with two conduction bands and two valence bands of  $(\text{Bi},\text{Sb})_2\text{Te}_3$  compounds [75]. As discussed above, the composition of  $\text{Bi}_{0.5}\text{Sb}_{1.5}\text{Te}_3$  has been found to have the best thermoelectric performance, while the reasons have in recent years been explained by Kim et al. to be band convergence [19].

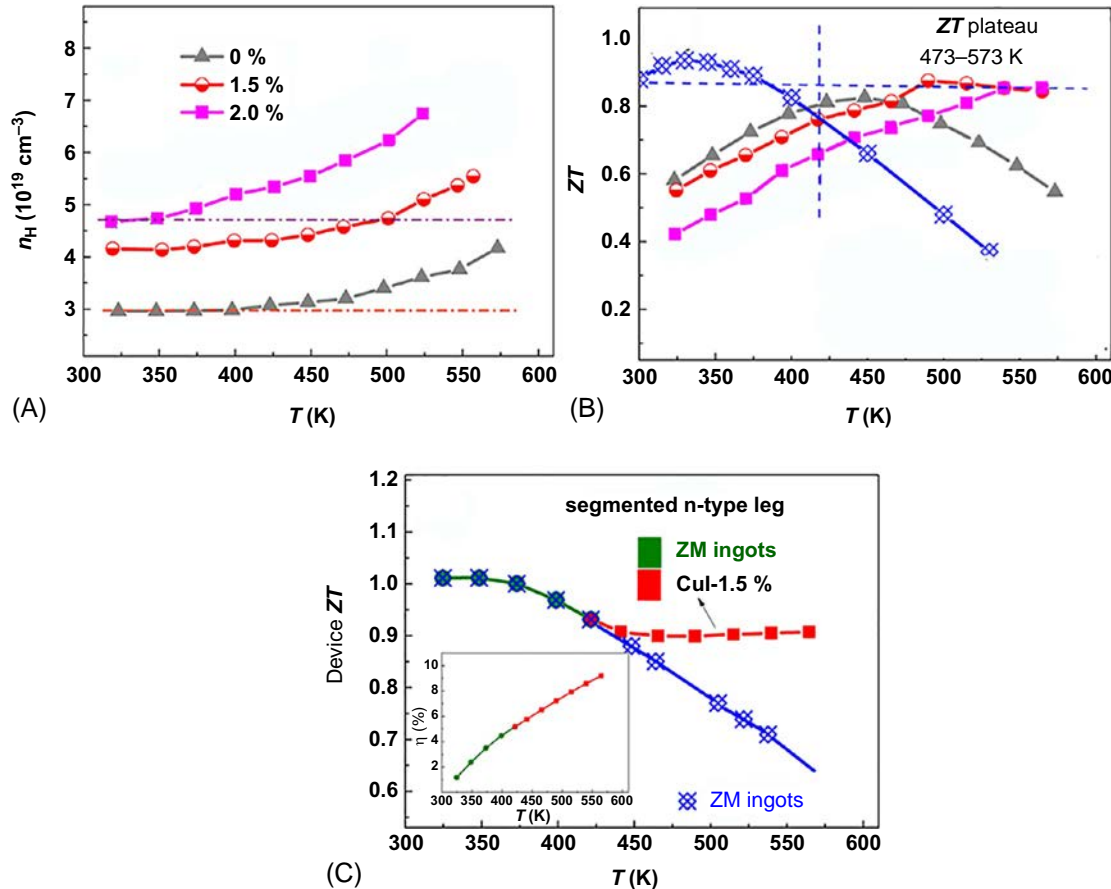


**Fig. 2.1.6** Temperature dependence of (A) carrier concentration and (B)  $ZT$  values of Cu-doped  $\text{Bi}_2\text{Te}_{2.2}\text{Se}_{0.8}$ -SiC composite. (C) Temperature dependence of calculated device  $ZT$  of segmented leg composed of zone melting ingots and the Cu-doped  $\text{Bi}_2\text{Te}_{2.2}\text{Se}_{0.8}$ -SiC composite, inset is the calculated efficiency of the segmented leg [51].

Figures are modified from Y. Pan, U. Aydemir, F.-H. Sun, C.-F. Wu, T.C. Chasapis, G.J. Snyder, J.-F. Li, Adv. Sci. 4 (2017) 1700259.

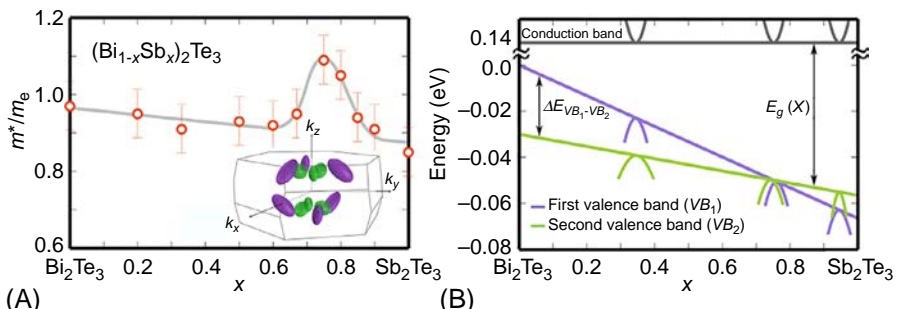


**Fig. 2.1.7** (A) Effective mass of  $\text{Bi}_{2-x}\text{Sb}_x\text{Te}_3$ , inset shows the hole pockets for the first (purple) and second (green) valence band in the Brillouin zone of  $\text{Bi}_2\text{Te}_3$  and (B) illustration of the crossing of the first and the second valence band [19].

Figures are modified from H.-S. Kim, N.A. Heinz, Z.M. Gibbs, Y. Tang, S.D. Kang, G.J. Snyder, Mater. Today 20 (2017) 452.

Through developing a two-band model, the experimental transport properties are satisfactorily explained. As shown in Fig. 2.1.7, an increased band effective mass is obtained at the composition of  $\text{Bi}_{0.5}\text{Sb}_{1.5}\text{Te}_3$ , which is due to the convergence of the two different valence bands that cross as the Bi/Sb ratio changes [19]. Such explanations are consistent with low-temperature measurements and the theory indicating a complex band structure.

### 2.1.3.4 Microstructure engineering

Thermoelectric properties of polycrystalline materials are greatly influenced by their microstructures including anisotropy, grain size, dislocations, nanoinclusions, etc., which are sensitive to the preparation processes and the starting materials. In the past 10 years, many efforts have been focused on nanostructured polycrystalline materials to improve  $ZT$  by reducing the thermal conductivity [30, 76–80]. As mentioned above, the electrical performance of p-type  $(\text{Bi},\text{Sb})_2\text{Te}_3$  materials is less influenced by the microstructure while the situation is much more complicated for n-type  $\text{Bi}_2(\text{Te},\text{Se})_3$ . That is why most of the high performance obtained from microstructure engineering via advanced processing technologies are reported in p-type  $(\text{Bi},\text{Sb})_2\text{Te}_3$ . This section will give a few novel examples of the microstructure engineering in p-type  $(\text{Bi},\text{Sb})_2\text{Te}_3$  and one example in the case of n-type  $\text{Bi}_2(\text{Te},\text{Se})_3$ . These methods reduce the thermal conductivity in a way that avoids obviously degrading electrical conductivity, which therefore results in better thermoelectric performance.

Firstly, for p-type  $(\text{Bi},\text{Sb})_2\text{Te}_3$ , ball milling [28], melt spinning [81], hot deformation [82], etc. have been widely applied to introduce nanostructures. In these works, enhanced interface scattering of phonons (focused on low-frequency phonons) is responsible for the reduction of thermal conductivity. One of the most instructive examples is reported by Poudel et al. in 2008 [28]. By simply ball milling and hot pressing the zone melting  $\text{Bi}_{0.5}\text{Sb}_{1.5}\text{Te}_3$  ingots, fine-grained samples with plenty of

nanostructures (Fig. 2.1.8A) are produced. These lead to a large reduction in thermal conductivity (Fig. 2.1.8B) and improve the  $ZT_{max}$  from 1.0 to over 1.4 (Fig. 2.1.8C) [28]. Since then, ball milling combined with hot pressing and spark plasma sintering have gained increasing attention. Similarly, melt spinning combined with hot pressing or spark plasma sintering has also demonstrated to be efficient in enhancing  $ZT$  by decreasing thermal conductivity because of nanostructuring effect [83].

Further reduction of the thermal conductivity relies on a broader scattering of phonons. Conventional nanostructuring and alloying target the low and high-frequency phonons via interface and point defect scattering, respectively. Additional strain scattering by dislocations can impede the transport of mid-frequency phonons and thus further decrease the thermal conductivity [84, 85]. In 2015, Kim et al. have shown

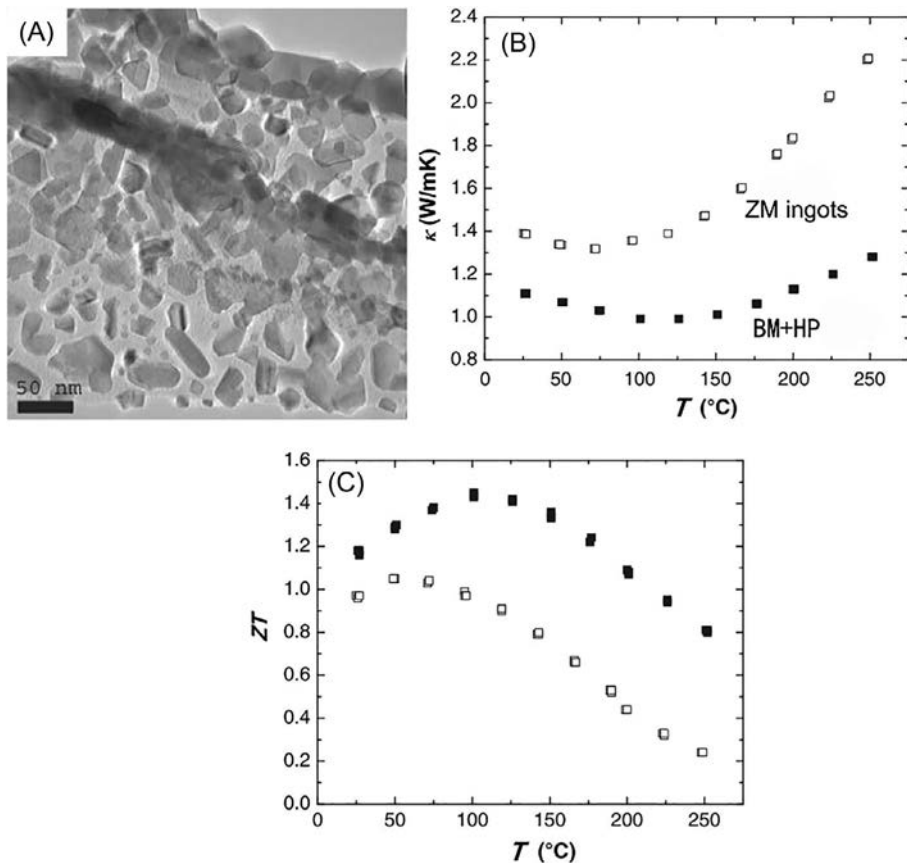


**Fig. 2.1.8** (A) Microstructure, (B) thermal conductivity, and (C)  $ZT$  values of fine-grained p-type  $\text{Bi}_{0.5}\text{Sb}_{1.5}\text{Te}_3$  polycrystalline made by ball milling and hot pressing [28]. Figures are modified from B. Poudel, Q. Hao, Y. Ma, Y. Lan, A. Minnich, B. Yu, X. Yan, D. Wang, A. Muto, D. Vashaee, X. Chen, J. Liu, M.S. Dresselhaus, G. Chen, Z. Ren, Science 320 (2008) 634.

a dramatic improvement of  $ZT$  in  $\text{Bi}_{0.5}\text{Sb}_{1.5}\text{Te}_3$  samples by introducing dense dislocation arrays at the grain boundaries [39]. This is realized by quickly squeezing out excess Te liquid during compaction of melt-spun  $\text{Bi}_{0.5}\text{Sb}_{1.5}\text{Te}_3$ -25 wt% Te composites. As illustrated in Fig. 2.1.9A, dislocation scattering further shrink the middle-frequency phonons contribution to thermal conductivity [39]. Compared to the conventional ball-milled and melt-spun samples, additional dislocation scattering results in lower thermal conductivity (Fig. 2.1.9B) [39]. Broad-spectrum phonon scattering dramatically enhances the  $ZT$  to 1.86 at 320 K (Fig. 2.1.9C) [39]. Unfortunately, it is difficult to repeat this record-high  $ZT$ , as pointed out by Deng et al. by reproducing the same method [86].

In addition to phonon scattering, reducing the thermal conductance can also be used to decrease the thermal conductivity. Pan et al. report an unconventional melt-centrifugation technique to produce a unique microstructure in  $(\text{Bi},\text{Sb})_2\text{Te}_3$  with large porosity and dense dislocations [59]. Melt-centrifugation engineers the microstructure via separating the liquid eutectic phase mixture from the solid  $(\text{Bi},\text{Sb})_2\text{Te}_3$  phase under strong centrifugal force. During centrifugation, the randomly distributed liquid phase is forced out of the bulk sample to the bottom of the silica ampoule,

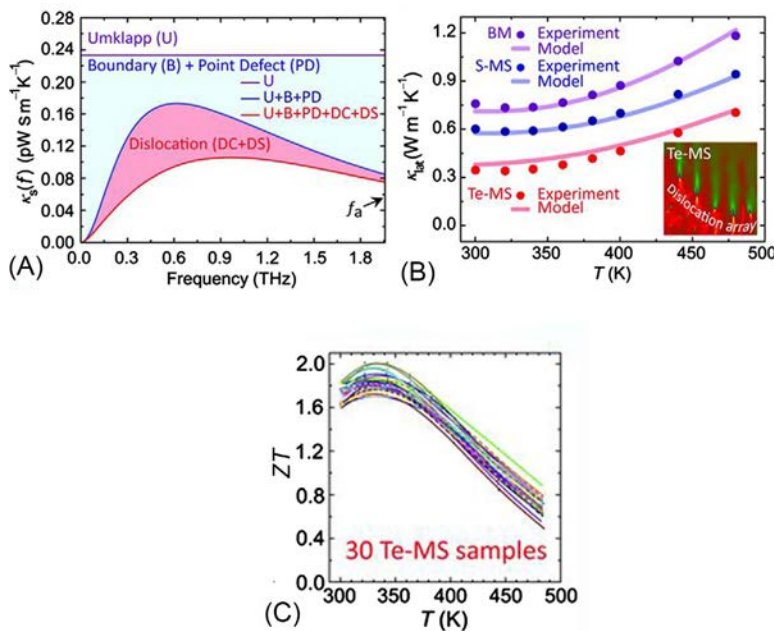


**Fig. 2.1.9** (A) Illustration of phonons scattering by Umklapp, boundary (or interface), point defect and dislocation in full-spectrum, (B) lattice thermal conductivity of  $\text{Bi}_{0.5}\text{Sb}_{1.5}\text{Te}_3$ -25 wt% Te melt-spun samples, with a comparison to ball-milled and melt-spun samples, and (C)  $ZT$  values of  $\text{Bi}_{0.5}\text{Sb}_{1.5}\text{Te}_3$ -25 wt% Te melt-spun samples [39].

Figures are modified from Sang Il Kim, Kyu Hyoung Lee, Hyeon A Mun, Hyun Sik Kim, Sung Woo Hwang, Jong Wook Roh, Dae Jin Yang, Weon Ho Shin, Xiang Shu Li, Young Hee Lee, G. Jeffrey Snyder, Sung Wng Kim, Science 348 (2015) 109.

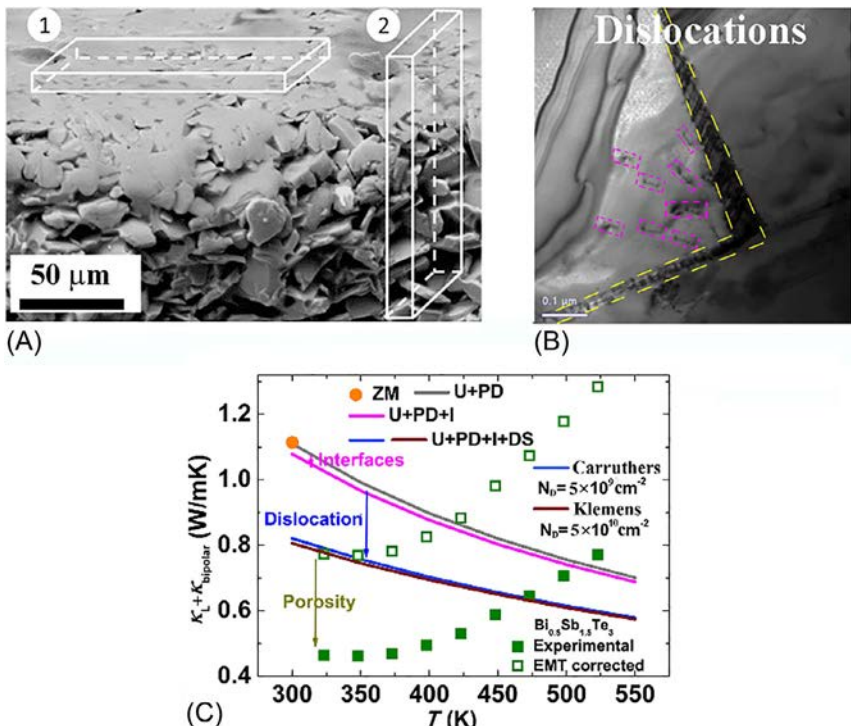


**Fig. 2.1.10** (A) Porous structure, (B) dislocation arrays, and (C) thermal conductivity of melt centrifuged  $\text{Bi}_{0.5}\text{Sb}_{1.5}\text{Te}_3$  [59].

Figures are modified from Y. Pan, U. Aydemir, J.A. Grovogui, I.T. Witting, R. Hanus, Y. Xu, J. Wu, C.F. Wu, F.H. Sun, H.L. Zhuang, J.F. Dong, J.F. Li, V.P. Dravid, G.J. Snyder, *Adv. Mater.* 30 (2018) 1802016.

leaving behind nearly pure  $(\text{Bi},\text{Sb})_2\text{Te}_3$  with a low density (Fig. 2.1.10A) [59]. Additionally, the grains form large misfit as facilitated by the uniaxial centrifugal force and liquid extrusion, which is then accommodated by dense dislocations (Fig. 2.1.10B) [59]. Consequently, a liquid-fused material with microscale dislocation arrays and large porosity has been achieved. Both the large porosity and the dense dislocations play a significant role in the reduction of the thermal conductivity (Fig. 2.1.10C) [59]. Despite the porous feature, the samples framework still show good electrical transport performance because of the fused framework.

In n-type  $\text{Bi}_2(\text{Te},\text{Se})_3$ , since the electrical transport properties have a strong dependence on the microstructure, microstructure engineering should pay attention to the maintenance of high electrical performance when decreasing thermal conductivity. Usually, the electrical transport properties are obviously deteriorated in polycrystalline materials because of two main reasons. Firstly, the charge carrier mobility is strongly related to the layer structure. Isotropic fine-grained sintered materials have

much lower mobility than layer structured zone melting-made ingots. Secondly, the charge carrier concentration changes greatly in polycrystalline sintered materials, making it far beyond the optimal range. The former requires the material to be layer structured while the latter is addressed by adjusting the composition (see Section 2.1.3.1). In this case, a hierarchical microstructure combined with a layer structure, fine grains and nanostructure can be advantageous to maximize the ratio of electrical conductivity to thermal conductivity.

Pan et al. have developed a repeated spark plasma sintering technique to introduce forged intriguing textures, defect clusters, and dislocation loops into n-type  $\text{Bi}_2(\text{Te}, \text{Se})_3$  alloys [58]. As illustrated in Fig. 2.1.11A, repeated spark plasma sintering forged a layer structure with larger grains (but still fine grains) in the sample [58]. With the in-plane textured structure, the mobility of the texture processing (TP) samples are boosted compared to the ball-milled sample (Fig. 2.1.11B) [58]. While at the same time the fine-grained structure along with the distorted defects help trap heat, leading to a comparably low lattice thermal conductivity (Fig. 2.1.11C) [58]. By tuning the repeated spark plasma sintering temperature (from 400°C to 500°C) to optimize

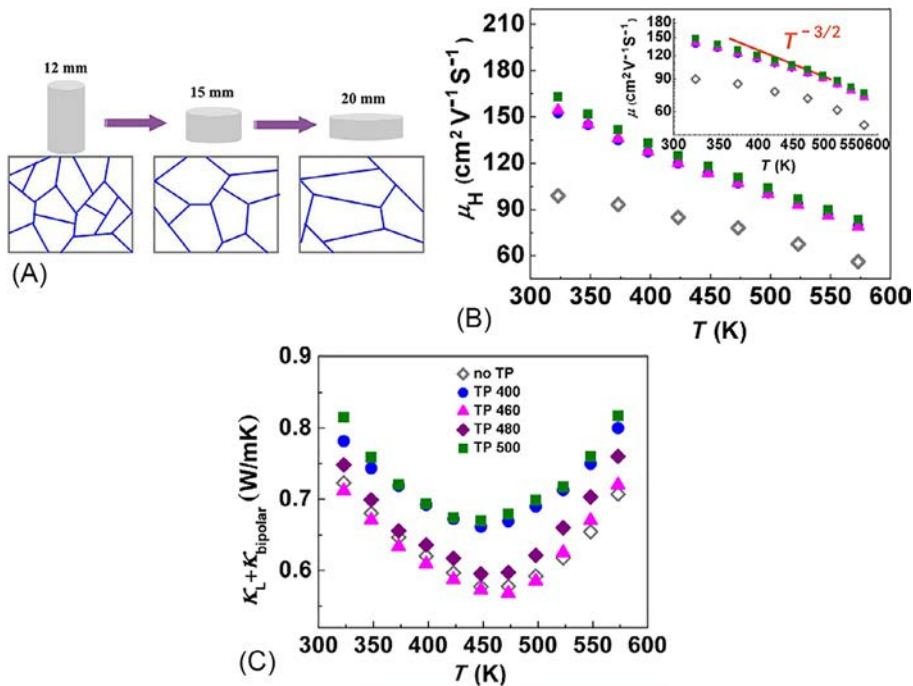


**Fig. 2.1.11** (A) Schematic illustration of repeated hot forging process, (B) Hall mobility, and (C) lattice and bipolar thermal conductivity of texture processed samples, with a comparison to the non-textured samples. Different hot forging temperatures are adopted, which are 400, 460, 480, and 500°C [58].

Figures are modified from Y. Pan, J.-F. Li, NPG Asia Mater. 8, e275.

the ratio of textures to defects, a maximum enhancement of 35% in  $ZT$  is achieved compared to the non-textured samples. Similarly, results based on top-to-bottom hot deformation method has been conducted by Hu et al. [57]

### 2.1.4 Nanocomposites

Incorporating nanoscale heterogeneity into a thermoelectric alloy matrix often by in situ precipitation or simple mixing can be effective in  $ZT$  enhancement. Although effective medium theory predicts that the performance would not exceed the better of the two individual components, the situation can be different if the components interact with each other. For example, with coherent interfaces formed through in situ precipitation, the nanoscopic inhomogeneity effectively reduces the thermal conductivity of the whole material by enhancing phonon scattering but can have fewer influences on its electrical conductivity. The difficulty of this method is to find such a combination of second-phase inclusions in a matrix so that thermal conductivity is reduced while its electrical conductivity is not reduced significantly at the same time. SiC particles are firstly demonstrated to be effective in enhancing the  $ZT$  of  $\text{Bi}_2\text{Te}_3$  [87, 88]. In the following years, it is applied in ternary  $(\text{Bi},\text{Sb})_2\text{Te}_3$  matrix. Li et al. demonstrated that adding SiC nanoparticles into the p-type  $(\text{Bi},\text{Sb})_2\text{Te}_3$  matrix is effective for its thermoelectric property enhancement [89]. As shown in Fig. 2.1.12A and B, SiC nanoparticles can efficiently scatter the low energy (LE) charge carrier while high energy (HE) carrier can still transport because of the coherent boundaries [89]. This would lead to an enhanced Seebeck coefficient based on the energy filtering effect. Along with the relatively low thermal conductivity (Fig. 2.1.12C), a high  $ZT$  value up to 1.33 at 373 K is obtained in  $\text{Bi}_{0.3}\text{Sb}_{1.7}\text{Te}_3$  alloys (Fig. 2.1.12D) [89].

The introduction of hard SiC nanoparticles can improve the mechanical properties of  $\text{Bi}_2\text{Te}_3$ -based thermoelectric materials. Fig. 2.1.13 summarizes the mechanical strength of SiC- $\text{Bi}_2\text{Te}_3$ -based composites [51]. By additional SiC nanoparticles, Young's modulus, flexural strength, Vickers hardness, and also fracture toughness are all enhanced [51, 88, 90]. The enhanced mechanical strength is advantageous for mechanical stability and module applications. More studies on nanocomposites with different second-phase inclusions have also been conducted by other groups [91–97].

### 2.1.5 Additional considerations

In addition to the thermoelectric performance, other considerations should also be considered in the thermoelectric field, for example, reproducibility. Based on experimental experiences, p-type  $(\text{Bi},\text{Sb})_2\text{Te}_3$  usually have better reproducibility than n-type  $\text{Bi}_2(\text{Te},\text{Se})_3$ . The poor reproducibility of n-type  $\text{Bi}_2(\text{Te},\text{Se})_3$  can be caused by the easy change of point defect concentration due to Se evaporation.

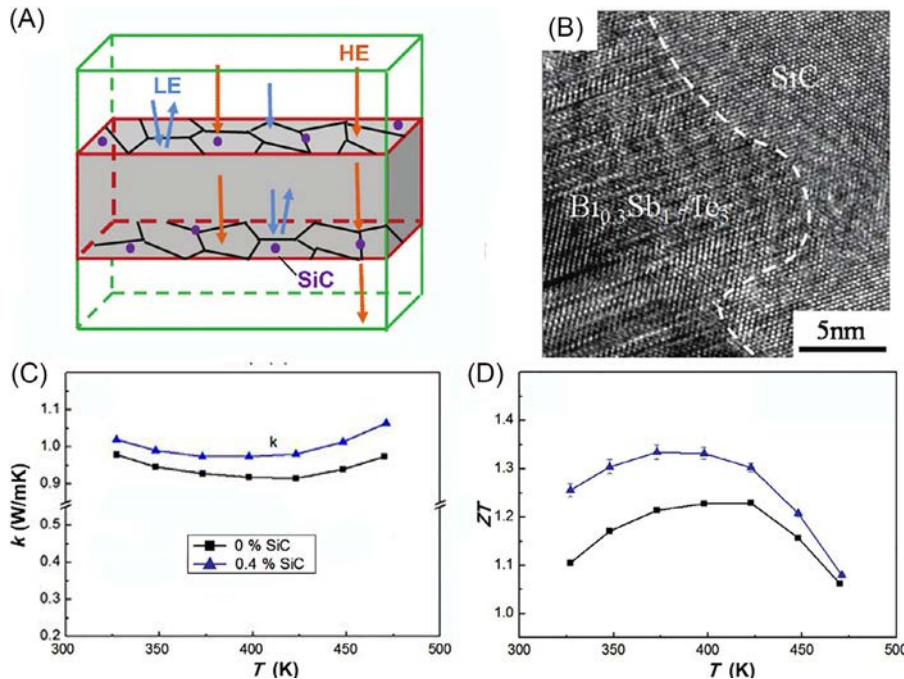


**Fig. 2.1.12** (A) Schematic illustration of the energy filtering effect of SiC in  $\text{Bi}_{0.3}\text{Sb}_{1.7}\text{Te}_3$ , (B) TEM images show the coherent boundary of SiC and  $\text{Bi}_{0.3}\text{Sb}_{1.7}\text{Te}_3$ , (C) thermal conductivity, and (D) ZT values of  $\text{Bi}_{0.3}\text{Sb}_{1.7}\text{Te}_3$ -SiC composite, with a comparison to the pure  $\text{Bi}_{0.3}\text{Sb}_{1.7}\text{Te}_3$  [89].

Figures are modified from J. Li, Q. Tan, J.-F. Li, D.-W. Liu, F. Li, Z.-Y. Li, M. Zou, K. Wang, Adv. Funct. Mater. 23 (2013) 4317–4323.

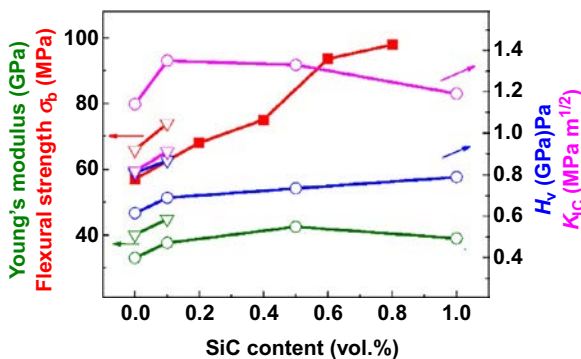


**Fig. 2.1.13** Mechanical properties of  $\text{Bi}_2\text{Te}_3$ -based alloys-SiC composites including Young's modulus, flexural strength, Vickers hardness, and fracture toughness.

Figures are from Y. Pan, U. Aydemir, F.-H. Sun, C.-F. Wu, T.C. Chasapis, G.J. Snyder, J.-F. Li, Adv. Sci. 4 (2017) 1700259.

## 2.1.6 Summary

In summary,  $\text{Bi}_2\text{Te}_3$  alloyed with  $\text{Sb}_2\text{Te}_3$  and  $\text{Bi}_2\text{Se}_3$  show excellent thermoelectric performance at near room temperature due to complex multi-valley structure, high mobility, and low thermal conductivity. Thermoelectric performance enhancement can be realized through defect chemistry manipulation, carrier concentration optimization, band convergence, and more widely adopted microstructure engineering. The  $ZT$  value of p-type fine-grained polycrystalline  $(\text{Bi},\text{Sb})_2\text{Te}_3$  is generally higher than n-type  $\text{Bi}_2(\text{Te},\text{Se})_3$ , due to the large deterioration of electrical performance of n-type  $\text{Bi}_2(\text{Te},\text{Se})_3$  which is strongly dependent on the layer structure. More researches on broadening the temperature range of high  $ZT$  values, reproducibility, interface problem in the nanocomposites, adding organic polymers as second-phase mixture, etc. can be conducted in the future.

## Acknowledgments

This work was supported by the Basic Science Center Project of NSFC No. 51788104 and National Key R&D Program of China 2018YFB0703603. Y. P. acknowledges the financial support from the Alexander von Humboldt Foundation. We thank Hua-Lu Zhuang for help with proofreading.

## References

- [1] W.M. Yim, F.D. Rosi, Solid State Electron. 15 (1972) 1121.
- [2] M.H. Francombe, Br. J. Appl. Phys. 9 (1958) 415.
- [3] R.T. Delves, A.E. Bowley, D.W. Hazelden, H.J. Goldsmid, Proc. Phys. Soc. 78 (1961) 838.
- [4] J.H. Dennis, Adv. Energy Convers. 1 (1961) 99–105.
- [5] M. Situmorang, H.J. Goldsmid, Phys. Status Solidi (b) 134 (1986) K83.
- [6] H.J. Goldsmid, J. Appl. Phys. 32 (1961) 2198.
- [7] Y.L. Chen, J.G. Analytis, J.-H. Chu, Z.K. Liu, S.-K. Mo, X.L. Qi, H.J. Zhang, D.H. Lu, X. Dai, Z. Fang, S.C. Zhang, I.R. Fisher, Z. Hussain, Z.-X. Shen, Science 325 (2009) 178.
- [8] R. Sew, L.R. Testardi, J. Phys. Chem. Solids 23 (1962) 1219.
- [9] I.G. Austin, A. Sheard, J. Electron. Control 3 (1957) 236–237.
- [10] I.T. Witting, T.C. Chasapis, F. Ricci, M. Peters, N.A. Heinz, G. Hautier, G.J. Snyder, Adv. Electron. Mater. 5 (2019) 1800904.
- [11] S.J. Youn, A.J. Freeman, Phys. Rev. B (2001) 63.
- [12] B.Y. Yavorsky, N.F. Hinsche, I. Mertig, P. Zahn, Phys. Rev. B 84 (2011) 165208.
- [13] J.R. Drabble, Proc. Phys. Soc. Lond. 72 (1958) 380–390.
- [14] J.R. Drabble, R.D. Groves, R. Wolfe, Proc. Phys. Soc. Lond. 71 (1958) 430–443.
- [15] H.A. Ashworth, J.A. Rayne, R.W. Ure, Phys. Rev. B 3 (1971) 2646–2661.
- [16] R.B. Mallinson, J.A. Rayne, R.W. Ure, Phys. Rev. 175 (1968) 1049–1056.
- [17] C.B. Satterthwaite, R.W. Ure, Phys. Rev. 108 (1957) 1164–1170.
- [18] G.R. Miller, C.-Y. Li, J. Phys. Chem. Solids 26 (1965) 173.
- [19] H.-S. Kim, N.A. Heinz, Z.M. Gibbs, Y. Tang, S.D. Kang, G.J. Snyder, Mater. Today 20 (2017) 452.
- [20] Y. Pan, T.-R. Wei, C.-F. Wu, J.-F. Li, J. Mater. Chem. C 3 (2015) 10583.

- [21] F. Yang, T. Ikeda, G.J. Snyder, C. Dames, *J. Appl. Phys.* 108 (2010) 034310.
- [22] X. Chen, H.D. Zhou, A. Kiswandhi, I. Miotkowski, Y.P. Chen, P.A. Sharma, A.L.L. Sharma, M.A. Hekmaty, D. Smirnov, Z. Jiang, *Appl. Phys. Lett.* 99 (2011) 261912.
- [23] O. Yamashita, S. Tomiyoshi, K. Makita, *J. Appl. Phys.* 93 (2003) 368.
- [24] O. Yamashita, S. Tomiyoshi, *J. Appl. Phys.* 95 (2004) 6277.
- [25] J.Y. Yang, T. Aizawa, A. Yamamoto, T. Ohta, *J. Alloys Compd.* 312 (2000) 326.
- [26] S. Miura, Y. Sato, K. Fukuda, K. Nishimura, K. Ikeda, *Mater. Sci. Eng. A* 277 (2000) 244.
- [27] J.-F. Li, J. Liu, *Phys. Status Solidi (a)* 203 (2006) 3768.
- [28] B. Poudel, Q. Hao, Y. Ma, Y. Lan, A. Minnich, B. Yu, X. Yan, D. Wang, A. Muto, D. Vashaee, X. Chen, J. Liu, M.S. Dresselhaus, G. Chen, Z. Ren, *Science* 320 (2008) 634.
- [29] J.M. Schultz, J.P. McHugh, W.A. Tiller, *J. Appl. Phys.* 33 (1962) 2443.
- [30] Y. Lan, A.J. Minnich, G. Chen, Z. Ren, *Adv. Funct. Mater.* 20 (2010) 357–376.
- [31] M. Zhou, J.-F. Li, T. Kita, *J. Am. Chem. Soc.* 130 (2008) 4527–4532.
- [32] W. Liu, H.S. Kim, S. Chen, Q. Jie, B. Lv, M. Yao, Z. Ren, C.P. Opeil, S. Wilson, C.W. Chu, Z. Ren, *Proc. Natl. Acad. Sci. U. S. A.* 112 (2015) 3269–3274.
- [33] X. Yan, W. Liu, S. Chen, H. Wang, Q. Zhang, G. Chen, Z. Ren, *Adv. Energy Mater.* 3 (2013) 1195–1200.
- [34] G. Joshi, H. Lee, Y. Lan, X. Wang, G. Zhu, D. Wang, R.W. Gould, D.C. Cuff, M.Y. Tang, M.S. Dresselhaus, *Nano Lett.* 8 (2008) 4670–4674.
- [35] W. Kim, *J. Mater. Chem. C* 3 (2015) 10336.
- [36] B.R. Ortiz, H. Peng, A. Lopez, P.A. Parilla, S. Lany, E.S. Toberer, *Phys. Chem. Chem. Phys.* 17 (2015) 19410–19423.
- [37] Z. Chen, X. Zhang, Y. Pei, *Adv. Mater.* 30 (2018) e1705617.
- [38] X. Tang, W. Xie, H. Li, W. Zhao, Q. Zhang, M. Niino, *Appl. Phys. Lett.* 90 (2007) 012102.
- [39] K.H.L.S.I. Kim, H. Amun, H.S. Kim, S.W. Hwang, J.W. Roh, D.J. Yang, W.H. Shin, X.S. Li, Y.H. Lee, G.J. Snyder, S.W. Kim, *Science* 348 (2015) 109.
- [40] R.F. Brebrick, *J. Phys. Chem. Solids* 30 (1969) 719.
- [41] Z. Stary, J. Horak, M. Stordeur, M. Stolzer, *J. Phys. Chem. Solids* 49 (1988) 29–34.
- [42] T. Thonhauser, G.S. Jeon, G.D. Mahan, J.O. Sofo, *Phys. Rev. B* 68 (2003) 205207.
- [43] J. Navratil, Z. Stary, T. Plechacek, *Mater. Res. Bull.* 31 (1996) 1559.
- [44] W.-S. Liu, Q. Zhang, Y. Lan, S. Chen, X. Yan, Q. Zhang, H. Wang, D. Wang, G. Chen, Z. Ren, *Adv. Energy Mater.* 1 (2011) 577–587.
- [45] L.D. Zhao, B.P. Zhang, J.F. Li, M. Zhou, W.S. Liu, *Phys. B Condens. Matter* 400 (2007) 11–15.
- [46] L.D. Zhao, B.P. Zhang, J.F. Li, H.L. Zhang, W.S. Liu, *Solid State Sci.* 10 (2008) 651–658.
- [47] L.P. Hu, X.H. Liu, H.H. Xie, J.J. Shen, T.J. Zhu, X.B. Zhao, *Acta Mater.* 60 (2012) 4431–4437.
- [48] J. Horak, K. Cermak, L. Koudelka, *J. Phys. Chem. Solids* 47 (1986) 805.
- [49] L. Hu, T. Zhu, X. Liu, X. Zhao, *Adv. Funct. Mater.* 24 (2014) 5211–5218.
- [50] T. Zhu, L. Hu, X. Zhao, J. He, *Adv. Sci.* 3 (2016) 1600004.
- [51] Y. Pan, U. Aydemir, F.-H. Sun, C.-F. Wu, T.C. Chasapis, G.J. Snyder, J.-F. Li, *Adv. Sci.* 4 (2017) 1700259.
- [52] Y. Pan, T.-R. Wei, Q. Cao, J.-F. Li, *Mater. Sci. Eng. B* 197 (2015) 75–81.
- [53] Y. Zheng, Q. Zhang, X. Su, H. Xie, S. Shu, T. Chen, G. Tan, Y. Yan, X. Tang, C. Uher, G.J. Snyder, *Adv. Energy Mater.* 5 (2015) 1401391.
- [54] L. Hu, H. Gao, X. Liu, H. Xie, J. Shen, T. Zhu, X. Zhao, *J. Mater. Chem.* 22 (2012) 16484.
- [55] F. Hao, P. Qiu, Y. Tanga, S. Bai, T. Xing, H.-S. Chu, Q. Zhang, P. Lu, T. Zhang, D. Ren, J. Chen, X. Shi, L. Chen, *Energy Environ. Sci.* 9 (2016) 3120–3127.
- [56] F. Hao, P. Qiu, Q. Song, H. Chen, P. Lu, D. Ren, X. Shi, L. Chen, *Materials* 10 (2017) 251.

- [57] L. Hu, H. Wu, T. Zhu, C. Fu, J. He, P. Ying, X. Zhao, *Adv. Energy Mater.* 5 (2015) 1500411.
- [58] Y. Pan, J.-F. Li, *NPG Asia Mater.* 8 (2016) e275.
- [59] Y. Pan, U. Aydemir, J.A. Grovogui, I.T. Witting, R. Hanus, Y. Xu, J. Wu, C.F. Wu, F.H. Sun, H.L. Zhuang, J.F. Dong, J.F. Li, V.P. Dravid, G.J. Snyder, *Adv. Mater.* 30 (2018) 1802016.
- [60] W. Xie, X. Tang, Y. Yan, Q. Zhang, T.M. Tritt, *Appl. Phys. Lett.* 94 (2009) 102111.
- [61] A. Soni, Y. Shen, M. Yin, Y. Zhao, L. Yu, X. Hu, Z. Dong, K.A. Khor, M.S. Dresselhaus, Q. Xiong, *Nano Lett.* 12 (2012) 4305–4310.
- [62] G.R. Miller, C.-Y. Li, C.W. Spencer, *J. Appl. Phys.* 34 (1963) 1398.
- [63] L.-P. Hu, T.-J. Zhu, Y.-G. Wang, H.-H. Xie, Z.-J. Xu, X.-B. Zhao, *NPG Asia Mater.* 6 (2014) e88.
- [64] C.H. Champness, W.B. Muir, P.T. Chiang, *Can. J. Phys.* 45 (1967) 3611.
- [65] F.D. Rosi, B. Abeles, R.V. Jensen, *J. Phys. Chem. Solids* 10 (1959) 191.
- [66] D.B. Hyun, J.S. Hwang, T.S. Oh, J.D. Shim, N.V. Kolomolets, *J. Phys. Chem. Solids* 59 (1998) 1039–1044.
- [67] T.E. Svechnikova, P.P. Konstantinov, G.T. Alekseeva, *Inorg. Mater.* 36 (2000) 677.
- [68] D.B. Hyun, J.S. Hwang, B.C. You, T.S. Oh, C.W. Hwang, *J. Mater. Sci.* 33 (1998) 5595.
- [69] O.C. Yelgel, G.P. Srivastava, *Phys. Rev. B* 85 (2012) 125207.
- [70] T.A. McCarthy, H.J. Goldsmids, *Energy Convers.* 10 (1970) 125.
- [71] H. Kitagawa, N. Mimura, K. Takimura, S. Morito, K. Kikuchi, *J. Electron. Mater.* 45 (2016) 1523–1528.
- [72] K.H. Lee, S.-M. Choi, S.I. Kim, J.W. Roh, D.J. Yang, W.H. Shin, H.J. Park, K. Lee, S. Hwang, J.H. Lee, H. Mun, S.W. Kim, *Curr. Appl. Phys.* 15 (2015) 190–193.
- [73] K.H. Lee, S.I. Kim, H. Mun, B. Ryu, S.-M. Choi, H.J. Park, S. Hwang, S.W. Kim, *J. Mater. Chem. C* 3 (2015) 10604–10609.
- [74] Z. Xu, H. Wu, T. Zhu, C. Fu, X. Liu, L. Hu, J. He, X. Zhao, *NPG Asia Mater.* 8 (2016) e302.
- [75] M. Volotsky, T. Gudkin, Z. Dashevsky, V. Kaidanov, I. Sgibnev, *Sov. Phys. Semicond.* 8 (1974) 682–683.
- [76] C.J. Vineis, A. Shakouri, A. Majumdar, M.G. Kanatzidis, *Adv. Mater.* 22 (2010) 3970–3980.
- [77] J.-F. Li, Y. Pan, C. Wu, F. Sun, T. Wei, *Sci. China Technol. Sci.* 60 (2017) 1347–1364.
- [78] A.J. Minnich, M.S. Dresselhaus, Z.F. Ren, G. Chen, *Energy Environ. Sci.* 2 (2009) 466.
- [79] J.-F. Li, W.-S. Liu, L.-D. Zhao, M. Zhou, *NPG Asia Mater.* 2 (2010) 152–158.
- [80] H. Mun, S.M. Choi, K.H. Lee, S.W. Kim, *ChemSusChem* 8 (2015) 2312–2326.
- [81] W. Xie, X. Tang, Y. Yan, Q. Zhang, T.M. Tritt, *J. Appl. Phys.* 105 (2009) 113713.
- [82] J.-J. Shen, T.-J. Zhu, X.-B. Zhao, S.-N. Zhang, S.-H. Yang, Z.-Z. Yin, *Energy Environ. Sci.* 3 (2010) 1519–1523.
- [83] W. Xie, J. He, H.J. Kang, X. Tang, S. Zhu, M. Laver, S. Wang, J.R. Copley, C.M. Brown, Q. Zhang, T.M. Tritt, *Nano Lett.* 10 (2010) 3283–3289.
- [84] P. Carruthers, *Phys. Rev.* 114 (1959) 995–1001.
- [85] H.-S. Kim, S.D. Kang, Y. Tang, R. Hanus, G. Jeffrey Snyder, *Mater. Horiz.* 3 (2016) 234–240.
- [86] R. Deng, X. Su, Z. Zheng, W. Liu, Y. Yan, Q. Zhang, V.P. Dravid, C. Uher, M.G. Kanatzidis, X. Tang, *Sci. Adv.* 4 (2018) eaar5606.
- [87] J.-F. Li, J. Liu, *Phys. Status Solidi (a)* 203 (2006) 3768–3773.
- [88] L.-D. Zhao, B.-P. Zhang, J.-F. Li, M. Zhou, W.-S. Liu, J. Liu, *J. Alloys Compd.* 455 (2008) 259–264.

- [89] J. Li, Q. Tan, J.-F. Li, D.-W. Liu, F. Li, Z.-Y. Li, M. Zou, K. Wang, *Adv. Funct. Mater.* 23 (2013) 4317–4323.
- [90] D.-W. Liu, J.-F. Li, C. Chen, B.-P. Zhang, *J. Electron. Mater.* 40 (2010) 992–998.
- [91] X.B. Zhao, X.H. Ji, Y.H. Zhang, T.J. Zhu, J.P. Tu, X.B. Zhang, *Appl. Phys. Lett.* 86 (2005) 062111.
- [92] B. Xu, M.T. Agne, T. Feng, T.C. Chasapis, X. Ruan, Y. Zhou, H. Zheng, J.H. Bahk, M.G. Kanatzidis, G.J. Snyder, Y. Wu, *Adv. Mater.* 29 (2017) 1605140.
- [93] N. Gothard, *Dissertations*, 2008.
- [94] S. Ganguly, C. Zhou, D. Morelli, J. Sakamoto, C. Uher, S.L. Brock, *J. Solid State Chem.* 184 (2011) 3195–3201.
- [95] W. Liu, X. Yan, G. Chen, Z. Ren, *Nano Energy* 1 (2012) 46–52.
- [96] Y. Xiao, G. Chen, H. Qin, M. Wu, Z. Xiao, J. Jiang, J. Xu, H. Jiang, G. Xu, *J. Mater. Chem. A* 2 (2014) 8512.
- [97] Q. Zhang, X. Ai, L. Wang, Y. Chang, W. Luo, W. Jiang, L. Chen, *Adv. Funct. Mater.* 25 (2015) 966–976.

# Thermoelectric properties of skutterudites

2.2

Ctirad Uher

University of Michigan, Ann Arbor, MI, United States

## 2.2.1 Introduction

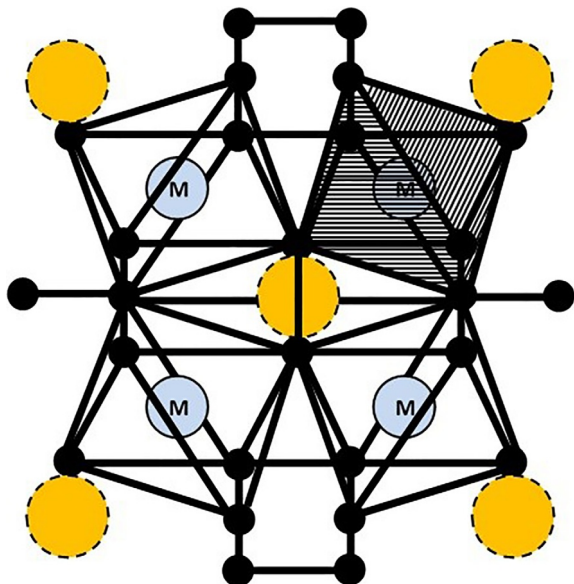
Since 1994, when Slack [1] proposed that the skutterudite structure is an excellent candidate for exploring his phonon-glass electron-crystal (PGEC) concept, skutterudites have gained worldwide attention as one of the most prospective novel thermoelectric materials for efficient power-generating applications in the temperature range between 500 and 900K, where a lot of industrial waste heat is generated. Apart from their premier place in the field of thermoelectricity, the importance and acclaim of skutterudites extend to many other fields. For instance, several members of the skutterudite family display exotic superconducting behavior [2] and varieties of magnetic ground states [3], some of them harbor heavy Fermions [4, 5] and, with minor modifications, the skutterudite structure may even reveal aspects of topological physics [6, 7]. Staying within the realm of thermoelectricity, I will briefly review the structural aspects and different forms of skutterudites, note various synthesis routes to prepare the material, outline the key band structure and phonon dispersion features, give examples of the thermoelectric performance achieved, and describe where we stand in the development of thermoelectric modules based on skutterudites. In this review, it is not possible to capture all aspects of skutterudites, and thus I focus on the more recent developments and provide ample references to works not being covered in more details.

## 2.2.2 Structural forms of skutterudites

### 2.2.2.1 Binary skutterudites

Skutterudites are binary structures with a chemical formula  $\text{MX}_3$ , where M represents column 9 transition metals Co, Rh, and Ir, and X stands for the pnictogen elements P, As, and Sb. Skutterudites crystallize with the body-centered-cubic lattice in the space group  $Im\bar{3}$ , which was first identified by Oftedal in 1928 [8]. The unit cell of the skutterudite structure, centered over a void at (0,0,0), is shown in Fig. 2.2.1. An important structural aspect of skutterudites is an infinite three-dimensional array of slightly distorted and tilted  $\text{MX}_6$  octahedrons that share corners with six neighboring octahedrons. The tilt does two things: it gives rise to the formation of the planar rectangular four-membered rings of pnictogen atoms  $\text{X}_4$ , and it creates a relatively open crystalline

**Fig. 2.2.1** The unit cell of the skutterudite structure centered over a void at (0,0,0). The octahedral coordination of the transition metal M by the pnictogen atoms (black circles) is highlighted by stripes. The tilt of the  $\text{MX}_6$  corner-sharing octahedrons gives rise to the formation of the planar rectangular four-membered pnictogen rings  $\text{X}_4$  arranged in linear arrays along the [100], [010], and [001] crystallographic directions, with adjacent rings being orthogonal to each other.



environment with two large structural voids (often called cages) per unit cell. The structure is fully specified by its lattice parameter  $a$  and the two positional parameters  $y$  and  $z$  that give the exact position of the pnictogen atom on the ring. In terms of the positional parameters and the lattice constant, the sides of the rectangle with pnictogen atoms at its vertices are given as

$$d_1(X-X) = 2az \quad \text{and} \quad d_2(X-X) = a(1-2y) \quad (2.2.1)$$

The ratio  $d_2/d_1$  in binary skutterudites varies between 1.03 and 1.05. Apart from having two other pnictogen atoms as the nearest neighbors, each pnictogen atom X also bonds with two nearest transition metal atoms M. The bond length in this case is

$$D(M-X) = a \left[ \left(\frac{1}{4}\right)^2 + \left(y - \frac{1}{4}\right)^2 + \left(z - \frac{1}{4}\right)^2 \right]^{1/2}. \quad (2.2.2)$$

The pnictogen ring structure  $\text{X}_4$  is held together via  $\sigma$  bonds, where each pentavalent pnictogen atom ( $\text{ns}^2\text{np}^3$ ) contributes two valence electrons, one each to bond with its two nearest X atoms, and the remaining three valence electrons participating in bonding with the two nearest metal atoms M. As there are six pnictogen atoms in octahedral coordination around each M atom, the pnictogen atoms contribute  $(5-2) \times \frac{1}{2} \times 6 = 9$  electrons toward the  $\text{MX}_6$  octahedral complex. This is just a perfect match to engage nine valence electrons of column 9 transition metal ( $\text{d}^7\text{s}^2$ ) to form the 18-electron rare-gas configuration that favors diamagnetism and semiconducting behavior. From the perspective of the metal atom M, it contributes  $6 \times \frac{1}{2} = 3$  electrons for bonding with the six neighboring pnictogen atoms. These electrons form the octahedral  $\text{d}^2\text{sp}^3$  hybrid

orbitals, the essence of the M-X bonding. Since there is no M-M bonding, the transition metal is left with six nonbonding electrons. Because binary skutterudites are all diamagnetic materials, column 9 transition metal M must be in the nonmagnetic state, i.e., having no unpaired electrons. Consequently, the M atom is left in the 3+ state with six nonbonding electrons spin-paired in a zero spin d<sup>6</sup> configuration. This is essentially the bonding scheme proposed originally by Dudkin and Abrikosov [9]. It is also relevant that the electronegativity of pnictogens is very close to that of Co-like metals so that the M-X bond has only a small degree of ionicity.

While all nine MX<sub>3</sub> binary skutterudites with M=Co, Rh, Ir, and X=P, As, Sb can be synthesized, binary skutterudites with Fe-like transition metals do not form in nature, although FeSb<sub>3</sub> was stabilized as a thin film using modulated elemental reaction synthesis [10] and molecular beam epitaxy [11]. NiP<sub>3</sub> has been known to exist since 1910 [12], and its extra delocalized electron leads to metallic conductivity and paramagnetism [13].

The inability to synthesize binary skutterudites with transition metals other than those of column 9 does not mean that a partial replacement of Co by either Fe or Ni cannot be made. Indeed, up to about 10 at.% of Co can be replaced by Ni and perhaps as much as 25 at.% of Fe can substitute for Co in CoSb<sub>3</sub> [14]. Even as little as 0.5 at.% of Fe has a profound impact on the transport, causing the structure to become metallic [15]. Arsenide skutterudites are more tolerant to Ni than to Fe and can accommodate as much as 65 at.% of Ni compared to just 16 at.% of Fe [16]. An interesting symmetrical substitution, where two Co atoms are replaced by an atom each of Fe and Ni, is also possible. In this case, the total number of electrons is preserved, and all ions are in the low-spin d<sup>6</sup> configuration, making such Fe<sub>0.5</sub>Ni<sub>0.5</sub>X<sub>3</sub> a diamagnetic solid [17–19]. In addition, one can form solid solutions between binary skutterudites, with some of them forming complete series, such as CoP<sub>3-x</sub>As<sub>x</sub> [20]. Unfortunately, the solid solutions more relevant to thermoelectricity, such as CoAs<sub>3-x</sub>Sb<sub>x</sub> [20] and Co<sub>1-x</sub>Ir<sub>x</sub>Sb<sub>3</sub> [21], are more restrictive with miscibility gaps of 0.4 < x < 2.8 and 0.2 < x < 0.65, respectively.

### 2.2.2.2 Ternary skutterudites

Ternary skutterudites are man-made modifications of binary skutterudites. The aim here is to make isoelectronic substitutions (keeping the valence electron count at 72) on either the cation site by a pair of elements from columns 8 and 10, forming, e.g., Fe<sub>0.5</sub>Ni<sub>0.5</sub>Sb<sub>3</sub> [22], or at the anion site with a pair of elements from columns 14 (Ge, Sn) and 16 (S, Se, Te), forming, e.g., CoGe<sub>1.5</sub>Se<sub>1.5</sub> [23]. It is also possible to substitute simultaneously on both the cation and anion sites and form Fe<sub>4</sub>Sb<sub>8</sub>Te<sub>4</sub>≡FeSb<sub>2</sub>Te by replacing divalent Fe for trivalent Co and compensating for it on the anion site by replacing one pentavalent Sb atom with a hexavalent Te atom [24]. In an extreme case, one can consider partial substitutions on both cation and anion sites, such as forming PtSn<sub>1.2</sub>Sb<sub>1.8</sub> from IrSb<sub>3</sub> [25].

In general, making isoelectronic substitutions on the cation site fully preserves the cubic structure and, apart from a somewhat larger lattice parameter, the band structure of such ternary skutterudites is not significantly different from the corresponding

binary skutterudites. In contrast, making isoelectronic substitutions on the anion site leads to more impacting structural changes. First of all, the homogeneous environment of the pnictogen rings of binary skutterudites suffers a major disruption as it must now accommodate two foreign atoms, one from column 14 and one from column 16. This gives rise to two crystallographically distinct and distorted four-membered rings, which lowers the symmetry of the structure from cubic to rhombohedral with the space group  $R\bar{3}$  [26, 27]. Many reports have depicted the ternary skutterudites, such as  $\text{IrGe}_{1.5}\text{S}_{1.5}$  and  $\text{RhSn}_{1.5}\text{Te}_{1.5}$ , as single-phase structures [28–30]. High-resolution powder neutron diffraction studies [31] have cast doubt on such claims, revealing the presence of up to 10 at.%  $\text{IrGe}$  and  $\text{RhTe}_2$ .

Many kinds of ternary skutterudites have been synthesized over the years and, as such, have greatly expanded the family of skutterudites. From the perspective of thermoelectricity, the main goal has always been to degrade the otherwise high thermal conductivity of binary skutterudites by enhancing phonon scattering on the alloy disorder. While this has, indeed, been accomplished, the same disorder has unfortunately even greater impact on electronic transport, and no ternary skutterudite has, as yet, emerged as a prospective thermoelectric material.

### 2.2.2.3 Skutterudites filled with electropositive fillers

The large structural voids arising from the tilting of the  $\text{MX}_6$  octahedrons can be filled with a variety of species, resulting in filled skutterudites, which were first synthesized by Jeitschko and Braun in 1977 [32] in the form of phosphide skutterudites. Shortly after, filled skutterudites with arsenide-based [33] and antimode-based [34] frameworks were also prepared. Until 1995, when Slack identified filled skutterudites as candidates for his PGEC concept, the structures remained more or less esoteric, albeit intriguing, compounds displaying surprising physical properties, most notably superconductivity with a rather high transition temperature above 10K in the case of  $\text{LaRu}_4\text{As}_{12}$  [35]. Acting on the idea of Slack, the same year Morelli and Meissner [36] verified that the presence of a filler, indeed, dramatically suppresses the lattice thermal conductivity of skutterudites. Soon after, Sales et al. [37] correlated the low lattice thermal conductivity of filled skutterudites with an exceptionally large atomic displacement parameter of the filler, documenting that the reduction in the thermal conductivity is tied with the “rattling” nature of the filler species within the skutterudite structural voids. From then on, thermoelectric aspects of skutterudites have received intense worldwide attention.

With column 9 transition metal in the  $[\text{M}_4\text{X}_{12}]$  framework, such as filled skutterudites of the from  $\text{R}_y\text{Co}_4\text{Sb}_{12}$ , the fillers R entering as electropositive ions very quickly saturate the structure electronically, resulting in considerably less than full void occupancy,  $y << 1$ . Filling fraction limits for various fillers in the  $[\text{Co}_4\text{Sb}_{12}]$  framework are listed in Table 2.2.1.

If higher void occupancies are desired, one must charge compensate. The most effective in this sense is a partial or complete replacement of column 9 transition metal M with a column 8 Fe-like transition metal T, forming  $\text{RCo}_{4-x}\text{Fe}_x\text{Sb}_{12}$  structures. It is

**Table 2.2.1** Filling fractions of various fillers in the framework of CoSb<sub>3</sub> with relevant references.

<b>Na</b>	<b>K</b>	<b>Rb</b>	<b>Ca</b>	<b>Sr</b>	<b>Ba</b>	<b>La</b>	<b>Ce</b>	<b>Nd</b>	<b>Eu</b>	<b>Yb</b>	<b>Ga</b>	<b>In</b>	<b>Tl</b>	<b>Sn</b>
0.65 [38]	0.60 [39]	0.25 [39]	0.20 [40]	0.40 [41]	0.45 [42]	0.23 [43]	0.09 [44]	0.13 [45]	0.44 [46]	0.25 [47]	0.02 [48]	0.22 [49]	0.22 [50]	1.0 [51]

important to recognize that in this case, it is not the neutral  $[M_4X_{12}] = [MX_3]$  framework of binary skutterudites but the charged complex  $[T_4X_{12}]^{4-}$  that forms the basis of filled skutterudites. Since only U and Th form  $R^{4+}$  ions in skutterudites, all other filled skutterudites  $R_yT_4X_{12}$  have the valence electron count smaller than 72 and are paramagnetic metals, unless magnetic interactions set in at low temperatures or the structure becomes a superconductor. For thermoelectricity, this is not an optimal situation as metals tend to have rather small Seebeck coefficients. To bring the skutterudite back into the realm of semiconductors with the electron count of 72, the structure must be charge compensated. The charge compensation can be done either on the pnictogen rings by substituting column 14 elements Ge or Sn, or at the site of Fe-like metal. Such substitutions, carried in the spirit of the Zintl concept, not only greatly expand the scope of skutterudites but also give rise to a plethora of fascinating physical properties that go well beyond thermoelectric applications [52].

During the late 1990s, the focus centered on finding the most effective filler species that can reduce the relatively large thermal conductivity of binary skutterudites. On account of its intermediate valence between  $2+$  and  $3+$ , and thus somewhat higher void occupancy, coupled with its rather heavy mass, Yb was identified as one of the most effective fillers [53–58] to degrade the thermal conductivity. The actual void occupancy by Yb has been obviously of intense interest, and it was shown [59] that it depends on the annealing conditions, with higher annealing temperatures ( $\sim 800^\circ\text{C}$ ) for an extended period of time (7 days) resulting in significantly increased occupancy reaching 40%. Moreover, ball milling followed by hot pressing was shown [60] to lead to occupancies approaching 50%, the value achieved previously by charge compensating on the site of Sb with Sn [61] or Ge [62]. To rationalize such a wide range of void occupancies by Yb, Tang et al. [63] carried out a detailed evaluation of the equilibrium isothermal section of the phase diagram of Yb-Co-Sb at various temperatures and verified a strong dependence of the filling fraction of Yb on the temperature and on the initial stoichiometry of Co and Sb. It was also shown that, in general, the filler occupancies can be greatly enhanced, and species unable to fill the voids under ambient pressure syntheses can do so using high-pressure synthesis [64–66].

By picturing rattling of a filler as an independent Einstein-like oscillator of a fixed frequency that resonantly disturbs normal phonon modes of the structure, it was soon recognized and experimentally verified that multiple filling is more effective than filling with a single type of atom [67–69]. By modeling rattling of a filler as a mass  $m$  attached at the end of a spring with the spring constant  $k$  that makes displacements  $x$  from the center position of the void, Yang et al. [70] calculated rattling frequencies  $\omega_0 = (k/m)^{1/2}$  for numerous filler species. The wide range of frequencies spanning from  $42\text{ cm}^{-1}$  for the heavy ytterbium to  $141\text{ cm}^{-1}$  for the light potassium provided further impetus for multifilling studies. Thus, while with single filled skutterudites the highest values of the dimensionless thermoelectric figure of merit  $ZT$  cluster around unity with occasional reports of  $ZT \sim 1.2$  [49, 71] and exceptionally 1.5 [72], the carefully chosen double-filling combinations raise the  $ZT$  to a range of 1.3–1.4 [73–76], and several notable triple-filling attempts [77–80] have culminated in the record-high  $ZT = 1.7$  for  $\text{Ba}_{0.08}\text{La}_{0.05}\text{Yb}_{0.04}\text{Co}_4\text{Sb}_{12}$  [81]. Comparable  $ZT$  values for n-type skutterudites were also obtained by filling the  $[\text{Co}_4\text{Sb}_{12}]$  framework with Mischmetal

(commercially available mixture of rare earth elements consisting of 50.8% Ce, 28.1% La, 16.1% Nd, and 5.0% Pr) in combination with Sm [82]. Moreover, filling with didymium (commercially available 4.76 mass% of Pr with 95.24 mass% of Nd and designated as DD) in combination with Ba and Yb, and with the assistance of applied high-pressure torsion (HPT) that generates severe plastic deformation with enhanced dislocation density, a much increased number of grain boundaries, and a greatly reduced crystallite size, the value was further enhanced to  $ZT \sim 1.9$  [83]. For p-type skutterudites, the highest reported  $ZT \sim 1.3$  was obtained for  $DD_{0.70}Fe_{2.7}Co_{1.3}Sb_{11.8-Sn_{0.2}}$  [84]. Previously synthesized p-type  $DD_{0.60}Fe_3CoSb_{12}$  subjected to HPT was claimed to reach  $ZT \sim 1.4$  [85].

It has been assumed that filling voids in binary skutterudites is a random process. While this is likely true at low filling fractions, ab initio calculations combined with the cluster expansion method by Kim et al. [86] have shown that in  $Ba_xCo_4Sb_{12}$  at higher filling fractions, the interaction between filler species may overcome entropy, and the filler species partially order. The presence of order-disorder phase transitions and the two-phase mixture for  $0.25 < x < 0.50$  was confirmed by positron annihilation measurements by Zhang et al. [87] and has implications on the thermal conductivity.

Beyond the obvious geometrical constraints that the filler ion must be smaller than the void radius but not too small so that it can establish bonding (albeit weak) with the pnictogen atoms, are there some fundamental reasons, why certain species can fill the voids while others cannot? The early theoretical studies of filling concerned specific fillers, such as La, Y, and Sc in  $CoP_3$  [88], and addressed the dual aspect of Sn that can act as a filler as well as substitute for Sb [89]. The key question concerning the universal criterion for filling had to wait for the detailed DFT studies of the filling fraction limit by Shi et al. [90, 91], which established that a filler R should be able to enter the void in  $CoSb_3$  if its Pauling electronegativity  $x_R$  with respect to the electronegativity of Sb (2.05) satisfies

$$x_{Sb} - x_R > 0.80. \quad (2.2.3)$$

Since the calculations assumed absolute zero temperature, the numerical value might be slightly altered by temperature effects. Nevertheless, at least for rare earth, alkaline earth, and some alkali metal fillers (Na, K, Rb), the agreement with the experimental results is excellent. The largest and the smallest alkali metal atoms, Cs and Li, could not be synthesized at that time. Cs is nearly the size as the void, while Li is too small to establish bonding with Sb. However, upon applying high pressures of 3–4 GPa for a couple of hours at 1073 K,  $Li_xCo_4Sb_{12}$  with up to  $x = 0.4$  was successfully prepared later [66].

The filling criterion in Eq. (2.2.3) fails miserably in the case of column 13 elements Ga, In, and Tl, which, with their Pauling electronegativities of 1.81, 1.78, and 2.04, respectively, should not be able to fill the voids of  $CoSb_3$ . Yet, they undoubtedly enter the skutterudite voids and, in the case of Tl, with a rather large filling fraction of 20%–25% [50, 92]. Filling of Ga and In comes with a surprising twist, as both Ga and In behave as amphoteric impurities, meaning that they act as both donors and acceptors depending on the lattice site they enter [48, 93]. The filling limit of Ga

is, however, very low. Indium was originally believed to have maximum occupancy of  $y=0.22$  [49, 94], later extended to  $y=0.26$  [95]. However, it was also noted that  $\text{Ce}_x\text{In}_y\text{Co}_4\text{Sb}_{12}$  with the indium content less than  $y=0.15$  [76], and  $\text{Yb}_x\text{In}_y\text{Co}_4\text{Sb}_{12}$  with indium less than  $y=0.20$  [77], both contained an InSb impurity phase, suggesting that the filling fraction limit of In might be considerably smaller than  $y=0.22$ . Indeed, indium was found at the grain boundaries when its nominal content approached 20 at. % [96, 97]. Studying phase relations in the In-Co-Sb system, Grytsiv et al. [98] reported that there are actually two solubility limits for indium in  $\text{In}_y\text{Co}_4\text{Sb}_{12}$ , depending on the exact Co/Sb ratio in the starting composition. Such a seemingly conflicting result was placed into a proper perspective by Tang et al. [99], who studied the ternary In-Co-Sb phase diagram in the proximity of  $\text{CoSb}_3$  by DFT calculations that were supported by experiment. They confirmed the dual character of In, but unlike the case of Ga, indium donates a single electron when it enters a void, while when it substitutes for Sb, the skutterudite becomes deficient by two electrons per In atom. In other words, the perfectly charge-balanced skutterudite is  $\text{In}_{2y/3}\text{Co}_4\text{Sb}_{12-y/3}(\text{InSb})_{y/3}$ .

#### **2.2.2.4 Skutterudites with the $[\text{Pt}_4\text{Ge}_{12}]$ framework**

Within a week of each other in 2007, two research groups [100, 101] submitted their discovery of an entirely new skutterudite framework based on the  $[\text{Pt}_4\text{Ge}_{12}]$  polyanion. The role of the filler species here is to transfer the charge to the polyanion and thus stabilize the structure. Apart from the voids of the new framework being somewhat smaller than the voids in  $\text{CoSb}_3$ , the fundamental structural aspects of the new filled skutterudites are essentially identical with the pnictogen-based skutterudites. Table 2.2.2 illustrates the key structural parameters of several filled skutterudites having the  $[\text{Pt}_4\text{Ge}_{12}]$  framework.

Although the  $\text{APt}_4\text{Ge}_{12}$  skutterudites display a plethora of fascinating physical properties, including unusual forms of superconductivity, different magnetic ground states, and heavy Fermion character, in my opinion, they will not make a significant impact as thermoelectric materials because of the high cost of platinum and germanium.

#### **2.2.2.5 Skutterudites filled with electronegative fillers**

So far, all filler species in  $\text{RT}_4\text{X}_{12}$  and  $\text{RPt}_4\text{Ge}_{12}$  skutterudites were electron donors (cations) supplying electrons to the respective frameworks to stabilize the structure. In 2010, Fukuoka and Yamanaka [106] reported that they filled  $\text{RhSb}_3$  with iodine to a remarkably high 95% void occupancy and, rather than transferring electrons to the framework, the iodine drew electrons from the framework, i.e., it acted as an electronegative (acceptor) filler with the valence  $1^-$ . In principle, such electronegative fillers are appealing as they make the structure naturally p-type with no need to charge compensate to counteract electrons generated by the usual filling with electropositive fillers. A potential benefit is thus much-reduced charge carrier scattering on the structural disorder as no chemical adjustments on the framework need be made. Structural analysis of  $\text{IRh}_4\text{Sb}_{12}$  indicated that while the Rh—Sb bond length is essentially

**Table 2.2.2** Lattice constant  $a$ , interatomic distances, cage radius, all in Å, and the ratio of the cage radius to the filler' ion radius for several RPt<sub>4</sub>Ge<sub>12</sub> skutterudites.

	SrPt <sub>4</sub> Ge <sub>12</sub>	BaPt <sub>4</sub> Ge <sub>12</sub>	LaPt <sub>4</sub> Ge <sub>12</sub>	CePt <sub>4</sub> Ge <sub>12</sub>	PrPt <sub>4</sub> Ge <sub>12</sub>	NdPt <sub>4</sub> Ge <sub>12</sub>	EuPt <sub>4</sub> Ge <sub>12</sub>	ThPt <sub>4</sub> Ge <sub>12</sub>	UPt <sub>4</sub> Ge <sub>12</sub>
$a$	8.6509	8.6838	8.6235	8.610	8.6111	8.602	8.6435	8.5931	8.5887
R-Ge	3.3468	3.3706	3.3290	3.3207	3.3175	3.3142	3.3289	3.321	3.2927
Pt-Ge	2.4983	2.5050	2.4870	2.4843	2.4828	2.4814	2.4899	2.481	2.4729
$d_1$	2.5052	2.4906	2.5014	2.5077	2.5090	2.5112	2.5140	2.482	2.528
$d_2$	2.6309	2.6623	2.6169	2.6081	2.6052	2.6022	2.6150	2.604	2.584
$r_{\text{cage}}$	2.06	2.08	2.05	2.04	2.04	2.04	2.05	2.05	2.01
$r_{\text{cage}}/r_{\text{ion}}$	1.64	1.51	1.77	1.79	1.81	1.84	1.71	1.95	2.01

Most of the entries are from the data of Gumeniuk et al. [102]. The data for SrPt<sub>4</sub>Ge<sub>12</sub> are from Bauer et al. [100], and the data for ThPt<sub>4</sub>Ge<sub>12</sub> and UPt<sub>4</sub>Ge<sub>12</sub> are from Bauer et al. [103]. Lattice constants of CePt<sub>4</sub>Ge<sub>12</sub> and NdPt<sub>4</sub>Ge<sub>12</sub> are from Toda et al. [104] and that of EuPt<sub>4</sub>Ge<sub>12</sub> from Grytsiv et al. [105].

unchanged (2.63 Å in  $\text{IRh}_4\text{Sb}_{12}$  versus 2.621 Å in  $\text{RhSb}_3$ ), the  $[\text{Sb}]_4$  ring distances  $d_1 = 2.88$  Å and  $d_2 = 2.96$  Å were somewhat longer than in  $\text{RhSb}_3$  ( $d_1 = 2.80$  Å and  $d_2 = 2.92$  Å). Likewise, the I—Sb bond length of 3.48 Å was slightly larger than in a typical rare earth-filled  $\text{LaFe}_4\text{Sb}_{12}$  (3.41 Å) or alkaline earth-filled  $\text{BaFe}_4\text{Sb}_{12}$  (3.46 Å). X-ray photoelectron spectroscopy confirmed the oxidation state of iodine as 1<sup>-</sup>. No signs of any phase transition were detected down to 2 K of the otherwise metallic electrical resistivity.

As expected, such a surprising discovery was followed by several other attempts to synthesize skutterudites with electronegative fillers. The first in line was Li et al. [107], who showed that high pressure can trap iodine also in  $\text{CoSb}_3$ . Trying nominal iodine contents  $y = 0.4$ , 0.8, and 1.2 returned the actual filling fractions of 0.13, 0.72, and 0.79. Thus, the maximum iodine occupancy in  $\text{CoSb}_3$  is about 0.8, still a very high filling fraction. In a subsequent study, the same research team [108] explored the interplay between the filling fraction of iodine  $y$  and the content of Fe in  $\text{I}_y\text{Fe}_x\text{Co}_{4-x}\text{Sb}_{12}$ . Although an electronegative iodine filler is an exciting discovery, two aspects make it questionable whether it could become a useful thermoelectric: an expensive and difficult to scale synthesis relying on high-pressure apparatus, and the thermally unstable nature of the structure that decomposes at temperatures where one would expect skutterudites to operate. Perhaps other halides might fare better, and in this regard, Ortiz et al. [109] synthesized bromine-filled  $\text{Br}_y\text{CoSb}_4\text{Sb}_{12}$  with the filling fraction of  $y = 0.40$  under a more manageable pressure of 80 MPa. Duan et al. [110] succeeded in filling  $\text{CoSb}_3$  with Cl and, surprisingly, with S and Se, all acting as electronegative fillers. Most recently, Te was successfully entered into voids of the  $\text{Co}_4\text{Sb}_{12}$  framework under high pressure as an electronegative filler, acting electronically opposite to its usual donor role when substituting for Sb at 24 g sites [111].

### 2.2.2.6 Composite skutterudites

Composite skutterudites can be divided into two classes: intrinsic composites that form in situ as a result of segregation of secondary phases due to large deviations in stoichiometry or due to rapid quenching; and extrinsic composites prepared by intentionally adding unrelated phases into the skutterudite matrix. The intent to form composites stems from a desire to maximize phonon scattering to lower the lattice thermal conductivity. In some instances, there is an opportunity to enhance the Seebeck coefficient due to energy-dependent scattering of electrons (energy filtering) at the interface of nanoinclusions and the matrix, provided the barrier is optimized. Both types of composites are richly documented in the literature.

#### 2.2.2.6.1 Intrinsic skutterudite composites

The early work concerned the formation of  $\text{FeSb}_2$  in  $\text{Co}_{1-x}\text{Fe}_x\text{Sb}_3$  when  $x > 0.25$  [112], and  $\text{NiSb}_2$  (actually NiSb and Sb as  $\text{NiSb}_2$  decomposed) in  $\text{Co}_{1-x}\text{Ni}_x\text{Sb}_3$  [113] when  $x > 0.1$ . Later, composites based on the ternary skutterudite matrix  $\text{FeSb}_2\text{Te}$  were studied where the formation of the secondary InSb phase was promoted [114, 115], and the  $ZT$  as high as 0.76 was achieved at 800 K, some 15% higher than

the structure with no second phase. Filled skutterudites offer an additional route to form intrinsic composites by using overstoichiometric amounts of the filler that can be oxidized [57, 116], form secondary phases [76, 117–119], or are expelled upon cooling [120, 121]. Here I wish to mention two composites. One formed by triple-filled  $\text{Sr}_{0.09}\text{Ba}_{0.11}\text{Yb}_{0.05}\text{Co}_4\text{Sb}_{12}$  with the in situ-formed  $\text{Yb}_2\text{O}_3$  phase due to an intentional excess of Yb in the starting composition. The composite attained  $ZT=1.6$  at 838 K, which was enhanced to  $ZT=1.9$  upon applying severe plastic deformation by high-pressure torsion [82]. The second composite was prepared using a grossly indium-overstoichiometric starting composition  $\text{In}_1\text{Co}_4\text{Sb}_{12}$  with some 10 at.% excess of Sb, which resulted in an in situ-formed InSb phase that strongly enhanced the electrical conductivity and decreased the thermal conductivity, yielding  $ZT=1.5$  at 725 K, the highest figure of merit for a single-filled skutterudite [72].

#### 2.2.2.6.2 Extrinsic skutterudite composites

The first extrinsic skutterudite composite consisted of dispersing a powder  $\text{FeSb}_2$  in a matrix of  $\text{CoSb}_3$  by long-term (up to 40 h) ball milling [122, 123], which yielded  $ZT=0.46$  at 756 K, far exceeding the maximum  $ZT$  of similarly prepared  $\text{CoSb}_3$ . The work was followed by dispersing nanoparticles of oxides, including, among others,  $\text{MoO}_2$ ,  $\text{WO}_2$ , and  $\text{Al}_2\text{O}_3$  [124],  $\text{ZnO}$  [125],  $\text{ZrO}_2$  [126, 127], and  $\text{CeO}_2$  [128] in  $\text{CoSb}_3$ ,  $\text{TiO}_2$  in  $\text{Ba}_{0.22}\text{Co}_4\text{Sb}_{12}$  [129, 130], and  $\text{CeO}_2$  in  $\text{In}_{0.25}\text{Co}_4\text{Sb}_{12}$  [131]. Apart from insulating oxides, semiconducting and metallic nanoparticles were frequently used as additives in  $\text{CoSb}_3$ , including  $\text{NiSb}$  [113],  $\text{PbTe}$  [132],  $\text{WTe}_2$  [133], carbon-based particles, such as  $\text{C}_{60}$  [134], graphene [135], multiwalled carbon nanotubes in  $\text{La}_{0.3}\text{Co}_4\text{Sb}_{12}$  [136], and Ag nanoparticles in  $\text{Ba}_{0.3}\text{Co}_4\text{Sb}_{12}$  [137, 138]. Finally, there are several reports on dispersing  $\text{CoSb}_3$  nanoparticles in the micron-sized  $\text{CoSb}_3$  matrix [139–141] or its filled skutterudite matrix [142, 143]. While in all cases the thermal conductivity of composite structures was reduced below the value of the thermal conductivity of the matrix, a major gain in the figure of merit was not always materialized, as the electronic transport suffered comparable damage. In the case of “homo” composites formed by dispersing a  $\text{CoSb}_3$  nanophasse in the larger grain size  $\text{CoSb}_3$  matrix, rigorous annealing studies are needed to assess the stability of such composites, as the nanophasse might ripen or perhaps even dissolve in the matrix when exposed to elevated temperatures for long periods of time.

### 2.2.3 Synthesis of skutterudites

Skutterudites are the highest pnictogen-content compounds that form by fusing with the transition metals. However, the reaction is of the peritectic nature, i.e., the skutterudite phase cannot be accessed by cooling the equilibrium melt. Rather, it is obtained in a peritectic reaction (at 873°C in the case of  $\text{CoSb}_3$ ) from the  $\text{CoSb}_2$  phase and the liquid phase [144]. Since the kinetics are very slow, the peritectic reaction is not fully completed, and long-term annealing (several days to a couple of weeks) is

needed to obtain the skutterudite phase. Over the years, numerous synthesis approaches have been explored. The early favored method to prepare  $\text{CoSb}_3$  was dissolving stoichiometric quantities of cobalt in antimony, cooling the material to room temperature, and annealing for a week or two [145, 146]. Full density was achieved by hot pressing the crushed powder. Single crystals can be prepared by any one of the following methods: growing from nonstoichiometric melts [147]; by flux-assisted growth using molten fluxes such as Sn [12, 148–150] or Sb where, in the latter case, the flux is a constituent of the skutterudite [151], or, in the case of arsenide skutterudites, by lowering the melting point of As (pressures over 3.5 MPa at its melting point of 817°C!) by adding Cd [152]; and by rather slow and size-limited chemical vapor transport [153]. There are also rapid fabrication techniques available, such as melt-spinning [154–156], melt atomizing [157], microwave-assisted synthesis [158, 159], self-propagating high-temperature synthesis [160, 161], selective laser melting [162], and hydrothermal growth of nanometer-size powders [163–172]. Interestingly, the very popular and versatile ball milling does not directly fuse the elemental powders into the skutterudite phase even after more than 50 h of milling [173, 174]. However, the skutterudite phase forms easily during the consolidation of the resulting fine-grained powder by SPS. A special fabrication process is high-pressure synthesis. It serves well in the preparation of skutterudites that are difficult or cannot be formed via conventional techniques at ambient pressure [51, 64–66, 175, 176], it tends to enhance the occupancy of voids [177], and it was essential in the synthesis of skutterudites with electronegative fillers [106].

Thin film forms of skutterudites have been prepared by DC and RF sputtering [178–185], including multilayer sputtering followed by annealing [186, 187], co-deposition of Co and Sb [188], and deposition of partially Yb-filled  $\text{CoSb}_3$  [189]; by electron beam evaporation [190]; by pulsed laser deposition [191–194], including deposition of filled skutterudites [195–197], and noting a strong influence of the laser wavelength on the formation and quality of the deposited films [198, 199]; by modulated elemental reaction method [10, 200, 201] with special emphasis on preparing thin films of  $\text{FeSb}_3$  [202–204], the structure that does not exist in nature nor can be synthesized in bulk form; by MBE deposition of  $\text{CoSb}_3$  [205, 206],  $\text{FeSb}_3$  [11], and  $\text{Y}_{y}\text{Co}_4\text{Sb}_{12}$  with  $0 < y < 0.27$  [207]; and by electrodeposition. Although electrodeposition of skutterudites is hampered by the vastly different reduction potentials of cobalt and antimony [208], quasi-one-dimensional wires of  $\text{CoSb}_3$  in porous anodic aluminum oxide templates were prepared [209–211] and so were thin films of  $\text{CoSb}_3$  [212, 213] from aqueous solutions using the basic recipe developed by Sadana and Kumar [214] and from ethylene glycol-based electrolyte [215]. Electrodeposition of  $\text{CoP}_3$  from molten salts was documented [216], but it requires rather high temperatures ( $\sim 700^\circ\text{C}$ ). In all cases of thin film deposition, the thermal expansion coefficient of the film and substrate should be similar, otherwise cracking of the film will happen upon annealing or during measurements at elevated temperatures. With the linear thermal expansion coefficient of skutterudites in the range  $(8.5\text{--}9.1) \times 10^{-6} \text{ K}^{-1}$  [217], there is no usual substrate that perfectly matches. In fact, the often used thermally oxidized Si is a particularly poor choice as its thermal expansion is only  $2.6 \times 10^{-6} \text{ K}^{-1}$ .

Another issue with thin films is their thermal stability at elevated temperatures. In general, thin films of  $\text{CoSb}_3$  start to decompose at temperatures some 200°C lower than their bulk forms. Films having a slight overstoichiometry of Sb fair somewhat better than Co-rich films [218].  $\text{FeSb}_3$  thin films prepared by the modulated elemental reaction synthesis decomposed above 500°C [10].

## 2.2.4 Electronic energy bands

### 2.2.4.1 Binary skutterudites

Calculations of the electronic energy band structure must reflect the key structural features of binary skutterudites, namely the octahedral coordination of transition metal M and the near-square planar configuration of pnictogen rings  $X_4$ . Until the early 1990s, self-consistent band structure calculations of skutterudites were considered too difficult. With the improved algorithms, Singh and Pickett [219] calculated the band structure of  $\text{CoSb}_3$ ,  $\text{IrSb}_3$ , and  $\text{CoAs}_3$  within the local-density approximation (LDA) using an extended general-potential linearized augmented-plane-wave (LAPW) method. The results for  $\text{CoSb}_3$  are shown in Fig. 2.2.2 and reveal two important aspects: a clear separation between the valence and conduction band manifolds, referred to as a pseudogap, and a single band crossing the gap and touching (or nearly so) the triply degenerate conduction band minimum at  $\Gamma$ . Both the valence and conduction bands derive from hybridized combinations of transition metal d-states and pnictogen p-states. The single gap-crossing band in  $\text{CoSb}_3$  and  $\text{IrSb}_3$

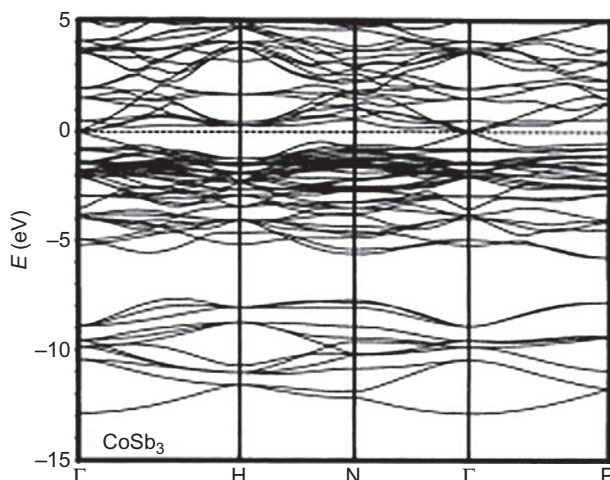


**Fig. 2.2.2** Scalar relativistic electronic energy band structure of  $\text{CoSb}_3$ .

Reproduced from D.J. Singh, W.E. Pickett, Phys. Rev. B 50 (1994) 11235. With permission from the American Physical Society.

has remarkable properties in that it features linear dispersion over most of the zone. As a consequence, the Seebeck coefficient within the constant relaxation time approximation becomes

$$S = - \left( \frac{2\pi k_B^2 T}{3e\alpha} \right) \left( \frac{\pi}{3n} \right)^{1/3}, \quad (2.2.4)$$

where  $\alpha = -3.10 \text{ eV}\text{\AA}$  is the slope of the linearly dispersing region and  $n$  is the carrier concentration. The weaker doping dependence of the Seebeck coefficient compared to the usual parabolically dispersing band makes it more challenging to optimize the power factor. Using ever more sophisticated algorithms and treatments of the exchange-correlation potential, the band structure of  $\text{CoSb}_3$  was described in numerous subsequent publications [220–242]. Although minor details can be noted, particularly a very wide range of bandgap values from 0.003 eV [224] to 0.66 eV [231], depending on the degree of hybridization between p-states of Sb on the ring, the choice of the exchange-correlation functional, and whether one adopts the optimized or measured lattice parameters, the bands themselves do not change much in different calculations. I like to highlight two theoretical works that had a particularly strong influence on the study of transport properties of  $\text{CoSb}_3$ . The first one describes calculations of the electronic transport parameters based on the DFT-derived band structure by Chaput et al. [229] that documented the validity of the rigid band model upon doping  $\text{CoSb}_3$ , clarified the use of the free-electron formula for the carrier concentration based on measurements of the Hall effect and showed that a more appropriate Lorenz number (a parameter used to evaluate the electronic thermal conductivity from measurements of the electrical conductivity via the Wiedemann-Franz law) for  $\text{CoSb}_3$  has a value of  $2 \times 10^{-8} \text{ V}^2 \text{ K}^{-2}$  rather than the metallic (Sommerfeld) value of  $2.45 \times 10^{-8} \text{ V}^2 \text{ K}^{-2}$ . As the lattice thermal conductivity  $\kappa_L$  is invariably assessed by subtracting the electronic thermal conductivity  $\kappa_e$  from the total measured thermal conductivity,  $\kappa_L = \kappa - \kappa_e$ , using the Sommerfeld value significantly underestimates the lattice thermal conductivity. The other report is by Tang et al. [240] and points out the importance of multivalley bands in  $\text{CoSb}_3$  (the conduction band at  $\Gamma$  being triply degenerate, and one of the bands having a higher-lying minimum along the  $\Gamma$ -N direction about 0.11 eV above the main conduction band edge) and their convergence at elevated temperatures, Fig. 2.2.3. The authors argued that it is this multiband nature of conduction bands that explains the high values of the Seebeck coefficient even at high electron concentrations. This arises as a consequence of a dramatically increased number of electron conduction valleys (the original  $N_v = 3$  augmented by  $N_v = 12$ ) as the secondary conduction band converges with the primary ( $\Gamma$  point) conduction band upon increasing the temperature. The convergence was documented by the temperature-dependent optical absorption in the range 300–700 K.

Band structures of other binary skutterudites can be found in Refs. [6, 224, 241–245] for semiconducting  $\text{RhSb}_3$ , in Refs. [219, 224, 241, 243, 246] for semiconducting  $\text{IrSb}_3$ , in Refs. [219, 224, 241] for semiconducting  $\text{CoAs}_3$ , in Refs. [224, 241] for semiconducting  $\text{RhAs}_3$ , in Refs. [224, 241] for semiconducting  $\text{IrAs}_3$ , in Refs. [80, 225, 241, 244, 247–249] for metallic  $\text{CoP}_3$ , in Refs. [224, 241] for

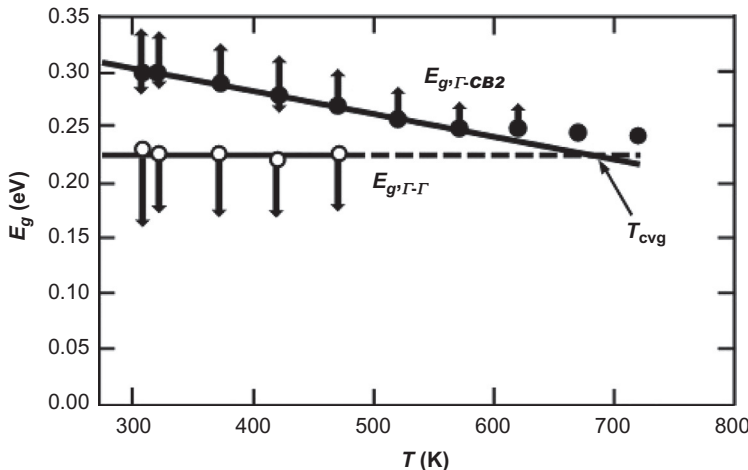


**Fig. 2.2.3** Temperature-dependent bandgap for the direct  $E_{g,\Gamma-\Gamma}$  and indirect  $E_{g,\Gamma-CB2}$  transitions indicating band convergence of conduction bands in  $\text{CoSb}_3$  near 700 K as determined from optical absorption edge measurements [239]. Since the interpretation of such measurements might be affected by defect states, error bars indicate the spread of uncertainties arising from the optical determination of the bandgap values in both transitions measured on numerous doped samples as well as Yb- and Na-filled  $\text{CoSb}_3$ .

The graph is constructed from the data of Y. Tang, Z.M. Gibbs, L.A. Agapito, G.D. Li, H.-S. Kim, M.B. Nardelli, S. Curtarolo, G.J. Snyder, Nat. Mater. 14 (2015) 1223.

metallic  $\text{RhP}_3$ , in Refs. [224, 241] for semiconducting  $\text{IrP}_3$ , and in Refs. [224, 249] for metallic  $\text{NiP}_3$ .

### 2.2.4.2 Band structure of ternary skutterudites

The fact that the band structure depends sensitively on the positional parameters  $y$  and  $z$ , and these are significantly altered by substituting column 14 (Ge, Sn) and column 16 (S, Se, Ye) atoms for pnictogen atoms, leads to modifications of the electronic bands of ternary skutterudites. DFT-based calculations by Bertini and Cenedese [231] indicated enhanced charge transfer and, consequently, a more ionic character of the bonds. Detailed DFT calculations by Volja et al. [19] for several ternary skutterudites revealed their much larger band gaps (perhaps by as much as a factor of 2–3) in comparison to  $\text{CoSb}_3$ . While a single linearly dispersing valence band toward the  $\Gamma$  point is preserved, its linearity is weakened and a second, heavier valence band of multivalley character lies close by. Finding ways to close the separation further would benefit the Seebeck coefficient. Large band gaps and even closer proximity of the second, heavier valence band to the linear valence band (separation merely 0.2 eV) was also found in recent calculations by Zevalkink et al. [22]. A similar situation pertains to the conduction band edge at  $\Gamma$ , where two degenerate conduction bands are separated from the slightly higher-lying conduction band by only 0.04 eV, and the multiband conduction could be easily explored.

### 2.2.4.3 Band structure of filled skutterudites

Early calculations of the band structure of filled skutterudites focused on phosphide-based materials because they showed superconductivity with relatively high transition temperatures [27]. Calculations were carried out using the tight-binding method [250] and referred strictly to the  $[Fe_4P_{12}]^{3-}$  polyanion. Although fillers generally do not have a dramatic effect on the band structure, omitting them completely in the calculations is not appropriate. The first DFT calculations were made by Nordström and Singh [251] for  $CeFe_4P_{12}$  and  $CeFe_4Sb_{12}$  using an approach similar to Ref. [219] and including spin-orbit interactions. In both cases, Ce was shown to be trivalent and thus one would expect a metal. This was not the case as the calculations indicated rather significant gaps of 0.34 and 0.10 eV for P- and Sb-based skutterudites, respectively. Strong hybridization of Ce 4f states with Fe 3d and pnicogen p-states was invoked as the origin of the band gap. The calculations also revealed the presence of considerably heavy valence and conduction bands, the feature generic to all filled skutterudites. Subsequently, DFT calculations have been carried out for many filled skutterudites [7, 242, 252–266] indicating a few of them as having small band gaps while most are metallic systems. For example, DFT calculations were carried out by Harima and Takegahara [267] who evaluated the progression of electronic bands in  $LaFe_4X_{12}$  from phosphide to arsenides to antimonides, shown in Fig. 2.2.4. In all cases, the Fermi level intersects similar valence band manifolds (p-type metals) with the density of states (DOS) at the Fermi level increasing dramatically from the phosphides (13.97 states/eV) to the arsenides (18.16 states/eV) to antimonides (25.2 states/eV).

### 2.2.4.4 Band structure of skutterudites with the $[Pt_4Ge_{12}]$ framework

The computed DOS and, occasionally the “spaghetti” diagrams, were usually presented as part of the original discoveries of skutterudites with the  $[Pt_4Ge_{12}]$  framework and many subsequent computations [105, 106, 109, 112, 266, 268–283]. Fig. 2.2.5 indicates a typical case of the electronic DOS of  $SrPt_4Ge_{12}$ . The major difference with the pnicogen-based skutterudites is the dominant role of Ge 4p states near the Fermi energy and no effect whatsoever of the filler species in this energy range. The fillers are important for their charge transfer to the framework that stabilizes the structure but have little effect on the transport and superconducting properties.

### 2.2.4.5 Band structure of skutterudites with electronegative fillers

Skutterudites with electronegative fillers, sometimes also called inverse skutterudites, have generated much interest in recent years. Supporting their discovery of iodine acting as an electronegative filler in  $RhSb_3$ , Fukuoka and Yamanaka [106] included LAPW calculations (WIEN2k code) of the band structure that revealed the presence of the familiar near-linearly dispersing  $\Gamma$ -point valence band typical of  $RhSb_3$  and

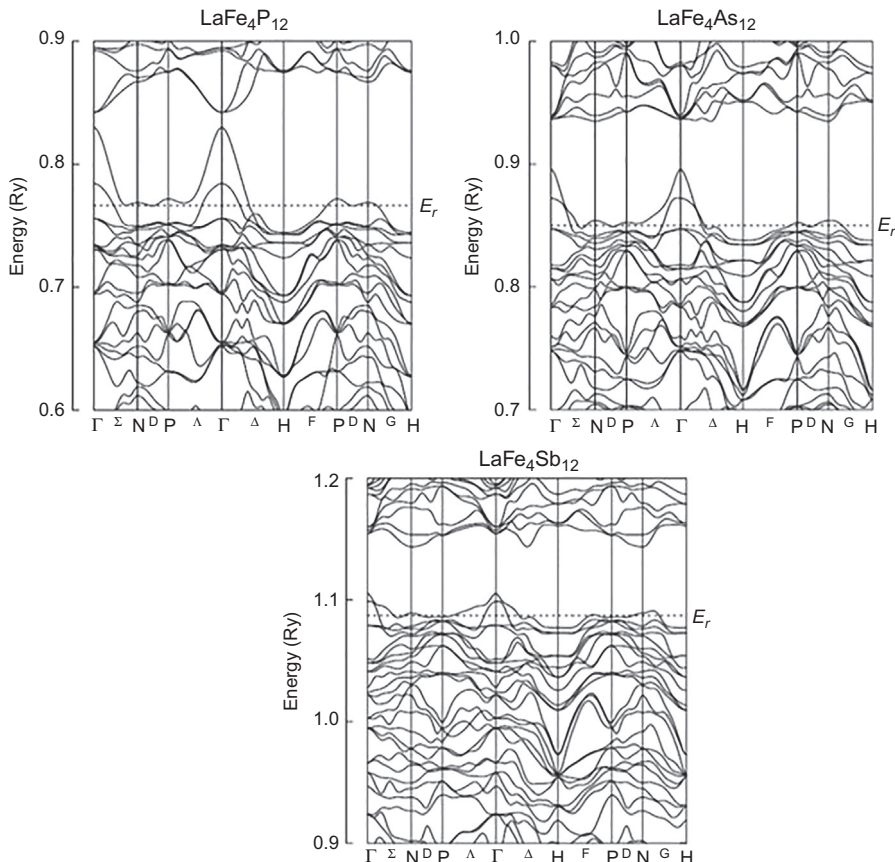


**Fig. 2.2.4** Electronic band structure of LaFe<sub>4</sub>P<sub>12</sub>, LaFe<sub>4</sub>As<sub>12</sub>, and LaFe<sub>4</sub>Sb<sub>12</sub> calculated by the FP-LAPW method. In all cases, the Fermi energy intersects the valence bands manifold, making the structures p-type metals.

Reproduced from H. Harima, K. Takegahara, Physica B 328 (2003) 26. With permission from Elsevier.

CoSb<sub>3</sub>. In this case, however, the Fermi level crosses the valence band, making IRh<sub>4</sub>Sb<sub>12</sub> a metal. The bands near the Fermi energy are dominated by Rh p- and d-states and by Sb p-states, with p-states of iodine lying well below the Fermi level. A similar outcome, i.e., little effect of iodine on the band structure, except for shifting the Fermi level down so that it intersects more than a single valence band, was obtained in band structure calculations for IC<sub>0.4</sub>Sb<sub>12</sub> [107], shown in Fig. 2.2.6. Band structure calculations [110] for Br<sub>0.063</sub>Co<sub>4</sub>Sb<sub>12</sub> (p-type metal) and S<sub>0.063</sub>Co<sub>4</sub>Sb<sub>11.5</sub>Te<sub>0.5</sub> (n-type metal on account of Te doping on the site of Sb) also indicate only very small contributions of electronegative fillers in the vicinity of the Fermi energy.

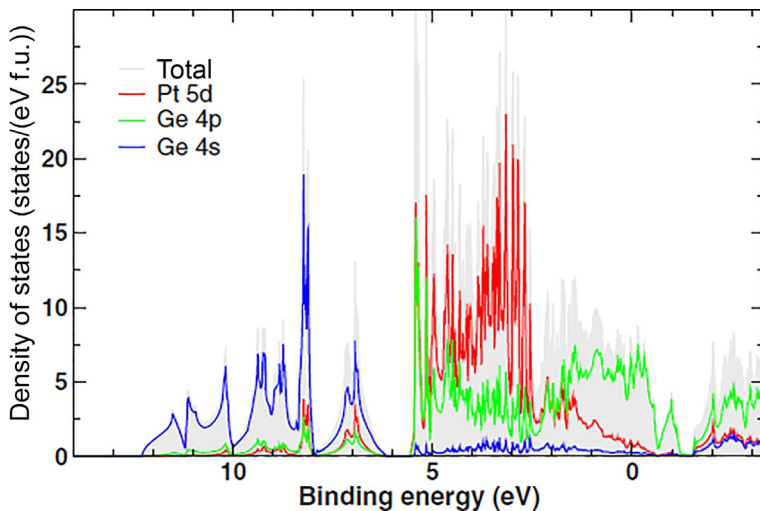


**Fig. 2.2.5** Calculated total and atom-resolved partial electronic density of states of  $\text{SrPt}_4\text{Ge}_{12}$ . The Fermi level is at zero binding energy. Note the dominant role of Ge 4p states in the vicinity of the Fermi energy, while Pt 5d states represent the bulk of the states in the energy range from about 2.5 to 5 eV. There is a negligible contribution of the filler species to the density of states close to the Fermi energy.

Reproduced from H. Rosner, J. Gegner, D. Regesch, W. Schnelle, R. Gumeniuk, A. Leithe-Jasper, H. Fujiwara, T. Haupricht, T.C. Koethe, H.-H. Hsieh, H.-J. Lin, C.T. Chen, A. Ormeci, Yu. Grin, L.H. Tjeng, Phys. Rev. B 80 (2009) 075114. With permission from the American Physical Society.

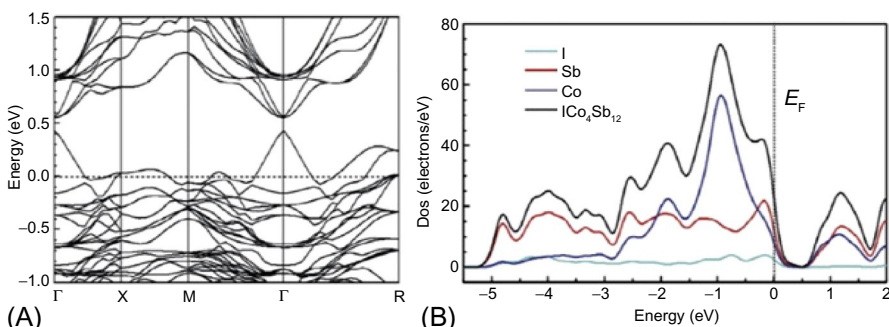


**Fig. 2.2.6** The band structure (A) and the density of states (B) near the Fermi energy for  $\text{ICo}_4\text{Sb}_{12}$ .

Reproduced from X.-D. Li, B. Xu, L. Zhang, F.-F. Duan, X.-L. Yan, J.-Q. Yang, Y.-J. Tian, J. Alloys Compd. 615 (2014) 177. With permission from Elsevier.

## 2.2.5 Transport properties of skutterudites

The dimensionless thermoelectric figure of merit is defined as  $ZT = \frac{S^2\sigma}{\kappa} T$ , where  $S$  is the Seebeck coefficient,  $\sigma$  is the electrical conductivity,  $\kappa$  stands for the total thermal conductivity (consisting of the electronic  $\kappa_e$  and lattice  $\kappa_L$  contributions), and  $T$  is the absolute temperature. Thus, there are three electronic transport parameters,  $S$ ,  $\sigma$ , and  $\kappa_e$ , and one thermal transport parameter,  $\kappa_L$ , that directly enter into considerations of the material and device efficiency maximization. In reality, only  $S$  and  $\sigma$  are subject to experimental studies because the electronic thermal conductivity is tied to the electrical conductivity via the Wiedemann-Franz law and the value of the Lorenz number, which, for a given system, is fixed. However, in order to properly assess the carrier dynamics, the Hall effect is an additional indispensable transport coefficient that informs one about the carrier concentration and, in conjunction with the electrical conductivity, the carrier mobility, and thus the type and strength of scattering.

### 2.2.5.1 Electronic transport properties

#### 2.2.5.1.1 Electronic transport in binary skutterudites

Early transport measurements on pure and doped  $\text{CoSb}_3$  were carried out by Dudkin and colleagues during the second half of the 1950s [9]. They established  $\text{CoSb}_3$  as a small bandgap extrinsic semiconductor with high room temperature mobility of  $290 \text{ cm}^2 \text{ V}^{-1} \text{ s}^{-1}$ , and the carrier type strongly dependent on the exact stoichiometry [14]. At elevated temperatures, the conductivity became dominated by intrinsic excitations with the hole mobility greatly exceeding the electron mobility and the Seebeck coefficient attaining positive values. The team also explored the influence of dopants on the Co sites as well as on the Sb sites [145, 268], in both cases noting a strong dependence on even minute amounts of the dopant, and the structure attaining a metal-like conductivity. Transport studies on arsenide skutterudites were carried out by Pleass and Heyding in 1962 [16]. Limited work on phosphide skutterudites was done by Ackermann and Wold in 1977 on their chemical vapor transport-synthesized crystals of  $\text{CoP}_3$  [153], and the flux-grown  $\text{RhP}_3$  was measured by Odile et al. a year later [149].

The renewed interest in thermoelectricity in the early 1990s brought skutterudites into the forefront of the field, and the initial effort was led by researchers at the Jet Propulsion Laboratory (JPL). The work focused not only on the thermoelectric properties but also on the understanding of the phase diagram [269] and the growth of single-crystalline specimens [147]. Shortly thereafter, skutterudites started to be explored in laboratories worldwide, with  $\text{CoSb}_3$  drawing by far the greatest interest. Fig. 2.2.7 illustrates the temperature dependence of the electrical resistivity of undoped p-type  $\text{CoSb}_3$  plotted on a semilogarithmic graph to highlight its semiconducting behavior. The data include four samples, three of them single crystals prepared by different methods, and also a very pure polycrystalline specimen. Regardless of the nature of the samples, their high-temperature resistivity attained

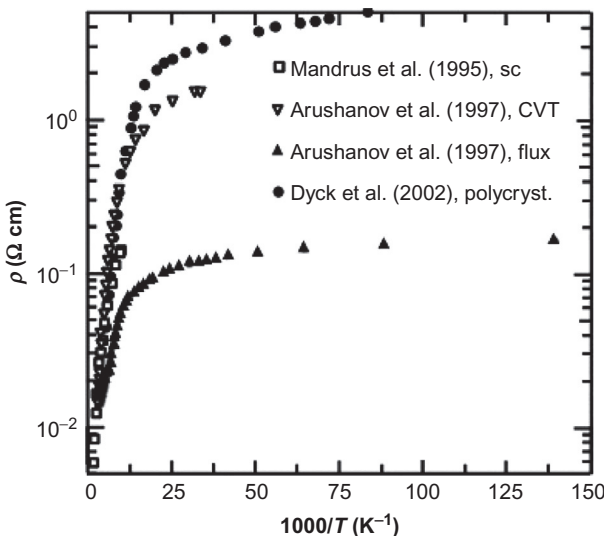


**Fig. 2.2.7** Electrical resistivity of several specimens of p-type  $\text{CoSb}_3$ . A single crystal of Mandrus et al. [151], had room temperature carrier concentration (holes) of  $7.0 \times 10^{16} \text{ cm}^{-3}$ ; single crystals of Arushanov et al. [270], were prepared by chemical vapor transport (*open triangles*) and by the flux method (*solid triangles*) and had hole carrier concentrations of  $1.24 \times 10^{17} \text{ cm}^{-3}$  and  $1.37 \times 10^{17} \text{ cm}^{-3}$ , respectively; and the polycrystalline sample of Dyck et al. [271], had  $1.4 \times 10^{18}$  holes per  $\text{cm}^3$ .

a similar slope from which the band gaps in the range 30–100 meV followed. Low-temperature resistivity and the Hall effect measurements on single crystals were explained assuming two acceptor levels (a shallow band and a deep level) [270], while for the polycrystalline sample one acceptor level sufficed [271]. However, below about 30 K, the resistivity followed the Mott variable range hopping,  $\rho(T) = \rho_0 \exp \left[ \left( \frac{T_0}{T} \right)^{1/4} \right]$ , with the characteristic temperature  $T_0 = 584 \text{ K}$ . General shapes of the temperature-dependent resistivity similar to that of  $\text{CoSb}_3$  were also observed with  $\text{CoAs}_3$  and  $\text{RhAs}_3$  [16]. The electrical resistivity of  $\text{IrSb}_3$  is metallic above about 60 K [21, 272], but rises with decreasing temperature below 50 K [273].  $\text{CoP}_3$  shows a weak semiconducting dependence, with the resistivity starting to increase with the temperature above about 400 K [274].

Binary skutterudites possess very high mobilities, with the room temperature values of  $3445 \text{ cm}^2 \text{ V}^{-1} \text{ s}^{-1}$  for crystals of  $\text{CoSb}_3$  with the carrier density of  $4 \times 10^{17} \text{ cm}^{-3}$  [275], and a spectacular value of near  $8000 \text{ cm}^2 \text{ V}^{-1} \text{ s}^{-1}$  for the p-type  $\text{RhSb}_3$  crystal having the carrier density of  $3.5 \times 10^{18} \text{ cm}^{-3}$  [284]. A collection of room temperature mobilities and carrier densities for several binary skutterudites can be found in my 2001 review [285]. A detailed assessment of electronic transport properties of pure  $\text{CoSb}_3$  below ambient temperature, including both the impurity band conduction and the nonparabolicity of the valence band, can be found in Ref. [286].

Representative Seebeck coefficient data for undoped but naturally p-type  $\text{CoSb}_3$  at low and high temperatures are illustrated in Fig. 2.2.8. Low-temperature values of the

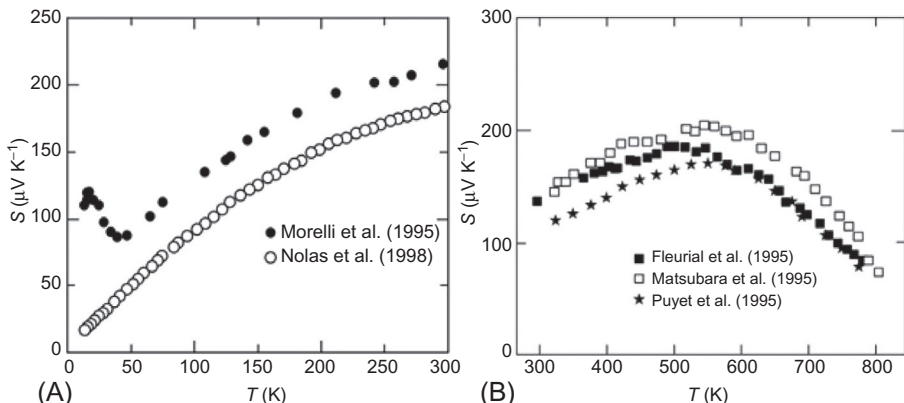


**Fig. 2.2.8** Temperature dependence of the Seebeck coefficient of  $\text{CoSb}_3$  measured (A) below ambient temperature and (B) above ambient temperature. Note a pronounced phonon drag effect observed on a single crystalline sample (solid circles) below 50 K. The phonon drag is missing on a polycrystalline sample (open circles) due to strong phonon boundary scattering. Low-temperature data come from Ref. [287] (solid circles) and Ref. [43] (open circles). High-temperature data are from Ref. [284] (solid squares), Ref. [288] (open squares), and Ref. [40] (stars).

Seebeck coefficient measured on a single-crystal sample (solid circles) [287] reveal a pronounced phonon drag effect at temperatures below 50 K, which does not develop in polycrystalline samples due to strong boundary scattering. High-temperature Seebeck coefficients on a single crystal (solid squares) [284] and polycrystalline samples (open squares [288] and stars [40]) keep rising with temperature up to about 500–550 K, at which point intrinsic excitations start to take place and the magnitude of the Seebeck coefficient rapidly diminishes on account of the presence of minority charge carriers. A comparative study of binary skutterudites, including antimonide and arsene samples, was made by Sharp et al. [289], but the quality of the samples was not uniform,  $\text{CoAs}_3$  having a low mass density of only about 50% of the theoretical value. N-type  $\text{CoSb}_3$  crystals, grown with the addition of a minute amount of Te, show exceptionally large values of the Seebeck coefficient, up to  $-500 \mu\text{V K}^{-1}$ , depending on the doping, but the low-doped structures become p-type at temperatures above about 570 K, as the intrinsic holes have much higher mobility than electrons [275,290]. Numerous doping studies have indicated a strong effect on the carrier concentration and, therefore, on the electrical conductivity and the Seebeck coefficient. Moreover, as the carrier concentration increases, the effective mass of holes and electrons increases, with electrons being at least an order of magnitude heavier than holes [290,291]. The respective dependences of the effective mass on the carrier concentration are illustrated in Fig. 2.2.9. As follows from Fig. 2.2.9A, the effective mass of holes is quite small and seems to follow the  $p^{1/3}$  dependence, where  $p$  is the carrier concentration of holes obtained from the Hall effect measurements. The very light mass of holes contributes to their exceptionally high mobility. While the effective mass of electrons ( $\text{CoSb}_3$  doped n-type with different dopants) shown in Fig. 2.2.9B also increases with the concentration of electrons, the value of the effective mass of electrons

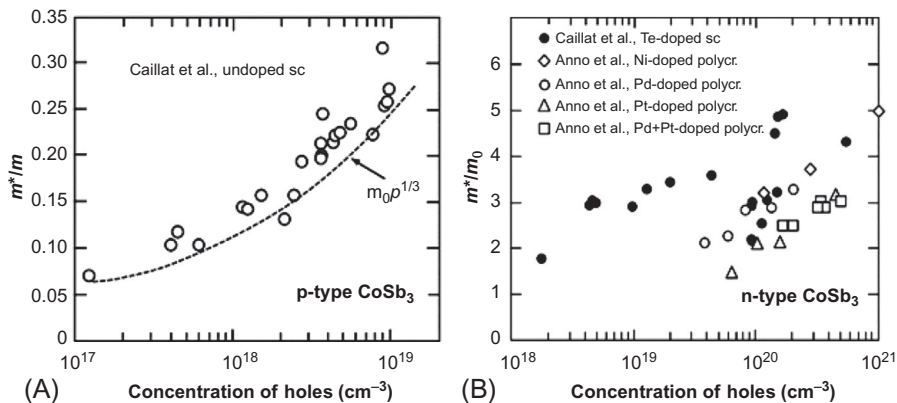


**Fig. 2.2.9** Effective masses of holes (A) and electrons (B) as a function of the carrier concentration based on the Hall effect measurements. The data of Caillat et al. [290] for an undoped p-type single-crystal follow a  $p^{1/3}$  dependence, consistent with the band structure model of Singh and Pickett [219]. A collection of various intentionally n-type doped samples of  $\text{CoSb}_3$  shown in (B) also indicates a rising trend in the effective mass with the concentration of electrons, but the effective masses here are an order of magnitude larger. Such large effective masses of electrons support a large magnitude of the Seebeck coefficient of n-type  $\text{CoSb}_3$ . The n-type effective masses refer to measurements by Caillat et al. [290] and Anno et al. [291].

is high. High effective masses are beneficial to the Seebeck coefficient. In fact, the maximum power factors of n- and p-type  $\text{CoSb}_3$  are comparable in magnitude, but peak at different carrier concentrations, in p-type samples between  $10^{18}$  and  $10^{19} \text{ cm}^{-3}$ , while in n-type samples above  $10^{20} \text{ cm}^{-3}$  [290]. High Seebeck coefficient coupled with good electrical conductivity results in room temperature power factors ( $S^2\sigma$ ) of  $\text{CoSb}_3$  of up to  $3.5 \text{ mW m}^{-1} \text{ K}^{-2}$  [290]. Unfortunately, a too high thermal conductivity of  $\text{CoSb}_3$  ( $\sim 10 \text{ W m}^{-1} \text{ K}^{-1}$  at 300 K) (see Section 2.2.5.2.1) prevents  $\text{CoSb}_3$  from being a useful thermoelectric material. The thermoelectric figure of merit  $ZT$  at 300 K does not exceed 0.02, while among the best values for pure  $\text{CoSb}_3$  at elevated temperatures is  $ZT=0.17$  at 610 K [292]. However, upon filling, a skutterudite becomes a very interesting thermoelectric prospect, as we shall see in the following paragraphs.

### 2.2.5.1.2 Electronic transport in filled skutterudites

While the most obvious benefit of filled skutterudites is a drastically reduced thermal conductivity (discussed in Section 2.2.5.2.2), the process of filling is also an exceptionally effective way of increasing the density of electrons as the filler has its valence electrons stripped and they go into the conduction band. Unless the structure is charge compensated (doped by Sn or Ge on Sb sites, or Co is partly or fully replaced by Fe), or one uses electronegative fillers, filling always leads to an n-type skutterudite. The actual concentration of electrons depends solely on the filling fraction and the effective charge state of the filler.

As noted in [Section 2.2.4.3](#), while the band structure of filled skutterudites is more complicated, the critical regions near the conduction and valence band edges are substantially unaffected by filling, and good electronic properties of binary skutterudites are more or less preserved.

In early studies attempting to increase the filling fraction, Fe was often used to substitute for Co and charge compensate for the structure. This resulted in p-type filled skutterudites, which initially had a superior thermoelectric performance with the  $ZT$  on the order of unity. However, once effective filler concentrations were identified and multiple filling strategies were developed, n-type skutterudites quickly caught up with the performance of p-type skutterudites and have led the way ever since.

Detailed theoretical studies of electronic transport properties revealed [\[293\]](#) that the optimal carrier concentration in n-type skutterudites that yields the maximum power factor is around 0.5 electrons per formula unit. This implies that a monovalent filler should fill about 50% of voids, a divalent filler about 25% of voids, and a trivalent filler around 17% of voids, assuming full ionization. The estimates are broadly supported by numerous experimental investigations, e.g., Refs. [\[38,42,73,294–299\]](#). Thus, from the electronic perspective, all fillers having the same charge state should be equally effective at the same filling fraction.

Upon filling or substantial doping, the semiconducting character of  $\text{CoSb}_3$  changes into that of a heavy degenerate system with metal-like electrical conductivity, but with a large Seebeck coefficient supported by the heavy mass of electrons. [Fig. 2.2.10](#) represents a collection of power factors obtained with different forms of n-type skutterudites, including the highest reported values in the range  $5\text{--}6.5 \text{ mW m}^{-1} \text{ K}^{-2}$  that were obtained on triple-filled forms of the structure [\[81, 83\]](#). The power factor  $S^2\sigma$  is truly a comprehensive measure of the electronic contribution to the thermoelectric performance. As shown by Rogl and colleagues [\[83\]](#), although the high-pressure torsion (HPT) enhances the figure of merit because of the strongly suppressed thermal conductivity, the power factor is degraded by this process because the Seebeck coefficient does not change much while the electrical conductivity suffers from the presence of additional defects introduced during the HPT process. While some defects and microcracks created by HPT are annealed out upon the first measurement heating, the resistivity does not fully recover its pre-HPT value. This is the reason for a significantly lower power factor, which actually was obtained upon cooling, after which the structure seemed stabilized [\[83\]](#). Very high power factors were also observed in single-filled  $\text{Yb}_{0.22}\text{Co}_4\text{Sb}_{12}$  with the nominal Yb content of 0.30, which, in fact, was an intrinsic composite skutterudite since it contained a precipitated  $\text{YbSb}_2$  phase [\[47\]](#). An unfilled double-doped skutterudite, in as-prepared form, attained a rather ordinary  $ZT \sim 0.7$  at 800 K. However, upon a 15 h annealing near 900 K, it more than doubled its  $ZT$  and reached a remarkably high value of 1.6 at 800 K [\[300\]](#), by far the highest  $ZT$  for an unfilled skutterudite! The reason was a dramatically reduced lattice thermal conductivity (close to the glass limit) as phonons scattered on a myriad of pores with dimensions from hundreds of nanometers to several micrometers that formed during the annealing as the excess Te either evaporated or was squeezed out during SPS. Again, the power factor was significantly degraded as a consequence of enhanced charge carrier scattering on the defected structure. A single-filled

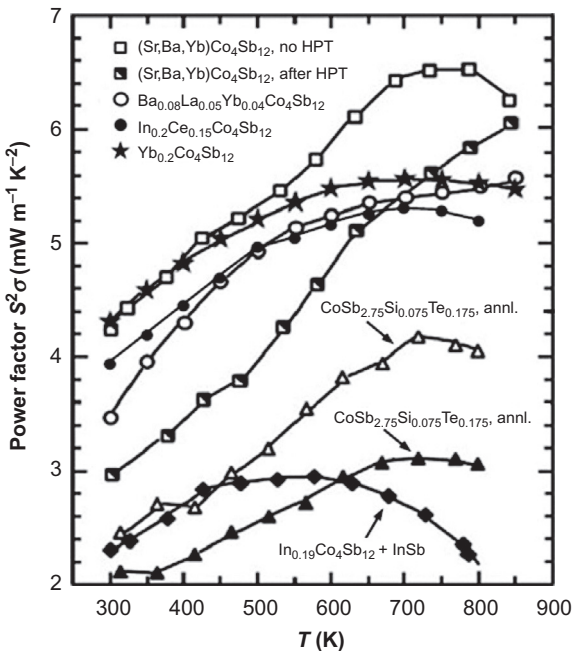


**Fig. 2.2.10** Power factors obtained on a variety of n-type skutterudites, some of them with the highest reported values. The data include triple-filled  $(\text{Sr},\text{Ba},\text{Yb})\text{Co}_4\text{Sb}_{12}$  from Ref. [83] both before the application of the high-pressure torsion (HPT) (*open square symbols*), and after being subjected to HPT (*half-filled squares*); triple-filled  $\text{Ba}_{0.08}\text{La}_{0.05}\text{Yb}_{0.04}\text{Co}_4\text{Sb}_{12}$  from Ref. [81] (*open circles*), on which  $ZT = 1.7$  was reported; a double-filled  $\text{In}_{0.2}\text{Ce}_{0.15}\text{Co}_4\text{Sb}_{12}$  skutterudite from Ref. [76] that contained an InSb nanophase (*solid circles*); a single-filled composite  $\text{Yb}_{0.22}\text{Co}_4\text{Sb}_{12}$  skutterudite from Ref. [47], which had the nominal Yb composition  $y = 0.30$  and contained  $\text{YbSb}_2$  precipitates (*star symbols*); a single-filled composite  $\text{In}_{0.19}\text{Co}_4\text{Sb}_{12}$  with InSb nanoinclusions from Ref. [72], which had the nominal In content of  $y = 1$  and was reported with very high  $ZT = 1.5$  at 750 K (*solid diamonds*); and unfilled double-doped  $\text{CoSb}_{2.95}\text{Si}_{0.064}\text{Te}_{0.256}$  from Ref. [300] with a significant excess of Te prior to annealing (*open triangles*) and after high-temperature annealing (*filled triangles*), which created a spectrum of pores with sizes from hundreds of nanometers to micrometers. The  $ZT$  after annealing doubled to 1.6 around 800 K compared to that before annealing.

$\text{In}_{0.19}\text{Co}_4\text{Sb}_{12}$  synthesized from the nominal In content of  $y = 1$  possessed a large density of InSb nanoinclusions, again representing an intrinsic composite skutterudite [72]. It reached  $ZT = 1.5$  at 750 K, but obviously, its carrier density was not very high as the power factor attained its maximum near 550 K and turned down on account of intrinsic excitations setting in.

Unless filled with electronegative fillers, p-type skutterudites are prepared by a partial or full replacement of Co by Fe, or by heavy p-type doping on the sites of Sb. Already the early studies indicated [44,301] that the replacement of Co by Fe can be carried out to any desirable extent, provided enough fillers are present to charge

compensate and stabilize the structure. In fact, the level of void filling is tied to the degree of Fe replacing Co. This results in high carrier densities of holes on the order of  $10^{20}$ – $10^{21} \text{ cm}^{-3}$ . Of course, such high carrier concentrations are detrimental to the magnitude of the Seebeck coefficient. In  $\text{CoSb}_3$ , the highly dispersing nondegenerate  $\Gamma$ -point valence band, due mostly to the Sb 5p orbital nature, has a very low density of states and thus contributes little to the Seebeck coefficient of p-type binary skutterudites. As the presence of Fe on the Co sites increases, the more flat and heavy 3d bands of Fe increase the density of states and support larger values of the Seebeck coefficient. Unfortunately, the increased effective mass also reduces the mobility of holes. Consequently, the power factors of p-type skutterudites are generally significantly lower in comparison to their n-type cousins, and rarely exceed values of  $3 \text{ mW m}^{-1} \text{ K}^{-2}$ . Moreover, the flat bands require high carrier concentrations to attain optimal doping levels, and this likely leads to enhanced carrier-phonon scattering, which keeps the electrical conductivity low.

As with n-type filled skutterudites, vast amounts of literature have covered attempts to prepare efficient p-type skutterudites. I mention here only those that led to very high TE performance or presented some unique aspects of p-type skutterudites. A collection of power factors of p-type skutterudites is shown in Fig. 2.2.11. The data include the record-high values reported by Rogl et al. in a series of papers on p-type didymium-filled skutterudites [302–307], with some

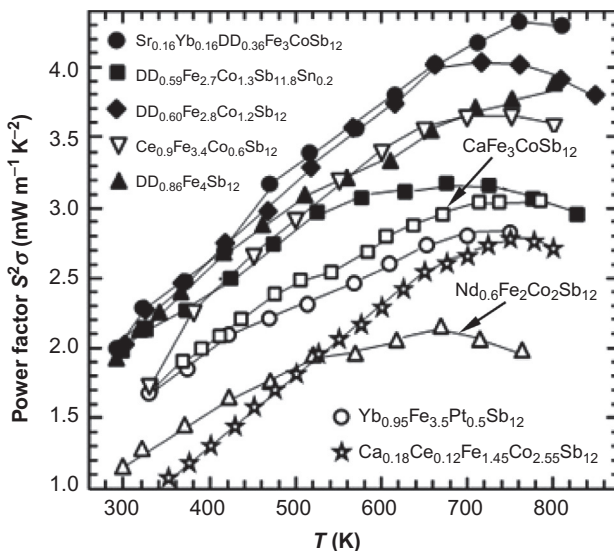


**Fig. 2.2.11** Power factors of selected p-type skutterudites, including those showing record-high values. Solid symbols are from measurements by Rogl et al. that contained didymium as a single filler or in combination with other fillers: *solid circles* [302], *solid diamonds*, and *solid squares* [84], *solid triangles* [303]. Open symbols are power factors measured on single-filled and double-filled p-type skutterudites: *open circles* [310], *open stars* [312], *open squares* [313], *open up triangles* [119], and *open down triangles* [314].

of the structures approaching or even slightly exceeding power factor values of  $4 \text{ mW m}^{-1} \text{ K}^{-2}$ . The measurements with didymium fillers included a comparison of thermoelectric properties based on the  $[\text{Fe}_x\text{Co}_{4-x}\text{Sb}_{12}]$  and  $[\text{Fe}_x\text{Ni}_{4-x}\text{Sb}_{12}]$  frameworks having similar valence counts (remember, substituting one Ni atom for one Fe atom is equivalent to substituting one Fe atom with two Co atoms). The interest was driven by two factors: by ab initio calculations for  $\text{RFe}_3\text{NiSb}_{12}$  ( $\text{R} = \text{Ca}, \text{Sr}, \text{and Ba}$ ) [308] that indicated the presence of heavy band states of Fe 3d origin just below the valence band edge, accessible by appropriate doping; and by the cost of potential modules, with Ni being significantly less expensive than Co. Measurements indicated that there is only a slight advantage in the performance of  $\text{R}_y\text{Co}_{4-x}\text{Fe}_x\text{Sb}_{12}$  skutterudites over  $\text{R}_y\text{Ni}_{4-x}\text{Fe}_x\text{Sb}_{12}$  structures having the same electron count, and it is notable only above 500 K, where the Seebeck coefficient of the  $[\text{Co}_{4-x}\text{Fe}_x\text{Sb}_{12}]$  framework is marginally higher than the one supported by the  $[\text{Ni}_{4-x}\text{Fe}_x\text{Sb}_{12}]$  framework, the latter tending to decrease at somewhat lower temperatures. Beyond doping, the heavy Fe 3d bands in the  $[\text{Ni}_{4-x}\text{Fe}_x\text{Sb}_{12}]$  framework could also be reached by increasing the fraction of Fe. Indeed, by raising the Fe content to 3.5 in compounds  $\text{Yb}_{y}\text{Ni}_{0.5}\text{Fe}_{3.5}\text{Sb}_{12}$  with  $0.8 \leq y \leq 1$ , the Seebeck coefficient was considerably enhanced, and the power factor approached  $3 \text{ mW m}^{-1} \text{ K}^{-2}$  at 700 K [309]. However, the figure of merit did not exceed 0.6, as the rather small bandgap resulted in an early onset of intrinsic processes that prevented the power factor from reaching higher values. Increasing the bandgap by replacing Ni with Pt and keeping the large Fe/Pt ratio, a comparable power factor of  $2.7 \text{ mW m}^{-1} \text{ K}^{-2}$  was obtained, and the figure of merit reached 0.9 at 740 K for  $\text{Yb}_{0.95}\text{Fe}_{3.5}\text{Pt}_{0.5}\text{Sb}_{12}$ , the enhancement obtained chiefly as a consequence of the onset of intrinsic excitations being shifted to a higher temperature near 750 K [310]. The data in Fig. 2.2.11 also include the power factor of a Nd-filled skutterudite,  $\text{Nd}_{0.6}\text{Fe}_2\text{Co}_2\text{Sb}_{12}$ . In terms of the effectiveness of reducing the lattice thermal conductivity, Nd is actually even better than Yb, and several studies have attempted to use it to obtain high TE conversion efficiency [119,311]. Unfortunately, the power factor of all Nd-filled skutterudites turned out to be unimpressive, and even the record-low values of the lattice thermal conductivity could not bring the figure of merit to values much better than unity. A small amount of Ge substituted on the Sb rings improved the figure of merit to about  $ZT = 1.1$  at 700 K by lowering the thermal conductivity, but it also seriously affected the power factor, decreasing it from about  $2.2 \text{ mW m}^{-1} \text{ K}^{-2}$  at its peak value in  $\text{Nd}_{0.6}\text{Fe}_2\text{Co}_2\text{Sb}_{12}$  down to  $1.6 \text{ mW m}^{-1} \text{ K}^{-2}$  in  $\text{Nd}_{0.6}\text{Fe}_2\text{Co}_2\text{Sb}_{11.7}\text{Ge}_{0.3}$ . A similar degradation of the power factor upon substitutions on the pnictogen rings is also documented in Fig. 2.2.11 by comparing  $\text{DD}_{0.59}\text{Fe}_{2.7}\text{Co}_{1.3}\text{Sb}_{11.8}\text{Sn}_{0.2}$  (solid squares) with  $\text{DD}_{0.60}\text{Fe}_{2.8}\text{Co}_{1.2}\text{Sb}_{12}$  (solid diamonds), the two skutterudites with essentially the same didymium content and Fe/Co ratio. I also want to mention that the HPT process, which might improve the figure of merit by perhaps 10% above 700 K by introducing severe plastic deformation (high density of dislocations and finer grain size that increases the scattering of phonons and further degrades the lattice thermal conductivity), is also highly damaging to the carrier mobility and lowers the power factor [85].

Singh pointed out [315] that Ru and Os, with their far less localized 4d, respectively, 5d might have enhanced hole mobilities compared to Fe-based skutterudites.

Calculations, indeed, indicated [316] that the effective mass at the top of the  $\Gamma$ -point valence band decreases dramatically from  $3.1\text{ m}_e$  for  $\text{LaFe}_4\text{Sb}_{12}$  to  $1.5\text{ m}_e$  for  $\text{LaRu}_4\text{Sb}_{12}$  and further to  $0.9\text{ m}_e$  for  $\text{LaOs}_4\text{Sb}_{12}$ . The resulting predicted power factor of over  $5\text{ mW m}^{-1}\text{ K}^{-2}$  would then rival the best power factors of n-type skutterudites. Except for its intrinsic scientific value, I do not see much profit from following this route as the cost of the materials would be prohibitive.

### 2.2.5.2 Phonon transport

As discussed in the preceding sections, skutterudites have outstanding electronic transport properties that predispose them to be excellent candidates for thermoelectric energy conversion. Unfortunately, they also possess far too high thermal conductivity that disqualifies binary skutterudites from considerations as efficient thermoelectrics. It was an idea of Slack that filling the voids in the skutterudite structure might lead to serious degradation of their heat conducting ability, which gave hope for developing skutterudites into thermoelectric materials. Before discussing the effect of filling, I briefly mention key issues pertaining to heat transport in binary skutterudites.

#### 2.2.5.2.1 Thermal conductivity of binary skutterudites

Being a semiconducting structure, heat conduction in skutterudites proceeds by two distinct channels, charge carriers, and lattice vibrations. The first channel contributes the electronic thermal conductivity  $\kappa_e$  tied via the Wiedemann-Franz law to the electrical conductivity  $\sigma$  by  $\kappa_e = \sigma LT$ , where  $L$  is the Lorenz number, dependent on the degeneracy of the system. In highly degenerate systems, such as metals, it has a value  $2.45 \times 10^{-8}\text{ V}^2\text{ K}^{-2}$ . In skutterudites, a more appropriate value is  $2 \times 10^{-8}\text{ V}^2\text{ K}^{-2}$ . There is little one can do to alter the Lorenz number, and the electronic thermal conductivity is basically determined by the value of the electrical conductivity. In semiconductors, such as skutterudites, the electronic term is typically much smaller (even in heavily doped  $\text{CoSb}_3$  it rarely exceeds 20%) than the contribution due to lattice vibrations, known in quantized form as phonons. Since the lattice vibrations are essentially independent of the charge carriers, the aim is to disturb them to the maximum extent so that their contribution would approach the lowest possible value known as the minimum thermal conductivity [317,318]. Given that the calculated minimum thermal conductivity of  $\text{CoSb}_3$  is about  $0.3\text{ W m}^{-1}\text{ K}^{-1}$ , while the measured room temperature total thermal conductivity is around  $10\text{ W m}^{-1}\text{ K}^{-1}$ , there is ample room to attempt to degrade the lattice thermal conductivity and make skutterudites competitive thermoelectrics.

In the  $Im\bar{3}$  the symmetry of skutterudites, 45 zone center vibrations decompose into 19 distinct zone center phonon modes. Some of these modes were measured [319] and, in combination with DFT calculations, Feldman and Singh [320] computed the phonon density of states of  $\text{CoSb}_3$  shown in Fig. 2.2.12. The notable features are the parabolic dependence up to about  $70\text{ cm}^{-1}$  dominated by acoustic phonons and interrupted by the presence of optic modes, a gap near  $100\text{ cm}^{-1}$  (in later studies [321] a strong depression but not zero PDOS), and a wide gap between about 180

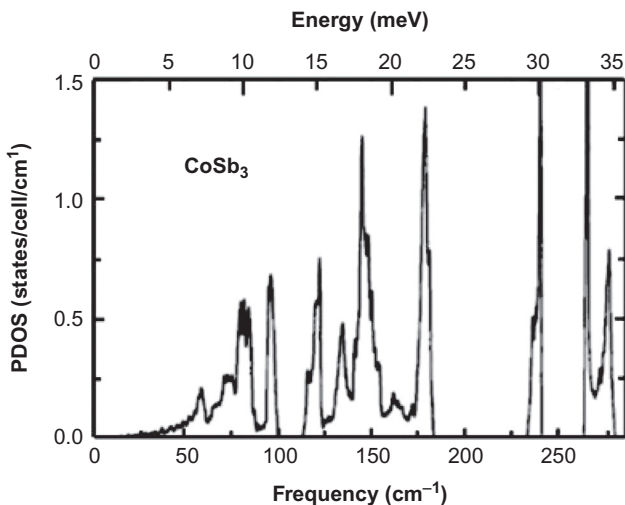


**Fig. 2.2.12** Phonon density-of-states of  $\text{CoSb}_3$  based on the model of Feldman and Singh. Modified from J.L. Feldman, D.J. Singh, Phys. Rev. B 53 (1996) 6273.

and  $230 \text{ cm}^{-1}$  that separates the essentially Sb modes from the higher frequency transition metal modes.

It is clear that to affect the thermal conductivity, which is given mostly by low-frequency acoustic phonons, it is imperative to strongly scatter Sb-related phonon modes. This can be done in a number of ways, such as introducing defects into the structure including doping, forming solid solutions, and enhancing boundary scattering by making samples with a very small grain size. Although such approaches reduce the thermal conductivity, the reduction is not large enough. It was only upon filling the structural voids that the impact on heat transport enabled the development of skutterudites as thermoelectrics.

### 2.2.5.2.2 Thermal conductivity of filled skutterudites

The idea of Slack [1], referred to as the phonon-glass electron-crystal (PGEC) paradigm, centered on a notion that a weakly bonded filler, behaving as an independent Einstein-like low-frequency oscillator vibrates (rattles) in an oversized void and resonantly scatters low-frequency normal phonon modes, thus seriously impeding their ability to propagate. Supporting evidence for this picture are very large atomic displacement parameters of the filler species compared to the vibrational amplitudes of the framework atoms [37,322,323], neutron inelastic scattering [324–336], nuclear resonance inelastic scattering [337–340], inelastic X-ray scattering [341–344], Raman scattering [345–352], ultrafast spectroscopy [353] and, above all, the fact that many partially filled skutterudites, indeed, attained the glass-like thermal conductivity, with the value approaching the minimum thermal conductivity. However, Slack's PGEC paradigm, underpinned by the assumption that the fillers “rattle” independently and incoherently with respect to the atoms of the framework has been seriously challenged

in the context of skutterudites by high-resolution time-of-flight neutron measurements by Koza et al. [332–336]. The experiments documented that the motion of the fillers is actually correlated with the motion of the framework atoms, and the authors argued that umklapp scattering rather than resonant scattering by the fillers is the mechanism suppressing the lattice thermal conductivity. The denial of the relevance of the PGEC concept in filled skutterudites on microscopic grounds has been controversial and not universally accepted. There is no question that the fillers form local modes, and the PGEC concept has successfully guided the improvement of the TE performance of skutterudites, but it is also true that weaknesses in the concept were pointed out already much earlier [230,354–356]. After all, even the well-known fact that partial filling rather than a full filling is more effective in reducing the lattice thermal conductivity does not exactly conform to the PGEC idea. With the ever more sophisticated algorithms and the dramatically increased computing power, reliable ab initio studies of the thermal conductivity became a reality in the past half-a-dozen years [357], and were applied to skutterudites [235,358–364]. Although the actual computed values of the intrinsic lattice thermal conductivity of skutterudites sometimes miss the target [365], the physical insight gained, by being able to judiciously vary input parameters, has been invaluable in pointing out the key structural features affecting thermal transport in skutterudites.

Selected lattice thermal conductivities of n- and p-type skutterudites are presented in Fig. 2.2.13. The data chosen reflect the lowest values of  $\kappa_L$  measured on different forms of skutterudites. In the case of n-type skutterudites, multifilling is clearly the most effective approach, including using mischmetal as fillers [81–83], although low values of  $\kappa_L$  are occasionally found even in single-filled structures, particularly when the filler is Yb [63]. The lattice thermal conductivity can be further degraded by introducing severe plastic deformation via the high-pressure torsion (HPT) process [83]. Among p-type skutterudites, particularly low values of  $\kappa_L$  are achieved with didymium and Nd fillers [84, 119], and the HPT process [307] is equally effective in lowering the lattice thermal conductivity, as in the case of n-type skutterudites, with the  $\kappa_L$  approaching the minimum thermal conductivity.

## 2.2.6 Thermoelectric performance

Over the past two decades, thermoelectric properties of skutterudites have been improved significantly, and the highest  $ZT$  values for both n-type and p-type structures are collected in Fig. 2.2.14. N-type forms of skutterudites have notably higher  $ZT$  values than their p-type cousins, primarily due to their considerably higher power factors. The best n-type skutterudites reach values between 1.5 and 1.8 at temperatures 800–850 K, while p-type skutterudites attain their maximum figure of merit of 1.1–1.3 near 750 K. In general, multiple-filled skutterudites reach higher  $ZT$  values, benefitting from a strong suppression of the lattice thermal conductivity caused by the normal phonon modes being scattered over a wider range of frequencies by the Einstein modes of the filler species. Moreover, several different fillers also offer more flexibility in tuning the carrier concentration to its optimal value. With n-type

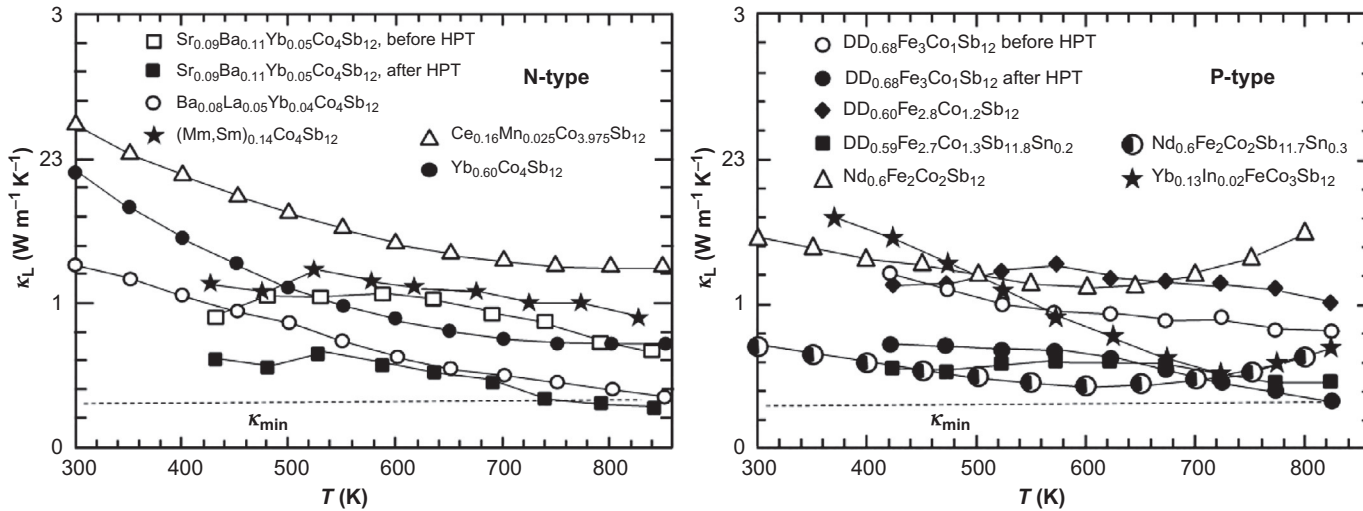


**Fig. 2.2.13** Lattice thermal conductivity of selected n-type (left-hand panel) and p-type (right-hand panel) skutterudites, showing the lowest lattice thermal conductivities reported. N-type skutterudites include triple-filled  $\text{Ba}_{0.08}\text{La}_{0.05}\text{Yb}_{0.04}\text{Co}_4\text{Sb}_{12}$  (open circles) from Ref. [81], triple-filled  $\text{Sr}_{0.09}\text{Ba}_{0.11}\text{Yb}_{0.05}\text{Co}_4\text{Sb}_{12}$  before (open squares) and after (solid squares) HPT processing was applied from Ref. [83], mischmetal-filled skutterudite  $(\text{Mm},\text{Sm})_{0.34}\text{Co}_4\text{Sb}_{12}$  (stars) from Ref. [82], double-filled  $\text{Ce}_{0.16}\text{Mn}_{0.025}\text{Co}_{3.975}\text{Sb}_{12}$  (open triangles) from Ref. [366], and a single-filled  $\text{Yb}_{0.30}\text{Co}_4\text{Sb}_{12}$  (solid circles) from Ref. [63]. Among p-type skutterudites are the didymium-filled  $[\text{Fe}_x\text{Co}_{4-x}\text{Sb}_{12}]$  frameworks with (solid squares) and without (solid diamonds) doping by Sn on the Sb site from Ref. [84], didymium-filled  $\text{DD}_{0.68}\text{Fe}_3\text{Co}_1\text{Sb}_{12}$  before (open circles) and after (solid circles) HPT processing was applied from Ref. [307],  $\text{Nd}_{0.6}\text{Fe}_2\text{Co}_2\text{Sb}_{12}$  with (half-filled circles) and without (open triangles) Sn substituting for a fraction of Sb from Ref. [119], and  $\text{Yb}_{0.13}\text{In}_{0.02}\text{FeCo}_3\text{Sb}_{12}$  (stars) from Ref. [367]. In each case, the lattice thermal conductivity was determined from the measured total thermal conductivity by subtracting the electronic thermal conductivity computed from the measured electrical conductivity using the Lorenz number of  $2 \times 10^{-8} \text{ V}^2 \text{ K}^{-2}$ .

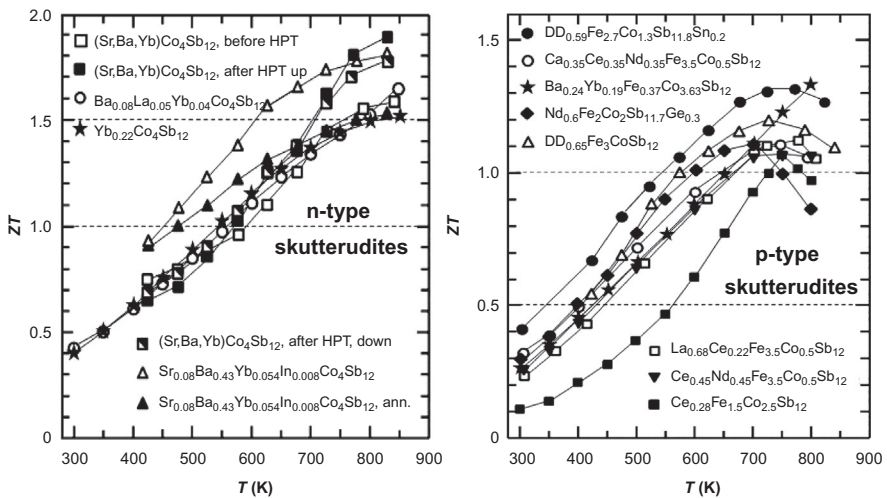


**Fig. 2.2.14** The highest thermoelectric figures of merit obtained on n-type (*left panel*) and p-type (*right panel*) skutterudites. N-type skutterudites include triple-filled  $(\text{Sr},\text{Ba},\text{Yb})\text{Co}_4\text{Sb}_{12}$  from Ref. [83] before and after applying high-pressure torsion (HPT); a quaternary-filled  $\text{Sr}_{0.08}\text{Ba}_{0.43}\text{Yb}_{0.054}\text{In}_{0.008}\text{Co}_4\text{Sb}_{12}$  skutterudite before and after high-temperature annealing synthesized by ball milling  $(\text{Sr}_{0.33}\text{Ba}_{0.33}\text{Yb}_{0.33})_{0.35}\text{Co}_4\text{Sb}_{12}$  with 9.1 wt% of  $\text{In}_{0.4}\text{Co}_4\text{Sb}_{12}$  from Ref. [371]; a triple-filled  $\text{Ba}_{0.08}\text{La}_{0.05}\text{Yb}_{0.04}\text{Co}_4\text{Sb}_{12}$  from Ref. [81]; and a single-filled  $\text{Yb}_{0.22}\text{Co}_4\text{Sb}_{12}$  (nominal Yb content 0.30) with a surprisingly high value of  $ZT$  topping 1.5 from Ref. [47]. P-type skutterudites include a didymium-filled  $\text{DD}_{0.65}\text{Fe}_3\text{CoSb}_{12}$  from Ref. [305]; a didymium-filled and Sn-substituted  $\text{DD}_{0.59}\text{Fe}_{2.7}\text{Co}_{1.3}\text{Sb}_{11.8}\text{Sn}_{0.2}$  from Ref. [84]; a triple-filled  $\text{Ca}_{0.35}\text{Ce}_{0.35}\text{Nd}_{0.35}\text{Fe}_{3.5}\text{Co}_{0.5}\text{Sb}_{12}$  from Ref. [372]; double-filled skutterudites  $\text{Ce}_{0.45}\text{Nd}_{0.45}\text{Fe}_{3.5}\text{Co}_{0.5}\text{Sb}_{12}$  from Ref. [373], [374] and  $\text{La}_{0.68}\text{Ce}_{0.22}\text{Fe}_{3.5}\text{Co}_{0.5}\text{Sb}_{12}$  from Ref. [375]; a single-filled  $\text{Ce}_{0.28}\text{Fe}_{1.5}\text{Co}_{2.5}\text{Sb}_{12}$  from Ref. [369], and  $\text{Nd}_{0.6}\text{Fe}_2\text{Co}_2\text{Sb}_{11.7}\text{Ge}_{0.3}$  from Ref. [119].

skutterudites, an application of high-pressure torsion (HPT) was found to enhance the figure of merit to values near  $ZT \sim 2$  [83, 84]. The reader interested in details of the HPT process and its effect on the structural and transport parameters are referred to Ref. [302]. Although the figure of merit of n-type skutterudites seems to benefit from HPT, the defects introduced are partly annealed already upon the first measuring cycle to high temperatures, as the comparison of curves in the left-hand panel of Fig. 2.2.14 indicates (open, solid, and half-filled squares), and taking into account an expensive and not readily available HPT instrumentation, the technique is unlikely to make a major impact on the fabrication of skutterudites. In p-type skutterudites, a very effective filler was found in didymium [305–307], which is a commercially available mixture of 95.24 wt% of Nd and 4.76 wt% Pr, with Nd being known as an even more effective filler than Yb in reducing the thermal conductivity in fully filled skutterudites [368].  $ZT$  values of 1.2 obtained with didymium-filled  $[\text{Fe}_x\text{Co}_{4-x}\text{Sb}_{12}]$  frameworks were subsequently enhanced to 1.3 upon substituting a small fraction of Sn for Sb [84]. High-pressure torsion has not improved the performance of p-type

skutterudites substantially. Clearly, multifilled skutterudites have superior TE properties. However, one occasionally finds reports of an exceptional TE performance even with single-filled skutterudites, as documented by  $\text{Yb}_{0.22}\text{Co}_4\text{Sb}_{12}$  reaching  $ZT=1.5$  [47] in the case of n-type skutterudites, and  $\text{Ce}_{0.28}\text{Fe}_{1.5}\text{Co}_{2.5}\text{Sb}_{12}$  with  $ZT=1.1$  in the case of p-type skutterudites [369], and even an unfilled triple-doped  $\text{Co}_4\text{Sb}_{11}\text{Ge}_{0.2}\text{Te}_{0.70}\text{Se}_{0.10}$  was reported to reach  $ZT=0.99$  at 775 K [370].

In view of the strategic importance of rare earth elements, and consequently their cost, attempts have been made to replace them entirely by fillers from the family of alkaline earth. There have been several early studies with Ba, Sr, and Ca-filled skutterudites, which indicated quite high filling fractions but only modest reductions in the lattice thermal conductivity of Ba-filled [42,70,71,73,86,368,369,376,377], Sr-filled [41,368,378], and Ca-filled [40,298,368,379–381] skutterudites. A more recent work with Ca fillers in nearly fully filled single-phase  $\text{CaCo}_{4-x}\text{Fe}_x\text{Sb}_{12}$  with  $2 \leq x \leq 3.5$  prepared by melt spinning followed by SPS [313], resulted in quite high (measured by p-type standards) power factors of  $3.3 \text{ mW m}^{-1} \text{ K}^{-2}$ , which, combined with the low lattice thermal conductivity of  $0.84 \text{ W m}^{-1} \text{ K}^{-1}$  near 700 K, yielded a very respectable  $ZT=0.9$  at 773 K for  $\text{CaFe}_3\text{CoSb}_{12}$ . The surprisingly low value of the lattice thermal conductivity of  $\text{CaFe}_3\text{CoSb}_{12}$  (much lower than the lattice thermal conductivity of Ba- and Sr-filled structures even though Ca is lighter than Ba and Sr) was similar to that measured on  $\text{CaFe}_4\text{Sb}_{12}$  [368] and stimulated the authors to perform lattice dynamics calculations for an explanation. The calculations revealed the presence of a low-frequency mode of Ca ( $\sim 7 \text{ meV}$ ) with flat dispersion and thus very low group velocity. Such phonon features were apparently responsible for the lattice thermal conductivity of Ca-filled skutterudites being exceptionally low and comparable to that of  $\text{LaFe}_4\text{Sb}_{12}$ . Interestingly, double filling with Ca and Yb in equal amounts has not improved the  $ZT$  to any significant degree, apparently because both fillers affect the same normal phonon modes.

I would also like to mention two more studies that reported rather high  $ZT$  values. In the first one, various combinations of up to seven fillers with the rather high total filling fraction  $0.4 < y < 0.7$  were synthesized by partially replacing Co with Fe. The highest figure of merit  $ZT=1.5$  at about 800 K was achieved with n-type  $\text{Ba}_{0.1}\text{Yb}_{0.2}\text{Al}_{0.1}\text{La}_{0.05}\text{Eu}_{0.05}\text{Ga}_{0.1}\text{In}_{0.1}\text{Co}_{3.75}\text{Fe}_{0.25}\text{Sb}_{12}$  [382]. The second report [300] described an n-type, completely unfilled skutterudite of composition  $\text{Co}_{23.4}\text{Sb}_{69.1}\text{Si}_{1.5}\text{Te}_{6.0}$  ( $\text{Co}_4\text{Sb}_{11.81}\text{Si}_{0.256}\text{Te}_{1.025}$  if normalized to the Co constituency of four), annealed at 873 K for 15 h, that achieved an unprecedented  $ZT=1.6$  as a consequence of the presence of numerous nanometer—to micrometer size pores, which dramatically lowered the lattice thermal conductivity. The porous architecture was left behind upon high-temperature annealing as the excess of Te evaporated.

## 2.2.7 Mechanical properties of skutterudites

Long service life and reliability of TE modules operating under harsh conditions of high cycling temperatures require thermoelectric materials to possess robust elastic moduli to withstand external and internal strains. In skutterudites, processing and

microstructure play an important role in the overall mechanical properties. For instance, the fracture strength depends inversely on the square of the grain size [383]. Thus, the cast ingots, with grain sizes typically tens of microns, have a significantly lower fracture strength than samples consolidated from submicron powders prepared by ball milling, e.g., Ref. [384]. As already mentioned, in spite of possessing structural voids, the skutterudite structure is remarkably stable and, in the case of IrSb<sub>3</sub>, does not collapse under the pressure of at least 42 GPa generated in diamond anvil cells [385]. Indeed, experimental studies of mechanical properties have documented superior performance of skutterudites over other thermoelectric materials [386–388]. The eventual catastrophic failure of a single crystal of CoSb<sub>3</sub> under uniaxial tension and compression has been visualized by molecular dynamics simulations [389]. The three elastic constants appropriate for the cubic structure of CoSb<sub>3</sub>, C<sub>11</sub>=185.13 GPa, C<sub>12</sub>=46.95 GPa, and C<sub>44</sub>=43.02 GPa computed at 300 K, are in excellent agreement with the first-principles computed values and decrease monotonically with increasing temperature on account of softening of the structure. The Young's modulus, the Poisson ratio, and the ultimate strength under virtual tension at 300 K turned out to be 165.9 GPa, 0.193, and 22.18 GPa, respectively. Under virtual compression, CoSb<sub>3</sub> is distinctly more robust than under tension with the corresponding values at 300 K of 181.6 GPa, 0.206, and 39.44 GPa. The ultimate compressive strength of 39.44 GPa is consistent with the experimental report of CoSb<sub>3</sub> withstanding pressures well above 20 GPa [390]. The eventual catastrophic failure of CoSb<sub>3</sub> is in accord with the behavior of conventional brittle materials. An atomistic explanation of brittle fracture in CoSb<sub>3</sub> was offered recently [391] based on large-scale molecular dynamics simulations of the shear response along the most plausible (010)/(100) slip system. The simulations revealed that the brittle fracture in CoSb<sub>3</sub> is initiated by the failure of the shorter Sb—Sb bond within the Sb<sub>4</sub> ring, accompanied by the slippage of Co octahedrons. This, in turn, causes the breakdown of the Co—Sb bond, leading to the destruction of the Co octahedrons, and the ensuing propagating cavitation, i.e., the opening of the crack. At 300 K, this happens at the ultimate shear stress of 14.04 GPa when the failure shear strain reaches 0.4436. The ultimate shear stress decreases to 13.46 GPa at 800 K.

Fatigue resulting from cycling loading of CoSb<sub>3</sub>-based skutterudites was investigated by Ruan et al. [392]. The test involved repeated loading of well-compacted (99% theoretical density) CoSb<sub>3</sub> and Ce<sub>0.5</sub>Fe<sub>1.5</sub>Co<sub>2.5</sub>Sb<sub>12</sub> samples with 60% and 80% maximum compressive strength (an average value obtained on several identical samples was 384 MPa) and measuring the residual compressive strength after a predetermined number of cycles as well as measuring the number of cycles prior to a complete failure. Catastrophic cracks formed as a result of local stress accumulation at the preexisting defect sites, such as tiny nanopores and microcracks, and propagated along the grain boundaries, a situation typical of brittle solids. After 5000 loading cycles with 60% of compressive strength, the fatigue tests indicated the residual strength reduced by 19% (312 MPa). After 18,000 loading cycles, the residual strength decreased by 42% (222 MPa). Higher percentage loading (80% of the compressive strength) resulted in halving the number of cycles the samples could survive (from 35,000 to 45,000 of cycles at 60% compressive strength down to around 20,000 of

cycles at 80% compressive strength). The results documented a considerable cyclic fatigue effect on the residual compressive strength in skutterudites.

The porosity of a structure affects the TE performance. Phonon scattering at pores reduces the lattice thermal conductivity, as shown long ago [393]. Moreover, an inhomogeneous distribution of the pores is more effective in degrading the thermal conductivity than are uniformly distributed pores [394]. What is less obvious is that the porous structures always have an enhanced absolute value of the Seebeck coefficient, which arises as a consequence of the increased entropy in porous structures. However, in this case, it is substantially irrelevant whether the pores are distributed homogeneously or whether there are various distributions of pore sizes [395]. Porous structures have recently attracted considerable interest as a means of enhancing the thermoelectric performance, chiefly by having much-reduced lattice thermal conductivity. In the case of skutterudites, the pivotal work was the observation of exceptionally high  $ZT \sim 1.6$  at 800 K upon 15 h high-temperature annealing of unfilled double-doped  $\text{CoSb}_{2.95}\text{Si}_{0.064}\text{Te}_{0.256}$ , during which the excess of Te evaporated and left behind pores with dimensions spanning from several hundred nanometers to several micrometers [300]. Although an exciting discovery, a question looms regarding the mechanical stability of structures containing pores. Indeed, extensive molecular dynamics simulations show [396] that both the tensile and compressive elastic moduli decrease with the increasing degree of porosity, halving the strain a single crystal of  $\text{CoSb}_3$  can withstand prior to breaking. The effect does not seem to depend in any major way on the radius of pores in the range 10–30 Å. Perhaps not surprisingly, the tensile strength is affected far more than the compressive strength.

Since power-generating TE modules operate over a wide range of temperatures, and n- and p-type legs are not of the same material, thermal expansion is an important parameter relevant to the structural stability of the module. Any significant asymmetrical strain developed between the n- and p-type elements may lead to a fracture, rendering the module useless. Over the years, thermal expansion has been measured numerous times on a vast variety of skutterudites. The most comprehensive table of thermal expansion coefficients obtained on skutterudites can be found in Ref. [217]. The  $\text{CoSb}_3$ -based skutterudites have the linear thermal expansion coefficient around  $10 \times 10^{-6} \text{ K}^{-1}$ , with p-type skutterudites marginally larger than n-type skutterudites.

## 2.2.8 Thermal stability of skutterudites

While possessing excellent thermoelectric properties during laboratory measurements, the critical issue with skutterudites is their stability following exposure to air under high-temperature operations. As originally envisaged, based on their thermoelectric parameters, the intent was to use skutterudites in power generation applications in the temperature range roughly between 500 and 800 K, the range where many opportunities exist for waste heat recovery, including in the operations of gasoline and diesel-powered vehicles.

However, as recognized early on [397–400], there are serious decomposition and oxidation issues with skutterudites, commencing already around 600 K. A thorough evaluation was needed to find effective strategies for minimizing the degradation of the material. Detailed assessments of decomposition routes and oxide reactions taking place in  $\text{CoSb}_3$  as a function of temperature under various atmospheres are given in [401–404]. The activation energy for the sublimation of Sb was found to be 44.5 kJ/mol [405], while the oxidation activation energy of  $\text{CoSb}_3$  was stated as 37.4 kJ/mol [406]. Similar problems were found with filled skutterudites [59,407–411]. Even though the figure of merit did not decrease dramatically at elevated temperatures, the structural integrity of the samples was compromised. In the case of a nanocomposite of 1 vol% of TiN dispersed in  $\text{Co}_4\text{Sb}_{11.5}\text{Te}_{0.5}$ , the figure of merit actually increased by 20% after annealing at 773 K in vacuum for 100 h, but the porosity increased as some Sb evaporated [412]. It should also be noted that the desire to prepare nanometer-scale grain sizes expected to strongly scatter heat-conducting phonons is seriously undermined by heating skutterudites to high temperatures, where the grain growth is intensified [413]. The conclusion that, without effective protection, the long-term operation of skutterudite-based modules in air and temperatures above 700 K would be compromised, brought into the forefront the urgent need to find ways of mitigating the harmful effect of oxidation amplified by the volatilization of Sb.

Initial attempts to stop the evaporation of Sb consisted of magnetron sputter-deposited thin metallic coatings on the skutterudite legs. This included metals, such as Mo, V, Ta, and Ti [414,415], and proved effective. Further aging tests with Ti [416] have shown that the sublimation of Sb can be blocked to temperatures of about 923 K. A double-layer Al-Ni coating on  $\text{Yb}_{0.3}\text{Co}_4\text{Sb}_{12}$  applied via electrochemical deposition [417] performed well in accelerated aging tests at 873 K for 30 days, indicating essentially no change in the structure and excellent protection from oxidation and Sb sublimation. However, not all metal coatings performed so well. For instance, coatings with Cr-5Si lost their effectiveness above 873 K due to cracking [418]. Of course, from the practical point of view, metal coatings are not a solution, at least not applied directly to the skutterudite legs, as they electrically short the resistance of the thermoelectric material. The interest thus shifted toward electrically insulating coatings, such as enamel layers [419,420], aerogels [421,422], and inorganic/organic silica layers, often containing dispersed glass or granular alumina particles that were supposed to inhibit cracking during solidification of the gel [423,424]. Such layers performed well in aging tests to 873 K in a vacuum, although some diffusion of Sb was detected in the coated layer. Undoubtedly, efforts will continue to find effective protective coatings for skutterudites that withstand the harsh conditions of cycling to high temperatures with minimal deterioration.

## 2.2.9 Thermoelectric modules based on skutterudites

Although spectacular results have been obtained during the past 10 years regarding the thermoelectric figure of merit for both n- and p-type skutterudites, the success has not resulted in the development of commercial TE modules based on skutterudites. In fact,

no skutterudite-based power-generating module can be purchased currently on the market. While the  $ZT$  values reported for skutterudite materials are clearly superior to other families of thermoelectrics intended for power generation applications in the temperature range of 500–800 K, the market remains dominated by  $\text{Bi}_2\text{Te}_3$  and  $\text{PbTe}$  technology. The state of the affairs persists in spite of skutterudites also having advantages as far as the mechanical strength, environmental considerations, and the cost advantage are concerned. It is not entirely clear why this is so, but perhaps it is the reluctance to invest in a venture that does not immediately offer financial rewards. The fact that the operation of skutterudite modules at elevated temperatures requires protective coatings to prevent volatilization of Sb and oxidation when operated in the air is an added complexity that may hamper investments. Moreover, the largest and truly mass-scale anticipated application of skutterudites as power generators converting waste exhaust heat of gasoline and diesel-powered vehicles has substantially lost its appeal with plans for electrification of a new generation of cars. Regarding skutterudites, in particular, the proposed location of thermoelectric generators along the exhaust system is too far down the pipe, where available exhaust gas temperatures are low, rendering skutterudites uncompetitive with well-developed technology based on  $\text{Bi}_2\text{Te}_3$ -type modules. Much higher temperatures are available closer to the engine block, where skutterudites would truly show their advantage, but automotive engineers do not like to consider this option as the rapid warming of the catalytic converter is the number one priority in satisfying emission standards.

However, the lack of commercially available skutterudite modules does not mean that several larger research groups have not tried to assemble quite efficient skutterudite-based thermoelectric modules. In this section, I will describe several of them.

The first effort to make modules based on skutterudites goes back some 20 years when Caillat et al. [425,426] assembled unicouples consisting of a Te-doped  $\text{CoSb}_3$  n-type leg combined with a  $\text{Ce}_{0.8}\text{Fe}_{3.5}\text{Co}_{0.5}\text{Sb}_{12}$  p-type leg that generated the maximum power output of 1.3 W at a current of 15 A (efficiency of about 10%). The measured internal resistance of the unicouple was  $5.46\text{ m}\Omega$ . By brazing an Nb metal bridge across the n- and p-type elements at the hot end and using a Bi-Sn solder to attach the cold end of the legs to Cu-plated  $\text{Al}_2\text{O}_3$ , the unicouple operated with the hot side at 873 K, and the cold side maintained at 363 K. The authors also proposed and developed the technology for segmented unicouples comprising short segments of n- and p-type  $\text{Bi}_2\text{Te}_3$ -based materials to generate power at the low-temperature end while the skutterudite segments would be effective above 500 K.

For successful operation of high-temperature TE modules, it is critical to develop strategies to prevent diffusion between thermoelectric legs and electrodes, keep the internal resistance to a minimum, and make the module mechanically robust to withstand cycling to high temperatures. Experience with skutterudite modules has been gained through successive experimental efforts. N-type  $\text{Yb}_{0.25}\text{Co}_4\text{Sb}_{12}/\text{Yb}_2\text{O}_3$  (excess Yb oxidized when the ingot was processed into a fine powder in the air prior to SPS) and p-type  $\text{Ce}_{0.45}\text{Co}_{2.5}\text{Fe}_{1.5}\text{Sb}_{12}$  were used to assemble modules consisting of two n-p couples [427]. A diffusion barrier in the form of plasma-sprayed Mo was applied to both ends of the TE elements. The hot end of the legs was attached to a 1-mm thick

Mo-Cu plate (comparable coefficient of thermal expansion as  $\text{CoSb}_3$ ). The actual joints were made by a short SPS process at 1023K under 10–20 MPa using Ag-Cu solder. The cold side of the legs was connected to Cu electrodes in an alumina substrate using ordinary Sn-based solder. The couples operated across a 490K temperature difference, generating 210mV open voltage with the maximum power output of 140mW when the load resistance matched the internal resistance of 73 m $\Omega$ . While the theoretical conversion efficiency was projected at 8.4%, the experimental efficiency at 6.4% was lower, due to the contact resistance and the heat loss. Mo proved a good diffusion barrier and no deterioration in the performance was observed after five repeated thermal cycles. More on the development of modules, their testing, and the incorporation of aerogel-based thermal insulation is described in Ref. [422]. Multifilled skutterudites ( $n\text{-Yb}_{0.3}\text{Ca}_{0.1}\text{Co}_{3.75}\text{Fe}_{0.25}\text{Sb}_{12}$  and  $p\text{-La}_{0.7}\text{Ba}_{0.1}\text{Fe}_3\text{CoSb}_{12}$  with maximum  $ZTs$  of 1.0 and 0.65, respectively) served as active elements in a 32-unicouple module assembled with Co-Fe-Ni-based alloys serving as both diffusion barriers and electrodes [428]. The alloy composition was adjusted to match the thermal expansion of the n- and p-type legs. The module developed a maximum power output of 32 W with a conversion efficiency of 8% when operated with a 550K temperature difference between the hot and cold junctions (the hot junction kept at 873 K). Subjected to 100 heating/cooling cycles between 873 and 473 K with further continuous heating at 873 K for 240h in a vacuum, no changes in the output power were detected, and no significant interdiffusion was observed at the skutterudite-diffusion barrier interface even after 1 month annealing at 873 K. Such a successful outcome was not observed [429] with a 9-unicouple module that used skutterudites with a composition similar to that in Ref. [425]. The module operated with the temperatures at the hot junction not exceeding 575 K. Even though a rather low temperature, the authors noted a dramatic increase in the internal resistance of the module after just four thermal cycles, which they attributed to the degradation of the electrical contacts because the tests were carried out in the air.

During the past dozen or so years, most of the major car companies have engaged in and supported research into recovery and conversion of waste exhaust heat produced by gasoline and diesel engines in order to improve fuel consumption by reducing the load on an alternator. The GM Global Research & Development team [430,431] described the design, assembly, performance, and properties of the critical parts of 32-couple skutterudite-based modules intended to operate under the temperature difference of 460K (hot junction at 773K). The modules generated a power output between 8.5 and 11.5 W, representing up to 7.5% conversion efficiency, depending on the loading pressure and the nature of the interface materials. In particular, the team documented the importance of minimizing parasitic losses arising during the module assembly that can rapidly degrade the performance of otherwise excellent thermoelectric materials. The team also developed a protective silica-based enamel coating for the TE elements to suppress oxidation and sublimation when operating in air at high temperatures [420]. Several other groups have developed skutterudite-based modules. An interesting variant was a unicouple arranged in an in-line configuration rather than the usual  $\Pi$ -formation (see Fig. 2.2.15) that used  $\text{Yb}_{0.35}\text{Co}_4\text{Sb}_{12}$  for the n-type leg and  $\text{NdFe}_{3.5}\text{Co}_{0.5}\text{Sb}_{12}$  for the p-type leg [432]. As electrodes were used  $\text{CoSi}_2$  for the n-leg

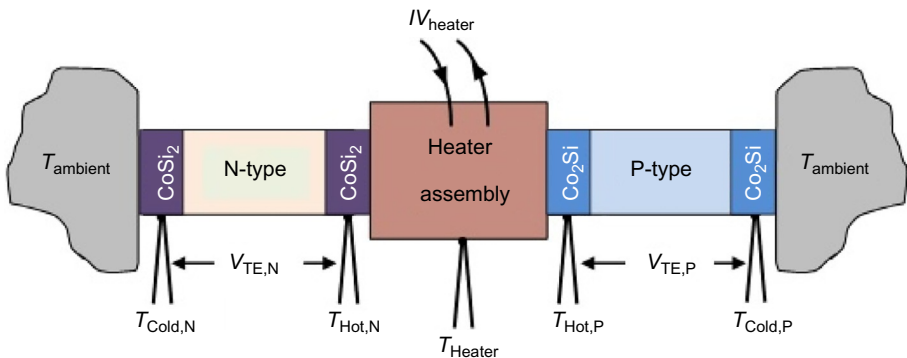


**Fig. 2.2.15** Schematic layout of an in-line arrangement of n- and p-legs of a unicouple.

(contact resistances  $0.7\text{--}2 \times 10^{-10} \Omega \text{m}^2$ ) and  $\text{Co}_2\text{Si}$  for the p-leg (contact resistances  $1.2\text{--}2.3 \times 10^{-10} \Omega \text{m}^2$ ) represent 2.3%–5.1% of the total resistance of the legs. The authors used the effective values of the transport parameters to define the effective  $ZT_{\text{eff}}$  of the legs (0.74 for the n-type leg operated between 325 and 868 K, and 0.51 for the p-type leg operated between 343 and 823 K), and the maximum efficiency of their n-p unicouple reached 9.1% when kept between about 343 and 823 K. The Tsukuba Development Center [433] assembled a 32-couple module from multifilled n-type  $(\text{Yb,Ca,Al,Ga,In})_{0.7}\text{Fe}_{0.25}\text{Co}_{3.75}\text{Sb}_{12}$  and p-type  $(\text{La,Ba,Ga,Ti})_{0.9}\text{Fe}_3\text{CoSb}_{12}$  with diffusion barriers prepared by SPS during the consolidation of the skutterudite powders. The module, operated with the hot side at 873 K while the cold side was maintained at 323 K, generated the power output of about 25 W with the efficiency as high as 7.2%. Although the efficiency was much below the theoretical value of nearly 13%, the module had excellent stability even when operating at 873 K for more than 1000 h. Subsequently, the authors used improved skutterudite materials and the efficiency increased to 8.5%.

I have already pointed out that composites of skutterudites with various forms of graphite have shown high figures of merit. One such form, reduced graphene oxide (rGO), was used as an additive in n-type  $\text{Yb}_{0.27}\text{Co}_4\text{Sb}_{12}$  (0.72 vol% of rGO) and in p-type  $\text{Ce}_{0.85}\text{Fe}_3\text{CoSb}_{12}$  (1.4 vol% of rGO) to build a 16-couple module [434]. The operation of the module was compared to a similar 16-couple module with the same skutterudite elements but with no rGO additives. Operating both modules with 873 K hot and 296 K cold temperatures, the module using composite skutterudite elements attained the highest power output of 3.8 W and the efficiency of 8.4%, while the modules with no rGO additives reached the highest power output of only 3.1 W and the lower efficiency of 6.8%. By far the best thermoelectric performance has been achieved recently by Zhang et al. [435] using 8-couple modules with rationally designed short segmented legs of  $\text{Bi}_2\text{Te}_3$ -type materials (2.1 mm n-type and 2.3 mm p-type) with longer legs of n- and p-type skutterudites (9.9 mm n-type and 9.7 mm p-type), for the total length of the segmented legs of 12 mm. The numerical analysis took into account the temperature-dependent thermoelectric properties of the materials and various parasitic losses. The modules were operated under a temperature difference of 541 K with the hot side at 849 K and delivered 5.7 W power at an efficiency

of 12%. The skutterudite segments were prepared by one-step SPS sintering of the skutterudite powder (n-type  $\text{Yb}_{0.3}\text{Co}_4\text{Sb}_{12}$ , p-type  $\text{CeFe}_{3.85}\text{Mn}_{0.15}\text{Sb}_{12}$ ), Ti-Al powder, and Ni foil subsequently brazed to a  $\text{Mo}_{50}\text{Cu}_{50}$  electrode. The composition of the Ti-Al barrier layer was carefully optimized so that the contact resistance between Ti-Al and skutterudite joints was below  $10 \mu\Omega\text{cm}^2$ . Exposed to 384 h at 873 K under vacuum, the  $\text{Ti}_{0.88}\text{Al}_{12}$ /skutterudite contact remained under  $10 \mu\Omega\text{cm}^2$ , demonstrating its superior performance. The  $\text{Bi}_2\text{Te}_3$ -type materials were n-type  $\text{Bi}_{2}\text{Te}_{2.5}\text{Se}_{0.5}$  and p-type  $\text{Bi}_{0.4}\text{Sb}_{1.6}\text{Te}_3$  disks metallized on both faces with Ni, and subsequently diced into the desired size and soldered to the skutterudite segments. The total interfacial resistivity of all contacts was about  $40 \mu\Omega\text{cm}^2$ , contributing no more than 2% loss in the maximum conversion efficiency. All segmented legs were of fixed  $4 \times 4\text{mm}^2$  cross section, with a 1 mm gap between the n- and p-legs. To minimize radiation and convection losses within the module, low thermal conductivity glass fibers were used to fill the gaps between the legs. A schematic representation of the segmented couple and the efficiency of the 8-couple module as a function of the current under different operating temperatures are presented in Fig. 2.2.16.

Most recently, a 14-couple module, constructed from n-type  $\text{Yb}_{0.15}\text{Co}_4\text{Sb}_{12}$  and p-type  $\text{CeFe}_3\text{CoSb}_{12}$  with Ag sheet electrodes bonded to the skutterudite elements with an Ag-23 mass% Pd paste sintered at 723 K for 7 h in a vacuum under the uniaxial pressure of 14.7 MPa, was tested in the air [436]. No deterioration in the performance was observed for long-term exposure at 573 K. However, raising the hot side temperature to 673 K resulted in an increased resistivity and decreased power output, with  $\text{Sb}_2\text{O}_3$  detected at the hot end of the p-type elements. The overall performance of the module suffered greatly from very inefficient n-type legs having the  $ZT$  considerably inferior to that of the p-type elements.

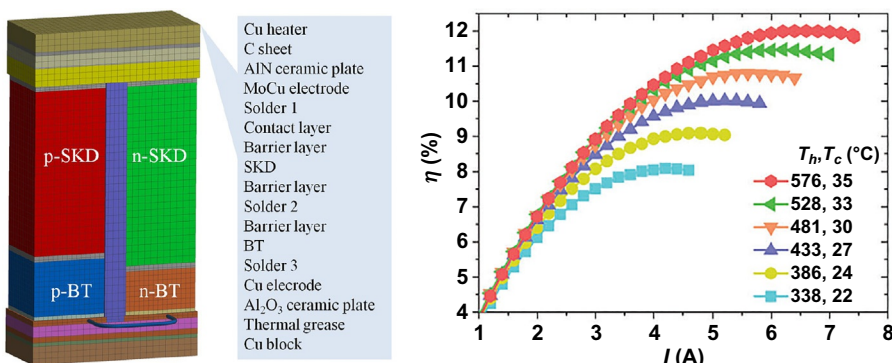


**Fig. 2.2.16** The left panel shows a schematic layout of the segmented couple with the legend indicating the sequence of layers. The right-hand panel presents the measured conversion efficiency at various temperatures of an 8-couple module assembled from the segmented legs shown in the left-hand panel.

Reproduced and modified from Q.H. Zhang, J.C. Liao, Y.S. Tang, M. Gu, C. Ming, R.F. Qiu, S. Q. Bai, X. Shi, C. Uher, L.D. Chen, Energy Environ. Sci. 10 (2017) 956. With permission from the Royal Society of Chemistry.

## 2.2.10 Conclusion

Intensive worldwide research efforts during the past two decades have established skutterudites as a premier family of thermoelectric materials. By judicious doping, multiple filling, forming interesting composite structures, and developing innovative processing methods, both n-type and p-type forms of the material have attained thermoelectric figures of merit well in excess of unity. In fact, some n-type skutterudites have been approaching the previously unheard of  $ZT \sim 2$ . In the process of developing efficient skutterudite materials, much has been learned about their physical, chemical, and mechanical properties, and the structure has often served as a test bed on which to verify various proposals to enhance the thermoelectric performance by invoking imaginative modifications of the electronic band structure and phonon dispersion. By any measure, the progress in the material aspects of skutterudites has been spectacular.

Unfortunately, the same cannot be said about the development of thermoelectric modules based on skutterudites. In fact, apart from local efforts of some larger research groups developing and testing their skutterudite-based prototype modules, one cannot purchase any skutterudite module because there is simply no one manufacturing them. This unhappy state of affairs persists in spite of skutterudites being clearly one of the most affordable thermoelectric materials in terms of the availability and cost of the constituent elements. Unfortunately, skutterudites require protective coatings when operated at temperatures above 700 K to limit the loss of Sb and to prevent oxidation when used in air. Such protective coatings represent processing complications, but not insurmountable ones. Although the anticipated replacement of gasoline and diesel engines by electrically driven motors has taken away one of the most prospective mass-scale applications of skutterudites intended to convert the heat of exhaust gases into electricity, there are plenty of other opportunities where efficient and structurally sound thermoelectric modules operating in the 500–800 K temperature range should find great use. The lack of commercially available modules, however, does not allow even exploratory work in such areas of waste heat recovery.

## Acknowledgments

I am grateful to my graduate student, Trevor P. Bailey, for proofreading the manuscript. My research is supported by a grant from the US Department of Energy DE-SC0018941.

## References

- [1] G.A. Slack, in: D.M. Rowe (Ed.), *CRC Handbook of Thermoelectrics*, CRC Press, Boca Raton, FL, 1995, p. 407.
- [2] M.B. Maple, E. Bauer, N.A. Frederick, P.-C. Ho, W.A. Yuhasz, V.S. Zapf, *Physica B* 328 (2003) 29.
- [3] H. Sato, H. Sugawara, Y. Aoki, H. Harima, *Handbook of Magnetic Materials*, vol. 18, Elsevier, 2009, p. 1 (Chapter 1).

- [4] E. Bauer, N.A. Frederick, P.-C. Ho, V.S. Zapf, M.B. Maple, Phys. Rev. B 65 (2002) 100506(R).
- [5] H. Sugawara, T.D. Matsuda, K. Abe, Y. Aoki, H. Sato, S. Nojiri, Y. Inada, R. Settai, Y. Ônuki, Phys. Rev. B 66 (2002) 134411.
- [6] V. Pardo, J.C. Smith, W.E. Pickett, Phys. Rev. B 85 (2012) 214531.
- [7] B.H. Yan, L. Müchler, X.-L. Qi, S.-C. Zhang, C. Felser, Phys. Rev. B 85 (2012) 165125.
- [8] I. Oftedal, Z. Kristallogr. A66 (1928) 517.
- [9] L.D. Dudkin, N.K. Abrikosov, Zh. Neorg. Khim. 1 (1956) 2096.
- [10] M.D. Hornbostel, E.J. Hyer, J. Thiel, D.C. Johnson, J. Am. Chem. Soc. 119 (1997) 2665.
- [11] M.V. Daniel, L. Hammerschmidt, C. Schmidt, F. Timmermann, J. Franke, N. Jöhrmann, M. Hietschold, D.C. Johnson, B. Paulus, M. Albrecht, Phys. Rev. B 91 (2015) 085410.
- [12] P. Jolibois, C. R. Acad. Sci. 150 (1910) 106.
- [13] F. Hulliger, Helv. Phys. Acta 34 (1961) 782.
- [14] L.D. Dudkin, N.K. Abrikosov, Zh. Neorg. Khim. 2 (1957) 212.
- [15] J. Yang, G.P. Meisner, C. Uher, Proceedings of the 18<sup>th</sup> International Conference on Thermoelectrics, IEEE Catalog Number 99TH8407, Piscataway, NJ, 1999, p. 458.
- [16] C.M. Pleass, R.D. Heyding, Can. J. Chem. 40 (1962) 590.
- [17] E.H. Nickel, Chem. Geol. 5 (1969) 233.
- [18] W. Jeitschko, A.J. Foecker, D. Paschke, M.V. Dewalsky, C.B.H. Evers, B. Künnen, A. Lang, G. Kotzyba, U.C. Rodewald, M.H. Möller, Z. Anorg. Allg. Chem. 626 (2000) 1112.
- [19] H.D. Lutz, G. Kliche, J. Solid State Chem. 40 (1981) 64.
- [20] A. Borshchevsky, J.-P. Fleurial, E. Allevato, T. Caillat, Proceedings of the 13<sup>th</sup> International Conference on Thermoelectrics, American Institute of Physics, Kansas City, MO, 1995, p. 3.
- [21] G.A. Slack, V.G. Tsoukala, J. Appl. Phys. 76 (1994) 1665.
- [22] A. Kjekshus, T. Rakke, Acta Chem. Scand. A 28 (1974) 99.
- [23] R. Korenstein, S. Soled, A. Wold, G. Collin, Inorg. Chem. 16 (1977) 2344.
- [24] J.-P. Fleurial, T. Caillat, A. Borshchevsky, Proceedings of the 16<sup>th</sup> International Conference on Thermoelectrics, IEEE Catalog Number 97TH8291, Piscataway, NJ, 1997, p. 1.
- [25] T. Caillat, J. Kulleck, A. Borshchevsky, J.-P. Fleurial, J. Appl. Phys. 79 (1996) 8419.
- [26] P. Vaqueiro, G.G. Sobany, A.V. Powell, K.S. Knight, J. Solid State Chem. 179 (2006) 2047.
- [27] D. Volja, B. Kozinsky, A. Li, D. Wee, N. Marzari, M. Fornari, Phys. Rev. B 85 (2012) 245211.
- [28] A. Lyons, R.P. Gruska, C. Case, S.N. Subbarao, A. Wold, Mater. Res. Bull. 13 (1978) 125.
- [29] M. Partik, C. Krings, H.D. Lutz, Z. Kristallogr. 211 (1996) 304.
- [30] A. Zevalkink, K. Star, U. Aydemir, G.J. Snyder, J.-P. Fleurial, S. Bux, T. Vo, P. von Allmen, J. Appl. Phys. 118 (2015) 035107.
- [31] P. Vaqueiro, G.G. Sobany, M. Stindl, J. Solid State Chem. 181 (2008) 768.
- [32] W. Jeitschko, D.J. Braun, Acta Crystallogr. B 33 (1977) 3401.
- [33] D.J. Braun, W. Jeitschko, J. Less-Common Met. 72 (1980) 147.
- [34] D.J. Braun, W. Jeitschko, J. Solid State Chem. 32 (1980) 357.
- [35] G.P. Meisner, Physica B&C 108 (1981) 763.
- [36] D.T. Morelli, G.P. Meisner, J. Appl. Phys. 77 (1995) 3777.
- [37] B.C. Sales, D. Mandrus, B.C. Chakoumakos, V. Keppens, J.R. Thompson, Phys. Rev. B 56 (1997) 15081.
- [38] Y.Z. Pei, L.D. Chen, W.Q. Zhang, X. Shi, S.Q. Bai, X.Y. Zhao, Z.G. Mei, X.Y. Li, Appl. Phys. Lett. 89 (2006) 221107.

- [39] Z.G. Mei, J. Yang, Y.Z. Pei, W.Q. Zhang, L.D. Chen, J. Yang, *Phys. Rev. B* 77 (2008) 045202.
- [40] M. Puyet, B. Lenoir, A. Dauscher, M. Dehmas, C. Stiewe, E. Müller, *J. Appl. Phys.* 95 (2004) 4852.
- [41] X.Y. Zhao, X. Shi, L.D. Chen, W. Zhang, W.B. Zhang, Y.Z. Pei, *J. Appl. Phys.* 99 (2006) 053711.
- [42] L.D. Chen, T. Kawahara, X.F. Tang, T. Goto, T. Hirai, J.S. Dyck, W. Chen, C. Uher, *J. Appl. Phys.* 90 (2001) 1864.
- [43] G.S. Nolas, J.L. Cohn, G.A. Slack, *Phys. Rev. B* 58 (1998) 164.
- [44] B. Chen, J.X. Xu, C. Uher, D.T. Morelli, G.P. Meisner, J.-P. Fleurial, T. Caillat, A. Borshchevsky, *Phys. Rev. B* 55 (1997) 1476.
- [45] V.L. Kuznetsov, L.A. Kuznetsova, D.M. Rowe, *J. Phys. Condens. Matter* 15 (2003) 5035.
- [46] S. Berger, C. Paul, E. Bauer, A. Grytsiv, P. Rogl, D. Kaczorowski, A. Saccone, R. Ferro, C. Godart, Proceedings of the 20<sup>th</sup> International Conference on Thermoelectrics, IEEE Catalog 01TH8589, Piscataway, NJ, 2001, p. 77.
- [47] S. Wang, J.R. Salvador, J. Yang, P. Wei, B. Duan, J. Yang, *NPG Asia Mater.* 8 (2016) e285.
- [48] A. Harnwunggmoung, K. Kurosaki, T. Plirdpring, T. Sugihara, Y. Ohishi, H. Muta, S. Yamanaka, *J. Appl. Phys.* 110 (2011) 013521.
- [49] T. He, J.Z. Chen, H.D. Rosenfeld, M.A. Subramanian, *Chem. Mater.* 18 (2006) 759.
- [50] B.C. Sales, B.C. Chakoumakos, D. Mandrus, *Phys. Rev. B* 61 (2000) 2475.
- [51] H. Takizawa, K. Okazaki, K. Uheda, T. Endo, G.S. Nolas, *Mater. Res. Soc. Symp. Proc.* 691 (2002) 37.
- [52] H. Luo, J.W. Krizan, L. Muechler, N. Haldolaarachchige, T. Klimczuk, W. Xie, M.K. Fuccillo, C. Felser, R.J. Cava, *Nat. Commun.* 6 (2015) 6489.
- [53] G.S. Nolas, M. Kaeser, R.T. Littleton, T.M. Tritt, *Appl. Phys. Lett.* 77 (2000) 1855.
- [54] H. Anno, Y. Nagamoto, K. Ashida, E. Taniguchi, T. Koyanagi, K. Matsubara, in: D.M. Rowe (Ed.), Proceedings of the 19<sup>th</sup> International Conference on Thermoelectrics, Babrow Press, UK, 2000, p. 90.
- [55] B.C. Sales, B.C. Chakoumakos, D. Mandrus, *Mater. Res. Soc. Symp. Proc.* 626 (2000) Z7.1.1.
- [56] J. Nagao, D. Nataraj, M. Ferhat, T. Uchida, S. Takeya, T. Ebinuma, H. Anno, K. Matsubara, E. Hatta, K. Musaka, *J. Appl. Phys.* 92 (2002) 4135.
- [57] X.Y. Zhao, X. Shi, L.D. Chen, W.Q. Zhang, S.Q. Bai, Y.Z. Pei, X.Y. Li, T. Goto, *Appl. Phys. Lett.* 89 (2006) 092121.
- [58] H. Li, X.F. Tang, Q.J. Zhang, C. Uher, *Appl. Phys. Lett.* 93 (2008) 252109.
- [59] X. Xia, P. Qui, X. Shi, X. Li, X. Huang, L.D. Chen, *J. Electron. Mater.* 41 (2012) 2225.
- [60] J. Yang, Q. Hao, H. Wang, Y. Lan, Q. He, A. Minnich, D. Wang, J. Harriman, V. Varki, M.S. Dresselhaus, G. Chen, Z. Ren, *Phys. Rev. B* 80 (2009) 115329.
- [61] J. Yang, G.P. Meisner, W. Chen, J.S. Dyck, C. Uher, Proceedings of the 20<sup>th</sup> International Conference on Thermoelectrics, IEEE Catalog Number 01TH 8589, Piscataway, NJ, 2001, p. 73.
- [62] G.A. Lamberton, R.H. Tedstrom, T.M. Tritt, G.S. Nolas, *J. Appl. Phys.* 97 (2005) 113715.
- [63] Y. Tang, S.-W. Chen, G.J. Snyder, *J. Materomics* 1 (2015) 75.
- [64] C. Sekine, H. Saito, T. Uchihami, A. Sakai, I. Shirotani, *Solid State Commun.* 106 (1998) 441.
- [65] H. Takizawa, K. Miura, M. Ito, T. Suzuki, T. Endo, *J. Alloys Compd.* 282 (1999) 79.

- [66] J. Zhang, B. Xu, L.-M. Wang, D. Yu, Z. Liu, J. He, Y. Tian, *Appl. Phys. Lett.* **98** (2011) 072109.
- [67] D. Bérardan, C. Godart, E. Alleno, S. Berger, E. Bauer, *J. Alloys Compd.* **351** (2003) 18.
- [68] D. Bérardan, E. Alleno, C. Godart, M. Puyet, B. Lenoir, *J. Appl. Phys.* **98** (2005) 033710.
- [69] Q.M. Lu, J.X. Zhang, X. Zhang, Y.Q. Liu, M.D. Liu, M.L. Zhou, *J. Appl. Phys.* **98** (2005) 106107.
- [70] J. Yang, W.Q. Zhang, S.Q. Bai, Z. Mei, L.D. Chen, *Appl. Phys. Lett.* **90** (2007) 192111.
- [71] J.S. Dyck, W. Chen, C. Uher, L.D. Chen, X.F. Tang, T. Hirai, *J. Appl. Phys.* **91** (2002) 3698.
- [72] V.V. Khovaly, T.A. Korolkov, A.I. Voronin, M.V. Gorshenkov, A.T. Burkov, *J. Mater. Chem. A* **5** (2017) 3541.
- [73] X. Shi, H. Kong, C.-P. Li, C. Uher, J. Yang, J.R. Salvador, H. Wang, L.D. Chen, W.Q. Zhang, *Appl. Phys. Lett.* **92** (2008) 182101.
- [74] S.Q. Bai, Y.Z. Pei, L.D. Chen, W.Q. Zhang, X.Y. Zhao, J. Yang, *Acta Mater.* **57** (2009) 3135.
- [75] W. Zhao, P. Wei, Q.J. Zhang, C.L. Dong, L. Liu, X.F. Tang, *J. Am. Chem. Soc.* **131** (2009) 3713.
- [76] H. Li, X.F. Tang, Q.J. Zhang, C. Uher, *Appl. Phys. Lett.* **94** (2009) 102114.
- [77] J. Graff, S. Zhu, T. Holgate, J. Peng, J. He, T.M. Tritt, *J. Electron. Mater.* **40** (2011) 696.
- [78] L. Zhang, A. Grytsiv, P. Rogl, E. Bauer, M. Zehetbauer, *J. Phys. D Appl. Phys.* **42** (2009) 225405.
- [79] G. Rogl, A. Grytsiv, N. Melnychenko-Koblyuk, E. Bauer, S. Laumann, P. Rogl, *J. Phys. Condens. Matter* **23** (2011) 275601.
- [80] S. Ballikaya, N. Uzar, S. Yildirim, J.R. Salvador, C. Uher, *J. Solid State Chem.* **193** (2012) 31.
- [81] X. Shi, J. Yang, J.R. Salvador, M.F. Chi, J.Y. Cho, H. Wang, S.Q. Bai, J.H. Yang, W.Q. Zhang, L.D. Chen, *J. Am. Chem. Soc.* **133** (2011) 7837.
- [82] G. Rogl, A. Grytsiv, P. Rogl, E. Bauer, M. Hochhenhofer, R. Anbalagan, R.C. Mallik, E. Schafler, *Acta Mater.* **76** (2014) 434.
- [83] G. Rogl, A. Grytsiv, P. Rogl, N. Peranio, E. Bauer, M. Zehetbauer, O. Eibl, *Acta Mater.* **63** (2014) 30.
- [84] G. Rogl, A. Grytsiv, P. Heinrich, E. Bauer, P. Kumar, N. Peranio, O. Eibl, J. Horky, M. Zehetbauer, P. Rogl, *Acta Mater.* **91** (2015) 227.
- [85] G. Rogl, A. Grytsiv, P. Rogl, E. Royanian, E. Bauer, J. Horky, D. Setman, E. Schafler, M. Zehetbauer, *Acta Mater.* **61** (2013) 6778.
- [86] H. Kim, M. Kaviany, J.C. Thomas, A. van der Ven, C. Uher, B. Huang, *Phys. Rev. Lett.* **105** (2010) 265901.
- [87] T. Zhang, K. Zhou, X.F. Li, Z.Q. Chen, X.L. Su, X.F. Tang, *J. Appl. Phys.* **117** (2015) 055103.
- [88] O.M. Løvvik, Ø. Prytz, *Phys. Rev. B* **70** (2004) 195119.
- [89] L. Bertini, C. Gatti, *J. Chem. Phys.* **121** (2004) 8983.
- [90] X. Shi, W.Q. Zhang, L.D. Chen, J. Yang, *Phys. Rev. Lett.* **95** (2005) 185503.
- [91] X. Shi, W.Q. Zhang, L.D. Chen, J. Yang, C. Uher, *Phys. Rev. B* **75** (2007) 235208.
- [92] A. Harnwunggmoung, K. Kurosaki, H. Muta, S. Yamanaka, *Appl. Phys. Lett.* **96** (2010) 202107.
- [93] Y. Qiu, L. Xi, X. Shi, P. Qiu, W. Zhang, L.S. Chen, J.R. Salvador, J.Y. Cho, J. Yang, Y.-C. Chien, S.-W. Chen, Y. Tang, G.J. Snyder, *Adv. Funct. Mater.* **23** (2013) 3194.
- [94] R.C. Mallik, C. Stiewe, G. Karpinski, R. Hassdorf, E. Müller, *J. Electron. Mater.* **38** (2009) 1337.

- [95] J. Leszczynski, V. Da Ros, B. Lenoir, A. Dauscher, C. Candolfi, P. Masschelein, J. Hejtmánek, K. Kutasinski, J. Tobola, R.I. Smith, C. Stiewe, E. Müller, *J. Phys. D Appl. Phys.* 46 (2013) 495106.
- [96] A. Sesselmann, T. Dasgupta, K. Kelm, E. Müller, S. Perlt, S. Zastrow, *J. Mater. Res.* 26 (2011) 1820.
- [97] E. Visnow, C.P. Heinrich, A. Schmitz, J. de Boor, P. Leidich, B. Klobes, R.P. Hermann, E. Müller, W. Tremel, *Inorg. Chem.* 54 (2015) 7818.
- [98] A. Grytsiv, P. Rogl, H. Michor, E. Bauer, G. Giester, *J. Electron. Mater.* 42 (2013) 2940.
- [99] Y. Tang, Y. Qiu, L. Xi, X. Shi, W. Zhang, L.D. Chen, S.-M. Tseng, S.-W. Chen, G.J. Snyder, *Energy Environ. Sci.* 7 (2014) 812.
- [100] E. Bauer, A. Grytsiv, X.-Q. Chen, N. Melnychenko-Koblyuk, G. Hilscher, H. Kaldarar, H. Michor, E. Royanian, G. Giester, M. Rotter, R. Podloucky, P. Rogl, *Phys. Rev. Lett.* 99 (2007) 217001.
- [101] R. Gumeniuk, W. Schnelle, H. Rosner, M. Nicklas, A. Leithe-Jasper, Y. Grin, *Phys. Rev. Lett.* 100 (2008) 017002.
- [102] R. Gumeniuk, H. Borrman, A. Ormeci, H. Rosner, W. Schnelle, M. Nicklas, Y. Grin, A. Leithe-Jasper, *Z. Kristallogr.* 225 (2010) 531.
- [103] E. Bauer, X.-Q. Chen, P. Rogl, G. Hilscher, H. Michor, E. Royanian, R. Podloucky, G. Giester, O. Sologub, A.P. Gonçalves, *Phys. Rev. B* 78 (2008) 064516.
- [104] M. Toda, H. Sugawara, K. Magishi, T. Saito, K. Koyama, Y. Aoki, H. Sato, *J. Phys. Soc. Jpn.* 77 (2008) 124702.
- [105] A. Grytsiv, X.-Q. Chen, N. Melnychenko-Koblyuk, P. Rogl, E. Bauer, G. Hilscher, H. Kaldarar, H. Michor, E. Royanian, R. Podloucky, M. Rotter, G. Giester, *J. Phys. Soc. Jpn.* 77 (2008) 121.
- [106] H. Fukuoka, S. Yamanaka, *Chem. Mater.* 22 (2010) 47.
- [107] X.-D. Li, B. Xu, L. Zhang, F.-F. Duan, X.-L. Yan, J.-Q. Yang, Y.-J. Tian, *J. Alloys Compd.* 615 (2014) 177.
- [108] L. Zhang, B. Xu, X.-D. Li, F.-F. Duan, X.-L. Yan, Y.-J. Tian, *Mater. Lett.* 139 (2015) 249.
- [109] B.R. Ortiz, C.M. Crawford, R.W. McKinney, P.A. Parilla, E.S. Toberer, *J. Mater. Chem. A* 4 (2016) 8444.
- [110] B. Duan, J. Yang, J.R. Salvador, Y. He, B. Zhao, S. Wang, P. Wei, F.S. Ohuchi, W.Q. Zhang, R.P. Hermann, O. Gourdon, S.X. Mao, Y.W. Cheng, C.M. Wang, J. Liu, P.C. Zhai, X.F. Tang, Q.J. Zhang, J. Yang, *Energy Environ. Sci.* 9 (2016) 2090.
- [111] R. Chetty, J. Tobola, P. Klimczyk, L. Jaworska, K.T. Wojciechowski, *J. Alloys Compd.* 809 (2019) 151477.
- [112] S. Katsuyama, Y. Shichijo, M. Ito, K. Majima, H. Nagai, *J. Appl. Phys.* 84 (1998) 6708.
- [113] S. Katsuyama, M. Watanabe, M. Kuroki, T. Maehata, M. Ito, *J. Appl. Phys.* 93 (2003) 2758.
- [114] G. Tan, Y. Zheng, X.F. Tang, *Appl. Phys. Lett.* 103 (2013) 183904.
- [115] G. Tan, H. Chi, W. Liu, Y. Zheng, X.F. Tang, J. He, C. Uher, *J. Mater. Chem. C* 3 (2015) 8372.
- [116] J. Ding, H. Gu, P.F. Qiu, X.H. Chen, Z. Xiong, Q. Zheng, X. Shi, L.D. Chen, *J. Electron. Mater.* 42 (2012) 382.
- [117] A. Gharleghi, P.-C. Hung, F.-H. Lin, C.-J. Liu, *ACS Appl. Mater. Interfaces* 8 (2016) 35123.
- [118] J. Eilertsen, S. Rouvimov, M.A. Subramanian, *Acta Mater.* 60 (2012) 2178.
- [119] L. Zhang, F.F. Duan, X.D. Li, X.L. Yan, W.T. Hu, L.M. Wang, Z.Y. Liu, Y.J. Tian, B. Xu, *J. Appl. Phys.* 114 (2013) 083715.
- [120] Z. Xiong, X. Chen, X.Y. Huang, S.Q. Bai, L.D. Chen, *Acta Mater.* 58 (2010) 3995.

- [121] Z. Xiong, L. Xi, J. Ding, X. Chen, X.Y. Huang, H. Gu, L.D. Chen, W.Q. Zhang, *J. Mater. Res.* 26 (2011) 1848.
- [122] S. Katsuyama, Y. Kanayama, M. Ito, K. Majima, H. Nagai, Proceedings of the 17<sup>th</sup> International Conference on Thermoelectrics, IEEE Catalog Number 98TH8365, Piscataway, NJ, 1998, p. 342.
- [123] S. Katsuyama, Y. Kanayama, M. Ito, K. Majima, H. Nagai, *J. Appl. Phys.* 88 (2000) 3484.
- [124] S. Katsuyama, H. Kusaka, M. Ito, K. Majima, H. Nagai, Proceedings of the 18<sup>th</sup> International Conference on Thermoelectrics, IEEE Catalog Number 99TH8407, Piscataway, NJ, 1999, p. 348.
- [125] C. Chubilleau, B. Lenoir, P. Masschelein, A. Dauscher, C. Godart, *J. Electron. Mater.* 41 (2012) 1181.
- [126] Z. He, C. Stiewe, D. Platzek, G. Karpinski, E. Müller, *J. Appl. Phys.* 191 (2007) 043707.
- [127] Z. He, C. Stiewe, D. Platzek, G. Karpinski, E. Müller, S.H. Li, M. Toprak, M. Muhammed, *Nanotechnology* 18 (2007) 235602.
- [128] E. Alleno, L. Chen, C. Chubilleau, B. Lenoir, O. Rouleau, M.F. Trichet, B. Villeroy, *J. Electron. Mater.* 39 (2010) 1966.
- [129] Z. Xiong, X. Chen, X.Y. Zhao, S.Q. Bai, X.G. Huang, L.D. Chen, *Solid State Sci.* 11 (2009) 1612.
- [130] X.Y. Zhou, G.W. Wang, L.J. Guo, H. Chi, G. Wang, Q. Zhang, C.Q. Chen, T. Thompson, J. Sakamoto, V.P. Dravid, G.Z. Cao, C. Uher, *J. Mater. Chem. A* 2 (2014) 20629.
- [131] M. Benyahia, V. Ohorodniichuk, E. Leroy, A. Dauscher, B. Lenoir, E. Alleno, *J. Alloys Compd.* 735 (2018) 1096.
- [132] C. Chubilleau, B. Lenoir, A. Dauscher, C. Godart, *Intermetallics* 22 (2012) 47.
- [133] A. Gharleghi, Y.F. Liu, M.H. Zhou, J. He, T.M. Tritt, C.-J. Liu, *J. Mater. Chem. A* 4 (2016) 13874.
- [134] X. Shi, L.D. Chen, J. Yang, G.P. Meisner, *Appl. Phys. Lett.* 84 (2004) 2301.
- [135] B. Feng, J. Xie, G.S. Cao, T.J. Zhu, X.B. Zhao, *J. Mater. Chem. A* 1 (2013) 13111.
- [136] P. Che, B.B. Wang, C.Y. Sun, Y.S. Han, W.J. Li, *J. Alloys Compd.* 695 (2017) 1908.
- [137] R.D. Schmidt, E.D. Case, Z. Lobo, T.R. Thompson, J.S. Sakamoto, X.Y. Zhou, C. Uher, *J. Mater. Sci.* 49 (2014) 7192.
- [138] K. Peng, L. Guo, G. Wang, X. Su, X.Y. Zhou, X.F. Tang, C. Uher, *Sci. Adv. Mater.* 7 (2015) 1.
- [139] X. Ji, J. He, P. Alboni, Z. Su, N. Godard, B. Zhang, T.M. Tritt, J.W. Kolis, *Phys. Status Solidi (RRL)* 1 (2007) 229.
- [140] J.L. Mi, X.B. Zhao, T.J. Zhu, J.P. Tu, *Appl. Phys. Lett.* 91 (2007) 172116.
- [141] L. Yang, H.H. Hng, D. Li, Q.Y. Yan, J. Ma, T.J. Zhu, X.B. Zhao, H. Huang, *J. Appl. Phys.* 106 (2009) 013705.
- [142] P.N. Alboni, X. Ji, J. He, N. Gothard, T.M. Tritt, *J. Appl. Phys.* 103 (2008) 113707.
- [143] J.L. Mi, X.B. Zhao, T.J. Zhu, J.P. Tu, *J. Phys. D Appl. Phys.* 41 (2008) 205403.
- [144] P. Feschotte, D. Lorin, *J. Less-Common Met.* 155 (1989) 255.
- [145] B.N. Zobrina, L.D. Dudkin, *Sov. Phys. Solid State* 1 (1959) 1668.
- [146] N. Nakagawa, H. Tanaka, A. Kasama, K. Miyamura, H. Masumoto, K. Matsubara, Proceedings of the 15<sup>th</sup> International Conference on Thermoelectrics, IEEE Catalog Number 96TH8169, Piscataway, NJ, 1996, p. 117.
- [147] T. Caillat, J.-P. Fleurial, A. Borshchevsky, *J. Cryst. Growth* 166 (1996) 722.
- [148] W. Biltz, H. Heimbrech, *Z. Anorg. Allg. Chem.* 237 (1938) 132.
- [149] J.P. Odile, S. Soled, C.A. Castro, A. Wold, *Inorg. Chem.* 17 (1978) 283.
- [150] M.S. Torikachvili, J.W. Chen, Y. Dalichaouch, R.P. Czuerdin, M.W. McElfresh, C. Rossel, M.B. Maple, G.P. Meisner, *Phys. Rev. B* 36 (1987) 8660.

- [151] D. Mandrus, A. Maglioni, T.W. Darling, M.F. Hundley, E.J. Peterson, J.D. Thompson, *Phys. Rev. B* 52 (1995) 4926.
- [152] Z. Henkie, M.B. Maple, A. Pietraszko, R. Wawryk, T. Cichorek, R.E. Baumbach, W.M. Yuhasz, P.-C. Ho, *J. Phys. Soc. Jpn.* 77 (2008) 128.
- [153] J. Ackermann, A. Wold, *J. Phys. Chem. Solid* 38 (1977) 1013.
- [154] T. Morimura, H. Kitagawa, M. Hasaka, S. Kondo, Proceedings of the 16<sup>th</sup> International Conference on Thermoelectrics, IEEE Catalog Number 97TH8291, Piscataway, NJ, 1997, p. 356.
- [155] H. Kitagawa, M. Hasaka, T. Morimura, S. Kondo, Proceedings of the 17<sup>th</sup> International Conference on Thermoelectrics, IEEE Catalog Number 98TH8365, Piscataway, NJ, 1998, p. 338.
- [156] G. Tan, W. Liu, S. Wang, Y. Yan, H. Li, X.F. Tang, C. Uher, *J. Mater. Chem. A* 1 (2013) 12657.
- [157] H. Uchida, V. Crnko, H. Tanaka, A. Kasama, K. Matsubara, Proceedings of the 17<sup>th</sup> International Conference on Thermoelectrics, IEEE Catalog Number 98TH8365, Piscataway, NJ, 1998, p. 330.
- [158] K.J. Rao, B. Vaidhyanathan, M. Ganguli, P.A. Ramakrishnan, *Chem. Mater.* 11 (1999) 882.
- [159] K. Biswas, S. Muir, M. Subramanian, *Mater. Res. Bull.* 46 (2011) 2288.
- [160] X. Su, F. Fu, Y. Yan, G. Zheng, T. Liang, Q. Zhang, X. Cheng, D. Yang, H. Chi, X.F. Tang, Q.-J. Zhang, C. Uher, *Nat. Commun.* 5 (2014) 4908.
- [161] T. Liang, X. Su, Y. Yan, G. Zheng, Q.-J. Zhang, H. Chi, X.F. Tang, C. Uher, *J. Mater. Chem. A* 2 (2014) 17914.
- [162] Y. Yan, H.Q. Ke, J. Yang, C. Uher, X.F. Tang, *ACS Appl. Mater. Interfaces* 10 (2018) 13669.
- [163] M. Wang, Y. Zhang, M. Muhammed, *Nanostruct. Mater.* 12 (1999) 237.
- [164] H. Liu, J.-Y. Wang, X. Hu, L.-X. Li, F. Gu, S.-R. Zhao, M.-Y. Gu, R.I. Boughton, M.-H. Jiang, *J. Alloys Compd.* 334 (2002) 313.
- [165] A. Gharleghi, Y.H. Pai, F.H. Lin, J.-C. Liu, *J. Mater. Chem. C* 2 (2014) 4213.
- [166] A. Gharleghi, Y.H. Chu, F.H. Lin, Z.R. Yang, Y.H. Pai, J.-C. Liu, *ACS Appl. Mater. Interfaces* 8 (2016) 5205.
- [167] J. Xie, X.B. Zhao, J.-L. Mi, G.-S. Cao, J.-P. Tu, *J. Zhejiang Univ. Sci. A* 5 (2004) 1504.
- [168] J.L. Mi, T.J. Zhu, X.B. Zhao, J. Ma, *J. Appl. Phys.* 101 (2007) 054314.
- [169] X.-H. Ji, J. He, P.N. Alboni, T.M. Tritt, J.W. Kolis, *Mater. Res. Soc. Symp. Proc.* 1044 (2008) 3.
- [170] A. Bhaskar, Y.-W. Yang, C.-J. Liu, *Ceram. Int.* 41 (2015) 6381.
- [171] K. Kadel, W. Li, *Crystal Res. Technol.* 49 (2014) 135.
- [172] A. Bhaskar, Y.-W. Yang, Z.-R. Yang, F.-H. Lin, C.-J. Liu, *Ceram. Int.* 41 (2015) 7989.
- [173] J.Y. Yang, Y.H. Chen, J.Y. Peng, X.L. Song, W. Zhu, J.F. Su, R. Chen, *J. Alloys Compd.* 375 (2004) 229.
- [174] J.Y. Yang, Y.H. Chen, W. Zhu, J.Y. Peng, S. Bao, X. Fan, X. Duan, *J. Solid State Chem.* 179 (2006) 212.
- [175] C. Sekine, T. Uchiumi, I. Shirotani, K. Matsuhira, T. Sakakibara, T. Goto, T. Yagi, *Phys. Rev. B* 62 (2000) 11581.
- [176] I. Shirotani, Y. Shimaya, K. Kihou, C. Sekine, T. Yagi, *J. Solid State Chem.* 174 (2003) 32.
- [177] K. Tanaka, Y. Kawahito, Y. Yonezawa, D. Kikuchi, H. Aoki, K. Kuwahara, M. Ichihara, H. Sugawara, Y. Aoki, H. Sato, *J. Phys. Soc. Jpn.* 76 (2007) 103704.
- [178] H. Anno, K. Matsubara, Y. Notohara, T. Sakakibara, K. Kishimoto, T. Koyanagi, Proceedings of the 15<sup>th</sup> International Conference on Thermoelectrics, IEEE Catalog Number 96TH8169, Piscataway, NJ, 1996, p. 435.

- [179] H. Anno, T. Sakakibara, Y. Notohara, H. Tashiro, T. Koyanagi, H. Kaneko, K. Matsubara, Proceedings of the 16<sup>th</sup> International Conference on Thermoelectrics, IEEE Catalog Number 97TH8291, Piscataway, NJ, 1997, p. 338.
- [180] Z.-H. Zheng, M. Wei, F. Li, J.-T. Luo, H.-L. Ma, G.-X. Liang, X.-H. Zhang, P. Fan, *J. Mater. Sci. Mater. Electron.* 28 (2017) 17221.
- [181] Z.-H. Zheng, M. Wei, F. Li, J.-T. Luo, G.-X. Liang, H.-L. Ma, X.-H. Zhang, P. Fan, *Coatings* 7 (2017) 205.
- [182] Z.-H. Zheng, F. Li, Y.-Z. Li, P. Fan, J.-T. Luo, G.-X. Liang, B. Fan, A.-H. Zhong, *Thin Solid Films* 632 (2017) 88.
- [183] P. Fan, Y. Zhang, Z.-H. Zheng, W.-F. Fan, J.-T. Luo, G.-X. Liang, D.-P. Zhang, *J. Electron. Mater.* 44 (2015) 630.
- [184] V. Savchuk, A. Boulouz, S. Chakraborty, J. Schumann, H. Vinzelberg, *J. Appl. Phys.* 92 (2002) 5319.
- [185] V. Savchuk, J. Schumann, B. Schüpp, G. Behr, N. Mattern, D. Soupel, *J. Alloys Compd.* 351 (2003) 248.
- [186] Z.-H. Zheng, P. Fan, Y. Zhang, J.-T. Luo, Y. Huang, G.-X. Liang, *J. Alloys Compd.* 639 (2015) 74.
- [187] Z.-H. Zheng, M. Wei, J.-T. Luo, F. Li, G.-X. Liang, Y. Liang, J. Hao, H.-L. Ma, X.-H. Zhang, P. Fan, *Inorg. Chem. Front.* 5 (2018) 1409.
- [188] A. Ahmed, S. Han, *Appl. Surf. Sci.* 408 (2017) 88.
- [189] G.S. Fu, L. Zuo, J. Chen, M. Lu, L.Y. Yu, *J. Appl. Phys.* 117 (2015) 125304.
- [190] B. Chen, J.-H. Xu, S. Hu, C. Uher, *Mat. Res. Soc. Symp. Proc.* 452 (1997) 1037.
- [191] H.M. Christen, D.G. Mandrus, D.P. Norton, L.A. Boatner, B.C. Sales, *Mater. Res. Soc. Symp. Proc.* 478 (1997) 217.
- [192] J.C. Caylor, A.M. Stacy, T. Sands, G. Gronsky, *Mater. Res. Soc. Symp. Proc.* 545 (1999) 327.
- [193] J.C. Caylor, A.M. Stacy, G. Gronsky, T. Sands, *J. Appl. Phys.* 89 (2001) 3508.
- [194] H.-A. Durant, K. Nishimoto, K. Ito, I. Kataoka, *Appl. Surf. Sci.* 154–155 (2000) 387.
- [195] A. Suzuki, *Jpn. J. Appl. Phys.* 42 (2003) 2843.
- [196] R. Zeipl, J. Walachová, J. Lorinčík, S. Leshkov, M. Josieková, M. Jelinek, T. Kocourek, K. Jurek, J. Navrátil, L. Beneš, T. Plecháček, *J. Vac. Sci. Technol. A* 28 (2010) 523.
- [197] S.R.S. Kumar, A. Alyamani, J.W. Graff, T.M. Tritt, H.N. Alshareef, *J. Mater. Sci.* 26 (2011) 1836.
- [198] A. Dauscher, M. Puyet, B. Lenoir, D. Conceag, M. Dinescu, *Appl. Phys. A* 79 (2004) 1465.
- [199] D. Conceag, A. Dauscher, B. Lenoir, V. DaRos, R. Birjega, A. Moldovan, M. Dinescu, *Appl. Surf. Sci.* 253 (2007) 8097.
- [200] H. Sellinschegg, D.C. Johnson, G.S. Nolas, G.A. Slack, S.B. Schujman, F. Mohammed, T.M. Tritt, E. Nelson, Proceedings of the 17<sup>th</sup> International Conference on Thermoelectrics, IEEE Catalog Number 98TH8365, Piscataway, NJ, 1998, p. 338.
- [201] A.L.E. Smalley, S. Kim, D.C. Johnson, *Chem. Mater.* 15 (2003) 3847.
- [202] M.D. Hornbostel, E.J. Hyer, J.H. Edvalson, D.C. Johnson, *Inorg. Chem.* 36 (1997) 4270.
- [203] J.R. Williams, M. Johnson, D.C. Johnson, *J. Am. Chem. Soc.* 123 (2001) 1645.
- [204] A. Möchel, I. Sergueev, N. Nguyen, G.J. Long, F. Grandjean, D.C. Johnson, R.P. Hermann, *Phys. Rev. B* 84 (2011) 064302.
- [205] M.V. Daniel, C. Brombacher, G. Beddies, N. Jöhrmann, M. Hietschold, D.C. Johnson, Z. Aabdin, N. Peranio, O. Eibl, M. Albrecht, *J. Alloys Compd.* 624 (2015) 216.
- [206] M.V. Daniel, M. Lindorf, M. Albrecht, *J. Appl. Phys.* 120 (2016) 125306.
- [207] M. Lonsky, S. Heinz, M.V. Daniel, M. Albrecht, J. Müller, *J. Appl. Phys.* 120 (2016) 142101.

- [208] P. Vanysek, in: W.M. Hayes (Ed.), *Handbook of Chemistry and Physics*, ninety-third ed., Chemical Rubber Company, 2012, p. 5.
- [209] J.F. Behnke, A.L. Prieto, A.M. Stacy, T. Sands, Proceedings of the 18<sup>th</sup> International Conference on Thermoelectrics, IEEE Catalog Number 99TH8407, Piscataway, NJ, 1999, p. 451.
- [210] L.-J. Chen, H. Hu, Y.-X. Li, G.-F. Chen, S.-Y. Yu, G.-H. Wu, *Chem. Lett.* 35 (2006) 170.
- [211] D.V. Quach, R. Vidu, J.R. Groza, P. Stroeve, *Ind. Eng. Chem. Res.* 49 (2010) 11385.
- [212] H. Cheng, H.H. Hng, J. Ma, X.J. Xu, *J. Mater. Res.* 23 (2008) 3013.
- [213] S. Yadav, B.S. Yadav, S. Chaudhary, D.K. Pandya, *RSC Adv.* 7 (2017) 20336.
- [214] Y.N. Sadana, R. Kumar, *Surf. Technol.* 11 (1980) 37.
- [215] H. Yamamoto, M. Morishita, Y. Mizuta, A. Masubuchi, *Surf. Coat. Technol.* 206 (2012) 3415.
- [216] R.C. DeMattei, A. Watcharapasorn, R.S. Feigelson, *J. Electrochem. Soc.* 148 (2001) D109.
- [217] G. Rogl, L. Zhang, P. Rogl, A. Grytsiv, M. Falmbigl, D. Rajs, M. Kriegisch, H. Müller, E. Bauer, J. Koppensteiner, W. Schranz, M. Zehetbauer, Z. Henkie, M.B. Maple, *J. Appl. Phys.* 107 (2010) 043507.
- [218] M.V. Daniel, M. Friedemann, J. Franke, M. Albrecht, *Thin Solid Films* 589 (2015) 203.
- [219] D.J. Singh, W.E. Pickett, *Phys. Rev. B* 50 (1994) 11235.
- [220] J.O. Sofo, G.D. Mahan, *Mater. Res. Soc. Symp. Proc.* 545 (1999) 315.
- [221] K. Akai, H. Kurisu, T. Shimura, M. Matsuura, Proceedings of the 16<sup>th</sup> International Conference on Thermoelectrics, IEEE Catalog Number 97TH8291, Piscataway, NJ, 1997, p. 334.
- [222] K. Koga, K. Akai, K. Oshiro, M. Matsuura, Proceedings of the 20<sup>th</sup> International Conference on Thermoelectrics, IEEE Catalog Number 01TH8589, Piscataway, NJ, 2001, p. 105.
- [223] I. Lefebvre-Devos, M. Lassalle, X. Wallart, J. Olivier-Fourcade, L. Monconduit, J. Jumas, *Phys. Rev. B* 63 (2001) 125110.
- [224] K. Takegahara, H. Harima, *Physica B* 328 (2003) 74.
- [225] K.T. Wojciechowski, J. Tobola, J. Leszczynski, *J. Alloys Compd.* 361 (2003) 19.
- [226] L. Bertini, C. Stiewe, M. Toprak, S. Williams, D. Platzek, A. Mrotzek, Y. Zhang, C. Gatti, E. Müller, M. Muhammed, M. Rowe, *J. Appl. Phys.* 93 (2003) 438.
- [227] E.Z. Kurmaev, A. Moewes, I.R. Shtein, L.D. Finkelstein, A.L. Ivanovski, H. Anno, *J. Phys. Condens. Matter* 16 (2004) 979.
- [228] K. Koga, K. Akai, K. Oshiro, M. Matsuura, *Phys. Rev. B* 71 (2005) 155119.
- [229] L. Chaput, P. Pecheur, J. Tobola, H. Scherrer, *Phys. Rev. B* 72 (2005) 085126.
- [230] P. Ghosez, M. Veithen, *J. Phys. Condens. Matter* 19 (2007) 096002.
- [231] L. Bertini, S. Cenedese, *Phys. Status Solidi (RRL)* 1 (2007) 244.
- [232] W. Wei, Z.Y. Wang, L.L. Wang, H.J. Liu, R. Xiong, J. Shi, X.F. Tang, *J. Phys. D Appl. Phys.* 42 (2009) 115403.
- [233] P.-X. Lu, Q.-H. Ma, Y. Li, X. Hu, *J. Magn. Magn. Mater.* 322 (2010) 3080.
- [234] C.-H. Park, Y.-S. Kim, *Phys. Rev. B* 81 (2010) 085206.
- [235] D. Wee, B. Kozinsky, N. Marzari, M. Fornari, *Phys. Rev. B* 81 (2010) 045204.
- [236] S. Li, X. Jia, H. Ma, *Chem. Phys. Lett.* 549 (2012) 22.
- [237] H.A.R. Aliabad, M. Ghazanfari, I. Ahmad, M.A. Saeed, *Comput. Mater. Sci.* 65 (2012) 509.
- [238] L. Hammerschmidt, S. Schlecht, B. Paulus, *Phys. Status Solidi A* 210 (2013) 131.
- [239] S. Sharma, S.K. Pandey, *Comput. Mater. Sci.* 85 (2014) 340.
- [240] Y. Tang, Z.M. Gibbs, L.A. Agapito, G.D. Li, H.-S. Kim, M.B. Nardelli, S. Curtarolo, G.J. Snyder, *Nat. Mater.* 14 (2015) 1223.

- [241] B. Khan, H.A.R. Aliabad, S. Jalali-Asadabadi, I. Khan, I. Ahmad, J. Alloys Compd. 647 (2015) 364.
- [242] C.Z. Hu, X.Y. Zeng, Y.F. Liu, M.H. Zhou, H.J. Zhao, T.M. Tritt, J. He, J. Jakowski, P.R.C. Kent, J.S. Huang, B.G. Sumpter, Phys. Rev. B 95 (2017) 165204.
- [243] K. Akai, K. Oshiro, M. Matsuura, Proceedings of the 18<sup>th</sup> International Conference on Thermoelectrics, IEEE Catalog Number 99TH8407, Piscataway, NJ, 1999, p. 444.
- [244] M. Fornari, D.J. Singh, Appl. Phys. Lett. 74 (1999) 3666.
- [245] A. Kolezynski, W. Szczypka, J. Alloys Compd. 691 (2017) 299.
- [246] Y. Yin, Y. Huang, Y. Wu, G. Chen, W.-J. Yin, S.-H. Wei, X. Gong, Chem. Mater. 29 (2017) 9429.
- [247] V.P. Zhukov, Phys. Status Solidi 38 (1996) 90.
- [248] H. Harima, Prog. Theor. Phys. Suppl. 138 (2000) 117.
- [249] M. Llunell, P. Alemany, S. Alvarez, V.P. Zhukov, Phys. Rev. B 53 (1996) 10605.
- [250] D.W. Jung, M.-H. Whangbo, S. Alvarez, Inorg. Chem. 29 (1990) 2252.
- [251] L. Nordström, D.J. Singh, Phys. Rev. B 53 (1996) 1103.
- [252] D.J. Singh, I.I. Mazin, Phys. Rev. B 56 (1997) 1650(R).
- [253] H. Harima, J. Magn. Magn. Mater. 177–181 (1998) 321.
- [254] M. Fornari, D.J. Singh, Phys. Rev. B 59 (1999) 9722.
- [255] K. Akai, K. Koga, K. Oshiro, M. Matsuura, Proceedings of the 20<sup>th</sup> International Conference on Thermoelectrics, IEEE Catalog Number 01TH8589, Piscataway, NJ, 2001, p. 93.
- [256] K. Takegahara, H. Harima, J. Phys. Soc. Jpn. 71 (2002) 240.
- [257] H. Sugawara, S. Osaki, S.R. Saha, Y. Aoki, H. Sato, Y. Inada, H. Shishido, R. Settai, Y. Onuki, H. Harima, K. Oikawa, Phys. Rev. B 66 (2002) 220504(R).
- [258] H. Harima, K. Takegahara, Physica B 312–313 (2002) 843.
- [259] D.J. Singh, Mater. Res. Soc. Symp. Proc. 691 (2002) 15.
- [260] H. Harima, K. Takegahara, J. Phys. Condens. Matter 15 (2003) S2081.
- [261] H. Harima, K. Takegahara, Physica B 359–361 (2005) 920.
- [262] K. Takegahara, H. Harima, J. Phys. Soc. Jpn. 77 (2008) 193.
- [263] G.Z. Xing, X.F. Fan, W.T. Zheng, Y.M. Ma, H.L. Shi, D.J. Singh, Sci. Rep. 5 (2015) 10782.
- [264] A.H. Reshak, J. Alloys Compd. 651 (2015) 176.
- [265] A. Shankar, D.P. Rai, Sandeep, M.P. Ghimire, R.K. Thapa, Indian J. Phys. 91 (2017) 17.
- [266] H.M. Tütüncü, E. Karaca, G.P. Srivastava, Phys. Rev. B 95 (2017) 214514.
- [267] H. Harima, K. Takegahara, Physica B 328 (2003) 26.
- [268] L.D. Dudkin, N.K. Abrikosov, Sov. Phys. Solid State 1 (1959) 126.
- [269] T. Caillat, A. Borshchevsky, J.-P. Fleurial, J. Alloys Compd. 199 (1993) 207.
- [270] E. Arushanov, K. Fess, W. Kaefer, C. Kloc, E. Bucher, Phys. Rev. B 56 (1997) 1911.
- [271] J.S. Dyck, W. Chen, J. Yang, G.P. Meisner, C. Uher, Phys. Rev. B 65 (2002) 115204.
- [272] T. Caillat, A. Borshchevsky, J.-P. Fleurial, in: B. Mathiprakasam (Ed.), Proceedings of the 13<sup>th</sup> International Conference on Thermoelectrics, American Institute of Physics, NY, 1995, p. 98.
- [273] T.M. Tritt, G.S. Nolas, G.A. Slack, A.C. Ehrlich, D.J. Gillespie, J.L. Cohn, J. Appl. Phys. 79 (1996) 8412.
- [274] A. Watcharapasorn, R.C. DeMattei, R.S. Feigelson, T. Caillat, A. Borshchevsky, G.J. Snyder, J.-P. Fleurial, J. Appl. Phys. 86 (1999) 6213.
- [275] T. Caillat, A. Borshchevsky, J.-P. Fleurial, in: B. Mathiprakasam (Ed.), Proceedings of the 13<sup>th</sup> International Conference on Thermoelectrics, American Institute of Physics, NY, 1995, p. 58.

- [276] R. Gumeniuk, H. Rosner, W. Schnelle, M. Nicklas, A. Leithe-Jasper, Y. Grin, *Phys. Rev. B* 78 (2008), 052504.
- [277] E. Bauer, A. Grytsiv, X.-Q. Chen, N. Melnychenko-Koblyuk, G. Hilscher, H. Kaldaar, H. Michor, E. Royanian, M. Rotter, R. Podloucky, P. Rogl, *Adv. Mater.* 20 (2008) 1325.
- [278] D.H. Galvan, *J. Supercond. Nov. Magn.* 22 (2009) 367.
- [279] V.H. Tran, B. Nowak, A. Jezierski, D. Kaczorowski, *Phys. Rev. B* 79 (2009) 144510.
- [280] V.H. Tran, D. Kaczorowski, W. Müller, A. Jezierski, *Phys. Rev. B* 79 (2009), 054520.
- [281] H. Rosner, J. Gegner, D. Regesch, W. Schnelle, R. Gumeniuk, A. Leithe-Jasper, H. Fujiwara, T. Haupricht, T.C. Koethe, H.-H. Hsieh, H.-J. Lin, C.T. Chen, A. Ormeci, Y. Grin, L.H. Tjeng, *Phys. Rev. B* 80 (2009), 075114.
- [282] R. Gumeniuk, M. Schöneich, A. Leithe-Jasper, W. Schnelle, M. Nicklas, H. Rosner, A. Ormeci, U. Burkhardt, M. Schmidt, U. Schwarz, M. Ruck, Y. Grin, *New J. Phys.* 12 (2010) 103035.
- [283] L.S. Sharath Chandra, M.K. Chatopadhyay, S.B. Roy, S.K. Pandey, *Philos. Mag.* 96 (2016) 2161.
- [284] J.-P. Fleurial, T. Caillat, A. Borshchevsky, in: B. Mathiprakasam (Ed.), *Proceedings of the 13<sup>th</sup> International Conference on Thermoelectrics*, American Institute of Physics, NY, 1995, p. 40.
- [285] C. Uher, in: T.M. Tritt (Ed.), *Semiconductors and Semimetals*, vol. 69, Academic Press, San Diego, CA, 2001, pp. 139–253.
- [286] Y. Kajikawa, *J. Appl. Phys.* 116 (2014) 153710.
- [287] D.T. Morelli, T. Caillat, J.-P. Fleurial, A. Borshchevsky, J. Vandersande, B. Chen, C. Uher, *Phys. Rev. B* 51 (1995) 9622.
- [288] K. Matsubara, T. Sakakibara, Y. Notohara, H. Anno, H. Shimizu, T. Koyanagi, *Proceedings of the 15<sup>th</sup> International Conference on Thermoelectrics*, IEEE, 1996, p. 96.
- [289] J.W. Sharp, E.C. Jones, R.K. Williams, P.M. Martin, B.C. Sales, *J. Appl. Phys.* 78 (1995) 1013.
- [290] T. Caillat, A. Borshchevsky, J.-P. Fleurial, *J. Appl. Phys.* 80 (1996) 4442.
- [291] H. Anno, K. Matsubara, Y. Notohara, T. Sakakibara, H. Tashiro, *J. Appl. Phys.* 86 (1999) 3780.
- [292] L. Bertini, K. Billqvist, M. Christensen, C. Gatti, L. Holmgren, B. Iversen, E. Müller, M. Muhammed, G. Noriega, A. Palmqvist, D. Platzek, D.M. Rowe, A. Saramat, C. Stiewe, M. Toprak, S.G. Williams, Y. Zhang, *Proceedings of the 22nd International Conference on Thermoelectrics*, IEEE Catalog Number 03TH8726, Piscataway, NJ, 2003, p. 48.
- [293] J. Yang, Y. Xi, W. Zhang, L.D. Chen, J. Yang, *J. Electron. Mater.* 38 (2009) 1397.
- [294] D.T. Morelli, G.P. Meisner, B.X. Chen, S.Q. Hu, C. Uher, *Phys. Rev. B* 56 (1997) 7376.
- [295] G.S. Nolas, H. Takizawa, T. Endo, H. Sellinschegg, D.C. Johnson, *Appl. Phys. Lett.* 77 (2000) 52.
- [296] G.A. Lamberton Jr., S. Bhattacharya, R.T. Littleton IV, M.A. Kaeser, R.H. Tedstrom, T.M. Tritt, J. Yang, G.S. Nolas, *Appl. Phys. Lett.* 80 (2002) 598.
- [297] X.Y. Li, L.D. Chen, J.F. Fan, W.B. Zhang, T. Takahara, T. Hirai, *J. Appl. Phys.* 98 (2005) 083702.
- [298] M. Puyet, A. Dauscher, B. Lenoir, M. Dehmas, C. Stiewe, E. Müller, J. Hejtmánek, *J. Appl. Phys.* 97 (2005) 083712.
- [299] Y.Z. Pei, J. Yang, L.D. Chen, W. Zhang, J.R. Salvador, J.H. Yang, *Appl. Phys. Lett.* 95 (2009) 042101.
- [300] A.U. Khan, K. Kobayashi, D.-M. Tang, Y. Yamauchi, K. Hasegawa, M. Mitome, Y. Xue, B. Jiang, K. Tsuchiya, D. Goldberg, Y. Bando, T. Mori, *Nano Energy* 31 (2017) 152.

- [301] X.F. Tang, L.D. Chen, T. Goto, T. Hirai, *J. Mater. Res.* 16 (2001) 837.
- [302] G. Rogl, A. Grytsiv, J. Bursik, J. Horky, R. Anbalagan, E. Bauer, R.C. Mallik, P. Rogl, M. Zehetbauer, *Phys. Chem. Chem. Phys.* 17 (2015) 3715.
- [303] G. Rogl, A. Grytsiv, M. Falmbigl, P. Rogl, E. Bauer, M. Zehetbauer, Y. Gelbstein, *J. Alloys Compd.* 537 (2012) 242.
- [304] G. Rogl, A. Grytsiv, E. Bauer, P. Rogl, M. Zehetbauer, *Intermetallics* 18 (2010) 57.
- [305] G. Rogl, A. Grytsiv, E. Bauer, P. Rogl, M. Zehetbauer, *Intermetallics* 19 (2011) 546.
- [306] G. Rogl, A. Grytsiv, E. Bauer, P. Rogl, M. Zehetbauer, *Solid State Phenom.* 170 (2011) 240.
- [307] G. Rogl, A. Grytsiv, P. Rogl, E. Bauer, M.B. Kerber, M. Zehetbauer, S. Puchegger, *Intermetallics* 18 (2010) 2435.
- [308] D.J. Singh, M.H. Du, *Phys. Rev. B* 82 (2010) 075115.
- [309] J.Y. Cho, Z. Ye, M.M. Tessema, R.A. Waldo, J.R. Salvador, J. Yang, W. Cai, H. Wang, *Acta Mater.* 60 (2012) 2104.
- [310] J.Y. Cho, Z.X. Ye, M.M. Tessema, J.R. Salvador, R.A. Waldo, J. Yang, W.Q. Zhang, J. Yang, W. Cai, H. Wang, *J. Appl. Phys.* 113 (2013) 143708.
- [311] N. Shaheen, X.C. Shen, M.S. Javed, H. Zhan, L.J. Guo, R. Alsharafi, T.Y. Huang, X. Lu, G.Y. Wang, X.Y. Zhou, *J. Electron. Mater.* 46 (2017) 2958.
- [312] X.F. Tang, H. Li, Q.J. Zhang, M. Niino, T. Goto, *J. Appl. Phys.* 100 (2006) 123702.
- [313] D.R. Thompson, C. Liu, J. Yang, J.R. Salvador, D.B. Haddad, N.D. Ellison, R.A. Waldo, J. Yang, *Acta Mater.* 92 (2015) 152.
- [314] S. Lee, K.H. Lee, Y.-M. Kim, H.S. Kim, G.J. Snyder, S. Baik, S.W. Kim, *Acta Mater.* 142 (2018) 8.
- [315] D.J. Singh, in: T.M. Tritt (Ed.), *Recent Trends in Thermoelectric Materials II, Semiconductors and Semimetals*, vol. 70, Academic Press, San Diego, CA, 2001 (Chapter 5).
- [316] J. Yang, R. Liu, Z. Chen, L. Xi, J. Yang, W. Zhang, L.D. Chen, *Appl. Phys. Lett.* 101 (2012) 022101.
- [317] G.A. Slack, in: F. Seitz, D. Turnbull (Eds.), *Solid State Physics*, vol. 34, Academic Press, NY, 1979, p. 1.
- [318] D.G. Cahill, R.O. Pohl, *Solid State Commun.* 70 (1989) 927.
- [319] H.D. Lutz, G. Kliche, *Phys. Status Solidi B* 112 (1982) 549.
- [320] J.L. Feldman, D.J. Singh, *Phys. Rev. B* 53 (1996) 6273.
- [321] M. Rotter, P. Rogl, A. Grytsiv, W. Wolf, M. Krisch, A. Mirone, *Phys. Rev. B* 77 (2008) 144301.
- [322] B.C. Sales, B.C. Chakoumakos, D. Mandrus, J.W. Sharp, *J. Solid State Chem.* 146 (1999) 528.
- [323] J. Yamaura, Z. Hiroi, *J. Phys. Soc. Jpn.* 80 (2011) 054601.
- [324] V. Keppens, D. Mandrus, B.C. Sales, B.C. Chakoumakos, P. Dai, R. Coldea, M.B. Maple, D.A. Gajewski, E.J. Freeman, S. Bennington, *Nature (London)* 395 (1998) 876.
- [325] R.P. Hermann, R.Y. Jin, W. Schweika, F. Grandjean, D. Mandrus, B.C. Sales, G.J. Long, *Phys. Rev. Lett.* 90 (2003) 135505.
- [326] R. Viennois, L. Girard, M.M. Koza, H. Mutka, D. Ravot, F. Terki, S. Charar, J.-C. Tedenac, *Phys. Chem. Chem. Phys.* 7 (2005) 1617.
- [327] J.L. Feldman, P.C. Dai, T. Enck, B.C. Sales, D. Mandrus, D.J. Singh, *Phys. Rev. B* 73 (2006) 014306.
- [328] I.K. Dimitrov, M.E. Manley, S.M. Shapiro, J. Yang, W.Q. Zhang, L.D. Chen, Q. Jie, G. Ehlers, A. Podlesnyak, J. Camacho, Q. Li, *Phys. Rev. B* 82 (2010) 174301.
- [329] A. Möchel, I. Sergueev, H.-C. Wille, J. Voigt, M. Prager, M.B. Stone, B.C. Sales, Z. Guguchia, A. Shengelaya, V. Keppens, R.P. Hermann, *Phys. Rev. B* 84 (2011) 184306.

- [330] J.Y. Peng, W. Xu, Y.G. Yan, J.Y. Yang, L.W. Fu, H.J. Kang, J. He, *J. Appl. Phys.* **112** (2012) 024909.
- [331] K. Iwasa, M. Kohgi, H. Sugawara, H. Sato, *Physica B* **378–380** (2006) 194.
- [332] M.M. Koza, M.R. Johnson, R. Viennois, H. Mutka, L. Girard, D. Ravot, *Nat. Mater.* **7** (2008) 805.
- [333] M.M. Koza, L. Capogna, A. Leithe-Jasper, H. Rosner, W. Schnelle, H. Mutka, M.R. Johnson, C. Ritter, Y. Grin, *Phys. Rev. B* **81** (2010) 174302.
- [334] M.M. Koza, A. Leithe-Jasper, H. Rosner, W. Schnelle, H. Mutka, M.R. Johnson, M. Krisch, L. Capogna, Y. Grin, *Phys. Rev. B* **84** (2011) 014306.
- [335] M.M. Koza, A. Leithe-Jasper, H. Rosner, W. Schnelle, H. Mutka, M.R. Johnson, Y. Grin, *Phys. Rev. B* **89** (2014) 014302.
- [336] M.M. Koza, M. Boehm, E. Sischka, W. Schnelle, H. Mutka, A. Leithe-Jasper, *Phys. Rev. B* **91** (2015) 014305.
- [337] G.J. Long, R.P. Hermann, F. Grandjean, E.E. Alp, W. Sturhahn, C.E. Johnson, D.E. Brown, O. Leupold, R. Rüffer, *Phys. Rev. B* **71** (2005) 140302(R).
- [338] S. Tsutsui, H. Kobayashi, J. Umemura, Y. Yoda, H. Onodera, H. Sugawara, D. Kikuchi, H. Sato, C. Sekine, I. Shirotani, *Physica B* **383** (2006) 142.
- [339] S. Tsutsui, H. Kobayashi, J.P. Sutter, H. Uchiyama, A.Q.R. Baron, Y. Yoda, D. Kikuchi, H. Sugawara, C. Sekine, I. Shirotani, A. Ochiai, H. Sato, *J. Phys. Soc. Jpn.* **77** (2008) 257.
- [340] H.-C. Wille, R.P. Hermann, I. Sergueev, O. Leupold, P. van der Linden, B.C. Sales, F. Grandjean, G.J. Long, R. Rüffer, Y.V. Shvyd'ko, *Phys. Rev. B* **76** (2007) 140301(R).
- [341] S. Tsutsui, Y. Yoda, H. Kobayashi, *J. Phys. Soc. Jpn.* **76** (2007) 065003.
- [342] S. Tsutsui, H. Kobayashi, D. Ishikawa, J.P. Sutter, A.Q.R. Baron, T. Hasegawa, N. Ogita, M. Udagawa, Y. Yoda, H. Onodera, D. Kikuchi, H. Sugawara, C. Sekine, I. Shirotani, H. Sato, *J. Phys. Soc. Jpn.* **77** (2008) 033601.
- [343] S. Tsutsui, M. Mizumaki, M. Tsubota, H. Tanida, T. Uruga, Y. Murakami, D. Kikuchi, H. Sugawara, H. Sato, *J. Phys. Conf. Ser.* **150** (2009) 042220.
- [344] S. Tsutsui, H. Uchiyama, J.P. Sutter, A.Q.R. Baron, H. Sugawara, J. Yamaura, Z. Hiroi, A. Ochiai, H. Sato, *J. Phys. Conf. Ser.* **200** (2010) 012213.
- [345] J.L. Feldman, D.J. Singh, C. Kendziora, D. Mandrus, B.C. Sales, *Phys. Rev. B* **68** (2003) 094301.
- [346] L.X. Li, H. Liu, J.Y. Wang, X.B. Hu, S.R. Zhao, H.D. Jiang, Q.J. Huang, H.H. Wang, Z.F. Li, *Phys. Chem. Lett.* **347** (2001) 373.
- [347] N. Ogita, T. Kondo, T. Hasegawa, M. Udagawa, H. Sugawara, H. Sato, C. Sekine, I. Shirotani, *AIP Conf. Proc.* **850** (2006) 1331.
- [348] N. Ogita, R. Kojima, T. Hasegawa, Y. Takasu, M. Udagawa, T. Kondo, S. Narazu, T. Takabatake, N. Takeda, Y. Ishikawa, H. Sugawara, T. Ikeno, D. Kikuchi, H. Sato, C. Sekine, I. Shirotani, *J. Phys. Soc. Jpn.* **77** (2008) 251.
- [349] J.G. Peng, X.Y. Liu, J. He, J.Y. Yang, *Proc. Eng.* **27** (2012) 121.
- [350] T.X. Liu, X.F. Tang, H. Li, X.L. Su, Q.J. Zhang, *Acta Phys. Sin.* **57** (2008) 7078.
- [351] J.L. Li, B. Duan, H.J. Yang, H.T. Wang, G.D. Li, J. Yang, G. Chen, P.C. Zha, *J. Mater. Chem. C* **7** (2019) 8079.
- [352] Y. Wang, X.F. Xu, J. Yang, *Phys. Rev. Lett.* **102** (2009) 175508.
- [353] L. Guo, X. Xu, J.R. Salvador, G.P. Meisner, *J. Electron. Mater.* **42** (2013) 1978.
- [354] J.L. Feldman, D.J. Singh, I.I. Mazin, D. Mandrus, B.C. Sales, *Phys. Rev. B* **61** (2000) R9209.
- [355] C.H. Lee, I. Hase, H. Sugawara, H. Yoshizawa, H. Sato, *J. Phys. Soc. Jpn.* **75** (2006) 123602.

- [356] M. Christensen, A.B. Abrahamsen, N.B. Christensen, F. Juranyi, N.H. Andersen, K. Lefmann, J. Andreasson, C.R.H. Bahl, B.B. Iversen, *Nat. Mater.* 7 (2008) 811.
- [357] W. Li, L. Lindsey, D.A. Broido, D.A. Stewart, N. Mingo, *Phys. Rev. B* 86 (2012) 174307.
- [358] T. Hasegawa, Y. Takasu, N. Ogita, M. Udagawa, *J. Phys. Soc. Jpn.* 77 (2008) 248.
- [359] B. Huang, M. Kaviani, *Acta Mater.* 58 (2010) 4516.
- [360] N. Bernstein, J.L. Feldman, D.J. Singh, *Phys. Rev. B* 81 (2010) 134301.
- [361] J.L. Feldman, D.J. Singh, N. Bernstein, *Phys. Rev. B* 89 (2014) 224304.
- [362] W. Li, N. Mingo, *Phys. Rev. B* 90 (2014) 094302.
- [363] W. Li, N. Mingo, *Phys. Rev. B* 89 (2014) 184304.
- [364] Y.H. Fu, D.J. Singh, W. Li, L.J. Zhang, *Phys. Rev. B* 94 (2016) 075122.
- [365] W. Li, N. Mingo, *Phys. Rev. B* 91 (2015) 144304.
- [366] P.F. Qiu, X. Shi, Y.T. Qiu, X.G. Huang, S. Wan, W.Q. Zhang, L.D. Chen, J. Yang, *Appl. Phys. Lett.* 103 (2013) 062103.
- [367] D. Hobbis, Y. Liu, K. Wei, T.M. Tritt, G.S. Nolas, *Crystals* 7 (2017) 256.
- [368] P.F. Qiu, J. Yang, R.H. Liu, X. Shi, X.Y. Huang, G.J. Snyder, W. Zhang, L.D. Chen, *J. Appl. Phys.* 109 (2011) 063713.
- [369] X.F. Tang, Q.J. Zhang, L.D. Chen, T. Goto, T. Hirai, *J. Appl. Phys.* 97 (2005) 093712.
- [370] B. Duan, P.C. Zhai, L.S. Liu, Q.J. Zhang, *J. Electron. Mater.* 41 (2011) 1120.
- [371] G. Rogl, A. Grytsiv, K. Yubuta, S. Puchagger, E. Bauer, C. Raja, R.C. Mallik, P. Rogl, *Acta Mater.* 95 (2015) 201.
- [372] T. Dahal, Q. Jie, W. Liu, K. Dahal, C.F. Guo, Y.C. Lan, Z.F. Ren, *J. Alloys Compd.* 623 (2015) 104.
- [373] Q. Jie, H.Z. Wang, W.S. Liu, H. Wang, G. Chen, Z.F. Ren, *Phys. Chem. Chem. Phys.* 15 (2013) 6809.
- [374] S. Ballikaya, C. Uher, *J. Alloys Compd.* 585 (2014) 168.
- [375] T. Dahal, H.S. Kim, S. Gahlawat, K. Dahal, Q. Jie, W.S. Liu, Y.C. Lan, K. White, Z.F. Ren, *Acta Mater.* 117 (2016) 13.
- [376] Y.Z. Pei, L.D. Chen, S.Q. Bai, X.Y. Zhao, X.Y. Li, *Scr. Mater.* 56 (2007) 621.
- [377] L. Guo, X. Xu, J.R. Salvador, G.P. Meissner, *Appl. Phys. Lett.* 102 (2013) 111905.
- [378] G.S. Nolas, M. Kaeser, R.T. Littlton IV, T.M. Tritt, H. Sellinschegg, D.C. Johnson, E. Nelson, *Mater. Res. Soc. Symp. Proc.* 626 (2000) Z10.1.
- [379] M. Puyet, B. Lenoir, A. Daucher, P. Weisbecker, S.J. Clarke, *J. Solid State Chem.* 177 (2004) 2138.
- [380] Y.G. Yan, W. Wong-Ng, L. Li, I. Levin, J.A. Kaduk, M.R. Suchomel, X. Sun, G.J. Tan, X.F. Tang, *J. Solid State Chem.* 218 (2014) 221.
- [381] X.H. Li, Q. Zhang, Y.L. Kang, C. Chen, L. Zhang, D.L. Yu, Y.J. Tian, B. Xu, *J. Alloys Compd.* 677 (2016) 61.
- [382] M. Matsubara, R. Asahi, *J. Electron. Mater.* 45 (2016) 1669.
- [383] R.W. Rice, *Mechanical Properties of Ceramics and Composites: Grains and Particle Effects*, Marcel-Dekker, N.Y., 2000.
- [384] J. Jiang, L.D. Chen, S.Q. Bai, Q. Yao, Q. Wang, *Scr. Mater.* 52 (2005) 347.
- [385] T.S. Snider, J.V. Badding, S.B. Schujiman, G.A. Slack, *Chem. Mater.* 12 (2000) 697.
- [386] C. Recknagel, N. Reinfried, P. Höhn, W. Schnelle, H. Rosner, Y. Grin, A. Leithe-Jasper, *Sci. Technol. Adv. Mater.* 8 (2007) 357.
- [387] J.R. Salvador, J. Yang, X. Shi, A.A. Wereszczak, H. Kong, C. Uher, *Philos. Mag.* 89 (2009) 1517.
- [388] L. Zhang, G. Rogl, A. Grytsiv, S. Puchegger, J. Koppensteiner, F. Spieckermann, H. Kabelka, M. Reinecker, P. Rogl, W. Schranz, M. Zehetbauer, M.A. Carpenter, *Mater. Sci. Eng. B* 170 (2010) 26.

- [389] X.Q. Yang, P.C. Zhai, L.S. Liu, Q.J. Zhang, *J. Appl. Phys.* 109 (2011) 123517.
- [390] A.C. Kraemer, M.R. Gallas, J.A.H. da Jornada, C.A. Perottoni, *Phys. Rev. B* 75 (2007) 024105.
- [391] G.D. Li, Q. An, W.A. Goddard III, R. Hanus, P.C. Zhai, Q.J. Zhang, G.J. Snyder, *Acta Mater.* 103 (2016) 775.
- [392] Z.-W. Ruan, L.-S. Liu, P.-C. Zhai, P.-F. Wen, Q.-J. Zhang, *J. Electron. Mater.* 39 (2010) 2029.
- [393] H.W. Russell, *J. Am. Ceram. Soc.* 18 (1935) 1.
- [394] R.H. Tarkhanyan, D.G. Niarchos, *Int. J. Therm. Sci.* 67 (2013) 107.
- [395] R.H. Tarkhanyan, D.G. Niarchos, *J. Mater. Res.* 28 (2013) 2316.
- [396] W.J. Li, G.D. Li, X.Q. Yang, L.S. Liu, P.C. Zhai, *J. Electron. Mater.* 44 (2015) 1477.
- [397] L.J. Wilson, S.A. Mikhail, *Thermochim. Acta* 156 (1989) 107.
- [398] K.T. Wojciechowski, J. Leszczybski, R. Gajerski, Proceedings of the 7<sup>th</sup> European Workshop on Thermoelectrics, Pamplona, Spain, 2002.
- [399] R. Hara, S. Inoue, H.T. Kaibe, S. Sano, *J. Alloys Compd.* 349 (2003) 297.
- [400] G.J. Snyder, T. Caillat, TE Workshop, San Diego, Feb. 17-20, 2004.
- [401] A.C. Sklad, M.W. Gaulois, A.P. Grosvenor, *J. Alloys Compd.* 505 (2010) L6.
- [402] E. Godlewska, K. Zawadzka, A. Adamczyk, M. Mitoraj, K. Mars, *Oxid. Met.* 74 (2010) 113.
- [403] J. Leszczynski, K.T. Wojciechowski, A.L. Malecki, *J. Therm. Anal. Calorim.* 105 (2011) 211.
- [404] P.F. Wen, P. Li, Q.J. Zhang, F.J. Yi, L.S. Liu, P.C. Zhai, *J. Electron. Mater.* 38 (2009) 1200.
- [405] D.G. Zhao, C.W. Tian, Y.T. Liu, C.W. Zhan, L.D. Chen, *J. Alloys Compd.* 509 (2011) 3166.
- [406] D.G. Zhao, C.W. Tian, S.Q. Tang, Y.T. Liu, L.D. Chen, *J. Alloys Compd.* 504 (2010) 552.
- [407] P. Wei, W.Y. Zhao, C.L. Dong, X. Yang, J. Yu, Q.J. Zhang, *Acta Mater.* 59 (2011) 3244.
- [408] K. Biswas, M.A. Subramanian, M.S. Good, K.C. Roberts, T.J. Hendricks, *J. Electron. Mater.* 41 (2011) 1615.
- [409] K.-H. Park, S.-W. You, S.-C. Ur, I.-H. Kim, S.-M. Choi, W.-S. Seo, *J. Electron. Mater.* 41 (2012) 1051.
- [410] M.Y. Tafti, M. Saleemi, M. Johnsson, A. Jacquot, M.S. Toprak, *Mater. Res. Soc. Symp. Proc.* 1735 (2015) 14.
- [411] P.F. Wen, Y. Zhu, J. Chen, H.J. Yang, P.C. Zhai, *J. Mater. Eng. Perform.* 25 (2016) 4764.
- [412] P.F. Wen, B. Duan, P.C. Zhai, P. Li, Q.J. Zhang, *J. Mater. Sci. Mater. Electron.* 24 (2013) 5155.
- [413] P.F. Wen, P. Li, Q.J. Zhang, Z.W. Ruan, L.S. Liu, P.C. Zhai, *J. Electron. Mater.* 42 (2013) 1443.
- [414] M.S. El-Genk, H.H. Saber, T. Caillat, J.S. Sakamoto, *Energy Convers. Manag.* 47 (2006) 174.
- [415] M.S. El-Genk, H.H. Saber, T. Caillat, J.S. Sakamoto, *Energy Convers. Manag.* 48 (2007) 1383.
- [416] D. Zhao, M. Zuo, Z. Wang, X. Teng, H. Geng, *Appl. Surf. Sci.* 305 (2014) 86.
- [417] X. Bao, M. Gu, Q.H. Zhang, Z.H. Wu, S.Q. Bai, L.D. Chen, H.Q. Xie, *J. Electron. Mater.* 48 (2019) 5523.
- [418] E. Godlewska, K. Zawadzka, K. Mars, R. Mania, K. Wojciechowski, A. Opoka, *Oxid. Met.* 74 (2010) 205.
- [419] K. Zawadzka, E. Godlewska, K. Mars, M. Nocun, *AIP Conf. Proc.* 1449 (2012) 231.

- [420] Y.-S. Park, T. Thompson, Y. Kim, J.R. Salvador, J.S. Sakamoto, *J. Mater. Sci.* 50 (2015) 1500.
- [421] J.S. Sakamoto, G.J. Snyder, T. Caillat, J.-P. Fleurial, S.M. Jones, J.-A. Paik, US Patent Application No. 20060090475 A1, 2006.
- [422] J.S. Sakamoto, H. Schock, T. Caillat, J.-P. Fleurial, R. Maloney, M. Lyle, T. Ruckle, E. Timm, L. Zhang, *Sci. Adv. Mater.* 3 (2011) 621.
- [423] H. Dong, X. Li, Y. Tang, J. Zou, X. Huang, Y. Zhou, W. Jiang, G. Zheng, L.D. Chen, *J. Alloys Compd.* 527 (2012) 247.
- [424] H. Dong, X. Li, X. Huang, Y. Zhou, W. Jiang, L.D. Chen, *Ceram. Int.* 39 (2013) 4551.
- [425] T. Caillat, J.-P. Fleurial, G.J. Snyder, A. Zoltan, D. Zoltan, A. Borshchevsky, Proceedings of the 18<sup>th</sup> International Conference on Thermoelectrics, IEEE Catalog Number 99TH8407, 1999, p. 473.
- [426] T. Caillat, J.-P. Fleurial, G.J. Snyder, A. Borshchevsky, Proceedings of the 20<sup>th</sup> International Conference on Thermoelectrics, IEEE Catalog Number 01TH8589, 2001, p. 282.
- [427] D. Zhao, C.W. Tian, S.Q. Tang, Y.T. Liu, L.K. Jiang, L.D. Chen, *Mater. Sci. Semicond. Process.* 13 (2010) 221.
- [428] J.Q. Guo, H.Y. Geng, T. Ochi, S. Suzuki, M. Kikuchi, Y. Yamaguchi, S. Ito, *J. Electron. Mater.* 41 (2012) 1036.
- [429] Garcia-Cañadas, A.V. Powell, A. Kaltzoglou, P. Vaqueiro, G. Min, *J. Electron. Mater.* 42 (2013) 1369.
- [430] J.R. Salvador, J.Y. Cho, Z.X. Ye, J.E. Moczygemba, A.J. Thompson, J.W. Sharp, J.D. König, R. Maloney, T. Thompson, J. Sakamoto, H. Wang, A.A. Wereszczak, G.P. Meisner, *J. Electron. Mater.* 42 (2013) 1389.
- [431] J.R. Salvador, J.Y. Cho, Z.X. Ye, J.E. Moczygemba, A.J. Thompson, J.W. Sharp, J.D. König, R. Maloney, T. Thompson, J. Sakamoto, H. Wang, A.A. Wereszczak, *Phys. Chem. Chem. Phys.* 16 (2014) 12510.
- [432] A. Muto, J. Yang, B. Poudel, Z.F. Ren, G. Chen, *Adv. Energy Mater.* 3 (2013) 245.
- [433] G. Nie, S. Suzuki, T. Tomida, A. Sumiyoshi, T. Ochi, K. Mukaiyama, M. Kikuchi, J.Q. Guo, A. Yamamoto, H. Obara, *J. Electron. Mater.* 46 (2017) 2640.
- [434] P.A. Zong, R. Hanus, M. Dylla, Y.S. Tang, J.C. Liao, Q.H. Zhang, G.J. Snyder, L.D. Chen, *Energy Environ. Sci.* 10 (2017) 183.
- [435] Q.H. Zhang, J.C. Liao, Y.S. Tang, M. Gu, C. Ming, R.F. Qiu, S.Q. Bai, X. Shi, C. Uher, L.D. Chen, *Energy Environ. Sci.* 10 (2017) 956.
- [436] S. Katsuyama, W. Yamakawa, Y. Matsumura, R. Funahashi, *J. Electron. Mater.* 48 (2019) 5257.

# Recent developments in half-Heusler thermoelectric materials

2.3

*Jan-Willem G. Bos*

Institute of Chemical Sciences and Centre for Advanced Energy Storage and Recovery,  
School of Engineering and Physical Sciences, Heriot-Watt University, Edinburgh, Scotland

## 2.3.1 Introduction

The semiconducting nature of the XNiSn (X = Ti, Zr, and Hf) half-Heusler (HH) compounds was first reported by Aliev et al. in the late 1980s [1, 2]. This started a period of intensive research where many of the basic properties of HH alloys were established, including band structure studies confirming the presence of a bandgap and exploration of feasible thermoelectric compositions [3–15]. This work identified n-type XNiSn and p-type XCoSb as promising materials with figures of merit,  $ZT$  near 1 and 0.6, respectively [7, 8]. Furthermore, doping using Sb and Sn to control the carrier concentration and alloying on the X-site with Ti, Zr, and Hf to reduce the lattice thermal conductivity ( $\kappa_{lat}$ ), were established as the best route to optimize the thermoelectric performance [7, 8, 10, 14].

Following on from this early work two main design approaches gained prominence: these are nanostructuring and electronic band structure engineering. Nanostructuring routes include mechanical reduction of grain sizes [16, 17] and use of phase segregation to form composite materials [18–24]. Both of these approaches lead to decreases in  $\kappa_{lat}$ , while electronic enhancements have been reported for HHs with nano-inclusions [25–27].

The use of band structure engineering concepts has been driven by the wider availability of density functional theory (DFT) calculations [28, 29], but also by the routine availability of Hall measurements and empirical semiconductor band modeling [30, 31]. These advances have enabled the underpinning electronic parameters for good thermoelectric performance to be assessed in a much more rigorous manner. This has led to the discovery of several highly promising materials, including p-type NbFeSb, which looks likely to replace ZrCoSb [31–33] and ZrCoBi [34]. In terms of thermal transport, phonon calculations and use of the Callaway model have enabled deeper insight into the main factors affecting thermal transport [35–38].

Many of the recent advances in HH performance have occurred in parallel with improved synthetic methodologies. In particular, the use of a processing sequence involving arc or levitation melting, mechanical milling and consolidation through spark plasma sintering or hot pressing, has been one of the main drivers for the

improved materials quality [17,39–42]. In some instances, mechanical alloying of elemental precursors followed by consolidation has been demonstrated to be sufficient to achieve very high sample qualities, enabling much faster synthesis times [34].

This chapter reviews major recent developments in HH materials for use at higher temperatures. As such it does not include the related MgAgSb phase, with  $ZT \sim 1$  near room temperature [43, 44]. Section 2.3.2 covers general background and the single parabolic band (SPB) model that is needed to understand many of the recent advances. The latest developments in the established XNiSn and XCoSb compositions are covered in Section 2.3.3. The new p- and n-types that have recently gained prominence are discussed in Sections 2.3.4 and 2.3.5. The chapter concludes with an outlook in Section 2.3.6.

## 2.3.2 Background

The XYZ HH structure consists of a face centered cubic arrangement of main group atoms (Z) with electropositive X metals occupying all octahedral sites, while the Y metals (usually a late first-row transition metal, e.g., Fe, Co, or Ni) occupy half of the tetrahedral sites (Fig. 2.3.1). This structural description readily leads to the common Zintl electron counting model of the chemical bonding, where the electropositive  $X^{n+}$  atoms transfer their valence electrons to a covalently bonded zincblende  $(YZ)^{n-}$  network. This leads to semiconducting behavior for 18 valence electrons as both the Y and Z atoms have filled valence shells [45,46]. In reality, the X elements are not spectators when it comes to the electronic properties but are hybridized via their d-orbitals to form part of the valence and conduction band [45,46].

The Zintl electron counting can be extended to include the oxidation numbers of the elements. These need to be charge balanced for semiconducting behavior and also form a good indicator to predict structural stability [48]. This is particularly useful for establishing the viability of hypothetical nonstoichiometric (i.e., not 1:1:1) compositions. For example, in case of the X-site deficient compositions discussed in Section 2.3.5,  $(Nb^{5+})_{0.8}Co^{-1}Sb^{-3}$  is charge balanced and is found to be stable. By contrast, the hypothetical Y-site deficient composition  $Nb^{5+}(Co^{-1})_{0.89}Sb^{3-}$  is not charge balanced and therefore not stable, despite having 18 electrons [48].

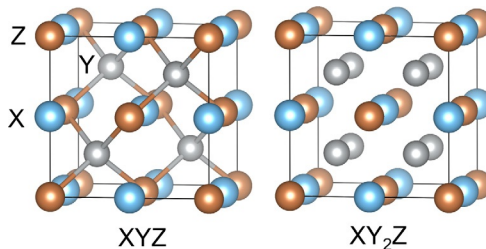


**Fig. 2.3.1** Atomic models of the XYZ and XY<sub>2</sub>Z half- and full-Heusler structures with the covalent  $(YZ)^{z-}$  zincblende substructure indicated. Structures were generated using the VESTA software [47].

Filling of the vacant tetrahedral position (often referred to as the interstitial site) leads to the XY<sub>2</sub>Z full-Heusler (FH) structure (Fig. 2.3.1). In principle, substitutions can be made on any of the X, Y, and Z positions in the HH structure, while the interstitial site typically has low solubility. The notable exception is the TiNiSn system, where significant amounts of interstitial Ni and Cu are possible, as discussed in Section 2.3.3.

The increased use of electronic band structure engineering concepts has been one of the main drivers for the discovery of new high-ZT compositions and has placed materials development on a firmer footing [30–32]. The SPB model is the simplest approximation of the band structure of a semiconductor and has been applied widely to HH alloys [30–33, 49]. This model is widely discussed in the literature and we will only give a few essential points [50, 51]. In case of acoustic phonon scattering dominated transport, which is valid for most thermoelectrics, the Seebeck coefficient,  $S \propto m_{DOS}^* = N_v^{2/3} m_b^*$ . Here,  $m_{DOS}^*$  is electronic density of states effective mass,  $N_v$  is the valley degeneracy and  $m_b^*$  is the electron (or hole) band mass [50, 51]. This shows that  $S$  is proportional to both  $N_v$  and  $m_b^*$ . By contrast, the charge carrier mobility,  $\mu \propto 1/(m_b^{*3/2} m_l E_{def}^2)$  is inversely dependent on  $m_b^*$ , the carrier inertial mass ( $m_l$ , which is equal to  $m_b^*$  for an isotropic band) and the deformation potential ( $E_{def}$ ), which quantifies the coupling between acoustic phonons and charge carriers [50, 51]. The main conclusion from this analysis is that a large  $N_v$  is favorable as this enhances  $S$  without detriment to  $\mu$ , while increasing  $m_b^*$  leads to a trade-off between an increased  $S$  but reduced  $\mu$ . In case of multiple contributing bands at the same point in the Brillouin zone, an effective degeneracy,  $N = N_v \times N_b$  and average  $m_b^*$  are often used. Here,  $N_b$  is the number of contributing bands. The HHs are characterized by relatively high  $N_v$  and  $N_b$  but also by heavy electrons and holes,  $m_b^* = 1\text{--}3 m_e$ . However, this is compensated by a weak coupling between lattice and charge carriers (a low  $E_{def} = 10\text{--}15 \text{ eV}$ ), which enables relatively high Hall mobilities  $\mu_H = 2\text{--}50 \text{ cm}^2 \text{ V}^{-1} \text{ s}^{-1}$ , considering the large  $m_b^*$  [30]. Furthermore, alloying does not strongly reduce  $\mu$  in the HHs, whereas it does efficiently suppress  $\kappa_{lat}$  [30, 52]. The combination of large  $m_{DOS}^*$  and low  $E_{def}$  is favorable and enables large  $S^2\sigma$ , but high levels of carrier doping are needed to achieve peak performance (typical Hall concentrations  $n_H = 10^{20}\text{--}10^{22} \text{ cm}^{-3}$ ), which can sometimes be difficult to achieve experimentally [33].

**Table 2.3.1** provides an overview of the valley ( $N_v$ ) and band ( $N_b$ ) degeneracies, density of states effective mass from Hall measurements ( $m_{DOS}^*$ ), average band mass ( $m_b^*$ ), peak power factor ( $S^2\sigma$ ), and *figures of merit* (ZT) values for the main HH materials. For the n-type materials, the conduction band maximum usually occurs at the X-point of the Brillouin zone ( $N_v = 3$ ), while the valence band (VB) maximum occurs at either the  $\Gamma$  ( $N_v = 1$ ) or L ( $N_v = 4$ ) points. ZrCoBi appears to be a unique example where bands at both  $\Gamma$  and L points contribute [34]. Overall, the electron masses tend to be smaller than the hole masses. The notable exception is the new p-type NbFeSb, with  $m_b^* = 1.8 m_e$ , which is relatively close to  $m_b^* \sim 1.3 m_e$  for the XNiSn n-types. By contrast, the previous state of the art ZrCoSb p-types have  $m_b^* \sim 3 m_e$ , which at least partly explains their lower  $S^2\sigma \sim 3 \text{ mW m}^{-1} \text{ K}^{-2}$  (Table 2.3.1). The final point from Table 2.3.1 is that the peak ZT values for the best n- and p-types now reproducibly exceed unity, which is an important milestone for applications.

**Table 2.3.1** An overview of selected electronic parameters of the main half-Heusler materials.

Composition	Type	$N_v^{\text{a}}$	$N_b$	$m_{DOS}^*$ ( $\text{m}_e$ )	$m_b^*$ ( $\text{m}_e$ )	Peak $S^2\sigma$ ( $\text{mW m}^{-1} \text{K}^{-2}$ )	Peak ZT	Refs.
TiNiSn	n	3	1	2.8	1.3	4	0.45 @ 723K	[53]
TiNi <sub>1+y</sub> Sn	n	3	1	3.1	1.5	3–4	0.6 @ 723K	[53–55]
(Zr/Hf)Ni(Sn/Sb)	n	3	1	2.7	1.3	5–6	1.2 @ 900K	[39,56]
(Ti/Zr/Hf)Ni(Sn/Sb)	n	3	1	—	—	5–6	1.3 @ 825K	[19, 20, 57, 58]
TiNiCu <sub>y</sub> Sn	n	3	2	—	—	4	0.6 @ 773K	[59]
(Ti/Zr/Hf)NiCu <sub>y</sub> Sn	n	4	2	4.1	1.2	4	0.8 @ 773K	[60]
(Zr/Hf)Co(Sb/Sn)	p	4	2	12.5	3.1	3–3.5	0.9 @ 1123K	[61, 62]
(Ti/Zr/Hf)Co(Sb/Sn)	p	—	—	—	—	3.5	0.9 @ 973K	[63]
(Zr/Hf)(CoNi)Sb	n	3	1	6.5	3.1	3.3	1.0 @ 1073K	[64]
(V/Nb/Ti)FeSb	p	4	2	10.0	2.5	3	0.8 @ 900K	[31]
(NbTi)FeSb	p	4	2	6.4	1.6	4.5	1.1 @ 1100K	[32,42,65]
(Nb/Hf)FeSb	p	4	2	6.9	1.7	5.5	1.5 @ 1200K	[33]
(Ta/Ti)FeSb	p	4	2	—	—	5.3	1.5 @ 973K	[66]
ZrCoBi	p	1+4	2+2	—	—	4	1.4 @ 973K	[34]
NbCoSn	n	3	2	6.0	1.8	3.2	0.6 @ 1000K	[67]
Nb <sub>0.8+x</sub> CoSb	n	—	—	7.7	—	2.5	0.9 @ 1073K	[68, 69]

$N_v$  is the valley degeneracy,  $N_b$  is the number of contributing bands,  $m_{DOS}^*$  and  $m_b^*$  are the density of states and band masses from the single parabolic band model (in units of electron rest mass,  $m_e$ ). Indicative peak power factors ( $S^2\sigma$ ) and ZT values are also given.

<sup>a</sup>  $N_v = 3$  (X-point);  $N_v = 4$  (L point);  $N_v = 1$  ( $\Gamma$ -point).

### 2.3.3 Recent developments in XNiSn and XCoSb

The initial work on XNiSn and XCoSb established the effectiveness of Sb and Sn as dopants [7, 8, 15], and alloying with mixtures of Ti, Zr, and Hf as the main route to reduce  $\kappa_{lat}$  [5]. This period also saw the report of a very high  $ZT = 1.5$  at 673 K in the  $Ti_{1-x}(Zr_{0.25}Hf_{0.25})_xNi(Sn,Sb)$  system in 2005 [9]. This outstanding performance was due to the combination of a large  $S^2\sigma = 5\text{--}6 \text{ mW m}^{-1} \text{ K}^{-2}$  and very low  $\kappa_{lat} \sim 2 \text{ W m}^{-1} \text{ K}^{-1}$ . This generated much interest with the low  $\kappa_{lat}$  linked to the immiscibility of Ti and Zr/Hf and possible nanostructuring due to phase separation [19, 20, 57].

This early work also included the first studies into the impact of grain size reduction on  $\kappa_{lat}$  in XNiSn-based systems [70]. This was expanded upon in the early 2010s by more systematic studies that reduced the grain size further to 200–300 nm, followed by rapid consolidation to maintain the nanostructure [16, 17]. This enabled substantial improvements in  $ZT$  in both n- and p-types due to reductions in  $\kappa_{lat}$ . For example,  $ZT$  was improved from  $\sim 0.5$  to  $\sim 0.8$  in nanostructured  $(Zr,Hf)Co(Sb,Sn)$ , demonstrating the usefulness of this approach, which continues to be widely applied [16].

Phase segregation has also been widely explored as a route for performance enhancements. This has focused on two main areas: The first is segregation of the X-site elements [23, 24, 71] and is linked to the large size difference between Ti and Zr/Hf. The second is the limited solubility of metals on the vacant tetrahedral site, causing segregation into HH and FH phases [21–23]. These two types of segregation (X-site and HH/FH) will be briefly discussed in the following.

*X-site segregation:* Here, the thermodynamics is described by that of a solid solution between identical end-member structures, where a positive enthalpy of mixing ( $\Delta H > 0$ ), is compensated by the configurational entropy of mixing ( $-T\Delta S$ ). Solid-solution formation is achieved over the full range between Zr-Hf, reflecting the small size difference of these elements [23, 24]. However, the large size difference between Ti and Zr/Hf ( $\sim 3\%$  lattice mismatch compared to  $< 1\%$  for ZrNiSn and HfNiSn) leads to a miscibility gap, e.g., an upper solubility limit of  $\sim 9\%$  Zr in TiNiSn and  $\sim 7\%$  Ti in ZrNiSn (at 1000°C) and possible spinodal decomposition for intermediate compositions, affording a route to nanostructuring [23, 24, 57]. In samples processed via the melt, there indeed is a 1:1 correlation between Zr and Hf, while Ti is found to surround Zr/Hf domains, at first glance consistent with phase segregation [19, 20]. A typical microstructure for melted samples is shown in Fig. 2.3.2A.

By contrast, samples prepared using a powder metallurgy route show a much more continuous compositional distribution for the X-site elements, where all three elements are found to mix, as illustrated in Fig. 2.3.2B. This phase distribution reflects the initial mixing of the metal powder precursors, while Ni and Sn are entirely homogeneous [71, 72]. These different behaviors are likely linked to kinetic constraints during the synthesis of these materials. In particular, defect calculations show that creating vacancies on the X-sites carries a large energy penalty [24].

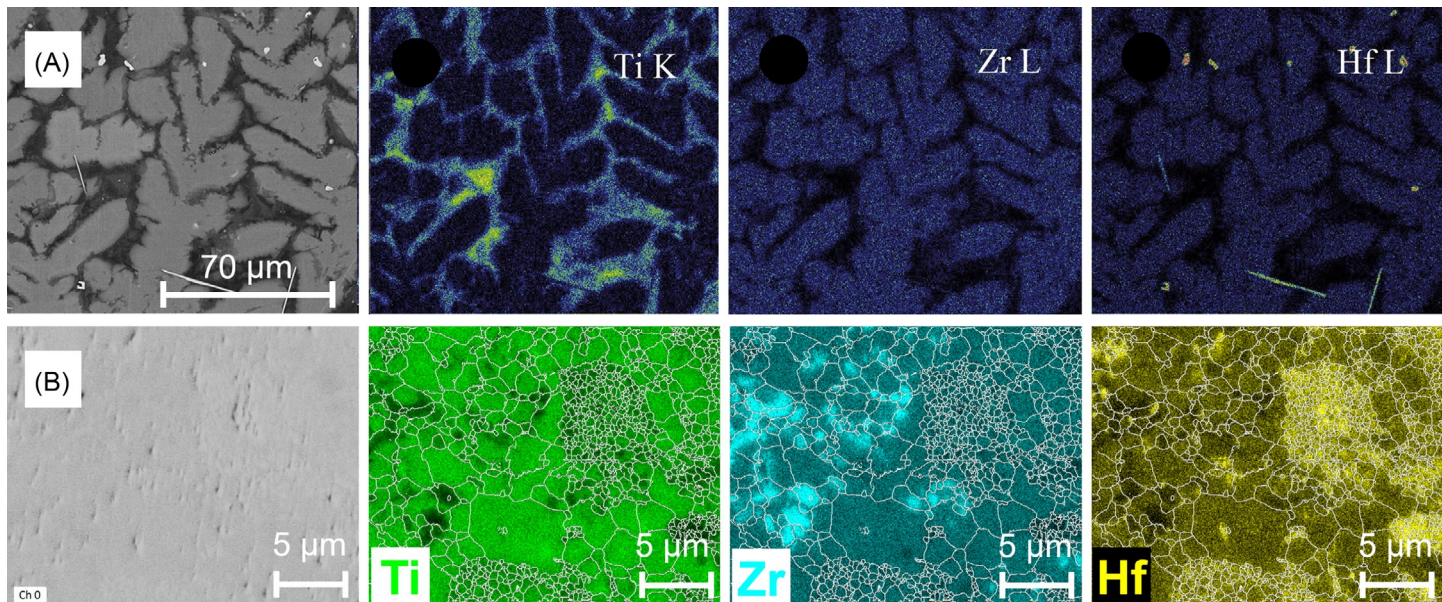


**Fig. 2.3.2** Comparison of microstructures for  $(\text{Ti},\text{Zr},\text{Hf})\text{NiSn}$  samples prepared via (A) arc melting and (B) solid-state routes.  
Panel (A) is reproduced from S. Populoh, M.H. Aguirre, O.C. Brunko, K. Galazka, Y. Lu, A. Weidenkaff, *Scr. Mater.* 66 (2012) 1073–1076 (with permission) and panel (B) from S.A. Barczak, R.J. Quinn, J.E. Halpin, K. Domosud, R.I. Smith, A.R. Baker, E. Don, I. Forbes, K. Refson, D.A. MacLaren, J.W.G. Bos, *J. Mater. Chem. A* 7 (2019) 27124–27134 (CC-BY license).

This energy barrier strongly impedes the X-metal diffusion at typical annealing temperatures (900–1000°C). This suggests that the melt-processed and powder microstructures are “frozen-in” and do not fully reflect the thermodynamics of the phase diagram. One possible solution is to use mineralizers (liquid phase assisted reactions) to improve the reaction kinetics. In this regard, the addition of small amounts of Cu has recently been shown to significantly improve the chemical homogeneity and to afford increased grain growth [60].

The impact of X-site segregation on  $\kappa_{lat}$  has not been fully quantified. Calculations suggest that most of the heat-carrying phonons in the HHs have mean free paths  $<1\text{--}2\,\mu\text{m}$  [35]. By contrast, the X-site segregation typically occurs over greater length scales (illustrated in Fig. 2.3.2), suggesting that these microstructures may not have a strong impact on  $\kappa_{lat}$ . Accurately modeling  $\kappa_{lat}$  remains challenging due to the complex compositions and range of length scales involved. For this reason, the relative importance of alloying, grain size reduction and segregation on phonon scattering remains poorly understood. Nevertheless, great improvements in  $ZT$  values have been made in XNiSn HHs. Several groups have now reported  $ZT = 1.2\text{--}1.3$  at 800–900 K, both by exploiting mixtures of all three elements but also by only alloying with Zr and Hf, which affords higher  $\mu$  and  $S^2\sigma$  (Table 2.3.1) [57, 58, 73]. However, it remains a challenge to fully reproduce the high  $ZT = 1.5$  at 673 K reported in 2005.

The peak performance of the p-type XCoSb samples has also been improved significantly in samples with and without X-site segregation, with a peak  $ZT = 1$  at 973 K. (Table 2.3.1) [61, 62]. This has been achieved by better processing and using optimal ratios of X-site alloying elements, coupled to grain size reduction. A recent study focused on the underpinning electronic parameters revealed a large  $m_{DoS}^* = 12.5\,m_e$  with a large valley ( $N_v = 4$ ) and band ( $N_b = 2$ ) degeneracy, yielding  $m_b^* = 3.1\,m_e$  within the SPB model (Table 2.3.1). This large carrier mass is in keeping with the moderate peak  $S^2\sigma = 3\text{--}3.5\,\text{mW m}^{-1}\,\text{K}^{-2}$  for these p-types that has limited their  $ZT$  values [62]. Remarkably, the XCoSb parent has recently been shown to support good n-type properties with  $ZT = 1$  at 1073 K (Table 2.3.1), offering the promise of generator devices with legs of near identical composition [64].

**HH-FH segregation:** This focuses on the tie-line between XYZ and XY<sub>2</sub>Z phases, which is characterized by the low solubility of additional Y atoms in the HH structure, leading to segregation into HH and FH domains [21, 22, 74]. This low solubility results from the disruption of the stable semiconducting band structure [21, 22, 74]. One of the first targeted studies of Y metal-rich HHs was undertaken on TiNi<sub>1+y</sub>Sn ( $y < 0.1$ ), where the data were interpreted in terms of Ni interstitials [75]. This was followed by work on the (Zr/Hf)Ni<sub>1+y</sub>Sn system, where segregation of 5–10 nm FH nano-inclusions was reported using a solid-state reaction between powder precursors [25]. This led to improvements in  $S^2\sigma$ , attributed to carrier filtering due to energy barriers between the FH inclusions and the HH matrix [25, 26]. In addition,  $\kappa_{lat}$  was reduced, leading to a peak  $ZT \sim 0.8$  [25]. Doping with Sb eliminates the carrier filtering effect as the band filling increases [76]. Similar carrier filtering effects were reported by the same group in p-type (Zr/Hf)Co<sub>1+y</sub>(Sb/Sn) systems [27].

As observed for X-site segregation, the final microstructure depends strongly on the processing route. Chai et al. pioneered the use of zone refining, where a molten

zone is moved through the sample. This leads to a pronounced segregation into HH and FH domains [23, 77, 78]. A typical example for a zone refined ZrNi<sub>1.1</sub>Sn sample is shown in Fig. 2.3.3. Immediately after melting, the microstructure contains many well-defined large FH plates of  $\sim 1 \mu\text{m}$  size. These anneal out above  $\sim 800^\circ\text{C}$ , leading to the dissolution of the large plates and conversion into smaller semicoherent inclusions, which occur in greater numbers (Fig. 2.3.3) [79, 80]. This change to a more dispersed microstructure leads to a reduction of  $\kappa_{lat}$  and improvement in  $ZT$  but occurs at the detriment of  $S^2\sigma$ . This elegant work illustrates the highly complex microstructures that are accessible and highlights the need for quantitative models that capture the impact of FH segregation to guide thermoelectric optimization.

TiNiSn is able to accommodate a much larger amount of interstitial Ni (e.g., 8% site occupancy at  $900^\circ\text{C}$ , versus <2%–3% for the Zr and Hf compositions) before segregation of FH phases occurs [53, 55, 72, 81–83]. The cause of this discrepancy is not fully understood but the interstitials strongly impact on the thermoelectric properties:  $\kappa_{lat}$  is severely reduced through strong point defect scattering [55, 59], but unfortunately  $\mu$  is also affected, limiting the observed improvements in  $ZT$  [53, 55]. The highest reported  $ZT$  values for Ni-rich samples without alloying are 0.6–0.7 at 800K [54, 82, 83], with one report demonstrating  $ZT \sim 1$  based on a highly suppressed  $\kappa_{lat}$  [57].

In terms of the electronic structure, interstitial Ni causes localized states within the semiconducting bandgap, reducing  $E_g$  to  $\sim 0.15 \text{ eV}$  from  $0.5 \text{ eV}$  for defect-free TiNiSn [81, 84, 85]. These localized Ni states have a formal +1 charge from defect calculations and are weak n-type dopants with thermally activated doping into the conduction band [86, 87]. The reduction in  $\mu$  caused by the Ni interstitials may be related to this formal charge and the close proximity of the localized energy states to the conduction band minimum.

First-principles defect calculations have afforded greatly improved insight into the prevalent defects depending on growth conditions [86, 88]. A systematic way to address all experimentally accessible growth conditions has been labeled phase boundary mapping [89]. This approach has been explored for the Ti-Ni-Sn system, where six unique phase regions and two stable TiNiSn boundary compositions were identified (Fig. 2.3.4) [53]. These are stoichiometric TiNiSn and TiNi<sub>1.06</sub>Sn, which were found to have substantially different thermoelectric properties. The stoichiometric samples are characterized by higher  $S^2\sigma$  but also a higher  $\kappa_{lat}$ , while the Ni-rich sample has a smaller  $\kappa_{lat}$  but reduced  $\mu$  (Fig. 2.3.4B and C) limiting  $S^2\sigma$ . Overall, the samples with Ni interstitials have a higher  $ZT \sim 0.55$ , compared to  $ZT \sim 0.45$  at 723 K (Fig. 2.3.4D).

Finally, the TiNiSn-system also affords the incorporation of significant amounts of interstitial Cu, leading to  $ZT = 0.6$  at 773 K for TiNiCu<sub>0.05</sub>Sn and  $ZT = 0.8$  at 773 K for alloyed compositions with mixtures of Ti, Zr, and Hf (Table 2.3.1). Structural analysis shows that up to  $\sim 12\%$  site occupancy is possible at  $900^\circ\text{C}$ , but the thermoelectric properties are optimized at much lower Cu concentrations (2%–5%) [59, 60, 81]. Interstitial Cu is an effective dopant n-type dopant with its 4s<sup>1</sup> electron delocalized into the conduction band, thus affording identical doping efficiency as Sb [60]. The introduction of Cu also reduces  $\kappa_{lat}$  but in contrast to interstitial Ni does not negatively impact on  $\mu$  [60].

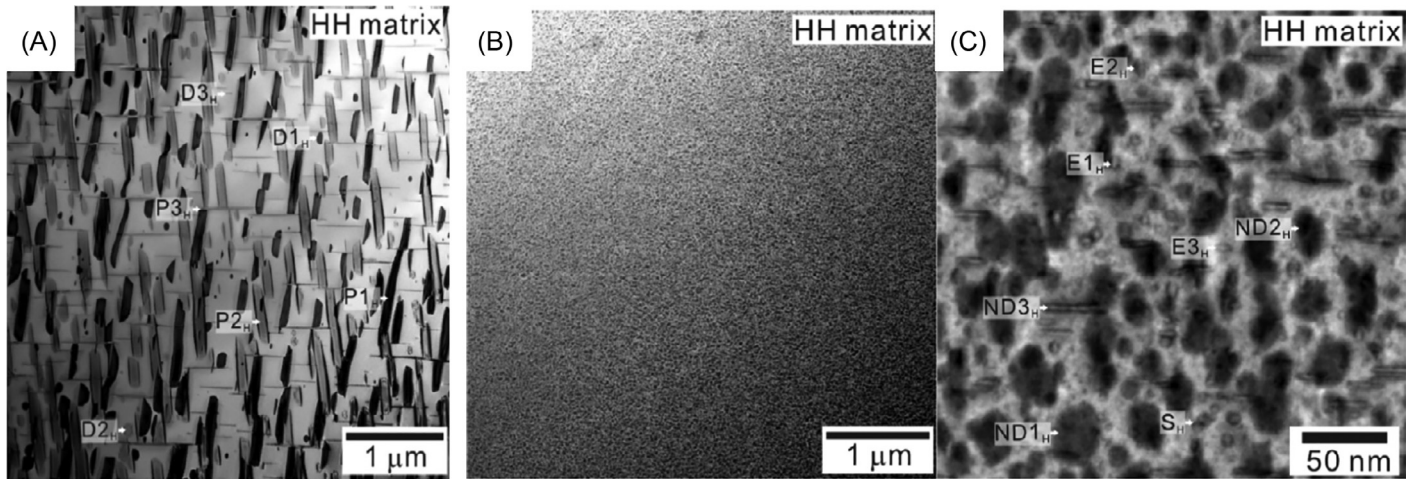


**Fig. 2.3.3** Microstructures for zone refined  $\text{ZrNi}_{1.1}\text{Sn}$ . Panel (A) microstructure immediately after zone refining (B, C) microstructure after annealing at 800°C, revealing a loss of larger FH precipitates and conversion to smaller partially coherent FH inclusions.  
Reproduced from Ref. Y.W. Chai, T. Oniki, Y. Kimura, *Acta Mater.* 85 (2015) 290–300 (with permission).

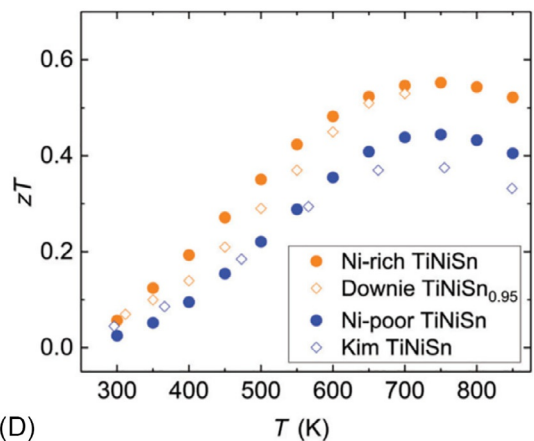
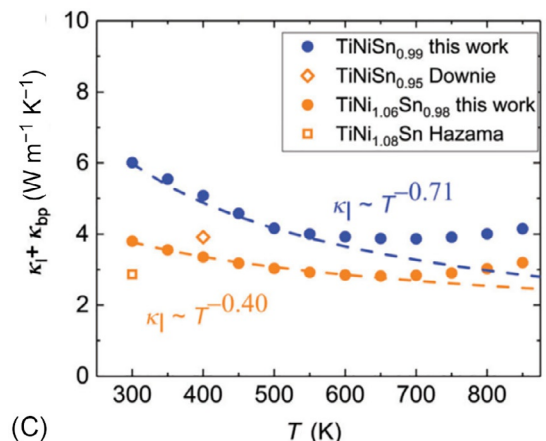
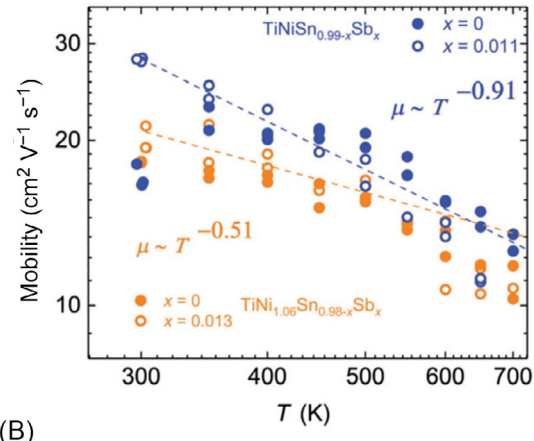
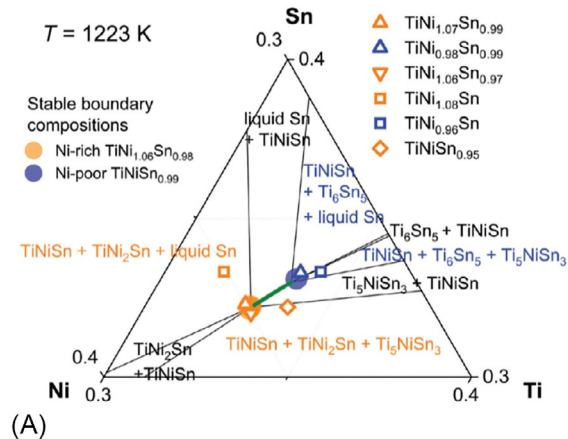


**Fig. 2.3.4** The phase boundary mapping approach to controlling the defect chemistry of  $\text{TiNiSn}$ . (A) At least six unique phase domains and two stable boundary  $\text{TiNiSn}$  compositions were found: stoichiometric  $\text{TiNiSn}$  and  $\text{TiNi}_{1.06}\text{Sn}$ . The impact of interstitial Ni on (B) the Hall carrier mobility, (C) thermal conductivity and (D) the figure of merit.

Reproduced from Y.L. Tang, X.S. Li, L.H.J. Martin, E.C. Reyes, T. Ivas, C. Leinenbach, S. Anand, M. Peters, G.J. Snyder, C. Battaglia, Energy Environ. Sci. 11 (2018) 311–320 (with permission from RSC publishing).

## 2.3.4 New p-types

During the past decade, a significant number of new p-types have been reported. The most prominent of these is NbFeSb. The promise of this material was first demonstrated in 2014 by Fu et al. showing that  $(V_{0.6}Nb_{0.4})_{1-x}Ti_xFeSb$  supports  $ZT=0.8$  at 900 K [31]. This was attributed to a large valley and ( $N_v=4$ ) band ( $N_b=2$ ) degeneracy and low  $E_{def}$ , which results in a relatively high  $\mu_H=5\text{--}10\text{ cm}^2\text{ V}^{-1}\text{ s}^{-1}$  and  $S^2\sigma=3\text{ mW m}^{-1}\text{ K}^{-2}$ , despite the large  $m_b^*=2.5\text{ m}_e$ . The high  $ZT$  was obtained at the solubility limit for Ti ( $x\sim 0.15$ ) with better performance predicted if higher p-type carrier concentrations could be achieved. Subsequent improvements relied on the use of electronic band structure engineering concepts. The first strategy used was to remove V and increase the band dispersion. Experimentally, a lower  $m_b^*=1.6\text{ m}_e$  was indeed found for  $Nb_{1-x}Ti_xFeSb$  without V alloying. This reduction of  $m_b^*$  moves the peak  $S^2\sigma$  to lower  $n_H$ , so that this falls within the solubility limit of Ti, while the lighter hole mass yields improved  $\mu_H=15\text{--}25\text{ cm}^2\text{ V}^{-1}\text{ s}^{-1}$  [32]. This enables a 50% improved  $S^2\sigma\sim 4.5\text{ mW m}^{-1}\text{ K}^{-2}$  and  $ZT=1.1$  at 1100 K [32].

Further improvements to  $ZT=1.5$  at 1200 K have been realized by using Zr and Hf as dopant elements [33], which affords a higher  $\mu_H$  due to a reduction in lattice strain [52]. This strategy enables  $S^2\sigma=5\text{--}6\text{ mW m}^{-1}\text{ K}^{-2}$ , while the large mass difference between Nb and Hf leads to a low  $\kappa_{lat}$ . The evolution of the key thermoelectric properties in the NbFeSb system utilizing Ti, Zr, and Hf as dopants is summarized in Fig. 2.3.5.

In parallel, He et al. obtained very large 300 K  $S^2\sigma$  in  $Nb_{1-x}Ti_xFeSb$  by promoting grain growth using higher consolidation temperatures [65]. Increasing the hot press temperature from 850°C to 1100°C improves  $\mu_H$  from  $\sim 15$  to  $\sim 26\text{ cm}^2\text{ V}^{-1}\text{ s}^{-1}$  at 300 K, enabling very large  $S^2\sigma\sim 10\text{ mW m}^{-1}\text{ K}^{-2}$  at 300 K for the best samples. At higher temperatures,  $S^2\sigma$  tends toward  $5\text{--}6\text{ mW m}^{-1}\text{ K}^{-2}$  as observed in other studies and similar peak  $ZT\sim 1$  values are found. This study affirms the importance of grain boundary control to extract the maximum performance from materials near room temperature. This is very significant for device applications, which depend on the temperature-averaged properties, and very large power outputs have been reported for single leg devices [40]. Large room temperature  $S^2\sigma$  values have also been reported for the other  $Nb_{1-x}A_xFeSb$  ( $A=\text{Zr}$  and  $\text{Hf}$ ) HHs, while multielement alloying and multiscale structural controlled have all been used to optimize the thermoelectric performance [41,42,90].

The related TaFeSb composition also supports excellent thermoelectric performance with peak  $ZT=1.5$  at 973 K and a temperature-averaged  $ZT=0.8\text{--}0.9$  between 300 and 973 K (Table 2.3.1) [66]. This outstanding performance is enabled by a near temperature-independent  $S^2\sigma\sim 5\text{ mW m}^{-1}\text{ K}^{-2}$  and a low  $\kappa_{lat}\sim 3\text{ W m}^{-1}\text{ K}^{-1}$  at 300 K. The low  $\kappa_{lat}$  is the main performance differentiator compared to NbFeSb and is due to a lower velocity of sound  $\sim 2900\text{ m s}^{-1}$  (cf.  $\sim 3500\text{ m s}^{-1}$  for NbFeSb) and the large mass difference between Ta and Ti, causing a strong alloying phonon scattering effect.

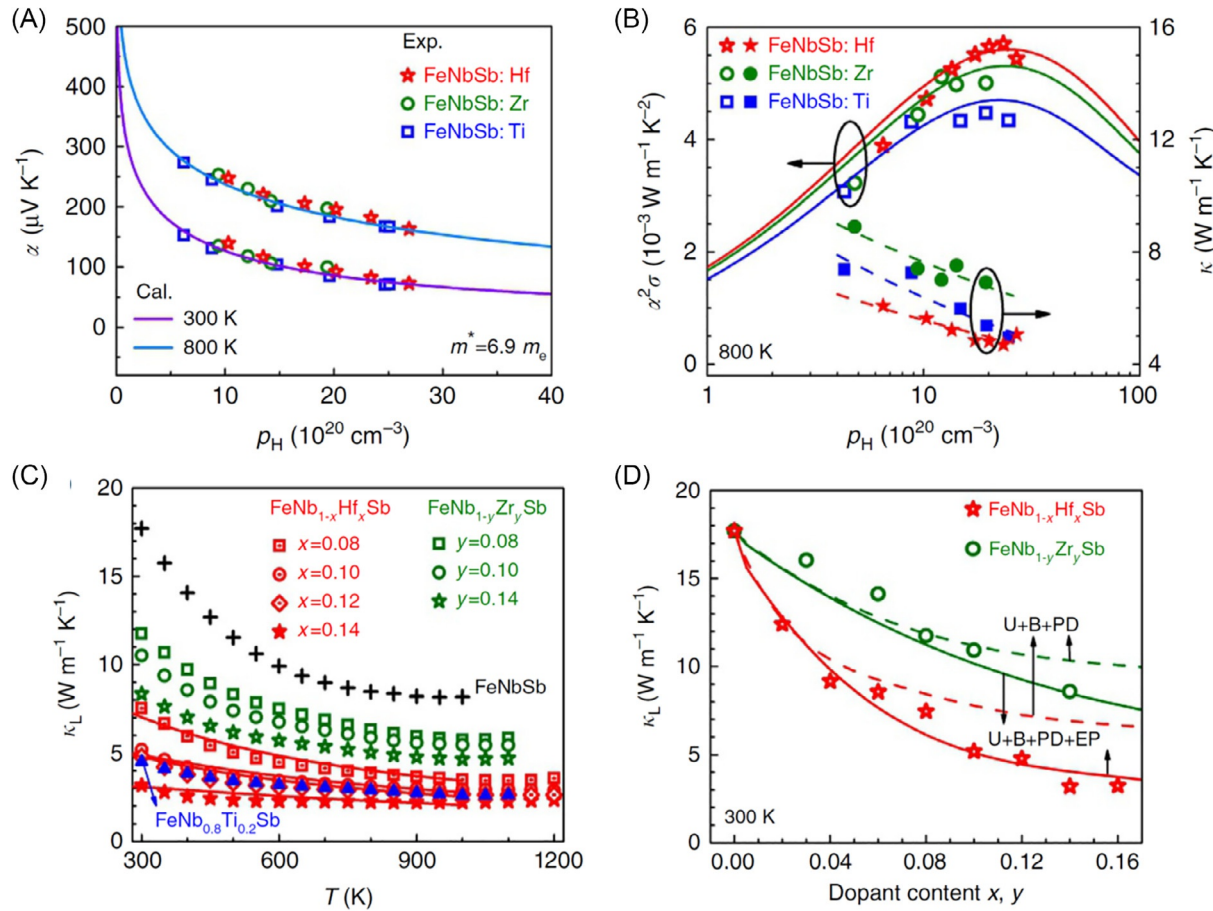


**Fig. 2.3.5** Overview of the key thermoelectric properties of the NbFeSb p-types. (A) Pisarenko plot revealing similar  $m_{DoS}^* = 6.9 m_e$  for Ti, Zr, and Hf alloyed samples, note that the alloying element is also the source of the p-type carriers. (B) Improved  $S^2\sigma$  in samples without alloying size disorder, i.e., the Zr and Hf systems. (C, D) Large reduction of  $\kappa_{lat}$  through alloying, with electron-phonon scattering suggested to be important in highly doped samples. Reproduced from C.G. Fu, S.Q. Bai, Y.T. Liu, Y.S. Tang, L.D. Chen, X.B. Zhao, T.J. Zhu, Nat. Commun. 6 (2015) 8144 (CC-BY license).

The final new high- $ZT$  p-type that must be mentioned is ZrCoBi. A reinvestigation of this composition [34], now synthesized using a milling and rapid consolidation approach, yielded samples with outstanding thermoelectric performance; i.e.,  $ZT=1.4$  at 973K. This results from a low  $\kappa_{lat}=2.5\text{ W m}^{-1}\text{ K}^{-1}$  at 300K and peak  $S^2\sigma=3.5\text{--}4\text{ mW m}^{-1}\text{ K}^{-2}$ . The good electrical properties have been attributed to a favorable electronic band structure with multiple contributing bands at the  $\Gamma$  and L points (Table 2.3.1). The low  $\kappa_{lat}$  is due to a low velocity of sound ( $2850\text{ m s}^{-1}$ ), combined with effective main group alloying using Sb and Sn (the p-type dopant) with significant mass differences.

### 2.3.5 New n-type compositions

The increased interest in HH thermoelectrics has led to the reinvestigation and discovery of several promising n-types. NbCoSn-based compositions were investigated in the early 2000s [91–93], with peak  $ZT<0.4$ . A recent reinvestigation using a melting, milling and rapid consolidation (1000°C and 80 MPa for 2 min) approach has enabled an increase to  $ZT=0.6$  for  $\text{NbCoSn}_{0.9}\text{Sb}_{0.1}$  at 1000K (Table 2.3.1) [67]. This material has peak  $S^2\sigma\sim3\text{ mW m}^{-1}\text{ K}^{-2}$  and  $\kappa_{lat}\sim8\text{ W m}^{-1}\text{ K}^{-1}$  at 300K. DFT calculations place the CB minimum at the X-point with two contributing bands, while the VB maximum is at the W point with  $N_v=12$ , which should enable excellent p-type properties [67]. However, attempts at p-type doping this composition have remained unsuccessful and reveal poor p-type electrical conductivities [94]. SPB analysis yields  $m_{DOS}^*=6m_e$  for the n-types, suggesting  $m_b^*=1.8m_e$ , which is significantly larger than  $m_b^*=1.3m_e$  for the  $X\text{NiSn}$  n-types, and consistent with the lower  $S^2\sigma$  in these compositions.

Another highlight of the recent literature has been the work on the so-called 19 valence electron HHs, exemplified by VCoSb and NbCoSb [95, 96]. These nominal 1:1:1 compositions were reported with promising  $ZT\sim0.5$  at 1000K, despite having a metallic electron count not associated with good thermoelectric performance. Subsequent work showed that these phases form with X-site vacancies with compositions closer to  $\text{V}_{0.9}\text{CoSb}$  and  $\text{Nb}_{0.85}\text{CoSb}$  [69, 94, 97]. The  $\text{A}_{0.8}\text{CoSb}$  stoichiometry corresponds a valence balanced 18-electron system, and the best way to express their compositions is therefore  $\text{A}_{0.8+x}\text{CoSb}$ , where the free electron concentration is proportional to  $x$ . The observation of different preferred values of  $x$  for the  $\text{A}=\text{V}$  ( $x\sim0.1$ ), Nb ( $\sim0.05$ ), and Ta ( $x\sim0$ ) can be explained by the increasing cost of filling antibonding electronic states due to a decreasing  $m_b^*$  [69, 98]. Despite the thermodynamic preference for a specific composition, it is possible to control the value of  $x$  by changing the nominal composition (and through temperature) [68, 98]. The most investigated of the HHs with intrinsic vacancies is  $\text{Nb}_{0.8+x}\text{CoSb}$ , where a maximum  $ZT=0.9$  was reported at 1100K for  $x\sim0.03$  [68]. This is based on a peak  $S^2\sigma\sim2.5\text{ mW m}^{-1}\text{ K}^{-2}$  and  $\kappa_{lat}\sim4\text{ W m}^{-1}\text{ K}^{-1}$  at room temperature. Hall measurements yield  $m_{DOS}^*=7.7m_e$  and  $\mu_H\sim4\text{ cm}^2\text{ V}^{-1}\text{ s}^{-1}$ , demonstrating that this is another HH system with heavy charge carriers. The highest reported  $ZT$  values for  $\text{V}_{0.8+x}\text{CoSb}$  and  $\text{Ta}_{0.8+x}\text{CoSb}$  are  $ZT=0.5$  at 950K and  $ZT=0.3$  at 950K, respectively, where the

V compound is characterized by an unusually low  $\kappa_{lat}$  and the refractory Ta material is characterized by very fine grains [69].

The realization that non 1:1:1 composition can be stable HHs, has led to an emerging interest in other complex compositions [48, 99]. Compositions with multiple elements on the X, Y, and Z sites have been dubbed “double half-Heuslers” and offer a large class of materials for further exploration [99]. An initial study of the 1:1 combination of 17 electron TiFeSb and 19 electron TiNiSb demonstrated promising  $ZT=0.7\text{--}1$  values at 1000K for n- and p-types by varying the Fe/Ni ratio [100]. This performance is based on a low thermal conductivity ( $\sim 3 \text{ W m}^{-1} \text{ K}^{-1}$  at 1000K) and a modest  $S^2\sigma \sim 2 \text{ mW m}^{-1} \text{ K}^{-2}$ . The relatively poor electrical properties are not unexpected given the inherent atomic disorder within the crystal structure. The low observed low  $\kappa_{lat}$  is likely caused by bond disorder, given the absence of any significant mass and size differences, and is in keeping with results from simulations that suggest that this type of complex HHs have reduced thermal conductivities [99].

### 2.3.6 Conclusions and outlook

The past decade has seen great improvements in HH performance, including in established materials, but also through the exploration of new compositions. This has been driven by improved processing, use of nanostructuring and adaptation of electronic band structure engineering concepts. As outlined in this chapter, this has led to several n- and p-type HHs with peak  $ZT \geq 1$  and  $S^2\sigma \geq 5\text{--}6 \text{ mW m}^{-1} \text{ K}^{-2}$  (Table 2.3.1). These efficiencies and power outputs are sufficient for application in heat recovery applications, leading to increasing work on generator development. The recent literature on HH generators indicates that prototypes are operating at 5%–10% efficiency with  $5\text{--}8 \text{ W cm}^{-2}$  power outputs from a  $500^\circ\text{C}$  gradient [101–103]. Besides these performance metrics, it is particularly encouraging that electrical and thermal contacting, mechanical strength, and temperature stability issues appear less severe than for some other high-performance materials. This indicates that it is justified pursuing further improvements in materials performance. Furthermore, the increased focus on translation into generators offers additional possibilities for materials scientists with a need for stability studies to investigate material and device degradation pathways and develop mitigation strategies.

Future materials development should focus on improving the temperature averaged  $S^2\sigma$  and  $ZT$ , as this determines device performance. One immediate way this can be achieved is by targeting parasitic resistances (e.g., grain boundary resistances), which affect the low-temperature electrical transport most strongly. In terms of their electronic structures, most n- and p-types have their band extrema at similar positions in the Brillouin zone, limiting the possibility for band convergence through alloying strategies. This suggests that new approaches are needed to increase  $ZT$  beyond the current state of the art. These are likely to be driven by advanced modeling to discover new compositions and novel routes to manipulate electron and phonon transport in existing materials.

To conclude, this decade has seen important advances in understanding and performance of HH thermoelectrics with  $ZT \geq 1$  for both n- and p-types. This has made these materials a realistic prospect for application in viable generator modules, placing a premium on any further gains in materials performance.

## References

- [1] F.G. Aliev, V.V. Kozyrkov, V.V. Moshchalkov, R.V. Scolozdra, K. Durczewski, *Z. Phys. B Condens. Matter* 80 (1990) 353–357.
- [2] F.G. Aliev, N.B. Brandt, V.V. Moshchalkov, V.V. Kozyrkov, R.V. Skolozdra, A.I. Belgorokhov, *Z. Phys. B Condens. Matter* 75 (1989) 167–171.
- [3] C. Uher, J. Yang, S. Hu, D.T. Morelli, G.P. Meisner, *Phys. Rev. B* 59 (1999) 8615–8621.
- [4] S. Ogut, K.M. Rabe, *Phys. Rev. B* 51 (1995) 10443–10453.
- [5] J. Yang, G.P. Meisner, L. Chen, *Appl. Phys. Lett.* 85 (2004) 1140–1142.
- [6] Y. Xia, V. Ponnambalam, S. Bhattacharya, A.L. Pope, S.J. Poon, T.M. Tritt, *J. Phys. Condens. Matter* 13 (2001) 77–89.
- [7] Y. Xia, S. Bhattacharya, V. Ponnambalam, A.L. Pope, S.J. Poon, T.M. Tritt, *J. Appl. Phys.* 88 (2000) 1952–1955.
- [8] Q. Shen, L. Chen, T. Goto, T. Hirai, J. Yang, G.P. Meisner, C. Uher, *Appl. Phys. Lett.* 79 (2001) 4165–4167.
- [9] S. Sakurada, N. Shutoh, *Appl. Phys. Lett.* 86 (2005) 082105.
- [10] S.J. Poon, Electronic and thermoelectric properties of half-Heusler alloys, *Recent Trends in Thermoelectric Materials Research II*, vol. 70, Academic Press, 2001, pp. 37–75.
- [11] B.R.K. Nanda, I. Dasgupta, *J. Phys. Condens. Matter* 15 (2003) 7307–7323.
- [12] K. Mastronardi, D. Young, C.C. Wang, P. Khalifah, R.J. Cava, A.P. Ramirez, *Appl. Phys. Lett.* 74 (1999) 1415–1417.
- [13] P. Larson, S.D. Mahanti, S. Sportouch, M.G. Kanatzidis, *Phys. Rev. B* 59 (1999) 15660–15668.
- [14] P. Larson, S.D. Mahanti, M.G. Kanatzidis, *Phys. Rev. B* 62 (2000) 12754–12762.
- [15] S. Bhattacharya, A.L. Pope, R.T. Littleton, T.M. Tritt, V. Ponnambalam, Y. Xia, S.J. Poon, *Appl. Phys. Lett.* 77 (2000) 2476–2478.
- [16] X.A. Yan, G. Joshi, W.S. Liu, Y.C. Lan, H. Wang, S. Lee, J.W. Simonson, S.J. Poon, T.M. Tritt, G. Chen, Z.F. Ren, *Nano Lett.* 11 (2011) 556–560.
- [17] G. Joshi, X. Yan, H.Z. Wang, W.S. Liu, G. Chen, Z.F. Ren, *Adv. Energy Mater.* 1 (2011) 643–647.
- [18] Y. Kimura, H. Ueno, Y. Mishima, *J. Electron. Mater.* 38 (2009) 934–939.
- [19] S. Populoh, M.H. Aguirre, O.C. Brunko, K. Galazka, Y. Lu, A. Weidenkaff, *Scr. Mater.* 66 (2012) 1073–1076.
- [20] M. Schwall, B. Balke, *Phys. Chem. Chem. Phys.* 15 (2013) 1868–1872.
- [21] K. Kirievsky, Y. Gelbstein, D. Fuks, *J. Solid State Chem.* 203 (2013) 247–254.
- [22] A. Page, C. Uher, P.F. Poudeu, A. Van der Ven, *Phys. Rev. B* 92 (2015) 174102.
- [23] Y. Kimura, Y.W. Chai, *JOM* 67 (2015) 233–245.
- [24] A. Page, A. Van der Ven, P.F.P. Poudeu, C. Uher, *J. Mater. Chem. A* 4 (2016) 13949–13956.
- [25] J.P.A. Makongo, D.K. Misra, X.Y. Zhou, A. Pant, M.R. Shabetai, X.L. Su, C. Uher, K.L. Stokes, P.F.P. Poudeu, *J. Am. Chem. Soc.* 133 (2011) 18843–18852.
- [26] Y.F. Liu, P. Sahoo, J.P.A. Makongo, X.Y. Zhou, S.J. Kim, H. Chi, C. Uher, X.Q. Pan, P.F.P. Poudeu, *J. Am. Chem. Soc.* 135 (2013) 7486–7495.

- [27] P. Sahoo, Y.F. Liu, J.P.A. Makongo, X.L. Su, S.J. Kim, N. Takas, H. Chi, C. Uher, X.Q. Pan, P.F.P. Poudeu, *Nanoscale* 5 (2013) 9419–9427.
- [28] J. Yang, H.M. Li, T. Wu, W.Q. Zhang, L.D. Chen, J.H. Yang, *Adv. Funct. Mater.* 18 (2008) 2880–2888.
- [29] R. Gautier, X.W. Zhang, L.H. Hu, L.P. Yu, Y.Y. Lin, T.O.L. Sunde, D. Chon, K.R. Poeppelmeier, A. Zunger, *Nat. Chem.* 7 (2015) 308–316.
- [30] H.H. Xie, H. Wang, Y.Z. Pei, C.G. Fu, X.H. Liu, G.J. Snyder, X.B. Zhao, T.J. Zhu, *Adv. Funct. Mater.* 23 (2013) 5123–5130.
- [31] C.G. Fu, T.J. Zhu, Y.Z. Pei, H.H. Xie, H. Wang, G.J. Snyder, Y. Liu, Y.T. Liu, X.B. Zhao, *Adv. Energy Mater.* 4 (2014) 1400600.
- [32] C.G. Fu, T.J. Zhu, Y.T. Liu, H.H. Xie, X.B. Zhao, *Energy Environ. Sci.* 8 (2015) 216–220.
- [33] C.G. Fu, S.Q. Bai, Y.T. Liu, Y.S. Tang, L.D. Chen, X.B. Zhao, T.J. Zhu, *Nat. Commun.* 6 (2015) 8144.
- [34] H.T. Zhu, R. He, J. Mao, Q. Zhu, C.H. Li, J.F. Sun, W.Y. Ren, Y.M. Wang, Z.H. Liu, Z.J. Tang, A. Sotnikov, Z.M. Wang, D. Broido, D.J. Singh, G. Chen, K. Nielsch, Z.F. Ren, *Nat. Commun.* 9 (2018) 2497.
- [35] J. Shiomi, K. Esfarjani, G. Chen, *Phys. Rev. B* 84 (2011) 104302.
- [36] J. Carrete, W. Li, N. Mingo, S.D. Wang, S. Curtarolo, *Phys. Rev. X* 4 (2014) 011019.
- [37] A. Katre, J. Carrete, N. Mingo, *J. Mater. Chem. A* 4 (2016) 15940–15944.
- [38] S.N.H. Eliassen, A. Katre, G.K.H. Madsen, C. Persson, O.M. Lovvik, K. Berland, *Phys. Rev. B* 95 (2017) 045202.
- [39] C. Yu, T.J. Zhu, R.Z. Shi, Y. Zhang, X.B. Zhao, J. He, *Acta Mater.* 57 (2009) 2757–2764.
- [40] G. Joshi, R. He, M. Engber, G. Samsonidze, T. Pantha, E. Dahal, K. Dahal, J. Yang, Y.C. Lan, B. Kozinsky, Z.F. Ren, *Energy Environ. Sci.* 7 (2014) 4070–4076.
- [41] J.J. Yu, C.G. Fu, Y.T. Liu, K.Y. Xia, U. Aydemir, T.C. Chasapis, G.J. Snyder, X.B. Zhao, T.J. Zhu, *Adv. Energy Mater.* 8 (2018) 1701313.
- [42] W.Y. Ren, H.T. Zhu, Q. Zhu, U. Saparamadu, R. He, Z.H. Liu, J. Mao, C. Wang, K. Nielsch, Z.M. Wang, Z.F. Ren, *Adv. Sci.* 5 (2018) 1800278.
- [43] H.Z. Zhao, J.E. Sui, Z.J. Tang, Y.C. Lan, Q.G. Jie, D. Kraemer, K.N. McEnaney, A. Guloy, G. Chen, Z.F. Ren, *Nano Energy* 7 (2014) 97–103.
- [44] D. Kraemer, J. Sui, K. McEnaney, H. Zhao, Q. Jie, Z.F. Ren, G. Chen, *Energy Environ. Sci.* 8 (2015) 1299–1308.
- [45] T. Graf, C. Felser, S.S.P. Parkin, *Prog. Solid State Chem.* 39 (2011) 1–50.
- [46] W.G. Zeier, J. Schmitt, G. Hautier, U. Aydemir, Z.M. Gibbs, C. Felser, G.J. Snyder, *Nat. Rev. Mater.* 1 (2016) 16032.
- [47] K. Momma, F. Izumi, *J. Appl. Crystallogr.* 44 (2011) 1272–1276.
- [48] S. Anand, K. Xia, V.I. Hegde, U. Aydemir, V. Kocevski, T. Zhu, C. Wolverton, G.J. Snyder, *Energy Environ. Sci.* 11 (2018) 1480–1488.
- [49] T.J. Zhu, C.G. Fu, H.H. Xie, Y.T. Liu, X.B. Zhao, *Adv. Energy Mater.* (2015) 5.
- [50] A.F. May, G.J. Snyder, *Introduction to modeling thermoelectric transport at high temperatures, Materials, Preparation, and Characterization in Thermoelectrics, Thermoelectrics and Its Energy Harvesting*, CRC Press, 2012, pp. K1–K18.
- [51] Y.Z. Pei, H. Wang, G.J. Snyder, *Adv. Mater.* 24 (2012) 6125–6135.
- [52] Y.T. Liu, C.G. Fu, K.Y. Xia, J.J. Yu, X.B. Zhao, H.G. Pan, C. Felser, T.J. Zhu, *Adv. Mater.* 30 (2018) 1800881.
- [53] Y.L. Tang, X.S. Li, L.H.J. Martin, E.C. Reyes, T. Ivas, C. Leinenbach, S. Anand, M. Peters, G.J. Snyder, C. Battaglia, *Energy Environ. Sci.* 11 (2018) 311–320.

- [54] R.A. Downie, D.A. MacLaren, R.I. Smith, J.W.G. Bos, *Chem. Commun.* 49 (2013) 4184–4186.
- [55] S.A. Barczak, J. Buckman, R.I. Smith, A.R. Baker, E. Don, I. Forbes, J.W.G. Bos, *Materials* 11 (2018) 536.
- [56] L. Chen, S. Gao, X. Zeng, A.M. Dehkordi, T.M. Tritt, S.J. Poon, *Appl. Phys. Lett.* 107 (2015) 041902.
- [57] M. Gurth, G. Rogl, V.V. Romaka, A. Grytsiv, E. Bauer, P. Rogl, *Acta Mater.* 104 (2016) 210–222.
- [58] G. Rogl, P. Sauerschnig, Z. Rykavets, V.V. Romaka, P. Heinrich, B. Hinterleitner, A. Grytsiv, E. Bauer, P. Rogl, *Acta Mater.* 131 (2017) 336–348.
- [59] S.A. Barczak, J.E. Halpin, J. Buckman, R. Decourt, M. Pollet, R.I. Smith, D.A. MacLaren, J.W.G. Bos, *ACS Appl. Mater. Interfaces* 10 (2018) 4786–4793.
- [60] S.A. Barczak, R.J. Quinn, J.E. Halpin, K. Domosud, R.I. Smith, A.R. Baker, E. Don, I. Forbes, K. Refson, D.A. MacLaren, J.W.G. Bos, *J. Mater. Chem. A* 7 (2019) 27124–27134.
- [61] X. Yan, W.S. Liu, S. Chen, H. Wang, Q. Zhang, G. Chen, Z.F. Ren, *Adv. Energy Mater.* 3 (2013) 1195–1200.
- [62] C. Hu, K. Xia, X. Chen, X. Zhao, T. Zhu, *Mater. Today Phys.* 7 (2018) 69–76.
- [63] E. Rausch, B. Balke, S. Ouardi, C. Felser, *Phys. Chem. Chem. Phys.* 16 (2014) 25258–25262.
- [64] R. He, H.T. Zhu, J.Y. Sun, J. Mao, H. Reith, S. Chen, G. Schierning, K. Nielsch, Z.F. Ren, *Mater. Today Phys.* 1 (2017) 24–30.
- [65] R. He, D. Kraemer, J. Mao, L. Zeng, Q. Jie, Y.C. Lan, C.H. Li, J. Shuai, H.S. Kim, Y. Liu, D. Broido, C.W. Chu, G. Chen, Z. Ren, *Proc. Natl. Acad. Sci. U. S. A.* 113 (2016) 13576–13581.
- [66] H.T. Zhu, J. Mao, Y.W. Li, J.F. Sun, Y.M. Wang, Q. Zhu, G.N. Li, Q.C. Song, J.W. Zhou, Y.H. Fu, R. He, T. Tong, Z.H. Liu, W.Y. Ren, L. You, Z.M. Wang, J. Luo, A. Sotnikov, J.M. Bao, K. Nielsch, G. Chen, D.J. Singh, Z.F. Ren, *Nat. Commun.* 10 (2019) 270.
- [67] R. He, L.H. Huang, Y.M. Wang, G. Samsonidze, B. Kozinsky, Q.Y. Zhang, Z.F. Ren, *APL Mater.* 4 (2016) 104804.
- [68] K. Xia, Y. Liu, S. Anand, G.J. Snyder, J. Xin, J. Yu, X. Zhao, T. Zhu, *Adv. Funct. Mater.* (2018) 1705845.
- [69] D.A. Ferluccio, J.E. Halpin, K.L. MacIntosh, R.J. Quinn, E. Don, R.I. Smith, D.A. MacLaren, J.-W.G. Bos, *J. Mater. Chem. C* 7 (2019) 6539.
- [70] S. Bhattacharya, M.J. Skove, M. Russell, T.M. Tritt, Y. Xia, V. Ponnambalam, S.J. Poon, N. Thadhani, *Phys. Rev. B* 77 (2008) 184203.
- [71] R.A. Downie, D.A. MacLaren, J.W.G. Bos, *J. Mater. Chem. A* 2 (2014) 6107–6114.
- [72] R.A. Downie, S.A. Barczak, R.I. Smith, J.W.G. Bos, *J. Mater. Chem. C* 3 (2015) 10534–10542.
- [73] G. Rogl, K. Yubuta, V.V. Romaka, H. Michor, E. Schafler, A. Grytsiv, E. Bauer, P. Rogl, *Acta Mater.* 166 (2019) 466–483.
- [74] D.T. Do, S.D. Mahanti, J.J. Pulikkoti, *J. Phys. Condens. Matter* 26 (2014) 275501.
- [75] H. Hazama, M. Matsubara, R. Asahi, T. Takeuchi, *J. Appl. Phys.* 110 (2011) 063710.
- [76] Y.F. Liu, A. Page, P. Sahoo, H. Chi, C. Uher, P.F.P. Poudeu, *Dalton Trans.* 43 (2014) 8094–8101.
- [77] Y.W. Chai, Y. Kimura, *Appl. Phys. Lett.* 100 (2012) 033114.
- [78] Y.W. Chai, Y. Kimura, *Acta Mater.* 61 (2013) 6684–6697.
- [79] Y.W. Chai, T. Oniki, Y. Kimura, *Acta Mater.* 85 (2015) 290–300.

- [80] Y.W. Chai, T. Oniki, T. Kenjo, Y. Kimura, *J. Alloys Compd.* 662 (2016) 566–577.
- [81] R.A. Downie, R.I. Smith, D.A. MacLaren, J.W.G. Bos, *Chem. Mater.* 27 (2015) 2449–2459.
- [82] J.E. Douglas, C.S. Birkel, N. Verma, V.M. Miller, M.S. Miao, G.D. Stucky, T.M. Pollock, R. Seshadri, *J. Appl. Phys.* 115 (2014) 043720.
- [83] C.S. Birkel, J.E. Douglas, B.R. Lettiere, G. Seward, N. Verma, Y.C. Zhang, T.M. Pollock, R. Seshadri, G.D. Stucky, *Phys. Chem. Chem. Phys.* 15 (2013) 6990–6997.
- [84] J. Schmitt, Z.M. Gibbs, G.J. Snyder, C. Felser, *Mater. Horiz.* 2 (2015) 68–75.
- [85] C.G. Fu, M.Y. Yao, X. Chen, L.Z. Maulana, X. Li, J. Yang, K. Imasato, F.F. Zhu, G.W. Li, G. Auffermann, U. Burkhardt, W. Schnelle, J.S. Zhou, T.J. Zhu, X.B. Zhao, M. Shi, M. Dressel, A.V. Pronin, G.J. Snyder, C. Felser, *Adv. Sci.* (2019), <https://doi.org/10.1002/advs.201902409>.
- [86] Y.G.G. Yu, X.W. Zhang, A. Zunger, *Phys. Rev. B* 95 (2017) 085201.
- [87] A. Berche, P. Jund, *Materials* 11 (2018) 868.
- [88] R. Stern, B. Dongre, G.K.H. Madsen, *Nanotechnology* 27 (2016) 334002.
- [89] S. Ohno, U. Aydemir, M. Amsler, J.H. Pohls, S. Chanakian, A. Zevalkink, M.A. White, S.K. Bux, C. Wolverton, G.J. Snyder, *Adv. Funct. Mater.* 27 (2017) 1606361.
- [90] J.J. Shen, C.G. Fu, Y.T. Liu, X.B. Zhao, T.J. Zhu, *Energy Storage Mater.* 10 (2018) 69–74.
- [91] Y. Kimura, Y. Tamura, T. Kita, *Appl. Phys. Lett.* 92 (2008) 012105.
- [92] Y. Kawaharada, K. Kurosaki, H. Muta, M. Uno, S. Yamanaka, *J. Alloys Compd.* 377 (2004) 312–315.
- [93] Y. Kawaharada, K. Kurosaki, H. Muta, M. Uno, S. Yamanaka, *J. Alloys Compd.* 384 (2004) 303–307.
- [94] D.A. Ferluccio, R.I. Smith, J. Buckman, J.-W.G. Bos, *Phys. Chem. Chem. Phys.* 20 (2018) 3979–3987.
- [95] L.H. Huang, R. He, S. Chen, H. Zhang, K. Dahal, H.Q. Zhou, H. Wang, Q.Y. Zhang, Z.F. Ren, *Mater. Res. Bull.* 70 (2015) 773–778.
- [96] H. Zhang, Y. Wang, L. Huang, S. Chen, H. Dahal, D. Wang, Z. Ren, *J. Alloys Compd.* 654 (2016) 321–326.
- [97] W.G. Zeier, S. Anand, L.H. Huang, R. He, H. Zhang, Z.F. Ren, C. Wolverton, G.J. Snyder, *Chem. Mater.* 29 (2017) 1210–1217.
- [98] S. Anand, K. Xia, T. Zhu, C. Wolverton, G.J. Snyder, *Adv. Energy Mater.* 28 (2018) 1801409.
- [99] S. Anand, M. Wood, Y. Xia, C. Wolverton, G.J. Snyder, *Joule* 3 (2019) 1226–1238.
- [100] Z. Liu, S. Guo, Y. Wu, J. Mao, Q. Zhu, H. Zhu, Y. Pei, J. Sui, Y. Zhang, Z. Ren, *Adv. Funct. Mater.* 29 (2019) 1905044.
- [101] K. Bartholomé, B. Balke, D. Zuckermann, M. Köhne, M. Müller, K. Tarantik, J. König, *J. Electron. Mater.* 43 (2014) 1775–1781.
- [102] Y.L. Zhang, M. Cleary, X.W. Wang, N. Kempf, L. Schoensee, J. Yang, G. Joshi, L. Meda, *Energy Convers. Manag.* 105 (2015) 946–950.
- [103] Y.F. Xing, R.H. Liu, J.C. Liao, Q.H. Zhang, X.G. Xia, C. Wang, H. Huang, J. Chu, M. Gu, T.J. Zhu, C.X. Zhu, F.F. Xu, D.X. Yao, Y.P. Zeng, S.Q. Bai, C. Uher, L.D. Chen, *Energy Environ. Sci.* 12 (2019) 3390–3399.

# Pseudogap engineering of Fe<sub>2</sub>VAI-based thermoelectric Heusler compounds

2.4

*Yoichi Nishino*

Department of Physical Science and Engineering, Nagoya Institute of Technology,  
Nagoya, Japan

## 2.4.1 Introduction

Heusler compounds with composition X<sub>2</sub>YZ, where X and Y denote metallic elements and Z indicates a metalloid, exhibit a rich variety of exotic behaviors in their electronic, magnetic, and transport properties [1]. According to Webster and Ziebeck [2], Fe<sub>2</sub>VAI forms a single-phase intermetallic compound with the Heusler (*L*2<sub>1</sub>) structure. The Fe<sub>2</sub>VAI compound has been found to show a semiconductor-like behavior of electrical resistivity over a wide temperature range of up to 1200K and beyond [3]. This Heusler compound can be derived from the (Fe<sub>1-x</sub>V<sub>x</sub>)<sub>3</sub>Al system, where Fe<sub>3</sub>Al ( $x=0$ ) is a ferromagnetic alloy, but Fe<sub>2</sub>VAI ( $x=1/3$ ) is proved to be in a marginally magnetic state [3]. To create a framework for understanding the unusual resistivity behavior, electronic structure calculations have been reported [4–8], all of which clearly demonstrate that Fe<sub>2</sub>VAI is a nonmagnetic semimetal with a deep pseudogap centered right at the Fermi level. The existence of a pseudogap has been confirmed by infrared [9, 10] and photoelectron spectroscopy [11, 12].

Owing to the formation of a sharp pseudogap at the Fermi level, Fe<sub>2</sub>VAI-based compounds exhibit electronic properties that are potentially interesting for thermoelectric applications [13, 14]. In reference to the site selectivity of doping elements, it is possible to dope into one of the Fe, V, and Al sites in Fe<sub>2</sub>VAI for n-type [15–23] and into the Fe or V site for p-type [24, 25]. In spite of a semiconductor-like resistivity behavior of Fe<sub>2</sub>VAI, the doping of quaternary elements results in a remarkable reduction in the electrical resistivity along with a significant enhancement of the Seebeck coefficient. The coexistence of a large Seebeck coefficient *S* and a low electrical resistivity  $\rho$  for Fe<sub>2</sub>VAI-based compounds leads to a high power factor,  $P=S^2/\rho$ , comparable to that for Bi<sub>2</sub>Te<sub>3</sub> alloys. Besides, Fe<sub>2</sub>VAI-based compounds are composed of earth-abundant and nontoxic elements that are environmentally friendly and economical for wide-spread use. High mechanical strength together with excellent oxidation resistance is further favorable to their practical thermoelectric applications.

The performance of thermoelectric materials is quantified by the dimensionless figure of merit,  $ZT=S^2T/\rho\kappa$ , involving the thermal conductivity  $\kappa$  and the absolute temperature *T*. To increase the efficiency of thermoelectric power generation, a

low thermal conductivity is highly desirable to keep the temperature difference between the heating and cooling sides. One of the issues for thermoelectric  $\text{Fe}_2\text{VAl}$ -based compounds is to reduce the thermal conductivity as much as possible while maintaining the high-power factor. This section aims to systematically survey recent studies based on the pseudogap engineering and related research for the development of  $\text{Fe}_2\text{VAl}$ -based thermoelectric materials. In particular, heavy-element doping combined with the off-stoichiometric effect results in a large increase in  $ZT$ . Further, high-pressure torsion (HPT) processing is suitable to enhance the thermoelectric performance because of the production of an ultrafine-grained structure.

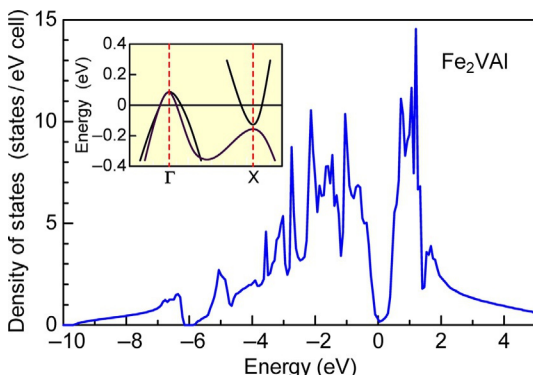
## 2.4.2 Pseudogap engineering of thermoelectric materials

**Fig. 2.4.1** shows the total density of states (DOS) for  $\text{Fe}_2\text{VAl}$ , calculated using the linear muffin tin orbital method with local density approximation [4]. The inset shows a blowup of the electronic band structure near the Fermi level. It is noted that no magnetic state can be stabilized, and as such, the bands are nonspin-polarized. The DOS spectrum is characterized by the disjointedness between the occupied valence bands and unoccupied conduction bands. In general, the electronic structure of  $\text{Fe}_2\text{VAl}$  consists of two peaks in the DOS, which are separated by a very deep pseudogap at the Fermi level. The creation of the pseudogap can be related to very strong hybridization of the  $s$  and  $p$  bands with the  $d$  bands, which would lead to increased stability of the  $L2_1$  structure [4]. The clear separation of the antibonding states from the completely full bonding states also indicates that the cohesive energy is maximized [26].

The calculated band structure in **Fig. 2.4.1** demonstrates that  $\text{Fe}_2\text{VAl}$  is a semimetal with the Fermi surface consisting of small hole pockets at the  $\Gamma$  point and an electron pocket at the  $X$  point. The hole pockets originate from the Fe 3d-dominant bands ( $t_{2g}$  character), while the electron pocket is of mainly V 3d- $e_g$  character [4–6]. However, both the electron and hole pockets are very small, thus producing a very low carrier density. The DOS at the Fermi level  $E_F$  for  $\text{Fe}_2\text{VAl}$  is  $N(E_F) \approx 0.08$  states/eV atom [4] and about an order of magnitude smaller than that for  $\text{Fe}_3\text{Al}$ . All the band calculations reported so far for  $\text{Fe}_2\text{VAl}$  are consistent with the above findings of the deep

**Fig. 2.4.1** Calculated electronic structure of  $\text{Fe}_2\text{VAl}$ . The inset shows a blowup of the band structure near the Fermi level, which is denoted by the horizontal line at 0 eV.

Reference G.Y. Guo, G.A. Botton, Y. Nishino, J. Phys. Condens. Matter 10 (1998) L119–L126; modified.



pseudogap at  $E_F$ . According to Weht and Pickett [6], the pseudogap is actually affected by the presence of Al states but the resulting carriers exhibit only minor Al character. A more realistic approach was reported by Bansil et al. [8] for the Heusler-type Fe<sub>3-x</sub>V<sub>x</sub>Al alloys:  $E_F$  moves down relative to the pseudogap with increasing Fe content, rather than up, as in the simple rigid-band picture. The unusual transport properties of Fe<sub>2</sub>VAL have been interpreted as arising from spin fluctuations [4, 5] or excitonic correlations [6].

In metallic systems, the Seebeck coefficient  $S$  at temperature  $T$  is expressed by the well-known formula [27]:

$$S(T) = \frac{\pi^2 k_B^2}{3(-e)} T \left( \frac{\partial \ln \sigma(E)}{\partial E} \right)_{E=E_F} \quad (2.4.1)$$

where  $\sigma(E)$  is the electrical conductivity and  $k_B$  is the Boltzmann constant. Since  $\sigma(E)$  is directly proportional to the DOS,  $N(E)$ , a large Seebeck coefficient arises from a low  $N(E)$  combined with its steep slope  $\partial N(E)/\partial E$  in the vicinity of  $E_F$ . As the DOS rises sharply on both sides of the pseudogap in Fe<sub>2</sub>VAL, we expect the Seebeck coefficient to be well enhanced by shifting  $E_F$  slightly upon doping. The doping process leads to the variation in valence electron concentration (VEC), which is an important factor for enhancing the Seebeck coefficient with a positive or negative sign. The VEC represents the number of electrons per atom, including the  $d$ -electrons involved in the valence band [28]: Fe<sub>2</sub>VAL has VEC of 6.0 as it possesses 24 valence electrons per formula unit.

Based on the pseudogap engineering, the energy position of the Fermi level can be tuned due to doping into one of the Fe, V, and Al sites in Fe<sub>2</sub>VAL or off-stoichiometric composition changes, which leads to a large enhancement of the Seebeck coefficient. Fig. 2.4.2 summarizes the Seebeck coefficient at 300 K for Fe<sub>2</sub>VAL-based compounds as a function of VEC [13]. The Seebeck coefficient  $S$  including its sign varies dramatically around VEC = 6.0, and the sign of  $S$  is positive at VEC  $\leq 6.0$  but becomes negative at VEC  $> 6.0$ . Since the VEC dependence of the Seebeck coefficient falls on a

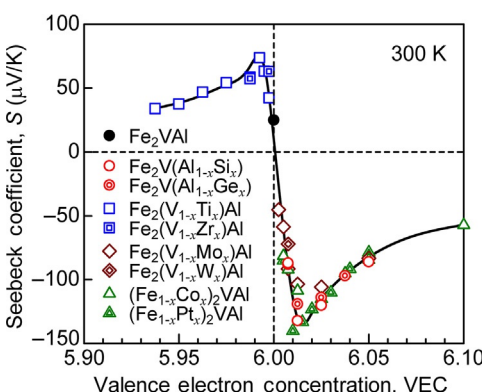


**Fig. 2.4.2** Seebeck coefficient at 300 K for various Fe<sub>2</sub>VAL-based compounds as a function of VEC.

Reference Y. Nishino, IOP Conf. Series: Mater. Sci. Eng. 18 (2011) 142001; partly modified.

universal curve regardless of doping elements, the variation in the Seebeck coefficient for  $\text{Fe}_2\text{VAl}$ -based compounds shows a rigid-band-like behavior [13]. Thus, a large increase in the Seebeck coefficient arises from a slight deviation of VEC from the stoichiometric value of 6.0. As the DOS within the pseudogap is very small, even a small change in composition due to doping causes a substantial shift of the Fermi level from the center of the pseudogap without modifying the band structure.

The Heusler compounds with  $\text{VEC}=6.0$  are considered to be one of the potential candidates for thermoelectric applications, and many such compounds have been synthesized to achieve good thermoelectric properties, including  $\text{Fe}_2\text{VAl}_{1-x}\text{Si}_x$  [15–17],  $\text{Fe}_2\text{VAl}_{1-x}M_x$  with  $M=\text{Si}$ ,  $\text{Ge}$  [18],  $M=\text{B}$ ,  $\text{In}$ ,  $\text{Si}$  [19] and  $M=\text{Si}$ ,  $\text{Sn}$  [20],  $\text{Fe}_2\text{V}_{1-x}\text{Nb}_x\text{Al}$  [21],  $\text{Fe}_{2-x}\text{Co}_x\text{VAl}$  [22, 29],  $\text{Fe}_2\text{V}_{1-x}\text{W}_x\text{Al}$  [23],  $\text{Fe}_2\text{V}_{1-x}\text{Ti}_x\text{Al}$  [24],  $\text{Fe}_{2-x}\text{Re}_x\text{VAl}$  [25],  $\text{Fe}_{2-x}\text{Ni}_x\text{VAl}$  [30], and  $\text{Fe}_{2-x}\text{Ti}_{1+x}\text{Sn}$  [31, 32]. However, simultaneous achievement of an increased power factor and a reduced thermal conductivity is still difficult for Fe-based Heusler compounds. Recently, Ru-based Heusler compounds have been developed, which contain heavier constituent elements, keeping  $\text{VEC}=6.0$ , e.g.,  $\text{Ru}_2\text{TaAl}$  [33],  $\text{Ru}_2\text{NbGa}$  [34], and  $\text{Ru}_2\text{VAl}_{1-x}\text{Ga}_x$  [35], where both Ru and Ta are heavier than Fe and V. Although the Seebeck coefficient is not as large as that for  $\text{Fe}_2\text{VAl}$ -based alloys, the thermal conductivity reaches  $7 \text{ W/mK}$  at room temperature [33], in contrast to  $28 \text{ W/mK}$  for the stoichiometric  $\text{Fe}_2\text{VAl}$  compound [18].

### 2.4.3 Fe/V off-stoichiometric effect

A large improvement in thermoelectric performance has been found for off-stoichiometric  $\text{Fe}_2\text{VAl}$  alloys:  $(\text{Fe}_{2/3}\text{V}_{1/3})_{100-y}\text{Al}_y$  [36],  $\text{Fe}_{2-x}\text{V}_{1+x}\text{Al}$  [37–39], and  $\text{Fe}_2\text{V}_{1+x}\text{Al}_{1-x}$  [40]. In the case of  $(\text{Fe}_{2/3}\text{V}_{1/3})_{100-y}\text{Al}_y$  alloys, a small change in the Al composition from the stoichiometric  $y=25.0$  results in an enhancement of the Seebeck coefficient of up to  $-130 \mu\text{V/K}$  for the Al-poor alloy and  $75 \mu\text{V/K}$  for the Al-rich alloys, together with a drastic decrease in the electrical resistivity [36]. Also,  $\text{Fe}_{2-x}\text{V}_{1+x}\text{Al}$  alloys show a large value of the Seebeck coefficient  $S$  [37–39], and its sign is negative or positive for the V-rich or V-poor composition, respectively, which however disagrees with the rigid-band picture but signifies a considerable change in the pseudogap due to the Fe/V off-stoichiometry. Further, a significant enhancement of  $S$  with a negative sign has been found for a slightly V-rich alloy ( $x>0$ ), in conjunction with an anomalous upturn of the resistivity at low temperatures [38]. Thus, Lue and Kuo [38] concluded that, although  $\text{Fe}_{2-x}\text{V}_{1+x}\text{Al}$  alloys possess a large Seebeck coefficient, their high resistivity renders them unsuited for thermoelectric applications.

Remarkably, a large Seebeck coefficient together with a low electrical resistivity has been observed for  $\text{Fe}_{2-x}\text{V}_{1+x}\text{Al}$  alloys only by doping of quaternary elements for tuning precisely the Fermi level [41, 42]. To study the off-stoichiometric effect on thermoelectric performance, it should be specified that, based on the VEC effect, which off-stoichiometric composition  $x$  in  $\text{Fe}_{2-x}\text{V}_{1+x}\text{Al}$  alloys, i.e., V-rich ( $x>0$ ) or V-poor ( $x<0$ ), is more appropriate for increasing the Seebeck coefficient due to

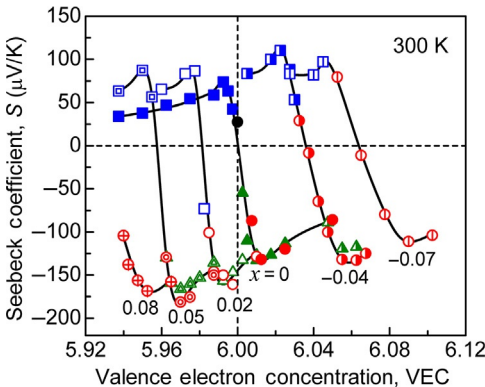


**Fig. 2.4.3** Seebeck coefficient at 300K against VEC in  $\text{Fe}_{2-x}\text{V}_{1+x}\text{Al}_{1-y}\text{Si}_y$  (circles),  $\text{Fe}_{2-x}\text{V}_{1+x-y}\text{Ti}_y\text{Al}$  (squares), and  $\text{Fe}_{2-x-y}\text{Ir}_y\text{V}_{1+x}\text{Al}$  (triangles). The closed and open symbols represent the data for the stoichiometric ( $x=0$ ) and off-stoichiometric alloys, respectively. Reference Y. Nishino, Y. Tamada, J. Appl. Phys. 115 (2014) 123707; partly modified.

doping while maintaining a low electrical resistivity. Fig. 2.4.3 plots the VEC dependence of the Seebeck coefficient at 300K for  $\text{Fe}_{2-x}\text{V}_{1+x}\text{Al}_{1-y}\text{Si}_y$ ,  $\text{Fe}_{2-x}\text{V}_{1+x-y}\text{Ti}_y\text{Al}$ , and  $\text{Fe}_{2-x-y}\text{Ir}_y\text{V}_{1+x}\text{Al}$  alloys [42]. For the stoichiometric  $x=0$  alloys, the sign of  $S$  is positive at  $\text{VEC} \leq 6.0$  but turns to negative at  $\text{VEC} > 6.0$ , so that the VEC dependence follows a universal curve regardless of doping elements, as shown by the closed symbols. This curve is just the same as that shown in Fig. 2.4.2. As plotted by the open symbols in Fig. 2.4.3, the VEC dependence for  $\text{Fe}_{2-x}\text{V}_{1+x}\text{Al}$ -based alloys falls on characteristic curves depending on the off-stoichiometric composition  $x$ , which are similar to the universal curve for the  $x=0$  alloys. Thus, a rigid-band-like change due to doping can be observed for both the stoichiometric and off-stoichiometric alloys. It is interesting to note that the curves for the V-poor alloys ( $x < 0$ ) appear at  $\text{VEC} > 6.0$ , while those for V-rich alloys ( $x > 0$ ) at  $\text{VEC} < 6.0$ . Eventually, a larger, positive Seebeck coefficient can be found for the V-poor alloys, e.g.,  $x = -0.04$ , whilst a larger, negative Seebeck coefficient is achievable for the V-rich alloys, e.g.,  $x = 0.05$  [42].

A possible origin of the enhanced Seebeck coefficient for  $\text{Fe}_{2-x}\text{V}_{1+x}\text{Al}$ -based alloys has been revealed by X-ray photoemission spectroscopy [43]. It is found that the valence-band electronic structure around the Fermi level  $E_F$  is significantly modified by the off-stoichiometric Fe/V composition change, while the energy position of  $E_F$  can be tuned due to doping of quaternary elements. Soda et al. [44] have proposed that nonrigid-band-like change in the electronic structure could be caused by the antisite defects-derived states in the pseudogap, which is responsible for the observed large Seebeck coefficient. These modifications in the electronic structure around  $E_F$  are also consistent with a supercell calculation of the band structure for  $\text{Fe}_{2-x}\text{V}_{1+x}\text{Al}$  [45]. However, a recent band structure calculation [46] disagrees with the experimental results, which posits that the thermoelectric performance of Fe<sub>2</sub>VAI is affected by the formation of antisite defects/disorder negatively.

In Fig. 2.4.4, the power factor is compared between the stoichiometric and off-stoichiometric alloys with the Si and Ti doping [42]. The power factor  $P$  for the stoichiometric  $\text{Fe}_2\text{VAl}_{0.90}\text{Si}_{0.10}$  alloy increases with temperature, reaching  $5.4 \times 10^{-3} \text{ W/mK}^2$  at 300K [15], which is substantially higher than that for a conventional

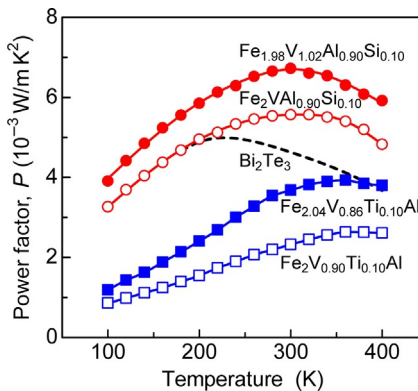


**Fig. 2.4.4** Temperature dependence of power factor  $P$  in off-stoichiometric  $\text{Fe}_{1.98}\text{V}_{1.02}\text{Al}_{0.90}\text{Si}_{0.10}$  and  $\text{Fe}_{2.04}\text{V}_{0.86}\text{Ti}_{0.10}\text{Al}$  alloys and stoichiometric  $\text{Fe}_2\text{VAl}_{0.90}\text{Si}_{0.10}$  and  $\text{Fe}_2\text{V}_{0.90}\text{Ti}_{0.10}\text{Al}$  alloys. The dotted curve indicates the data for  $\text{Bi}_2\text{Te}_3$ . Reference Y. Nishino, Y. Tamada, J. Appl. Phys. 115 (2014) 123707; partly modified.

thermoelectric material like  $\text{Bi}_2\text{Te}_3$  [47]. Moreover, the off-stoichiometric  $\text{Fe}_{1.98}\text{V}_{1.02}\text{Al}_{0.90}\text{Si}_{0.10}$  alloy exhibits a higher  $P$  than the stoichiometric alloy at all temperatures, and the maximum value of  $P$  is  $6.7 \times 10^{-3} \text{ W/mK}^2$  at 300 K [42]. On the other hand, the p-type Ti-doped alloys achieve  $P = 2.6 \times 10^{-3} \text{ W/mK}^2$  for the stoichiometric alloy [24] and  $P = 3.9 \times 10^{-3} \text{ W/mK}^2$  for the off-stoichiometric alloy [42]. It is noted that the value of  $P$  for  $\text{Fe}_{2.04}\text{V}_{0.86}\text{Ti}_{0.10}\text{Al}$  is almost equivalent to that for  $\text{Bi}_2\text{Te}_3$  at around 400 K so that these off-stoichiometric alloys demonstrate a remarkable enhancement of the power factor for both p-type and n-type.

#### 2.4.4 V/Al off-stoichiometric effect

Based on the band calculations of  $\text{Fe}_2\text{VAl}$  [4, 8], the Fe sublattice plays an important role in determining its physical and crystalline properties. We expect that, while keeping the Fe sublattice unchanged, the replacement of V or Al atoms with Al or V, respectively, induces a large number of carriers without modifying the Heusler-type structure. Thus, off-stoichiometric  $\text{Fe}_2\text{V}_{1+x}\text{Al}_{1-x}$  alloys have been developed, where the Al- and V-rich alloys correspond to hole- and electron-doping, respectively, since the number of valence electrons for V atoms is larger than that for Al atoms. Owing to the hole- or electron-doping, the Fermi level  $E_F$  in  $\text{Fe}_2\text{V}_{1+x}\text{Al}_{1-x}$  alloys shifts to a lower or higher energy side, respectively, from the bottom of the pseudogap.

**Fig. 2.4.5A** shows the temperature dependence of the Seebeck coefficient  $S$  for  $\text{Fe}_2\text{V}_{1+x}\text{Al}_{1-x}$  alloys with compositions of  $-0.12 \leq x \leq 0$  [40]. While the value of  $S$  for  $\text{Fe}_2\text{VAl}$  ( $x=0$ ) is positive and centered around  $20-30 \mu\text{V/K}$ , its sign is also positive for the Al-rich alloys ( $x < 0$ ), and the value of  $S$  increases up to  $100 \mu\text{V/K}$  at 400 K for  $x = -0.03$ . This enhancement of  $S$  is larger than that for typical p-type  $\text{Fe}_2\text{V}_{1-x}\text{Ti}_x\text{Al}$  alloys [24] and is almost equivalent to that for the Fe/V off-stoichiometric alloys with

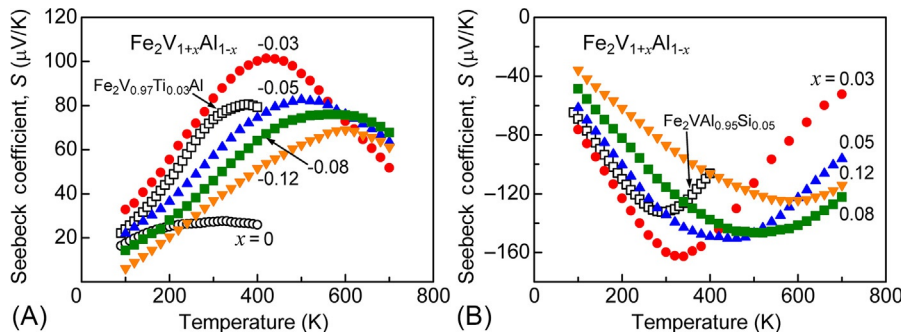


**Fig. 2.4.5** Temperature dependence of Seebeck coefficient  $S$  in  $\text{Fe}_2\text{V}_{1+x}\text{Al}_{1-x}$  with (A)  $-0.12 \leq x \leq 0$  and (B)  $0.03 \leq x \leq 0.12$ . For comparison, the data for  $\text{Fe}_2\text{V}_{0.97}\text{Ti}_{0.03}\text{Al}$  and  $\text{Fe}_2\text{VAI}_{0.95}\text{Al}_{0.05}$  are also plotted.

Reference H. Miyazaki, S. Tanaka, N. Ide, K. Soda, Y. Nishino, Mater. Res. Express 1 (2014) 015901; partly modified.

the Ti doping, as shown in Fig. 2.4.3. Surprisingly, the peak temperature of  $S$  rises to 500–600K with increasing  $|x|$ , whereas the peak value of  $S$  decreases in conjunction with the peak broadening. On the other hand, as shown in Fig. 2.4.5B, the sign of  $S$  is negative for the V-rich alloys ( $x>0$ ), and the absolute value of  $S$  increases up to  $160 \mu\text{V/K}$  at 320K for  $x=0.03$  [40], which is larger than that for typical n-type  $\text{Fe}_2\text{VAI}_{1-x}\text{Si}_x$  alloys [15] but slightly lower than that for the Fe/V off-stoichiometric alloys with the Si doping, as shown in Fig. 2.4.3. Further, as  $x$  increases, there occurs the peak temperature shift of  $S$  up to 500–600K, which is very different from  $\text{Fe}_2\text{VAI}_{1-x}\text{Si}_x$  alloys where the peak temperature is only 300–400K [15]. The  $\text{Fe}_2\text{V}_{1+x}\text{Al}_{1-x}$  system exhibits the highest peak temperature of  $S$  among Fe-based Heusler compounds reported so far.

Along with an enhancement of the Seebeck coefficient for  $\text{Fe}_2\text{V}_{1+x}\text{Al}_{1-x}$  alloys, the -semiconductor-like resistivity disappears rapidly, and as  $|x|$  increases, the low-temperature resistivity decreases. The substantial reduction in the electrical resistivity above room temperature is favorable for developing good thermoelectric materials. Fig. 2.4.6A shows the temperature dependence of the power factor  $P$  for p-type  $\text{Fe}_2\text{V}_{1+x}\text{Al}_{1-x}$  alloys with  $-0.12 \leq x \leq -0.03$  [40]. The value of  $P$  reaches  $4.3 \times 10^{-3} \text{ W/mK}^2$  for  $x=-0.03$ , which is superior to that for p-type half-Heusler compound  $\text{Zr}_{0.5}\text{Hf}_{0.5}\text{CoSb}_{0.8}\text{Sn}_{0.2}$  [48], Sb-based skutterudite  $\text{YbFe}_4\text{Sb}_{12}$  [49], and  $\text{Mn}_{0.98}\text{V}_{0.02}\text{Si}_{1.74}$  [50] in the temperature range below 500–600K. Also shown in Fig. 2.4.6B is the temperature dependence of the power factor  $P$  for n-type  $\text{Fe}_2\text{V}_{1+x}\text{Al}_{1-x}$  alloys with  $0.03 \leq x \leq 0.12$  [40]. As  $x$  increases, the value of  $P$  increases up to  $6.8 \times 10^{-3} \text{ W/mK}^2$  for  $x=0.05$ , which is almost equivalent to that for the Fe/V off-stoichiometric alloy with the Si doping, as shown in Fig. 2.4.4. Moreover, the peak position of  $P$  shifts to higher temperatures, in association with the peak shift of the Seebeck coefficient. As compared with the data on half-Heusler compound  $\text{Hf}_{0.6}\text{Zr}_{0.4}\text{NiSn}_{0.995}\text{Sb}_{0.005}$  [51], Sb-based skutterudite  $\text{Ba}_{0.10}\text{La}_{0.05}\text{Yb}_{0.07}\text{Co}_4\text{Sb}_{12}$  [52], Sb-doped  $\text{Mg}_2\text{Si}$  [53], and  $\text{Mg}_2\text{Si}_{0.3}\text{Sn}_{0.7}$  [54], all of which are n-type materials,

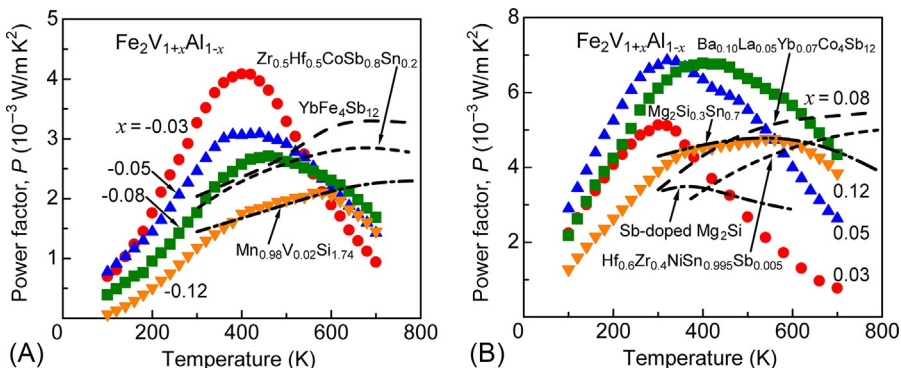


**Fig. 2.4.6** Temperature dependence of power factor  $P$  in  $\text{Fe}_2\text{V}_{1+x}\text{Al}_{1-x}$  with (A)  $-0.12 \leq x \leq -0.03$  and (B)  $0.03 \leq x \leq 0.12$ . The data for  $\text{Zr}_{0.5}\text{Hf}_{0.5}\text{CoSb}_{0.8}\text{Sn}_{0.2}$  [48],  $\text{YbFe}_4\text{Sb}_{12}$  [49],  $\text{Mn}_{0.98}\text{V}_{0.02}\text{Si}_{1.74}$  [50],  $\text{Hf}_{0.6}\text{Zr}_{0.4}\text{NiSn}_{0.995}\text{Sb}_{0.005}$  [51],  $\text{Ba}_{0.10}\text{La}_{0.05}\text{Yb}_{0.07}\text{Co}_4\text{Sb}_{12}$  [52],  $\text{Mg}_2\text{Si}(\text{Sb})$  [53], and  $\text{Mg}_2\text{Si}_{0.3}\text{Sn}_{0.7}$  [54] are also plotted. Reference H. Miyazaki, S. Tanaka, N. Ide, K. Soda, Y. Nishino, Mater. Res. Express 1 (2014) 015901; partly modified.

the power factor for  $\text{Fe}_2\text{V}_{1+x}\text{Al}_{1-x}$  alloys is always higher at least in the temperature range below 700 K.

## 2.4.5 Synergistic effect of off-stoichiometry and Ta doping

It has been found that off-stoichiometric  $\text{Fe}_2\text{V}_{1+x}\text{Al}_{1-x}$  alloys exhibit the highest power factor ever reached by  $\text{Fe}_2\text{VAl}$ -based thermoelectric materials [40]. Indeed, the off-stoichiometric alloys still retain a high thermal conductivity  $\kappa$  of approximately 15  $\text{W/mK}$ . In order to enhance the thermoelectric performance, the  $\kappa$  value should be reduced as much as possible, while maintaining the high power factor. If the exceeding V atoms in  $\text{Fe}_2\text{V}_{1+x}\text{Al}_{1-x}$  alloys are substituted by Ta atoms, leading to isoelectronic  $\text{Fe}_2\text{VTa}_x\text{Al}_{1-x}$ , this replacement results in the same doping effect as that of the V/Al off-stoichiometry, together with an atomic mass effect, which is effective in reducing the thermal conductivity.

A detailed local crystal structure of  $\text{Fe}_2\text{VTa}_x\text{Al}_{1-x}$  has been determined by Rietveld analyses of X-ray diffraction patterns [55]. Fig. 2.4.7A compares the site occupancy of Fe, V, and Al atoms in the corresponding site against the Ta composition  $x$ . The site occupancy of Fe atoms maintains a constant value of 1 within the error range, regardless of the Ta doping, which means that Fe atoms always occupy the Fe site. As Al atoms are substituted by Ta atoms in  $\text{Fe}_2\text{VTa}_x\text{Al}_{1-x}$ , there is a decrease in the number of Al atoms in the Al site. This decrease occurs in conjunction with a decrease in the number of V atoms in the V site so that there is a modification in the position of these atoms compared to pristine  $\text{Fe}_2\text{VAl}$ . Because Fe atoms always occupy the Fe site, the Al site is the only available position for V atoms. This suggests that Ta atoms have to

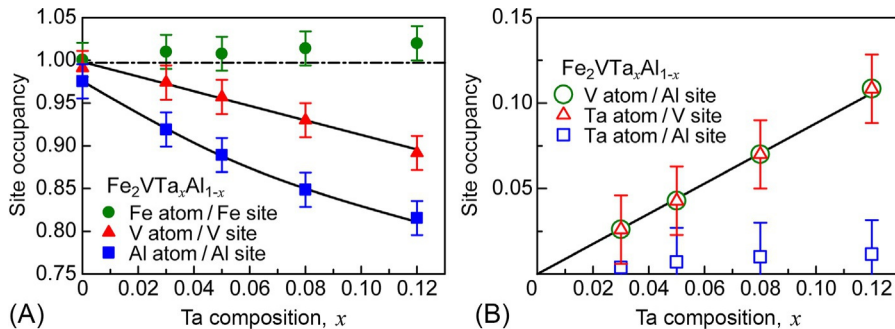


**Fig. 2.4.7** Site occupancy as a function of Ta composition  $x$  for  $\text{Fe}_2\text{VTa}_x\text{Al}_{1-x}$ .

Reference K. Renard, A. Mori, Y. Yamada, S. Tanaka, H. Miyazaki, Y. Nishino, J. Appl. Phys. 115 (2014) 033707; partly modified.

occupy the vacant V site. As seen in Fig. 2.4.7B, the site occupancy of V atoms in the Al site and that of Ta atoms in the V site increase concurrently with the Ta composition, whilst the number of Ta atoms in the Al site keeps almost zero. Thus, in  $\text{Fe}_2\text{VTa}_x\text{Al}_{1-x}$  alloys, Ta atoms indeed occupy the V site, whereas the ejected V atoms are displaced to the Al site [55]. The formula of  $\text{Fe}_2\text{VTa}_x\text{Al}_{1-x}$ , therefore, can be expressed as  $\text{Fe}_2(\text{V}_{1-x}\text{Ta}_x)\text{Al}_{1-x}\text{V}_x$ . This demonstrates the synergistic effect of V/Al off-stoichiometry as in  $\text{Fe}_2\text{V}_{1+x}\text{Al}_{1-x}$  alloys [40] and heavy element Ta doping as in  $\text{Fe}_2\text{V}_{1-x}\text{W}_x\text{Al}$  alloys [23].

The thermal conductivity  $\kappa$  for  $\text{Fe}_2\text{VTa}_x\text{Al}_{1-x}$  alloys is displayed in Fig. 2.4.8 along with the electronic ( $\kappa_e$ ) and lattice ( $\kappa_{ph}$ ) components at 300 K against the Ta composition  $x$  [55]. Although the  $\kappa$  value for  $\text{Fe}_2\text{VAI}$  ( $x=0$ ) is 27 W/mK, the Ta doping causes a drastic decrease to 7 W/mK for  $x=0.12$ . As shown in Fig. 2.4.8, the  $\kappa$  value for  $\text{Fe}_2\text{V}_{1+x}\text{Al}_{1-x}$  alloys also decreases with the off-stoichiometric composition  $x$ , which

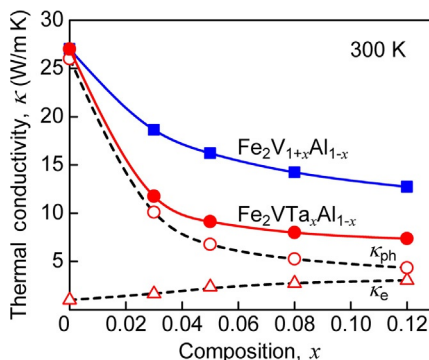


**Fig. 2.4.8** Thermal conductivity  $\kappa$  for  $\text{Fe}_2\text{VTa}_x\text{Al}_{1-x}$  as a function of Ta composition  $x$ : the data for  $\text{Fe}_2\text{V}_{1+x}\text{Al}_{1-x}$  are also plotted.  $\kappa$  is provided by the sum of electronic component  $\kappa_e$  and lattice component  $\kappa_{ph}$ .

Reference K. Renard, A. Mori, Y. Yamada, S. Tanaka, H. Miyazaki, Y. Nishino, J. Appl. Phys. 115 (2014) 033707; partly modified.

is however not so rapid as in  $\text{Fe}_2\text{VTa}_x\text{Al}_{1-x}$  alloys. Meanwhile, the two components,  $\kappa_e$  and  $\kappa_{ph}$ , change very differently. While  $\kappa_e$  increases slightly with the Ta composition  $x$ ,  $\kappa_{ph}$  first decreases sharply but then tends to saturate above  $x=0.08$ . Therefore, the overall reduction in the thermal conductivity  $\kappa$  is regulated by a significant decrease in  $\kappa_{ph}$  at a low doping level.

The dimensionless figure of merit for  $\text{Fe}_2\text{VTa}_x\text{Al}_{1-x}$  alloys reaches  $ZT=0.21\text{--}0.22$  at 400–500K for  $x=0.05$  [55]. This enhancement of  $ZT$  arises from the improvement in the power factor along with its peak temperature shift with increasing Ta composition, in addition to a reduction in the thermal conductivity. The optimal composition for these alloys is  $\text{Fe}_2\text{VTa}_{0.05}\text{Al}_{0.95}$ , that exhibits the best performance at temperatures up to 600K. This can be compared with heavy-element W doping for  $\text{Fe}_2\text{V}_{0.80}\text{W}_{0.20}\text{Al}$ , of which  $ZT$  is around 0.20 at 400K but drops to about 0.14 even at 500K [23]. To further enhance the thermoelectric performance, ways of reducing the grain size while maintaining the high power factor have to be explored.

## 2.4.6 High-pressure torsion processing

It is common knowledge that a smaller grain size results in a lower thermal conductivity because of enhanced phonon scattering at interfaces and lattice defects such as dislocations [56]. Powder metallurgical process is a simple method to fabricate fine-grained bulk materials, and sintered  $\text{Fe}_2\text{VAl}$ -based alloys have been produced by pulse-current sintering using powders synthesized by mechanical milling [57]. However, grain growth during sintering often prevents a significant decrease in the thermal conductivity. An alternative method for grain refinement is high-pressure torsion (HPT) processing which, due to severe plastic deformation, produces ultrafine-grained or nanostructured bulk materials along with a high density of crystal imperfections [58, 59].

Despite low plastic deformability of  $\text{Fe}_2\text{VAl}$ -based alloys, severe plastic deformation can be achieved by HPT deformation without crack formation at room temperature. During HPT, a disc-like specimen is subjected to a torsional strain under high hydrostatic pressure, so that practically unlimited strain can be introduced [59]. The thermal conductivity for  $\text{Fe}_2\text{VTa}_{0.05}\text{Al}_{0.95}$  is approximately 10W/mK at 300K, as shown in Fig. 2.4.8 but, after HPT deformation, reaches 5.0W/mK [60]. HPT processing effectively reduces the thermal conductivity but also leads to a drastic degradation of the power factor due to the disappearance of the  $L2_1$ -ordered structure. Hence, after HPT deformation, appropriate heat treatment is necessary to restore the  $L2_1$  ordering without causing grain coarsening.

When subjected to annealing at 873K, the Seebeck coefficient for the HTP-deformed samples can be recovered to almost the same level as that for the arc-melted samples [60]. The temperature dependence of the thermal conductivity  $\kappa$  is shown in Fig. 2.4.9 for (A)  $\text{Fe}_2\text{V}_{1.05}\text{Al}_{0.95}$  and (B)  $\text{Fe}_2\text{VTa}_{0.05}\text{Al}_{0.95}$  [60]. Although the  $\kappa$  value for the HPT-deformed sample of  $\text{Fe}_2\text{V}_{1.05}\text{Al}_{0.95}$  is around 5.5W/mK at 300K, it increases quickly with temperature, as shown in Fig. 2.4.9A. In addition, the  $\kappa$  value

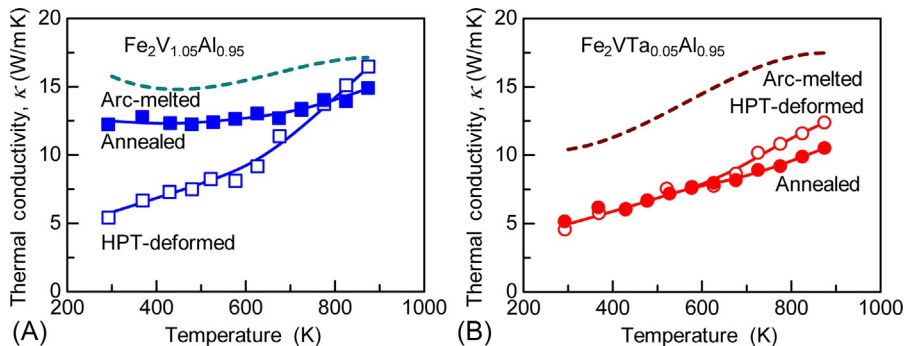


**Fig. 2.4.9** Temperature dependence of thermal conductivity for HPT-deformed and annealed samples of (A)  $\text{Fe}_2\text{V}_{1.05}\text{Al}_{0.95}$  and (B)  $\text{Fe}_2\text{VTa}_{0.05}\text{Al}_{0.95}$ : the data for arc-melted samples are plotted by broken curves.

Reference S. Masuda, K. Tsuchiya, J. Qiang, H. Miyazaki, Y. Nishino, J. Appl. Phys. 124 (2018) 035106; partly modified.

for the annealed sample of  $\text{Fe}_2\text{V}_{1.05}\text{Al}_{0.95}$  increases up to 12 W/m K at 300 K, because grain growth occurs during annealing. On the other hand, as shown in Fig. 2.4.9B, the  $\kappa$  value for  $\text{Fe}_2\text{VTa}_{0.05}\text{Al}_{0.95}$  also decreases due to HPT deformation. Notably, the annealed sample of  $\text{Fe}_2\text{VTa}_{0.05}\text{Al}_{0.95}$  demonstrates a low  $\kappa$  of 5.0 W/m K at 300 K [60], which is comparable to that for the HPT-deformed sample. The difference in the thermal conductivity before and after annealing is believed to originate from their microstructure changes.

The microstructures of the annealed samples with and without the Ta doping are characterized by transmission electron microscopy (TEM), which demonstrates an ultrafine-grained structure with a grain size of almost 80 nm for  $\text{Fe}_2\text{VTa}_{0.05}\text{Al}_{0.95}$ , unlike  $\text{Fe}_2\text{V}_{1.05}\text{Al}_{0.95}$  with large grains of approximately 270 nm [60]. Further, according to energy-dispersive X-ray (EDX) analysis for  $\text{Fe}_2\text{VTa}_{0.05}\text{Al}_{0.95}$ , the solute segregation of Ta occurs at grain boundaries and also at recrystallization interfaces. Thus, the retardation of recrystallization by the Ta doping could arise from the solute drag effect, which leads to the suppression of grain coarsening during annealing. In case the average grain size is about 100 nm or less, the lattice thermal conductivity  $\kappa_{\text{ph}}$  can be reduced by 50% or more compared with the arc-melted sample [60].

Finally,  $ZT$  can be evaluated from the measured thermoelectric properties. Fig. 2.4.10 shows the temperature dependence of  $ZT$  for  $\text{Fe}_2\text{V}_{1.05}\text{Al}_{0.95}$  and  $\text{Fe}_2\text{VTa}_{0.05}\text{Al}_{0.95}$  [60]. It is seen that the annealed sample of  $\text{Fe}_2\text{V}_{1.05}\text{Al}_{0.95}$  exhibits a lower  $ZT$  than the arc-melted sample because the electrical resistivity is still higher after annealing. Remarkably, the annealed sample of  $\text{Fe}_2\text{VTa}_{0.05}\text{Al}_{0.95}$  possesses  $ZT$  that is approximately 50% higher than that for the arc-melted sample, achieving  $ZT=0.30$  at 500 K, which is the highest value ever reported for Fe<sub>2</sub>VAL-based compounds [60]. The enhancement of  $ZT$  for  $\text{Fe}_2\text{VTa}_{0.05}\text{Al}_{0.95}$  subjected to HPT deformation essentially arises from a significant decrease in the thermal conductivity, in conjunction with the recovery of the high power factor after annealing.

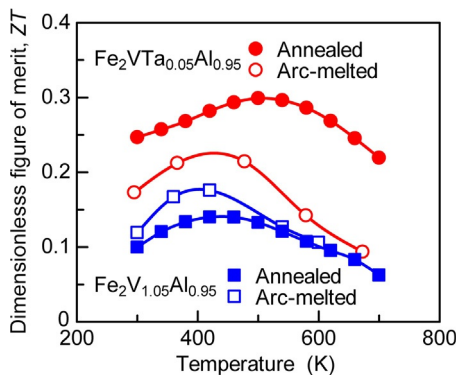


**Fig. 2.4.10** Temperature dependence of  $ZT$  for annealed and arc-melted samples of  $\text{Fe}_2\text{V}_{1.05}\text{Al}_{0.95}$  and  $\text{Fe}_2\text{Vta}_{0.05}\text{Al}_{0.95}$ .

Reference S. Masuda, K. Tsuchiya, J. Qiang, H. Miyazaki, Y. Nishino, J. Appl. Phys. 124 (2018) 035106; partly modified.

## 2.4.7 Concluding remarks

The Heusler-type  $\text{Fe}_2\text{VAl}$  compound is widely considered as one of the potential thermoelectric materials. As the DOS rises sharply on both valence- and conduction-band sides of the pseudogap, the Seebeck coefficient enhances by shifting the Fermi level slightly upon doping. Further enhancement of the Seebeck coefficient can be achieved by doping for off-stoichiometric  $\text{Fe}_{2-x}\text{V}_{1+x}\text{Al}$  alloys: hence, a large Seebeck coefficient with a negative sign is obtained for the V-rich alloys, while good p-type materials are consistently available from the V-poor alloys. Meanwhile, off-stoichiometric  $\text{Fe}_2\text{V}_{1+x}\text{Al}_{1-x}$  alloys exhibit a large Seebeck coefficient with a positive or negative sign, in association with its peak temperature shift up to 500–600 K. The maximum power factor for n-type  $\text{Fe}_2\text{V}_{1.05}\text{Al}_{0.95}$  reaches  $6.8 \times 10^{-3} \text{ W/mK}^2$ , which is actually higher than that for half-Heusler  $\text{ZrNiSn}$  compounds, Sb-based skutterudite, and Sb-doped  $\text{Mg}_2\text{Si}$  in the same temperature range. The heavy-element Ta doping for the V/Al off-stoichiometric alloys causes a drastic decrease in the thermal conductivity, leading to  $ZT = 0.21$ – $0.22$  for  $\text{Fe}_2\text{Vta}_{0.05}\text{Al}_{0.95}$  at 400–500 K. HPT processing further reduces the thermal conductivity because of the production of ultrafine-grained structures with a grain size of almost 80 nm, which can be obtained through the suppression of grain coarsening due to the Ta doping during annealing. Thus, a reduced thermal conductivity of approximately  $5.0 \text{ W/mK}$  for  $\text{FeVta}_{0.05}\text{Al}_{0.95}$ , combined with the high power factor, leads to  $ZT = 0.30$  at 500 K.

## References

- [1] T. Graf, C. Felser, S.S.P. Parkin, Prog. Solid State Chem. 39 (2011) 1–50.
- [2] P.J. Webster, K.R.A. Ziebeck, Phys. Lett. A 98 (1983) 51–53.
- [3] Y. Nishino, M. Kato, S. Asano, K. Soda, M. Hayasaka, U. Mizutani, Phys. Rev. Lett. 79 (1997) 1909–1912.

- [4] G.Y. Guo, G.A. Botton, Y. Nishino, *J. Phys. Condens. Matter* 10 (1998) L119–L126.
- [5] D.J. Singh, I.I. Mazin, *Phys. Rev. B* 57 (1998) 14352–14356.
- [6] R. Weht, W.E. Pickett, *Phys. Rev. B* 58 (1998) 6855–6861.
- [7] M. Weinert, R.E. Watson, *Phys. Rev. B* 58 (1998) 9732–9740.
- [8] A. Bansil, S. Kaprzyk, P.E. Mijnarends, J. Tobola, *Phys. Rev. B* 60 (1999) 13392–13412.
- [9] H. Okamura, J. Kawahara, T. Nanba, S. Kimura, K. Soda, U. Mizutani, Y. Nishino, M. Kato, I. Shimoyama, H. Miura, K. Fukui, K. Nakagawa, H. Nakagawa, T. Kinoshita, *Phys. Rev. Lett.* 84 (2000) 3674–3677.
- [10] Y. Feng, J.Y. Rhee, T.A. Wiener, D.Y. Lynch, B.E. Hubbard, A.J. Sievers, D.L. Schlagel, T.A. Lograsso, L.L. Miller, *Phys. Rev. B* 63 (2001) 165109.
- [11] K. Soda, T. Mizutani, O. Yoshimoto, S. Yagi, U. Mizutani, H. Sumi, Y. Nishino, Y. Yamada, T. Yokoya, S. Shin, A. Sekiyama, S. Suga, *J. Synchrotron Rad.* 9 (2002) 233–236.
- [12] K. Soda, H. Murayama, K. Shimba, S. Yagi, J. Yuhara, T. Takeuchi, U. Mizutani, H. Sumi, M. Kato, H. Kato, Y. Nishino, A. Sekiyama, S. Suga, T. Matsushita, Y. Saito, *Phys. Rev. B* 71 (2005) 245112.
- [13] Y. Nishino, in: T.B. Massalski, P.E. Turchi (Eds.), *The Science of Complex Alloy Phases*, TMS, Warrendale, 2005, pp. 325–344.
- [14] Y. Nishino, *IOP Conf. Series: Mater. Sci. Eng.* 18 (2011) 142001.
- [15] H. Kato, M. Kato, Y. Nishino, U. Mizutani, S. Asano, *J. Jpn. Inst. Metals* 65 (2001) 652–656.
- [16] M. Vasundhara, V. Srinivas, V.V. Rao, *J. Phys. Condens. Matter* 17 (2005) 6025–6036.
- [17] C.S. Lue, C.F. Chen, J.Y. Lin, Y.T. Yu, Y.K. Kuo, *Phys. Rev. B* 75 (2007), 064204.
- [18] Y. Nishino, S. Deguchi, U. Mizutani, *Phys. Rev. B* 74 (2006) 115115.
- [19] M. Vasundhara, V. Srinivas, V.V. Rao, *Phys. Rev. B* 77 (2008) 224415.
- [20] E.J. Skoug, C. Zhou, Y. Pei, D.T. Morelli, *J. Electron. Mater.* 38 (2009) 1221–1223.
- [21] C.S. Lue, R.F. Liu, M.Y. Song, K.K. Wu, Y.K. Kuo, *Phys. Rev. B* 78 (2008) 165117.
- [22] W. Lu, W. Zhang, L. Chen, *J. Alloys Compd.* 484 (2009) 812–815.
- [23] M. Mikami, Y. Kinemuchi, K. Ozaki, Y. Terazawa, T. Takeuchi, *J. Appl. Phys.* 111 (2012), 093710.
- [24] H. Matsuura, Y. Nishino, U. Mizutani, S. Asano, *J. Jpn. Inst. Metals* 66 (2002) 767–771.
- [25] F. Kobayashi, N. Ide, Y. Nishino, *J. Jpn. Inst. Metals* 71 (2007) 208–212.
- [26] G. Trambly de Laissardi  re, D. Nguyen Manh, L. Magaud, J.P. Julien, F. Cyrot-Lackmann, D. Mayou, *Phys. Rev. B* 52 (1995) 7920–7933.
- [27] N.F. Mott, H. Jones, *The Theory of the Properties of Metals*, Oxford, Clarendon Press, 1936.
- [28] U. Mizutani, *Hume-Rothery Rules for Structurally Complex Alloy Phases*, CRC Press, Boca Raton, 2011, pp. 249–283.
- [29] C. Liu, D.T. Morelli, *J. Electron. Mater.* 41 (2012) 1632–1635.
- [30] I. Knapp, B. Budinska, D. Milosavljevic, P. Heinrich, S. Khmelevskyi, R. Moser, R. Podloucky, P. Prenninger, E. Bauer, *Phys. Rev. B* 96 (2017), 045204.
- [31] C.S. Lue, Y.-K. Kuo, *J. Appl. Phys.* 96 (2004) 2681–2683.
- [32] M.L.C. Buffon, G. Laurita, L. Lamontagne, E.E. Levin, S. Mooraj, D.L. Lloyd, N. White, T.M. Pollock, R. Seshadri, *J. Phys. Condens. Matter* 29 (2017) 405702.
- [33] C.W. Tseng, C.N. Kuo, H.W. Lee, K.F. Chen, R.C. Huang, C.-M. Wei, Y.K. Kuo, C.S. Lue, *Phys. Rev. B* 96 (2017) 125106.
- [34] C.N. Kuo, H.W. Lee, C.-M. Wei, Y.H. Lin, Y.K. Kuo, C.S. Lue, *Phys. Rev. B* 94 (2016) 205116.

- [35] B. Ramachandran, Y.H. Lin, Y.K. Kuo, C.N. Kuo, A.A. Gippius, C.S. Lue, *Intermetallics* 92 (2018) 36–41.
- [36] Y. Nishino, H. Kato, M. Kato, U. Mizutani, *Phys. Rev. B* 63 (2001) 233303.
- [37] Y. Hanada, R.O. Suzuki, K. Ono, *J. Alloys Compd.* 329 (2001) 63–68.
- [38] C.S. Lue, Y.-K. Kuo, *Phys. Rev. B* 66 (2002), 085121.
- [39] T. Nakama, Y. Takaesu, K. Yagasaki, T. Naka, A. Matsushita, K. Fukuda, Y. Yamada, *J. Phys. Soc. Jpn.* 74 (2005) 1378–1381.
- [40] H. Miyazaki, S. Tanaka, N. Ide, K. Soda, Y. Nishino, *Mater. Res. Express* 1 (2014), 015901.
- [41] T. Sugiura, Y. Nishino, *J. Jpn. Inst. Metals* 73 (2009) 846–851.
- [42] Y. Nishino, Y. Tamada, *J. Appl. Phys.* 115 (2014) 123707.
- [43] K. Soda, S. Harada, M. Kato, S. Yagi, M. Inukai, H. Miyazaki, Y. Sandaiji, Y. Tamada, S. Tanaka, T. Sugiura, Y. Nishino, *J. Electron Spectrosc. Relat. Phenom.* 184 (2011) 236–239.
- [44] K. Soda, S. Harada, M. Kato, S. Yagi, Y. Sandaiji, Y. Nishino, *IOP Conf. Ser.: Mater. Sci. Eng.* 18 (2011) 142004.
- [45] S. Fujii, Y. Ikenaga, S. Ishida, S. Asano, *J. Phys. Soc. Jpn.* 72 (2003) 698–704.
- [46] D.I. Bilc, P. Ghosez, *Phys. Rev. B* 83 (2011) 205204.
- [47] H. Scherrer, S. Scherrer, in: D.M. Rowe (Ed.), *CRC Handbook of Thermoelectrics*, CRC Press, Boca Raton, 1995, pp. 211–237.
- [48] X. Yan, G. Joshi, W. Liu, Y. Lan, H. Wang, S. Lee, J.W. Simonson, S.J. Poon, T.M. Tritt, G. Chen, Z.F. Ren, *Nano Lett.* 11 (2011) 556–560.
- [49] P.F. Qiu, J. Yang, R.H. Liu, X. Shi, X.Y. Huang, G.J. Snyder, W. Zhang, L.D. Chen, *J. Appl. Phys.* 109 (2011), 063713.
- [50] Y. Miyazaki, H. Hamada, K. Hayashi, K. Yubuta, *J. Electron. Mater.* 46 (2017) 2705–2709.
- [51] L. Chen, X. Zeng, T.M. Tritt, S.J. Poon, *J. Electron. Mater.* 45 (2016) 5554–5560.
- [52] X. Shi, J. Yang, J.R. Salvador, M. Chi, J.Y. Cho, H. Wang, S. Bai, J. Yang, W. Zhang, L. Chen, *J. Am. Chem. Soc.* 133 (2011) 7837–7846.
- [53] K. Kambe, H. Udon, *J. Electron. Mater.* 43 (2014) 2212–2217.
- [54] W. Liu, X. Tan, K. Yin, H. Liu, X. Tang, J. Shi, Q. Zhang, C. Uher, *Phys. Rev. Lett.* 108 (2012) 166601.
- [55] K. Renard, A. Mori, Y. Yamada, S. Tanaka, H. Miyazaki, Y. Nishino, *J. Appl. Phys.* 115 (2014), 033707.
- [56] C.M. Bhandari, in: D.M. Rowe (Ed.), *Thermoelectric Handbook: Micro to Nano*, CRC Press, Boca Raton, 2005, pp. 1–15 (Chapter 14).
- [57] M. Mikami, M. Inukai, H. Miyazaki, Y. Nishino, *J. Electron. Mater.* 45 (2016) 1284–1289.
- [58] R.Z. Valiev, Y.V. Ivanisenko, E.F. Rauch, B. Baudelet, *Acta Mater.* 44 (1996) 4705–4712.
- [59] G. Rogl, D. Setman, E. Schafler, J. Horky, M. Kerber, M. Zehetbauer, M. Falmbigl, P. Rogl, E. Royanian, E. Bauer, *Acta Mater.* 60 (2012) 2146–2157.
- [60] S. Masuda, K. Tsuchiya, J. Qiang, H. Miyazaki, Y. Nishino, *J. Appl. Phys.* 124 (2018), 035106.

# Zintl phases for thermoelectric applications

2.5

Susan M. Kauzlarich, Kasey P. Devlin, and Christopher J. Perez  
Chemistry Department, University of California, Davis, CA, United States

## 2.5.1 Introduction

While thermoelectric materials have been studied for quite some time, recently Zintl phases have found prominence in this field [1–5]. This interest results from the initial discovery of high  $zT$  for a compound of the  $\text{Ca}_{14}\text{AlSb}_{11}$  structure type,  $\text{Yb}_{14}\text{MnSb}_{11}$  [6–9], and the promise of high  $zT$  in a compound of the  $\text{CaAl}_2\text{Si}_2$  structure type,  $\text{Ca}_x\text{Yb}_{1-x}\text{Zn}_2\text{Sb}_2$  [10–14]. The Zintl or Zintl-Klemm concept is a powerful idea connecting solid-state compounds to structural principles that can be easily understood and exploited by scientists [15–19]. The Zintl concept starts with the idea that some intermetallic compounds can be viewed as valence precise and charge balanced in the idealized case, where electropositive species donate their electrons to the more electronegative species, which further form bonding interactions to satisfy valence. Zintl phases exhibit both ionic and covalent bonding, allowing for a wide variety of structures and compositions. Due to the filled valence states of the anion or polyanion array and the empty valence states of the electropositive electron donors, semiconducting behavior is expected for the resulting compounds. The extremes of bonding allow Zintl phases to exhibit semiconducting (or even insulating) to metallic properties within this classification, depending on how the bonding can be adjusted from ionic to polar covalent. Therefore, the Zintl concept provides a simple, yet effective bonding description that allows for the application of chemical ideas to tune carrier concentration and mobility in a semiconductor. Additionally, because of the structural and bonding complexity, Zintl phases can have quite low lattice thermal conductivity, allowing for optimization of the Seebeck coefficient and transport properties to enable a high  $zT$ . Therefore, Zintl phases have become an exciting new area for the search of promising thermoelectric materials.

There are a number of good reviews on Zintl phases [9, 20], along with more recent reviews related to Zintl phases that have been investigated for their thermoelectric properties [1, 2, 5]. A simple search of publications of Zintl phases and thermoelectrics shows that this is a growing field. Fig. 2.5.1 shows the interest in the field of Zintl phases and thermoelectrics and Zintl phases by documenting the number of publications vs year with those key word searches. In 2018, almost half of the papers published on Zintl phases have also reported thermoelectric data. Clearly, as a class of compounds, there is great interest in these compounds for their thermoelectric properties. Historically, Zintl phases consisted of main group metalloids with alkali or

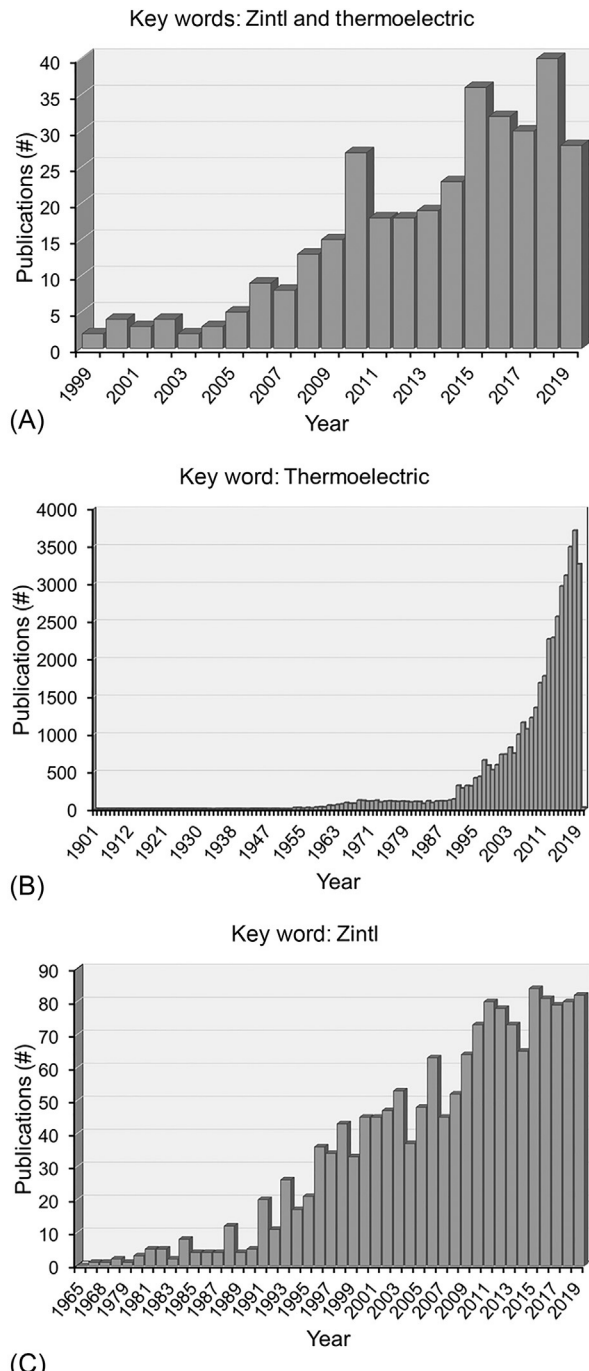


**Fig. 2.5.1** Publications vs year from Web of Science showing the trend in Zintl phases for thermoelectric applications with key words: (A) Zintl and thermoelectric, (B) thermoelectric, and (C) Zintl.

alkaline earth cations. This has been expanded to include transition and rare earth metal Zintl phases and mixtures of both transition and rare earth metals. There are examples of transition metal Zintl phases involving the closed-shell metals from the left- and right-hand side of the transition metal series. Their structure and bonding can be described in a similar fashion as their main-group analogs and have been included in the classification of Zintl phases. There are also examples from the middle of the periodic table, including those of  $\text{Ca}_{14}\text{AlSb}_{11}$  structure type, Skutterudites, and Clathrates. Since Clathrates [20–22] and Skutterudite [23–25] structures have extensive literature associated with them as well as several recent reviews, they will not be covered here. This chapter covers the structures and thermoelectric properties of Zintl compounds with an aim to provide an overview of the area.

## 2.5.2 What is a Zintl phase?

Zintl phases are named after Eduard Zintl (1898–1941), a German scientist who worked on compounds that were composed of main group metalloids, combining them with highly electropositive metals [26]. Therefore, a Zintl phase is the product of a reaction between a group 1 (alkali metal) or group 2 (alkaline earth) elements and any post-transition metal or metalloid (i.e., from groups 13, 14, 15, or 16). Since these phases are made up of all metals, they are a subgroup of intermetallics. However, unlike intermetallic compounds, Zintl phases are typically a specific composition with very little phase width and the bonding can be understood by considering ionic bonding from the electropositive element to the more electronegative elements and then covalent (or polar covalent) bonding within the electronegative metalloids, if there are not enough electrons to form an isolated anion. Zintl recognized that there was electron transfer from the electropositive cation to the metalloids that allowed the metalloid clusters or anions to satisfy valence. The structure of the Zintl anion or polyanion should be considered based on the available electrons and the resulting electronic state. The classic example of a Zintl phase is  $\text{NaTl}$  and can be considered as an ionic formula  $(\text{Na}^+)(\text{Tl}^-)$ . In this case,  $\text{Tl}^-$  is isoelectronic with group 14 and, similar to group 14 elements, forms a four-bonded diamond framework with  $\text{Na}^+$  cations in interstitial sites in the structure. The idea that the polyanionic structure should be similar to an isoelectronic element was postulated by Klemm and there are many examples of this with the simple binary compounds [27]. A thermoelectric relevant phase,  $\text{Mg}_3\text{Sb}_2$  can be considered a Zintl phase. In the simplest interpretation, the ionic description of  $3(\text{Mg}^{2+})2(\text{Sb}^{3-})$  seems like it holds [15]. However, this description does not adequately describe the bonding within the structure (Fig. 2.5.2). A more complete understanding of the bonding in this structure arises from the fact that Mg can be ionic, like the rest of the alkaline earth metals although it has a fairly high electronegativity value, or covalent because of its small size giving rise to polar covalent bonds in solids, similar to Al in its bonding behavior. A recent review of Mg—group 15 containing compounds points to this dichotomy for Mg [28]. Since Mg can be considered either covalent or ionic, recognizing that it is isostructural to  $\text{CaAl}_2\text{Si}_2$  and considering it as  $\text{MgMg}_2\text{Sb}_2$  with  $\text{Mg}^{2+}$  acting like  $\text{Ca}^{2+}$  between the layers, and

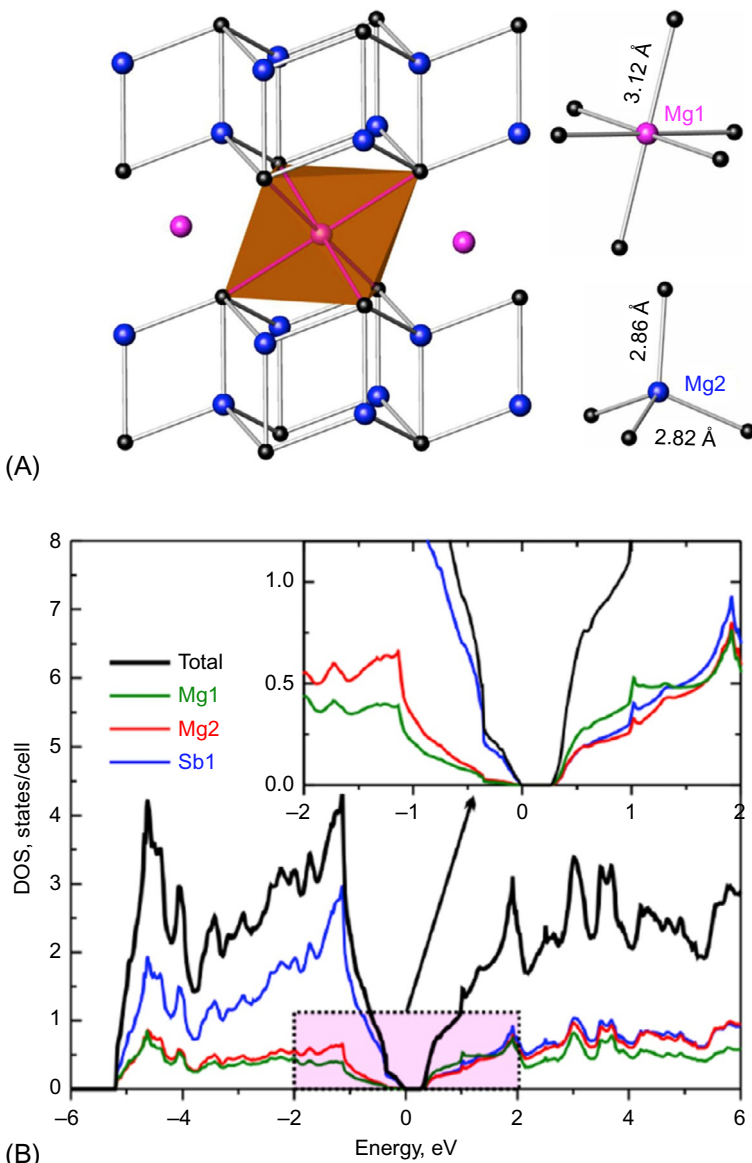


**Fig. 2.5.2** (A) A view of the structure of  $\text{Mg}_3\text{Sb}_2$  showing the relationship to the  $\text{CaAl}_2\text{Si}_2$  structure type. (B) Density of states with an enlarged inset showing the contributions of the two Mg sites near the Fermi level. Both sites contribute to the top of the valence band and bottom of conduction band. In addition, calculated Crystal Orbital Hamilton Population (COHP) indicates stronger Mg2-Sb1 interactions as compared with Mg1-Sb1.

Adapted with permission from reference J. Wang, J. Mark, K.E. Woo, J. Voyles, K. Kovnir, Chemical flexibility of mg in pnictide materials: structure and properties diversity, *Chem. Mater.* 31 (20) (2019) 8286–8300. Copyright (2019) American Chemical Society.

covalently bonded within layers of  $[\text{Mg}_2\text{Sb}_2]^{2-}$  provides some insight into the low thermal conductivity observed.  $\text{Mg}_3\text{Sb}_2$  crystallizes in the anti- $\text{La}_2\text{O}_3$  structure type and compounds with this structure type can be described as either fully ionic or fully covalent. While these different structural descriptions,  $\text{CaAl}_2\text{Si}_2$  vs anti- $\text{La}_2\text{O}_3$ , make for a useful construct depending on the application, electronic calculations suggest that the bonding of the two types of Mg, based on coordination, are similar and should be considered polar covalent [28].  $\text{Mg}_3\text{Sb}_2$  is an example where the application of the ideas of Zintl is useful in either case, the fully ionic or mixed ionic-(polar)covalent structural models; but it should be recognized that the real nature of the bonding is not well described by either model. However, there are many compounds which do show formal charge transfer and follow the 8-N rule (where N is the number of valence electrons) with resultant structural features which can be considered Zintl phases.

This is a good place to point out the 8-N rule for understanding polyanions. From a chemistry perspective, an understanding of electron counting starts with the octet rule for main group elements and is formulated from having s- and p-orbitals fully filled and a coordination number of 4. So, for example, carbon is typically four bonded with eight total electrons. In the case of a Zintl phase, their structure can be understood by a formal electron transfer from the electropositive elements to the more electronegative element. Therefore, the valence electron concentration (VEC) of the more electronegative element is increased to fulfill an octet (if there are enough electropositive elements). If there are not enough electrons to fulfill an octet, then the element will form bonds according to the 8-N rule to satisfy the anion valence, in a similar manner as an isovalent electronic element. For example, heteroanions with tetrahedral units can be described according to the analogous oxides, so the isolated tetrahedron  $[\text{GeAs}_4]^{8-}$  in the Zintl phase,  $\text{Ba}_4\text{GeAs}_4$  [29], is isoelectronic with  $[\text{GeO}_4]^{4-}$  and is balanced by alkaline earth cations [27, 29]. With this idea, Zintl phases can be composed of anions and/or polyanions that are chains, planes, or three-dimensional structures formed to satisfy valence. There are numerous binary and multinary phases that can be treated as Zintl phases, making this simplistic manner of considering crystal structures and properties of some intermetallics very powerful. However, there are limitations to this approach which can arise when compounds are metallic or have a phase width. Also, while the ideas of Zintl can be employed for transition metal-containing phases [9, 18, 30–32], many of these are compounds with metals that have either zero, half-filled, or completely filled d-bands, requiring additional considerations. In the case of metals, it can be easier to consider a total valence electron count rather than the 8-N rules. For this review, we will consider a few transition metal-containing Zintl phases but will consider the d orbitals localized and the bonding in an analogous manner as for main group metals. Ideas of Zintl and electron counting work quite well in some cases and have been described for Skutterudites [25] and Clathrates [20], providing insight and guidance into new compositions with potential for thermoelectric applications.

The ideas of Zintl electron counting allow for chemical intuition [3, 6, 7, 33] and rational design [34] to be employed and can lead to optimization of the thermoelectric properties. A good starting place for a complex phase with no significant band structure calculation is carrier concentration and bandgap engineering [1]. In the case of a Zintl phase, since you can count electrons, you can add or subtract through alio-valent

substitutions such as replacing an alkaline earth by a rare earth to add or an alkali metal to subtract. In some cases, the polyanion(s) can also be either isovalently or aliovalently substituted to tune the electron count. In addition, since these phases are semiconductors, employing isovalent substitutions can increase or decrease the bandgap depending on whether they contribute to increasing or decreasing the bond strength of the corresponding orbitals near the Fermi level, thereby impacting both the magnitude of the Seebeck coefficient and the temperature at which bipolar conduction appears. The magnitude of the Seebeck coefficient depends on the density of state (DOS) at the Fermi level and temperature onset of bipolar conduction depends on activation of carriers across the bandgap, so the size of the bandgap. Employing isovalent periodic group substitutions such as As vs Sb gives rise to stronger bonding states and thereby a larger gap. If instead, the cation is exchanged for a larger sized isovalent substitution such as Sr for Ca, the bonding states of the polyanions are weakened by the expansion of the unit cell, again leading to a larger gap. In some cases, a larger gap and changes in the density of states (DOS) at the Fermi level results in eliminating bipolar conduction at the high temperatures and increasing the Seebeck coefficient. With substitutions, in addition to band engineering, point defect phonon scattering and defect concentrations are affected thereby making optimization of properties difficult or even counter intuitive [14]. As a phase become technologically important, the application of and insight gained from detailed band structure calculations allow for additional optimization [35, 36].

### 2.5.3 Zintl phases and thermoelectrics

There are a number of other structure types that can be considered as Zintl phases to be considered for thermoelectric properties. The compounds with compositions,  $AB_2X_2$ ,  $A_{14}MPn_{11}$ ,  $A_2MPn_2$ , and  $A_{11}M_6Pn_{12}$  will be presented and discussed. Compounds of the composition  $A_5M_2Pn_6$ ,  $A_3MPn_3$ , and  $A_9M_4Pn_9$  have been recently reviewed; therefore, will not be described herein [4]. Fig. 2.5.3 provides a survey view of several Zintl phase materials with efficient  $zTs$  reported to date. The band structures and bonding characteristics of these structure types can be adjusted by elemental substitutions, dopants, and alloying to improve the thermoelectric performance further.

### 2.5.4 Compounds with the $AB_2X_2$ composition

The first published example of an identified Zintl phase with promising thermoelectric properties of the  $AB_2X_2$  (1-2-2) composition was the study of the  $Ca_xYb_{1-x}Zn_2Sb_2$  solid solution [10]. This solid solution crystallizes in the  $CaAl_2Si_2$  structure type (trigonal  $P-3m1$ ). The general formula of  $AB_2X_2$  with this structure type typically has A as either an alkaline earth or rare earth element, B is a main group element or transition metal and X is either group 14 or 15 elements. The structure is shown in Fig. 2.5.4. It is composed of alternating cationic A layers separated by anionic  $B_2X_2$  layers. While the anionic part of the structure can be understood with Zintl electron counting with both

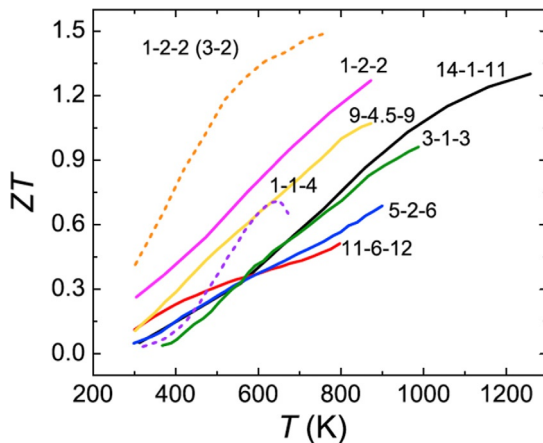


**Fig. 2.5.3** The  $zT$  values of a variety of recently reviewed Zintl phases with  $p$ -type and  $n$ -type are indicated by solid and dashed lines. The compositions are indicated as numbers: 14-1-11 ( $\text{Yb}_{14}\text{Mn}_{0.2}\text{Al}_{0.8}\text{Sb}_{11}$ ), 11-6-12 ( $\text{Eu}_{11}\text{Cd}_{4.5}\text{Zn}_{1.5}\text{Sb}_{11}$ ), 5-2-6 ( $\text{Ca}_5\text{In}_{1.9}\text{Zn}_{0.1}\text{Sb}_6$ ), 3-1-3 ( $\text{Sr}_3\text{Ga}_{0.93}\text{Zn}_{0.07}\text{Sb}_3$ ), 9-4-9 ( $\text{Ca}_9\text{Zn}_{4.5}\text{Sb}_9$ ), 1-2-2 ( $\text{Eu}_{0.2}\text{Yb}_{0.2}\text{Ca}_{0.4}\text{Mg}_2\text{Bi}_2$ ), n-type 1-2-2 ( $\text{Mg}_{3.05}\text{Nb}_{0.15}\text{Sb}_{1.5}\text{Bi}_{0.49}\text{Te}_{0.01}$ ), and n-type 1-1-4 ( $\text{K}_{0.99}\text{Ba}_{0.01}\text{AlSb}_4$ ).

Reprinted with permission from reference J. Shuai, J. Mao, S. Song, Q. Zhang, G. Chen, Z. Ren, Recent progress and future challenges on thermoelectric Zintl materials, Mater. Today Phys. 1 (2017) 74–95. Copyright (2017) Elsevier.

B and X being four-bonded, the total number of valence electrons per formula unit tends to be 16. Within the  $\text{B}_2\text{X}_2$  layers, the B atoms are tetrahedrally coordinated by X atoms. The tetrahedra share three edges to form a layer. As mentioned above for the example of  $\text{Mg}_3\text{Sb}_2$  which can be alternatively written as  $\text{Mg}(\text{Mg}_2\text{Sb}_2)$ , as the electronegativity difference between the B and X element becomes larger, this structural description is no longer accurate [37]. Most of the antimonide and bismuthide compounds have been demonstrated as narrow bandgap semiconductors and good thermoelectric properties have been established in many members of this structural family [14]. While these phases have been shown to have relatively high thermal conductivity, they have been found to possess light effective mass, leading to high electron mobility compared with other Zintl thermoelectrics [38]. Probably one of the most important guiding principles in bandgap engineering in this system is recognizing that strong B-X bonding will lead to a large gap due to difference in energy between the bonding and antibonding bands which are B-X in origin [14].

Another very common  $\text{AB}_2\text{X}_2$  structure type is the  $\text{ThCr}_2\text{Si}_2$  structure type (tetragonal,  $I4/mmm$ ), but most of these compounds have been shown to be metallic and there have been no notable high-efficiency thermoelectric materials with this structure type discovered to date. However, related oxychalcogenide phases which crystallize in complex building blocks that included the anti- $\text{ThCr}_2\text{Si}_2$  structure type are found for  $[\text{A}_2\text{O}_2]\text{Te}$  ( $\text{A} = \text{La-Nd, Sm-Ho, Bi}$ ) and  $\text{Bi}_2\text{O}_2\text{Se}$  and some show reasonable  $zTs$  with  $p$ -type  $\text{Bi}_{1-x}\text{Sr}_x\text{OCuSe}$  providing a  $zT$  of 0.76 at 873 K [39]. There are other structure types with the 1-2-2 composition that have been investigated for

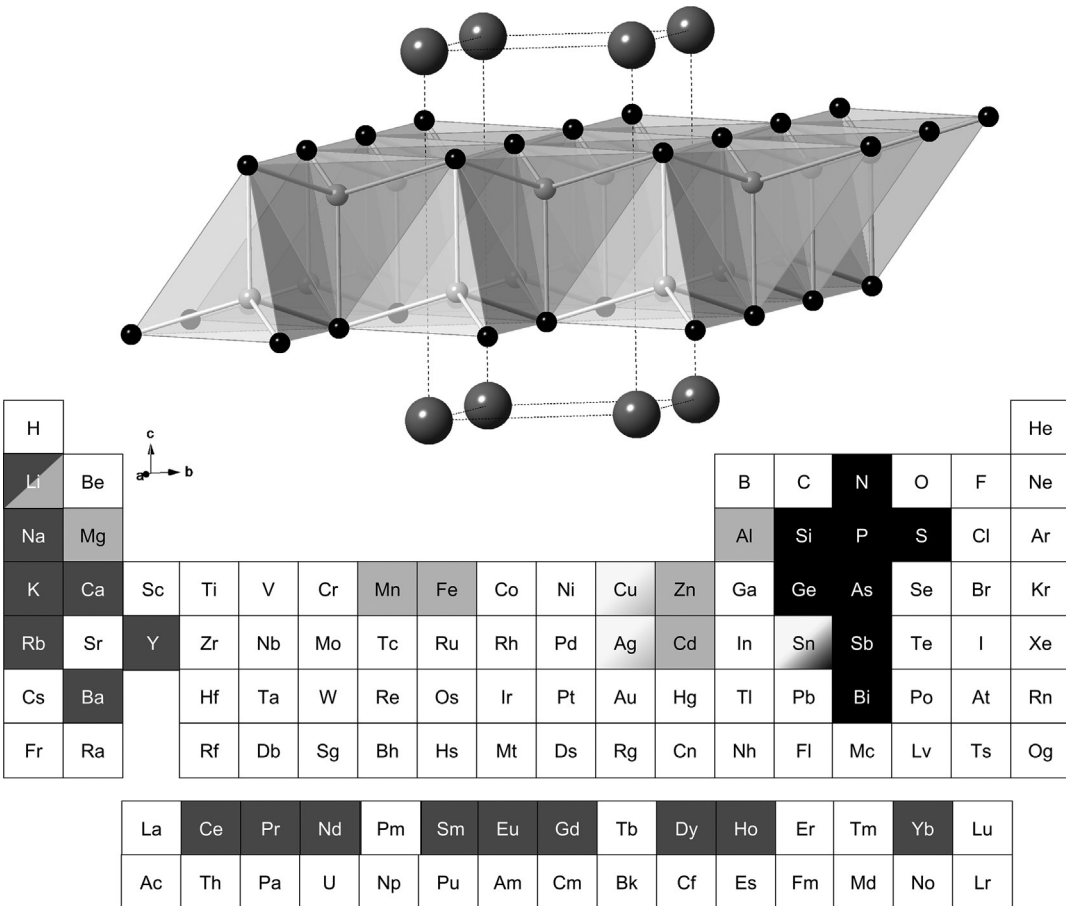


**Fig. 2.5.4** The CaAl<sub>2</sub>Si<sub>2</sub> (AB<sub>2</sub>X<sub>2</sub>) structure type with the A, B, and X sites indicated by large dark gray, smaller light gray, and black spheres, respectively. The periodic table is colored to indicate the elements that can occupy the sites with the same colors as the atoms in the structure type; partial shading indicates nonstoichiometry.

thermoelectric properties, such as a few crystallizing in the  $\alpha$ -BaCu<sub>2</sub>S<sub>2</sub> structure type (orthorhombic, *Pnma*). The compounds (Ba,Na)-Cu<sub>2</sub>Se<sub>2</sub>, BaZn<sub>2</sub>Sb<sub>2</sub>, and Ba<sub>1-x</sub>K<sub>x</sub>Zn<sub>2</sub>As<sub>2</sub> have been investigated and show *zT* values of 1.0 at 773 K, 0.31 at 675 K, and 0.67 at 900 K, respectively [40–42].

## 2.5.5 Compounds with the A<sub>14</sub>MPn<sub>11</sub> composition

The Ca<sub>14</sub>AlSb<sub>11</sub> structure type (Fig. 2.5.5) has a high degree of chemical flexibility. Generally described as A<sub>14</sub>MPn<sub>11</sub>, this structure type can accommodate the cations, Sr, Ba, Eu, Yb, and Ca as “A”, In, Nb, Mn, Zn, Cd, Al, and Ga as “M”, and Bi, Sb, As, and P as “Pn” [4, 8, 43]. The structure type has been described in detail recently [4, 8]. In brief, Zintl counting can be used to describe the structure as follows:

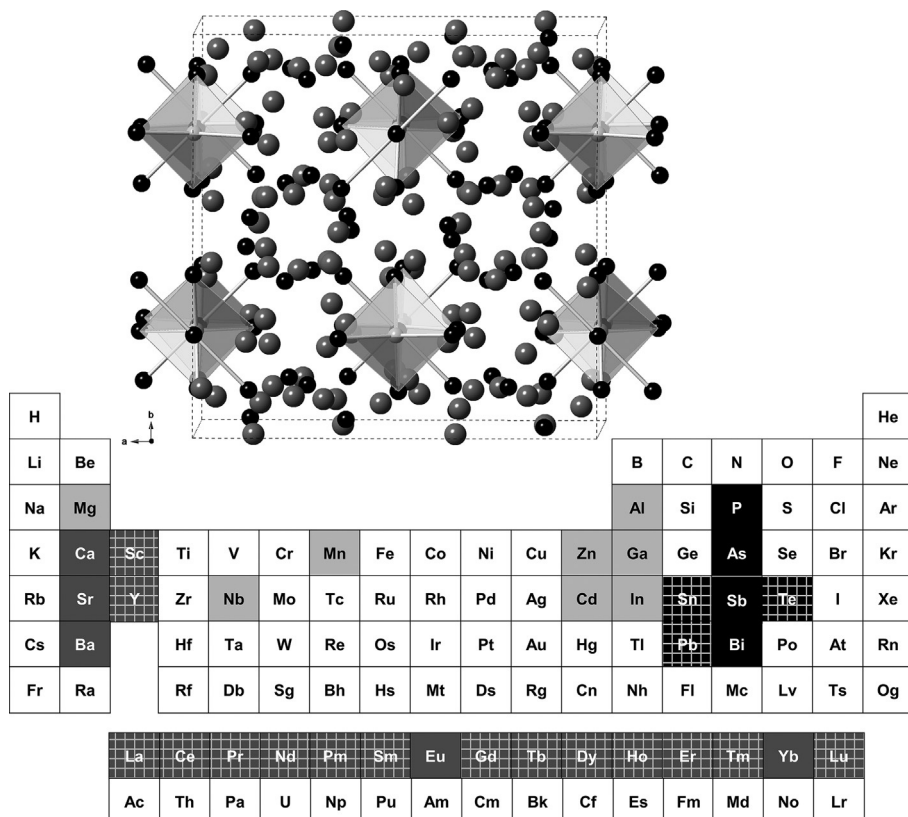


**Fig. 2.5.5** The A<sub>14</sub>MPn<sub>11</sub> structure with the A, M, and Pn sites is indicated by large dark gray, smaller light gray, and black spheres, respectively. The periodic table is highlighted with the elements that can occupy the corresponding sites with cross-hatched pattern given to alio-valent substituents.

one formula unit comprises 14 isolated  $A^{2+}$  cations which are charge balanced by one tetrahedral unit  $[MPn_4]^{9-}$ , one linear unit  $[Pn_3]^{7-}$ , and four isolated anions  $Pn^{3-}$  [44].  $A_{14}MPn_{11}$  structure crystallizes in the tetragonal  $I4_1/acd$  space group. The unit cell of the  $A_{14}MPn_{11}$  structure has 208 atoms leading to an inherently low thermal conductivity [45]. The complexity of the unit cell coupled with the large mass differences in  $A_{14}MPn_{11}$  structures leads to an almost temperature-independent thermal conductivity (Fig. 2.5.6) for a large variety of different A, M, and Pn constituents [49]. The anti-monide analogs of  $A_{14}MPn_{11}$  have thermal conductivities on the order of magnitude of glass ( $\sim 0.8 \text{ W/mK}$ ) and is much lower than other state of the art thermoelectric materials such as  $Bi_2Te_3$  and Skutterudites ( $\sim 2 \text{ W/mK}$ ) [49–51].

The chemical flexibility and low thermal conductivity suggested that the  $Ca_{14}AlSb_{11}$  structure type would be a good thermoelectric material. This was proven correct in 2006 by Brown et al. [6] when single crystals of  $Yb_{14}MnSb_{11}$  grown by via a Sn flux and hot-pressed into pellets were measured to have a  $zT$  of 1 at 1223 K. At the time, this  $zT$  was a 60% improvement on the state of the art material ( $p\text{-Si}_{0.8}\text{Ge}_{0.2}$ ) [6, 49, 52]. The high performance of  $Yb_{14}MnSb_{11}$  spurred a flurry of  $Yb_{14}MnSb_{11}$  doping studies including Zn [53], Al [45], La [54], Ca [55], Te [56], Pr [57], Sm [57], Mg [47], Y [58], and Sc [58], the results of which are well summarized by Shuai, et al. [4]. The most successful was the reduction of the carrier concentration ( $1.3 \times 10^{21} \text{ cm}^{-3}$ ) and spin disorder scattering of  $Yb_{14}MnSb_{11}$  by replacing some Mn with Al ( $Yb_{14}Mn_{1-x}Al_xSb_{11}$ ,  $x=0.6, 0.8$ ) which provided the peak  $zT$  (1.3) for the flux synthesis route (Fig. 2.5.7) [45]. Flux synthesis created issues of Sn contamination which were overcome by high-energy milling and reactive hot pressing with reported  $zTs$  as high as

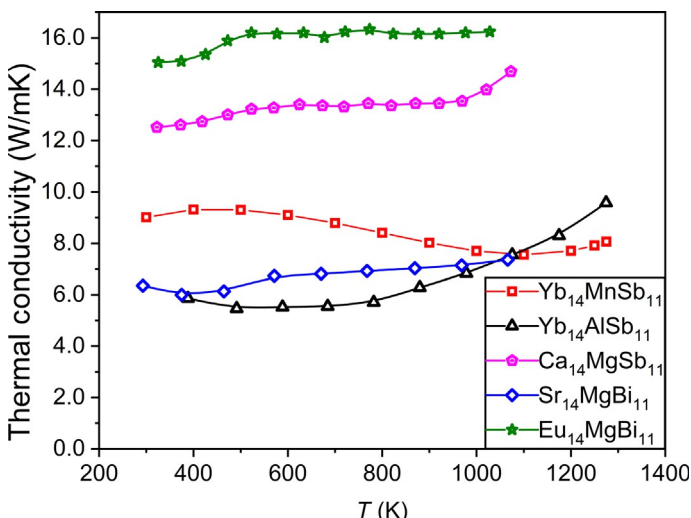


**Fig. 2.5.6** Thermal conductivity vs temperature is adapted from literature for  $A_{14}MPn_{11}$  [46–48]. The low thermal conductivity of the  $A_{14}MSb_{11}$  compounds is shown with different A and M. The almost temperature-independent nature of the thermal conductivity is seen through different A, M, and Pn constituents.

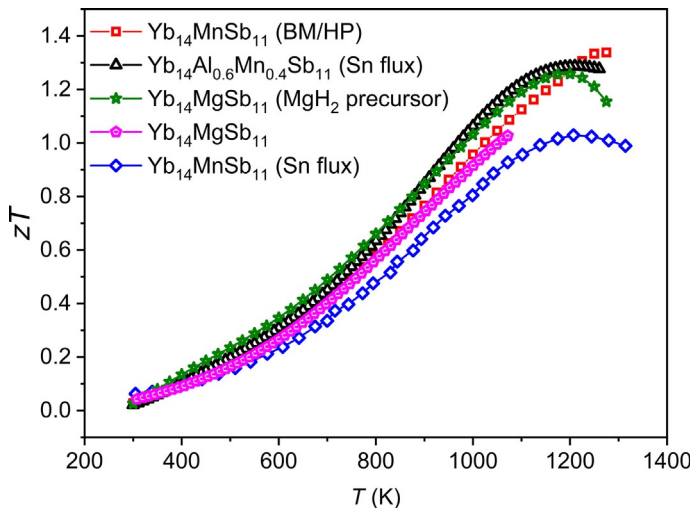


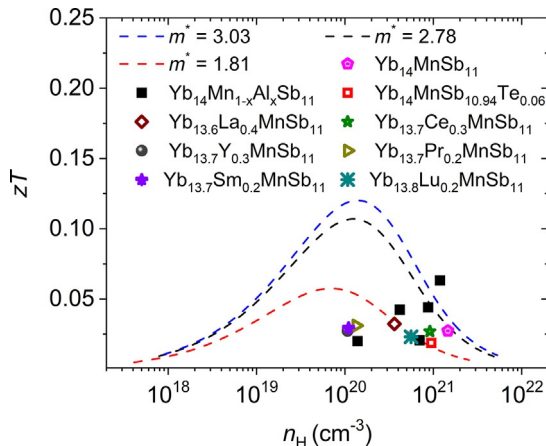
**Fig. 2.5.7**  $zT$  vs temperature is adapted from literature for  $\text{Yb}_{14}\text{MnSb}_{11}$  ball-milled (BM) and reactively hot-pressed (HP) [46],  $\text{Yb}_{14}\text{MnSb}_{11}$  and  $\text{Yb}_{14}\text{Al}_{0.6}\text{Mn}_{0.4}\text{Sb}_{11}$  from hot-pressed single crystals synthesized by Sn flux [6, 45], and  $\text{Yb}_{14}\text{MgSb}_{11}$  high temperature annealed and consolidated by SPS from Mg metal [47] and MgH<sub>2</sub> [59].

1.33 for  $\text{Yb}_{14}\text{MnSb}_{11}$  [46]. Another high  $zT$  phase is  $\text{Yb}_{14}\text{MgSb}_{11}$ , first reported by Hu et al. [47] with a  $zT$  of 1 at 1073 K [47], it has since been followed up by Justl et al. [59]. Using MgH<sub>2</sub> as a clean, easy to disperse Mg source, a peak  $zT$  of 1.25 at 1200 K was achieved for  $\text{Yb}_{14}\text{MgSb}_{11}$  with a higher average  $zT$  than  $\text{Yb}_{14}\text{MnSb}_{11}$  [59].  $\text{Yb}_{14}\text{MgSb}_{11}$  has lower carrier concentration ( $5.3 \times 10^{20} \text{ cm}^{-3}$ ) than  $\text{Yb}_{14}\text{MnSb}_{11}$  (provided above) resulting in an increased Seebeck coefficient and resistivity [59]. Additionally, replacing the d<sup>5</sup> Mn<sup>2+</sup> with d<sup>0</sup> Mg<sup>2+</sup> effectively eliminates spin disorder scattering associated with the coupling of the d<sup>5</sup> electrons with holes in the structure making  $\text{Yb}_{14}\text{MgSb}_{11}$  a simpler structural platform for exploring doping effects [45].

Future improvement of  $zT$  for compounds of the  $\text{Ca}_{14}\text{AlSb}_{11}$  structure type should be aided by computation. Fig. 2.5.8 (adapted from Hu, Cerretti, Wille, Bux, and Kauzlarich [8]) shows the measured carrier concentration vs  $zT$  predicted by a single parabolic band model, and measured data points. As discussed by Wille et al. and seen in Fig. 2.5.8, the model does not fit the data well [60]. Future computational studies on  $\text{A}_{14}\text{MPn}_{11}$  should explore a better multiple band model with which to predict the optimal carrier concentration of the  $\text{Ca}_{14}\text{AlSb}_{11}$  structure type. Another option for the further optimization of the thermoelectric properties of  $\text{Yb}_{14}\text{MnSb}_{11}$  may be done by compositing which works well in the Skutterudite, PbTe, Bi<sub>2</sub>Te<sub>3</sub>, and Half-Heusler systems which not only helps the thermoelectric properties, but can also improve the mechanical properties which are important for device fabrication [61, 62]. Preliminary studies find that compositing W with  $\text{Yb}_{14}\text{MnSb}_{11}$  does not provide a  $zT$  improvement, but shows that the two phases can be composited without reaction, and the material qualitatively becomes harder as a result of compositing [63].

**Fig. 2.5.8**  $zT$  vs carrier concentration predicted by single parabolic band model.

Adapted with permission from reference Y. Hu, G. Cerretti, E.L. Kunz Wille, S.K. Bux, S.M. Kauzlarich, The remarkable crystal chemistry of the  $\text{Ca}_{14}\text{AlSb}_{11}$  structure type, magnetic and thermoelectric properties, *J. Solid State Chem.* 271 (2019) 88–102. Copyright (2019) Elsevier.



Furthermore, exploiting the chemical flexibility of the structure, the limits of alloy scattering should be explored by inserting more than two atoms on one site with drastically different masses. This could improve  $zT$  by providing samples with extremely low thermal conductivity. Lastly, using precursors such as  $\text{MgH}_2$ ,  $\text{MnSb}$ ,  $\text{AlSb}$ , and  $\text{YbH}_2$  can help overcome the difficulties of reaction kinetics and handling soft metals such as the alkaline earths, Yb, and Eu.

## 2.5.6 Compounds of the $\text{A}_2\text{MPn}_2$ composition

$\text{A}_2\text{MPn}_2$  intermetallic compounds can adopt a number of different crystal structure types. There are three main structure types shown in Fig. 2.5.9, described by  $\text{Sr}_2\text{ZnP}_2$  ( $P6_3/mmc$ ) [64],  $\text{Yb}_2\text{CdSb}_2$  ( $Cmc2_1$ ) [65–67], and  $\text{K}_2\text{MnS}_2$  ( $Ibam$ ) [68], with the elemental compositions reported to date. Additionally, there is another polymorph of  $\text{Yb}_2\text{CdSb}_2$  which forms when  $\text{Yb}^{2+}$  is replaced by  $\text{Ca}^{2+}$ ,  $\text{Ca}_2\text{CdSb}_2$  ( $Pnma$ ) structure type that is closely structurally related [65].  $\text{Ca}_2\text{CdSb}_2$  is the centrosymmetric version of  $\text{Yb}_2\text{CdSb}_2$  where the layers are identical and simply differ by the stacking [65]. In this chapter, the focus is on the first two members of this composition whose thermoelectric properties have been measured:  $\text{Eu}_2\text{ZnSb}_2$  ( $P6_3/mmc$ ) [64] and  $\text{Yb}_{2-x}\text{Eu}_x\text{CdSb}_2$  ( $Cmc2_1$ ) [69].  $\text{Eu}_2\text{ZnSb}_2$  crystallizes in the hexagonal space group  $P6_3/mmc$ ; the idealized structure can be described as flat honeycomb layers made up of Zn and Sb separated by  $\text{Eu}^{2+}$  cations which occupy hexagonal prisms between the layers. The Zn site is only 50% occupied and the structure has been described in detail [64]. The  $\text{Yb}_2\text{CdSb}_2$  crystal structure type is represented in the non-centrosymmetric orthorhombic space group  $Cmc2_1$ . This structure can be described as a two-dimensional  $[\text{CdSb}_2]^{4-}$  polyanionic layer extended in the  $ac$  plane as a result of corner sharing of the  $\text{CdSb}_4$  tetrahedra along the  $a$ - and  $c$ -crystallographic

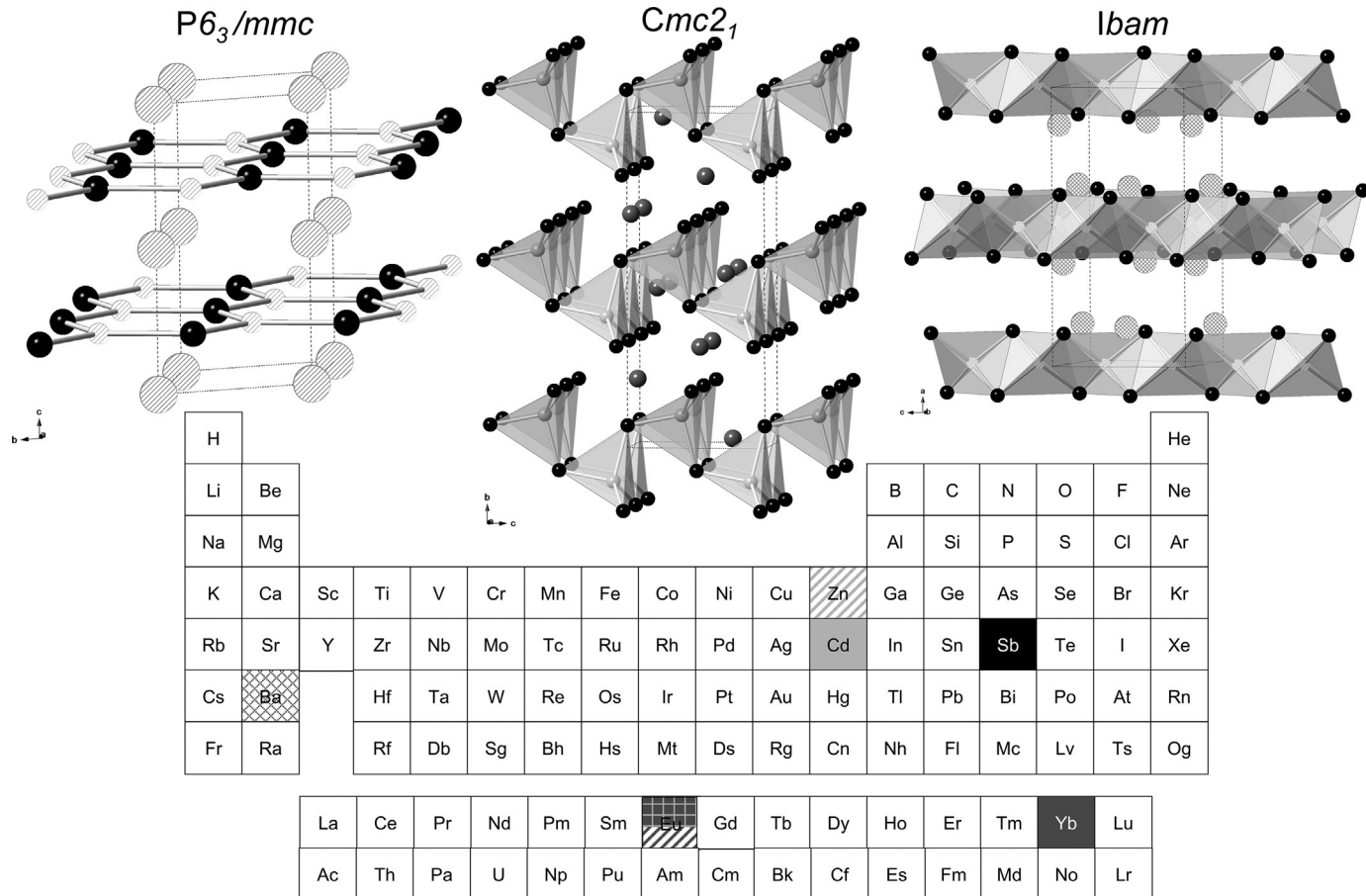


**Fig. 2.5.9** The structure types, Sr<sub>2</sub>ZnP<sub>2</sub> (*P6<sub>3</sub>/mmc*), Yb<sub>2</sub>CdSb<sub>2</sub> (*Cmc<sub>2</sub>1*), and K<sub>2</sub>MnS<sub>2</sub> (*Ibam*) with shading according to A<sub>2</sub>MPn<sub>2</sub> with the A, M, and Pn sites are indicated by large patterned or gray, smaller patterned or light gray, and black spheres, respectively. The periodic table is shaded with the elements that can occupy the corresponding shaded or patterned sites.

directions. The  $\text{Yb}^{2+}$  cations occupy the space between the adjacent polyanionic layer. Those compounds that crystallize in the  $\text{K}_2\text{MnS}_2$  structure type display infinite linear chains of edge-sharing  $\text{ZnPn}_4$  tetrahedra in their anionic substructure and is only observed for the  $\text{Ba}_2\text{ZnPn}_2$  ( $\text{Pn} = \text{As, Sb, Bi}$ ) compounds [68].

These structures can be rationalized as charge-balanced Zintl phases by the Zintl concept as  $[\text{A}^{2+}]_2[\text{M}^{2+}][\text{Pn}^{3-}]_2$ . Various Zintl compounds with the  $\text{Yb}_2\text{CdSb}_2$  structure type have been synthesized. Most belong to the more electronegative pnictogen analogues such as  $\text{Ca}_2\text{CdP}_2$ ,  $\alpha\text{-Ca}_2\text{CdAs}_2$ ,  $\text{Sr}_2\text{CdAs}_2$   $\text{Ba}_2\text{CdAs}_2$ , and  $\text{Eu}_2\text{CdAs}_2$  [66]. The only  $\text{A}_2\text{MPn}_2$  rare earth antimonide compounds ( $\text{A} = \text{Yb or Eu}$ ; and  $\text{X} = \text{Sb}$ ) with the  $\text{Ca}_2\text{CdSb}_2$  crystal structure reported to date is  $\text{Ca}_2\text{CdSb}_2$  itself.  $\text{Eu}_2\text{CdSb}_2$  does not exist except in solid solutions such as  $\text{Sr}_{2-x}\text{Eu}_x\text{CdSb}_2$ ,  $\text{Ba}_{2-x}\text{Eu}_x\text{CdSb}_2$ , and  $\text{Yb}_{2-x}\text{Eu}_x\text{CdSb}_2$  [67].  $\text{Yb}_{2-x}\text{Eu}_x\text{CdSb}_2$  solid solution has been investigated and preserves the  $\text{Yb}_2\text{CdSb}_2$  crystal structure in an incomplete phase width up to approximately  $x \sim 1$ , in the crystal structures [67, 69]. Fig. 2.5.10 shows the best  $zT$ s of the compounds measured to date:  $\text{Eu}_2\text{ZnSb}_2$  ( $P6_3/mmc$ ) [64] and  $\text{Yb}_{2-x}\text{Eu}_x\text{CdSb}_2$  ( $Cmc2_1$ ),  $x = 0, 0.4$  [69].  $\text{A}_2\text{MX}_2$  compounds are interesting for the thermoelectric applications due to the narrow gap semiconducting properties predicted by their electronic band structures. Although the thermoelectric properties calculation of  $\alpha\text{-Ca}_2\text{CdAs}_2$  ( $Cmc2_1$ ) compounds in this family should provide promising results [70], these phases have not yet been investigated for the thermoelectric properties. Theoretical calculations for the  $\alpha\text{-Ca}_2\text{CdAs}_2$  structure suggest a bandgap of 0.96 eV and a relatively high  $zT$  value of  $\sim 0.8$  at 800 K with the Seebeck coefficient, electrical conductivity, and thermal conductivity of  $266 \mu\text{V/K}$ ,  $2.8 (\Omega\text{ms})^{-1}$ , and  $2.1 \text{ W}/(\text{mK})$ , respectively.

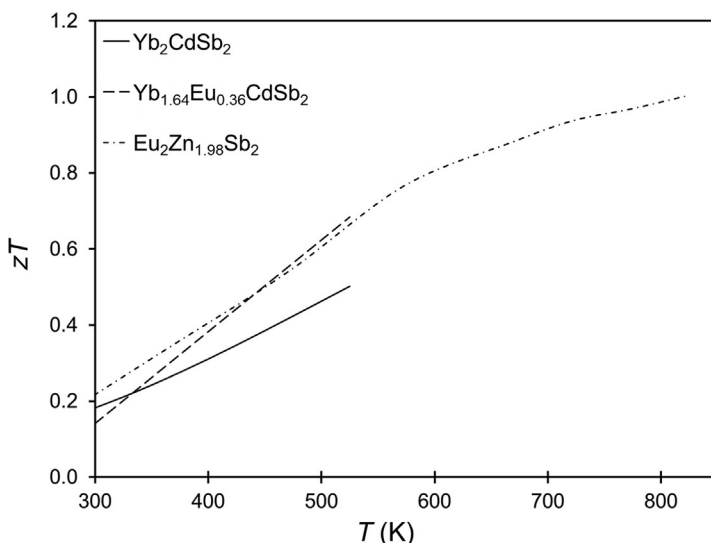
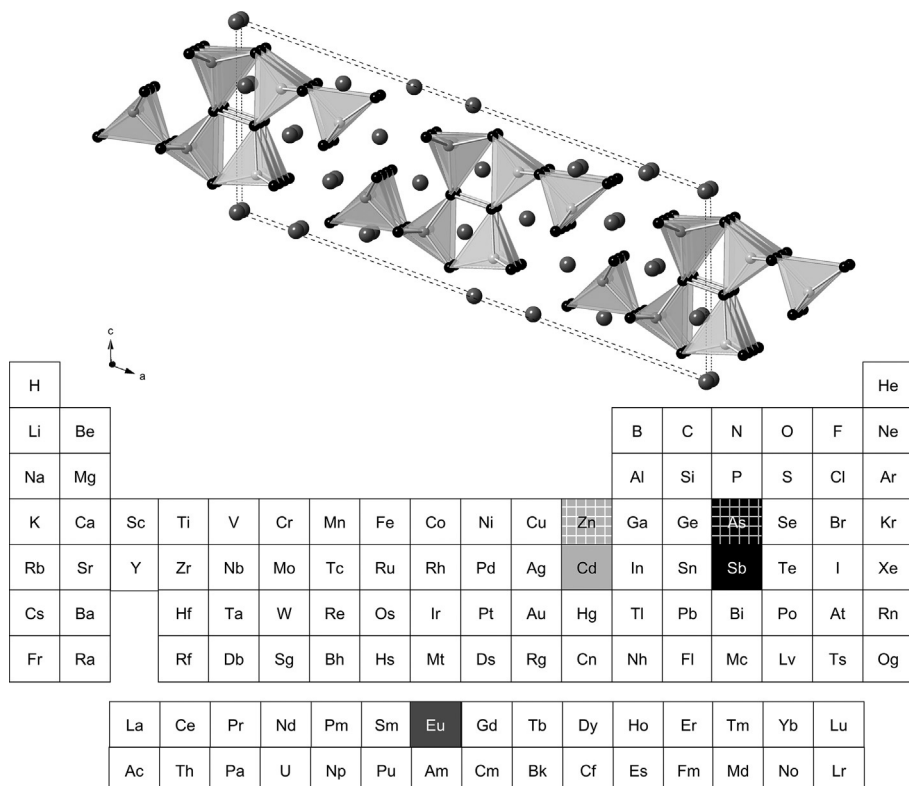


Fig. 2.5.10  $zT$  vs temperature for  $\text{Yb}_2\text{CdSb}_2$ ,  $\text{Yb}_{1.64}\text{Eu}_{0.36}\text{CdSb}_2$ , and  $\text{Eu}_2\text{Zn}_{1.96}\text{Sb}_2$  [67, 69].

## 2.5.7 Compounds of the $A_{11}M_6Pn_{12}$ composition

Compounds of the composition 11-6-12 (monoclinic,  $C2/m$ ) with the  $Sr_{11}Cd_6Sb_{12}$  structure type [71] is shown in Fig. 2.5.11 and has been only moderately investigated. This structure can be described as infinite, one-dimensional tubes of two edge-fused pentagons. There are 15 crystallography unique atomic positions in the asymmetric unit comprised of 6 Sr, 6 Sb, and 3 Cd sites and preferred site substitution was demonstrated in a few compositions to date [1, 72–74]. The transport properties measurements on  $Eu_{11}Cd_6Sb_{12}$  show exceptionally low lattice thermal conductivities of 0.78–0.49 W/mK and high  $p$ -type Seebeck coefficient of +118 to 153  $\mu$ V/K. These compounds also show relatively high mobilities of 20–55  $\text{cm}^2/\text{V s}$ . It is the high resistivity values of 7–13  $\text{m}\Omega\text{cm}$  that results in a low  $zT$  value of 0.23 at 774 K. Theoretical calculation on the compound  $Eu_{11}Cd_6Sb_{12}$  show that the Zintl formalism does not adequately describe the bonding in this compound as mixing of Eu and Sb orbitals is



**Fig. 2.5.11** A view of the  $Sr_{11}Cd_6Sb_{12}$  structure type with the Sr, Cd, and Pn sites is indicated as large gray, light gray, and black spheres, respectively. The periodic table is colored with the elements that can occupy the corresponding shaded sites with a cross-hatched pattern given to dopants.

observed in the vicinity of the Fermi level [72], contrasting with the expected ionic interaction between cation (in this case, Eu<sup>2+</sup>) and the anionic network described by Zintl concept. These compounds are better described as polar intermetallics rather than Zintl compounds [72, 75].

### 2.5.8 *n*-Type Zintl phases

The majority of Zintl phases have been observed as *p*-type semiconductors. There have been attempts to dope *p*-type structures into *n*-type semiconductors [76, 77]. In 2019, Gorai et al. investigated a computational method for guiding the synthesis of doped *n*-type Zintl phases via computational defect diagrams [78]. The limitations of doping Zintl phases from *p*- to *n*-type semiconductors results from the native defects of a material having low formation energy. This type of acceptor defect is referred to as an electron “killer” and can make it difficult or impossible to dope a material *n*-type [78]. However, there are a few Zintl phases that have been discovered to be *n*-type or doped *n*-type in recent years: KGaSb<sub>4</sub> [79, 80], KAlSb<sub>4</sub> [81, 82], and Zr<sub>3</sub>Ni<sub>3</sub>Sb<sub>4</sub> [83].

### 2.5.9 KAlSb<sub>4</sub> structure type

KAlSb<sub>4</sub> and KGaSb<sub>4</sub> crystallize in the orthorhombic *Pnma* space group, Fig. 2.5.12. This structure type is described by infinite corner-shared MSb<sub>4</sub> tetrahedral chains extending the *b*-direction that are connected by two trigonal pyramidal Sb chains and a zig-zag Sb chain. These linked chains create infinite channels of K ions parallel to the *b*-axis [79, 81]. The structure is charged balanced with the infinite polyanionic structure, MSb<sub>4</sub><sup>-</sup>, surrounding K<sup>+</sup> ions. This structure type has been explored for both *p*-type and *n*-type doping to enhance the thermoelectric properties. The pure-phase polycrystalline powder of these materials were synthesized by high-energy ball milling followed by uniaxial hot pressing [80, 82].

The KAlSb<sub>4</sub> parent compound has a large negative Seebeck coefficient across the measured temperature range with a maximum of -495  $\mu\text{V/K}$  at 200°C [82]. The Ga analog, KGaSb<sub>4</sub>, experiences a *p*- to *n*-transition around 275°C with a maximum Seebeck coefficient of  $\pm 200 \mu\text{V/K}$  at 175°C and 400°C, respectively, Fig. 2.5.13A [80].

The *n*-type thermoelectric properties of these two materials were studied via Ba-doping on the K site. The K<sub>1-x</sub>Ba<sub>x</sub>AlSb<sub>4</sub> ( $x = 0.003, 0.005, 0.010, 0.030, 0.050$ ) and K<sub>1-x</sub>Ba<sub>x</sub>GaSb<sub>4</sub> ( $x = 0.005, 0.010, 0.015, 0.020, 0.025$ ) structures have a Ba solubility limit of  $x = 0.007$  and  $x = 0.020$ , respectively. In Fig. 2.5.13, the parent compounds have been plotted with squares while the doped compositions resulting in the largest Seebeck coefficient (triangles) and the doped compositions resulting in the largest *zT* (circles) are also plotted. The electrical resistivity of the KMSb<sub>4</sub> compounds decreases with increased Ba doping (Fig. 2.5.13B) while the thermal conductivity increases slightly (Fig. 2.5.13C). As expected, the carrier concentration increases with the

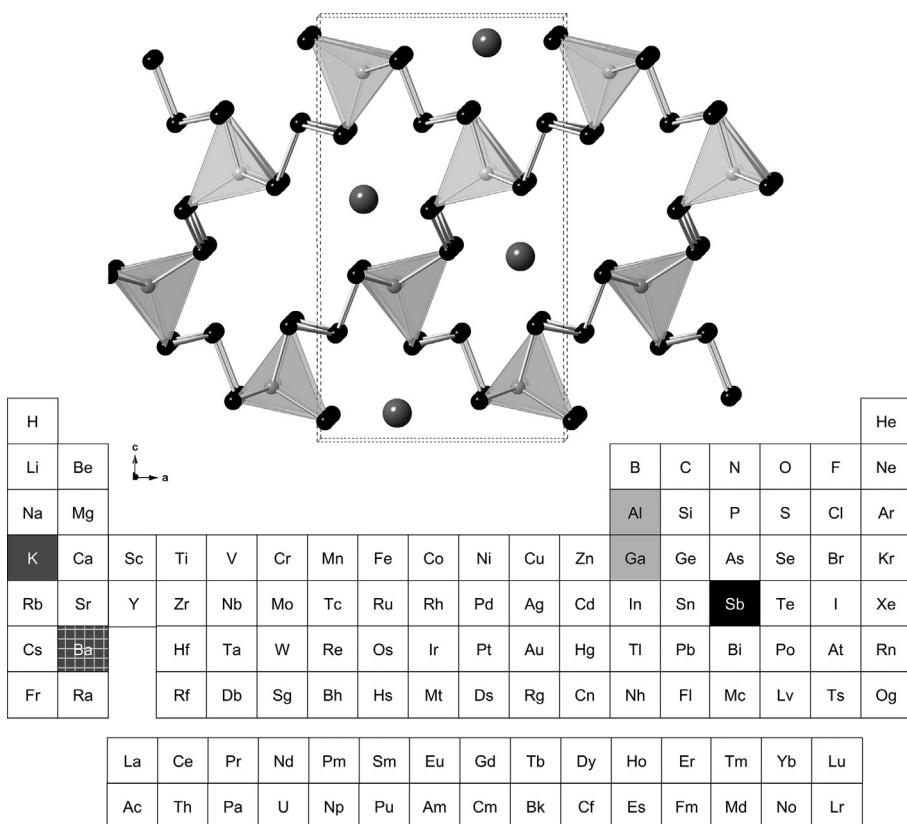


**Fig. 2.5.12** The structure of KMSb<sub>4</sub> viewed down the *b*-axis with the K, M, and Pn sites is indicated by large dark gray, small light gray, and black spheres, respectively. The periodic table is shaded with the elements that can occupy the corresponding sites with a cross-hatched pattern given to the *n*-type dopant.

increased Ba doping (Fig. 2.5.13D). The electron mobility, Fig. 2.5.13E, is increased with Ba doping for the K<sub>1-x</sub>Ba<sub>x</sub>GaSb<sub>4</sub> samples; however, the electron mobility is decreased by Ba doping in K<sub>1-x</sub>Ba<sub>x</sub>AlSb<sub>4</sub>. The K<sub>1-x</sub>Ba<sub>x</sub>AlSb<sub>4</sub> produced a maximum *zT* of 0.7 at 370°C when *x*=0.010, Fig. 2.5.13F. The absolute Seebeck coefficient of these materials is decreased from the undoped parent compound, but the electrical resistivity is improved significantly, yielding an increased *zT*. Similarly, the K<sub>1-x</sub>Ba<sub>x</sub>GaSb<sub>4</sub> material has a maximum *zT* of 0.92 at 400°C when *x*=0.015. When Ba is doped, even at the smallest amount (*x*=0.005), the Seebeck remains negative over the entire temperature range and the electrical resistivity is dramatically reduced leading to the improved *zT*. The small amount of dopants would be difficult to quantify but leads to dramatic changes in the carrier concentrations of these materials [82].

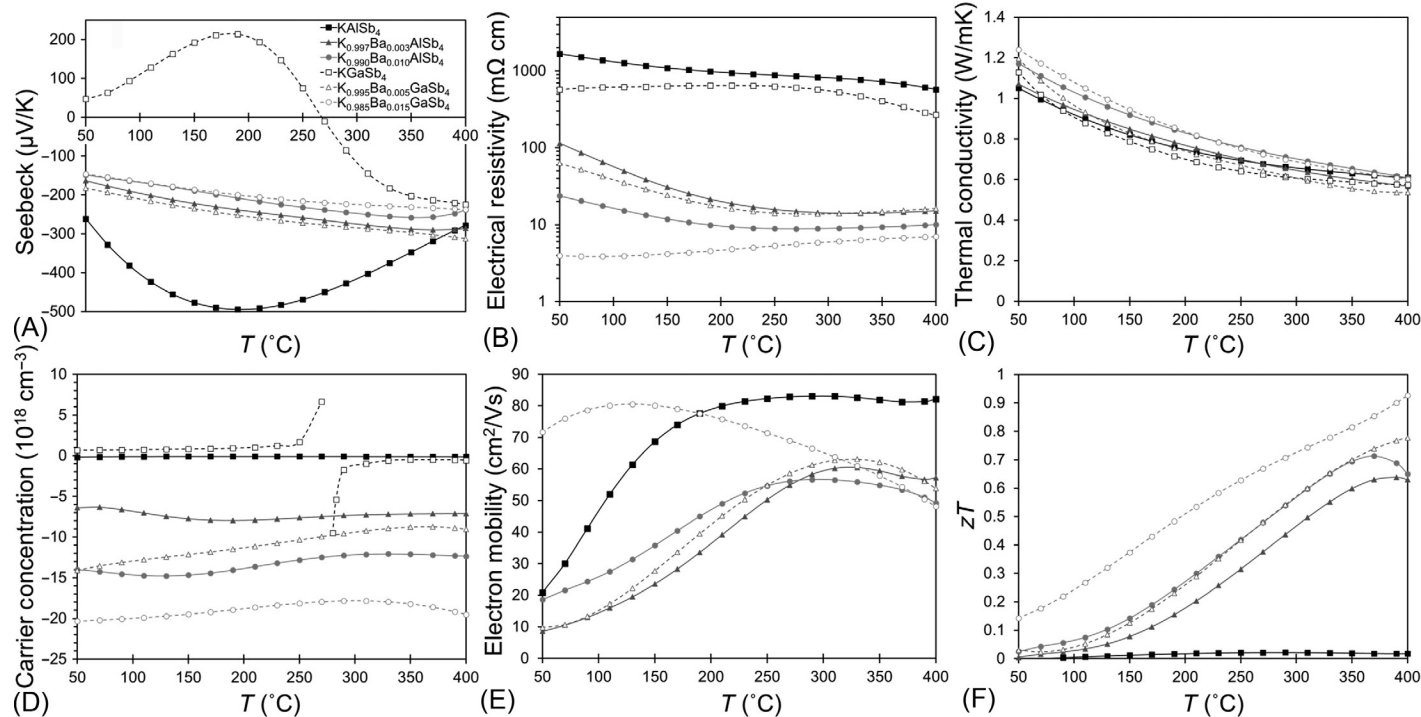


**Fig. 2.5.13** Measurements on pristine KGaSb<sub>4</sub> are not shown for carrier concentration or electron mobility due to the sign change associated with the bipolar transition from *p*-type to *n*-type transport at high temperatures. (A) Seebeck coefficient, (B) electrical resistivity, (C) thermal conductivity, (D) carrier concentration, (E) electron mobility, and (F)  $zT$  of the parent compositions of KMSb<sub>4</sub> (squares), the compositions with the highest Seebeck coefficient of the Ba-doped series (triangles), and the compositions with the highest  $zT$  of the Ba-doped series (circles) are plotted for KAISb<sub>4</sub> (closed symbols) and KGaSb<sub>4</sub> (open symbols).

Adapted from references B.R. Ortiz, P. Gorai, V. Stevanovic, E.S. Toberer, Thermoelectric performance and defect chemistry in n-type Zintl KGaSb<sub>4</sub>, Chem. Mater. 29 (10) (2017) 4523–4534; B.R. Ortiz, P. Gorai, L. Krishna, R. Mow, A. Lopez, R. McKinney, V. Stevanovic, E.S. Toberer, Potential for high thermoelectric performance in n-type Zintl compounds: a case study of Ba doped KAISb<sub>4</sub>. J. Mater. Chem. A 5 (8) (2017) 4036–4046.

## 2.5.10 $\text{Zr}_3\text{Ni}_3\text{Sb}_4$ structure type

$\text{Zr}_3\text{Ni}_3\text{Sb}_4$  is a *p*-type thermoelectric material crystallizing in the cubic space group  $I-43d$  [84] with a maximum  $zT$  of  $\sim 0.11$  at 550 K (Fig. 2.5.14) [77, 85].  $\text{Zr}_3\text{Ni}_3\text{Sb}_4$  adopts the  $\text{Y}_3\text{Au}_3\text{Sb}_4$  structure which is a filled variant of the prevalent  $\text{Th}_3\text{P}_4$  structure type. The structure is complicated and makes a simple description difficult. The Zr atoms are coordinated to eight Sb atoms via two interpenetrating tetrahedra. The Ni atoms are coordinated to four Sb atoms along the  $-4$  axis. The “ $\text{Zr}_3\text{Sb}_4$ ” network, consisting of metal-centered dodecahedra that share edges and faces in all directions, is the  $\text{Th}_3\text{P}_4$  structure type. The remaining tetrahedral holes filled with Ni atoms results in the space-filling structure of  $\text{Y}_3\text{Au}_3\text{Sb}_4$  [84]. Simplistically, the Zintl counting can be thought of as 3  $\text{Zr}^{4+}$  cations and the extended  $[\text{Ni}_3\text{Sb}_4]^{-12}$  array; however,  $\text{Zr}_3\text{Ni}_3\text{Sb}_4$  is not a true Zintl phase due to the short ( $2.7746(2)$  Å) Zr-Ni bond distance

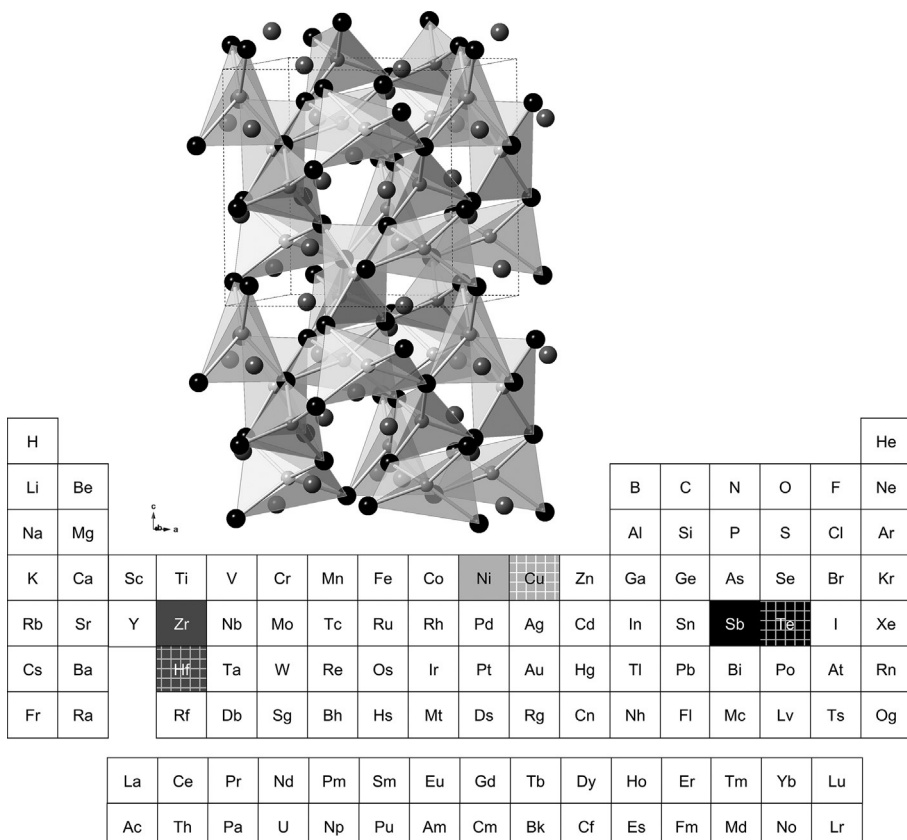


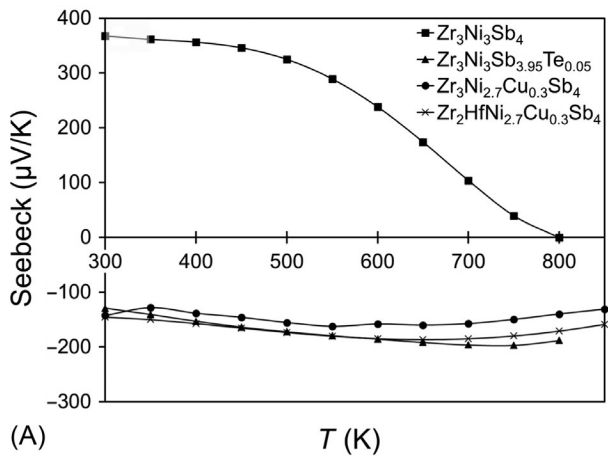
**Fig. 2.5.14** The structure of  $\text{Zr}_3\text{Ni}_3\text{Sb}_4$  viewed down the  $b$ -axis with elements substituting on the Zr, Ni, and Sb sites is indicated by large dark gray, small light gray, and black spheres, respectively. The known compositions are highlighted in the periodic table with the *n*-type dopant marked with a cross-hatched pattern.

resulting in a metal-metal bond. The Zr<sup>4+</sup> is an extreme and the Zr-Ni bonding would reduce the actual charge. The presence of a Zr-Ni bond is supported by DFT calculations because the predicted charges of +0.53 for Zr, -0.07 for Ni, and -0.35 for Sb are reduced compared to the initial electron counting [84]. It may be possible for Zr<sub>3</sub>Ni<sub>3</sub>Sb<sub>4</sub> to become a Zintl phase by substituting Zr with a more electropositive element.

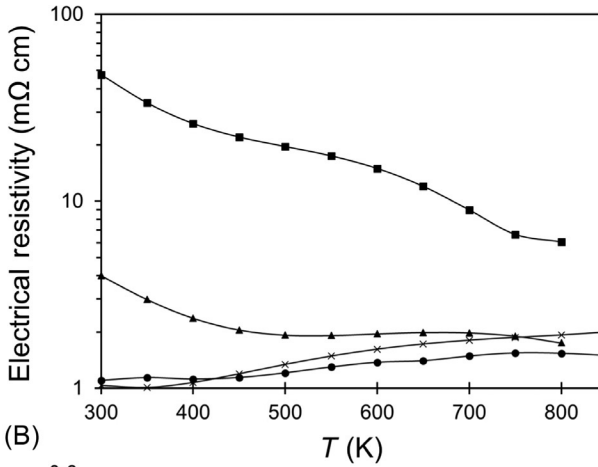
The parent Zr<sub>3</sub>Ni<sub>3</sub>Sb<sub>4</sub> compound experiences bipolar conduction resulting in a downturn in the Seebeck coefficient below 550 K. The *n*-type thermoelectric properties of this compound have been studied via Te doping on the Sb site (Zr<sub>3</sub>Ni<sub>3</sub>Sb<sub>4-x</sub>Te<sub>x</sub>;  $x = 0.025, 0.05, 0.1, 0.2$ ), Cu doping on the Ni site (Zr<sub>3</sub>Ni<sub>3-x</sub>Cu<sub>x</sub>Sb<sub>4</sub>;  $x = 0.1, 0.3, 0.5$ ), and Hf doping on the Zr site in conjunction with Cu doping on the Ni site (Zr<sub>2-x</sub>Hf<sub>x</sub>Ni<sub>2.7</sub>Cu<sub>0.3</sub>Sb<sub>4</sub>;  $x = 1, 2, 3$ ). In Fig. 2.5.15, the thermoelectric properties of the compositions with the highest  $zT$ 's are summarized [77, 83, 85]. Slight doping on any site results in a negative Seebeck coefficient along the entire temperature range with the largest Seebeck coefficient belonging to Zr<sub>3</sub>Ni<sub>3</sub>Sb<sub>3.95</sub>Te<sub>0.05</sub>, Fig. 2.5.15A. The resistivity of the parent compound is large and doping reduces the resistivity of the material, Fig. 2.5.15B. The thermal conductivity for Te- and Cu- doped samples is larger at room temperature compared to the undoped and HfCu<sub>0.3</sub>-doped samples, Fig. 2.5.15C. The improvements in the Seebeck coefficient and the resistivity of the material results in a large increase for the  $zT$  of each of the doped compounds, Fig. 2.5.15D. The largest increase is with the Zr<sub>3</sub>Ni<sub>3</sub>Sb<sub>3.95</sub>Te<sub>0.05</sub> doped material showing a maximum  $zT$  of 0.59 at 750 K.

## 2.5.11 Summary and outlook

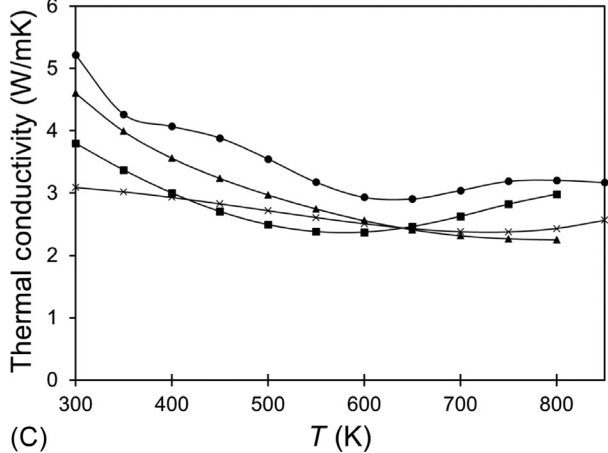
Thermoelectric generators have the potential to provide clean, reliable electricity through waste heat recovery or cogeneration. As current generator efficiencies are insufficient for widespread application, new and optimized thermoelectric materials hold the key as the primary enabling component. Material improvements have been challenging because of the interdependent nature of the Seebeck coefficient, electrical resistivity, and thermal conductivity through the free carrier concentration. There are a wide variety of materials that are under investigation for thermoelectric applications. Zintl phases, in particular, have several features, such as the combination of ionic and covalent bonding and their complex structures that make them ideal candidates for thermoelectric materials. Since many complex Zintl phases have low thermal conductivity, most of the effort on optimization can focus on carrier concentration and bandgap engineer. Tuning the electronics by isovalent or alio-valent elements is one strategy for these phases which tend to have very low thermal conductivity due to the complexity of the structure. Iso-valent substitutions within a periodic group allow for subtle tuning whereas electrons or holes can be added via Period ±1 elemental substitutions. In effect, there is a “small knob” and a “large knob” for electron tuning in Zintl phases. Clearly, while the Zintl concept provides an initial starting point for considering how to tune compounds, more advanced theoretical investigations are necessary to provide insight for further advancement. The potential for new discoveries within this classification of compounds is great, as it is the latest addition to



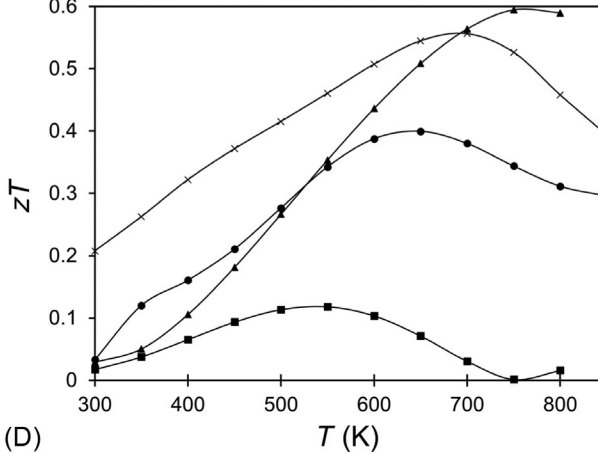
(A)  $T$  (K)



(B)  $T$  (K)



(C)  $T$  (K)



(D)  $T$  (K)

**Fig. 2.5.15** (A) Seebeck coefficient, (B) electrical resistivity, (C) thermal conductivity, and (D)  $zT$  of the compositions with the highest resulting  $zT$ , from each  $n$ -type doping study [77, 83, 85].

materials for thermoelectric applications. The ideas of Zintl and the progress in structure and bonding will lend themselves to many more discoveries. There are still many opportunities to discover more efficient thermoelectric materials as many compositions have not been investigated. The surprising discovery of *n*-type behavior [86] for Mg<sub>3</sub>Sb<sub>2</sub> also suggests that successes in *n*-type doping are likely to progress further in this area.

The structure types described herein are good starting places for further efforts to discover high efficiency thermoelectrics. Each has a significant number of combinations of elements that will lead to changes in the DOS, bandgap, and therefore, the resulting thermoelectric properties. Considering the few exciting materials discovered to date, there is a high probability that new Zintl compounds will be discovered with even more promising thermoelectric properties and that rational design will yield even higher efficiency materials.

## Acknowledgments

The authors thank the National Science Foundation, which has funded the majority of the Zintl crystal chemistry research in the Kauzlarich group. Currently, the research on Zintl phases is supported through DMR-1709382 and DMR-2001156-0. The authors also thank the groups of Jean-Pierre Fleurial and Sabah K. Bux at the Jet Propulsion Laboratory (JPL) and current and past members of the JPL Advanced ThermOelectric Materials (ATOM) and Fundamental Advanced Thermoelectric Materials (FANTOM) projects for insight and useful discussion.

## References

- [1] N. Kazem, S.M. Kauzlarich, Thermoelectric properties of zintl antimonides, in: J.-C. Bünzli, V. Pecharsky (Eds.), *Handbook on the Physics and Chemistry of Rare Earths*, vol. 50, Elsevier, Holland, 2016, pp. 177–208.
- [2] X. Shi, L. Chen, C. Uher, Recent advances in high-performance bulk thermoelectric materials, *Int. Mater. Rev.* 61 (6) (2016) 379–415.
- [3] S.M. Kauzlarich, A. Zevalkink, E. Toberer, G.J. Snyder, Zintl phases: recent developments in thermoelectrics and future outlook, in: I. Nandhakumar, N.M. White, S. Beeby (Eds.), *Thermoelectric Materials and Devices*, vol. 17, The Royal Society of Chemistry, 2017, pp. 1–26.
- [4] J. Shuai, J. Mao, S. Song, Q. Zhang, G. Chen, Z. Ren, Recent progress and future challenges on thermoelectric Zintl materials, *Mater. Today Phys.* 1 (2017) 74–95.
- [5] K.-F. Liu, S.-Q. Xia, Recent progresses on thermoelectric Zintl phases: structures, materials and optimization, *J. Solid State Chem.* 270 (2019) 252–264.
- [6] S.R. Brown, S.M. Kauzlarich, F. Gascoin, G.J. Snyder, Yb<sub>14</sub>MnSb<sub>11</sub>: new high efficiency thermoelectric material for power generation, *Chem. Mater.* 18 (7) (2006) 1873–1877.
- [7] S.M. Kauzlarich, S.R. Brown, G. Jeffrey Snyder, Zintl phases for thermoelectric devices, *Dalton Trans.* 21 (2007) 2099–2107.
- [8] Y. Hu, G. Cerretti, E.L. Kunz Wille, S.K. Bux, S.M. Kauzlarich, The remarkable crystal chemistry of the Ca<sub>14</sub>AlSb<sub>11</sub> structure type, magnetic and thermoelectric properties, *J. Solid State Chem.* 271 (2019) 88–102.

- [9] A. Ovchinnikov, S. Bobev, Zintl phases with group 15 elements and the transition metals: a brief overview of pnictides with diverse and complex structures, *J. Solid State Chem.* 270 (2019) 346–359.
- [10] F. Gascoin, S. Ottensmann, D. Stark, S.M. Haile, G.J. Snyder, Zintl phases as thermoelectric materials: tuned transport properties of the compounds  $\text{Ca}_x\text{Yb}_{1-x}\text{Zn}_2\text{Sb}_2$ , *Adv. Funct. Mater.* 15 (11) (2005) 1860–1864.
- [11] J.-P. Fleurial, Thermoelectric power generation materials: technology and application opportunities, *JOM* 61 (4) (2009) 79–85.
- [12] E.S. Toberer, A.F. May, G.J. Snyder, Zintl chemistry for designing high efficiency thermoelectric materials, *Chem. Mater.* 22 (3) (2010) 624–634.
- [13] K. Guo, Q. Cao, J. Zhao, Zintl phase compounds  $\text{AM}_2\text{Sb}_2$  ( $\text{A} = \text{Ca}, \text{Sr}, \text{Ba}, \text{Eu}, \text{Yb}; \text{M} = \text{Zn}, \text{Cd}$ ) and their substitution variants: a class of potential thermoelectric materials, *J. Rare Earths* 31 (11) (2013) 1029–1038.
- [14] W. Peng, S. Chanakian, A. Zevalkink, Crystal chemistry and thermoelectric transport of layered  $\text{AM}_2\text{X}_2$  compounds, *Inorg. Chem. Front.* 5 (8) (2018) 1744–1759.
- [15] H. Schäfer, B. Eisenmann, W. Müller, Zintl phases: transitions between metallic and ionic bonding, *Angew. Chem. Int. Ed.* 12 (9) (1973) 694–712.
- [16] H. Schäfer, On the problem of polar intermetallic compounds: the stimulation of E. Zintl's work for the modern chemistry of intermetallics, *Annu. Rev. Mater. Sci.* 15 (1985) 1–42.
- [17] R. Hoffmann, C. Zheng, Making and breaking bonds in the solid-state—the THCR<sub>2</sub>Si<sub>2</sub> structure, *J. Phys. Chem.* 89 (20) (1985) 4175–4181.
- [18] S.M. Kauzlarich, A rational approach to solid state synthesis—the Zintl concept, *Comment Inorg. Chem.* 10 (2–3) (1990) 75–88.
- [19] S.M. Kauzlarich, *Chemistry, Structure, and Bonding of Zintl Phases and Ions*, VCH Publishers, Inc., New York, 1996.
- [20] A.V. Shevelkov, K. Kovnir, Zintl clathrates, in: T. Fässler (Ed.), *Struct Bond*, vol. 139, Springer-Verlag, Berlin, 2010, pp. 97–142.
- [21] G.S. Nolas, J.L. Cohn, G.A. Slack, S.B. Schujman, Semiconducting Ge clathrates: promising candidates for thermoelectric applications, *Appl. Phys. Lett.* 73 (2) (1998) 178–180.
- [22] G.S. Nolas, Semiconductor clathrates: a PGEC (Phonon Glass Electron Crystal) system with potential for thermoelectric applications, in: *Materials Research Society Symposium Proceedings*, vol. 545, 1999, pp. 435–442 (Thermoelectric Materials 1998—The Next Generation Materials for Small-Scale Refrigeration and Power Generation Applications).
- [23] B.C. Sales, D. Mandrus, R.K. Williams, Filled skutterudite antimonides: a new class of thermoelectric materials, *Science (Washington, DC)* 272 (5266) (1996) 1325–1328.
- [24] G.S. Nolas, M. Kaeser, R.T.I. Littleton, T.M. Tritt, High figure of merit in partially filled ytterbium skutterudite materials, *Appl. Phys. Lett.* 77 (12) (2000) 1855–1857.
- [25] H. Luo, J.W. Krizan, L. Muechler, N. Haldolaarachchige, T. Klimczuk, W. Xie, M.K. Fuccillo, C. Felser, R.J. Cava, A large family of filled skutterudites stabilized by electron count, *Nat. Commun.* 6 (2015) 6489.
- [26] R. Kniep, Introduction Eduard Zintl: his life and scholarly work, in: S.M. Kauzlarich (Ed.), *Chemistry, Structure, and Bonding of Zintl Phases and Ions*, VCH Publishers, Inc., New York, 1996, pp. xvii–xxx.
- [27] R. Nesper, The Zintl-Klemm concept – a historical survey, *Z. Anorg. Allg. Chem.* 640 (14) (2014) 2639–2648.
- [28] J. Wang, J. Mark, K.E. Woo, J. Voyles, K. Kovnir, Chemical flexibility of mg in Pnictide materials: structure and properties diversity, *Chem. Mater.* 31 (20) (2019) 8286–8300.
- [29] B. Eisenmann, H. Jordan, H. Schäfer,  $\text{Ba}_4\text{SiAs}_4$  and  $\text{Ba}_4\text{GeAs}_4$ , Zintl phases with isolated  $\text{SiAs}_4^{8-}$  and  $\text{GeAs}_4^{8-}$  anions, *Angew. Chem. Int. Ed. Engl.* 20 (2) (1981) 197–198.

- [30] W. Jeitschko, M. Reehuis, Zintl counting with transition metals, *J. Phys. Chem. Solids* 48 (1987) 667.
- [31] S.M. Kauzlarich, T.Y. Kuromoto, M.M. Olmstead, Preparation and structure of a new ternary transition-metal Zintl compound containing high spin Mn(III) $\text{Bi}_4$  tetrahedra, *J. Am. Chem. Soc.* 111 (20) (1989) 8041–8042.
- [32] S.M. Kauzlarich, Transition metal Zintl compounds, in: S.M. Kauzlarich (Ed.), *Chemistry, Structure, and Bonding of Zintl Phases and Ions*, VCH Publishers, Inc., New York, 1996, pp. 245–274.
- [33] W.G. Zeier, A. Zevalkink, Z.M. Gibbs, G. Hautier, M.G. Kanatzidis, G.J. Snyder, Thinking like a chemist: intuition in thermoelectric materials, *Angew. Chem.* 55 (24) (2016) 6826–6841.
- [34] G. Tan, L.D. Zhao, M.G. Kanatzidis, Rationally designing high-performance bulk thermoelectric materials, *Chem. Rev.* 116 (19) (2016) 12123–12149.
- [35] J. Zhang, L. Song, B.B. Iversen, Insights into the design of thermoelectric Mg<sub>3</sub>Sb<sub>2</sub> and its analogs by combining theory and experiment, *npj Comput. Mater.* 5 (1) (2019).
- [36] Y. Grin, Inhomogeneity and anisotropy of chemical bonding and thermoelectric properties of materials, *J. Solid State Chem.* 274 (2019) 329–336.
- [37] X.-J. Wang, M.-B. Tang, H.-H. Chen, X.-X. Yang, J.-T. Zhao, U. Burkhardt, Y. Grin, Synthesis and high thermoelectric efficiency of Zintl phase YbCd<sub>2-x</sub>Zn<sub>x</sub>Sb<sub>2</sub>, *Appl. Phys. Lett.* 94 (9) (2009), 092106.
- [38] E.S. Toberer, A.F. May, B.C. Melot, E. Flage-Larsen, G.J. Snyder, Electronic structure and transport in thermoelectric compounds AZn<sub>2</sub>Sb<sub>2</sub> (A = Sr, Ca, Yb, Eu), *Dalton Trans.* 39 (4) (2010) 1046–1054.
- [39] S.D.N. Luu, P. Vaqueiro, Layered oxychalcogenides: structural chemistry and thermoelectric properties, *J. Mater.* 2 (2) (2016) 131–140.
- [40] J. Li, L.-D. Zhao, J. Sui, D. Berardan, W. Cai, N. Dragoe, BaCu<sub>2</sub>Se<sub>2</sub> based compounds as promising thermoelectric materials, *Dalton Trans.* (2015) 2285–2293.
- [41] X.-J. Wang, M.-B. Tang, J.-T. Zhao, H.-H. Chen, X.-X. Yang, Thermoelectric properties and electronic structure of Zintl compound BaZn<sub>2</sub>Sb<sub>2</sub>, *Appl. Phys. Lett.* 90 (23) (2007) 232107-1–232107-3.
- [42] K. Kihou, H. Nishiate, A. Yamamoto, C.H. Lee, Thermoelectric properties of As-based Zintl compounds Ba<sub>1-x</sub>K<sub>x</sub>Zn<sub>2</sub>As<sub>2</sub>, *Inorg. Chem.* 56 (6) (2017) 3709–3712.
- [43] N. Kazem, S.M. Kauzlarich, J.-C.G. Bünzli, V.K. Pecharsky (Eds.), *Thermoelectric properties of Zintl antimonides*, in: Including Actinides, vol. 50, Elsevier, 2016, pp. 177–208.
- [44] G. Cordier, H. Schafer, M. Stelter, Darstellung und Struktur der Verbindung Ca<sub>14</sub>AlSb<sub>11</sub>, *Z. Anorg. Allg. Chem.* 519 (12) (1984) 183–188.
- [45] E.S. Toberer, C.A. Cox, S.R. Brown, T. Ikeda, A.F. May, S.M. Kauzlarich, G.J. Snyder, Traversing the metal-insulator transition in a Zintl phase: rational enhancement of thermoelectric efficiency in Yb<sub>14</sub>Mn<sub>1-x</sub>Al<sub>x</sub>Sb<sub>11</sub>, *Adv. Funct. Mater.* 18 (18) (2008) 2795–2800.
- [46] J.H. Grebenkemper, Y.F. Hu, D. Barrett, P. Gogna, C.K. Huang, S.K. Bux, S.M. Kauzlarich, High temperature thermoelectric properties of Yb<sub>14</sub>MnSb<sub>11</sub> prepared from reaction of MnSb with the elements, *Chem. Mater.* 27 (16) (2015) 5791–5798.
- [47] Y. Hu, J. Wang, A. Kawamura, K. Kovnir, S.M. Kauzlarich, Yb<sub>14</sub>MgSb<sub>11</sub> and Ca<sub>14</sub>MgSb<sub>11</sub>—new mg-containing Zintl compounds and their structures, bonding, and thermoelectric properties, *Chem. Mater.* 27 (1) (2014) 343–351.
- [48] W. Tan, Z. Wu, M. Zhu, J. Shen, T. Zhu, X. Zhao, B. Huang, X.T. Tao, S.Q. Xia, A<sub>14</sub>MgBi<sub>11</sub> (A = Ca, Sr, Eu): magnesium bismuth based Zintl phases as potential thermoelectric materials, *Inorg. Chem.* 56 (17) (2017) 10576–10583.

- [49] A. Möchel, I. Sergueev, H.C. Wille, F. Juranyi, H. Schober, W. Schweika, S.R. Brown, S.M. Kauzlarich, R.P. Hermann, Lattice dynamics in the thermoelectric Zintl compound  $\text{Yb}_{14}\text{MnSb}_{11}$ , Phys. Rev. B 84 (18) (2011) 184303.
- [50] G.P. Meisner, D.T. Morelli, S. Hu, J. Yang, C. Uher, Structure and lattice thermal conductivity of fractionally filled skutterudites: solid solutions of fully filled and unfilled end members, Phys. Rev. Lett. 80 (16) (1998) 3551–3554.
- [51] F.R. Yu, J.J. Zhang, D.L. Yu, J.L. He, Z.Y. Liu, B. Xu, Y.J. Tian, Enhanced thermoelectric figure of merit in nanocrystalline  $\text{Bi}_2\text{Te}_3$  bulk, J. Appl. Phys. 105 (9) (2009), 094303.
- [52] O. Yamashita, N. Sadatomi, Thermoelectric properties of  $\text{Si}_{1-x}\text{Ge}_x$  ( $x \leq 0.10$ ) with alloy and dopant segregations, J. Appl. Phys. 88 (1) (2000) 245–251.
- [53] S.R. Brown, E.S. Toberer, T. Ikeda, C.A. Cox, F. Gascoin, S.M. Kauzlarich, G.J. Snyder, Improved thermoelectric performance in  $\text{Yb}_{14}\text{Mn}_{1-x}\text{Zn}_x\text{Sb}_{11}$  by the reduction of spin-disorder scattering, Chem. Mater. 20 (10) (2008) 3412–3419.
- [54] E.S. Toberer, S.R. Brown, T. Ikeda, S.M. Kauzlarich, G. Jeffrey Snyder, High thermoelectric efficiency in lanthanum doped  $\text{Yb}_{14}\text{MnSb}_{11}$ , Appl. Phys. Lett. 93 (6) (2008), 062110.
- [55] C.A. Cox, S.R. Brown, G.J. Snyder, S.M. Kauzlarich, Effect of Ca doping on the thermoelectric performance of  $\text{Yb}_{14}\text{MnSb}_{11}$ , J. Electron. Mater. 39 (9) (2010) 1373–1375.
- [56] T.H. Yi, M.N. Abdusalyamova, F. Makhmudov, S.M. Kauzlarich, Magnetic and transport properties of Te doped  $\text{Yb}_{14}\text{MnSb}_{11}$ , J. Mater. Chem. 22 (29) (2012) 14378–14384.
- [57] Y.F. Hu, S.K. Bux, J.H. Grebenkemper, S.M. Kauzlarich, The effect of light rare earth element substitution in  $\text{Yb}_{14}\text{MnSb}_{11}$  on thermoelectric properties, J. Mater. Chem. C 3 (40) (2015) 10566–10573.
- [58] J.H. Grebenkemper, S. Klemenz, B. Albert, S.K. Bux, S.M. Kauzlarich, Effects of Sc and Y substitution on the structure and thermoelectric properties of  $\text{Yb}_{14}\text{MnSb}_{11}$ , J. Solid State Chem. 242 (2016) 55–61.
- [59] A.P. Justl, G. Cerretti, S.K. Bux, S.M. Kauzlarich, Hydride assisted synthesis of the high temperature thermoelectric phase:  $\text{Yb}_{14}\text{MgSb}_{11}$ , J. Appl. Phys. 126 (16) (2019) 165106.
- [60] E.L. Kunz Wille, N.S. Grewal, S.K. Bux, S.M. Kauzlarich, Seebeck and figure of Merit enhancement by rare earth doping in  $\text{Yb}_{14-x}\text{RE}_x\text{ZnSb}_{11}$  ( $x = 0.5$ ), Materials (Basel) 12 (5) (2019) 731.
- [61] G. Rogl, P. Rogl, How nanoparticles can change the figure of merit, ZT, and mechanical properties of skutterudites, Mater. Today Phys. 3 (2017) 48–69.
- [62] W.S. Liu, X. Yan, G. Chen, Z.F. Ren, Recent advances in thermoelectric nanocomposites, Nano Energy 1 (1) (2012) 42–56.
- [63] G. Cerretti, O. Villalpando, J.P. Fleurial, S.K. Bux, Improving electronic properties and mechanical stability of  $\text{Yb}_{14}\text{MnSb}_{11}$  via W compositing, J. Appl. Phys. 126 (17) (2019) 175102.
- [64] D.K. Wilson, B. Saparov, S. Bobev, Synthesis, crystal structures and properties of the Zintl phases  $\text{Sr}_2\text{ZnP}_2$ ,  $\text{Sr}_2\text{ZnAs}_2$ ,  $\text{A}_2\text{ZnSb}_2$  and  $\text{A}_2\text{ZnBi}_2$  ( $\text{A} = \text{Sr}$  and  $\text{Eu}$ ), Z. Anorg. Allg. Chem. 637 (13) (2011) 2018–2025.
- [65] S.-Q. Xia, S. Bobev, Cation-anion interactions as structure directing factors: structure and bonding of  $\text{Ca}_2\text{CdSb}_2$  and  $\text{Yb}_2\text{CdSb}_2$ , J. Am. Chem. Soc. 129 (13) (2007) 4049–4057.
- [66] J. Wang, M. Yang, M.Y. Pan, S.Q. Xia, X.T. Tao, H. He, G. Darone, S. Bobev, Synthesis, crystal and electronic structures, and properties of the new pnictide semiconductors  $\text{A}_2\text{CdPn}_2$  ( $\text{A} = \text{Ca}, \text{Sr}, \text{Ba}, \text{Eu}; \text{Pn} = \text{P}, \text{As}$ ), Inorg. Chem. 50 (17) (2011) 8020–8027.
- [67] B. Saparov, M. Saito, S. Bobev, Syntheses, and crystal and electronic structures of the new Zintl phases  $\text{Na}_2\text{ACdSb}_2$  and  $\text{K}_2\text{ACdSb}_2$  ( $\text{A} = \text{Ca}, \text{Sr}, \text{Ba}, \text{Eu}, \text{Yb}$ ): structural relationship with  $\text{Yb}_2\text{CdSb}_2$  and the solid solutions  $\text{Sr}_{2-x}\text{A}_x\text{CdSb}_2$ ,  $\text{Ba}_{2-x}\text{A}_x\text{CdSb}_2$  and  $\text{Eu}_{2-x}\text{Yb}_x\text{CdSb}_2$ , J. Solid State Chem. 184 (2) (2011) 432–440.

- [68] B. Saparov, S. Bobev, Isolated (1)(infinity) ZnPn(2) (4-) chains in the Zintl phases Ba(2) ZnPn(2) (Pn = As, Sb, Bi)-synthesis, structure, and bonding, *Inorg. Chem.* 49 (11) (2010) 5173–5179.
- [69] J.A. Cooley, P. Promkhan, S. Gangopadhyay, D. Donadio, W.E. Pickett, B.R. Ortiz, E.S. Toberer, S.M. Kauzlarich, High seebeck coefficient and unusually low thermal conductivity near ambient temperatures in layered compound  $Yb_{2-x}Eu_xCdSb_2$ , *Chem. Mater.* 30 (2) (2018) 484–493.
- [70] W. Khan, J. Minar, Theoretical study on optical and thermoelectric properties of the direct band gap [small alpha]/[small beta]-Ca<sub>2</sub>CdAs<sub>2</sub> pnictide semiconductors, *RSC Adv.* 4 (87) (2014) 46791–46799.
- [71] S.-M. Park, S.-J. Kim, Sr<sub>11</sub>Cd<sub>6</sub>Sb<sub>12</sub>: a new Zintl compound with infinite chains of pentagonal tubes, *J. Solid State Chem.* 177 (10) (2004) 3418–3422.
- [72] N. Kazem, W. Xie, S. Ohno, A. Zevalkink, G.J. Miller, G.J. Snyder, S.M. Kauzlarich, High-temperature thermoelectric properties of the solid-solution Zintl phase Eu<sub>11</sub>Cd<sub>6</sub>Sb<sub>12-x</sub>As<sub>x</sub> (x < 3), *Chem. Mater.* 26 (3) (2014) 1393–1403.
- [73] N. Kazem, A. Hurtado, F. Sui, S. Ohno, A. Zevalkink, J.G. Snyder, S.M. Kauzlarich, High temperature thermoelectric properties of the solid-solution Zintl phase Eu<sub>11</sub>Cd<sub>6-x</sub>Zn<sub>x</sub>Sb<sub>12</sub>, *Chem. Mater.* 27 (12) (2015) 4413–4421.
- [74] N. Kazem, J. Cooley, E.C. Burks, K. Liu, S.M. Kauzlaricht, Synthesis, characterization, and low temperature transport properties of Eu<sub>11-x</sub>Yb<sub>x</sub>Cd<sub>6</sub>Sb<sub>12</sub> solid-solution Zintl phases, *Inorg. Chem.* 55 (23) (2016) 12230–12237.
- [75] S.-Q. Xia, S. Bobev, Are Ba<sub>11</sub>Cd<sub>6</sub>Sb<sub>12</sub> and Sr<sub>11</sub>Cd<sub>6</sub>Sb<sub>12</sub> Zintl phases or not? A density-functional theory study, *J. Comput. Chem.* 29 (13) (2008) 2125–2133.
- [76] E.S. Toberer, A.F. May, C.J. Scanlon, G.J. Snyder, Thermoelectric properties of p-type LiZnSb: assessment of ab initio calculations, *J. Appl. Phys.* 105 (6) (2009), 063701.
- [77] Z.H. Liu, J. Mao, S.Y. Peng, B.Q. Zhou, W.H. Gao, J.H. Sui, Y.Z. Pei, Z.F. Ren, Tellurium doped n-type Zintl Zr<sub>3</sub>Ni<sub>3</sub>Sb<sub>4</sub> thermoelectric materials: balance between carrier-scattering mechanism and bipolar effect, *Mater. Today Phys.* 2 (2017) 54–61.
- [78] P. Gorai, A. Goyal, E.S. Toberer, V. Stevanovic, A simple chemical guide for finding novel n-type dopable Zintl pnictide thermoelectric materials, *J. Mater. Chem. A* 7 (33) (2019) 19385–19395.
- [79] G. Cordier, H. Ochmann, Crystal-structure of potassium Tecto-Tetraantimonidogallate, KGaSb<sub>4</sub>, *Z. Kristallogr.* 195 (3–4) (1991) 306–307.
- [80] B.R. Ortiz, P. Gorai, V. Stevanovic, E.S. Toberer, Thermoelectric performance and defect chemistry in n-type Zintl KGaSb<sub>4</sub>, *Chem. Mater.* 29 (10) (2017) 4523–4534.
- [81] G. Cordier, H. Ochmann, Crystal-structure of potassium tecto-tetraantimonidoaluminate, KAlSb<sub>4</sub>, *Z. Kristallogr.* 195 (3–4) (1991) 308–309.
- [82] B.R. Ortiz, P. Gorai, L. Krishna, R. Mow, A. Lopez, R. McKinney, V. Stevanovic, E.S. Toberer, Potential for high thermoelectric performance in n-type Zintl compounds: a case study of Ba doped KAlSb<sub>4</sub>, *J. Mater. Chem. A* 5 (8) (2017) 4036–4046.
- [83] H. Tamaki, T. Kanno, A. Sakai, K. Takahashi, Y. Yamada, Thermoelectric properties and electronic transport analysis of Zr<sub>3</sub>Ni<sub>3</sub>Sb<sub>4</sub>-based solid solutions, *J. Appl. Phys.* 118 (5) (2015), 055103.
- [84] M. Wang, R. McDonald, A. Mar, M<sub>3</sub>Ni<sub>3</sub>Sb<sub>4</sub> (M = Zr, Hf) and Zr<sub>3</sub>Pt<sub>3</sub>Sb<sub>4</sub> ternary antimonides with the Y<sub>3</sub>Au<sub>3</sub>Sb<sub>4</sub> structure, *Inorg. Chem.* 38 (14) (1999) 3435–3438.
- [85] J.R. Salvador, X. Shi, J. Yang, H. Wang, Synthesis and transport properties of M<sub>3</sub>Ni<sub>3</sub>Sb<sub>4</sub> (M=Zr and Hf): an intermetallic semiconductor, *Phys. Rev. B* 77 (23) (2008) 235217.
- [86] H. Tamaki, H.K. Sato, T. Kanno, Isotropic conduction network and defect chemistry in Mg<sup>3+</sup>delta Sb<sup>2-</sup>-based layered Zintl compounds with high thermoelectric performance, *Adv. Mater.* 28 (46) (2016) 10182–10187.

# High-performance sulfide thermoelectric materials

2.6

*Anthony V Powell*

Department of Chemistry, University of Reading, Reading, United Kingdom

## 2.6.1 Introduction

The efficiency of a thermoelectric (TE) device is directly related to the performance of the TE materials of which it is composed. This is embodied in a dimensionless figure of merit,  $ZT = S^2\sigma T/\kappa$ , comprising the Seebeck coefficient ( $S$ ), electrical conductivity ( $\sigma$ ), and thermal conductivity ( $\kappa$ ). Thermal conductivity has contributions from the lattice vibrations ( $\kappa_L$ ) and charge carriers ( $\kappa_e$ ). The contributions to  $ZT$  cannot be independently optimized, presenting considerable challenges in the design of high-performance materials. Commercial TE devices are based on  $\text{Bi}_2\text{Te}_3$ , with a maximum figure of merit ( $(ZT)_{\max} \approx 1$ ) close to ambient temperature. Performance falls off at higher temperatures, making  $\text{Bi}_2\text{Te}_3$ -based devices unsuitable for energy-recovery applications in the medium-to-high temperature range. This has stimulated a growth in the search for new, high-performance materials for TE applications at elevated temperatures. Much of the recent interest in materials for use in the technologically important region of  $373 \leq T/K \leq 573$ , where *ca.* 80% of waste heat from industrial processes is released [1], has focused on sulfides. This has been driven in part by the much greater terrestrial abundance of sulfur (*ca.*  $10^5$  ppb) compared to tellurium (1 ppb) [2].

The relatively low mass of sulfur gives rise to higher vibrational frequencies in solid-state sulfides, making attainment of low thermal conductivities more challenging than in the heavier congeners. The relatively high electronegativity of sulfur, results in narrower bands and thus a higher effective mass of carriers, than in the corresponding selenides and tellurides. Despite its relatively low atomic mass, the polarizability of the sulfide anion is high, giving rise to a pronounced bonding anisotropy, reflected in the adoption of a variety of low-dimensional structures. Low dimensionality may confer advantages in achieving high Seebeck coefficients [3], due to the highly structured density of states (DOS). The Mott relationship [4] relates the Seebeck coefficient to the derivative of the DOS at the Fermi level ( $E_F$ ). Tuning  $E_F$  to a discontinuity in the DOS can thus enhance the Seebeck coefficient, although in bulk materials reductions in thermal conductivity due to interface scattering of phonons may play a more dominant role. The highly polarizable sulfide anion also favors cation diffusion. Above a critical temperature, this may lead to the cation sublattice entering a liquid-like state within an effectively rigid anion matrix. The description phonon-liquid electron crystal (PLEC) has been applied to such materials, which show substantial reductions in thermal conductivity.

These properties of the sulfide anion provide the basis for a number of TE materials design strategies [5]. Examples of materials created using such approaches are presented in this chapter, the focus of which is necessarily on a subset of materials. Broader coverage of the families of sulfide thermoelectric is provided by a number of recent reviews [6–10].

## 2.6.2 Low-dimensional sulfides

### 2.6.2.1 Layered materials

The tendency to low dimensionality is exemplified by the layered structures of the transition-metal dichalcogenides, in which slabs of edge-sharing metal-centered octahedra (or trigonal prisms) are stacked in a direction perpendicular to the slabs. The van der Waals' interactions between  $\text{MS}_2$  units are weak, enabling guest species to be readily inserted within the interlayer gap by expansion of the interlayer space. This provides a means of tuning charge-carrier concentrations with minimal structural perturbation.

The electrical transport properties of single crystals of  $\text{TiS}_2$  are competitive with those of  $\text{Bi}_2\text{Te}_3$  [11]. Although the in-plane power factor reaches *ca.* 64% that of  $\text{Bi}_2\text{Te}_3$ , the relatively high in-plane thermal conductivity of  $6.8 \text{ W m}^{-1} \text{ K}^{-1}$  substantially reduces the figure of merit ( $ZT \approx 0.16$  at 300 K) from that of  $\text{Bi}_2\text{Te}_3$ . This has stimulated efforts to exploit chemical substitution to improve the electron-transport properties and reduce the thermal conductivity of  $\text{TiS}_2$ . Mass fluctuation in phases of the form  $\text{Ti}_{1-x}\text{M}_x\text{S}_2$  ( $\text{M} = \text{Nb}$  [12],  $\text{Ta}$  [13]) has been used to effect reductions in thermal conductivity, while intercalation (Fig. 2.6.1) provides a means of tuning the charge-carrier density.  $\text{TiS}_2$  commonly exhibits self-intercalation ( $\text{Ti}_{1+x}\text{S}_2$ ) whereby excess titanium cations are accommodated in the van der Waals' gap [14]. The resulting charge transfer to  $t_{2g}$ -derived bands has an impact on the electron-transport properties. Disorder of the intercalated titanium ions increases phonon scattering, reducing thermal conductivity, enabling the figure of merit to reach  $(ZT)_{\max} = 0.48$  at 700 K for  $x = 0.025$ .

While the increased carrier concentration, resulting from charge transfer from the guest ion to the  $\text{TiS}_2$  host, increases the electrical conductivity, it simultaneously reduces the Seebeck coefficient and also increases  $\kappa_e$ . These changes compete with the reduction in  $\kappa_L$ , arising from the structural disorder of guest species introduced into the interlayer space. The optimum TE properties are therefore generally found at low levels of intercalation, where the balance between the deleterious impact of the increased carrier concentration and the beneficial effects of structural disorder is optimized. This is exemplified by the *n*-type materials  $\text{Co}_x\text{TiS}_2$  ( $0.0 \leq x \leq 0.75$ ) [15], which with increasing cobalt content, progress from a disordered array of cobalt ions in the interlayer space to a series of vacancy-ordered phases. At cobalt contents  $x > 0.1$ , the reduction in thermal conductivity is insufficient to compensate for the decrease in power factors ( $S^2\sigma$ ), which reach values  $< 0.5 \mu\text{W cm}^{-1} \text{ K}^{-2}$  at 300 K. However, at lower levels of cobalt intercalation ( $x < 0.1$ ) the reduction in  $\kappa_L$ , due to

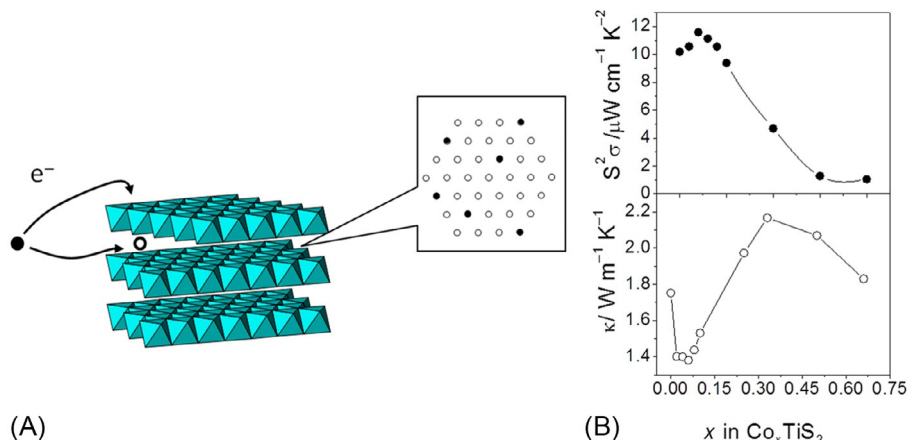


**Fig. 2.6.1** (A) The two-dimensional structure of  $\text{TiS}_2$  illustrating the competing factors of electron transfer to the host, which increases electrical (and thermal) conductivity but decreases the Seebeck coefficient, and the disorder of the guest in the interlayer space, which reduces  $\kappa_L$ . (B) Compositional dependence of the in-plane power factors for  $\text{Co}_x\text{TiS}_2$  at 575 K (upper plot) and cross-plane thermal conductivity (lower plot) illustrating the competition between the two contributions to  $ZT$ .

disorder, outweighs the increase in  $\kappa_e$  due to increased carrier concentration and the total thermal conductivity is reduced. Compositions in the range  $0.04 \leq x \leq 0.08$  exhibit the relatively high value, for an  $n$ -type sulfide, of  $(ZT)_{\max} = 0.30$  at 573 K.

Similar levels of performance are achieved in  $\text{Cu}_x\text{TiS}_2$  ( $0.02 \leq x \leq 0.1$ ) consolidated by Spark Plasma Sintering (SPS) to create high-density monoliths [16], for which  $(ZT)_{\max} = 0.46$  at 825 K has been reported for  $\text{Cu}_{0.1}\text{TiS}_2$ . Similarly, the intercalation of silver increases the figure of merit to  $(ZT)_{\max} = 0.45$  at 700 K for compositions,  $\text{Ag}_x\text{TiS}_2$ , in the range  $0.02 \leq x \leq 0.1$  [17]. While it has been reported that intercalation of Bi, [18], Gd [19], and Nd [20] also enhances the figure of merit, the baseline performance of the binary sulfide is poorer than that reported in other studies, suggesting the samples may not be fully dense. Efforts to incorporate tin [21] result in the formation of trace amounts of a material,  $(\text{SnS})_{1+m}(\text{TiS}_{2-\delta})_n$ , with a misfit layered structure. The figure of merit is increased to  $(ZT)_{\max} = 0.46$  at 623 K for 5 mol% tin incorporation, principally due to a marked increase in electrical conductivity.

Investigation of materials with reduced dimensionality has extended to a variety of alternative structure types, including layered SnS ( $(ZT)_{\max} = 0.8$  at 873 K) [22],  $\text{Cs}_{1.43}\text{Cd}_{1.43}\text{Bi}_{2.57}\text{S}_6$  [23], which exhibits a low thermal conductivity ( $< 0.5 \text{ W m}^{-1} \text{ K}^{-1}$ ) but relatively high resistivity,  $\text{CuCrS}_2$ , for which there are conflicting reports of thermoelectric performance [24–26] and materials in the pavonite family, including  $\text{Cd}_2\text{Pb}_2\text{Bi}_4\text{S}_9$  ( $(ZT)_{\max} = 0.53$  at 775 K) [27]. A recent example of a pavonite-related material is provided by the  $n$ -type  $\text{ABi}_4\text{S}_7$  ( $\text{A} = \text{Fe}, \text{Mn}$ ) [28] phases. The structure (Fig. 2.6.2A) contains  $\text{AS}_6$  octahedra that share vertices with  $\text{BiS}_6$  octahedra and edges with  $\text{BiS}_5$  square pyramids. The sulfur vertex common to  $\text{AS}_6$  and  $\text{BiS}_6$  octahedra

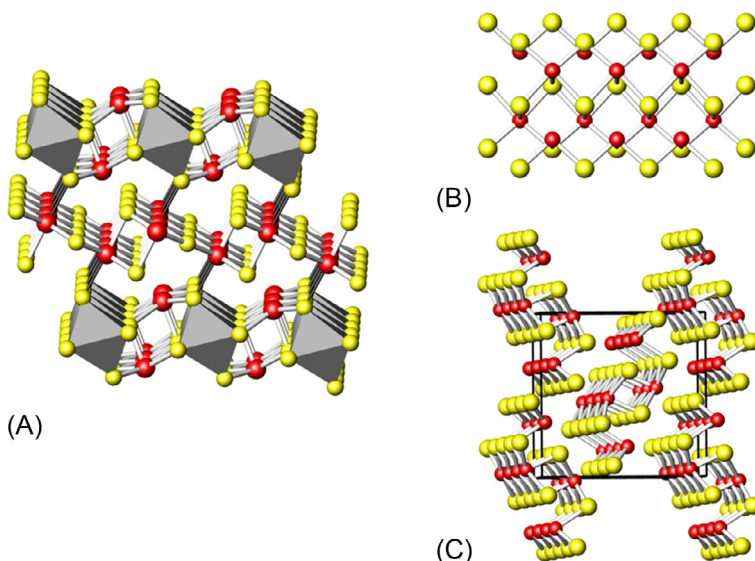


**Fig. 2.6.2** Low dimensionality in the structures of  $\text{MnBi}_4\text{S}_7$  and  $\text{Bi}_2\text{S}_3$ . (A) The structure of  $\text{MnBi}_4\text{S}_7$  viewed along [010] in which two-dimensional units are linked through longer Bi-S interactions shown as solid lines. (B) A single chain of  $\text{Bi}_2\text{S}_3$  viewed along [110] and (C) the structure of  $\text{Bi}_2\text{S}_3$  viewed along [001], with the unit cell outlined. Key: bismuth, solid circles; sulfur open circles; manganese-centered octahedra are shaded in (A).

is located at a relatively long Bi-S distance. This confers layer-like characteristics on the structure. A combination of a low-symmetry layered structure, strong bond anharmonicity and low-energy optic modes, contribute to a low thermal conductivity ( $< 1 \text{ W m}^{-1} \text{ K}^{-1}$  in the range  $300 \leq T/\text{K} \leq 700$ ). The anharmonicity may be associated with a stereochemically active electron lone pair of  $\text{Bi}^{3+}$ . Band structure calculations reveal the presence of a mixture of heavy and light bands near the conduction band minimum. The former contributes to a relatively high Seebeck coefficient, despite a metal-like  $\rho(T)$  behavior. This results in comparatively high power factors, which coupled with the low thermal conductivity, leads to  $(ZT)_{\max} = 0.21$  at 700 K in  $\text{MnBi}_4\text{S}_7$ .

### 2.6.2.2 Bismuth sulfide

Promising TE performance has also been demonstrated in systems of lower dimensionality. For example, the structure of  $\text{Bi}_2\text{S}_3$  (Fig. 2.6.2B) comprises chains of distorted  $\text{BiS}_6$  octahedra (Fig. 2.6.2C) directed along [001]. The pristine material is a semiconductor, with a bandgap,  $E_g \approx 1.3 \text{ eV}$ , resulting in a relatively high electrical resistivity. Efforts have focused on *n*-type doping to enhance TE performance. Doping with  $\text{BiCl}_3$  results in a high degree of anisotropy in the as-prepared ingots [29], which exhibit preferential growth of crystallites along the chain direction. Carrier

concentrations increase monotonically with  $\text{BiCl}_3$  content leading to marked increases in electrical conductivity and power factor (to  $600\text{--}700\,\mu\text{W m}^{-1}\text{ K}^{-1}$  in the range  $300 \leq T/K \leq 700$ ) along the growth direction. Thermal conductivity also decreases, leading to  $(ZT)_{\max} = 0.60$  at 760 K for 0.5 mol% doping. Similar results have been obtained in mechanochemically alloyed samples, consolidated by SPS [30]. Alternative dopants, such as Cu [31] and Ag [32], produce inferior performance to that achieved with Cl, which calculations confirm to be the optimum dopant [33].

### 2.6.2.3 Derivatives of shandite: A pseudo-two-dimensional material

Low dimensionality may manifest itself through the presence of low-dimensional structural motifs within an otherwise three-dimensional structure. For example, phases of general formula,  $\text{A}_3\text{M}_2\text{S}_2$ , ( $\text{A} = \text{Ni, Co, Rh, Pd}$ ;  $\text{M} = \text{Pb, In, Sn, Ti}$ ) related to the mineral shandite, adopt a structure (Fig. 2.6.3A) containing kagome-like  $\text{A}_3\text{M}$  layers, with sulfur atoms located above and below triangular  $\text{A}_3$  units, linked into a three-dimensional structure by additional M atoms at interlayer sites. The two-dimensional character is evident in the highly structured DOS (Fig. 2.6.3B), particularly in the region of  $E_F$ . This may be responsible for the relatively high Seebeck coefficient (*c.*  $50\,\mu\text{V K}^{-1}$ ) of  $\text{Co}_3\text{Sn}_2\text{S}_2$ , despite its metallic character.

The presence of narrow bands of predominantly Co-based *d*-states in the vicinity of  $E_F$  has stimulated efforts to exploit the tuning of  $E_F$  to increase the Seebeck coefficient. Partial replacement of cobalt by either nickel or iron effects electron and hole doping, respectively [34].  $\text{Co}_{3-x}\text{Ni}_x\text{Sn}_2\text{S}_2$  ( $0.0 \leq x \leq 3.0$ ) shows increasingly metallic character with increasing nickel content, resulting in a deterioration of TE properties. By contrast, iron substitution in  $\text{Co}_{3-x}\text{Fe}_x\text{Sn}_2\text{S}_2$  ( $0.0 \leq x \leq 0.6$ ), progressively increases  $|S|$  and reduces  $\sigma$ , producing an increase of up to 30% in power factor at 300 K.  $\kappa_e$  also decreases with iron content, while  $\kappa_L$  is effectively invariant, due to the negligible mass difference between iron and cobalt. The total thermal conductivity is reduced and the figure of merit reaches  $(ZT)_{\max} = 0.2$  at the comparatively modest temperature of 525 K.

Similar levels of improvement in TE properties may be achieved through substitution of the main-group element [35].  $\text{Co}_3\text{Sn}_{2-x}\text{In}_x\text{S}_2$  ( $0 \leq x \leq 2$ ) shows an unusual double metal-to-semiconductor-to-metal transition [36] with increasing indium content, as the upper conduction band is progressively depopulated (Fig. 2.6.3C) and  $E_F$  moves into the band gap at  $x = 1.0$ . At  $x > 1.0$ , holes are created in the valence band and there is a change from *n*-type ( $x < 1.0$ ) to *p*-type ( $x > 1.0$ ) behavior. The marked increase in  $|S|$  as the metal-semiconductor transition is approached, contributes to a significant improvement in the figure of merit (Fig. 2.6.3D), which reaches  $(ZT)_{\max} = 0.32$  at 673 K for  $\text{Co}_3\text{Sn}_{1.6}\text{In}_{0.4}\text{S}_2$ . Simultaneous substitution at the transition-metal and main-group metal sites in series,  $\text{Co}_{3-x}\text{Fe}_x\text{Sn}_{2-y}\text{In}_y\text{S}_2$  [37] also produces improvements in TE performance, with the figure of merit of  $\text{Co}_{2.667}\text{Fe}_{0.333}\text{Sn}_{1.6}\text{In}_{0.4}\text{S}_2$  reaching  $(ZT)_{\max} = 0.29$  at temperatures as low as 573 K.

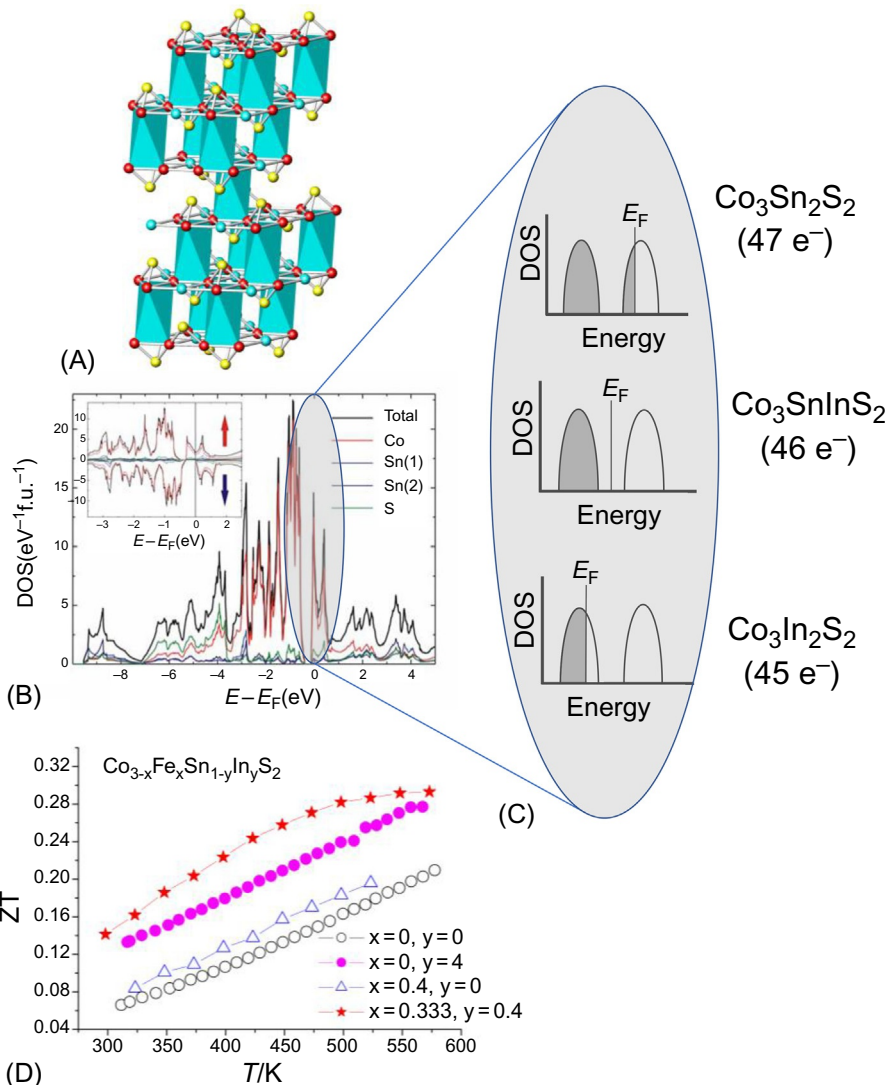


**Fig. 2.6.3** (A) The pseudo-two-dimensional shandite structure adopted by  $\text{Co}_3\text{Sn}_2\text{S}_2$ . (B) The calculated electronic density of states (DOS) of  $\text{Co}_3\text{Sn}_2\text{S}_2$ . (C) Tuning of the Fermi level,  $E_F$ , through progressive substitution of tin by indium, resulting in a change from an  $n$ -type metal (47  $e^-$ ) to a semiconductor (46  $e^-$ ) to a  $p$ -type metal (45  $e^-$ ). (D) Improvements in the thermoelectric figure of merit,  $ZT$ , through tuning of  $E_F$  by chemical substitution at the transition-metal site, main-group metal site and both sites simultaneously.

Figure (B) from Y.S. Dedkov, et al. J. Phys.: Conf. Ser. (2008) 100, 072,011 used under license CC BY 4.0.

## 2.6.3 Phonon-liquid electron crystal and related materials

### 2.6.3.1 Binary copper sulfides and their derivatives

The high TE performance of Cu<sub>2</sub>Se (ZT = 1.5 at 1000 K) [38] has motivated investigations of the sulfide congener, which at high temperatures adopts the same cubic antifluorite structure (Fig. 2.6.4) comprising CuS<sub>4</sub> tetrahedra sharing edges and vertices. The structural chemistry at lower temperatures is complex [39] and temperature-induced structural phase transitions occur at 373 and 743 K. Nonstoichiometry of the form Cu<sub>2-x</sub>S introduces further complexity [40], with both djurleite (0.04 ≤ x ≤ 0.07) and digenite (x ≥ 0.2) structures being observed. All compositions adopt an antifluorite-type structure at high temperature, passing through a sequence of structural phase transitions similar to those of the stoichiometric phase.

Cu<sub>2</sub>S is an intrinsic semiconductor and copper vacancies lead to *p*-type behavior [41]. Increasing hole concentrations increase the electrical conductivity, while suppressing the Seebeck coefficient. The copper content has a less marked effect on thermal conductivity, which remains low (<0.6 W m<sup>-1</sup> K<sup>-1</sup>) for all compositions in the range 0 ≤ x ≤ 0.02. Electronic states near the band edge are little affected by the copper stoichiometry [42] and electrical properties are determined principally by the anion sublattice, suggesting the material behaves as an electron crystal. The weak temperature dependence of thermal conductivity in the high-temperature phase, suggests the emergence of a liquid-like copper sublattice, consistent with PLEC behavior. The remarkable TE performance of Cu<sub>1.97</sub>S ((ZT)<sub>max</sub> = 1.7 at 1000 K) [41] is associated with an exceptionally low lattice thermal conductivity, the origin of which appears

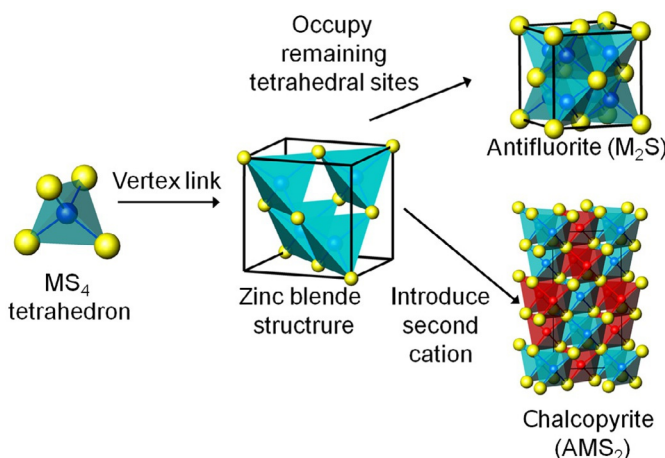


**Fig. 2.6.4** Vertex linking of metal-centered tetrahedra gives rise to the zinc-blende structure, which contains vacant tetrahedral sites, occupation of which by cations produces the antifluorite structure, adopted by Cu<sub>2-x</sub>S phases at elevated temperatures. Ordering of two different cations over the vertex-linked tetrahedra of zinc-blende (denoted by *light* and *dark* shading of tetrahedra) results in the chalcopyrite structure adopted by CuFeS<sub>2</sub>.

to lie in the softness of the shear modes that reduce the transverse phonon velocity and the average speed of sound in the liquid-like state [41]. Significantly, the calculated minimum value of  $\kappa_L$  lies below the minimum thermal conductivity determined from the Cahill formula [43], suggesting that only a fraction of the modes contribute to heat propagation.

The ion mobility that leads to a liquid-like copper sublattice, which contributes to the exceptional TE performance of PLEC-type phases, also creates significant stability problems under device operating conditions. The electric field produced when a device is subjected to a temperature gradient, leads to migration of the mobile copper ions, which deposit at one end of the thermoelement. In the case of Cu<sub>2</sub>S, this leads to compositional changes, cracking, and loss of performance [44]. The more defective digenite (Cu<sub>1.8</sub>S) appears to be more robust, with no evidence for degradation even at high current densities.

Cu<sub>1.8</sub>S prepared mechanochemically and consolidated by SPS [45] exhibits  $(ZT)_{\max} = 0.5$  at 673 K. Consolidation at the higher temperature of 973 K results in a lower thermal conductivity. This is associated with the formation of micro-precipitates of a Cu-rich phase (Cu<sub>1.96</sub>S) and pores with dimensions 100–500 nm, resulting from partial decomposition. Efforts to improve the TE properties of Cu<sub>1.8</sub>S have included doping with sodium [46], titanium [47], and bismuth [48]. Sodium doping enhances the Seebeck coefficient through reductions in carrier concentration and results in the creation of nanopores and nanograins, which reduce the thermal conductivity and increase the figure of merit to  $(ZT)_{\max} = 1.1$  at 773 K in Na<sub>0.01</sub>Cu<sub>1.8</sub>S. Titanium and bismuth produce more modest performance enhancements, with  $(ZT)_{\max} = 0.54$  and 0.61, respectively, at 673 K. In both cases, sulfur volatilization results in the formation of binary and ternary sulfides. Alloying of digenite with small amounts of PbS [49] appears to suppress sulfur volatilization. Electrical transport properties are maintained and the introduction of point defects and interfaces reduces the thermal conductivity. This more than doubles the figure of merit to  $(ZT)_{\max} = 1.1$  at 773 K for Cu<sub>1.8</sub>S containing 2 wt% PbS.

Cu<sub>1.8</sub>S containing 3 wt% of In<sub>2</sub>S<sub>3</sub> exhibits  $(ZT)_{\max} = 1.4$  at 773 K [50]. Powder X-ray diffraction, coupled with electron microscopy, reveals the material is effectively a composite, suggesting that the observed reduction in thermal conductivity is associated with increased interface scattering. Nanocomposites of Cu<sub>1.8</sub>S, incorporating nanoparticulates of a second unrelated phase, including WSe<sub>2</sub> [51], graphene [52], and Bi<sub>2</sub>S<sub>3</sub> and Bi<sub>2</sub>S<sub>3</sub>@Bi core-shell nanorods [53] show a similar effect. Significantly, such composites show greater reproducibility in electrical properties on repeated cycling than the binary sulfides.

### 2.6.3.2 Ternary copper sulfides

In an effort to address the stability problems associated with Cu-ion diffusion, attention has turned to ternary and higher-order materials constructed from CuS<sub>4</sub> tetrahedra [54]. This includes variants of the *n*-type sulfide mineral chalcopyrite, CuFeS<sub>2</sub> (Fig. 2.6.4). Although the TE properties of mineral samples are fairly modest [55, 56], both naturally occurring and synthetic Cu-rich materials possess large Seebeck

coefficients (up to  $|S|=713\,\mu\text{VK}^{-1}$  at 300K), due to a heavy-effective-mass conduction band [57–59]. This reduces mobility and results in a low electrical conductivity. Efforts have focused on the use of chemical substitution to increase the charge-carrier concentration and hence electrical conductivity, albeit with a concomitant reduction in the Seebeck coefficient. TE performance is also limited by the high thermal conductivity ( $\kappa=9.3\,\text{W m}^{-1}\,\text{K}^{-1}$ ) of CuFeS<sub>2</sub>, although calculations indicate that reducing the grain size to  $d\approx20\,\text{nm}$  would decrease this sufficiently to achieve  $ZT=0.8$  at 700K, in an optimally doped material [57].

Efforts to effect control of the carrier concentration through chemical means have included varying the Cu:Fe ratio [60] and the partial substitution of copper [57]. Both Cu<sub>1-x</sub>Fe<sub>1+x</sub>S<sub>2</sub> ( $x=0.03, 0.05$ ) and Zn<sub>0.03</sub>Cu<sub>0.97</sub>FeS<sub>2</sub> retain the *n*-type behavior of the parent phase and power factors are increased almost five-fold from that of the stoichiometric ternary phase. The maximum figure of merit at 400K is limited to  $(ZT)_{\max}=0.07$ , due principally to a thermal conductivity that remains relatively high ( $\kappa\approx6\,\text{W m}^{-1}\,\text{K}^{-1}$ ). Li et al. [61] reported  $(ZT)_{\max}=0.33$  at 700K for Cu<sub>0.97</sub>Fe<sub>1.03</sub>S<sub>2</sub>, arising from reductions in thermal conductivity due to a disordered distribution of iron cations. Theoretical work [62] suggests 3%, may not be the optimum doping level and an increase in power factor by a factor of 2.5 is predicted at lower doping levels (<1%).

The presence of a magnetic ion (Fe<sup>3+</sup>) increases the carrier mass (to 3.5m<sub>0</sub>–5.6m<sub>0</sub>) through interaction with the magnetic moment and also increases scattering of charge carriers. This has stimulated efforts to substitute magnetic ions at the copper site [63, 64] in Cu<sub>1-x</sub>M<sub>x</sub>FeS<sub>2-y</sub> (M=Mn, Co, Ni;  $x\leq0.5$ ;  $y\leq0.02$ ). The manganese-containing phases show the highest figures of merit, with  $(ZT)_{\max}=0.20$  at 623K. Palladium substitution [65] in Cu<sub>1-x</sub>Pd<sub>x</sub>FeS<sub>2</sub> leads at  $x>0.02$  to the formation of microprecipitates of PdS, analogous to the ZnS inclusions identified in Cu<sub>1-x</sub>Zn<sub>x</sub>FeS<sub>2</sub> [66]. The inclusions scatter phonons, thereby reducing  $\kappa_L$ , while the power factor shows little compositional variation at  $x>0.05$  and the figure of merit reaches  $(ZT)_{\max}=0.19$  at 573K for Cu<sub>0.9</sub>Pd<sub>0.1</sub>FeS<sub>2</sub>. Partial substitution of iron by the heavier isovalent element indium has little impact on band structure but reduces  $\kappa_L$  by 60% at the solid solution limit of 8 mol% [67], contributing to a 30% increase in the figure of merit to  $(ZT)_{\max}=0.17$  at 630K. Sulfur deficiency in chalcopyrites improves TE properties and CuFeS<sub>1.80</sub> exhibits  $ZT=0.21$  at 573K [68]. When coupled with the partial replacement of copper by a magnetic cation in Cu<sub>0.98</sub>Co<sub>0.02</sub>FeS<sub>1.98</sub>,  $(ZT)_{\max}$  reaches 0.20 at 673K [63].

Alternative synthesis methods [69–71] have been exploited for the production of nanoparticles of CuFeS<sub>2</sub>. In contrast with the *n*-type conduction of the bulk phase, nanoparticulate forms are *p*-type, suggesting there are deviations from stoichiometry. Alternative approaches to enhancing the TE performance of chalcopyrite-type phases include the use of high-pressure torsion [72] to create defects and dislocations that achieve significant reductions in thermal conductivity and rapid ignition of pelletized mixtures of the elements [73]. A reaction mixture of stoichiometry CuFeS<sub>2.3</sub>, produces a two-phase product with  $(ZT)_{\max}=0.23$  at 625K. This has the characteristics of a nanocomposite; in particular, the enhanced scattering of low-energy phonons that may occur at interfaces between the phases.

Bornite,  $\text{Cu}_5\text{FeS}_4$  adopts a cubic antifluorite-like structure above 540 K [74, 75], in which cation vacancies, and copper and iron cations are statistically distributed over tetrahedral sites (Fig. 2.6.5A). Vacancy ordering on cooling produces a cubic (2a) phase [76], in which zinc blende and antifluorite subcells alternate, doubling each of the unit cell dimensions. Below 460 K, the orthorhombic (4a) structure [77] is stabilized in which the unit cell is quadrupled along the  $b$ -axis (Fig. 2.6.5B).

Stoichiometric  $\text{Cu}_5\text{FeS}_4$  exhibits a remarkably low thermal conductivity ( $<0.5 \text{ W m}^{-1} \text{ K}^{-1}$ ), comparable to that of  $\text{Cu}_{2-x}\text{S}$ , over a wide temperature range [78] and ball-milled samples exhibit  $(ZT)_{\max}=0.55$  at 543 K [79]. The presence of iron on tetrahedral sites appears to suppress Cu-ion migration and a test sample subjected to a constant current shows no signs of the degradation evident in  $\text{Cu}_{2-x}\text{S}$  [78]. Mössbauer and spectroscopic data indicate the formal oxidation states  $\text{Cu}^+$  and  $\text{Fe}^{3+}$  [80], making the stoichiometric phase a semiconductor. Efforts have focused on improving the relatively poor electrical-transport properties by creating holes in the valence band, through chemical substitution. The impact of changing both the carrier

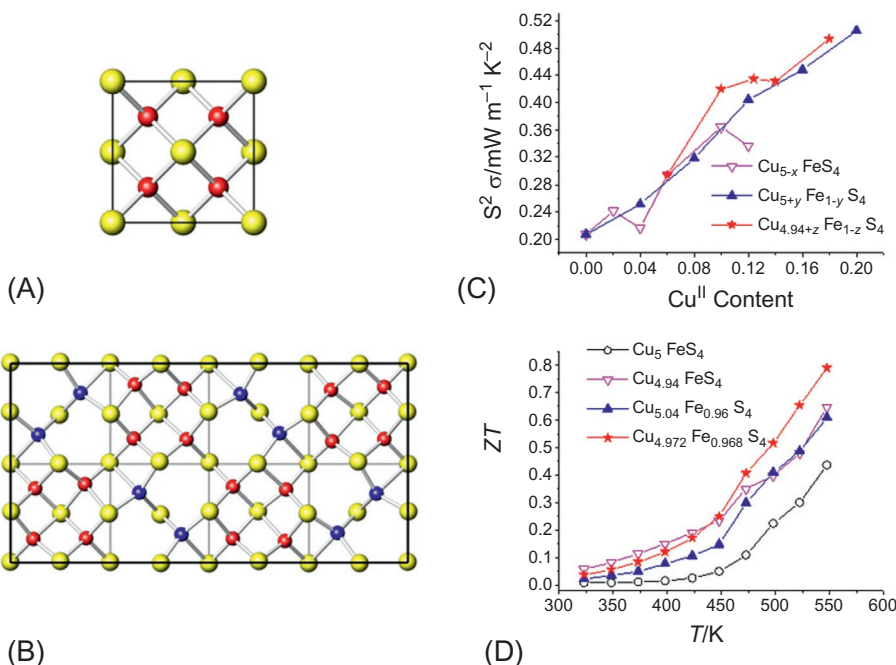


**Fig. 2.6.5** (A) The defective antifluorite structure adopted by  $\text{Cu}_5\text{FeS}_4$  at high temperature, in which there is a disordered distribution of copper and iron cations and cation vacancies at the center of each tetrahedron. (B) The ambient temperature (4a) phase that is adopted below 460 K. Cations within the antifluorite and zinc blende subcells are denoted by small black and gray spheres, respectively, sulfide anions by large white spheres. (C) The near linear dependence of power factor ( $S^2 \sigma$ ) on nominal Cu(II) content for three series of chemically modified bornite-type phases. (D) Temperature dependence of the figure of merit for members of each of the series presented in (C).

and vacancy concentrations has been explored [81] through preparation of nonstoichiometric series  $\text{Cu}_{5-x}\text{FeS}_4$  ( $x \leq 0.1$ ) and  $\text{Cu}_{5+y}\text{Fe}_{1-y}\text{S}_4$  ( $y \leq 0.08$ ) (Fig. 2.6.5). The electrical conductivity increases with increasing numbers of copper vacancies and the figure of merit rises to  $(ZT)_{\max} \approx 0.6$  at 550 K in each series. Further enhancement to  $(ZT)_{\max} = 0.79$  at 550 K is achieved by adjusting the hole concentration, while simultaneously controlling the number of cation vacancies. The highest figures of merit are observed when *ca.* 1% of vacancies are present in materials containing 2%–2.8% of  $\text{Cu}^{2+}$ , producing materials with  $(ZT)_{\max} = 0.79$  at 550 K, among the highest for a sulfide at this temperature. Chemical substitution at both the copper and iron sites of bornite has also been investigated. The figure of merit of  $\text{Cu}_5\text{Fe}_{1-x}\text{Mn}_x\text{S}_4$  [79] is comparable with that of the ternary phase. Partial substitution of copper by both cobalt [82] and zinc [83] has been achieved. The figure of merit of  $\text{Cu}_{4.96}\text{Co}_{0.04}\text{FeS}_4$  reaches  $(ZT)_{\max} = 0.5$  at 590 K. This is increased further through double substitution in  $\text{Cu}_{4.96}\text{Co}_{0.04}\text{Fe}_{0.96}\text{Zn}_{0.04}\text{S}_4$  for which  $(ZT)_{\max} = 0.6$  at 590 K [83].

## 2.6.4 Conclusions

Sulfides are promising candidate materials for thermoelectric applications in the mid-range of temperatures, where it is not possible to use  $\text{Bi}_2\text{Te}_3$  as it degrades. While atmospheric oxidation does not appear to be a significant problem in the probable temperature range of operation, the materials discussed here present challenges in terms of materials stability. In particular, the volatilization of sulfur during synthesis or consolidation commonly occurs, leading to compositional changes and the formation of microprecipitates of secondary phases by exsolution. These may have a beneficial impact on thermal transport properties, through the creation of additional interfaces at which phonons may be scattered. However, partial decomposition introduces questions both over the reproducibility of a given fabrication process and with respect to the long-term stability of a device. Furthermore, PLEC materials exhibit instability due to Cu-ion migration under device operating conditions. The compositional changes that result from deposition of copper, degrade both performance and mechanical integrity. The introduction of nonmobile cations can improve reproducibility of properties, as exemplified by the bornite-related phases.

## References

- [1] T. Kajikawa, in: D.M. Rowe (Ed.), *Thermoelectrics Handbook: Macro to Nano*, CRC Press, Boca Raton, 2006, p. 804. Chapter 50.
- [2] CRC Handbook of Chemistry, Physics, eighty-seventh ed., Taylor & Francis, Boca Raton, 2006.
- [3] L.D. Hicks, M.S. Dresselhaus, *Phys. Rev. B* **47** (1993) 16631.
- [4] N.F. Mott, E.A. Davis, *Electronic Processes in Non-Crystalline Materials*, Clarendon Press, Oxford, 1979.

- [5] A.V. Powell, P. Vaqueiro, in: I. Nandhakumar, N.M. White, S. Beeby (Eds.), *Thermoelectric Materials and Devices*, Royal Society of Chemistry, Cambridge, 2017, p. 27. Chapter 2.
- [6] G.J. Snyder, E.S. Toberer, *Nat. Mater.* 7 (2008) 105.
- [7] K. Suekuni, T. Takabatake, *APL Mater.* 4 (2016) 104503.
- [8] P. Ren, Y. Liu, J. He, T. Lv, J. Gao, G. Xu, *Inorg. Chem. Front.* 5 (2018) 2380.
- [9] Z.-H. Ge, L.-D. Zhao, D. Wu, X. Liu, B.-P. Zhang, J.-F. Li, J. He, *Mater. Today* 19 (2016) 227.
- [10] R. Chetty, A. Bali, R.C. Mallik, *J. Mater. Chem. C* 3 (2015) 12364.
- [11] H. Imai, Y. Shimakawa, Y. Kubo, *Phys. Rev. B* 64 (2001) 241104.
- [12] M. Beaumale, T. Barbier, Y. Bréard, B. Raveau, Y. Kinemuchi, R. Funahashi, E. Guilmeau, *J. Electron. Mater.* 43 (2014) 1590.
- [13] M. Beaumale, T. Barbier, Y. Bréard, S. Hébert, Y. Kinemuchi, E. Guilmeau, *J. Appl. Phys.* 115 (2014), 043704.
- [14] M. Beaumale, T. Barbier, Y. Bréard, G. Guélou, A.V. Powell, P. Vaqueiro, E. Guilmeau, *Acta Mater.* 78 (2014) 86.
- [15] G. Guélou, P. Vaqueiro, J. Prado-Gonjal, T. Barbier, S. Hébert, E. Guilmeau, W. Kockelmann, A.V. Powell, *J. Mater. Chem. C* 4 (2016) 1871.
- [16] E. Guilmeau, Y. Bréard, A. Maignan, *Appl. Phys. Lett.* 99 (2011), 052107.
- [17] T. Barbier, O.I. Lebedev, V. Roddatis, Y. Bréard, A. Maignan, E. Guilmeau, *Dalton Trans.* 44 (2015) 7887.
- [18] D. Li, X.Y. Qin, J. Zhang, L. Wang, H.J. Li, *Solid State Commun.* 135 (2005) 237.
- [19] D. Li, X.Y. Qin, J. Zhang, *J. Mater. Res.* 21 (2006) 480.
- [20] D. Li, X.Y. Qin, J. Zhang, H.J. Li, *Phys. Lett. A* 348 (2006) 379.
- [21] A. Ramakrishnan, S. Raman, L.-C. Chen, K.-H. Chen, *J. Electron. Mater.* 47 (2017) 3091.
- [22] H.-Q. Yang, X.-Y. Wang, H. Wu, B. Zhang, D.D. Xie, Y.J. Chen, X. Lu, X.D. Han, L. Miao, X.Y. Zhou, *J. Mater. Chem. C* 7 (2019) 3351.
- [23] J. Zhao, S.M. Islam, O.Y. Kontsevoi, G. Tan, C.C. Stoumpos, H. Chen, R.K. Li, M.G. Kanatzidis, *J. Am. Chem. Soc.* 139 (2017) 6978.
- [24] G.C. Tewari, T.S. Tripathi, A.K. Rastogi, *J. Electron. Mater.* 39 (2010) 1133.
- [25] Y.X. Chen, B.P. Zhang, Z.H. Ge, P.P. Shang, *J. Solid State Chem.* 186 (2012) 109.
- [26] A. Kaltzoglou, P. Vaqueiro, T. Barbier, E. Guilmeau, A.V. Powell, *J. Electron. Mater.* 43 (2014) 2029.
- [27] J. Zhao, S. Hao, S.M. Islam, H. Chen, G. Tan, S. Ma, C. Wolverton, M.G. Kanatzidis, *Chem. Mater.* 31 (2019) 3430.
- [28] J.-B. Labégorre, A. Virfeu, A. Bourhim, H. Willeman, T. Barbier, F. Appert, J. Juraszek, B. Malaman, A. Huguenot, R. Gautier, V. Nassif, P. Lemoine, C. Prestipino, E. Elkaim, L. Pautrot-d'Alençon, T. Le Mercier, A. Maignan, R.A.R. Al Orabi, E. Guilmeau, *Adv. Func. Mater.* 29 (2019) 1904112.
- [29] K. Biswas, L.-D. Zhao, M.G. Kanatzidis, *Adv. Energy Mater.* 2 (2012) 634.
- [30] X. Du, F. Cai, X. Wang, *J. Alloys Compd.* 587 (2014) 6.
- [31] Z.-H. Ge, B.-P. Xhang, Y. Liu, J.-F. Li, *Phys. Chem. Chem. Phys.* 14 (2012) 4475.
- [32] Z.-H. Ge, B.-P. Zhang, Y.-Q. Yu, P.P. Shang, *J. Alloys Compd.* 514 (2012) 205.
- [33] R. Chmielowski, D. Pérez, C. Bera, I. Opahle, W. Xie, S. Jacob, F. Capet, P. Roussel, A. Weidenkaff, G.K.H. Madsen, G. Dennler, *J. Appl. Phys.* 117 (2015) 125103.
- [34] P. Mangelis, P. Vaqueiro, J.-C. Jumas, I. da Silva, R.I. Smith, A.V. Powell, *J. Solid State Chem.* 251 (2017) 204.
- [35] J. Corps, P. Vaqueiro, A. Aziz, R. Grau-Crespo, W. Kockelmann, J.-C. Jumas, A.V. Powell, *Chem. Mater.* 27 (2015) 3946.

- [36] J. Corps, P. Vaqueiro, A.V. Powell, *J. Mater. Chem. A* 1 (2013) 6553.
- [37] P. Mangelis, P. Vaqueiro, A.V. Powell, *ACS Appl. Energy Mater.* 3 (2020) 2168.
- [38] H. Liu, X. Shi, F. Xu, L. Zhang, W. Zhang, L. Chen, Q. Li, C. Uher, T. Day, G.J. Snyder, *Nat. Mater.* 11 (2012) 422.
- [39] D.J. Chakrabarti, D.E. Laughlin, *Bull. Alloy Phase Diagr.* 4 (1983) 254.
- [40] P. Qiu, Y. Zhu, Y. Qin, X. Shi, L. Chen, *APL Mater.* 4 (2016) 104805.
- [41] Y. He, T. Day, T. Zhang, H. Liu, X. Shi, L. Chen, G.J. Snyder, *Adv. Mater.* 26 (2014) 3974.
- [42] Y. Sun, L. Xi, J. Yang, L. Wu, X. Shi, L. Chen, G. Snyder, J. Yang, W. Zhang, *J. Mater. Chem. A* 5 (2017) 5098.
- [43] D.G. Cahill, S.K. Watson, R.O. Pohl, *Phys. Rev. B* 46 (1992) 6131.
- [44] G. Dennler, R. Chmielowski, S. Jacob, F. Capet, P. Roussel, S. Zastrow, K. Nielsch, I. Opahle, G.K.H. Madsen, *Adv. Energy Mater.* 4 (2014) 1301581.
- [45] Z.-H. Ge, B.-P. Zhang, Y.-X. Chen, Z.-X. Yu, Y. Liu, J.-F. Li, *Chem. Commun.* 47 (2011) 12697.
- [46] Z.-H. Ge, X. Liu, D. Feng, J. Lin, J. He, *Adv. Energy Mater.* 6 (2016) 1600607.
- [47] D.-D. Liang, B.-P. Zhang, L. Zou, *J. Alloys Compd.* 731 (2018) 577.
- [48] D.-D. Liang, Z.-H. Ge, H.-Z. Li, B.-P. Zhang, F. Li, *J. Alloys Compd.* 708 (2017) 169.
- [49] Y.-X. Zhang, Z. Ma, Z.-H. Ge, P. Qin, F. Zheng, J. Feng, *J. Alloys Compd.* 764 (2018) 738.
- [50] Z.-H. Ge, X. Chong, D. Feng, Y.-X. Zhang, Y. Qiu, L. Xie, P.-W. Guan, J. Feng, J. He, *Mater. Today Phys.* 8 (2019) 71.
- [51] P. Qin, Z.-H. Ge, Y.-X. Chen, X. Chong, J. Feng, J. He, *Nanotechnology* 29 (2018) 345402.
- [52] H. Tang, F.-H. Sun, J.-F. Dong, Asfandiyar, H.-L. Zhuang, Y. Pan, J.-F. Li, *Nano Energy* 49 (2018) 267.
- [53] Y.-X. Zhang, Z.-H. Ge, J. Feng, *J. Alloys Compd.* 727 (2017) 1076.
- [54] A.V. Powell, *J. Appl. Phys.* 126 (2019) 100901.
- [55] P. Wyzga, M. Bobnar, C. Hennig, A. Leithe-Jasper, T. Mori, R. Gumeniuk, *Z. Anorg. Allg. Chem.* 643 (2017) 858.
- [56] R. Ang, A.U. Khan, N. Tsujii, K. Takai, R. Nakamura, T. Mori, *Angew. Chem. Int. Ed.* 54 (2015) 12909.
- [57] N. Tsujii, T. Mori, *Appl. Phys. Express* 6 (2013), 043001.
- [58] H. Takaki, K. Kobayashi, M. Shimono, N. Kobayashi, K. Hirose, N. Tsujii, T. Mori, *Appl. Phys. Lett.* 110 (2017), 072107.
- [59] J. Park, Y. Xia, V. Ozoliņš, *J. Appl. Phys.* 125 (2019) 125102.
- [60] N. Tsujii, *J. Electron. Mater.* 42 (2013) 1974.
- [61] Y. Li, T. Zhang, Y. Qin, T. Day, G.J. Snyder, X. Shi, L. Chen, *J. Appl. Phys.* 116 (2014) 203705.
- [62] H. Takaki, K. Kobayashi, M. Shimono, N. Kobayashi, K. Hirose, N. Tsujii, T. Mori, *Mater. Today Phys.* 3 (2017) 85.
- [63] D. Berthebaud, O.I. Lebedev, A. Maignan, *J. Mater.* 1 (2015) 68.
- [64] R. Lefèvre, D. Berthebaud, M.-Y. Mychinko, O.I. Lebedev, T. Mori, F. Gascoin, A. Maignan, *RSC Adv.* 6 (2016) 55117.
- [65] J. Navratil, J. Kasparova, T. Plechacek, L. Benes, Z. Olmrova-Zmrhalova, V. Kucek, C. Drasar, *J. Electron. Mater.* 48 (2019) 1795.
- [66] H. Xie, X. Su, G. Zheng, T. Zhu, K. Yin, Y. Yan, C. Uher, M.G. Kanatzidis, X. Tang, *Adv. Energy Mater.* 7 (2017) 1601299.
- [67] H. Xie, X. Su, G. Zheng, Y. Yan, W. Liu, H. Tang, M.G. Kanatzidis, C. Uher, X. Tang, *J. Phys. Chem. C* 120 (2016) 27895.
- [68] J. Li, Q. Tan, J.-F. Li, *J. Alloys Compd.* 551 (2013) 143.

- [69] M. Singh, M. Miyata, S. Nishino, D. Mott, M. Koyano, S. Maenosono, *Nanomaterials* **5** (2015) 1820.
- [70] D. Liang, R. Ma, S. Jiao, G. Pang, S. Feng, *Nanoscale* **4** (2012) 6265.
- [71] S. Verma, M. Singh, D. Ahuja, H. Shimose, S. Nishino, M. Miyata, D. Mott, M. Koyano, S. Maenosono, *Jpn. J. Appl. Phys.* **53** (2014) 120301.
- [72] N. Tsujii, F. Meng, K. Tsuchiya, S. Maruyama, T. Mori, *J. Electron Mater.* **45** (2016) 1642.
- [73] H. Xie, X. Su, Y. Yan, W. Liu, L. Chen, J. Fu, J. Yang, C. Uher, X. Tang, *NPG Asia Mater.* **9** (2017), e390.
- [74] Y. Kanazawa, K. Koto, N. Morimoto, *Can. Mineral.* **16** (1978) 397.
- [75] N. Morimoto, *Acta Cryst.* **17** (1964) 351.
- [76] B.A. Grguric, A. Putnis, R.J. Harrison, *Am. Mineral.* **83** (1998) 1231.
- [77] K. Koto, N. Morimoto, *Acta Cryst.* **B31** (1975) 2268.
- [78] P. Qiu, T. Zhang, Y. Qiu, X. Shi, L. Chen, *Energy Environ. Sci.* **7** (2014) 4000.
- [79] G. Guélou, A.V. Powell, P. Vaqueiro, *J. Mater. Chem. C* **3** (2015) 10624.
- [80] M.G. Townshed, J.R. Gosselin, R.J. Tremblay, L.G. Ripley, D.W. Carson, W.B. Muir, *J. Phys. Chem. Solids* **38** (1977) 1153.
- [81] S.O.J. Long, A.V. Powell, P. Vaqueiro, S. Hull, *Chem. Mater.* **30** (2018) 456.
- [82] A.O. Moghaddam, A. Shokuhfar, A. Cabot, *J. Alloys Compd.* **750** (2018) 1.
- [83] A.O. Maghaddam, A. Shokuhfar, P. Guardia, Y. Zhang, A. Cabot, *J. Alloys Compd.* **773** (2019) 1064.

# Synthetic minerals tetrahedrites and colusites for thermoelectric power generation

2.7

Koichiro Suekuni<sup>a</sup>, Michihiro Ohta<sup>b</sup>, Toshiro Takabatake<sup>c</sup>,  
and Emmanuel Guilmeau<sup>d</sup>

<sup>a</sup>Department of Applied Science for Electronics and Materials, Interdisciplinary Graduate School of Engineering Sciences, Kyushu University, Fukuoka, Japan, <sup>b</sup>Global Zero Emission Research Center, National Institute of Advanced Industrial Science and Technology (AIST), Tsukuba, Ibaraki, Japan, <sup>c</sup>Department of Quantum Matter, Graduate School of Advanced Sciences of Matter, Hiroshima University, Higashi-Hiroshima, Japan, <sup>d</sup>Normandie Université, ENSICAEN, UNICAEN, CNRS, CRISMAT, Caen, France

## 2.7.1 Introduction

Thermoelectrics is the simplest technology for direct thermal-to-electrical energy conversion, and high-performance thermoelectric (TE) materials are crucial for the development of this field [1–3]. In the past half-century, a large variety of high-performance TE materials have been studied: PbTe and its alloys [4, 5], half-Heusler compounds [6, 7], filled skutterudites [6, 8], and intermetallic clathrates [9, 10]. These materials are adequate for the recovery of waste heat in the medium-temperature range, 500–900 K. However, most are composed of toxic and/or costly elements. Therefore, it is necessary to discover new materials using less toxic, earth-abundant, and inexpensive elements.

For the chalcogenides, tellurium (Te) should be replaced with a less-toxic homologous element, sulfur (S). Although TE sulfide have not been studied as extensively as tellurides, some materials have been discovered to have relatively high dimensionless figure of merit,  $ZT = S^2 T \rho^{-1} \kappa^{-1}$  ( $S$ : Seebeck coefficient;  $\rho$ , electrical resistivity;  $\kappa$ , thermal conductivity), over a decade ago:  $\text{CeS}_x$  [11],  $R_{3-x}\text{S}_4/R_{2+x}\text{S}_3$  ( $R$ : rare-earth elements) [12–15],  $\text{TiS}_2$  [16, 17],  $\text{PbS}$  [18, 19],  $\text{Bi}_2\text{S}_3$  [20, 21], and  $\text{Cu}_x\text{Mo}_6\text{S}_8$  [22, 23]. Recently, Cu–S-based minerals with complex structures have been investigated for novel TE materials. This trend started with the pioneering works on kesterite  $\text{Cu}_2\text{ZnSnS}_4$  [24], digenite  $\text{Cu}_{1.8}\text{S}$  [25], and chalcopyrite  $\text{CuFeS}_2$  [26, 27]; as well as selenides/telluride with analogous compositions, e.g., stannite  $\text{Cu}_2(\text{Zn}/\text{Cd})\text{SnSe}_4$  [24, 28],  $\text{Cu}_3\text{SbSe}_4$  [29],  $\text{Cu}_2\text{Se}$  [30], and  $\text{CuGaTe}_2$  [31]. Those studies led to the study of tetrahedrites  $\text{Cu}_{12-x}Tr_x\text{Sb}_4\text{S}_{13}$  ( $Tr = \text{Mn}, \text{Fe}, \text{Co}, \text{Ni}, \text{and Zn}$ ) [32–34]. Since then, several Cu–S-based materials have been studied: colusites  $\text{Cu}_{26}\text{V}_2\text{M}_6\text{S}_{32}$  ( $M = \text{Ge}, \text{Sn}$ ) [35, 36], chalcocite  $\text{Cu}_2\text{S}$  [37],  $\text{Cu}_3\text{SnS}_4$  [38], bornite  $\text{Cu}_5\text{FeS}_4$  [39], mohite  $\text{Cu}_2\text{SnS}_3$  [40],  $\text{Cu}_4\text{SnS}_4$  [41],  $\text{Cu}_4\text{Sn}_7\text{S}_{16}$  [42], stanoidite  $\text{Cu}_8\text{Fe}_3\text{Sn}_2\text{S}_{12}$  [43], isocubanite

$\text{CuFe}_2\text{S}_3$  [44], and germanite-derivative  $\text{Cu}_{22}\text{Fe}_8\text{Ge}_4\text{S}_{32}$  [45]. Some of the Cu–S-based materials undergo structural phase transitions due to the mobility of  $\text{Cu}^+$  ion and/or anharmonic vibration of Cu atoms [32, 37, 39, 41]. Such phase transitions have been studied from the viewpoint of solid-state physics and chemistry.

The TE properties of Cu–S-based materials have been reviewed in papers on sulfides [17, 46, 47], binary sulfides [48], Cu-based compounds [49], Cu–S-based synthetic minerals [50], copper sulfides [51], copper chalcogenides [52, 53], multinary diamond-like chalcogenides [54], and tetrahedrites [55–57]. Among the Cu–S-based materials, tetrahedrites and colusites have been attracting increasing attention as p-type TE materials due to their high performance at temperatures up to  $\sim 700\text{ K}$  [33, 34, 36]. Studies on the two materials have progressed to further improve their TE properties and to elucidate the physical mechanism related to their high power factor  $S^2\rho^{-1}$  and low lattice thermal conductivity  $\kappa_{\text{lat}}$ . Moreover, TE elements and power-generation modules have been fabricated and their thermal-to-electrical energy conversion efficiency evaluated [58]. This chapter is devoted to highlighting the progress in the research of tetrahedrites and colusites and is expected to serve as a basis for further development of more efficient TE materials and power-generation modules.

## 2.7.2 Tetrahedrites

Tetrahedrite is a common sulfosalt mineral with the chemical formula  $\text{Cu}_{12-x}\text{Tr}_x\text{Sb}_4\text{S}_{13}$ , where  $\text{Tr}=\text{Cu, Fe, Zn, Ag, Hg, and Cd}$  [59]. Tetrahedrites with various compositions have been synthesized to mimic the natural mineral. Some of them exhibit high  $S^2\rho^{-1}$  and quite low  $\kappa_{\text{lat}}$ , leading to rather high  $ZT$  at 673 K. The high  $S^2\rho^{-1}$  originates from the Cu–S structural network, whereas the low  $\kappa_{\text{lat}}$  stems from the anharmonic vibration of Cu atoms. This section summarizes research that focuses on enhancing the TE performance and that which aims to elucidate the interplay between the crystal and electronic structure and the TE properties.

Tetrahedrite crystallizes in a body-centered-cubic structure with the space group  $I\bar{4}3m$  at room temperature [60]. As shown in Fig. 2.7.1A and B (drawn with VESTA [61]), the structure for the “pristine” tetrahedrite,  $\text{Cu}_{12}\text{Sb}_4\text{S}_{13}$ , consists of three units:  $\text{CuS}_4$ ,  $\text{CuS}_3$ , and  $\text{SbS}_3$ . The  $\text{CuS}_4$  units share their corner to form a three-dimensional network, which is reminiscent of a sodalite framework ( $\text{Na}_8\text{Al}_6\text{Si}_6\text{O}_{24}\text{Cl}_2$ ) [62]. The  $\text{S}_4$  tetrahedron is formed by four S(1) atoms at the  $24g$  site, and the  $\text{S}_3$  triangle is formed by two S(1) atoms and one S(2) atom at the  $2a$  site. The Cu atoms occupying the tetrahedral  $12d$  and trigonal planar  $12e$  sites are denoted as Cu(1) and Cu(2), respectively. Cu(2) faces two Sb atoms, which occupy the  $8c$  sites at the apex of the  $\text{SbS}(1)_3$  trigonal pyramidal units (Fig. 2.7.1B). The Sb atom, which has a 3+ formal valence, has a lone pair of electrons above the apex [63]. The Cu(2) atom vibrates anharmonically perpendicular to the  $\text{S}_3$  triangle and toward the Sb atoms. A detailed explanation based on lattice dynamics is provided below.

Elemental combinations for synthetic tetrahedrites based on  $\text{Cu}_{12}\text{Sb}_4\text{S}_{13}$  are summarized in Fig. 2.7.1C. It has been reported that the Cu(1) atoms in the  $\text{S}_4$  tetrahedra are partially substituted by 3d transition metals ( $\text{Tr}=\text{Cr, Mn, Fe, Co, and Ni}$ ) [59, 64, 65],

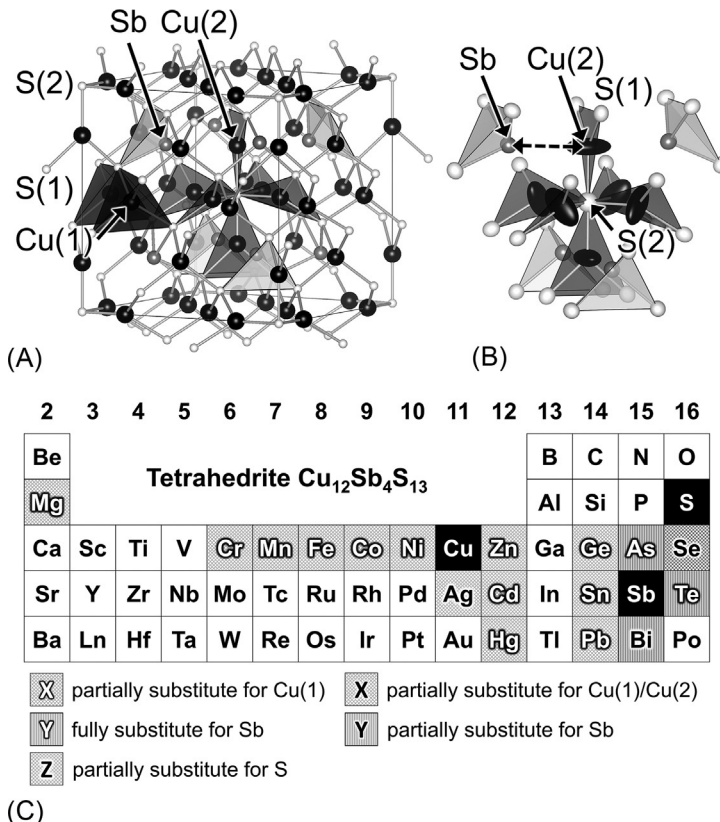


**Fig. 2.7.1** (A) Tetrahedrite crystal structure, (B) thermal ellipsoids of Cu(2) and its neighboring atoms (drawn with VESTA [61]), and (C) possible elemental combinations in the periodic table for the formation of tetrahedrites.

Ag [59, 63, 66], group 12 elements ( $Tr = \text{Zn}, \text{Cd}, \text{and Hg}$ ) [59, 64, 66], group 14 elements ( $M = \text{Ge}, \text{Sn}, \text{and Pb}$ ) [64, 67], and Mg [68]. Only Ag can replace Cu(2) in the  $\text{S}_3$  triangle [63, 66]. Furthermore, Sb can be fully replaced by As and Te [59, 69]. The As endmember,  $\text{Cu}_{12}\text{As}_4\text{S}_{13}$ , is referred to as tennantite, and the Te endmember,  $\text{Cu}_{10}\text{Te}_4\text{S}_{13}$ , is called goldfieldite. In contrast to As and Te, Bi can only substitute less than one of four Sb [70]. In addition, part of the S atoms in  $\text{Cu}_{12}\text{Sb}_4\text{S}_{13}$  can be replaced by Se [71]. It should be noted that non-substituted tetrahedrite has a broad composition range represented as  $\text{Cu}_{12+x}\text{Sb}_{4+y}\text{S}_{13}$ , in which additional Cu atoms occupy interstitial sites in the crystal structure [72].

First-principles electronic-structure calculations on  $\text{Cu}_{12}\text{Sb}_4\text{S}_{13}$  predicted its p-type degenerate-semiconducting electronic structure, where the Fermi level lies in the valence band [33, 73, 74]. The valence bands are mainly composed of the hybridized Cu 3d and S 3p orbitals, implying that the Cu–S network governs hole conduction [50]. The electronic density of states in the vicinity of the Fermi level has a

rather steep slope, which leads to a high  $S$  [74]. The calculations also showed a non-magnetic character of  $\text{Cu}_{12}\text{Sb}_4\text{S}_{13}$  with the monovalent state of Cu. Indeed, the Cu 2p X-ray photoemission spectroscopy on  $\text{Cu}_{12}\text{Sb}_4\text{S}_{13}$  confirmed such a monovalent state (absence of divalent Cu) [75]. Electronic-structure calculations on a Zn-substituted system  $\text{Cu}_{10}\text{Zn}_2\text{Sb}_4\text{S}_{13}$  showed that the Fermi level is lifted to the energy gap between the valence and conduction bands [33]. Similarly, the hole carrier concentration is expected to decrease by substituting  $\text{Cu}^+$  and  $\text{Sb}^{3+}$  with aliovalent cations, e.g.,  $\text{Tr}^{2+}$  and  $M^{4+}$  for  $\text{Cu}^{1+}$ , and  $\text{Te}^{4+}$  for  $\text{Sb}^{3+}$ .

TE properties of tetrahedrites have been extensively studied for the  $\text{Tr}$ -substituted series  $\text{Cu}_{12-x}\text{Tr}_x\text{Sb}_4\text{S}_{13}$  ( $\text{Tr}=\text{Mn, Fe, Co, Ni, and Zn}$ ). In 2012, the TE properties were first studied below 340 K for samples with  $x=0$  and  $x=2$  [32]. Fine tuning of the hole carrier concentration was then achieved for  $\text{Cu}_{12-x}(\text{Fe, Zn})_x\text{Sb}_4\text{S}_{13}$ , whose TE properties were measured up to  $\sim 700$  K [33]. A pristine sample exhibited a high  $ZT$  value of  $\sim 0.6$  at 673 K because of the combination of high  $S^2\rho^{-1}$  ( $1.2 \text{ mWK}^{-2} \text{ m}^{-1}$ ) and low  $\kappa$  ( $1.5 \text{ W K}^{-1} \text{ m}^{-1}$ ). Here, the  $\kappa_{\text{lat}}$  value below  $0.5 \text{ W K}^{-1} \text{ m}^{-1}$  is surprisingly low for crystalline systems. As the Fe and Zn content increases, the values of  $\rho$  and  $S$  monotonically increased, indicating a decrease in the hole carrier concentration, as expected from the electronic-structure calculations [33]. The power factor  $S^2\rho^{-1}$  was reduced after the substitution, and the charge carrier component of the thermal conductivity  $\kappa_{\text{car}}$  was more drastically decreased. As a result,  $ZT$  was enhanced to 0.8 at 700 K for  $\text{Cu}_{11.5}\text{Fe}_{0.5}\text{Sb}_4\text{S}_{13}$  and  $\text{Cu}_{11}\text{Zn}_1\text{Sb}_4\text{S}_{13}$  (Fig. 2.7.2A). Similarly, when substituting Cu with Ni,  $ZT$  was enhanced at 665 K to 0.7 for  $\text{Cu}_{12-x}\text{Ni}_x\text{Sb}_4\text{S}_{13}$  with  $x=1.0-1.5$  (Fig. 2.7.2A) [34].

In 2014, tetrahedrite-based TE elements with contact and diffusion barrier metal layers were fabricated by Alphabet Energy Inc. [76, 77]. They launched a power-generation module measuring  $1.6 \times 1.9$  in. composed of p-type tetrahedrites and n-type Mg–(Si,Sn)-based elements. The maximum output power generated by the module reached 9.2 W when the hot- and cold-side temperatures were maintained at 673 and 373 K, respectively [76].

Further efforts have been devoted to enhance  $ZT$  by various substitutions to tune the hole carrier concentration. As a result, not only  $\text{Cu}_{12-x}\text{Tr}_x\text{Sb}_4\text{S}_{13}$  ( $\text{Tr}=\text{Cr, Mn, Fe, Co, Ni, Zn, and Cd}$ ) [65, 78–88], but also  $\text{Cu}_{12-x}M_x\text{Sb}_4\text{S}_{13}$  ( $M=\text{Ge, Sn, and Pb}$ ) [89, 90],  $\text{Cu}_{12-x}\text{Mg}_x\text{Sb}_4\text{S}_{13}$  [68],  $\text{Cu}_{12}\text{Sb}_{4-y}\text{Te}_y\text{S}_{13}$  [74, 91], and  $\text{Cu}_{12}\text{Sb}_{4-y}\text{Bi}_y\text{S}_{13}$  [92] showed  $ZT$  values comparable to those described above (Fig. 2.7.2A and B). A doubly substituted sample,  $\text{Cu}_{10.5}\text{Ni}_{1.0}\text{Zn}_{0.5}\text{Sb}_4\text{S}_{13}$ , exhibited a  $ZT \sim 1.0$  at 700 K (Fig. 2.7.2A) [93]. Other attempts of double-substitution, e.g.,  $\text{Cu}_{12-x}(\text{Ni, Zn})_x\text{Sb}_4\text{S}_{13}$  and  $\text{Cu}_{12-x}(\text{Co, Ni, Zn})_x\text{Sb}_{4-y}\text{Te}_y\text{S}_{13}$ , resulted in  $ZT$  of 0.7–0.8 [81, 94–96]. In most of these substitutions, the value of  $ZT$  was maximized when 1.0–1.5 electrons per formula unit are doped into the valence band [56].

Doping of Cu into interstitial sites of  $\text{Cu}_{12+x}\text{Sb}_4\text{S}_{13}$  ( $x=0.3-2.0$ ) is also effective for tuning the carrier concentration [97, 98]. Samples were found to decompose into a “copper-poor” phase with a nearly stoichiometric composition and a “copper-rich” phase at room temperature. The two phases were coalesced into a single one with the help of mobile Cu ions at temperatures between 493 and 553 K [97]. Despite the complicated phase/structure characteristics of samples,  $\rho$  and  $S$  tended to increase

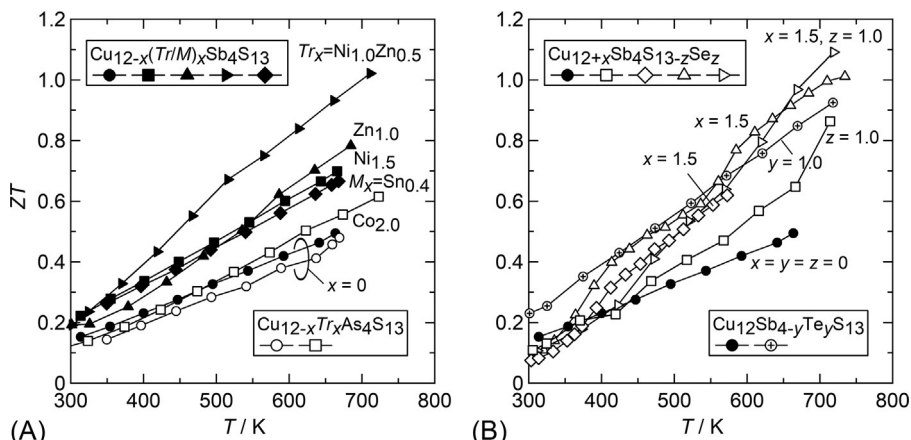


**Fig. 2.7.2** Temperature dependence of dimensionless figures of merit  $ZT$  for (A)  $\text{Cu}_{12-x}(\text{Tr}/\text{M})_x\text{Sb}_4\text{S}_{13}$ , (B)  $\text{Cu}_{12+x}\text{Sb}_4\text{S}_{13-z}\text{Se}_z$ , and (B)  $\text{Cu}_{12}\text{Sb}_{4-y}\text{Te}_y\text{S}_{13}$  tetrahedrites and (A)  $\text{Cu}_{12-x}\text{Tr}_x\text{As}_4\text{S}_{13}$  tennantites.

Data from X. Lu, D. T. Morelli, Y. Xia, F. Zhou, V. Ozolins, H. Chi, X. Zhou, C. Uher, High performance thermoelectricity in earth-abundant compounds based on natural mineral tetrahedrites, *Adv. Energy Mater.* 3 (2013) 342–348. <https://doi.org/10.1002/aenm.201200650>, K. Suekuni, K. Tsuruta, M. Kunii, H. Nishiate, E. Nishibori, S. Maki, M. Ohta, A. Yamamoto, M. Koyano, High-performance thermoelectric mineral  $\text{Cu}_{12-x}\text{Ni}_x\text{Sb}_4\text{S}_{13}$  tetrahedrite, *J. Appl. Phys.* 113 (2013) 043712/1–5. <https://doi.org/10.1063/1.4789389>, X. Lu, D. T. Morelli, Y. Wang, W. Lai, Y. Xia, V. Ozolins, Phase stability, crystal structure, and thermoelectric properties of  $\text{Cu}_{12}\text{Sb}_4\text{S}_{13-x}\text{Se}_x$  solid solutions, *Chem. Mater.* 28 (2016) 1781–1786. <https://doi.org/10.1021/acs.chemmater.5b04796>, Y. Kosaka, K. Suekuni, K. Hashikuni, Y. Bouyrie, M. Ohta, T. Takabatake, Effects of Ge and Sn substitution on the metal–semiconductor transition and thermoelectric properties of  $\text{Cu}_{12}\text{Sb}_4\text{S}_{13}$  tetrahedrite, *Phys. Chem. Chem. Phys.* 19 (2017) 8874–8879. <https://doi.org/10.1039/c7cp00351j>, X. Lu, D. Morelli, The effect of Te substitution for Sb on thermoelectric properties of tetrahedrite, *J. Electron. Mater.* 43 (2014) 1983–1987. <https://doi.org/10.1007/s11664-013-2931-2>, X. Lu, D. T. Morelli, Y. Xia, V. Ozolins, Increasing the thermoelectric figure of merit of tetrahedrites by co-doping with nickel and zinc, *Chem. Mater.* 27 (2015) 408–413. <https://doi.org/10.1021/cm502570b>, P. Vaqueiro, G. Guélou, A. Kaltzoglou, R. I. Smith, T. Barbier, E. Guilmeau, A. V. Powell, The influence of mobile copper ions on the glass-like thermal conductivity of copper-rich tetrahedrites, *Chem. Mater.* 29 (2017) 4080–4090. <https://doi.org/10.1021/acs.chemmater.7b00891>, Y. Yan, H. Wu, G. Wang, X. Lu, X. Zhou, High thermoelectric performance balanced by electrical and thermal transport in tetrahedrites  $\text{Cu}_{12+x}\text{Sb}_4\text{S}_{12}\text{Se}$ , *Energy Storage Mater.* 13 (2018) 127–133. <https://doi.org/10.1016/j.ensm.2018.01.006>, K. Suekuni, C. H. Lee, H. I. Tanaka, E. Nishibori, A. Nakamura, H. Kasai, H. Mori, H. Usui, M. Ochi, T. Hasegawa, M. Nakamura, S. Ohira-Kawamura, T. Kikuchi, K. Kaneko, H. Nishiate, K. Hashikuni, Y. Kosaka, K. Kuroki, T. Takabatake, *Adv. Mater.* 30 (2018) 1706230/1–6. <https://doi.org/10.1002/adma.201706230>, P. Levinsky, C. Candolfi, A. Dauscher, J. Tobola, J. Hejtmanek, B. Lenoir, Thermoelectric properties of the tetrahedrite–tennantite solid solutions  $\text{Cu}_{12}\text{Sb}_{4-x}\text{As}_x\text{S}_{13}$  and  $\text{Cu}_{10}\text{Co}_{2}\text{Sb}_{4-y}\text{As}_y\text{S}_{13}$  ( $0 \leq x, y \leq 4$ ), *Phys. Chem. Chem. Phys.* 21 (2019) 4547–4555. <https://doi.org/10.1039/C9CP00213H>.

with increasing  $x$  due to the decrease in carrier concentration. Furthermore, the “liquid-like” behavior of Cu ions lowered  $\kappa_{\text{lat}}$  to  $0.4 \text{ W K}^{-1} \text{ m}^{-1}$ , similar to superionic conductors Cu<sub>2</sub>Se and Cu<sub>2</sub>S [30, 37, 97]. As a result, ZT at 573 K increased from 0.4 for  $x=0$  to 0.6 for  $x=1.5$  and 2.0 (Fig. 2.7.2B) [97]. When the temperature increased to 723 K, ZT reaches 1.0 for  $x=1.5$  [98] (Fig. 2.7.2B).

A “band-engineering” strategy was proposed for the Se-substituted system, Cu<sub>12</sub>Sb<sub>4</sub>S<sub>13-z</sub>Se<sub>z</sub> ( $z \leq 2$ ) [71, 99]. The substitution led to a decrease in  $\rho$  while keeping S intact, thus enhancing  $S^2\rho^{-1}$ . These “decoupled” variations in  $\rho$  and S were attributed to an upward displacement of the valence bands with low effective masses above the Fermi level. Furthermore, the reduction in  $\kappa_{\text{lat}}$  resulted in an enhanced ZT at 720 K, from 0.6 ( $z=0$ ) to 0.9 ( $z=1$ ) (Fig. 2.7.2B). Furthermore, the simultaneous Se substitution and Cu doping yielded the highest ZT, 1.1 at 723 K (Fig. 2.7.2B) [98].

In contrast to tetrahedrites, few studies have been conducted on tennantites, Cu<sub>12-x</sub>Tr<sub>x</sub>As<sub>4</sub>S<sub>13</sub> [100, 101]. Their TE properties are very similar to those of tetrahedrites (Fig. 2.7.2A), but the toxic character of tennantites hinders their practical use. High-performance thermoelectricity (ZT = 1.0 at 700 K) was demonstrated also for samples composed of mixed natural tetrahedrites/tennantites (semiconducting) and synthetic Cu<sub>12</sub>Sb<sub>4</sub>S<sub>13</sub> (metallic) [33, 102, 103]. These results opened a path for the synthesis of new high-performance TE materials by directly using minerals with little additional processing.

Hereafter, the structural traits and lattice dynamics of tetrahedrites responsible for the low  $\kappa_{\text{lat}}$  are described. A structural analysis on Cu<sub>12</sub>Sb<sub>4</sub>S<sub>13</sub> revealed that the trigonally bonded Cu(2) atom vibrates in an anisotropic and highly anharmonic way perpendicular to the S<sub>3</sub> triangle [60]. Alternatively, the Cu(2) atom vibrates with a large atomic displacement parameter (0.13 Å<sup>2</sup> at 300 K) along the out-of-plane direction [34], as shown in Fig. 2.7.1B. Two possible mechanisms were proposed for the unique vibration of Cu(2): weak out-of-plane bonding between Cu(2) and Sb induced by the lone-pair electrons of Sb [104] (Fig. 2.7.1B), and inherent chemical pressure in the trigonal plane to squeeze Cu(2) out of the plane [100]. The latter inference was derived from an experimental fact; the out-of-plane atomic displacement parameter of Cu(2) increases and the energy of the rattling mode simultaneously decreases with decreasing S<sub>3</sub> triangle area when going from Cu<sub>10</sub>Zn<sub>2</sub>Sb<sub>4</sub>S<sub>13</sub> to Cu<sub>12</sub>Sb<sub>4</sub>S<sub>13</sub>, then Cu<sub>10</sub>Zn<sub>2</sub>As<sub>4</sub>S<sub>13</sub> and finally Cu<sub>12</sub>As<sub>4</sub>S<sub>13</sub>. For Cu<sub>12</sub>Sb<sub>4</sub>S<sub>13</sub>, first-principles calculations predicted that optical phonon branches involving the out-of-plane vibrations of Cu(2) exist at  $\sim 4$  meV [104]. Indeed, inelastic neutron scattering studies revealed the low-lying modes, as shown in Fig. 2.7.3A and B [100, 105]. Furthermore, inelastic neutron scattering on a naturally occurring single crystal [69] revealed a “flat” mode at 3.5 meV and the suppression of scattering intensity from acoustic modes in the energy interval from 3.5 to 6 meV. Above 6 meV, acoustic phonon peaks were retrieved but were strongly broadened. Data regarding the acoustic phonon modes were interpreted as a result of lifetime suppression, which was attributed to an “additional” Umklapp scattering via low-lying optical modes [106]. Thus, the low  $\kappa_{\text{lat}}$  for the tetrahedrites likely originates from the existence of low-energy modes involving the out-of-plane vibrations of the Cu(2) atoms.

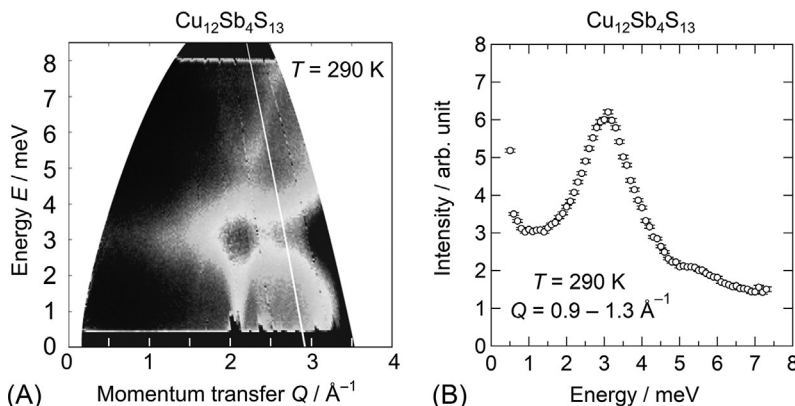


**Fig. 2.7.3** (A) Inelastic neutron scattering intensity map of  $\text{Cu}_{12}\text{Sb}_4\text{S}_{13}$  tetrahedrite at 290 K. (B) Energy dependence ( $E$ ) of the integrated scattering intensity in the momentum transfer ( $Q$ ) range of  $0.9\text{--}1.3 \text{\AA}^{-1}$ . Phonon modes involving the out-of-plane vibration of Cu appear at around 3 meV.

Data from K. Suekuni, C. H. Lee, H. I. Tanaka, E. Nishibori, A. Nakamura, H. Kasai, H. Mori, H. Usui, M. Ochi, T. Hasegawa, M. Nakamura, S. Ohira-Kawamura, T. Kikuchi, K. Kaneko, H. Nishiura, K. Hashikuni, Y. Kosaka, K. Kuroki, T. Takabatake, *Adv. Mater.* 30 (2018) 1706230/1–6. <https://doi.org/10.1002/adma.201706230>.

## 2.7.3 Colusites

Colusite is a sulfosalts mineral with a composition of  $\text{Cu}_{24+x}\text{V}_2(\text{As}, \text{Sb})_{6-x}(\text{Ge}, \text{Sn})_x\text{S}_{32}$  ( $x=0\text{--}2$ ) [107]. As and Sb were replaced with less toxic elements,  $\text{Cu}_{26}\text{V}_2\text{M}_6\text{S}_{32}$  ( $\text{M}=\text{Ge}, \text{Sn}$ ), and different derivatives were synthesized. Similar to tetrahedrites, the superior TE performances of the colusites originate from the combination of relatively high  $S^2\rho^{-1}$  and quite low  $\kappa_{\text{lat}}$ . The former originates from the —Cu—S network and the latter from atomic-scale phonon scatterers. Remarkably, a modification in the —Cu—S network drastically enhances the  $S^2\rho^{-1}$  value. In this section, we summarize the structural characteristics and TE properties of colusites, which are closely related. Furthermore, power generation from a TE module made of colusite with diffusion barriers is presented.

The colusite crystallizes in a simple cubic structure with the space group  $P\bar{4}3n$  [107, 108]. As shown in Fig. 2.7.4A (drawn with VESTA [61]), for  $\text{Cu}_{26}\text{V}_2\text{M}_6\text{S}_{32}$ ,  $\text{CuS}_4$  and  $\text{MS}_4$  units share their corners to form a three-dimensional network, where V atoms occupy tetrahedral voids formed by the  $\text{CuS}_4$  units. There are seven non-equivalent crystallographic sites: three for Cu ( $6d, 8e, 12f$ ), one for V ( $2a$ ), one for  $M$  ( $6c$ ), and two for S ( $8e, 24i$ ). This structure derives from sphalerite (ZnS) by an ordered distribution of Cu and  $M$  on the Zn site with two additional V (or transition metals A) located in the empty tetrahedral sites [108, 109]. Remarkably, the  $[\text{AS}_4]\text{Cu}_6$  complex centered at the A site (Fig. 2.7.4B) is important for the electronic properties because of the metal-like Cu—A interactions [109]. In 2014, colusites  $\text{Cu}_{26}\text{V}_2\text{M}_6\text{S}_{32}$  ( $\text{M}=\text{Ge}, \text{Sn}$ ) were first synthesized [35, 36]. Thereafter, a large variety of elemental

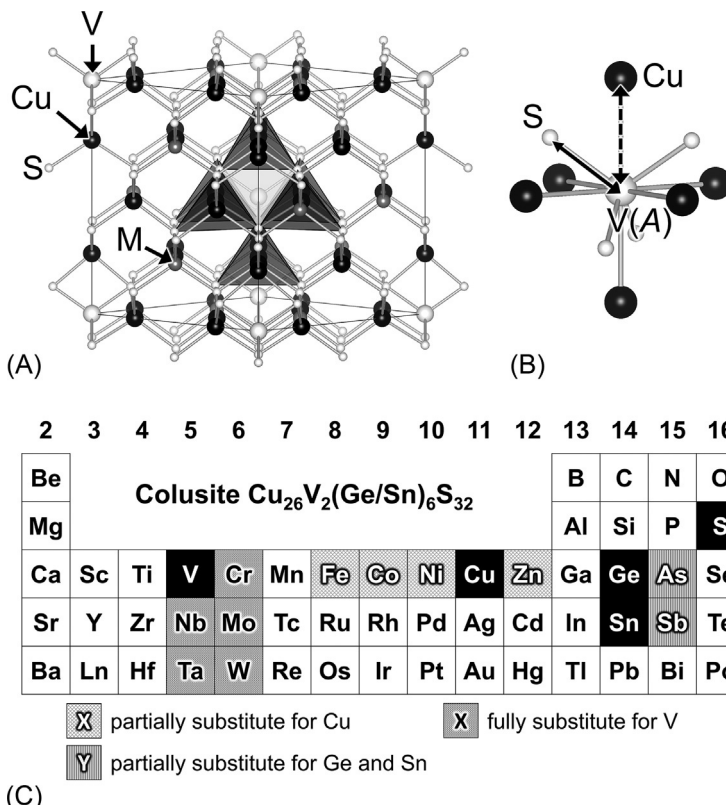


**Fig. 2.7.4** (A) Colusite crystal structure containing the  $[VS_4]Cu_6$  ( $[AS_4]Cu_6$ ) octahedral complex shown in (B) (drawn with VESTA [61]). (C) Possible elemental combinations in the periodic table for the formation of colusites.

combinations has been reported. A part of Cu atoms can be replaced by  $Tr=Fe, Co, Ni$ , and Zn, [110–112] whereas V can be fully substituted by  $A=Nb, Ta, Cr, Mo$ , and W [109, 113], Fig. 2.7.4C.

For  $Cu_{26}V_2M_6S_{32}$  ( $M=Ge, Sn$ ), first-principles electronic-structure calculations showed their  $p$ -type degenerate-semiconducting and nonmagnetic nature [36], as in  $Cu_{12}Sb_4S_{13}$  tetrahedrite. The valence band is mainly composed of the hybridized Cu 3d and S 3p orbitals, implying that the —Cu—S network is responsible for hole conduction.

TE properties of the Zn-substituted systems,  $Cu_{26-x}Zn_xV_2M_6S_{32}$  ( $x \leq 4$ ,  $M=Ge, Sn$ ), were first studied below 300 K in 2014 [35]. The system was tuned from metallic to semiconducting through the substitution of Zn for Cu, which led to the decrease in the hole carrier concentration, similar to tetrahedrite. In a subsequent study, TE performances were evaluated for  $Cu_{26}V_2M_6S_{32}$  ( $M=Ge, Sn$ ) up to 663 K [36]. The colusites exhibited relatively high  $S^2\rho^{-1}$  ( $0.5\text{--}0.6 \text{ mW K}^{-2} \text{ m}^{-1}$ ) and quite low  $\kappa_{lat}$  ( $0.3\text{--}0.4 \text{ W K}^{-1} \text{ m}^{-1}$ ), leading to  $ZT$  values of 0.5–0.7 at 663 K (Fig. 2.7.5A). Equivalent or higher  $ZT$  values were then reported for  $Cu_{26}V_2Sn_6S_{32}$  [114],  $Cu_{26}A_2M_6S_{32}$

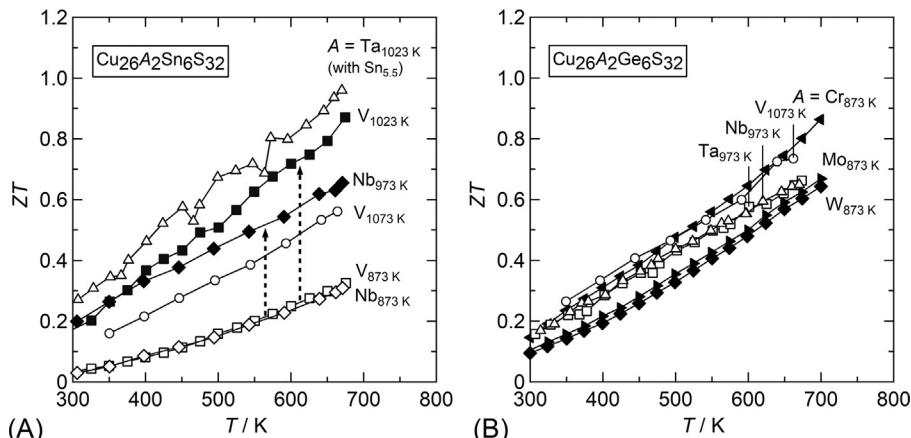


**Fig. 2.7.5** Temperature dependence of dimensionless figures of merit  $ZT$  for (A)  $\text{Cu}_{26}\text{A}_2\text{Sn}_6\text{S}_{32}$  and (B)  $\text{Cu}_{26}\text{A}_2\text{Ge}_6\text{S}_{32}$  colusites with  $A = \text{V}, \text{Nb}, \text{Ta}, \text{Cr}, \text{Mo}$ , and  $\text{W}$ . The subscript denotes the sintering temperature.

Data from K. Suekuni, F. S. Kim, H. Nishiate, M. Ohta, H. I. Tanaka, T. Takabatake, High-performance thermoelectric minerals: colusites  $\text{Cu}_{26}\text{V}_2\text{M}_6\text{S}_{32}$  ( $\text{M} = \text{Ge}, \text{Sn}$ ), *Appl. Phys. Lett.* 105 (2014) 132107/1–4. <https://doi.org/10.1063/1.4896998>, V. P. Kumar, A. R. Supka, P.

Lemoine, O. I. Lebedev, B. Raveau, K. Suekuni, V. Nassif, R. A. R. A. Orabi, M. Fornari, E. Guilmeau, High power factors of thermoelectric colusites  $\text{Cu}_{26}\text{T}_2\text{Ge}_6\text{S}_{32}$  ( $\text{T} = \text{Cr}, \text{Mo}, \text{W}$ ): toward functionalization of the conductive “Cu–S” network, *Adv. Energy Mater.* 9 (2018) 1803249/1–11. <https://doi.org/10.1002/aenm.201803249>, Y. Bouyrie, M. Ohta, K. Suekuni, P. Jood, T. Takabatake, Addition of Co, Ni, Fe and their role in the thermoelectric properties of colusite  $\text{Cu}_{26}\text{Nb}_2\text{Ge}_6\text{S}_{32}$ , *J. Alloys Compd.* 735 (2018) 1838–1845. <https://doi.org/10.1016/j.jallcom.2017.11.199>, C. Bourgès, Y. Bouyrie, A. R. Supka, R. A. R. A. Orabi, P. Lemoine, O. I. Lebedev, M. Ohta, K. Suekuni, V. Nassif, V. Hardy, R. Daou, Y. Miyazaki, M. Fornari, E. Guilmeau, High-performance thermoelectric bulk colusite by process controlled structural disordering, *J. Am. Chem. Soc.* 140 (2018) 2186–2195. <https://doi.org/10.1021/jacs.7b11224>, Y. Bouyrie, M. Ohta, K. Suekuni, Y. Kikuchi, P. Jood, A. Yamamoto, T. Takabatake, Enhancement in the thermoelectric performance of colusites  $\text{Cu}_{26}\text{A}_2\text{E}_6\text{S}_{32}$  ( $\text{A} = \text{Nb}, \text{Ta}; \text{E} = \text{Sn}, \text{Ge}$ ) using E-site non-stoichiometry, *J. Mater. Chem. C* 5 (2017) 4174–4184. <https://doi.org/10.1039/c7tc00762k>, K. Suekuni, Y. Shimizu, E. Nishibori, H. Kasai, H. Saito, D. Yoshimoto, K. Hashikuni, Y. Bouyrie, R. Chetty, M. Ohta, E. Guilmeau, T. Takabatake, K. Watanabe, M. Ohtaki, Atomic-scale phonon scatterers in thermoelectric colusites with a tetrahedral framework structure, *J. Mater. Chem. A* 7 (2019) 228–235. <https://doi.org/10.1039/c8ta08248k>.

( $\text{A} = \text{Nb}, \text{Ta}; \text{M} = \text{Ge}, \text{Sn}$ ) [112, 113] and  $\text{Cu}_{24}\text{Tr}_2\text{V}_2\text{Ge}_6\text{S}_{32}$  ( $\text{Tr} = \text{Ni}, \text{Co}$ ) (Fig. 2.7.5A and B) [111]. Furthermore, samples with off-stoichiometric compositions, e.g.,  $\text{Cu}_{26}\text{Ta}_2\text{Sn}_{5.5}\text{S}_{32}$ , exhibit an even higher  $ZT$  ( $\sim 1$ ) at 670 K (Fig. 2.7.5A) [115].

It should be noted that the value of  $\kappa_{\text{lat}}$  for  $\text{Cu}_{26}\text{V}_2\text{Sn}_6\text{S}_{32}$  strongly depends on the sintering temperature: at 673 K; it decreased from 0.6 to 0.3  $\text{W K}^{-1}\text{m}^{-1}$  when the sintering temperature increased from 873 to 1023 K, as shown in Fig. 2.7.6A [114]. A similar reduction in  $\kappa_{\text{lat}}$  with increasing sintering temperature was confirmed for  $\text{Cu}_{26}\text{Nb}_2\text{Sn}_6\text{S}_{32}$  [116]. The decrease in  $\kappa_{\text{lat}}$  is triggered by sulfur sublimation during

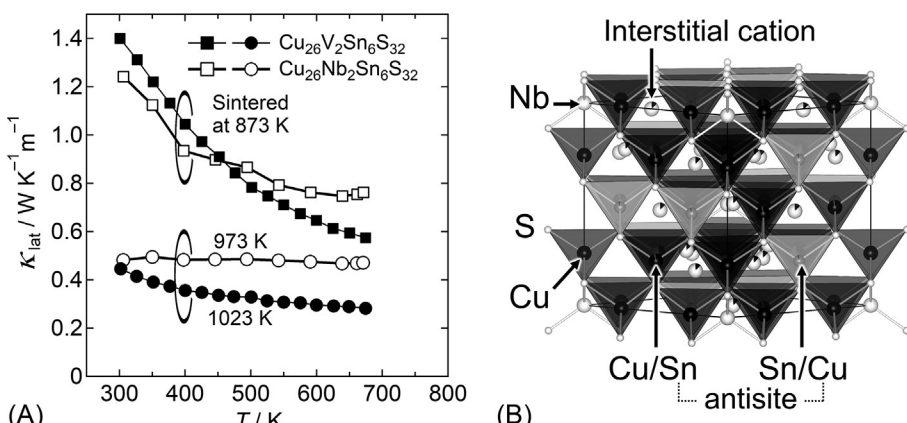


**Fig. 2.7.6** (A) Temperature dependence of lattice thermal conductivity  $\kappa_{\text{lat}}$  for the  $\text{Cu}_{26}\text{V}_2\text{Sn}_6\text{S}_{32}$  and  $\text{Cu}_{26}\text{Nb}_2\text{Sn}_6\text{S}_{32}$  samples sintered at 873 and 973/1023 K. (B) The modified colusite structure for  $\text{Cu}_{26}\text{Nb}_2\text{Sn}_6\text{S}_{32}$  (drawn with VESTA [61]) that reduces  $\kappa_{\text{lat}}$  [116]. Panel A: Data from C. Bourgès, Y. Bouyrie, A. R. Supka, R. A. R. A. Orabi, P. Lemoine, O. I. Lebedev, M. Ohta, K. Suekuni, V. Nassif, V. Hardy, R. Daou, Y. Miyazaki, M. Fornari, E. Guilmeau, High-performance thermoelectric bulk colusite by process controlled structural disordering, *J. Am. Chem. Soc.* 140 (2018) 2186–2195. <https://doi.org/10.1021/jacs.7b11224> and K. Suekuni, Y. Shimizu, E. Nishibori, H. Kasai, H. Saito, D. Yoshimoto, K. Hashikuni, Y. Bouyrie, R. Chetty, M. Ohta, E. Guilmeau, T. Takabatake, K. Watanabe, M. Ohtaki, Atomic-scale phonon scatterers in thermoelectric colusites with a tetrahedral framework structure, *J. Mater. Chem. A* 7 (2019) 228–235. <https://doi.org/10.1039/c8ta08248k>.

the sintering process above  $\sim 973$  K, as described later. However, the reduction in hole carrier concentration associated with the loss of sulfur did not alter the  $S^2\rho^{-1}$  value at 673 K [114, 116]. As a result,  $ZT$  was enhanced when the sintering temperature was elevated above 973 K, as shown in Fig. 2.7.5A.

The reduced  $\kappa_{\text{lat}}$  in  $\text{Cu}_{26}\text{V}_2\text{Sn}_6\text{S}_{32}$  was attributed to the several kinds of phonon scatterers, i.e., vacancies at S sites, Cu/Sn antisite defects, and chemical disorder on the metal ion sublattices [36, 113, 114, 116]. The disordered region/phase with face-centered-cubic structure is spontaneously formed in the “ordered” (colusite) matrix [116], which was reported also for natural minerals [107]. Further structural analysis on  $\text{Cu}_{26}\text{Nb}_2\text{Sn}_6\text{S}_{32}$  with the “ordered” structure revealed that sulfur sublimation induces atomic-scale defects/disordered states, including interstitial defects, antisites defects, and site splitting, which function as strong phonon scatterers (Fig. 2.7.6B). It should be noted that first-principles phonon-structure calculations predicted the existence of low-energy modes involving the vibration of Cu atoms [114]. The role of low-energy modes in reducing  $\kappa_{\text{lat}}$  should be further examined.

An important relationship between the —Cu—S network and the electronic properties was found for  $\text{Cu}_{26}A_2\text{Ge}_6\text{S}_{32}$  with  $A = \text{Cr}, \text{Mo}$ , and  $\text{W}$  [109]. When  $A$  goes from  $\text{W}$  to  $\text{Mo}$ , then  $\text{Cr}$ , the value of  $S^2\rho^{-1}$  at 300 K/700 K increased from 0.7/1.2 to 1.5/1.9 mW K $^{-2}$  m $^{-1}$ . As a result, despite the relatively high  $\kappa_{\text{lat}}$  due to the absence of aforementioned phonon scatterers, the  $A = \text{Cr}$  sample exhibited a  $ZT$  of 0.9 at 700 K (Fig. 2.7.5B). Note that the

value of  $S^2\rho^{-1}$  ( $1.9 \text{ mWK}^{-2}\text{m}^{-1}$ ) is the highest for Cu–S-based materials. The enhancement of S in the  $A = \text{Cr}$  system was attributed to a modification of the —Cu–S network that flattens the valence bands near the Fermi level, whereas the reduction in  $\rho$  (increased mobility of holes) was attributed to the enhanced metal-like  $A$ –Cu interactions in the  $[\text{As}_4]\text{Cu}_6$  complex (Fig. 2.7.4B) and to the smaller electronegativity for Cr compared to Mo and W [109]. Such “functionalization” of the —Cu–S network could be used as a new approach to enhance  $S^2\rho^{-1}$  for Cu–S-based materials. By combining the two independent ways to enhance  $S^2\rho^{-1}$  and reduce  $\kappa_{\text{lat}}$  described above, a still higher  $ZT$  is expected.

In anticipation of their practical use for power generation, colosite-based TE single elements with a diffusion barrier layer were fabricated (Fig. 2.7.7A) [117]. They were directly prepared by sintering  $\text{Cu}_{26}\text{Nb}_2\text{Ge}_6\text{S}_{32}$  colosite powder, which was

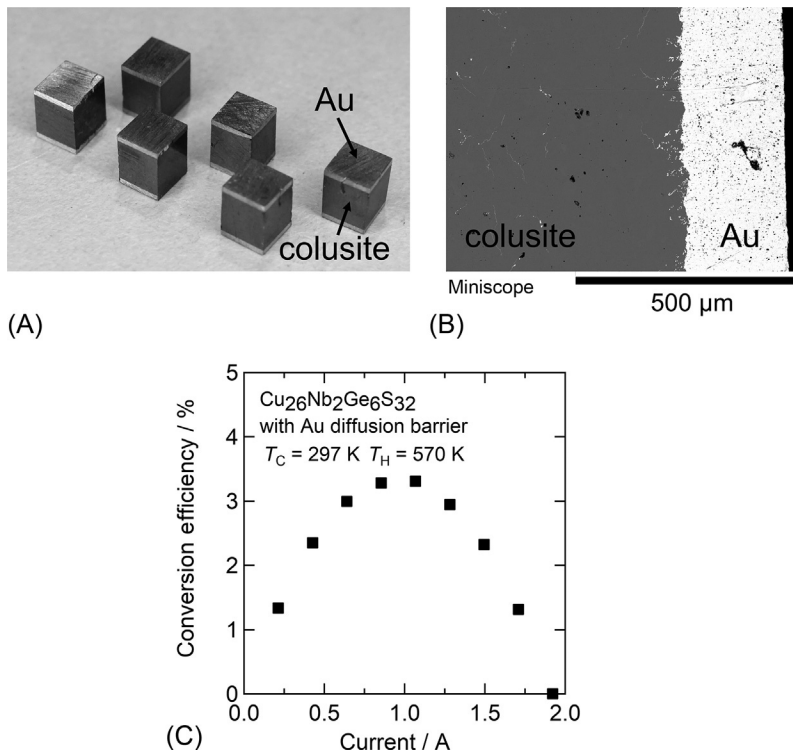


**Fig. 2.7.7** (A) Thermoelectric single elements composed of  $\text{Cu}_{26}\text{Nb}_2\text{Ge}_6\text{S}_{32}$  colosite and Au diffusion barrier. (B) Scanning electron microprobe image shows good contact between colosite and Au. (C) Conversion efficiency with respect to the electric current for the single element. The test was performed when the hot- and cold-side temperatures,  $T_H$  and  $T_C$ , were maintained at 570 and 297 K, respectively.

Data from R. Chetty, Y. Kikuchi, Y. Bouyrie, P. Jood, A. Yamamoto, K. Suekuni, M. Ohta, Power generation from the  $\text{Cu}_{26}\text{Nb}_2\text{Ge}_6\text{S}_{32}$ -based single thermoelectric element with au diffusion barrier, *J. Mater. Chem. C* 7 (2019) 5184–5192. <https://doi.org/10.1039/c9tc00868c>.

sandwiched by powders/foils of diffusion barrier materials. Among the tested elements (Ti, Pt, Ni, or Au), the Au layer had the best electrical and physical contact (no cracking) with the colusite because of no reaction product and good match in the coefficient of thermal expansion between Au and colusite (Fig. 2.7.7B). The output power of a single element of  $3 \times 3 \times 5$  (height) mm<sup>3</sup> with a gold-film contact reached a maximum of 17.8 mW when the hot- and cold-side temperatures were maintained at 570 and 297 K, respectively. Here, the maximum thermal-to-energy conversion efficiency is 3.3% (Fig. 2.7.7C). This value is lower than the maximum efficiency of 4.5% calculated by the three-dimensional finite-element simulation without parasitic ohmic and radiative heat losses for the Cu<sub>26</sub>Nb<sub>2</sub>Ge<sub>6</sub>S<sub>32</sub>-based TE element. Further optimization of the design would improve both the electrical and thermal contact, leading to a higher conversion efficiency.

## 2.7.4 Conclusion and perspective

In this chapter, we reviewed the investigations related to tetrahedrite- and colusite-based high-performance TE materials that mimic naturally occurring minerals. The electronic properties for both systems are governed by the electron-deficient (hole-conductive) —Cu—S structural networks. Earlier efforts were devoted to tuning the hole carrier concentration by chemical substitutions. Recent studies have revealed the possibility to tune the band degeneracy in tetrahedrite and to modify the —Cu—S network by including metal-metal interactions in the colusite. These insights for the enhancement of the power factor  $S^2\rho^{-1}$  offer the opportunity to boost the  $ZT$  values of Cu—S-based materials. In addition to the high  $S^2\rho^{-1}$ , both tetrahedrite and colusite present low  $\kappa_{\text{lat}}$ . The strong phonon scattering in tetrahedrite originates from the anharmonic vibration of Cu atoms. In the colusite, this is caused by atomic-scale defects and disordered arrangement of the metal ions. The elucidation of such mechanisms should be useful for the design/search of materials with low  $\kappa_{\text{lat}}$ . It is expected that reducing the  $\kappa_{\text{lat}}$  would lead to a high “average  $ZT$ ” at temperatures between 300 and 700 K for the Cu<sub>26</sub>Cr<sub>2</sub>Ge<sub>6</sub>S<sub>32</sub> colusite with superior  $S^2\rho^{-1}$ .

As for the fabrication of the TE elements and power-generation modules based on —Cu—S materials, less efforts have been devoted. Recently, Au diffusion barrier was used on colusite-based TE element. Its success opens a way for the fabrication of efficient power-generation modules. Further investigations are required to examine the degree of migration of Cu ions in TE elements made of tetrahedrites and colusites when they are subjected to large temperature gradients and high current density. Even if some Cu ions migrate, a doping strategy would solve this problem, as reported for Cu<sub>2</sub>S [118]. As an *n*-type counterpart of *p*-type tetrahedrites and colusites to form a series of II-shaped modules, TiS<sub>2</sub>-based materials are suitable for reducing costs of preparation and for an easy fabrication process. Particularly, a large amount of powder of these compounds could be synthesized by mechanical alloying in a very short time at room temperature [85, 109, 114]. The combination of similar S-based materials would allow the use of the same apparatus for the synthesis and sintering. We hope that this overview on tetrahedrites and colusites will serve as a basis for further development of more efficient TE materials and modules based on Cu and S.

## References

- [1] F.J. DiSalvo, Thermoelectric cooling and power generation, *Science* 285 (1999) 703–706, <https://doi.org/10.1126/science.285.5428.703>.
- [2] L.E. Bell, Cooling, heating, generating power, and recovering waste heat with thermoelectric systems, *Science* 321 (2008) 1457–1461, <https://doi.org/10.1126/science.1158899>.
- [3] T. Zhu, Y. Liu, C. Fu, J.P. Heremans, G.J. Snyder, X. Zhao, Compromise and synergy in high-efficiency thermoelectric materials, *Adv. Mater.* 29 (2017) 1605884/1–26, <https://doi.org/10.1002/adma.201605884>.
- [4] A.D. LaLonde, Y. Pei, H. Wang, G.J. Snyder, Lead telluride alloy thermoelectrics, *Mater. Today* 14 (2011) 526–532, [https://doi.org/10.1016/S1369-7021\(11\)70278-4](https://doi.org/10.1016/S1369-7021(11)70278-4).
- [5] L.D. Zhao, V.P. Dravid, M.G. Kanatzidis, The panoscopic approach to high performance thermoelectrics, *Energy Environ. Sci.* 7 (2014) 251–268, <https://doi.org/10.1039/C3EE43099E>.
- [6] G. Schierning, R. Chavez, R. Schmechel, B. Balke, G. Rogl, P. Rogl, Concepts for medium-high to high temperature thermoelectric heat-to-electricity conversion: a review of selected materials and basic considerations of module design, *Transl. Mater. Res.* 2 (2015) 025001/1–26, <https://doi.org/10.1088/2053-1613/2/2/025001>.
- [7] T. Zhu, C. Fu, H. Xie, Y. Liu, X. Zhao, High efficiency half-heusler thermoelectric materials for energy harvesting, *Adv. Energy Mater.* 5 (2015) 1500588/1–13, <https://doi.org/10.1002/aenm.201500588>.
- [8] M. Rull-Bravo, A. Moure, J.F. Fernández, M. Martín-González, Skutterudites as thermoelectric materials: revisited, *RSC Adv.* 5 (2015) 41653–41667, <https://doi.org/10.1039/C5RA03942H>.
- [9] M. Christensen, S. Johnsen, B.B. Iversen, Thermoelectric clathrates of type I, *Dalton Trans.* 39 (2010) 978–992, <https://doi.org/10.1039/B916400F>.
- [10] T. Takabatake, K. Suekuni, T. Nakayama, E. Kaneshita, Phonon-glass electron-crystal thermoelectric clathrates: experiments and theory, *Rev. Mod. Phys.* 86 (2014) 669–716, <https://doi.org/10.1103/RevModPhys.86.669>.
- [11] F.M. Ryan, N. Greenberg, F.L. Carter, R.C. Miller, Thermoelectric properties of some cerium sulfide semiconductors from 4° to 1300°K, *J. Appl. Phys.* 33 (1962) 864–868, <https://doi.org/10.1063/1.1777182>.
- [12] C. Wood, A. Lockwood, J. Parker, A. Zoltan, D. Zoltan, L.R. Danielson, V. Raag, Thermoelectric properties of lanthanum sulfide, *J. Appl. Phys.* 58 (1985) 1542–1547, <https://doi.org/10.1063/1.336088>.
- [13] J.F. Nakahara, T. Takeshita, M.J. Tschetter, B.J. Beaudry, K.A. Gschneidner Jr., Thermoelectric properties of lanthanum sulfide with Sm, Eu, and Yb additives, *J. Appl. Phys.* 63 (1988) 2331–2336, <https://doi.org/10.1063/1.341049>.
- [14] M. Ohta, S. Hirai, T. Mori, Y. Yajima, T. Nishimura, K. Shimakage, Effect of non-stoichiometry on thermoelectric properties of  $\gamma\text{-Tb}_2\text{S}_{3-x}$ , *J. Alloys Compd.* 418 (2006) 209–212, <https://doi.org/10.1016/j.jallcom.2005.10.065>.
- [15] M. Ohta, S. Hirai, Thermoelectric properties of  $\text{NdGd}_{1+x}\text{S}_3$  prepared by  $\text{CS}_2$  sulfurization, *J. Electron. Mater.* 38 (2009) 1287–1292, <https://doi.org/10.1007/s11664-009-0660-3>.
- [16] E. Guilmeau, A. Maignan, C. Wan, K. Koumoto, On the effects of substitution, intercalation, non-stoichiometry and block layer concept in  $\text{TiS}_2$  based thermoelectrics, *Phys. Chem. Chem. Phys.* 17 (2015) 24541–24555, <https://doi.org/10.1039/C5CP01795E>.
- [17] P. Jood, M. Ohta, Hierarchical architecturing for layered thermoelectric sulfides and chalcogenides, *Materials* 8 (2015) 1124–1149, <https://doi.org/10.3390/ma8031124>.

- [18] S. Johnsen, J. He, J. Androulakis, V.P. Dravid, I. Todorov, D.Y. Chung, M.G. Kanatzidis, Nanostructures boost the thermoelectric performance of PbS, *J. Am. Chem. Soc.* 133 (2011) 3460–3470, <https://doi.org/10.1021/ja109138p>.
- [19] D. Greig, Thermoelectricity and thermal conductivity in the lead sulfide group of semiconductors, *Phys. Rev.* 120 (1960) 358–365, <https://doi.org/10.1103/PhysRev.120.358>.
- [20] B. Chen, C. Uher, L. Iordanidis, M.G. Kanatzidis, Transport properties of  $\text{Bi}_2\text{S}_3$  and the ternary bismuth sulfides  $\text{KBi}_{6.33}\text{S}_{10}$  and  $\text{K}_2\text{Bi}_8\text{S}_{13}$ , *Chem. Mater.* 9 (1997) 1655–1658, <https://doi.org/10.1021/cm970033m>.
- [21] K. Biswas, L.D. Zhao, M.G. Kanatzidis, Tellurium-free thermoelectric: the anisotropic n-type semiconductor  $\text{Bi}_2\text{S}_3$ , *Adv. Energy Mater.* 2 (2012) 634–638, <https://doi.org/10.1002/aenm.201100775>.
- [22] T. Tsubota, M. Ohtaki, K. Eguchi, Thermoelectric properties of chevrel-type sulfides  $\text{AMo}_6\text{S}_8$  ( $A=\text{Fe, Ni, Ag, Zn, Sn, Pb, Cu}$ ), *J. Ceram. Soc. Jpn.* 107 (1999) 697–701, <https://doi.org/10.2109/jcersj.107.697>.
- [23] M. Ohta, A. Yamamoto, H. Obara, Preparation and thermoelectric properties of chevrel-phase  $\text{Cu}_x\text{Mo}_6\text{S}_8$  ( $2.0 \leq x \leq 4.0$ ), *Mater. Trans.* 50 (2009) 2129–2133, <https://doi.org/10.2320/matertrans.MAW200918>.
- [24] M.L. Liu, F.Q. Huang, L.D. Chen, I.W. Chen, A wide-band-gap p-type thermoelectric material based on quaternary chalcogenides of  $\text{Cu}_2\text{ZnSn}Q_4$  ( $Q=\text{S,Se}$ ), *Appl. Phys. Lett.* 94 (2009) 202103/1–3, <https://doi.org/10.1063/1.3130718>.
- [25] Z.H. Ge, B.P. Zhang, Y.X. Chen, Z.X. Yu, Y. Liu, J.F. Li, Synthesis and transport property of  $\text{Cu}_{1.8}\text{S}$  as a promising thermoelectric compound, *Chem. Commun.* 47 (2011) 12697–12699, <https://doi.org/10.1039/C1CC16368J>.
- [26] J. Li, Q. Tan, J.F. Li, Synthesis and property evaluation of  $\text{CuFeS}_{2-x}$  as earth-abundant and environmentally-friendly thermoelectric materials, *J. Alloys Compd.* 551 (2013) 143–149, <https://doi.org/10.1016/j.jallcom.2012.09.067>.
- [27] N. Tsujii, T. Mori, High thermoelectric power factor in a carrier-doped magnetic semiconductor  $\text{CuFeS}_2$ , *Appl. Phys. Express* 6 (2013) 043001/1–4, <https://doi.org/10.7567/APEX.6.043001>.
- [28] M.L. Liu, I.W. Chen, F.Q. Huang, L.D. Chen, Improved thermoelectric properties of cu-doped quaternary chalcogenides of  $\text{Cu}_2\text{CdSnSe}_4$ , *Adv. Mater.* 21 (2009) 3808–3812, <https://doi.org/10.1002/adma.200900409>.
- [29] E.J. Skoug, J.D. Cain, D.T. Morelli, High thermoelectric figure of merit in the  $\text{Cu}_3\text{SbSe}_4$ - $\text{Cu}_3\text{SbS}_4$  solid solution, *Appl. Phys. Lett.* 98 (2011) 261911/1–3, <https://doi.org/10.1063/1.3605246>.
- [30] H. Liu, X. Shi, F. Xu, L. Zhang, W. Zhang, L. Chen, Q. Li, C. Uher, T. Day, G.J. Snyder, Copper ion liquid-like thermoelectrics, *Nat. Mater.* 11 (2012) 422–425, <https://doi.org/10.1038/nmat3273>.
- [31] T. Plirdprong, K. Kurosaki, A. Kosuga, T. Day, S. Firdosy, V. Ravi, G.J. Snyder, A. Harnwunggmoung, T. Sugahara, Y. Ohishi, H. Muta, S. Yamanaka, Chalcopyrite  $\text{CuGaTe}_2$ : a high-efficiency bulk thermoelectric material, *Adv. Mater.* 24 (2012) 3622–3626, <https://doi.org/10.1002/adma.201200732>.
- [32] K. Suekuni, K. Tsuruta, T. Ariga, M. Koyano, Thermoelectric properties of mineral tetrahedrites  $\text{Cu}_{10}\text{Tr}_2\text{Sb}_4\text{S}_{13}$  with low thermal conductivity, *Appl. Phys. Express* 5 (2012) 051201/1–3, <https://doi.org/10.1143/APEX.5.051201>.
- [33] X. Lu, D.T. Morelli, Y. Xia, F. Zhou, V. Ozolins, H. Chi, X. Zhou, C. Uher, High performance thermoelectricity in earth-abundant compounds based on natural mineral tetrahedrites, *Adv. Energy Mater.* 3 (2013) 342–348, <https://doi.org/10.1002/aenm.201200650>.

- [34] K. Suekuni, K. Tsuruta, M. Kunii, H. Nishiate, E. Nishibori, S. Maki, M. Ohta, A. Yamamoto, M. Koyano, High-performance thermoelectric mineral  $\text{Cu}_{12-x}\text{Ni}_x\text{Sb}_4\text{S}_{13}$  tetrahedrite, *J. Appl. Phys.* 113 (2013) 043712/1–5, <https://doi.org/10.1063/1.4789389>.
- [35] K. Suekuni, F.S. Kim, T. Takabatake, Tunable electronic properties and low thermal conductivity in synthetic colusites  $\text{Cu}_{26-x}\text{Zn}_x\text{V}_2\text{M}_6\text{S}_{32}$  ( $x \leq 4$ , M = Ge, Sn), *J. Appl. Phys.* 116 (2014) 063706/1–5, <https://doi.org/10.1063/1.4892593>.
- [36] K. Suekuni, F.S. Kim, H. Nishiate, M. Ohta, H.I. Tanaka, T. Takabatake, High-performance thermoelectric minerals: colusites  $\text{Cu}_{26}\text{V}_2\text{M}_6\text{S}_{32}$  (M = Ge, Sn), *Appl. Phys. Lett.* 105 (2014) 132107/1–4, <https://doi.org/10.1063/1.4896998>.
- [37] Y. He, T. Day, T. Zhang, H. Liu, X. Shi, L. Chen, G.J. Snyder, High thermoelectric performance in non-toxic earth-abundant copper sulfide, *Adv. Mater.* 26 (2014) 3974–3978, <https://doi.org/10.1002/adma.201400515>.
- [38] Y. Goto, Y. Sakai, Y. Kamihara, M. Matoba, Electronic structure and transport properties of cu-deficient kuramite  $\text{Cu}_{3-x}\text{SnS}_4$ , *Jpn. J. Appl. Phys.* 54 (2015) 021801/1–5, <https://doi.org/10.7567/JJAP.54.021801>.
- [39] P. Qiu, T. Zhang, Y. Qiu, X. Shi, L. Chen, Sulfide bornite thermoelectric material: a natural mineral with ultralow thermal conductivity, *Energy Environ. Sci.* 7 (2014) 4000–4006, <https://doi.org/10.1039/C4EE02428A>.
- [40] Q. Tan, W. Sun, Z. Li, J.F. Li, Enhanced thermoelectric properties of earth-abundant  $\text{Cu}_2\text{SnS}_3$  via in doping effect, *J. Alloys Compd.* 672 (2016) 558–563, <https://doi.org/10.1016/j.jallcom.2016.02.185>.
- [41] A. Suzumura, N. Nagasako, Y. Kinoshita, M. Watanabe, T. Kita, R. Asahi, Presence of a doubly-splitting site and its effect on thermoelectric properties of  $\text{Cu}_4\text{SnS}_4$ , *Mater. Trans.* 56 (2015) 858–863, <https://doi.org/10.2320/matertrans.E-M2015804>.
- [42] C. Bourgès, P. Lemoine, O.I. Lebedev, R. Daou, V. Hardy, B. Malaman, E. Guilmeau, Low thermal conductivity in ternary  $\text{Cu}_4\text{Sn}_7\text{S}_{16}$  compound, *Acta Mater.* 97 (2015) 180–190, <https://doi.org/10.1016/j.actamat.2015.06.046>.
- [43] V.P. Kumar, T. Barbier, V. Caignaert, B. Raveau, R. Daou, B. Malaman, G.L. Caér, P. Lemoine, E. Guilmeau, Copper hyper-stoichiometry: the key for the optimization of thermoelectric properties in stannoidite  $\text{Cu}_{8+x}\text{Fe}_{3-x}\text{Sn}_2\text{S}_{12}$ , *J. Phys. Chem. C* 121 (2017) 16454–16461, <https://doi.org/10.1021/acs.jpcc.7b02068>.
- [44] T. Barbier, D. Berthebaud, R. Frésard, O.I. Lebedev, E. Guilmeau, V. Eyerta, A. Maignan, Structural and thermoelectric properties of n-type isocubanite  $\text{CuFe}_2\text{S}_3$ , *Inorg. Chem. Front.* 4 (2017) 424–432, <https://doi.org/10.1039/C6QI00510A>.
- [45] V.P. Kumar, L. Paradis-Fortin, P. Lemoine, V. Caignaert, B. Raveau, B. Malaman, G.L. Caér, S. Cordier, E. Guilmeau, Designing a thermoelectric copper-rich sulfide from a natural mineral: synthetic germanite  $\text{Cu}_{22}\text{Fe}_8\text{Ge}_4\text{S}_{32}$ , *Inorg. Chem.* 56 (2017) 13376–13381, <https://doi.org/10.1021/acs.inorgchem.7b02128>.
- [46] S. Hébert, D. Berthebaud, R. Daou, Y. Bréard, D. Pelloquin, E. Guilmeau, F. Gascoin, O. Lebedev, A. Maignan, Searching for new thermoelectric materials: some examples among oxides, sulfides and selenides, *J. Phys. Condens. Matter* 28 (2016) 013001/1–23, <https://doi.org/10.1088/0953-8984/28/1/013001>.
- [47] M. Ohta, P. Jood, M. Murata, C.H. Lee, A. Yamamoto, H. Obara, An integrated approach to thermoelectrics: combining phonon dynamics, nanoengineering, novel materials development, module fabrication, and metrology, *Adv. Energy Mater.* 9 (2019) 1801304/1–29, <https://doi.org/10.1002/aenm.201801304>.
- [48] Z.H. Ge, L.D. Zhao, D. Wu, X. Liu, B.P. Zhang, J.F. Li, J. He, Low-cost, abundant binary sulfides as promising thermoelectric materials, *Mater. Today* 19 (2016) 227–239, <https://doi.org/10.1016/j.mattod.2015.10.004>.

- [49] P. Qiu, X. Shi, L. Chen, Cu-based thermoelectric materials, *Energy Storage Mater.* 3 (2016) 85–97, <https://doi.org/10.1016/j.ensm.2016.01.009>.
- [50] K. Suekuni, T. Takabatake, Research update: Cu–S based synthetic minerals as efficient thermoelectric materials at medium temperatures, *APL Mater.* 4 (2016) 104503/1–11, <https://doi.org/10.1063/1.4955398>.
- [51] R. Mulla, M.H.K. Rabinal, Copper sulfides: earth-abundant and low-cost thermoelectric materials, *Energy Technol.* 7 (2019) 1800850/1–34, <https://doi.org/10.1002/ente.201800850>.
- [52] T.R. Wei, Y. Qin, T. Deng, Q. Song, B. Jiang, R. Liu, P. Qiu, X. Shi, L. Chen, Copper chalcogenide thermoelectric materials, *Sci. Chin. Mater.* 62 (2019) 8–24, <https://doi.org/10.1007/s40843-018-9314-5>.
- [53] P. Kush, S. Deka, Multifunctional copper-based quaternary chalcogenide semiconductors toward state-of-the-art energy applications, *ChemNanoMat* 5 (2019) 373–402, <https://doi.org/10.1002/cnma.201800321>.
- [54] D. Zhang, H.C. Bai, Z.L. Li, J.L. Wang, G.S. Fu, S.F. Wang, Multinary diamond-like chalcogenides for promising thermoelectric application, *Chin. Phys. B* 27 (2018) 047206/1–11, <https://doi.org/10.1088/1674-1056/27/4/047206>.
- [55] R. Chetty, A. Bali, R.C. Mallik, Tetrahedrites as thermoelectric materials: an overview, *J. Mater. Chem. C* 3 (2015) 12364–12378, <https://doi.org/10.1039/C5TC02537K>.
- [56] X. Lu, D.T. Morelli, in: C. Uher (Ed.), *Tetrahedrites: Earth-Abundant Thermoelectric Materials with Intrinsically Low Thermal Conductivity*, in: *Materials Aspects of Thermoelectricity*, CRC Press, Taylor and Francis Group, Boca Raton, FL, 2016, pp. 473–488, <https://doi.org/10.1201/9781315197029>. Chap. 16.
- [57] C. Candolfi, Y. Bouyrie, S. Sassi, A. Dauscher, B. Lenoir, Tetrahedrites: prospective novel thermoelectric materials, in: S. Skipidarov, M. Nikitin (Eds.), *Thermoelectrics for Power Generation—A Look at Trends in the Technology*, InTech, 2016, pp. 73–91, <https://doi.org/10.5772/65638>. Chap. 4.
- [58] M. Ohta, High performance thermoelectrics for power generation using earth-abundant and low toxicity elements—toward developing an innovative waste heat recovery system—, *Synthesiology* 10 (2017) 63–74. [https://www.aist.go.jp/aist\\_j/aistinfo/synthesiology/paper\\_point.html#10\\_2](https://www.aist.go.jp/aist_j/aistinfo/synthesiology/paper_point.html#10_2).
- [59] N.E. Johnson, J.R. Craig, J.D. Rimstidt, Compositional trends in tetrahedrite, *Can. Mineral.* 24 (1986) 385–397. <https://pubs.geoscienceworld.org/canmin/article-abstract/24/2/385/11883/compositional-trends-in-tetrahedrite?redirectedFrom=fulltext>.
- [60] A. Pfitzner, M. Evain, V. Petricek,  $\text{Cu}_{12}\text{Sb}_4\text{S}_{13}$ : a temperature-dependent structure investigation, *Acta Crystallogr. B* 53 (1997) 337–345, <https://doi.org/10.1107/S0108768196014024>.
- [61] K. Momma, F. Izumi, VESTA 3 for three-dimensional visualization of crystal, volumetric and morphology data, *J. Appl. Crystallogr.* 44 (2011) 1272–1276, <https://doi.org/10.1107/S0021889811038970>.
- [62] N.E. Johnson, J.R. Craig, J.D. Rimstidt, Crystal chemistry of tetrahedrite, *Am. Mineral.* 73 (1988) 389–397. <https://pubs.geoscienceworld.org/msa/ammin/article-abstract/73/3-4/389/42147/crystal-chemistry-of-tetrahedrite?redirectedFrom=PDF>.
- [63] M.L. Johnson, C.W. Burnham, Crystal structure refinement of an arsenic-bearing argentian tetrahedrite, *Am. Mineral.* 70 (1985) 165–170. <https://pubs.geoscienceworld.org/msa/ammin/article-abstract/70/1-2/165/41660/crystal-structure-refinement-of-an-arsenic-bearing?redirectedFrom=fulltext>.
- [64] E. Makovicky, S. Karup Møller, Exploratory studies on substitution of minor elements in synthetic tetrahedrite. Part I. Substitution by Fe, Zn, Co, Ni, Mn, Cr, V and Pb. Unit-cell

- parameter changes on substitution and the structural role of "Cu<sup>2+</sup>", N. Jb. Mineral. (Abh.) 167 (1994) 89–123. w/o DOI and URL.
- [65] D.S.P. Kumar, S. Tippireddy, A. Ramakrishnan, K.H. Chen, P. Malar, R.C. Mallik, Thermoelectric and electronic properties of chromium substituted tetrahedrite, Semicond. Sci. Technol. 34 (2019) 035017/1–14, <https://doi.org/10.1088/1361-6641/aafa31>.
  - [66] R.A.D. Patrick, A.J. Hall, Silver substitution into synthetic zinc, cadmium, and iron tetrahedrites, Mineral. Mag. 47 (1983) 441–451, <https://doi.org/10.1180/minmag.1983.047.345.05>.
  - [67] M.H. Klünder, E. Makovicky, S. Karup-Møller, Exploratory studies on substitutions in tetrahedrite-tennantite solid solution. Part IV. Substitution of germanium and tin, N. Jb. Mineral. (Abh.) 179 (2003) 43–71, <https://doi.org/10.1127/0077-7757/2003/0179-0043>.
  - [68] P. Levinsky, C. Candolfi, A. Dauscher, B. Lenoir, J. Hejtmánek, Thermoelectric properties of magnesium-doped tetrahedrite Cu<sub>12-x</sub>Mg<sub>x</sub>Sb<sub>4</sub>S<sub>13</sub>, J. Electron. Mater. 48 (2019) 1926–1931, <https://doi.org/10.1007/s11664-019-07032-w>.
  - [69] Y. Bouyrie, C. Candolfi, S. Pailhès, M.M. Koza, B. Malaman, A. Dauscher, J. Tobola, O. Boisron, L. Saviot, B. Lenoir, From crystal to glass-like thermal conductivity in crystalline minerals, Phys. Chem. Chem. Phys. 17 (2015) 19751–19758, <https://doi.org/10.1039/c5cp02900g>.
  - [70] M.H. Klünder, S. Karup-Møller, E. Makovicky, Exploratory studies on substitutions in the tetrahedrite-tennantite solid solution series Part III. The solubility of bismuth in tetrahedrite-tennantite containing iron and zinc, N. Jb. Mineral. (Abh.) 2003 (2003) 153–175, <https://doi.org/10.1127/0028-3649/2003/2003-0153>.
  - [71] X. Lu, D.T. Morelli, Y. Wang, W. Lai, Y. Xia, V. Ozolins, Phase stability, crystal structure, and thermoelectric properties of Cu<sub>12</sub>Sb<sub>4</sub>S<sub>13-x</sub>Se<sub>x</sub> solid solutions, Chem. Mater. 28 (2016) 1781–1786, <https://doi.org/10.1021/acs.chemmater.5b04796>.
  - [72] E. Makovicky, B.J. Skinner, Studies of the sulfosalts of copper; VI, low-temperature exsolution in synthetic tetrahedrite solid solution, Cu<sub>12+x</sub>Sb<sub>4+y</sub>S<sub>13</sub>, Can. Mineral. 16 (1978) 611–623. <https://pubs.geoscienceworld.org/canmin/article-abstract/16/4/611/11283/studies-of-the-sulfosalts-of-copper-vi-low?redirectedFrom=fulltext>.
  - [73] K. Suekuni, Y. Tomizawa, T. Ozaki, M. Koyano, Systematic study of electronic and magnetic properties for Cu<sub>12-x</sub>TM<sub>x</sub>Sb<sub>4</sub>S<sub>13</sub> (TM=Mn, Fe, Co, Ni, and Zn) tetrahedrite, J. Appl. Phys. 115 (2014) 143702/1–5, <https://doi.org/10.1063/1.4871265>.
  - [74] Y. Bouyrie, C. Candolfi, V. Ohorodniichuk, B. Malaman, A. Dauscher, J. Tobola, B. Lenoir, Crystal structure, electronic band structure and high-temperature thermoelectric properties of Te-substituted tetrahedrites Cu<sub>12</sub>Sb<sub>4-x</sub>Te<sub>x</sub>S<sub>13</sub> (0.5 ≤ x ≤ 2.0), J. Mater. Chem. C 3 (2015) 10476–10487, <https://doi.org/10.1039/C5TC01636C>.
  - [75] H.I. Tanaka, K. Suekuni, K. Umeo, T. Nagasaki, H. Sato, G. Kutluk, E. Nishibori, H. Kasai, T. Takabatake, Metal–semiconductor transition concomitant with a structural transformation in tetrahedrite Cu<sub>12</sub>Sb<sub>4</sub>S<sub>13</sub>, J. Phys. Soc. Jpn. 85 (2016) 014703/1–6, <https://doi.org/10.7566/JPSJ.85.014703>.
  - [76] N. Seltenrich, Thermoelectrics: An Old, New Tech, Berkeley Engineer, Spring, 2016, pp. 14–17. <https://engineering.berkeley.edu/magazine/spring-2016/thermoelectrics-old-new-tech>.
  - [77] L. Miller, J.P. Reifenberg, D. Crane, A. Lorimer, M. Aguirre, J. Chase, M.L. Scullin, Electrical and Thermal Contacts for Bulk Tetrahedrite Material, and Methods of Making the Same, U.S. Patent 20160190420A1, <https://patents.google.com/patent/WO2016109202A1/ja>.
  - [78] R. Chetty, D.S. Prem Kumar, G. Rogl, P. Rogl, E. Bauer, H. Michor, S. Suwas, S. Puchegger, G. Giester, R.C. Mallik, Thermoelectric properties of a Mn substituted synthetic

- tetrahedrite, *Phys. Chem. Chem. Phys.* 17 (2015) 1716–1727, <https://doi.org/10.1039/C4CP04039B>.
- [79] J. Wang, X. Li, Y. Bao, Thermoelectric properties of Mn doped  $\text{Cu}_{12-x}\text{Mn}_x\text{Sb}_4\text{S}_{13}$  tetrahedrites, *Mater. Sci. Forum* 847 (2016) 161–165, <https://doi.org/10.4028/www.scientific.net/MSF.847.161>.
- [80] R. Chetty, A. Bali, M.H. Naik, G. Rogl, P. Rogl, M. Jain, S. Suwas, R.C. Mallik, Thermoelectric properties of Co substituted synthetic tetrahedrite, *Acta Mater.* 100 (2015) 266–274, <https://doi.org/10.1016/j.actamat.2015.08.040>.
- [81] Y. Bouyrie, S. Sassi, C. Candolfi, J.-B. Vaney, A. Dauscher, B. Lenoir, Thermoelectric properties of double-substituted tetrahedrites  $\text{Cu}_{12-x}\text{Co}_x\text{Sb}_{4-y}\text{Te}_y\text{S}_{13}$ , *Dalton Trans.* 45 (2016) 7294–7302, <https://doi.org/10.1039/C6DT00564K>.
- [82] S.Y. Kim, G.E. Lee, I.H. Kim, Thermoelectric properties of mechanically-alloyed and hot-pressed  $\text{Cu}_{12-x}\text{Co}_x\text{Sb}_4\text{S}_{13}$  tetrahedrites, *J. Korean Phys. Soc.* 74 (2019) 967–971, <https://doi.org/10.3938/jkps.74.967>.
- [83] T. Barbier, P. Lemoine, S. Gascoin, O.I. Lebedev, A. Kaltzoglou, P. Vaqueiro, A.V. Powell, R.I. Smith, E. Guilmeau, Structural stability of the synthetic thermoelectric ternary and nickel-substituted tetrahedrite phases, *J. Alloys Compd.* 634 (2015) 253–262, <https://doi.org/10.1016/j.jallcom.2015.02.045>.
- [84] T. Barbier, S. Rollin-Martinet, P. Lemoine, F. Gascoin, A. Kaltzoglou, P. Vaqueiro, A.V. Powell, E. Guilmeau, Thermoelectric materials: a new rapid synthesis process for non-toxic and high-performance tetrahedrite compounds, *J. Am. Ceram. Soc.* 99 (2016) 51–56, <https://doi.org/10.1111/jace.13838>.
- [85] T. Barbier, P. Lemoine, S. Martinet, M. Eriksson, M. Gilmas, E. Hug, G. Guélou, P. Vaqueiro, A.V. Powell, E. Guilmeau, Up-scaled synthesis process of sulphur-based thermoelectric materials, *RSC Adv.* 6 (2016) 10044–10053, <https://doi.org/10.1039/C5RA23218J>.
- [86] S.G. Kwak, G.E. Lee, I.H. Kim, Electronic transport and thermoelectric properties of  $\text{Cu}_{12-x}\text{Zn}_x\text{Sb}_4\text{S}_{13}$  tetrahedrites prepared by mechanical alloying and hot pressing, *Korean J. Met. Mater.* 57 (2019) 1–6, <https://doi.org/10.3365/KJMM.2019.57.5.328>.
- [87] D.S.P. Kumar, R. Chetty, P. Rogl, G. Rogl, E. Bauer, P. Malar, R.C. Mallik, Thermoelectric properties of cd doped tetrahedrite:  $\text{Cu}_{12-x}\text{Cd}_x\text{Sb}_4\text{S}_{13}$ , *Intermetallics* 78 (2016) 21–29, <https://doi.org/10.1016/j.intermet.2016.08.003>.
- [88] S. Tippireddy, R. Chetty, M.H. Naik, M. Jain, K. Chattopadhyay, R.C. Mallik, Electronic and thermoelectric properties of transition metal substituted tetrahedrites, *J. Phys. Chem. C* 122 (2018) 8735–8749, <https://doi.org/10.1021/acs.jpcc.7b12214>.
- [89] Y. Kosaka, K. Suekuni, K. Hashikuni, Y. Bouyrie, M. Ohta, T. Takabatake, Effects of Ge and Sn substitution on the metal–semiconductor transition and thermoelectric properties of  $\text{Cu}_{12}\text{Sb}_4\text{S}_{13}$  tetrahedrite, *Phys. Chem. Chem. Phys.* 19 (2017) 8874–8879, <https://doi.org/10.1039/c7cp00351j>.
- [90] L.L. Huang, Y.S. Wang, C. Zhu, R. Xu, J.M. Li, J.H. Zhang, D. Li, Z.M. Wang, L. Wang, C.J. Song, H.X. Xin, J. Zhang, X.Y. Qin, Preparation and enhanced thermoelectric performance of Pb-doped tetrahedrite  $\text{Cu}_{12-x}\text{Pb}_x\text{Sb}_4\text{S}_{13}$ , *J. Alloys Compd.* 69 (2018) 478–483, <https://doi.org/10.1016/j.jallcom.2018.07.335>.
- [91] X. Lu, D. Morelli, The effect of Te substitution for Sb on thermoelectric properties of tetrahedrite, *J. Electron. Mater.* 43 (2014) 1983–1987, <https://doi.org/10.1007/s11664-013-2931-2>.
- [92] D.S.P. Kumar, R. Chetty, O.E. Femi, K. Chattopadhyay, P. Malar, R.C. Mallik, Thermoelectric properties of Bi doped tetrahedrite, *J. Electron. Mater.* 46 (2017) 2616–2622, <https://doi.org/10.1007/s11664-016-4826-5>.

- [93] X. Lu, D.T. Morelli, Y. Xia, V. Ozolins, Increasing the thermoelectric figure of merit of tetrahedrites by co-doping with nickel and zinc, *Chem. Mater.* 27 (2015) 408–413, <https://doi.org/10.1021/cm502570b>.
- [94] Y. Bouyrie, C. Candolfi, J.B. Vaney, A. Dauscher, B. Lenoir, High temperature transport properties of tetrahedrite  $\text{Cu}_{12-x}M_x\text{Sb}_{4-y}\text{Te}_y\text{S}_{13}$  ( $M = \text{Zn}, \text{Ni}$ ) compounds, *J. Electron. Mater.* 45 (2016) 1601–1605, <https://doi.org/10.1007/s11664-015-4128-3>.
- [95] S. Battiston, C. Fanciulli, S. Fiameni, A. Famengo, S. Fasolin, M. Fabrizio, One step synthesis and sintering of Ni and Zn substituted tetrahedrite as thermoelectric material, *J. Alloys Compd.* 702 (2017) 75–83, <https://doi.org/10.1016/j.jallcom.2017.01.187>.
- [96] D.P. Weller, D.T. Morelli, Rapid synthesis of zinc and nickel co-doped tetrahedrite thermoelectrics by reactive spark plasma sintering and mechanical alloying, *J. Alloys Compd.* 710 (2017) 794–799, <https://doi.org/10.1016/j.jallcom.2017.03.272>.
- [97] P. Vaqueiro, G. Guélou, A. Kaltzoglou, R.I. Smith, T. Barbier, E. Guilmeau, A.V. Powell, The influence of mobile copper ions on the glass-like thermal conductivity of copper-rich tetrahedrites, *Chem. Mater.* 29 (2017) 4080–4090, <https://doi.org/10.1021/acs.chemmater.7b00891>.
- [98] Y. Yan, H. Wu, G. Wang, X. Lu, X. Zhou, High thermoelectric performance balanced by electrical and thermal transport in tetrahedrites  $\text{Cu}_{12+x}\text{Sb}_4\text{S}_{12}\text{Se}$ , *Energy Storage Mater.* 13 (2018) 127–133, <https://doi.org/10.1016/j.ensm.2018.01.006>.
- [99] X. Lu, W. Yao, G. Wang, X. Zhou, D. Morelli, Y. Zhang, H. Chi, S. Hui, C. Uher, Band structure engineering in highly degenerate tetrahedrites through isovalent doping, *J. Mater. Chem. A* 4 (2016) 17096–17103, <https://doi.org/10.1039/c6ta07015a>.
- [100] K. Suekuni, C.H. Lee, H.I. Tanaka, E. Nishibori, A. Nakamura, H. Kasai, H. Mori, H. Usui, M. Ochi, T. Hasegawa, M. Nakamura, S. Ohira-Kawamura, T. Kikuchi, K. Kaneko, H. Nishiate, K. Hashikuni, Y. Kosaka, K. Kuroki, T. Takabatake, Retreat from stress: rattling in a planar coordination, *Adv. Mater.* 30 (2018) 1706230/1–6, <https://doi.org/10.1002/adma.201706230>.
- [101] P. Levinsky, C. Candolfi, A. Dauscher, J. Tobola, J. Hejtmánek, B. Lenoir, Thermoelectric properties of the tetrahedrite–tenantite solid solutions  $\text{Cu}_{12}\text{Sb}_{4-x}\text{As}_x\text{S}_{13}$  and  $\text{Cu}_{10}\text{Co}_2\text{Sb}_{4-y}\text{As}_y\text{S}_{13}$  ( $0 \leq x, y \leq 4$ ), *Phys. Chem. Chem. Phys.* 21 (2019) 4547–4555, <https://doi.org/10.1039/C9CP00213H>.
- [102] X. Lu, D.T. Morelli, Natural mineral tetrahedrite as a direct source of thermoelectric materials, *Phys. Chem. Chem. Phys.* 15 (2013) 5762–5766, <https://doi.org/10.1039/C3CP50920F>.
- [103] X. Lu, D.T. Morelli, Rapid synthesis of high-performance thermoelectric materials directly from natural mineral tetrahedrite, *MRS Commun.* 3 (2013) 129–133, <https://doi.org/10.1557/mrc.2013.26>.
- [104] W. Lai, Y. Wang, D.T. Morelli, X. Lu, From bonding asymmetry to anharmonic rattling in  $\text{Cu}_{12}\text{Sb}_4\text{S}_{13}$  tetrahedrites: when lone-pair electrons are not so lonely, *Adv. Funct. Mater.* 25 (2015) 3648–3657, <https://doi.org/10.1002/adfm.201500766>.
- [105] A.F. May, O. Delaire, J.L. Niedziela, E. Lara-Curcio, M.A. Susner, D.L. Abernathy, M. Kirkham, M.A. McGuire, Structural phase transition and phonon instability in  $\text{Cu}_{12}\text{Sb}_4\text{S}_{13}$ , *Phys. Rev. B* 93 (2016) 064104/1–8, <https://doi.org/10.1103/PhysRevB.93.064104>.
- [106] C.H. Lee, I. Hase, H. Sugawara, H. Yoshizawa, H. Sato, Low-lying optical phonon modes in the filled skutterudite  $\text{CeRu}_4\text{Sb}_{12}$ , *J. Phys. Soc. Jpn.* 75 (2006) 123602/1–5, <https://doi.org/10.1143/JPSJ.75.123602>.
- [107] P.G. Spry, S. Merlino, S. Wang, X. Zhang, P.R. Buseck, New occurrences and refined crystal chemistry of colusite, with comparisons to arsenosulvanite, *Am. Mineral.* 79 (1994) 750–763. <https://pubs.geoscienceworld.org/msa/ammin/article-abstract/79/7-8/750/42892/New-occurrences-and-refined-crystal-chemistry-of?redirectedFrom=fulltext>.

- [108] O.V. Frank-Kamenetskaya, I.V. Rozhdestvenskaya, L.A. Yanulova, New data on the crystal structures of colusites and arsenosulvanites, *J. Struct. Chem.* 43 (2002) 89–100, <https://doi.org/10.1023/A:1016077917390>.
- [109] V.P. Kumar, A.R. Supka, P. Lemoine, O.I. Lebedev, B. Raveau, K. Suekuni, V. Nassif, R. A.R.A. Orabi, M. Fornari, E. Guilmeau, High power factors of thermoelectric colusites  $\text{Cu}_{26}T_2\text{Ge}_6\text{S}_{32}$  ( $T = \text{Cr}, \text{Mo}, \text{W}$ ): toward functionalization of the conductive “Cu–S” network, *Adv. Energy Mater.* 9 (2018) 1803249/1–11, <https://doi.org/10.1002/aenm.201803249>.
- [110] F.S. Kim, K. Suekuni, H. Nishiate, M. Ohta, H.I. Tanaka, T. Takabatake, Tuning the charge carrier density in the thermoelectric colusite, *J. Appl. Phys.* 119 (2016) 175105/1–5, <https://doi.org/10.1063/1.4948475>.
- [111] Y. Bouyrie, V. Ohorodniichuk, S. Sassi, P. Masschelein, A. Dauscher, C. Candolfi, B. Lenoir, High-temperature transport properties of colusite  $\text{Cu}_{24}T_2\text{V}_2\text{Ge}_6\text{S}_{32}$  ( $T = \text{Ni}, \text{Co}$ ), *J. Electron. Mater.* 46 (2017) 2684–2690, <https://doi.org/10.1007/s11664-016-4893-7>.
- [112] Y. Bouyrie, M. Ohta, K. Suekuni, P. Jood, T. Takabatake, Addition of Co, Ni, Fe and their role in the thermoelectric properties of colusite  $\text{Cu}_{26}\text{Nb}_2\text{Ge}_6\text{S}_{32}$ , *J. Alloys Compd.* 735 (2018) 1838–1845, <https://doi.org/10.1016/j.jallcom.2017.11.199>.
- [113] Y. Kikuchi, Y. Bouyrie, M. Ohta, K. Suekuni, M. Aihara, T. Takabatake, Vanadium-free colusites  $\text{Cu}_{26}\text{A}_2\text{Sn}_6\text{S}_{32}$  ( $\text{A} = \text{Nb}, \text{Ta}$ ) for environmentally friendly thermoelectrics, *J. Mater. Chem. A* 4 (2016) 15207–15214, <https://doi.org/10.1039/c6ta05945g>.
- [114] C. Bourgès, Y. Bouyrie, A.R. Supka, R.A.R.A. Orabi, P. Lemoine, O.I. Lebedev, M. Ohta, K. Suekuni, V. Nassif, V. Hardy, R. Daou, Y. Miyazaki, M. Fornari, E. Guilmeau, High-performance thermoelectric bulk colusite by process controlled structural disordering, *J. Am. Chem. Soc.* 140 (2018) 2186–2195, <https://doi.org/10.1021/jacs.7b11224>.
- [115] Y. Bouyrie, M. Ohta, K. Suekuni, Y. Kikuchi, P. Jood, A. Yamamoto, T. Takabatake, Enhancement in the thermoelectric performance of colusites  $\text{Cu}_{26}\text{A}_2\text{E}_6\text{S}_{32}$  ( $\text{A} = \text{Nb}, \text{Ta}; \text{E} = \text{Sn}, \text{Ge}$ ) using E-site non-stoichiometry, *J. Mater. Chem. C* 5 (2017) 4174–4184, <https://doi.org/10.1039/c7tc00762k>.
- [116] K. Suekuni, Y. Shimizu, E. Nishibori, H. Kasai, H. Saito, D. Yoshimoto, K. Hashikuni, Y. Bouyrie, R. Chetty, M. Ohta, E. Guilmeau, T. Takabatake, K. Watanabe, M. Ohtaki, Atomic-scale phonon scatterers in thermoelectric colusites with a tetrahedral framework structure, *J. Mater. Chem. A* 7 (2019) 228–235, <https://doi.org/10.1039/c8ta08248k>.
- [117] R. Chetty, Y. Kikuchi, Y. Bouyrie, P. Jood, A. Yamamoto, K. Suekuni, M. Ohta, Power generation from the  $\text{Cu}_{26}\text{Nb}_2\text{Ge}_6\text{S}_{32}$ -based single thermoelectric element with an diffusion barrier, *J. Mater. Chem. C* 7 (2019) 5184–5192, <https://doi.org/10.1039/c9tc00868c>.
- [118] Q.L. Meng, S. Kong, Z. Huang, Y. Zhu, H.C. Liu, X. Lu, P. Jiang, X. Bao, Simultaneous enhancement in the power factor and thermoelectric performance of copper sulfide by  $\text{In}_2\text{S}_3$  doping, *J. Mater. Chem. A* 4 (2016) 12624–12629, <https://doi.org/10.1039/C6TA03780A>.

# High-performance thermoelectrics based on metal selenides

2.8

Tanmoy Ghosh<sup>a</sup>, Moinak Dutta<sup>a</sup>, and Kanishka Biswas<sup>a,b,c</sup>

<sup>a</sup>New Chemistry Unit, Jawaharlal Nehru Centre for Advanced Scientific Research (JNCASR), Bangalore, India, <sup>b</sup>School of Advanced Materials, Jawaharlal Nehru Centre for Advanced Scientific Research (JNCASR), Bangalore, India, <sup>c</sup>International Centre of Materials Science, Jawaharlal Nehru Centre for Advanced Scientific Research (JNCASR), Bangalore, India

## 2.8.1 Introduction

Thermoelectric materials based on metal chalcogenide (S, Se, and Te-based) semiconductors are being used in thermoelectric applications for a long time, and in recent years, there has been a tremendous improvement in their thermoelectric performance [1]. These advancements can be primarily attributed to the development of new material processing techniques and our improved understanding, as well as manipulation capabilities, of electron and phonon transports. The key advantages of these heavy metal-chalcogenide-based thermoelectric materials are their intrinsically low lattice thermal conductivity because of heavy atomic masses of the constituent atoms and relatively easy composition manipulability to achieve the desired electronic and thermal properties. However, out of these S, Se and Te-based chalcogenides, Te-based chalcogenides, such as LAST [2], TAGS [3],  $\text{Bi}_2\text{Te}_3/\text{Sb}_2\text{Te}_3$  [4], etc., received the most attention in the early days of development of high-performance thermoelectrics. While Se is the more earth abundant element compared to Te and has a much lower market price, the development of Se-based thermoelectric materials was much slower. One of the major drawbacks is the Se evaporation when subjected to high temperatures because of the lower melting point of Se (493 K) compared to Te (723 K), which degrades the material's thermoelectric performance. Se compounds, such as  $\text{Cu}_2\text{Se}$ , are known in the thermoelectric community for a long time and research on  $\text{Cu}_2\text{Se}$  was actively pursued in 1960s and 1970s for practical applications [5]. However, material degradation due to copper ion migration was so detrimental that research and development stopped eventually. In addition, Se has a lower atomic mass compared to Te because of which Se compounds tend to have higher lattice thermal conductivity compared to Te compounds. High-performance Se-based thermoelectric materials, such as PbSe [6], SnSe [7], and  $\text{In}_4\text{Se}_3$  [8], have emerged in the last decade only. Several ternary selenides such as  $\text{AgSbSe}_2$ ,  $\text{AgBiSe}_2$ ,  $\text{AgCuSe}$ ,  $\text{AgCrSe}_2$ , and oxy-selenides such as  $\text{BiCuSeO}$  are also generating impressive popularity in thermoelectrics owing to their innate low lattice thermal

conductivity. In this chapter, we discuss the fundamentals of correlation among the electronic, thermal, and structural properties of several high-performance metal selenide thermoelectrics and their recent progress.

## 2.8.2 State-of-the-art materials

### 2.8.2.1 *Binary metal selenides*

#### 2.8.2.1.1 *PbSe*

Lead telluride (PbTe)-based materials are generally considered to be in the forefront in terms of power generating efficiency in the mid-temperature (600–900 K) region. The major bottleneck, however, lies in the lack of natural abundance, and subsequently the high cost of Te, which obstructs its manufacturing for mass market applications. More abundant Se, which lies just above Te in the chalcogenide family, is thus seen as a cost-effective analog to PbTe. PbSe, like its Te counterpart, have rock-salt-type cubic structure wherein Pb resides in the cation position and Se in the anion position. PbSe has a bandgap of  $\sim 0.27$  eV, melting point of  $\sim 1357$  K, and intrinsically lower thermal conductivity, which makes it a viable alternative to PbTe. In this part, we discuss the recent developments in PbSe, which renders them high-performance thermoelectric material and the associated concepts.

The electronic structure of PbSe is quite similar to that of PbTe. It is a direct bandgap semiconductor, having the primary bandgap at the L point. It has a second valence band at the  $\Sigma$  point with an energy offset of around 0.3 eV [9]. Band convergence by reducing the  $\Delta E(L - \Sigma)$  can increase the valley degeneracy of the system, which in turn increases the Seebeck coefficient ( $S$ ) without disrupting the carrier propagation. NaSbSe<sub>2</sub>-alloyed PbSe exhibits convergence of these two valence bands, which results in an increase in the Seebeck coefficient value but do not hinder the electronic conductivity drastically. Added to the fact that Na and Sb occupy the Pb position in the lattice offers enhanced point defect scattering and lowers the lattice thermal conductivity ( $\kappa_L$ ), which ranges between 1 and 0.55 W/mK in the 400–873 K temperature range. NaSbSe<sub>2</sub>, which has a bandgap of  $\sim 1.1$  eV, on alloying with PbSe widens the principal bandgap of PbSe [9]. After a certain alloying concentration, the L and  $\Sigma$  bands flatten out and both these bands contribute to electrical transport properties. As a result, a higher power factor of  $\sim 15$   $\mu\text{W}/\text{cm K}^2$  is obtained at 873 K in Na<sub>1.1</sub>Pb<sub>10</sub>Sb<sub>0.9</sub>Se<sub>12</sub>. Added to the low lattice thermal conductivity of this material, it exhibits a superior *p*-type thermoelectric figure of merit (zT) of 1.4 at 873 K [9].

A similar band convergence has also been observed in HgSe-alloyed PbSe. From a chemical perspective, the valence band edge in PbSe is dominated by the contributions from the 6s<sup>2</sup> lone pairs of Pb<sup>2+</sup> cation. The replacement of Pb<sup>2+</sup> with Hg<sup>2+</sup>, which is devoid of such lone pairs, will aid in lowering the primary band edge at the L point. Indeed, it has been observed that HgSe alloying leads to an increase in bandgap from 0.27 eV for pristine PbSe to 0.33 eV for 6 mol% HgSe-alloyed PbSe [10]. This resulted in the lowering of band offset between the L and  $\Sigma$  valence bands (Fig. 2.8.1A) and at about 550 K, one can observe the contributions of both bands in the transport properties. This, in turn, results in a high power factor ( $\sigma S^2$ ) of  $\sim 20$   $\mu\text{W}/\text{cm K}^2$  for 2 mol%

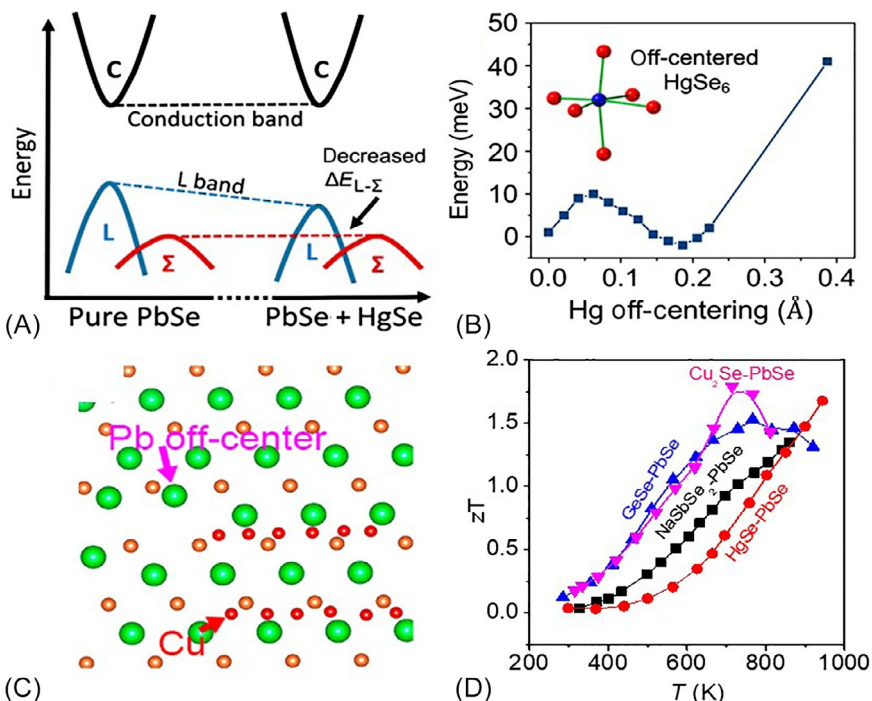


**Fig. 2.8.1** (A) Schematic illustration showing a decrease in the energy offset between L and  $\Sigma$  valence bands of PbSe with HgSe incorporation. (B) Decrease in the total energy of PbSe with Hg off-centering in  $\text{HgSe}_6$  octahedra. (C) Schematic of Cu atoms residing in interstitial positions in PbSe, which off-centers Pb due to Coulombic repulsion. (D) Thermoelectric figure of merit (zT) of some state-of-the-art PbSe-HgSe thermoelectrics.

Figures (A) and (B) are reproduced with permission from reference J.M. Hodges, S. Hao, J.A. Grovogui, X. Zhang, T.P. Bailey, X. Li, Z. Gan, Y.-Y. Hu, C. Uher, V.P. Dravid, C. Wolverton, M.G. Kanatzidis, Chemical insights into  $\text{PbSe}-x\%\text{HgSe}$ : high power factor and improved thermoelectric performance by alloying with discordant atoms, *J. Am. Chem. Soc.* 140 (2018) 18115. <https://doi.org/10.1021/jacs.8b11050> © 2018 American Chemical Society. Figure (C) is reproduced with permission from reference C. Zhou, Y. Yu, Y.K. Lee, O. Cojocaru-Miredin, B. Yoo, S.-P. Cho, J. Im, M. Wuttig, T. Hyeon, I. Chung, High-performance n-type PbSe-Cu<sub>2</sub>Se thermoelectrics through conduction band engineering and phonon softening, *J. Am. Chem. Soc.* 140 (2018) 15535. <https://doi.org/10.1021/jacs.8b10448> © 2018 American Chemical Society.

HgSe alloyed Pb<sub>0.98</sub>Na<sub>0.02</sub>Se<sub>2</sub> at 923 K. Hg atoms, due to the relativistic effects, rarely achieve octahedral coordination in either solid solutions or molecular compounds. Pb atoms, which reside in an octahedral environment in PbSe, make an intriguing case for Hg incorporation in its position. Also, HgSe has a zinc-blende structure with metallic character (bandgap,  $E_g = 0\text{ eV}$ ), wherein Hg atoms occupy the tetrahedral holes in the compound. Therefore, it is counterintuitive that HgSe alloying in PbSe would increase the bandgap of PbSe and in direct contradiction to the experimental observations. Therefore, it is only logical to think that HgSe alloying in PbSe results in

an unusual bonding environment wherein the  $\text{Hg}^{2+}$  resides in the off-centered sites. This off-centering is locally guided as the powder X-ray diffraction (PXRD) shows a global cubic arrangement. Locally distorted atoms are known to provide emergent properties like low lattice thermal conductivity in a compound. It is worth remembering that PbSe in itself shows “emphanisis” behavior as is seen from pair distribution function (PDF) analysis [11].  $^{199}\text{Hg}$  and  $^{77}\text{Se}$  solid-state NMR data shows a pronounced anisotropic shift for Hg in the PbSe-6%HgSe alloy signifying a distorted environment, which is in accordance with general prediction as its tendency to avoid octahedral coordination. First-principles density functional theory (DFT) calculations also show that off-centering of Hg by  $\sim 0.2\text{\AA}$  is energetically more favorable (Fig. 2.8.1B), which further corroborates the experimental observations. This off-centering of  $\text{Hg}^{2+}$  has a profound effect on the lattice thermal conductivity as it acts as an effective scattering center of acoustic phonons. This off-centering leads to a low lattice thermal conductivity value of  $0.68\text{ W/mK}$  at  $\sim 950\text{ K}$  as compared to  $0.88\text{ W/mK}$  for pristine PbSe. The combined effects of off-centered  $\text{Hg}^{2+}$  cations and valence band convergence lead to an unprecedented  $zT$  of  $\sim 1.7$  in Hg-alloyed *p*-type PbSe [10].

This off-centering nature of cations in PbSe is not restricted to *p*-type materials only. In fact, GeSe-alloyed PbSe shows a peak *n*-type  $zT$  of  $\sim 1.54$  at  $773\text{ K}$  and an excellent  $ZT_{\text{avg}}$  of  $\sim 1.14$  for the temperature range of  $400\text{--}900\text{ K}$  [12]. The primary driving force for this high  $zT$  and  $ZT_{\text{avg}}$  values is the ultralow lattice thermal conductivity of this alloy. Pristine  $\text{Pb}_{0.9955}\text{Sb}_{0.0045}\text{Se}$  shows lattice thermal conductivity of  $\sim 1.84\text{ W/mK}$  at room temperature, while the same for 12% GeSe-alloyed  $\text{Pb}_{0.9955}\text{Sb}_{0.0045}\text{Se}$  is  $\sim 0.96\text{ W/mK}$ . The lattice thermal conductivity further decreases with increasing temperature and reaches an ultralow value of  $0.36\text{ W/mK}$  at  $573\text{ K}$ . First-principles DFT calculations show that Ge atoms in PbSe do not sit in the Pb position but are rhombohedrally off-centered by about  $0.3\text{\AA}$  from their parent positions. The most plausible explanation of this distortion is the presence of stereochemically active  $4s^2$  lone pairs of Ge, which occupy the space and distort the octahedral arrangement. The reduction in lattice thermal conductivity is similar to the PbSe-HgSe case, but the influence of off-centering is much more pronounced as Ge is much smaller than Hg and has the ability to induce anharmonicity in the lattice at a much larger scale than Hg. The electrical conductivity ( $\sigma$ ), however, decreases on Ge doping from  $\sim 4370\text{ S/cm}$  for  $\text{Pb}_{0.9955}\text{Sb}_{0.0045}\text{Se}$  to  $\sim 970\text{ S/cm}$  for  $\text{Pb}_{0.9955}\text{Sb}_{0.0045}\text{Se-12\%GeSe}$  at  $300\text{ K}$ . This decrease in electrical conductivity is due to the decrease in carrier concentration as Ge contributes to intrinsic hole vacancies in the lattice. Seebeck coefficient value, however, increases from  $-49\text{ }\mu\text{V/K}$  for  $\text{Pb}_{0.9955}\text{Sb}_{0.0045}\text{Se}$  to  $-80\text{ }\mu\text{V/K}$ , and this increment is largely due to the decrease in the carrier concentrations. Power factor decreases from  $21\text{ }\mu\text{W/cmK}^2$  at  $773\text{ K}$  for  $\text{Pb}_{0.9955}\text{Sb}_{0.0045}\text{Se}$  to  $\sim 16\text{ }\mu\text{W/cmK}^2$  at  $600\text{ K}$  for  $\text{Pb}_{0.9955}\text{Sb}_{0.0045}\text{Se-14\%GeSe}$ . The decreases in the power factor is not so significant as compared to the decrease in lattice thermal conductivity, and as a result, an impressive *n*-type  $zT$  of  $\sim 1.54$  is achieved in  $\text{Pb}_{0.9955}\text{Sb}_{0.0045}\text{Se-12\%GeSe}$  at  $773\text{ K}$  [12].

The convergence of conduction bands for achieving higher *n*-type thermoelectric performance in PbSe is almost impossible as the energy offset between the two nearest conduction bands is  $\sim 0.5\text{ eV}$ . To increase the Seebeck coefficient value of *n*-type

PbSe, the common approach is to introduce resonant states. Al doping in PbSe has been shown to be effective in inducing resonant states in PbSe [13]. The room temperature Seebeck coefficient of Al-doped PbSe lies far above the theoretical Pisarenko Plot calculated with a single parabolic band (SPB) model indicating the formation of resonance level, and the consequent distortion in the electronic density of states. The room temperature Seebeck coefficient increases from  $-80\text{ }\mu\text{V/K}$  for 0.2% Cl-doped PbSe to  $-106\text{ }\mu\text{V/K}$  in 2% Al-doped PbSe. Further, the lattice thermal conductivity also decreases with an increase in Al doping due to the formation of nanosized pores and small crystalline grains. The lattice thermal conductivity decreases from  $\sim 0.9\text{ W/mK}$  for pristine to  $0.58\text{ W/mK}$  in 3% Al-doped PbSe. This reduction in lattice thermal conductivity coupled with the increase in Seebeck coefficient resulted in a peak  $zT \sim 1.3$  in 1% Al-doped PbSe with *n*-type conduction [13].

Several other well-known methods of increasing the  $zT$  have also been applied in PbSe in recent years. Notably, it has been seen that although Sb and Bi reside in the same group of the periodic table, their inclusion in PbSe results in quite contrasting effects [14]. Sb, due to its size mismatch with Pb, forms nanoprecipitates quite easily. Even 0.25 mol% Sb doping is sufficient to form nanoprecipitates which are effective in reducing the lattice thermal conductivity by scattering the heat-carrying acoustic phonons. Bi, on the other hand, has comparable size with Pb and do not form such precipitates and, as a result, does not lower the lattice thermal conductivity effectively. This contrasting effect of Bi and Sb on the microstructure and lattice thermal conductivity markedly affects the  $zT$ . While  $\text{Pb}_{0.9975}\text{Sb}_{0.0025}\text{Se}$  shows an *n*-type peak  $zT \sim 1.45$  at 830 K, Bi-doped PbSe reaches a maximum *n*-type  $zT$  of  $\sim 0.89$  at 920 K in  $\text{Pb}_{0.995}\text{Bi}_{0.005}\text{Se}$  [14].  $\text{Cu}_2\text{Se}$ -doped PbSe showcases an interesting case of conduction band flattening where Cu gets incorporated into the lattice voids of PbSe [15]. Cu atoms act as guest atoms in cages because of their small sizes and behave like rattlers, and thus effectively decrease the lattice thermal conductivity. Electrostatic repulsions between Pb and Cu result in Pb being locally off-centered from its mean position along the [110] direction which further induces lattice anharmonicity (Fig. 2.8.1C). Finally, bandgap also increases from 0.17 eV for PbSe to 0.24 eV in PbSe-3% $\text{Cu}_2\text{Se}$ . This increase in bandgap leads to an increase in effective mass ( $m^*$ ) by almost 10-fold from  $0.109m_e$  for pristine PbSe to  $1.023m_e$  in 3 mol%  $\text{Cu}_2\text{Se}$ -doped PbSe. This increase in  $m^*$  leads to higher DOS adjacent to the Fermi level while the higher bandgap means the charge carriers will possess high polarity. Both these factors enhance the Seebeck coefficient, particularly at higher temperatures. This increase in Seebeck coefficient value combined with ultralow lattice thermal conductivity leads to an impressive *n*-type  $zT$  of  $\sim 1.8$  at 723 K and  $ZT_{avg}$  of  $\sim 1.1$  for the temperature range of 300–823 K [15]. Fig. 2.8.1D shows a thermoelectric performance of some state-of-the-art PbSe-based thermoelectric materials.

Several general approaches of improving the thermoelectric performance like carrier modulation, hierarchical scattering has also been applied to PbSe to achieve impressive  $zT$  values. Na and Cd co-doped PbSe shows *p*-type peak  $zT$  of  $\sim 1.6$  at 923 K, which has been attributed to hierarchical all-scale scattering as well as band convergence [16]. Similar observations have also been made in the case of Sr-doped PbSe [17], Cd-doped PbSe-PbTe alloy [18], Cu-doped PbSe [19], etc.

### 2.8.2.1.2 SnSe

SnSe has created a sensation in the thermoelectric community since the work of Zhao et al. in which they obtained  $zT = 2.6$  at 923 in pristine SnSe single crystal (Fig. 2.8.2C) and  $ZT_{dev} = 1.34$  for the temperature range 300–773 K in hole-doped SnSe single crystal along the crystallographic *b*-axis [7, 20]. The thermoelectric performance along the crystallographic *a*-axis is, however, much lower with a peak  $zT = 0.8$ . SnSe bears few very intriguing features as a thermoelectric material: intrinsically ultralow lattice thermal conductivity due to highly anharmonic bonding and high Seebeck coefficient

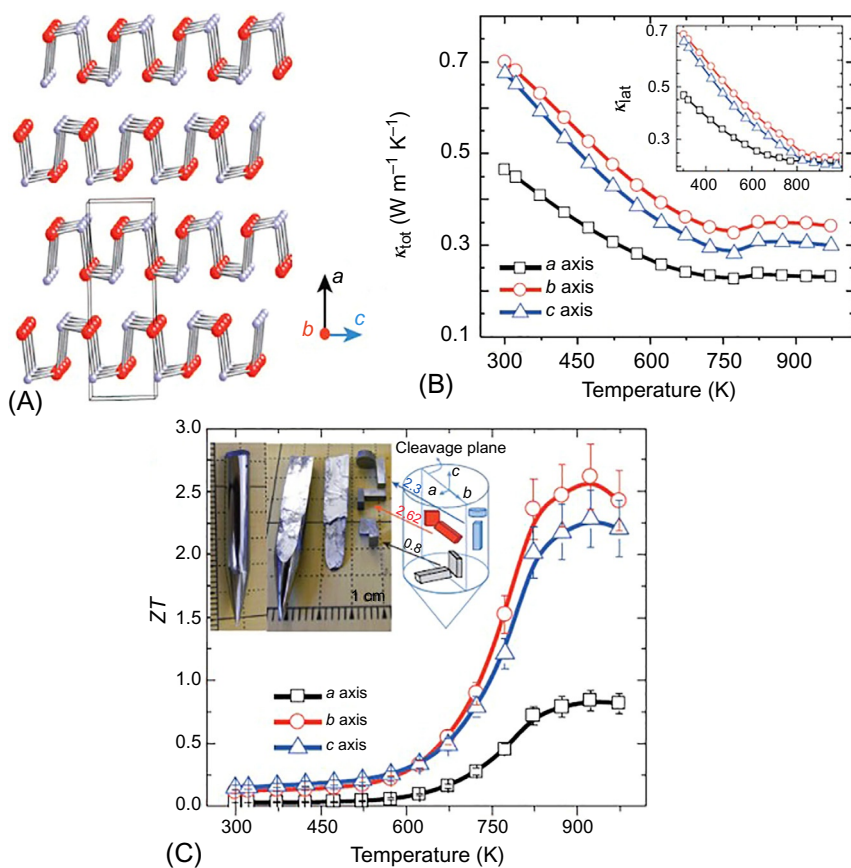


**Fig. 2.8.2** (A) Layered and corrugated crystal structure of SnSe at room temperature. (B) Temperature variation of total thermal conductivity ( $\kappa_{tot}$ ) along the crystallographic *a*-, *b*-, and *c*-axis. Inset shows the lattice thermal conductivity ( $\kappa_{lat}$ ). (C) Thermoelectric figure of merit ( $zT$ ) of single-crystalline *p*-type pristine SnSe.

Figures (A)–(C) are reproduced with permission from reference L.-D. Zhao, S.-H. Lo, Y. Zhang, H. Sun, G. Tan, C. Uher, C. Wolverton, V.P. Dravid, M.G. Kanatzidis, Ultralow thermal conductivity and high thermoelectric figure of merit in SnSe crystals, *Nature* 508 (2014) 373–377. <https://doi.org/10.1038/nature13184> © 2014 Springer Nature.

due to the presence of multiple valence bands within closely spaced energy levels. These features are strongly correlated with the intriguing crystal structure of SnSe. SnSe has a layered orthorhombic crystal structure (space group *Pnma*, Fig. 2.8.2A) in ambient conditions [21]. This layered structure can be considered as an NaCl type structure having three-dimensional distortion. The layered structure consists of a two-atom thick slab in the *b-c* plane. These layers are stacked along the crystallographic *a*-axis and have strong Sn-Se intralayer bonds. The Sn-Se bonds along the crystallographic *a*-axis (out-of-plane direction) is, however, much weaker. Further, the structure comprises a distorted  $\text{SnSe}_7$  polyhedra, which comprises three short and four long Sn-Se bonds. The long bonds are mainly interlayer in character and also accommodate stereochemically active  $\text{Sn}^{2+}$  lone pairs. This layered structure and anisotropic chemical bonding reflect in its highly anisotropic electrical and thermal transport properties. This ambient structure undergoes a reversible second-order displacive phase transition to a higher symmetry phase (space group *Cmcm*)  $\sim 800\text{K}$ . This high-temperature phase transition has been shown to be a two-step process, which occurs continuously over a broad temperature range of  $\sim 200\text{K}$  [22]. In the first step, which happens over a broad temperature and below the critical temperature, atomic positions get shifted continuously along the crystallographic *b*-axis. In the second step, which happens abruptly within a small temperature range, the *b/a* ratio changes from  $>1$  in the *Pnma* phase to  $<1$  in the *Cmcm* phase. This high-temperature higher symmetry phase has a lower bandgap (0.39 eV compared to ambient bandgap of 0.86 eV in the *Pnma* phase). Because of this lower bandgap and stable Sn vacancies in the high-temperature phase, carrier concentration increases. However, the lattice thermal conductivity decreases with increasing temperature due to the enhanced phonon softening and the three-phonon scattering process compared to the ambient orthorhombic *Pnma* phase [22, 23].

SnSe is an indirect bandgap semiconductor with an energy gap of  $\sim 0.86\text{eV}$ . The extremely high Seebeck coefficient of SnSe is because of its valence band structure, which comprises multiple valence bands within small energy difference to the valence band maximum [20, 24]. The conduction band minimum and the valence band maximum are mainly constituted by Sn-p orbitals and Se-p orbitals, respectively. The topmost valence band is present along the  $\Gamma$ -Z direction. A second valence band exists just 0.06 eV below the topmost valence band. The energy difference between the topmost two valence bands is much lower in SnSe compared to other state-of-the-art thermoelectric materials such as PbTe and SnTe. As a result, the contribution of a second valence band in transport properties starts at a much lower temperature or doping level, which in turn generates extremely high power factor at lower temperatures in hole-doped SnSe. In undoped SnSe, the *p*-type carriers are primarily generated from the intrinsic  $\text{Sn}^{2+}$  vacancies and have room temperature carrier concentration of  $\sim 10^{17}\text{cm}^{-3}$  [22]. It has been shown that the Fermi level reaches the second valence band when the *p*-type carrier concentration reaches  $\sim 4 \times 10^{19}\text{cm}^{-3}$ . As the *p*-type carrier concentration increases further, the other lower lying valence bands also start participating in the electronic transport. For example, the energy difference between the first and the third valence band is only 0.13 eV. This multiband electronic transport is also evident from the temperature variation of the Hall effect as the Hall coefficient increases continuously with increasing temperature [20]. The room temperature

Pisarenko plot of carrier concentration vs Seebeck coefficient also shows similar multiband transport features as the Pisarenko curve could not be fitted with a single parabolic band but requires a multiband model. Hole doping tremendously increases the room temperature electrical conductivity from  $\sim 12 \text{ S/cm}$  for pristine SnSe to  $\sim 1500 \text{ S/cm}$ . The room temperature Seebeck coefficient of hole-doped SnSe is  $\sim 160 \mu\text{V/K}$  which is lower compared to that of pristine SnSe which has a value of  $\sim 500 \mu\text{V/K}$ , but much higher than other state-of-the-art thermoelectric materials for a similar carrier concentration level of  $\sim 4 \times 10^{19} \text{ cm}^{-3}$ . This high Seebeck coefficient arising from the contribution of multiple valence bands results in ultrahigh power factor with a value of  $\sim 40 \mu\text{W/cm K}^2$  for the crystallographic *b*-axis at room temperature and high  $ZT_{\text{dev}}$  of  $\sim 1.34$  for the temperature range  $300\text{--}773 \text{ K}$  in hole-doped SnSe single crystals [20]. The effective masses of the topmost two valence bands are also highly anisotropic. The effective masses for the topmost two valence bands are  $m_{kx} = 0.76 m_0$ ,  $m_{ky} = 0.33 m_0$ , and  $m_{kz} = 0.14 m_0$  for the first valence band and  $m_{kx} = 2.49 m_0$ ,  $m_{ky} = 0.18 m_0$ , and  $m_{kz} = 0.19 m_0$  for the second valence band. Such anisotropic effective masses cause anisotropy in the carrier mobility, which reflects in their anisotropic electrical conductivity.

One of the most intriguing features of SnSe is its ultralow lattice thermal conductivity [7, 25]. The room temperature lattice thermal conductivities along the crystallographic *a*, *b*, and *c* axes are  $\sim 0.46$ ,  $\sim 0.70$ , and  $\sim 0.68 \text{ W/mK}$ , respectively (Fig. 2.8.2B). With increasing temperature, these lattice thermal conductivities decrease further. The lattice thermal conductivity reaches an ultralow value of  $0.23 \text{ W/mK}$  at  $973 \text{ K}$  for the crystallographic *a*-axis. This ultralow thermal conductivity is closely related to its layered structure and the resultant anharmonicity of the system. The strong anharmonic bonding is evident from the large value of the Grüneisen parameter [7]. The average Grüneisen parameters in the ambient orthorhombic phase for the crystallographic *a*-, *b*-, and *c*-axis are 4.1, 2.1, and 2.3, respectively. Along the crystallographic *a*-axis, the Grüneisen parameter reaches as high as 7.2. This large Grüneisen parameter for the crystallographic *a*-axis reflects the weak interlayer coupling for the out-of-plane direction and the resultant anharmonicity. The inelastic neutron scattering study further showed that this strong anharmonicity is caused by the presence of a lattice instability due to the condensation of soft transverse optical phonon modes [26]. The coupling of long-range *p*-orbital network of Se atoms with the stereochemically active  $5s^2$  lone pair of Sn causes this bonding instability. This weak chemical bonding along the *a*-axis has been further confirmed through inelastic neutron scattering study, which show softer transverse acoustic phonons for the crystallographic *a*-axis compared to the in-plane directions. As a result, lattice thermal conductivity along the crystallographic *a*-axis is much lower compared to the in-plane directions. Sn vacancy also significantly affects the lattice thermal conductivity.

Practical device applications based on single crystals are much more costly and time consuming. The highly anisotropic thermoelectric performance of the SnSe single crystal is also another major disadvantage of its practical applications. Because of its layered structure that cleaves easily along the (100) plane, the SnSe single crystal also gets cracked easily. Therefore, there is a continuous effort to improve the thermoelectric performance of polycrystalline SnSe [21, 27]. However, because of lower

carrier mobility (room temperature carrier mobility in polycrystalline samples is more than five times lower than the mobility of  $\sim 250 \text{ cm}^2/\text{Vs}$  along the crystallographic *b*-axis in single crystals) and higher thermal conductivity [28, 29], SnSe polycrystals have much inferior thermoelectric performance compared to their single crystalline counterpart. Polycrystal samples are, in general, expected to have lower lattice thermal conductivity because of excess grain boundary scattering than their single crystal counterpart. However, several reports showed that SnSe polycrystals have higher thermal conductivity than SnSe single crystals, which created significant controversy on whether the observed ultralow thermal conductivity of SnSe is intrinsic or not [30]. The higher thermal conductivity of polycrystals later clarified to arise as a result of either variation in stoichiometry or the surface oxidation. Off-stoichiometric SnSe has much lower lattice thermal conductivity compared to the stoichiometric SnSe [31]. The formation of  $\text{SnO}_2$  layer, which has much higher thermal conductivity (98 W/mK along the crystallographic *c*-axis and 55 W/mK along the crystallographic *a*-axis at room temperature) compared to SnSe, due to oxidation results in higher thermal conductivity in polycrystalline samples. Recently, Lee et al. have devised a strategy to remove these  $\text{SnO}_2$  layers using the  $\text{H}_2$  reduction process [32]. This resulted in an ultralow lattice thermal conductivity of  $\sim 0.11 \text{ W/mK}$  at 773 K in polycrystalline SnSe, which is much lower than the single crystalline counterpart and is in accordance to the general expectation. The removal of  $\text{SnO}_2$  layers increases the carrier mobility and electrical conductivity as well. As a result, an enhanced *zT* of  $\sim 2.5$  is achieved at 773 K, which makes the thermoelectric performance polycrystalline SnSe at par with the single-crystalline counterpart. Recently, 2D SnSe nanoplates are also shown to have very high thermoelectric performance with a *zT* of  $\sim 2.1$  at 873 K [33].

While the *p*-type SnSe has created sensation with its ultrahigh thermoelectric performance, the design of practical thermoelectric devices requires compatible *n*-type thermoelectric material as well. Several theoretical studies have indicated that SnSe has a better *n*-type thermoelectric performance compared to its *p*-type thermoelectric performance [34, 35]. Theoretical calculations predict that this high *n*-type thermoelectric performance will be along the interlayer *a*-axis, contrary to the high *p*-type thermoelectric performance observed along the crystallographic *b*- and *c*-axis. Bi-doped SnSe single crystal was first shown to have high thermoelectric performance with a *zT* of  $\sim 2.2$  at 773 K, however, that is along the crystallographic *b*-axis [36]. However, a recent study has reported high *n*-type thermoelectric performance along the crystallographic *a*-axis with *zT* = 2.8 at 773 K. The origin of this high *n*-type thermoelectric performance has been ascribed to the electron orbital overlap along the interlayer direction, which increases electrical conductivity for this out-of-plane direction while thermal transport is hindered in the out-of-plane direction due to the layered crystal structure.

### 2.8.2.1.3 $\text{Cu}_2\text{Se}$

Thermoelectric properties of  $\text{Cu}_2\text{Se}$ , particularly in its high-temperature superionic  $\beta$ -phase, provides a new direction of rationally designing high-performance thermoelectric materials. While this compound is known for a long time [5], recent surge in interest has stemmed only after the work of Liu et al. [37]. At ambient conditions,

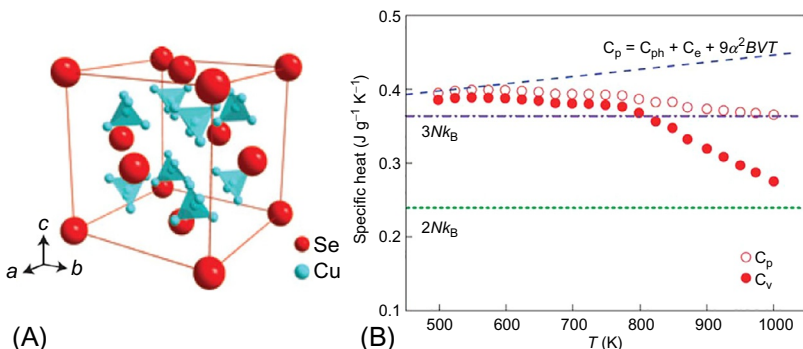


**Fig. 2.8.3** (A)  $\beta$ -phase crystal structure of  $\text{Cu}_2\text{Se}$  with Cu atoms occupying the 8c and 32f interstitial positions. (B) Temperature variation of heat capacity of  $\text{Cu}_2\text{Se}$ .

Figures (A) and (B) are reproduced with permission from reference H. Liu, X. Shi, F. Xu, L. Zhang, W. Zhang, L. Chen, Q. Li, C. Uher, T. Day, G.J. Snyder, Copper ion liquid-like thermoelectrics, Nat. Mater. 11 (2012) 422–425. <https://doi.org/10.1038/nmat3273> © 2012 Springer Nature.

$\text{Cu}_2\text{Se}$  possesses a monoclinic  $\alpha$ -phase (space group  $C2/c$ ) structure in which Cu atoms are orderly placed in the lattice [38]. This room temperature  $\alpha$ -phase undergoes a reversible superionic phase transition of  $\sim 400\text{ K}$  to an FCC structure. In the high-temperature  $\beta$ -phase, Se atoms form a rigid FCC network and the Cu atoms are randomly distributed in the tetrahedral and trigonal interstitial sites (Fig. 2.8.3A). The Cu diffusion rate ( $\sim 10^{-5}\text{--}10^{-7}\text{ cm}^2/\text{s}$ ) is very high in the high-temperature  $\beta$ -phase [39]. Various strategies, such as nanostructuring, have been developed over the years to reduce the lattice thermal conductivity of crystalline materials for achieving high thermoelectric performance. In  $\text{Cu}_2\text{Se}$ , Liu et al. showed a new method of using liquid-like behaviors of highly disordered cations in an otherwise crystalline material to achieve ultralow thermal conductivity [37]. The traditional strategies, such as the inclusion of various dimensional defects in the lattice, of reducing the lattice thermal conductivity involve increasing the scattering of heat-carrying acoustic phonons so that the phonon mean free path decreases and thereby, the lattice thermal conductivity decreases as well. One can reduce the material's thermal conductivity to their glassy limit with these traditional strategies. However, Liu et al. demonstrated the idea of fundamentally eliminating several modes of heat propagation so that the material's heat capacity decreases. In analogy, heat propagation via transverse vibrations are absent in liquids because they lack the shear strength that is required to support the propagation of transverse vibrational modes. Liu et al. showed that highly disordered copper ions in the superionic  $\beta$ -phase of  $\text{Cu}_2\text{Se}$  also exhibit such liquid-like character around the crystalline Se sublattice [37]. They established the liquid-like character of copper ions by showing that heat capacity of  $\text{Cu}_2\text{Se}$  at constant volume is significantly less than the  $3Nk_B$  ( $k_B$  is the Boltzmann constant) value, which is expected in a crystalline material (Fig. 2.8.3B). In addition to the elimination of transverse modes of heat propagation, the highly disordered cations also scatter the acoustic phonons limiting their

mean free path, which further results in the lowering of lattice thermal conductivity. A recent neutron diffraction study by Voneshen et al., however, have shown the presence of transverse phonon modes at all temperatures and questions the validity of the liquid-like diffusion model in superionic compounds [39]. Liu et al. reported an extraordinary  $zT$  of  $\sim 1.5$  at 1000 K for  $\text{Cu}_2\text{Se}$ . The Seebeck coefficient in the  $\beta$ -phase ranges between 80 and  $300 \mu\text{V/K}$  for the temperature range 420–1000 K with electrical resistivity ( $\rho$ ) in the range of  $10^{-2}$ – $10^{-3} \Omega\text{-cm}$ . The high-temperature lattice thermal conductivity, however, is very low only  $0.4$ – $0.6 \text{ W/mK}$ .

Following the report of Liu et al., there is a surge in research interest to further improve the thermoelectric performance of  $\text{Cu}_2\text{Se}$ . Solid solution alloying with S and Te has been tried to improve the thermoelectric performance. Various nanostructuring approaches, such as introducing various dimensional defects via high-energy ball milling followed by spark plasma sintering and as well as chemically synthesized  $\text{Cu}_2\text{Se}$  nanoplates and thin film, have also been investigated to improve the thermoelectric performance [40, 41]. The introduction of various dimensional defects has been shown to be very effective in improving the thermoelectric performance via reducing the lattice thermal conductivity, which reaches to an ultralow value of  $\sim 0.34 \text{ W/mK}$  at 973 K. This processes have shown to be resulting in a peak  $zT$  of  $\sim 2.1$  at 973 K [40]. The doping of Al and Ag have also been used to improve the thermoelectric performance. Al doping is particularly effective due to the improvement in the formation of a highly aligned lamellar structure, which concentrates the superionic properties in a particular direction and results in an impressive peak  $zT$  of  $\sim 2.62$  at 1029 K [42]. Various composite and hybrid materials, such as carbon-reinforced  $\text{Cu}_2\text{Se}$  [43] and  $\text{Cu}_2\text{Se}/\text{carbon-nanotube}$  hybrid materials [44], have been synthesized which have improved thermoelectric performance.  $\text{Cu}_2\text{Se}/\text{carbon-nanotube}$  hybrid materials have a peak  $zT$  of  $\sim 2.4$  at 1000 K.

While  $zT$  in the superionic  $\beta$ -phase reaches a very high value, the low-temperature  $\alpha$ -phase has comparatively inferior thermoelectric performance because of high hole concentrations arising out of intrinsic Cu vacancies. Several attempts have been made to improve the thermoelectric performance of the low-temperature  $\alpha$ -phase, which does not have any chemical instability problem, such as using excess Cu addition and  $n$ -type I and Br doping [45].

While  $\text{Cu}_2\text{Se}$  has an impressive  $zT$ , their practical applicability is mainly limited due to Se evaporation and copper ion migration, which degrades the device quality very rapidly [5]. In inclusion in  $\text{Cu}_2\text{Se}$  lattice has been shown to improve the chemical stability, along with having a very high  $zT$  of  $\sim 2.6$  at 850 K [46]. A recent report on the thermoelectric module prepared using  $\text{Cu}_2\text{Se}$  and  $\text{Yb}_{0.3}\text{Co}_4\text{Sb}_{12}$  exhibited a thermoelectric efficiency of 9.1% for  $\Delta T = 680 \text{ K}$  [47].

#### 2.8.2.1.4 $\text{In}_4\text{Se}_3$

$\text{In}_4\text{Se}_3$  is one of the most intriguing mid-temperature (500–900 K)  $n$ -type thermoelectric materials in the selenide family. The high  $zT$  achieved in  $\text{In}_4\text{Se}_3$  is the result of a low-dimensional electronic transport phenomenon, which is called the charge density wave (CDW) [8]. This low-dimensional electronic transport causes strong electron–phonon

coupling due to the breakdown of the translational symmetry of the lattice, which consequently results in an ultralow lattice thermal conductivity.  $\text{In}_4\text{Se}_3$  has an orthorhombic crystal structure (space group  $Pnnm$ , Fig. 2.8.4A), which supports this low-dimensional anisotropic transport behavior [48]. The crystal structure of  $\text{In}_4\text{Se}_3$  comprises the stacking of the anionic  $[\text{In}_3\text{Se}_3]^{1-}$  layer along the crystallographic  $a$ -axis. This anionic  $[\text{In}_3\text{Se}_3]^{1-}$  layer forms a two-dimensional sheet in the  $b$ - $c$  plane, which are weakly connected to each other along the crystallographic  $a$ -axis via  $\text{In}^{1+}$  atoms. The two-dimensional  $[\text{In}_3\text{Se}_3]^{1-}$  layer in the  $b$ - $c$  plane also has another intriguing feature: multiple zigzag quasi-one-dimensional In/Se chains running along the crystallographic  $c$ -axis. The quantum confinement effect in these quasi-one-dimensional chains are also believed to be the reason behind the observed relatively high Seebeck coefficient of  $\text{In}_4\text{Se}_3$ .  $\text{In}_4\text{Se}_3$  has gained wide attention in the thermoelectric community since the work of Rhyee et al. on Se-deficient single-crystal  $\text{In}_4\text{Se}_{3-\delta}$  ( $\delta=0.22$  and  $0.65$ ) [8]. They showed a very high  $n$ -type  $zT$  of  $\sim 1.48$  at  $705\text{K}$  in the  $b$ - $c$  plane for  $\delta=0.65$ . The temperature variations of electrical conductivity and Seebeck coefficient of  $\text{In}_4\text{Se}_3$  are consistent with its semiconducting nature and  $n$ -type electronic transport. However, the thermal conductivity exhibits ultralow values with highly anisotropic behavior between  $a$ - $b$  and  $b$ - $c$  planes (Fig. 2.8.4B). For example, the room temperature thermal conductivity in the  $b$ - $c$  plane is  $\sim 1.2\text{ W/mK}$ , which further decreases to  $0.74\text{ W/mK}$  at  $705\text{ K}$ . More surprisingly, the thermal conductivity in the  $b$ - $c$  plane is lower than that in the  $a$ - $b$  plane at all temperatures. In layered materials, one expects the in-plane thermal and electrical conductivities to be greater than that along the out-of-plane direction. Further, the carrier concentration in the  $b$ - $c$  plane is also lower than that in the  $a$ - $b$  plane (inset of Fig. 2.8.4C), which indicates the role of some novel mechanism behind this ultralow and anisotropic thermal transport. A careful analysis by HRTEM, electron diffraction, and theoretical analysis revealed that Peierls instability and the associated charge density wave is the reason behind the extraordinary thermal transport behavior of  $\text{In}_4\text{Se}_{3-\delta}$ . These experimental and theoretical works indicated a quasi-one-dimensional Peierls instability and a consequent long-range lattice modulation with the charge-density wave. The charge density gap in the  $b$ - $c$  plane lowers the carrier concentration. The heat-carrying acoustic phonons experience significantly enhanced scattering due to the lattice distortion and Peierls instability in the  $b$ - $c$  plane. As a result, thermal conductivity in the  $b$ - $c$  plane is lower compared to that in the  $a$ - $b$  plane. While  $\text{In}_4\text{Se}_{3-\delta}$  ( $\delta=0.22$  and  $0.65$ ) has impressive peak  $zT$ , the average  $zT$  over a wide temperature range is low, which has been subsequently improved via Cl doping [49].

Single-crystalline  $\text{In}_4\text{Se}_3$  has highly anisotropic thermoelectric properties: while  $zT$  in the  $b$ - $c$  plane reaches  $1.48$  at  $705\text{ K}$ , the  $zT$  in the  $a$ - $b$  plane has very low values,  $\sim 0.3$  at  $600\text{ K}$ . Such anisotropic thermoelectric performance is a significant concern for practical applications. This has led researchers to improve the thermoelectric performance of polycrystalline  $\text{In}_4\text{Se}_3$ , which has significantly lower anisotropic thermoelectric performance [50]. The most notable examples are the Pb/Sn-co-doping and Pb/Cu/I multiple heteroatoms doping, which resulted in a peak  $zT \sim 1.4$  and improved the thermoelectric performance of polycrystalline  $\text{In}_4\text{Se}_3$  to a level similar to that of the single-crystalline bulk ingot [51, 52].

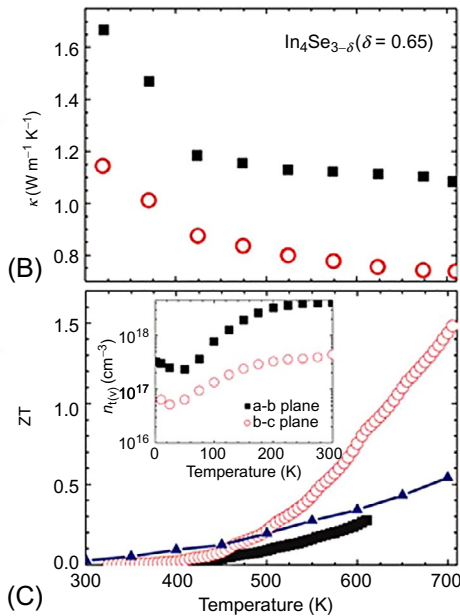
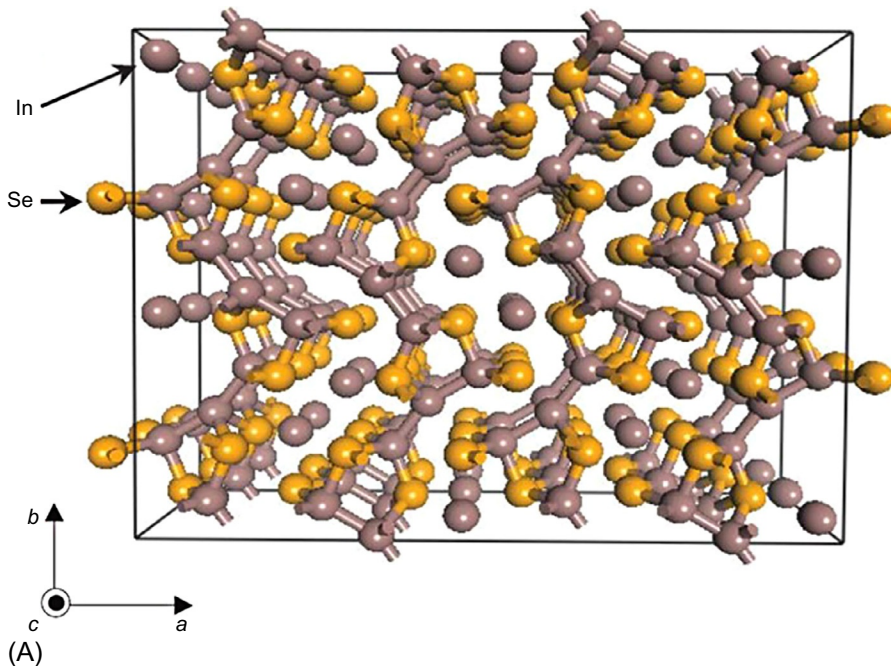


**Fig. 2.8.4** (A) Crystal structure of  $\text{In}_4\text{Se}_3$ . The unit cell is orthorhombic with space group  $Pnnm$ . (B) Thermal conductivity ( $\kappa$ ) and (C) thermoelectric figure of merit ( $zT$ ) of  $\text{In}_4\text{Se}_{3-\delta}$  ( $\delta = 0.65$ ) single crystal as a function of temperature. The inset in (C) shows the temperature variation of carrier concentration.

Figures (A)–(C) are reproduced with permission from reference J.-S. Rhyee, K.H. Lee, S.M. Lee, E. Cho, S.I. Kim, E. Lee, Y.S. Kwon, J.H. Shim, G. Kotliar, Peierls distortion as a route to high thermoelectric performance in  $\text{In}_4\text{Se}_{3-\delta}$  crystals, *Nature* 459 (2009) 965–968. <https://doi.org/10.1038/nature08088> © 2009 Springer Nature.

### 2.8.2.1.5 GeSe

Following the success in SnSe, there has been a great attention in the investigation of structurally similar compounds in the IV–VI chalcogenide semiconductors to achieve high thermoelectric performance. Out of these, germanium selenide (GeSe), which has the layered orthorhombic crystal structure [space group *Pnma*, Fig. 2.8.5A (left panel)], same as SnSe, has received a lot of attention. Theoretical investigations also predicted that a minimum lattice thermal conductivity of 0.39 W/mK can be obtained in GeSe [53] and hole-doped orthorhombic GeSe can have *p*-type zT as high as 2.5 at 800 K along the crystallographic *b*-axis for an optimal hole concentration of

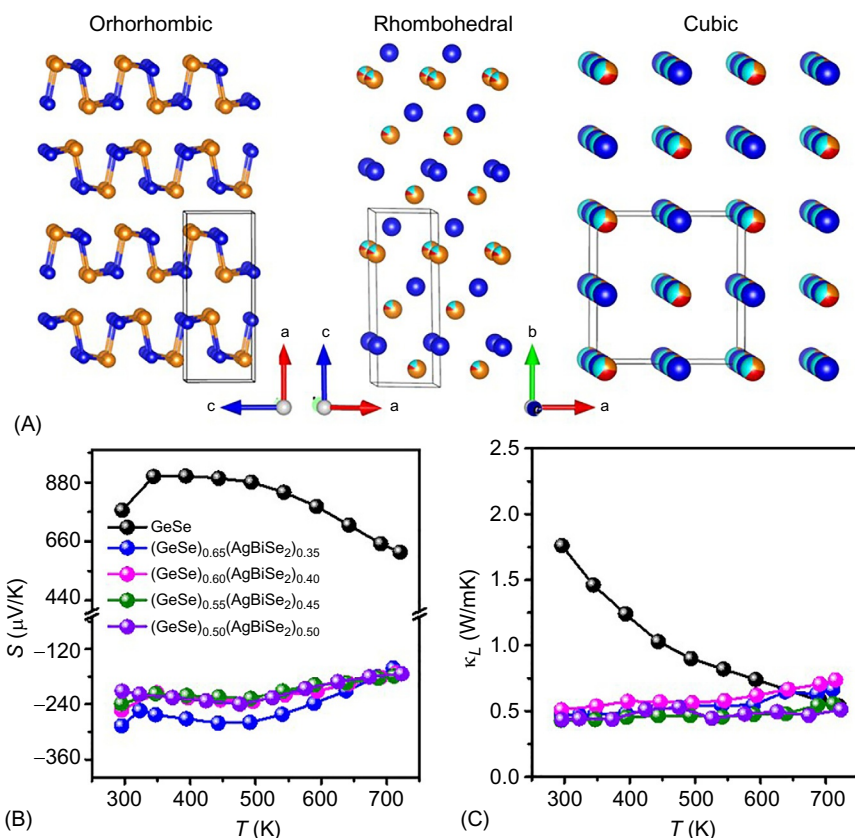


**Fig. 2.8.5** (A) Orthorhombic, rhombohedral, and cubic phase of  $(\text{GeSe})_{1-x}(\text{AgBiS}_2)_x$ . Ge Yellow, Se/Te blue, Ag red, Bi cyan. (B) Seebeck coefficient ( $S$ ) and (C) lattice thermal conductivity ( $\kappa_L$ ) of  $(\text{GeSe})_{1-x}(\text{AgBiS}_2)_x$  as a function of temperature.

Figures (A)–(C) are reproduced with permission from reference S. Roychowdhury, T. Ghosh, R. Arora, U.V. Waghmare, K. Biswas, Stabilizing n-type cubic GeSe by entropy-driven alloying of AgBiSe<sub>2</sub>: ultralow thermal conductivity and promising thermoelectric performance, Angew. Chem. Int. Ed. 57 (2018) 15167–15171. <https://doi.org/10.1002/anie.201809841> © 2018 John Wiley and Sons.

$\sim 5 \times 10^{19} \text{ cm}^{-3}$  [54]. However, pristine orthorhombic GeSe has a carrier concentration of  $\sim 10^{16} \text{ cm}^{-3}$ , and it turns out that improving the hole concentration in the desired limit is very challenging. Various attempts have been made to improve the hole concentration; however, the effort remained unsuccessful with a maximum obtained carrier concentration of  $\sim 10^{18} \text{ cm}^{-3}$  in Ag/Sn co-doped GeSe and a maximum zT of  $\sim 0.2$  at 700 K [55].

Following these unsuccessful attempts, Huang et al. realized the similarities of GeSe with another high-performance thermoelectric material in the IV-VI chalcogenide family, GeTe, which has a rhombohedral structure (space group  $R\bar{3}m$ ) at ambient conditions [56]. They have been able to realize the rhombohedral phase of GeSe (Fig. 2.8.5A, middle panel) via alloying with  $\text{AgSbSe}_2$ . Under ambient conditions, the rhombohedral phase forms in  $\text{GeAg}_x\text{Sb}_x\text{Se}_{1+2x}$  for  $x \geq 0.1$ . This results in a dramatic increase in hole carrier concentration in this rhombohedral phase to  $\sim 10^{20} \text{ cm}^{-3}$ . The increase in carrier concentration, however, decreases the room temperature Seebeck coefficient from  $\sim 600 \mu\text{V/K}$  for pristine GeSe to  $\sim 100$ – $200 \mu\text{V/K}$  in  $\text{GeAg}_x\text{Sb}_x\text{Se}_{1+2x}$ . Overall, the power factor increases: from  $56 \mu\text{W/mK}^2$  in pristine GeSe to  $1233 \mu\text{W/mK}^2$  in  $\text{GeAg}_{0.15}\text{Sb}_{0.15}\text{Se}_{1.3}$  at 710 K. Because of the solid solution point defects, lattice thermal conductivity also decreases in  $\text{GeAg}_x\text{Sb}_x\text{Se}_{1+2x}$ : typically, the lattice thermal conductivity decreases from  $2.9 \text{ W/mK}$  in pristine GeSe to  $0.85 \text{ W/mK}$  at  $x = 0.3$  in  $\text{GeAg}_x\text{Sb}_x\text{Se}_{1+2x}$  at 710 K. This increased power factor and decreased thermal conductivity lead to a high zT of  $\sim 0.86$  at 710 K in  $\text{GeAg}_{0.2}\text{Sb}_{0.2}\text{Se}_{1.4}$ . In a following study, Yan et al. found a similar rhombohedral phase by alloying with  $\text{AgSbTe}_2$  and achieved a zT of  $\sim 1$  at 754 K in  $\text{GeSeAg}_{0.2}\text{Sb}_{0.2}\text{Te}_{0.4}$  [57].

These works have established GeSe as a promising thermoelectric material. However, there is scope to further improve the thermoelectric performance of GeSe by lowering the thermal conductivity and by stabilizing the high-temperature cubic rock-salt phase [space group  $Fm\bar{3}m$ , Fig. 2.8.5A (right panel)] under ambient conditions. Theoretical calculations show that the rock-salt phase could be stabilized by applying a pressure of greater than 7 GPa [58]. Roychowdhury et al. have recently been able to stabilize this cubic rock-salt phase at ambient conditions by entropy-driven alloying with  $\text{AgBiSe}_2$  [59]. When GeSe is alloyed with  $\text{AgBiSe}_2$ , the transition temperature to the high-temperature cubic rock-salt phase decreases with increasing  $\text{AgBiSe}_2$  concentration. The ambient structure of  $(\text{GeSe})_{1-x}(\text{AgBiSe}_2)_x$  evolves from orthorhombic at  $x = 0$  to rhombohedral at  $x = 0.1$  and with further increase in  $\text{AgBiSe}_2$  concentration; the cubic rock-salt phase stabilizes under ambient conditions above  $x = 0.3$ . The cubic  $(\text{GeSe})_{1-x}(\text{AgBiSe}_2)_x$  is notable for its n-type thermoelectric properties. Because of intrinsic Ge vacancies, which moves the Fermi level deep inside the valence band, Ge chalcogenides generally show p-type thermoelectric properties. Cubic  $(\text{GeSe})_{1-x}(\text{AgBiSe}_2)_x$  is the first report on the n-type behavior in Ge chalcogenides. Typically, the Seebeck coefficient has a value of  $-210 \mu\text{V/K}$  at room temperature, which decreases to  $-174 \mu\text{V/K}$  at 723 K in  $(\text{GeSe})_{50}(\text{AgBiSe}_2)_{50}$  (Fig. 2.8.5B). The thermal conductivity of this system is also ultralow (Fig. 2.8.5C): only  $0.43 \text{ W/mK}$  at room temperature in  $(\text{GeSe})_{50}(\text{AgBiSe}_2)_{50}$ , which makes this system a promising thermoelectric material. The obtained highest zT is 0.45 at 677 K in  $(\text{GeSe})_{50}(\text{AgBiSe}_2)_{50}$ .

### 2.8.2.1.6 BiSe

BiSe has recently emerged as a promising *n*-type thermoelectric material with intriguing structural and electronic properties [60]. BiSe has a natural Van der Waals heterostructure from the  $(\text{Bi}_2)_m(\text{Bi}_2\text{Se}_3)_n$  homologous family comprising a Bi-bilayer sandwiched between two  $\text{Bi}_2\text{Se}_3$  quintuple layers with weak Van der Waals force of interaction [61]. Recently, BiSe is also turned out to be a weak topological insulator [62]. Samanta et al. have recently demonstrated very low lattice thermal conductivity in BiSe [60]. The room temperature lattice thermal conductivity is  $\sim 0.6 \text{ W/mK}$ , which remains flat throughout the 300–650 K temperature range. Interestingly, the lattice thermal conductivity of BiSe ( $\sim 0.6 \text{ W/mK}$  at 300 K) is much lower compared to that of  $\text{Bi}_2\text{Se}_3$  ( $\kappa_{\text{lat}} \sim 1.8 \text{ W/mK}$  at 300 K), despite the fact that both the compounds belong to the same  $(\text{Bi}_2)_m(\text{Bi}_2\text{Se}_3)_n$  homologous family. This observation gives clear indication that the Bi-bilayer plays an important role in minimizing the lattice thermal conductivity of BiSe. The measurement of low-temperature heat capacity and an analysis of the lattice dynamics of BiSe show that localized vibrations of the Bi-bilayer induce low-frequency optical modes, which strongly couple with the heat-carrying acoustic modes and scatter the acoustic phonons, resulting in the low lattice thermal conductivity in BiSe. They achieved the highest *zT* of  $\sim 0.8$  at 425 K in  $\text{Bi}_{0.7}\text{Sb}_{0.3}\text{Se}$ , which is an important advancement for *n*-type thermoelectric materials with high thermoelectric performance for near room temperature applications.

## 2.8.2.2 Ternary metal selenides

### 2.8.2.2.1 AgSbSe<sub>2</sub>

$\text{AgSbSe}_2$  has intrinsically low lattice thermal conductivity, which varies in the range of  $\sim 0.25$ – $0.4 \text{ W/mK}$  for the temperature range of 300–725 K [63]. This low lattice thermal conductivity makes it an ideal candidate for thermoelectric purposes.  $\text{AgSbSe}_2$  has a cubic rock-salt structure under ambient conditions in which the cation positions are taken up by Ag and Sb atoms, while the anion positions are taken up by Se atoms. The presence of two cations (Ag and Sb) in the crystallographically equivalent positions creates a disorder in the lattice, and this disorder in turn increases the scattering of heat-carrying acoustic phonons in the system. Furthermore, Sb having  $5s^2$  lone pairs induces a strong lattice anharmonicity, which further helps in acoustic phonon scattering and lowers the lattice thermal conductivity. This dual effects of disorder and lone pairs result in an ultralow lattice thermal conductivity in  $\text{AgSbSe}_2$ . The bandgap of  $\text{AgSbSe}_2$  is  $\sim 0.7 \text{ eV}$ , which makes it a typical narrow bandgap semiconductor. Pristine  $\text{AgSbSe}_2$  shows a peak *zT* of  $\sim 0.4$  at 673 K. This is mainly due to the high Seebeck coefficient which has the room temperature value of  $\sim 310 \mu\text{V/K}$  and linearly increases to  $\sim 461 \mu\text{V/K}$  at 705 K. However, the main disadvantage of  $\text{AgSbSe}_2$  is its low electrical conductivity. The room temperature value is  $\sim 4.5 \text{ S/cm}$ , which initially increases with temperature and reaches to a value of  $\sim 15 \text{ S/cm}$  at 500 K. Subsequently, bipolar nature kicks in with further increase in temperature and the electrical conductivity decreases with further increase in temperature and reaches to  $\sim 10 \text{ S/cm}$  at 705 K.

Increase of hole concentration by doping aliovalent  $\text{Pb}^{2+}$  in place of  $\text{Sb}^{3+}$  results in an increase in electrical conductivity and the room temperature value increases to  $\sim 61 \text{ S/cm}$  in  $\text{AgSb}_{0.96}\text{Pb}_{0.04}\text{Se}_2$ . The increased electrical conductivity aids in the increment of the power factor from  $\sim 2 \mu\text{W}/\text{cm K}^2$  for pristine  $\text{AgSbSe}_2$  to  $\sim 6 \mu\text{W}/\text{cm K}^2$  in  $\text{AgSb}_{0.96}\text{Pb}_{0.04}\text{Se}_2$  at 623 K. Coupled with the low lattice thermal conductivity, an impressive *p*-type  $zT \sim 1$  is obtained in  $\text{AgSb}_{0.96}\text{Pb}_{0.04}\text{Se}_2$  at 610 K [63]. Similarly, 2 mol% Bi doping also improves the  $zT$  of  $\sim 1.15$  at 685 K [63] (Fig. 2.8.6A). Cd $^{2+}$  substitution in the  $\text{Sb}^{3+}$  position also improves the electrical transport property and results in  $zT$  of  $\sim 1$  at 640 K in  $\text{AgSb}_{0.98}\text{Cd}_{0.02}\text{Se}_2$  [64]. Likewise, a  $zT$  of  $\sim 1$  is achieved at 610 K by controlling Sb deficiency in  $\text{AgSb}_{0.99}\text{Se}_2$  and  $\text{AgSb}_{0.9925}\text{Se}_2$  [65]. Na doping, on the other hand, forms nanoscale stacking faults which further decreases the lattice thermal conductivity while simultaneously increasing the electrical conductivity which leads to a peak  $zT \sim 0.92$  at 673 K [66]. The formation of hierarchical architectures via Ca doping also leads to a low lattice thermal conductivity of  $\sim 0.27 \text{ W/mK}$  and, thus, enhances  $zT$  of  $\text{AgSbSe}_2$  to 1.2 [67]. Mg and Ba doping in  $\text{AgSbSe}_2$  also successfully results in high  $zT$  values close to unity [68]. Sn-doped  $\text{AgSbSe}_2$  have a  $zT$  of  $\sim 1.21$ , which can be attributed to the enhanced power factor and ultralow lattice thermal conductivity [69].

### 2.8.2.2 $\text{AgBiSe}_2$

$\text{AgBiSe}_2$ , unlike its  $\text{AgSbSe}_2$  counterpart, has a hexagonal crystal structure (space group  $P\bar{3}ml$ ), which transforms to a rhombohedral phase (space group  $R\bar{3}m$ ) at 410 K. As the temperature increases further, it undergoes a second structural transition from rhombohedral to cubic (space group  $Fm\bar{3}m$ ) at 580 K (Fig. 2.8.6B). These phase changes bring forth interesting electronic and phonon transport properties in  $\text{AgBiSe}_2$ . Xiao et al. showed that nanocrystalline  $\text{AgBiSe}_2$  undergoes a reversible *p-n-p*-type conduction switching [70]. The room temperature hexagonal structure consists of 11 atomic repeating Se-Ag-Se-Bi chains along the crystallographic *c*-axis followed by a Bi-layer, while the rhombohedral layer consists of Bi atoms present in identical chemical environments. The cubic phase is the one where all the Ag and Bi atoms are randomly distributed in the cationic sites. During the rhombohedral to cubic phase transformation, Ag and Bi atoms exchange their atomic positions which aids in the *p-n-p* transition. These Ag-Bi exchange leads to a quasi-metallic state and a consequent change in the majority carriers from hole to electrons and thus, the electronic transport switches from *p*- to *n*-type [70]. After the full cationic disordering in the cubic phase, the bandgap further opens up, which leads to the second switching from *n*- to *p*-type. This complete disordering of cations also increases the phonon-phonon Umklapp scattering, which increases the anharmonicity in the lattice and results in the intrinsically ultralow lattice thermal conductivity. This low lattice thermal conductivity makes cubic  $\text{AgBiSe}_2$  a promising thermoelectric material with a  $zT$  of  $\sim 1.5$  at 700 K in the nanocrystalline form [70]. Bulk  $\text{AgBiSe}_2$ , however, unlike its nanocrystalline counterpart, do not show such *p-n-p*-type conduction switching. It remains *n*-type throughout the temperature range of 20–773 K [71]. Seebeck coefficient of  $\text{AgBiSe}_2$  increases from  $-154 \mu\text{V/K}$  at room temperature to  $-270 \mu\text{V/K}$  at 773 K.

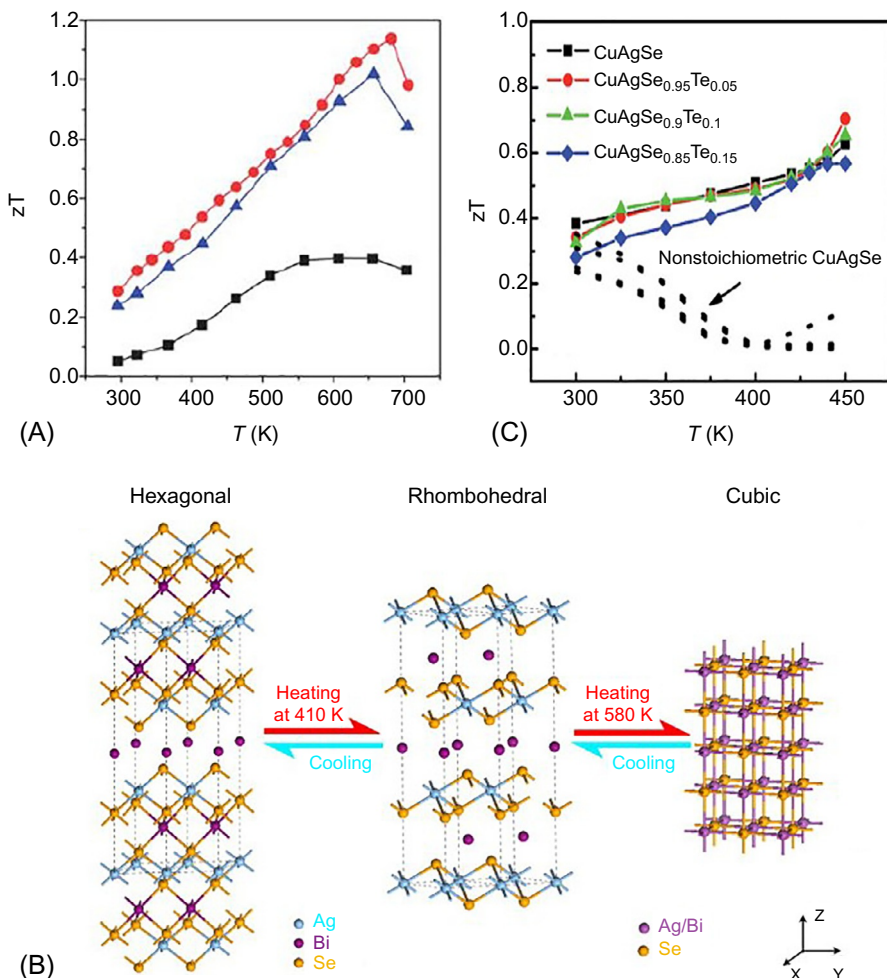


**Fig. 2.8.6** (A) Temperature-dependent thermoelectric figure of merit ( $zT$ ) of  $\text{AgSbSe}_2$ . (B) Crystal structure of  $\text{AgBiSe}_2$  at different temperature regimes. (C) Thermoelectric figure of merit ( $zT$ ) of  $\text{CuAgSe}$  as a function of temperature.

Figure (A) is reproduced with permission from reference S.N. Guin, A. Chatterjee, D.S. Negi, R. Datta, K. Biswas, High thermoelectric performance in tellurium free p-type  $\text{AgSbSe}_2$ , *Energy Environ. Sci.* 6 (2013) 2603–2608. <https://doi.org/10.1039/C3EE41935E> © 2013 Royal Society of Chemistry. Figure (B) is reproduced with permission from reference C. Xiao, X. Qin, J. Zhang, R. An, J. Xu, K. Li, B. Cao, J. Yang, B. Ye, Y. Xie, High thermoelectric and reversible p-n-p conduction type switching integrated in dimetal chalcogenide *J. Am. Chem. Soc.* 134 (2012) 18460. <https://doi.org/10.1021/ja308936b> © 2012 American Chemical Society.

Figure (C) is reproduced with permission from reference P.F. Qiu, X.B. Wang, T.S. Zhang, X. Shi, L.D. Chen, Thermoelectric properties of Te-doped ternary  $\text{CuAgSe}$  compounds, *J. Mater. Chem. A* 3 (2015) 22454–22461. <https://doi.org/10.1039/C5TA06780D> © 2015 Royal Society of Chemistry.

Niobium (Nb), which mainly resides in  $\text{Nb}^{3+}$  oxidation state, doping on the Ag site provides extra electrons in the lattice. This increases the carrier concentration of the system, and hence the electrical conductivity also increases. It has been found that the carrier concentration increases from  $\sim 1.5 \times 10^{19} \text{ cm}^{-3}$  for pristine  $\text{AgBiSe}_2$  to  $\sim 6.5 \times 10^{19} \text{ cm}^{-3}$  in  $\text{Ag}_{0.96}\text{Nb}_{0.04}\text{BiSe}_2$  [71]. This increase in carrier concentration directly correlates to the decrease in electrical resistivity ( $\rho$ ). The room temperature electrical conductivity decreases from  $13.8 \text{ m}\Omega\text{-cm}$  for pristine  $\text{AgBiSe}_2$  to  $4.3 \text{ m}\Omega\text{-cm}$  in  $\text{Ag}_{0.96}\text{Nb}_{0.04}\text{BiSe}_2$ . Similarly, the room temperature Seebeck coefficient decreases to  $85 \mu\text{V/K}$  in 4 mol% Nb-doped  $\text{AgBiSe}_2$ . The room temperature lattice thermal conductivity also decreases from  $\sim 0.6 \text{ W/mK}$  for pristine  $\text{AgBiSe}_2$  to  $\sim 0.53 \text{ W/mK}$  in 4 mol% Nb-doped  $\text{AgBiSe}_2$ . At higher temperatures, pristine  $\text{AgBiSe}_2$  has a lattice thermal conductivity of  $\sim 0.41 \text{ W/mK}$  at 773 K, whereas  $\text{Ag}_{0.96}\text{Nb}_{0.04}\text{BiSe}_2$  has the value of  $\sim 0.27 \text{ W/mK}$  at 623 K. A  $zT$  of  $\sim 1$  at 773 K is achieved in  $\text{Ag}_{0.96}\text{Nb}_{0.04}\text{BiSe}_2$ , which can be mainly attributed to an increase in carrier concentration and a decrease in lattice thermal conductivity of the compound [71]. Halogen doping in the selenium site results in a peak  $zT$  of  $\sim 0.9$  at 810 K in  $\text{AgBiSe}_{1.98}\text{Cl}_{0.02}$  [72]. This increment in  $zT$  with halogen doping is mainly a result of increased carrier concentration and ultralow lattice thermal conductivity ( $\sim 0.27 \text{ W/mK}$  at 810 K). Similarly, GeSe-alloyed  $\text{AgBiSe}_2$  has a peak  $n$ -type  $zT$  of  $\sim 1.05$  at 750 K [73]. This high  $zT$  value obtained after GeSe alloying is due to the formation of  $\text{Bi}_2\text{Se}_3$  nanoprecipitates, which drastically enhances the scattering of acoustic phonons. Moiré fringes having a periodicity of 0.25 nm has also been observed, which indicates additional phonon scattering due to the presence of superlattice and local mass fluctuations. These factors lead to an ultralow lattice thermal conductivity of  $\sim 0.3 \text{ W mK}$ , which aids in obtaining such a high  $zT$  value [73]. Other doping effects like Te substitution on Se site has also been successful in increasing the  $n$ -type  $zT$  value to 0.6 [74].

### 2.8.2.2.3 CuAgSe

“Phonon-Glass-Electron-Crystal” (PGEC) property is an important criterion for a material to exhibit superior thermoelectric performance. It implies that the phonon transport in the materials resembles glass-like conduction due to strong phonon scattering, while the system allows electrons (or holes) to flow seamlessly.  $\beta$ -CuAgSe, which consists of alternating stacks of  $\text{Cu}_2\text{Se}$  and Ag layers, show promising thermoelectric performance near room temperature. The Seebeck coefficient value is *negative* at lower temperatures, however, switches from *n*- to *p*-type at  $\sim 400 \text{ K}$ . This switching is indicative of the semimetallic band structure of  $\beta$ -CuAgSe, wherein the major carrier type shifts from electron to hole with an increase in temperature. The resistivity increases with an increase in temperature, which is also indicative of the semimetallic behavior of  $\beta$ -CuAgSe. At 470 K, both Seebeck coefficient and resistivity show anomalies, which can be attributed to the formation of high-temperature superionic  $\alpha$ -CuAgSe.  $\alpha$ -CuAgSe possess disordered face-centered cubic structure wherein the cations ( $\text{Ag}^+/\text{Cu}^+$ ) are disordered and are weakly bonded to the lattice. The Se atoms, on the other hand, form a rigid face-centered substructure. The feebly bonded cations are responsible for the superionic conduction in  $\alpha$ -CuAgSe [75]. Also, this weak chemical bonding leads to a significant

bonding inhomogeneity and the consequent anharmonicity lowers the lattice thermal conductivity akin to glass-like thermal conduction. The solid Se substructure, on the other hand, makes for a stable pathway for the electron conduction, which is essential for thermoelectrics. The presence of these two substructures makes CuAgSe a potential PGEC compound [75]. It has been found that 10% Ni doping increases the  $zT$  value from 0.02 for pristine  $\beta$ -CuAgSe to 0.1 at 100 K. The  $zT$  value increases with an increase in temperature and reaches 0.25 at 300 K in 10 mol% Ni-doped CuAgSe [75]. The substitution of Te in the Se position further decreases the lattice thermal conductivity. The thermal conductivity decreases from 1.6 W/mK for pristine  $\beta$ -CuAgSe to 0.9 W/mK in  $\text{CuAgSe}_{0.85}\text{Te}_{0.15}$ . The carrier concentration also decreases with an increase in Te doping, which results in lower electrical conductivity but similar Seebeck coefficient with respect to the pristine CuAgSe. This results in an  $n$ -type  $zT$  of  $\sim 0.7$  at 450 K in  $\text{CuAgSe}_{0.95}\text{Te}_{0.05}$  [76] (Fig. 2.8.6C). CuAgSe nanoparticles also show an impressive  $zT$  of  $\sim 0.9$  at 623 K, which can be attributed to its intrinsically low lattice thermal conductivity [77].

#### 2.8.2.2.4 $\text{AgCrSe}_2$

$\text{AgCrSe}_2$  has an intriguing phonon transport property wherein its transverse acoustic phonons are fully suppressed due to the dynamic cation disorder and its longitudinal acoustic phonons also get heavily scattered but survives. This is akin to the heat transportation in liquids, which employs the vibrations arising from longitudinal acoustic phonons only. At room temperature,  $\text{AgCrSe}_2$  has hexagonal crystal structure (space group  $R\bar{3}m$ ) comprising alternating Ag layers (which lies in tetrahedral interstitial sites) and  $\text{CrSe}_6$  octahedra. However, at 450 K,  $\text{AgCrSe}_2$  undergoes an order-disorder transition from  $R\bar{3}m$  to  $R\bar{3}m$ , wherein the Ag atoms become mobile and hop from one tetrahedral hole to another. This leads to the suppression of transverse phonons and ultimately leads to the liquid-like transition in  $\text{AgCrSe}_2$  [78]. The vibration of these  $\text{Ag}^+$  cations are shown to be localized in nature [79].  $\text{AgCrSe}_2$  shows an ultralow lattice thermal conductivity of  $\sim 0.6$  W/mK at room temperature, which further decreases to  $\sim 0.2$  W/mK at 523 K. This low lattice thermal conductivity leads to a peak  $zT$  of  $\sim 1$  at 523 K when the thermal conductivity is calculated based on experimentally observed heat capacity value. However,  $zT$  is  $\sim 0.4$  only if one uses the lattice thermal conductivity based on the Dulong-Petit heat capacity value [80]. CuCrSe<sub>2</sub>-alloyed  $\text{AgCrSe}_2$  nanocomposites show a peak  $zT$  of  $\sim 1.4$ , which can be attributed to its intrinsically low lattice thermal conductivity [81].

#### 2.8.2.3 Oxy-selenides

##### 2.8.2.3.1 $\text{BiCuSeO}$

Thermoelectric materials are generally subjected to high temperatures, which lead to material degradation due to oxidation and evaporation. One of the major advantages of  $\text{BiCuSeO}$  is its robust chemical stability against oxidation. The oxy-selenide  $\text{BiCuSeO}$  is a relatively new addition to the chalcogenide thermoelectric family. This material

was first explored for superconductivity for its similarity with the well-known superconductor LaFeAsO. While superconductivity was never found in BiCuSeO, it has been later realized as a potential thermoelectric material for its high Seebeck coefficient and ultralow thermal conductivity, and the research interest has surged since the work of Zhao et al. in 2010 [82]. BiCuSeO has a layered structure with a tetragonal unit cell (space group  $P4/nmm$ ). The crystal structure comprises alternate stacking of positively charged  $[Bi_2O_2]^{2+}$  and negatively charged  $[Cu_2Se_2]^{2-}$  layer along the crystallographic  $c$ -axis (Fig. 2.8.7A). The positively charged  $[Bi_2O_2]^{2+}$  layer is insulating

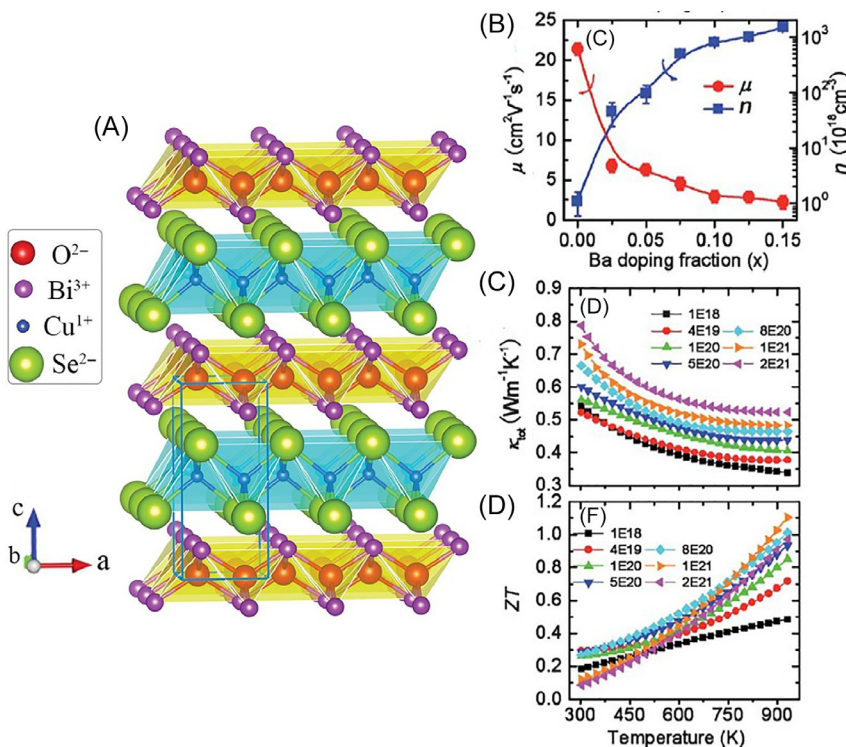


**Fig. 2.8.7** (A) Layered tetragonal crystal structure of BiCuSeO, (B) change in room temperature carrier concentration ( $n$ ) and mobility ( $\mu$ ) of Ba-doped BiCuSeO as a function of Ba concentration, (C) total thermal conductivity ( $\kappa_{\text{tot}}$ ), and (D) thermoelectric figure of merit ( $ZT$ ) of Ba-doped BiCuSeO at various carrier concentration levels as a function of temperature.

Figure (A) is reproduced with permission from reference Y. Liu, L.-D. Zhao, Y. Zhu, Y. Liu, F. Li, M. Yu, D.-B. Liu, W. Xu, Y.-H. Lin, C.-W. Nan, Synergistically optimizing electrical and thermal transport properties of BiCuSeO via a dual-doping approach, *Adv. Energy Mater.* 6 (2016) 1502423. <https://doi.org/10.1002/aenm.201502423> © 2016 John Wiley and Sons.

Figures (B)–(D) are reproduced with permission from reference J. Li, J. Sui, Y. Pei, C. Barreteau, D. Berardan, N. Dragoe, W. Cai, J. He, L.-D. Zhao, A high thermoelectric figure of merit  $ZT > 1$  in Ba heavily doped BiCuSeO oxyselelenides, *Energy Environ. Sci.* 5 (2012) 8543–8547. <https://doi.org/10.1039/C2EE22622G> © 2012 Royal Society of Chemistry.

in nature and most of the electronic transport occurs through the conducting  $[\text{Cu}_2\text{Se}_2]^{2-}$  layer. BiCuSeO is an indirect multiband semiconductor with a bandgap of 0.8 eV [83]. The valence band maximum occurs along the  $\Gamma$ -M line with primary contributions from the hybridized Cu-3d and Se-4p orbitals. The conduction band minimum occurs at the Z point and is primarily made up of Bi-6p states. The *p*-type electronic character mainly originates from the intrinsic Cu vacancies. Because of its layered structure, BiCuSeO shows anisotropic electrical and thermal transports between the in-plane and out-of-plane directions [84]. The main disadvantage of BiCuSeO for thermoelectric applications is its low carrier concentration and the corresponding low electrical conductivity. The room temperature electrical conductivity is only  $\sim 1.12 \text{ S/cm}$  and the corresponding carrier concentration and carrier mobility are  $\sim 10^{18} \text{ cm}^{-3}$  and  $\sim 22 \text{ cm}^2/\text{Vs}$ , respectively. The Seebeck coefficient, however, is very high; the room temperature Seebeck coefficient value is  $350 \mu\text{V/K}$ , which increases with increasing temperature and reaches  $425 \mu\text{V/K}$  at 923 K. This large Seebeck coefficient is primarily ascribed to the low dimensional structure of this material. Owing to this high Seebeck coefficient, the power factor reaches  $2.5 \mu\text{W/cmK}^2$  at 923 K. The most intriguing property is, however, the ultralow lattice thermal conductivity of BiCuSeO. The lattice thermal conductivity varies between  $0.6 \text{ W/mK}$  at room temperature and  $0.4 \text{ W/mK}$  at 923 K. Combining this ultralow thermal conductivity and moderate power factor, a sizable *zT* of 0.5 can be achieved at 923 K in pristine BiCuSeO. Several theoretical and experimental works have been carried out to understand the origin of this intrinsically ultralow thermal conductivity of BiCuSeO. Earlier works mainly ascribed the origin of this low lattice thermal conductivity to acoustic-optical phonon coupling and anharmonic vibration caused by large atomic displacements and lone pair electrons associated with Bi [85, 86]. The high anharmonicity is evident from the large Grüneisen parameter, which reaches to as high as 6 for the low-frequency vibrational modes [85]. The average Grüneisen parameter value is 2.5, which is very high and signifies strong anharmonicity in the system. Recent neutron diffraction and theoretical calculation results, however, have indicated the primary role of localized low-energy vibrational modes associated with the weak bonding of Cu as the primary source of scattering of the heat-carrying acoustic phonons [87]. Another obvious reason is the weak bonding present in the system because of its layered structure, which is evident from the low value of Young modulus, which is only  $76.5 \text{ GPa}$  at 300 K [88].

As can be seen, the main limiting factor of improving the thermoelectric performances is the low carrier concentration. Cu deficiency has been used as a tool to improve the carrier concentration and, consequently, electrical conductivity increases by an order of magnitude [89]. Dual vacancy, vacancies at both Bi and Cu sites, further improves the thermoelectric performance [90]. The interlayer charge transfer of holes from the  $[\text{Bi}_2\text{O}_2]^{2+}$  layer to the  $[\text{Cu}_2\text{Se}_2]^{2-}$  layer, created due to Bi vacancy, further increases the electrical performance, while simultaneously decreasing the lattice thermal conductivity because of increased phonon scattering at the vacancy sites. The use of another innovative strategy, called 3D modulation doping, improves the carrier

mobility by a factor of 2 [91]. In this approach, bulk material is synthesized in such a way that it comprises regions of varying doping concentrations so that the heavily doped regions act as a source of charge carriers, while the lower doped regions effectively transport the generated charge carriers in the heavily doped regions with less charge carrier scattering and thus maintaining high charge carrier mobility. This approach results in a peak  $zT$  of  $\sim 1.4$  at 923 K in Ba-doped BiCuSeO. Taking the advantage of layered structure and consequent anisotropic electrical and thermal transport properties, textured microstructure with oriented grains has also been used to boost the thermoelectric performance of BiCuSeO [92]. As discussed before, one of the main drawbacks is the low carrier concentration and the consequent low electrical conductivity. Doping of divalent atoms such as Ca, Mg, Sr, Ba, and Pb in place of  $\text{Bi}^{3+}$  also increases the carrier concentration [84, 93]. These doping results in an increase of carrier concentration to a level of  $10^{21} \text{ cm}^{-3}$  for about 15 mol% of divalent atom doping. However, with an increase in carrier concentration, charge carrier mobility also degrades, lowering the overall electrical conductivity (Fig. 2.8.7B). The carrier mobility decreases from  $22 \text{ cm}^2/\text{Vs}$  to about  $1\text{--}2 \text{ cm}^2/\text{Vs}$  when the carrier concentration reaches  $10^{21} \text{ cm}^{-3}$  [84]. The lattice thermal conductivity also decreases because of the increased point defect scattering and reaches to an extremely low value of  $0.25 \text{ W/mK}$  at 923 K in Ba-doped BiCuSeO (Fig. 2.8.7C) [94]. These doping strategies resulted in an improved  $zT$  which reaches to a value as high as 1.1 at 923 K (Fig. 2.8.7D) [94]. Pb/Ca dual doping also has been used which resulted in a record high  $zT$  of  $\sim 1.5$  at 873 K. While Pb doping increases the power factor due to the increased carrier concentration and effective mass, dual Pb/Ca doping increases phonon scattering due to increased mass fluctuation and point defect scattering as well, which consequently results in the record high thermoelectric performance in BiCuSeO [95].

### 2.8.3 Future outlook

Thermoelectric performance of Se-based chalcogenide materials has improved tremendously in the last decade. This includes the improvement in thermoelectric performance of traditional materials such as PbSe with new strategies like band convergence as well as new understanding in thermoelectric transport properties of decade-old materials such as  $\text{Cu}_2\text{Se}$ . Several new intriguing materials such as SnSe,  $\text{In}_4\text{Se}_3$ , and BiCuSeO have also been discovered, which show high thermoelectric performance. Ternary selenides, such as CuAgSe and  $\text{AgCrSe}_2$ , with their intrinsically ultralow lattice thermal conductivity, lead a new direction of designing high-performance thermoelectric materials. Yet, there is still a tremendous scope to further improve the thermoelectric performance of these well-known materials with innovative material processing techniques or using intrinsic properties. Another oxy-selenide,  $\text{Bi}_2\text{O}_2\text{Se}$ , is also emerging as a promising  $n$ -type thermoelectric material with several key advantageous properties such as a layered structure, high charge carrier mobility, and ferroelectric properties [96–98] wherein lies a great scope to improve the thermoelectric performance of this material.

## References

- [1] J. He, T.M. Tritt, Advances in thermoelectric materials research: looking back and moving forward, *Science* 357 (2017) eaak9997, <https://doi.org/10.1126/science.aak9997>.
- [2] K.F. Hsu, S. Loo, F. Guo, W. Chen, J.S. Dyck, C. Uher, T. Hogan, E.K. Polychroniadis, M.G. Kanatzidis, Cubic  $\text{AgPb}_m\text{SbTe}_{2+m}$ : bulk thermoelectric materials with high figure of merit, *Science* 303 (2004) 818–821, <https://doi.org/10.1126/science.1092963>.
- [3] F.D. Rosi, J.P. Dismukes, E.F. Hockings, Semiconductor materials for thermoelectric power generation up to 700 °C, *Electr. Eng.* 79 (1960) 450–459, <https://doi.org/10.1109/EE.1960.6432651>.
- [4] R. Venkatasubramanian, E. Siivola, T. Colpitts, B. O’Quinn, Thin-film thermoelectric devices with high room-temperature figures of merit, *Nature* 413 (2001) 597–602, <https://doi.org/10.1038/35098012>.
- [5] D.R. Brown, T. Day, T. Caillat, G.J. Snyder, Chemical stability of  $(\text{Ag,Cu})_2\text{Se}$ : a historical overview, *J. Electron. Mater.* 42 (2013) 2014–2019, <https://doi.org/10.1007/s11664-013-2506-2>.
- [6] H. Wang, Y. Pei, A.D. LaLonde, G.J. Snyder, Heavily doped p-type PbSe with high thermoelectric performance: an alternative for PbTe, *Adv. Mater.* 23 (2011) 1366, <https://doi.org/10.1002/adma.201004200>.
- [7] L.-D. Zhao, S.-H. Lo, Y. Zhang, H. Sun, G. Tan, C. Uher, C. Wolverton, V.P. Dravid, M.G. Kanatzidis, Ultralow thermal conductivity and high thermoelectric figure of merit in SnSe crystals, *Nature* 508 (2014) 373–377, <https://doi.org/10.1038/nature13184>.
- [8] J.-S. Rhyee, K.H. Lee, S.M. Lee, E. Cho, S.I. Kim, E. Lee, Y.S. Kwon, J.H. Shim, G. Kotliar, Peierls distortion as a route to high thermoelectric performance in  $\text{In}_4\text{Se}_{3-\delta}$  crystals, *Nature* 459 (2009) 965–968, <https://doi.org/10.1038/nature08088>.
- [9] T.J. Slade, T.P. Bailey, J.A. Grovogui, X. Hua, X. Zhang, J.J. Kuo, I. Hader, G.J. Snyder, C. Wolverton, V.P. Dravid, C. Uher, M.G. Kanatzidis, High thermoelectric performance in PbSe–NaSbSe<sub>2</sub> alloys from valence band convergence and low thermal conductivity, *Adv. Energy Mater.* 9 (2019) 1901377, <https://doi.org/10.1002/aenm.201901377>.
- [10] J.M. Hodges, S. Hao, J.A. Grovogui, X. Zhang, T.P. Bailey, X. Li, Z. Gan, Y.-Y. Hu, C. Uher, V.P. Dravid, C. Wolverton, M.G. Kanatzidis, Chemical insights into PbSe–x %HgSe: high power factor and improved thermoelectric performance by alloying with discordant atoms, *J. Am. Chem. Soc.* 140 (2018) 18115, <https://doi.org/10.1021/jacs.8b11050>.
- [11] R. Yu, E.S. Bozin, M. Abeykoon, B. Sangiorgio, N.A. Spaldin, C.D. Malliakas, M.G. Kanatzidis, S.J.L. Billinge, Emphantitic anharmonicity in PbSe at high temperature and anomalous electronic properties in the PbQ (Q = S, Se, Te) system, *Phys. Rev. B* 98 (2018) 144108, <https://doi.org/10.1103/PhysRevB.98.144108>.
- [12] Z.-Z. Luo, S. Hao, X. Zhang, X. Hua, S. Cai, G. Tan, T.P. Bailey, R. Ma, C. Uher, C. Wolverton, V.P. Dravid, Q. Yan, M.G. Kanatzidis, Soft phonon modes from off-center Ge atoms lead to ultralow thermal conductivity and superior thermoelectric performance in n-type PbSe–GeSe, *Energy Environ. Sci.* 11 (2018) 3220–3230, <https://doi.org/10.1039/C8EE01755G>.
- [13] Q. Zhang, H. Wang, W. Liu, H. Wang, B. Yu, Q. Zhang, Z. Tian, G. Ni, S. Lee, K. Esfarjani, G. Chen, Z. Ren, Enhancement of thermoelectric figure-of-merit by resonant states of aluminium doping in lead selenide, *Energy Environ. Sci.* 5 (2012) 5246–5251, <https://doi.org/10.1039/C1EE02465E>.

- [14] Y. Lee, S.-H. Lo, C. Chen, H. Sun, D.-Y. Chung, T.C. Chasapis, C. Uher, V.P. Dravid, M.G. Kanatzidis, Contrasting role of antimony and bismuth dopants on the thermoelectric performance of lead selenide, *Nat. Commun.* 5 (2014) 1–11, <https://doi.org/10.1038/ncomms4640>.
- [15] C. Zhou, Y. Yu, Y.K. Lee, O. Cojocaru-Miredin, B. Yoo, S.-P. Cho, J. Im, M. Wuttig, T. Hyeon, I. Chung, High-performance n-type PbSe–Cu<sub>2</sub>Se thermoelectrics through conduction band engineering and phonon softening, *J. Am. Chem. Soc.* 140 (2018) 15535, <https://doi.org/10.1021/jacs.8b10448>.
- [16] L.-D. Zhao, S. Hao, S.-H. Lo, C.-I. Wu, X. Zhou, Y. Lee, H. Li, K. Biswas, T.P. Hogan, C. Uher, C. Wolverton, V.P. Dravid, M.G. Kanatzidis, High thermoelectric performance via hierarchical compositionally alloyed nanostructures, *J. Am. Chem. Soc.* 135 (2013) 7364–7370, <https://doi.org/10.1021/ja403134b>.
- [17] H. Wang, Z.M. Gibbs, Y. Takagiwa, G.J. Snyder, Tuning bands of PbSe for better thermoelectric efficiency, *Energy Environ. Sci.* 7 (2014) 804–811, <https://doi.org/10.1039/C3EE43438A>.
- [18] G. Tan, S. Hao, S. Cai, T.P. Bailey, Z. Luo, I. Hadar, C. Uher, V.P. Dravid, C. Wolverton, M.G. Kanatzidis, All-scale hierarchically structured p-type PbSe alloys with high thermoelectric performance enabled by improved band degeneracy, *J. Am. Chem. Soc.* 141 (2019) 4480–4486, <https://doi.org/10.1021/jacs.9b00967>.
- [19] L. You, Y. Liu, X. Li, P. Nan, B. Ge, Y. Jiang, P. Luo, S. Pan, Y. Pei, W. Zhang, G.J. Snyder, J. Yang, J. Zhang, J. Luo, Boosting the thermoelectric performance of PbSe through dynamic doping and hierarchical phonon scattering, *Energy Environ. Sci.* 11 (2018) 1848–1858, <https://doi.org/10.1039/C8EE00418H>.
- [20] L.-D. Zhao, G. Tan, S. Hao, J. He, Y. Pei, H. Chi, H. Wang, S. Gong, H. Xu, V.P. Dravid, C. Uher, G.J. Snyder, C. Wolverton, M.G. Kanatzidis, Ultrahigh power factor and thermoelectric performance in hole-doped single-crystal SnSe, *Science* 351 (2016) 141, <https://doi.org/10.1126/science.aad3749>.
- [21] L.-D. Zhao, C. Chang, G. Tan, M.G. Kanatzidis, SnSe: a remarkable new thermoelectric material, *Energy Environ. Sci.* 9 (2016) 3044–3060, <https://doi.org/10.1039/C6EE01755J>.
- [22] A. Dewandre, O. Hellman, S. Bhattacharya, A.H. Romero, G.K.H. Madsen, M.J. Verstraete, Two-step phase transition in SnSe and the origins of its high power factor from first principles, *Phys. Rev. Lett.* 117 (2016) 276601, <https://doi.org/10.1103/PhysRevLett.117.276601>.
- [23] J.M. Skelton, L.A. Burton, S.C. Parker, A. Walsh, C.-E. Kim, A. Soon, J. Buckeridge, A.A. Sokol, C.R.A. Catlow, A. Togo, I. Tanaka, Anharmonicity in the high-temperature *Cmcm* phase of SnSe: soft modes and three-phonon interactions, *Phys. Rev. Lett.* 117 (2016), <https://doi.org/10.1103/PhysRevLett.117.075502>.
- [24] Q. Lu, M. Wu, D. Wu, C. Chang, Y.-P. Guo, C.-S. Zhou, W. Li, X.-M. Ma, G. Wang, L.-D. Zhao, L. Huang, C. Liu, J. He, Unexpected large hole effective masses in SnSe revealed by angle-resolved photoemission spectroscopy, *Phys. Rev. Lett.* 119 (2017) 116401, <https://doi.org/10.1103/PhysRevLett.119.116401>.
- [25] J. Carrete, N. Mingo, S. Curtarolo, Low thermal conductivity and triaxial phononic anisotropy of SnSe, *Appl. Phys. Lett.* 105 (2014) 101907, <https://doi.org/10.1063/1.4895770>.
- [26] C.W. Li, J. Hong, A.F. May, D. Bansal, S. Chi, T. Hong, G. Ehlers, O. Delaire, Orbitally driven giant phonon anharmonicity in SnSe, *Nat. Phys.* 11 (2015) 1063, <https://doi.org/10.1038/nphys3492>.
- [27] C. Chang, G. Tan, J. He, M.G. Kanatzidis, L.-D. Zhao, The thermoelectric properties of SnSe continue to surprise: extraordinary electron and phonon transport, *Chem. Mater.* 30 (2018) 7355, <https://doi.org/10.1021/acs.chemmater.8b03732>.

- [28] C.-L. Chen, H. Wang, Y.-Y. Chen, T. Day, G.J. Snyder, Thermoelectric properties of p-type polycrystalline SnSe doped with ag, *J. Mater. Chem. A* 2 (2014) 11171–11176, <https://doi.org/10.1039/C4TA01643B>.
- [29] S. Sassi, C. Candolfi, J.-B. Vaney, V. Ohorodniichuk, P. Masschelein, A. Dauscher, B. Lenoir, Assessment of the thermoelectric performance of polycrystalline p-type SnSe, *Appl. Phys. Lett.* 104 (2014) 212105, <https://doi.org/10.1063/1.4880817>.
- [30] P.-C. Wei, S. Bhattacharya, J. He, S. Neeleshwar, R. Podila, Y.Y. Chen, A.M. Rao, The intrinsic thermal conductivity of SnSe, *Nature* 539 (2016), <https://doi.org/10.1038/nature19832>.
- [31] D. Wu, L. Wu, D. He, L.-D. Zhao, W. Li, M. Wu, M. Jin, J. Xu, J. Jiang, L. Huang, Y. Zhu, M.G. Kanatzidis, J. He, Direct observation of vast off-stoichiometric defects in single crystalline SnSe, *Nano Energy* 35 (2017) 321, <https://doi.org/10.1016/j.nanoen.2017.04.004>.
- [32] Y.K. Lee, Z. Luo, S.P. Cho, M.G. Kanatzidis, I. Chung, Surface oxide removal for polycrystalline SnSe reveals near-single-crystal thermoelectric performance, *Joule* 3 (2019) 719–731, <https://doi.org/10.1016/j.joule.2019.01.001>.
- [33] S. Chandra, K. Biswas, Realization of high thermoelectric figure of merit in solution synthesized 2D SnSe nanoplates via Ge alloying, *J. Am. Chem. Soc.* 141 (2019) 6141–6145, <https://doi.org/10.1021/jacs.9b01396>.
- [34] K. Kutorasinski, B. Wiendlocha, S. Kaprzyk, J. Tobola, Electronic structure and thermoelectric properties of *n*- and *p*-type SnSe from first-principles calculations, *Phys. Rev. B* 91 (2015) 205201, <https://doi.org/10.1103/PhysRevB.91.205201>.
- [35] R. Guo, X. Wang, Y. Kuang, B. Huang, First-principles study of anisotropic thermoelectric transport properties of IV-VI semiconductor compounds SnSe and SnS, *Phys. Rev. B* 92 (2015) 115202, <https://doi.org/10.1103/PhysRevB.92.115202>.
- [36] A.T. Duong, V.Q. Nguyen, G. Duvnjir, V.T. Duong, S. Kwon, J.Y. Song, J.K. Lee, J.E. Lee, S. Park, T. Min, J. Lee, J. Kim, S. Cho, Achieving ZT=2.2 with Bi-doped n-type SnSe single crystals, *Nat. Commun.* 7 (2016) 1–6, <https://doi.org/10.1038/ncomms13713>.
- [37] H. Liu, X. Shi, F. Xu, L. Zhang, W. Zhang, L. Chen, Q. Li, C. Uher, T. Day, G.J. Snyder, Copper ion liquid-like thermoelectrics, *Nat. Mater.* 11 (2012) 422–425, <https://doi.org/10.1038/nmat3273>.
- [38] K. Yamamoto, S. Kashida, X-ray study of the average structures of Cu<sub>2</sub>Se and Cu<sub>1.8</sub>S in the room temperature and the high temperature phases, *J. Solid State Chem.* 93 (1991) 202–211, [https://doi.org/10.1016/0022-4596\(91\)90289-T](https://doi.org/10.1016/0022-4596(91)90289-T).
- [39] D.J. Voneshen, H.C. Walker, K. Refson, J.P. Goff, Hopping time scales and the phonon-liquid electron-crystal picture in thermoelectric copper selenide, *Phy. Rev. Lett.* 118 (2017) 145901, <https://doi.org/10.1103/PhysRevLett.118.145901>.
- [40] B. Gahtori, S. Bathula, K. Tyagi, M. Jayasimhadri, A.K. Srivastava, S. Singh, R.C. Budhani, A. Dhar, Giant enhancement in thermoelectric performance of copper selenide by incorporation of different nanoscale dimensional defect features, *Nano Energy* 13 (2015) 36–46, <https://doi.org/10.1016/j.nanoen.2015.02.008>.
- [41] B. Yu, W. Liu, S. Chen, H. Wang, H. Wang, G. Chen, Z. Ren, Thermoelectric properties of copper selenide with ordered selenium layer and disordered copper layer, *Nano Energy* 1 (2012) 472–478, <https://doi.org/10.1016/j.nanoen.2012.02.010>.
- [42] B. Zhong, Y. Zhang, W. Li, Z. Chen, J. Cui, W. Li, Y. Xie, Q. Hao, Q. He, High superionic conduction arising from aligned large lamellae and large figure of merit in bulk Cu<sub>1.94</sub>Al<sub>0.02</sub>Se, *Appl. Phys. Lett.* 105 (2014) 123902, <https://doi.org/10.1063/1.4896520>.
- [43] L. Zhao, S.M.K.N. Islam, J. Wang, D.L. Cortie, X. Wang, Z. Cheng, J. Wang, N. Ye, S. Dou, X. Shi, L. Chen, G.J. Snyder, X. Wang, Significant enhancement of figure-of-merit in carbon-reinforced Cu<sub>2</sub>Se nanocrystalline solids, *Nano Energy* 41 (2017) 164–171, <https://doi.org/10.1016/j.nanoen.2017.09.020>.

- [44] R. Nunna, P. Qiu, M. Yin, H. Chen, R. Hanus, Q. Song, T. Zhang, M.-Y. Chou, M.T. Agne, J. He, G.J. Snyder, X. Shi, L. Chen, Ultrahigh thermoelectric performance in Cu<sub>2</sub>Se-based hybrid materials with highly dispersed molecular CNTs, *Energy Environ. Sci.* 10 (2017) 1928–1935, <https://doi.org/10.1039/C7EE01737E>.
- [45] H. Liu, X. Yuan, P. Lu, X. Shi, F. Xu, Y. He, Y. Tang, S. Bai, W. Zhang, L. Chen, Y. Lin, L. Shi, H. Lin, X. Gao, X. Zhang, H. Chi, C. Uher, Ultrahigh thermoelectric performance by electron and phonon critical scattering in Cu<sub>2</sub>Se<sub>1-x</sub>I<sub>x</sub>, *Adv. Mater.* 25 (2013) 6612, <https://doi.org/10.1002/adma.201302660>.
- [46] A.A. Olvera, N.A. Moroz, P. Sahoo, P. Ren, T.P. Bailey, A.A. Page, C. Uher, P.F.P. Poudeu, Partial indium solubility induces chemical stability and colossal thermoelectric figure of merit in Cu<sub>2</sub>Se, *Energy Environ. Sci.* 10 (2017) 1668–1676, <https://doi.org/10.1039/C7EE01193H>.
- [47] P. Qiu, T. Mao, Z. Huang, X. Xia, J. Liao, M.T. Agne, M. Gu, Q. Zhang, D. Ren, S. Bai, X. Shi, G.J. Snyder, L. Chen, High-efficiency and stable thermoelectric module based on liquid-like materials, *Joule* 3 (2019) 1538–1548, <https://doi.org/10.1016/j.joule.2019.04.010>.
- [48] J.H.C. Hogg, H.H. Sutherland, D.J. Williams, The crystal structure of tetraindium triselenide, *Acta Crystallogr. B* 29 (1973) 1590–1593, <https://doi.org/10.1107/S056740873005108>.
- [49] J.-S. Rhyee, K. Ahn, K.H. Lee, H.S. Ji, J.-H. Shim, Enhancement of the thermoelectric figure-of-merit in a wide temperature range in In<sub>4</sub>Se<sub>3-x</sub>Cl<sub>0.03</sub> bulk crystals, *Adv. Mater.* 23 (2011) 2191–2194, <https://doi.org/10.1002/adma.201004739>.
- [50] X. Yin, J.-Y. Liu, L. Chen, L.-M. Wu, High thermoelectric performance of In<sub>4</sub>Se<sub>3</sub>-based materials and the influencing factors, *Acc. Chem. Res.* 51 (2018) 240–247, <https://doi.org/10.1021/acs.accounts.7b00480>.
- [51] Z.-S. Lin, L. Chen, L.-M. Wang, J.-T. Zhao, L.-M. Wu, A promising mid-temperature thermoelectric material candidate: Pb/Sn-codoped In<sub>4</sub>Pb<sub>x</sub>Sn<sub>y</sub>Se<sub>3</sub>, *Adv. Mater.* 25 (2013) 4800–4806, <https://doi.org/10.1002/adma.201302038>.
- [52] Y. Luo, J. Yang, M. Liu, Y. Xiao, L. Fu, W. Li, D. Zhang, M. Zhang, Y. Cheng, Multiple heteroatom induced carrier engineering and hierarchical nanostructures for high thermoelectric performance of polycrystalline In<sub>4</sub>Se<sub>2.5</sub>, *J. Mater. Chem. A* 3 (2014) 1251–1257, <https://doi.org/10.1039/C4TA05508J>.
- [53] G. Ding, G. Gao, K. Yao, High-efficient thermoelectric materials: the case of orthorhombic IV-VI compounds, *Sci. Rep.* 5 (2015) 9567, <https://doi.org/10.1038/srep09567>.
- [54] S. Hao, F. Shi, V.P. Dravid, M.G. Kanatzidis, C. Wolverton, Computational prediction of high thermoelectric performance in hole doped layered GeSe, *Chem. Mater.* 28 (2016) 3218–3226, <https://doi.org/10.1021/acs.chemmater.6b01164>.
- [55] X. Zhang, J. Shen, S. Lin, J. Li, Z. Chen, W. Li, Y. Pei, Thermoelectric properties of GeSe, *J. Mater. Sci.* 2 (2016) 331–337, <https://doi.org/10.1016/j.jmat.2016.09.001>.
- [56] Z. Huang, S.A. Miller, B. Ge, M. Yan, S. Anand, T. Wu, P. Nan, Y. Zhu, W. Zhuang, G.J. Snyder, P. Jiang, X. Bao, High thermoelectric performance of new rhombohedral phase of GeSe stabilized through alloying with AgSbSe<sub>2</sub>, *Angew. Chem. Int. Ed.* 56 (2017) 14113, <https://doi.org/10.1002/anie.201708134>.
- [57] M. Yan, X. Tan, Z. Huang, G. Liu, P. Jiang, X. Bao, Synergetic optimization of electronic and thermal transport for high-performance thermoelectric GeSe–AgSbTe<sub>2</sub> alloy, *J. Mater. Chem. A* 6 (2018) 8215–8220, <https://doi.org/10.1039/C8TA01393D>.
- [58] V.L. Deringer, R.P. Stoffel, R. Dronskowski, Vibrational and thermodynamic properties of GeSe in the quasiharmonic approximation, *Phys. Rev. B* 89 (2014), <https://doi.org/10.1103/PhysRevB.89.094303>.

- [59] S. Roychowdhury, T. Ghosh, R. Arora, U.V. Waghmare, K. Biswas, Stabilizing n-type cubic GeSe by entropy-driven alloying of AgBiSe<sub>2</sub>: ultralow thermal conductivity and promising thermoelectric performance, *Angew. Chem. Int. Ed.* 57 (2018) 15167–15171, <https://doi.org/10.1002/anie.201809841>.
- [60] M. Samanta, K. Pal, P. Pal, U.V. Waghmare, K. Biswas, Localized vibrations of bi bilayer leading to ultralow lattice thermal conductivity and high thermoelectric performance in weak topological insulator n-type BiSe, *J. Am. Chem. Soc.* 140 (2018) 5866, <https://doi.org/10.1021/jacs.8b02691>.
- [61] H. Lind, S. Lidin, U. Häussermann, Structure and bonding properties of (Bi<sub>2</sub>Se<sub>3</sub>)<sub>m</sub>(Bi<sub>2</sub>)<sub>n</sub> stacks by first-principles density functional theory, *Phys. Rev. B* 72 (2005) 184101, <https://doi.org/10.1103/PhysRevB.72.184101>.
- [62] K. Majhi, K. Pal, H. Lohani, A. Banerjee, P. Mishra, A.K. Yadav, R. Ganesan, B.R. Sekhar, U.V. Waghmare, P.S. Anil Kumar, Emergence of a weak topological insulator from the Bi<sub>x</sub>Se<sub>y</sub> family, *Appl. Phys. Lett.* 110 (2017) 162102, <https://doi.org/10.1063/1.4981875>.
- [63] S.N. Guin, A. Chatterjee, D.S. Negi, R. Datta, K. Biswas, High thermoelectric performance in tellurium free p-type AgSbSe<sub>2</sub>, *Energy Environ. Sci.* 6 (2013) 2603–2608, <https://doi.org/10.1039/C3EE41935E>.
- [64] S.N. Guin, A. Chatterjee, K. Biswas, Enhanced thermoelectric performance in p-type AgSbSe<sub>2</sub> by Cd-doping, *RSC Adv.* 4 (2014) 11811–11815, <https://doi.org/10.1039/C4RA00969J>.
- [65] S.N. Guin, K. Biswas, Sb deficiencies control hole transport and boost the thermoelectric performance of p-type AgSbSe<sub>2</sub>, *J. Mater. Chem. C* 3 (2015) 10415–10421, <https://doi.org/10.1039/C5TC01429H>.
- [66] S. Cai, Z. Liu, J. Sun, R. Li, W. Fei, J. Sui, Enhancement of thermoelectric properties by Na doping in Te-free p-type AgSbSe<sub>2</sub>, *Dalton Trans.* 44 (2015) 1046–1051, <https://doi.org/10.1039/C4DT03059A>.
- [67] W. Gao, Z. Wang, J. Huang, Z. Liu, Extraordinary thermoelectric performance realized in hierarchically structured AgSbSe<sub>2</sub> with ultralow thermal conductivity, *ACS Appl. Mater. Interfaces* 10 (2018) 18685–18692, <https://doi.org/10.1021/acsami.8b03243>.
- [68] Z. Liu, J. Shuai, H. Geng, J. Mao, Y. Feng, X. Zhao, X. Meng, R. He, W. Cai, J. Sui, Contrasting the role of Mg and Ba doping on the microstructure and thermoelectric properties of p-type AgSbSe<sub>2</sub>, *ACS Appl. Mater. Interfaces* 7 (2015) 23047–23055, <https://doi.org/10.1021/acsami.5b06492>.
- [69] D. Li, X.Y. Qin, T.H. Zou, J. Zhang, B.J. Ren, C.J. Song, Y.F. Liu, L. Wang, H.X. Xin, J.C. Li, High thermoelectric properties for Sn-doped AgSbSe<sub>2</sub>, *J. Alloys Compd.* 635 (2015) 87–91, <https://doi.org/10.1016/j.jallcom.2014.11.081>.
- [70] C. Xiao, X. Qin, J. Zhang, R. An, J. Xu, K. Li, B. Cao, J. Yang, B. Ye, Y. Xie, High thermoelectric and reversible p-n-p conduction type switching integrated in dimetal chalcogenide, *J. Am. Chem. Soc.* 134 (2012) 18460, <https://doi.org/10.1021/ja308936b>.
- [71] L. Pan, D. Bérardan, N. Dragoe, High thermoelectric properties of n-type AgBiSe<sub>2</sub>, *J. Am. Chem. Soc.* 135 (2013) 4914–4917, <https://doi.org/10.1021/ja312474n>.
- [72] S.N. Guin, V. Srihari, K. Biswas, Promising thermoelectric performance in n-type AgBiSe<sub>2</sub>: effect of aliovalent anion doping, *J. Mater. Chem. A* 3 (2014) 648–655, <https://doi.org/10.1039/C4TA04912H>.
- [73] H.-J. Wu, P.-C. Wei, H.-Y. Cheng, J.-R. Deng, Y.-Y. Chen, Ultralow thermal conductivity in n-type Ge-doped AgBiSe<sub>2</sub> thermoelectric materials, *Acta Mater.* 141 (2017) 217–229, <https://doi.org/10.1016/j.actamat.2017.09.029>.
- [74] Y. Goto, A. Nishida, H. Nishiate, M. Murata, C.H. Lee, A. Miura, C. Moriyoshi, Y. Kuroiwa, Y. Mizuguchi, Effect of Te substitution on crystal structure and transport

- properties of  $\text{AgBiSe}_2$  thermoelectric material, *Dalton Trans.* 47 (2018) 2575–2580, <https://doi.org/10.1039/C7DT04821A>.
- [75] S. Ishiwata, Y. Shiomi, J.S. Lee, M.S. Bahramy, T. Suzuki, M. Uchida, R. Arita, Y. Taguchi, Y. Tokura, Extremely high electron mobility in a phonon-glass semimetal, *Nat. Mater.* 12 (2013) 512–517, <https://doi.org/10.1038/nmat3621>.
- [76] P.F. Qiu, X.B. Wang, T.S. Zhang, X. Shi, L.D. Chen, Thermoelectric properties of Te-doped ternary CuAgSe compounds, *J. Mater. Chem. A* 3 (2015) 22454–22461, <https://doi.org/10.1039/C5TA06780D>.
- [77] C. Han, Q. Sun, Z.X. Cheng, J.L. Wang, Z. Li, G.Q. Max Lu, S.X. Dou, Ambient scalable synthesis of surfactant-free thermoelectric CuAgSe nanoparticles with reversible metallic-n-p conductivity transition, *J. Am. Chem. Soc.* 136 (2014) 17626–17633. doi:<https://doi.org/10.1021/ja510433j>.
- [78] B. Li, H. Wang, Y. Kawakita, Q. Zhang, M. Feygenson, H.L. Yu, D. Wu, K. Ohara, T. Kikuchi, K. Shibata, T. Yamada, X.K. Ning, Y. Chen, J.Q. He, D. Vaknin, R.Q. Wu, K. Nakajima, M.G. Kanatzidis, Liquid-like thermal conduction in intercalated layered crystalline solids, *Nat. Mater.* 17 (2018) 226–230, <https://doi.org/10.1038/s41563-017-0004-2>.
- [79] F. Damay, S. Petit, S. Rols, M. Braendlein, R. Daou, E. Elkaim, F. Gascoin, C. Martin, A. Maignan, Localised  $\text{Ag}^+$  vibrations at the origin of ultralow thermal conductivity in layered thermoelectric  $\text{AgCrSe}_2$ , *Sci. Rep.* 6 (2016) 23415, <https://doi.org/10.1038/srep23415>.
- [80] F. Gascoin, A. Maignan, Order-disorder transition in  $\text{AgCrSe}_2$ : a new route to efficient thermoelectrics, *Chem. Mater.* 23 (2011) 2510–2513, <https://doi.org/10.1021/cm200581k>.
- [81] S. Bhattacharya, A. Bohra, R. Basu, R. Bhatt, S. Ahmad, K.N. Meshram, A.K. Debnath, A. Singh, S.K. Sarkar, M. Navneethan, Y. Hayakawa, D.K. Aswal, S.K. Gupta, High thermoelectric performance of  $(\text{AgCrSe}_2)_{0.5}(\text{CuCrSe}_2)_{0.5}$  nano-composites having all-scale natural hierarchical architectures, *J. Mater. Chem. A* 2 (2014) 17122–17129, <https://doi.org/10.1039/C4TA04056B>.
- [82] L.D. Zhao, D. Berardan, Y.L. Pei, C. Byl, L. Pinsard-Gaudart, N. Dragoe,  $\text{Bi}_{1-x}\text{Sr}_x\text{CuSeO}$  oxyselenides as promising thermoelectric materials, *Appl. Phys. Lett.* 97 (2010) 092118, <https://doi.org/10.1063/1.3485050>.
- [83] D. Zou, S. Xie, Y. Liu, J. Lin, J. Li, Electronic structures and thermoelectric properties of layered  $\text{BiCuOCh}$  oxychalcogenides ( $\text{Ch} = \text{S}, \text{Se}$  and  $\text{Te}$ ): first-principles calculations, *J. Mater. Chem. A* 1 (2013) 8888–8896, <https://doi.org/10.1039/C3TA11222E>.
- [84] L.-D. Zhao, J. He, D. Berardan, Y. Lin, J.-F. Li, C.-W. Nan, N. Dragoe,  $\text{BiCuSeO}$  oxyselenides: new promising thermoelectric materials, *Energy Environ. Sci.* 7 (2014) 2900–2924, <https://doi.org/10.1039/C4EE00997E>.
- [85] J. Ding, B. Xu, Y. Lin, C. Nan, W. Liu, Lattice vibration modes of the layered material  $\text{BiCuSeO}$  and first principles study of its thermoelectric properties, *New J. Phys.* 17 (2015), <https://doi.org/10.1088/1367-2630/17/8/083012>.
- [86] S.K. Saha, Exploring the origin of ultralow thermal conductivity in layered  $\text{BiOCuSe}$ , *Phys. Rev. B* 92 (2015), <https://doi.org/10.1103/PhysRevB.92.041202>.
- [87] P. Vaqueiro, R.A.R.A. Orabi, S.D.N. Luu, G. Guélou, A.V. Powell, R.I. Smith, J.-P. Song, D. Wee, M. Fornari, The role of copper in the thermal conductivity of thermoelectric oxychalcogenides: do lone pairs matter? *Phys. Chem. Chem. Phys.* 17 (2015) 31735–31740, <https://doi.org/10.1039/C5CP06192J>.
- [88] F. Li, J.-F. Li, L.-D. Zhao, K. Xiang, Y. Liu, B.-P. Zhang, Y.-H. Lin, C.-W. Nan, H.-M. Zhu, Polycrystalline  $\text{BiCuSeO}$  oxide as a potential thermoelectric material, *Energy Environ. Sci.* 5 (2012) 7188–7195, <https://doi.org/10.1039/C2EE21274A>.

- [89] Y. Liu, L.-D. Zhao, Y. Liu, J. Lan, W. Xu, F. Li, B.-P. Zhang, D. Berardan, N. Dragoe, Y.-H. Lin, C.-W. Nan, J.-F. Li, H. Zhu, Remarkable enhancement in thermoelectric performance of BiCuSeO by Cu deficiencies, *J. Am. Chem. Soc.* 133 (2011) 20112–20115, <https://doi.org/10.1021/ja2091195>.
- [90] Z. Li, C. Xiao, S. Fan, Y. Deng, W. Zhang, B. Ye, Y. Xie, Dual vacancies: an effective strategy realizing synergistic optimization of thermoelectric property in BiCuSeO, *J. Am. Chem. Soc.* 137 (2015) 6587–6593, <https://doi.org/10.1021/jacs.5b01863>.
- [91] Y.-L. Pei, H. Wu, D. Wu, F. Zheng, J. He, High thermoelectric performance realized in a BiCuSeO system by improving carrier mobility through 3D modulation doping, *J. Am. Chem. Soc.* 136 (2014) 13902–13908, <https://doi.org/10.1021/ja507945h>.
- [92] J. Sui, J. Li, J. He, Y.-L. Pei, D. Berardan, H. Wu, N. Dragoe, W. Cai, L.-D. Zhao, Texturation boosts the thermoelectric performance of BiCuSeO oxyselenides, *Energy Environ. Sci.* 6 (2013) 2916–2920, <https://doi.org/10.1039/C3EE41859F>.
- [93] X. Zhang, C. Chang, Y. Zhou, L.-D. Zhao, BiCuSeO thermoelectrics: an update on recent progress and perspective, *Materials* 10 (2017) 198, <https://doi.org/10.3390/ma10020198>.
- [94] J. Li, J. Sui, Y. Pei, C. Barreteau, D. Berardan, N. Dragoe, W. Cai, J. He, L.-D. Zhao, A high thermoelectric figure of merit  $ZT > 1$  in Ba heavily doped BiCuSeO oxyselenides, *Energy Environ. Sci.* 5 (2012) 8543–8547, <https://doi.org/10.1039/C2EE22622G>.
- [95] Y. Liu, L.-D. Zhao, Y. Zhu, Y. Liu, F. Li, M. Yu, D.-B. Liu, W. Xu, Y.-H. Lin, C.-W. Nan, Synergistically optimizing electrical and thermal transport properties of BiCuSeO via a dual-doping approach, *Adv. Energy Mater.* 6 (2016) 1502423, <https://doi.org/10.1002/aenm.201502423>.
- [96] T. Ghosh, M. Samanta, A. Vasdev, K. Dolui, J. Ghatak, T. Das, G. Sheet, K. Biswas, Ultrathin free-standing nanosheets of  $\text{Bi}_2\text{O}_2\text{Se}$ : room temperature ferroelectricity in self-assembled charged layered heterostructure, *Nano Lett.* 19 (2019) 5703–5709, <https://doi.org/10.1021/acs.nanolett.9b02312>.
- [97] X. Tan, Y. Liu, R. Liu, Z. Zhou, C. Liu, J.-L. Lan, Q. Zhang, Y.-H. Lin, C.-W. Nan, Synergistical enhancement of thermoelectric properties in n-type  $\text{Bi}_2\text{O}_2\text{Se}$  by carrier engineering and hierarchical microstructure, *Adv. Energy Mater.* 9 (2019) 1900354, <https://doi.org/10.1002/aenm.201900354>.
- [98] J. Wu, H. Yuan, M. Meng, C. Chen, Y. Sun, Z. Chen, W. Dang, C. Tan, Y. Liu, J. Yin, Y. Zhou, S. Huang, H.Q. Xu, Y. Cui, H.Y. Hwang, Z. Liu, Y. Chen, B. Yan, H. Peng, High electron mobility and quantum oscillations in non-encapsulated ultrathin semiconducting  $\text{Bi}_2\text{O}_2\text{Se}$ , *Nat. Nanotechnol.* 12 (2017) 530–534, <https://doi.org/10.1038/nnano.2017.43>.

# Materials development and module fabrication in highly efficient lead tellurides

2.9

Michihiro Ohta<sup>a,\*</sup>, Priyanka Jood<sup>a,\*</sup>, Raju Chetty<sup>a</sup>, and Mercouri G. Kanatzidis<sup>b,c</sup>

<sup>a</sup>Global Zero Emission Research Center, National Institute of Advanced Industrial Science and Technology (AIST), Tsukuba, Ibaraki, Japan, <sup>b</sup>Department of Chemistry, Northwestern University, Evanston, IL, United States, <sup>c</sup>Materials Science Division, Argonne National Laboratory, Argonne, IL, United States

## 2.9.1 Introduction

Lead telluride (PbTe) is a traditional thermoelectric material that shows high performance within 600–900 K, and has been used in power generation technologies, such as radioisotope thermoelectric generators in space probes, since the 1960s [1, 2]. The thermoelectric figure of merit ( $ZT$ ) of PbTe was limited to approximately unity until the mid-2000s [3–6]. New design strategies for producing better thermoelectric materials, including nanostructuring/hierarchical architecturing and band engineering, have been developed, which has significantly increased the potential for using PbTe in thermoelectric applications [3–17]. Nanostructuring/hierarchical architecturing leads to effective scattering of heat-carrying phonons, reducing the lattice thermal conductivity ( $\kappa_{\text{lat}}$ ). Band engineering approaches, such as band convergence, improve the power factor ( $S^2/\rho$ ), where  $S$  is the Seebeck coefficient and  $\rho$  is the electrical resistivity. Moreover, nanostructuring/hierarchical architecturing and band engineering suppress bipolar (minority carrier) transport, leading to an enhancement in the  $S$  value and a reduction in electronic thermal conductivity ( $\kappa_{\text{el}}$ ) at high temperatures.

Table 2.9.1 lists the key stages in the development of the  $ZT$  value of PbTe since 2004. Over the past 15 years, the application of new strategies has dramatically enhanced this value, e.g.,  $ZT$  values of 2.5 at 923 K and 1.83 at 733 K were reported for p-type  $\text{Pb}_{0.98}\text{Na}_{0.02}\text{Te}$ –8% SrTe [34] and n-type PbTe–4% InSb [48], respectively. Moreover, thermoelectric modules using newly developed high- $ZT$  PbTe have recently been fabricated for use in power generation applications [8, 52]. A maximum conversion efficiency ( $\eta_{\text{max}}$ ) of ~8.8% at a hot-side temperature ( $T_h$ ) of 873 K and a cold-side temperature ( $T_c$ ) of 303 K has been demonstrated in the prototype nanostructured PbTe-based module [33]. Furthermore, a  $\eta_{\text{max}}$  of 12% was obtained by stacking a nanostructured PbTe-based module with high efficiency at higher temperatures on top of another  $\text{Bi}_2\text{Te}_3$ -based module with high efficiency at lower temperatures (a cascade-type module) [38].

\* These authors contributed equally to this work.

**Table 2.9.1** Important milestones related to the improvement in thermoelectric figure of merit ( $ZT$ ) of state-of-the-art PbTe-based thermoelectric materials developed since 2004.

Sample	Maximum ZT	Temperature (K)	Reference
<i>p-type</i>			
Ingots of $\text{Ag}_{0.5}\text{Pb}_6\text{Sn}_2\text{Sb}_{0.2}\text{Te}_{10}$	1.45	627	[18]
Ingots of $\text{Na}_{0.95}\text{Pb}_{20}\text{Sb}\text{Te}_{22}$	1.7	650	[19]
Sintered compact of $\text{Tl}_{0.02}\text{Pb}_{0.98}\text{Te}$	1.5	773	[20]
Ingots of $\text{Pb}_{0.9875-x}\text{K}_{0.0125}\text{Na}_x\text{Te}$ ( $x=0.006, 0.01$ )	1.3	700	[21]
Sintered compact of Na-doped PbTe	1.4	750	[22]
Ingots of PbTe–12% PbS-doped 2% Na	1.8	800	[23]
Sintered compact of $\text{Pb}_{0.98}\text{Na}_{0.02}\text{Te}_{0.85}\text{Se}_{0.15}$	1.8	850	[24]
Ingots of PbTe–6% CaTe doped with 1% Na <sub>2</sub> Te	1.5	765	[25]
Ingots of PbTe–2% SrTe doped with 1% Na	1.7	800	[26]
Ingots of PbTe–2% MgTe doped with 2% Na <sub>2</sub> Te	1.6	780	[27]
Sintered compact of PbTe–4% SrTe doped with 2% Na	2.2	915	[28]
Sintered compact of $\text{Pb}_{0.98}\text{K}_{0.020}\text{Te}_{0.85}\text{Se}_{0.15}$	1.6	773	[29]
Sintered compact of PbTe–2% HgTe–1% Na <sub>2</sub> Te	1.64	770	[30]
Sintered compact of $\text{Pb}_{0.98}\text{Na}_{0.020}\text{Te}–6\%$ MgTe	2.0	823	[31]
Sintered compact of 2% Na-doped $(\text{PbTe})_{0.86}(\text{PbSe})_{0.07}(\text{PbS})_{0.07}$	2.0	823	[32]
Sintered compact of PbTe–2% MgTe doped with 4% Na	1.8	810	[33]
Sintered compact of $\text{Pb}_{0.98}\text{Na}_{0.020}\text{Te}–8\%$ SrTe	2.5	923	[34]
Sintered compact of $\text{Pb}_{0.945}\text{Na}_{0.025}\text{Eu}_{0.03}\text{Te}$	2.2	850	[35]
Sintered compact of $\text{Pb}_{0.98}\text{Te}_{0.85}\text{Se}_{0.15}–2\%\text{Na}–4\%$ SrTe	2.3	923	[36]
Sintered compact of $\text{Pb}_{0.97}\text{Na}_{0.03}\text{Te}–1\text{ mol\% Ba}_{0.5}\text{Ca}_{0.5}\text{Te}$	2.2	823	[37]
Sintered compact of $\text{Pb}_{0.953}\text{Na}_{0.040}\text{Ge}_{0.007}\text{Te}$	1.9	805	[38]
<i>n-type</i>			
Ingots of $\text{AgPb}_{18}\text{Sb}\text{Te}_{20}$	1.7	700	[39]
Ingots of $(\text{Pb}_{0.95}\text{Sn}_{0.05}\text{Te})_{0.92}(\text{PbS})_{0.08}$	1.5	642	[40]
Ingots of PbTe–Pb (0.5%)–Sb (2%)	1.4	700	[41]

**Table 2.9.1** Continued

Sample	Maximum ZT	Temperature (K)	Reference
Ingot of $\text{Ag}_{0.05}\text{Pb}_{0.99}\text{La}_{0.01}\text{Te}$	1.2	720	[42]
Ingot of $\text{PbTe}-1\% \text{CdTe}-0.055\% \text{PbI}_2$	1.2	720	[43]
Sintered compact of $(\text{PbLa}_{0.03}\text{Te}_{1.03})_{0.945}(\text{Ag}_2\text{Te})_{0.055}$	1.6	775	[44]
Sintered compact of $\text{PbTe}_{0.996}\text{I}_{0.004}-1 \text{ mol\% MgTe}$	1.2	700	[45]
Sintered compact of $\text{PbTe}$ doped with 0.2% $\text{PbI}_2$	1.4	750	[33]
Sintered compact of $\text{Pb}_{0.9875}\text{Sb}_{0.0125}\text{Te}_{0.88}\text{S}_{0.12}$	1.4	900	[46]
Sintered compact of $\text{PbTe}-2\% \text{Cu}_2\text{Te}$	1.5	723	[47]
Sintered compact of $\text{PbTe}-4\% \text{InSb}$	1.83	773	[48]
Sintered compact of $\text{Pb}_{0.988}\text{Sb}_{0.12}\text{Te}-13\% \text{GeTe}$	1.38	623	[49]
Sintered compact of $\text{Pb}_{0.98}\text{Ga}_{0.02}\text{Te}$	1.34	766	[50]
Sintered compact of $\text{PbTe}-4\% \text{MnTe}$	1.6	773	[51]

This chapter examines recent attempts to develop PbTe-based materials and modules for thermoelectric waste heat recovery. First, the enhancement in  $ZT$  values of PbTe through approaches such as nanostructuring/hierarchical structuring, band convergence, and minority carrier blocking is discussed, followed by a consideration of bridging the technological valley between the development of materials and fabrication of modules in newly developed high- $ZT$  PbTe. Finally, the chapter concludes with a brief overview of future opportunities and potential challenges regarding the application of PbTe-based thermoelectrics in the context of power generation.

## 2.9.2 Nanostructuring and hierarchical structuring

In 2004, a reduction in  $\kappa_{\text{lat}}$  through nanostructuring was first demonstrated for the n-type  $\text{AgPb}_m\text{SbTe}_{2+m}$  system called the LAST [39]. The nanoscale precipitates of the Ag-Sb-rich second phase embedded in bulk ingots of  $\text{AgPb}_m\text{SbTe}_{2+m}$  effectively scatter the heat-carrying phonons with medium mean free paths, leading to reduced  $\kappa_{\text{lat}}$  and enhanced  $ZT$  (Table 2.9.1). A  $ZT$  value of 1.7 at 700K was obtained for  $\text{AgPb}_{18}\text{SbTe}_{20}$ . Following the discovery of high  $ZT$  in the n-type  $\text{AgPb}_m\text{SbTe}_{2+m}$  system, high  $ZT$  values were achieved in p-type  $\text{Ag}(\text{Pb}_{1-y}\text{Sn}_y)_m\text{SbTe}_{2+m}$  [18] and p-type  $\text{Na}_{1-x}\text{Pb}_m\text{Sb}_y\text{Te}_{m+2}$  [19] systems. The most successful approach to  $ZT$  enhancement is nanostructuring, which has been commonly used for PbTe as well as other thermoelectric materials such as PbS [53, 54], GeTe [55, 56], SnTe [57], Skutterudite [58], and half-Heusler compounds [59]. Recently, this approach has evolved to become an all-scale hierarchical structuring (panoscopic) method for scattering

phonons having short-to-long mean free paths and further reducing  $\kappa_{\text{lat}}$  [16, 28]. For example, point defects and microscale grain boundaries can scatter phonons having short and long mean free paths, respectively.

In the PbTe system, nanostructures tend to form in the bulk as precipitates of the second phase through precipitation processes. Fig. 2.9.1A illustrates the general approach to embedding the nanoprecipitates within the bulk [16]. The solubility limit of the second phase must be low in its solid state; however, under high temperatures, the components of the second phase must completely dissolve in the liquid state. The second phase can be precipitated at nanoscales into the matrix by adjusting the precipitation process (such as modifying the cooling rate from the liquid to the solid state).

Nanostructures for PbTe are induced by adding the alkaline earth elements, Cd, Hg, Sb, InSb, Cu<sub>2</sub>Te, and Ge through spontaneous nucleation and growth and spinodal decomposition [16, 25–28, 30, 31, 33, 38, 40, 41, 43, 48, 60]. Fig. 2.9.1B shows a high-magnification transmission electron microscopy (TEM) image of nanostructures formed in the ingot and sintered compact of p-type Pb<sub>0.94</sub>Na<sub>0.04</sub>Mg<sub>0.02</sub>Te [27, 33] and the sintered compact of p-type Pb<sub>0.953</sub>Na<sub>0.040</sub>Ge<sub>0.007</sub>Te [38]. The nanoprecipitates are embedded with coherent interfaces within the PbTe matrix; the typical diameter of spherical nanoprecipitates is approximately 5 nm. The energy-dispersive X-ray spectroscopy (EDS) of the submicron precipitates (~150 nm) for the sintered compact of Pb<sub>0.94</sub>Na<sub>0.04</sub>Mg<sub>0.02</sub>Te is shown in Fig. 2.9.1C [33]. The chemical composition of the nanoprecipitates (Mg rich but Pb and Na deficient) reveals that the introduction of Mg induces nanoprecipitate formation.

The nanostructures effectively scatter heat-carrying phonons with medium mean free paths, essentially reducing the  $\kappa_{\text{lat}}$  and enhancing  $ZT$  values. Fig. 2.9.2A contains a comparison of  $\kappa_{\text{lat}}$  for ingots of p-type Pb<sub>0.96-x</sub>Na<sub>0.04</sub>Mg<sub>x</sub>Te ( $x=0, 0.02$ ) [27], a sintered compact of Pb<sub>0.94</sub>Na<sub>0.04</sub>Mg<sub>0.02</sub>Te [33], and ingot and sintered compact of PbTe–4% SrTe–2% Na [28].  $\kappa_{\text{lat}}$  decreases from  $\sim 2.5 \text{ W m}^{-1} \text{ K}^{-1}$  for non-nanostructured ingot of Pb<sub>0.96</sub>Na<sub>0.04</sub>Te to  $\sim 2.0 \text{ W m}^{-1} \text{ K}^{-1}$  for nanostructured ingot of Pb<sub>0.94</sub>Na<sub>0.04</sub>Mg<sub>0.02</sub>Te at room temperature [27]. Embedding nanostructures into the PbTe grains enhances the  $ZT$  from  $\sim 1.1$  for Pb<sub>0.96</sub>Na<sub>0.04</sub>Te to  $\sim 1.3$  for Pb<sub>0.94</sub>Na<sub>0.04</sub>Mg<sub>0.02</sub>Te at 710 K (Fig. 2.9.2B) [27].

Further reduction in  $\kappa_{\text{lat}}$  can be achieved in sintered compacts of nanostructured PbTe. The grain boundaries scatter phonons having long mean free paths. In Pb<sub>0.94</sub>Na<sub>0.04</sub>Mg<sub>0.02</sub>Te, the  $\kappa_{\text{lat}}$  of  $\sim 0.74 \text{ W m}^{-1} \text{ K}^{-1}$  for the ingot [27] decreases to  $\sim 0.57 \text{ W m}^{-1} \text{ K}^{-1}$  for the sintered compact at  $\sim 770 \text{ K}$  [33]. Similarly, the  $\kappa_{\text{lat}}$  of the sintered compact of PbTe–4% SrTe–2% Na is significantly low ( $\sim 0.5 \text{ W m}^{-1} \text{ K}^{-1}$  at 915 K) [28]. Because of all-scale hierarchical structures, peak  $ZT$  values of 1.8 at 780 K and  $\sim 2.2$  at 915 K were achieved for the sintered compacts of Pb<sub>0.94</sub>Na<sub>0.04</sub>Mg<sub>0.02</sub>Te and PbTe–4% SrTe–2% Na, respectively [28, 33] (Fig. 2.9.2B).

The decoupling of the charge carrier and the phonon transport processes is crucial for achieving high  $ZT$  values. In addition to phonon scattering, the introduction of nanostructures into the host materials can reduce the mobility of the charge carrier. This effect can be mitigated by the application of the concept of band alignment with a small offset for majority carriers between the matrix phase and the nanostructured

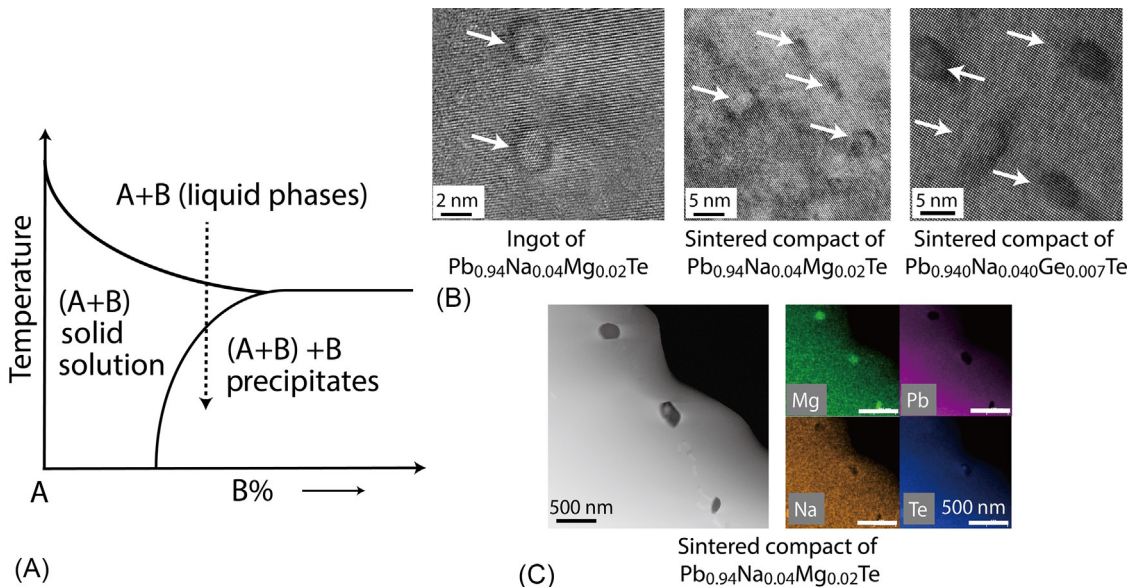


**Fig. 2.9.1** (A) Schematic representation of a general approach for the formation of nanoprecipitates (B phase) in the bulk (A phase) [16]. (B) High-magnification transmission electron microscopy (TEM) image of nanostructures formed in the ingot and sintered compact of p-type  $\text{Pb}_{0.94}\text{Na}_{0.04}\text{Mg}_{0.02}\text{Te}$  [27, 33] and the sintered compact of p-type  $\text{Pb}_{0.953}\text{Na}_{0.040}\text{Ge}_{0.007}\text{Te}$  [38]. (C) Energy-dispersive X-ray spectroscopy (EDS) of the submicron precipitates ( $\sim 150$  nm) for the sintered compact of  $\text{Pb}_{0.94}\text{Na}_{0.04}\text{Mg}_{0.02}\text{Te}$  [33].

(B) Reproduced with permission from M. Ohta, K. Biswas, S.-H. Lo, J.Q. He, D.Y. Chung, V.P. Dravid, M.G. Kanatzidis, Enhancement of thermoelectric figure of merit by the insertion of MgTe nanostructures in p-type PbTe doped with  $\text{Na}_2\text{Te}$ , *Adv. Energy Mater.* 2 (2012) 1117–1123. <https://doi.org/10.1002/aenm.201100756> (web archive link); P. Jood, M. Ohta, A. Yamamoto, M.G. Kanatzidis, Excessively doped PbTe with Ge-induced nanostructures enables high-efficiency thermoelectric modules, *Joule* 2 (2018) 1339–1355. <https://doi.org/10.1016/j.joule.2018.04.025> (web archive link) with permission of John Wiley and Sons and Elsevier, respectively; (B) and (C) reproduced with permission from X.K. Hu, P. Jood, M. Ohta, M. Kunii, K. Nagase, H. Nishiate, M.G. Kanatzidis, A. Yamamoto, Power generation from nanostructured PbTe-based thermoelectrics: comprehensive development from materials to modules, *Energy Environ. Sci.* 9 (2016) 517–529. <https://doi.org/10.1039/c5ee02979a> (web archive link) with permission of The Royal Society of Chemistry.

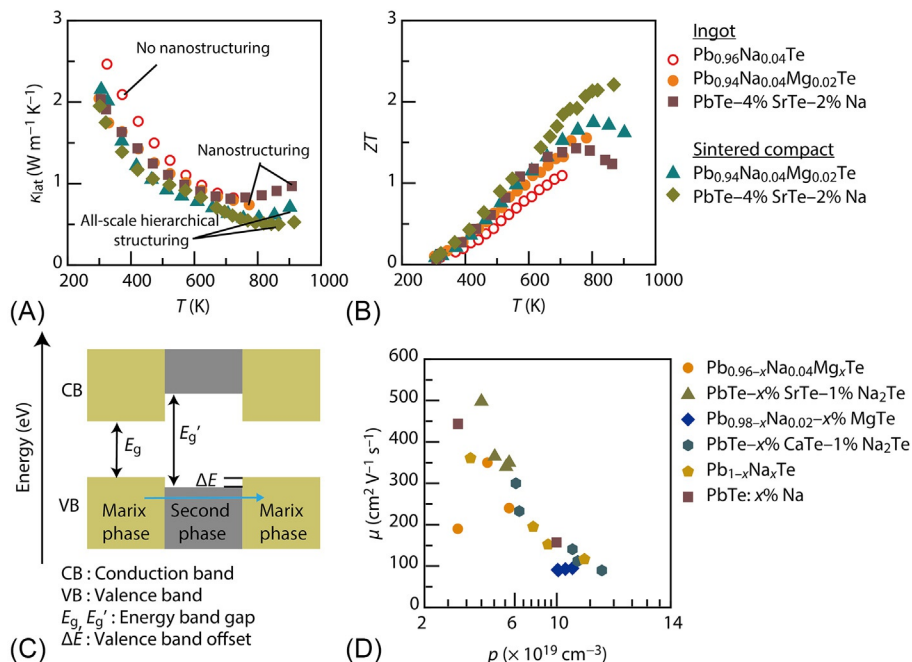


**Fig. 2.9.2** Temperature dependence of (A) lattice thermal conductivity  $\kappa_{\text{lat}}$  and (B) thermoelectric figure of merit  $ZT$  for the ingots of p-type  $\text{Pb}_{0.96-x}\text{Na}_{0.04}\text{Mg}_x\text{Te}$  ( $x=0, 0.02$ ) [27], the sintered compact of p-type  $\text{Pb}_{0.94}\text{Na}_{0.04}\text{Mg}_{0.02}\text{Te}$  [33], and the ingot and sintered compact of p-type  $\text{PbTe}-4\% \text{SrTe}-2\% \text{Na}$  [28]. (C) Schematic representation of band alignment with slight band offset ( $\Delta E$ ) between the matrix phase and nanostructured second phase. The arrow indicates the smooth transmission of the charge carrier through the nanostructured phase. (D) Charge carrier mobility ( $\mu$ ) versus carrier concentration ( $p$ ) for p-type ingots of  $\text{Pb}_{0.96-x}\text{Na}_{0.04}\text{Mg}_x\text{Te}$  ( $x=0, 0.01, 0.02, 0.03$ ) [27],  $\text{PbTe}-x\% \text{SrTe}-1\% \text{Na}_2\text{Te}$  ( $x=0, 0.5, 1.0, 2.0$ ) [26],  $\text{PbTe}-x\% \text{CaTe}-1\% \text{Na}_2\text{Te}$  ( $x=1.0, 2.0, 3.0, 5.0, 6.0$ ) [25],  $\text{PbTe}:x\% \text{Na}$  ( $0.1 \leq x \leq 2.5$ ) [21, 25], and sintered compacts of  $\text{Pb}_{0.98}\text{Na}_{0.02}-x\% \text{MgTe}$  ( $x=0, 1.0, 2.0, 4.0$ ) [31] and  $\text{Pb}_{1-x}\text{Na}_x\text{Te}$  ( $0.005 < x < 0.02$ ) [22].

second phase, as shown in Fig. 2.9.2C [16, 26]. Band alignment can promote high mobility of the charge carrier simultaneously with strong phonon scattering. Moreover, while one set of bands for majority carriers may be aligned (e.g., valence bands), the other set of bands for minority carriers (e.g., conduction bands) may be misaligned, causing minority carrier blocking [61, 62]. Fig. 2.9.2D shows charge carrier mobility as a function of carrier concentration for the p-type ingots of  $\text{Pb}_{0.96-x}\text{Na}_{0.04}\text{Mg}_x\text{Te}$  ( $x=0, 0.01, 0.02, 0.03$ ) [27],  $\text{PbTe}-x\% \text{SrTe}-1\% \text{Na}_2\text{Te}$  ( $x=0, 0.5, 1.0, 2.0$ ) [26],  $\text{PbTe}-x\% \text{CaTe}-1\% \text{Na}_2\text{Te}$  ( $x=1.0, 2.0, 3.0, 5.0, 6.0$ ) [25],  $\text{PbTe}:x\% \text{Na}$  ( $0.1 \leq x \leq 2.5$ ) [21, 25], and sintered compacts of  $\text{Pb}_{0.98}\text{Na}_{0.02}-x\% \text{MgTe}$  ( $x=0, 1.0, 2.0, 4.0$ ) [31] and  $\text{Pb}_{1-x}\text{Na}_x\text{Te}$  ( $0.005 < x < 0.02$ ) [22]. The mobility of the charge carrier decreases as the carrier concentration for the nanostructured PbTe increases, which follows a trend similar to that of the nonnanostructured PbTe. This indicates

that carrier mobility is unaffected by the introduction of nanostructures. A higher content of MT<sub>x</sub> (M = Mg, Sr) in PbTe systems affects *S* and bipolar thermal conductivity properties, which is discussed in the following subsection.

### 2.9.3 Band convergence

As a thermoelectric material, PbTe has a highly attractive band structure because it possesses two valence bands lying closely in energy. The highest energy band is known as the light mass band, and it demonstrates band extrema at the *L* point of the Brillouin zone (*L* band). The closer but lower-energy second band has a heavy effective mass, and it is called the  $\Sigma$  band. The latter lies at approximately 0.17 eV at 0 K below the *L* band (Fig. 2.9.3A) [63]. Because of the small offset between the two valence bands, their involvement in electrical transport can be improved by adjusting the material's alloying and doping properties for maximum thermoelectric performance, as will be demonstrated here. The contribution of each band to electrical transport is determined by temperature (Fig. 2.9.3A) and carrier concentration (Fig. 2.9.3B). The *L* band dominates electrical transport at low temperatures of <350–400 K. As the temperature increases, the *L* band reduces its energy and its gap with the  $\Sigma$  band edge allowing the  $\Sigma$  band to contribute more to charge transport [2, 63, 64]. The narrowing of this gap is often referred to as band convergence. The convergence of both bands leads to a high effective mass of carriers (defined as  $m^* = N_v^{2/3} m_b^*$ , where  $m_b^*$  is the single valley effective mass) from the resulting high valley degeneracy number ( $N_v$ ), which is 4 for the *L* band and increases to 12 for the  $\Sigma$  band [63, 65]. Because carrier mobility  $\mu$  is proportional to  $1/m_b^*$ , it is mostly

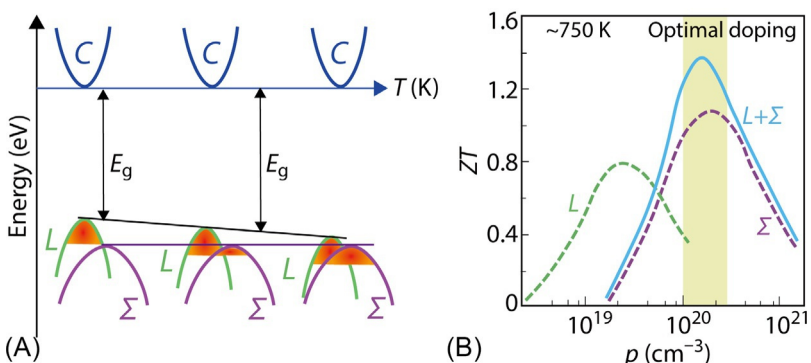


**Fig. 2.9.3** (A) Schematic representation showing the movement of energy bands with temperature in PbTe. The colored areas in each band indicate the population of holes [2]. *C*, *L*, and  $\Sigma$  represent the conduction band, light-mass valence band, and heavy-mass valence band, respectively. (B) Theoretical *ZT* as a function of p-type carrier (hole) concentration (*p*) for PbTe is shown here for transport contribution from *L* and  $\Sigma$  bands individually as well for the combined contribution (*L* +  $\Sigma$ ) from both bands. It is suggested that the interaction between both bonds facilitates high *ZT* [2, 14].

unaffected by the increase in  $N_v$ . Even if intervalley scattering slightly decreases  $\mu$ , a considerable enhancement in  $m^*$  results in an overall increase in  $S^2/\rho$  [66].

The contribution of both valence bands at high temperatures can be further modified by varying the carrier concentration, as shown in Fig. 2.9.3B [2, 14]. Optimum performance of PbTe can be obtained when both bands contribute to electrical transport with appropriate doping levels. For example, heavily Na-doped PbTe [22] and K/Na co-doped PbTe [21] achieved a peak  $ZT$  of  $\sim 1.4$  at 750K and  $\sim 1.3$  at 700K, respectively (Table 2.9.1) by tuning the interaction of both valence bands. These  $ZT$  values are comparable with that of  $\text{Ti}_{0.02}\text{Pb}_{0.98}\text{Te}$  with its Ti-resonant states ( $ZT \sim 1.5$  at 773K) (Table 2.9.1) [20]. It should be noted that one study [22] based on multiparabolic bands predicted  $ZT$  values as high as 1.7 for heavily doped ( $10^{20} \text{ cm}^{-3}$ ) p-type PbTe at 750K. This value is twice that of n-type PbTe (which does not benefit from a second band contribution) owing to heavy-mass hole contribution from the  $\Sigma$  band in the former, which is responsible for a large  $S$ . Much higher  $S$  values for p-type PbTe ( $\sim 300 \mu\text{V K}^{-1}$ ) [22] were reported compared with that for n-type PbTe ( $\sim -180 \mu\text{V K}^{-1}$ ) [45, 67] at  $\sim 750$ K at the same doping levels of  $\sim 4 \times 10^{19} \text{ cm}^{-3}$ .

As the band energy offsets of the  $L$  and  $\Sigma$  bands are small (comparable with several  $k_B T$ , where  $k_B$  is the Boltzmann constant), band convergence is possible even at room temperature through alloying of PbTe with MgTe [31, 68], SrTe [34, 36], PbSe [24, 36], etc. For example, substituting Pb with Mg or Sr increases the bandgap between the  $L$  valence band and the  $C$  conduction band, which consequently pushes the  $L$  band within a few  $k_B T$  of the  $\Sigma$  band (Fig. 2.9.4A). Owing to the small electronegativity difference between Pb and Te and the presence of a lone pair, Pb takes the form of pure PbTe [17] in the valence band. SrTe with a large electronegativity difference between Sr and Te has a much larger bandgap ( $\sim 3.5$ eV) compared with PbTe ( $\sim 0.3$ eV) and the valence band mostly comprises Te states. Therefore, when Sr substitutes Pb, it reduces the contribution of the  $6s^2$  electrons from the top of the valence band; this causes the light hole  $L$  band to lower its energy and consequently decreases the  $L-\Sigma$  separation and also increases the bandgap [17].

The Pisarenko relation between  $S$  and the carrier (hole) concentration in p-type samples clearly exhibits the  $S$  enhancement at room temperature due to the alloying-induced band convergence in PbTe (Fig. 2.9.4B). The solid black line in Fig. 2.9.4B is a theoretical line representing the decrease in  $S$  with increasing hole concentration until  $\sim 5 \times 10^{19} \text{ cm}^{-3}$ , considering a single parabolic band model [27, 33, 63, 66]. At a high hole concentration (for degenerate doping levels), the  $\Sigma$  band starts populating with carriers, which results in an almost constant relation between  $S$  and  $p$ . This is demonstrated by the dashed Pisarenko line, which considers the two-valence-band model of PbTe [27, 33, 63, 66]. It is evident from Fig. 2.9.4B that PbTe samples alloyed with 4%–8% SrTe [34, 36] and 6% MgTe [31] (the higher content level) have up to twice the  $S$  than the nonalloyed 2% Na-doped PbTe [22], which lies on the theoretical line for the two-valence-band model (dashed line). This indicates the dramatically enhanced  $m^*$  resulting from the contribution from both valence bands, as explained above.

Therefore, band convergence has produced one of the best power factors ( $S^2/\rho$ ) ever achieved in p-type PbTe systems, with values reaching as high as

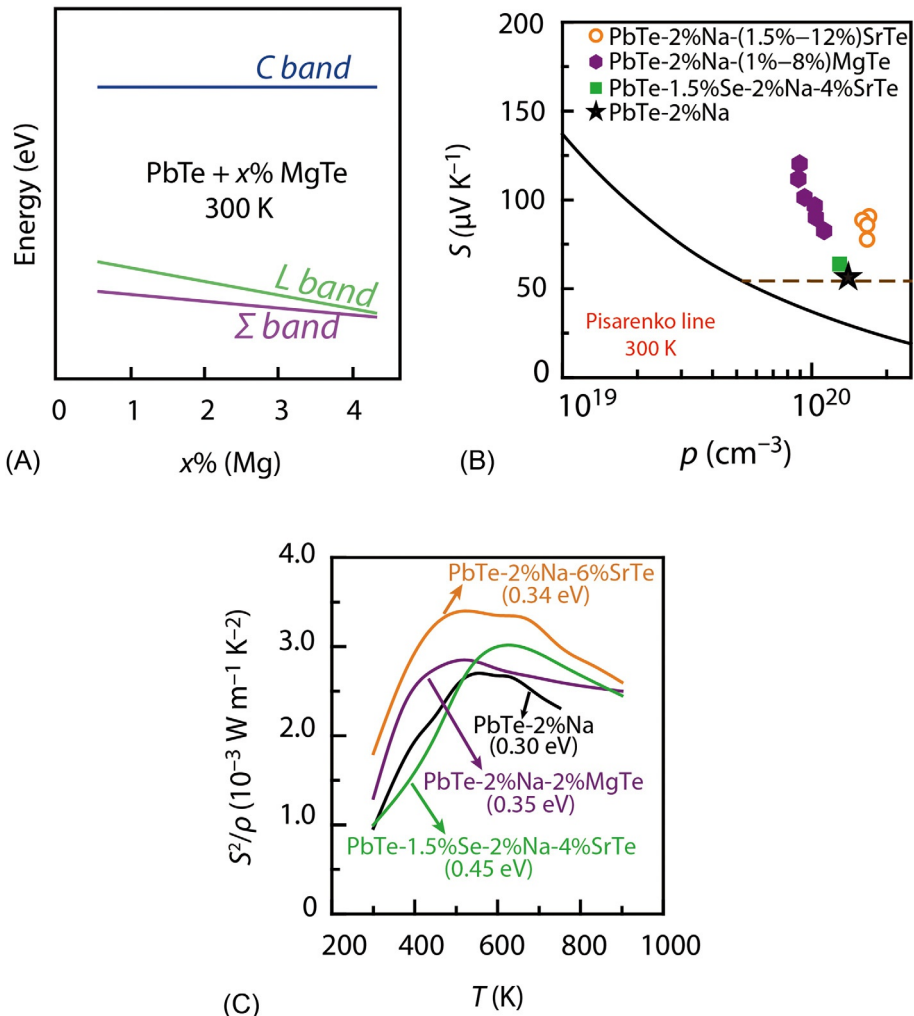


**Fig. 2.9.4** (A) Positioning of the *C* conduction band, the *L* light mass valence band, and the  $\Sigma$  heavy mass valence band as a function of MgTe alloying clearly shows the valence band convergence and enlargement of bandgap [31]. (B) Pisarenko plot (Seebeck coefficient ( $S$ ) versus p-type carrier (hole) concentration ( $p$ ) at 300 K). The *solid line* is the theoretical line that considers a single parabolic band. The *dashed line* stretching out at higher  $p$  shows the two-valence-band structure of PbTe. The enhancement of  $S$  is evident owing to alloying [22, 31, 34, 36] as they all lie above the Pisarenko theoretical line. (C) Power factor ( $S^2/\rho$ ) as a function of temperature for several alloyed compositions [22, 31, 34, 36] of PbTe, along with their bandgaps in parentheses.

$\sim 3.5 \times 10^{-3} \text{ W m}^{-1} \text{ K}^{-2}$  at  $\sim 500 \text{ K}$  ( $\text{Pb}_{0.98}\text{Na}_{0.02}\text{Te}-2\% \text{ SrTe}$ ) [34]. Significant enhancement in  $S^2/\rho$  of PbTe after alloying with MgTe and SrTe is evident from Fig. 2.9.4C, which also reveals the bandgap values for each composition. When the solubility limit of the alloying compounds in PbTe is reached, additional amounts

can precipitate and increase impurities. This results in increased phonon and carrier scattering, i.e., decreased lattice thermal conductivity and also electrical conductivity [31, 34, 36, 69]. The latter can be avoided by using the concept of band alignment, as described earlier.

Band engineering also contributes to suppressing bipolar thermal conductivity ( $\kappa_{bi}$ ) arising from the diffusion of electron-hole pairs. Owing to the narrow bandgap of PbTe, an increase in temperature facilitates minority carrier (electrons in the case of p-type PbTe) jumps across the bandgap [63]. These minority carriers should be blocked because they not only contribute to total thermal conductivity but also counteract the  $S$  from the majority carrier with their opposite  $S$ , eventually reducing the overall  $S$ . The energy required for bipolar diffusion ( $E_g^*$ ) should be higher than the bandgap and can be estimated from  $\kappa_{bi} = A \exp\left(-\frac{E_g^*}{2k_B T}\right)$ , where  $A$  is a constant,  $k_B$  the Boltzmann constant, and  $T$  is the temperature [31]. Proper alloying with a second phase can lead to an enlarged bandgap, which suppresses this bipolar effect. MgTe alloying in PbTe increases the bandgap from  $\sim 0.30$  to  $\sim 0.40$  eV, which leads to an almost 90% reduction in  $\kappa_{bi}$  [31]. The combined effect of band convergence along with all-scale phonon scattering in systems like  $Pb_{0.98}Na_{0.020}Te$ –6% MgTe [31],  $Pb_{0.98}Na_{0.020}Te$ –8% SrTe [34], and  $Pb_{0.98}Te_{0.85}Se_{0.15}$ –2% Na–4% SrTe [36] has produced very high  $ZT$  values of 2.0 at 823 K, 2.5 at 923 K, and 2.3 at 923 K, respectively (Table 2.9.1).

## 2.9.4 Power generation module made of nanostructured lead telluride

The  $\eta_{max}$  of PbTe-based modules was limited to  $\sim 6\%$  until the mid-2000s; therefore, such modules were conventionally used for thermoelectric power generation only in niche markets, such as space missions [1, 70]. Because of dramatic improvements in  $ZT$  values of PbTe-based materials, new opportunities to build more efficient modules now exist. To boost a module's  $\eta_{max}$ , technology transfer between material development and module fabrication has commenced in newly developed high- $ZT$  PbTe, particularly in nanostructured PbTe [8, 52]. However, it is challenging to demonstrate high conversion efficiency rates in a new module. The creation of stable and low-resistance electrical contacts between thermoelectric materials and electrodes and reducing heat losses in various parts of the module are crucial to module fabrication [71–74]. A discussion of current progress in fabricating modules made of nanostructured PbTe [33, 38] follows.

Recently, three prototypical modules (single stage, segment type, and cascade type) from nanostructured PbTe-based materials have been fabricated. Nanostructured  $Pb_{0.94}Mg_{0.02}Na_{0.04}Te$  with a peak  $ZT$  of  $\sim 1.8$  at 810 K or  $Pb_{0.953}Ge_{0.007}Na_{0.040}Te$  with a peak  $ZT$  of  $\sim 1.9$  at 805 K was used in p-type legs, and nonnanostructured  $PbTe_{0.996}I_{0.004}$  with a peak  $ZT$  of  $\sim 1.4$  at 750 K or  $PbTe_{0.9964}I_{0.0036}$  with a peak  $ZT$  of  $\sim 1.3$  K at 780 K was used in n-type legs [33, 38] (Fig. 2.9.5A).

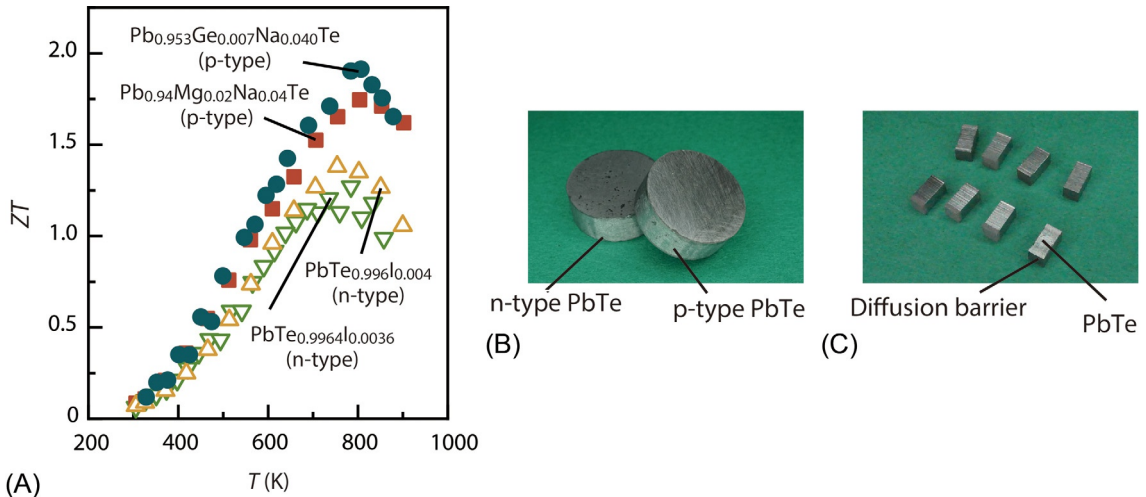


**Fig. 2.9.5** (A) Temperature dependence of the thermoelectric figure of merit ( $ZT$ ) in nanostructured  $Pb_{0.94}Mg_{0.02}Na_{0.04}Te$  (p-type) [33], nonnanostructured  $PbTe_{0.996}I_{0.004}$  (n-type) [33], nanostructured  $Pb_{0.953}Ge_{0.007}Na_{0.040}Te$  (p-type) [38], and nonnanostructured  $PbTe_{0.9964}I_{0.0036}$  (n-type) [38] without diffusion barriers. (B) Wafers and (C) legs of  $Pb_{0.953}Na_{0.040}Ge_{0.007}Te$  (p-type) and  $PbTe_{0.9964}I_{0.0036}$  (n-type) with diffusion barriers [38].

(B) and (C) Reproduced with permission from P. Jood, M. Ohta, A. Yamamoto, M.G. Kanatzidis, Excessively doped PbTe with Ge-induced nanostructures enables high-efficiency thermoelectric modules, Joule 2 (2018) 1339–1355. <https://doi.org/10.1016/j.joule.2018.04.025> (web archive link) with permission of Elsevier.

The PbTe-based module typically operates under a large temperature gradient. The hot side of the PbTe-based module must be exposed to a high operating temperature range of 600–900 K. Therefore, unwanted chemical reactions and/or atomic diffusion at the interfaces between thermoelectric materials and electrodes can occur during operation, resulting in high contact resistance and degradation. To prevent these phenomena, a diffusion barrier is required between the electrodes and thermoelectric materials. For PbTe-based modules, Fe-, Ni-, Nb-, and Ti-based alloys were also investigated as diffusion barriers [70, 75–78]. The diffusion barriers used in newly developed prototypical module for p-type  $\text{Pb}_{0.953}\text{Ge}_{0.007}\text{Na}_{0.040}\text{Te}$  and n-type  $\text{PbTe}_{0.9964}\text{I}_{0.0036}$  were Fe and 80% Co-20% Fe, respectively.

The wafers (sintered compacts) of p- and n-type PbTe (diameter: 15 mm) were sintered with diffusion barriers by pressure-assisted sintering (Fig. 2.9.5B) [33, 38]. The thermoelectric legs (including PbTe-based thermoelectric material and diffusion barrier) were prepared by grinding, polishing, and dicing of the wafers (Fig. 2.9.5C). For the cold side, the p- and n-type legs were alternately positioned on the insulated metal (Cu or Al) substrates with high thermal conductivity, where Cu patterns were printed on the insulated polymer film. On the hot side, the legs were interconnected by Cu electrodes. For example, in the single-stage module, Ag-based paste and Pb-Sn-based solder were used to connect the legs and Cu interconnecting electrodes at the hot and cold sides, respectively. Fig. 2.9.6A shows a photograph of a single-stage module.

To boost the average  $ZT$  value of the entire module, the p- and n-type PbTe-based legs can be stacked on top of the p- and n-type  $\text{Bi}_2\text{Te}_3$ -based legs, respectively (Fig. 2.9.6B) [33]. The  $\text{Bi}_2\text{Te}_3$ - and PbTe-based materials possess high  $ZT$  values across a low and high temperature range of 280–400 K and 600–900 K, respectively. Therefore, the segmented  $\text{Bi}_2\text{Te}_3/\text{PbTe}$  legs achieve high  $ZT$  over a broader temperature range. Moreover, to improve conversion efficiency over a wider temperature range, a cascaded thermoelectric module was fabricated by stacking a PbTe-based module on top of a  $\text{Bi}_2\text{Te}_3$ -based module (Fig. 2.9.6C) [38].

The power generation characteristics of a single-stage nanostructured PbTe module (p-type:  $\text{Pb}_{0.953}\text{Ge}_{0.007}\text{Na}_{0.040}\text{Te}$ ; n-type:  $\text{PbTe}_{0.9964}\text{I}_{0.0036}$ ) [38], segmented  $\text{Bi}_2\text{Te}_3$ /nanostructured PbTe module (p-type:  $\text{Pb}_{0.94}\text{Mg}_{0.02}\text{Na}_{0.04}\text{Te}$ ; n-type:  $\text{PbTe}_{0.996}\text{I}_{0.004}$ ) [33], and cascaded  $\text{Bi}_2\text{Te}_3$ /nanostructured PbTe module (p-type:  $\text{Pb}_{0.953}\text{Ge}_{0.007}\text{Na}_{0.040}\text{Te}$ ; n-type:  $\text{PbTe}_{0.9964}\text{I}_{0.0036}$ ) [38] were investigated under vacuum ( $10^{-2}$ – $10^{-3}$  Pa) in a home-built testing system (Fig. 2.9.6D) [52, 79]. Table 2.9.2 summarizes the measured values of the internal resistance ( $R_{in}$ ), maximum power output ( $P_{max}$ ), open-circuit heat flow ( $Q_{oc}$ ), and maximum conversion efficiency ( $\eta_{max}$ ) for the hot-side temperature ( $T_h$ ) of 873 K and cold-side temperature ( $T_c$ ) of 283 K.  $P_{max}$  (~2.23 W) and  $\eta_{max}$  (~8.5%) were obtained in the single-stage module. Segment-type and cascade-type modules enhance  $P_{max}$  and  $\eta_{max}$  because low-temperature performance is improved by the use of a  $\text{Bi}_2\text{Te}_3$  leg/module. A  $\eta_{max}$  value of ~12% was demonstrated in the cascade-type modules [38].

Good durability in  $\eta_{max}$  was demonstrated over a 24-h stability test under a hot-side temperature of 773 K or below [38] (Fig. 2.9.6E). Under the largest temperature gradient (590 K) and highest temperature of the hot side (873 K), a slight decrease in  $\eta_{max}$

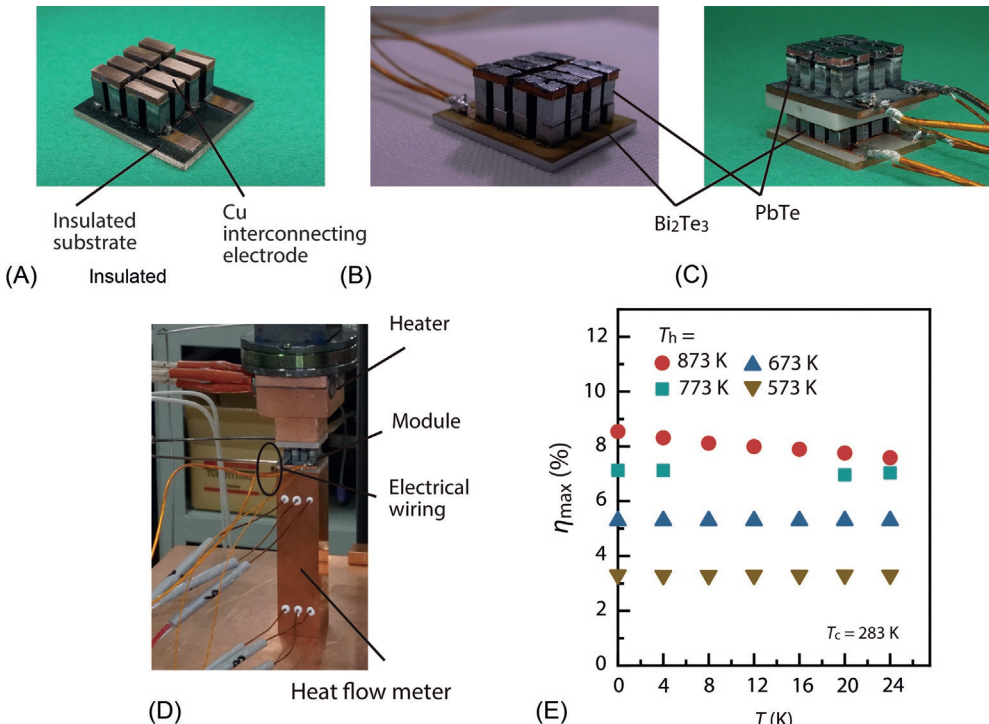


**Fig. 2.9.6** (A) Single-stage nanostructured PbTe module (p-type:  $\text{Pb}_{0.953}\text{Ge}_{0.007}\text{Na}_{0.040}\text{Te}$ , n-type:  $\text{PbTe}_{0.9964}\text{I}_{0.0036}$ ) [38], (B) segmented  $\text{Bi}_2\text{Te}_3$ /nanostructured PbTe module (p-type:  $\text{Pb}_{0.94}\text{Mg}_{0.02}\text{Na}_{0.04}\text{Te}$ , n-type:  $\text{PbTe}_{0.996}\text{I}_{0.004}$ ) [33], and (C) cascaded  $\text{Bi}_2\text{Te}_3$ /nanostructured PbTe module (p-type:  $\text{Pb}_{0.953}\text{Ge}_{0.007}\text{Na}_{0.040}\text{Te}$ , n-type:  $\text{PbTe}_{0.9964}\text{I}_{0.0036}$ ) [38]. (A–C) Dimension of insulated metal substrate:  $18\text{ mm} \times 15\text{ mm} \times 1\text{ mm}$ . (D) Home-built testing system for a thermoelectric power generation module [38]. (E) A 24-h stability test of maximum conversion efficiency ( $\eta_{\max}$ ) as a function of time (hours) with  $T_h = 873, 773, 673$ , and  $573\text{ K}$  and  $T_c = 283\text{ K}$  in a single-stage module [38].

(A), (C), and (D) Reproduced with permission from P. Jood, M. Ohta, A. Yamamoto, M.G. Kanatzidis, Excessively doped PbTe with Ge-induced nanostructures enables high-efficiency thermoelectric modules, Joule 2 (2018) 1339–1355. <https://doi.org/10.1016/j.joule.2018.04.025> (web archive link) with permission of Elsevier; (B) adapted from X. Hu, P. Jood, M. Ohta, M. Kunii, K. Nagase, H. Nishiate, M.G. Kanatzidis, A. Yamamoto, Power generation from nanostructured PbTe-based thermoelectrics: comprehensive development from materials to modules, Energy Environ. Sci. 9 (2016) 517–529. <https://doi.org/10.1039/c5ee02979a> (web archive link) with permission of The Royal Society of Chemistry.

**Table 2.9.2** Measured and simulated internal resistance ( $R_{in}$ ), maximum power output ( $P_{max}$ ), open-circuit heat flow ( $Q_{oc}$ ), and maximum conversion efficiency ( $\eta_{max}$ ) in a single-stage nanostructured PbTe module (p-type:  $Pb_{0.953}Ge_{0.007}Na_{0.040}Te$ ; n-type:  $PbTe_{0.996}I_{0.0036}$ ) [38], segmented  $Bi_2Te_3$ /nanostructured PbTe module (p-type:  $Pb_{0.94}Mg_{0.02}Na_{0.04}Te$ ; n-type:  $PbTe_{0.996}I_{0.004}$ ) [33], and cascaded  $Bi_2Te_3$ /nanostructured PbTe module (p-type:  $Pb_{0.953}Ge_{0.007}Na_{0.040}Te$ ; n-type:  $PbTe_{0.996}I_{0.0036}$ ) [38] for a hot-side temperature ( $T_h$ ) of 773–873 K and cold-side temperature ( $T_c$ ) of 283 K.

Module configuration	$T_h$ (K)	$T_c$ (K)		$R_{in}$ ( $\Omega$ )	$P_{max}$ (W)	$Q_{oc}$ (W)	$\eta_{max}$ (%)
Single stage	773	283	Measured	0.237	1.57	21.0	6.9
			Simulated	0.192	1.84	18.1	9.2
	873	283	Measured	0.288	2.23	24.0	8.5
			Simulated	0.242	2.58	20.6	11.1
Segment type	773	283	Measured	0.327	1.82	13.4	10
			Simulated	0.311	1.90	9.1	13.9
	873	283	Measured	0.371	2.34	15.8	11
			Simulated	0.35	2.55	10.8	15.6
Cascade type	773	283	Measured	—	1.27	11.2	10
	873	283	Measured	—	1.77	13.2	12

due to a small increase in  $R_{in}$  was observed after testing. The small increase in  $R_{in}$  may be due to the deterioration of interfaces between the legs and electrodes and/or the volatilization of Te on the hot side.

The power generation characteristics of single-stage and segment-type modules were calculated by three-dimensional finite-element simulations using the measured  $S$ ,  $\rho$ , and  $\kappa_{total}$  values of the materials [33, 38]. Table 2.9.2 compares the simulated values of  $R_{in}$ ,  $P_{max}$ ,  $Q_{oc}$ , and  $\eta_{max}$  for  $T_h=873$  K and  $T_c=283$  K with experimentally measured values. The measured values of  $R_{in}$  (0.288  $\Omega$  for single-stage module and 0.371  $\Omega$  for segment-type module) are greater than the simulated values (0.242  $\Omega$  for single-stage module and 0.35  $\Omega$  for segment-type module), leading to a lower measured  $P_{max}$ . The values of the measured  $P_{max}$  are 2.23 W for the single-stage module and 2.34 W for the segment-type module; these values are 10%–15% lower than the simulated values. This is attributed to parasitic electrical resistances, which result in ohmic losses at the material interfaces. Moreover, the measured values of  $Q_{oc}$  (24.0 W for single stage and 15.8 W for segment type) are higher than the simulated values (20.6 W for single stage and 10.8 W for segment type). This difference arises from various parasitic heat losses within a module, including poor thermal contact between the hot source and hot side as well as heat leakage through radiation from the hot to cold sides (in the free spaces between p- and n-type legs) and from the leg surfaces. The ohmic losses and parasitic heat losses reduce the measured  $\eta_{max}$ . The values of measured  $\eta_{max}$  for single-stage and segment-type modules are 20%–30% lower than the simulated values. Future module design should be optimized to reduce ohmic losses and parasitic heat losses to enhance  $P_{max}$  and  $\eta_{max}$ .

An improvement in the mechanical properties of the legs is crucial for the fabrication and reliable operation of thermoelectric modules [80]. Several efforts have been made to enhance mechanical strength (fracture toughness and hardness) of PbTe-based materials by doping/alloying [81–85].

## 2.9.5 Conclusions and insights for the future

PbTe-based materials started as conventional thermoelectric materials and with high performance within 600–900 K. The thermoelectric figure of merit ( $ZT$ ) for both p- and n-type PbTe was limited to approximately unity until the mid-2000s, but thanks to advances in the understanding of these materials have led to dramatically enhanced  $ZT$  values of more than 2.5 for p-type samples and more than 1.8 for n-type samples. New strategies such as nanostructuring/hierarchical architecturing, band alignment, and electronic band engineering have been found to be particularly effective in enabling these improvements. These approaches have achieved dramatic reductions in lattice thermal conductivity and enhancements in the power factor. Recently, high conversion efficiency was demonstrated in modules fabricated using some of the newly developed high- $ZT$  PbTe materials. A maximum conversion efficiency of 12% was obtained in cascade-type modules of nanostructured PbTe and  $\text{Bi}_2\text{Te}_3$ . To enable the application of such developments in the field of power generation, more effort should be devoted to improving the mechanical strength and thermal stability of the materials, the thermal stability of the electrical and thermal contacts between materials and electrodes, and the geometrical configuration of the modules.

## Acknowledgment

The authors thank Mr. Atsushi Yamamoto of the AIST for plentiful, stimulating discussions.

## References

- [1] R.D. Abelson, Space missions and applications, in: D.M. Rowe (Ed.), *Thermoelectrics Handbook: Macro to Nano*, CRC Press, Boca Raton, FL, 2006, pp. 56:1–56:29.
- [2] A.D. Lalonde, Y.H. Pei, H. Wang, G.J. Snyder, Lead telluride alloy thermoelectrics, Mater. Today 14 (2011) 526–532, [https://doi.org/10.1016/S1369-7021\(11\)70278-4](https://doi.org/10.1016/S1369-7021(11)70278-4).
- [3] G.J. Snyder, E.S. Toberer, Complex thermoelectric materials, Nat. Mater. 7 (2008) 105–114, <https://doi.org/10.1038/nmat2090>.
- [4] J.P. Heremans, M.S. Dresselhaus, L.E. Bell, D.T. Morelli, When thermoelectrics reached the nanoscale, Nat. Nanotechnol. 8 (2013) 471–473, <https://doi.org/10.1038/nnano.2013.129>.
- [5] T.J. Zhu, Y.T. Liu, C.G. Fu, J.P. Heremans, J.G. Snyder, X.B. Zhao, Compromise and synergy in high-efficiency thermoelectric materials, Adv. Mater. 29 (2017) 1605884:1–1605884:26, <https://doi.org/10.1002/adma.201605884>.
- [6] J. He, T.M. Tritt, Advances in thermoelectric materials research: looking back and moving forward, Science 357 (2017) eaak9997:1–eaak9997:9, <https://doi.org/10.1126/science.aak9997>.

- [7] L. Yang, Z.-G. Chen, M.S. Dargusch, J. Zou, High performance thermoelectric materials: progress and their applications, *Adv. Energy Mater.* 8 (2018) 1701797:1–1701797:28, <https://doi.org/10.1002/aenm.201701797>.
- [8] G.J. Tan, M. Ohta, M.G. Kanatzidis, Thermoelectric power generation: from new materials to devices, *Philos. Trans. R. Soc. A Math. Phys. Eng. Sci.* 377 (2019) 20180450:1–20180450:28, <https://doi.org/10.1098/rsta.2018.0450>.
- [9] H.J. Wu, L.-D. Zhao, F.S. Zheng, D. Wu, Y.L. Pei, X. Tong, M.G. Kanatzidis, J.Q. He, Broad temperature plateau for thermoelectric figure of merit  $ZT > 2$  in phase-separated  $\text{PbTe}_{0.7}\text{S}_{0.3}$ , *Nat. Commun.* 5 (2014) 4515:1–4515:9, <https://doi.org/10.1038/ncomms5515>.
- [10] J.R. Sootsman, D.Y. Chung, M.G. Kanatzidis, New and old concepts in thermoelectric materials, *Angew. Chem. Int. Ed.* 48 (2009) 8616–8639, <https://doi.org/10.1002/anie.200900598>.
- [11] M.G. Kanatzidis, Nanostructured thermoelectrics: the new paradigm? *Chem. Mater.* 22 (2010) 648–659, <https://doi.org/10.1021/cm902195j>.
- [12] C.J. Vineis, A. Shakouri, A. Majumdar, M.G. Kanatzidis, Nanostructured thermoelectrics: big efficiency gains from small features, *Adv. Mater.* 22 (2010) 3970–3980, <https://doi.org/10.1002/adma.201000839>.
- [13] Y.C. Lan, A.J. Minnich, G. Chen, Z.F. Ren, Enhancement of thermoelectric figure-of-merit by a bulk nanostructuring approach, *Adv. Funct. Mater.* 20 (2010) 357–376, <https://doi.org/10.1002/adfm.200901512>.
- [14] Y.Z. Pei, H. Wang, G.J. Snyder, Band engineering of thermoelectric materials, *Adv. Mater.* 24 (2012) 6125–6135, <https://doi.org/10.1002/adma.201202919>.
- [15] K. Nielsch, J. Bachmann, J. Kimling, H. Böttner, Thermoelectric nanostructures: from physical model systems towards nanograinined composites, *Adv. Energy Mater.* 1 (2011) 713–731, <https://doi.org/10.1002/aenm.201100207>.
- [16] L.-D. Zhao, V.P. Dravid, M.G. Kanatzidis, The panoscopic approach to high performance thermoelectrics, *Energy Environ. Sci.* 7 (2014) 251–268, <https://doi.org/10.1039/C3EE43099E>.
- [17] W.G. Zeier, A. Zevalkink, Z.M. Gibbs, G. Hautier, M.G. Kanatzidis, G.J. Snyder, Thinking like a chemist: intuition in thermoelectric materials, *Angew. Chem. Int. Ed. Engl.* 55 (2016) 6826–6841, <https://doi.org/10.1002/anie.201508381>.
- [18] J. Androulakis, K.F. Hsu, R. Pcionek, H. Kong, C. Uher, J.J. D’Angelo, A. Downey, T. Hogan, M.G. Kanatzidis, Nanostructuring and high thermoelectric efficiency in p-type  $\text{Ag}(\text{Pb}_{1-y}\text{Sn}_y)_m\text{SbTe}_{2+m}$ , *Adv. Mater.* 18 (2006) 1170–1173, <https://doi.org/10.1002/adma.200502770>.
- [19] P.F.P. Poudeu, J. D’Angelo, A.D. Downey, J.L. Short, T.P. Hogan, M.G. Kanatzidis, High thermoelectric figure of merit and nanostructuring in bulk p-type  $\text{Na}_{1-x}\text{Pb}_m\text{Sb}_y\text{Te}_{m+2}$ , *Angew. Chem. Int. Ed.* 45 (2006) 3835–3839, <https://doi.org/10.1002/anie.200600865>.
- [20] J.P. Heremans, V. Jovovic, E.S. Toberer, A. Saramat, K. Kurosaki, A. Charoenphakdee, S. Yamanaka, G.J. Snyder, Enhancement of thermoelectric efficiency in PbTe by distortion of the electronic density of states, *Science* 321 (2008) 554–557, <https://doi.org/10.1126/science.1159725>.
- [21] J. Androulakis, I. Todorov, D.-Y. Chung, S. Ballikaya, G.Y. Wang, C. Uher, M.G. Kanatzidis, Thermoelectric enhancement in PbTe with K or Na codoping from tuning the interaction of the light- and heavy-hole valence bands, *Phys. Rev. B* 82 (2010) 115209, <https://doi.org/10.1103/PhysRevB.82.115209>.
- [22] Y.Z. Pei, A. LaLonde, S. Iwanaga, G.J. Snyder, High thermoelectric figure of merit in heavy hole dominated PbTe, *Energy Environ. Sci.* 4 (2011) 2085–2089, <https://doi.org/10.1039/c0ee00456a>.

- [23] S.N. Girard, J.Q. He, X.Y. Zhou, D. Shoemaker, C.M. Jaworski, C. Uher, V.P. Dravid, J.P. Heremans, M.G. Kanatzidis, High performance Na-doped PbTe–PbS thermoelectric materials: electronic density of states modification and shape-controlled nanostructures, *J. Am. Chem. Soc.* 133 (2011) 16588–16597, <https://doi.org/10.1021/ja206380h>.
- [24] Y.Z. Pei, X.Y. Shi, A. LaLonde, H. Wang, L.D. Chen, G.J. Snyder, Convergence of electronic bands for high performance bulk thermoelectrics, *Nature* 473 (2011) 66–69, <https://doi.org/10.1038/nature09996>.
- [25] K. Biswas, J.Q. He, G.Y. Wang, S.-H. Lo, C. Uher, V.P. Dravid, M.G. Kanatzidis, High thermoelectric figure of merit in nanostructured p-type PbTe–MTe (M = Ca, Ba), *Energy Environ. Sci.* 4 (2011) 4675–4684, <https://doi.org/10.1039/c1ee02297k>.
- [26] K. Biswas, J.Q. He, Q.C. Zhang, G.Y. Wang, C. Uher, V.P. Dravid, M.G. Kanatzidis, Strained endotaxial nanostructures with high thermoelectric figure of merit, *Nat. Chem.* 3 (2011) 160–166, <https://doi.org/10.1038/nchem.955>.
- [27] M. Ohta, K. Biswas, S.-H. Lo, J.Q. He, D.Y. Chung, V.P. Dravid, M.G. Kanatzidis, Enhancement of thermoelectric figure of merit by the insertion of MgTe nanostructures in p-type PbTe doped with Na<sub>2</sub>Te, *Adv. Energy Mater.* 2 (2012) 1117–1123, <https://doi.org/10.1002/aenm.201100756>.
- [28] K. Biswas, J.Q. He, I.D. Blum, C.-I. Wu, T.P. Hogan, D.N. Seidman, V.P. Dravid, M.G. Kanatzidis, High-performance bulk thermoelectrics with all-scale hierarchical architectures, *Nature* 489 (2012) 414–418, <https://doi.org/10.1038/nature11439>.
- [29] Q. Zhang, F. Cao, W.S. Liu, K. Lukas, B. Yu, S. Chen, C. Opeil, D. Broido, G. Chen, Z.F. Ren, Heavy doping and band engineering by potassium to improve the thermoelectric figure of merit in p-type PbTe, PbSe, and PbTe<sub>1-y</sub>Se<sub>y</sub>, *J. Am. Chem. Soc.* 134 (2012) 10031–10038, <https://doi.org/10.1021/ja301245b>.
- [30] K. Ahn, K. Biswas, J.Q. He, I. Chung, V. Dravid, M.G. Kanatzidis, Enhanced thermoelectric properties of p-type nanostructured PbTe–MTe (M = Cd, Hg) materials, *Energy Environ. Sci.* 6 (2013) 1529–1537, <https://doi.org/10.1039/c3ee40482j>.
- [31] L.D. Zhao, H.J. Wu, S.Q. Hao, C.I. Wu, X.Y. Zhou, K. Biswas, J.Q. He, T.P. Hogan, C. Uher, C. Wolverton, V.P. Dravid, M.G. Kanatzidis, All-scale hierarchical thermoelectrics: MgTe in PbTe facilitates valence band convergence and suppresses bipolar thermal transport for high performance, *Energy Environ. Sci.* 6 (2013) 3346–3355, <https://doi.org/10.1039/c3ee42187b>.
- [32] R.J. Korkosz, T.C. Chasapis, S.H. Lo, J.W. Doak, Y.J. Kim, C.-I. Wu, E. Hatzikraniotis, T. P. Hogan, D.N. Seidman, C. Wolverton, V.P. Dravid, M.G. Kanatzidis, High ZT in p-type (PbTe)<sub>1-2x</sub>(PbSe)<sub>x</sub>(PbS)<sub>x</sub> thermoelectric materials, *J. Am. Chem. Soc.* 136 (2014) 3225–3237, <https://doi.org/10.1021/ja4121583>.
- [33] X.K. Hu, P. Jood, M. Ohta, M. Kunii, K. Nagase, H. Nishiate, M.G. Kanatzidis, A. Yamamoto, Power generation from nanostructured PbTe-based thermoelectrics: comprehensive development from materials to modules, *Energy Environ. Sci.* 9 (2016) 517–529, <https://doi.org/10.1039/c5ee02979a>.
- [34] G.J. Tan, F.Y. Shi, S.Q. Hao, L.-D. Zhao, H. Chi, X.M. Zhang, C. Uher, C. Wolverton, V. P. Dravid, M.G. Kanatzidis, Non-equilibrium processing leads to record high thermoelectric figure of merit in PbTe–SrTe, *Nat. Commun.* 7 (2016) 12167:1–12167:9, <https://doi.org/10.1038/ncomms12167>.
- [35] Z.W. Chen, Z.Z. Jian, W. Li, Y.J. Chang, B.H. Ge, R. Hanus, J. Yang, Y. Chen, M.X. Huang, G.J. Snyder, Y.Z. Pei, Lattice dislocations enhancing thermoelectric PbTe in addition to band convergence, *Adv. Mater.* 29 (2017) 1606768:1–1606768:8, <https://doi.org/10.1002/adma.201606768>.

- [36] Y.L. Pei, G.J. Tan, D. Feng, L. Zheng, Q. Tan, X.B. Xie, S.K. Gong, Y. Chen, J.-F. Li, J.Q. He, M.G. Kanatzidis, L.-D. Zhao, Integrating band structure engineering with all-scale hierarchical structuring for high thermoelectric performance in PbTe system, *Adv. Energy Mater.* 7 (2017) 1601450:1–1601450:11, <https://doi.org/10.1002/aenm.201601450>.
- [37] S. Sarkar, X.M. Zhang, S.Q. Hao, X. Hua, T.P. Bailey, C. Uher, C. Wolverton, V.P. Dravid, M.G. Kanatzidis, Dual alloying strategy to achieve a high thermoelectric figure of merit and lattice hardening in p-type nanostructured PbTe, *ACS Energy Lett.* 3 (2018) 2593–2601, <https://doi.org/10.1021/acsenergylett.8b01684>.
- [38] P. Jood, M. Ohta, A. Yamamoto, M.G. Kanatzidis, Excessively doped PbTe with Ge-induced nanostructures enables high-efficiency thermoelectric modules, *Joule* 2 (2018) 1339–1355, <https://doi.org/10.1016/j.joule.2018.04.025>.
- [39] K.F. Hsu, S. Loo, F. Guo, W. Chen, J.S. Dyck, C. Uher, T. Hogan, E.K. Polychroniadis, M. G. Kanatzidis, Cubic  $\text{AgPb}_m\text{SbTe}_{2+m}$ : bulk thermoelectric materials with high figure of merit, *Science* 303 (2004) 818–821, <https://doi.org/10.1126/science.1092963>.
- [40] J. Androulakis, C.-H. Lin, H.-J. Kong, C. Uher, C.-I. Wu, T. Hogan, B.A. Cook, T. Caillat, K.M. Paraskevopoulos, M.G. Kanatzidis, Spinodal decomposition and nucleation and growth as a means to bulk nanostructured thermoelectrics: enhanced performance in  $\text{Pb}_{1-x}\text{Sn}_x\text{Te}-\text{PbS}$ , *J. Am. Chem. Soc.* 129 (2007) 9780–9788, <https://doi.org/10.1021/ja071875h>.
- [41] J.R. Sootsman, H. Kong, C. Uher, J.J. D'Angelo, C.-I. Wu, T.P. Hogan, T. Caillat, M.G. Kanatzidis, Large enhancements in the thermoelectric power factor of bulk PbTe at high temperature by synergistic nanostructuring, *Angew. Chem. Int. Ed.* 47 (2008) 8618–8622, <https://doi.org/10.1002/anie.200803934>.
- [42] K. Ahn, C.P. Li, C. Uher, M.G. Kanatzidis, Improvement in the thermoelectric figure of merit by La/Ag cosubstitution in PbTe, *Chem. Mater.* 21 (2009) 1361–1367, <https://doi.org/10.1021/cm803437x>.
- [43] K. Ahn, M.-K. Han, J.Q. He, J. Androulakis, S. Ballikaya, C. Uher, V.P. Dravid, M.G. Kanatzidis, Exploring resonance levels and nanostructuring in the PbTe-CdTe system and enhancement of the thermoelectric figure of merit, *J. Am. Chem. Soc.* 132 (2010) 5227–5235, <https://doi.org/10.1021/ja910762q>.
- [44] Y.Z. Pei, J. Lensch-Falk, E.S. Toberer, D.L. Medlin, G.J. Snyder, High thermoelectric performance in PbTe due to large nanoscale  $\text{Ag}_2\text{Te}$  precipitates and La doping, *Adv. Funct. Mater.* 21 (2011) 241–249, <https://doi.org/10.1002/adfm.201000878>.
- [45] P. Jood, M. Ohta, M. Kunii, X.K. Hu, H. Nishiate, A. Yamamoto, M.G. Kanatzidis, Enhanced average thermoelectric figure of merit of n-type  $\text{PbTe}_{1-x}\text{I}_x-\text{MgTe}$ , *J. Mater. Chem. C* 3 (2015) 10401–10408, <https://doi.org/10.1039/C5TC01652E>.
- [46] G.J. Tan, C.C. Stoumpos, S. Wang, T.P. Bailey, L.-D. Zhao, C. Uher, M.G. Kanatzidis, Subtle roles of Sb and S in regulating the thermoelectric properties of N-type PbTe to high performance, *Adv. Energy Mater.* 7 (2017) 1700099:1–1700099:9, <https://doi.org/10.1002/aenm.201700099>.
- [47] Y. Xiao, H.J. Wu, W. Li, M.J. Yin, Y.L. Pei, Y. Zhang, L.W. Fu, Y.X. Chen, S.J. Pennycook, L. Huang, J.Q. He, L.-D. Zhao, Remarkable roles of Cu To synergistically optimize phonon and carrier transport in n-type PbTe-Cu<sub>2</sub>Te, *J. Am. Chem. Soc.* 139 (2017) 18732–18738, <https://doi.org/10.1021/jacs.7b11662>.
- [48] J. Zhang, D. Wu, D.S. He, D. Feng, M.J. Yin, X.Y. Qin, J.Q. He, Extraordinary thermoelectric performance realized in n-type PbTe through multiphase nanostructure engineering, *Adv. Mater.* 29 (2017) 1703148:1–1703148:7, <https://doi.org/10.1002/adma.201703148>.
- [49] Z.-Z. Luo, X.M. Zhang, X. Hua, G.J. Tan, T.P. Bailey, J.W. Xu, C. Uher, C. Wolverton, V. P. Dravid, Q.Y. Yan, M.G. Kanatzidis, High thermoelectric performance in supersaturated

- solid solutions and nanostructured n-type PbTe-GeTe, *Adv. Funct. Mater.* 28 (2018) 1801617:1–1801617:10, <https://doi.org/10.1002/adfm.201801617>.
- [50] X.L. Su, S.Q. Hao, T.P. Bailey, S. Wang, I. Hadar, G.J. Tan, T.-B. Song, Q.J. Zhang, C. Uher, C. Wolverton, X.F. Tang, M.G. Kanatzidis, Weak Electron phonon coupling and deep level impurity for high thermoelectric performance  $\text{Pb}_{1-x}\text{Ga}_x\text{Te}$ , *Adv. Energy Mater.* 8 (2018) 1800659:1–1800659:11, <https://doi.org/10.1002/aenm.201800659>.
- [51] Y. Xiao, H.J. Wu, J. Cui, D.Y. Wang, L.W. Fu, Y. Zhang, Y. Chen, J.Q. He, S.J. Pennycook, L.-D. Zhao, Realizing high performance n-type PbTe by synergistically optimizing effective mass and carrier mobility and suppressing bipolar thermal conductivity, *Energy Environ. Sci.* 11 (2018) 2486–2495, <https://doi.org/10.1039/C8EE01151F>.
- [52] M. Ohta, P. Jood, M. Murata, C.H. Lee, A. Yamamoto, H. Obara, An integrated approach to thermoelectrics: combining phonon dynamics, nanoengineering, novel materials development, module fabrication, and metrology, *Adv. Energy Mater.* 9 (2018) 1801304:1–1801304:29, <https://doi.org/10.1002/aenm.201801304>.
- [53] S. Johnsen, J.Q. He, J. Androulakis, V.P. Dravid, I. Todorov, D.Y. Chung, M.G. Kanatzidis, Nanostructures boost the thermoelectric performance of PbS, *J. Am. Chem. Soc.* 133 (2011) 3460–3470, <https://doi.org/10.1021/ja109138p>.
- [54] L.-D. Zhao, S.-H. Lo, J.Q. He, H. Li, K. Biswas, J. Androulakis, C.-I. Wu, T.P. Hogan, D.-Y. Chung, V.P. Dravid, M.G. Kanatzidis, High performance thermoelectrics from earth-abundant materials: enhanced figure of merit in PbS by second phase nanostructures, *J. Am. Chem. Soc.* 133 (2011) 20476–20487, <https://doi.org/10.1021/ja208658w>.
- [55] M. Samanta, K. Biswas, Low thermal conductivity and high thermoelectric performance in  $(\text{GeTe})_{1-2x}(\text{GeSe})_x(\text{GeS})_x$ : competition between solid solution and phase separation, *J. Am. Chem. Soc.* 139 (2017) 9382–9391, <https://doi.org/10.1021/jacs.7b05143>.
- [56] M. Hong, J. Zou, Z.G. Chen, Thermoelectric GeTe with diverse degrees of freedom having secured superhigh performance, *Adv. Mater.* 31 (2019) 1807071:1–1807071:23, <https://doi.org/10.1002/adma.201807071>.
- [57] G.J. Tan, L.-D. Zhao, F.Y. Shi, J.W. Doak, S.-H. Lo, H. Sun, C. Wolverton, V.P. Dravid, C. Uher, M.G. Kanatzidis, High thermoelectric performance of p-type SnTe via a synergistic band engineering and nanostructuring approach, *J. Am. Chem. Soc.* 136 (2014) 7006–7017, <https://doi.org/10.1021/ja500860m>.
- [58] G. Rogl, A. Grytsiv, P. Rogl, E. Bauer, M. Hochenhofer, R. Anbalagan, R.C. Mallik, E. Schafler, Nanostructuring of p- and n-type skutterudites reaching figures of merit of approximately 1.3 and 1.6, respectively, *Acta Mater.* 76 (2014) 434–448, <https://doi.org/10.1016/j.actamat.2014.05.051>.
- [59] W.J. Xie, A. Weidenkaff, X.F. Tang, Q.J. Zhang, J. Poon, T.M. Tritt, Recent advances in nanostructured thermoelectric half-heusler compounds, *Nanomaterials*. 2 (2012) 379–412, <https://doi.org/10.3390/nano2040379>.
- [60] L.W. Fu, M.J. Yin, D. Wu, W. Li, D. Feng, L. Huang, J.Q. He, Large enhancement of thermoelectric properties in n-type PbTe via dual-site point defects, *Energy Environ. Sci.* 10 (2017) 2030–2040, <https://doi.org/10.1039/C7EE01871A>.
- [61] J.-H. Bahk, A. Shakouri, Enhancing the thermoelectric figure of merit through the reduction of bipolar thermal conductivity with heterostructure barriers, *Appl. Phys. Lett.* 105 (2014) 52106:1–52106:5, <https://doi.org/10.1063/1.4892653>.
- [62] H.R. Yang, J.-H. Bahk, T. Day, A.M.S. Mohammed, G.J. Snyder, A. Shakouri, Y. Wu, Enhanced thermoelectric properties in bulk nanowire heterostructure-based nanocomposites through minority carrier blocking, *Nano Lett.* 15 (2015) 1349–1355, <https://doi.org/10.1021/nl504624r>.

- [63] U.I. Ravich, B.A. Efimova, I.A. Smirnov, *Semiconducting Lead Chalcogenides*, Plenum Press, New York, 1970.
- [64] J. Zhao, C.D. Malliakas, K. Wijayaratne, V. Karlapati, N. Appathurai, D.Y. Chung, S. Rosenkranz, M.G. Kanatzidis, U. Chatterjee, Spectroscopic evidence for temperature-dependent convergence of light- and heavy-hole valence bands of PbQ (Q = Te, Se, S), *Europhys. Lett.* 117 (2017) 27006:1–27006:6, <https://doi.org/10.1209/0295-5075/117/27006>.
- [65] A.J. Crocker, L.M. Rogers, Valence band structure of PbTe, *Le, J. Phys. Colloq.* 29 (1968) C4-129–C4-132, <https://doi.org/10.1051/jphyscol:1968418>.
- [66] Y. Xiao, L.-D. Zhao, Charge and phonon transport in PbTe-based thermoelectric materials, *Npj Quantum Mater.* 3 (2018) 55:1–55:12, <https://doi.org/10.1038/s41535-018-0127-y>.
- [67] Y.Z. Pei, Z.M. Gibbs, A. Gloskovskii, B. Balke, W.G. Zeier, G.J. Snyder, Optimum carrier concentration in n-type PbTe thermoelectrics, *Adv. Energy Mater.* 4 (2014) 1400486:1–1400486:12, <https://doi.org/10.1002/aenm.201400486>.
- [68] Y.Z. Pei, A.D. LaLonde, N.A. Heinz, X.Y. Shi, S. Iwanaga, H. Wang, L.D. Chen, G.J. Snyder, Stabilizing the optimal carrier concentration for high thermoelectric efficiency, *Adv. Mater.* 23 (2011) 5674–5678, <https://doi.org/10.1002/adma.201103153>.
- [69] Y.Z. Pei, N.A. Heinz, A. LaLonde, G.J. Snyder, Combination of large nanostructures and complex band structure for high performance thermoelectric lead telluride, *Energy Environ. Sci.* 4 (2011) 3640–3645, <https://doi.org/10.1039/c1ee01928g>.
- [70] Y. Hori, T. Ito, Fabrication of 500°C class thermoelectric module and evaluation of its high temperature stability, in: *Proceedings of the 25th International Conference on Thermoelectrics*, 2006, pp. 642–645.
- [71] M. Zebarjadi, K. Esfarjani, M.S. Dresselhaus, Z.F. Ren, G. Chen, Perspectives on thermoelectrics: from fundamentals to device applications, *Energy Environ. Sci.* 5 (2012) 5147–5162, <https://doi.org/10.1039/C1EE02497C>.
- [72] Q.H. Zhang, X.Y. Huang, S.Q. Bai, X. Shi, C. Uher, L.D. Chen, Thermoelectric devices for power generation: recent progress and future challenges, *Adv. Eng. Mater.* 18 (2016) 194–213, <https://doi.org/10.1002/adem.201500333>.
- [73] H.S. Kim, W.S. Liu, Z.F. Ren, The bridge between the materials and devices of thermoelectric power generators, *Energy Environ. Sci.* 10 (2017) 69–85, <https://doi.org/10.1039/C6EE02488B>.
- [74] R. He, G. Schierning, K. Nielsch, Thermoelectric devices: a review of devices, architectures, and contact optimization, *Adv. Mater. Technol.* 3 (2017) 1700256:1–1700256:17, <https://doi.org/10.1002/admt.201700256>.
- [75] A. Singh, S. Bhattacharya, C. Thinaharan, D.K. Aswal, S.K. Gupta, J.V. Yakhmi, K. Bhanumurthy, Development of low resistance electrical contacts for thermoelectric devices based on n-type PbTe and p-type TAGS-85 ((Ag<sub>0.8</sub>Sb<sub>0.15</sub>Te<sub>0.05</sub>)<sub>0.15</sub>(GeTe)<sub>0.85</sub>), *J. Phys. D Appl. Phys.* 42 (2009) 015502:1–015502:6, <https://doi.org/10.1088/0022-3727/42/1/015502>.
- [76] H.Y. Xia, F. Drymiotis, C.-L. Chen, A.P. Wu, G.J. Snyder, Bonding and interfacial reaction between Ni foil and n-type PbTe thermoelectric materials for thermoelectric module applications, *J. Mater. Sci.* 49 (2014) 1716–1723, <https://doi.org/10.1007/s10853-013-7857-9>.
- [77] H.Y. Xia, C.-L. Chen, F. Drymiotis, A.P. Wu, Y.-Y. Chen, G.J. Snyder, Interfacial reaction between Nb foil and n-type PbTe thermoelectric materials during thermoelectric contact fabrication, *J. Electron. Mater.* 43 (2014) 4064–4069, <https://doi.org/10.1007/s11664-014-3350-8>.

- [78] C.-C. Yu, H.J. Wu, M.T. Agne, I.T. Witting, P.-Y. Deng, G.J. Snyder, J.P. Chu, Titanium-based thin film metallic glass as diffusion barrier layer for PbTe-based thermoelectric modules, *APL Mater.* 7 (2019) 013001:1–013001:8, <https://doi.org/10.1063/1.5046826>.
- [79] H. Wang, R. McCarty, J.R. Salvador, A. Yamamoto, J. König, Determination of thermoelectric module efficiency: a survey, *J. Electron. Mater.* 43 (2014) 2274–2286, <https://doi.org/10.1007/s11664-014-3044-2>.
- [80] W.S. Liu, Q. Jie, H.S. Kim, Z.F. Ren, Current progress and future challenges in thermoelectric power generation: from materials to devices, *Acta Mater.* 87 (2015) 357–376, <https://doi.org/10.1016/j.actamat.2014.12.042>.
- [81] Q.Y. Zhang, H.Z. Wang, Q.A. Zhang, W.S. Liu, B. Yu, H. Wang, D.Z. Wang, G. Ni, G. Chen, Z.F. Ren, Effect of silicon and sodium on thermoelectric properties of thallium-doped lead telluride-based materials, *Nano Lett.* 12 (2012) 2324–2330, <https://doi.org/10.1021/nl3002183>.
- [82] Y. Zhang, L.H. Wu, J.Y. Zhang, J.J. Xing, J. Luo, Eutectic microstructures and thermoelectric properties of MnTe-rich precipitates hardened PbTe, *Acta Mater.* 111 (2016) 202–209, <https://doi.org/10.1016/j.actamat.2016.03.059>.
- [83] A. Schmitz, J. de Boor, K. Mull, E. Müller, Tailoring the mechanical properties of thermoelectric lead telluride by alloying with non-doping calcium, *J. Mater. Sci.* 51 (2016) 6933–6943, <https://doi.org/10.1007/s10853-016-9980-x>.
- [84] G.D. Li, U. Aydemir, B. Duan, M.T. Agne, H.T. Wang, M. Wood, Q.J. Zhang, P.C. Zhai, W.A. Goddard, G.J. Snyder, Micro- and macromechanical properties of thermoelectric lead chalcogenides, *ACS Appl. Mater. Interfaces* 9 (2017) 40488–40496, <https://doi.org/10.1021/acsmami.7b15651>.
- [85] L.W. Fu, J. Cui, Y. Yu, Y. Huang, Y.F. Wang, Y. Chen, J.Q. He, Achieving a fine balance between the strong mechanical and high thermoelectric properties of n-type PbTe–3% Sb materials by alloying with PbS, *J. Mater. Chem. A* 7 (2019) 6304–6311, <https://doi.org/10.1039/C9TA00400A>.

# Oxide thermoelectric materials: Compositional, structural, microstructural, and processing challenges to realize their potential

2.10

*Slavko Bernik*

Jožef Stefan Institute, Department for Nanostructured Materials, Ljubljana, Slovenia

## 2.10.1 Introduction

When it comes to oxide thermoelectric materials, it is usually highlighted that in contrast to state-of-the-art thermoelectric alloys they are stable in an oxidizing atmosphere of up to high temperatures and are made of nontoxic, abundant, and hence low-cost materials [1–3]. These characteristics are a strong motivation for the development of oxide thermoelectric materials and oxide-based thermoelectric technologies for mid-temperature and, in particular, high-temperature applications [4]. They are also important for expanding thermoelectric technologies to various areas of application; environmental and economic criteria are nowadays, in general, mandatory and have to be properly considered and satisfied in any technology and human activity [5]. However, without proper thermoelectric characteristics and efficiency, with  $zT$  values currently much lower than the values for the state-of-the-art thermoelectric materials and also the somewhat arbitrary “threshold” value 1, all the advantages of oxide materials are in vain.

For a broader perspective on the topic of oxide thermoelectric materials, it is important to stress that metal oxides already have a key role in numerous advanced technologies for electronics and energetics [6]. We are talking about technologies that already have a tremendous impact on society and the lives of every one of us. In this sense, it is important that they can directly support our striving for sustainability. In general, they enable the intelligent and effective use of natural resources and a minimum impact on the environment, while improving the quality of life. Furthermore, it is also very important that metal oxides have promising potentials for further progress, which could give way to the development of novel, even more effective electronics, devices, and ecological technologies. Such a role of metal oxides derives from a variety of physical properties they possess that enable and support different functionalities as required by applications. However, the potential of metal oxides is fully realized by the possibility for fine-tuning their functionality to the specific needs of the

application via chemical composition, structure, microstructure, and processing. Their applicability is further extended by the fact that they can be synthesized and processed with a wide variety of methods, including classic solid-state synthesis, wet chemical techniques (i.e., coprecipitation, sol-gel, hydrothermal, etc.), electrodeposition, chemical/physical deposition (PLD, laser ablation, RF magnetron sputtering, etc.), and various sintering methods (classic, hot pressing, spark plasma, microwave, etc.) [5]. Accordingly, they can be prepared in 1D, 2D, and 3D forms of different dimensionalities from the nano-to-macrorange for optimal design and integration into a certain device.

Metal oxides are already present in many other technologies for energy generation, storage, conversion, and emission control, including solar cells, fuel cells, nuclear reactors, energy harvesting, batteries, supercapacitors, hydrogen economy, thermochemical cycles, AC power transportation and transformation, and catalytic converters in exhaust systems [6]. All these technologies also represent a strong background for the development of oxide thermoelectric materials and oxide-based thermoelectric devices. At the same time, specific challenges in the research and development of oxide thermoelectric materials dealing with fundamental issues of charge and heat transport are also of great significance to any other applications of metal oxides, which gives them a broader perspective going beyond the topic of thermoelectrics.

Thermoelectric properties of oxide materials are perhaps still a long way behind the state-of-the-art classic thermoelectric alloys [7]. Also, some other families of newer thermoelectric materials such as scutterudites [8], tetrahedrites [9, 10], and chalcogenides [11] show  $zT$  values of above 1 and even above 2. However, the topic of oxides as thermoelectrics is rather new; it has to be stressed that just over 20 years ago they were considered as unsuitable candidates for thermoelectric materials, until the breakthrough report of Terasaki et al. about  $\text{NaCo}_2\text{O}_2$  [12]. This was understandable and justified when considering the many shortcomings of oxides in complying with the well-known criteria for a good thermoelectric material. In general, oxides have a mixed nature of bonding; besides covalent they also have a more or less expressed ionic nature, which leads to largely polarized metal-oxide bonds. Hence, they often have a low charge-carrier concentration, but if perhaps relatively high, their mobility is often low, even two or three orders of magnitude lower in comparison to the entirely covalent materials. Also, the large bonding energies and the small atomic mass of oxygen, and often also cation atoms, result in higher vibration frequencies of the crystal lattice and hence a high lattice thermal conductivity. In addition, many oxides have a small unit cell, composed of a small number of atoms and a small variety of atoms (i.e., elements), and a simple structure without any other structural elements causing phonon scattering. Hence, the problem of high thermal conductivity in oxides is even more severe [13–15]. Consequently, oxides likely have a low electrical conductivity, which also means a lower power factor, despite the relatively high values of the Seebeck coefficient,  $S$ , that they exhibit. And their thermal conductivity,  $\kappa$ , is much too high for a good thermoelectric material, which would typically have a value of  $\kappa < 2 \text{ W/mK}$ . However, Terasaki et al. [12] found that a single crystal of metallic layered  $\text{NaCo}_2\text{O}_4$  has a large Seebeck coefficient and a power factor comparable to a typical

thermoelectric material such as  $\text{Bi}_2\text{Te}_3$ , and recognized  $\text{NaCo}_2\text{O}_4$  as a promising thermoelectric material. The report triggered worldwide research in oxide thermoelectric materials, which is reflected in the increasing number of scientific publications over the past two decades, up to a few hundred every year. Such an intensity of research and development activities has been driven by fundamental questions of controlling the charge and heat transport for an enhanced figure of merit ( $zT$ ) of oxide materials. They were also strongly stimulated by the expected advantages of using chemically and temperature stable, nontoxic, and cheap oxide materials in technologies for harvesting electricity from high-temperature heat sources. As a result the family of oxide thermoelectric materials became wide and contains numerous chemically and structurally very different narrow- or wide-bandgap semiconductors of the n- and p-type [3, 14–18]. The narrow-bandgap thermoelectric oxides are compounds such as  $\text{Na}_x\text{CoO}_2$ ,  $\text{Ca}_3\text{Co}_4\text{O}_9$ ,  $\text{BiCuSeO}$ , and  $\text{CaMnO}_3$ . The group of the wide-bandgap semiconductors mainly includes transition-metal oxides with most known  $\text{ZnO}$ -,  $\text{TiO}_2$ -,  $\text{In}_2\text{O}_3$ -based materials, and  $\text{SrTiO}_3$  [19]. Looking at the timeline for the highest obtained figure of merit,  $zT$ , for oxide thermoelectric materials is very illustrative [20–22]. The p-type materials are ahead of the n-type materials. In the form of single crystals and whiskers, layered cobaltites ( $\text{NaCo}_2\text{O}_4$ ,  $\text{Ca}_3\text{Co}_4\text{O}_9$ , and  $\text{Bi}_2\text{Sr}_2\text{Co}_2\text{O}_y$ ) have values of  $zT$  in the range 1–1.2 at 1000 K, while as a polycrystalline bulk material the value is 0.8. The n-type thermoelectric materials are not available as single crystals, and in the form of polycrystalline bulk their highest  $zT$  value is 0.65 at 1247 K (0.47 at 1000 K) for Al- and Ga-doped  $\text{ZnO}$ . However, a two-dimensional electron gas (2-DEG) formed at the interfaces of an n-type  $\text{SrTiO}_3/\text{SrO}$  superlattice structure in epitaxial thin films showed values of  $zT \approx 2.447$  [23]. Similarly, for the in-plane direction of ribbon-like single crystals of p-type  $\text{Ca}_3\text{Co}_4\text{O}_9$ ,  $zT$  values in the range 1.2–2.7 at 873 K were estimated [24]. Although obtained in 2D-confined systems, such high  $zT$  values are certainly encouraging for possible enhancement of the thermoelectric performance of bulk polycrystalline oxide materials. They also indicate that the key is in decoupling and an independent control of charge carriers and phonons (i.e., charge and heat transport). The complexity of this task is well reflected in the fact that despite extensive research activities, which are reported in more than 1300 articles, the highest  $zT$  values given for the oxide materials in a timeline graph almost a decade ago still hold.

This chapter on oxide thermoelectric materials will be limited to the topic of polycrystalline volume ceramics, which is itself already extensive enough. The challenges of developing polycrystalline volume ceramics with the required thermoelectric properties of applications in waste-heat harvesting most directly and comprehensively cover the complexity of the problem, both in terms of understanding the fundamental physical properties and their control as well as the processing of the material itself. The use of single crystals is limited for well-known reasons (availability, quantity, and price). And the thermoelectric thin films are by themselves a specific case, which certainly needs to be addressed separately; the thermoelectric material is 2D confined, typically in contact with a substrate of a different type of material, so the thermoelectric properties are essentially affected by the dimensional confinement of the thermoelectric material, the interface with the substrate, and the characteristics of the substrate [1, 25–29]. Accordingly, the chapter will present the open problems and

challenges in the development of thermoelectric polycrystalline oxide ceramic materials for higher  $zT$  values, based on the scientific publications in the past decade.

## 2.10.2 The n-type oxide thermoelectric materials

### 2.10.2.1 Transition-metal oxides

The oxides of transition metals are an interesting group of n-type thermoelectric materials with  $\text{ZnO}$ ,  $\text{TiO}_2$ , and  $\text{In}_2\text{O}_3$  as the most widely studied representatives [19]. In general, their thermopower,  $S$ , is relatively high ( $>100\,\mu\text{V/K}$ ); however, for a high power factor they have a too low conductivity due to the low charge-carrier concentration ( $n < 10^{17}\,\text{cm}^3$ ) and despite the high charge-carrier mobility ( $>100\,\text{cm}^2/\text{Vs}$ ), while their effective mass,  $m^*$  is low. Although quite different, their structures are relatively simple with high bonding energies and hence they have a high thermal conductivity. Below, recent research in the field of thermoelectric  $\text{ZnO}$  ceramics will be presented, while in recently published articles more is available with respect to  $\text{TiO}_2$  and some other oxides of transition metal (Nb, Mo, W) [15, 30] and  $\text{In}_2\text{O}_3$  [31].

#### 2.10.2.1.1 Zinc oxide ( $\text{ZnO}$ )

$\text{ZnO}$  is already widely used in various technological applications for overvoltage protection in electronics and optoelectronic devices due to its very interesting semiconducting, piezoelectric, pyroelectric, and optical properties, which can be fine-tuned by doping. It is also important that  $\text{ZnO}$  is earth abundant, low-cost, nontoxic, and stable at high temperatures. With a direct wide bandgap of  $3.4\,\text{eV}$  and a large exciton binding energy of  $60\,\text{meV}$  at room temperature it should be an insulator; however, due to the slightly nonstoichiometric composition  $\text{Zn}_{1+x}\text{O}$  with excess zinc and hence with the presence of intrinsic donors, interstitial zinc ( $\text{Zn}_i$ ) and oxygen vacancies ( $\text{O}_V$ ), it has the character of an n-type semiconductor. Typically, it has a hexagonal wurtzite-type structure where each Zn atom is surrounded by four oxygen atoms. It could also be in a cubic zinc-blende structure, and rarely in a rock-salt structure.  $\text{ZnO}$  can be synthesized in various morphologies (spheres, rods, disks) using wet-chemical (solvothermal, hydrothermal) and vapor-phase methods.  $\text{ZnO}$  likely has the largest family of different nanostructures, like nanorods, nanobelts, nanorings, nanosprings, and hierarchical nanostructures (i.e., nanorod arrays) [32–38].

$\text{ZnO}$  is considered as one of the most promising n-type thermoelectric oxide materials. Since  $\text{ZnO}$  is also known as a transparent conducting oxide, like  $\text{SnO}_2$ ,  $\text{TiO}_2$ , and  $\text{In}_2\text{O}_3$ , it is noteworthy that it also shows the photo-Seebeck effect [39, 40]. Pure  $\text{ZnO}$  has a high Seebeck coefficient,  $S$ , of about  $-400\,\mu\text{V/K}$  due to having a low charge-carrier concentration below  $10^{18}\,\text{cm}^{-3}$ , usually in the range of  $10^{14}\text{--}10^{17}\,\text{cm}^{-3}$ . However, it has a large charge-carrier mobility of about  $200\,\text{cm}^2/\text{Vs}$  due to a light electronic effective mass of  $0.30m_0$  as the nondegenerative conduction bands are mainly made by the Zn 4s band, while the degenerate valence bands are mainly composed of the O 2p band [16, 32, 41]. Pure  $\text{ZnO}$  also has a high thermal conductivity,  $\kappa$ , of about  $40\,\text{W/mK}$  at  $300\,\text{K}$  and about  $10\,\text{W/mK}$  at  $1000\,\text{K}$  [42].

ZnO is very accommodating with respect to doping. Hence, the electrical properties of ZnO could be significantly improved by doping and bandgap engineering. The transition-metal elements of Ti, Cr, Mn, Co, and Ni are standard dopants in ZnO-based varistor ceramics to enhance their current-voltage (*I-U*) nonlinearity by increasing the electrical conductivity of ZnO grains [43–45]. Also, Cr, Mn, Co, and Ni are key dopants in the development of ZnO-based dilute magnetic semiconductors [46–49]. In recent years, some studies on the effect of Co [50, 51] and Ni doping [52, 53] on the thermoelectric properties of ZnO have been reported. Doping with Co up to 10 at.% increased the electrical conductivity,  $\sigma$ , of the  $Zn_{1-x}Co_xO$  samples synthesized with the sol-gel method and sintered in a vacuum by SPS at 900°C from 4 S/cm to about 35 S/cm at 680 K for a maximum power factor, PF, of about  $3 \times 10^{-4}$  W/mK<sup>2</sup>. By Co-doping the thermal conductivity,  $\kappa$ , was reduced from 36 to 11 W/mK at 300 K and from 10 to 3.3 W/mK at 830 K. [50] Wu et al. [51] also reported that incorporating organic nanoparticles into the  $Zn_{1-x}Co_xO$  samples resulted in an increase of  $\sigma$  to 190 S/cm and PF to about  $8 \times 10^{-4}$  W/mK<sup>2</sup>, while  $\kappa$  slightly decreased; hence, the  $zT$  increased from 0.04 to 0.22 at 860 K. By Ni doping the thermoelectric characteristics of the ZnO ceramics were not improved much [52, 53]. This could also be attributed to the fact that they were prepared by classic sintering at 1400°C in air and not with the SPS method, which is generally recognized as an effective processing method to enhance the thermoelectric performance of materials and also oxides [7, 16].

Probably the most promising and hence widely studied donor dopants for ZnO are Group III elements, i.e., Al, In, and Ga. According to numerous reported results, Al certainly showed to be by far the most effective donor dopant in ZnO [54–68], resulting in maximum values of  $\sigma$ , depending on the morphology, up to 7000 S/cm [61] and PF up to a maximum of  $22 \times 10^{-4}$  W/mK<sup>2</sup> [3]. However, the increase in  $\sigma$  is due to an increase in the charge-carrier concentration up to the values of  $n \approx 10^{20}$  cm<sup>-3</sup>, which results in a huge decrease of S to values of even less than one-fourth of the value for pure ZnO, somewhere in the range between –25 and –150 μV/mK. A comparison of the results presented in Refs. [53–67] shows that, in general, higher  $\sigma$ , and consequently also PF values, are obtained by classic sintering in an inert atmosphere of N<sub>2</sub> or Ar, and by SPS in Ar or in vacuum. Berardan et al. [57] directly compared samples sintered at 1400°C under a flow of air or nitrogen (N<sub>2</sub> < 3 ppm O<sub>2</sub>) and confirmed a 20 times higher  $\sigma$  with N<sub>2</sub> sintering (2 times higher PF), which was explained by the presence of oxygen vacancies (V<sub>O</sub>) as donors in the samples with compositions close to Zn<sub>0.995</sub>Al<sub>0.005</sub>O<sub>0.98</sub>. Ullah et al. [69] confirmed the benefits of sintering in argon. Tian et al. [70] demonstrated the significance of defect engineering for the thermoelectric properties of ZnO. They showed the importance of eliminating from the grain boundaries the intrinsic acceptor states, zinc vacancies (V<sub>Zn</sub>) and oxygen interstitials (O<sub>i</sub>), to prevent the formation of electrostatic Schottky barriers that trap electrons. Accordingly, by sintering in a reducing atmosphere of N<sub>2</sub>+CO they increased the  $\sigma$  of ZnO ceramics doped with Al, Mg, and Ti to 1900 S/cm at 310 K (1000 S/cm at 1000 K), which is several orders of magnitude larger than in samples sintered in N<sub>2</sub> or in air. They also found that sintering under a reducing atmosphere increases the solid solubility of Al in ZnO. Finally, by creating highly defective ZnO grains (high concentration of oxygen vacancies, V<sub>O</sub>, and increased

incorporation of Al) via multiple doping and sintering conditions, the lattice thermal conductivity,  $\kappa_L$ , of the samples sintered in a reducing atmosphere was strongly decreased. In further work Tian et al. [71] compared the SPS method in vacuum with sintering in a reducing ( $N_2 + CO$ ) atmosphere; while both eliminate the Schottky barriers, there are important differences that essential for a further improvement of the thermoelectric materials. The SPS processing with an extremely fast heating rate reduced the formation of the  $Zn_2TiO_4$  phase and increased the solubility of Ti in ZnO grains, which results in a higher charge-carrier concentration ( $n \approx 2.5 \times 10^{20} \text{ cm}^{-3}$ ) and hence a higher  $\sigma$  (2300 S/cm) in comparison with the samples sintered in a reducing atmosphere ( $n \approx 1 \times 10^{20} \text{ cm}^{-3}$ ). The SPS samples also had lower  $\kappa$ , noticeably at 310 K and slightly at 980 K.

In most studies Al is added to ZnO in amounts much above the solubility limit, which is less than 0.3 at.-% [72, 73]. Hence, typically  $ZnAl_2O_4$  is formed in the samples and it was confirmed that fine  $ZnAl_2O_4$  precipitates contribute to reduced thermal conductivity. Using fine nanopowders and nanocomposites, mostly in combination with SPS processing, which resulted in a fine-grained microstructure with nanoprecipitates of  $ZnAl_2O_4$ , proved very beneficial for the thermoelectric properties of Al-doped ZnO [56, 58–64, 68, 74–78]. In comparison to coarse-grained samples, such samples likely have a lower  $\sigma$  and more importantly a significantly lower  $\kappa$ ; it is reduced from typical values of about 30 W/mK at 300 K and 5 W/mK at 1000 K to values of 5–10 W/mK and 1–2 W/mK, respectively. The interesting possibility to decrease the thermal conductivity of ZnO ceramics is the addition of fine inclusions of some other phases, like organic nanoparticles, carbon nanotubes, and ZnS [51, 79–81]. In the studies of Al-doped ZnO, mostly values of  $zT$  in the range from about 0.1 to 0.36 were obtained, while the highest reported value was 0.44 at 1000 K [75].

$Ga_2O_3$ , as well as  $In_2O_3$  and  $Fe_2O_3$ , are not standard donor dopants, but they result in a Wurtzite structure of ZnO in the formation of extended 2D defects, the so-called multiple inversion boundaries (IBs). With the ordering of IBs, homologous phases  $(ZnO)_kM_2O_3$  ( $k = \text{integer}$ , M = In, Ga, Fe) having compositional and structural homogeneity are formed [82, 83]. Recent reports of Liang et al. [84–89] on the influence of natural superlattice interfaces (IBs) on charge and heat transport resulting in a strongly increased electrical and decreased thermal conductivity greatly contribute to a better understanding of the phenomenon, which could help in designing ZnO ceramics with an enhanced thermoelectric performance.

The highest  $zT$  values for ZnO ceramics were so far obtained with proper Ga and Al doping, 0.47 at 1000 K and 0.65 at 1247 K [90]. Recent studies have shown the influence of processing on the thermoelectric characteristics of Al- and Ga-doped ZnO [91–96] and the highest  $zT$  was reported by Brockway et al. [96]. They prepared bulk samples from Al- and Ga-doped ZnO nanowires by SPS at 1200°C in vacuum and obtained a  $zT$  value of 0.6 at 1273 K for the composition  $Zn_{0.97}Al_{0.02}Ga_{0.01}O$ , which was attributed to the resonant scattering of phonons in connection with preserved nanostructuring after the consolidation. Single Ga doping of ZnO resulted in much lower  $zT$  values, and while the thermal conductivity is strongly reduced, the electrical conductivity is too low [84, 97–99]. An important insight into the structural and thermoelectric characteristics of the Ga:ZnO system was given in a recent report of

Guilmeau et al. [100], showing that IBs are already formed with the addition of 1 at.% of Ga and strongly affect the charge-carrier concentration and the mobility, while already the addition of up to 4 at.% drastically reduces the thermal conductivity in the temperature range 300 to 1000 K.

In the ZnO-In<sub>2</sub>O<sub>3</sub> system, Košir et al. [101] recently explained the mechanism of formation of the (ZnO)<sub>*k*</sub>In<sub>2</sub>O<sub>3</sub> (*k*=5, 7, 9, ...) homologous phases in accordance with an internal diffusion mechanism that controls the formation of IBs [102], and how their formation influences the microstructure development and thermoelectric characteristics, depending on the degree of compositional and structural homogeneity. Other studies also confirmed that better compositional and structural homogeneity result in higher *zT* values of up to about 0.20 at 1000 K [103–106]. The influence of phase equilibria in the ZnO-In<sub>2</sub>O<sub>3</sub> system on the thermoelectric properties was also well presented by Liang and Clark [107]. A very significant recent report was that of Labegorre et al. [108], showing that IBs are formed already during the addition of 0.25 at.% of In, which markedly effects the charge-carrier concentration and mobility, increases the electrical, and decreases the thermal conductivity, as you can see in Fig. 2.10.1. Accordingly, the samples with the addition of only 2 at.% of In showed *zT* values of 0.075 at 960 K, which are comparable to the compositions with a much higher addition of In [101]. Furthermore, the presence of IBs for such low levels of In indicates the absence of a classic solid solubility and shows a more complex charge creation, which needs to be explained.

A study of possible n-type carrier sources in (ZnO)<sub>*k*</sub>In<sub>2</sub>O<sub>3</sub> was reported by Peng et al. [109]. Dual doping of ZnO with In and Al [110, 111] resulted in much lower *zT* values, with highest being 0.22 at 1073 K [111]. Košir et al. [112] confirmed that Al substitutes In on both primary sites in the Zn<sub>5</sub>(In<sub>1-x</sub>Al<sub>x</sub>)<sub>2</sub>O<sub>8</sub> homologous phase and shrinks the unit cell, and hence reduces the charge-carrier concentration and effects their mobility. This could explain the poorer thermoelectric characteristics in comparison to the (Ga,Al)-doped ZnO. Also, dual In and Ga doping of ZnO resulted in *zT* values of less than 0.20 [113, 114].

A completely new view of the Al doping of ZnO, with exciting implications for the thermoelectric characteristics, was opened with the recent reports of Hoemke et al. [67, 115–117] about the presence of multiple inversion boundaries in ZnO doped with Al and co-doped either with Mn or Sn.

### 2.10.2.2 Perovskite-type thermoelectric materials

Oxide materials with a perovskite structure of CaTiO<sub>3</sub> and a general chemical formula ABO<sub>3</sub> represent a large family of materials having a variety of physical and chemical properties, which are already widely used in electronics (capacitors, infrared detectors, thermistors, resonators, oscillators, filters, gas sensors, electrodes, etc.) and are also for quite some time interesting candidates for thermoelectric applications. An extensive review of the development of the broad family of n- and p-type perovskite and hybrid perovskite materials for thermoelectric applications was recently published by Wu and Gao [118]. In general, for the relatively high Seebeck coefficient of perovskite materials, the main challenge is increasing their low electrical

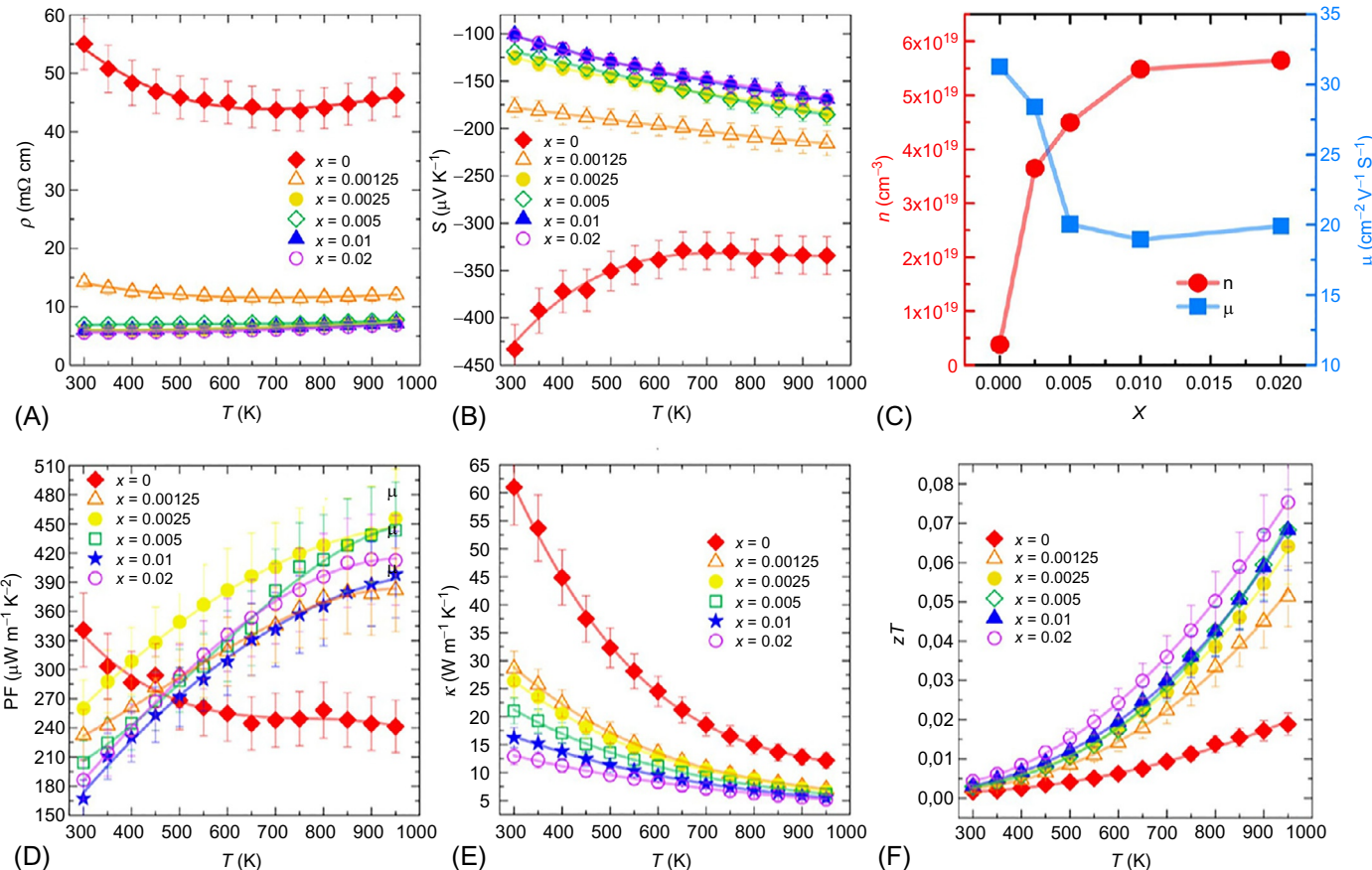


**Fig. 2.10.1** Thermoelectric properties of  $\text{Zn}_{1-x}\text{In}_x\text{O}$  ceramics as a function of composition and temperature: (A) electrical resistivity ( $\rho$ ), (B) Seebeck coefficient ( $S$ ), (C) dependence of carrier concentration ( $n$ ) and Hall mobility ( $\mu$ ), (D) power factor (PF), (E) thermal conductivity ( $\kappa$ ), and (F) figure of merit ( $zT$ ). Reprinted (and adapted) with permission from J.B. Labegorre, O.I. Lebedev, C. Bourges, A. Recnik, M. Kosir, S. Bernik, A. Maignan, T. Le Mercier, L. Pautrot-d'Alenccon, E. Guilmeau, Phonon scattering and electron doping by 2D structural defects in In/ZnO, ACS Appl. Mater. Interfaces 10 (2018) 6415–6423. Copyright 2019 American Chemical Society.

conductivity and in the case of oxide perovskites decreasing their high thermal conductivity. Accordingly, doping, the introduction of oxygen vacancies, nanostructuring, and an increased structural complexity are approaches used to enhance the thermoelectric performance of perovskite materials. These are certainly well recognized as promising and hence extensively studied, such as thermoelectric oxide perovskites of n-type, e.g.,  $\text{SrTiO}_3$  and  $\text{CaMnO}_3$  [14, 119].

### 2.10.2.2.1 Strontium titanate ( $\text{SrTiO}_3$ )

Stoichiometric  $\text{SrTiO}_3$  has an isotropic cubic perovskite structure  $\text{ABO}_3$ , where the oxygen anions form an octahedron with one  $\text{Ti}^{4+}$  ion in the center and a high melting point at 2080°C. With a bandgap of 3.2 eV stoichiometric  $\text{SrTiO}_3$  acts as an insulator, having a low carrier concentration much below  $10^{15} \text{ cm}^{-3}$ . However, by substitutional donor doping of  $\text{Sr}^{2+}$  ions on A sites with  $\text{M}^{3+}$  ions (i.e.,  $\text{La}^{3+}$ ) and  $\text{Ti}^{4+}$  ions on B sites with  $\text{M}^{5+}$  ions (i.e.,  $\text{Nb}^{5+}$ ), and the creation of oxygen vacancies by sintering under reducing conditions, the charge-carrier concentration can be increased up to values of  $10^{21} \text{ cm}^{-3}$  and the electrical conductivity tuned over a very broad range from insulating to metallic. The positive effect of oxygen vacancies on an increase of the electrical conductivity and a decrease of the lattice thermal conductivity by phonon scattering was clearly shown by studies of the undoped and Nb-doped  $\text{SrTiO}_3$  over a wide range of partial pressures of oxygen  $P(\text{O}_2)$  [120, 121]. However, using only a single approach to adding free electrons to  $\text{SrTiO}_3$  to raise the Fermi energy from the forbidden to the conduction band was shown to be much less effective. Just substitutional donor doping with higher-valence elements to A and B sites is restricted by the limited solubility of the dopants in the range 0.27–0.37 and hence results in lower concentrations of charge carriers, which are also partially localized; hence, in the case of unreduced La- and Nb-doped materials the conductivities are typically below 100 S/cm, for a charge-carriers mobility in the range of 1–4  $\text{cm}^2/\text{Vs}$ . On the other hand, during the excess creation of oxygen vacancies the distance among them reduces to a critical value and they gather into clusters; consequently, a small mid-gap is formed at the bottom of the conduction band, while the density of the free electrons is reduced.

Hence, with a possible high electrical conductivity and a large Seebeck coefficient in the range from about –100 to about –350  $\mu\text{V}/\text{mK}$  and due to a high electron mobility of up to  $100 \text{ cm}^2/\text{Vs}$  and a large effective mass ( $m^* \approx 2\text{--}16 m_0$ ),  $\text{SrTiO}_3$  has also been recognized as a promising n-type oxide thermoelectric material. However,  $\text{SrTiO}_3$  also has a high thermal conductivity of about 10 W/mK at 300 K and  $>3$  W/mK at 1000 K [3, 14–16]. Accordingly, the research emphasis in the development of thermoelectric  $\text{SrTiO}_3$ -based materials is on heterovalent and homovalent doping of the A and B sites to increase the charge-carrier concentration, electrical conductivity, and power factor of  $\text{SrTiO}_3$ ; since the defect equilibrium is highly dependent on the partial pressure of oxygen  $P(\text{O}_2)$ , as reported by Blennow et al. [122], sintering in a reducing atmosphere is normally used. Also important for obtaining a higher  $zT$  is reducing the thermal conductivity of doped  $\text{SrTiO}_3$ . Heavy doping with La or Nb was reported to increase the charge-carrier concentration even up to about  $3 \times 10^{21} \text{ cm}^{-3}$ , which with a large Seebeck effect of about –350  $\mu\text{V}/\text{mK}$  resulted in the highest power factor (PF) of

$36 \times 10^{-4}$  W/mK<sup>2</sup> [3]. Li et al. [123] reported  $zT$  values of about 0.42 from 769 to 1009 K for bulk polycrystalline  $\text{Sr}_{0.93}\text{La}_{0.07}\text{Ti}_{0.93}\text{Nb}_{0.07}\text{O}_3$  with a charge-carrier concentration of  $1.8 \times 10^{21}$  cm<sup>-3</sup> and a power factor of  $18 \times 10^{-4}$  W/mK<sup>2</sup> at 600 K, obtained by the hydrothermal synthesis of La- and Nb-doped  $\text{SrTiO}_3$  powder and its sintering with carbon in vacuum at 1300°C. They attributed the decrease in thermal conductivity to the in-situ precipitation of NbC and  $\text{TiO}_{2-\delta}$  secondary phases, causing additional phonon scattering to the Nb and La point defects. Wang et al. [124] reported even higher  $zT$  values of 0.65 at 1100 K in  $\text{SrTiO}_3$  doped with 10 mol.% of La and Nb, showing that the simultaneous enhancement of all three key thermoelectric parameters is possible by nanoscale co-doping using the appropriate combination of hydrothermal synthesis and an effective sintering method. In the composite of undoped  $\text{SrTiO}_3$  and LaNb-doped  $\text{SrTiO}_3$  prepared by using the same preparation methods, a simultaneous increase of the Seebeck coefficient and a decrease of the thermal conductivity were obtained [125].

Studies also have shown that doping of the A and B sites can contribute to reduced thermal conductivity. Daniels et al. [126] reported that by tuning the size of cations at the A and B sites it is possible to affect the degree of octahedral distortion and hence the structural symmetry, which results in the effect of phonon glass and reducing the thermal conductivity to about 2.3 W/mK at 300 K. Yaremchenko et al. [127] reported that in Ta-substituted  $\text{SrTiO}_3$  high power factors of up to about  $14 \times 10^{-4}$  W/mK at 400 K are obtained with the appropriate presence of strontium and oxygen vacancies, while a higher content of oxygen vacancies also strongly reduced the thermal conductivity to values below 3 W/mK, giving a maximum  $zT$  value of 0.37 at 1230 K. Several reports confirmed the benefits of simultaneous substitutional A-site donor doping and the formation of A-site vacancies to increase the electrical conductivity and power factor, and to decrease the thermal conductivity of  $\text{SrTiO}_3$ . Kovalevsky et al. [128, 129] showed that a large increase in PF to values of about  $15 \times 10^{-4}$  W/mK<sup>2</sup> can be obtained with heavily substitutional donor doping with Pr to A-sites or Nb to B-sites, while a significant decrease in thermal conductivity to about 2 W/mK is related to the presence of oxygen vacancies in A-site deficit materials; they reported maximum  $zT$  values of 0.23 for Nb-doped at 1050 K and 0.34 at 1175 K for Pr-doped  $\text{SrTiO}_3$ . Dehkordi et al. [130–132] also reported a large PF of  $16.8 \times 10^{-4}$  W/mK, a reduced thermal conductivity, and a  $zT$  of 0.35 at 773 K for Pr-doped  $\text{SrTiO}_3$ , which was explained by the formation of Pr-rich grain boundaries, resulting in the substantial enhancement of carrier mobility, while the nonuniform distribution of dopants induces structural transitions at the grain boundaries for extra phonon scattering. Similar  $zT$  values of 0.25–0.345 at 700–1000 K for simultaneously La- and Nb-doped  $\text{SrTiO}_3$ , with the emphasized role of A-site and oxygen vacancies, were also reported by Srivastava et al. [133]. Azough et al. [134] reported that by the simultaneous interplay of La-substitution to the A sites and A-site vacancies with the formation of a layered structure, thermal conductivity can be reduced and controlled from about 5.5 W/mK at 325 K, and 4 W/mK at 1150 K to about 2.7 W/mK for the whole temperature range; the highest  $zT$  value of 0.27 at 1070 K was obtained in the sample with the composition  $\text{Sr}_{1-x}\text{La}_{2x/3}\text{TiO}_3$  for  $x=0.50$  with half of the A-sites occupied by La and vacancies. Just recently, Popuri et al. [135] confirmed that La-doped  $\text{SrTiO}_3$  becomes a phonon

glass with a thermal conductivity of about 2.5 W/mK from 300 to 900 K for large numbers of A-site vacancies. They also explained that the electron-crystal properties for high electrical conductivity are reduced due to the core-shell grain structure. The highest  $zT$  for the La-substituted and A-site-deficient  $\text{SrTiO}_3$  of 0.41 at 973 K was reported by Lu et al. [136] for the sample with the composition  $\text{Sr}_{1-3x/2}\text{La}_x\text{TiO}_{3-\delta}$  ( $x=0.15$ ); the influence of composition on  $zT$  is shown in Fig. 2.10.2.

A substantial decrease in thermal conductivity at room temperature without a significant influence on electrical conductivity in La- and Mn-doped  $\text{SrTiO}_3$  was reported by Okuda et al. [137], while the relation of structural properties to the thermal conductivity was reported by Kajimoto et al. [138]. An increase in the electrical conductivity and a decrease in thermal conductivity were reported also for La and Dy co-doped Sr-deficient  $\text{SrTiO}_3$ , leading to a  $zT$  value of 0.29 at 773 K in the  $\text{Sr}_{0.75}\text{La}_{0.1}\text{Dy}_{0.1}\text{TiO}_3$  sample [139]. In contrast, Y-substitution to A-sites of Sr- and O-deficient  $\text{Sr}_{1-1.5x}\text{Y}_x\text{TiO}_{3-\delta}$  resulted in a larger decrease in electrical conductivity than the thermal conductivity and hence a reduced thermoelectric performance and a lower  $zT$  with an increasing amount of Y for  $x \geq 0.08$  when the  $\text{Y}_2\text{Ti}_2\text{O}_7$  secondary phase starts to form [140].

An interesting possibility for the microstructural enhancement of the thermoelectric characteristics was shown by Tkach et al. [141] and is schematically presented in Fig. 2.10.3. Using exaggerated grain growth they prepared heavily Nd-doped  $\text{SrTiO}_3$  ceramics with a distinct bimodal microstructure of large 60  $\mu\text{m}$  grains in a fine matrix of 2  $\mu\text{m}$ , bringing a  $zT$  value of 0.36 at 970 K, which is about three times larger than for ceramics with the same composition and a uniform grain size of about 8  $\mu\text{m}$ .

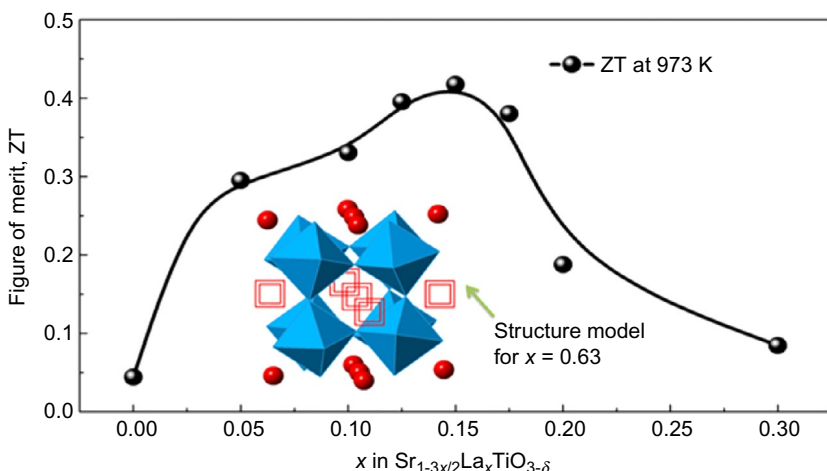


**Fig. 2.10.2** The influence of La-substitution of Sr-sites in A-site-deficient  $\text{Sr}_{1-3x/2}\text{La}_x\text{TiO}_{3-\delta}$  ceramics on the thermoelectric characteristics and their structural model showing a random distribution of A-site vacancies hindering long-range symmetry.

From Z. Lu, H. Zhang, W. Lei, D.C. Sinclair, I.M. Reaney, High-figure-of-merit thermoelectric La-doped A-site-deficient  $\text{SrTiO}_3$  ceramics, Chem. Mater. 28 (2016) 925–935.

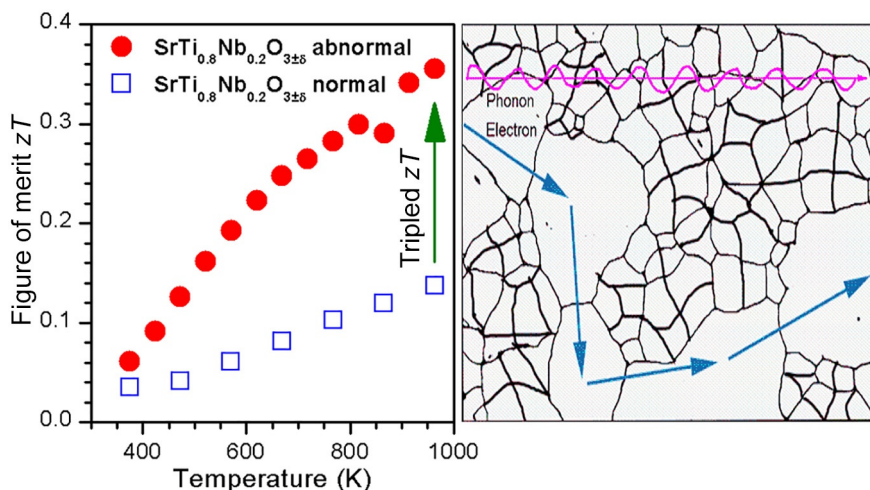


**Fig. 2.10.3** Abnormal grain growth and thereby bimodal grain size distribution in  $\text{SrTi}_{0.8}\text{Nb}_{0.2}\text{O}_{3\pm\delta}$  ceramics result in a significant increase of  $zT$ ; while the large grains provide a conducting path for the electrons for a substantial enhancement of electrical conductivity, the fine-grained part of the microstructure results in phonon scattering and a lower thermal conductivity.

Reprinted with permission from A. Tkach, J. Resende, K.V. Saravanan, M.E. Costa, P. Diaz-Chao, E. Guilmeau, O. Okhay, P.M. Vilarinho, Abnormal grain growth as a method to enhance the thermoelectric performance of Nb-doped strontium titanate ceramics, ACS Sustain. Chem. Eng. 6 (2018) 15988–15994. Copyright 2019 American Chemical Society.

The influence of microstructure with a distinct bimodal grain size on the thermoelectric characteristics of Nb-doped  $\text{SrTiO}_3$  was also demonstrated by Wang et al. [142].

The enhancement of the PF in  $\text{Sr}_{0.9}\text{Nd}_{0.1}\text{TiO}_3$  to  $20 \times 10^{-4} \text{ W/mK}^2$  and the  $zT$  value to 0.37 at 1015 K through control of the nanostructure and microstructure with the addition of  $\text{B}_2\text{O}_3$  and  $\text{ZrO}_2$  was also reported by Ekren et al. [143]; while  $\text{B}_2\text{O}_3$  reduced the sintering temperature, the Zr doping improved the compositional homogeneity for a uniform distribution of Nd and Sr in the structure, resulting in greatly enhanced carrier mobility. Buscaglia et al. [144] showed that a fine microstructure with nanosized grains can strongly reduce thermal conductivity, especially for a grain size of less than 35 nm; ceramics with a grain size of 24 nm had a glass-like behavior and a  $\kappa$  of 1.2 W/mK at 300 K; however, it also had low electrical conductivity. It was reported that the problem of the electrostatic Schottky barriers at the grain boundaries reducing their electrical conductivity could be addressed by the addition of graphene [145, 146], reduced graphene oxide (RGO) [147–149] or metallic micro/nano inclusions [150, 151], resulting in an increase of the carrier concentration and also carrier mobility. The thermopower of the nano- $\text{SrTiO}_3$  could also be enhanced by tuning the nature of the grain boundaries with the addition of rare-earth elements [152].

In comparison to  $\text{SrTiO}_3$ , the layered perovskite  $\text{SrO}(\text{SrTi}_n\text{O}_3)_n$  ( $n=1,2,3,\dots,\infty$ ) Ruddlesden-Popper (RP) homologous compounds with a natural quasi-two-dimensional

superlattice structure have a much lower thermal conductivity [153–157]. The introduction of platelet grains of the RP-phase into  $\text{Sr}(\text{Ti}_{0.8}\text{Nb}_{0.2})\text{O}_3$  ceramics by SrO and CaO doping [158] or the addition of RP crystals synthesized by the molten-salt method [159] resulted in a decrease in the thermal and an increase in electrical conductivity.

### 2.10.2.2.2 Calcium manganite ( $\text{CaMnO}_3$ )

$\text{CaMnO}_3$  has an orthorhombic perovskite structure, an indirect bandgap of around 0.7 eV, an insulating character with a high Seebeck coefficient of about  $-350 \mu\text{V/K}$  at room temperature, and a low thermal conductivity of about  $3\text{W/mK}$ . The high resistivity is the main drawback of  $\text{CaMnO}_3$ , hence doping for an increased charge-carrier concentration was still the focus of research in recent years [16, 119, 160]. So far the substitution of Ca for Bi or rare-earth (RE) elements, i.e., the larger radius of RE was more effective (i.e., Yb) and the substitution of Mn for transition metals (Nb, Ta, Mo, Ru, W) in limited (optimal) amounts was the most effective; electrical conductivity can be increased by a few orders of magnitude to values from about  $350\text{S/cm}$  at  $300\text{K}$  to about  $100\text{S/cm}$  at  $1000\text{K}$ . However, with such donor doping the Seebeck coefficient typically has values in the range from  $-100$  to  $-200 \mu\text{V/K}$ . In comparison to pristine, doped  $\text{CaMnO}_3$  typically has lower thermal conductivity in the range  $1.5\text{--}2\text{W/mK}$ . While standard solid-state processing results in a grain size of several micrometers, wet-chemical synthesis methods resulted in nanostructuring and a crystallite size of less than  $200\text{nm}$ , which decreased the thermal conductivity to values between 0.5 and  $1\text{W/mK}$ . Within such thermoelectric parameters, the obtained  $zT$  values of doped  $\text{CaMnO}_3$  stayed below 0.3 at  $1000\text{K}$  [16, 119, 161–170]. The breakthrough was a report by Song et al. [171] showing that optimal doping in combination with microstructural engineering can lead to strongly enhanced thermoelectric characteristics as shown in Fig. 2.10.4; they obtained a  $zT$  value of 0.67 at  $773\text{ K}$  in  $\text{Ca}_{0.97}\text{Bi}_{0.03}\text{MnCu}_{0.04}\text{O}_{3-\delta}$  ceramics with a CuO secondary phase segregated at the grain boundaries, prepared by the sol-gel synthesis method and sintering at  $1100^\circ\text{C}$  in an oxygen flow.

## 2.10.3 The p-type oxide thermoelectric materials

### 2.10.3.1 Layered cobalt oxides

Certainly the most prominent group of p-type oxide thermoelectric materials is the layered cobalt oxides, represented by  $\text{Na}_x\text{CoO}_3$ ,  $\text{Ca}_3\text{Co}_4\text{O}_9$ , and  $\text{Bi}_2\text{Sr}_2\text{Co}_2\text{O}_9$ , having quite a high thermopower, good electrical conductivity, and a relatively low thermal conductivity. While  $\text{Ca}_3\text{Co}_4\text{O}_9$  is generally considered as stable, the other two suffer from Na and Bi volatility at higher temperatures, and the  $\text{Na}_x\text{CoO}_3$  is also sensitive to humidity [2, 14, 16, 172]. It would be extremely beneficial and convenient for thermoelectric applications to also have n-type layered cobalt oxides. Recently, Gong et al. [173] reported that they prepared by sintering and annealing in a reducing atmosphere an n-type (Ag,La) co-doped Ca-Co-O ceramic with a very high electrical

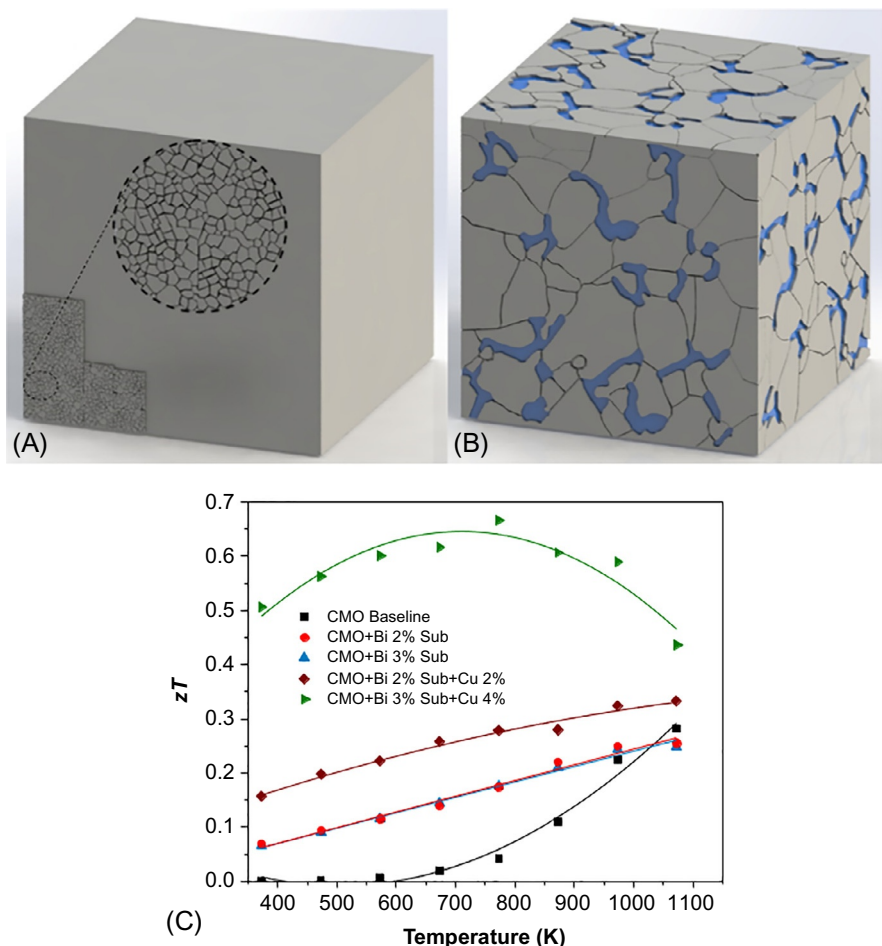


**Fig. 2.10.4** Evolution of the grain morphology and formation of the grain-boundary network upon Cu addition in  $\text{Ca}_{1-x}\text{B}_{\text{x}}\text{MnCu}_y\text{O}_{3-\delta}$  samples: (A)  $\text{CaMnO}_{3-\delta}$ , (B) Bi-doped  $\text{CaMnO}_{3-\delta}$  with Cu addition. (C) Temperature dependence of  $zT$  of  $\text{Ca}_{1-x}\text{B}_{\text{x}}\text{MnCu}_y\text{O}_{3-\delta}$  samples.

Reprinted (and adapted) with permission from X. Song, S.A. Paredes Navia, L. Liang, C. Boyle, C.O. Romo-De-La-Cruz, B. Jackson, A. Hinerman, M. Wilt, J. Prucz, Y. Chen, Grain boundary phase segregation for dramatic improvement of the thermoelectric performance of oxide ceramics, ACS Appl. Mater. Interfaces 10 (2018) 39018–39024. Copyright 2019 American Chemical Society.

conductivity of above 3000 S/cm, a Seebeck coefficient of  $-56 \mu\text{V/K}$ , a maximum power factor of  $15.36 \times 10^{-4} \text{ W/mK}^2$ , and a  $zT$  value of 0.39 at 823 K.

In many respects, layered cobalt oxides are very different from other oxide thermoelectric materials, which largely comes from their complex layered structure. In general, their structure is composed of two structurally and chemically different types of layers (structural blocks), which alternate in the direction of the crystallographic

*c*-axis. Hence, the transport of electrons and phonons follows different paths. The ordered CdI<sub>2</sub>-type CoO<sub>2</sub> layers, which are common to all three types of compounds, serve as the transport path for charge carriers (electrons/holes). The structural blocks in between the CoO<sub>2</sub> layers, i.e., either disordered Na layers or rock-salt Ca<sub>2</sub>CoO<sub>3</sub> layers and Bi<sub>2</sub>Sr<sub>2</sub>O<sub>4</sub> layers, serve as phonon-scattering regions responsible for the low thermal conductivity. At the same time, they act as a charge reservoir for the CoO<sub>2</sub> layers. In Ca<sub>3</sub>Co<sub>4</sub>O<sub>9</sub> and Bi<sub>2</sub>Sr<sub>2</sub>Co<sub>2</sub>O<sub>9</sub>, the structure mismatch between both types of structural blocks (i.e., the misfit layered structure) results in additional phonon scattering, reducing the thermal conductivity. Accordingly, such a structural anisotropy reflects in the thermoelectric characteristics; while the thermopower is rather isotropic, electrical and thermal conductivity are highly anisotropic, much higher in the *a*-*b* planes than in the *c*-direction perpendicular to the structural layers. Generally, in the single crystals, fully expressed properties are primarily related to the composition and crystal structure. However, a disadvantage of the polycrystalline ceramics of layered cobaltites caused by the complex microstructural features is even more expressed with the anisotropy of the physical characteristics, also due to the more or less anisotropic plate-like morphology of the grains and hence the additional marked effect of a degree of texturing. Hence, the thermoelectric characteristics of ceramics based on these layered p-type oxide compounds showed a high sensitivity to the synthesis and processing methods, with the opportunity to improve the thermoelectric characteristics via an optimization of the microstructure (density, grain size and grain size distribution, connectivity among the grains, grain orientation). At the same time a complex charge balance between both structural units strongly affects the possibilities to enhance the electrical conductivity by doping.

In this chapter, Ca<sub>3</sub>Co<sub>4</sub>O<sub>9</sub>, which is generally considered as stable, will be presented in more detail. Other two types of layered cobalt oxides suffer from Na and Bi volatility at higher temperatures, while the Na<sub>x</sub>CoO<sub>3</sub> is also sensitive to humidity. More about them can be found elsewhere and in particular in the recent report of Ji [2] about Na<sub>x</sub>CoO<sub>3</sub> and Ang [172] about Bi<sub>2</sub>Sr<sub>2</sub>Co<sub>2</sub>O<sub>y</sub>.

#### 2.10.3.1.1 Calcium cobalt oxide (Ca<sub>3</sub>Co<sub>4</sub>O<sub>9</sub>)

Good resistance to environmental influences, temperature stability up to the decomposition temperature at 926°C, and prospects for further enhancement of the thermoelectric characteristics are advantages that make Ca<sub>3</sub>Co<sub>4</sub>O<sub>9</sub> the most attractive among the p-type oxide thermoelectric materials. Single crystals of Ca<sub>3</sub>Co<sub>4</sub>O<sub>9</sub> have, in the *a*-*b* planes, a high Seebeck coefficient *S* of about 240 µV/K, a relatively high electrical conductivity *σ* of about 430 S/cm, and a relatively high thermal conductivity *κ* of about 3 W/mK, and hence a good *zT* value of 0.87 at 973 K. However, for the polycrystalline Ca<sub>3</sub>Co<sub>4</sub>O<sub>9</sub> ceramics, which are much more feasible for use, *zT* values much below 0.1 are mostly obtained, and result from a much lower electrical conductivity *σ* typically below 50 S/cm, a lower Seebeck coefficient of about 150 µV/K, and a lower thermal conductivity of about 1–1.5 W/mK [174–179]. Such poor thermoelectric characteristics are also a consequence of the highly porous microstructure composed of randomly oriented plate-like grains that are weakly connected to each other.

The synthesis of the  $\text{Ca}_3\text{Co}_4\text{O}_9$  compound is straightforward using powders of  $\text{CaCO}_3$  and  $\text{CoO}$ , and is usually carried out at a temperature of about  $900^\circ\text{C}$ , just below its decomposition temperature. However, the solid-state reaction of the  $\text{Ca}_3\text{Co}_4\text{O}_9$  phase formation is very sluggish and often incomplete with residues of the starting reagents, even after prolonged heat treatment for several days with intermediate grindings. In addition, a random growth in all directions of distinct platelet grains of  $\text{Ca}_3\text{Co}_4\text{O}_9$  with a length/width of up to about  $5\ \mu\text{m}$  and a thickness of less than  $1\ \mu\text{m}$  prevents densification as such a grain morphology inevitably creates empty space in between them, so that the obtained ceramics have a density of only about 50%–70% of the theoretical (i.e.,  $4.68\ \text{g}/\text{cm}^3$ ). Presečnik et al. showed that either using fine attrition milled sub-micrometer powders of the starting reagents [180] or a mechano-chemical treatment of the starting powder mixture with high-energy milling [181] significantly enhances the solid-state reaction, resulting in the formation of a pure, fine-grained  $\text{Ca}_3\text{Co}_4\text{O}_9$  phase with a single calcination for just several hours at significantly lower temperatures of  $760^\circ\text{C}$ ; the resulting highly porous ceramics had a  $zT$  of about 0.1 at  $900\text{K}$ . Furthermore, reports showed that sol-gel and other wet-chemical methods enable the synthesis at even lower temperatures in the range from  $650^\circ\text{C}$  to  $800^\circ\text{C}$  and with short firing times so that the obtained single-phase  $\text{Ca}_3\text{Co}_4\text{O}_9$  has a much finer (i.e., smaller and thinner) plate-like grains and noticeably higher  $zT$  values in the range from 0.1 to 0.29 [182–185].

As the synthesis of  $\text{Ca}_3\text{Co}_4\text{O}_9$  typically results in highly porous ceramics with randomly oriented plate-like grains, while the thermoelectric characteristics are highly anisotropic, the microstructure optimization was intensively studied. With the expectation of a significantly enhanced  $zT$ , the focus was on the development of a dense and highly textured microstructure using different processing methods, such as hot pressing (HP), cold high-pressure pressing, templated grain growth, and spark-plasma sintering (SPS). The SPS and especially free-edge SPS (SPT) were shown to be very effective in processing dense and highly textured  $\text{Ca}_3\text{Co}_4\text{O}_9$  ceramics [186–188]. Presečnik et al. [180] compared the influence of different processing methods while using the same starting  $\text{Ca}_3\text{Co}_4\text{O}_9$  powder on the microstructure and thermoelectric characteristics of the  $\text{Ca}_3\text{Co}_4\text{O}_9$  ceramics. Besides HP and SPT they also used novel approaches, such as free-edge cold pressing (CPT) of the calcined  $\text{Ca}_3\text{Co}_4\text{O}_9$  pellets; it resulted in modestly textured and porous  $\text{Ca}_3\text{Co}_4\text{O}_9$  ceramics with a very low thermal conductivity of about  $0.5\ \text{W}/(\text{m}\cdot\text{K})$  and a  $zT$  value of 0.31 at  $900\text{K}$ . In contrast to the general expectation of perfect textures and fully dense materials, ceramics prepared by the edge-free SPS (SPT) had a much lower  $zT$  value of 0.17, similar to other reports in the literature, handicapped by a three times higher thermal conductivity. The thermoelectric characteristic  $zT$  and the microstructures of the  $\text{Ca}_3\text{Co}_4\text{O}_9$  ceramics as prepared by single calcination at  $760^\circ\text{C}$ , the CPT processed ceramics and the SPT processed ceramics are presented in Fig. 2.10.5. In general, many reports confirmed that the synthesis and use of very fine  $\text{Ca}_3\text{Co}_4\text{O}_9$  powders and appropriate processing methods to make properly porous ceramics, while preserving fine plate-like morphology of the grains, enable the enhancement of the thermoelectric characteristics of pristine  $\text{Ca}_3\text{Co}_4\text{O}_9$  to  $zT$  values of up to about 0.4 [183, 189–194].

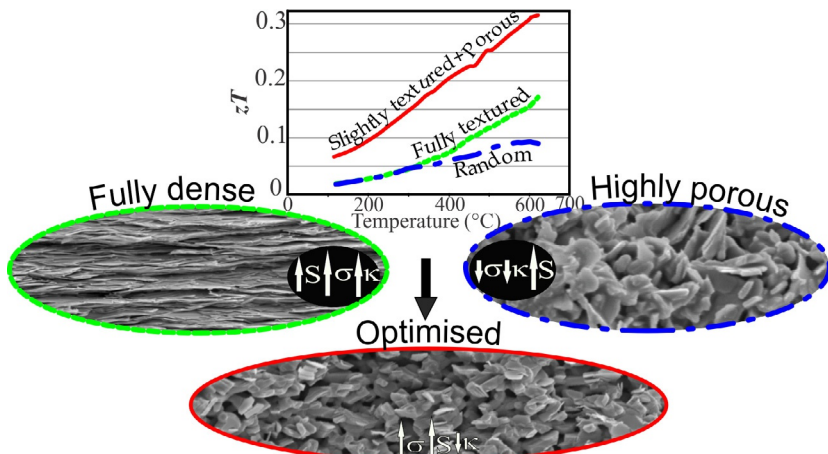


**Fig. 2.10.5** Influence of microstructure (i.e., texturing, porosity) on the thermoelectric characteristics and  $zT$  of the p-type  $\text{Ca}_3\text{Co}_4\text{O}_9$  ceramics as synthesized by a single calcination at 760°C (blue), processed by the free-edge spark plasma sintering (green) and processed by free-edge cold pressing (red).

Sintering in an oxygen atmosphere also proved beneficial [195, 196]. In addition, the addition of platelet  $\text{Ca}_3\text{Co}_4\text{O}_9$  template seeds [197] and a transition liquid-phase-sintering additive [198] was reported to enhance the thermoelectric characteristics of  $\text{Ca}_3\text{Co}_4\text{O}_9$  ceramics via microstructure development.

Doping of the  $\text{Ca}_3\text{Co}_4\text{O}_9$  was intensively studied to further enhance the thermoelectric characterization by tuning the charge-carrier concentration and mobility for a higher electrical conductivity and to create phonon-scattering sites for a lower thermal conductivity. Accordingly, the influence of dopants aimed to substitute either Ca-sites or Co-sites was examined; alkaline and alkaline earth metals or rare-earth elements primarily went to Ca-sites, while the transition metals went to Co-sites. In general, it showed that doping the Ca-sites mainly changes the charge-carrier concentration of the system and has less influence on the band structure. Doping on the Co sites, especially in the  $\text{CoO}_2$  layer, however, can affect the band structure and the transport mechanism.

Rare-earth elements ( $\text{RE}^{3+}$ ) generally decrease the electrical and thermal conductivity and increase the Seebeck coefficient [22, 199–209]. With  $\text{RE}^{3+}$  substitution of the  $\text{Ca}^{2+}$ , the share of  $\text{Co}^{2+}$  is increased with respect to the  $\text{Co}^{3+}$  to prevent the charge neutrality of the  $\text{Ca}_2\text{CoO}_3$  layers, which consequently affects the lower concentration of holes in the conducting  $\text{CoO}_2$  layers. In these studies, values of  $zT$  below 0.30 were mostly obtained. The highest  $zT$  value of 0.74 at 800 K was reported by Saini et al. [204] for Tb-doped  $\text{Ca}_{2.5}\text{Tb}_{0.5}\text{Co}_4\text{O}_9$  ceramics with a very large Seebeck coefficient of about 325  $\mu\text{V/K}$ . A high  $zT$  of 0.61 was also obtained in dually Lu- and Ag-doped  $\text{Ca}_{2.8}\text{Ag}_{0.05}\text{Lu}_{0.15}\text{Co}_4\text{O}_{9+\delta}$  ceramics [22].

Attempts at doping the Ca sites with the alkali (Na, K) [175, 210–212] and alkali-earth elements (Sr, Ba) [213–218] also showed segregation of the doping element at

the grain boundaries, affecting the microstructure development; they mostly resulted in an increase in the electrical conductivity and the Seebeck coefficient, and a decrease in thermal conductivity, giving  $zT$  values typically in the range from about 0.20–0.35. The highest  $zT$  value of 0.52 at 1073K was obtained by Carvillo et al. [214] in ceramics with the composition  $\text{Ca}_3\text{Ba}_{0.05}\text{Co}_4\text{O}_9$ , which was attributed to Ba segregation at the grain boundaries of Ba-free  $\text{Ca}_3\text{Co}_4\text{O}_9$  grains causing energy filtering for increased thermopower S, and also to increase the electrical conductivity and decrease the thermal conductivity. Among other dopants aimed at the Ca sites, especially Bi was positive [219–221], resulting in an enhancement of all three thermoelectric parameters to bring  $zT$  to values of about 0.40; Bi segregates at the grain boundaries, enhances the grain growth, and improves the crystal texture. The doping of Cd to Ca sites resulted in a  $zT$  value of 0.35 at 1000K [222].

For doping of Co sites, mostly the effects of transition elements such as Ti, Mn, Fe, Cu, Ni, and Zn were studied [223–230], and  $zT$  values up to about 0.30 were obtained, while the highest value of about 0.40 at 1000K was reported for the Fe-doped composition  $\text{Ca}_3\text{Co}_{3.9}\text{Fe}_{0.1}\text{O}_{9+\delta}$ . A  $zT$  value of 0.40 was also obtained by dual Bi and Fe doping in  $\text{Ca}_{2.7}\text{Bi}_{0.3}\text{Co}_{3.9}\text{Fe}_{0.1}\text{O}_{9+\delta}$  ceramics [231]. The substitution of Ga for Co also resulted in  $zT$  values of about 0.30 [177, 232]. Dual doping with rare-earth elements (Ce, Eu, or Lu) to Ca sites and the transition metal (Fe, or Ni) to Co sites was also studied, affecting the lower electrical and thermal conductivity and the higher Seebeck coefficient, while the reported  $zT$  values are much below 0.1 [233–235].

The influence of Co substitution with high valence 6+ ions of Cr [178, 236–238] and W [239, 240] was also studied. In general, it results in a higher Seebeck coefficient and a lower thermal conductivity. However, due to the decrease in electrical conductivity with the decrease in charge-carrier concentration (i.e., the valence of the dopant is higher than the average valence of Co and acts as an electron donor, reducing the hole concentration), the obtained  $zT$  values remained quite similar to the undoped  $\text{Ca}_3\text{Co}_4\text{O}_9$  ceramics at values below 0.20.

It appears from these studies that the main difficulty in obtaining even higher  $zT$  values of the  $\text{Ca}_3\text{Co}_4\text{O}_9$ -based ceramics still remains in the relatively low electrical conductivity; despite all the efforts it is still much lower in comparison to the single crystals, reaching values of typically just a few 100S/cm, which is at least several times if not for an order of magnitude too low for a significant breakthrough in the obtained  $zT$  values. Nanostructuring, optimization of microstructure, and doping have so far been effective in the enhancement of the thermopower S to the values for single crystals, and also to decrease the thermal conductivity to 1W/mK and lower, much below that for single crystals of  $\text{Ca}_3\text{Co}_4\text{O}_9$ .

## 2.10.4 A toolbox to enhance the thermoelectric performance of oxide materials

A top-down approach in the research and development of thermoelectric oxide materials in recent decades has resulted in extensive knowledge with an insight into the influence of composition, structure, and microstructure on the phenomena of charge

and heat transport and consequently their thermoelectric performance. Basically, we have tools now for tailoring the thermoelectric performance of oxide materials. Doping proved to be an effective way for significant enhancement of electrical conductivity, but often in combination with a reduced thermopower caused by an increased charge-carrier concentration. However, we have good examples that appropriate doping enables a simultaneous increase in electrical conductivity and thermopower. In different ways, doping could also be effectively used to reduce thermal conductivity, while electrical conductivity is increased or not affected: (i) point defects increasing the disorder in the crystal lattice, (ii) segregation of fine nano-precipitates of secondary phases, and (iii) creation of additional interfaces in the grains like inversion boundaries. Grain boundaries can also reduce thermal conductivity; however, only at grain sizes of less than 100 nm. In this regard, the use of wet-chemical and other synthesis methods that result in fine nanopowders was confirmed as a winning approach, but only in combination with processing methods that preserve a fine-grained microstructure, like spark plasma sintering. At the same time these methods enable much better control of the chemical composition from the nanometer level, which was confirmed to bring forward also other advantages related to doping, either due to better compositional homogeneity, the possibility to create a compositional gradient, and a core-shell structure, and others. Nano- and mezzo-porosity can also contribute to reduced thermal conductivity without affecting either the electrical conductivity or the mechanical properties. A large density of grain boundaries in fine-grained ceramics unfortunately results in a decreased electrical conductivity. The problem could be effectively resolved by adding an appropriate conductive secondary phase to the grain boundaries, which can also be used to tune their energy-filtering effect for a higher thermopower.

Accordingly, we should start to consider the richness of structural and microstructural features as tools that open a challenging opportunity for us to enhance the thermoelectric performance of the polycrystalline oxide materials to values of  $zT$  beyond those of the single crystals. So now we have to find a way for bottom-up tailoring [241] of the oxide thermoelectric materials in a way to exploit through chemistry, synthesis, and processing different structural and microstructural features at all levels from nano to micro in an optimal way for the goal.

## 2.10.5 Summary

The main challenges in the development of thermoelectric polycrystalline oxide materials to reach  $zT$  values of 1 and higher, complying with the demands of applications, still remains the same; i.e., how to simultaneously control the transport of charge and heat for a high electrical conductivity and a high thermopower to gain a high power factor, and to obtain a low thermal conductivity. While these may be general guidelines, it could be perceived from the literature that each material requires a completely individual approach to addressing these challenges. In the case of ZnO and SrTiO<sub>3</sub>, high conductivities and power factors can be achieved by doping, while the reduction of thermal conductivity below 2 W/mK due to a simple structure composed of

lightweight elements represents a major milestone. In contrast, thermal conductivities below 1 W/mK are usual for  $\text{Ca}_3\text{Co}_4\text{O}_9$  with a complex misfit layered structure; however, raising the electrical conductivity to much more than several 100 S/cm is still unattainable. The limitations of individual solutions and the importance of integrating together from the nanolevel to the microlevel compositional, structural, and microstructural elements in a way to achieve the desired effect and thermoelectric properties are increasingly recognized in all these studies. How to achieve this begins to represent the essence of the problem, which brings to the forefront also the whole process of making the oxide materials.

## References

- [1] P. Brinks, M. Huijben, Thermoelectric oxides, in: G. Koster, M. Huijben, G. Rijnders (Eds.), *Epitaxial Growth of Complex Metal Oxides*, Elsevier, 2015, pp. 397–441.
- [2] L. Ji, Metal oxide-based thermoelectric materials, in: Y. Wu (Ed.), *Metal Oxides in Energy Technologies*, Elsevier, 2018, pp. 49–72.
- [3] Y. Feng, X. Jiang, E. Ghafari, B. Kucukgok, C. Zhang, I. Ferguson, N. Lu, Metal oxides for thermoelectric power generation and beyond, *Adv. Compos. Hybrid Mater.* 1 (2017) 114–126.
- [4] R. Funahashi, T. Barbier, E. Combe, Thermoelectric materials for middle and high temperature ranges, *J. Mater. Res.* 30 (2015) 2544–2557.
- [5] Y. Wu, T. van Ree, Introduction: Energy technologies and their role in our life, in: Y. Wu (Ed.), *Metal Oxides in Energy Technologies*, Elsevier, 2018, pp. 1–16.
- [6] Metal Oxides in Energy Technologies, Elsevier, 2019.
- [7] X. Zhang, L.-D. Zhao, Thermoelectric materials: energy conversion between heat and electricity, *J. Materiom.* 1 (2015) 92–105.
- [8] G. Rogl, P. Rogl, Skutterudites, a most promising group of thermoelectric materials, *Curr. Opin. Green Sustain. Chem.* 4 (2017) 50–57.
- [9] J. Heo, G. Laurita, S. Muir, M.A. Subramanian, D.A. Kesler, Enhanced thermoelectric performance of synthetic tetrahedrites, *Chem. Mater.* 26 (2014) 2047–2051.
- [10] Y. Yan, H. Wu, G. Wang, X. Lu, X. Zhou, High thermoelectric performance balanced by electrical and thermal transport in tetrahedrites  $\text{Cu}_{12+x}\text{Sb}_4\text{S}_{12}\text{Se}$ , *Energy Storage Mater.* 13 (2018) 127–133.
- [11] S.C. Shi Yixuan, Kleinke Holger Chalcogenides as thermoelectric materials, *J. Solid State Chem.* 270 (2019) 273–279.
- [12] I. Terasaki, Y. Sasago, K. Uchinokura, Large thermoelectric power in  $\text{NaCo}_2\text{O}_4$  single crystals, *Phys. Rev. B* 56 (1997), R12685.
- [13] G. Ren, J. Lan, C. Zeng, Y. Liu, B. Zhan, S. Butt, Y.-H. Lin, C.-W. Nan, High performance oxides-based thermoelectric materials, *JOM* 67 (2014) 211–221.
- [14] A. Nag, V. Shubha, Oxide thermoelectric materials: a structure–property relationship, *J. Electron. Mater.* 43 (2014) 962–977.
- [15] M. Backhaus-Ricoult, J. Rustad, L. Moore, C. Smith, J. Brown, Semiconducting large bandgap oxides as potential thermoelectric materials for high-temperature power generation? *Appl. Phys. A* 116 (2014) 433–470.
- [16] Y. Yin, B. Tudu, A. Tiwari, Recent advances in oxide thermoelectric materials and modules, *Vacuum* 146 (2017) 356–374.

- [17] J.W. Fergus, Oxide materials for high temperature thermoelectric energy conversion, *J. Eur. Ceram. Soc.* 32 (2012) 525–540.
- [18] K. Koumoto, Y. Wang, R. Zhang, A. Kosuga, R. Funahashi, Oxide thermoelectric materials: a nanostructuring approach, *Annu. Rev. Mat. Res.* 40 (2010) 363–394.
- [19] S. Walia, S. Balendhran, H. Nili, S. Zhuiykov, G. Rosengarten, Q.H. Wang, M. Bhaskaran, S. Sriram, M.S. Strano, K. Kalantar-zadeh, Transition metal oxides—thermoelectric properties, *Progr. Mater. Sci.* 58 (2013) 1443–1489.
- [20] M. Ohtaki, Recent aspects of oxide thermoelectric materials for power generation from mid-to-high temperature heat source, *J. Cerma. Soc. Jpn.* 119 (2011) 770–775.
- [21] J. He, Y. Liu, R. Funahashi, Oxide thermoelectrics: The challenges, progress, and outlook, *J. Mater. Res.* 26 (2011) 1762–1772.
- [22] N. Van Nong, N. Pryds, S. Linderoth, M. Ohtaki, Enhancement of the thermoelectric performance of p-type layered oxide  $\text{Ca}_3\text{Co}_4\text{O}_{9+\delta}$  through heavy doping and metallic nanoinclusions, *Adv. Mater.* 23 (2011) 2484–2490.
- [23] H. Ohta, S. Kim, Y. Mune, T. Mizoguchi, K. Nomura, S. Ohta, T. Nomura, Y. Nakanishi, Y. Ikuhara, M. Hirano, H. Hosono, K. Koumoto, Giant thermoelectric Seebeck coefficient of a two-dimensional electron gas in  $\text{SrTiO}_3$ , *Nat. Mater.* 6 (2007) 129–134.
- [24] R. Funahashi, I. Matsubara, H. Ikuta, T. Takeuchi, U. Mizutani, S. Sodeoka, An oxide single crystal with high thermoelectric performance in air, *Jpn. J. Appl. Phys.* 39 (2000) L1127.
- [25] J. Ravichandran, Thermoelectric and thermal transport properties of complex oxide thin films, heterostructures and superlattices, *J. Mater. Res.* 32 (2017) 183–203.
- [26] M.-H. Hong, H. Choi, D.I. Shim, H.H. Cho, J. Kim, H.-H. Park, Study of the effect of stress/strain of mesoporous Al-doped ZnO thin films on thermoelectric properties, *Solid State Sci.* 82 (2018) 84–91.
- [27] P. Mele, S.J. Singh, S. Saini, A.K. Jha, M.I. Adam, Nanostructured oxide thin films for sustainable development, *Proc. Eng.* 171 (2017) 201–206.
- [28] A.T.T. Pham, H.K.T. Ta, Y.-r. Liu, M. Aminzare, D.P. Wong, T.H. Nguyen, N.K. Pham, T.B.N. Le, T. Seetawan, H. Ju, S. Cho, K.-H. Chen, V.C. Tran, T.B. Phan, Effect of annealing temperature on thermoelectric properties of Ga and In dually doped-ZnO thin films, *J. Alloys Compd.* 747 (2018) 156–165.
- [29] T. Schulz, T. Reimann, A. Bochmann, A. Vogel, B. Capraro, B. Mieller, S. Teichert, J. Töpfer, Sintering behavior, microstructure and thermoelectric properties of calcium cobaltite thick films for transversal thermoelectric multilayer generators, *J. Eur. Ceram. Soc.* 38 (2018) 1600–1607.
- [30] G. Kieslich, G. Cerretti, I. Veremchuk, R.P. Hermann, M. Panthöfer, J. Grin, W. Tremel, A chemists view: Metal oxides with adaptive structures for thermoelectric applications, *Phys. Status Solidi A* 213 (2016) 808–823.
- [31] G. Korotcenkov, V. Brinzari, M.-H. Ham,  $\text{In}_2\text{O}_3$ -based thermoelectric materials: the state of the art and the role of surface state in the improvement of the efficiency of thermoelectric conversion, *Crystals* 8 (2018) 14.
- [32] V.A. Coleman, C. Jagadish, *Basic properties and applications of ZnO, Zinc Oxide Bulk, Thin Films and Nanostructures*, Elsevier, 2006.
- [33] A. Janotti, C.G. Van de Walle, Fundamentals of zinc oxide as a semiconductor, *Rep. Prog. Phys.* 72 (2009) 126501.
- [34] K. Ellmer, A. Bikowski, Intrinsic and extrinsic doping of ZnO and ZnO alloys, *J. Phys. D Appl. Phys.* 49 (2016) 413002.
- [35] A. Janotti, C.G. Van de Walle, Native point defects in ZnO, *Phys. Rev. B* 76 (2007) 165202.

- [36] K. Tang, S.-L. Gu, J.-D. Ye, S.-M. Zhu, R. Zhang, Y.-D. Zheng, Recent progress of the native defects and p-type doping of zinc oxide, *Chin. Phys. B* 26 (2017), 047702.
- [37] Y.-B. Hahn, Zinc oxide nanostructures and their applications, *Korean J. Chem. Eng.* 28 (2011) 1797–1813.
- [38] A.B. Djurišić, X. Chen, Y.H. Leung, A. Man Ching Ng, ZnO nanostructures: growth, properties and applications, *J. Mater. Chem.*, 22 (2012) 6526.
- [39] R. Okazaki, A. Horikawa, Y. Yasui, I. Terasaki, Photo-seebeck effect in ZnO, *J. Physical Soc. Japan* 81 (2012) 114722.
- [40] A. Horikawa, T. Igarashi, I. Terasaki, R. Okazaki, Photo-seebeck effect in polycrystalline ZnO, *J. Appl. Phys.* 118 (2015), 095101.
- [41] J.G. Reynolds, C.L. Reynolds, Progress in ZnO acceptor doping: What is the best strategy? *Adv. Condens. Matter Phys.* 2014 (2014) 1–15.
- [42] L.J.W. Xufei, V. Vikas, J.L. Wohlwend, K. Roy Ajit, L. Tengfei, Thermal conductivity of Wurtzite zinc-oxide from first-principles lattice dynamics—a comparative study with gallium nitride, *Sci. Rep.* 6 (2016) 10.
- [43] T.K. Gupta, Application of zinc oxide varistors, *J. Am. Ceram. Soc.* 73 (1990) 1817–1840.
- [44] D.R. Clarke, Varistor ceramics, *J. Am. Ceram. Soc.* 82 (1999) 485–502.
- [45] S. Bernik, N. Daneu, Characteristics of ZnO-based varistor ceramics doped with Al<sub>2</sub>O<sub>3</sub>, *J. Eur. Ceram. Soc.* 27 (2007) 3161–3170.
- [46] R. Seshadri, Zinc oxide-based diluted magnetic semiconductors, *Curr. Opin. Solid State Mater. Sci.* 9 (2005) 1–7.
- [47] S. Lany, H. Raebiger, A. Zunger, Magnetic interactions of Cr – Cr and Co – Co impurity pairs in ZnO within a band-gap corrected density functional approach, *Phys. Rev. B* 77 (2008).
- [48] Y. Li, Y. Li, M. Zhu, T. Yang, J. Huang, H. Jin, Y. Hu, Structure and magnetic properties of Cr-doped ZnO nanoparticles prepared under high magnetic field, *Solid State Commun.* 150 (2010) 751–754.
- [49] C.-L. Tsai, Y.-J. Lin, J.-H. Chen, H.-C. Chang, Y.-H. Chen, L. Horng, Y.-T. Shih, On the origin of the ferromagnetism in Zn<sub>0.8</sub>Mn<sub>0.2</sub>O having a higher Curie temperature than Zn<sub>0.8</sub>Co<sub>0.2</sub>O, *Solid State Commun.* 152 (2012) 488–492.
- [50] Z.H. Wu, H.Q. Xie, Y.B. Zhai, Preparation and thermoelectric properties of Co-doped ZnO synthesized by sol-gel, *J. Nanosci. Nanotechnol.* 15 (2015) 3147–3150.
- [51] X.H.W. Zihua, W. Yuanyuan, X. Jiaoqiao, M. Jianhui, Thermoelectric properties of co-doped ZnO by incorporating organic nanoparticles, *Rare Met. Mater. Eng.* 47 (2018) 452–456.
- [52] A. Baranovskiy, I. Koresh, Y. Amouyal, Tuning transport properties of nickel-doped zinc oxide for thermoelectric applications, *MRS Commun.* 8 (2018) 858–864.
- [53] I. Koresh, Y. Amouyal, Effects of microstructure evolution on transport properties of thermoelectric nickel-doped zinc oxide, *J. Eur. Ceram. Soc.* 37 (2017) 3541–3550.
- [54] M. Ohtaki, T. Tsubota, K. Eguchi, H. Arai, High-temperature thermoelectric properties of (Zn<sub>1-x</sub>Al<sub>x</sub>)O, *J. Appl. Phys.* 79 (1996) 1816–1818.
- [55] T. Tsubota, M. Ohtaki, K. Eguchi, H. Arai, Thermoelectric properties of Al-doped ZnO as a promising oxidematerial for high-temperature thermoelectric conversion, *J. Mater. Chem.* 7 (1997) 85–90.
- [56] K.F. Cai, E. Müller, C. Drašar, A. Mrotzek, Preparation and thermoelectric properties of Al-doped ZnO ceramics, *Mater. Sci. Eng. B* 104 (2003) 45–48.
- [57] D. Bérardan, C. Byl, N. Dragoe, Influence of the preparation conditions on the thermoelectric properties of Al-doped ZnO, *J. Am. Ceram. Soc.* 93 (2010) 2352–2358.

- [58] N. Ma, J.F. Li, B.P. Zhang, Y.H. Lin, L.R. Ren, G.F. Chen, Microstructure and thermoelectric properties of  $Zn_{1-x}Al_xO$  ceramics fabricated by spark plasma sintering, *J. Phys. Chem. Solid* 71 (2010) 1344–1349.
- [59] X. Qu, W. Wang, S. Lv, D. Jia, Thermoelectric properties and electronic structure of Al-doped ZnO, *Solid State Commun.* 151 (2011) 332–336.
- [60] W.H. Nam, Y.S. Lim, S.-M. Choi, W.-S. Seo, J.Y. Lee, High-temperature charge transport and thermoelectric properties of a degenerately Al-doped ZnO nanocomposite, *J. Mater. Chem.* 22 (2012) 14633–14638.
- [61] L. Han, N. Van Nong, W. Zhang, L.T. Hung, T. Holgate, K. Tashiro, M. Ohtaki, N. Pryds, S. Linderoth, Effects of morphology on the thermoelectric properties of Al-doped ZnO, *RSC Adv.* 4 (2014) 12353.
- [62] Y. Zhao, B. Chen, A. Miner, S. Priya, Low thermal conductivity of Al-doped ZnO with layered and correlated grains, *RSC Adv.* 4 (2014) 18370.
- [63] P. Díaz-Chao, F. Giovannelli, O. Lebedev, D. Chateigner, L. Lutterotti, F. Delorme, E. Guilmeau, Textured Al-doped ZnO ceramics with isotropic grains, *J. Eur. Ceram. Soc.* 34 (2014) 4247–4256.
- [64] D. Gautam, M. Engenhorst, C. Schilling, G. Schierning, R. Schmeichel, M. Winterer, Thermoelectric properties of pulsed current sintered nanocrystalline Al-doped ZnO by chemical vapour synthesis, *J. Mater. Chem. A* 3 (2015) 189–197.
- [65] D.-B. Zhang, B.-P. Zhang, D.-S. Ye, Y.-B. Zhu, Thermoelectric properties of textured  $Zn_{1-x}Al_xO$  ceramics prepared by spark plasma sintering of hydrothermally synthesized rod-shaped powders, *Ceram. Int.* 41 (2015) 14627–14634.
- [66] S. Jantrasee, P. Moontragoon, S. Pinitsoontorn, Thermoelectric properties of Al-doped ZnO: experiment and simulation, *J. Semicond.* 37 (2016), 092002.
- [67] J. Hoemke, A.U. Khan, H. Yoshida, T. Mori, E. Tochigi, N. Shibata, Y. Ikuhara, Y. Sakka, Sintering characteristics and thermoelectric properties of Mn-Al co-doped ZnO ceramics, *J. Cerma. Soc. Jpn.* 124 (2016) 515–522.
- [68] D.-B. Zhang, H.-Z. Li, B.-P. Zhang, D.-d. Liang, M. Xia, Hybrid-structured ZnO thermoelectric materials with high carrier mobility and reduced thermal conductivity, *RSC Adv.* 7 (2017) 10855–10864.
- [69] M. Ullah, W. Chunlei, W. Su, D. Liu, A. Zaman, Thermoelectric properties of Al-doped zinc oxide-based ceramics sintered at high temperature under different atmospheres, *J. Mater. Sci. Mater. Electron.* 30 (2019) 8611–8618.
- [70] T. Tian, L. Cheng, L. Zheng, J. Xing, H. Gu, S. Bernik, H. Zeng, W. Ruan, K. Zhao, G. Li, Defect engineering for a markedly increased electrical conductivity and power factor in doped ZnO ceramic, *Acta Mater.* 119 (2016) 136–144.
- [71] T. Tian, L. Cheng, J. Xing, L. Zheng, Z. Man, D. Hu, S. Bernik, J. Zeng, J. Yang, Y. Liu, G. Li, Effects of sintering on the microstructure and electrical properties of ZnO-based thermoelectric materials, *Mater. Des.* 132 (2017) 479–485.
- [72] O.T. Shirouzu Keita, M.H. Mikinory, E. Naoya, H. Junichi, Distribution and solubility of Al in  $Al_2O_3$  doped ZnO sintered body, *J. Chem. Soc. Jpn.* 115 (2007) 254–258.
- [73] H. Serier, M. Gaudon, M. Ménétrier, Al-doped ZnO powdered materials: Al solubility limit and IR absorption properties, *Solid State Sci.* 11 (2009) 1192–1197.
- [74] K.V. Zakharchuk, M. Widemann, D.O. Alikin, W. Xie, S. Populoh, S.M. Mikhalev, A. Tselev, J.R. Frade, A. Weidenkaff, A.V. Kovalevsky, A self-forming nanocomposite concept for ZnO-based thermoelectrics, *J. Mater. Chem. A* 6 (2018) 13386–13396.
- [75] P. Jood, R.J. Mehta, Y. Zhang, G. Peleckis, X. Wang, R.W. Siegel, T. Borca-Tasciuc, S.X. Dou, G. Ramanath, Al-doped zinc oxide nanocomposites with enhanced thermoelectric properties, *Nano Lett.* 11 (2011) 4337–4342.

- [76] S. Yang, F. Chen, Q. Shen, L. Zhang, Microstructure and electrical property of aluminum doped zinc oxide ceramics by isolating current under spark plasma sintering, *J. Eur. Ceram. Soc.* 36 (2016) 1953–1959.
- [77] F. Giovannelli, C. Chen, P. Díaz-Chao, E. Guilmeau, F. Delorme, Thermal conductivity and stability of Al-doped ZnO nanostructured ceramics, *J. Eur. Ceram. Soc.* 38 (2018) 5015–5020.
- [78] D.-B. Zhang, B.-P. Zhang, P.-P. Shang, C. Gao, Y.-Q. Zhang, Effect of  $ZnAl_2O_4$  phase on thermoelectric properties of Al doped ZnO ceramics fabricated by spark plasma sintering, *Mater. Res. Innovat.* 18 (2014) S4-110–S114-115.
- [79] C. Dreßler, R. Löhnert, J. Gonzalez-Julian, O. Guillou, J. Töpfer, S. Teichert, Effect of Carbon Nanotubes on Thermoelectric Properties in  $Zn_{0.98}Al_{0.02}O$ , *J. Electron. Mater.* 45 (2015) 1459–1463.
- [80] W.H. Nam, B.B. Kim, Y.S. Lim, K.S. Dae, W.S. Seo, H.H. Park, J.Y. Lee, Phonon-glass electron-crystals in ZnO-multiwalled carbon nanotube nanocomposites, *Nanoscale* 9 (2017) 12941–12948.
- [81] B. Zhu, D. Li, T. Zhang, Y. Luo, R. Donelson, T. Zhang, Y. Zheng, C. Du, L. Wei, H.H. Hng, The improvement of thermoelectric property of bulk ZnO via ZnS addition: Influence of intrinsic defects, *Ceram. Int.* 44 (2018) 6461–6465.
- [82] J. Barf, T. Walther, W. Mader, Twin boundaries in zinc oxide with additions of gallium oxide, *Interface Sci.* 12 (2004) 213–226.
- [83] H. Schmid, E. Okunishi, T. Oikawa, W. Mader, Structural and elemental analysis of iron and indium doped zinc oxide by spectroscopic imaging in Cs-corrected STEM, *Micron* 43 (2012) 49–56.
- [84] X. Liang, Thermoelectric transport properties of naturally nanostructured Ga-ZnO ceramics: Effect of point defect and interfaces, *J. Eur. Ceram. Soc.* 36 (2016) 1643–1650.
- [85] X. Liang, L. Shen, C. Wang, Origin of anisotropy and compositional dependence of phonon and electron transport in ZnO based natural superlattices and role of atomic layer interfaces, *Nano Energy* 59 (2019) 651–666.
- [86] X. Liang, M. Baram, D.R. Clarke, Thermal (Kapitza) resistance of interfaces in compositional dependent ZnO-In<sub>2</sub>O<sub>3</sub> superlattices, *Appl. Phys. Lett.* 102 (2013) 223903.
- [87] X. Liang, Remarkable enhancement in the Kapitza resistance and electron potential barrier of chemically modified In<sub>2</sub>O<sub>3</sub>(ZnO)<sub>9</sub> natural superlattice interfaces, *Phys. Chem. Chem. Phys.* 17 (2015) 29655–29660.
- [88] X. Liang, D.R. Clarke, Single layer In-O atomic sheets as phonon and electron barriers in ZnO-In<sub>2</sub>O<sub>3</sub> natural superlattices: Implications for thermoelectricity, *J. Appl. Phys.* 124 (2018), 025101.
- [89] X. Liang, Recasting the Callaway and von Baeyer thermal conductivity model on defective oxide materials: the ZnO-In<sub>2</sub>O<sub>3</sub> system as an example, *Phys. Chem. Chem. Phys.* 17 (2015) 27889–27893.
- [90] M. Ohtaki, K. Araki, K. Yamamoto, High thermoelectric performance of dually doped ZnO ceramics, *J. Electron. Mater.* 38 (2009) 1234–1238.
- [91] P. Sikam, P. Moontragoon, Z. Ikonic, T. Kaewmaraya, P. Thongbai, The study of structural, morphological and optical properties of (Al, Ga)-doped ZnO: DFT and experimental approaches, *Appl. Surf. Sci.* 480 (2019) 621–635.
- [92] M. Ullah, W. Bin Su, A. Manan, A.S. Ahmad, A.A. Shah, Z. Yao, Phase, microstructural investigation and thermoelectric properties of Ga-doped zinc oxide-based ceramics sintered under an argon atmosphere, *Ceram. Int.* 44 (2018) 17873–17877.
- [93] C.L. Matiullah, W.B. Wang, A. Su, I. Zaman, J.Z. Ullah, D.K. Zhai, Liu, Effects of sintering atmospheres on thermoelectric properties, phase, microstructure and lattice

- parameters c/a ratio of Al, Ga dual doped ZnO ceramics sintered at high temperature, *J. Mater. Sci. Mater. Electron.* 29 (2018) 9555–9563.
- [94] L. Han, L.T. Hung, N. van Nong, N. Pryds, S. Linderoth, The influence of spark plasma sintering temperature on the microstructure and thermoelectric properties of Al,Ga dual-doped ZnO, *J. Electron. Mater.* 42 (2012) 1573–1581.
  - [95] K.-H. Jung, S.-M. Choi, C.-H. Lim, W.-S. Seo, H.-H. Park, Phase analysis and thermoelectric properties of  $Zn_{1-x}M_xO$  ( $M = Al, Ga$ ) samples, *Surf. Interface Anal.* 44 (2012) 1507–1510.
  - [96] L. Brockway, V. Vasiraju, M.K. Sunkara, S. Vaddiraju, Engineering efficient thermoelectrics from large-scale assemblies of doped ZnO nanowires: nanoscale effects and resonant-level scattering, *ACS Appl. Mater. Interfaces* 6 (2014) 14923–14930.
  - [97] S. Jantrasee, P. Moontragoon, S. Pinitsoontorn, C. Ruttanapun, Enhancing thermoelectric properties of nanostructure Ga-doped ZnO prepared by microwave-hydrothermal synthesizing with comparing to calculation results, *Mater. Res. Expr.* 6 (2019), 045047.
  - [98] D.T. Alvarez-Ruiz, F. Azough, D. Hernandez-Maldonado, D.M. Kepartsoglou, Q.M. Ramasse, S.J. Day, P. Svec, P. Svec, R. Freer, Utilising unit-cell twinning operators to reduce lattice thermal conductivity in modular structures: Structure and thermoelectric properties of  $Ga_2O_3(ZnO)_9$ , *J. Alloys Compd.* 762 (2018) 892–900.
  - [99] Y. Michiue, H. Nishijima, Y. Suzuki, T. Mori, Synthesis and thermoelectric properties of composite oxides in the pseudobinary system  $ZnO$ - $Ga_2O_3$ , *Solid State Sci.* 65 (2017) 29–32.
  - [100] E. Guilmeau, P. Diaz-Chao, O.I. Lebedev, A. Recnik, M.C. Schafer, F. Delorme, F. Giovannelli, M. Kosir, S. Bernik, Inversion boundaries and phonon scattering in  $Ga$ :ZnO thermoelectric compounds, *Inorg. Chem.* 56 (2017) 480–487.
  - [101] M. Košir, M. Podlogar, N. Daneu, A. Rečnik, E. Guilmeau, S. Bernik, Phase formation, microstructure development and thermoelectric properties of  $(ZnO)_kIn_2O_3$  ceramics, *J. Eur. Ceram. Soc.* 37 (2017) 2833–2842.
  - [102] A. Rečnik, N. Daneu, S. Bernik, Nucleation and growth of basal-plane inversion boundaries in ZnO, *J. Eur. Ceram. Soc.* 27 (2007) 1999–2008.
  - [103] L.M. Wang, C.-Y. Chang, S.-T. Yeh, S.W. Chen, Z.A. Peng, S.C. Bair, D.S. Lee, F.C. Liao, Y.K. Kuo, Synthesis and post-annealing effects on the transport properties of thermoelectric oxide  $(ZnO)_mIn_2O_3$  ceramics, *Ceram. Int.* 38 (2012) 1167–1174.
  - [104] M. Amani, I.M. Tougas, O.J. Gregory, G.C. Fralick, High-temperature thermoelectric properties of compounds in the system  $Zn_xIn_yO_{x+1.5y}$ , *J. Electron. Mater.* 42 (2012) 114–120.
  - [105] L.-J. Cui, Z.-H. Ge, P. Qin, J. Feng, Enhanced thermoelectric properties of  $In_2O_3(ZnO)_5$  intrinsic superlattice ceramics by optimizing the sintering process, *RSC Adv.* 7 (2017) 49883–49889.
  - [106] M. Ullah, W. Chunlei, W.-B. Su, A. Manan, A.S. Ahmad, A.U. Rehman, Thermoelectric properties of indium-doped zinc oxide sintered in an argon atmosphere, *J. Mater. Sci. Mater. Electron.* 30 (2019) 4813–4818.
  - [107] X. Liang, D.R. Clarke, Relation between thermoelectric properties and phase equilibria in the  $ZnO$ - $In_2O_3$  binary system, *Acta Mater.* 63 (2014) 191–201.
  - [108] J.B. Labegorre, O.I. Lebedev, C. Bourges, A. Recnik, M. Kosir, S. Bernik, A. Maignan, T. Le Mercier, L. Pautrot-d'Alencon, E. Guilmeau, Phonon scattering and electron doping by 2D structural defects in In/ZnO, *ACS Appl. Mater. Interfaces* 10 (2018) 6415–6423.
  - [109] H. Peng, J.-H. Song, E.M. Hopper, Q. Zhu, T.O. Mason, A.J. Freeman, Possible n-type carrier sources in  $In_2O_3(ZnO)_k$ , *Chem. Mater.* 24 (2011) 106–114.

- [110] M. Ullah, C. Wang, W.-B. Su, J. Li, A. Manan, I. Ullah, M. Idrees, Thermoelectric properties, phase analysis, microstructural investigation and lattice parameters c/a ratio of Al<sup>3+</sup> and In<sup>3+</sup> dual-doped zinc oxide-based ceramics sintered at high temperature under an argon atmosphere, *Mater. Sci. Semicond. Process.* 87 (2018) 202–206.
- [111] X. Liang, L. Shen, Optimizing interfacial transport properties of InO<sub>2</sub> single atomic layers in In<sub>2</sub>O<sub>3</sub>(ZnO)<sub>4</sub> natural superlattices for enhanced high temperature thermoelectrics, *Nanoscale* 10 (2018) 4500–4514.
- [112] M. Košir, M. Čeh, C.W. Ow-Yang, E. Guilmeau, S. Bernik, Structural features and thermoelectric properties of Al-doped (ZnO)<sub>5</sub>In<sub>2</sub>O<sub>3</sub> homologous phases, *J. Am. Ceram. Soc.* 100 (2017) 3712–3721.
- [113] D.T. Alvarez-Ruiz, F. Azough, M. Hernandez, D.M.K. David, Q.M. Ramasse, P. Svec, P. Svec, R. Freer, Enhancement of electrical conduction and phonon scattering in Ga<sub>2</sub>O<sub>3</sub>(ZnO)<sub>9</sub>-In<sub>2</sub>O<sub>3</sub>(ZnO)<sub>9</sub> compounds by modification of interfaces at the nanoscale, *J. Electron. Mater.* 48 (2018) 1818–1826.
- [114] H. Takemoto, K. Fugane, P. Yan, J. Drennan, M. Saito, T. Mori, H. Yamamura, Reduction of thermal conductivity in dually doped ZnO by design of three-dimensional stacking faults, *RSC Adv.* 4 (2014) 2661–2672.
- [115] J. Hoemke, E. Tochigi, T. Tohei, H. Yoshida, N. Shibata, Y. Ikuhara, Y. Sakka, Inversion domain boundaries in Mn and Al dual-doped ZnO: Atomic structure and electronic properties, *J. Am. Ceram. Soc.* 100 (2017) 4252–4262.
- [116] J. Hoemke, E. Tochigi, T. Tohei, H. Yoshida, N. Shibata, Y. Ikuhara, Y. Sakka, Inversion domain network stabilization and spinel phase suppression in ZnO, *J. Am. Ceram. Soc.* 101 (2018) 2616–2626.
- [117] J. Hoemke, A.U. Khan, H. Yoshida, T. Mori, E. Tochigi, N. Shibata, Y. Ikuhara, Y. Sakka, Microstructural analysis and thermoelectric properties of Sn-Al co-doped ZnO ceramics, *AIP Conf. Proc.* 1763 (2016). 050004.
- [118] T. Wu, P. Gao, Development of Perovskite-type materials for thermoelectric application, *Materials* 11 (2018) 999.
- [119] H. Wang, W. Su, J. Liu, C. Wang, Recent development of n-type perovskite thermoelectrics, *J. Materiom.* 2 (2016) 225–236.
- [120] J.U. Rahman, W.H. Nam, N. Van Du, G. Rahman, A.U. Rahman, W.H. Shin, W.-S. Seo, M.H. Kim, S. Lee, Oxygen vacancy revived phonon-glass electron-crystal in SrTiO<sub>3</sub>, *J. Eur. Ceram. Soc.* 39 (2019) 358–365.
- [121] P.A. Sharma, H.J. Brown-Shaklee, J.F. Ihlefeld, Oxygen partial pressure dependence of thermoelectric power factor in polycrystalline n-type SrTiO<sub>3</sub>: Consequences for long term stability in thermoelectric oxides, *Appl. Phys. Lett.* 110 (2017) 173901.
- [122] P. Blennow, A. Hagen, K. Hansen, L. Wallenberg, M. Mogensen, Defect and electrical transport properties of Nb-doped SrTiO<sub>3</sub>, *Solid State Ion.* 179 (2008) 2047–2058.
- [123] J.-B. Li, J. Wang, J.-F. Li, Y. Li, H. Yang, H.-Y. Yu, X.-B. Ma, X. Yaer, L. Liu, L. Miao, Broadening the temperature range for high thermoelectric performance of bulk polycrystalline strontium titanate by controlling the electronic transport properties, *J. Mater. Chem. C* 6 (2018) 7594–7603.
- [124] J. Wang, B.-Y. Zhang, H.-J. Kang, Y. Li, X. Yaer, J.-F. Li, Q. Tan, S. Zhang, G.-H. Fan, C.-Y. Liu, L. Miao, D. Nan, T.-M. Wang, L.-D. Zhao, Record high thermoelectric performance in bulk SrTiO<sub>3</sub> via nano-scale modulation doping, *Nano Energy* 35 (2017) 387–395.
- [125] K.-X. Wang, J. Wang, Y. Li, T. Zou, X.-H. Wang, J.-B. Li, Z. Cao, W.-J. Shi, X. Yaer, Enhancement of thermoelectric properties of SrTiO<sub>3</sub>/LaNb–SrTiO<sub>3</sub> composite by different doping levels, *Chin. Phys. B* 27 (2018), 048401.

- [126] L.M. Daniels, S. Ling, S.N. Savvin, M.J. Pitcher, M.S. Dyer, J.B. Claridge, B. Slater, F. Corà, J. Alaria, M.J. Rosseinsky, A and B site doping of a phonon-glass perovskite oxide thermoelectric, *J. Mater. Chem. A* 6 (2018) 15640–15652.
- [127] A.A. Yaremchenko, S. Populoh, S.G. Patrício, J. Macías, P. Thiel, D.P. Fagg, A. Weidenkaff, J.R. Frade, A.V. Kovalevsky, Boosting thermoelectric performance by controlled defect chemistry engineering in Ta-substituted strontium titanate, *Chem. Mater.* 27 (2015) 4995–5006.
- [128] A.V. Kovalevsky, A.A. Yaremchenko, S. Populoh, A. Weidenkaff, J.R. Frade, Effect of A-site cation deficiency on the thermoelectric performance of donor-substituted strontium titanate, *J. Phys. Chem. C* 118 (2014) 4596–4606.
- [129] A.V. Kovalevsky, M.H. Aguirre, S. Populoh, S.G. Patrício, N.M. Ferreira, S.M. Mikhalev, D.P. Fagg, A. Weidenkaff, J.R. Frade, Designing strontium titanate-based thermoelectrics: insight into defect chemistry mechanisms, *J. Mater. Chem. A* 5 (2017) 3909–3922.
- [130] A.M. Dehkordi, S. Bhattacharya, J. He, H.N. Alshareef, T.M. Tritt, Significant enhancement in thermoelectric properties of polycrystalline Pr-doped  $\text{SrTiO}_3-\delta$  ceramics originating from nonuniform distribution of Pr dopants, *Appl. Phys. Lett.* 104 (2014) 193902.
- [131] A.M. Dehkordi, S. Bhattacharya, T. Darroudi, J.W. Graff, U. Schwingenschlögl, H.N. Alshareef, T.M. Tritt, Large thermoelectric power factor in Pr-doped  $\text{SrTiO}_3-\delta$  ceramics via grain-boundary-induced mobility enhancement, *Chem. Mater.* 26 (2014) 2478–2485.
- [132] A.M. Dehkordi, S. Bhattacharya, T. Darroudi, H.N. Alshareef, T.M. Tritt, New insights on the synthesis and electronic transport in bulk polycrystalline Pr-doped  $\text{SrTiO}_3-\delta$ , *J. Appl. Phys.* 117 (2015), 055102.
- [133] D. Srivastava, C. Norman, F. Azough, M.C. Schafer, E. Guilmeau, D. Kepaptsoglou, Q.M. Ramasse, G. Nicotra, R. Freer, Tuning the thermoelectric properties of A-site deficient  $\text{SrTiO}_3$  ceramics by vacancies and carrier concentration, *Phys. Chem. Chem. Phys.* 18 (2016) 26475–26486.
- [134] F. Azough, S.S. Jackson, D. Ekren, R. Freer, M. Molinari, S.R. Yeandel, P.M. Panchmatia, S.C. Parker, D.H. Maldonado, D.M. Kepaptsoglou, Q.M. Ramasse, Concurrent La and A-Site vacancy doping modulates the thermoelectric response of  $\text{SrTiO}_3$ : experimental and computational evidence, *ACS Appl. Mater. Interfaces* 9 (2017) 41988–42000.
- [135] S.R. Popuri, R. Decourt, J.A. McNulty, M. Pollet, A.D. Fortes, F.D. Morrison, M.S. Senn, J.W.G. Bos, Phonon-glass and heterogeneous electrical transport in A-site-deficient  $\text{SrTiO}_3$ , *J. Phys. Chem. C* 123 (2019) 5198–5208.
- [136] Z. Lu, H. Zhang, W. Lei, D.C. Sinclair, I.M. Reaney, High-figure-of-merit thermoelectric La-doped A-site-deficient  $\text{SrTiO}_3$  ceramics, *Chem. Mater.* 28 (2016) 925–935.
- [137] T. Okuda, H. Hata, T. Eto, S. Sobaru, R. Oda, H. Kaji, K. Nishina, H. Kuwahara, M. Nakamura, R. Kajimoto, Effects of Mn substitution on the thermoelectric properties and thermal excitations of the electron-doped perovskite  $\text{Sr}_{1-x}\text{La}_x\text{TiO}_3$ , *J. Physical Soc. Japan* 85 (2016), 094717.
- [138] R. Kajimoto, M. Nakamura, N. Murai, S.I. Shamoto, T. Honda, K. Ikeda, T. Otomo, H. Hata, T. Eto, M. Noda, H. Kuwahara, T. Okuda, Elastic and dynamical structural properties of La and Mn-doped  $\text{SrTiO}_3$  studied by neutron scattering and their relation with thermal conductivities, *Sci. Rep.* 8 (2018) 9651.
- [139] J. Han, Q. Sun, Y. Song, Enhanced thermoelectric properties of La and Dy co-doped, Sr-deficient  $\text{SrTiO}_3$  ceramics, *J. Alloys Compd.* 705 (2017) 22–27.
- [140] C. Chen, T. Zhang, R. Donelson, T.T. Tan, S. Li, Effects of yttrium substitution and oxygen deficiency on the crystal phase, microstructure, and thermoelectric properties of  $\text{Sr}_{1-1.5x}\text{Y}_x\text{TiO}_3-\delta$  ( $0 \leq x \leq 0.15$ ), *J. Alloys Compd.* 629 (2015) 49–54.

- [141] A. Tkach, J.O. Resende, K.V. Saravanan, M.E. Costa, P. Diaz-Chao, E. Guilmeau, O. Okhay, P.M. Vilarinho, Abnormal grain growth as a method to enhance the thermoelectric performance of Nb-doped strontium titanate ceramics, *ACS Sustain. Chem. Eng.* 6 (2018) 15988–15994.
- [142] J. Wang, X. Ye, X. Yaer, B. Zhang, W. Ma, L. Miao, High thermoelectric performance of niobium-doped strontium titanate bulk material affected by all-scale grain boundary and inclusions, *Scr. Mater.* 99 (2015) 25–28.
- [143] D. Ekren, F. Azough, A. Gholinia, S.J. Day, D. Hernandez-Maldonado, D.M. Kepaptsoglou, Q.M. Ramasse, R. Freer, Enhancing the thermoelectric power factor of  $\text{Sr}_{0.9}\text{Nd}_{0.1}\text{TiO}_3$  through control of the nanostructure and microstructure, *J. Mater. Chem. A* 6 (2018) 24928–24939.
- [144] M.T. Buscaglia, F. Maglia, U. Anselmi-Tamburini, D. Marré, I. Pallecchi, A. Ianculescu, G. Canu, M. Viviani, M. Fabrizio, V. Buscaglia, Effect of nanostructure on the thermal conductivity of La-doped  $\text{SrTiO}_3$  ceramics, *J. Eur. Ceram. Soc.* 34 (2014) 307–316.
- [145] X. Feng, Y. Fan, N. Nomura, K. Kikuchi, L. Wang, W. Jiang, A. Kawasaki, Graphene promoted oxygen vacancies in perovskite for enhanced thermoelectric properties, *Carbon* 112 (2017) 169–176.
- [146] Y. Lin, C. Norman, D. Srivastava, F. Azough, L. Wang, M. Robbins, K. Simpson, R. Freer, I.A. Kinloch, Thermoelectric power generation from lanthanum strontium titanium oxide at room temperature through the addition of graphene, *ACS Appl. Mater. Interfaces* 7 (2015) 15898–15908.
- [147] J.U. Rahman, N.V. Du, W.H. Nam, W.H. Shin, K.H. Lee, W.S. Seo, M.H. Kim, S. Lee, Grain boundary interfaces controlled by reduced graphene oxide in nonstoichiometric  $\text{SrTiO}_{3-\delta}$  thermoelectrics, *Sci. Rep.* 9 (2019) 8624.
- [148] C. Wu, J. Li, Y. Fan, J. Xing, H. Gu, Z. Zhou, X. Lu, Q. Zhang, L. Wang, W. Jiang, The effect of reduced graphene oxide on microstructure and thermoelectric properties of Nb-doped A-site-deficient  $\text{SrTiO}_3$  ceramics, *J. Alloys Compd.* 786 (2019) 884–893.
- [149] O. Okhay, S. Zlotnik, W. Xie, K. Orlinski, M.J. Hortiguela Gallo, G. Otero-Irurueta, A.J.S. Fernandes, D.A. Pawlak, A. Weidenkaff, A. Tkach, Thermoelectric performance of Nb-doped  $\text{SrTiO}_3$  enhanced by reduced graphene oxide and Sr deficiency cooperation, *Carbon* 143 (2019) 215–222.
- [150] D. Srivastava, C. Norman, F. Azough, M.C. Schäfer, E. Guilmeau, R. Freer, Improving the thermoelectric properties of  $\text{SrTiO}_3$ -based ceramics with metallic inclusions, *J. Alloys Compd.* 731 (2018) 723–730.
- [151] M. Qin, F. Gao, G. Dong, J. Xu, M. Fu, Y. Wang, M. Reece, H. Yan, Microstructure characterization and thermoelectric properties of  $\text{Sr}_{0.9}\text{La}_{0.1}\text{TiO}_3$  ceramics with nano-sized Ag as additive, *J. Alloys Compd.* 762 (2018) 80–89.
- [152] Y. Kinemuchi, K.-i. Mimura, K. Kato, Enhanced thermopower in nano- $\text{SrTiO}_3$  via rare earth doping, *J. Electron. Mater.* 44 (2014) 1773–1776.
- [153] Y.E. Putri, S.M. Said, R. Refinel, M. Ohtaki, S. Syukri, Low thermal conductivity of RE-doped  $\text{SrO}(\text{SrTiO}_3)_1$  Ruddlesden Popper phase bulk materials prepared by molten salt method, *Electron. Mater. Lett.* 14 (2018) 556–562.
- [154] Z. Lu, D.C. Sinclair, I.M. Reaney, X. Tan, The influence of La doping and heterogeneity on the thermoelectric properties of  $\text{Sr}_3\text{Ti}_2\text{O}_7$  ceramics, *J. Am. Ceram. Soc.* 99 (2016) 515–522.
- [155] R.R. Sun, L.N. Liu, G.L. Guo, J. Zhang, Y.S. Zhang, C.J. Tang, J.F. Su, D.M. Zhang, X.Y. An, Fabrication and thermoelectric properties of n-type Ruddlesden-Popper phase  $\text{Sr}_3(\text{Ti}_{1-x}\text{Ta}_x)_2\text{O}_7$  oxides, *ECS J. Solid State Sci. Technol.* 5 (2015) P151–P154.

- [156] R.R. Sun, X.Y. Qin, L.L. Li, D. Li, J. Zhang, Y.S. Zhang, C.J. Tang, The effects of elements doping on transport and thermoelectric properties of  $\text{Sr}_3\text{Ti}_2\text{O}_7$ , *J. Phys. Chem. Solid* 75 (2014) 629–637.
- [157] A.H. Reshak, Thermoelectric properties of  $\text{Sr}_{n+1}\text{Ti}_n\text{O}_{3n+1}$  ( $n=1, 2, 3, \infty$ ) Ruddlesden–Popper homologous series, *Renew. Energy* 76 (2015) 36–44.
- [158] M. Jerič, J. de Boor, J. Zavašnik, M. Čeh, Lowering the thermal conductivity of  $\text{Sr}(\text{Ti}_{0.8}\text{Nb}_{0.2})\text{O}_3$  by SrO and CaO doping: microstructure and thermoelectric properties, *J. Mater. Sci.* 51 (2016) 7660–7668.
- [159] M. Jerič, J. de Boor, B. Jančar, M. Čeh, An enhanced thermoelectric figure of merit for  $\text{Sr}(\text{Ti}_{0.8}\text{Nb}_{0.2})\text{O}_3$  based on a Ruddlesden–Popper-polytype-induced microstructure, *J. Eur. Ceram. Soc.* 36 (2016) 1177–1182.
- [160] K. Koumoto, R. Funahashi, E. Guilmeau, Y. Miyazaki, A. Weidenkaff, Y. Wang, C. Wan, X.D. Zhou, Thermoelectric ceramics for energy harvesting, *J. Am. Ceram. Soc.* 96 (2013) 1–23.
- [161] H. Kawakami, M. Saito, H. Takemoto, H. Yamamura, Y. Isoda, Y. Shinohara, Thermoelectric properties of perovskite-type oxide Ca-Mn-O system in relation to A-site vacancies, *Mater. Trans.* 54 (2013) 1818–1822.
- [162] B. Zhan, J. Lan, Y. Liu, Y. Lin, Y. Shen, C. Nan, High temperature thermoelectric properties of Dy-doped  $\text{CaMnO}_3$  ceramics, *J. Mater. Sci. Technol.* 30 (2014) 821–825.
- [163] M. Molinari, D.A. Tompsett, S.C. Parker, F. Azough, R. Freer, Structural, electronic and thermoelectric behaviour of  $\text{CaMnO}_3$  and  $\text{CaMnO}_{3-\delta}$ , *J. Mater. Chem. A* 2 (2014) 14109–14117.
- [164] R. Kabir, R. Tian, T. Zhang, R. Donelson, T.T. Tan, S. Li, Role of Bi doping in thermoelectric properties of  $\text{CaMnO}_3$ , *J. Alloys Compd.* 628 (2015) 347–351.
- [165] D. Srivastava, F. Azough, R. Freer, E. Combe, R. Funahashi, D.M. Kepaptsoglou, Q.M. Ramasse, M. Molinari, S.R. Yeandel, J.D. Baran, S.C. Parker, Crystal structure and thermoelectric properties of Sr-Mo substituted  $\text{CaMnO}_3$ : a combined experimental and computational study, *J. Mater. Chem. C* 3 (2015) 12245–12259.
- [166] R. Kabir, T. Zhang, D. Wang, R. Donelson, R. Tian, T.T. Tan, S. Li, Improvement in the thermoelectric properties of  $\text{CaMnO}_3$  perovskites by W doping, *J. Mater. Sci.* 49 (2014) 7522–7528.
- [167] S. Paengson, P. Pilasuta, K. Singsoog, W. Namhongsa, W. Impho, T. Seetawan, Improvement in thermoelectric properties of  $\text{CaMnO}_3$  by Bi doping and hot pressing, *Mater. Today: Proc.* 4 (2017) 6289–6295.
- [168] T. Yang, T. Cheng, Effects of La, Sm and Yb doping on thermoelectric properties of  $\text{Ca}_{0.98}\text{Er}_{0.02}\text{MnO}_3$  at high temperature, *RSC Adv.* 7 (2017) 44659–44664.
- [169] C. Li, Q. Chen, Y. Yan, Effects of Pr and Yb dual doping on the thermoelectric properties of  $\text{CaMnO}_3$ , *Materials* 11 (2018) 1807.
- [170] A. Sotelo, M.A. Torres, M.A. Madre, J.C. Diez, Influence of Ag on the properties of  $\text{Ca}_{0.9}\text{Yb}_{0.1}\text{MnO}_3$  sintered ceramics, *Materials* 11 (2018) 2503.
- [171] X. Song, S.A. Paredes Navia, L. Liang, C. Boyle, C.O. Romo-De-La-Cruz, B. Jackson, A. Hinerman, M. Wilt, J. Prucz, Y. Chen, Grain boundary phase segregation for dramatic improvement of the thermoelectric performance of oxide ceramics, *ACS Appl. Mater. Interfaces* 10 (2018) 39018–39024.
- [172] R. Ang, Layered cobaltites and natural chalcogenides for thermoelectrics, in: M. Nikitin (Ed.), *Thermoelectrics for Power Generation—A Look at Trends in the Technology*, Intech, 2016 (Chapter 1).

- [173] C. Gong, Z. Shi, Y. Zhang, Y. Chen, J. Hu, J. Gou, M. Qin, F. Gao, Fabrication and thermoelectric properties of Ca-Co-O ceramics with negative Seebeck coefficient, *Results Phys.* 9 (2018) 1233–1238.
- [174] H. Wang, X. Sun, X. Yan, D. Huo, X. Li, J.-G. Li, X. Ding, Fabrication and thermoelectric properties of highly textured  $\text{Ca}_9\text{Co}_{12}\text{O}_{28}$  ceramic, *J. Alloys Compd.* 582 (2014) 294–298.
- [175] G. Constantinescu, S. Rasekh, M.A. Torres, P. Bosque, J.C. Diez, M.A. Madre, A. Sotelo, Effect of Na doping on the  $\text{Ca}_3\text{Co}_4\text{O}_9$  thermoelectric performance, *Ceram. Int.* 41 (2015) 10897–10903.
- [176] D. Kenfau, D. Chateigner, M. Gomina, J.G. Noudem, Anisotropy of the mechanical and thermoelectric properties of hot-pressed single-layer and multilayer thick  $\text{Ca}_3\text{Co}_4\text{O}_9$  ceramics, *Int. J. Appl. Ceram. Technol.* 8 (2011) 214–226.
- [177] G. Constantinescu, M.A. Madre, S. Rasekh, M.A. Torres, J.C. Diez, A. Sotelo, Effect of Ga addition on Ca-deficient  $\text{Ca}_3\text{Co}_4\text{O}_y$  thermoelectric materials, *Ceram. Int.* 40 (2014) 6255–6260.
- [178] J.C. Diez, M.A. Torres, S. Rasekh, G. Constantinescu, M.A. Madre, A. Sotelo, Enhancement of  $\text{Ca}_3\text{Co}_4\text{O}_9$  thermoelectric properties by Cr for Co substitution, *Ceram. Int.* 39 (2013) 6051–6056.
- [179] Y. Huang, B. Zhao, S. Lin, R. Ang, W. Song, Y. Sun, M.A. White, Strengthening of thermoelectric performance via Ir doping in layered  $\text{Ca}_3\text{Co}_4\text{O}_9$  system, *J. Am. Ceram. Soc.* 97 (2014) 798–804.
- [180] M. Presečnik, J. de Boor, S. Bernik, Synthesis of single-phase  $\text{Ca}_3\text{Co}_4\text{O}_9$  ceramics and their processing for a microstructure-enhanced thermoelectric performance, *Ceram. Int.* 42 (2016) 7315–7327.
- [181] M. Presečnik, S. Bernik, Influence of a mechano-chemical treatment on the synthesis and characteristics of p-type thermoelectric  $\text{Ca}_3\text{Co}_4\text{O}_9$  ceramics, *J. Alloys Compd.* 686 (2016) 708–716.
- [182] S. Chen, X. Song, X. Chen, Y. Chen, E.J. Barbero, E.L. Thomas, P.N. Barnes, Effect of precursor calcination temperature on the microstructure and thermoelectric properties of  $\text{Ca}_3\text{Co}_4\text{O}_9$  ceramics, *J. Sol-Gel Sci. Technol.* 64 (2012) 627–636.
- [183] M. Gunes, M. Ozenbas, Effect of grain size and porosity on phonon scattering enhancement of  $\text{Ca}_3\text{Co}_4\text{O}_9$ , *J. Alloys Compd.* 626 (2015) 360–367.
- [184] N. Wu, T.C. Holgate, N. Van Nong, N. Pryds, S. Linderoth, High temperature thermoelectric properties of  $\text{Ca}_3\text{Co}_4\text{O}_{9+\delta}$  by auto-combustion synthesis and spark plasma sintering, *J. Eur. Ceram. Soc.* 34 (2014) 925–931.
- [185] N. Prasoetsopha, S. Pinitsoontorn, V. Amornkitbamrung, Synthesis and thermoelectric properties of  $\text{Ca}_3\text{Co}_4\text{O}_9$  prepared by a simple thermal hydro-decomposition method, *Electron. Mater. Lett.* 8 (2012) 305–308.
- [186] J.G. Noudem, D. Kenfau, D. Chateigner, M. Gomina, Toward the enhancement of thermoelectric properties of lamellar  $\text{Ca}_3\text{Co}_4\text{O}_9$  by edge-free spark plasma texturing, *Scr. Mater.* 66 (2012) 258–260.
- [187] M.E. Song, H. Lee, M.G. Kang, W. Li, D. Maurya, B. Poudel, J. Wang, M.A. Meeker, G.A. Khodaparast, S.T. Huxtable, S. Priya, Nanoscale texturing and interfaces in compositionally modified  $\text{Ca}_3\text{Co}_4\text{O}_9$  with enhanced thermoelectric performance, *ACS Omega* 3 (2018) 10798–10810.
- [188] D. Kenfau, M. Gomina, J.G. Noudem, D. Chateigner, Anisotropy of transport properties correlated to grain boundary density and quantified texture in thick oriented  $\text{Ca}_3\text{Co}_4\text{O}_9$  ceramics, *Materials* 11 (2018) 1224.

- [189] N. Puri, R.P. Tandon, A.K. Mahapatro, Significant enhancement in thermoelectric power factor of bulk nanostructured calcium cobalt oxide ceramics, *ACS Appl. Energy Mater.* 2 (2018) 269–277.
- [190] M. Bittner, L. Helmich, F. Nietschke, B. Geppert, O. Oeckler, A. Feldhoff, Porous  $\text{Ca}_3\text{Co}_4\text{O}_9$  with enhanced thermoelectric properties derived from sol-gel synthesis, *J. Eur. Ceram. Soc.* 37 (2017) 3909–3915.
- [191] A. Soffientini, I.G. Tredici, S. Boldrini, A. Famengo, G. Spinolo, U. Anselmi-Tamburini, Synthesis and characterization of bulk nanostructured thermoelectric  $\text{Ca}_3\text{Co}_4\text{O}_9$ , *J. Nanosci. Nanotechnol.* 17 (2017) 1674–1680.
- [192] Y. Yin, S. Saini, D. Magginetti, K. Tian, A. Tiwari, Thermoelectric response of porous  $\text{Ca}_3\text{Co}_4\text{O}_9$  prepared by an eco-friendly technique, *Ceram. Int.* 43 (2017) 9505–9511.
- [193] F. Delorme, D. Ovono Ovono, P. Marudhachalam, C. Fernandez Martin, O. Fraboulet, Effect of precursors size on the thermoelectric properties of  $\text{Ca}_3\text{Co}_4\text{O}_9$  ceramics, *Mater. Res. Bull.* 47 (2012) 1169–1175.
- [194] A. Sotelo, S. Rasekh, M.A. Torres, P. Bosque, M.A. Madre, J.C. Diez, Effect of synthesis methods on the  $\text{Ca}_3\text{Co}_4\text{O}_9$  thermoelectric ceramic performances, *J. Solid State Chem.* 221 (2015) 247–254.
- [195] C. Boyle, L. Liang, C.-O. Romo-De-La-Cruz, R. Johnson, Y. Chen, J. Prucz, E. Cakmak, T.R. Watkins, E. Lara-Curzio, X. Song, Improving the thermoelectric performance and thermal stability of  $\text{Ca}_3\text{Co}_4\text{O}_{9+\delta}$  ceramics by sintering in oxygen atmosphere, *J. Sol-Gel Sci. Technol.* 85 (2018) 712–722.
- [196] N. Kanas, S.P. Singh, M. Rotan, M. Saleemi, M. Bittner, A. Feldhoff, T. Norby, K. Wiik, T. Grande, M.-A. Einarsrud, Influence of processing on stability, microstructure and thermoelectric properties of  $\text{Ca}_3\text{Co}_{4-x}\text{O}_{9+6}$ , *J. Eur. Ceram. Soc.* 38 (2018) 1592–1599.
- [197] Z. Shi, J. Xu, J. Zhu, Y. Zhang, T. Gao, M. Qin, H. Sun, G. Dong, F. Gao, Effect of platelet template seeds on microstructure and thermoelectric properties of  $\text{Ca}_3\text{Co}_4\text{O}_9$  ceramics, *Ceram. Int.* 45 (2019) 1977–1983.
- [198] A. Sotelo, F.M. Costa, N.M. Ferreira, A. Kovalevsky, M.C. Ferro, V.S. Amaral, J.S. Amaral, S. Rasekh, M.A. Torres, M.A. Madre, J.C. Diez, Tailoring  $\text{Ca}_3\text{Co}_4\text{O}_9$  microstructure and performances using a transient liquid phase sintering additive, *J. Eur. Ceram. Soc.* 36 (2016) 1025–1032.
- [199] S. Butt, Y.-C. Liu, J.-L. Lan, K. Shehzad, B. Zhan, Y. Lin, C.-W. Nan, High-temperature thermoelectric properties of La and Fe co-doped Ca–Co–O misfit-layered cobaltites consolidated by spark plasma sintering, *J. Alloys Compd.* 588 (2014) 277–283.
- [200] S. Rasekh, G. Constantinescu, M.A. Torres, J.C. Diez, M.A. Madre, A. Sotelo, Thermoelectric properties of rare earth doped  $\text{Ca}_{3-x}\text{RE}_x\text{Co}_4\text{O}_9$  ( $\text{RE} = \text{Dy}, \text{Er}, \text{Gd}, \text{and Tb}; x = 0, 0.01, 0.03, \text{and } 0.05$ ), *J. Electroceram.* 32 (2014) 376–382.
- [201] Y. Liu, L. Zhang, S.E. Shirasath, J. Zheng, Y. Liu, C. Ulrich, S. Li, Manipulation of charge carrier concentration and phonon scattering via spin-entropy and size effects: Investigation of thermoelectric transport properties in La-doped  $\text{Ca}_3\text{Co}_4\text{O}_9$ , *J. Alloys Compd.* 801 (2019) 60–69.
- [202] J.S. Cha, D.H. Kim, H.Y. Hong, G.H. Kim, K. Park, Effect of  $\text{La}^{3+}$  substitution on the structural and thermoelectric properties of  $\text{Ca}_{3-x}\text{La}_x\text{Co}_4\text{O}_{9+d}$ , *J. Eur. Ceram. Soc.* 39 (2019) 3320–3326.
- [203] J.S. Cha, S.M. Choi, G.H. Kim, S.J. Kim, K. Park, High-temperature thermoelectric properties of  $\text{Sm}^{3+}$ -doped  $\text{Ca}_3\text{Co}_4\text{O}_{9+d}$  fabricated by spark plasma sintering, *Ceram. Int.* 44 (2018) 6376–6383.

- [204] S. Saini, H.S. Yaddanapudi, K. Tian, Y. Yin, D. Magginetti, A. Tiwari, Terbium ion doping in  $\text{Ca}_3\text{Co}_4\text{O}_9$ : a step towards high-performance thermoelectric materials, *Sci. Rep.* 7 (2017) 44621.
- [205] G. Kiirat, M.A. Aksan, S. Rasekh, M.A. Madre, J.C. Diez, A. Sotelo, Decrease of  $\text{Ca}_3\text{Co}_4\text{O}_{9+\delta}$  thermal conductivity by Yb-doping, *Ceram. Int.* 41 (2015) 12529–12534.
- [206] G. Tang, F. Xu, D. Zhang, Z. Wang, Improving the spin entropy by suppressing  $\text{Co}^{4+}$  concentration in thermoelectric  $\text{Ca}_3\text{Co}_4\text{O}_{9+\delta}$ , *Ceram. Int.* 39 (2013) 1341–1344.
- [207] X. Song, Y. Chen, S. Chen, E. Barbero, E.L. Thomas, P. Barnes, Significant enhancement of electrical transport properties of thermoelectric  $\text{Ca}_3\text{Co}_4\text{O}_{9+\delta}$  through Yb doping, *Solid State Commun.* 152 (2012) 1509–1512.
- [208] N.V. Nong, C.-J. Liu, M. Ohtaki, High-temperature thermoelectric properties of late rare earth-doped  $\text{Ca}_3\text{Co}_4\text{O}_{9+\delta}$ , *J. Alloys Compd.* 509 (2011) 977–981.
- [209] Y. Wang, Y. Sui, F. Li, L. Xu, X. Wang, W. Su, X. Liu, Thermoelectrics in misfit-layered oxides  $[(\text{Ca},\text{Ln})_2\text{CoO}_3]_{0.62}[\text{CoO}_2]$ : From bulk to nano, *Nano Energy* 1 (2012) 456–465.
- [210] B. Özkurt, M.E. Aytekin, M.A. Madre, A. Sotelo, M.A. Torres, Improving thermoelectric properties of  $\text{Ca}_3\text{Co}_4\text{O}_{9+\delta}$  through both Na doping and K addition at optimal values, *J. Mater. Sci. Mater. Electron.* 30 (2019) 8832–8837.
- [211] C. Romo-De-La-Cruz, L. Liang, S.A.P. Navia, Y. Chen, J. Prucz, X. Song, Role of oversized dopant potassium on the nanostructure and thermoelectric performance of calcium cobaltite ceramics, *Sustain. Energy Fuels* 2 (2018) 876–881.
- [212] Y. Huang, B. Zhao, S. Lin, Y. Sun, Enhanced thermoelectric performance induced by misplaced substitution in layered  $\text{Ca}_3\text{Co}_4\text{O}_9$ , *J. Phys. Chem. C* 119 (2015) 7979–7986.
- [213] M.A. Torres, F.M. Costa, D. Flahaut, K. Touati, S. Rasekh, N.M. Ferreira, J. Allouche, M. Depriester, M.A. Madre, A.V. Kovalevsky, J.C. Diez, A. Sotelo, Significant enhancement of the thermoelectric performance in  $\text{Ca}_3\text{Co}_4\text{O}_9$  thermoelectric materials through combined strontium substitution and hot-pressing process, *J. Eur. Ceram. Soc.* 39 (2019) 1186–1192.
- [214] P. Carvillo, Y. Chen, C. Boyle, P.N. Barnes, X. Song, Thermoelectric performance enhancement of calcium cobaltite through barium grain boundary segregation, *Inorg. Chem.* 54 (2015) 9027–9032.
- [215] G. Constantinescu, S. Rasekh, M.A. Torres, M.A. Madre, A. Sotelo, J.C. Diez, Improvement of thermoelectric properties in  $\text{Ca}_3\text{Co}_4\text{O}_9$  ceramics by Ba doping, *J. Mater. Sci. Mater. Electron.* 26 (2015) 3466–3473.
- [216] S. Butt, Y. Ren, M.U. Farooq, B. Zhan, R.U.R. Sagar, Y. Lin, C.-W. Nan, Enhanced thermoelectric performance of heavy-metals (M: Ba, Pb) doped misfit-layered ceramics:  $(\text{Ca}_{2-x}\text{M}_x\text{CoO}_3)_{0.62}(\text{CoO}_2)$ , *Energ. Conver. Manage.* 83 (2014) 35–41.
- [217] G. Constantinescu, S. Rasekh, M.A. Torres, J.C. Diez, M.A. Madre, A. Sotelo, Effect of Sr substitution for Ca on the  $\text{Ca}_3\text{Co}_4\text{O}_9$  thermoelectric properties, *J. Alloys Compd.* 577 (2013) 511–515.
- [218] F. Delorme, C.F. Martin, P. Marudhachalam, D. Ovono Ovono, G. Guzman, Effect of Ca substitution by Sr on the thermoelectric properties of  $\text{Ca}_3\text{Co}_4\text{O}_9$  ceramics, *J. Alloys Compd.* 509 (2011) 2311–2315.
- [219] C. Boyle, P. Carvillo, Y. Chen, E.J. Barbero, D. McIntyre, X. Song, Grain boundary segregation and thermoelectric performance enhancement of bismuth doped calcium cobaltite, *J. Eur. Ceram. Soc.* 36 (2016) 601–607.
- [220] J.-Y. Cho, O.J. Kwon, Y.K. Chung, J.-S. Kim, W.-S. Kim, K.J. Song, C. Park, Effect of trivalent Bi doping on the seebeck coefficient and electrical resistivity of  $\text{Ca}_3\text{Co}_4\text{O}_9$ , *J. Electron. Mater.* 44 (2015) 3621–3626.

- [221] C. Boyle, L. Liang, Y. Chen, J. Prucz, E. Cakmak, T.R. Watkins, E. Lara-Curzio, X. Song, Competing dopants grain boundary segregation and resultant seebeck coefficient and power factor enhancement of thermoelectric calcium cobaltite ceramics, *Ceram. Int.* 43 (2017) 11523–11528.
- [222] S. Butt, W. Xu, W.Q. He, Q. Tan, G.K. Ren, Y. Lin, C.-W. Nan, Enhancement of thermoelectric performance in Cd-doped  $\text{Ca}_3\text{Co}_4\text{O}_9$  via spin entropy, defect chemistry and phonon scattering, *J. Mater. Chem. A* 2 (2014) 19479–19487.
- [223] L. Xu, F. Li, Y. Wang, High-temperature transport and thermoelectric properties of  $\text{Ca}_3\text{Co}_{4-x}\text{Ti}_x\text{O}_9$ , *J. Alloys Compd.* 501 (2010) 115–119.
- [224] M.A. Torres, S. Rasekh, P. Bosque, G. Constantinescu, M.A. Madre, J.C. Diez, A. Sotelo, Decrease of electrical resistivity in  $\text{Ca}_3\text{Co}_4\text{O}_9$  thermoelectric ceramics by Ti doping, *J. Mater. Sci. Mater. Electron.* 26 (2014) 815–820.
- [225] Y. Wang, Y. Sui, X. Wang, W. Su, X. Liu, Enhanced high temperature thermoelectric characteristics of transition metals doped  $\text{Ca}_3\text{Co}_4\text{O}_{9+\delta}$  by cold high-pressure fabrication, *J. Appl. Phys.* 107 (2010), 033708.
- [226] T. Wu, T.A. Tyson, J. Bai, K. Pandya, C. Jaye, D. Fischer, On the origin of enhanced thermoelectricity in Fe doped  $\text{Ca}_3\text{Co}_4\text{O}_9$ , *J. Mater. Chem. C* 1 (2013) 4114.
- [227] W. Wong-Ng, T. Luo, W. Xie, W.H. Tang, J.A. Kaduk, Q. Huang, Y. Yan, S. Chattopadhyay, X. Tang, T. Tritt, Phase diagram, crystal chemistry and thermoelectric properties of compounds in the Ca–Co–Zn–O system, *J. Solid State Chem.* 184 (2011) 2159–2166.
- [228] Y. Xu, X. Qu, S. Lü, Y. Qian, J. Hu, Q. Meng, Microstructure and electrical transport properties of  $\text{Ca}_3\text{Co}_{4-x}\text{Mn}_x\text{O}_{9+d}$  ceramics fabricated under two-step external magnetic field, *Ceram. Int.* 42 (2016) 6107–6114.
- [229] G. Constantinescu, M.A. Torres, S. Rasekh, P. Bosque, M.A. Madre, J.C. Diez, A. Sotelo, Thermoelectric properties in  $\text{Ca}_3\text{Co}_{4-x}\text{Mn}_x\text{O}_y$  ceramics, *Adv. Appl. Ceram.* 114 (2014) 303–308.
- [230] L. Liang, C.-O. Romo-De-La-Cruz, P. Carvilo, B. Jackson, E. Gemmen, S.A. Paredes-Navia, J. Prucz, Y. Chen, X. Song, Difference between transition metal cation substitution and nonstoichiometric addition on nanostructure and thermoelectric performance of complex oxide ceramics, *J. Solid State Chem.* 277 (2019) 427–433.
- [231] R. Tian, T. Zhang, D. Chu, R. Donelson, L. Tao, S. Li, Enhancement of high temperature thermoelectric performance in Bi, Fe co-doped layered oxide-based material  $\text{Ca}_3\text{Co}_4\text{O}_{9+\delta}$ , *J. Alloys Compd.* 615 (2014) 311–315.
- [232] N. Prasoetsopha, S. Pinitsoontorn, T. Kamwanna, K. Kurosaki, Y. Ohishi, H. Muta, S. Yamanaka, Thermoelectric properties of  $\text{Ca}_3\text{Co}_{4-x}\text{Ga}_x\text{O}_{9+\delta}$  prepared by thermal hydro-decomposition, *J. Electron. Mater.* 43 (2014) 2064–2071.
- [233] W. Yang, H. Qian, J. Gan, W. Wei, Z. Wang, G. Tang, Effects of Lu and Ni substitution on thermoelectric properties of  $\text{Ca}_3\text{Co}_4\text{O}_{9+\delta}$ , *J. Electron. Mater.* 45 (2016) 4171–4176.
- [234] G.D. Tang, W.C. Yang, Y. He, Z.H. Wang, Enhanced thermoelectric properties of  $\text{Ca}_3\text{Co}_4\text{O}_{9+\delta}$  by Ni, Ce co-doping, *Ceram. Int.* 41 (2015) 7115–7118.
- [235] D.W. Zhang, X.N. Mi, Y.H. Zhang, Q.S. Wu, Y.C. Bao, Effects of Eu and Fe co-doping on thermoelectric properties of misfit-layered  $\text{Ca}_3\text{Co}_4\text{O}_{9+\delta}$ , *J. Mater. Sci. Mater. Electron.* 26 (2015) 7490–7495.
- [236] N. Prasoetsopha, S. Pinitsoontorn, T. Kamwanna, V. Amornkitbamrung, K. Kurosaki, Y. Ohishi, H. Muta, S. Yamanaka, The effect of Cr substitution on the structure and properties of misfit-layered  $\text{Ca}_3\text{Co}_{4-x}\text{Cr}_x\text{O}_{9+\delta}$  thermoelectric oxides, *J. Alloys Compd.* 588 (2014) 199–205.

- [237] Y. Huang, B. Zhao, S. Lin, R. Ang, Y. Sun, M.A. White, Enhanced thermoelectric performance induced by Cr doping at Ca-sites in  $\text{Ca}_3\text{Co}_4\text{O}_9$  system, *J. Am. Ceram. Soc.* 97 (2014) 3589–3596.
- [238] Y. Fu, S. Lin, Y. Huang, R. Shi, B. Zhao,  $\text{Cr}^{6+}$  ion doping effects in layered  $\text{Ca}_3\text{Co}_4\text{O}_9$  system, *J. Alloys Compd.* 613 (2014) 87–92.
- [239] M. Presečnik, S. Bernik, Microstructural and thermoelectric properties of  $\text{WO}_3$ -doped  $\text{Ca}_3\text{Co}_4\text{O}_9$  ceramics, *Ceram. Int.* 42 (2016) 16103–16108.
- [240] Y. Fu, B. Zhao, Y. Huang, J. Dai, Y. Sun, Enhanced electrical correlation in the W-doped cobaltite  $\text{Ca}_3\text{Co}_4\text{O}_9$  ceramics, *Phys. B: Condens. Matter* 414 (2013) 16–20.
- [241] S. Yazdani, M.T. Pettes, Nanoscale self-assembly of thermoelectric materials: a review of chemistry-based approaches, *Nanotechnology* 29 (2018) 432001.

# Oxide thermoelectric materials **2.11**

Dursun Ekren, Feridoon Azough, and Robert Freer

School of Materials, University of Manchester, Manchester, United Kingdom

## 2.11.1 Introduction

Originally, oxides were not considered as candidates for thermoelectrics because of low charge carrier mobility ( $\mu$ ) and high thermal conductivity. Nevertheless, reports of promising thermoelectric properties for cobaltites in the 1990s [1] initiated research into several families of materials. For most oxides, the raw materials are earth-abundant, low-cost elements, in comparison to the heavy, toxic, and rare elements (Pb, Te, etc.) in traditional materials [2]. Oxides exhibit higher chemical and thermal stability, offering advantages in hostile environments. Furthermore, the chemical versatility and structural complexity of oxides can be exploited to tune the thermoelectric properties.

Over the last 30 years, the development of high ZT oxides has been challenging. Although single crystal p-type oxides with  $ZT \approx 1$  were synthesized, the preparation of comparable n-type oxides was less successful. However, the larger bandgap in oxides encourages high Seebeck coefficients ( $S$ ) and peak ZT values at a higher temperature. Additionally, advances in the preparation of nanostructured materials and predictions of first-principles calculations suggest that high ZT oxide thermoelectric materials could be obtained in the near future. This short review considers oxides in two groups: (i) p-type and (ii) n-type; the p-type are mainly layered cobaltites,  $\text{LaCoO}_3$  and  $\text{CuAlO}_2$  while n-type oxides include perovskites ( $\text{CaMnO}_3$ ,  $\text{SrTiO}_3$ , etc.),  $\text{ZnO}$ -based materials, Magnéli phases, and tungsten bronze structured materials.

## 2.11.2 P-type oxides

### 2.11.2.1 Layered cobaltites

Among the p-type layered cobaltites,  $\text{Na}_x\text{CoO}_2$  (NCO) [1, 3–6],  $\text{Ca}_3\text{Co}_4\text{O}_9$  (CCO) [7–14], and  $\text{Bi}_2\text{Sr}_2\text{Co}_2\text{O}_y$  (BSCO) [13, 15–26] exhibit the most promising properties. Typically they have a layered structure along  $c$ -axis which is formed by stacking of  $\text{CoO}_2$  and rock salt (RS)-type layers [27]. The former provides high charge carrier mobility, enabling high electrical conductivity ( $\sigma$ ) while the latter has an insulating nature and the origin of low thermal conductivity ( $\kappa$ ) in these materials [5].

### 2.11.2.1.1 Sodium cobaltite

The report of a high power factor ( $\sigma S^2$ ) ( $5000 \mu\text{W m}^{-1} \text{K}^{-2}$ ) for NCO single crystals by Terasaki et al. [1] paved the way for the research into oxides as thermoelectric materials. Unexpectedly, NCO has both high  $\mu$  ( $\sim 13 \text{ cm}^2 \text{V}^{-1} \text{s}^{-1}$  at 300 K) and a large  $S$  ( $\sim 100 \mu\text{VK}^{-1}$  at 300 K) as a result of the strong degeneracy of charge carriers and strong correlation of 3d electrons [4]. The preparation of high-quality bulk polycrystalline NCO materials is still a challenge because of the preferential growth of planar grains [28]. The crystallinity and densification of polycrystalline NCO can be improved by hot pressing (HP) [3], which results in increased  $\sigma$  and lower  $\kappa$ . However, the maximum ZT ( $ZT_{\max}$ ) was still limited to 0.11 at 473 K, very much lower than for single crystals. Thus, conventional processing methods are inadequate for achieving high-performance NCO materials. In contrast, the use of a polymerized complex (PC) route for NCO powders and then the production of NCO+10% Ag composites yielded a  $ZT_{\max}$  of up to 0.92 at 960 K [6].

### 2.11.2.1.2 Calcium cobaltite

$\text{Ca}_3\text{Co}_4\text{O}_9$  is formed by stacking layers of  $\text{CaO}$  and  $\text{CoO}$ , with an unequal mismatch, along the  $b$ -axis [13, 29]. The electronic properties are sensitive to oxygen deficiency and an increase in the vacancy concentration leads to a decrease in  $\sigma$  and increase in  $S$  because of the change in the  $\text{Co}^{4+}/\text{Co}^{3+}$  ratio and the increase in charge carrier entropy [12]. For CCO single crystals, a  $ZT_{\max}$  value of  $\sim 0.87$  at 973 K was reported [7], while for polycrystalline CCO the  $ZT_{\max}$  was limited to  $\sim 0.43$  at 1073 K for Bi or Ba doped ceramics [9, 14]. Due to the anisotropic nature of the grains, polycrystalline materials need to be textured to maximize the performance; for example, a maximum  $\sigma S^2$  of  $27,700 \mu\text{W m}^{-1} \text{K}^{-2}$  at 1000 K was achieved for Bi-doped CCO by texturing [11]. Experiments on dual doping of Ca-sites in CCO with heavy and light alkaline earth elements [7, 8, 11] in combination with the ab initio calculations [13] indicate a route for the preparation of high-quality CCO materials.

### 2.11.2.1.3 Bismuth strontium cobaltite

$\text{Bi}_2\text{Sr}_2\text{Co}_2\text{O}_y$  is a further misfit layered cobaltite, with a structure comprising  $\text{CoO}_2$  layers and rock salt (RS)-type  $\text{BiO}$  and  $\text{SrO}$  layers [27]. BSCO is characterized by low  $\kappa$  ( $\sim 1.3 \text{ W m}^{-1} \text{K}^{-1}$ ), relatively high  $S$  ( $\sim 100 \mu\text{VK}^{-1}$ ), and high  $\sigma$  ( $1 \times 10^4 \text{ S cm}^{-1}$ ) [15]. In whisker form Funahashi and Shikano [19] achieved a  $ZT_{\max}$  of 1.1 at 973 K, but values were very much smaller for polycrystalline ceramics because of the orientation-dependent properties [13, 16], highlighting the necessity for textured ceramics to maximize performance. Doping BSCO single crystals with Pb reduced the anisotropy in  $\sigma$  while having a limited effect on  $S$  [20]. For ceramics, a range of dopants have been explored including Ag, Y, and Ca on Sr sites, and Zr, Al, and Mo on Co sites; it was demonstrated that doping Sr sites was most effective to increase electronic properties and Ca was the best to tune thermoelectric properties [24]. Recent computational work on the misfit layered cobaltites [13, 17] revealed that dual doping of the RS layers by isovalent cations could induce strain and lead to

charge transfer and thereby tune thermoelectric properties. Additionally, a deficiency of Bi can increase electronic transport properties and reduce  $\kappa$  (Fig. 2.11.1) [17].

Combe et al. [26] explored the effect of processing method on BCSO ceramics and demonstrated that partial melting (PM) led to improved microstructure and superior thermoelectric performance (with a  $ZT_{max}$  of 0.25 at 973 K) in comparison to hot pressing. Diez et al. [21, 22] showed that texturing, by use of laser floating zone technique, significantly improved the  $\sigma S^2$  of BSCO ceramics. By employing a composite approach, through adding Ag to BSCO, Wang et al. [25] were able to both increase  $\sigma S^2$  and reduce  $\kappa$ . At the optimum level of Ag addition (3 wt%) they achieved a  $ZT_{max}$  value of 0.26 at 973 K, while Sotelo et al. [23] were able to double the  $\sigma S^2$  of textured BSCO ceramics with only 1 wt% Ag addition.

### 2.11.2.2 Other p-type oxides

#### 2.11.2.2.1 $LaCoO_3$

$LaCoO_3$  (LCO) is a perovskite structured p-type oxide [30]; the Seebeck coefficients are sensitive to processing conditions with reports of both n-type [31–33] and p-type [34–39] behavior at room temperature. However, a transition from n-type to p-type behavior at 400–500 K [31–33] has been linked to a change in the thermally activated spin state for  $Co^{3+}$  [30]. Although undoped LCO exhibits a high  $S$  ( $640 \mu V K^{-1}$  at 300 K [30]) and low  $\kappa$  ( $1 W m^{-1} K^{-1}$  at 300 K [31]), its ZT is limited by low  $\sigma$  ( $\sim 6 S m^{-1}$  at 300 K [34]). A variety of doping strategies have been employed to improve the thermoelectric performance [31–34, 37–41], including Sr [40, 41], Pb [31], and Na [31] doping on the La site, Ni [32] and Cu [33] on the Co site, and co-doping on La/Co sites (by Ni/Ti [34], Ni/Fe [37], and Ni/Sr [38]). It was demonstrated that Pb doping was most effective, increasing  $\sigma S^2$  and reducing  $\kappa$ , leading to a  $ZT_{max}$  of 0.2 at 600 K, the highest ZT value obtained for  $LaCoO_3$ . The simultaneous introduction of La/O vacancies increased  $\sigma$  and  $S$ , by increasing carrier concentration ( $n$ ), and reduced  $\kappa$ , leading to a  $ZT_{max}$  of 0.18 at 300 K for  $La_{0.92}CoO_{2.93}$  [35]. Finally, it was shown that  $B_2O_3$ -CuO additions reduced the sintering temperature by 200 K, improved  $\sigma S^2$  and reduced  $\kappa$  [36], enhancing  $ZT_{max}$  by 50%.

#### 2.11.2.2.2 $CuAlO_2$

$CuAlO_2$  (CAO) having a natural superlattice structure (with a delafossite structure (space group:  $R\bar{3}m$ ) [42]), and based on low-cost starting materials, has attracted much interest as a thermoelectric [42–57]. It exhibits p-type behavior due to the presence of copper vacancies ( $V_{Cu}'$ ) and/or interstitial oxygen ( $O_i''$ ) [58]. Undoped CAO has an  $\sigma$  of  $\sim 1 S cm^{-1}$  and a  $S$  of  $\sim 500 \mu V K^{-1}$  at 550 K [53] and a maximum  $\sigma S^2$  of  $4.98 \times 10^{-5} W m^{-1} K^{-2}$  at 1140 K was reported [51]; thermal conductivity is relatively high ( $5.5 W m^{-1} K^{-1}$  at 573 K) [47]. The thermoelectric properties can be tuned by doping on the Cu-site [50, 54], the Al-site [46, 52, 53, 55], by excess oxygen [56] or use of additives [45, 47, 49]. The best performance was achieved by dual doping on the Cu

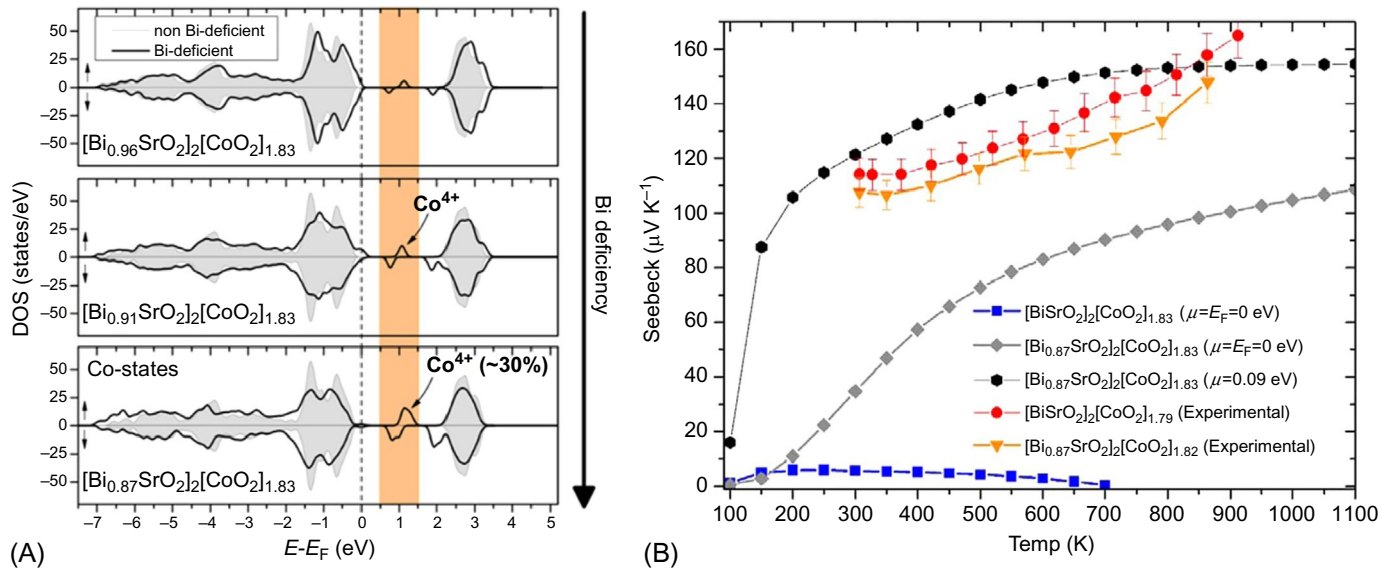


**Fig. 2.11.1** (A) Evaluation of DOS from first-principle calculations for the Co states of  $[Bi_{0.87}SrO_2]_2[CoO_2]_{1.83}$  with increasing Bi deficiency and (B) comparison of calculated and experimental  $S$  values for BSCO with and without Bi deficiency.

Reproduced with permission from J.D. Baran, D. Kepaptsoglou, M. Molinari, N. Kulwongwit, F. Azough, R. Freer, Q.M. Ramasse, S.C. Parker, Role of structure and defect chemistry in high-performance thermoelectric bismuth strontium cobalt oxides, *Chem. Mater.* 28 (2016) 7470–7478. Copyright © 2016, American Chemical Society.

site, giving a maximum  $\sigma S^2$  of  $1.26 \times 10^{-4} \text{ W m}^{-1} \text{ K}^{-2}$  for  $\text{Cu}_{0.979}\text{Ag}_{0.02}\text{Zn}_{0.001}\text{AlO}_2$ , and the highest ZT (0.016 at 1060K) for CAO-based materials.

## 2.11.3 N-type oxides

### 2.11.3.1 Calcium manganite

The perovskite structured  $\text{CaMnO}_3$  (CMO) was one of the first n-type materials investigated. It goes through a metal-insulator transition at high temperature as a result of the change in the spin state of Mn ions [59]. Undoped CMO has low  $\sigma$  ( $\sim 50 \text{ S m}^{-1}$ ) and high  $S$  ( $\sim 350 \mu\text{V K}^{-1}$ ), and hence relatively low  $\sigma S^2$  [60]. Moreover, its high  $\kappa$  ( $\sim 3.5 \text{ W m}^{-1} \text{ K}^{-1}$ ) limits the  $ZT_{\max}$  [61], but the thermoelectric properties of CMO can be improved by substituting Ca with rare earths [59, 60, 62–65] and/or Mn with Nb [64, 66–69]. The resulting distortion of  $\text{MnO}_6$  octahedra and Mn-O-Mn bond angles modify the electronic band structure;  $\sigma$  was increased by doping with smaller ionic radius species [60]. Later, it was suggested that change in the average Mn valance was responsible for the improvement in  $\sigma$  [62]. Reduction in  $\kappa$  was achieved by replacement of Ca with smaller and heavier dopants [60] through strain/mass contrast. Significant improvement in CMO has been achieved and theoretical work predicts a  $ZT_{\max}$  value greater than 1.0 [63]. Nb is a particularly effective B-site dopant, able to tune the thermoelectric properties, as it is involved in conduction processes, unlike Ta, which acts as an impurity [66]. However, the 5+ species tend to increase  $\kappa$  due to the increasing contribution of electrons to thermal conduction. Dual doping can also be beneficial [64], increasing ZT to 0.11 at 1000K for  $\text{Ca}_{0.7}\text{Sr}_{0.3}\text{Mn}_{0.96}\text{Mo}_{0.04}\text{O}_3$ . Srivastava et al. [64] also showed (by modeling and experimental work) that the  $\kappa$  of CMO could be reduced by twin boundaries resulting from the cubic to tetragon structural transition on cooling after sintering.

The development of oxygen deficiency [68, 70] and optimum processing route [67] can improve the thermoelectric performance. CMO can accommodate high levels of oxygen deficiency, thereby increasing  $\sigma$  [70]. However, the stability of CMO in reducing atmospheres at elevated temperatures is of concern for applications [71]. Conversely, the microstructures are sensitive to the processing route [67]; soft chemistry (SC) leads to submicron grains with nanosized twinned domains in comparison to much larger average grain sizes reported for solid-state reaction (SSR). Therefore, significantly higher  $\sigma S^2$  ( $\sim 190\text{--}200 \mu\text{W m}^{-1} \text{ K}^{-2}$ ) and lower  $\kappa$  ( $< 1 \text{ W m}^{-1} \text{ K}^{-1}$ ) were obtained for the ceramics prepared via SC, leading to a  $ZT_{\max}$  of 0.32 at 1060K [67].

### 2.11.3.2 ZnO-based materials

#### 2.11.3.2.1 Zinc oxide

$\text{ZnO}$  (ZO) is a very promising n-type thermoelectric due to its high  $\mu$  [72–80]. Pure ZO exhibits a high power factor ( $\sim 368 \mu\text{W m}^{-1} \text{ K}^{-2}$  at 1273K) but also high  $\kappa$  ( $\sim 5 \text{ W m}^{-1} \text{ K}^{-1}$ ) as a result of the simple crystal structure [72]. To improve thermoelectric properties it is typically singly doped with Al [72] or dual doped with Al and

Ga [73]. Tsubota et al. attained a  $ZT_{max}$  of 0.30 at 1273 K with 2% Al doping [72], while Ohtaki et al. [73] showed dual doping to be more effective; the additional presence of Ga prevents the formation of  $ZnAl_2O_4$  phase, which limits  $\sigma$ . Therefore, a record ZT value of 0.65 was achieved for  $Zn_{0.96}Al_{0.02}Ga_{0.02}O$  at 1273 K [73]. However, these results have rarely been replicated by other researchers. More recent studies suggest that sample preparation under a  $N_2$  atmosphere induces oxygen vacancies which improve  $\sigma S^2$  [76], and  $\kappa$  is reduced by the presence of a  $Ga_2O_3(ZnO)_9$  secondary phase [79].

### 2.11.3.2.2 Homologous compounds

The encouraging thermoelectric results for ZO prompted work on the related, so-called, homologous compounds:  $In_2O_3(ZnO)_m$  (IZO) and  $Ga_2O_3(ZnO)_m$  (GZO) where  $m$  is an integer. Their structures comprise zinc oxide layers separated by  $m$  layers of indium/gallium oxide, enabling low  $\kappa$  while allowing the tuning of  $\sigma S^2$  by adjusting  $m$ . Initial work focused on IZO; Ohta et al. [81] suggested the optimum value of  $m$  to maximize thermoelectric performance was between 9 and  $\infty$ , while Kaga et al. [82] found it to lie between 3 and 5. It was noted that densification of compositions with  $m > 9$  was challenging [81]. Although a  $ZT_{max}$  value of 0.23 at 1053 K was achieved for the composition of  $m=3.5$ , doped with 2.5% Ca, it was subsequently reported that the ZT of such compounds could be enhanced by doping with transition metals which leads to lattice distortion [83, 84].

In the last few years attention has turned to the thermoelectric properties of GZO compounds [85–88]. Here the size of the superlattice and nano-twins in the structures can be controlled by adjusting  $m$ , which is effective for reducing  $\kappa$ ; however, a concurrent reduction in  $\sigma$  also occurs. For the pseudo-binary  $ZnO-Ga_2O_3$  system, Michiue et al. [88] showed that GZO could be formed when  $m=9\text{--}38$ ; higher  $m$  values led to the formation of a two-phase material ( $Ga_2O_3(ZnO)_{m \approx 38}$  + doped ZnO). The many nanoscale interfaces were effective in scattering both charge carriers and phonons [86, 89], such that higher values of  $m$  values enhanced  $\sigma$  while reducing  $\kappa$ . Alvarez-Ruiz et al. [90] characterized twin boundaries (TB) and inversion boundaries (IB) in  $Ga_2O_3(ZnO)_9$  (Fig. 2.11.2), and were able to show that Ga ions were located at the junctions of the boundaries [89]. By optimizing processing, a  $ZT_{max}$  of 0.06 was achieved at 900 K and then increased to 0.09 at 1000 K by adjusting Ga content [87]. In their more recent work, they [90] demonstrated that by incorporation of In into  $Ga_2O_3(ZnO)_9$  the thermoelectric properties could be tuned;  $\kappa$  was reduced to  $2\text{ W m}^{-1}\text{ K}^{-2}$  while  $\sigma S^2$  remained high at  $150\text{ }\mu\text{W m}^{-1}\text{ K}^{-2}$  for  $(Ga_{0.8}In_{0.2})_2O_3(ZnO)_9$ , leading to a  $ZT_{max}$  of 0.07 at 900 K.

### 2.11.3.3 $TiO_2$ and Magnéli phases

#### 2.11.3.3.1 $TiO_2$

There have been limited studies on the thermoelectric properties of  $TiO_2$  [91–93], but typically anatase exhibits higher  $\sigma$  and a lower  $\kappa$  ( $3\text{ W m}^{-1}\text{ K}^{-1}$  at 1000 K) than rutile, which has a higher  $S$  ( $-600\mu\text{V K}^{-1}$ ) [91, 92]. Overall, the  $ZT_{max}$  is limited due to the

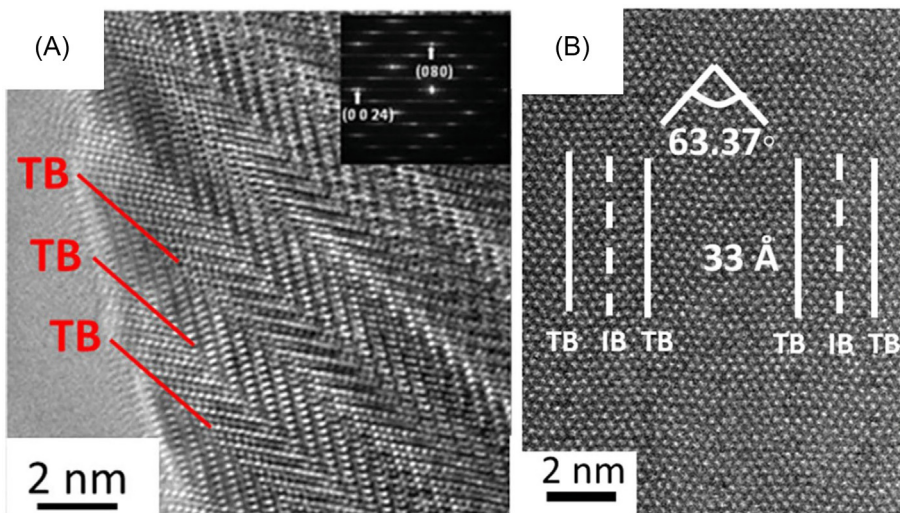


**Fig. 2.11.2** (A) Twin boundaries (TB) and (B) inversion boundaries (IB) in  $\text{Ga}_2\text{O}_3(\text{ZnO})_9$ . Reproduced with permission from D. Alvarez-Ruiz, F. Azough, D.T. Hernandez-Maldonado, D.M. Kepaptsoglou, Q.M. Ramasse, P. Svec, P. Svec Sr., R. Freer, Enhancement of electrical conduction and phonon scattering in  $\text{Ga}_2\text{O}_3(\text{ZnO})_9\text{-In}_2\text{O}_3(\text{ZnO})_9$  compounds by modification of interfaces at the nanoscale, J. Electron. Mater. 48 (2018) 1818–1826.

low  $\sigma$  [92]. However, first-principle calculations for rutile [93] suggested a  $ZT_{\max}$  of 0.93 at 2000K.

### 2.11.3.3.2 Magnéli phases

Due to the limitations of  $\text{TiO}_2$ , the Magnéli phases  $\text{Ti}_n\text{O}_{2n-1}$  ( $n=2, 3, \dots$ ) have been the subject of several investigations [94]. These phases can be formed by increasing the oxygen vacancy concentration in  $\text{TiO}_2$ , leading to the formation of planar shear defects [92]. The very small dimensions of such defects (0.2–2.0nm) means they do not scatter charges, but are effective for phonon scattering ( $l_{ph}$  of  $\text{TiO}_2 \approx 1\text{ nm}$ ) and thus help to reduce  $\kappa$  [95].

The preparation of single phase Magnéli phase is challenging and frequently more than one phase develops in bulk samples [96, 97]. Electronic transport properties are controlled by the oxygen nonstoichiometry [96, 98]; at higher levels of oxygen deficiency, the number of charge carriers increases,  $\sigma$  increases, and  $S$  is reduced. In samples prepared with an excess of 8 vol% Ti, a maximum  $\sigma S^2$  of  $1000\mu\text{W m}^{-1}\text{ K}^{-2}$  was achieved at 973K [99]. Furthermore,  $\kappa$  can also be tuned by adjusting oxygen deficiency [91, 92, 95, 96]; at room temperature  $\kappa$  was reduced from  $5.18\text{ W m}^{-1}\text{ K}^{-1}$  for  $\text{TiO}_2$  to  $2.04\text{ W m}^{-1}\text{ K}^{-1}$  for  $\text{TiO}_{1.80}$  [95]. Additionally, preparation of Magnéli phases by high-pressure, high-temperature (HPHT) techniques yields high-density ceramics with superior thermoelectric performance to conventionally prepared ceramics [100]. By optimizing processing conditions, Liu et al. [100] achieved a

$ZT_{max}$  of 0.35 at 973K for nonstoichiometric  $TiO_{2-x}$ , one of the highest values for the Magnéli phases. Finally, N doping [101] and Nb/N co-doping [102] of  $TiO_{2-x}$  phases have been very effective; Mikami and Ozaki [101] demonstrated a simultaneous increase in  $S$  and reduction in  $\kappa$  for  $Ti_n(O,N)_{2n-1}$  phases, giving a  $ZT_{max}$  of 0.40 at 1150K for  $Ti_8(O,N)_{15}$ . Similarly, by co-doping with Nb and N Liu et al. [102] increased  $\sigma S^2$  and reduced  $\kappa$  resulting in a  $ZT_{max}$  of 0.35 at 973K for  $Ti_{0.83}Nb_{0.17}(O,N)_{2\pm\delta}$ .

There are also other thermoelectric Magnéli phases based on niobium ( $Nb_{3n-1}O_{8n-2}$ ) and tungsten ( $W_nO_{3n-1}$ ), but their performance is modest; a  $ZT_{max}$  of 0.23 at 1000K was reported for composites made of  $NbO_x$  with TiN or W additions [92] while the  $ZT_{max}$  was only 0.15 at 1100K for composites of  $WO_{2.90}$  with  $Ta_2O_5$  [103].

#### 2.11.3.4 Tungsten bronze structured materials

Materials with the complex tungsten bronze structure, such as  $(Sr,Ba)Nb_2O_6$  (SBN) are expected to have low  $\kappa$  [104]. The structure of SBN consists of two A-sites, occupied by Sr (A1-site) and Sr/Ba atoms (A2-sites), B sites occupied by Nb atoms and vacant C-sites surrounded by O atoms [105–107]. Polarization along the  $c$ -axis [108] leads to anisotropy in the transport properties. Single crystal  $Sr_{0.61}Ba_{0.39}Nb_2O_6$  (SBN61) exhibits high  $\sigma S^2$  ( $2 \times 10^{-3} \text{ W m}^{-1} \text{ K}^{-2}$  at 516K) along the  $c$ -direction [109], which combined with the inherently low  $\kappa$  suggests that SBN could have high ZT values [109, 110]. Nonetheless, anisotropy in the transport properties indicates that ceramics need to be textured to maximize thermoelectric performance. For non-textured ceramics, Lee et al. [111] showed that properties were highest along the  $a$ -axis and that conductivity of the grain boundaries dominated charge transport in SBN. A variety of doping strategies were explored including La on Sr sites [112], substituting K and Y for Sr, and Zr and Mo for Nb [113, 114], F doping on O sites [115] and interstitial doping [116, 117]. It was shown that donor doping on the Sr site enhanced the  $\sigma S^2$  [112, 113] as a result of changes in the distance between  $NbO_6$  structural layers and weakening of metal-oxygen bonds [112]. On the other hand, F doping on O sites also increased  $\sigma S^2$  through changes to the band structure and increased carrier concentration [115]. Fluorine doping also helped to reduce  $\kappa$ , which led to a  $ZT_{max}$  of 0.21 at 1073K for  $Sr_{0.61}Ba_{0.39}Nb_2O_{5.95}F_{0.05}$ . Finally, interstitial doping with Yb [116] or K [117] improved the  $\sigma S^2$  through enhancement of  $\sigma$ ; Yb doping tended to reduce  $\kappa$ , whereas K interstitial doping led to an increase in  $\kappa$ . A  $ZT_{max}$  of 0.23 at 1073K was obtained for  $Sr_{0.7}Ba_{0.3}K_{0.1}Nb_2O_{6-\delta}$  [117].

The related ferroelectric  $Ba_{6-x}Nd_{8+2x}Ti_{18}O_{54}$  also has a tungsten bronze structure; it was demonstrated to have a high  $S$  ( $-210 \mu\text{VK}^{-1}$ ) and low  $\sigma$  ( $60 \text{ S cm}^{-1}$ ) [118]. Moreover, it exhibits a low and stable  $\kappa$  with temperature ( $\sim 1.45 \text{ W m}^{-1} \text{ K}^{-1}$ ), indeed one of the lowest  $\kappa$  values reported for thermoelectric oxides. By adjusting the Ba/Nd ratio, the thermoelectric performance could be maximized and a  $ZT_{max}$  of 0.16 was achieved at 1000K for  $Ba_{5.19}Nd_{8.54}Ti_{18}O_{54}$ . These results indicate that tungsten bronze structured oxides are promising thermoelectrics and using strategies such as texturing and different types of doping could further improve the thermoelectric performance.

### 2.11.3.5 *SrTiO<sub>3</sub>-based materials*

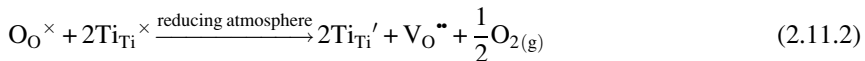
SrTiO<sub>3</sub> (STO) is one of the most promising thermoelectric oxides due to its chemical flexibility and high-temperature stability. It has an ideal cubic perovskite structure (Goldschmidt tolerance factor,  $\tau_G = 1.002$ ), a space group of  $Pm\bar{3}m$  with a lattice parameter of 3.905 Å at room temperature [119]. It has a mixed ionic-covalent nature due to covalent Ti—O and ionic Sr—O bonds. When processed in air STO is insulating [120–122], which limits  $\sigma S^2$  even though the S values are high ( $-380 \mu\text{VK}^{-1}$  at 300K). Another limiting factor is the high  $\kappa$  ( $9\text{--}12 \text{W m}^{-1} \text{K}^{-1}$ ) at room temperature [123, 124]. However, by optimizing the processing parameters,  $\sigma S^2$  can be maximized, even reaching values comparable to those of conventional thermoelectric materials such as Bi<sub>2</sub>Te<sub>3</sub> [120]. In contrast, the reduction of  $\kappa$  is more challenging due to the small mean free path ( $l_{ph} \leq 10 \text{nm}$ ) for the majority of phonons [125]. This makes the typical nanostructuring approach to reduce  $\kappa$  ineffective, necessitating atomic-scale defects, such as vacancies or doping.

The thermoelectric properties of STO have been examined in terms of the effects of processing [126–131], donor doping on A- [120, 123, 126–129, 132–136] and/or B-sites [130, 137–145], A-site vacancies [146–150] and STO-based composites [134, 138, 151–161]. By using different processing and doping strategies, ZT<sub>max</sub> values of 0.35–0.41 can be achieved (Table 2.11.1). However, the electronic and thermal properties depend on the processing route; it is possible to prepare ceramics with core-shell-type microstructures using spark plasma sintering (SPS) [136, 166] while the mixed oxide (MO) route, with or without hot pressing (HP), typically leads to single-phase, homogenous materials [126–128]. It is well established that STO-based ceramics must be prepared under reducing conditions to maximize thermoelectric performance [129–131]; the formation of oxygen vacancies (Eq. 2.11.1), helps to improve  $\sigma$  [167] and reduce  $\kappa$  [168]. Moreover, the reduction of Ti<sup>4+</sup> to Ti<sup>3+</sup> upon the formation of oxygen vacancies (Eq. 2.11.2) results in an increased  $n$ , leading to the improved  $\sigma$  [167]. Therefore, bulk STO ceramics are either directly sintered in reducing atmosphere or prepared in air and then annealed under reducing conditions.



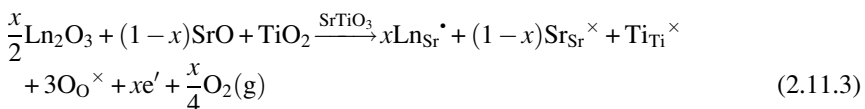
**Table 2.11.1** ZT<sub>max</sub> values for STO-based materials.

Formulation	Processing route	ZT <sub>max</sub>	Reference
Sr <sub>0.92</sub> La <sub>0.08</sub> TiO <sub>3</sub>	SPS	0.37 (1045K)	[135]
Sr <sub>0.9</sub> Dy <sub>0.1</sub> TiO <sub>3-δ</sub>	MO	0.41 (1073K)	[128]
Sr <sub>0.9</sub> Gd <sub>0.1</sub> TiO <sub>3-δ</sub>	SPS	0.37 (1006K)	[162]
SrTi <sub>0.80</sub> Nb <sub>0.20</sub> O <sub>3</sub>	HP	0.35 (1000K)	[163]
Sr <sub>0.83</sub> La <sub>0.1</sub> Dy <sub>0.07</sub> TiO <sub>3</sub>	MO	0.36 (1045K)	[164]
Sr <sub>0.775</sub> La <sub>0.15</sub> TiO <sub>3-δ</sub>	MO	0.41 (973K)	[147]
Sr <sub>0.70</sub> La <sub>0.16</sub> Ti <sub>0.80</sub> Nb <sub>0.20</sub> O <sub>3</sub>	MO	0.35 (1000K)	[165]

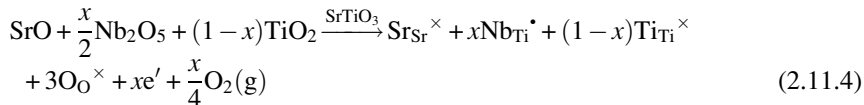


### 2.11.3.5.1 Donor-doped $\text{SrTiO}_3$

Donor doping of STO mainly focuses on replacing Sr by lanthanide series elements [127, 128, 132, 133, 136, 141, 166, 169–171] while some studies have doped Nb on the Ti site [130, 143]. There are also cases of dual doping on the A-site [164, 172] or B-site [145], and combined doping on both A- and B-sites [124, 173]. It was demonstrated that La-doped STO single crystals could have  $\sigma S^2$  values as high as  $2.8\text{--}3.6 \times 10^{-3} \text{ W m}^{-1} \text{ K}^{-2}$  [120], which is comparable with  $\text{Bi}_2\text{Te}_3$ . Lanthanide doping on A-sites leads to distortion of the  $\text{TiO}_6$  octahedra due to the ionic radius differences [174]. Hence, the solubility limit for lanthanides is typically 10 mol% [128] and a secondary  $\text{Ln}_2\text{Ti}_2\text{O}_7$  phase develops in heavily doped samples [128]. Furthermore, the distortion of the  $\text{TiO}_6$  octahedra leads to modification of the electronic band structure [175, 176] and an increase in  $n$  (Eq. 2.11.3). This improves  $\sigma S^2$ , through the increase in  $\sigma$  and negligible decrease in  $S$  due to the change in the effective mass of charge carriers ( $m^*$ ) with the reduction in the unit cell volume [176]. Conversely, lanthanide doping leads to a reduction of  $\kappa$  from improved phonon scattering, resulting from mass/strain contrast between host and dopant cations [127]. Strain contrast occurs as a result of introducing cations smaller than Sr on the A-site, and mass contrast occurs because of the significant mass difference between Sr and lanthanides. Therefore, doping with larger ionic radius lanthanides (La, Pr, etc.) leads to relatively higher  $\sigma S^2$  values while a lower  $\kappa$  is achieved upon doping with smaller ionic radius lanthanides (Dy, Yb, etc.) [127, 128].



The most common B-site dopants for STO are Nb [130, 143], Ta [144, 177], and W [145]. Doping with Nb leads to metallic conduction [142] and  $\sigma$  is improved by the increase in  $n$  [143] (Eq. 2.11.4). At the same time,  $S$  is improved because of the increase in effective mass  $m^*$  [143]. Therefore, Nb doping of STO enabled a maximum  $\sigma S^2$  of  $\sim 1500 \mu\text{W m}^{-1} \text{ K}^{-2}$  at 1000 K for  $\text{SrTi}_{0.6}\text{Nb}_{0.4}\text{O}_3$ , while a  $ZT_{\max}$  of 0.37 was obtained for  $\text{SrTi}_{0.8}\text{Nb}_{0.2}\text{O}_3$  epitaxial thin films at 1000 K [143]. In spite of similar structural effects when STO is doped by Ta [144], the covalent nature of Ta—O bonds results in a more noticeable reduction in  $\kappa$  compared to Nb [178]. As a result, a  $ZT_{\max}$  of 0.24 at 1000 K was achieved for  $\text{SrTi}_{0.9}\text{Ta}_{0.1}\text{O}_3$  [144]. The final dopant, W, has a much lower solubility in  $\text{SrTiO}_3$  (<6%) [145] which limits the improvement in  $\sigma$  and hence  $\sigma S^2$  even though  $\kappa$  is reduced. Thus, only a modest  $ZT_{\max}$  of 0.13 at 1000 K was achieved for  $\text{SrTi}_{0.97}\text{W}_{0.03}\text{O}_3$  [145].



Dual doping on both A- and/or B-sites has been examined to enhance the thermoelectric properties of STO [137, 173, 179]. It enables improvement of  $\sigma S^2$  by optimizing the  $n$  and reduction of  $\kappa$  by much-enhanced mass/strain contrast [145, 164, 172]. Therefore, by this approach a  $ZT_{\max}$  of 0.28 was obtained for  $\text{Sr}_{0.97}\text{Ti}_{0.8}\text{Nb}_{0.17}\text{W}_{0.03}\text{O}_{3\pm\delta}$  at 1270K [145] and 0.36 for  $\text{La}_{0.1}\text{Sr}_{0.83}\text{Dy}_{0.07}\text{TiO}_3$  at 1045K [164].

### 2.11.3.5.2 A-site deficient $\text{SrTiO}_3$

As the small mean free path for phonons in STO is comparable to the interatomic distances [180] it is necessary to introduce atomic scale defects to effectively scatter phonons to reduce  $\kappa$ . One approach for achieving such defects has been the introduction of A-site cation vacancies [146–150, 181, 182]. Typically, lanthanide doping and Sr vacancies are introduced together so that  $\kappa$  can be reduced while simultaneously improving the electronic transport properties, as in  $\text{SrTiO}_3\text{-Ln}_{2/3}\text{TiO}_3$  solid solutions [146–150]. Popuri et al. [146] were the first to demonstrate that it was possible to tune the  $\kappa$  of STO with A-site vacancies, achieving a glass-like, temperature-independent  $\kappa$ . The origin of such behavior was shown to be the combination of mass/strain contrast with doping, interface scattering of phonons due to the formation of a layered structure, and the presence of anti-phase and twin boundaries [146–148, 150]; A-site vacancies also localized the motions of Sr [149]. Furthermore, the electronic transport properties could be tuned by adjusting the Ln/vacancy concentration on A-sites [147, 148, 150]. The optimum Ln/vacancy concentration for maximum performance was achieved with vacancy concentrations of 3.3%–13.3% [147, 148, 150]. The majority of such studies reported  $ZT_{\max}$  values  $\sim 0.28$  at 870K regardless of processing approach and dopants used [147, 148, 150], although a  $ZT_{\max}$  of 0.41 was achieved for  $\text{Sr}_{0.775}\text{La}_{0.15}\text{TiO}_3$  at 973K [147], one of the highest ZT values reported for STO-based thermoelectric materials.

For the solid solution of STO and A-site deficient  $\text{La}_{1/3}\text{NbO}_3$  [165, 183], a  $ZT_{\max}$  of 0.25 at 1000K was achieved for  $\text{Sr}_{0.8}\text{La}_{0.067}\text{Ti}_{0.8}\text{Nb}_{0.2}\text{O}_3$  [165]. It was also demonstrated that excess La doping on Sr site and Nb doping on Ti site could improve performance, leading to a  $ZT_{\max}$  of 0.35 at 1000K with only 5% additional La doping.

### 2.11.3.5.3 $\text{SrTiO}_3$ -based composites

To further improve the properties of STO-based ceramics, different approaches have been utilized, by incorporating additives or inclusions to the STO matrix [154–158]. It was demonstrated that introducing yttria stabilized zirconia (YSZ) [159, 160], mesoporous silica (MS) [161], potassium niobate (KTO) nanowires [151], and  $\text{TiO}_2$  nanotube (TNT) [138] could improve  $\sigma S^2$  and/or reduce  $\kappa$ . The main limitation arising from such additives was the low density of ceramics processed conventionally; nevertheless, improvements in the transport properties were achieved [159, 160]. For example,

a  $ZT_{max}$  of 0.34 at 900K was obtained for  $\text{SrTi}_{0.85}\text{Nb}_{0.15}\text{O}_3$  ceramics containing 3 wt% KTO [151]. It was shown that high-density  $\text{Sr}_{0.9}\text{Nd}_{0.1}\text{TiO}_3$  could be achieved by the co-addition of  $\text{B}_2\text{O}_3$  and  $\text{ZrO}_2$  [184]; the  $\text{ZrO}_2$  promoted chemical homogeneity (Fig. 2.11.3) and a 30% improvement in the  $\sigma S^2$  ( $2.0 \times 10^{-3} \text{ W m}^{-1} \text{ K}^{-2}$  at 500K) while obtaining a respectable  $ZT_{max}$  value of 0.37 at 1015K from additions of 0.5 wt%  $\text{B}_2\text{O}_3$  and 0.3 wt%  $\text{ZrO}_2$ .

Recently, it was shown that incorporating metallic inclusions in the matrix [134, 158] could improve  $\sigma S^2$  by simultaneously increasing  $n$  and reducing  $\kappa$  (by the scattering of phonons at inclusion/matrix interface) leading to improved thermoelectric performance. For  $\text{Sr}_{0.9}\text{La}_{0.1}\text{TiO}_3$ , 15% Ag addition increased ZT from 0.08 to 0.18 at 960K [134]; for  $\text{Sr}_{0.8}\text{La}_{0.067}\text{Ti}_{0.8}\text{Nb}_{0.2}\text{O}_{3-\delta}$ , 2.5 wt% Cu increased ZT from 0.25 to 0.36 at 1000K [158].

Finally, the focus on STO-based composites moved to STO/graphene(oxide) composites [152, 153, 157, 185] after Lin et al. [157] reported that thermoelectric properties can be improved and the operational temperature window can be widened by incorporation of graphene [157]. Single crystal-like electronic transport behavior in a polycrystalline material was a further advantage [120]. It was demonstrated that the presence of graphene at the grain boundaries (GBs) promotes oxygen deficiency at GBs [152]; the single crystal-like charge conduction behavior was attributed to an increase in the weighted mobility [186]. Dylla et al. [186] also suggested that by optimizing the grain boundary structure,  $ZT_{max}$  greater than 0.5 could be obtained for  $T > 300\text{K}$ .

### 2.11.3.6 Other n-type oxides

#### 2.11.3.6.1 A-site deficient perovskites

The related A-site deficient perovskites, with complex/layered crystal structures,  $\text{La}_{1/3}\text{NbO}_3$  [183],  $\text{Pr}_{2/3}\text{TiO}_3$  [187], and  $\text{La}_{2/3}\text{TiO}_3$  [147] have also been investigated. The complexity of the crystal structures of these materials leads to a low  $\kappa$  ( $2 \text{ W m}^{-1} \text{ K}^{-1}$  at 500K for  $\text{La}_{1/3}\text{NbO}_3$  [183]) with reasonable  $\sigma S^2$  ( $S \approx -120 \mu\text{V K}^{-1}$  and  $\sigma \approx 180 \text{ S cm}^{-1}$  for  $\text{Pr}_{2/3}\text{TiO}_3$  [187]) as a result of the electronic band structure.

#### 2.11.3.6.2 Layered perovskite oxides

Layered perovskite oxides include (i) Ruddlesden-Popper phases, (ii) Dion-Jacobson phases, and (iii) Aurivillius phases. All have structural layers parallel to [001] and have a chemical formula of  $\text{AO}(\text{ABO}_3)_n$ ,  $\text{A}'(\text{A}_{n-1}\text{B}_n\text{O}_{3n+1})$ , and  $(\text{Bi}_2\text{O}_2)(\text{A}_{n-1}\text{B}_n\text{O}_{3n+1})$ , respectively. Among these, the Ruddlesden-Popper (RP) phases have been most studied for thermoelectric applications. The RP phase occurs in STO when excess Sr leads to  $\text{SrO}$  planar defects [188]; the crystal structure can be described as alternative stacking of STO perovskite slabs and  $\text{SrO}$  layers. An increase in the number of STO slabs between  $\text{SrO}$  layers ( $n \rightarrow \infty$ ) is required for enhancing electronic transport while shorter distances between  $\text{SrO}$  layers are necessary to reduce  $\kappa$  [189]. Studies of the effects of lanthanides on Sr site [189–191] and Nb

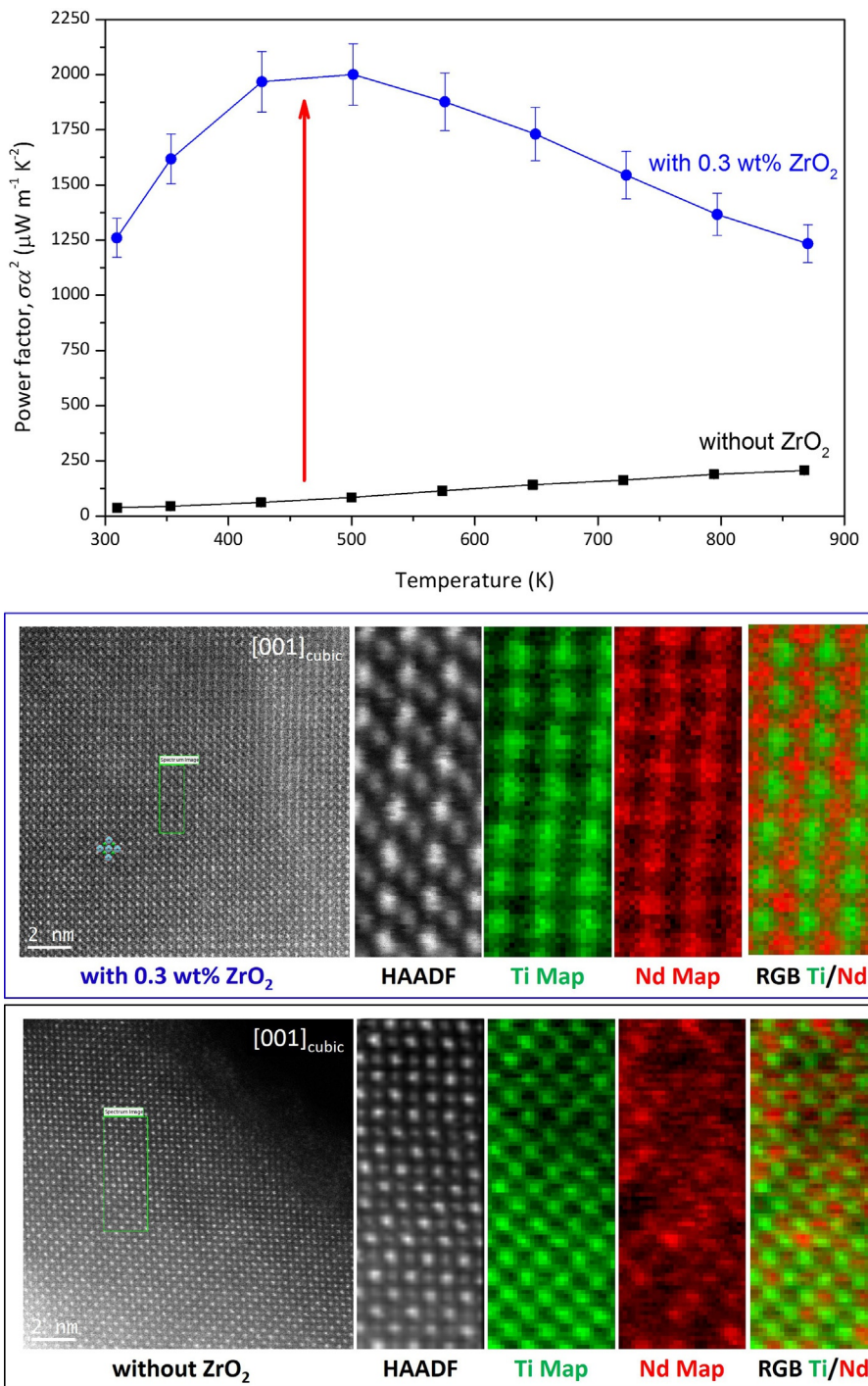


Fig. 2.11.3 See figure legend on next page.

on Ti site [192, 193] showed that the symmetry of  $\text{TiO}_6$  octahedra and the charge carrier scattering by  $\text{SrO}$  layers controlled the electronic transport properties. Thus, a larger number of perovskite slabs and net distance between  $\text{SrO}$  layers are required for higher thermoelectric  $\sigma S^2$ . Thus, optimization of the ZT is challenging and RP phases tend to exhibit modest  $ZT_{\max}$  values (0.14 at 1000 K [192]). However, by improving the symmetry of  $\text{TiO}_6$  octahedra and increasing  $n$ , Wang et al. [193] achieved a  $ZT_{\max}$  value of 0.24 at 1000 K for 5% Gd-doped  $\text{SrO}(\text{SrTiO}_3)_2$ .

Other layered perovskite oxides include  $\text{La}_2\text{Ti}_2\text{O}_7$  [194] and  $\text{Sr}_2\text{Nb}_2\text{O}_7$  [195]. Their complex and layered crystal structures are responsible for the low  $\kappa$  of these materials ( $1.3 \text{ W m}^{-1} \text{ K}^{-2}$  for  $\text{La}_2\text{Ti}_2\text{O}_7$  and  $1.5 \text{ W m}^{-1} \text{ K}^{-2}$  for  $\text{Sr}_2\text{Nb}_2\text{O}_7$ ). However, low  $\sigma$  generally limits the overall thermoelectric performance. A recent ab initio study of  $\text{La}_2\text{Ti}_2\text{O}_7$  [196] suggested that the ZT value could reach 2.6 at 1200 K by optimizing  $n$  to  $\sim 10^{20} \text{ cm}^{-3}$  [196]. However, optimization of  $n$  to such values remains challenging.

## 2.11.4 Applications

Oxide thermoelectric materials are usually considered for generating power from waste heat at high temperatures. Their thermal and chemical stability, low cost of raw materials, and nontoxic constituent elements make them attractive for such applications. Moreover, cascade devices with oxide materials on the high-temperature side could widen the operating temperature window of thermoelectric modules; commercial cascade modules based on  $\text{Bi}_2\text{Te}_3/\text{CaMnO}_3$  ([www.tecteg.com](http://www.tecteg.com)) and experimental work on other cascade systems supports this argument [197]. CCO-based materials are frequently the choice for p-type legs while different materials have been used for the n-type legs [197–205]. Power density values for oxide thermoelectrics are presented in Fig. 2.11.4. The data suggests that they could also be employed for applications where low power densities are required. Experimental data from the cascade modules [197, 207] shows that the performance of the existing modules could be improved and high power density devices can be obtained. In addition, widening of the operating window for such devices is important since there are thermoelectric materials with high  $ZT_{\max}$  values, but low average ZT values [208]. In this respect, the greatly enhanced operating window for STO-graphene composites [157] suggests composites could play an increasingly important role in future devices.

**Fig. 2.11.3** Improvement in the power factor and homogeneity of  $\text{Sr}_{0.9}\text{Nd}_{0.1}\text{TiO}_3$  by additions of 0.5 wt%  $\text{B}_2\text{O}_3$  and 0.3 wt%  $\text{ZrO}_2$ .

The figure is modified from D. Ekren, F. Azough, A. Gholinia, S.J. Day, D. Hernandez-Maldonado, D.M. Kepaptsoglou, Q.M. Ramasse, R. Freer, Enhancing the thermoelectric power factor of  $\text{Sr}_{0.9}\text{Nd}_{0.1}\text{TiO}_3$  through control of the nanostructure and microstructure, *J. Mater. Chem. A* 6 (2018) 24928–24939.

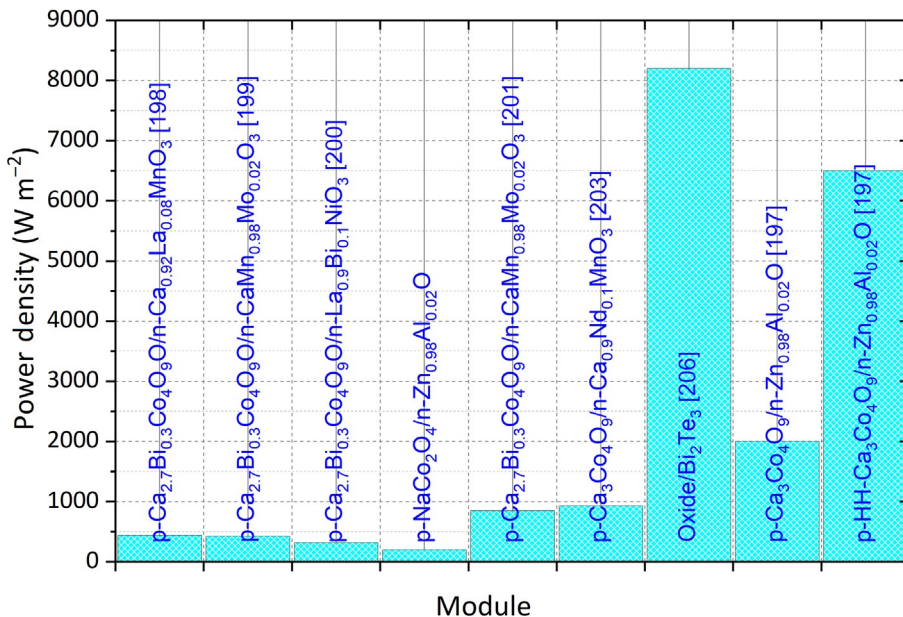


**Fig. 2.11.4** Power densities of oxide thermoelectric modules for p-Ca<sub>2.7</sub>Bi<sub>0.3</sub>Co<sub>4</sub>O<sub>9</sub>/n-Ca<sub>0.92</sub>La<sub>0.08</sub>MnO<sub>3</sub> [198], p-Ca<sub>2.7</sub>Bi<sub>0.3</sub>Co<sub>4</sub>O<sub>9</sub>/n-CaMn<sub>0.98</sub>Mo<sub>0.02</sub>O<sub>3</sub> [199], p-Ca<sub>2.7</sub>Bi<sub>0.3</sub>Co<sub>4</sub>O<sub>9</sub>/n-La<sub>0.9</sub>Bi<sub>0.1</sub>NiO<sub>3</sub> [200], p-NaCo<sub>2</sub>O<sub>4</sub>/n-Zn<sub>0.98</sub>Al<sub>0.02</sub>O [206], p-Ca<sub>2.7</sub>Bi<sub>0.3</sub>Co<sub>4</sub>O<sub>9</sub>/n-CaMn<sub>0.98</sub>Mo<sub>0.02</sub>O<sub>3</sub> [201], p-Ca<sub>3</sub>Co<sub>4</sub>O<sub>9</sub>/n-Ca<sub>0.9</sub>Nd<sub>0.1</sub>MnO<sub>3</sub> [203], oxide/Bi<sub>2</sub>Te<sub>3</sub> [207], p-Ca<sub>3</sub>Co<sub>4</sub>O<sub>9</sub>/n-Zn<sub>0.98</sub>Al<sub>0.02</sub>O [197], and p-HH-Ca<sub>3</sub>Co<sub>4</sub>O<sub>9</sub>/n-Zn<sub>0.98</sub>Al<sub>0.02</sub>O [197].

## 2.11.5 Outlook

The ZT<sub>max</sub> values for leading thermoelectric oxides are summarized in Fig. 2.11.5. It is clear that p-type single crystals with ZT<sub>max</sub> values reaching 1.2 could be employed in thermoelectric applications; however, the anisotropy of the properties makes it challenging to prepare bulk ceramics with similar performance. With advances in material processing, high quality textured ceramics could be prepared. On the other hand, n-type bulk oxides underperform in comparison to p-type oxides; nevertheless, recent reports of ZT<sub>max</sub> values  $\geq 0.6$  [212, 213] and stable ZT values for oxide-based composites [157] suggest that these materials could be employed for thermoelectric applications. Indeed, the high  $\sigma S^2$  values [120, 157, 184] and improved performance documented for STO-based superlattices [218] indicate that further improvement is possible. Recent first-principles calculations and theoretical predictions [110, 186, 214, 216, 217, 219] (see Fig. 2.11.5C) suggest that oxide materials with ZT<sub>max</sub> values  $>1$  could be prepared. Finally, the chemical flexibility, thermal stability, earth-abundant constituent elements, and environmental friendliness of oxides could lead to cost-effective thermoelectric devices competitive with conventional technologies and comply with the latest environment regulations.

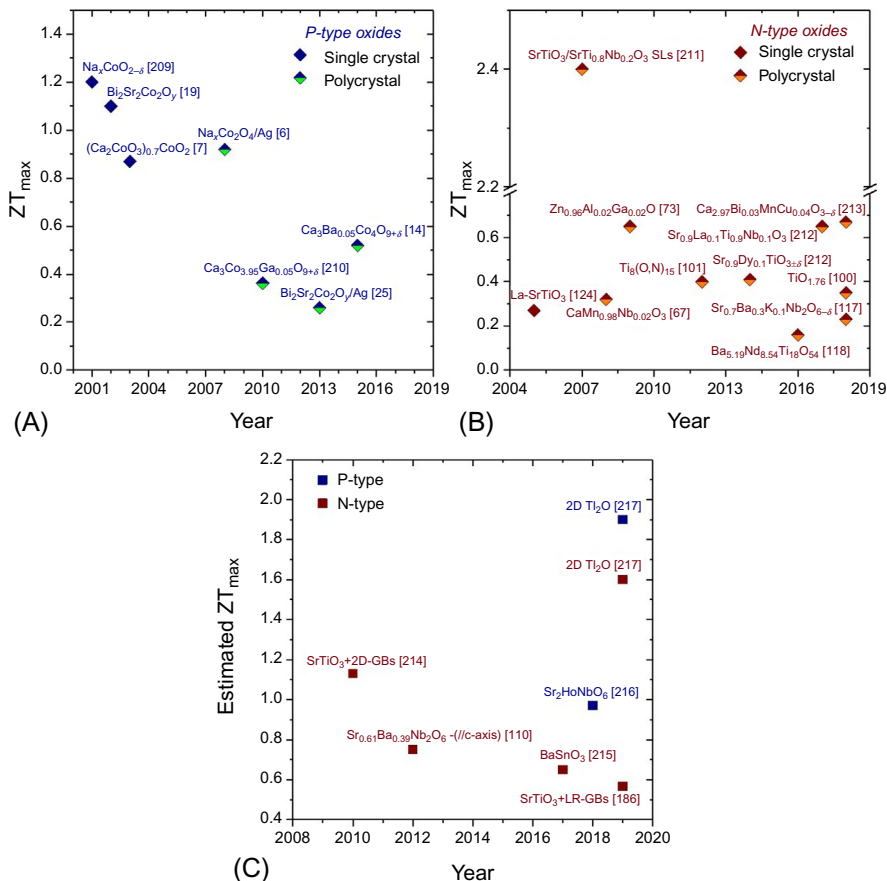


**Fig. 2.11.5**  $ZT_{\max}$  values reported for p-type (A) and n-type (B) thermoelectric oxides, and (C) estimated  $ZT_{\max}$  values for oxide thermoelectric materials;  $Na_xCoO_{2-\delta}$  [209],  $Bi_2Sr_2Co_2O_y$  [19],  $(Ca_2CoO_3)_{0.7}CoO_2$  [7],  $Na_xCo_2O_4/Ag$  [6],  $Ca_3Co_{3.95}Ga_{0.05}O_{9+\delta}$  [210],  $Bi_2Sr_2Co_2O_y/Ag$  [25],  $Ca_3Ba_{0.05}Co_4O_{9+\delta}$  [14], La-doped  $SrTiO_3$  [124],  $SrTiO_3/SrTi_{0.8}Nb_{0.2}O_3$  SLs [211],  $CaMn_{0.98}Nb_{0.02}O_3$  [67],  $Zn_{0.96}Al_{0.02}Ga_{0.02}O$  [73],  $Ti_8(O,N)_{15}$  [101],  $Sr_{0.9}Dy_{0.1}TiO_{3\pm\delta}$  [122],  $Ba_{5.19}Nd_{8.54}Ti_{18}O_{54}$  [118],  $Sr_{0.9}La_{0.1}Ti_{0.9}Nb_{0.1}O_3$  [212],  $TiO_{1.76}$  [100],  $Sr_{0.7}Ba_{0.3}K_{0.1}Nb_2O_{6-\delta}$  [117],  $Ca_{2.97}Bi_{0.03}MnCu_{0.04}O_{3-\delta}$  [213],  $SrTiO_3$  with 2D-GBs [214],  $Sr_{0.61}Ba_{0.39}Nb_2O_6$  [110],  $BaSnO_3$  [215],  $Sr_2HoNbO_6$  [216], 2D- $Tl_2O$  [217], and  $SrTiO_3$  with low resistivity GBs [186].

## Acknowledgments

The authors are grateful to the EPSRC for the provision of funding for this work (EP/H043462, EP/I036230/1, EP/L014068/1, EP/L017695/1 acknowledged by RF). All research data supporting this publication are directly available within the publication.

## References

- [1] I. Terasaki, Y. Sasago, K. Uchinokura, Large thermoelectric power in  $\text{NaCo}_2\text{O}_4$  single crystals, *Phys. Rev. B* 56 (1997) 685–687.
- [2] J. He, Y. Liu, R. Funahashi, Oxide thermoelectrics: the challenges, progress, and outlook, *J. Mater. Res.* 26 (2011) 1762–1772.
- [3] H. Yakabe, K. Kikuchi, I. Terasaki, Y. Sasago, K. Uchinokura, Thermoelectric properties of transition-metal oxide  $\text{NaCo}_2\text{O}_4$  system, in: XVI ICT '97. Proceedings ICT'97. 16th International Conference on Thermoelectrics (Cat. No.97TH8291), 1997, pp. 523–527.
- [4] W. Koshiba, K. Tsutsui, S. Maekawa, Thermopower in cobalt oxides, *Phys. Rev. B Condens. Matter Mater. Phys.* 62 (2000) 6869–6872.
- [5] Y. Miyazaki, Crystal structure and thermoelectric properties of the misfit-layered cobalt oxides, *Solid State Ionics* 172 (2004) 463–467.
- [6] M. Ito, D. Furumoto, Microstructure and thermoelectric properties of  $\text{Na}_x\text{Co}_2\text{O}_4/\text{Ag}$  composite synthesized by the polymerized complex method, *J. Alloys Compd.* 450 (2008) 517–520.
- [7] M. Shikano, R. Funahashi, Electrical and thermal properties of single-crystalline  $(\text{Ca}_2\text{Co}_3)_0.7\text{CoO}_2$  with a  $\text{Ca}_3\text{Co}_4\text{O}_9$  structure, *Appl. Phys. Lett.* 82 (2003) 1851–1853.
- [8] G. Xu, R. Funahashi, M. Shikano, I. Matsubara, Y. Zhou, Thermoelectric properties of the Bi- and Na-substituted  $\text{Ca}_3\text{Co}_4\text{O}_9$  system, *Appl. Phys. Lett.* 80 (2002) 3760–3762.
- [9] Q.M. Lu, J.X. Zhang, Q.Y. Zhang, Y.Q. Liu, D.M. Liu, Improved thermoelectric properties of  $\text{Ca}_{3-x}\text{Ba}_x\text{Co}_4\text{O}_9$  ( $x=0\sim0.4$ ) bulks by sol-gel and SPS method, in: Proceedings International Conference on Thermoelectrics, IEEE, 2006, pp. 66–69.
- [10] H. Fukutomi, Y. Konno, K. Okayasu, M. Hasegawa, H. Nakatsugawa, Texture development of  $\text{Ca}_3\text{Co}_4\text{O}_9$  thermoelectric oxide by high temperature plastic deformation and its contribution to the improvement in electric conductivity, *Mater. Sci. Eng. A* 527 (2009) 61–64.
- [11] H. Hao, Q. He, C. Chen, H. Sun, X. Hu, Textured structure and anisotropic thermoelectric properties of  $\text{Ca}_{2.7}\text{Bi}_{0.3}\text{Co}_4\text{O}_9$  oxide prepared by conventional solid-state reaction, *Int. J. Mod. Phys. B* 23 (2009) 87–95.
- [12] D. Moser, L. Karvonen, S. Populoh, M. Trottmann, A. Weidenkaff, Influence of the oxygen content on thermoelectric properties of  $\text{Ca}_{3-x}\text{Bi}_x\text{Co}_4\text{O}_{9+\delta}$  system, *Solid State Sci.* 13 (2011) 2160–2164.
- [13] J.D. Baran, M. Molinari, N. Kulwongwit, F. Azough, R. Freer, D. Kepaptsoglou, Q.M. Ramasse, S.C. Parker, Tuning thermoelectric properties of misfit layered cobaltites by chemically induced strain, *J. Phys. Chem. C* 119 (2015) 21818–21827.
- [14] C. Boyle, P. Carillo, Y. Chen, E.J. Barbero, D. McIntyre, X. Song, Grain boundary segregation and thermoelectric performance enhancement of bismuth doped calcium cobaltite, *J. Eur. Ceram. Soc.* 36 (2016) 601–607.
- [15] R. Funahashi, I. Matsubara, S. Sodeoka, Thermoelectric properties of  $\text{Bi}_2\text{Sr}_2\text{Co}_2\text{O}_x$  polycrystalline materials, *Appl. Phys. Lett.* 76 (2000) 2385.
- [16] J. Lingner, R. Funahashi, E. Combe, M. Letz, G. Jakob, Thermoelectric sintered glass-ceramics with a  $\text{Bi}_2\text{Sr}_2\text{Co}_2\text{O}_x$  phase, *Appl. Phys. A* (2015) 59–66.
- [17] J.D. Baran, D. Kepaptsoglou, M. Molinari, N. Kulwongwit, F. Azough, R. Freer, Q.M. Ramasse, S.C. Parker, Role of structure and defect chemistry in high-performance thermoelectric bismuth strontium cobalt oxides, *Chem. Mater.* 28 (2016) 7470–7478.
- [18] E. Combe, R. Funahashi, T. Barbier, F. Azough, R. Freer, Decreased thermal conductivity in  $\text{Bi}_2\text{Sr}_2\text{Co}_2\text{O}_x$  bulk materials prepared by partial melting, *J. Mater. Res.* 31 (2016) 1296–1305.

- [19] R. Funahashi, M. Shikano,  $\text{Bi}_2\text{Sr}_2\text{Co}_2\text{O}_y$  whiskers with high thermoelectric figure of merit, *Appl. Phys. Lett.* 81 (2002) 1459–1461.
- [20] T. Fujii, I. Terasaki, T. Watanabe, A. Matsuda, Large in-plane anisotropy on resistivity and thermopower in the misfit layered oxide  $\text{Bi}_{2-x}\text{Pb}_x\text{Sr}_2\text{C}_2\text{O}_y$ , *Jpn. J. Appl. Phys. 2 Lett.* 41 (2002) 3–7.
- [21] J.C. Diez, E. Guilmeau, M.A. Madre, S. Marinel, S. Lemonnier, A. Sotelo, Improvement of  $\text{Bi}_2\text{Sr}_2\text{Co}_{1.8}\text{O}_x$  thermoelectric properties by laser floating zone texturing, *Solid State Ionics* 180 (2009) 827–830.
- [22] J.C. Diez, S. Rasekh, G. Constantinescu, M.A. Madre, M.A. Torres, A. Sotelo, Effect of annealing on the thermoelectric properties of directionally grown  $\text{Bi}_2\text{Sr}_2\text{Co}_{1.8}\text{O}_x$  ceramics, *Ceram. Int.* 38 (2012) 5419–5424.
- [23] A. Sotelo, M.A. Torres, G. Constantinescu, S. Rasekh, J.C. Diez, M.A. Madre, Effect of Ag addition on the mechanical and thermoelectric performances of annealed  $\text{Bi}_2\text{Sr}_2\text{Co}_{1.8}\text{O}_x$  textured ceramics, *J. Eur. Ceram. Soc.* 32 (2012) 3745–3751.
- [24] L.H. Yin, R. Ang, Y.N. Huang, H.B. Jiang, B.C. Zhao, X.B. Zhu, W.H. Song, Y.P. Sun, The contribution of narrow band and modulation of thermoelectric performance in doped layered cobaltites  $\text{Bi}_2\text{Sr}_2\text{Co}_2\text{O}_y$ , *Appl. Phys. Lett.* 100 (2012) 173503.
- [25] S. Wang, Z. Bai, H. Wang, Q. Lü, J. Wang, G. Fu, High temperature thermoelectric properties of  $\text{Bi}_2\text{Sr}_2\text{Co}_2\text{O}_y/\text{Ag}$  composites, *J. Alloys Compd.* 554 (2013) 254–257.
- [26] E. Combe, R. Funahashi, F. Azough, R. Freer, Relationship between microstructure and thermoelectric properties of  $\text{Bi}_2\text{Sr}_2\text{Co}_2\text{O}_x$  bulk materials, *J. Mater. Res.* 29 (2014) 1376–1382.
- [27] H. Leligny, D. Grebille, O. Perez, A.C. Masset, M. Hervieu, B. Raveau, A five-dimensional structural investigation of the misfit layer compound  $[\text{Bi}_{0.87}\text{SrO}_2]_2[\text{CoO}_2]_{1.82}$ , *Acta Crystallogr. Sect. B Struct. Sci.* 56 (2000) 173–182.
- [28] H. Yamakawa, S. Lee, H. Takagi, C.A. Randall, Property-processing relations in developing thermoelectric ceramics:  $\text{Na}_{1-x}\text{Co}_2\text{O}_4$ , *J. Mater. Sci.* 46 (2011) 2064–2070.
- [29] M. Karppinen, H. Fjellvåg, T. Konno, Y. Morita, T. Motohashi, H. Yamauchi, Evidence for oxygen vacancies in misfit-layered calcium cobalt oxide,  $[\text{CoCa}_2\text{O}_3]_q\text{CoO}_2$ , *Chem. Mater.* 16 (2004) 2790–2793.
- [30] A. Maignan, D. Flahaut, S. Hébert, Sign change of the thermoelectric power in  $\text{LaCoO}_3$ , *Eur. Phys. J. B* 39 (2004) 145–148.
- [31] T. He, J. Chen, T.G. Calvarese, M.A. Subramanian, Thermoelectric properties of  $\text{La}_{1-x}\text{A}_x\text{CoO}_3$  ( $\text{A} = \text{Pb}, \text{Na}$ ), *Solid State Sci.* 8 (2006) 467–469.
- [32] F. Li, J.F. Li, Effect of Ni substitution on electrical and thermoelectric properties of  $\text{LaCoO}_3$  ceramics, *Ceram. Int.* 37 (2011) 105–110.
- [33] F. Li, J.F. Li, J.H. Li, F.Z. Yao, The effect of Cu substitution on microstructure and thermoelectric properties of  $\text{LaCoO}_3$  ceramics, *Phys. Chem. Chem. Phys.* 14 (2012) 12213–12220.
- [34] R. Robert, M.H. Aguirre, L. Bocher, M. Trottmann, A. Weidenkaff, Synthesis and high temperature thermoelectric properties of Ni and Ti substituted  $\text{LaCoO}_3$ , *J. Solid State Chem.* 179 (2006) 3893–3899.
- [35] Y. Wang, F. Li, L. Xu, Y. Sui, X. Wang, W. Su, X. Liu, Large thermal conductivity reduction induced by La/O vacancies in the thermoelectric  $\text{LaCoO}_3$  system, *Inorg. Chem.* 50 (2011) 4412–4416.
- [36] Y. Song, Q. Sun, Y. Lu, X. Liu, F. Wang, Low-temperature sintering and enhanced thermoelectric properties of  $\text{LaCoO}_3$  ceramics with  $\text{B}_2\text{O}_3\text{-CuO}$  addition, *J. Alloys Compd.* 536 (2012) 150–154.
- [37] V. Vulchev, L. Vassilev, S. Harizanova, M. Khristov, E. Zhecheva, R. Stoyanova, Improving of the thermoelectric efficiency of  $\text{LaCoO}_3$  by double substitution with nickel and iron, *J. Phys. Chem. C* 116 (2012) 13507–13515.

- [38] F. Li, J.F. Li, Enhanced thermoelectric performance of separately Ni-Doped and Ni/Sr-codoped LaCoO<sub>3</sub> nanocomposites, *J. Am. Ceram. Soc.* 95 (2012) 3562–3568.
- [39] R. Kun, S. Populoh, L. Karvonen, J. Gumbert, A. Weidenkaff, M. Busse, Structural and thermoelectric characterization of Ba substituted LaCoO<sub>3</sub> perovskite-type materials obtained by polymerized gel combustion method, *J. Alloys Compd.* 579 (2013) 147–155.
- [40] K. Berggold, M. Kriener, C. Zobel, A. Reichl, M. Reuther, R. Müller, A. Freimuth, T. Lorenz, Thermal conductivity, thermopower, and figure of merit of La<sub>1-x</sub>Sr<sub>x</sub>CoO<sub>3</sub>, *Phys. Rev. B Condens. Matter Mater. Phys.* 72 (2005) 1–7.
- [41] K. Iwasaki, T. Ito, T. Nagasaki, Y. Arita, M. Yoshino, T. Matsui, Thermoelectric properties of polycrystalline La<sub>1-x</sub>Sr<sub>x</sub>CoO<sub>3</sub>, *J. Solid State Chem.* 181 (2008) 3145–3150.
- [42] K. Koumoto, H. Koduka, W.S. Seo, Thermoelectric properties of single crystal CuAlO<sub>2</sub> with a layered structure, *J. Mater. Chem.* 11 (2001) 251–252.
- [43] M.V. Lalic, J. Mestnik-Filho, A.W. Carbonari, R.N. Saxena, M. Morales, Influence of Cd impurity on the electronic properties of CuAlO<sub>2</sub> delafossite: first-principles calculations, *J. Phys. Condens. Matter* 14 (2002) 5517–5528.
- [44] Y. Lu, T. Nozue, N. Feng, K. Sagara, H. Yoshida, Y. Jin, Fabrication of thermoelectric CuAlO<sub>2</sub> and performance enhancement by high density, *J. Alloys Compd.* 650 (2015) 558–563.
- [45] A. Sakulkalavek, R. Sakdanuphab, Power factor improvement of delafossite CuAlO<sub>2</sub> by liquid-phase sintering with Ag<sub>2</sub>O addition, *Mater. Sci. Semicond. Process.* 56 (2016) 313–323.
- [46] V. Siriwongrungson, A. Sakulkalavek, R. Sakdanuphab, Optimum sintering temperature for thermoelectric properties of low-cost CuAl<sub>0.90</sub>Fe<sub>0.10</sub>O<sub>2</sub> material, *J. Mater. Sci. Mater. Electron.* 27 (2016) 11102–11109.
- [47] S. Pantian, R. Sakdanuphab, A. Sakulkalavek, Enhancing the electrical conductivity and thermoelectric figure of merit of the p-type delafossite CuAlO<sub>2</sub> by Ag<sub>2</sub>O addition, *Curr. Appl. Phys.* 17 (2017) 1264–1270.
- [48] S. Pantian, R. Sakdanuphab, A. Sakulkalavek, Effect of starch addition on structural, electrical and thermal properties of delafossite CuAl<sub>0.9</sub>Fe<sub>0.1</sub>O<sub>2</sub>, *Mater. Sci. Eng. B Solid State Mater. Adv. Technol.* 226 (2017) 39–46.
- [49] N. Daichakomphu, R. Sakdanuphab, A. Harnwunggmoung, S. Pinitsoontorn, A. Sakulkalavek, Achieving thermoelectric improvement through the addition of a small amount of graphene to CuAlO<sub>2</sub> synthesized by solid-state reaction, *J. Alloys Compd.* 753 (2018) 630–635.
- [50] M.V. Lalić, J. Mestnik-Filho, A.W. Carbonari, R.N. Saxena, Changes induced by the presence of Zn or Ni impurity at Cu sites in CuAlO<sub>2</sub> delafossite, *Solid State Commun.* 125 (2003) 175–178.
- [51] K. Park, K.Y. Ko, W.S. Seo, Thermoelectric properties of CuAlO<sub>2</sub>, *J. Eur. Ceram. Soc.* 25 (2005) 2219–2222.
- [52] K. Park, K.Y. Ko, W.S. Seo, Effect of partial substitution of Ca for Al on the microstructure and high-temperature thermoelectric properties of CuAlO<sub>2</sub>, *Mater. Sci. Eng. B Solid State Mater. Adv. Technol.* 129 (2006) 1–7.
- [53] K. Park, K.Y. Ko, H.C. Kwon, S. Nahm, Improvement in thermoelectric properties of CuAlO<sub>2</sub> by adding Fe<sub>2</sub>O<sub>3</sub>, *J. Alloys Compd.* 437 (2007) 1–6.
- [54] S. Yanagiya, N. Van Nong, J. Xu, N. Pryds, The effect of (Ag, Ni, Zn)-addition on the thermoelectric properties of copper aluminate, *Materials (Basel)* 3 (2010) 318–328.
- [55] Y.C. Liou, L.S. Chang, Y.M. Lu, H.C. Tsai, U.R. Lee, Effects of mechanical milling on preparation and properties of CuAl<sub>1-x</sub>Fe<sub>x</sub>O<sub>2</sub> thermoelectric ceramics, *Ceram. Int.* 38 (2012) 3619–3624.

- [56] Y. Lu, K. Maeda, K. Sagara, L. Hao, Y.R. Jin, Improvement of thermoelectric properties of CuAlO<sub>2</sub> by excess oxygen doping in annealing, *Mater. Sci. Forum* 750 (2013) 134–137.
- [57] T. Suriwong, T. Thongtem, S. Thongtem, Thermoelectric and optical properties of CuAlO<sub>2</sub> synthesized by direct microwave heating, *Curr. Appl. Phys.* 14 (2014) 1257–1262.
- [58] M.A. Marquardt, N.A. Ashmore, D.P. Cann, Crystal chemistry and electrical properties of the delafossite structure, *Thin Solid Films* 496 (2006) 146–156.
- [59] T. Kobayashi, H. Takizawa, T. Endo, T. Sato, M. Shimada, H. Taguchi, M. Nagao, Metal-insulator transition and thermoelectric properties in the system (R<sub>1-x</sub>Ca<sub>x</sub>)MnO<sub>3-δ</sub> (R: Tb, Ho, Y), *J. Solid State Chem.* 92 (1991) 116–129.
- [60] D. Flahaut, T. Mihara, R. Funahashi, N. Nabeshima, K. Lee, H. Ohta, K. Koumoto, Thermoelectrical properties of A-site substituted Ca<sub>1-x</sub>Re<sub>x</sub>MnO<sub>3</sub> system, *J. Appl. Phys.* 100 (2006) 084911.
- [61] M. Ohtaki, H. Koga, T. Tokunaga, K. Eguchi, H. Arai, Electrical transport properties and high-temperature thermoelectric performance of (Ca<sub>0.9</sub>M<sub>0.1</sub>)MnO<sub>3</sub> (M = Y, La, Ce, Sm, In, Sn, Sb, Pb, Bi), *J. Solid State Chem.* 120 (1995) 105–111.
- [62] R. Funahashi, A. Kosuga, N. Miyasou, E. Takeuchi, S. Urata, K. Lee, H. Ohta, K. Koumoto, Thermoelectric properties of CaMnO<sub>3</sub> systems, in: International Conference on Thermoelectrics, 2007, pp. 124–128.
- [63] Y. Wang, Y. Sui, H. Fan, X. Wang, Y. Su, W. Su, X. Liu, High temperature thermoelectric response of electron-doped CaMnO<sub>3</sub>, *Chem. Mater.* 21 (2009) 4653–4660.
- [64] D. Srivastava, F. Azough, R. Freer, E. Combe, R. Funahashi, D.M. Kepaptsoglou, Q.M. Ramasse, M. Molinari, S.R. Yeandel, J.D. Baran, S.C. Parker, Crystal structure and thermoelectric properties of Sr–Mo substituted CaMnO<sub>3</sub>: a combined experimental and computational study, *J. Mater. Chem. C* 3 (2015) 12245–12259.
- [65] T. Wang, P. Nan, H. Wang, W. Su, A. Sotelo, J. Zhai, X. Wang, Y. Ran, T. Chen, C. Wang, Right heterogeneous microstructure for achieving excellent thermoelectric performance in Ca<sub>0.9</sub>R<sub>0.1</sub>MnO<sub>3-δ</sub> (R = Dy, Yb) ceramics, *Inorg. Chem.* 57 (2018) 9133–9141.
- [66] G. Xu, R. Funahashi, Q. Pu, B. Liu, R. Tao, G. Wang, Z. Ding, High-temperature transport properties of Nb and Ta substituted CaMnO<sub>3</sub> system, *Solid State Ionics* 171 (2004) 147–151.
- [67] L. Bocher, M.H. Aguirre, D. Logvinovich, A. Shkabko, R. Robert, M. Trottmann, A. Weidenkaff, CaMn<sub>1-x</sub>Nb<sub>x</sub>O<sub>3</sub> (x ≤ 0.08) perovskite-type phases as promising new high-temperature n-type thermoelectric materials, *Inorg. Chem.* 47 (2008) 8077–8085.
- [68] L. Bocher, M.H. Aguirre, R. Robert, D. Logvinovich, S. Bakardjieva, J. Hejtmanek, A. Weidenkaff, High-temperature stability, structure and thermoelectric properties of CaMn<sub>1-x</sub>Nb<sub>x</sub>O<sub>3</sub> phases, *Acta Mater.* 57 (2009) 5667–5680.
- [69] R. Kabir, T. Zhang, D. Wang, R. Donelson, R. Tian, T.T. Tan, S. Li, Improvement in the thermoelectric properties of CaMnO<sub>3</sub> perovskites by W doping, *J. Mater. Sci.* 49 (2014) 7522–7528.
- [70] M. Schrade, R. Kabir, S. Li, T. Norby, T.G. Finstad, High temperature transport properties of thermoelectric CaMnO<sub>3-δ</sub>—indication of strongly interacting small polarons, *J. Appl. Phys.* 115 (2014) 0–7.
- [71] M. Molinari, D.A. Tompsett, S.C. Parker, F. Azough, R. Freer, Structural, electronic and thermoelectric behaviour of CaMnO<sub>3</sub> and CaMnO<sub>(3-δ)</sub>, *J. Mater. Chem. A* 2 (2014) 14109.
- [72] T. Tsubota, M. Ohtaki, K. Eguchi, H. Arai, Thermoelectric properties of Al-doped ZnO as a promising oxide material for high-temperature thermoelectric conversion, *J. Mater. Chem.* 7 (1997) 85–90.

- [73] M. Ohtaki, K. Araki, K. Yamamoto, High thermoelectric performance of dually doped ZnO ceramics, *J. Electron. Mater.* 38 (2009) 1234–1238.
- [74] H. Cheng, X.J. Xu, H.H. Hng, J. Ma, Characterization of Al-doped ZnO thermoelectric materials prepared by RF plasma powder processing and hot press sintering, *Ceram. Int.* 35 (2009) 3067–3072.
- [75] N. Ma, J.F. Li, B.P. Zhang, Y.H. Lin, L.R. Ren, G.F. Chen, Microstructure and thermoelectric properties of  $ZnO_{1-x}Al_xO$  ceramics fabricated by spark plasma sintering, *J. Phys. Chem. Solid* 71 (2010) 1344–1349.
- [76] D. Bérardan, C. Byl, N. Dragoe, Influence of the preparation conditions on the thermoelectric properties of Al-doped ZnO, *J. Am. Ceram. Soc.* 93 (2010) 2352–2358.
- [77] X. Qu, W. Wang, S. Lv, D. Jia, Thermoelectric properties and electronic structure of Al-doped ZnO, *Solid State Commun.* 151 (2011) 332–336.
- [78] P. Jood, R.J. Mehta, Y. Zhang, G. Peleckis, X. Wang, R.W. Siegel, T. Borca-Tasciuc, S.X. Dou, G. Ramanath, Al-doped zinc oxide nanocomposites with enhanced thermoelectric properties, *Nano Lett.* 11 (2011) 4337–4342.
- [79] S.M. Choi, K.H. Lee, K.H. Jung, Y.S. Lim, W.S. Seo, Effects of process variable control on the thermoelectric properties of the  $Zn_{0.98}Ga(Al)_{0.02}O$  system, *J. Electron. Mater.* 42 (2013) 2056–2061.
- [80] S. Jantrasee, P. Moontragoon, S. Pinitsoontorn, Thermoelectric properties of Al-doped ZnO: experiment and simulation, *J. Semicond.* 37 (2016) 1–8.
- [81] H. Ohta, W.-S. Seo, K. Koumoto, Thermoelectric properties of homogenous compounds in  $ZnO-In_2O_3$  system, *J. Am. Ceram. Soc.* 79 (1996) 2193–2196.
- [82] H. Kaga, R. Asahi, T. Tani, Thermoelectric properties of doped  $(ZnO)_mIn_2O_3$ , *Jpn. J. Appl. Phys.* 43 (2004) 3540–3543.
- [83] M. Kazeoka, H. Hiramatsu, W.S. Seo, K. Koumoto, Improvement in thermoelectric properties of  $(ZnO)_5In_2O_3$  through partial substitution of yttrium for indium, *J. Mater. Res.* 13 (1998) 523–526.
- [84] Y. Masuda, M. Ohta, W.-S. Seo, W. Pitschke, K. Koumoto, Structure and thermoelectric transport properties of iso-electronically substituted  $(ZnO)_5In_2O_3$ , *J. Solid State Chem.* 150 (2000) 221–227.
- [85] Y. Michiue, T. Mori, A. Prytuliak, Y. Matsushita, M. Tanaka, N. Kimizuka, Electrical, optical, and thermoelectric properties of  $Ga_2O_3(ZnO)_9$ , *RSC Adv.* 1 (2011) 1788.
- [86] X. Liang, Thermoelectric transport properties of naturally nanostructured Ga-ZnO ceramics: effect of point defect and interfaces, *J. Eur. Ceram. Soc.* 36 (2016) 1643–1650.
- [87] E. Guilmeau, P. Díaz-Chao, O.I. Lebedev, A. Rečnik, M.C. Schäfer, F. Delorme, F. Giovannelli, M. Košir, S. Bernik, Inversion boundaries and phonon scattering in Ga:ZnO thermoelectric compounds, *Inorg. Chem.* 56 (2017) 480–487.
- [88] Y. Michiue, H. Nishijima, Y. Suzuki, T. Mori, Synthesis and thermoelectric properties of composite oxides in the pseudobinary system  $ZnO-Ga_2O_3$ , *Solid State Sci.* 65 (2017) 29–32.
- [89] D.T. Alvarez-Ruiz, F. Azough, D. Hernandez-Maldonado, D.M. Kepaptsoglou, Q.M. Ramasse, S.J. Day, P. Svec, P. Svec, R. Freer, Utilising unit-cell twinning operators to reduce lattice thermal conductivity in modular structures: structure and thermoelectric properties of  $Ga_2O_3(ZnO)_9$ , *J. Alloys Compd.* 762 (2018) 892–900.
- [90] D. Alvarez-Ruiz, F. Azough, D.T. Hernandez-Maldonado, D.M. Kepaptsoglou, Q.M. Ramasse, P. Svec, P. Svec Sr., R. Freer, Enhancement of electrical conduction and phonon scattering in  $Ga_2O_3(ZnO)_9-In_2O_3(ZnO)_9$  compounds by modification of interfaces at the nanoscale, *J. Electron. Mater.* 48 (2018) 1818–1826.
- [91] M. Backhaus-Ricoult, J.R.J.R. Rustad, D. Vargheese, I. Dutta, K. Work, Levers for thermoelectric properties in titania-based ceramics, *J. Electron. Mater.* 41 (2012) 1636–1647.

- [92] M. Backhaus-Ricoult, J. Rustad, L. Moore, C. Smith, J. Brown, Semiconducting large bandgap oxides as potential thermoelectric materials for high-temperature power generation? *Appl. Phys. A Mater. Sci. Process* 116 (2014) 433–470.
- [93] D. Bayerl, E. Kioupakis, Theoretical limits of thermoelectric figure of merit in n-type  $TiO_2$  polymorphs, *Phys. Rev. B* 91 (2015) 1–5.
- [94] S. Andersson, B. Collén, U. Kuylenstierna, A. Magnéli, Phase analysis studies on the titanium-oxygen system, *Acta Chem. Scand.* 11 (1957) 1641–1652.
- [95] S. Harada, K. Tanaka, H. Inui, Thermoelectric properties and crystallographic shear structures in titanium oxides of the Magnéli phases, *J. Appl. Phys.* 108 (2010) 083703.
- [96] Q. He, Q. Hao, G. Chen, B. Poudel, X. Wang, D. Wang, Z. Ren, Thermoelectric property studies on bulk  $TiO_x$  with  $x$  from 1 to 2, *Appl. Phys. Lett.* 91 (2007) 5–8.
- [97] K. Fuda, T. Shoji, S. Kikuchi, Y. Kunihiro, S. Sugiyama, Fabrication of titanium oxide-based composites by reactive SPS sintering and their thermoelectric properties, *J. Electron. Mater.* 42 (2013) 2209–2213.
- [98] M.K. Nowotny, T. Bak, J. Nowotny, Electrical properties and defect chemistry of  $TiO_2$  single crystal. II. Thermoelectric power, *J. Phys. Chem. B* 110 (2006) 16283.
- [99] Y. Lu, Y. Matsuda, K. Sagara, L. Hao, T. Otomitsu, H. Yoshida, Fabrication and thermoelectric properties of magneli phases by adding Ti into  $TiO_2$ , *Adv. Mat. Res.* 415–417 (2011) 1291–1296.
- [100] H. Liu, H. Ma, C. Wang, F. Wang, B. Liu, J. Chen, G. Ji, Y. Zhang, X. Jia, Enhanced thermoelectric properties of nonstoichiometric  $TiO_{1.76}$  with excellent mechanical properties induced by optimizing processing parameters, *Ceram. Int.* 44 (2018) 19859–19865.
- [101] M. Mikami, K. Ozaki, Thermoelectric properties of nitrogen-doped  $TiO_{2-x}$  compounds, *J. Phys. Conf. Ser.* 379 (2012) 012006.
- [102] C. Liu, L. Miao, J. Zhou, R. Huang, C.A.J. Fisher, S. Tanemura, Chemical tuning of  $TiO_2$  nanoparticles and sintered compacts for enhanced thermoelectric properties, *J. Phys. Chem. C* 117 (2013) 11487–11497.
- [103] G. Kieslich, U. Burkhardt, C.S. Birkel, I. Veremchuk, J.E. Douglas, M.W. Gaulois, I. Lieberwirth, R. Seshadri, G.D. Stucky, Y. Grin, W. Tremel, Enhanced thermoelectric properties of the n-type Magnéli phase  $WO_{2.90}$ : reduced thermal conductivity through microstructure engineering, *J. Mater. Chem. A* 2 (2014) 13492–13497.
- [104] J.A. Bock, S. Trolier-McKinstry, G.D. Mahan, C.A. Randall, Polarization-based perturbations to thermopower and electronic conductivity in highly conductive tungsten bronze structured  $(Sr,Ba)Nb_2O_6$ : relaxors vs normal ferroelectrics, *Phys. Rev. B Condens. Matter Mater. Phys.* 90 (2014) 1–8.
- [105] A.A. Ballman, H. Brown, The growth and properties of strontium barium metaniobate,  $Sr_{1-x}Ba_xNb_2O_6$ , a tungsten bronze ferroelectric, *J. Cryst. Growth* 1 (1967) 311–314.
- [106] P.B. Jamieson, S.C. Abrahams, J.L. Bernstein, Ferroelectric tungsten bronze-type crystal structures. I. Barium strontium niobate  $Ba_{0.27}Sr_{0.75}Nb_2O_{5.78}$ , *J. Chem. Phys.* 48 (1968) 5048–5057.
- [107] L.A. Bursill, P.J. Lin, Chaotic states observed in strontium barium niobate, *Philos. Mag. B* 54 (1986) 157–170.
- [108] J. Schneck, J.C. Toledano, R. Whatmore, F.W. Ainger, Incommensurate phases in ferroelectric tetragonal tungsten bronzes, *Ferroelectrics* 36 (1981) 327–330.
- [109] S. Lee, R.H.T. Wilke, S. Trolier-McKinstry, S. Zhang, C.A. Randall,  $Sr_xBa_{1-x}Nb_2O_{6-8}$  ferroelectric-thermoelectrics: crystal anisotropy, conduction mechanism, and power factor, *Appl. Phys. Lett.* 96 (2010) 031910.
- [110] S. Lee, J.A. Bock, S. Trolier-McKinstry, C.A. Randall, Ferroelectric-thermoelectricity and Mott transition of ferroelectric oxides with high electronic conductivity, *J. Eur. Ceram. Soc.* 32 (2012) 3971–3988.

- [111] S. Lee, S. Dursun, C. Duran, C.A. Randall, Thermoelectric power factor enhancement of textured ferroelectric  $\text{Sr}_x\text{Ba}_{1-x}\text{Nb}_2\text{O}_{6-\delta}$  ceramics, *J. Mater. Res.* 26 (2011) 26–30.
- [112] J. Li, H. Wang, W. Su, C. Wang, J. Liu, Y. Zhou, Y. Zhang, Y. Li, J. Zhai, Enhancement of thermoelectric performance of  $\text{Sr}_{0.7}\text{Ba}_{0.3}\text{Nb}_2\text{O}_{6-\delta}$  ceramics by lanthanum doping, *Ceram. Int.* 42 (2015) 1128–1132.
- [113] R. Ottini, C. Tealdi, C. Tomasi, I.G. Tredici, A. Soffientini, U. Anselmi-Tamburini, P. Ghigna, G. Spinolo, Feasibility of electron and hole injection in heavily doped strontium barium niobate (SBN50)  $\text{Sr}_{0.5}\text{Ba}_{0.5}\text{Nb}_2\text{O}_6$  for thermoelectric applications, *J. Appl. Phys.* 121 (2017) 085104.
- [114] R. Ottini, C. Tealdi, C. Tomasi, I.G. Tredici, A. Soffientini, R. Burriel, E. Palacios, M. Castro, U. Anselmi-Tamburini, P. Ghigna, G. Spinolo, Local environments and transport properties of heavily doped strontium barium niobates  $\text{Sr}_{0.5}\text{Ba}_{0.5}\text{Nb}_2\text{O}_6$ , *J. Solid State Chem.* 258 (2018) 99–107.
- [115] Y. Li, J. Liu, Z. Wang, Y.C. Zhou, C. Wang, J. Li, Y. Zhu, M. Li, L. Mei, Effects of fluorine doping on thermoelectric properties of  $\text{Sr}_{0.61}\text{Ba}_{0.39}\text{Nb}_2\text{O}_6$  ceramics, *Phys. Scr.* 90 (2015) 025801.
- [116] Y. Li, J. Liu, Y. Zhang, Y. Chen, J. Li, W. Su, H. Wang, C. Wang, Thermoelectric properties of ytterbium interstitial doped  $\text{Sr}_{0.7}\text{Ba}_{0.3}\text{Yb}_x\text{Nb}_2\text{O}_{6-\delta}$  ceramics, *Ceram. Int.* 43 (2017) 13345–13348.
- [117] Y. Li, Y. Zhang, J. Liu, Y. Chen, J. Li, W. Su, C. Wang, Effects of potassium interstitial doping on thermoelectric properties of  $\text{Sr}_{0.7}\text{Ba}_{0.3}\text{Nb}_2\text{O}_{6-\delta}$  ceramics, *J. Mater. Sci. Mater. Electron.* 29 (2018) 9137–9141.
- [118] F. Azough, R. Freer, S.R. Yeandel, J.D. Baran, M. Molinari, S.C. Parker, E. Guilmeau, D. Kepaptsoglou, Q. Ramasse, A. Knox, D. Gregory, D. Paul, M. Paul, A. Montecucco, J. Siviter, P. Mullen, W. Li, G. Han, E.A. Man, H. Baig, T. Mallick, N. Sellami, G. Min, T. Sweet,  $\text{Ba}_{6-3x}\text{Nd}_{8+2x}\text{Ti}_{18}\text{O}_{54}$  tungsten bronze: a new high-temperature n-type oxide thermoelectric, *J. Electron. Mater.* 45 (2016) 1894–1899.
- [119] T. Ishihara, *Perovskite Oxide for Solid Oxide Fuel Cells*, Springer, 2009.
- [120] T. Okuda, K. Nakanishi, S. Miyasaka, Y. Tokura, Large thermoelectric response of metallic perovskites:  $\text{Sr}_{1-x}\text{La}_x\text{TiO}_3$  ( $0 \leq x \leq 0.1$ ), *Phys. Rev. B* 63 (2001) 113104.
- [121] M. Ito, T. Matsuda, Thermoelectric properties of non-doped and Y-doped  $\text{SrTiO}_3$  polycrystals synthesized by polymerized complex process and hot pressing, *J. Alloys Compd.* 477 (2009) 473–477.
- [122] F. Gao, S. Yang, J. Li, M. Qin, Y. Zhang, H. Sun, Fabrication, dielectric, and thermoelectric properties of textured  $\text{SrTiO}_3$  ceramics prepared by RTGG method, *Ceram. Int.* 41 (2015) 127–135.
- [123] H. Muta, K. Kurosaki, S. Yamanaka, Thermoelectric properties of reduced and La-doped single-crystalline  $\text{SrTiO}_3$ , *J. Alloys Compd.* 392 (2005) 306–309.
- [124] S. Ohta, T. Nomura, H. Ohta, K. Koumoto, High-temperature carrier transport and thermoelectric properties of heavily La- or Nb-doped  $\text{SrTiO}_3$  single crystals, *J. Appl. Phys.* 97 (2005) 034106.
- [125] L. Feng, T. Shiga, J. Shiomi, Phonon transport in perovskite  $\text{SrTiO}_3$  from first principles, *Appl. Phys. Express* 8 (2015) 071501.
- [126] H. Muta, K. Kurosaki, S. Yamanaka, Thermoelectric properties of rare earth doped  $\text{SrTiO}_3$ , *J. Alloys Compd.* 350 (2003) 292–295.
- [127] J. Liu, C.L. Wang, Y. Li, W.B. Su, Y.H. Zhu, J.C. Li, L.M. Mei, Influence of rare earth doping on thermoelectric properties of  $\text{SrTiO}_3$  ceramics, *J. Appl. Phys.* 114 (2013) 223714.

- [128] A.V. Kovalevsky, A.A. Yaremchenko, S. Populoh, P. Thiel, D.P. Fagg, A. Weidenkaff, J. R. Frade, Towards a high thermoelectric performance in rare-earth substituted  $\text{SrTiO}_3$ : effects provided by strongly-reducing sintering conditions, *Phys. Chem. Chem. Phys.* 16 (2014) 26946–26954.
- [129] P. Shang, B. Zhang, J. Li, N. Ma, Effect of sintering temperature on thermoelectric properties of La-doped  $\text{SrTiO}_3$  ceramics prepared by sol–gel process and spark plasma sintering, *Solid State Sci.* 12 (2010) 1341–1346.
- [130] P. Blennow, A. Hagen, K.K. Hansen, L.R. Wallenberg, M. Mogensen, Defect and electrical transport properties of Nb-doped  $\text{SrTiO}_3$ , *Solid State Ionics* 179 (2008) 2047–2058.
- [131] S. Hashimoto, F.W.W. Poulsen, M. Mogensen, Conductivity of  $\text{SrTiO}_3$  based oxides in the reducing atmosphere at high temperature, *J. Alloys Compd.* 439 (2007) 232–236.
- [132] A.M. Dehkordi, S. Bhattacharya, J. He, H.N. Alshareef, T.M. Tritt, Significant enhancement in thermoelectric properties of polycrystalline Pr-doped  $\text{SrTiO}_{3-\delta}$  ceramics originating from nonuniform distribution of Pr dopants, *Appl. Phys. Lett.* 104 (2014) 193902.
- [133] Y. Kinemuchi, K.I. Mimura, A. Towata, K. Kato, Thermoelectric properties of rare earth-doped  $\text{SrTiO}_3$  nanocubes, *J. Electron. Mater.* 43 (2014) 2011–2016.
- [134] L. Hanbo, Z. Ganhong, D. Zhenxiang, Y. Zhenheng, W. Haiqiu, M. Yongqing, Thermoelectric properties of  $\text{Sr}_{0.9}\text{La}_{0.1}\text{TiO}_3$  and  $\text{Sr}_{2.7}\text{La}_{0.3}\text{Ti}_2\text{O}_7$  with 15% Ag addition, *J. Rare Earths* 32 (2014) 314–319.
- [135] A. Kikuchi, N. Okinaka, T. Akiyama, A large thermoelectric figure of merit of La-doped  $\text{SrTiO}_3$  prepared by combustion synthesis with post-spark plasma sintering, *Scr. Mater.* 63 (2010) 407–410.
- [136] A.M. Dehkordi, S. Bhattacharya, T. Darroudi, G. Jennifer, W.U. Schwingenschlögl, H.N. Alshareef, T.M. Tritt, A.M. Dehkordi, S. Bhattacharya, T. Darroudi, J.W. Graff, U. Schwingenschlögl, H.N. Alshareef, T.M. Tritt, Large thermoelectric power factor in Pr-doped  $\text{SrTiO}_{3-\delta}$  ceramics via grain-boundary-induced mobility enhancement, *Chem. Mater.* 26 (2014) 2478–2485.
- [137] Y. Wang, X. Zhang, L. Shen, N. Bao, C. Wan, N.-H. Park, K. Koumoto, A. Gupta, Nb-doped grain boundary induced thermoelectric power factor enhancement in La-doped  $\text{SrTiO}_3$  nanoceramics, *J. Power Sources* 241 (2013) 255–258.
- [138] N. Wang, H. He, X. Li, L. Han, C. Zhang, Enhanced thermoelectric properties of Nb-doped  $\text{SrTiO}_3$  polycrystalline ceramic by titanate nanotube addition, *J. Alloys Compd.* 506 (2010) 293–296.
- [139] J. Lingner, G. Jakob, M. Letz, Nb-doped  $\text{SrTiO}_3$  glass-ceramics as high temperature stable n-type oxide thermoelectrics, *AIP Conf. Proc.* 1449 (2012) 343–346.
- [140] J. Liu, C.L. Wang, W.B. Su, H.C. Wang, P. Zheng, J.C. Li, J.L. Zhang, L.M. Mei, Enhancement of thermoelectric efficiency in oxygen-deficient  $\text{Sr}_{1-x}\text{La}_x\text{TiO}_{3-\delta}$  ceramics, *Appl. Phys. Lett.* 95 (2009) 162110.
- [141] C. Chen, T. Zhang, R. Donelson, T.T. Tan, S. Li, Effects of yttrium substitution and oxygen deficiency on the crystal phase, microstructure, and thermoelectric properties of  $\text{Sr}_{1-1.5x}\text{Y}_x\text{TiO}_{3-\delta}$  ( $0 \leq x \leq 0.15$ ), *J. Alloys Compd.* 629 (2015) 49–54.
- [142] X.G. Guo, X.S. Chen, Y.L. Sun, L.Z. Sun, X.H. Zhou, W. Lu, Electronic band structure of Nb doped  $\text{SrTiO}_3$  from first principles calculation, *Phys. Lett. Sect. A Gen. At. Solid State Phys.* 317 (2003) 501–506.
- [143] S. Ohta, T. Nomura, H. Ohta, M. Hirano, H. Hosono, K. Koumoto, Large thermoelectric performance of heavily Nb-doped  $\text{SrTiO}_3$  epitaxial film at high temperature, *Appl. Phys. Lett.* 87 (2005) 97–100.
- [144] A.A. Yaremchenko, S. Populoh, S.G. Patrício, J. Macías, P. Thiel, D.P. Fagg, A. Weidenkaff, J.R. Frade, A.V. Kovalevsky, Boosting thermoelectric performance by

- controlled defect chemistry engineering in Ta-substituted strontium titanate, *Chem. Mater.* 27 (2015) 4995–5006.
- [145] A.V. Kovalevsky, S. Populoh, S.G. Patrício, P. Thiel, M.C. Ferro, D.P. Fagg, J.R. Frade, A. Weidenkaff, Design of SrTiO<sub>3</sub>-based thermoelectrics by tungsten substitution, *J. Phys. Chem. C* 119 (2015) 4466–4478.
  - [146] S.R. Popuri, A.J.M. Scott, R.A. Downie, M.A. Hall, E. Suard, R. Decourt, M. Pollet, J.-W.G. Bos, Glass-like thermal conductivity in SrTiO<sub>3</sub> thermoelectrics induced by A-site vacancies, *RSC Adv.* 4 (2014) 33720–33723.
  - [147] Z. Lu, H. Zhang, W. Lei, D.C. Sinclair, I.M. Reaney, High-figure-of-merit thermoelectric La-doped A-site-deficient SrTiO<sub>3</sub> ceramics, *Chem. Mater.* 28 (2016) 925–935.
  - [148] F. Azough, S.S. Jackson, D. Ekren, R. Freer, M. Molinari, S.R. Yeandel, P.M. Panchmatia, S.C. Parker, D.H. Maldonado, D.M. Kepaptsoglou, Q.M. Ramasse, Concurrent La and A-site vacancy doping modulates the thermoelectric response of SrTiO<sub>3</sub>: experimental and computational evidence, *ACS Appl. Mater. Interfaces* 9 (2017) 41988–42000.
  - [149] J.-W.G. Bos, J.A. McNulty, M. Pollet, S.R. Popuri, R. Decourt, F.D. Morrison, M.S. Senn, A.D. Fortes, Phonon-glass and heterogeneous electrical transport in A-site deficient SrTiO<sub>3</sub>, *J. Phys. Chem. C* 123 (2019) 5198–5208.
  - [150] D. Ekren, F. Azough, R. Freer, Enhancing the thermoelectric properties of Sr<sub>1-x</sub>Pr<sub>2x/3</sub>□<sub>x/3</sub>TiO<sub>3±δ</sub> through control of crystal structure and microstructure, *Philos. Trans. R. Soc. A Math. Phys. Eng. Sci.* 377 (2019) 20190037.
  - [151] N. Wang, H. He, Y. Ba, C. Wan, K. Koumoto, Thermoelectric properties of Nb-doped SrTiO<sub>3</sub> ceramics enhanced by potassium titanate nanowires addition, *J. Ceram. Soc. Japan* 118 (2010) 1098–1101.
  - [152] X. Feng, Y. Fan, N. Nomura, K. Kikuchi, L. Wang, W. Jiang, A. Kawasaki, Graphene promoted oxygen vacancies in perovskite for enhanced thermoelectric properties, *Carbon* 112 (2017) 169–176.
  - [153] O. Okhay, S. Zlotnik, W. Xie, K. Orlinski, M.J. Hortiguela Gallo, G. Otero-Irueta, A.J.S. Fernandes, D.A. Pawlak, A. Weidenkaff, A. Tkach, Thermoelectric performance of Nb-doped SrTiO<sub>3</sub> enhanced by reduced graphene oxide and Sr deficiency cooperation, *Carbon* 143 (2019) 215–222.
  - [154] L.D. Chen, X.Y. Huang, M. Zhou, X. Shi, W.B. Zhang, The high temperature thermoelectric performances of Zr<sub>0.5</sub>Hf<sub>0.5</sub>Ni<sub>0.8</sub>Pd<sub>0.2</sub>Sn<sub>0.99</sub>Sb<sub>0.01</sub> alloy with nanophase inclusions, *J. Appl. Phys.* 99 (2006) 064305.
  - [155] H. Li, X. Tang, Q. Zhang, C. Uher, High performance In<sub>x</sub>Ce<sub>y</sub>Co<sub>4</sub>Sb<sub>12</sub> thermoelectric materials with in situ forming nanostructured InSb phase, *Appl. Phys. Lett.* 94 (2009) 10–13.
  - [156] Y. Pei, J. Lensch-Falk, E.S. Toberer, D.L. Medlin, G.J. Snyder, High thermoelectric performance in PbTe due to large nanoscale Ag<sub>2</sub>Te precipitates and La doping, *Adv. Funct. Mater.* 21 (2011) 241–249.
  - [157] Y. Lin, C. Norman, D. Srivastava, F. Azough, L. Wang, M. Robbins, K. Simpson, R. Freer, I.A. Kinloch, Thermoelectric power generation from lanthanum strontium titanium oxide at room temperature through the addition of graphene, *ACS Appl. Mater. Interfaces* 7 (2015) 15898–15908.
  - [158] D. Srivastava, C. Norman, F. Azough, M.C. Schäfer, E. Guilmeau, R. Freer, Improving the thermoelectric properties of SrTiO<sub>3</sub>-based ceramics with metallic inclusions, *J. Alloys Compd.* 731 (2018) 723–730.
  - [159] N. Wang, H. Li, Y. Ba, Y. Wang, C. Wan, K. Fujinami, K. Koumoto, Effects of YSZ additions on thermoelectric properties of Nb-doped strontium titanate, *J. Electron. Mater.* 39 (2010) 1777–1781.

- [160] N. Wang, H. Chen, H. He, W. Norimatsu, M. Kusunoki, K. Koumoto, Enhanced thermoelectric performance of Nb-doped  $\text{SrTiO}_3$  by nano-inclusion with low thermal conductivity, *Sci. Rep.* 3 (2013) 3–7.
- [161] N. Wang, L. Han, H. He, Y. Ba, K. Koumoto, Effects of mesoporous silica addition on thermoelectric properties of Nb-doped  $\text{SrTiO}_3$ , *J. Alloys Compd.* 497 (2010) 308–311.
- [162] L. Li, Y. Liu, X. Qin, D. Li, J. Zhang, C. Song, L. Wang, Enhanced thermoelectric performance of highly dense and fine-grained  $(\text{Sr}_{1-x}\text{Gd}_x)\text{TiO}_{3-\delta}$  ceramics synthesized by sol–gel process and spark plasma sintering, *J. Alloys Compd.* 588 (2014) 562–567.
- [163] S. Ohta, H. Ohta, K. Koumoto, Grain size dependence of thermoelectric performance of Nb-doped  $\text{SrTiO}_3$  polycrystals, *J. Ceram. Soc. Japan* 114 (2006) 102–105.
- [164] H.C.C. Wang, C.L.L. Wang, W.B.B. Su, J. Liu, Y. Zhao, H. Peng, J.L.L. Zhang, M.L.L. Zhao, J.C.C. Li, N. Yin, L.M.M. Mei, Enhancement of thermoelectric figure of merit by doping Dy in  $\text{La}_{0.1}\text{Sr}_{0.9}\text{TiO}_3$  ceramic, *Mater. Res. Bull.* 45 (2010) 809–812.
- [165] D. Srivastava, C. Norman, F. Azough, M.C. Schäfer, E. Guilmeau, D. Kepartsoglou, Q. M. Ramasse, G. Nicotra, R. Freer, Tuning the thermoelectric properties of A-site deficient  $\text{SrTiO}_3$  ceramics by vacancies and carrier concentration, *Phys. Chem. Chem. Phys.* (2016) 26475–26486.
- [166] A.M. Dehkordi, S. Bhattacharya, T. Darroudi, H.N. Alshareef, T.M. Tritt, New insights on the synthesis and electronic transport in bulk polycrystalline Pr-doped  $\text{SrTiO}_{3-\delta}$ , *J. Appl. Phys.* 117 (2015) 055102.
- [167] S. Hashimoto, L. Kindermann, F.W. Poulsen, M. Mogensen, A study on the structural and electrical properties of lanthanum-doped strontium titanate prepared in air, *J. Alloys Compd.* 397 (2005) 245–249.
- [168] L. Zhang, N. Li, H.-Q. Wang, Y. Zhang, F. Ren, X.-X. Liao, Y.-P. Li, X.-D. Wang, Z. Huang, Y. Dai, H. Yan, J.-C. Zheng, Tuning the thermal conductivity of strontium titanate through annealing treatments, *Chin. Phys. B* 26 (2017) 016602.
- [169] J. Liu, C.L. Wang, W.B. Su, H.C. Wang, J.C. Li, J.L. Zhang, L.M. Mei, Thermoelectric properties of  $\text{Sr}_{1-x}\text{Nd}_x\text{TiO}_3$  ceramics, *J. Alloys Compd.* 492 (2010) 54–56.
- [170] A.V. Kovalevsky, A.A. Yaremenko, S. Populoh, A. Weidenkaff, J.R. Frade, Enhancement of thermoelectric performance in strontium titanate by praseodymium substitution, *J. Appl. Phys.* 113 (2013) 0–8.
- [171] S. Bhattacharya, A. Mehdizadeh Dehkordi, S. Tennakoon, R. Adebisi, J.R. Gladden, T. Darroudi, H.N. Alshareef, T.M. Tritt, Role of phonon scattering by elastic strain field in thermoelectric  $\text{Sr}_{1-x}\text{Y}_x\text{TiO}_{3-\delta}$ , *J. Appl. Phys.* 115 (2014) 223712.
- [172] J. Han, Q. Sun, Y. Song, Enhanced thermoelectric properties of La and Dy co-doped, Sr-deficient  $\text{SrTiO}_3$  ceramics, *J. Alloys Compd.* 705 (2017) 22–27.
- [173] D. Srivastava, F. Azough, M. Molinari, S.C. Parker, R. Freer, High-temperature thermoelectric properties of  $(1-x)\text{SrTiO}_3-(x)\text{La}_{0.66}\text{NbO}_3$  ceramic solid solution, *J. Electron. Mater.* 44 (2014) 1803–1808.
- [174] R.D. Shannon, Revised effective ionic radii and systematic studies of interatomic distances in halides and chalcogenides, *Acta Crystallogr.* 32 (1976) 751–767.
- [175] J.B. Goodenough, Covalency criterion for localized vs collective electrons in oxides with the perovskite structure, *J. Appl. Phys.* 37 (1966) 1415–1422.
- [176] H. Muta, K. Kurosaki, S. Yamanaka, Thermoelectric properties of doped  $\text{BaTiO}_3\text{-SrTiO}_3$  solid solution, *J. Alloys Compd.* 368 (2004) 22–24.
- [177] Y. Cui, J.R. Salvador, J. Yang, H. Wang, G. Amow, H. Kleinke, Thermoelectric properties of heavily doped n-type  $\text{SrTiO}_3$  bulk materials, *J. Electron. Mater.* 38 (2009) 1002–1007.

- [178] A. Kinaci, C. Sevik, T. Çağın, Electronic transport properties of  $\text{SrTiO}_3$  and its alloys:  $\text{Sr}_{1-x}\text{La}_x\text{TiO}_3$  and  $\text{SrTi}_{1-x}\text{M}_x\text{O}_3$  ( $\text{M}=\text{Nb}, \text{Ta}$ ), *Phys. Rev. B* 82 (2010) 155114.
- [179] H.C. Wang, C.L. Wang, W.B. Su, J. Liu, H. Peng, Y. Sun, J.L. Zhang, M.L. Zhao, J.C. Li, N. Yin, L.M. Mei, Synthesis and thermoelectric performance of Ta doped  $\text{Sr}_{0.9}\text{La}_{0.1}\text{TiO}_3$  ceramics, *Ceram. Int.* 37 (2011) 2609–2613.
- [180] Y. Wang, K. Fujinami, R. Zhang, C. Wan, N. Wang, Y. Ba, K. Koumoto, Interfacial thermal resistance and thermal conductivity in nanograined  $\text{SrTiO}_3$ , *Appl. Phys. Express* 3 (2010) 031101.
- [181] A.V. Kovalevsky, A.A. Yaremchenko, S. Populoh, A. Weidenkaff, J.R. Frade, Effect of A-site cation deficiency on the thermoelectric performance of donor-substituted strontium titanate, *J. Phys. Chem. C* 118 (2014) 4596–4606.
- [182] A.V. Kovalevsky, M.H. Aguirre, S. Populoh, S.G. Patrício, N.M. Ferreira, S.M. Mikhalev, D.P. Fagg, A. Weidenkaff, J.R. Frade, Designing strontium titanate-based thermoelectrics: insight into defect chemistry mechanisms, *J. Mater. Chem. A* 5 (2017) 3909–3922.
- [183] D. Kepaptsoglou, J.D. Baran, F. Azough, D. Ekren, D. Srivastava, M. Molinari, S.C. Parker, Q.M. Ramasse, R. Freer, Prospects for engineering thermoelectric properties in  $\text{La}_{1/3}\text{NbO}_3$  ceramics revealed via atomic-level characterization and modeling, *Inorg. Chem.* 57 (2017) 45–55.
- [184] D. Ekren, F. Azough, A. Gholinia, S.J. Day, D. Hernandez-Maldonado, D.M. Kepaptsoglou, Q.M. Ramasse, R. Freer, Enhancing the thermoelectric power factor of  $\text{Sr}_{0.9}\text{Nd}_{0.1}\text{TiO}_3$  through control of the nanostructure and microstructure, *J. Mater. Chem. A* 6 (2018) 24928–24939.
- [185] C. Wu, J. Li, Y. Fan, J. Xing, H. Gu, Z. Zhou, X. Lu, Q. Zhang, L. Wang, W. Jiang, The effect of reduced graphene oxide on microstructure and thermoelectric properties of Nb-doped A-site-deficient  $\text{SrTiO}_3$  ceramics, *J. Alloys Compd.* 786 (2019) 884–893.
- [186] M.T. Dylla, J.J. Kuo, I. Witting, G.J. Snyder, Grain boundary engineering nanostructured  $\text{SrTiO}_3$  for thermoelectric applications, *Adv. Mater. Interfaces* 6 (2019) 1900222.
- [187] N.A. Kirsanov, G.V. Bazuev, Electrical and magnetic properties of the  $\text{Pr}_{2/3}\text{TiO}_{3\pm y}$  perovskite phase, *Inorg. Mater.* 37 (2001) 487–490.
- [188] S.N. Ruddlesden, P. Popper, The compound  $\text{Sr}_3\text{Ti}_2\text{O}_7$  and its structure, *Acta Crystallogr.* 11 (1958) 54–55.
- [189] Y. Wang, C. Wan, X. Zhang, L. Shen, K. Koumoto, A. Gupta, N. Bao, Influence of excess  $\text{SrO}$  on the thermoelectric properties of heavily doped  $\text{SrTiO}_3$  ceramics, *Appl. Phys. Lett.* 102 (2013) 183905.
- [190] Y. Wang, K.H. Lee, H. Hyuga, H. Kita, H. Ohta, K. Koumoto, Enhancement of thermoelectric performance in rare earth-doped  $\text{Sr}_3\text{Ti}_2\text{O}_7$  by symmetry restoration of  $\text{TiO}_6$  octahedra, *J. Electroceram.* 24 (2010) 76–82.
- [191] R.R. Sun, X.Y. Qin, L.L. Li, D. Li, J. Zhang, Y.S. Zhang, C.J. Tang, The effects of elements doping on transport and thermoelectric properties of  $\text{Sr}_3\text{Ti}_2\text{O}_7$ , *J. Phys. Chem. Solid* 75 (2014) 629–637.
- [192] K.H. Lee, S.W. Kim, H. Ohta, K. Koumoto, Ruddlesden-Popper phases as thermoelectric oxides: Nb-doped  $\text{SrO}(\text{SrTiO}_3)_n$  ( $n=1,2$ ), *J. Appl. Phys.* 100 (2006) 063717.
- [193] Y. Wang, K.H. Lee, H. Ohta, K. Koumoto, Thermoelectric properties of electron doped  $\text{SrO}(\text{SrTiO}_3)_n$  ( $n=1,2$ ) ceramics, *J. Appl. Phys.* 105 (2009) 103701.
- [194] J. Khaliq, C. Li, K. Chen, B. Shi, H. Ye, A.M. Grande, H. Yan, M.J. Reece, Reduced thermal conductivity by nanoscale intergrowths in perovskite like layered structure  $\text{La}_2\text{Ti}_2\text{O}_7$ , *J. Appl. Phys.* 117 (2015) 075101.
- [195] T.D. Sparks, P.A. Fuierer, D.R. Clarke, Anisotropic thermal diffusivity and conductivity of La-doped strontium niobate  $\text{Sr}_2\text{Nb}_2\text{O}_7$ , *J. Am. Ceram. Soc.* 93 (2010) 1136–1141.

- [196] V. Fiorentini, R. Farris, E. Argiolas, M.B. MacCioni, High thermoelectric figure of merit and thermopower in layered perovskite oxides, *Phys. Rev. Mater.* 3 (2019) 1–8.
- [197] L.T. Hung, N. Van Nong, L. Han, R. Bjørk, P.H. Ngan, T.C. Holgate, B. Balke, G.J. Snyder, S. Linderoth, N. Pryds, Segmented thermoelectric oxide-based module for high-temperature waste heat harvesting, *Energy Technol.* 3 (2015) 1143–1151.
- [198] I. Matsubara, R. Funahashi, T. Takeuchi, S. Sodeoka, T. Shimizu, K. Ueno, Fabrication of an all-oxide thermoelectric power generator, *Appl. Phys. Lett.* 78 (2002) 3627–3629.
- [199] E.S. Reddy, J.G. Noudem, S. Hebert, C. Goupil, Fabrication and properties of four-leg oxide thermoelectric modules, *J. Phys. D Appl. Phys.* 38 (2005) 3751–3755.
- [200] R. Funahashi, M. Mikami, T. Mihara, S. Urata, N. Ando, A portable thermoelectric-power-generating module composed of oxide devices, *J. Appl. Phys.* 99 (2006) 2004–2007.
- [201] R. Funahashi, S. Urata, Fabrication and application of an oxide thermoelectric system, *Int. J. Appl. Ceram. Technol.* 4 (2007) 297–307.
- [202] S.M. Choi, K.H. Lee, C.H. Lim, W.S. Seo, Oxide-based thermoelectric power generation module using p-type  $\text{Ca}_3\text{Co}_4\text{O}_9$  and n-type  $(\text{ZnO})_7\text{In}_2\text{O}_3$  legs, *Energy Convers. Manag.* 52 (2011) 335–339.
- [203] C.-H. Lim, S.-M. Choi, W.-S. Seo, H.-H. Park, A power-generation test for oxide-based thermoelectric modules using p-type  $\text{Ca}_3\text{Co}_4\text{O}_9$  and n-type  $\text{Ca}_{0.9}\text{Nd}_{0.1}\text{MnO}_3$  legs, *J. Electron. Mater.* 41 (2011) 1247–1255.
- [204] K. Park, G.W. Lee, Fabrication and thermoelectric power of  $\pi$ -shaped  $\text{Ca}_3\text{Co}_4\text{O}_9/\text{CaMnO}_3$  modules for renewable energy conversion, *Energy* 60 (2013) 87–93.
- [205] P. Mele, H. Kamei, H. Yasumune, K. Matsumoto, K. Miyazaki, Development of thermoelectric module based on dense  $\text{Ca}_3\text{Co}_4\text{O}_9$  and  $\text{Zn}_{0.98}\text{Al}_{0.02}\text{O}$  legs, *Met. Mater. Int.* 20 (2014) 389–397.
- [206] T. Souma, M. Ohtaki, M. Shigeno, Y. Ohba, N. Nakamura, T. Shimozaki, Fabrication and power generation characteristics of p- $\text{NaCo}_2\text{O}_4$ /n-ZnO oxide thermoelectric modules, in: Proceedings International Conference on Thermoelectrics, ICT, 2006, pp. 603–606.
- [207] K. Koumoto, R. Funahashi, E. Guilmeau, Y. Miyazaki, A. Weidenkaff, Y. Wang, C. Wan, Thermoelectric ceramics for energy harvesting, *J. Am. Ceram. Soc.* 96 (2013) 1–23.
- [208] L.-D. Zhao, S.-H. Lo, Y. Zhang, H. Sun, G. Tan, C. Uher, C. Wolverton, V.P. Dravid, M. G. Kanatzidis, Ultralow thermal conductivity and high thermoelectric figure of merit in SnSe crystals, *Nature* 508 (2014) 373–377.
- [209] K. Fujita, T. Mochida, K. Nakamura, High-temperature thermoelectric properties of  $\text{Na}_x\text{CoO}_{2-\delta}$  single crystals, *Jpn. J. Appl. Phys.* 40 (2001) 4644–4647.
- [210] N.V. Nong, C.J. Liu, M. Ohtaki, Improvement on the high temperature thermoelectric performance of Ga-doped misfit-layered  $\text{Ca}_3\text{Co}_{4-x}\text{Ga}_x\text{O}_{9+\delta}$  ( $x = 0, 0.05, 0.1$ , and  $0.2$ ), *J. Alloys Compd.* 491 (2010) 53–56.
- [211] H. Ohta, S. Kim, Y. Mune, T. Mizoguchi, K. Nomura, S. Ohta, T. Nomura, Y. Nakanishi, Y. Ikuhara, M. Hirano, H. Hosono, K. Koumoto, Giant thermoelectric Seebeck coefficient of a two-dimensional electron gas in  $\text{SrTiO}_3$ , *Nat. Mater.* 6 (2007) 129–134.
- [212] J. Wang, B.Y. Zhang, H.J. Kang, Y. Li, X. Yaer, J.F. Li, Q. Tan, S. Zhang, G.H. Fan, C.Y. Liu, L. Miao, D. Nan, T.M. Wang, L.D. Zhao, Record high thermoelectric performance in bulk  $\text{SrTiO}_3$  via nano-scale modulation doping, *Nano Energy* 35 (2017) 387–395.
- [213] X. Song, S.A. Paredes Navia, L. Liang, C. Boyle, C.O. Romo-De-La-Cruz, B. Jackson, A. Hinerman, M. Wilt, J. Prucz, Y. Chen, Grain boundary phase segregation for dramatic improvement of the thermoelectric performance of oxide ceramics, *ACS Appl. Mater. Interfaces* 10 (2018) 39018–39024.

- [214] R.Z. Zhang, C.L. Wang, J.C. Li, K. Koumoto, Simulation of thermoelectric performance of bulk  $\text{SrTiO}_3$  with two-dimensional electron gas grain boundaries, *J. Am. Ceram. Soc.* 93 (2010) 1677–1681.
- [215] J. Li, Z. Ma, R. Sa, K. Wu, Improved thermoelectric power factor and conversion efficiency of perovskite barium stannate, *RSC Adv.* 7 (2017) 32703–32709.
- [216] S.A. Khandy, D.C. Gupta, Electronic structure, magnetism and thermoelectric properties of double perovskite  $\text{Sr}_2\text{HoNbO}_6$ , *J. Magn. Magn. Mater.* 458 (2018) 176–182.
- [217] H.H. Huang, G. Xing, X. Fan, D.J. Singh, W.T. Zheng, Layered  $\text{Tl}_2\text{O}$ : a model thermoelectric material, *J. Mater. Chem. C* 7 (2019) 5094–5103.
- [218] H. Ohta, Thermoelectrics based on strontium titanate, *Mater. Today* 10 (2007) 44–49.
- [219] H.R. Liu, J.H. Yang, H.J. Xiang, X.G. Gong, S.H. Wei, Origin of the superior conductivity of perovskite  $\text{Ba}(\text{Sr})\text{SnO}_3$ , *Appl. Phys. Lett.* 102 (2013) 112109.

# Thermoelectric materials-based on organic semiconductors

2.12

*Qingshuo Wei<sup>a</sup>, Masakazu Mukaida<sup>a</sup>, Kazuhiro Kirihsara<sup>a</sup>, and Takao Ishida<sup>b</sup>*

<sup>a</sup>Nanomaterials Research Institute, National Institute of Advanced Industrial Science and Technology, Tsukuba, Ibaraki, Japan, <sup>b</sup>Global Zero Emission Research Center, National Institute of Advanced Industrial Science and Technology, Tsukuba, Ibaraki, Japan

## 2.12.1 A short history of organic thermoelectrics

Thermoelectric materials are generally used for the direct conversion of heat energy into electricity. In most cases, this process relies on the Seebeck effect, which is a phenomenon of voltage production by conductors or semiconductors as a function of the temperature gradient and is named after the physicist Thomas Johann Seebeck, who confirmed this phenomenon approximately 200 years ago [1]. Previous studies on thermoelectric materials have mainly investigated for the inorganic compounds such as bismuth-telluride (Bi-Te) and metal oxides [2]. However, since several groups recently reported, especially after 2010, high power factors and excellent figures of merit ( $ZT$ ) for organic materials, researchers from different fields have started to consider their potential for thermal energy conversion applications.

Organic semiconductors have recently attracted attention as energy conversion materials. Moreover, their thermoelectric properties have been previously investigated; among them, the Seebeck effect has been used as a physical parameter to determine the carrier type and relative concentration in such materials. In 1957, Fielding et al. systematically studied the Seebeck effect of metal-free phthalocyanines and copper phthalocyanine single crystals, concluding that the holes are the majority carriers in both cases [3]. Pohl et al. reported that polyacene quinone radical polymers can show both p- and n-type properties depending on the structures by comparing the Seebeck coefficient ( $S$ ) (Fig. 2.12.1) [4]. In 2002, a research group from the Tokyo University of Science Yamaguchi observed thermal transporting properties of conducting polymers and calculated  $ZT$  for organic materials; due to the high electrical conductivity ( $\sigma$ ) of polyaniline films,  $ZT$  could reach  $10^{-3}$  at room temperature [5]. Since 2000, organic electronics, such as organic solar cells, transistors, and light emission diodes, have seen significant development and the physical and chemical properties of organic conducting polymers also approach those of inorganic semiconductors [6]. However, studies on heat energy harvesting by conducting polymers are limited.

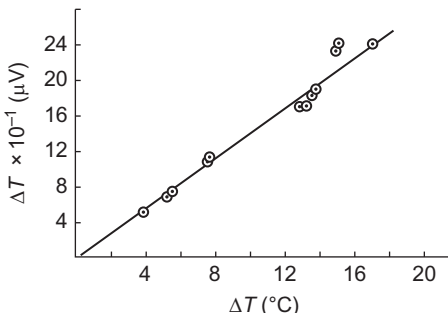


**Fig. 2.12.1** Thermoelectric properties of polyacene quinone radical polymers.

Data from H.A. Pohl, E.H. Engelhardt, Synthesis and characterization of some highly conjugated semiconducting polymers, *J. Phys. Chem.* 66 (11) (1962) 2085. Copyright 1962 American Chemical Society.

The situation started to change in 2011: Crispin et al. stated that the de-doping of in situ polymerized highly conductive poly(3,4-ethylenedioxothiophene):tosylate (PEDOT:tos) with tetrakis(dimethylamino)ethylene (TDAE) could generate a remarkable power factor ( $>300 \mu\text{W}/(\text{m K}^2)$ ) [7]. After their pioneering works, many researchers have joined the field of organic thermoelectrics, focusing on the materials, modules, and characterization methods.

## 2.12.2 Thermoelectric properties of heavily doped PEDOT during polymerization

The synthesis of PEDOT (Fig. 2.12.2) was reported for the first time in 1988 [8]. The product was designed and fabricated as a conducting polymer stable toward moisture and oxygen since existing conducting polymers, including polyacetylene, polyaniline, and polypyrrole, had exhibited low atmospheric stability, limiting their applications. The most common synthetic route for PEDOT is the oxidative polymerization from 3,4-ethylenedioxothiophene (EDOT). Conductive PEDOT carries positive charges. Therefore, counterions such as  $\text{Cl}^-$ , perchlorate  $\text{ClO}_4^-$ , tosylate  $\text{tos}^-$ , and poly(styrenesulfonate) ( $\text{PSS}^-$ ) can be found in all the oxidized forms of PEDOT due to charge balancing; they are normally called dopants, although such counterions cannot oxidize PEDOT.

Generally speaking, conductive PEDOT films can be obtained by two methods. The first method is the PEDOT synthesis during film formation and is called

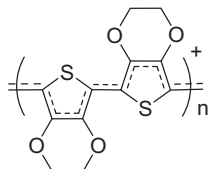


**Fig. 2.12.2** Chemical structure of doped poly(3,4-ethylenedioxothiophene).

in situ polymerization; a typical example is PEDOT<sup>+</sup>Cl<sup>-</sup>, which is produced by using FeCl<sub>3</sub> as an oxidant. The highest  $\sigma$  of such a thin film could exceed 6000 S/cm [9]. Single-crystal PEDOT nanowires have been synthesized under geometrically confined conditions with patterned substrates, achieving a  $\sigma$  of 8797 S/cm [10]. The metallic behavior of in situ polymerized PEDOT films has also been reported [11].

The second method is PEDOT coating from a stable dispersion. This approach is almost limited to the usage of PEDOT:PSS, which is a stable PEDOT dispersion commercially available on a large scale. PEDOT:PSS is also synthesized via oxidative polymerization from EDOT in solution. PSS helps the PEDOT dispersion. There are different grades of PEDOT:PSS depending on the application; PH1000 exhibits the highest  $\sigma$  (around 1000 S/cm) and could replace indium tin oxide as a transparent conducting substrate. Okuzaki et al. have recently developed a novel, fully soluble self-doped PEDOT (S-PEDOT) polymer with a  $\sigma$  higher than 1000 S/cm [12], which has been attributed to its high molecular weight.

Highly doped PEDOT generally shows respective thermoelectric performance because of the high  $\sigma$ . At the same time, the typical  $S$  is not high; for example, it is only 11  $\mu\text{V/K}$  for in situ polymerized PEDOT thin films [9] and around 17  $\mu\text{V/K}$  for PEDOT:PSS [13]. This is mainly attributed to the high carrier density in these materials. Thus, to further improve the thermoelectric properties, the control of the carrier density inside such films has been attempted, which is a typical approach in the field of inorganic thermoelectric materials.

In the abovementioned study of Crispin et al. (2011) on the de-doping of PEDOT:tos, a  $ZT$  of 0.25 was also observed, which is mainly attributed to a high  $S$  ( $>200\mu\text{V/K}$ ) [7]. Later studies from the same group pointed out the difficulties of in-plane thermal conductivity ( $\kappa$ ) measurements and accurately estimated the maximum  $ZT$  (0.11) for PEDOT:tos at an oxidation level of about 22% at room temperature (Fig. 2.12.3) [14]. They also successfully fabricated  $\pi$ -type thermoelectric generators by using these dedoped PEDOT:tos films.

Massonnet et al. developed a method based on the treatment of PEDOT:PSS films by drop-casting aqueous solutions containing reducing salts or organic reducing agents. Their most significant finding was that the  $S$  enhancement followed the trend of the redox potentials for aqueous solutions of reducing agents, reaching 104  $\mu\text{V/K}$  in the case of NaBH<sub>4</sub>-treated PEDOT:PSS (Table 2.12.1) [15]; it increased when decreasing  $\sigma$ . An enhanced power factor, compared with untreated PEDOT:PSS, was also achieved.

Our group focused on a different approach to precisely control the carrier density in PEDOT:PSS films. Wei et al. used a solid-state photoinduced charge-transfer reaction for the de-doping process [16, 17]. In this approach, a photobase generator is mixed with a conducting polymer to allow de-doping upon optical irradiation due to its photodecarboxylation reaction; varying the ultraviolet (UV) exposure time enables the precise carrier density control in these films, above three orders of magnitude. In addition, the carrier mobility in the film varies from  $10^{-3}$  to  $8.2\text{ cm}^2/(\text{Vs})$  depending on the carrier density. The  $S$  measured as a function of the irradiation time has revealed a maximum power factor of  $\sim 42\mu\text{W}/(\text{m K}^2)$  at a carrier density of  $\sim 5 \times 10^{20}\text{ cm}^{-3}$  (Fig. 2.12.4). This approach could provide a possible route to finely control and measure the doping density of a single device.

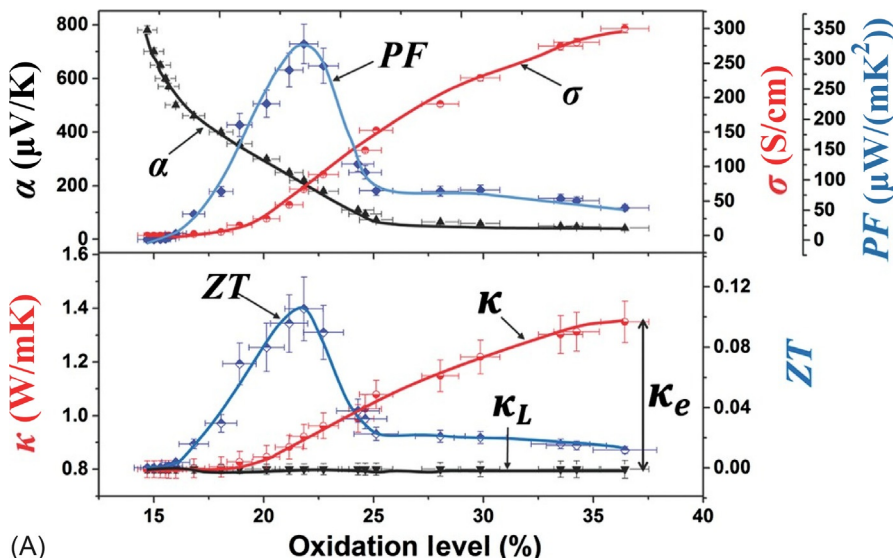


**Fig. 2.12.3** Seebeck coefficient, electrical conductivity, power factor ( $\sigma\alpha^2$ ), thermal conductivity, and figure of merit ( $ZT$ ) of poly(3,4-ethylenedioxythiophene):tosylate as a function of the oxidation level, at 300K.

Data from Z.U. Khan, J. Edberg, M.M. Hamed, R. Gabrielsson, H. Granberg, L. Wågberg, I. Engquist, M. Berggren, X. Crispin, Thermoelectric polymers and their elastic aerogels, *Adv. Mater.* 28 (2016) 4556. Copyright 2015 Wiley-VCH Verlag GmbH & Co.

**Table 2.12.1** Thermoelectric power enhancement of PEDOT:PSS films through treatment with aqueous and organic reducing agents.

Entry	Reducing agent	Redox potential $E^\circ$ (V/SHE)	EG-dipping	Seebeck coefficient ( $\mu\text{V}/\text{K}$ )
1	None	N/A	a	18
2	$\text{Na}_2\text{S}_2\text{O}_3$	-0.57	a	59
3	TDAE	-0.71 <sup>b</sup>	a	43
4	$\text{Na}_2\text{SO}_3$	-0.93	a	70
5	Hydrazine	-1.16	a	92
6	$\text{NaBH}_4$	-1.24	a	104

<sup>a</sup> EG dipping performed after the reduction step.

<sup>b</sup> Electrochemical potential measured in  $\text{CH}_3\text{CN}$ .

Data from N. Massonnet, A. Carella, O. Jaudouin, P. Rannou, G. Laval, C. Celle, J.-P. Simonato, Improvement of the Seebeck coefficient of PEDOT:PSS by chemical reduction combined with a novel method for its transfer using free-standing thin films, *J. Mater. Chem. C* 2 (2014) 1278. Copyright 2013 The Royal Society of Chemistry.

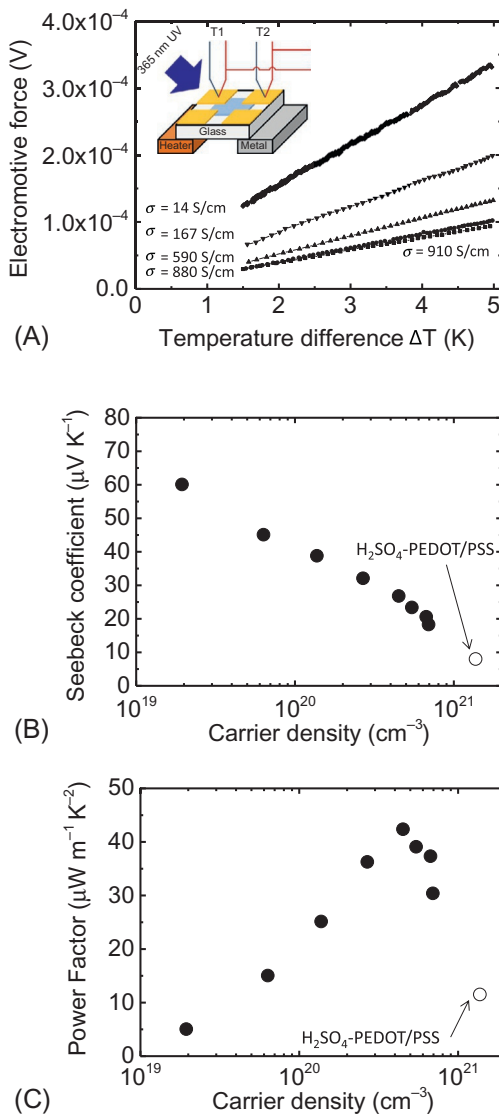


**Fig. 2.12.4** (A) Electromotive force as a function of the temperature difference for obtaining the Seebeck coefficient of a PEDOT:PSS film at a given ultraviolet irradiation time, (B) resulting Seebeck coefficient, and (C) power factor as a function of the carrier density.

Data from Q. Wei, M. Mukaida, K. Kirihara, Y. Naitoh, T. Ishida, Photoinduced dedoping of conducting polymers: an approach to precise control of the carrier concentration and understanding transport properties, ACS Appl. Mater. Interfaces 8 (2016) 2054. Copyright 2016 American Chemical Society.

## 2.12.3 Thermoelectric properties of organic semiconductors with controlled molecular doping

PEDOT:PSS is predoped during polymerization. Other organic semiconductors could be chemically doped by exposure to oxidative agents such as  $\text{Fe}^{3+}$ ,  $\text{I}_2$ ,  $\text{Br}_2$ , 7,7,8,8-tetracyano-2,3,5,6-tetrafluoroquinodimethane ( $\text{F}_4\text{TCNQ}$ ), and  $\text{NOPO}_6$  after the film formation. For a high  $\sigma$  via molecular doping, both doping density and carrier mobility must be considered: a high concentration of dopants could generate more changes, but

these dopants could also affect the molecular packing and the morphology, decreasing the carrier mobility. Although doping phthalocyanine and polyacetylene with I<sub>2</sub> leads to high conductivity, I<sub>2</sub> easily evaporates and, thus, provides an unstable conductive film.

Leclerc et al. reported for FeCl<sub>3</sub>-doped poly(2,7-carbazole) derivatives a  $\sigma$  up to 500 S/cm, resulting in a power factor of 19  $\mu\text{W}/(\text{m K}^2)$  [18]. Zhu et al. used iron (III) bis(trifluoromethanesulfonyl)imide as the dopant and studied the thermoelectric properties of poly(3-hexylthiophene) (P3HT), poly(2,5-bis(3-tetradecylthiophen-2-yl)thieno(3,2-*b*)thiophene) (PBTTT), and two donor-acceptor-type organic semiconductors. All these materials exhibited maximum power density at high doping levels; in particular, PBTTT showed the highest value, namely, 14  $\mu\text{W}/(\text{mK}^2)$  (Fig. 2.12.5) [19].

The efficient charge-transfer reaction between F<sub>4</sub>TCNQ and P3HT was observed by Kim et al. in 2008 [20]; resulting in a  $\sigma$  higher than 0.1 S/cm. By using the liquid crystal organic semiconductor PBTTT, which has higher carrier mobility than P3HT, Chabinyc et al. achieved a  $\sigma$  as high as 2 S/cm for PBTTT:F<sub>4</sub>TCNQ films [21]. Kang et al. studied the same materials and system but optimized the process by evaporating the F<sub>4</sub>TCNQ molecules on top of the PBTTT layer; as a consequence, the polymer retained its highly ordered lamellar microstructure with the dopant incorporated into the layer of side chains. This solid-state diffusion method allowed a  $\sigma$  much higher than 200 S/cm [22].

Kao et al. have demonstrated that hydrolyzed fluoroalkyl trichlorosilane (FTS) can act as another efficient dopant for P3HT and PBTTT [23]. It enabled the  $\sigma$  increase by up to six orders of magnitude, reaching 1000 S/cm for PBTTT and 50 S/cm for P3HT. Although not fully understood, the doping mechanism is tentatively attributed to the protonic doping and not the charge transfer. Patel et al. studied and compared the thermoelectric properties of FTS-doped PBTTT; they observed better thermoelectric performance (Seebeck coefficient and power factor of about 33  $\mu\text{V/K}$  and 100  $\mu\text{W}/(\text{m K}^2)$ , respectively), exceeding that of films doped with 4-ethylbenzenesulfonic acid [24]. Interestingly, this difference is not due to local structure perturbations by dopants but to changes in the carrier scattering in the disordered regions of the film or to the entropic vibrational component of  $S$ . The same research group also compared the thermoelectric properties of a series of semiconducting polymers having a  $\sigma$  of 10<sup>-5</sup>–1000 S/cm that were doped with either F<sub>4</sub>TCNQ or FTS. There was no obvious maximum in the power factor of these polymers, unlike what is typically observed for inorganic semiconductors (Fig. 2.12.6) [25]. The authors also pointed out that developing additional doping mechanisms yielding higher conductivities may further improve the power factor of organic semiconductors.

## 2.12.4 N-type organic thermoelectric materials

N-type organic thermoelectric materials must face significant challenges to achieve efficient doping and stability toward moisture and oxygen. Although the material combination is still limited, pioneering groups have demonstrated promising thermoelectric properties of these materials through molecular doping. Chabinyc et al.

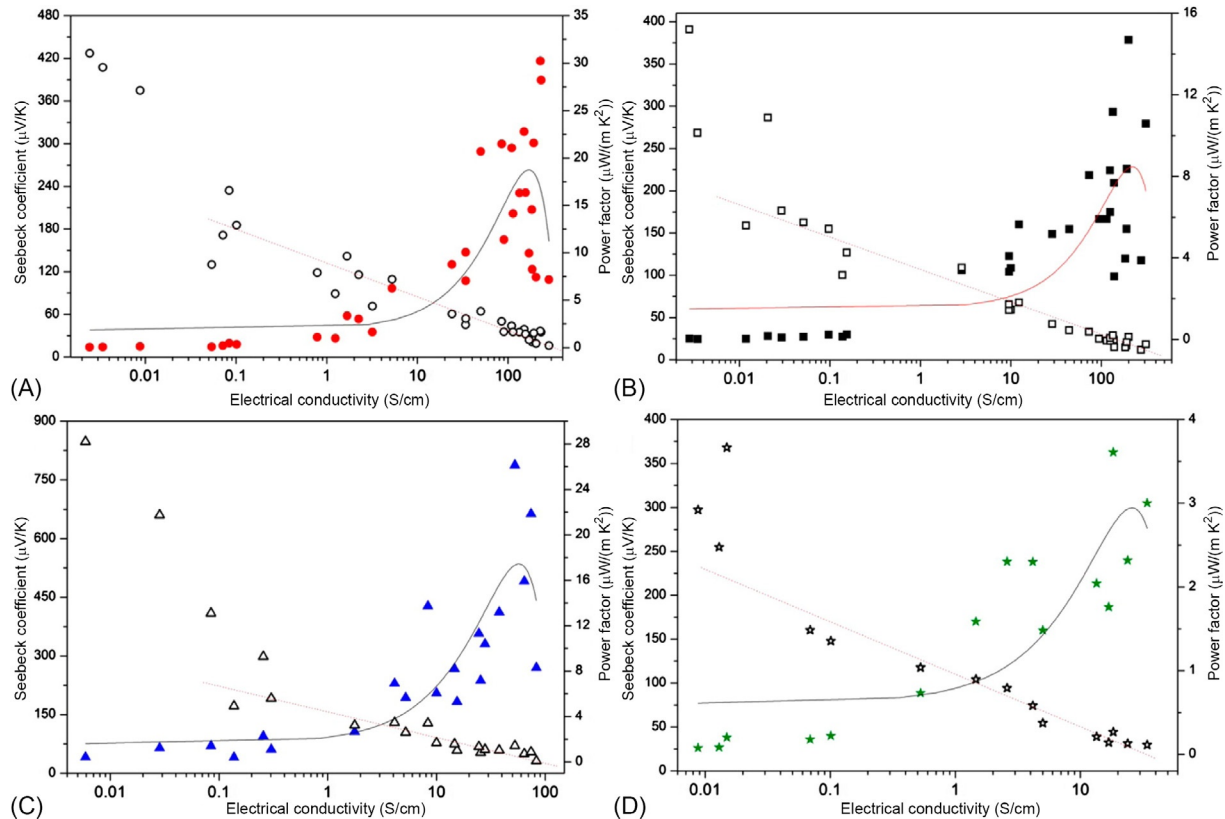


**Fig. 2.12.5** Optimization of the thermoelectric power factor with the doping time. Seebeck coefficient and power factor as functions of the electrical conductivity, in logarithm scale, for (A) poly(3-hexylthiophene), (B) poly(2,5-bis(3-tetradecylthiophen-2-yl)thieno(3,2-*b*)thiophene), (C) poly(diketopyrrolopyrrole-terthiophene), and (D) poly[(4,40-bis(2-ethylhexyl)dithieno[3,2-*b*:20,30-*d*]silole)-2,6-diyl-alt-(2,1,3-benzothiadiazole)-4,7-diyl]. The continuous lines help to guide the eye.

Data from Q. Zhang, Y. Sun, W. Xu, D. Zhu, What to expect from conducting polymers on the playground of thermoelectricity: lessons learned from four high-mobility polymeric semiconductors, *Macromolecules* 47 (2014) 609. Copyright 2014 American Chemical Society.

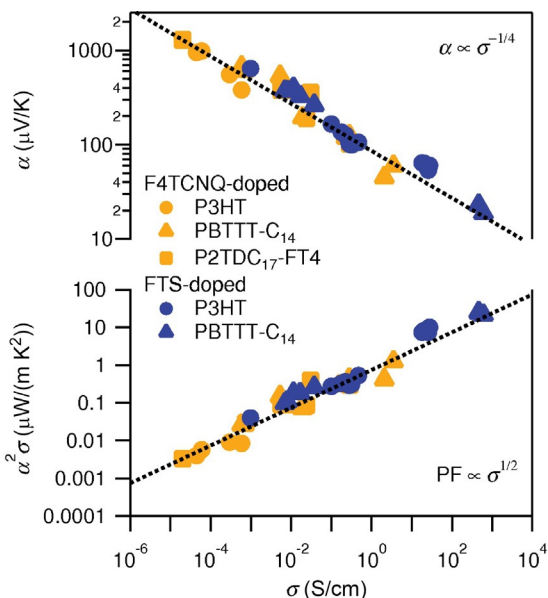


**Fig. 2.12.6** Thermopower (top) and power factor (bottom) as functions of the electrical conductivity for different polymers; the *dashed lines* indicate empirical fits of  $\alpha$  and PF, proportional to  $\sigma^{-1/4}$  and  $\sigma^{1/2}$ , respectively.

Data from Z.U. Khan, J. Edberg, M.M. Hamed, R. Gabrielsson, H. Granberg, L. Wågberg, I. Engquist, M. Berggren, X. Crispin, Thermoelectric polymers and their elastic aerogels, *Adv. Mater.* 28 (2016) 4556. Copyright 2015 Wiley-VCH Verlag GmbH & Co.

observed a  $\sigma$  of about  $10^{-2}$   $\text{S}/\text{cm}$  and power factors above  $0.1 \mu\text{W}/(\text{m K}^2)$  for solution mixtures of poly{[*N,N'*-bis(2-octyldecyl)-naphthalene-1,4,5,8-bis(dicarboximide)-2,6-diyl]-alt-5,5'-(2,2'-bithiophene)} and dihydro-1*H*-benzoimidazol-2-yl (N-DBI) derivatives [26]. Later, Segalman et al. reported a  $\sigma$  of  $0.5 \text{ S}/\text{cm}$  and power factors above  $1 \mu\text{W}/(\text{m K}^2)$  for self-doped perylene diimides [27]. Pei et al. synthesized a series of benzodifuranone-based poly(*p*-phenylene vinylene) (BDPPV) derivatives that exhibited an electron mobility up to  $1.70 \text{ cm}^2/(\text{Vs})$  under ambient conditions (Fig. 2.12.7) [28]. Due to low LUMO levels, these polymers showed an efficient electron transfer from N-DBI; spin-coating the BDPPV/N-DBI mixture allowed a  $\sigma$  of  $14 \text{ S}/\text{cm}$  and power factors up to  $28 \mu\text{W}/(\text{m K}^2)$  in thin solid films.  $\sigma$  reaches the highest values in n-type organic semiconductors. Kemerink et al. found that a [6,6]-phenyl-C<sub>61</sub>-butyric acid methyl ester coating on a previously cast 4-(1,3-dimethyl-2,3-dihydro-1*H*-benzoimidazol-2-yl)-*N,N*-diphenylaniline film could generate a power factor higher than  $35 \mu\text{W}/(\text{m K})$  and a high  $S (> 800 \mu\text{V}/\text{K})$  [29]. Compared with p-type organic thermoelectric materials, the performance of the n-type ones is still not high enough, especially in terms of  $\sigma$ . Nevertheless, recently efforts on organic thin film transistors have shown that they could achieve carrier mobility comparable with that of the p-type materials; moreover, an efficient dopant could significantly improve their performance.

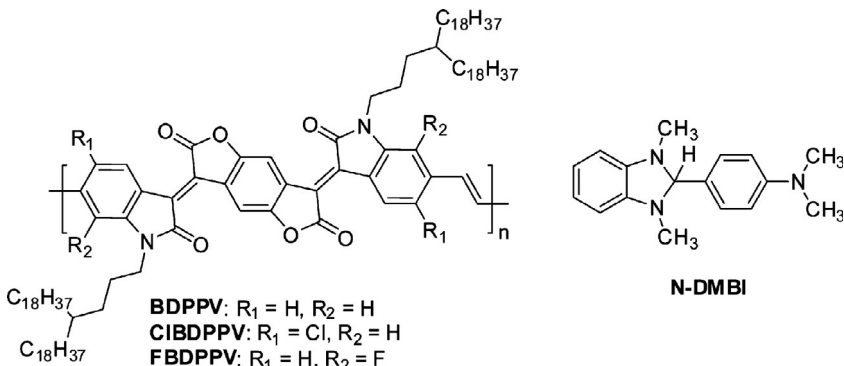


**Fig. 2.12.7** Chemical structures of benzodifurandione-based poly(*p*-phenylene vinylene) (BDPPV) derivatives and n-type dopant dihydro-1*H*-benzoimidazol-2-yl.

Data from K. Shi, F. Zhang, C.-A. Di, T.-W. Yan, Y. Zou, X. Zhou, D. Zhu, J.-Y. Wang, J. Pei, Toward high performance n-type thermoelectric materials by rational modification of BDPPV backbones, *J. Am. Chem. Soc.* 137 (2015) 6979. Copyright 2015 American Chemical Society.

## 2.12.5 Anisotropic thermal and electrical transport in organic semiconductors

Organic thermoelectric materials are often characterized by the in-plane  $\sigma$ , in-plane  $S$ , and through-plane  $\kappa$  of their thin films since it is difficult to obtain the through-plane  $\sigma$ , through-plane  $S$ , and in-plane  $\kappa$  for similar conducting polymer films. Since many organic semiconductors can form anisotropic films, such films would presumably exhibit anisotropic thermoelectric properties. Measuring the aforementioned charactering parameters is important for understanding the thermal and carrier transport mechanisms in conducting polymers to improve their thermoelectric performance, but it is challenging.

Weathers et al. directly measured all these three in-plane thermoelectric properties of the same suspended PEDOT thin films using suspended microdevices. [30] They observed an anisotropic  $\kappa$  that showed a general increase with  $\sigma$ , reaching 1.8 W/(mK) at  $\sigma$  around 500 S/cm; this increase exceeds that predicted by the Wiedemann-Franz law according to the Sommerfeld value of the Lorentz factor.

Liu et al. studied the in-plane  $\kappa$  of PEDOT:PSS films through time-domain thermoreflectance experiments [31] and similarly reported highly anisotropic  $\kappa$ . However, Wei et al. found that the  $\kappa$  increase is consistent with conventional Sommerfeld value of the Lorentz number by using the Wiedemann-Franz law.

The authors have studied both the in-plane and through-plane  $\kappa$ ,  $\sigma$ , and  $S$  of PEDOT:PSS thin films [32]. For the through-plane conductivity investigation, Wei et al. designed a coaxial four-point probe [33]; as shown in Fig. 2.12.8, the outer electrodes worked as the source probe (current probe) and the inner ones as the sense probe (voltage probe). All the probes consisted of gold-plated copper blocks and the controlled distance between the sense and the source probe ranged from 750 to 25  $\mu$ m.

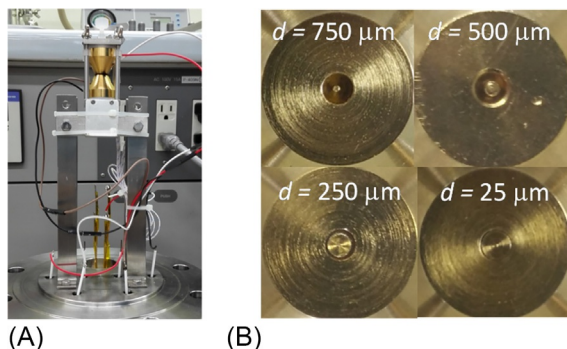


**Fig. 2.12.8** Images of (A) the four-point probe setup for measuring the through-plane electrical conductivity and (B) its source and sense probes.

Data from Q. Wei, H. Suga, I. Ikeda, M. Mukaida, K. Kirihara, Y. Naitoh, T. Ishida, An accurate method to determine the through-plane electrical conductivity and to study transport properties in film samples, Org. Electron. 38 (2016) 264. Copyright 2016 Elsevier.

As shown in Fig. 2.12.9A, the measured in-plane  $\sigma$  of the PEDOT:PSS films was  $820 \text{ S/cm}$ , which is identical to previously reported values, suggesting that the analyzed thick film had an ordered structure similar to the thin films. However, the through-plane  $\sigma$  showed a lower value of  $36 \text{ S/cm}$ . This anisotropic behavior was attributed to the morphology of the PEDOT:PSS films. The authors have also demonstrated that highly conductive PEDOT:PSS films have a layered structure and that PSS may isolate the PEDOT nanocrystals in the through-plane direction. The through-plane  $S$  was  $15 \mu\text{V/K}$  at room temperature, which is close to the corresponding in-plane value (Fig. 2.12.9B). The authors measured  $\kappa$  of large-area freestanding ordered PEDOT:PSS films via flash analysis, finding through- and in-plane values of  $0.15$  and  $0.84 \text{ W/(m K)}$ , respectively; this suggested an anisotropic nature of  $\kappa$  for the tested samples (Fig. 2.12.9C). The authors also estimated  $ZT$  at room temperature, obtaining  $8.4 \times 10^{-3}$  and  $1.6 \times 10^{-3}$  in the in-plane and through-plane direction, respectively. It was calculated based on in-plane  $\sigma$ , in-plane  $S$ , and through-plane  $\kappa$  gave an overestimated value of  $0.05$ ; this result indicates that, for an accurate  $ZT$  estimation, the three properties from the same direction should be used.

In this chapter, the authors have introduced the history of organic thermoelectric materials and summarized the recent efforts for improving the thermoelectric properties of p- and n-type organic materials. PEDOT predoped during polymerization and organic thermoelectric materials through molecular doping have also been described, along with a couple of examples of n-type organic thermoelectric materials. Such pioneering studies have opened new possibilities for the application of organic semiconductors; for further improvements, more efficient dopants for both high mobility p- and n-type semiconductors are needed. The anisotropy and stability should also be considered when characterizing such organic thermoelectric materials.

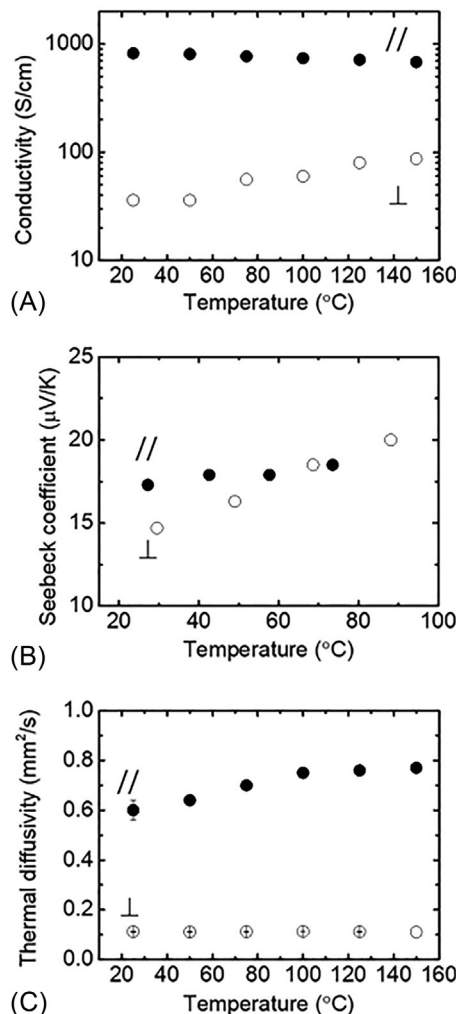


**Fig. 2.12.9** (A) Electrical conductivity, (B) Seebeck coefficient, and (C) thermal diffusivity of PEDOT:PSS films in the in-plane (*closed circles*) and through-plane (*open circles*) directions, plotted as functions of the temperature.

Data from Q. Wei, M. Mukaida, K. Kirihara, T. Ishida, Experimental studies on the anisotropic thermoelectric properties of conducting polymer films, ACS Macro Lett. 3 (2014) 948.

Copyright 2014 American Chemical Society.

## References

- [1] T.J. Seebeck, Ueber die magnetische Polarisation der Metalle und Erze durch Temperatur-Differenz, Ann. Phys. 82 (1826) 133–160.
- [2] G.J. Snyder, E.S. Toberer, Complex thermoelectric materials, Nat. Mater. 7 (2008) 105.

- [3] P.E. Fielding, F. Gutman, Electrical properties of phthalocyanines, *J. Chem. Phys.* 26 (1957) 411–419.
- [4] H.A. Pohl, E.H. Engelhardt, Synthesis and characterization of some highly conjugated semiconducting polymers, *J. Phys. Chem.* 66 (1962) 2085–2095.
- [5] H. Yan, N. Sada, N. Toshima, Thermal transporting properties of electrically conductive polyaniline films as organic thermoelectric materials, *J. Therm. Anal. Calorim.* 69 (2002) 881–887.
- [6] S.R. Forrest, M.E. Thompson, Introduction: organic electronics and optoelectronics, *Chem. Rev.* 107 (2007) 923–925.
- [7] O. Bubnova, Z.U. Khan, A. Malti, S. Braun, M. Fahlman, M. Berggren, X. Crispin, Optimization of the thermoelectric figure of merit in the conducting polymer poly(3,4-ethylenedioxothiophene), *Nat. Mater.* 10 (2011) 429.
- [8] A. Elschner, S. Kirchmeyer, W. Lovenich, U. Merker, K. Reuter, PEDOT: Principles and Applications of an Intrinsically Conductive Polymer, CRC Press, Boca Raton, FL, 2010.
- [9] X. Wang, X. Zhang, L. Sun, D. Lee, S. Lee, M. Wang, J. Zhao, Y. Shao-Horn, M. Dincă, T. Palacios, K.K. Gleason, High electrical conductivity and carrier mobility in oCVD PEDOT thin films by engineered crystallization and acid treatment, *Sci. Adv.* 4 (2018) eaat5780.
- [10] B. Cho, K.S. Park, J. Baek, H.S. Oh, Y.-E. Koo Lee, M.M. Sung, Single-crystal poly(3,4-ethylenedioxothiophene) nanowires with ultrahigh conductivity, *Nano Lett.* 14 (2014) 3321–3327.
- [11] N. Massonnet, A. Carella, A. de Geyer, J. Faure-Vincent, J.-P. Simonato, Metallic behaviour of acid doped highly conductive polymers, *Chem. Sci.* 6 (2015) 412–417.
- [12] H. Yano, K. Kudo, K. Marumo, H. Okuzaki, Fully soluble self-doped poly(3,4-ethylenedioxothiophene) with an electrical conductivity greater than  $1000 \text{ S cm}^{-1}$ , *Sci. Adv.* 5 (2019) eaav9492.
- [13] Q. Wei, M. Mukaida, K. Kirihara, Y. Naitoh, T. Ishida, Thermoelectric power enhancement of PEDOT:PSS in high-humidity conditions, *Appl. Phys. Express* 7 (2014) 031601.
- [14] Z.U. Khan, J. Edberg, M.M. Hamedi, R. Gabrielson, H. Granberg, L. Wågberg, I. Engquist, M. Berggren, X. Crispin, Thermoelectric polymers and their elastic aerogels, *Adv. Mater.* 28 (2016) 4556–4562.
- [15] N. Massonnet, A. Carella, O. Jaudouin, P. Rannou, G. Laval, C. Celle, J.-P. Simonato, Improvement of the Seebeck coefficient of PEDOT:PSS by chemical reduction combined with a novel method for its transfer using free-standing thin films, *J. Mater. Chem. C* 2 (2014) 1278–1283.
- [16] Q. Wei, M. Mukaida, K. Kirihara, Y. Naitoh, T. Ishida, Photoinduced dedoping of conducting polymers: an approach to precise control of the carrier concentration and understanding transport properties, *ACS Appl. Mater. Interfaces* 8 (2016) 2054–2060.
- [17] Q. Wei, M. Mukaida, T. Ishida, Extracting carrier mobility in conducting polymers using a photoinduced charge transfer reaction, *J. Phys. Chem. C* 122 (2018) 15922–15928.
- [18] R.B. Aich, N. Blouin, A. Bouchard, M. Leclerc, Electrical and thermoelectric properties of poly(2,7-carbazole) derivatives, *Chem. Mater.* 21 (2009) 751–757.
- [19] Q. Zhang, Y. Sun, W. Xu, D. Zhu, What to expect from conducting polymers on the playground of thermoelectricity: lessons learned from four high-mobility polymeric semiconductors, *Macromolecules* 47 (2014) 609–615.
- [20] K.-H. Yim, G.L. Whiting, C.E. Murphy, J.J.M. Halls, J.H. Burroughes, R.H. Friend, J.-S. Kim, Controlling electrical properties of conjugated polymers via a solution-based p-type doping, *Adv. Mater.* 20 (2008) 3319–3324.

- [21] J.E. Cochran, M.J.N. Junk, A.M. Glaudell, P.L. Miller, J.S. Cowart, M.F. Toney, C.J. Hawker, B.F. Chmelka, M.L. Chabinyc, Molecular interactions and ordering in electrically doped polymers: blends of PBTTT and F4TCNQ, *Macromolecules* 47 (2014) 6836–6846.
- [22] K. Kang, S. Watanabe, K. Broch, A. Sepe, A. Brown, I. Nasrallah, M. Nikolk, Z. Fei, M. Heeney, D. Matsumoto, K. Marumoto, H. Tanaka, S.-i. Kuroda, H. Sirringhaus, 2D coherent charge transport in highly ordered conducting polymers doped by solid state diffusion, *Nat. Mater.* 15 (2016) 896.
- [23] C.Y. Kao, B. Lee, L.S. Wielunski, M. Heeney, I. McCulloch, E. Garfunkel, L.C. Feldman, V. Podzorov, Doping of conjugated polythiophenes with alkyl silanes, *Adv. Funct. Mater.* 19 (2009) 1906–1911.
- [24] S.N. Patel, A.M. Glaudell, D. Kiefer, M.L. Chabinyc, Increasing the thermoelectric power factor of a semiconducting polymer by doping from the vapor phase, *ACS Macro Lett.* 5 (2016) 268–272.
- [25] A.M. Glaudell, J.E. Cochran, S.N. Patel, M.L. Chabinyc, Impact of the doping method on conductivity and thermopower in semiconducting polythiophenes, *Adv. Energy Mater.* 5 (2015) 1401072.
- [26] R.A. Schlitz, F.G. Brunetti, A.M. Glaudell, P.L. Miller, M.A. Brady, C.J. Takacs, C.J. Hawker, M.L. Chabinyc, Solubility-limited extrinsic n-type doping of a high electron mobility polymer for thermoelectric applications, *Adv. Mater.* 26 (2014) 2825–2830.
- [27] B. Russ, M.J. Robb, F.G. Brunetti, P.L. Miller, E.E. Perry, S.N. Patel, V. Ho, W.B. Chang, J.J. Urban, M.L. Chabinyc, C.J. Hawker, R.A. Segalman, Power factor enhancement in solution-processed organic n-type thermoelectrics through molecular design, *Adv. Mater.* 26 (2014) 3473–3477.
- [28] K. Shi, F. Zhang, C.-A. Di, T.-W. Yan, Y. Zou, X. Zhou, D. Zhu, J.-Y. Wang, J. Pei, Toward high performance n-type thermoelectric materials by rational modification of BDPPV backbones, *J. Am. Chem. Soc.* 137 (2015) 6979–6982.
- [29] G. Zuo, Z. Li, E. Wang, M. Kemerink, High Seebeck coefficient and power factor in n-type organic thermoelectrics, *Adv. Electron. Mater.* 4 (2018) 1700501.
- [30] A. Weathers, Z.U. Khan, R. Brooke, D. Evans, M.T. Pettes, J.W. Andreasen, X. Crispin, L. Shi, Significant electronic thermal transport in the conducting polymer poly(3,4-ethyl-enedioxythiophene), *Adv. Mater.* 27 (2015) 2101–2106.
- [31] J. Liu, X. Wang, D. Li, N.E. Coates, R.A. Segalman, D.G. Cahill, Thermal conductivity and elastic constants of PEDOT:PSS with high electrical conductivity, *Macromolecules* 48 (2015) 585–591.
- [32] Q. Wei, M. Mukaida, K. Kirihara, T. Ishida, Experimental studies on the anisotropic thermoelectric properties of conducting polymer films, *ACS Macro Lett.* 3 (2014) 948–952.
- [33] Q. Wei, H. Suga, I. Ikeda, M. Mukaida, K. Kirihara, Y. Naitoh, T. Ishida, An accurate method to determine the through-plane electrical conductivity and to study transport properties in film samples, *Org. Electron.* 38 (2016) 264–270.

# Organic thermoelectric materials and devices

2.13

Hong Wang<sup>a</sup> and Choongho Yu<sup>b</sup>

<sup>a</sup>Frontier Institute of Science and Technology, Xi'an Jiaotong University, Xi'an, PR China,

<sup>b</sup>Department of Mechanical Engineering, Texas A&M University, College Station, TX, United States

## 2.13.1 Introduction

Organic thermoelectric (TE) materials are typically lightweight, easy to process, inexpensive, and less toxic than their inorganic counterparts [1]. Flexible organic TE materials are advantageous in making close contacts with nonflat heat sources, such as human bodies, cylindrical pipes, heat engines, and power-consuming devices, to achieve effective energy conversion. These advantages have attracted significant interest in developing flexible, organic material-based TE devices. However, the performance (ZT value) of current organic TE materials is inferior to those of inorganic counterparts that have shown high ZT values of 2.5–3 at temperatures over 900K [2, 3] and ~1 at 300 K [4]. Only a few organic TE materials have been reported to have ZT values over 0.2 at 300 K [5–7].

The low TE performance of organic materials can be attributed to the difficulties in understanding and predicting charge transport, which widely varies depending on the molecular structure and morphology of the organic materials. For example, the crystallinity and morphology of polymers are easily altered depending on the sample preparation conditions such as temperature, humidity, and drying process, but slight changes in the crystallinity and morphology can make the charge transport properties very different. To date, there is still no robust transport model guiding us to further improve the TE performance of this complex system [8–10].

Nevertheless, recent progress in improving TE performance, understanding transport mechanisms, and fabricating modules has shown promising future applications, especially for portable and wearable applications. The performance of a TE material is typically indicated by the thermoelectric figure-of-merit called ZT, which is defined as  $S^2\sigma T/\kappa$ , where  $S$  is the Seebeck coefficient (or thermopower),  $\sigma$  is the electrical conductivity,  $\kappa$  is the thermal conductivity, and  $T$  is the absolute temperature. Ideal TE materials have high electrical conductivity, high Seebeck coefficient, and low thermal conductivity. However, these three key factors are adversely correlated. There have been considerable efforts to decouple the three key parameters by making composites, controlling the morphology, and tuning the doping level. For example, Yu and coworkers reported their insightful work

on decoupling the electrical conductivity and Seebeck coefficient in 2008 [11] and 2010 [12]. Bubnova et al. reported that a high-power factor ( $S^2\sigma$ ) could be obtained by tuning the oxidation level of poly(3,4-ethylenedioxythiophene):tosylate (PEDOT:Tos) in 2011 [5]. Wang et al. demonstrated that creating polymer composites with nonpercolated carbon nanotubes (CNTs) is an effective way to obtain materials with low thermal conductivity, high Seebeck coefficient, and decent electrical conductivity in 2015 [7]. Kang et al. reported a semiempirical model for the charge transport in conducting polymers in 2016 [10]. These exciting results have prompted researchers to pursue higher TE performance of organic materials because of their low cost and scalability even though the ZT values are lower than those of inorganic materials. The following sections present overviews of organic thermoelectric materials, including fundamental theory, chemical structures and compositions, and strategies for device development.

### 2.13.2 Charge transport in organic thermoelectric materials

The most distinct characteristics in organic materials compared with inorganic counterparts are the charge transport mechanisms. In general, electrically conducting organic materials have delocalized  $\pi$ -orbitals through which charge carriers can be injected. The injection of charge carriers is called “doping” for organic materials. A variety of oxidizing/reducing agents such as  $\text{FeCl}_3$ , 2,3,5,6-Tetrafluoro-7,7,8,8-tetracyanoquino-dimethane (F4TCNQ), and  $\text{I}_2$  have been used to dope organic materials, including poly(3-hexylthiophene) and polyacetylene [13]. Doping often generates polaronic charge carriers in organic materials. Charge transport occurs via hopping of polarons between localized states [14].

Conducting polymers are exemplary organic materials that are typically composed of spatially and energetically inhomogeneous domains [15]. Charge carriers can hop from one domain to another in conducting polymers. Electrical transport properties based on the Drude model may not accurately describe the charge carrier transport in conducting polymers. This model is typically valid for free hole/electron transport under spatially uniform electronic potentials. The transport models for disordered materials include variable range hopping (VRH) [16], nearest-neighbor hopping (NNH) [17], and Efros-Shklovskii hopping (ESH) [18,19]. Kang et al. recently reported an empirical charge carrier transport model for conducting polymers with factors that do not convey physical meanings [10]. These models are insufficient to connect the TE performance well with other key electronic parameters, including mobility, the highest occupied molecular orbital (HOMO), the lowest unoccupied molecular orbital (LUMO), Fermi level, and carrier concentration. Further work is necessary to facilitate development of high TE performance organic materials.

## 2.13.3 Thermoelectric materials: Polymers and small molecules

### 2.13.3.1 Developing thermoelectric materials based on polymers

#### 2.13.3.1.1 Tuning the carrier concentration via doping and dedoping

Tuning the carrier concentration is an effective way to find the peak power factor of polymers. Conducting polymers were discovered in the late 1970s by Heeger, Shirakawa, and Macdiarmid [20–22]. Later, a number of conducting polymers were developed with a high electrical conductivity up to  $10^4$  S/cm, which are called “synthetic metals” [22]. High electrical conductivity can be achieved after doping intrinsic conducting polymers that have electrical conductivity as low as  $10^{-9}$  S/cm. In fact, conducting polymers are typically heavily doped since their charge mobility is small, e.g., in the range of  $0.3\text{--}0.7\text{ cm}^2/(\text{Vs})$  (one or two orders of magnitude lower than those of inorganic materials) [4]. Heavy doping significantly increases the carrier concentration and subsequently increases the electrical conductivity of conducting polymers.

For many conducting polymers, the highest power factor often appears at a high doping level. For example, pristine polyacetylene has an electrical conductivity in the range of  $10^{-3}\text{--}10^{-8}$  S/cm and a Seebeck coefficient in the range of  $10^2\text{--}10^3\text{ }\mu\text{V/K}$ , leading to a low power factor less than  $1\text{ }\mu\text{W}/(\text{m K}^2)$  [23–25]. When polyacetylene is doped, the electrical conductivity can be increased to  $\sim 10^4$  S/cm with a Seebeck coefficient of  $\sim 20\text{ }\mu\text{V/K}$ . After doping, although the Seebeck coefficient is reduced, the large enhancement in electrical conductivity leads to a high-power factor of  $\sim 400\text{ }\mu\text{W}/(\text{m K}^2)$  for heavily doped polyacetylene [26].

Similar results have been observed for heavily doped polyaniline, showing a higher power factor than pristine polyaniline. A facile gas treatment method was reported by Wang et al. to adjust the doping level of polyaniline [27]. It was found that the power factor of polyaniline monotonically decreased upon lowering the carrier concentration by dedoping, as shown in Fig. 2.13.1 [27]. Here, doped polyaniline initially had a high electrical conductivity of 5700 S/m and a Seebeck coefficient of  $\sim 16\text{ }\mu\text{V/K}$ . While decreasing the doping level of polyaniline with ammonium hydroxide gas, the electrical conductivity rapidly dropped from 5700 to  $\sim 400$  S/m, but the Seebeck coefficient slowly increased from  $\sim 16$  to  $46\text{ }\mu\text{V/K}$  after 10 min of ammonium hydroxide treatment. Although a high Seebeck coefficient up to  $\sim 115\text{ }\mu\text{V/K}$  could be achieved with the gas treatment, the power factor continued to decrease during the entire dedoping process due to the large reduction in electrical conductivity. The maximum power factor of polyaniline, therefore, appeared with the highest electrical conductivity.

It has been proposed that a transition from a semiconductor to metal or semimetal can occur during a doping process. In general, undoped conducting polymers are semiconductors with large bandgaps, which can be identified by ultraviolet-visible-near infrared (UV-vis-NIR) spectroscopy. When the polymer is doped, semiconducting polymers can

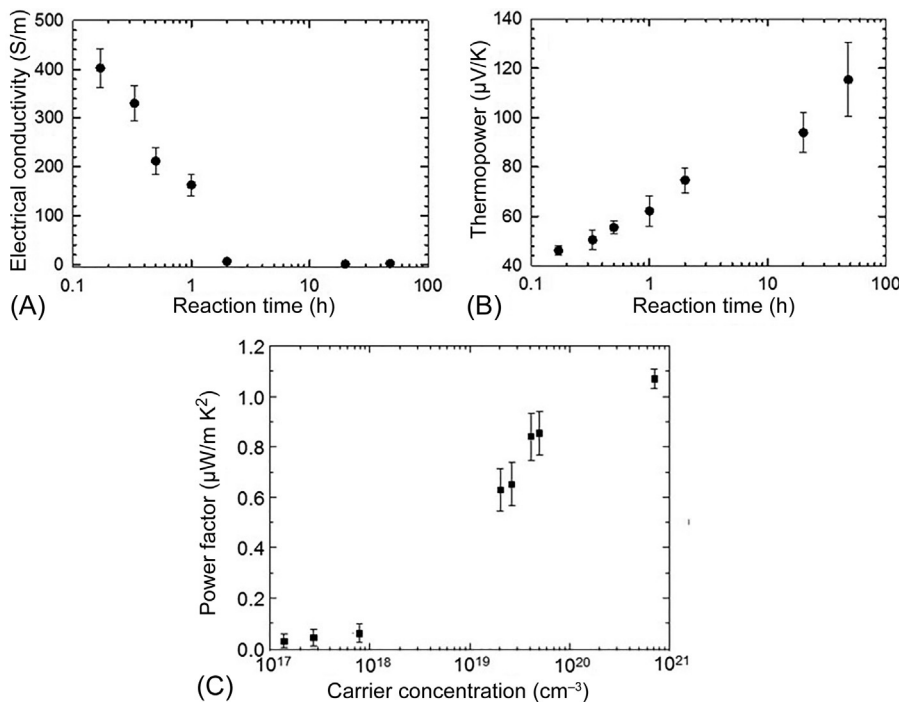


**Fig. 2.13.1** Electrical conductivity (A) and Seebeck coefficient (or thermopower) (B) of camphorsulfonic acid (CSA)-doped polyaniline (PANI) films treated with ammonium hydroxide for various time periods. (C) The correlation between the power factor ( $S^2\sigma$ ) and the charge carrier concentration. The charge mobility was assumed to be  $0.5 \text{ cm}^2/(\text{V s})$  [27].

be metallic since the extra carriers can destroy the bound states [28]. The change in the bandgap of polymers from semiconductor to metal has been observed in electron paramagnetic resonance (EPR) spectra [28]. Although doping for increasing the electrical conductivity typically reduces the Seebeck coefficient of polymers, the variation in electrical conductivity is often much larger than that of the Seebeck coefficient. As low doping levels significantly lower electrical conductivity, the maximum power factor typically appears at the highest electrical conductivity for conducting polymers.

Park et al. reported that the maximum power factor could be found by using an electrochemical method to tune the oxidation level of PEDOT [29]. Similar to the work reported by Bubnova et al., the oxidation/doping level is proportional to the oxidation electrochemical potential. When the potential was  $-2.0 \text{ V}$ , a relatively high Seebeck coefficient close to  $200 \mu\text{V/K}$  was observed by sacrificing the electrical conductivity. During the potential increase from  $-2.0 \text{ V}$ , the Seebeck coefficient and the electrical conductivity did not noticeably change until the potential was larger than  $-0.5 \text{ V}$ . Then, a sharp reduction in the Seebeck coefficient was observed (Fig. 2.13.2). The Seebeck coefficient became constant at  $\sim 40 \mu\text{V/K}$  between  $0.8$  and  $2.0 \text{ V}$ . In contrast, the very low electrical conductivity at a potential of  $-2.0 \text{ V}$

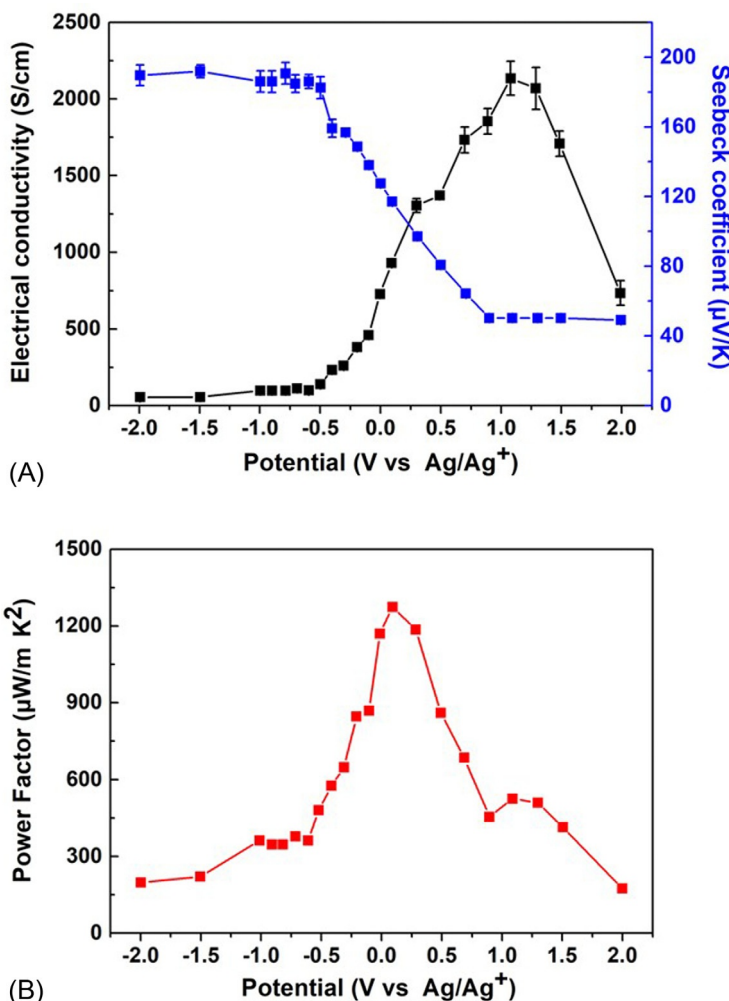


**Fig. 2.13.2** (A) The electrical conductivity and Seebeck coefficient of the PEDOT film prepared from a mixture of pyridine and poly(ethylene glycol)-block-poly(propylene glycol)-block-poly(ethylene glycol) triblock copolymer PEPG (PP-PEDOT) after application of different potentials. (B) The corresponding power factor of PP-PEDOT versus the application of potential [29].

was maintained until the potential reached  $-0.5\text{ V}$ , and then a sharp increase in the electrical conductivity was observed up to  $\sim 2000\text{ S/cm}$  at a potential of  $\sim 1.2\text{ V}$ . Then, the conductivity began to rapidly decrease and became  $\sim 600\text{ S/cm}$  at a potential of  $2.0\text{ V}$ . Here, the presence of the peak electrical conductivity despite further doping remains unclear. The maximum power factor was  $1270\text{ }\mu\text{W}/(\text{mK}^2)$  at  $0.1\text{ V}$  due to the high electrical conductivity. It should be noted that the thermal conductivity of highly electrically conducting polymers is likely to be higher than those of typical

polymers ( $0.1\text{--}0.5\text{ W}/(\text{m K})$  at room temperature) [30] due to the electronic contribution to the thermal conductivity.

There is another doping approach called “secondary” doping, which is different from the “primary” oxidation doping method. In the “secondary” doping method, a high boiling point solvent is used to remove excess insulating materials such as polystyrenesulfonate (PSS) in PEDOT:PSS. It has been shown that the electrical conductivity can be largely increased [31]. This method can also largely affect the TE performance of polymers. Kim et al. reported that the TE performance of PEDOT:PSS can be dramatically increased up to a high-power factor of  $469\text{ }\mu\text{W}/(\text{m K}^2)$  using a postsolvent treatment method (Fig. 2.13.3). PEDOT:PSS typically has a low power factor of  $1\text{--}10\text{ }\mu\text{W}/(\text{m K}^2)$  due to the low Seebeck coefficient caused by the high carrier concentration [32–34]. Hydrophilic solvents such as ethylene glycol (EG) and dimethyl sulfoxide (DMSO) can remove the PSS counterions from the polymer. The reduction in counterions can decrease the carrier concentration and subsequently increase the Seebeck coefficient. On the other hand, the removal of electrically insulating counterions can increase the electrical conductivity of the polymer. Therefore, the power factor can be raised after the treatment of EG and DMSO. The maximum power factor appears at the highest electrical conductivity close to  $\sim 10^3\text{ S/cm}$ , but this would result in nontrivial thermal conduction due to electrons.

On the other hand, a recent paper showed that it is possible for PEDOT to have a maximum power factor in the semiconducting region, although this is still under debate; the values may be influenced by ion transport under a temperature gradient called the Soret effect [35–37]. Bubnova reported that controlling the oxidation level of PEDOT could lead to a maximum power factor of  $324\text{ }\mu\text{W}/(\text{m K}^2)$  at room temperature in 2011 (Fig. 2.13.4) [5]. It was found that the doping level of PEDOT was strongly related to the oxidation level. To optimize the power factor value, PEDOT was exposed to the vapor of the reduction reagent tetrakis(dimethylamino)ethylene (TDAE), converting the oxidized PEDOT into a neutral state. When PEDOT was reduced, the electrical conductivity decreased and the Seebeck coefficient increased.

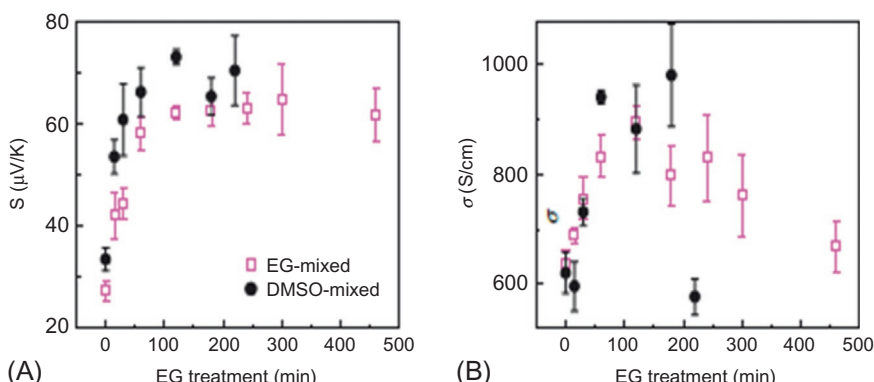


**Fig. 2.13.3** (A) Seebeck coefficient and (B) electrical conductivity of ethylene glycol (EG)-mixed and dimethyl-sulfoxide (DMSO)-mixed PEDOT:PSS measured during the EG treatment process at various dedoping times [6].

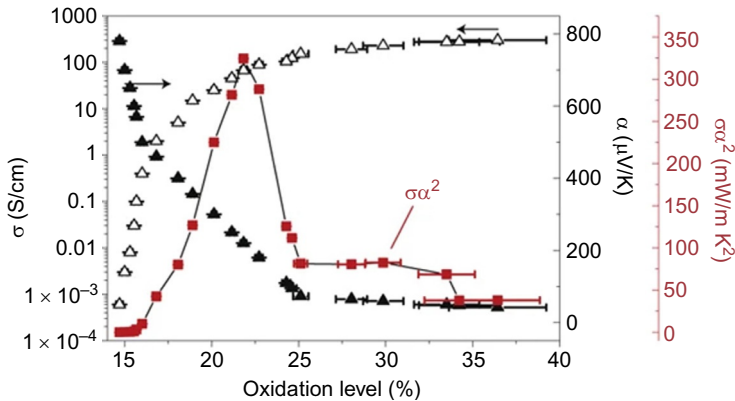


**Fig. 2.13.4** Seebeck coefficient  $\alpha$ , electrical conductivity  $\sigma$ , and corresponding power factor  $\sigma\alpha^2$  versus oxidation level for PEDOT [5].

The highest Seebeck coefficient for PEDOT was  $\sim 800 \mu\text{V}/\text{K}$  at the lowest oxidation level of approximately 15%. The maximum power factor was achieved at an oxidation level of  $\sim 22\%$ , where a relatively high Seebeck coefficient was observed due to the square term in the Seebeck coefficient despite a reduction in electrical conductivity.

### 2.13.3.1.2 Tuning the mobility via optimizing the morphology

The aforementioned doping method often adversely changes the electrical conductivity and the Seebeck coefficient at the same time, but increasing the electronic carrier mobility can raise electrical conductivity without considerably affecting the Seebeck coefficient. This can be qualitatively understood from the following equations [38]:

$$\sigma = \mu n q \quad (2.13.1)$$

$$S = \frac{1}{qT} \frac{\int \mu(E - E_f) E \frac{\partial f_o}{\partial E} D(E) dE}{\int \mu E \frac{\partial f_o}{\partial E} D(E) dE} \quad (2.13.2)$$

where  $\mu$ ,  $n$ ,  $q$ ,  $T$ ,  $E$ ,  $E_f$ ,  $f_o$ , and  $D$  are charge carrier mobility, carrier concentration, carrier charge, absolute temperature, energy, Fermi energy, Fermi-Dirac distribution, and density of states, respectively. Eq. (2.13.1) indicates that electrical conductivity is proportional to carrier mobility. Eq. (2.13.2) shows that carrier mobility minimally affects the Seebeck coefficient since it appears in both the numerator and denominator. Therefore, conducting polymers with high carrier mobility could be promising high-performance thermoelectric materials.

In general, polymers have amorphous structures whose backbones are randomly entangled, causing low carrier mobility. Increasing crystallinity could be a way to improve the mobility. Over the past decades, significant progress in improving carrier mobility has been made, resulting in  $\sim 26 \text{ cm}^2/(\text{Vs})$  [39,40]. While high carrier

mobility has shown enhanced performance in organic field-effect transistors and organic photovoltaics, the TE properties of high carrier mobility polymers have not been reported so far.

### 2.13.3.2 Developing thermoelectric materials based on small molecules

Conducting small molecules could be another group of promising TE materials in addition to conducting polymers. These small molecules are generally organic salts composed of a donor and an acceptor, which are called “organic metals” or “charge transfer compounds.” The most famous organic metal is tetrathiafulvalene-tetracyanoquinodimethane (TTF-TCNQ), which shows a good electrical conductivity of 600 S/cm at room temperature [41]. (Tetrathiatetracene)-triiodide also shows a high electrical conductivity up to 1000 S/cm [42]. In addition to high electrical conductivity, some organic metals such as (BEDT-TTF)Cu<sub>2</sub>Br<sub>4</sub> (BEDT=bis(ethylenedithio) and TTF-Ni(mnt)<sub>2</sub> (mnt=maleonitriledithiolato) show impressive Seebeck coefficients, -850 and -655  $\mu\text{V/K}$ , respectively. Nevertheless, due to the strong adverse relationship between electrical conductivity and the Seebeck coefficient, the power factor for small molecules is less than 100  $\mu\text{W}/(\text{mK}^2)$ . Kiyota et al. studied the TE performance of benzothienobenzothiophene-based organic metals. A series of [1]benzothieno[3,2-*b*][1]benzothiophene (BTBT):XF<sub>6</sub> (X=P, As, Sb, and Ta) was synthesized with a range of electrical conductivities from 640 to 4100 S/cm (Table 2.13.1). The power factors were only 55–88  $\mu\text{W}/(\text{mK}^2)$  due to the low Seebeck coefficients on the order of 10  $\mu\text{V/K}$  [43].

Recently, Huewe et al. demonstrated that organic metal microwires could have high TE performance (Fig. 2.13.5) [44]. P-type TTT<sub>2</sub>I<sub>3</sub> (TTT=tetrathiotetracene) microwire has a high electrical conductivity of  $2.1 \times 10^3$  S/cm and a positive Seebeck coefficient of 42  $\mu\text{V/K}$ . N-type (DMe-DCNQI)<sub>2</sub>Cu (DMe-DCNQI=dimethyl-dicyanoquinonediimine) has a high electrical conductivity of 10<sup>3</sup> S/cm and a negative

**Table 2.13.1** Room temperature conductivity  $\sigma$ , drift mobility  $\mu$ , activation energy Ea, Seebeck coefficient S, and power factor  $S^2\sigma$  of (BTBT)<sub>2</sub>XF<sub>6</sub> (X=P, As, Sb, and Ta) [43].

	PF <sub>6</sub>	AsF <sub>6</sub>	SbF <sub>6</sub>	TaF <sub>6</sub>
$\sigma_{\text{av}}$	1800	2600	1500	640
$\sigma_{\text{max}}$	2200	4100	2000	1700
$\mu_{\text{av}}$	6.9	10.1	6.0	2.6
$\mu_{\text{max}}$	8.4	15.9	7.9	6.8
Ea (K)	57	43	125	18
Ea with Apezon (K)	140	93	131	77
$S_{\text{av}}$ ( $\mu\text{V/K}$ )	15	15	15	15
$S^2\sigma_{\text{av}}$ ( $\mu\text{W}/(\text{mK}^2)$ )	38	55	38	17
$S^2\sigma_{\text{max}}$ ( $\mu\text{W}/(\text{mK}^2)$ )	47	88	48	40

The subscripts av and max indicate average and maximum values, respectively.

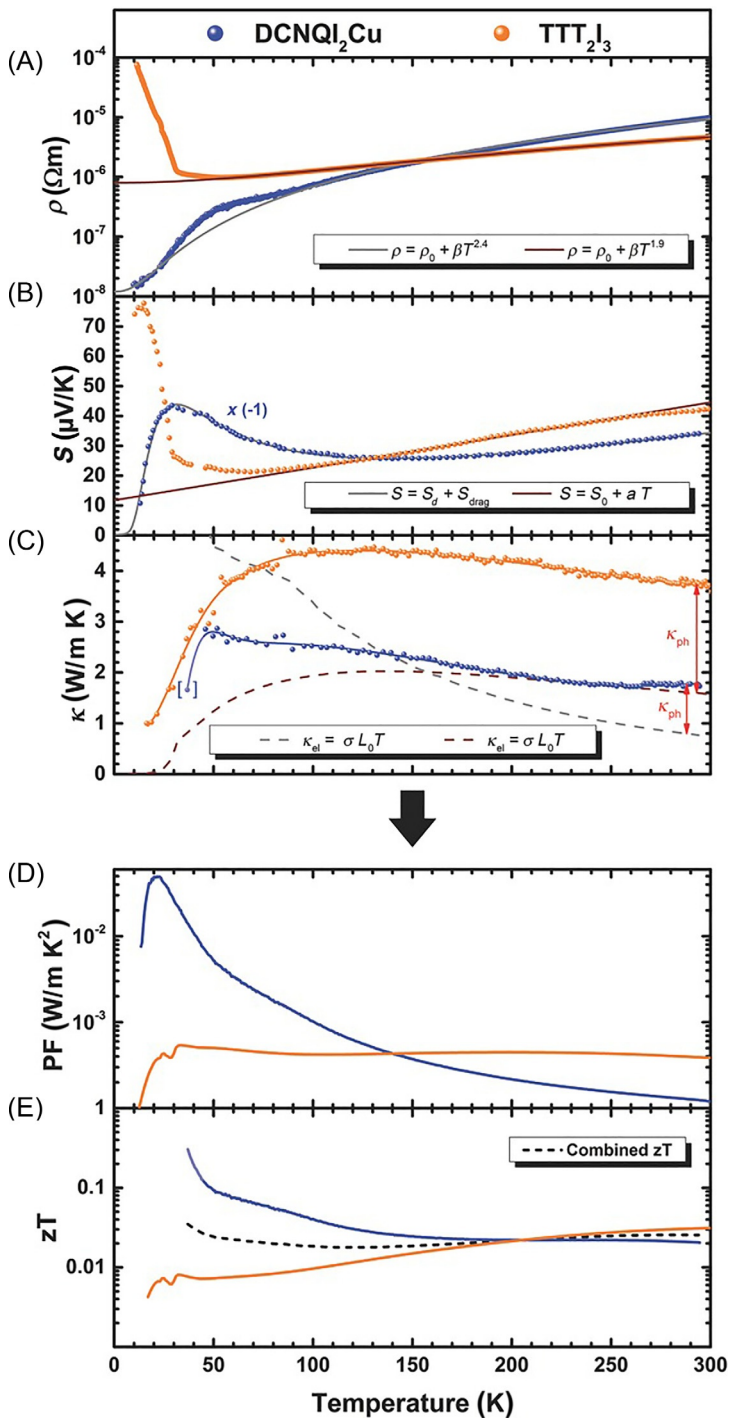


Fig. 2.13.5 See figure legend on next page

Seebeck coefficient of  $-34 \mu\text{V/K}$ . Their thermal conductivities were measured to be 3.7 and  $1.7 \text{ W/(mK)}$  for  $\text{TTT}_2\text{I}_3$  and  $(\text{DMe-DCNQI})_2\text{Cu}$ , respectively. Their power factors were relatively high, 370 and  $115.6 \mu\text{W/(mK}^2)$  for  $\text{TTT}_2\text{I}_3$  and  $(\text{DMe-DCNQI})_2\text{Cu}$ , respectively. The results suggest that organic metals with one-dimensional structures may provide better TE properties.

## 2.13.4 Thermoelectric materials: Polymer nanocomposites

It is difficult to have high electrical conductivity, high Seebeck coefficient, and low thermal conductivity at the same time in a single material due to the adverse relationship among these three key parameters. However, it may be possible to utilize the excellent properties of the individual components with composite structures for better TE performances. For example, the amorphous structures of polymers are advantageous for low thermal conductivity but are often detrimental to carrier mobility, resulting in low electrical conductivity. Here, introducing high carrier mobility components into polymers may bring synergistic effects beyond the general rule of mixtures. More specifically, it is possible to create junctions between polymers and fillers to increase the Seebeck coefficient due to the presence of energy barriers and suppression of thermal conductivity due to mismatch of the vibrational spectra [7,45]. Among the various polymer composites studied, several representative polymer composites are discussed in the following sections.

### 2.13.4.1 Decoupling electrical conductivity and the Seebeck coefficient

The adversely correlated electrical conductivity and Seebeck coefficient prohibit simultaneous improvement in most single materials. However, with composites, such undesirable behaviors can be avoided or alleviated. Wang et al. reported simultaneous enhancement in electrical conductivity and Seebeck coefficient for polyaniline composites, leading to a high-power factor of  $\sim 220 \mu\text{W/(mK}^2)$  (Fig. 2.13.6) [46].

---

**Fig. 2.13.5, cont'd** Thermoelectric properties of  $\text{TTT}_2\text{I}_3$  (p-type) and  $\text{DCNQI}_2\text{Cu}$  (n-type) crystals. (A) The temperature dependence of the electrical resistivity  $\rho = \rho_0 + \beta T\gamma$ , with  $\gamma > 1$ , for both materials, is typical for low-dimensional organic metals. (B) Absolute values of the Seebeck coefficient  $S$ . The linear fit in the metallic regime of  $\text{TTT}_2\text{I}_3$  yields a bandwidth of 632 meV. In the case of  $\text{DCNQI}_2\text{Cu}$ , an additional contribution of the phonon drag is considered, resulting in  $W_{\text{DCNQI}_2\text{Cu}} = 333 \text{ meV}$ . (C) Temperature dependence of the thermal conductivity  $\kappa$ , determined by means of  $3\omega$ -measurements. In addition, the electronic thermal conductivity  $\kappa_{\text{el}}$ , as calculated by the Wiedemann Franz law, is shown. The phonon contributions  $k_{\text{ph}}$  at room temperature for  $\text{TTT}_2\text{I}_3$  and  $\text{DCNQI}_2\text{Cu}$  are roughly estimated to be 2.1 and  $1 \text{ W/(mK)}$ , respectively. The quantities  $\rho$ ,  $S$ , and  $\kappa$ , all of which were measured on the same respective specimen, result in (D) the power factor  $S^2/\rho$  and (E) the dimensionless figure of merit  $zT$  [44].

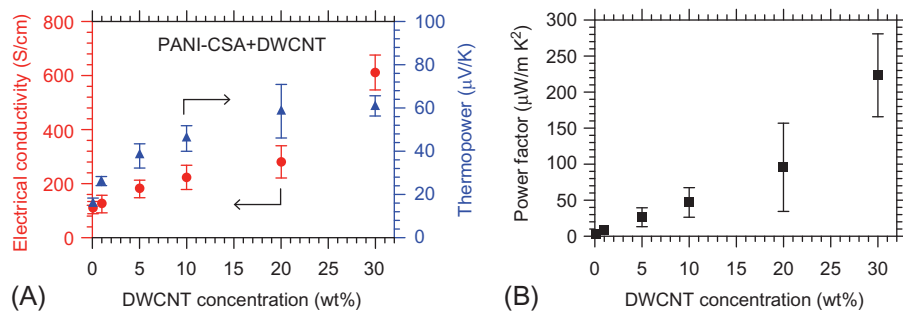


**Fig. 2.13.6** (A) Electrical conductivity and Seebeck coefficient of PANI-CSA composites. (B) The corresponding power factor for PANI-CSA composite [46].

Polyaniline doped with camphorsulfonic acid (PANI-CSA) has a low carrier mobility of  $\sim 0.15 \text{ cm}^2/(\text{Vs})$  and a high carrier concentration of  $\sim 2.1 \times 10^{21} \text{ cm}^{-3}$ . With the addition of CNTs, the carrier mobility was increased up to  $\sim 7.3 \text{ cm}^2/(\text{Vs})$ , and the carrier concentration decreased to  $\sim 5.6 \times 10^{20} \text{ cm}^{-3}$ . The large increase in the carrier mobility raised the electrical conductivity of the composite. Additionally, the reduction in the carrier concentration increased the Seebeck coefficient. The electrical conductivity of the optimized composite was  $\sim 610 \text{ S/cm}$  with a Seebeck coefficient of  $\sim 61 \mu\text{V/K}$ . This approach can be widely used for developing other high-performance polymer composites.

#### 2.13.4.2 Decoupling electrical conductivity and thermal conductivity

Thermal conductivity has two distinct contributions from electronic carriers (typically called electronic thermal conductivity) and atom vibrations (typically called lattice thermal conductivity). When the electrical conductivity is lower than  $1 \text{ S/cm}$ , the thermal conductivity from the electronic part is trivial according to the Wiedemann-Franz law [47]. Most traditional organic materials have low electrical conductivity, and their thermal conductivity values are typically in the range of  $0.1\text{--}0.5 \text{ W/(m K)}$  [30]. However, recently reported conducting polymers exhibit high electrical conductivities over  $100 \text{ S/cm}$ . In this case, the electronic thermal conductivity could be comparable to that of the lattice part, so the electronic part should be taken into consideration [48,49].

In another example, Wang et al. used a nonpercolated CNT network to create polymer composites (Fig. 2.13.7) [7]. Electrons may pass through CNT-polymer-CNT junctions by hopping, while vibron/phonon transport could be suppressed due to the mismatch in the vibrational spectra. Then, an extremely high power factor over  $1000 \mu\text{W}/(\text{m K}^2)$  was obtained. With a low thermal conductivity of  $\sim 0.6 \text{ W}/(\text{m K})$ , a strikingly high ZT of 0.5 for fully organic materials was observed at room temperature. This strategy could be extended to other polymer composites to achieve high TE performance.

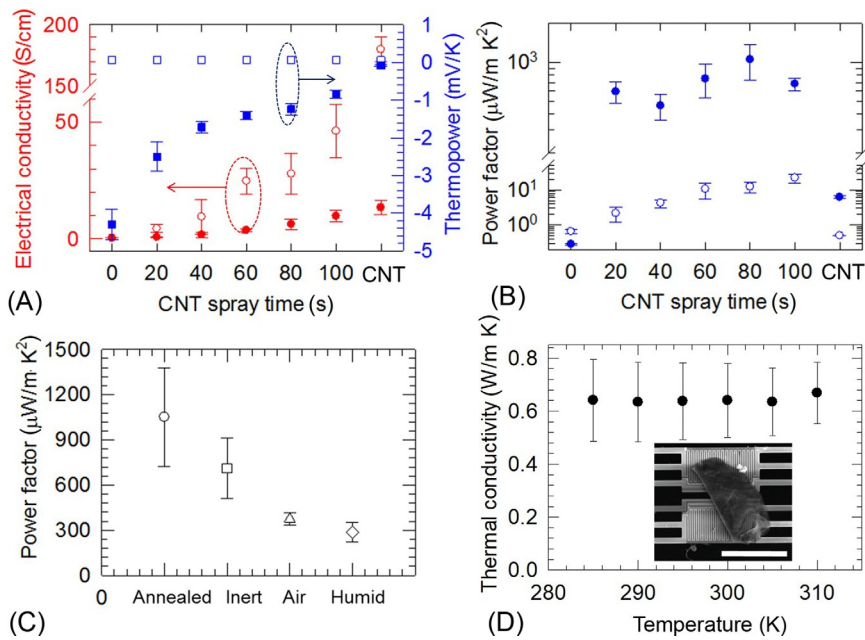


**Fig. 2.13.7** Characterization of electrical properties before and after TDAE treatment of CNT/PEDOT hybrids. (A) Electrical conductivity and Seebeck coefficient (or thermopower). (B) The corresponding power factor of CNT/PEDOT hybrids with 4.5%, 6.1%, 7.9%, 10.7%, and 15.8% CNT coverage. (C) Power factor when the hybrids (10.7% CNT) were annealed after TDAE treatment and measured in air (“annealed”; typical sample preparation method in this study); when they were measured in Ar (“inert”), air (“air”), and  $\text{H}_2\text{O}$ -saturated Ar (“humid”) environments with the annealing process. (D) Thermal conductivity of the hybrid near room temperature. A representative scanning electron microscope image of the hybrid bridged between two suspended membranes in a microdevice. The scale bar indicates  $30 \mu\text{m}$  [7].

### 2.13.4.3 Optimizing composite structures for high TE performances

Inorganic 1D nanomaterials often exhibit relatively higher TE performances than their bulk counterparts, so there have been various attempts to introduce high-performance nanowires/nanorods into polymer matrices. Kevin et al. reported the TE properties of core-shell structure hybrids with tellurium nanowires/nanorods as the core and PEDOT:PSS as the shell [50]. The ZT value of the composite was as high as 0.1 at room temperature. Here, the Seebeck coefficient has been raised, leading to a power factor of  $\sim 70 \mu\text{W}/(\text{m K}^2)$  while maintaining the polymer-like low thermal conductivity ( $\sim 0.2 \text{ W}/(\text{m K})$ ). This could be attributed to the Te nanorods encapsulated by PEDOT:PSS (Fig. 2.13.8), having polymer junctions impeding phonon propagation.

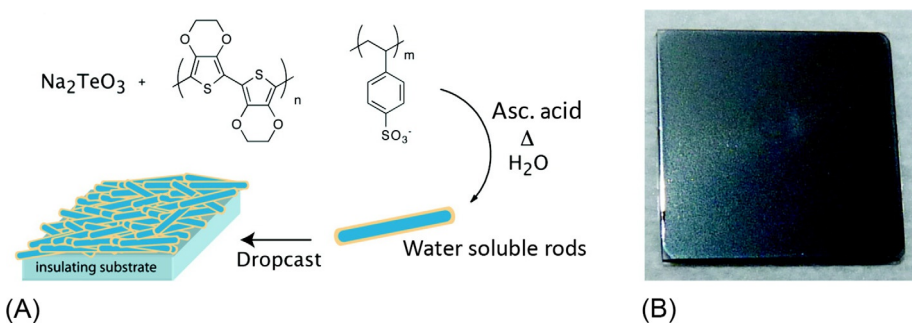


**Fig. 2.13.8** (A) Synthesis of PEDOT:PSS passivated Te nanorods, followed by the formation of smooth nanocomposite films during solution casting. (B) Picture of a typical drop-cast composite film on a quartz substrate, illustrating good film uniformity [50].

More systematic studies about the effects of such junctions have been reported in Hsu and Yu's work [45]. Here, PEDOT:PSS was placed between two CNT films in series so that electrons were transported through CNT-PEDOT:PSS-CNT junctions (Fig. 2.13.9). Then, the Fermi level of PEDOT:PSS was modulated by the gate bias voltage in an organic electrochemical transistor (OECT) configuration.

A series of experiments determined the key information about the electronic bands, such as HOMO, LUMO, and the Fermi level, which were determined by cyclic voltammetry (CV) measurements, ultraviolet photoelectron spectroscopy (UPS), and Kelvin probe force microscopy (KPFM) for single wall CNT (SWCNT), double wall CNT (DWCNT), multiwall CNT (MWCNT), and PEDOT:PSS (Fig. 2.13.10A). Then, band diagrams with band bending were constructed (Fig. 2.13.10B and C). It was found that the energy barrier created by PEDOT:PSS for hole carriers raised the Seebeck coefficient, remarkably increasing the power factor up to  $\sim 1.3 \times 10^3 \mu\text{W}/(\text{m K}^2)$ , which is an  $\sim 460\%$  improvement compared with that of the pristine CNT and is comparable to that of inorganic counterparts, despite reductions in the electrical conductivity due to the barriers.

## 2.13.5 Organic thermoelectric devices

Organic materials are often easier to use to make devices than inorganic counterparts because they can be readily cut into desired shapes and electrically connected. In addition, it is feasible to use 2D and 3D printing techniques. Mechanical flexibility is another large advantage that provides variability in processing, such as roll-to-roll (R2R) printing and deformation, for improving thermal contacts on nonflat surfaces.

Kim et al. synthesized n-type CNT films with polyethylenimine (PEI), diethylenetriamine (DETA), and  $\text{NaBH}_4$  in addition to p-type CNT films using a simple vacuum filtration method with aqueous CNT solutions [51]. CNTs exposed to air have p-type characteristics due to oxygen doping [52]. These films were easily cut with

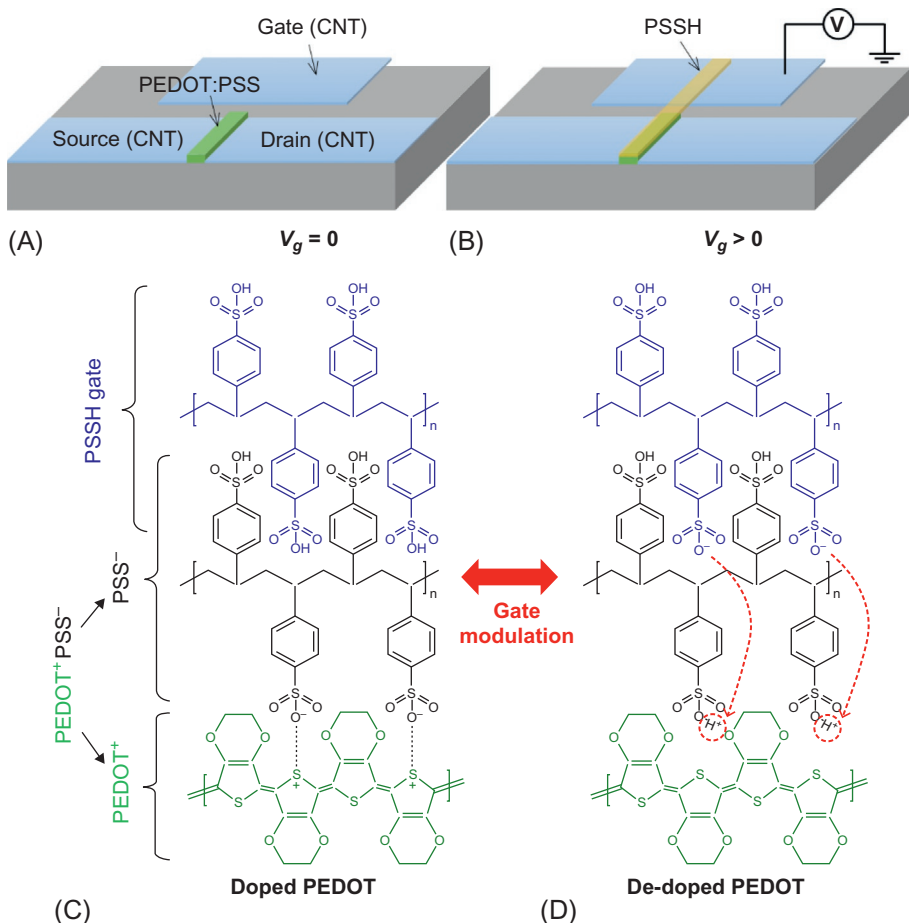


**Fig. 2.13.9** The OECT fabrication process (not to scale): (A) source, drain, and gate electrodes made of CNTs, and the PEDOT:PSS channel connecting the source and drain; (B) PSSH gate for bias voltage modulation. The substrate is orders of magnitude thicker than the CNTs and PEDOT:PSS films so that the temperature profile is linear along the source-to-drain direction when the thermopower was measured. Illustrations showing the PEDOT:PSS channel with the PSSH gate when the gate bias ( $V_g$ ) was (C) 0 V and (D) greater than 0 V [45].

razor blades, and 72 p-type and 72 n-type CNT films were alternatively connected in series and assembled in a thermally parallel direction (Fig. 2.13.11). This device generated a large voltage of  $\sim 0.5$  V at a temperature difference of 49 K and operated a glucose sensor with  $\sim 1.8 \mu\text{W}$  at a temperature difference of 32 K.

Wei et al. [53] screen-printed p-type PEDOT:PSS on flexible substrates and obtained a maximum output power of  $50 \mu\text{W}$  at a temperature difference of 100 K with thermal stability in air. Fang et al. [54] used a roll-to-roll method to fabricate TE modules with more than 100 legs of p-type PEDOT:PSS and n-type nickel (Fig. 2.13.12).

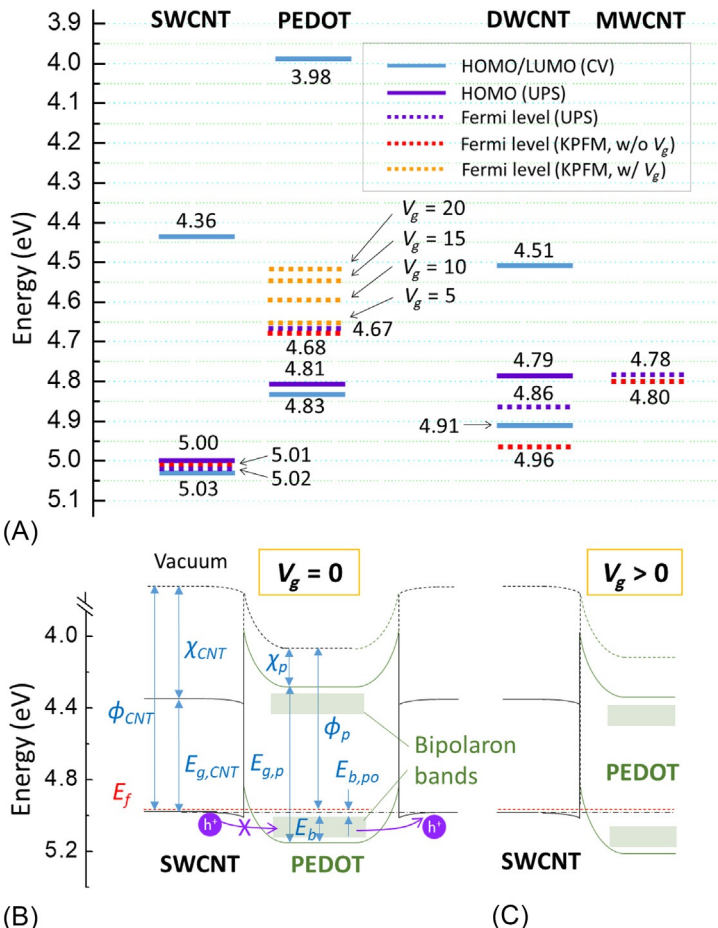


**Fig. 2.13.10** (A) HOMO, LUMO, and Fermi levels of PEDOT:PSS, SWCNT, DWCNT, and MWCNT determined by CV, UPS, and KPFM. The Fermi levels of PEDOT:PSS were measured when the gate voltage of the OECT was varied from 0 to 5, 10, 15, and 20 V. (B) The band diagram of the SWCNT-PEDOT:PSS-SWCNT junction without a gate voltage. Bipolaron bands are indicated by the shaded areas. It is expected that hole transport from the SWCNT to PEDOT is suppressed while holes could be injected from PEDOT to SWCNT. (C) The band diagram when  $V_g > 0$  V [45].

The assembled thermoelectric generator with 288 legs produced an output voltage of 0.26 V and an output power of 46  $\mu$ W at a temperature difference of 50 K.

Inorganic TE materials have been used together with polymers to utilize the benefits of organic TE materials, such as mechanical flexibility and easy module fabrication. Cai et al. [55] developed a power generator with 8 legs of PEDOT:PSS/polymer-functionalized (PF)-Te composite films on a polyimide flexible substrate. With a temperature difference between the forearm (305 K) and ambient air (292 K), the maximum output voltage was measured to be 13.4 mV. Li et al. [56] used

**Fig. 2.13.11** (A) Assembly process of p- and n-type carbon nanotube films. (B) One module (stack) consists of nine p-type and nine n-type films. (C) The module was bound by a Polytetrafluoroethylene (PTFE) tape. (D) A device design that maximizes the thermoelectric voltage generation for a given temperature gradient, and (E) a completed thermoelectric device consists of 144 films (72 p-type and 72 n-type) [51].

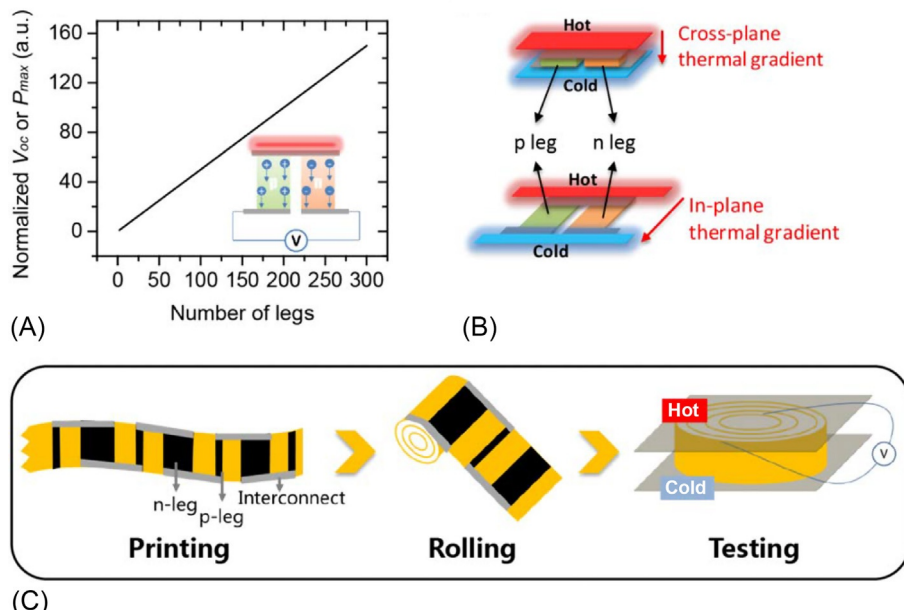
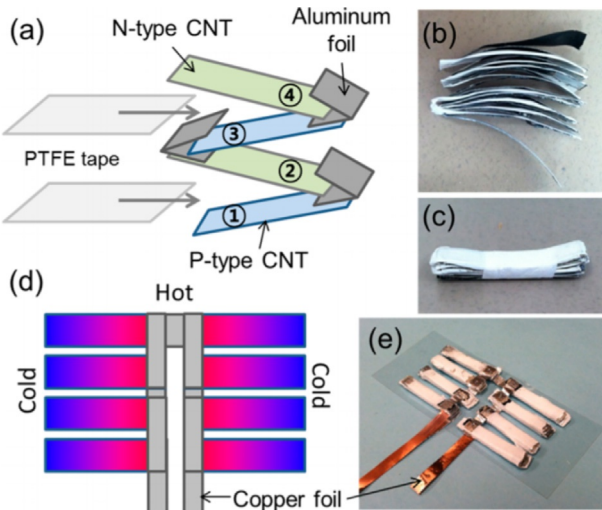


**Fig. 2.13.12** The rolled module design realizes large-scale fabrication of thermoelectric modules utilizing an in-plane thermal gradient. (A) Calculated  $V_{oc}$  (or  $P_{max}$ ) as a function of the number of legs. The maximum power from a thermoelectric module increases linearly with the number of p and n legs, which shows that the scalability of the fabrication methods is important. Solution-processable organic thermoelectric materials make it possible to use printing to fabricate thermoelectric modules on an industrial scale. The thickness of the printed films ranges from nanometers to millimeters, which make it difficult to maintain a significant temperature gradient along the cross-plane direction. Thus, an in-plane thermal gradient is more appropriate for printed modules, as shown in (B). Herein, we demonstrate a rolled module design as shown in (C). The thermoelectric materials were printed on a flexible substrate that was rolled into a compact cylinder. An axial thermal gradient is applied to generate a thermoelectric voltage [54].

PEDOT:PSS-based composite films as p-type legs and  $\text{Bi}_2\text{Te}_3$  film as n-type legs for constructing a thermoelectric device, generating an output power density of  $32 \mu\text{W cm}^{-2}$  and an output voltage of  $56 \text{ mV}$  at a temperature difference of  $60 \text{ K}$ . Wang et al. [57] used 10 legs with the optimized thermoelectric performance of the PEDOT:PSS/SiC-nanowire composite films to fabricate a thermoelectric generator with a maximum output power of  $927 \text{ nW}$  at a temperature difference of  $100 \text{ K}$ . Kang et al. [58] fabricated a TE generator consisting of 32 legs with PEDOT:PSS and tellurium-PEDOT:PSS hybrid composites, which were arranged in two rows to enhance the output power. There have been quite a few papers reporting the fabrication of organic TE modules, but other device aspects, such as device operation with the generated power, optimum circuit, and module design for flexible organic materials, and heat transfer analysis with less thermally conducting organic materials, have rarely been studied.

## 2.13.6 Summary

In this section, recent research achievements in organic TE research and related fundamental theory have been discussed. Despite the relatively short time period and efforts devoted to the organic TE area, significant progress has been made with TE performances gradually approaching those of inorganic TE materials. In 2008, the Yu research group reported a series of insightful works on polymer composites, which opened up the organic TE field [11,12,46,51,52,59]. They reported decoupling of electrical conductivity, the Seebeck coefficient, and thermal conductivity and developed organic TE modules with both p- and n-type materials. In 2011, the Crispin group showed a large improvement in the Seebeck coefficient of a representative conducting polymer, PEDOT, by tuning its oxidation level [5]. Later, Kim et al. reported that a solvent posttreatment method could be promising for improving the power factor [6]. Organic materials typically exhibit p-type behavior, so a significant improvement in the relatively inferior TE performances of n-type TE materials was necessary. In 2015, Wang et al. reported a record high thermoelectric performance with n-type PEDOT/CNT composites with a ZT value of 0.5 at room temperature, approaching that of inorganic materials [7]. The rapid development of this young research field suggests great potential for organic TE materials in converting heat to electricity or vice versa. The unique properties of organic materials compared with inorganic materials, such as mechanical flexibility, easy processing, and lightweight, make them suitable for wearable or disposable applications, such as continuous power supply for health monitoring devices and patch sensors on skin.

## References

- [1] H. Wang, C. Yu, Joule 3 (2019) 53–80.
- [2] L.-D. Zhao, S.-H. Lo, Y. Zhang, H. Sun, G. Tan, C. Uher, C. Wolverton, V.P. Dravid, M.G. Kanatzidis, Nature 508 (2014) 373.
- [3] W.M. Yim, F.D. Rosi, Solid State Electron. 15 (1972) 1121–1140.

- [4] M. Zebarjadi, K. Esfarjani, M.S. Dresselhaus, Z.F. Ren, G. Chen, *Energy Environ. Sci.* 5 (2012) 5147–5162.
- [5] O. Bubnova, Z.U. Khan, A. Malti, S. Braun, M. Fahlman, M. Berggren, X. Crispin, *Nat. Mater.* 10 (2011) 429–433.
- [6] G.H. Kim, L. Shao, K. Zhang, K.P. Pipe, *Nat. Mater.* 12 (2013) 719–723.
- [7] H. Wang, J.-H. Hsu, S.-I. Yi, S.L. Kim, K. Choi, G. Yang, C. Yu, *Adv. Mater.* 27 (2015) 6855–6861.
- [8] R. Noriega, J. Rivnay, K. Vandewal, F.P.V. Koch, N. Stingelin, P. Smith, M.F. Toney, A. Salleo, *Nat. Mater.* 12 (2013) 1038.
- [9] A.M. Glaudell, J.E. Cochran, S.N. Patel, M.L. Chabiny, *Adv. Energy Mater.* 5 (2015) 1401072.
- [10] S.D. Kang, G.J. Snyder, *Nat. Mater.* 16 (2017) 252.
- [11] C. Yu, Y.S. Kim, D. Kim, J.C. Grunlan, *Nano Lett.* 8 (2008) 4428–4432.
- [12] D. Kim, Y. Kim, K. Choi, J.C. Grunlan, C. Yu, *ACS Nano* 4 (2010) 513–523.
- [13] Q. Zhang, Y. Sun, W. Xu, D. Zhu, *Energy Environ. Sci.* 5 (2012) 9639–9644.
- [14] T.O. Poehler, H.E. Katz, *Energy Environ. Sci.* 5 (2012) 8110–8115.
- [15] O. Bubnova, X. Crispin, *Energy Environ. Sci.* 5 (2012) 9345–9362.
- [16] T.E. Whall, *J. Phys. C Solid State Phys.* 14 (1981) L887.
- [17] M. Cutler, N.F. Mott, *Phys. Rev.* 181 (1969) 1336–1340.
- [18] A.L. Efros, B.I. Shklovskii, *J. Phys. C Solid State Phys.* 8 (1975) L49.
- [19] C.O. Yoon, R.M.D. Moses, A.J. Heeger, *Phys. Rev. B* 49 (1994) 10851–10863.
- [20] H. Shirakawa, *Angew. Chem. Int. Ed.* 40 (2001) 2574–2580.
- [21] A.J. Heeger, *J. Phys. Chem. B* 105 (2001) 8475–8491.
- [22] A.G. MacDiarmid, *Angew. Chem. Int. Ed.* 40 (2001) 2581–2590.
- [23] A.B. Kaiser, *Rep. Prog. Phys.* 64 (2001) 1.
- [24] Y. Du, S.Z. Shen, K. Cai, P.S. Casey, *Prog. Polym. Sci.* 37 (2012) 820–841.
- [25] A. Shakouri, L. Suquan, *Thermoelectrics*, 1999. Eighteenth International Conference on Thermoelectrics, 1999, pp. 402–406.
- [26] Y.W. Park, *Synth. Met.* 45 (1991) 173–182.
- [27] H. Wang, L. Yin, X. Pu, C. Yu, *Polymer* 54 (2013) 1136–1140.
- [28] J.C.W. Chien, J.M. Warakomski, F.E. Karasz, W.L. Chia, C.P. Lillya, *Phys. Rev. B* 28 (1983) 6937–6952.
- [29] T. Park, C. Park, B. Kim, H. Shin, E. Kim, *Energy Environ. Sci.* 6 (2013) 788–792.
- [30] C. Huang, X. Qian, R. Yang, *Mater. Sci. Eng. R. Rep.* 132 (2018) 1–22.
- [31] Y. Cao, J. Qiu, P. Smith, *Synth. Met.* 69 (1995) 187–190.
- [32] C. Liu, B. Lu, J. Yan, J. Xu, R. Yue, Z. Zhu, S. Zhou, X. Hu, Z. Zhang, P. Chen, *Synth. Met.* 160 (2010) 2481–2485.
- [33] B. Zhang, J. Sun, H.E. Katz, F. Fang, R.L. Opila, *ACS Appl. Mater. Interfaces* 2 (2010) 3170–3178.
- [34] R. Yue, J. Xu, *Synth. Met.* 162 (2012) 912–917.
- [35] K. Choi, S.L. Kim, S.-i. Yi, J.-H. Hsu, C. Yu, *ACS Appl. Mater. Interfaces* 10 (2018) 23891–23899.
- [36] S.L. Kim, J.-H. Hsu, C. Yu, *Org. Electron.* 54 (2018) 231–236.
- [37] S.L. Kim, H.T. Lin, C. Yu, *Adv. Energy Mater.* 6 (2016) 1600546.
- [38] S.-i. Yi, C. Yu, *J. Appl. Phys.* 117 (2015) 035105.
- [39] H. Luo, C. Yu, Z. Liu, G. Zhang, H. Geng, Y. Yi, K. Broch, Y. Hu, A. Sadhanala, L. Jiang, P. Qi, Z. Cai, H. Sirringhaus, D. Zhang, *Sci. Adv.* 2 (2016) e1600076.
- [40] Y. Li, P. Sonar, L. Murphy, W. Hong, *Energy Environ. Sci.* 6 (2013) 1684–1710.

- [41] L.B. Coleman, M.J. Cohen, D.J. Sandman, F.G. Yamagishi, A.F. Garito, A.J. Heeger, *Solid State Commun.* 12 (1973) 1125–1132.
- [42] L.C. Isett, *Phys. Rev. B* 18 (1978) 439–447.
- [43] Y. Kiyota, T. Kadoya, K. Yamamoto, K. Iijima, T. Higashino, T. Kawamoto, K. Takimiya, T. Mori, *J. Am. Chem. Soc.* 138 (2016) 3920–3925.
- [44] F. Huewe, A. Steeger, K. Kostova, L. Burroughs, I. Bauer, P. Strohriegl, V. Dimitrov, S. Woodward, J. Pflaum, *Adv. Mater.* 29 (2017) 1605682.
- [45] J.-H. Hsu, C. Yu, *Nano Energy* 67 (2019) 104282.
- [46] H. Wang, S.-i. Yi, X. Pu, C. Yu, *ACS Appl. Mater. Interfaces* 7 (2015) 9589–9597.
- [47] R. Franz, G. Wiedemann, *Ann. Phys.* 15 (1853) 497–531.
- [48] J. Liu, X. Wang, D. Li, N.E. Coates, R.A. Segalman, D.G. Cahill, *Macromolecules* 48 (2015) 585–591.
- [49] A. Weathers, Z.U. Khan, R. Brooke, D. Evans, M.T. Pettes, J.W. Andreasen, A. Crispin, L. Shi, *Adv. Mater.* 27 (2015) 2101–2106.
- [50] K.C. See, J.P. Feser, C.E. Chen, A. Majumdar, J.J. Urban, R.A. Segalman, *Nano Lett.* 10 (2010) 4664–4667.
- [51] S.L. Kim, K. Choi, A. Tazebay, C. Yu, *ACS Nano* 8 (2014) 2377–2386.
- [52] C. Yu, A. Murali, K. Choi, Y. Ryu, *Energy Environ. Sci.* 5 (2012) 9481–9486.
- [53] Q. Wei, M. Mukaida, K. Kirihara, Y. Naitoh, T. Ishida, *RSC Adv.* 4 (2014) 28802–28806.
- [54] H. Fang, B.C. Popere, E.M. Thomas, C.-K. Mai, W.B. Chang, G.C. Bazan, M.L. Chabiny, R.A. Segalman, *J. Appl. Polym. Sci.* 134 (2016) 44208.
- [55] H. Song, K. Cai, *Energy* 125 (2017) 519–525.
- [56] C. Li, F. Jiang, C. Liu, W. Wang, X. Li, T. Wang, J. Xu, *Chem. Eng. J.* 320 (2017) 201–210.
- [57] X. Wang, F. Meng, T. Wang, C. Li, H. Tang, Z. Gao, S. Li, F. Jiang, J. Xu, *J. Alloys Compd.* 734 (2018) 121–129.
- [58] E.J. Bae, Y.H. Kang, K.S. Jang, S.Y. Cho, *Sci. Rep.* 6 (2016) 18805.
- [59] C. Yu, K. Choi, L. Yin, J.C. Grunlan, *ACS Nano* 5 (2011) 7885–7892.

# Thermoelectric materials and devices based on carbon nanotubes

2.14

*Yoshiyuki Nonoguchi*

Division of Materials Science, Nara Institute of Science and Technology, Ikoma, Japan

## 2.14.1 Introduction

In recent years, carbon nanotubes (CNT), especially single-walled carbon nanotubes (SWCNTs), have been recognized as candidates for new thermoelectric conversion materials. As a result of several breakthroughs such as high-quality raw materials and advanced structural control, the figure of merit  $zT$  of the SWCNT film near room temperature improved to about 0.1. This trend is also closely related to the influx of researchers following the recent energy harvesting boom toward the Internet of things (IoT). Thermal and thermoelectric properties of a single CNT were studied in the early 2000s, and a huge power factor and thermal conductivity were reported [1–3]. There may have been a possibility to improve the performance of thermoelectric materials by various measures, but it has been a long dawn before the CNT regains attention as a thermoelectric material. Since 2008, the number of papers on “carbon nanotubes” and “thermoelectric” seen in the Web of Science (as of February 28, 2020) has been increasing steadily, and the power factor has improved more than 100-fold in the past 10 years (Fig. 2.14.1). This fact is related to the fact that CNT manufacturing technology has been evolving rapidly in addition to new process technologies such as doping and orientation, and the performance as a material has been updated accordingly. Therefore, regarding “Enhanced Thermoelectric Properties,” which tends to be the title of the paper, it is necessary to distinguish between understanding of essential physics and materials chemistry and improving raw material quality. However, this is not always obvious. In this chapter, the characteristics of SWCNTs as thermoelectric conversion materials and recent research trends are summarized. The essential attractiveness and issues of the thermoelectric materials are discussed.

## 2.14.2 SWCNTs as thermoelectric materials

Here, we consider the characteristics of SWCNT by comparing it with various materials. As is widely known, bismuth telluride is highly promising from the viewpoint of thermoelectric properties near room temperature. When the authors started research around 2011, the thermoelectric power factor of the available SWCNT sheet

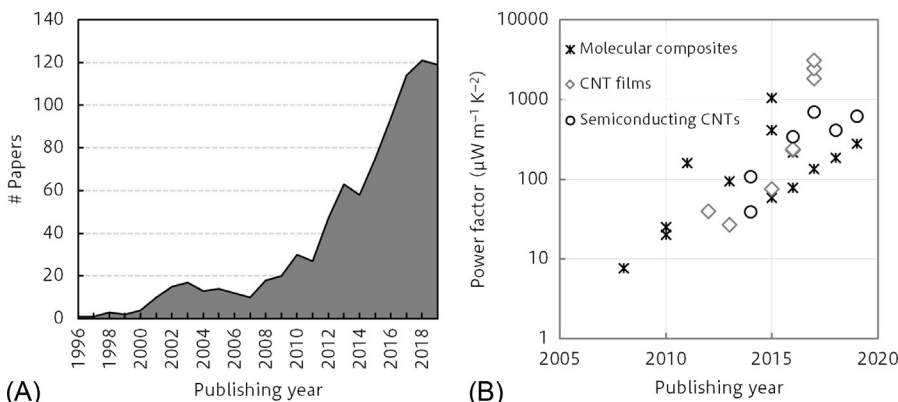


**Fig. 2.14.1** Changes in the number of related papers (A) and the power factor (B) in typical literature in recent years (February 28, 2020) [4–28].

(buckypaper) measured with PPMS (Quantum Design), was approximately  $10\text{ }\mu\text{W m}^{-1}\text{ K}^{-2}$ . The figure of merit  $zT$  near room temperature was then about  $10^{-4}$ . Currently, SWCNT sheets from Meijo Nanocarbon and OCSiAl distributed in Japan seem to have much better performance as high as  $zT$  up to 0.1. This progress seems to originate from the fact that the length and crystallinity of the nanotube were greatly improved at a single-nanotube level due to the progress of manufacturing technology, leading to a dramatic increase in conductivity. In fact, the thermoelectric properties of SWCNT sheets vary significantly depending on the SWCNT manufacturing and processing methods. In recent years, the field of materials chemistry has reported relatively excellent thermoelectric properties of SWCNT films in which functional dyes and the like are combined. Many examples mentioned the exotic effects such as energy filtering as the origin of the modulation, but many do not have basic verification such as carrier doping or morphology control, and the readership requires careful reading.

Initially, the motivation to use SWCNTs seemed to be in structural properties rather than performance. The superiority of SWCNTs has been proposed from the process point of view, such as the use of ink, but recently, high-quality ink processes have become possible even with inorganic semiconductors [29,30]. The density of SWCNT sheets and polymer composites is about  $0.5\text{--}2\text{ g cm}^{-3}$ . This is much lighter than ordinary semiconductor materials, which is an advantage. SWCNT is also widely considered as a component of flexible and stretchable electronics due to its structural flexibility. What is important in practical use is the flexibility of processing. Regarding the elasticity of the module, it is possible to use not only the softness of materials but also the structure of the origami/kirigami substrates [31].

Although the asbestos-like health hazards related to SWCNTs have been pointed out due to their fiber shape, the elements themselves are safe. An advantage in elemental strategy is that the SWCNT materials do not rely on rare elements. Recently,

safety-related purification technologies such as complete decomposition with hypochlorite have been developed [32].

### 2.14.3 Structure-property relationship

In order to study the essential physics, materials of uniform shape and orientation are required. In this regard, the thermoelectric transport of a single CNT is still under investigation, even though the network film shows moderate thermoelectric properties. Unlike common semiconductor materials, SWCNT films have complex, intertwined, nonuniform inhomogeneous network structures from a microscopic point of view (Fig. 2.14.2). It is also known that the electronic structure changes depending on how the graphene sheets are tailored into tubes (chirality). Depending on the presence or absence of the bandgap, it is roughly classified into metallic and semiconducting. In 2014, Maniwa et al. (Tokyo Metropolitan University) reported the power factor of high-purity semiconducting and metallic SWCNT films [24]. At this point, it was emphasized that (1) a larger power factor was observed in the semiconducting SWCNT film than in the metallic one, and (2) that the large Seebeck effect was caused by the contact between the semiconducting nanotubes. However, in 2018, it was reported that using a globally oriented SWCNT film, the Seebeck coefficient did not depend on the orientation angle, that is, the number of contacts [33]. The authors have recently mentioned that dispersants such as polymers remain in the SWCNT sheet, and affect the chemical doping (Fig. 2.14.3) [28]. This is important to use semiconducting SWCNTs as a practical sheet material. Given that electrical conductivity and thermal conductivity depend greatly on the number of contacts, an essential and systematic understanding of the thermoelectric properties of the film is expected. In addition, the effects of primary structures such as diameter distribution and defect density, and secondary structures such as entanglement and bundling, which are issues related to SWCNT, on thermoelectric properties are limited to fragmentary reports.

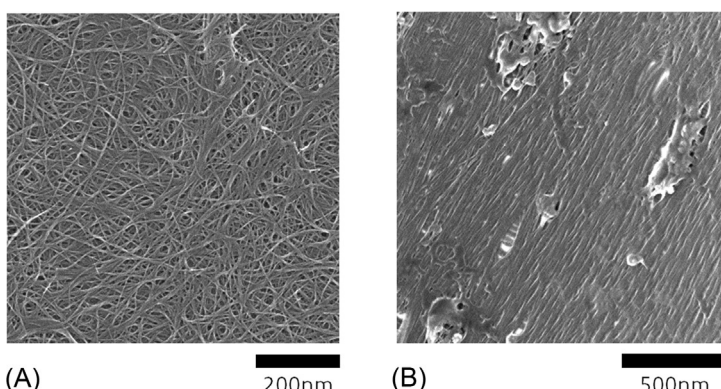


**Fig. 2.14.2** Scanning electron microscope images of (A) spaghetti-like and (B) highly oriented SWCNT films.

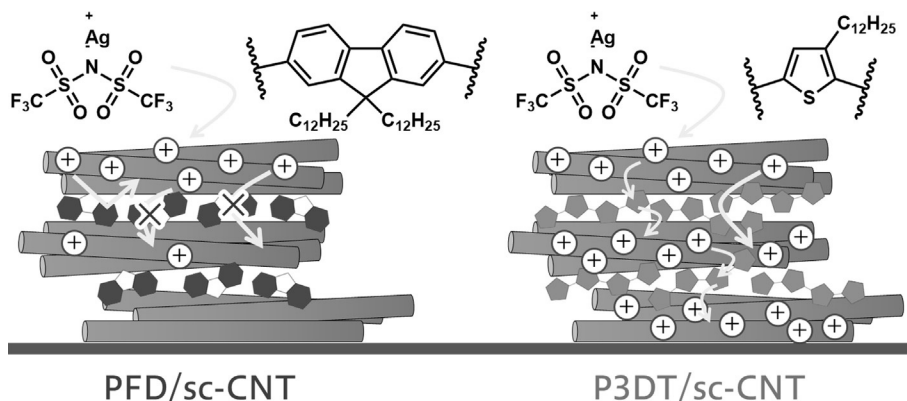


**Fig. 2.14.3** A schematic representation of dispersant effects on the uniformity of chemical doping to semiconducting SWCNT sheets.

## 2.14.4 Doping

Since thermoelectric properties are shown as a function of the Fermi level, precise carrier doping is inevitable. When using SWCNTs as a thermoelectric conversion material, a stable doping state must be created. Untreated SWCNTs are slightly oxidized by atmospheric oxygen and exhibit p-type transport. However, high-efficiency thermoelectric conversion modules are generally composed of a so-called  $\pi$ -type structure, so that both p-type and n-type substances are connected as series circuits. In this context, there is no doubt that reliable doping is necessary for thermoelectric research. At present, reliable carrier doping by elemental substitution has not been established in bulk synthesis, and electron transfer by the adsorption of redox molecules is used as a driving force for carrier injection in SWCNT electronic device applications. Metal-type electronic SWCNTs with no energy gap can easily become both p-type or n-type in the presence of electron acceptors and donors [34]. Oxidative doping with protic acids or reductive doping with hydride/hydrogen radicals is often used, but in most cases, no side reaction such as protonation is mentioned. In addition, the stability of semiconductor-type SWCNTs with a gap upon doping has not yet been systematically revealed. Particularly, n-type semiconducting SWCNTs having radical anionic properties are considered to be very sensitive to oxygen, and their stabilization would be a challenge. Polyethyleneimine, which is known as a strong base, has long been used as an n-type dopant for material applications [35]. From the viewpoint of electron transfer chemistry, the doping efficiency seems to be low and it is likely difficult to examine the structure correlation. In 2009, Lee et al. reported using reduced benzyl viologen, which acts as a two-electron reducing agent, enabling highly efficient n-type doping [36]. In 2010, Bao et al. (Stanford University) have reported the highly efficient n-type doping of fullerenes and SWCNTs using the dissociation of hydrides or hydrogen radicals from the dihydroimidazole skeleton [37]. Fujigaya et al. (Kyushu University) systematically studied the thermoelectric properties of n-type SWCNTs using this, and found the conditions for producing stable n-type nanotubes [38].

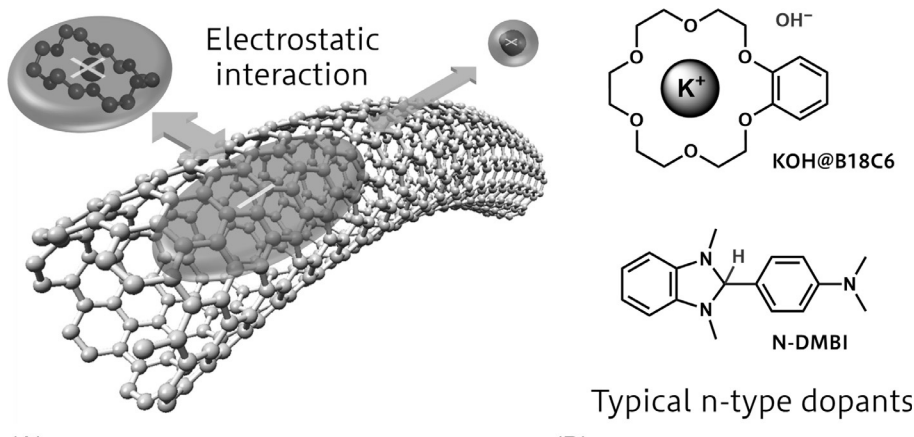


**Fig. 2.14.4** (A) Complex structure consisting of SWCNT anion and cationic complex.  
(B) Molecular structures of typical n-type dopants.

The authors have taken a different approach to produce n-type SWCNTs that are stable to air and heat [19]. The conduction band of a semiconducting SWCNT is deep enough (4.0–4.5 eV), so its reduced state is expected to be reasonably stable; but, it seems that most examples show a gradual deterioration. Therefore, sealing with a dense oxide film with low oxygen permeability was studied to kinetically stabilize n-type SWCNTs [27]. In contrast, the authors aimed for thermodynamic stabilization. In order to neutralize SWCNTs with counter charges while considering appropriate charge counterbalance, we comprehensively examined countercharge compounds with different sizes, shapes, and charge densities. It is considered that the charge on SWCNT is two-dimensionally delocalized, and therefore, it is important to use the counter ions having planar delocalized charges (Fig. 2.14.4). This is consistent with the empirical rule of hard and soft acid-base (HSAB) in solution. In particular, n-type SWCNT modified with a benzocrown ether complex maintained a negative Seebeck coefficient for more than 1 month even at 150°C. Yanagi and colleagues have realized deep doping using electrochemical transistors that use ionic liquids as electrolytes to study thermoelectric properties [25]. The size of the monovalent ion species used there is large for both positive and negative, and it is considered that a relatively stable doping state is realized from the viewpoint of the HSAB rule. The above-mentioned oxidized byproducts of the reduced benzyl viologen and dihydroimidazole derivatives are also highly planar and conjugated cationic compounds. These are considered to act as relatively appropriate counter ions for SWCNT anions.

## 2.14.5 Summary and outlook

In this chapter, we have focused on thermoelectric conversion materials using SWCNTs as active substrates. SWCNTs have a variety of functional aspects, and can be research targets ranging from the physical properties of low-dimensional

materials to realistic energy harvesting applications. Although not described in detail in this chapter, the study of appropriate measurement methods for thermophysical properties, including heat transfer of nanostructures, is also a new research subject. Molecular inclusions based on the unique cylindrical structure give rise to new phenomena from electron doping [18, 20] to heat conduction control through structural strain [39]. An SWCNT is a multifunctional material with various physical properties. SWCNTs have been widely studied as a flexible thermoelectric material. When the heating by the one-dimensional plasmon resonance found in the far infrared is used well, extremely sensitive terahertz electromagnetic wave detectors using thermoelectric conversion as a driving mechanism can be realized [40]. This is a seed of nondestructive inspection technology, and is based on a deep understanding of both photonics and phononics academically, and can be said to be a moonshot use of thermoelectric conversion. It is my hope that due to physical properties that contribute to the construction of theoretical systems and their application to thermoelectric materials, heat transfer engineering, materials chemistry, even truly innovative applications will emerge one after another.

## References

- [1] J.P. Small, K.M. Perez, P. Kim, Phys. Rev. Lett. 91 (2003) 256801.
- [2] L. Shi, D.Y. Li, C.H. Yu, W.Y. Jang, D.Y. Kim, Z. Yao, P. Kim, A. Majumdar, J. Heat Transf. 125 (2003) 1209.
- [3] M. Fujii, X. Zhang, H. Xie, H. Ago, K. Takahashi, T. Ikuta, H. Abe, T. Shimizu, Phys. Rev. Lett. 95 (2005) 065502.
- [4] C. Yu, Y.S. Kim, D. Kim, J.C. Grunlan, Nano Lett. 8 (2008) 4428.
- [5] D. Kim, Y. Kim, K. Choi, J.C. Grunlan, C. Yu, ACS Nano 4 (2010) 513.
- [6] Q. Yao, L.D. Chen, W.Q. Zhang, S.C. Liufu, X.H. Chen, ACS Nano 4 (2010) 2445.
- [7] C. Yu, K. Choi, L. Yin, J.C. Grunlan, ACS Nano 5 (2011) 7885.
- [8] N. Toshima, K. Oshima, H. Anno, T. Nishinaka, S. Ichikawa, A. Iwata, Y. Shiraishi, Adv. Mater. 27 (2015) 2246.
- [9] K. Suemori, Y. Watanabe, S. Hoshino, Appl. Phys. Lett. 106 (2015) 113902.
- [10] H. Wang, J.-H. Hsu, S.-I. Yi, S.L. Kim, K. Choi, G. Yang, C. Yu, Adv. Mater. 27 (2015) 6855.
- [11] C. Gao, G. Chen, J. Mater. Chem. A 4 (2016) 11299.
- [12] L. Wang, Q. Yao, J. Xiao, K. Zeng, S. Qu, W. Shi, Q. Wang, L. Chen, Chem. Asian J. 11 (2016) 1804.
- [13] G. Wu, Z.-G. Zhang, Y. Li, C. Gao, X. Wang, G. Chen, ACS Nano 11 (2017) 5746.
- [14] X. Cheng, X. Wang, G. Chen, J. Mater. Chem. A 6 (2018) 19030.
- [15] Y. Zhou, X. Yin, Y. Liu, X. Zhou, T. Wan, S. Wang, C. Gao, L. Wang, ACS Sustain. Chem. Eng. 7 (13) (2019) 11832.
- [16] C. Yu, A. Murali, K. Choi, Y. Ryu, Energy Environ. Sci. 5 (2012) 9481.
- [17] Y. Nonoguchi, K. Ohashi, R. Kanazawa, K. Ashiba, K. Hata, T. Nakagawa, C. Adachi, T. Tanase, T. Kawai, Sci. Rep. 3 (2013) 3344.
- [18] T. Fukumaru, T. Fujigaya, N. Nakashima, Sci. Rep. 5 (2015) 7951.
- [19] Y. Nonoguchi, M. Nakano, T. Murayama, H. Hagino, S. Hama, K. Miyazaki, R. Matsubara, M. Nakamura, T. Kawai, Adv. Funct. Mater. 26 (2016) 3021.

- [20] Y. Nonoguchi, Y. Iihara, K. Ohashi, T. Murayama, T. Kawai, *Chem. Asian J.* 11 (2016) 2423.
- [21] W. Zhou, Q. Fan, Q. Zhang, L. Cai, K. Li, X. Gu, F. Yang, N. Zhang, Y. Wang, H. Liu, W. Zhou, S. Xie, *Nat. Commun.* 8 (2017) 14886.
- [22] J. Choi, Y. Jung, S.J. Yang, J.Y. Oh, J. Oh, K. Jo, J.G. Son, S.E. Moon, C.R. Park, H. Kim, *ACS Nano* 11 (2017) 7608.
- [23] C.J. An, Y.H. Kang, H. Song, Y. Jeong, S.Y. Cho, *J. Mater. Chem. A* 5 (2017) 15631.
- [24] Y. Nakai, K. Honda, K. Yanagi, H. Kataura, T. Kato, T. Yamamoto, Y. Maniwa, *Appl. Phys. Express* 7 (2014) 025103.
- [25] K. Yanagi, S. Kanda, Y. Oshima, Y. Kitamura, H. Kawai, T. Yamamoto, T. Takenobu, Y. Nakai, Y. Maniwa, *Nano Lett.* 14 (2014) 6437.
- [26] A.D. Avery, B.H. Zhou, J. Lee, E.-S. Lee, E.M. Miller, R. Ihly, D. Wesenberg, K. S. Mistry, S.L. Guillot, B.L. Zink, Y.-H. Kim, J.L. Blackburn, A.J. Ferguson, *Nat. Energy* 1 (2016) 16033.
- [27] B.A. MacLeod, N.J. Stanton, I.E. Gould, D. Wesenberg, R. Ihly, Z.R. Owczarczyk, K. E. Hurst, C.S. Fewox, C.N. Folmar, K. Holman Hughes, B.L. Zink, J.L. Blackburn, A. J. Ferguson, *Energy Environ. Sci.* 10 (2017) 2168.
- [28] Y. Nonoguchi, A. Takata, C. Goto, T. Kitano, T. Kawai, *Sci. Technol. Adv. Mater.* 19 (2018) 581.
- [29] A. Chen, D. Madan, P.K. Wright, J.W. Evans, *J. Micromech. Microeng.* 21 (2011) 104006.
- [30] Y.C. Zhang, M.L. Snedaker, C.S. Birkel, S. Mubeen, X.L. Ji, Y.F. Shi, D.Y. Liu, X.N. Liu, M. Moskovits, G.D. Stucky, *Nano Lett.* 12 (2012) 1075.
- [31] K. Fukuie, Y. Iwata, E. Iwase, *Micromachines* 9 (2018) 315.
- [32] M. Zhang, Y. Deng, M. Yang, H. Nakajima, M. Yudasaka, S. Iijima, T. Okazaki, *Sci. Rep.* 9 (2019) 1284.
- [33] K. Fukuhara, Y. Ichinose, H. Nishidome, Y. Yomogida, F. Katsutani, N. Komatsu, W. Gao, J. Kono, K. Yanagi, *Appl. Phys. Lett.* 113 (2018) 243105.
- [34] P.G. Collins, K. Bradley, M. Ishigami, A. Zettl, *Science* 287 (2000) 1801.
- [35] M. Shim, A. Javey, N.W.S. Kam, H. Dai, *J. Am. Chem. Soc.* 123 (2001) 11512.
- [36] S.M. Kim, J.H. Jang, K.K. Kim, H.K. Park, J.J. Bae, W.J. Yu, I.H. Lee, G. Kim, D.D. Loc, U.J. Kim, E.-H. Lee, H.-J. Shin, J.-Y. Choi, Y.H. Lee, *J. Am. Chem. Soc.* 131 (2009) 327.
- [37] P. Wei, J.H. Oh, G. Dong, Z. Bao, *J. Am. Chem. Soc.* 132 (2010) 8852.
- [38] Y. Nakashima, N. Nakashima, T. Fujigaya, *Synth. Met.* 225 (2017) 76.
- [39] T. Kodama, M. Ohnishi, W. Park, T. Shiga, J. Park, T. Shimada, H. Shinohara, J. Shiomi, K.E. Goodson, *Nat. Mater.* 16 (2017) 892.
- [40] D. Suzuki, S. Oda, Y. Kawano, *Nat. Photonics* 10 (2016) 809.

# Higher manganese silicides

2.15

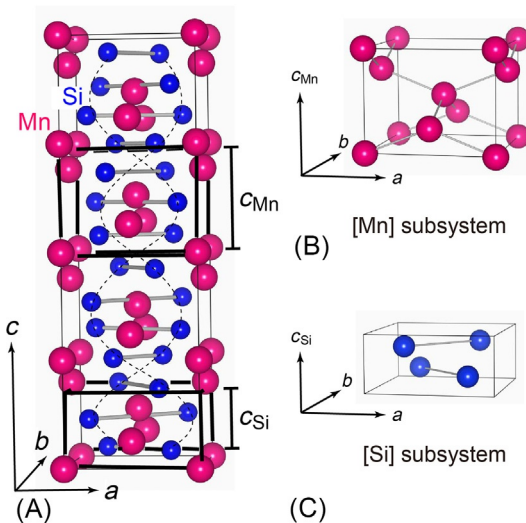
Yuzuru Miyazaki

Department of Applied Physics, Graduate School of Engineering, Tohoku University, Sendai, Japan

## 2.15.1 Introduction

The silicon-rich manganese silicide, having a chemical formula  $\text{MnSi}_{1.7}$ , is known as higher manganese silicide (HMS) [1–3]. In the 1960s, the silicide was already considered a p-type TE material suitable for mid-temperature range of 500–800K. HMS consists of naturally abundant and less-toxic elements, together with chemical stability and high oxidation resistance at operating temperature, and thus has several advantages for practical applications. However, the precise chemical formula of HMS was not identified for a long period due to its complicated crystal structure. Although the local arrangement of atoms is essentially identical, several chemical formulas— $\text{Mn}_4\text{Si}_7$  ( $\text{MnSi}_{1.75}$ ) [4, 5],  $\text{Mn}_{11}\text{Si}_{19}$  ( $\text{MnSi}_{1.7272\dots}$ ) [6],  $\text{Mn}_{15}\text{Si}_{26}$  ( $\text{MnSi}_{1.7333\dots}$ ) [7, 8], etc.—were proposed to represent HMS as different phases.  $\text{Mn}_4\text{Si}_7$  and  $\text{Mn}_{11}\text{Si}_{19}$  crystallize in a *primitive* tetragonal structure with the three-dimensional (3D) space group of  $\text{P}\bar{4}c2$  [4–6], while  $\text{Mn}_{15}\text{Si}_{26}$  crystallizes in a *body-centered* tetragonal structure with the 3D space group of  $\text{I}\bar{4}2d$  [7, 8]. Why would such a tiny change in the Mn:Si molar ratio cause a large symmetrical change from primitive to body-centered? Why are the *c*-axis lengths significantly different whereas the *a*-axis lengths are comparable? In 2008, the current author analyzed the detailed crystal structure of an HMS by utilizing the (3+1)-dimensional superspace formalism. According to their report [9], HMS is in fact a single incommensurate compound having a narrow compositional range around  $\text{MnSi}_{1.7}$  and consists of two tetragonal subsystems of [Mn] and [Si], having a common *a*-axis length but different *c*-axis lengths of  $c_{\text{Mn}}$  and  $c_{\text{Si}}$ . They defined the incommensurate *c*-axis length ratio as  $\gamma = c_{\text{Mn}}/c_{\text{Si}}$ , which is approximately 4.3/2.5 and hence results in the chemical formula  $\text{MnSi}_\gamma$ . The reason for using the Greek letter  $\gamma$  to represent the formula is that the  $\gamma$  value also denotes the modulation vector component between the two subsystems as  $\mathbf{k}=(\alpha\beta\gamma)=(00\gamma)$  according to definition [10]. The commensurate HMSs listed earlier are classified as members of incommensurate  $\text{MnSi}_\gamma$  with a small difference in  $\gamma$ . Fig. 2.15.1 shows the modulated crystal structure of an HMS with a  $\gamma$  value of 1.7361(1) [9]. The number in parenthesis represents the estimated standard deviation for the last significant digit. It should be noted that a conventional 3D *c*-axis length cannot be defined—it is usually infinite. Displacive modulation of atomic sites frequently occurs due to the size difference between the two subsystems. The structural feature is characterized by such a displacive modulation and has Nowotny chimney ladder (NCL)-type structure [11]. In this structure, the Mn atoms form a quadrangular chimney and the Si atoms are positioned to form a

**Fig. 2.15.1** Incommensurate crystal structure of  $\text{MnSi}_\gamma$  showing Mn and Si atoms in the range  $a \times a \times c_{\text{Mn}}$  (A). Unit cell of the [Mn] subsystem (B) and that of the [Si] subsystem (C) [9].



rotating ladder in the chimney along the  $c$ -axis. The structural modulation also gives rise to various types of defects, disorders, and stacking faults [12–16]. A detailed description of such modulated crystal structures is comprehensively given in Ref. [17]. In this chapter, we review the structural and derivative features of HMSs as well as recent efforts made to raise the TE performance of the system. To gain a more robust understanding of the subject matter, the reader should consult Refs. [18–20].

## 2.15.2 Unusual thermal expansion and striation problem

The two subsystems exhibit different thermal expansion due to their distinct chemical bonding nature. Fig. 2.15.2 shows the temperature evolution of lattice parameters— $a$ ,  $c_{\text{Mn}}$ ,  $c_{\text{Si}}$ , and  $\gamma = c_{\text{Mn}}/c_{\text{Si}}$ —of a melt-grown HMS sample with the nominal composition of  $\text{MnSi}_{1.74}$  [21]. Both  $a$  and  $c_{\text{Mn}}$  parameters show linear and reversible change against temperature  $T$ , as shown in Fig. 2.15.2A and B. However, the slope of the  $c_{\text{Si}}$ -axis length deviates above 800 K as  $T$  increases further (see Fig. 2.15.2C). Upon cooling, the  $c_{\text{Si}}$ -axis length depicts an almost linear  $T$ -dependence with decreasing  $T$  but does not overlap the initial values. This irreversible behavior observed in the  $c_{\text{Si}}$ -axis length has been confirmed to occur only when the sample is heated above 800 K. Thus, the  $\gamma$  value never returns to the initial value—approximately 1.743—when the sample is heated above 800 K (see Fig. 2.15.2D). High-temperature X-ray diffraction (HTXRD) study revealed the coefficient of thermal expansion (CTE) of the subsystems to be  $\alpha_a = 11.95(2) \times 10^{-6} (\text{K}^{-1})$ ,  $\alpha_{c_{\text{Mn}}} = 12.60(2) \times 10^{-6} (\text{K}^{-1})$ , and  $\alpha_{c_{\text{Si}}} = 10.71(5) \times 10^{-6} (\text{K}^{-1})$  at room temperature—this is comparable to that of typical metals [22]. The thermal expansion of HMS near room temperature appears to be isotropic despite the highly anisotropic crystal structure. The CTE values for the [Si] subsystem along

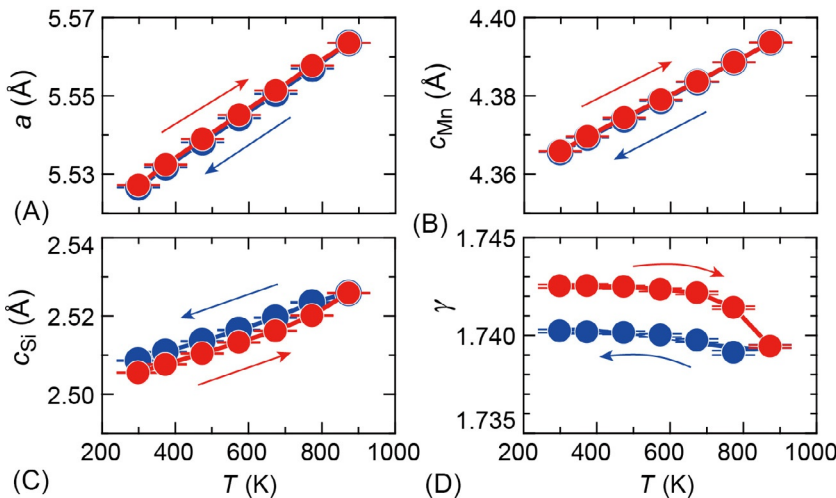


**Fig. 2.15.2** Temperature evolution of the lattice parameters,  $a$  (A),  $c_{\text{Mn}}$  (B),  $c_{\text{Si}}$  (C), and  $\gamma$  (D) of the  $\text{MnSi}_\gamma$  sample with the nominal composition of  $\gamma = 1.74$ .

the  $c$ -axis, however, becomes tripled— $\alpha_a = 11.82(2) \times 10^{-6} (\text{K}^{-1})$ ,  $\alpha_{c_{\text{Mn}}} = 12.46(2) \times 10^{-6} (\text{K}^{-1})$ , and  $\alpha_{c_{\text{Si}}} = 32.81(4) \times 10^{-6} (\text{K}^{-1})$ —at 1173 K [22]. This change in CTE along the  $c$ -axis is considered to be the primary cause of  $\text{MnSi}$  striations—formed nearly parallel to each other along the  $c$ -axis of the HMS—having intervals of 10–120  $\mu\text{m}$  and typical thickness of 1–10  $\mu\text{m}$  [23–25].

A more robust HTXRD study revealed that the  $\gamma$  value is close to 1.72 just below the peritectic temperature (melting point)—approximately 1420 K. Fig. 2.15.3 shows a partial phase diagram of HMS considering the results from HTXRD. From the liquid (L) +  $\text{MnSi}$  mixture, HMS crystalizes with a  $\gamma$  value of approximately 1.72. Upon cooling, the  $\gamma$  value increases gradually toward 1.74 at 800 K. According to the lever rule, about 3 mol% of  $\text{MnSi}$  should coexist with HMS at lower temperatures as follows:  $\text{MnSi}_{1.72}$  (1420 K) = 0.03  $\text{MnSi}$  + 0.97  $\text{MnSi}_{1.74}$  (below 800 K). The volume fraction of  $\text{MnSi}$  agrees with that of the observed striations.

$\text{MnSi}$  is a metallic conductor but the striations are usually polycrystalline and no particular crystallographic relationship between the HMS/ $\text{MnSi}$  interfaces has been reported [26]. Hence, the presence of such striations would lower the electrical conductivity and mechanical strength—both of which brings negative effect for the practical application as TE legs.

### 2.15.3 Dissipation of $\text{MnSi}$ striations

Based on the discussion made earlier, the formation of  $\text{MnSi}$  striations can be reduced by controlling the  $\gamma$  value to approximately 1.72 even at room temperature and/or kept independent of temperature. Abrikosov et al. first observed that a small amount of Ge substitution on Si sites can effectively reduce and eventually dissipate the  $\text{MnSi}$

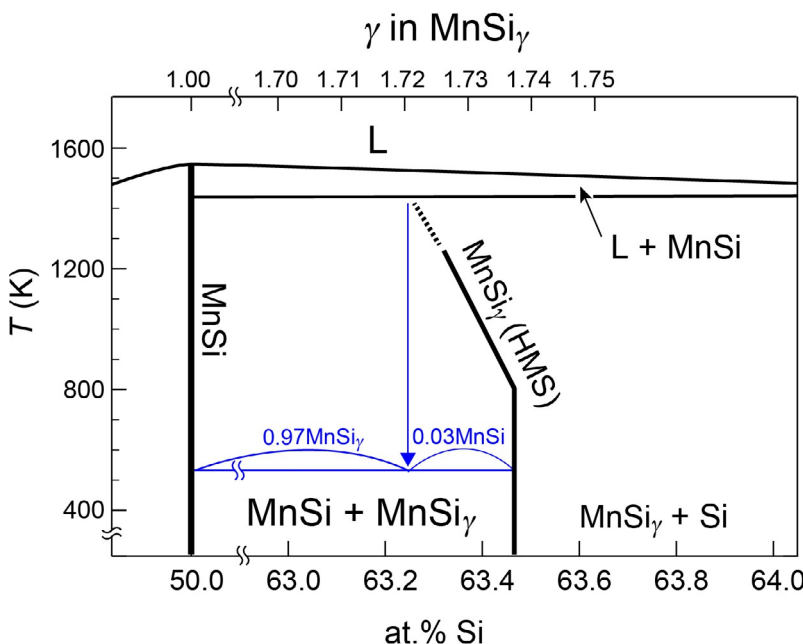


**Fig. 2.15.3** A proposed partial phase diagram of Mn-Si binary system based on the high-temperature X-ray diffraction.

striations in HMS [27]. Aoyama et al. have investigated the effect of Ge content on the microstructure of HMS. They confirmed that the complete dissipation of MnSi striations occurs when 0.5 mol% of Si is substituted with Ge [28]. However, the mechanism of this dissipation is yet to be fully understood. Miyazaki et al. investigated the effect of Ge content,  $y$ , on the lattice parameters of  $\text{Mn}(\text{Si}_{1-y}\text{Ge}_y)_\gamma$  solid solutions—the nominal  $\gamma$  value was fixed to 1.74 [29]. Fig. 2.15.4A–D shows that Ge substitution can effectively decrease the  $\gamma$  value to below 1.73. The data of the effect of V substitution is also included in the figures for comparison. The decrease in  $\gamma$  in the Ge solid solutions is due to the sudden increase in  $c_{\text{Si}}$ -axis length while keeping the  $a$ - and  $c_{\text{Mn}}$ -axis lengths nearly constant. The Ge-substituted samples exhibited a significant reduction in MnSi striations in microstructure—similar to that reported by Aoyama et al.—however, it was unable to dissipate the MnSi striations completely. Zhou et al. have recently proposed that Ge substitution can reduce the number of MnSi striations but cannot fully dissipate it because the solubility limit of Ge is relatively small—approximately 1 at.% [30].

MnSi striations can also be decreased and completely dissipated by partially substituting the Mn sites with Cr, V, or Co. [29, 31–33] For the case of V or Co substitution, the  $\gamma$  value is reduced to approximately 1.72 [29, 31, 32], whereas the Cr-substituted samples have  $\gamma$  values above 1.75 [33]. With the analysis done so far, the approximate  $\gamma$  value of 1.72 is not a sufficient condition for MnSi

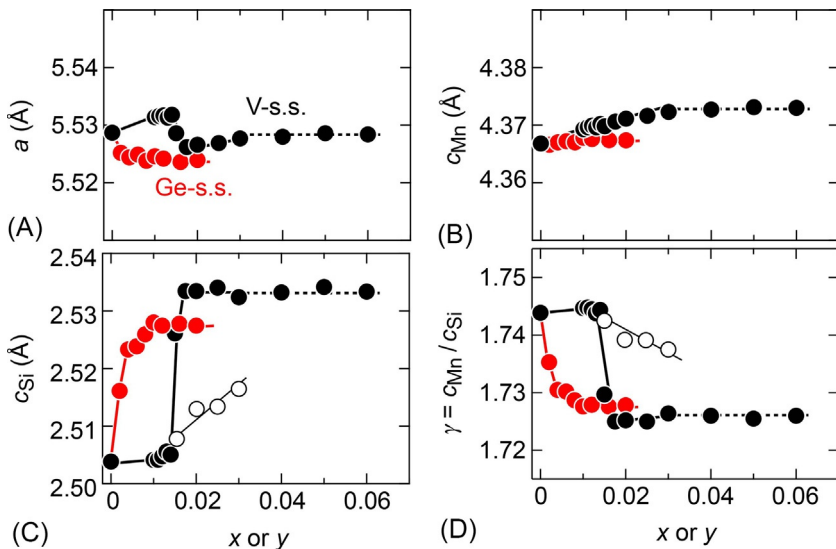


**Fig. 2.15.4** Effect of Ge-content,  $y$ , on the lattice parameters of a (A),  $c_{\text{Mn}}$  (B),  $c_{\text{Si}}$  (C), and  $\gamma$  (D) for the melt-grown  $\text{Mn}(\text{Si}_{1-y}, \text{Ge}_y)_\gamma$  samples with the nominal composition of  $\gamma = 1.74$ . The data of  $(\text{Mn}_{1-x}\text{V}_x)\text{Si}_{1.74}$  samples are also included for comparison [29].

striations. However, temperature-independent  $\gamma$  value would be a required condition to completely dissipate MnSi striations. HTXRD of such solid solutions is necessary to confirm the idea.

## 2.15.4 Theoretical approach

It is impossible to calculate the electronic structure and density of states (DOS) of HMSs due to the complicated incommensurate crystal structure. To do this, we need to assume a commensurate crystal structure model. Imai et al. first calculated the DOS of  $\text{Mn}_4\text{Si}_7$  and  $\text{Mn}_{11}\text{Si}_{19}$  using first-principles pseudopotential approach [34, 35]. The electronic structures of four commensurate phases— $\text{Mn}_4\text{Si}_7$ ,  $\text{Mn}_{11}\text{Si}_{19}$ ,  $\text{Mn}_{15}\text{Si}_{26}$ , and  $\text{Mn}_{27}\text{Si}_{47}$ —were later computed by Migas et al., based on the first-principles pseudopotential method [36]. In Fig. 2.15.5, we have shown the computed DOS of  $\text{Mn}_4\text{Si}_7$  using the full-potential augmented plane-wave as well as local orbital method [37]. The obtained result is similar to those reported by Imai et al. and Migas et al. [36].  $\text{Mn}_4\text{Si}_7$  is an intrinsic semiconductor with Fermi level,  $E_F$ , located at the top of the valence band (VB). The conduction band (CB) is separated from the VB with a bandgap of approximately 0.7 eV. The VB contains a broadband, ranging from -4 to -1 eV (mainly Mn-d and Si-p characters), and a steep band, ranging from -1 to 0 eV (mainly Mn-d characters). Another steep band is observed at the bottom of the CB, which is also a mixture of Mn-d and Si-p characters. The Seebeck coefficient is negatively proportional to the energy derivative of DOS at  $E_F$ , thus a large positive

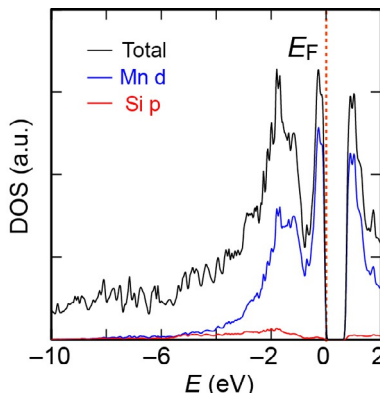


**Fig. 2.15.5** The total density of states (DOS) of  $\text{Mn}_4\text{Si}_7$  evaluated on the basis of first-principles calculation [37].

Based on the data given in Y. Miyazaki, J. Jpn. Inst. Metals 79 (2015) 530 (in Japanese).

Seebeck coefficient is expected. However, quite a small amount of DOS is observed at  $E_F$ . This implies that the electrical conductivity of  $\text{Mn}_4\text{Si}_7$  should be theoretically low. In the case of  $\text{Mn}_{11}\text{Si}_{19}$ ,  $E_F$  is shifted slightly below the top of the VB, which indicates a higher electrical conductivity and power factor (PF) [36]. Similar PF can also be expected for  $\text{Mn}_{15}\text{Si}_{26}$  and  $\text{Mn}_{27}\text{Si}_{47}$  as  $E_F$ , in these cases, is located slightly above the VB [36]. It must be noted that in the actual compound, the  $\gamma$  value is incommensurate around 1.73–1.74 and  $E_F$  should be slightly below the top of the VB.

The concept of VEC—valence electron counts per number of transition elements—is much convenient to use, compared to the time-consuming theoretical calculation of electronic structures and DOSs. The VEC of commensurate  $\text{Mn}_4\text{Si}_7$  is 14. This is because the valence electron numbers of Mn and Si are 7 and 4, respectively. Most of the NCL phases have VEC values around 14, according to the 14 electron rule [38, 39]. The VECs of other commensurate— $\text{Mn}_{11}\text{Si}_{19}$ ,  $\text{Mn}_{15}\text{Si}_{26}$ , and  $\text{Mn}_{27}\text{Si}_{47}$ —are determined to be 13.91, 13.93, and 13.96, respectively. The VEC of incommensurate HMSs can similarly be obtained using the expression:  $\text{VEC} = 7 + 4\gamma$ , where the  $\gamma$  value is evaluated from Le Bail analyses of XRD data based on superspace symmetry [17]. The VEC determines the relative position of  $E_F$  under the rigid band picture. When the VEC value is below 14,  $E_F$  is located in the VB and thus the compound should exhibit p-type conduction—a positive Seebeck coefficient. Smaller VEC corresponds to higher hole concentration and the most preferred value to obtain the highest PF is around 13.90 [33]. Similarly, n-type conduction can be realized for the HMS-based solid solutions having  $\text{VEC} > 14$ .

Studies on phonon and lattice dynamics have recently been reported by Chen et al. [40] They performed inelastic neutron scattering experiments on a single-crystalline HMS and discussed the lattice dynamics based on the phonon calculations of commensurate  $\text{Mn}_4\text{Si}_7$  model. The low lattice thermal conductivity of HMS obtained was attributed to a very low-lying optical phonon polarization—approximately 10–25 meV—which is associated with the twisting motions of the Si ladders relative

to the Mn chimney. Based on their calculations, the lattice thermal conductivity  $\kappa_L$  can be reduced to approximately 50% at 300 K, if the phonon mean free path is reduced to  $\sim 10$  nm [40]. The mean free path of hole carriers is in the range of 1–2 nm, thus the crystallite size between 5 and 10 nm would be effective to double the dimensionless figure-of-merit  $zT$  of HMSs.

## 2.15.5 Formation of HMS-based solid solutions

A large number of researchers have reported the effect of partial substitution of Mn and/or Si sites on the solubility range, crystal structure, and TE properties. Single substitution of V [29, 31, 41], Cr [42–45], Fe [44–49], Co [32, 46, 50], Re [51–54], or Ru [55, 56] for Mn sites and Ge [27–30] or Al [33] for Si sites have been studied. Multiple substitution of Mn and/or Si sites have also been reported [57–60]. However, it is difficult to conclude on the solubility range of substituent elements because a variety of chemical formulas were used by each author. The  $\gamma$  value also changes with partial substitution. Furthermore, the solubility range may be affected by the starting composition, preparation method, and thermal history of samples. For instance, the solubility limit of Cr for Mn is known to be around 20% using the standard arc-melting and annealing process but it expands to  $\sim 40\%$  when the melt-grown process is used. The melt-grown process involves heating a sample above the melting temperature—1423 K—cooled at the rate of 1 K/h down to 1373 K, and then cooled to room temperature in the furnace. The prepared sample is usually in a single-crystalline form. Fig. 2.15.6A–D shows the plot of the lattice parameters of partially substituted melt-grown samples and the nominal composition of  $(\text{Mn}_{1-x}M_x)\text{Si}_{1.74}$ , with  $M = \text{V, Cr, Fe, Co, and Ru}$ , based on the data given in Ref. [20]. A solid solution of  $x > 0.30$  can be prepared for the case of  $M = \text{Cr}$  and  $\text{Fe}$  and the complete solid solution is found for the Ru substitution (data with  $x > 0.5$  is not shown). The solubility limit of  $x$  approximately equal to 0.03 has been confirmed for V and Co, whereas the solubility limit for Re, Mo, Ta, Nb, W, Rh, and Ir is quite small— $x < 0.02$  (their results are not shown in the figure). The solubility limit of the other elements for the Mn site is negligibly small ( $x < 0.01$ ). The Si site can also be partially substituted with Al [33] and Ge [27–30], but the solubility limit was less than 0.01 for both elements. However, the Ge substitution effectively expands  $c_{\text{Si}}$ -axis to cause a significant reduction in the  $\gamma$  value down to approximately 1.72, as shown in Fig. 2.15.4C. Cr is the only element that increases the  $\gamma$  value to above 1.75 when the solid solution is formed (see Fig. 2.15.6D) [20].

## 2.15.6 Thermoelectric performance of HMS-based solid solutions

The properties of single-crystalline (SC) HMSs when measured parallel to the  $a$ -axis include Seebeck coefficient,  $S_a = 80\text{--}100 \mu\text{V/K}$ ; electrical conductivity,  $\sigma_a = 600\text{--}800 \text{ S/cm}$ ; thermal conductivity,  $\kappa_a = 3.2\text{--}3.6 \text{ W/Km}$ ; and resultant  $zT \sim 0.05$

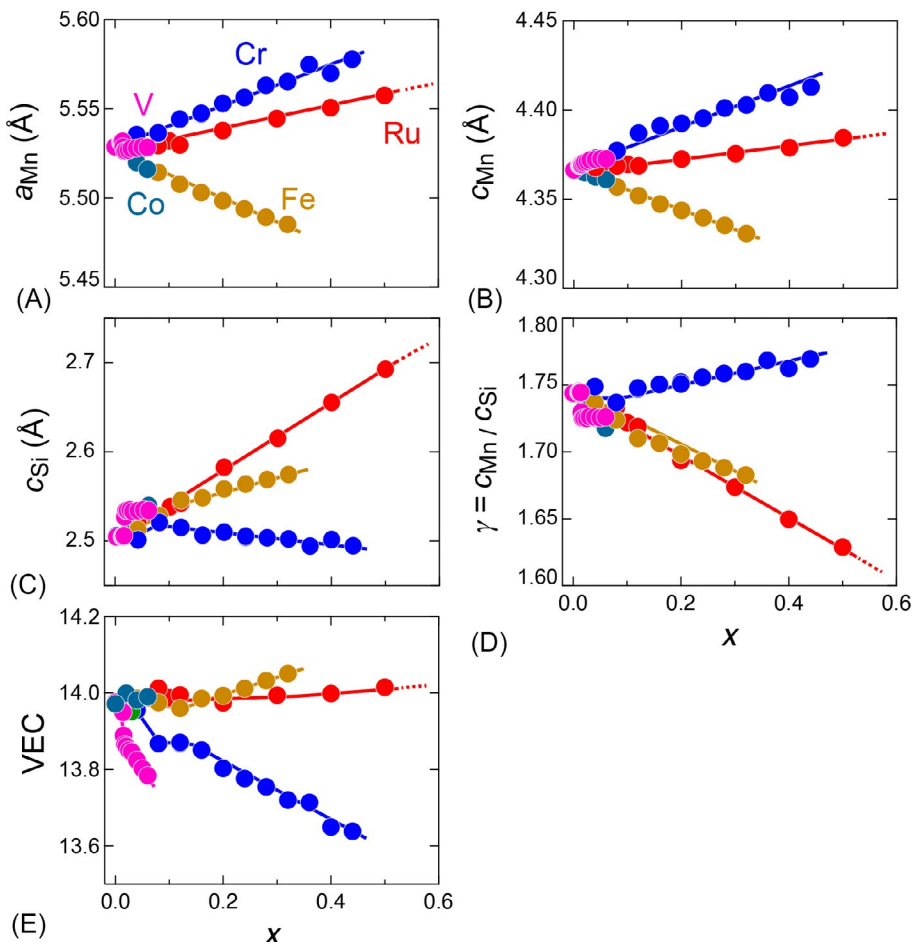


**Fig. 2.15.6** The determined lattice parameters,  $a$  (A),  $c_{\text{Mn}}$  (B),  $c_{\text{Si}}$  (C), and  $\gamma$  (D) of the melt-grown  $(\text{Mn}_{1-x}M_x)\text{Si}_{1.74}$ , solid solutions with  $M = \text{V}, \text{Cr}, \text{Fe}, \text{Co}$ , and  $\text{Ru}$ . The VEC values of the solid solutions (E).

at around 300 K [2]. Such SC samples exhibit metallic behavior in which the Seebeck coefficient gradually increases while the electrical conductivity decreases with  $T$  until 800 K—where bipolar diffusion takes place. The typical TE properties are  $S_a = 180\text{--}200 \mu\text{V/K}$ ,  $\sigma_a = 300\text{--}500 \text{S/cm}$ , and thermal conductivity  $\kappa_a = 3.5\text{--}4.5 \text{W/Km}$  at  $T = 800 \text{K}$ , where the highest  $zT = 0.20\text{--}0.30$  is achieved. Anisotropy in transport exists due to highly anisotropic structure. Typical SC HMSs exhibit lower  $zT$  values of approximately 0.15 at 800 K,  $250 \mu\text{V/K}$  for  $S_c$ ,  $80 \text{S/cm}$  for  $\sigma_c$ , and around  $2.8 \text{ W/Km}$  for  $\kappa_c$ —when the transport is measured parallel to the  $c$ -axis, being the less electrically conductive direction. Polycrystalline (PC) samples exhibit an average property with typical  $zT$  values of about 0.2 at around 800 K [2].

The partial substitution of Mn and/or Si site(s) introduces either hole or electron carriers [20]. Substituting Cr or V for the Mn site corresponds to hole doping as expected from the decrease in VEC value shown in Fig. 2.15.6E. The VEC of the solid solutions depends not only on the substitution amount  $x$ , but also on the  $c$ -axis length ratio  $\gamma$ —being directly related to the atomic radius,  $r_M$ , of the substituting elements. Thus, it can be represented as  $\text{VEC} = 7(1-x) + V_M x + 4\gamma$ , where  $V_M$  denotes the valence electron number of partially substituting elements  $M$ . The effect of  $x$  on VEC is much significant for  $M=\text{V}$  compared with  $M=\text{Cr}$  in  $(\text{Mn}_{1-x}M_x)\text{Si}_y$  solid solutions. The readers may suppose that it is due to the large difference in both the valence electron number and  $r_M$  between V and Mn atoms ( $r_{\text{Mn}}=0.161\text{ nm}$  and  $r_{\text{V}}=0.171\text{ nm}$ ), which will expand [Mn] subsystem upon substitution [61]. However, [Mn] subsystem in fact shows little expansion and a sudden expansion in  $c_{\text{Si}}$  significantly lowers the  $\gamma$  value (such trends can be more clearly recognized in Fig. 2.15.4A–D, identical plot but the  $x$  region is enlarged), leading to an abrupt decrease in VEC in the V-substituted samples at  $x \sim 0.015$ . In other words, V substitution is quite effective to adequately lower VEC—equivalent with optimizing hole concentration. The explanation for this significant change in VEC is currently unknown. A  $zT$  value of 0.6 at around 800K—being almost doubled relative to that of the substitution-free samples—has been reported for the V- or Cr-substituted melt-grown samples ( $x=0.02$  for V and  $x=0.08$  for Cr-solid solutions) [33].

Takeuchi et al. have recently reported the highest value of  $zT$  as approximately 1 at 900K for the Re-substituted supersaturated samples [51]. From the chemical formula,  $\text{Mn}_{30.4}\text{Re}_{6.0}\text{Si}_{63.6}$ , it can be rewritten as  $(\text{Mn}_{0.835}\text{Re}_{0.165})\text{Si}_{1.747}$  with  $\text{VEC}=13.988$ . Melt-spinning and subsequent spark plasma sintering (SPS) process can be used to yield a supersaturated solid solution of Re since the solubility limit of Re is less than 0.02 under a typical preparation method. The highest PF can be achieved with the VEC value, which is nearly an ideal value when compared with that of V-substituted samples of approximately  $2.3\text{ mW/K}^2\text{m}$  [29, 31], but a substantial decrease in the total thermal conductivity was recorded. The thermal conductivity of their sample is as low as  $2\text{ W/Km}$ , which is nearly half of that of typical bulk samples. A subsequent study on the nanostructure using transmission electron microscopy (TEM) has revealed lots of “sublattice dislocations (SDs)”—meaning only the arrangement of Si atoms is discontinuous in the Re-substituted samples [53]. Such a discontinuity can effectively block the propagation of phonons to reduce lattice thermal conductivity.

Considering the practical application of TE modules, it is required that both p- and n-type legs are made of compounds with similar crystal structures from the viewpoint of thermal expansion. N-type HMS-based solid solution can be obtained by controlling the VEC to a value larger than 14. Fig. 2.15.6E shows that it may be possible to obtain n-type samples through partial substitution of Co, Fe, or Ru. The experimental transition from p- to n-type conduction has been reported for Fe-substituted samples [45, 47, 48, 62] and Ru-substituted [55, 56] samples. For the case of Ru substitution, the crossover from p-type to n-type was reported to occur at  $x \sim 0.45$  in the formula  $(\text{Mn}_{1-x}\text{Ru}_x)\text{Si}_y$ —the original representation is  $x=0.55$  in  $\text{Ru}_{1-x}\text{Mn}_x\text{Si}_y$ . The composition of such a transition was expected considering the change in VEC from Fig. 2.15.6E, where the VEC becomes larger than 14 at  $x$  approximately equal to

0.5. The TE properties of n-type samples are much lower than that of p-type samples because the electrical conductivity remains as low as  $5\text{--}10 \times 10^3 \text{ S/m}$  at around 800 K. This is caused by a low carrier mobility due to the discontinuity of atomic-scale substitution and the emergence of a unique inhomogeneous distribution of Mn and Ru atoms in their microstructure [55, 56]. Considering Fe-solid solutions, the crossover is also observed at the point where VEC becomes larger than 14;  $x=0.25\text{--}0.30$ . The Fe-solid solutions exhibit similar electrical conductivity with the Ru-solid solutions, although the absolute value of the Seebeck coefficient is comparable to that of p-type samples. The  $zT$  value is reported to be approximately equal to 0.07 at 640 K for the  $x=0.30$  sample [62]. By using the melt-spinning and subsequent SPS process, a doubly substituted supersaturated sample of  $(\text{Mn}_{0.5}\text{Fe}_{0.4}\text{W}_{0.1})\text{Si}_{1.74}$  was found to exhibit a  $zT$  value of  $\sim 0.51$  at 700 K—the highest  $zT$  value for an n-type HMS-based solid solutions [63].

## 2.15.7 Domain separation

Characteristic domain separation has been observed for a partially substituted solid solution [29, 33]. The emergence of inhomogeneous distribution of some atoms—Cr/Mn and Ru/Mn in microstructure—has been already mentioned in Section 2.15.6, but the present domain separation is different and occurs in nanoscale. Fig. 2.15.7A represents part of a typical XRD pattern of V-solid solution,  $(\text{Mn}_{1-x}\text{V}_x)\text{Si}_{1.74}$  [31, 33]. The dominant peak 2110 does not show any remarkable change, but a significant change in the position and shape of the 1101 peak has been observed. The 2110 peak corresponds to the 211 reflection from the [Mn] subsystem, while the 1101 peak corresponds to the 111 reflection from the [Si] subsystem, which contains lots of disorder. Without any substitution, the 1101 peak is broad with overlapping of  $\text{K}_{\alpha 1}$  and

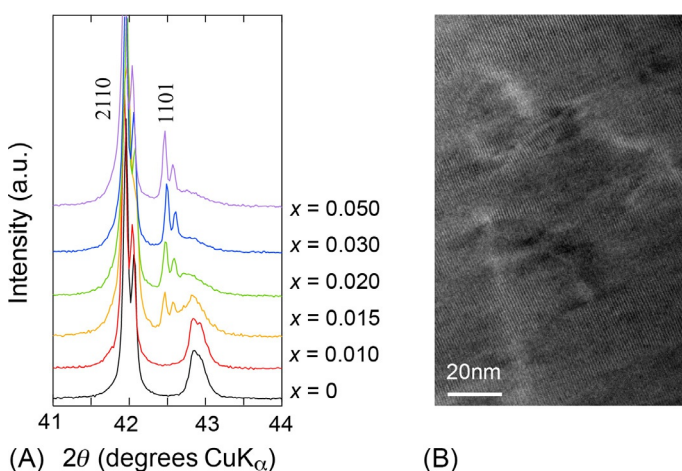


**Fig. 2.15.7** A part of X-ray diffraction patterns of the melt-grown  $(\text{Mn}_{1-x}\text{V}_x)\text{Si}_{1.74}$  samples (A). Transmission electron microscopy (TEM) image of the  $x=0.02$  sample (B).

$K_{\alpha 2}$ . By introducing a small amount of V substitution,  $x=0.015$ , the peak becomes obscure and an even sharp doublet appears at around  $2\theta$  which is approximately 42.5 degrees. The doublet and broad peaks (shoulder) both belong to the 1101 reflection. The peak width contains information on the crystallinity, crystallite size, and the degree of disorder. The existence of both lower-angle sharper doublet and higher-angle broader peak implies that the sample contains regular and highly disordered domains of Si atoms. Fig. 2.15.7B is a TEM image of the  $x=0.02$  sample, wherein several white streaks—a highly disordered domain of Si atoms—are recognized apart from the regular arrangement of Si atoms [20]. The volume fraction of the regular and disordered domain (area) approximately corresponds to the integrated intensity of lower-angle peak doublet and higher-angle shoulders of XRD patterns. A further increase in  $x$  reduces the shoulder height and the sharp doublet dominates at  $x>0.020$ . In contrast, little changes in the arrangement of Mn atoms are expected for all the compositions. Similar domain separation has been observed in Cr- and Co- substituted samples for the Mn sites, and Ge-substituted samples for the Si sites. Hence, such a nanosized domain separation is quite a common phenomenon in HMS-based solid solutions. The distribution of such domains is roughly estimated to be 10–50 nm, thus lattice thermal conductivity can effectively be reduced if the size and distribution are accurately controlled as described in Section 2.15.4 [40].

## 2.15.8 Summary

HMSs have a unique incommensurate crystal structure in which a variety of structural disorder of Si atoms are present. Partial substitution of Mn and/or Si sites is quite effective to tune-up TE properties but it appears that the PF has a maximum value of about  $2.5 \text{ mW/K}^2\text{m}$  at around 800 K, even if the VEC—electronic structure—is appropriately tuned. In contrast, the thermal conductivity can further be reduced through a careful control of micro-/nanostructure, with the help of a characteristic domain separation phenomenon. As the price-performance is quite high among inorganic TE materials, HMS-based TE materials have much potential for practical applications and we hope that the present review brings some motivation to the readers.

## Acknowledgment

The author is indebted to Dr. Yuta Kikuchi, Dr. Hiroki Nagai, Mr. Haruki Hamada, Mr. Yutaro Kawasaki, Professor Kei Hayashi, and Professor Kunio Yubuta, for their contribution to this project.

## References

- [1] V.K. Zaitsev, in: D.M. Rowe (Ed.), CRC Handbook of Thermoelectrics, CRC Press, New York, 1995. Sect. 25.
- [2] M.I. Fedorov, V.K. Zaitsev, in: D.M. Rowe (Ed.), Thermoelectrics Handbook: Macro to Nano, CRC Press, Boca Raton, FL, 2006. Sect. 31.
- [3] I. Nishida, in: M. Sakata (Ed.), Thermoelectrics—Principles and Applications, Realize Inc., Tokyo, 2001, p. 273 (in Japanese).

- [4] O.G. Karpinskii, B.A. Evseev, Izv. Akad. Nauk SSSR Neorg. Mater. 5 (1969) 525.
- [5] U. Gottlieb, A. Sulpice, B. Lambert-Andron, O. Laborde, J. Alloys Compd. 361 (2003) 13.
- [6] O. Schwomma, A. Preisinger, H. Nowotny, A. Wittmann, Monatsh. Chem. 95 (1964) 1527.
- [7] H.W. Knott, M.H. Mueller, L. Heaton, Acta Crystallogr. 23 (1967) 549.
- [8] G. Flieher, H. Völlenkle, H. Nowotny, Monatsh. Chem. 98 (1967) 2173.
- [9] Y. Miyazaki, D. Igarashi, K. Hayashi, T. Kajitani, K. Yubuta, Phys. Rev. B 78 (2008) 214104.
- [10] A. Yamamoto, Acta Crystallogr. A49 (1993) 831.
- [11] H. Nowotny, in: L. Eyring, M. O'keeffe (Eds.), The Chemistry of Extended Defects in Non-Metallic Solids, North Holland, Amsterdam, 1970, p. 223.
- [12] R. De Ridder, S. Amelinckx, Mater. Res. Bull. 6 (1971) 1223.
- [13] R. De Ridder, G. Van Tendeloo, S. Amelinckx, Phys. Status Solidi (a) 30 (1975) K99.
- [14] R. De Ridder, G. Van Tendeloo, S. Amelinckx, Phys. Status Solidi (a) 33 (1976) 383.
- [15] H.Q. Ye, S. Amelinckx, J. Solid State Chem. 61 (1986) 8.
- [16] L. Akselrud, R.C. Gil, M. Wagner-Reetz, Y. Grin, Acta Crystallogr. B71 (2015) 707.
- [17] Y. Miyazaki, in: I. Khidirov (Ed.), Neutron Diffraction, Intech Open Access Book, Rijeka, 2011 (Chapter 11).
- [18] Y. Miyazaki, Y. Kikuchi, in: K. Koumoto, T. Mori (Eds.), Thermoelectric Nanomaterials, Springer Series in Materials Science, Springer, Heidelberg, 2013 (Chapter 7).
- [19] Y. Miyazaki, in: C. Uher (Ed.), Materials Aspect of Thermoelectricity, CRC Press, Boca Raton, FL, 2016 (Chapter 13).
- [20] Y. Miyazaki, Jpn. J. Appl. Phys. 59 (2020) SF0802.
- [21] Y. Kawasaki, Master Thesis, Tohoku University, 2019 (in Japanese).
- [22] Y. Kikuchi, T. Nakajo, K. Hayashi, Y. Miyazaki, J. Alloys Compd. 616 (2014) 263.
- [23] L.D. Ivanova, N.K. Abrikosov, E.I. Elagina, V.D. Khvostikova, Izv. Akad. Nauk SSSR Neorg. Mater. 5 (1969) 1933.
- [24] T. Kojima, I. Nishida, T. Sakata, J. Cryst. Growth 47 (1979) 589.
- [25] I. Kawasumi, M. Sakata, I. Nishida, K. Masumoto, J. Cryst. Growth 49 (1980) 651.
- [26] E.I. Suvorova, V.V. Klechkovskaya, Crystallogr. Rep. 58 (2013) 854.
- [27] N.K. Abrikosov, L.D. Ivanova, V.G. Muravev, Izv. Akad. Nauk SSSR Neorg. Mater. 8 (1972) 1194.
- [28] I. Aoyama, M.I. Fedorov, V.A. Zaitsev, F.Y. Solomkin, I.S. Eremin, A.Y. Samunin, M. Mukoujima, S. Sano, T. Tsuji, Jpn. J. Appl. Phys. 44 (2005) 8562.
- [29] Y. Miyazaki, H. Hamada, H. Nagai, K. Hayashi, Materials 11 (2018) 926.
- [30] A.J. Zhou, T.J. Zhu, X.B. Zhao, S.H. Yang, T. Dasgupta, C. Stiewe, R. Hassdorf, E. Mueller, J. Electron. Mater. 39 (2010) 2002.
- [31] Y. Miyazaki, H. Hamada, K. Hayashi, K. Yubuta, J. Electron. Mater. 46 (2017) 2705.
- [32] H. Nagai, H. Hamada, K. Hayashi, Y. Miyazaki, J. Electron. Mater. 48 (2019) 1902.
- [33] H. Nagai, PhD Thesis, Tohoku University, 2019 (in Japanese).
- [34] Y. Imai, M. Mukaida, T. Tsunoda, Intermetallics 8 (2000) 381.
- [35] Y. Imai, A. Watanabe, Intermetallics 13 (2005) 233.
- [36] D.B. Migas, V.L. Shaposhnikov, A.B. Filonov, V.E. Borisenko, N.N. Dorozhkin, Phys. Rev. B 77 (2008) 075205.
- [37] Y. Miyazaki, J. Jpn. Inst. Metals 79 (2015) 530 (in Japanese).
- [38] W. Jeitschko, E. Parthe, Acta Crystallogr. 22 (1967) 417.
- [39] D.C. Fredrickson, S. Lee, R. Hoffmann, Inorg. Chem. 43 (2004) 6159.
- [40] X. Chen, A. Weathers, J. Carrete, S. Mukhopadhyay, O. Delaire, D.A. Stewart, N. Mingo, S.N. Girard, J. Ma, D.L. Abernathy, J. Yan, R. Sheshka, D.P. Sellan, F. Meng, S. Jin, J. Zhou, L. Shi, Nat. Commun. 6 (2015) 7723.

- [41] S.L. Tonquesse, V. Dorcet, L. Joanny, V. Demange, C. Prestipino, Q. Guo, D. Barthebaud, T. Mori, M. Pasturel, *J. Alloys Compd.* 816 (2020) 15257.
- [42] Y. Kikuchi, Y. Miyazaki, Y. Saito, K. Hayashi, K. Yubuta, T. Kajitani, *Jpn. J. Appl. Phys.* 51 (2012) 085801.
- [43] S. Ghodke, A. Yamamoto, M. Omprakash, H. Ikuta, T. Takeuchi, *Mater. Trans.* 58 (2017) 160.
- [44] V. Ponnambalam, D.T. Morelli, *J. Electron. Mater.* 41 (2012) 1389.
- [45] E.N. Nikitin, V.I. Tarasov, *Fiz. Tverd. Tela* 13 (1971) 3473.
- [46] G. Flieher, H. Völlenkle, H. Nowotny, *Monatsh. Chem.* 99 (1968) 2408.
- [47] V.K. Zaitsev, V.I. Tarasov, A.A. Adilbekov, *Fiz. Tverd. Tela* 17 (1975) 581.
- [48] V.I. Tarasov, E.N. Nikitin, L.N. Shumilova, *Izv. Akad. Nauk SSSR Neorg. Mater.* 11 (1975) 1038.
- [49] T. Yamada, Y. Miyazaki, H. Yamane, *Thin Solid Films* 519 (2011) 8524.
- [50] Y. Miyazaki, Y. Saito, K. Hayashi, K. Yubuta, T. Kajitani, *Adv. Sci. Technol.* 74 (2010) 22.
- [51] A. Yamamoto, S. Ghodke, H. Miyazaki, M. Inukai, Y. Nishino, M. Matsunami, T. Takeuchi, *Jpn. J. Appl. Phys.* 55 (2016) 020301.
- [52] X. Chen, S.N. Girard, F. Meng, E. Lara-Curzio, S. Jin, J.B. Goodenough, J. Zhou, L. Shi, *Adv. Energy Mater.* 4 (2014) 1400452.
- [53] T. Homma, T. Kamata, N. Naito, S. Ghodke, T. Takeuchi, *J. Alloys Compd.* 776 (2019) 8.
- [54] S. Ghodke, A. Yamamoto, H. Hu, S. Naito, T. Matsunaga, D. Byeon, H. Ikuta, T. Takeuchi, *ACS Appl. Mater. Interfaces* 11 (2019) 31169.
- [55] N.L. Okamoto, T. Koyama, K. Kishida, K. Tanaka, H. Inui, *Acta Mater.* 57 (2009) 5036.
- [56] N.L. Okamoto, T. Koyama, K. Kishida, K. Tanaka, H. Inui, *J. Electron. Mater.* 39 (2010) 1640.
- [57] I. Aoyama, H. Kaibe, L. Rauscher, T. Kanda, M. Mukoujima, S. Sano, T. Tsuji, *Jpn. J. Appl. Phys.* 44 (2005) 4275.
- [58] V. Ponnambalam, D.T. Morelli, S. Bhattacharya, T. Tritt, *J. Alloys Compd.* 580 (2013) 598.
- [59] S.A. Barczak, R.A. Downie, S.R. Popuri, R. Decourt, M. Pollet, J.W.G. Bos, *J. Solid State Chem.* 227 (2015) 55.
- [60] D.Y.N. Truong, D. Berthebaud, F. Gascoin, H. Kleinke, *J. Electron. Mater.* 44 (2015) 3603.
- [61] E. Clementi, D.L. Raimondi, W.P. Reinhardt, *J. Chem. Phys.* 47 (1967) 1300.
- [62] Y. Miyazaki, Y. Saito, K. Hayashi, K. Yubuta, T. Kajitani, *Jpn. J. Appl. Phys.* 50 (2011) 035804.
- [63] S. Ghodke, N. Hiroishi, A. Yamamoto, H. Ikuta, M. Matsunami, T. Takeuchi, *J. Electron. Mater.* 45 (2016) 5279.

# Silicide materials: Thermoelectric, mechanical properties, and durability for Mg-Si and Mn-Si

2.16

Tsutomu Iida<sup>a</sup>, Ryo Inoue<sup>b</sup>, Daishi Shiojiri<sup>a</sup>, Naomi Hirayama<sup>c</sup>, Noriaki Hamada<sup>d,e</sup>,  
and Yasuo Kogo<sup>a</sup>

<sup>a</sup>Department of Materials Science & Technology, Tokyo University of Science, Tokyo, Japan,

<sup>b</sup>Department of Mechanical Engineering, Tokyo University of Science, Tokyo, Japan, <sup>c</sup>Next Generation TATARA Co-Creation Centre, Shimane University, Shimane, Japan, <sup>d</sup>Center for Spintronics Research Network, Osaka University, Osaka, Japan, <sup>e</sup>Faculty of Science and Technology, Tokyo University of Science, Chiba, Japan

## 2.16.1 Basic thermoelectric characteristics by impurity doping and thermal durability

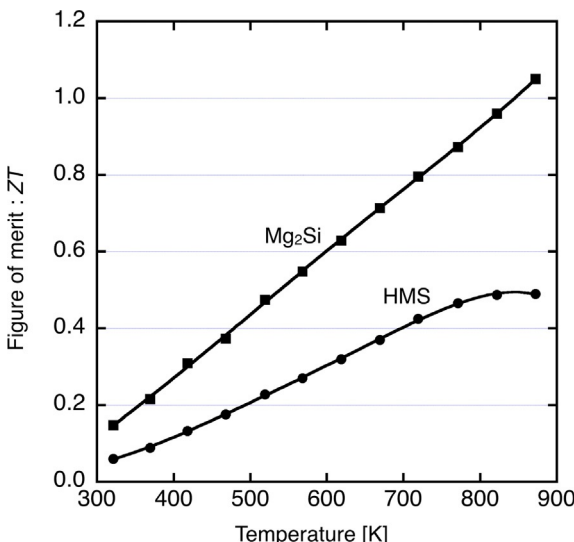
Developing greener TEG also requires a consideration of the environmental impact of the materials used in the production. Magnesium silicide ( $Mg_2Si$ ), magnesium tin silicide ( $MgSiSn$ ), and manganese silicide, including the so-called higher manganese silicide (HMS), all have the benefit of being environmentally benign and have sufficient performance to enable improvements in the overall energy efficiency of combustion systems, such as automotive engines and industrial furnaces. In contrast to other mid-temperature range thermoelectric materials,  $Mg_2Si$  and HMS have the merit of being nontoxic and sustainable materials and the cost of their production is relatively low. Lighter and tougher TE power generators in the mid-temperature range are easier to implement into automotive engines and industrial furnaces, but sometimes the application environment is not easy on the materials themselves.

As possible mid-temperature TE materials, the use of  $Mg_2Si$ ,  $MgSiSn$ , and HMS have been suggested for many years 1–47. The basic material properties of  $Mg_2Si$  and HMS, such as narrow bandgap 1–3,10–13,26,27 and carrier controllability by impurity doping 4–10,12–24,28–33 can provide design flexibility in terms of a thermal impedance adjustment for practical TE devices when the device is installed to a practical thermoelectric system. As for the  $Mg_2Si$ , many theoretical calculations have been made to understand and optimize the doping characteristics 6,19,34–40. Since  $Mg_2Si$  exhibits n-type conductivity, primarily due to the native defects 23, and HMS p-type behavior, the  $\pi$ -structure TE module requires a combination of n- and p-elements which therefore can use  $Mg_2Si$  and HMS. So far, the highest ZT values of  $Mg_2Si$  and HMS were ~1.2 48 and ~1.0 29,30, respectively. The basic TE characteristics

for the Mg<sub>2</sub>Si and HMS can be referenced from the above articles. However, much less work has been reported on the material durability in the operational temperature range. Therefore, the thermal stability of Mg<sub>2</sub>Si and HMS is studied in this work, since it is important in the practical application of TE chip and TE modules. For the durability tests, Mg<sub>2</sub>Si used was double doped with Sb and Zn, and undoped HMS (MnSi1.75), where the TE chips of Mg<sub>2</sub>Si and HMS used were initiated from the all-molten chunk of Mg<sub>2</sub>Si and MnSi1.75, respectively. Then the pulverized powder was sintered by a plasma-assisted sintering (PAS) method to form TE chips. The measured figure of merit, ZT values of the Mg<sub>2</sub>Si and HMS TE chips used in the experiments are plotted in Fig. 2.16.1.

Mg<sub>2</sub>Si has been known to be easily oxidized at the expected operational temperature. However, Mg<sub>2</sub>Si prepared by an all-molten method with no residual metallic-Mg exhibited atmospheric durability at 873 K for  $\sim 1000$  h [48](#). For further durability, however, some measures to promote resistance to oxidation are required otherwise the sample surfaces tend to deteriorate slightly. A surface passivation coating to block oxygen transmission is one of the measures to inactivate the surface of Mg<sub>2</sub>Si. The Mg<sub>2</sub>Si surface is highly reactive due to the existence of the Mg, showing a low value of the standard Gibbs free energy of formation of MgO. To form a surface passivation layer of  $\sim 10\text{-}\mu\text{m}$  thickness, an alkaline conditioner was used to stabilize the Mg<sub>2</sub>Si surface. Then the surface was dip coated with coating agent composed of SiO<sub>2</sub>, ZrO<sub>2</sub>, and mica produced by Nihon Parkerizing Co., Ltd. [49](#). Fig. 2.16.2 shows the results of aged  $3 \times 3 \times 7\text{ mm}^3$  size Mg<sub>2</sub>Si TE chips with an anti-oxidation passivation coating at 873 K for 7000 h in atmospheric conditions. The surfaces of the tested TE chips were seen to be durable during the experiments and the measured resistivities of the matrix were relatively stable at  $3.36\text{--}3.60 \times 10^{-6}\text{ }\Omega\text{-m}$  before aging and  $3.45\text{--}3.73 \times 10^{-6}\text{ }\Omega\text{-m}$  after 7000 h of aging.

**Fig. 2.16.1** Measured figure of merit (ZT) values for the Mg<sub>2</sub>Si and HMS TE chips used in the thermal durability experiments. TE chips were fabricated by plasma-activated sintering initiated from the all-molten synthesized source materials.



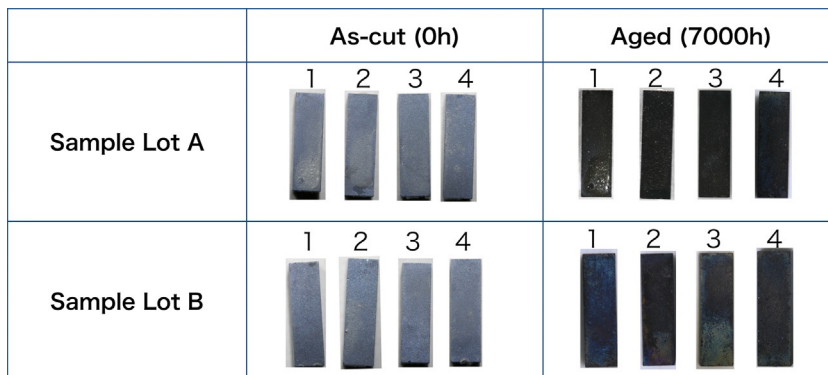


**Fig. 2.16.2** Appearance of doped  $\text{Mg}_2\text{Si}$  TE chips with anti-oxide coating after an accelerated aging test at 873 K for 7000 h in atmospheric conditions. The  $\text{Mg}_2\text{Si}$  samples were double doped with Sb 0.5 at%/Zn 0.5 at% (Sample lot A) and Sb 1.0 at%/Zn 1.0 at% (Sample lot B)

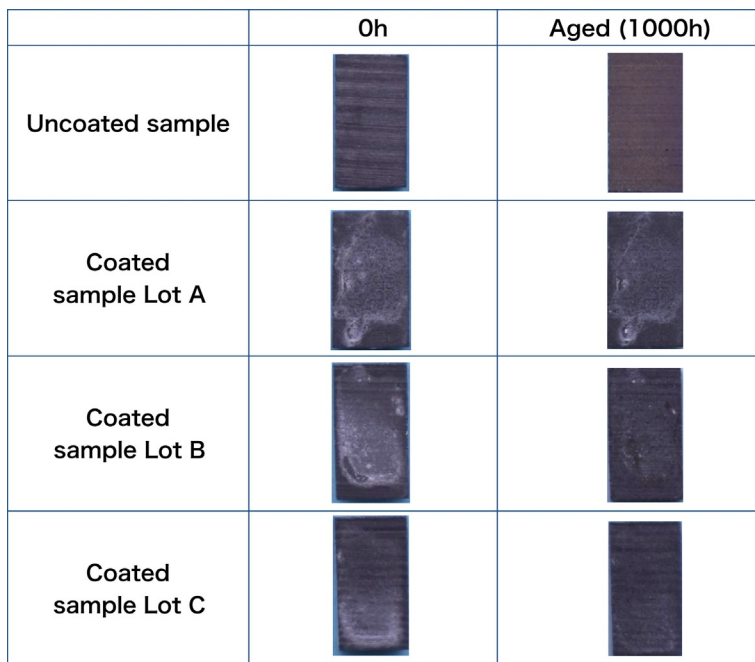


**Fig. 2.16.3** Appearance of undoped HMS TE chips with/without an anti-oxide coating after an accelerated aging test at 873 K for 1000 h in atmospheric conditions.

**Fig. 2.16.3** shows the results of aged  $3 \times 3 \times 5 \text{ mm}^3$  HMS TE chips with and without an anti-oxidation passivation coating at 873 K for 1000 h in atmospheric conditions. The TE chip used was initiated from an all-molten chunk of  $\text{MnSi}_{1.75}$  and then the pulverized powder was sintered by a plasma-assisted sintering (PAS) method. Although HMS is known to have a robust characteristic for oxidation at operation

temperature range, the uncoated sample exhibited slight traces of degradation on the surface which was subsequently confirmed to be due to oxidation by SEM-EDX analysis. The resistivity of the uncoated specimen was changed from  $2.43$  to  $2.52 \times 10^{-6}$   $\Omega\text{-m}$  after  $1000\text{ h}$  after aging and coated ones showed a smaller variation in the range of  $2.58\text{--}2.62 \times 10^{-6}$   $\Omega\text{-m}$  before aging to  $2.58\text{--}2.67 \times 10^{-6}$   $\Omega\text{-m}$  ( $1000\text{ h}$  aged) 49, indicating that the coating applied to the HMS is effective.

## 2.16.2 Electrode formation with low contact resistance

For a practical TEG fabrication, the formation of an appropriate electrode with low contact resistance at the interface between the electrode material and the  $\text{Mg}_2\text{Si}$  and HMS is important. Also, thermal stability is needed up to the operating temperature of  $\sim 900\text{ K}$ . A promising electrode formation method to adapt to large-scale production is metallic paste printing.

Since thermoelectric silicides are conventional semiconductor materials, extraction of the electricity generated by the TE chip under the temperature difference can be enhanced by a combination between the electrode material and matrix. The loss-less power gain from the TE chip requires optimized properties of the electrode materials, such as low resistivity, the ohmic-contact capability to the matrix with low contact resistance, and chemical stability with the surrounding substances at elevated temperatures. At the moment, not much exploratory experimentation regarding electrodes on TE silicides has been done, at least in a systematic manner. We have performed extensive studies aiming to obtain a thermally stable electrode on  $\text{Mg}_2\text{Si}$  and HMS and have also examined the interface profile, the thermal diffusion, alloy formation, and the durability for mid-temperature operation.

The tested electrode materials of  $\text{Mg}_2\text{Si}$  and HMS are listed in Table 2.16.1 with their material properties. Ni is known as one of the most promising electrode metallic material for  $\text{Mg}_2\text{Si}$ , with a sufficiently low contact resistivity of  $<1 \times 10^{-9}$   $\Omega\text{m}^2$ . However, in operational heat cycles up to  $\sim 900\text{ K}$ , it can give rise to the formation of Ni-silicide at the  $\text{Mg}_2\text{Si}/\text{Ni}$  interface. This formation of Ni-silicide at the electrode interface leads to a draw on the Si in the matrix, then the Mg left behind turns into  $\text{MgO}$  and this degrades the  $\text{Mg}_2\text{Si}/\text{Ni}$  interface. Regarding the electrode candidate for HMS, Ni is a possible material which has a good contact resistivity of the order of  $10^{-9}$   $\Omega\text{m}^2$  after formation, but exfoliation becomes a major issue at elevated temperatures. There is no notable report for chemically and thermodynamically stable electrode materials to HMS at the moment.

The electrode materials to be tested were determined in terms of low resistivity and comparable work function value to the host matrix. In order to realize a reproducible electrode formation process, a metallic paste printing method was used as the dominant electrode formation method. A usable electrode material was prepared with printing paste of the order of  $\sim \mu\text{m}$  size of metallic powder. Ni-based mixed metallic paste such as Ni-Au, Ni-Pd, and Ni-Al was tested for the  $\text{Mg}_2\text{Si}$  and a singular metallic paste of Ag, Cu, and Ti were used for the HMS, respectively.

**Table 2.16.1** Physical properties of Mg<sub>2</sub>Si, HMS and candidate material for electrode 50–56.

	Mg <sub>2</sub> Si	HMS	Ni	Cu	Au	Ag	Pd	Al	Ti
Resistivity [ $\times 10^{-8} \Omega\text{m}$ ]	$2.50 \times 10^2$	$3.30 \times 10^3$	7.04	1.70	2.20	1.61	10.55	5.92	43.1
Melting point [K]	1375	1423	1728	1358	1338	1234	1827	693	1941
Work function [eV]	3.59–4.61		4.5	4.9	4.5	4.3	5.1	4.3	4.3
Coefficient of thermal expansion [ $\times 10^{-6}/\text{K}$ ]	15.4	11.9	13.4	16.5	14.2	18.9	23.1	30.2	8.6
Powder size [ $\mu\text{m}$ ]	–	–	0.4	1.0	0.8	3.0	0.9	4.0	20

Mg<sub>2</sub>Si, Ni-Au, and Ni-Pd pastes with 0.1–0.5 at% Au and 0.1–0.5 at% Pd, respectively, were printed into sintered pellets which were compacted more than 98% density by plasma activated sintering (PAS) method. The pellets were used to print the 300-μm electrodes, which were then preheated at ~550 K to remove chemicals in the paste, and then baked at ~900–1100 K to form a ~100-μm thick metallic electrode and interdiffusion layers. As for the Ni-Al electrode, the Al content was 10 at% and heat treatment (baking) process was performed under a pressurized environment at 17 MPa, because of the risk of surface oxidation of the Ni-Al in the paste. The formed electrode with Ni-Au, Ni-Pd, and Ni-Al exhibited an ohmic contact and the evaluated contact resistance between the Mg<sub>2</sub>Si matrix and the electrode, which was measured by the four-point probe method with a 20-μm scan step of the probe made of tungsten carbide, as shown in Fig. 2.16.4. For all specimens, the observed contact resistivities ranged between  $0.5 \times 10^{-10}$  and  $1.0 \times 10^{-10} \Omega\text{m}^2$ . On the contrary, the samples with Ni-Au and Ni-Pd electrode showed a deterioration of the contact resistivities down to the order of  $10^{-9}$ – $10^{-8} \Omega\text{m}^2$  after the accelerated aging test at 873 K for 500 h in atmospheric conditions. It was revealed from an analysis at the matrix/electrode interface in detail that incorporated Au or Pd precipitated at the interface and that this gave rise to significant diffusion and local precipitation at the interface.

Fig. 2.16.5 shows the SEM observations and EDS line analysis of the Mg<sub>2</sub>Si-matrix/electrode interface for the Ni-Al specimen prepared under pressurized baking at 973 and 1073 K. The interface elemental profiles have clear and abrupt characteristics with no notable precipitation, indicating that the interdiffusion of constituent elements was unlikely for the combination of the Ni-Al electrode. However, it is apparent that the heat treatment can form an intermediate at the Mg<sub>2</sub>Si-matrix/electrode interface and it is seen that an increase in the heat treatment temperature encourages a widening of this layer thickness of the intermediate layers. The Mg<sub>2</sub>Si with Ni-Al specimen showed a thermally stable Mg<sub>2</sub>Si-matrix/electrode interface even after an

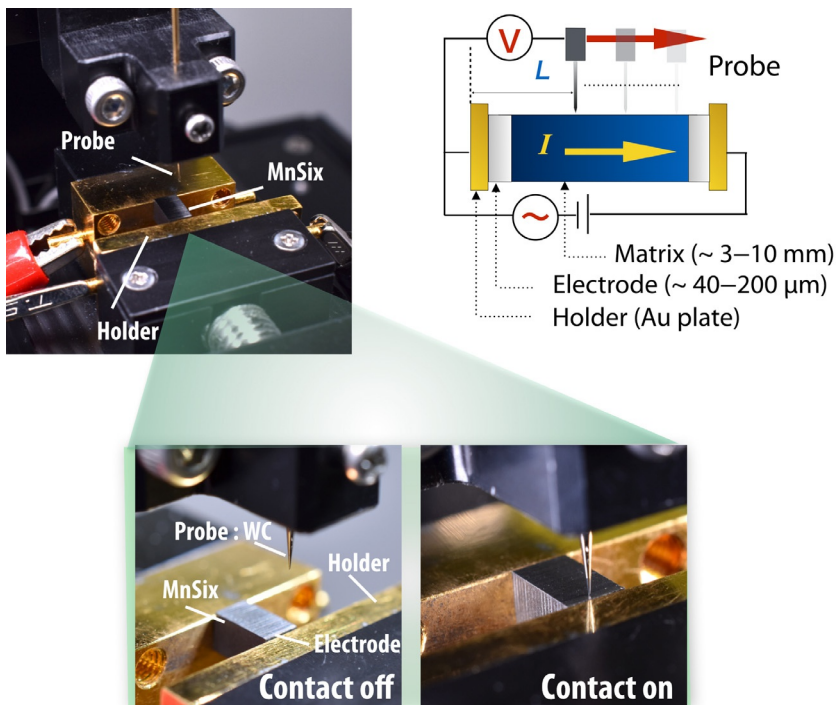


**Fig. 2.16.4** The four-terminal measurement apparatus to measure contact resistance between matrix and formed electrode.

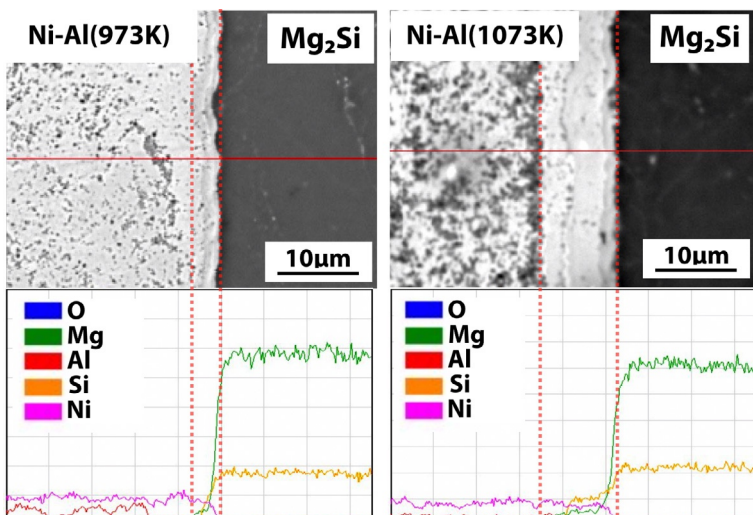


**Fig. 2.16.5** SEM image and EDS line analysis at the  $\text{Mg}_2\text{Si}$ -matrix/electrode interface for Ni-Al specimens which were prepared under a pressurized baking process at 973 and 1073 K.

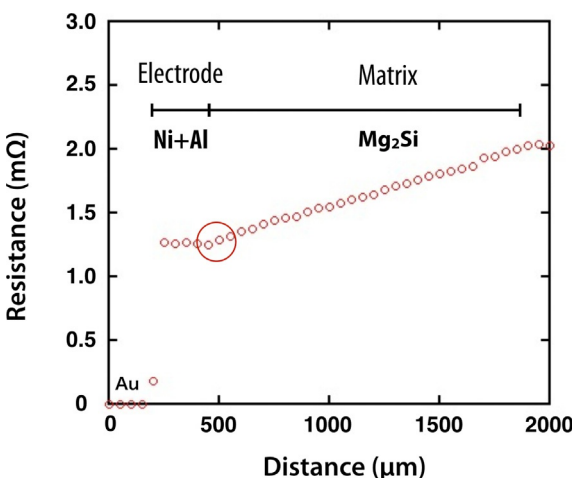
accelerated aging test at 873 K for 100 h in atmospheric conditions, with contact resistivities  $< 1 \times 10^{-9} \Omega\text{m}^2$ . For a simple durability test, where the TE chip is located between a pair of heat block under a temperature difference between 873 and 373 K (similar conditions to an actual power generation environment), no notable deterioration was observed. Fig. 2.16.6 indicates a speculative model for interface interdiffusion at the  $\text{Mg}_2\text{Si}/\text{Ni-Al}$  interface and subsequent  $\text{Ni}_3\text{Si}$  formation, which then seems a rather stable layer.

Fig. 2.16.7 shows the results of contact resistance measurement for the sample of  $\text{Mg}_2\text{Si}$  with an Ni-Al electrode. The sample was cut and polished after the aging test and the obtained resistivity value was  $0.41 \times 10^{-9} \Omega\text{m}^2$  at the  $\text{Mg}_2\text{Si}/\text{Ni-Al}$  interface.

As for the electrode formation to the HMS, an HMS sample was obtained from an all-molten synthesized  $\text{MnSi}_{1.75}$  chunk and then pulverized to a powder (25–45- $\mu\text{m}$  grain size) and sintered at 1203 K using the PAS method. For the HMS specimens, electrodes were processed under a pressurized environment of 18 MPa at 973–1073 K. This is to try and suppress the peeling of the electrode layers. After the formation of the electrode layers for Ni, Ag, Ti, and Cu, the specimens were stabilized to observe



**Fig. 2.16.6** A conceivable model for the  $\text{Mg}_2\text{Si}$ -matrix/electrode interface for the Ni-Al specimen after thermal treatment.



**Fig. 2.16.7** Results of the contact resistance measurement for  $\text{Mg}_2\text{Si}$  equipped with a Ni-Al electrode obtained by the four-terminal measurement method.

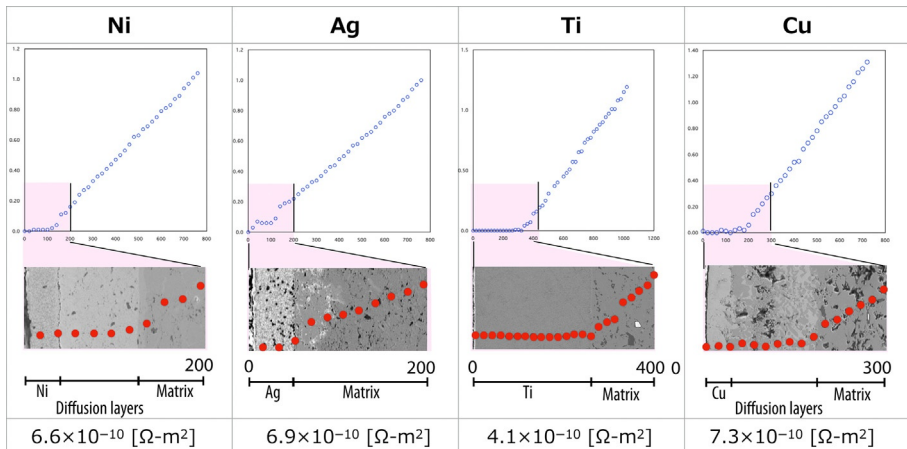


**Fig. 2.16.8** SEM image and results of the contact resistance measurement for the HMS equipped with electrodes of Ni, Ag, Ti, and Cu.

their surface using SEM and to proceed to cutting and polishing for a contact resistance measurement. Fig. 2.16.8 represents the results of the contact resistance measurement for the HMS equipped with electrodes of Ni, Ag, Ti, and Cu accompanied by SEM images of the HMS-matrix/electrode interface. For all the electrode materials sufficiently low values ( $< 1 \times 10^{-9} \Omega \cdot m^2$ ) of the contact resistivity were observed at the HMS-matrix interface. As shown in Fig. 2.16.8, the Ti electrode exhibited a rather abrupt and homogeneous interface as compared to the other materials and it is seen that only a minimal intermediate layer with the lowest contact resistivity at HMS-matrix/electrode interface was formed, which is associated with a clear change point in the resistance profile.

On the other hand, an accelerated aging test at 873 K revealed incomplete HMS-matrix/electrode interface adhesion; that is, the Ni and Ag electrodes exhibited peeling which is closely associated with a formation of Mn-O and Si-O at the matrix/electrode interface. The Cu electrode showed no notable peeling, however, there is a large diffusive penetration of Cu into the matrix resulting in a local crack formation at the matrix/electrode interface and about one order of magnitude lower contact resistivity value. For the Ti electrode, this was very stable with no peeling nor a sudden increase in contact resistance.

In order to investigate further the behavior of the HMS-matrix/Ti-electrode interface, EDS analysis was performed in detail. Fig. 2.16.9 shows the SEM images and EDS line/point analyses of the HMS-matrix/Ti-electrode interface for the Ti electrode sample. The accelerated aging test was performed at 873 K for 100 h in air and in Ar. It is seen that the interface was affected by the heat treatment and exhibited a local compositional change at the interface by forming MnSi and Ti-Si as intermediate substances. However, the observed characteristics for the HMS-matrix/Ti-electrode contact were reproducible and have sufficiently low contact resistivity. It seems that the Ti electrode processed with the current method is one possibility for a good stable HMS electrode.

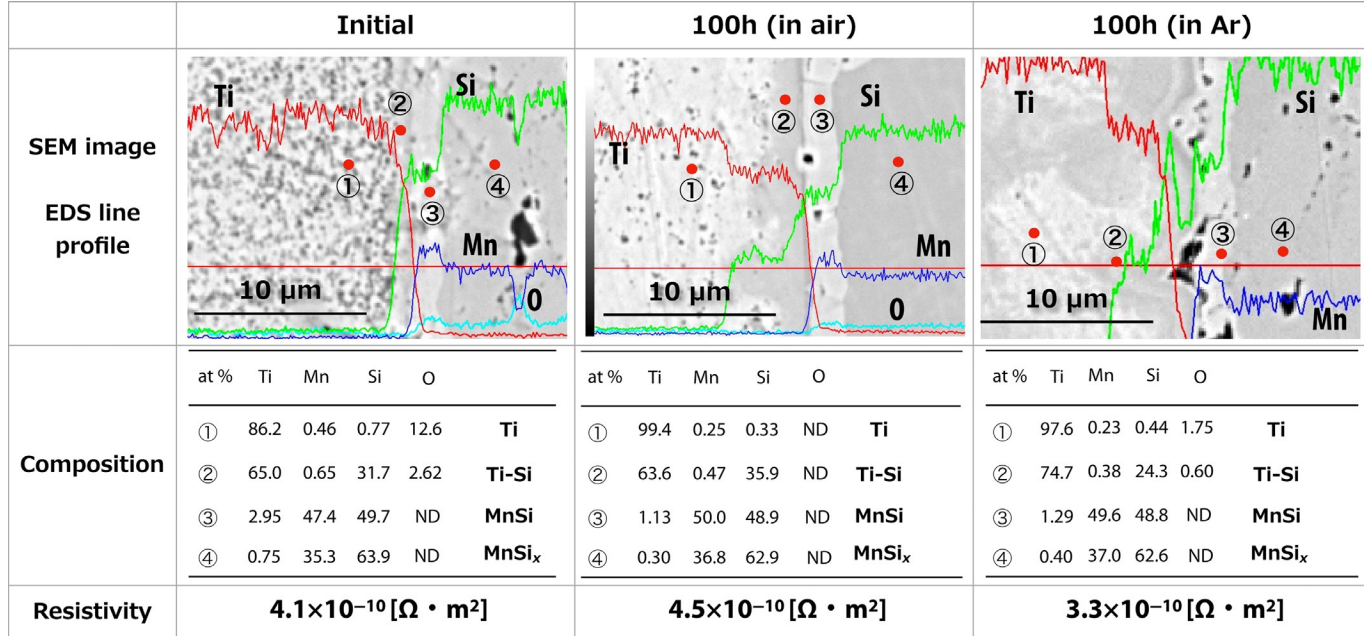


**Fig. 2.16.9** SEM images and EDS line analyses at the HMS-matrix/Ti-electrode interface. The accelerated aging test was performed at 873 K for 100 h in air and in Ar.

## 2.16.3 Mechanical properties of Mg- and Mn-based silicides

In order to establish reliable thermoelectric generators (TEG), TE materials are required to be, stiff, strong, and tough both at room temperature and at elevated temperatures. Recently, Liu et al. 57 has summarized the mechanical properties of various TE materials including  $\text{Bi}_2\text{Te}_3$ ,  $\text{PbTe}$ ,  $\text{PbSe}$ ,  $\text{PbS}$ ,  $\text{CoSb}_3$ ,  $\text{Zn}_4\text{Sb}_3$ ,  $\text{Ca}_3\text{Co}_4\text{O}_9$ , half-Heusler alloys, and  $\text{SiGe}$ . It is expected that thermoelectric generators will be used in a wide variety of applications, utilizing the heat generated from fuel cells, furnaces, and auto exhausts, etc. Fig. 2.16.10 shows TE materials classified according to their operating temperature. In the mid-temperature (573–873 K), magnesium (Mg), and manganese (Mn)-based silicides are candidate materials because of their high conversion efficiency at 873 K. There have been many attempts to integrate these two silicides into TEGs for automobile applications 58–61. To do so, technical problems such as their mechanical robustness, chemical stability, and toxicity had to be solved, manufacturing costs reduced, and mass production enabled 62–65.

Improving the mechanical properties of TE materials is critical for practical applications because TEGs are likely to be subjected to mechanical loading induced by vibration and thermal stress induced by the mismatch between the thermal and elastic properties of the constituent materials during heat cycling. The loading is affected not

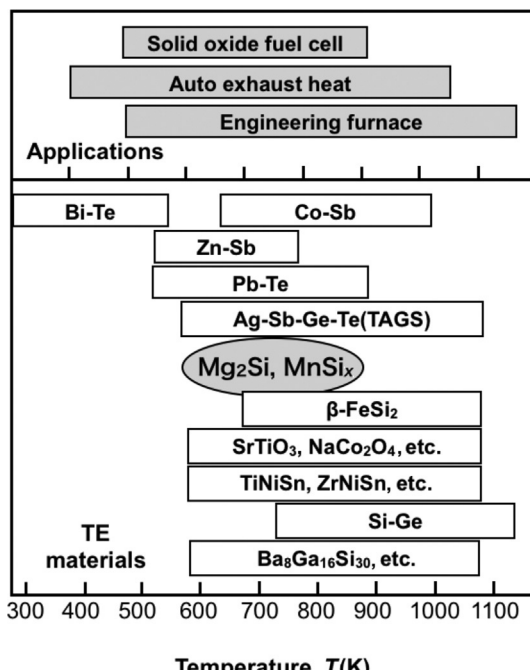


Fig. 2.16.10 Classification of TE materials as a function of operating temperature.

only by the shape and geometry of the TEG 66 but also by the thermal and mechanical properties of each element. Of these properties, the toughness of the silicides has been widely studied because most TE materials are brittle. Although the toughness of these silicides is relatively large compared with other TE materials, it is almost in the same range as that of brittle ceramics and intermetallics. In this chapter, recent studies in which the mechanical properties of Mg- and Mn-silicides have been examined are reviewed.

### 2.16.3.1 Modulus and hardness

In the past 10 years, many studies of the mechanical properties of TE materials have been carried out. Recent work examining the mechanical properties of Mg- and Mn-silicides at both room and elevated temperatures are summarized in Table 2.16.2. Each of the properties is described in the following section.

Elastic modulus is one of the most important parameters for a structural component because it tells us how a material will deform when a mechanical load is applied. The elastic modulus is a physical property that depends on the material. Most measurements of Young's modulus reported in the literature were obtained by bending, compression, or indentation tests. Moreover, the pulse-echo method and resonance ultrasound spectroscopy (RUS) have been used 66,68–72,74,79,80. An indentation test enables us to measure the local modulus and its distribution, although it is sensitive to sample preparation and microstructural heterogeneity, such as the grain size and crystal orientation. The pulse-echo and RUS methods are noncontact characterization techniques, which can be used to obtain elastic constants by measuring the time of flight of sound pulses in bulk materials. The natural frequency of the elastic vibrations and the number of normal modes together with the shape and mass of the sample can also be found. Both of these techniques are applicable to a wide range of sample sizes.

The elastic constant of single-crystal  $Mg_2Si$  was measured in pioneering work by Whitten et al. 67.  $Mg_2Si$  has a cubic structure ( $Fm\bar{3}m$ ) and has three elastic constants;  $c_{11}$ ,  $c_{12}$ , and  $c_{44}$ . For  $Mg_2Si$ ,  $C_{11}$ ,  $C_{12}$ , and  $C_{44}$  are  $121 \pm 0.2$ ,  $22 \pm 0.2$ , and  $46.4 \pm 0.05$  GPa, respectively. These elastic constants are almost the same as those obtained by first principle calculations 83. Manganese silicides have a wide range of atomic compositions, e.g., manganese mono-silicide ( $MnSi$ ),  $Mn_4Si_7$ ,  $Mn_7Si_{12}$ ,  $Mn_{11}Si_{19}$ ,  $Mn_{15}Si_{19}$ ,  $Mn_{26}Si_{45}$ ,  $Mn_{27}Si_{47}$ , and  $Mn_{39}Si_{68}$ . The crystal structures of these have also been determined and these have been found to depend on their atomic composition. In the case of single-crystalline  $MnSi$ , which has a cubic B20 crystal structure ( $P2_13$ ) with a lattice parameter of  $4.5598 \text{ \AA}$ ,  $C_{11}$ , and  $C_{44}$  are  $\sim 335$ , and  $\sim 123$  GPa, respectively 84.

Silicide-based TE materials are often fabricated by conventional metallurgical processes, i.e., hot-pressing (HP), and spark or activated plasma-sintering processes (PAS/SPS). The overall modulus ranges from 58 to 121 GPa for polycrystalline  $Mg_2Si$ , and 160 to 280 GPa for high manganese silicides (see Tables 2.16.2 and 2.16.3).

**Table 2.16.2** Overview of the mechanical properties of silicide-based TE materials.

Materials	Young's modulus, <i>E</i> (GPa)	Shear modulus, <i>G</i> (GPa)	Hardness, <i>Hv</i> (GPa)	Bending strength (MPa)	Compressive strength (MPa)	Fracture toughness (MPa $\text{m}^{1/2}$ )	Reference
<b>Magnesium silicide</b>							
Mg <sub>2</sub> Si (Single crystal)	C11: 121±0.2 C12: 22±0.2 C44: 46.4±0.05	N.A.	N.A.	N.A.	N.A.	N.A.	Whittenet al. 67
Sb-doped polycrystalline Mg <sub>2</sub> Si	105 (Ultrasonic) 102 (4PT bending) 143 (indentation)	N.A.	N.A.	55.4±6.4	430.5±44.4	0.62±0.05	Inoue et al. 68, Ishikawa et al. 69, Nakamura et al. 70, unpublished data
Mg <sub>2</sub> Si Mg <sub>2</sub> Si <sub>1-x</sub> Sn <sub>x</sub> ( <i>x</i> =0.4–0.6)	117.3 83±25 (compression) 58 (indentation)	49.5 N.A.	4.8–5.6 3.54	N.A. 79±10	N.A. 492±80	0.7–1.3(IF) 0.99 (IF)	Schmidt et al. 71 Gelbstein et al. 72
Mg <sub>2.15</sub> (Si <sub>0.3</sub> Sn <sub>0.7</sub> ) <sub>0.98</sub> Sb <sub>0.02</sub> Sb-doped Mg <sub>2</sub> Si (PM) Sb-doped Mg <sub>2</sub> Si (VM)	N.A. 113.6±0.3 (RUS) 110.4±0.2 (RUS)	N.A. 48.3±0.1 46.9±0.1	2.7±0.14 5.18±1.15 4.85±0.17	72±4 NA	458±81 NA	0.905±0.033 0.75±0.27 (IF) 0.73±0.11 (IF) ~0.82	Yin et al. 73 Schmidt et al. 74
Mg <sub>1.96</sub> Al <sub>0.04</sub> Si <sub>0.97</sub> Bi <sub>0.03</sub>	N.A.	N.A.	N.A.	N.A.	N.A.	N.A.	Kim et al. 2017 75, 76 2018, 2019 77, 2019 78

Table 2.16.2 Continued

Materials	Young's modulus, <i>E</i> (GPa)	Shear modulus, <i>G</i> (GPa)	Hardness, <i>Hv</i> (GPa)	Bending strength (MPa)	Compressive strength (MPa)	Fracture toughness (MPa·m <sup>1/2</sup> )	Reference
Mg <sub>2</sub> Si <sub>0.6</sub> Sn <sub>0.4</sub>	90 (impulse excitation) 82(at 500°C)	N.A.	4.5±0.15	NA	NA	1.0±3 (SENB) 0.1±0.15 (IF)	Mejri et al. <a href="#">79</a>
Mg <sub>2.08</sub> Si <sub>0.4-x</sub> Sn <sub>0.6</sub>	88.13±0.15 (RUS)	36.87±0.04	3.07±0.06	NA	NA	0.48±0.05 (IF)	Gao et al. <a href="#">80</a>
Bi- and Al-doped Mg <sub>2</sub> Si	Tensile strength: 0.8 MPa (un-doped), 1.4 MPa (Bi-doped), 1.6 MPa (Al-doped)						Satyala et al. <a href="#">81</a>
<b><i>MnSi</i></b>							
MnSi	N.A.	N.A.	N.A.	130–150	1146±120	N.A.	Inoue et al. unpublished work <a href="#">82</a>
HMS	160±30 (compression) 182 (indentation) 281 (impulse excitation) 263(at 500°C)	N.A.	11.85 (GPa)	178±10	1083±150	1.63	Gelstein et al. <a href="#">72</a>
MnSi <sub>1.77</sub>		N.A.	16.0±1.1 (GPa)	N.A.	N.A.	2.5±3 (SENB) 1.6±0.15 (IF)	Mejri et al. <a href="#">79</a>

**Table 2.16.3** Overview of the mechanical properties of silicide-based TE materials with various second-phase additives.

Materials	Young's modulus, $E$ (GPa)	Shear modulus, $G$ (GPa)	Hardness $H_V$ (GPa)	Bending strength, $\sigma_B$ (MPa)	Compressive strength, $\sigma_c$ (MPa)	Fracture toughness, $K_c$ (MPa·m $^{1/2}$ )	Reference
Sb-doped polycrystalline Mg <sub>2</sub> Si	112±0.26 114±0.28	N.A.	N.A.	N.A.	N.A.	0.62±0.05 0.79±0.08	Inoue et al. <a href="#">68</a>
1.0 vol%-SiC nanoparticle (intergranular)	119±0.12					0.92±0.07	
5.0 vol%-SiC nanoparticle (intergranular)	118±0.11					0.90±0.08	
5.0 vol%-SiC nanoparticle (intragranular)	121					0.95±0.06	
1.0 vol%-SiC nanoparticle (intragranular)	131±0.16					1.02±0.10	
5.0 vol%-SiC nanoparticle (intragranular)							
10.0 vol%-SiC nanoparticle (intragranular)							
Mg <sub>2</sub> Si <sub>1-x</sub> Sn <sub>x</sub>	N.A.	N.A.	2.7±0.14	72±4	458±81	0.905±0.03	Yin et al. <a href="#">73</a>
0.002-SiC nanoparticle			2.93±0.1	71.3±6.4	490±52	1.17±0.03	
0.004 SiC nanoparticle			2.97±0.12	72.7±5.1	521±64	1.23±0.06	
0.006 SiC nanoparticle			3.00±0.14	71.7±8.2	558±76	1.27±0.03	
0.008 SiC nanoparticle			3.02±0.12	72.4±7.7	599±53	1.29±0.04	
0.002-SiC nano-whisker	N.A.	N.A.	2.85±0.12	72.9±5.4	474±62	1.18±0.04	
0.004 SiC nano-whisker			2.92±0.1	75.7±7.1	500±72	1.25±0.06	
0.006 SiC nano-whisker			2.96±0.09	79.8±2.3	533±85	1.31±0.05	
0.008 SiC nano-whisker			2.99±0.12	84.5±4.5	568±80	1.36±0.04	
Sb-doped Mg <sub>2</sub> Si (PM)	113.6±0.3	48.3±0.1	5.66±0.71	NA	NA	0.862±0.14	Schmidt et al. <a href="#">74</a>
0.5 vol SiC nanoparticle	112.9±0.3	47.5±0.1	4.84±0.13			0.723±0.12	
1.0 vol- SiC nanoparticle	111.2±0.3	46.1±0.1	4.78±0.1			1.14±0.21	
1.5 vol SiC nanoparticle	105.8±0.4	43.3±0.1	4.79±0.15			0.46±0.08	

2.0 vol SiC nanoparticle	$118.1 \pm 0.2$	$50.3 \pm 0.1$	$4.51 \pm 0.24$			$0.899 \pm 0.10$		
3.0 vol SiC nanoparticle	$116.7 \pm 0.2$	$49.7 \pm 0.1$	$4.64 \pm 0.21$			$0.814 \pm 0.12$		
4.0 vol SiC nanoparticle	$114.5 \pm 0.6$	$49.7 \pm 0.2$	$4.71 \pm 0.16$			$0.673 \pm 0.1$		
Sb-doped Mg <sub>2</sub> Si (VM)	$110.4 \pm 0.2$	$46.9 \pm 0.1$	$4.58 \pm 0.11$	NA	NA	$0.694 \pm 0.05$		
0.5 vol SiC nanoparticle	$107.6 \pm 0.4$	$44.7 \pm 0.1$	$4.73 \pm 0.15$			$0.601 \pm 0.05$		
1.0 vol SiC nanoparticle	$113.4 \pm 0.2$	$48.3 \pm 0.1$	$4.60 \pm 0.09$			$0.602 \pm 0.04$		
1.5 vol SiC nanoparticle	$113.0 \pm 0.2$	$48.1 \pm 0.1$	$4.71 \pm 0.12$			$0.628 \pm 0.05$		
2.0 vol SiC nanoparticle	$111.3 \pm 0.3$	$47.5 \pm 0.1$	$4.63 \pm 0.11$			$0.684 \pm 0.07$		
Mg <sub>1.96</sub> Al <sub>0.04</sub> Si <sub>0.97</sub> Bi <sub>0.03</sub>	N.A.	N.A.	N.A.	N.A.	N.A.	$0.82 \pm 0.05$	Kim et al. <a href="#">77</a>	
1.0 vol rGO (graphene oxide)						$1.06 \pm 0.09$		
2.0 vol rGO (graphene oxide)						$1.42 \pm 0.34$		
3.0 vol rGO (graphene oxide)						$1.90 \pm 0.21$		
4.0 vol rGO (graphene oxide)						$2.19 \pm 0.57$		
Mg <sub>1.96</sub> Al <sub>0.04</sub> Si <sub>0.97</sub> Bi <sub>0.03</sub>	N.A.	N.A.	N.A.	N.A.	N.A.	$0.809 \pm 0.03$	Kim et al. <a href="#">76</a>	
0.3 Sn						$0.965 \pm 0.06$		
0.6						$1.03 \pm 0.05$		
0.9						$1.05 \pm 0.08$		
1.2						$1.07 \pm 0.08$		
1.8						$1.09 \pm 0.10$		
2.4						$1.14 \pm 0.12$		
Mg <sub>1.96</sub> Al <sub>0.04</sub> Si <sub>0.97</sub> Bi <sub>0.03</sub>	N.A.	N.A.	N.A.	N.A.	N.A.	$0.809 \pm 0.03$	Kim et al. <a href="#">75</a>	
0.6 vol Cu						$0.949 \pm 0.11$		
0.6 vol Al						$1.06 \pm 0.11$		
0.6 vol Sn						$1.03 \pm 0.05$		

The modulus of polycrystalline materials is also related to their porosity (P) and can be determined from some empirical equations 85. Schmidt et al. has reported that Young's modulus of sintered Mg<sub>2</sub>Si can be obtained with the following equation 74:

$$E = E_0(1 - \alpha P) \quad (2.16.1)$$

where  $E_0$  is Young's modulus of pore-free material,  $\alpha$  is a material-dependent constant, typically between 2 and 6 for a wide range of materials. Thus, the formation of pores should be prevented in order to increase the overall modulus of polycrystalline TE materials. The sintering conditions, such as the pressure, temperature, sintering time, etc., must be optimized.

### 2.16.3.2 Toughness

The formation of defects, such as cracks and pores, is inevitable during the manufacturing process as well as operation at elevated temperatures. When TE modules are subjected to mechanical and thermal stresses, significantly higher stress occurs at defects compared with the average stress because cracks propagate easily in brittle materials even if the external load is low.

The fracture toughness of TE materials is often measured by an indentation fracture (IF) technique and/or a bending test on a single-edge notched beam (SENB) specimen. In the case of conventional structural materials such as metals, a compact tension (CT) specimen is widely used; however, it is difficult to prepare CT specimens because they cannot be machined, and the specimen size is small. The IF technique is applicable even if the specimen is quite small. A pyramidal diamond indenter is impressed into the specimen surface, and the toughness is measured by the length of the crack from the corner of the indenter. The toughness,  $K_c$ , is measured by the length of the crack, which nucleates from the corner of the indenter, and the dimensions of the Vickers indentation. The relationship between the crack length and the indentation toughness,  $K_c$ , is expressed as 86

$$K_c = 0.016 \frac{E^{\frac{1}{2}} P^{\frac{1}{2}} a}{c^{\frac{3}{2}}} \quad (2.16.2)$$

where  $P$  is the applied load,  $E$  is Young's modulus of the composite,  $c$  is the mean crack length, and  $a$  is half the length of the diagonal of the impression. It should be noted that this equation can be used in the case of the formation of median/radial cracks.

The SENB test is also widely used as a standard test method for brittle intermetallics, ceramics, and composites. Mejri et al. 79 reported that the toughness of Mg<sub>2</sub>Si<sub>0.6</sub>Sn<sub>0.4</sub> and HMS are  $1.0 \pm 0.1 \text{ MPa}\cdot\text{m}^{1/2}$  and  $2.5 \pm 0.3 \text{ MPa}\cdot\text{m}^{1/2}$ , respectively. These values are in the same range as glass, which is a typical brittle material.

As mentioned in Ref. 87, improving the toughness of silicide-based materials is recognized as a critical problem for practical usage and much effort has gone into improving the toughness of various materials (described in [Section 2.16.3.5](#)).

### 2.16.3.3 Strength

The strength of TE materials is determined by the toughness and the crack length based on a fracture mechanics approach. The strength is often measured by a bending test using a rectangular specimen. A four-point bending test is widely conducted for brittle materials because the stress concentration at the contact area between the specimen and the loading device can be reduced compared with a three-point bending test. When a bending load is applied, a stress gradient is generated through the thicker part of the specimen. The maximum tensile/compressive stress occurs at the surfaces of the specimen. In the case of dense material, failure initiates from surface flaws and unstable crack propagation occurs for a moment. Assuming the crack propagates from the tensile surface at the critical load, the bending strength ( $\sigma_b$ ) can be calculated from the following equations:

$$\sigma_b = \frac{3Pl_s}{2bh^2} \text{ (for three - point bending)} \quad (2.16.3)$$

$$\sigma_b = \frac{3P(l_s - l_L)}{2bh^2} \text{ (for four - point bending)} \quad (2.16.4)$$

where  $l_s$  and  $l_L$  are the distances between the support points and the load points, respectively. The research group of Tokyo University of Science has investigated the strength of polycrystalline Mg<sub>2</sub>Si and High-Manganese-Silicide (HMS) fabricated by SPS. Their bending strengths at room temperature are 57 MPa for Sb-doped Mg<sub>2</sub>Si [69](#) and 130–150 MPa for HMS, respectively.

Recently, some new experimental techniques have been applied to measure the strength of TE materials under various stress states. Satyala et al. [81](#) also reported on a uniaxial diametral compression test for measuring the tensile strength of Mg<sub>2</sub>Si with glass inclusions. They concluded that the tensile strength was ~2 MPa. Ren et al. [88](#) and Morrison et al. [89](#) also characterized the biaxial flexure strength of lead-antimony-silver-tellurium (LAST) and lead-antimony-silver-tellurium-Tin (LAST-T) compounds, by means of a ball-on-ring and a ring-on-ring test. These techniques avoid the complication of specimen failure from the edge, which is often a problem in uniaxial testing of brittle materials [85](#). They also tried to evaluate the scatter in the fracture strength of LAST and LAST-T. The fracture strength of brittle materials is often determined by the size of the defects and flaws. In order to reduce the size and amount of these, the processing conditions were optimized; however, they could not eliminate them completely. Scatter in the strength is inevitable. This factor should be taken into account when designing TEGs; however, statistical approaches on the strength of TE materials are quite limited [88,90](#), and this type of work is still in progress.

### 2.16.3.4 Mechanical properties at elevated temperatures and long-term durability

Most studies have focused on the mechanical properties at room temperature. Studies examining the properties at elevated temperatures are quite limited. The overall modulus at elevated temperatures has been examined by free resonance with impulse excitation. Ishikawa et al. 69 reported on the temperature dependence of the overall modulus of polycrystalline Mg<sub>2</sub>Si. This can be expressed as a function of temperature  $E(T)$

$$E(T) = -10^{-8}T^3 + 2 \times 10^{-5}T^2 - 0.0296T + 113.36 \quad (2.16.5)$$

where  $T$  is the temperature. Mejri et al. 17 also reported that the modulus of Mg<sub>2</sub>Si<sub>0.6</sub>Sn<sub>0.4</sub> is

$$E(T) = 90.66 - 14.910^{-3}T - 310^{-6}T^2 - 410^{-9}T^3 \text{ (for Mg}_2\text{Si}_{0.6}\text{Sn}_{0.4}) \quad (2.16.6)$$

$$E(T) = 280.70 - 2610^{-3}T - 2010^{-6}T^2 + 610^{-9}T^3 \text{ (for MnSi}_{1.77}) \quad (2.16.7)$$

Generally, the modulus reduces with increasing temperature. In other words, the material easily deforms above the yield stress although it has large deformation. The temperature dependence of the modulus is required in order to simulate the stress/strain distribution of TEGs by computational and numerical analysis.

Fig. 2.16.11 shows the compressive stress-displacement curves of two representative silicides (Mg<sub>2</sub>Si and HMS) at room temperature and elevated temperature

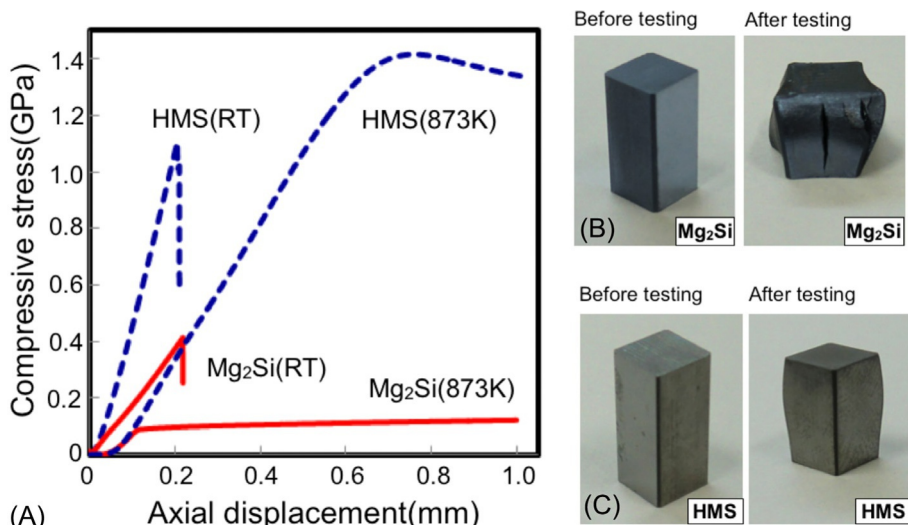


**Fig. 2.16.11** (A) Compressive stress-axial displacement curves of Mg<sub>2</sub>Si and HMS fabricated by an SPS process. (B) and (C) Appearance of Mg<sub>2</sub>Si and HMS specimens before and after the tests at elevated temperature.

(873 K). A linear stress-strain relationship is seen at room temperature. Then, the stress reaches a maximum and drops catastrophically. At 873 K, the slopes of the curves decrease, and failure occurs at low stress with large deformation. Barreling and lateral cracking are seen. Takeuchi et al. 91 also examined the compressive behavior of coarse-grained Mg<sub>2</sub>Si. They reported that the yield stress is lower than 10 MPa above ~903 K. Li et al. 92 also reported that the ductile-brittle transition temperature (DBTT) of Mg<sub>2</sub>Si is 793 K and that the DBTT is dependent on the Al content. This is also a critical issue because it is easily deformed at low stress.

For practical usage, creep and fatigue are important for predicting lifetime because TEGs are subjected to mechanical loads and thermal cycles for long periods. However, investigations of the long-term durability of TE materials have been limited. Michi et al. 93 reported on the compressive creep behavior of hot-pressed Mg<sub>1.96</sub>Al<sub>0.04</sub>Si<sub>0.97</sub>Bi<sub>0.03</sub>. The relationship between the applied stress ( $\sigma$ ) and the minimum strain rate,  $\dot{\varepsilon}$ , is given by

$$\dot{\varepsilon} = A\sigma^n \exp\left(-\frac{Q}{R_g T}\right), \quad (2.16.8)$$

where  $A$ ,  $n$ ,  $R_g$ , and  $Q$ , are a constant, the stress exponent, gas constant, and the activation energy for creep, respectively. They discussed the stress components of the materials and the deformation mechanism. They mentioned that grain boundary sliding is pinned by Bi-, Al-, and O-rich particles and concluded that Mg<sub>1.96</sub>Al<sub>0.04</sub>-Si<sub>0.97</sub>Bi<sub>0.03</sub> has good creep resistance compared with other TE materials such as PbTe and Bi<sub>2</sub>Te. Case et al. 94,95 also pointed out the importance of understanding the degradation mechanisms of TE materials under thermal fatigue. However, a comprehensive knowledge of the degradation of TE materials by creep and fatigue is still not well established.

### 2.16.3.5 Toughening of TE materials

As mentioned above, the toughness of silicide-based TE materials is in the same range as that of glass, although the toughness values are relatively higher than that of other TE materials. For structural usage, toughening is an important issue because unexpected failure occurs through the application of external loads and the generation of thermal stress. The way to improve toughness from the microstructural viewpoint is either by “grain refinement” or the “addition of a second phase.”

Grain refinement is an effective way of simultaneously increasing the toughness and strength of brittle polycrystalline materials. Refining the grain can limit the size of preexisting microcracks. Here, the failure stress ( $\sigma_f$ ) is expressed based on a linear elastic fracture mechanics (LEFM) approach

$$\sigma_f = \frac{K}{Y \sqrt{\pi a_{cri}}} \quad (2.16.9)$$

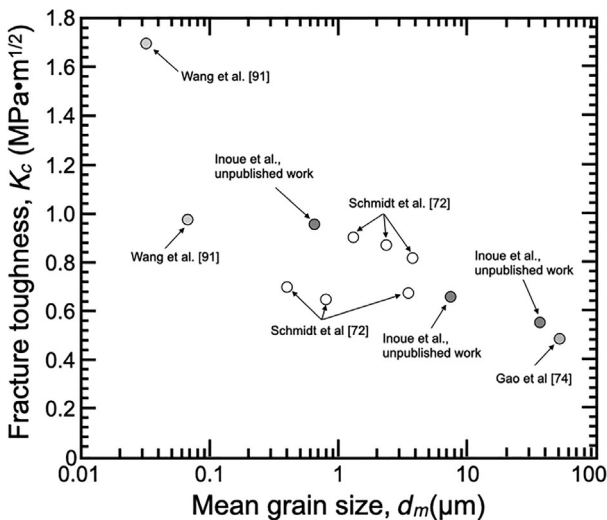


**Fig. 2.16.12** Plot of fracture toughness as a function of mean grain size.

where  $K$ ,  $a_{cri}$ , and  $Y$  are the stress intensity factor, the critical crack length, and a constant depending on the specimen shape and the loading conditions, respectively. In many works the toughening effect of grain refinement has been examined in various oxides and non-oxide ceramics (e.g., Ref. 96). **Fig. 2.16.12** shows the relationship between the mean grain size ( $d_m$ ) and the toughness ( $K_c$ ) of polycrystalline TE materials. Conventional milling techniques such as vibratory and planetary ball milling have been used to reduce grain size. Wang et al. 97 also reported that hot-pressed nano-sized ( $d=33\text{ nm}$ ) polycrystalline  $\text{Mg}_2\text{Si}$ , synthesized by a mechanically activated solid-state reaction reaches a toughness of  $1.67\text{ MPa}\cdot\text{m}^{1/2}$ , which is the highest value reported in the literature.

The addition of a second phase is also effective for enhancing toughness. In the case of brittle matrix composites, fibers, whiskers, flakes, and particles are added. The toughening mechanisms for ceramics and their composites have been reviewed (e.g., Refs. 98–100). **Fig. 2.16.13** shows plots of the toughness of  $\text{Mg}_2\text{Si}$  with second-phase additives. In the case of particulate composites with a volume fraction of  $\sim 10\%$ , the toughness was increased by up to  $\sim 2.2\text{ MPa}\cdot\text{m}^{1/2}$  77.

In the case of particulate composites, the main toughening mechanism is crack deflection at the interface between the silicide grains and the second phase. Toughening is achieved by changing the loading mode at the tip of the crack. Theoretical analysis showed that the toughness depends on the volume fraction of the second-phase additive and its aspect ratio 39,40. To toughen polycrystalline materials, micro-sized and nano-sized metal/ceramic particles are used for the second-phase additive. The mechanical and thermal properties of second-phase additives are also important. In the case of  $\text{Mg}_2\text{Si}$ , oxides 101–103, carbides 71,72,77,97, and metals 40–42,74 have been used for reinforcement. The addition of metal particles is an

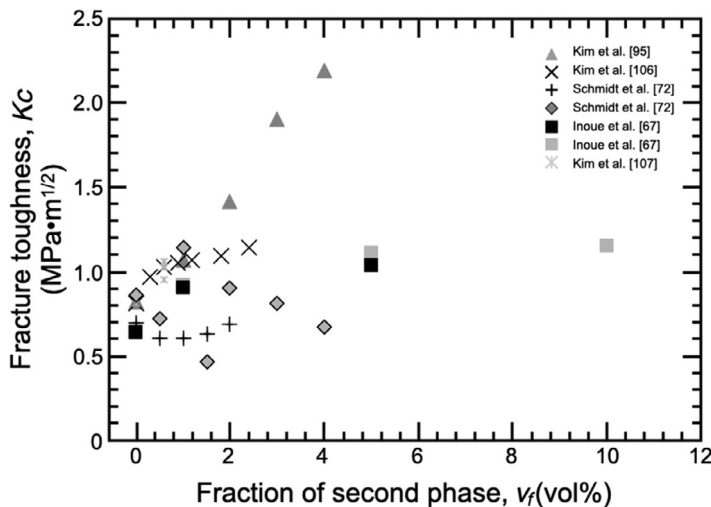


**Fig. 2.16.13** Plot of fracture toughness as a function of the volume fraction of second-phase additives.

attractive way of increasing toughness because the fracture energy dissipates by plastic deformation, as reviewed in Ref. 104; however, the melting point of metal particles is generally lower than that of  $\text{Mg}_2\text{Si}$  (1358 K). Of the ceramic particles, silicon carbide has been widely used as a second-phase additive because they have low density, high melting point, and high modulus, etc. SiC additives with various dimensions and shapes are available. Of these factors, the aspect ratio of the reinforcement strongly contributes to toughening even if the volume fraction is the same. The toughening effect due to rods (aspect ratio:  $R=12$ ) is 2–3 times larger than that due to particles ( $R=1$ ). Toughening mechanisms are classified into two categories: shielding and non-shielding mechanisms. In the case of a large aspect ratio, the second-phase additive sustains the load directly by crack bridging and the failure energy dissipates during pull out of the reinforcement as often seen in structural fiber reinforced ceramics. Previous studies by Yin et al. 73 and Kim et al. 78 have also shown that the addition of reinforcements with high aspect ratios (SiC-nano wires, and graphene oxide) strongly contribute to enhancing the toughness by crack bridging.

### 2.16.3.6 Simultaneous enhancement of toughness and ZT

Grain refinement and the addition of a second phase have the potential for improving the toughness above  $2 \text{ MPa}\cdot\text{m}^{1/2}$ . However, these are predominantly distributed at the grain boundaries and they reduce the transport properties. Fig. 2.16.14 shows the relationship between the volume fraction of the second phase, the fracture toughness, and ZT at 873 K. As the second-phase additives are increased, a significant decrease in ZT is seen. An excessive amount of the second phase is not effective for maintaining the transport properties of silicides.

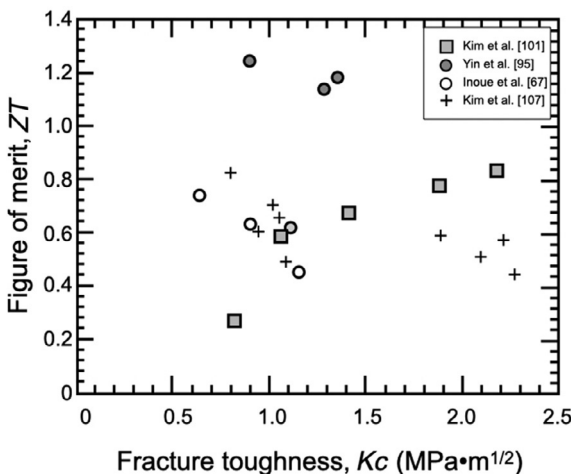


**Fig. 2.16.14** Relationship between fracture toughness, and ZT at the maximum temperature.

Theoretical analyses showed that the effectiveness of grain refinement on the transport properties increases if the grain size is less than 100 nm 103,104. However, the production of bulk materials with nano-sized grains is quite difficult because it is easy to form impurities by preferential oxidation of the surface. Oxidation proceeds easily as the grain diameter decreases because the fine grains have a significantly higher specific surface 105. Recently, the formation of impurities at the grain boundaries has been recognized as a critical problem. In the case of Mg<sub>2</sub>Si, preferential oxidation occurs via the following reaction 106:



As a result, large amounts of MgO are formed as the grain diameter decreases. de Boor et al. 107 investigated the thermoelectric properties of Mg<sub>2</sub>Si with different grain sizes of 13–56 μm. They also conducted a quantitative analysis of the effect of the MgO content on the figure of merit (ZT) and boundary scattering by a single parabolic band (SPB) model. Their results showed that 7 wt% of MgO contributes to a 30% reduction in ZT 107. There have been many attempts to optimize processing parameters such as the grain size, the process temperature, the sintering pressure, etc. 77,103, to inhibit the formation of MgO; however, an effective way of fabricating high purity Mg<sub>2</sub>Si without impurities has not yet been established. It is a critical problem to achieve a simultaneous increase of TE and improvement in the mechanical properties.

Attempts to break through the trade-off relationship between toughness and ZT have also been done. Inoue et al. 68 reported on the toughness and ZT of an intragranular Mg<sub>2</sub>Si composite. They introduced second-phase additives into the Mg<sub>2</sub>Si grains by a melting process. They successfully fabricated an intragranular Mg<sub>2</sub>Si/SiC composite with 10 vol% SiC with a small reduction in electrical conductivity. Kim et al. 78,82 also reported that the use of multidimensional dual nano-additives is an effective way to increase toughness without reducing ZT.

### 2.16.3.7 Current status and future works

In this chapter, an overview of recent work on the mechanical properties is presented. Various techniques are applicable for understanding the fundamental mechanical properties and failure behavior of TE materials. For practical applications, the lack of experimental data on long-term durability such as creep, and fatigue is still a problem. The data is also insufficient for statistical analysis. The brittleness can be improved by various methods such as grain refinement and the addition of a second phase. Some material designs have also been proposed to achieve an increase in toughness without reducing the transport properties.

## 2.16.4 Theoretical and computational study: The electronic, structural, and thermoelectric properties of impurity-doped Mg<sub>2</sub>Si

This portion reviews the theoretical research on environmentally friendly thermoelectric material, Mg<sub>2</sub>Si, and related materials. This research aims to develop high-quality thermoelectric materials with high performance and good stability by doping with impurities. Impurity doping is a well-established method used to improve the thermoelectric performance of Mg<sub>2</sub>Si; however, it requires higher thermoelectric conversion efficiency than is currently available if it is to achieve widespread application. Doping with impurity atoms that have a different valence number from that of the matrix is expected to change the carrier density and the structural properties of the material (e.g., the lattice parameter). Evidently, it is likely the electronic states near the Fermi level are affected by the formation of impurity states. These effects should determine the thermoelectric performance of the system; however, direct observation of the effects of impurity doping on the detailed electronic states is quite difficult in general. Therefore, first-principles calculations have been utilized to determine the electronic, structural, and carrier transport properties of thermoelectric materials.

We briefly explain first-principles calculation methods based on density-functional theory (DFT). The method determines the ground-state electronic structure of a crystal without empirical parameters by solving the following Kohn-Sham equation for a given potential  $V_{\text{eff}}$  that reduces the many-body problem for electronic states to an effective single-particle problem:

$$\left( -\frac{\hbar^2}{2m} \nabla^2 + V_{\text{eff}} \right) \psi_i = \varepsilon_i \psi_i, \quad (2.16.11)$$

where  $\psi_i$  is the Kohn-Sham orbital and  $\varepsilon_i$  is the corresponding orbital energy. The electron density for an  $N$ -particle system is given by  $\rho(\mathbf{r}) = \sum_{i=1,N} |\psi_i(\mathbf{r})|^2$ . A single electron algorithm that can be used to solve Eq. (2.16.11) under periodic boundary conditions utilizes the full-potential linearized augmented plane wave (FLAPW) method. This method provides electronic states with high accuracy. However, as it is computationally quite expensive, techniques to reduce the computational cost are often needed for its application to supercells doped with impurities. Another

method within the DFT framework is a pseudo-potential calculation, which has a more reasonable computational cost. The potential  $V_{eff}$  in Eq. (2.16.11) contains an exchange-correlation term, the treatment of which can also be important for the calculation results. Two of the most common methods are a local density approximation (LDA) and a generalized gradient approximation (GGA). However, a typical issue when using LDA or GGA is underestimating the value of the bandgap. For instance, it is estimated to be approximately 0.17 eV using LDA for Mg<sub>2</sub>Si 108,109 which is much smaller than the experimental value, 0.61–0.78 eV 110–112. Several alternative methods exist; e.g., DFT+U adds the Hubbard parameter U to correct the self-interaction errors of these standard DFT functionals. However, it cannot substantially improve the value of the bandgap; this may be because the conduction and valence band edges of Mg<sub>2</sub>Si consist mainly of s and p orbitals. Another type of function is the modified Becke-Johnson (mBJ) potential 113, which has been reported to considerably improve the calculated value of the bandgap such that it agrees with the experimental result 114. The Heyd-Scuseria-Ernzerhof hybrid functional also reproduces the experimental bandgap 115. Although these methods are computationally expensive, they are useful for overcoming the limitations of these standard DFT functionals.

Hereinafter, in reviewing previous work using first-principles calculations, we outline several theoretical techniques used to manage impurity-doped systems which may be useful for the computational design of Mg<sub>2</sub>Si and related materials.

#### 2.16.4.1 Electronic and thermoelectric properties of n-type and p-type Mg<sub>2</sub>Si

Fig. 2.16.15A shows the electronic states of pure Mg<sub>2</sub>Si obtained using the full-potential linearized augmented-plane-wave (FLAPW) method in the all-electron band-structure calculation package (ABCAP) 116. We employed the LDA and plane-wave cutoff energy of 60.0 Ha. Brillouin zone sampling was performed using

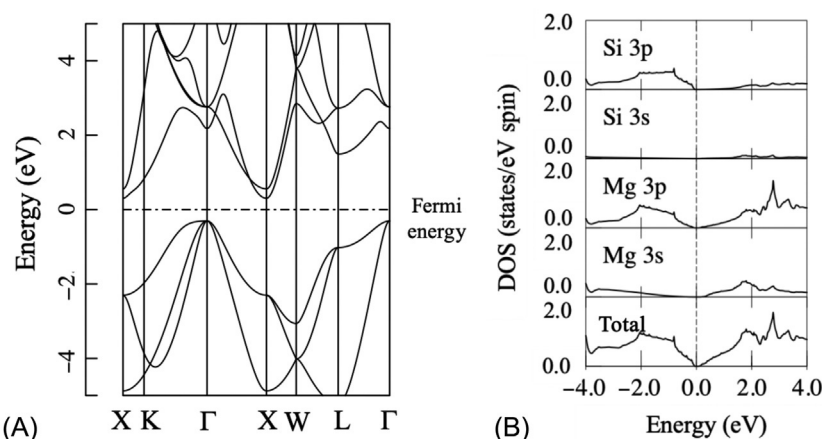


**Fig. 2.16.15** (A) Electronic band dispersion and (B) density of states (DOS) for the pure Mg<sub>2</sub>Si that was obtained using the FLAPW method in the ABCAP code.

a  $k$ -point grid with a (12, 12, 12) mesh for the unit cell. For self-consistent field calculations, the convergence threshold of the total energy was  $3.0 \times 10^{-7}$  eV.

The band dispersion has an indirect gap between the  $\Gamma$  point at the top of the valence band and the X point at the bottom of the conduction band. The calculated bandgap was approximately 0.173 eV, which is much smaller than the experimental value, as is typical with DFT. The top of the valence bands degenerates at the  $\Gamma_{15}$  point, as per the BSW notation 117. The upper two bands consist of Si 3p and Mg 3p states, and the lowest energy band is assigned to the Si 3p and Mg 3s orbitals. This result agrees with an experiment result obtained by Bevolo and Shanks using Auger spectroscopy 118. As they pointed out, this result suggests the covalency of  $Mg_2Si$ . As to the bottom of the conduction band at the X point, two bands exist with an energy difference of approximately 0.3 eV. The first and second conduction bands belong to different irreducible representations of the point group ( $X_1$  and  $X_3$ , respectively). The predominant contributions to the first band are Si 3s and Mg 2p orbitals; the second band consists mainly of an Mg 3s orbital without hybridization with the other atomic orbitals.

Fig. 2.16.15B shows the density of states (DOS) of  $Mg_2Si$ . The DOS rapidly increases at the valence band edge due to band degeneracy at the  $\Gamma$  point. As the steepness of the DOS around the Fermi level is essentially related to the magnitude of the Seebeck coefficient, carrier tuning is necessary to achieve high thermoelectric efficiency.

Based on the obtained band dispersion, we can calculate the group velocity of the carriers and thus, the effective mass was obtained under the effective mass approximation (see Ref. 109 for the details of the calculation). For slight n-type doping, the energy isosurface in  $k$ -space in the vicinity of the conduction-band minima is located at the X point. The energy isosurface is assumed to have the form of a spheroid with the principal axis along the  $\langle 100 \rangle$  direction, as depicted in Fig. 2.16.16. There are

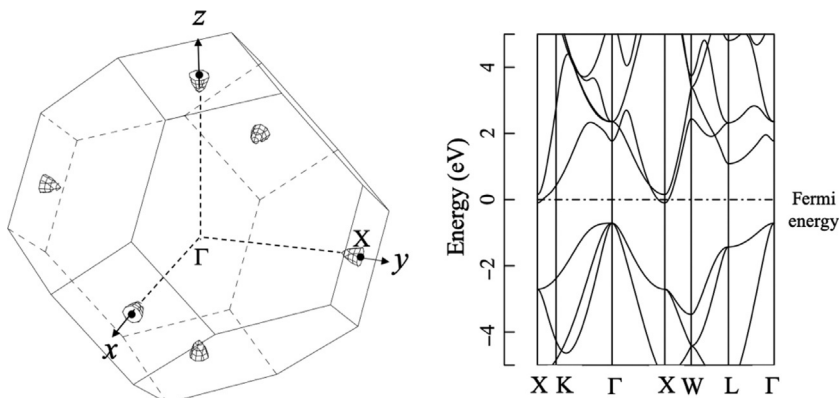


**Fig. 2.16.16** Equi-energy surfaces of the conduction band bottom in the Brillouin zone where the concentration of carriers is  $3 \times 10^{19} \text{ cm}^{-3}$  (left) and the corresponding electronic states (right). As shown in the band, the Fermi energy is located on the conduction band with the lowest energy.

three equivalent anisotropic minima at the X valley; one longitudinal mass along the  $<100>$  direction,  $m_L^*$ , and two transverse masses in the perpendicular directions,  $m_T^*$ . Using the ABCAP code with LDA,  $m_L$  and  $m_T$  were calculated to be  $0.582m_0$  and  $0.201m_0$ , respectively ( $m_0$  is the electron rest mass), under the effective mass approximation. The results are consistent with a calculation 119 performed using the modified Perdew-Burke-Emzerth of generalized gradient approximation (PBEsol GGA):  $m_L=0.582m_0$  and  $m_T=0.187m_0$ . The DOS mass  $m_{\text{DOS}}^*$  is  $0.596m_0$ , calculated from the geometric average:  $m_{\text{DOS}}^*=N_m^{2/3}(m_L m_T^2)^{1/3}$ , where the number of equivalent minima  $N_m=3$  for the X minima of Mg<sub>2</sub>Si. This successfully reproduced the experimental data obtained from Hall measurements ( $m_{\text{DOS}}^*=0.57m_0$ ) 111. The results show that first-principles calculation based on the FLAPW method effectively reproduces the electronic states of Mg<sub>2</sub>Si around the Fermi level. Although the experimental bandgap cannot be reproduced using LDA and GGA, as described above, the results validate FLAPW as an efficient tool for analyzing the electronic and carrier transport properties of this material.

[Fig. 2.16.17](#) represents the thermoelectric properties: the Seebeck coefficient S, the electrical conductivity  $\sigma/\tau$ , and the power factor PF for n-type Mg<sub>2</sub>Si calculated using the Boltzmann transport theorem with the constant relaxation time ( $\tau$ ) approximation. In the calculations, we assumed n-type doping using the rigid band approximation, i.e., we shifted the Fermi level to the position corresponding to the assumed carrier concentration without changes to the electronic band dispersion or crystal lattice from that of pure Mg<sub>2</sub>Si. In addition, before the thermoelectric calculation, the bandgap was corrected to the experimental value obtained from the following function:  $E_g=E_{g0}+\beta T$ , where  $E_{g0}=0.78$  eV,  $\beta=-5 \times 10^{-4}$  eV/K 110,120 (a scissors operation). [Fig. 2.16.17](#) shows that the PF is significantly affected by the carrier doping concentration, as expected from the above discussion. Therefore, because of this high sensitivity of the thermoelectric performance to the carrier concentration, fine-tuning of the carrier concentration by impurity doping is required to maximize the performance.

Before proceeding to the next topic, we comment the correspondence between the calculated and experimental observations. Evidently, the rigid band approximation is valid only when the added dopants supply carriers to the system without significant changes in the band dispersion adjacent to the Fermi level. Despite this rough treatment, the values of S obtained from the FLAPW calculations with LDA quantitatively agree with the experimental data over a wide temperature range for undoped Mg<sub>2</sub>Si 108 and doped systems with Bi 108 and Sb 121 (n-type) at 350–850K and Ag 108 (p-type) at 350–600K.

#### 2.16.4.2 Screening of impurity elements in Mg<sub>2</sub>Si

To examine the feasible sites and the stability of candidates for impurity dopants for Mg<sub>2</sub>Si, we performed variable-cell relaxation calculations for systems doped with the impurities. Mg<sub>2</sub>Si has an antifluorite crystal structure with the Fm-3m space group. We assumed three types of impurity sites: substitutional Mg- and Si-sites and interstitial insertion into the cell at the 4b site, as shown in [Fig. 2.16.18](#). The conventional

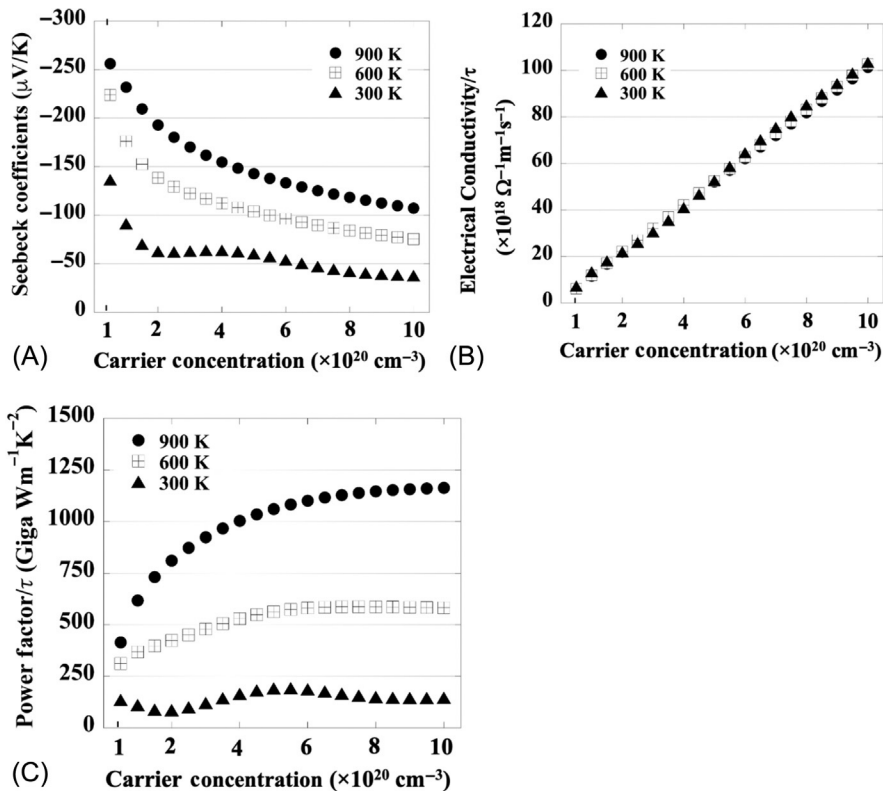


**Fig. 2.16.17** Dependences of thermoelectric properties: (A)  $S$ , (B)  $\sigma/\tau$ , and (C)  $PF/\tau$  of  $n$ -type  $\text{Mg}_2\text{Si}$  on the doping concentration. The temperature is assumed to be 300 K. The band gap value was corrected to match the experimental values corresponding to temperature before calculation was performed.

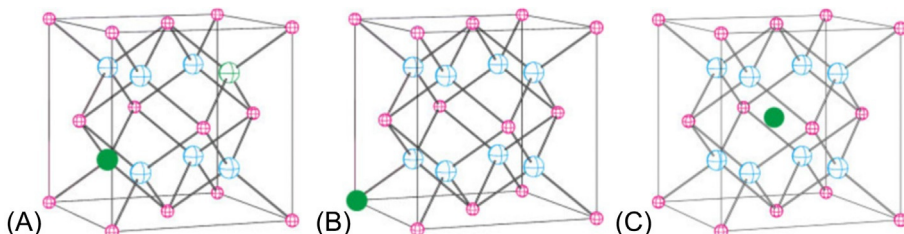


**Fig. 2.16.18** Three types of impurity sites are depicted; an impurity atom is substituted for (A) Mg and (B) Si atoms, and (C) it is inserted into the 4b site.

unit cell contains 12 (4 Si and 8 Mg) atoms; thus, assuming simple cubic (sc) periodicity for the atomic positions of the impurities, their atomic fraction in the cell, i.e., the doping concentration  $x$  (at%), is equal to 8.333 at%. Although experimental systems have lower values of  $x$ , it is computationally expensive to use such systems because it requires a larger cell containing more atoms. Therefore, we assumed the value of  $x$  to

**Table 2.16.4** Parameters used in the variable-cell relaxation calculations for impurity-doped systems.

Cell size	$1 \times 1 \times 1$
Doping site	Mg-, Si-, or 4b-site
Impurity concentration	8.3333%
Calculation code	Quantum Espresso
Pseudo-potential	Norm conserving
Electron correlation	GGA-PBE
Threshold on total energy	$10^{-5}$ Ry/Bohr
Threshold on forces	$10^{-4}$ Ry/Bohr
Kinetic energy cutoff for wave functions	60 Ry
K-points	8 8 8

be 8.333 at% in the present study as the first step to screening the candidate dopants. A variable cell relaxation calculation was performed using the Broyden-Fletcher-Goldfarb-Shanno quasi-newton algorithm in order to obtain stable structures. The calculation was performed using the pseudo-potential method, which is suitable for cell relaxation calculations because of its low computational cost. The calculation conditions are given in Table 2.16.4.

For the stable structures obtained, we calculated the following formation energies, on the basis of which we discuss the site occupation by the impurity atoms:

$$\Delta E(Mg_{2-\xi}Si : A_\xi) = E(Mg_{2-\xi}SiA_\xi) + \xi E(Mg) - E(Mg_2Si) - \xi E(A), \quad (2.16.12)$$

$$\Delta E(Mg_{2-\xi}Si : A_\xi) = E(Mg_{2-\xi}SiA_\xi) + \xi E(Si) - E(Mg_2Si) - \xi E(A), \quad (2.16.13)$$

$$\Delta E(Mg_{2-\xi}Si : A_\xi) = E(Mg_{2-\xi}SiA_\xi) - E(Mg_2Si) - \xi E(A). \quad (2.16.14)$$

Eqs. (2.16.12)–(2.16.14) correspond to the case of impurity atom A occupying the Mg-, Si-, and 4b-sites, respectively. Here  $\xi E(A)$  denotes the total energy of single-crystalline A per  $\xi$  mol.

Fig. 2.16.19 shows the lattice constants and the formation energies for systems doped with impurity atoms up to the sixth period in the periodic table. The lattice constant depends on the ionic radius of the impurity atom for all occupation sites.

On the other hand, the formation energy strongly depends on the atomic size only of the impurity atom for substitution into Si, such that it has higher values as the size of the impurity atom increases. As a result, the impurity species that are suggested to be stable at the Si site are B, C, P, Ge, As, Sn, Sb, Te, Pb, Bi, and Po. Of these, changes in the lattice constant larger than 1% were observed for B (-2.16%), C (-3.27%), Sn (1.85%), Sb (1.85%), Te (2.29%), Pb (2.14%), Bi (3.17%), and Po (3.17%). According to experimental studies, Sn, Sb, and Bi have been reported to be potential n-type dopants with the ZT values being 1.3 at 700 K as solid solution

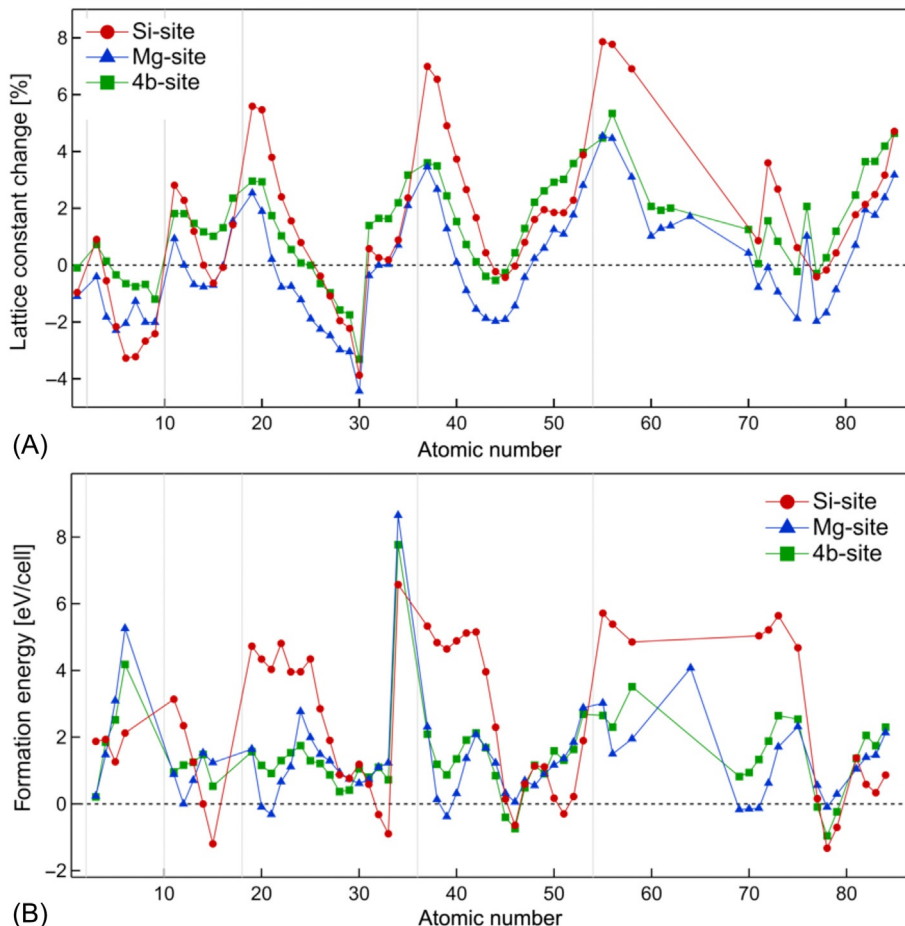


**Fig. 2.16.19** (A) Changes in the lattice constant and (B) the formation energies for the Mg, Si, and 4b sites when impurities are doped with 8.333 at%.

Mg<sub>2</sub>Si<sub>0.3</sub>Sn<sub>0.7</sub>, 0.87 at 873 K, and 0.86 at 862 K, respectively 122–124. Although As, Sb, Te, Pb, and Po have low formation energies, from an industrial point of view, they are not favorable for practical usage in energy conversion devices due to their high toxicity. Furthermore, the calculation shows that B and C are *p*-type and equivalent impurities, respectively. See also the next section for detailed analyses with regard to B. Our recent experimental study revealed that C is a promising impurity candidate because it gives *ZT* of 0.89 at 870 K, which is comparable with Sb (a typical dopant for Mg<sub>2</sub>Si) 125.

Almost none of the elements can be used for selective doping at the 4b site; i.e., the formation energy for the 4b site is comparable or more than those for the other sites, except for the six transition metals (Cr, Mn, Fe, Co, Ni, and Cu). However, as the formation energies for both of 4b and Mg sites are similar, they are not potential candidates for which carrier tuning is controllable.

Al, Ca, Sc, Ga, Sr, Y, Zr, Ga, Ba, Ce, Tm, Yb, Lu, and Hf were selectively substituted at the Mg site. Large changes in the lattice constant were observed for Ca (1.89%), Sr (2.67%), Y (1.28%), Ba (4.46%), and Ce (3.10%). Regarding these elements, there are few experimental reports of ZT, and only Al, Sr, and Y have been reported, with the ZT values being n-type 0.50 at 873 K, p-type 0.24 at 700 K, and n-type 0.23 at 873 K, respectively [126–128](#).

The present calculations were, in most cases, completed within 3 days using a single-core computer. For lanthanoid impurities, the calculations did not converge; this may be due to their large ionic radii, which can make the systems doped with them unstable. In addition, it may be attributed to the treatment of the transition metal elements, magnetic elements, and/or 4f electrons, which require further research.

#### **2.16.4.3 Instability of *p*-type systems and new candidates for acceptors**

$\text{Mg}_2\text{Si}$  intrinsically possesses *n*-type conductivity, and *n*-type dopants are generally used for improving its thermoelectric performance; however, despite the multiple attempts to find suitable acceptors, the development of *p*-type  $\text{Mg}_2\text{Si}$  is currently hindered by the difficulties in achieving stable *p*-type conductivity. For example, according to the results of one experimental study [108](#), Ag-doped  $\text{Mg}_2\text{Si}$  exhibited a change in conductivity from *p*-type to *n*-type at temperatures above 650 K.

The major origin of the instability of *p*-type conductivity could be the simultaneous generation of electrons and holes in the intrinsic semiconductor region. Furthermore, the transport properties can be affected by imperfections in the crystal structure, such as native defects. Indeed, it has been reported that the existence of native defects strongly affects the carrier transport in  $\text{Mg}_2\text{Si}$  [129–131](#); in particular, Mg atoms interstitially inserted into the cell act as dopants. According to a theoretical study, the aforementioned intrinsic *n*-type conductivity is attributable to this type of defect [129](#). Our previous theoretical study [132](#) suggested that the number of electrons generated by interstitial Mg doping could compensate for the number of holes produced by intentional impurity doping and even potentially exceed it if a system contains interstitial Mg defects with a comparable number of acceptors. This can be understood as the added impurities generating approximately one hole; whereas, interstitial Mg may become  $\text{Mg}^{2+}$ , supplying two electrons to the system. Thus, the presence of interstitial Mg defects must be a reason for the difficulty of achieving stable *p*-type conductivity.

In our previous work [133](#), we also addressed this issue in terms of structural stability. We examined  $\text{Mg}_2\text{Si}$  with various impurity atoms using first-principles pseudo-potential calculations. We computationally dealt with the impurity-doped structures by the supercell method. A system with a doping concentration  $x$  of 1 at% (or less), which is generally used in experiments, can be expressed as a  $2 \times 2 \times 2$  (or more) supercell. In this study,  $2 \times 2 \times 2$  supercells, consisting of eight unit cells with 96 (32 Si and 64 Mg) atomic sites, each with an impurity atom was optimized by

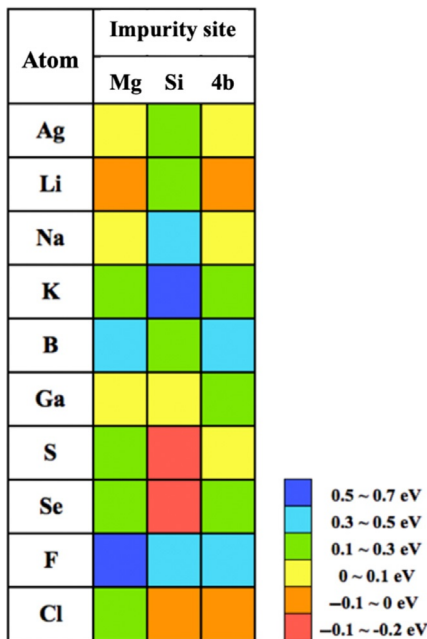


**Fig. 2.16.20** Formation energies per impurity atom for Mg, Si, and 4b sites calculated based on the optimized structures. In the calculation, the  $2 \times 2 \times 2$  supercell structure with an impurity atom was assumed; therefore, the concentration of impurities is 1.04 at%.

considering the localized shifts of individual atoms and by optimizing the lattice constants using the cell-relaxation technique of the quantum espresso package. In all the calculations, norm-conserving pseudo-potentials and the GGA-PBE functional were utilized (see Ref. 133 for details of the calculation).

The obtained formation energies for several species are shown in Fig. 2.16.20. Note that the Ag-doped system exhibits comparable  $\Delta E$  for different sites (Mg, Si, and interstitial 4b), which may at least partially explain the experimental instability of their *p*-type conductivity 108 because it suggests the possibility of the simultaneous doping of holes and electrons during synthesis; moreover, the Ag atoms occupying Mg sites would be driven towards the other sites at elevated temperatures, which also causes electron doping. A similar phenomenon is observed for systems incorporating alkali metals (Li 134, Na, and K) as they have similar  $\Delta E$  values for the Mg (*p*-type) and 4b (*n*-type) sites. Although Li 134 is a potentially promising acceptor for  $\text{Mg}_2\text{Si}$  because of its negative formation energy, the simultaneous occupation of 4b and Mg sites owing to them having almost the same  $\Delta E$  poses a challenge in achieving stable *p*-type conduction. Among the boron group elements (Ga and B), Ga is found to be favorable for hole doping because it exhibits a relatively small  $\Delta E$  for the Si (*p*-type) site. Furthermore, from the calculations, we predict new candidates for acceptors by the interstitial insertion of Cl and F atoms into the crystal lattice that leads to hole doping because of their high electronegativity.

#### 2.16.4.4 Other strategies for improving the thermoelectric efficiency

Even though we mainly focus on impurity doping in this study, we briefly show another strategy for improving the thermoelectric performance of Mg<sub>2</sub>Si: isotropic strain, proposed by H. Balout et al. 135. According to their theoretical work 135, the lattice constant is dominant in determining the transport properties such as  $\sigma$  and  $S$  for  $n$ -type Mg<sub>2</sub>Si. They revealed that  $PF$  is drastically enhanced under tensile strain. Kaur et al. 136 revealed that the variation in  $S$  under an applied strain is related to the change in the DOS using first-principles calculations. In addition, the author's previous study 109 using FLAPW calculations found a twofold improvement in  $PF$  by increasing the lattice constant, owing to enhancement of both  $\sigma$  and  $S$ . This is attributable to the effective conduction band degeneracy as well as the increase in effective mass caused by the structural change. The above theoretical findings provide new insight into the effects of structural changes on the thermoelectric performance of Mg<sub>2</sub>Si, suggesting the possibility that the thermoelectric properties can be controlled by adjusting the structural properties. It is expected that this will pave the way for important further developments based on Mg<sub>2</sub>Si.

As noted previously, Mg<sub>2</sub>Si<sub>1-x</sub>Sn<sub>x</sub> has been recognized as a potential thermoelectric material. The electronic states at the band edge are also important for its thermoelectric performance; i.e., the increase in  $PF$  originating from band convergence at  $x=0.65\text{--}0.7$  was predicted in a theoretical study 137; in fact, experimental  $ZT$  values higher than Mg<sub>2</sub>Si were observed at  $x=0.6$ , such as 1.1–1.3 138,139. Thus, we conclude that not only electron density tuning, but also electronic band engineering is significant for realizing an excellent thermoelectric material based on Mg<sub>2</sub>Si.

#### 2.16.4.5 Current status and future works

As of 2020, the calculation of a highly symmetric system such as Mg<sub>2</sub>Si using a pseudo-potential method is feasible using a single-core computer, even when doped with impurities at several at%. Such calculations typically converge within several days for a supercell consisting of 50 or fewer atoms, although this depends on the calculation conditions, such as the cut-off energy and the number of  $k$ -points. First-principles calculations are playing an increasingly important role in materials development, reflecting the recent rapid improvement in computational performance. For Mg<sub>2</sub>Si, in particular, calculation-based DFT has worked well for understanding the electronic and thermoelectric properties in many cases, as we have seen in some of the examples in this paper. In summary, based on the electronic band structures obtained using the FLAPW method, the effective mass for electrons agreed with the experimental data, and, notably, the calculated Seebeck coefficients quantitatively agreed with experimental systems doped with Sb, Bi ( $n$ -type), and Ag ( $p$ -type). Furthermore, pseudo-potential calculations were utilized to optimize the impurity-doped structures and predict the dopant species potentially possessing good stability at their target sites. In addition, several theoretical studies proposed strategies to pave the way for band engineering; for example, a solid solution of Mg(Si,Sn) and isotropic negative pressure were introduced.

Sizable supercells incorporating impurities and/or defects at concentrations used in experiments (1% or less) are expected to be computationally dealt with in the near future. If this is possible, first-principles calculations, in conjunction with experimental observations, will result in further understanding of the electronic states and thermoelectric carrier transport in actual systems. In addition, high-throughput screening of novel materials with good performance using machine learning has recently become more widely used in material development. As Mg<sub>2</sub>Si is manageable by calculations with relatively low costs, first-principles calculations can be utilized at the data collection stage when machine learning methods can be used for predicting suitable compositions and structures to obtain promising thermoelectric materials.

## References

- [1] R.G. Morris, R.D. Redin, G.C. Danielson, Phys. Rev. 109 (1958) 1909.
- [2] P. Koenig, D.W. Lynch, G.C. Danielson, J. Phys. Chem. Solids 20 (1961) 122.
- [3] A. Stella, A.D. Brotherrs, H. Hopkings, D.W. Lynch, Phys. Status Solidi 23 (1967) 697.
- [4] J. Tani, H. Kido, Physica B 223 (2005) 364.
- [5] G.S. Nolas, G.A. Slack, D.T. Modeli, T.M. Tritt, A.C. Ehrlich, J. Appl. Phys. 79 (1996) 4002.
- [6] V.K. Zaitsev, M.I. Fedorov, E.A. Gurieva, I.S. Eremin, P.P. Konstantinov, A.Y. Samunin, M.V. Vedernikov, Phys. Rev. B 74 (2006), 045207.
- [7] J. Tani, H. Kido, Intermetallics 15 (2007) 1202.
- [8] J. Tani, H. Kido, J. Alloys Compd. 466 (2008) 335.
- [9] M. Akasaka, T. Iida, A. Matsumoto, K. Yamanaka, Y. Takanashi, T. Imai, N. Hamada, J. Appl. Phys. 104 (2008), 013703.
- [10] P. Pandit, S.P. Sanyal, Ind. J. Pure Appl. Phys. 49 (2011) 692.
- [11] W. Liu, X. Tan, K. Yin, H. Liu, X. Tang, J. Shi, Q. Zhang, C. Uher, Phys. Rev. Lett. 108 (2012) 166601.
- [12] T. Sakamoto, T. Iida, N. Fukushima, Y. Honda, M. Tada, Y. Taguchi, Y. Mito, H. Taguchi, Y. Takanashi, Thin Solid Films 519 (2011) 8528.
- [13] S. Battiston, S. Fiameni, M. Saleemi, S. Boldrini, A. Famengo, F. Agresti, M. Stingaciu, M.S. Toprak, M. Fabrizio, S. Barison, J. Electron. Mater. 42 (2013) 1956.
- [14] M. Ioannou, G. Polymeris, E. Hatzikraniotis, A.U. Khan, K.M. Paraskevopoulos, T. Kyritsi, J. Electron. Mater. 42 (2013) 1827.
- [15] G. Kim, H. Lee, J. Kim, J.W. Roh, I. Lyo, B.-W. Kim, K.H. Lee, W. Lee, Up-scaled solid state reaction for synthesis of doped Mg<sub>2</sub>Si, Scr. Mater. 128 (2017) 53–56.
- [16] J. Li, X. Li, C. Chen, W. Hu, F. Yu, Z. Zhao, L. Zhang, D. Yu, Y. Tian, B. Xu, Enhanced thermoelectric performance of bismuthdoped magnesium silicide synthesized under high pressure, J. Mater. Sci. 53 (12) (2018) 9091–9098.
- [17] K. Kambe, H. Udon, Convenient melt-growth method for thermoelectric Mg<sub>2</sub>Si, J. Electron. Mater. 43 (6) (2014) 2212–2217.
- [18] J. Boor, D. Droste, C. Schneider, J. Janek, E. Mueller, Thermal stability of magnesium silicide/nickel contacts, J. Electron. Mater. 45 (10) (2016) 5313–5320.
- [19] Y. Isoda, S. Tada, H. Kitagawa, Y. Shinohara, Thermoelectric properties of Sb-doped Mg<sub>2</sub>Si prepared using different silicon sources, J. Electron. Mater. 45 (3) (2015) 1772–1778.

- [20] Y. Kang, L. Brockway, S. Vaddiraju, A simple phase transformation strategy for converting silicon nanowires into metal silicide nanowires: magnesium silicide, *Mater. Lett.* 100 (2013) 106–110.
- [21] X. Yang, S. Chen, H. Zhang, F. Lv, W. Fan, W.W. Zuhair, A. Munir, Thermoelectric properties and transport mechanism of pure and Bi-doped SiNWs-Mg<sub>2</sub>Si, *Phys. Status Solidi A Appl. Mater. Sci.* 215 (5) (2018) 1700742.
- [22] N. Satyala, D. Vashaee, Modeling of thermoelectric properties of magnesium silicide (Mg<sub>2</sub>Si), *J. Electron. Mater.* 41 (6) (2012) 1785–1791.
- [23] A. Kato, T. Yagi, N. Fukusako, First-principles studies of intrinsic point defects in magnesium silicide, *J. Phys. Condens. Matter* 21 (2009) 205801.
- [24] A. Nozariasbmarz, A. Agarwal, Z.A. Coutant, M.J. Hall, J. Liu, R. Liu, A. Malhotra, P. Norouzzadeh, M.C. Öztürk, V.P. Ramesh, Y. Sargolzaeiaval, F. Suarez, D. Vashaee, Thermoelectric silicides: a review, *Jpn. J. Appl. Phys.* 56 (2017), 05DA04.
- [25] P. Boulet, M.J. Verstraete, J.-P. Crocombette, M. Briki, M.-C. Record, *Comput. Mater. Sci.* 50 (2011) 847.
- [26] D.P. Spitzer, Lattice thermal conductivity of semiconductors: a chemical bond approach, *J. Phys. Chem. Solids* 31 (1970) 19.
- [27] M.V. Vedernikov, A.E. Engalychev, V.K. Ordin, M.I. Fedorov, K.R. Rao (Eds.), Thermoelectric properties of materials based on the higher manganese silicide and cobalt monosilicide, Proc. 7th Int. Conf. On Thermoelectric Energy Conversion, University of Texas at Arlington, Arlington, Texas, 1988, p. 151.
- [28] H. Nagai, H. Hamada, K. Hayashi, A.Y. Miyazaki, Effects of cobalt substitution on crystal structure and thermoelectric properties of melt-grown higher manganese silicides, *J. Electron. Mater.* 48 (4) (2019) 1902–1908.
- [29] A. Yamamoto, S. Ghodke, H. Miyazaki, M. Inukai, Y. Nishino, M. Matsunami, T. Takeuchi, Thermoelectric properties of supersaturated Re solid solution of higher manganese silicides, *Jpn. J. Appl. Phys.* 55 (2016), 020301.
- [30] T. Homma, T. Kamata, N. Saito, S. Ghodke, T. Takeuchi, Effects of Re substitution for Mn on microstructures and properties in Re-substituted higher manganese silicide thermoelectric material, *J. Alloys Compd.* 776 (5) (2019) 8–15.
- [31] W.-D. Liu, Z.-G. Chen, J. Zou, Eco-friendly higher manganese silicide thermoelectric materials: progress and future challenges, *Adv. Energy Mater.* 8 (19) (2018) 1800056.
- [32] Y. Miyazaki, D. Igarashi, K. Hayashi, T. Kajitani, K. Yubuta, Modulated crystal structure of chimney-ladder higher manganese silicides MnSi  $\gamma$  ( $\gamma \sim 1.74$ ), *Phys. Rev. B* 78 (2008) 214104.
- [33] Y. Miyazaki, H. Hamada, H. Nagai, K. Hayashi, Crystal structure and thermoelectric properties of lightly substituted higher manganese silicides, *Materials* 11 (6) (2018) 926.
- [34] P. Zwolenski, J. Tobola, S. Kaprzyk, *J. Electron. Mater.* 40 (2011) 889.
- [35] H. Wang, W. Chu, H. Jin, *Comput. Mater. Sci.* 60 (2012) 224.
- [36] N. Satyala, D. Vashaee, *J. Electron. Mater.* 41 (2012) 1785.
- [37] J.J. Pulikkotil, D.J. Singh, S. Auluck, M. Saravanan, D.K. Misra, A. Dhar, R.C. Budhani, *Phys. Rev. B* 86 (2012) 155204.
- [38] N. Hirayama, T. Iida, S. Morioka, M. Sakamoto, K. Nishio, Y. Kogo, Y. Takanashi, N. Hamada, *Jpn. J. Appl. Phys.* 54 (2015). 7S2 07JC05-1.
- [39] N. Hirayama, T. Iida, H. Funashima, S. Morioka, M. Sakamoto, K. Nishio, Y. Kogo, Y. Takanashi, N. Hamada, *J. Electron. Mater.* 44 (2014) 1656.
- [40] N. Hirayama, T. Iida, S. Morioka, M. Sakamoto, K. Nishio, Y. Kogo, Y. Takanashi, N. Hamada, *J. Mater. Res.* 30 (2015) 2564.

- [41] M. Søndergaard, M. Christensen, K.A. Borup, H. YinBo, B. Iversen, Thermal stability and thermoelectric properties of Mg<sub>2</sub>Si0.4Sn0.6 and Mg<sub>2</sub>Si0.6Sn0.4, *J. Mater. Sci.* 48 (5) (2013) 2002–2008.
- [42] N. Farahi, C. Stiewe, D.Y.N. Truong, J. de Boor, E. Muller, High efficiency Mg<sub>2</sub>(Si,Sn)-based thermoelectric materials: scale-up synthesis, functional homogeneity, and thermal stability, *RSC Adv.* 9 (2019) 23021.
- [43] G.S. Polymeris, N. Vlachos, E. Symeou, T. Kyritsi, Thermoelectric properties of Bi-doped Mg<sub>2</sub>Si0.6Sn0.4 solid solutions synthesized by two-step low temperature reaction combined with hot pressing, *Phys. Status Solidi A Appl. Mater. Sci.* 215 (17) (2018) 1800136.
- [44] S. Aryan, P. Akash, K. Hasbuna, Y. Mohammad, F. Nader, M. Eckhard, B. de Johannes, Mechanical alloying of optimized Mg-2(Si,Sn) solid solutions: understanding phase evolution and tuning synthesis parameters for thermoelectric applications, *ACS Appl. Energy Mater.* 1 (2) (2018) 531–542.
- [45] X. Li, S. Li, S. Feng, H. Zhong, Thermoelectric properties prediction of n-type Mg<sub>2</sub>Si1-x Sn (x) compounds by first principles calculation, *J. Electron. Mater.* 47 (2) (2018) 1022–1029.
- [46] H.L. Andersen, J. Zhang, H. Yin, B.B. Iversen, Structural stability and thermoelectric properties of cation-and anion-doped Mg<sub>2</sub>Si0.4Sn0.6, *Inorg. Chem. Front.* 4 (3) (2017) 456–467.
- [47] X. Tang, G. Wang, Y. Zheng, Y. Zhang, K. Peng, L. Guo, S. Wang, M. Zeng, J. Dai, G. Wang, X. Zhou, Ultra rapid fabrication of p-type Li-doped Mg<sub>2</sub>Si0.4Sn0.6 synthesized by unique melt spinning method, *Scr. Mater.* 115 (2016) 52–56.
- [48] T. Iida, Y. Kogo, A. Yasumori, K. Nishio, N. Hirayama, Silicide modules: practical issues in developing Mg<sub>2</sub>Si with good stability for generating power from waste heat sources, in: Z. Ren, Y. Lan, Q. Zhang (Eds.), *Advanced Thermoelectrics: Materials, Contacts, Devices, and Systems*, CRC Press, New York, 2018, pp. 697–717.
- [49] T. Sueuchi et al., To be submitted to the *J. of Alloys and compound*.
- [50] F. Ikeda et al., To be submitted to the *J. of Alloys and compound*.
- [51] Kawamura et al., To be submitted to the *J. of Alloys and compound*.
- [52] American Institute of Physics Handbook, McGraw-Hill Book Company, 1982.
- [53] The Japan Institute of Metals and Materials, Metal Databook, Maruzen, 2004.
- [54] K. Sekino, M. Midonoya, H. Udon, Y. Yamada, Preparation of Schottky contacts on n-type Mg<sub>2</sub>Si single crystalline substrate, *Phys. Procedia* (2011) p171–p173.
- [55] A. Atanassov, M. Baleva, *Thin Solid Films* 515 (5) (2007) 3046–3051.
- [56] (a) Y. Miyazaki, et al., *J. Jpn. Soc. Powder Powder Metall.* 64 (8) (2017) 461–466.  
(b) Y. Miyazaki, et al., *J. Japan Inst. Met. Mater.* 79 (11) (2015) 530–537.
- [57] W.-S. Liu, Q. Jie, H.S. Kim, Z. Ren, *Acta Metall.* 87 (2015) 357–376.
- [58] T. Sakamoto, T. Iida, Y. Ohno, M. Ishikawa, Y. Kogo, N. Hirayama, K. Arai, T. Nakamura, K. Nishio, Y. Takanashi, *J. Electron. Mater.* 43 (2013) 1620–1629.
- [59] T. Nemoto, T. Iida, J. Sato, Y. Oguni, A. Matsumoto, T. Miyata, T. Sakamoto, T. Nakajima, H. Taguchi, K. Nishio, Y. Takanashi, *J. Electron. Mater.* 39 (2010) 1572–1578.
- [60] H.S. Kim, K. Kikuchi, T. Itoh, T. Iida, M. Taya, *Mater. Sci. Eng. B* 185 (2014) 45–52.
- [61] J. de Boor, C. Gloanec, H. Kolb, R. Sottong, P. Ziolkowski, E. Müller, *J. Alloys Compd.* 632 (2015) 348–353.
- [62] E. Hatzikraniotis, K.T. Zorbas, I. Samaras, T. Kyritsi, K.M. Paraskevopoulos, *J. Electron. Mater.* 39 (2009) 2112–2116.
- [63] K. Singsoog, T. Seetawan, *Phys. B Phys. Condens. Matter* 566 (2019) 1–5.

- [64] G. Skomedal, L. Holmgren, H. Middleton, I.S. Eremin, G.N. Isachenko, M. Jaegle, K. Tarantik, N. Vlachos, M. Manoli, T. Kyratsi, D. Berthebaud, N.Y. Dao Truong, F. Gascoin, *Energy Convers. Manag.* 110 (2016) 13–21.
- [65] G. Skomedal, N.R. Kristiansen, M. Engvoll, H. Middleton, *J. Electron. Mater.* 43 (2013) 1946–1951.
- [66] A.S. Al-Merbat, B.S. Yilbas, A.Z. Sahin, *Appl. Therm. Eng.* 50 (2013) 683–692.
- [67] W.B. Whitten, P.L. Chung, G.C. Danielson, *J. Phys. Chem. Solids* 26 (1965) 49–56.
- [68] R. Inoue, J. Nakano, T. Nakamura, T. Ube, T. Iida, Y. Kogo, *J. Alloys Compd.* 775 (2019) 657–666.
- [69] M. Ishikawa, T. Nakamura, S. Hirata, T. Iida, K. Nishio, Y. Kogo, *Jpn. J. Appl. Phys.* 54 (2015), 07JC03–8.
- [70] T. Nakamura, R. Inoue, S. Hasegawa, Y. Kogo, T. Iida, *MRS Adv.* (2017) 1–7.
- [71] R.D. Schmidt, E.D. Case, J. Giles, J.E. Ni, T.P. Hogan, *J. Electron. Mater.* 41 (2012) 1210–1216.
- [72] Y. Gelbstein, J. Tunbridge, R. Dixon, M.J. Reece, H. Ning, R. Gilchrist, R. Summers, I. Agote, M.A. Lagos, K. Simpson, C. Rouaud, P. Feulner, S. Rivera, R. Torrecillas, M. Husband, J. Crossley, I. Robinson, *J. Electron. Mater.* 43 (2014) 1703–1711.
- [73] K. Yin, X. Su, Y. Yan, H. Tang, M.G. Kanatzidis, C. Uher, X. Tang, *Scr. Mater.* 126 (2017) 1–5.
- [74] R.D. Schmidt, X. Fan, E.D. Case, P.B. Sarac, *J. Mater. Sci.* 50 (2015) 4034–4046.
- [75] G. Kim, H. Lee, J. Kim, J.W. Roh, I. Lyo, B.-W. Kim, K.H. Lee, W. Lee, *Ceram. Int.* 43 (2017) 12979–12982.
- [76] G. Kim, H. Lee, H.J. Rim, J. Kim, K. Kim, J.W. Roh, S.-M. Choi, B.-W. Kim, K.H. Lee, W. Lee, *J. Alloys Compd.* 769 (2018) 53–58.
- [77] G. Kim, S.W. Kim, H.J. Rim, H. Lee, J. Kim, J.W. Roh, B.-W. Kim, K.H. Lee, W. Lee, *Scr. Mater.* 162 (2019) 402–407.
- [78] G. Kim, H.J. Rim, H. Lee, J. Kim, J.W. Roh, K.H. Lee, W. Lee, *J. Alloys Compd.* 801 (2019) 234–238.
- [79] M. Mejri, Y. Thimont, B. Malard, C. Estournès, *Scr. Mater.* 172 (2019) 28–32.
- [80] P. Gao, I. Berkun, R.D. Schmidt, M.F. Luzenski, X. Lu, P. Bordon Sarac, E.D. Case, T.P. Hogan, *J. Electron. Mater.* 43 (2014) 1790–1803.
- [81] N. Satyala, J.S. Krasinski, D. Vashaee, *Acta Metall.* 74 (2014) 141–150.
- [82] G. Kim, W. Kim, Intercorrelated relationship between the thermoelectric performance and mechanical reliability of Mg<sub>2</sub>Si-reduced graphene oxide nanocomposites, *Electron. Mater. Lett.* 16 (2) (2020) 174–179.
- [83] S. Ganeshan, S.L. Shang, Y. Wang, Z.K. Liu, *J. Alloys Compd.* 498 (2010) 191–198.
- [84] A.E. Petrova, V.N. Krasnorussky, A.A. Shikov, W.M. Yuhasz, T.A. Lograsso, J.C. Lashley, S.M. Stishov, *Phys. Rev. B* 82 (2010) 194–198.
- [85] J.B. Wachtman, W.R. Cannon, M.J. Matthewson, *Mechanical Properties of Ceramics*, John Wiley & Sons, Hoboken, NJ, USA, 2009.
- [86] G.R. Anstis, P. Chantikul, B.R. Lawn, D.B. Marshall, *J. Am. Ceram. Soc.* 64 (1981) 533–538.
- [87] S. Gahlawat, K. White, Z. Ren, Y. Kogo, T. Iida, *Advanced Thermoelectrics*, first ed., Series in Materials Science and Engineering, CRC Press, Taylor & Francis Group, Boca Raton, FL, 2017, pp. 555–602.
- [88] F. Ren, E.D. Case, E.J. Timm, M.D. Jacobs, H. Schock, *Philos. Mag. Lett.* 86 (2006) 673–682.

- [89] A.Q. Morrison, E.D. Case, F. Ren, A.J. Baumann, D.C. Kleinow, J.E. Ni, M.J. Hoffmann, J. D'Angelo, N. Matchanov, T. Hendricks, N.K. Karri, C. Cauchy, J. Barnard, M.G. Kanatzidis, Mater. Chem. Phys. 134 (2012) 973–987.
- [90] S.S. Razavi-Tousi, Y.C. Tseng, J. Alloys Compd. 764 (2018) 745–754.
- [91] S. Takeuchi, T. Hashimoto, K. Suzuki, Intermetallics 4 (1996) S147–S150.
- [92] A. Li, X.-P. Zhao, H.-Y. Huang, Y. Ma, L. Gao, Y.-J. Su, P. Qian, Int. J. Miner. Metall. Mater. 26 (2019) 507–515.
- [93] R.A. Michi, G. Kim, B.-W. Kim, W. Lee, D.C. Dunand, Scr. Mater. 148 (2018) 10–14.
- [94] E.D. Case, J. Electron. Mater. 41 (2012) 1811–1819.
- [95] J.E. Ni, E.D. Case, J. Electron. Mater. 42 (2012) 1382–1388.
- [96] R.W. Rice, Mechanical Properties of Ceramics and Composites, CRC Press, 2000.
- [97] L. Wang, X.Y. Qin, W. Xiong, X.G. Zhu, Mater. Sci. Eng. A 459 (2007) 216–222.
- [98] P.F. Becher, J. Am. Ceram. Soc. 74 (1991) 255–269.
- [99] A.G. Evans, J. Am. Ceram. Soc. 73 (1990) 187–206.
- [100] W.B. Hillig, Annu. Rev. Mater. Sci. 17 (2012) 1–44.
- [101] J.-I. Tani, H. Kido, Intermetallics 32 (2013) 72–80.
- [102] S. Fiameni, A. Famengo, S. Boldrini, S. Battiston, M. Saleemi, M. Stingaci, M. Jhonsson, S. Barison, M. Fabrizio, J. Electron. Mater. 42 (2013) 2062–2066.
- [103] T. Itoh, A. Tominaga, Mater. Trans. 57 (2016) 1088–1093.
- [104] L.S. Sigl, P.A. Mataga, B.J. Dagleish, R.M. McMeeking, A.G. Evans, Acta Metall. 36 (1988) 945–953.
- [105] J. de Boor, C. Compere, T. Dasgupta, C. Stiewe, H. Kolb, A. Schmitz, E. Mueller, J. Mater. Sci. 49 (2014) 3196–3204.
- [106] J.-I. Tani, M. Takahashi, H. Kido, J. Alloys Compd. 488 (2009) 346–349.
- [107] J. de Boor, T. Dasgupta, H. Kolb, C. Compere, K. Kelm, E. Mueller, Acta Metall. 77 (2014) 68–75.
- [108] M. Akasaka, T. Iida, A. Matsumoto, K. Yamanaka, Y. Takanashi, T. Imai, N. Hamada, The thermoelectric properties of bulk crystalline n- and p-type Mg<sub>2</sub>Si prepared by the vertical Bridgman method, J. Appl. Phys. 104 (2008), 013703.
- [109] N. Hirayama, Y. Imai, N. Hamada, Conduction band engineering of Mg<sub>2</sub>Si by isotropic strain for enhancement of thermoelectric performance: a first-principles study, J. Appl. Phys. 127 (2020) 205107.
- [110] R.G. Morris, R.D. Redin, G.C. Danielson, Semiconducting properties of Mg<sub>2</sub>Si single crystals, Phys. Rev. 109 (1958) 1909.
- [111] H. Udono, H. Tajima, M. Uchikoshi, M. Itakura, Crystal growth and characterization of Mg<sub>2</sub>Si for IR-detectors and thermoelectric applications, Jpn. J. Appl. Phys. 54 (2015), 07JB06.
- [112] D. Tamura, R. Nagai, K. Sugimoto, H. Udono, I. Kikuma, H. Tajima, I.J. Ohsugi, Melt growth and characterization of Mg<sub>2</sub>Si bulk crystals, Thin Solid Films 515 (2007) 8272.
- [113] F. Tran, P. Blaha, Accurate band gaps of semiconductors and insulators with a semilocal exchange-correlation potential, Phys. Rev. Lett. 102 (2009) 226401.
- [114] J.J. Pulikkotil, D.J. Singh, S. Auluck, M. Saravanan, D.K. Misra, A. Dhar, R.C. Budhani, Doping and temperature dependence of thermoelectric properties in Mg<sub>2</sub>(Si,Sn), Phys. Rev. B 86 (2012) 155204.
- [115] B. Ryu, S. Park, E. Choi, et al., Hybrid-functional and quasi-particle calculations of band structures of Mg<sub>2</sub>Si, Mg<sub>2</sub>Ge, and Mg<sub>2</sub>Sn, J. Korean Phys. Soc. 75 (2019) 144–152.

- [116] H. Kasai, H. Akai, H. Yoshida, *Introduction to Computational Materials Design*, Osaka University Press, Osaka, 2005. in Japanese.
- [117] L.P. Bouckaert, R. Smoluchowski, E. Wigner, Theory of Brillouin zones and symmetry properties of wave functions in crystals, *Phys. Rev.* 50 (1936) 58.
- [118] A.J. Bevolo, H.R. Shanks, Valence band study of Mg<sub>2</sub>Si by Auger spectroscopy, *J. Vac. Sci. Technol. A* 1 (1983) 574.
- [119] S. Sharma, S.K. Pandey, A first principle study of electronic band structures and effective mass tensors of thermoelectric materials: PbTe, Mg<sub>2</sub>Si, FeGa<sub>3</sub> and CoSb<sub>3</sub>, *Comput. Mater. Sci.* 85 (2014) 340.
- [120] P. Koenig, D.W. Lynch, G.C. Danielson, Infrared absorption in magnesium silicide and magnesium germanide, *J. Phys. Chem. Solids* 20 (1961) 122.
- [121] N. Hirayama, T. Iida, S. Morioka, M. Sakamoto, K. Nishio, Y. Kogo, Y. Takanashi, N. Hamada, First-principles investigation of structural, electronic, and thermoelectric properties of n- and p-type Mg<sub>2</sub>Si, *J. Mater. Res.* 30 (2015) 2564–2577.
- [122] W. Liu, K. Yin, Q. Zhang, C. Uher, X. Tang, Eco-friendly high-performance silicide thermoelectric materials, *Natl. Sci. Rev.* 4 (4) (2017) 611–626.
- [123] Y. Oto, T. Iida, T. Sakamoto, R. Miyahara, A. Natsui, K. Nishio, Y. Kogo, N. Hirayama, Y. Takanashi, Thermoelectric properties and durability at elevated temperatures of impurity doped n-type Mg<sub>2</sub>Si, *Phys. Status Solidi C* 10 (12) (2013) 1857–1861.
- [124] J.-i. Tani, H. Kido, Thermoelectric properties of Bi-doped Mg<sub>2</sub>Si semiconductors, *Physica B* 364 (2005) 218–224.
- [125] D. Shiojiri et al., To be submitted to *J. Electron. Mater.*
- [126] S. Battiston, S. Fiameni, M. Saleemi, S. Boldrini, A. Famengo, F. Agresti, M. Stingaciu, M.S. Toprak, M. Fabrizio, S. Barison, Synthesis and characterization of Al-doped Mg<sub>2</sub>Si thermoelectric materials, *J. Electron. Mater.* 42 (7) (2013) 1956–1959.
- [127] T. Kajitani, M. Kubouchi, S. Kikuchi, K. Hayashi, T. Ueno, Y. Miyazaki, K. Yubuta, High-performance p-type magnesium silicon thermoelectrics, *J. Electron. Mater.* 42 (7) (2013) 1855–1863.
- [128] Q.S. Meng, W.H. Fan, R.X. Chen, Z.A. Munir, Thermoelectric properties of Sc- and Y-doped Mg<sub>2</sub>Si prepared by field-activated and pressure-assisted reactive sintering, *J. Alloys Compd.* 509 (30) (2011) 7922–7926.
- [129] A. Kato, T. Yagi, T.N. Fukusako, First-principles studies of intrinsic point defects in magnesium silicide, *J. Phys. Condens. Matter* 21 (2009) 205801.
- [130] P. Jund, R. Viennois, C. Colinet, G. Hug, M. Fevre, J.-C. Tedenac, Lattice stability and formation energies of intrinsic defects in Mg<sub>2</sub>Si and Mg<sub>2</sub>Ge via first principles simulations, *J. Phys. Condens. Matter* 25 (2013), 035403.
- [131] M. Kubouchi, K. Hayashi, Y. Miyazaki, Quantitative analysis of interstitial Mg in Mg<sub>2</sub>Si studied by single crystal X-ray diffraction, *J. Alloys Compd.* 617 (2014) 3309.
- [132] N. Hirayama, T. Iida, K. Nishio, Y. Kogo, K. Takarabe, N. Hamada, Influence of native defects on structural and electronic properties of magnesium silicide, *Jpn. J. Appl. Phys.* 56 (2017), 05DC05.
- [133] N. Hirayama, T. Iida, M. Sakamoto, K. Nishio, N. Hamada, Substitutional and interstitial impurity p-type doping of thermoelectric Mg<sub>2</sub>Si: a theoretical study, *Sci. Technol. Adv. Mater.* 20 (2019) 160–172.
- [134] A. Kolezynski, P. Nieroda, K.T. Wojciechowski, Li doped Mg<sub>2</sub>Si p-type thermoelectric material: theoretical and experimental study, *Comput. Mater. Sci.* 100 (2015) 8488.
- [135] H. Balout, P. Boulet, M.-C. Record, Electronic and transport properties of Mg<sub>2</sub>Si under isotropic strains, *Intermetallics* 50 (2014) 8.

- [136] K. Kaur, S. Dhiman, R. Kumar, Strain engineering on thermoelectric performance of Mg<sub>2</sub>Si, *Mater. Res. Express* 4 (2017), 075509.
- [137] W. Liu, X. Tan, K. Yin, H. Liu, X. Tang, J. Shi, Q. Zhang, C. Uher, Convergence of conduction bands as a means of enhancing thermoelectric performance of n-Type Mg<sub>2</sub>Si<sub>1-x</sub>Sn<sub>x</sub> solid solutions, *Phys. Rev. Lett.* 108 (2012) 166601.
- [138] V.K. Zaitsev, M.I. Fedorov, E.A. Gurieva, I.S. Eremin, P.P. Konstantinov, A.Y. Samulin, M.V. Vedernikov, Highly effective Mg<sub>2</sub>Si<sub>1-x</sub>Sn<sub>x</sub> thermoelectrics, *Phys. Rev. B* 74 (2006), 045207.
- [139] T. Dasgupta, C. Stiewe, J. de Boor, E. Müller, Influence of power factor enhancement on the thermoelectric figure of merit in Mg<sub>2</sub>Si<sub>0.4</sub>Sn<sub>0.6</sub> based materials, *Phys. Status Solidi (a)* 211 (2014) 1250.

# Highly efficient Mg<sub>2</sub>Si-based thermoelectric materials:

2.17

## A review on the micro- and nanostructure properties and the role of alloying

Georgios S. Polymeris<sup>a</sup>, Euripides Hatzikraniotis<sup>b</sup>, and Theodora Kyratsi<sup>c</sup>

<sup>a</sup>Institute of Nanoscience and Nanotechnology, NCSR "Demokritos", Athens, Greece,

<sup>b</sup>Department of Physics, Aristotle University of Thessaloniki, Thessaloniki, Greece,

<sup>c</sup>Department of Mechanical and Manufacturing Engineering, University of Cyprus, Nicosia, Cyprus

### 2.17.1 Introduction

The key to a more widespread acceptance of thermoelectric (hereafter TEs) is the development of materials for thermal energy conversion especially using less expensive, more earth-abundant, nontoxic materials to meet the environmental regulations that are capable of higher conversion efficiency. Commonly used TE compounds often contain elements, such as Pb, Te, and Bi, which are toxic, rare in the Earth's crust as well as expensive; thus using them in a more wide range of TE applications—particularly at levels that could impact global energy use—is uncertain. The application of the appropriate materials in TE generators, especially for the automotive and space-airborne industry, requires other characteristics beyond TE performance such as plastic deformation and high fracture toughness in order to survive mechanical stress due to vibrations and temperature cycling [1, 2]. Moreover, these generators, in particular, should be as light as possible, with low mass density materials having the advantage over the more common PbTe, CoSb<sub>3</sub>, and Bi<sub>2</sub>Te<sub>3</sub> with densities between 6.5 and 8.5 g cm<sup>-3</sup> [3, 4].

In a pioneer study of 2006 by Zaitsev and coworkers, Mg<sub>2</sub>Si<sub>0.4</sub>Sn<sub>0.6</sub> was reported to yield a dimensionless figure of merit ZT higher than 1 at about 700 K with adequate doping [5, 6]. Furthermore, Mg<sub>2</sub>Si and Mg<sub>2</sub>Si-based materials exhibit fascinating aspects, such as low density (1.98–2.76 g cm<sup>-3</sup>), which encourages the growth of light and economically advantageous systems, along with very good thermophysical properties, including high melting point—1085°C, elevated compression strength—1640 MPa, as well as elevated Young's modulus—120 GPa and low thermal expansion coefficient [7]. Moreover, it consists of elements in the earth's crust and in conjunction with their nontoxicity, which is consistent with the priority for a technology that is safe for both

the environment and humans, makes them environmentally friendly. The constituent elements of Mg<sub>2</sub>Si are among the most abundant in the earth's crust: Si and Mg are the second and eighth most abundant elements, respectively, giving this class a crucial advantage in view of potential large-scale applications and economical attractiveness [8, 9]. This weight advantage is higher for the binary Mg<sub>2</sub>Si or Si-rich compositions but gives magnesium silicides (of any composition) an advantage where weight is crucial, and realistic industrial scaling-up approach becomes of major interest for practical use in device operation [10].

Despite the poor room-temperature ductility and low toughness, standing as major shortcomings, the favorable combination of all these aforementioned physical and chemical properties makes these compounds interesting candidate TE materials [5, 11, 12]. Indeed, these compounds have drawn much attention as an advantageous choice for TEs with applications in automotive waste heat recovery and aeronautics. Especially the automotive sector, due to its global ubiquity and transition of the current combustion engines to more environmental friendly as well as cheap technologies, has a very high potential to benefit from these emerging technologies to improve overall vehicle efficiency. A large fraction of the potentially available waste heat can be generated in the mid-temperature region between 500 and 800 K, which is too hot for the commercially available TE generators based on other materials. Magnesium-based TE materials possess the right characteristics to address these challenges while exhibiting high conversion efficiencies in the medium-to-high-temperature range (250–650°C), making them the target of great research interest for the cases on exhaust heat recovery. Nevertheless, the degradation of high-temperature Mg<sub>2</sub>Si TE devices via oxidation is one of the primary instability mechanisms, as in the presence of O<sub>2</sub>, Mg<sub>2</sub>Si decomposes to form MgO and Si [13], not to mention a significant drawback [14, 15]. Mg<sub>2</sub>Si oxidation takes place in two steps, including a mild initial oxidation process with a temperature threshold of 300°C and an abrupt one after 500°C [16]. A variety of solutions has been suggested towards circumventing this problem, including the formation of a humidity-resistant layer on the surface of Mg<sub>2</sub>Si [17] or alternatively boron nitride (BN) coating [18] in order to prevent Mg loss and oxidation [19].

## 2.17.2 Synthesis and groups of bulk materials

There are different synthesis strategies to produce Mg<sub>2</sub>Si-based materials, including melting or solid-state or solid-liquid approaches. Evidently, in most of the cases, there is a densification step (i.e., hot pressing, spark plasma sintering, etc.) which is necessary to process the powdery samples.

In the past, bulk Mg<sub>2</sub>Si has been typically prepared by solid-state reaction [20–22] and self-propagating high-temperature synthesis (SHS) [23, 24], while other types of synthesis methods such as induction melting [25], microwave [26–28], mechanical alloying [29], vertical Bridgman growth [30], reactive sintering [31–35], arc melting [36], or various combinations of the above [23, 37] are less common.

More specifically, it is difficult to synthesize Mg<sub>2</sub>Si via melting due to the large difference in melting points and vapor pressures of the constituent elements. Furthermore, control of its composition is also difficult, mainly due to the volatilization and oxidation of Mg. On the other hand, mechanical alloying, which is usually preferred for industrial-scale applications, is not an effective technique for this material since severe agglomeration during milling is known to be a major problem. Dry milling is not practical under various conditions [38], while the wet ball-milling process was found to be a useful tool only to fabricate nanocrystalline material when using Mg<sub>2</sub>Si as the starting powder [39]. In general, solid-state reactions are preferable because they are relatively easier, better to control, and demand simpler equipment [37], although the low yield is a major disadvantage for device-scale preparation. Bulk Mg<sub>2</sub>Si is commonly prepared with solid-state reaction in combination with hot pressing or SPS for the development of high-quality pellets [40].

In addition to the binary system, bulk multinary Mg<sub>2</sub>Si-based materials can be found in two different chemical forms, namely pseudo-binary solid solutions, (Mg<sub>2</sub>Si)<sub>1-x</sub>(Mg<sub>2</sub>Sn)<sub>x</sub>, and pseudo-ternary solid solutions, (Mg<sub>2</sub>Si)<sub>1-x-y</sub>(Mg<sub>2</sub>Sn)<sub>x</sub>(Mg<sub>2</sub>Ge)<sub>y</sub>. In such cases, more sophisticated synthesis techniques were applied, which comprise a number of specific synthesis steps. The synthesis of the solid solutions yielding the highest efficiency typically includes (i) solid-state reaction combined with spark plasma sintering [41–43], (ii) mixing of all commercially available elements (Mg, Si, Sn, and Bi); combination of short time ball milling and annealing for successful solid-state reaction; hot pressing to obtain highly dense pellets [37], and (iii) induction melting followed by spark plasma sintering [44] while other techniques have been also investigated (i.e., melt spinning by [45]). Furthermore, mechanical-assisted alloying synthesis combined with sintering (hot pressing or SPS) has been more recently developed for the highly efficient bulk multinary materials [46–48] as an advantageous technique for large-scale production of powders of different chemical compounds, easier development and integration in the production line, and easier handling and shaping for module fabrication. Interestingly, different synthesis methods lead to various microstructural features that affect ZT values for materials with the same compositions, as discussed below. Overall, powder/solid-state techniques seem to have an advantage since they combine complex microstructures (nano-features, distribution of grain sizes, secondary phases, etc.), high figure of merit and can be integrated in a material/device production line.

## 2.17.3 Structural properties and alloying

### 2.17.3.1 Microstructure

Magnesium silicide is a narrow bandgap semiconductor of dark blue color [49] which crystallizes in the face-centered cubic (FCC) CaF<sub>2</sub>-type structure with the structural symmetry corresponding to the Fm3m space group. The unit cell is composed of 12 atoms, from which the eight centered tetrahedral (8c, 1/4, 1/4, 1/4) sites are occupied by Mg; the four face-centered cubic positions (4a, 0, 0, 0) are occupied by Si but can be

also occupied by Sn and Ge [50]. Considering the cubic crystal structure of  $Mg_2Si$  consisting of a face-centered lattice of Si with an embedded simple cubic lattice of Mg (Fig. 2.17.1A), the central part of the unit cell is unfilled, providing thus enough space for stable interstitial defects [51]. Thereby, both the phase purity and microstructure of the  $Mg_2Si$ -based materials are difficult to control by conventional techniques mainly because of the easy volatilization and oxidation of Mg which causes structural defects. Theoretical investigations of structural defects in  $Mg_2Si$  lattice proposed that the central 4b site ( $\frac{1}{2}, \frac{1}{2}, \frac{1}{2}$ ) is the only stable position for interstitial atoms [52]. These results are consistent with previous studies reporting that  $Mg_2Si$  crystals may contain a small amount of Mg at the 4b interstitial site and that vacancy and interstitial defects are more likely to occur in  $Mg_2Si$  compared with other point defects [52, 53] (Fig. 2.17.1B).

Fig. 2.17.2A shows the powder X-ray diffraction (PXRD hereafter) patterns for Bi-doped members of three different family groups, namely binary  $Mg_2Si$ , pseudo-binary  $(Mg_2Si)_{0.6}(Mg_2Sn)_{0.4}$ , and pseudo-ternary  $(Mg_2Si)_{0.55}(Mg_2Sn)_{0.4}(Mg_2Ge)_{0.05}$ . For the compacted samples, besides the binary  $Mg_2Si$ ,  $MgO$  (the strongest at  $\sim 43$  degrees) can be identified as a secondary phase. This is due to the chemical instability of  $Mg_2Si$  with respect to  $MgO$  and is usually observed in the material [54, 55]. It can be deduced that the  $MgO$  phase is formed during a synthesis step including either intensive heating or compaction. Finally, especially in binary materials, intermetallic phases can be detected as traces, such as  $Mg_3Bi_2$  [39, 56],  $Mg_3Sb_2$  [57, 58], and  $Mg_3Ga_2$  [59] which are formed by dopants and components of the matrix and pure, unreacted Mg [40].

As this figure is going to reveal further, the incorporation of Sn within the matrix results in diffraction peaks which are shifted to lower angles, indicating thus a gradual increase in the lattice constant. Both qualitative and quantitative analyses prove that all materials are of a pure crystallographic structure and no other compounds were

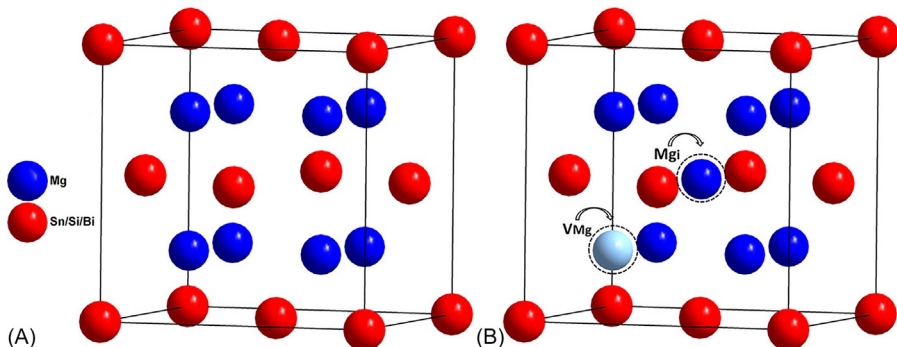


**Fig. 2.17.1** Crystal structure of  $Mg_2(Si, Sn, Ge):Bi$  or  $Sb$  at ambient conditions. (A) Unit cell of the original cubic antifluorite  $CaF_2$ -type structure; and (B) illustrative model of the unit cell with one Mg ion shifted from its regular position toward the interstitial site ( $4b, \frac{1}{2}, \frac{1}{2}, \frac{1}{2}$ ) and one Mg vacancy ( $8c, \frac{1}{4}, \frac{1}{4}, \frac{1}{4}$ ).

From L.R. Macario, X. Cheng, D. Ramirez, T. Mori, H. Kleinke, ACS Appl. Mater. Interfaces 10 (2018) 40585–40591.

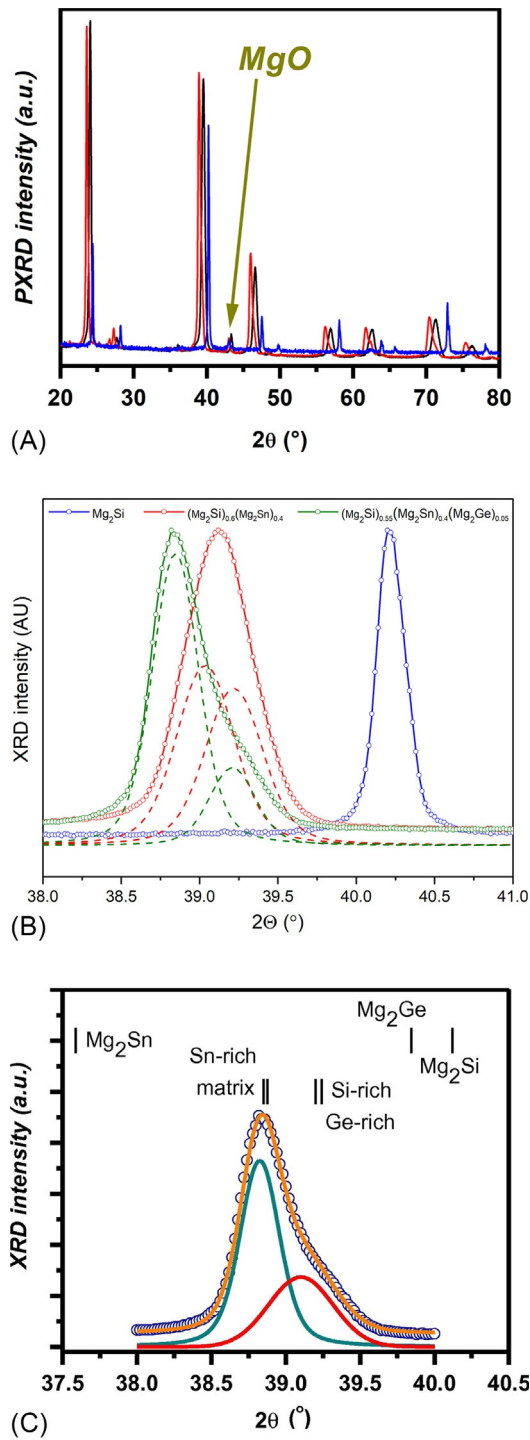


Fig. 2.17.2 See figure legend on next page

detected, apart from MgO which is inevitably formed at low concentration [39, 57, 60, 61]. The strong peak around 40 degrees is presented in Fig. 2.17.2B for each member of these three aforementioned groups. According to this latter figure, a single (and relative narrow) peak is observed solely for the case of binary Mg<sub>2</sub>Si. This peak becomes much wider in the case of a pseudo-binary group (Mg<sub>2</sub>Si)<sub>0.6</sub>(Mg<sub>2</sub>Sn)<sub>0.4</sub> and finally becomes a doublet, with a clear shoulder for the case of a pseudo-ternary group of materials (Mg<sub>2</sub>Si)<sub>0.55</sub>(Mg<sub>2</sub>Sn)<sub>0.4</sub>(Mg<sub>2</sub>Ge)<sub>0.05</sub>. The wide peak for the pseudo-binary materials may be analyzed with a single peak at  $2\theta = 39.12$  degrees [62], or with 2 unresolved peaks 1 at the Sn-richer size at  $2\theta = 39.04$  degrees and another at Si-richer side at  $2\theta = 39.22$  degrees, respectively, as shown in Fig. 2.17.2B [62, 63]. Interestingly, the shoulder for the case of the pseudo-ternary materials is located in the same Bragg angle ( $2\theta = 39.22$  degrees), indicating the formation of a Si-rich phase that is monitored at the same composition in both pseudo-binary and pseudo-ternary compounds. The main peak for the pseudo-ternary is at  $2\theta = 38.85$  degrees, indicating that the corresponding phase is slightly shifted toward to the Sn-richer side of the composition. These PXRD features, which include either shifting or splitting of the main XRD peak were frequently reported for pseudo-binary (Mg<sub>2</sub>Si)<sub>1-x</sub>(Mg<sub>2</sub>Sn)<sub>x</sub> compounds within the range  $0.3 < x < 0.75$  [19, 45, 47, 51, 61–72].

Fig. 2.17.3 presents examples of backscattered scanning electron microscopy (SEM hereafter) images for various members of groups of doped Mg<sub>2</sub>Si-based materials. Fig. 2.17.3A presents a uniform image with a smooth continuum, corresponding to Bi-doped binary Mg<sub>2</sub>Si. Only a few white spots are monitored, corresponding to the presence of intermetallic phases, such as Mg<sub>3</sub>Bi<sub>2</sub> [56] or Mg<sub>3</sub>Sb<sub>2</sub> [57]. Such uniform SEM images are characteristic in all cases of binary Mg<sub>2</sub>Si [54, 73, 74]. Fig. 2.17.3B presents an SEM image together with the corresponding elemental mapping using energy dispersive X-ray (EDX hereafter) analysis again for binary Mg<sub>2</sub>Si. The back-scattered electron image shows the Mg<sub>2</sub>Si matrix (a) as well as grain boundaries (b) and bright inclusions boundaries and Si enrichment at the bright spots. While oxygen is clearly enriched at the grain boundaries and at the bright spots, Mg is slightly deficient at the grain boundaries. The Si mapping shows Si deficiency at the grain. The oxygen enrichment together with the slight Mg deficiency at the grain boundaries can

---

**Fig. 2.17.2, cont'd** (A) Typical PXRD patterns for the cases of a binary (blue), a pseudo-binary (black), and a pseudo-ternary (red) compound. It is worth mentioning that even though the pseudo-binary and -ternary compounds yield the same nominal Sn content and similar Bi-level, the peak is shifted; (B) deconvolution of the main diffraction peak at 40 degrees for the cases of pseudo-binary and -ternary compounds of the previous figure; the peak for the binary material is also presented for comparison reasons; (C) the dominant (220) XRD peak for the case of the pseudo-ternary compound, deconvolved into its two individual components. Vertical lines indicate the theoretical  $2\theta_{max}$  values for either the binary materials or all the phases yielded by EDX analysis. Each one of these components corresponds to a doublet of unresolved phases, owing to the close proximity of the corresponding lattice constants.

(C) From G.S. Polymeris, N. Vlachos, A.U. Khan, E. Hatzikraniotis, C.B. Lioutas, A. Delimitis, E. Pavlidou, K.M. Paraskevopoulos, T. Kyrtasi, Acta Mater. 83 (2015) 285–293.

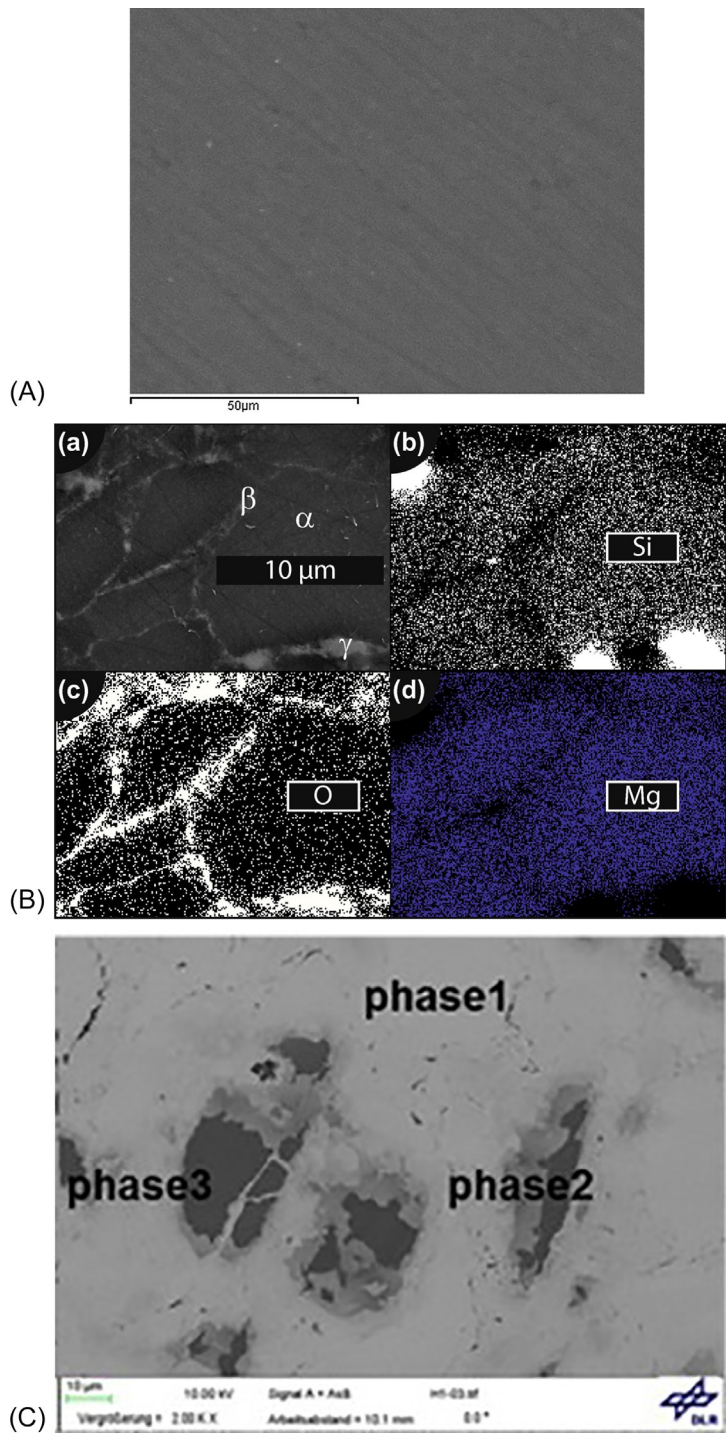
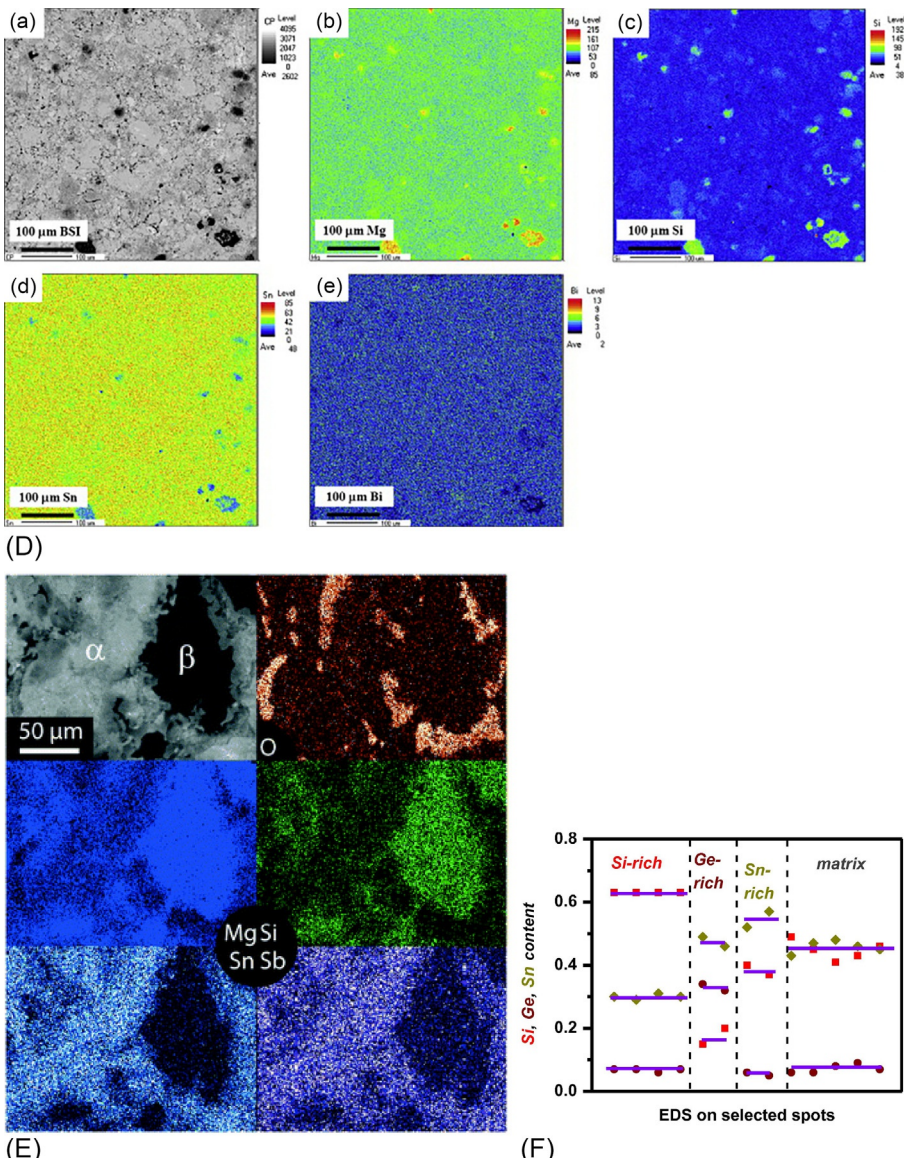


Fig. 2.17.3

(continued)



**Fig. 2.17.3** See figure legend on opposite page

be explained by MgO decorating the grain boundaries [75]. In other words, small MgO particles are located at the grain boundaries between the  $Mg_2Si$  crystallites, in excellent agreement with other related studies on  $Mg_2Si$  [39, 76].

Nevertheless, a mosaic-like texture, similar to those of Fig. 2.17.3C, D-(a), and E-(a), is yielded for the cases of both pseudo-binary and pseudo-ternary compounds.

This texture consists of regions of different gray-color shades, in a light gray background which corresponds to the matrix, with a composition close to the nominal. Besides the main parent matrix and the magnesium oxide, other Mg<sub>2</sub>X-type secondary groups of phases were identified; one with enhanced silicon content along with one containing extra tin. These phases were termed as Si-rich and Sn-rich, respectively, and are monitored in the majority of the cases of pseudo-binary (Mg<sub>2</sub>Si)<sub>1-x</sub>(Mg<sub>2</sub>Sn)<sub>x</sub> compounds within the range 0.3 < x < 0.75 [24,61,63,65,66,69–71,77,78]. In the cases where Ge is added, one additional phase is monitored, containing well higher germanium content than the stoichiometric ratios; these Ge-rich phases are monitored for the case of pseudo-ternary compounds [62,70,79]. The dominance of each element in each phase was verified by SEM-EDX elemental mapping analysis; typical mapping images are presented in Fig. 2.17.3D and E. All of them were ubiquitously present in the microscale (Fig. 2.17.3F), as SEM coupled with EDS indicated [62,63,70,79,80]. It is quite interesting to note that, within this mosaic-like texture, the Sn-rich phases are monitored as droplets inside the matrix. On the contrary, both Si-rich and Ge-rich phases (where available) are monitored as bi-continuous net inside the matrix.

The results indicated by SEM coupled with EDS clearly indicate the presence of at least two groups of different phases with varying tin content, besides the main parent matrix family and the magnesium oxide. However, the values for lattice parameters of these secondary phases result in XRD peaks with angles expected to be centered very close to each other for the case of the Sn-rich phase and matrix (x = 0.4, Fig. 2.17.2C); this is exactly the case for Si-rich and Ge-rich phases, for the pseudo-ternary materials. For the case of pseudo-ternary material, the lattice constant for the matrix and Sn-rich phases is 6.477 and 6.481 Å, respectively, while for the Si-rich and Ge-rich ones is 6.579 and 6.583 Å [62]. Eventually, each one of the two main XRD peaks in the case of both pseudo-binary and pseudo-ternary compounds corresponds to the mixture of

---

**Fig. 2.17.3, cont'd** Typical SEM micrographs for the cases of (A and B) Bi-doped binary compounds. In micrograph B, apart from the matrix (a), grain boundaries and bright inclusions are clearly visible. The corresponding elemental mappings with respect to (b) silicon, (c) oxygen, and (d) Mg are also shown. The mappings indicate MgO formation at the Mg<sub>2</sub>Si grain boundaries; (C) a Bi-doped Mg<sub>2</sub>Si<sub>0.4</sub>Sn<sub>0.6</sub> specimen showing the presence of secondary phases; (D) Mg<sub>2.16</sub>(Si<sub>0.4</sub>Sn<sub>0.6</sub>)<sub>1-y</sub>Bi<sub>y</sub> (0 ≤ y ≤ 0.03) solid solutions; besides the backscattered image (a) the elemental mapping distributions (b)–(e) are also presented; (E) an Sb-doped Mg<sub>2</sub>Si<sub>0.8</sub>Sn<sub>0.2</sub> specimen showing the presence of the main phase α along with the Mg<sub>2</sub>Si-like phase β. Plot (F) presents the contents of the basic elements at various EDS spots on a Mg<sub>2</sub>Si<sub>0.53</sub>Sn<sub>0.4</sub>Ge<sub>0.05</sub>:Bi<sub>0.02</sub> specimen indicating the presence of four different groups, each one corresponding to a different phase.

(A and B) From J. de Boor, T. Dasgupta, H. Kolb, C. Compere, K. Kelm, E. Mueller, *Acta Mater.* 77 (2014) 68–75. (C) From T. Dasgupta, C. Stiewe, J. de Boor, E. Müller, *Phys. Status Solidi A* 211 (2014) 1250–1254. (D) From W. Liu, Q. Zhang, K. Yin, H. Chi, X. Zhou, X. Tang, C. Uher, *J. Solid State Chem.* 203 (2013) 333–339. (E) From J. de Boor, S. Gupta, H. Kolb, T. Dasgupta, E. Mueller, *J. Mater. Chem. C* 3 (2015) 10467. (F) From G.S. Polymeris, N. Vlachos, A.U. Khan, E. Hatzikraniotis, C.B. Lioutas, A. Delimitis, E. Pavlidou, K.M. Paraskevopoulos, T. Kyrtatsi, *Acta Mater.* 83 (2015) 285–293.

the phases. Due to the two groups of close lattice constants, the first peak, at lower  $2\theta$  angles, corresponds to a doublet of unresolved PXRD phases observed in SEM, namely the Sn-rich phases and the matrix, while the one at higher  $2\theta$  angles corresponds to another doublet of unresolved phases, namely the Si-rich and Ge-rich ones; thus the major peak 40 degrees appears as a doublet. This latter conclusion is clearly revealed in Fig. 2.17.2C.

### 2.17.3.2 Nanostucture

The presence of phases with dominant Si and Sn components for pseudo-binary  $(\text{Mg}_2\text{Si})_{1-x}(\text{Mg}_2\text{Sn})_x$  compounds within the range  $0.3 < x < 0.75$ , along with the presence of a Ge-rich phase when germanium is incorporated, in conjunction to the MgO content, was verified by both PXRD and SEM-EDS techniques in macro- and micro-scales, respectively. However, these were reported to be ubiquitously present in all relevant length scales, including the nanoscale, by transmission electron microscopy (TEM hereafter) and high-resolution TEM (HR-TEM hereafter) measurements coupled with EDS [42,45,48,62,63,69–72,77,79,81–85]. A selection of typical electron diffraction patterns is presented for the high ZT  $\text{Mg}_2\text{Si}_{0.53}\text{Sn}_{0.40}\text{Ge}_{0.05}\text{:Bi}_{0.02}$  material in Fig. 2.17.4, from different areas, for the sake of comparison. The growth of single crystals with sizes up to a few microns is verified by the periodically arranged spots, indicated by black dots in the left-hand image. The existence of the MgO is revealed with very good accuracy in both images by green arcs in the left image as well as by gray images in the right image. The rings of discrete spots verify the growth of a polycrystalline material; the deduced d-spacings show the coexistence of both Si-rich and Sn-rich single crystals. The blue and red arcs of the middle image correspond to the theoretically expected positions of spots for the FCC cubic phases (NaCl type structure) of  $\text{Mg}_2\text{Sn}$  and  $\text{Mg}_2\text{Si}$ , respectively. This latter image verifies the presence of Si-rich and Sn-rich crystallites, implying the corresponding presence of Si-rich and Sn-rich phases in the nanoscale. Nevertheless, the image is composite, showing a compilation of two different images. A characteristic dispersion of these rings is revealed, providing proofs toward the coexistence of at least two phases (inset in presents an enlarged image of the rings), with tin contents of 0.3 and 0.7, according to the corresponding radii of the rings. Fig. 2.17.5 shows a typical high-angle annular dark-field (HAADF) image from the  $\text{Mg}_2\text{Si}_{0.6}\text{Sn}_{0.4}\text{Sb}_{0.013}$  sample, using the (220) strong reflection. EDS mapping in either one or two dimensions indicates the presence of high Sn content, higher than the nominal one, corresponding thus to an Sn-rich phase.

These phases span from a micro-meter scale down to the nanoscale for both pseudo-binary and pseudo-ternary compounds. This feature is strongly supported by Fig. 2.17.6, where detailed high-resolution TEM (HRTEM) combined with EDS studies and EDS mapping revealed that Sn-rich and Si-rich phases, in conjunction to the MgO nano-phase, appear within one crystalline grain. Two types of nano-phases are observed; elongated nano-crystallites which correspond to pseudo-ternary material phases and two considerably smaller almost circular in shape nano-MgO which are most likely located at the phase boundaries. Material nano-phases are most likely found imbedded inside a larger phase of the “opposite type.” For example, in

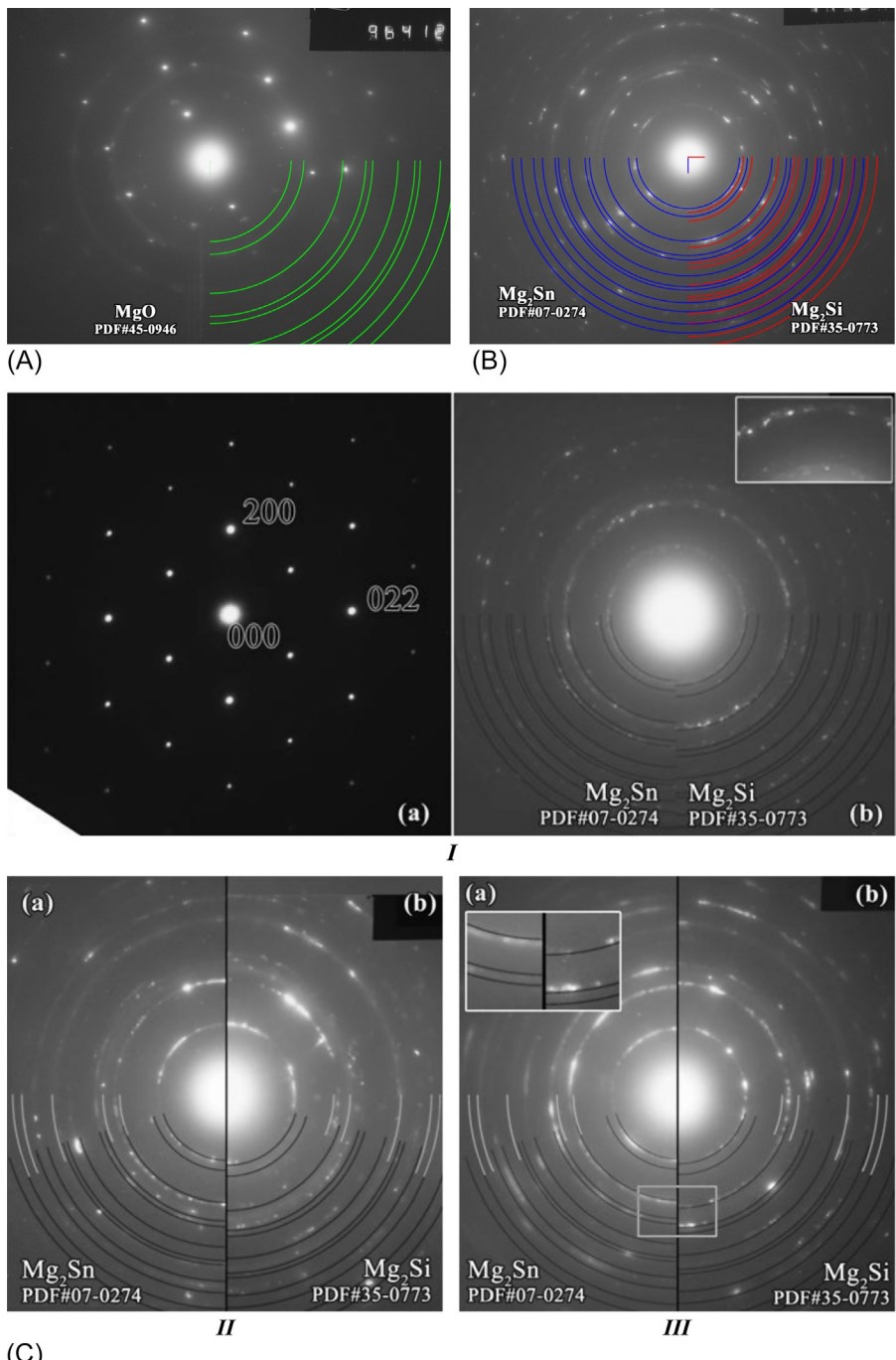


**Fig. 2.17.4** See figure legend on next page

**Fig. 2.17.6C** an elongated Si-rich phase is found imbedded in a Sn-rich phase of much larger size. The size distribution of the nano-crystallites was measured using both dark-field images and HR-TEM and is presented in **Fig. 2.17.7** for both undoped and two doped members of the  $Mg_2Si_{0.53}Sn_{0.40}Ge_{0.05}$  compounds. The distribution can be modeled by two clearly defined Log-Normal distributions for both undoped and doped samples. Based on the inverse Fast Fourier Transform (iFFT) analysis (**Fig. 2.17.6C**), the distribution with the lower crystallite sizes corresponds to MgO while the one with the larger sizes to the pseudo-quaternary material. The sizes of the quaternary material nanocrystallites are in the order of 20–25 nm, for both undoped and doped materials, suggesting the *in situ* formation of a bulk nanostructured material.

As it was verified by the previous **Figs. 2.17.4–2.17.7**, nanocomposite made by powder metallurgy methods exhibits some general features: (i) a distribution range of grain size from a couple of hundreds of nanometers to several nanometers; (ii) nano-inclusions due to compositional fluctuation; and (iii) secondary-phase nanoparticles at grain boundaries. It should be noted that the average grain size in different materials could be different due to the different grain growth behaviors and also the ratio between the hot-pressing (when applicable) temperature ( $T_{HP}$ ) and the melting point ( $T_m$ ). In many cases, TEM and HRTEM techniques have verified the presence of nanostructuring even for binary materials [24,86].

### 2.17.3.3 Dopant-stimulated phase separation, miscibility gap, and thermodynamics of phase separation

The dopant element is incorporated into the Si/Sn sublattice in the  $Mg_2(Si,Sn(Ge))$ -type crystal structure acting as an electron donor and significantly influences the electrical transport properties. However, the dopant content exhibits an increasing trend from Si-rich to Ge-rich phases (case of pseudo-ternary compounds) and, finally, to Sn-rich phases (cases of both pseudo-binary and pseudo-ternary compounds). Clearly, the dopant enhances phase separation, leading to an increase on the Sn-rich phase at the expense of the “matrix,” implying that the dopant content is not expected to be homogeneously distributed in all phases [62, 70]. It seems more likely for Bi/Sb to substitute

**Fig. 2.17.4, cont'd** TEM diffraction images of  $Mg_2Si_{0.53}Sn_{0.40}Ge_{0.05}:Bi_{0.02}$ . (A) Single crystal electron diffraction image, along with obvious presence of two rings corresponding to MgO; green arcs correspond to the theoretically expected positions of spots for the MgO. (B) Electron diffraction from the polycrystalline area. Red and blue arcs correspond to the theoretically expected positions of the diffracted beams according to the corresponding PDF files for  $Mg_2Si$  and  $Mg_2Sn$ , respectively. (C) ED patterns from two different polycrystalline areas, indicating the coexistence of Si-rich and Sn-rich crystallites. More possible stoichiometry around  $x=0.3$  and  $x=0.7$ .

From G.S. Polymeris, N. Vlachos, A.U. Khan, E. Hatzikraniotis, C.B. Lioutas, A. Delimitis, E. Pavlidou, K.M. Paraskevopoulos, T. Kyrtatsi, *Acta Mater.* 83 (2015) 285–293.

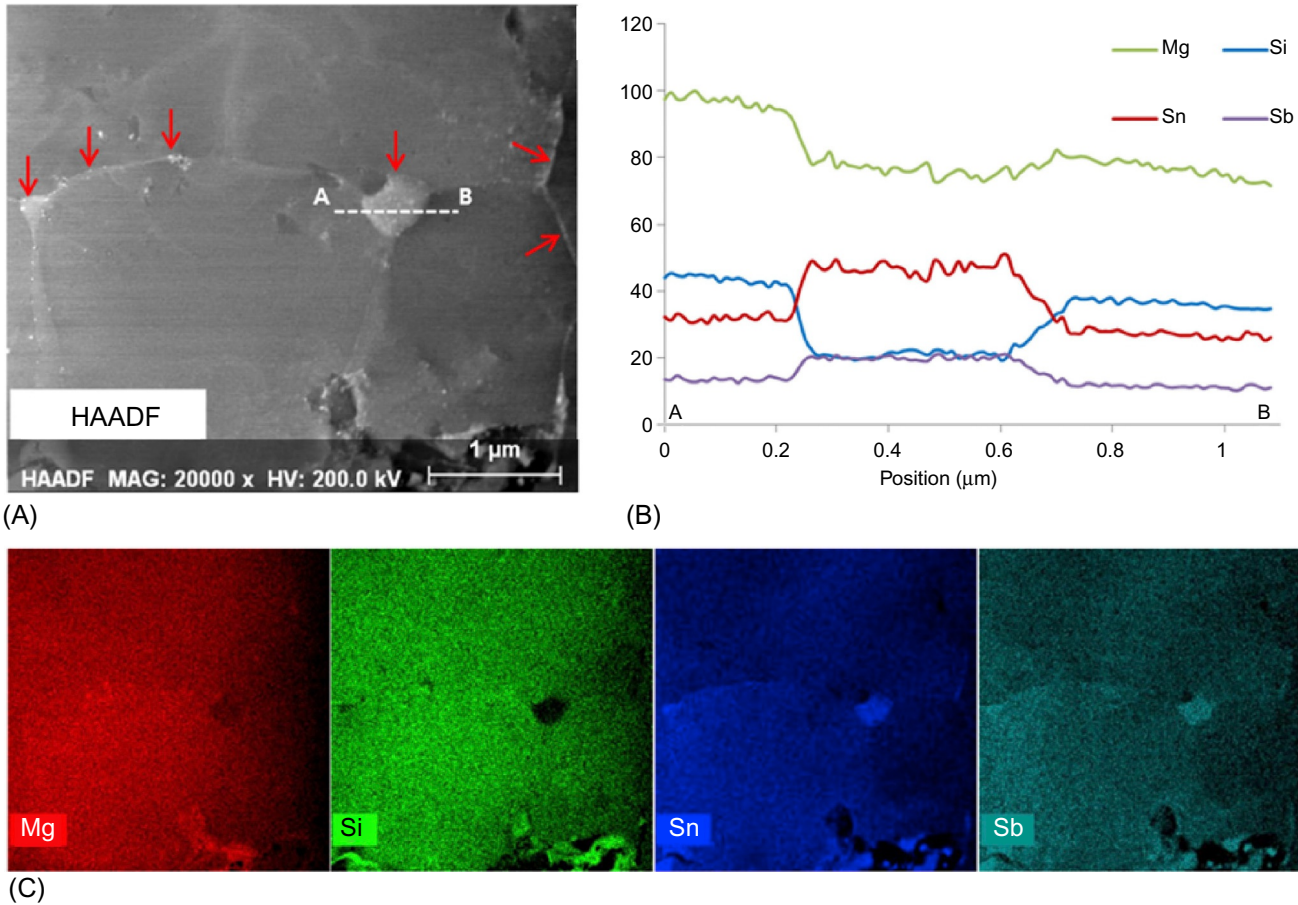


**Fig. 2.17.5** Plot (A) presents a high-angle annular dark-field (HAADF) image of  $\text{Mg}_2\text{Si}_{0.6}\text{Sn}_{0.4}\text{Sb}_{0.013}$  sample; the Sn-rich nano-phase is indicated by red arrows. Plot (B) presents the compositional line scan from point A to point B in plot (A), while images (C) depict elemental mapping images. From J. Jang, B. Ryu, S.-J. Joo, B.-S. Kim, B.-K. Min, H.-W. Lee, S.-D. Park, H.S. Lee, J.E., Lee, J. Alloys Compd. 739 (2018) 129-138.

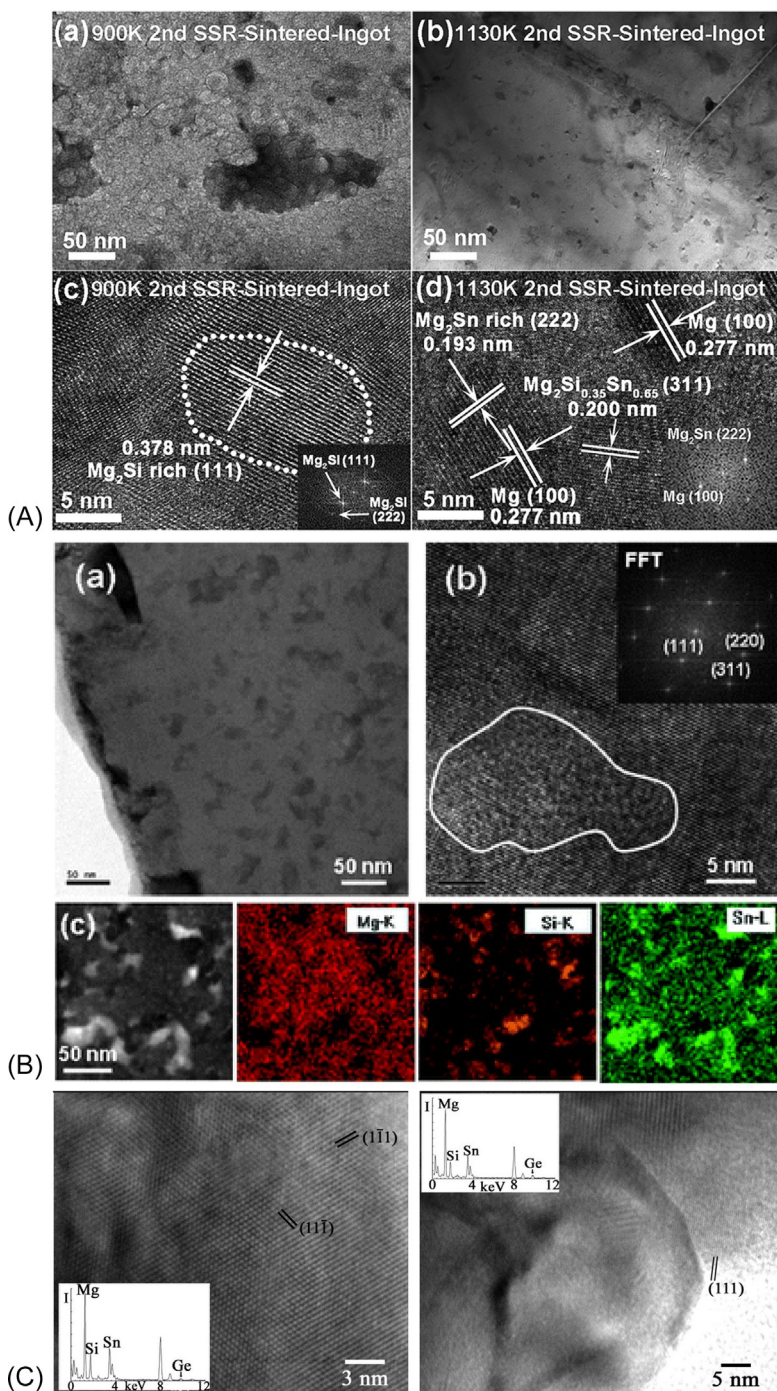


Fig. 2.17.6 See figure legend on opposite page

Sn than other elements. Consequently, the Sn-rich phase should contain more dopant, than the other phases. This feature is further supported by Fig. 2.17.8A and B and by both SEM-EDS and TEM-EDS measurements of the Bi versus the Si/Sn/Ge contents of Mg<sub>2</sub>Si<sub>0.53</sub>Sn<sub>0.40</sub>Ge<sub>0.05</sub>:Bi<sub>0.02</sub> compound. This feature could be attributed to element size considerations, as tin yields the largest volume. Therefore, the large atoms of Sb or Bi prefer occupying unit cells with larger volumes, such as those of the Sn-rich phase. For the Si-rich leftover phase, which dominates, doping takes place at a much slower rate. Tin replaces Si in the cases of both pseudo-binary and pseudo-ternary compounds in all scales; please refer to Fig. 2.17.8C. For the case of pseudo-ternary compounds, the Ge-rich phase attains doping easily, because it is also rich in tin; the presence of the group of Ge-rich phases stands as a strong argument that germanium also stimulates phase separation. Dopant selective substitution/in-homogeneities are also monitored in the meso-scale, using micro-FTIR mapping. Micro-FTIR spectra were analyzed using a specific effective medium theory (EMT). The main outcome of the modeling procedure includes various parameters, among which, for each group phase, the plasma frequency  $\omega_p$  is related to the variation in the dopant concentration, while the variation in  $\epsilon_{INF}$  is related to the Sn content and thus the identification of various phases in the meso-scale. The data extracted from the analysis for the majority of the samples successfully identified three distinct groups, each one corresponding to a different phase. Moreover, the plasma frequency (i.e., the dopant content) seems to be higher for higher  $\epsilon_{INF}$  values (i.e., Sn-rich phases). An example of  $\omega_p$  mapping is presented in Fig. 2.17.8D.

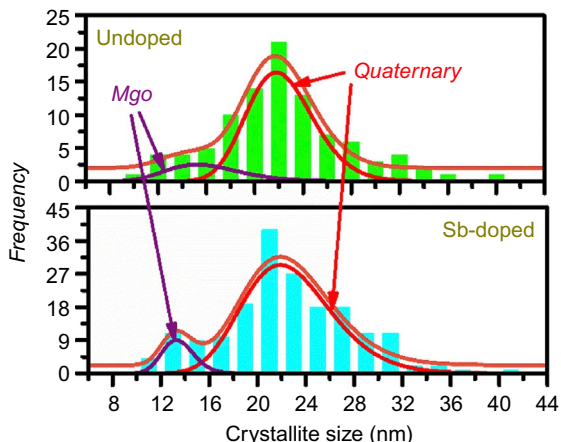
Besides the main matrix and the MgO, three more groups of secondary phases are monitored, which extend with uniform composition from nanoscale to macroscale, as observed by HRTEM (atomic scale), TEM (nanoscale), SEM studies coupled with EDS (microscale), micro-FTIR (mesoscale), and PXRD (macroscale). All these length-scale observations verified the presence of a hierarchical structure extending from few millimeters down to a few nanometers, with uniform, narrow distribution of nanoparticles, even in the case of MgO. While from the theoretical point of view

---

**Fig. 2.17.6, cont'd** HR-TEM images of pseudo-binary and pseudo-ternary compounds for the cases of: (A) Mg<sub>2.16</sub>(Si<sub>0.30</sub>Sn<sub>0.70</sub>)<sub>0.98</sub>Sb<sub>0.02</sub> solid solution; (a) and (b) correspond to low magnification images while (c) and (d) are high magnification images of the compound following the second SSR synthesis step quenched at 900 and 1130 K, respectively. The insets in (c) and (d) show the corresponding fast Fourier transform (FFT) patterns; (B) Mg<sub>2.16</sub>(Si<sub>0.4</sub>Sn<sub>0.6</sub>)<sub>0.985</sub>Sb<sub>0.015</sub> along with elemental maps of Mg, Si, and Sn. The insert in (b) shows the fast Fourier transform pattern of the matrix; (C) Mg<sub>2</sub>Si<sub>0.53</sub>Sn<sub>0.40</sub>Ge<sub>0.05</sub>:Bi<sub>0.02</sub> indicating an Sn-rich and (left image) and a Ge-rich (middle image) nano-crystallite. The corresponding EDS spectra are presented as insets, with the differences in the EDS peak intensities being outlined. Image reconstruction via IFFT depicts nanocrystals of Sn-rich and Si-rich phases, along with those of MgO (left image); the MgO nanocrystallites are generally smaller.

(A) From K. Yin, X. Su, Y. Yan, C. Uher, X. Tang, RSC Adv. 6 (2016) 16824–16831. (B) From W. Liu, X. Tang, H. Li, K. Yin, J. Sharp, X. Zhou, C. Uher, J. Mater. Chem. 22 (2012) 13653. (C) From G.S. Polymeris, N. Vlachos, A.U. Khan, E. Hatzikraniotis, C.B. Lioutas, A. Delimitis, E. Pavlidou, K.M. Paraskevopoulos, T. Kyriatsi, Acta Mater. 83 (2015) 285–293.

**Fig. 2.17.7** Crystallite size distribution for the cases of undoped  $Mg_2Si_{0.53}Sn_{0.40}Ge_{0.05}$  as well as  $Mg_2Si_{0.55-y}Sn_{0.40}Ge_{0.05}$ :  $X_y$  compounds for the cases of  $X: Sb, y=0.0125$  (from Ref. [70]) and  $X: Bi, y=0.02$  (unpublished data), yielded from Dark Field TEM images.



$Mg_2Si$  and  $Mg_2Ge$  form a complete solid solution, pseudo-binary  $Mg_2Si$ - $Mg_2Sn$  and  $Mg_2Ge$ - $Mg_2Sn$  phase diagrams show a miscibility gap at low temperature [5,6,11,87,88], especially in the Si-rich part (Fig. 2.17.9).  $Mg_2Si$  and  $Mg_2Sn$  are known to form solid solutions of  $Mg_2Si_{1-x}Sn_x$ ; however, within the range  $0.4 < x < 0.6$ , a special  $Mg_2Si_{1-x}Sn_x$  microstructure is expected to occur, owing to the features of the pseudo-binary phase diagram of  $Mg_2Si$ - $Mg_2Sn$  of Fig. 2.17.9 [5, 6, 11]. This expected miscibility gap and its special features is the reason why the majority of the corresponding TEM and HR-TEM studies were performed for nominal tin contents which are situated in the boundary between the region of the formation of  $Mg_2Si_{1-x}Sn_x$  solid solutions and the theoretically expected miscibility gap, namely  $x=0.6$  [42,45,48,72,77,79,81,82,85] and  $x=0.4$  [62, 63, 69, 70]. Some scarce studies also focus on  $x=0.7$  tin content [71,83].

Sn-rich group of phases with Sn:Si ratio of the order of 60/40 seems to be thermodynamically favored; nevertheless the exact Sn and Si contents of the Sn-rich and Si-rich phases correspondingly slightly change upon the dopant content [25,61,62,70,85]. Surprisingly, the Sn content in these later citations ranged between 60% and 70% Sn. The formation of this, specific, secondary phase with values of  $x$  equal to, or even larger than, 0.6 is thermodynamically favored owing to the presence of the  $Mg_2Si_{1-x}Sn_x$  miscibility gap itself, as the thermodynamically favored composition of tin is just above the expected boundary between the region of the formation of  $Mg_2Si_{1-x}Sn_x$  solid solutions and the miscibility gap. Doping clearly promotes the phase separation of  $Mg_2Si$ - $Mg_2Sn$  solid solutions and selectively dopes the grain boundary phase, implying that the addition of dopant affects the Sn/Si ratio in the  $Mg_2Si$ -rich matrix phase via shifting of the boundaries of the miscibility gap, which was corroborated by EDS analysis. Nevertheless, among these groups of secondary phases, besides the Sn-rich, the rest falls within the miscibility gap. Concentrations of tin in the range between 0.4 and 0.6, namely within the known miscibility gap, not only were monitored; moreover were proven very stable, thus verifying the dependence of either its presence or its precise extent on the synthesis process [64].

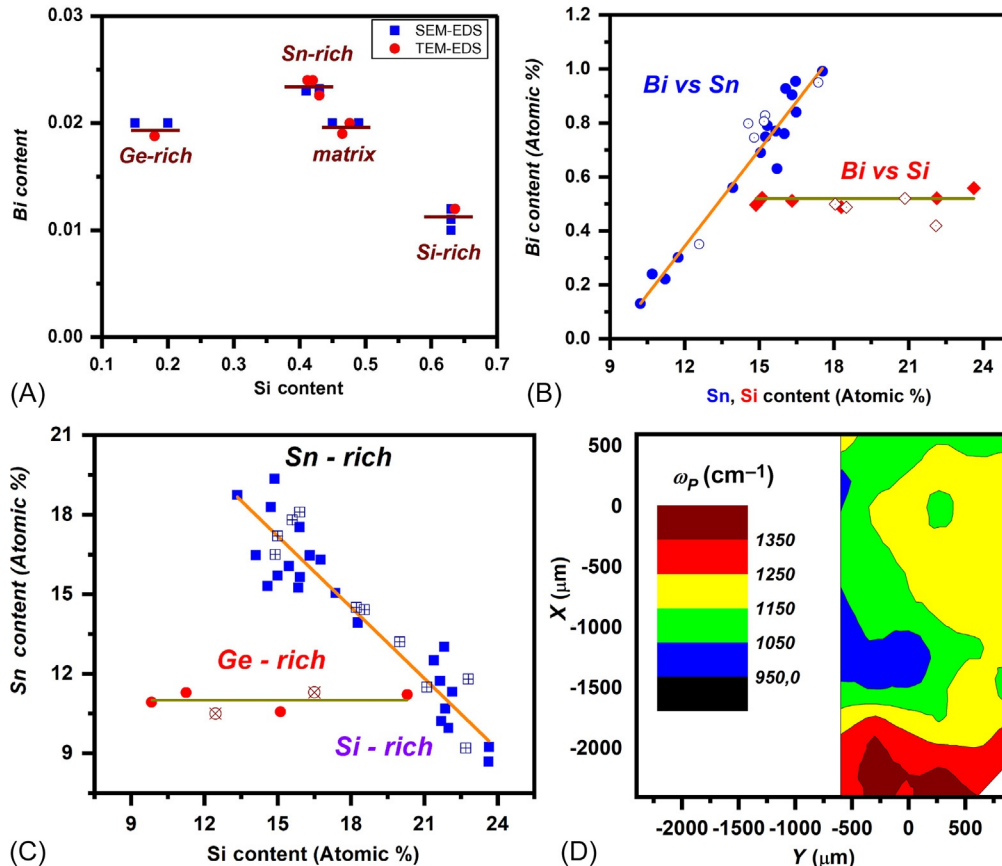


**Fig. 2.17.8** SEM-EDS (solid dots) and TEM-EDS (open dots) elemental analysis regarding the doping level on the Sn/Si/Ge-rich phases (plots A and B) as well as both Sn and Ge contents versus the Si content (plot C) for the case of  $Mg_2Si_{0.53}Sn_{0.40}Ge_{0.05}$  as well as  $Mg_2Si_{0.53}Sn_{0.40}Ge_{0.05}:Bi_{0.02}$  compound. Plot (D) presents a micro-FTIR mapping of the plasma frequency of the same material.  
 Plot (A) from G.S. Polymeris, N. Vlachos, A.U. Khan, E. Hatzikraniotis, C.B. Lioutas, A. Delimitis, E. Pavlidou, K.M. Paraskevopoulos, T. Kyriatsi, Acta Mater. 83 (2015) 285–293.

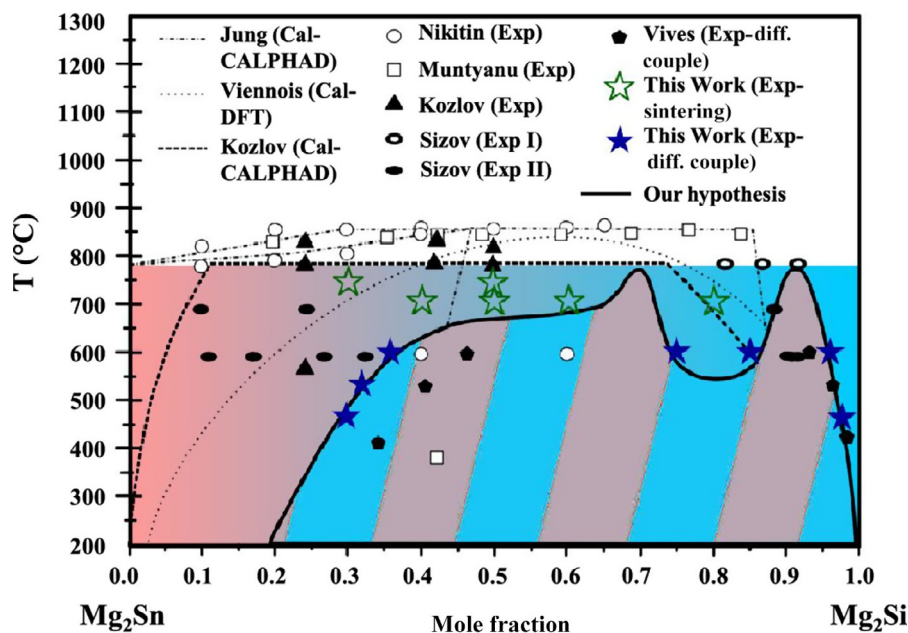


**Fig. 2.17.9** Available phase diagrams of  $\text{Mg}_2\text{Si}-\text{Mg}_2\text{Sn}$  (data according to Refs. [88–90]). Nikitin et al. [91] and Muntyanu et al. [92] had carried out XRD, thermal analysis, microhardness measurements, and density measurements to obtain boundaries of the miscibility gap. Also, Kozlov et al. [87] had obtained their experimental data by differential scanning calorimetry and thermal analysis. Sizov et al. [93] had conducted homogenization experiments (Exp I) and obtained Si-rich single-phase solid solutions (*empty ovals*). The solid solutions were then annealed at lower temperatures (Exp II) which then underwent phase separation to form Si-rich and Sn-rich phases (*filled ovals*). Both *filled* and *empty stars with blue* show the experimental data of Yasseri et al. [94], including experimental data with  $\text{Mg}_2(\text{Si},\text{Sn})$  compositions at which formation of a homogenous solid solution was proven, indicating the solubility limits (boundaries of the miscibility gap at 450–600°C). The *solid black line* is plotted as a guide to the eye to indicate a hypothesis for the position of the miscibility gap. *Black solid and blue solid curves* show bimodal and spinodal lines, respectively.

From M. Yasseri, A. Sankhla, H. Kamila, R. Orenstein, D.Y. Nhi Truong, N. Farahi, J. de Boor, E. Mueller, *Acta Mater.* 185 (2020) 80–88.

The phase separation phenomena in  $\text{Mg}_2\text{Si}_{1-x}\text{Sn}_x$  alloys are neither studied in detail [93,95,96] nor yet fully understood. According to the different phase diagrams, an alloy decomposes spinodally in the area of a miscibility gap, where the second derivative of the free energy vs composition (calculated for each temperature) is negative; if the second derivative is positive, decomposition should follow the mechanism of nucleation and growth. Each of these mechanisms indicates different SEM microstructure features; while the microstructure formed during nucleation and growth consists of “islands” of one phase in a matrix of another, spinodal decomposition allows the formation of continuous endotaxial lamellae-like clusters [93,97]. Based on the SEM features presented previously both microstructural features were observed,

implying thus that both mechanisms coexist, depending on the content of the secondary phases. For the secondary phases yielding compositions close to that of the matrix, spinodal decomposition is responsible [95].

The study of the miscibility or solid solution gap of compounds has received relatively limited attention, considering its importance for the stability of these materials when they are subject to high operating temperature and thermal cycling. Viennois et al. [88] suggested that the miscibility gap is wider than what has been previously accepted, and these authors conclude that reports on high ZT TEs are likely not single-phase materials; this statement stands in good agreement to the reported literature. Indeed, even Fig. 2.17.9 suggests that various authors have suggested different phase diagrams, representing varying existence of limits and transformations of compounds in thermodynamic equilibrium [87,90,93,94]. The variation in the reported miscibility gap of Mg<sub>2</sub>Si<sub>1-x</sub>Sn<sub>x</sub> is considered to be a result of the kinetics of the formation of Sn- or Si-rich phases [65,89] suggesting a relationship with the synthesis method, the Mg-stoichiometry, and the temperature applied during synthesis. Moreover, the miscibility gap is expected to be different for the pseudo-ternary compounds, due to the miscibility gaps of both Mg<sub>2</sub>Si-Mg<sub>2</sub>Sn and Mg<sub>2</sub>Ge-Mg<sub>2</sub>Sn alloys. Finally, Yi et al. [98] have discussed the possibility of strain-induced suppression of the miscibility gap in nanostructured Mg<sub>2</sub>Si-Mg<sub>2</sub>Sn solid solutions.

## 2.17.4 Thermoelectric properties

### 2.17.4.1 Experimentally achieved ZT<sub>max</sub> values and doping

In general, the electrical transport properties of the undoped magnesium silicide TE alloys and solid solutions are poor for the undoped material; therefore optimization of the TE properties by doping becomes mandatory. Impurity doping drastically affects the TE properties of Mg<sub>2</sub>Si compounds and their solid solutions. A plethora of dopants has been proposed in order to improve its TE properties, while for practical applications thermodynamically stable dopants are required to ensure long-lifetime operation at elevated temperatures.

In a theoretical study, Zwolenski et al. [99] have focused on the influence of chemical disorder on electronic properties, emphasizing site selectivity, the n/p character of dopants, and the effect of dopants on the thermopower. They have adapted the fully self-consistent Korringa-Kohn-Rostoker method with the coherent potential approximation (KKR-CPA hereafter) to treat various types of chemical disorders and to calculate an electronic band structure with complex energy. In their work, they have studied several impurities (Al, P, Zn, Ga, Ag, Cd, In, Sb) and found that In, Cd, Ag, and Zn act as p-type dopants, occupying preferentially the Mg site, whereas in others occupy the chalcogen site, acting as n-type.

Over the voluminous literature already published, very few p-type dopants have been suggested, including gallium [50,100], silver [74,101,102], and lithium [44,103], indicating that effective p-type doping seems more difficult to be achieved. For the case of n-type, it was suggested that elements from groups Ib, IIIb, and Vb

could be primarily located at Si sites in Mg<sub>2</sub>Si, as well as substituting Sn and/or Ge in pseudo-binary and pseudo-ternary solid solutions and can, therefore, be used as donors [60,104,105]. It is noteworthy that elements Bi and Sb from the Vb group were found to be much more effective in enhancing the TE properties of n-type Mg<sub>2</sub>Si-based materials than other group elements by improving the n-type electrical conductivity through increasing the carrier concentration to the order of 10<sup>20</sup>–10<sup>21</sup> cm<sup>-3</sup> at 300 K [106]. The atomic radius for Si and Sn is 110 and 145 pm, respectively, while for Sb and Bi is 140 and 160 pm, and this may explain the easier substitution of Sn (or Si) by Sb than by Bi. The formation energies of both Sb and Bi in the Sn (or Si) site substitution are negative at the Mg-rich and the Sn (or Si) rich limits, suggesting that these impurities have good solubility. Despite the most frequent use of Sb, calculations from first principles show that Bi is the most stable element in Mg<sub>2</sub>Si compared with the other dopants, mostly due to its low melting point of 545 K [107] while it is nearly twice as heavy and has a larger radius than other n-type dopants such as Sb. Following the pioneer publication of Tani and Kido [12], several studies were published, applying Bi-doping. In any case, both Bi and Sb were proven to be effective dopants, as 2% Bi doping or 1.5% Sb results in carrier concentration barely 10<sup>20</sup> cm<sup>-3</sup> for the binary Mg<sub>2</sub>Si [60, 70]. The doping efficiency is considerably increased (2.06 × 10<sup>20</sup> and 5.2 × 10<sup>20</sup> cm<sup>-3</sup>) for the case of pseudo-binary [63,70,79] and pseudo ternary materials [70,79]. In a recent review, it was suggested that dopant solubility in general increases while moving from Mg<sub>2</sub>Si toward the Mg<sub>2</sub>Sn side [8]. The excess of Bi that is not dissolved in the lattice as dopant, is most likely accumulated in the grain boundaries [73]. The carrier concentration further increases with double doping [40,77,83,108–110].

Fig. 2.17.10 presents the maximum TE figure of merit ( $ZT_{max}$ ) values that have been reported so far in the literature for Mg<sub>2</sub>Si-Mg<sub>2</sub>Sn(-Mg<sub>2</sub>Ge) compounds and various doping elements (including the cases of multidoping); these  $ZT_{max}$  values are plotted versus tin content  $x$  and are grouped according to their dopant. The data of this latter figure were collected based on an extended literature review up to January 2020 for both n-type and p-type compounds. The following results could be easily revealed according to Fig. 2.17.10:

- (a) For the case of binary Mg<sub>2</sub>Si compounds, the maximum ZT value does not exceed 0.9; moreover, the majority of the studies on the binary n-type compound report doping with Bi.
- (b) For all compositions, p-type materials (plotted as open symbols) are much inferior to n-type as far as the reported maximum ZT value is concerned [8, 44]. The maximum reported ZT value for p-type materials is 0.72 [44, 111].
- (c) The majority of the studies on both pseudo-binary and -ternary compounds is devoted to specific (stoichiometric) compounds, namely  $x=0.4$ ,  $x=0.6$ , and  $x=0.7$ ; for the same tin content, a wide range of  $ZT_{max}$  values has been reported, with the  $ZT_{max}$  and all related properties depending on the synthesis procedure.
- (d) For the majority of both pseudo-binary and -ternary compounds, Sb doping was applied.
- (e) There is an increasing trend of the  $ZT_{max}$  on the tin content up to 0.7, and a decreasing trend for higher Sn concentrations. The maximum ZT value is being achieved for  $x=0.7$  and co-doping using Bi and Cr [83], being around 1.72.

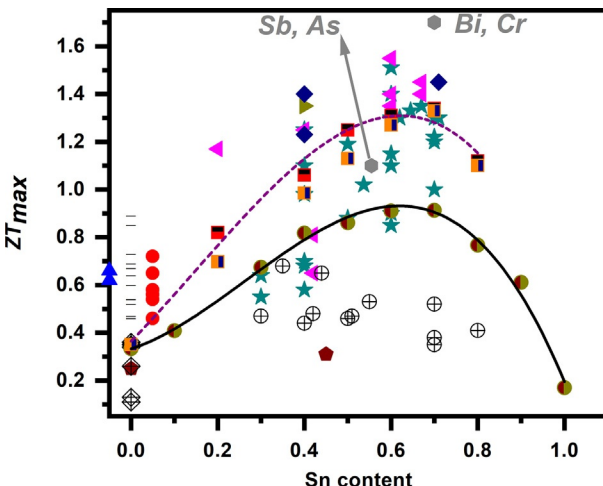


**Fig. 2.17.10** The maximum ZT values reported so far in the literature (until January 2020) plotted versus the tin content  $x$  for the cases of (a) binary Mg<sub>2</sub>Si doped with Bi (black thin lines), Sb (red dots), and Al (blue triangles), (b) pseudo-binary Mg<sub>2</sub>Si<sub>1-x</sub>Sn<sub>x</sub> solid solutions doped with Bi (pink triangles) and Sb (green stars), (c) pseudo-ternary solid solutions doped with Bi (dark yellow triangles), and Sb (dark blue diamonds), (d) undoped compounds (dark red pentagons), (e) co-doped compounds (dark gray hexagons; the co-dopants are also indicated), (f) p-type Mg<sub>2</sub>Si (open diamonds) and Mg<sub>2</sub>Si<sub>1-x</sub>Sn<sub>x</sub> (open dots) solid solutions. Double colored dots correspond to the data of Søndergaard et al. [112] measured at 700 K, while the double-colored squares correspond to the data of Liu et al. [42]; orange-blue double-colored squares also correspond to measurements at 700 K. Continuous curves provide a guide for the eye for the datasets of these two aforementioned reports.

(f) For the same composition, there is a range of  $ZT_{max}$  values. Such variations can be attributed to the different microstructural features resulted from the different synthesis routes.

Each filled data point presented in Fig. 2.17.10 corresponds to the  $ZT_{max}$  value of n-type compounds with a specific nominal contribution. Two studies, by Søndergaard et al. [112] and Liu et al. [42] cover the entire composition area, ranging from  $x=0$  up to  $x=1$  in the system Mg<sub>2</sub>Si<sub>1-x</sub>Sn<sub>x</sub>. In both cases, the dopant was Sb resulting in n-type of compounds. The data from both two aforementioned studies are also presented in Fig. 2.17.10 as double-colored dots and double colored squares respectively, while the continuous lines provide a guide for the eye regarding these two datasets. Most of the reported  $ZT_{max}$  values fall between these two lines, while some are well above the top line. The same trend is also monitored for both data sets, namely increasing ZT values for  $x$  values up to 0.8, being followed by decreasing ZT values for  $x$  above 0.8. Maximum ZT is somehow misleading, since various authors have adopted different methods of synthesis and processing, and different dopant and doping concentration, while  $ZT_{max}$  does not occur at the same temperature at all compositions. For example,  $ZT_{max}$  for the case of Liu et al. [42, 43] is not achieved at 700 K, a temperature at which the  $ZT_{max}$  values are reported by Søndergaard et al. [112].

The discrepancy between the  $ZT_{max}$  values that was observed for the two aforementioned papers for the same temperature could be attributed to the Mg content, as for the case of Liu et al. [42] compounds have been synthesized with an excess of magnesium  $\delta$  [113,114]. It is known that some quantity of Mg is “lost” in the synthesis/processing and Mg deficiency acts as acceptor, reducing the free carriers. Therefore, though the samples of Søndergaard et al. [112] have higher dopant content compared to those of Liu et al. [42] (0.75% vs 0.6% respectively), the free carrier concentration in the case of Søndergaard et al. [112] samples is lower than in Liu et al. [42], resulting in lower conductivity and lower power factor, though Seebeck coefficient practically coincides for the two authors.

#### 2.17.4.2 Band features and modeling of TE properties

$Mg_2Si$  is an indirect bandgap semiconductor with a forbidden band gap of  $E = 0.78\text{ eV}$  at  $0\text{ K}$  [115,116] and a direct gap of  $1.88\text{ eV}$  [117]. This bandgap was reported to decrease with the temperature almost linearly, with a wide range of different values for the temperature coefficient of the bandgap ( $dE_g/dT$ ) [115,118].

The modeling of TE properties is performed based on the Boltzmann transport theory, where the transport coefficients (conductivity, Seebeck, etc.) are calculated explicitly by transport integrals through nonlinear differential equations in relation to the distribution function of the electron gas. The distribution would indicate how carriers are distributed in the momentum space ( $k$ -space) and thus how the transport properties can be evaluated. To apply the Boltzmann transport theory, one needs to know either the detailed band structure of the material or to assume a parabolic (or nonparabolic) shape of the bands. Therefore, there are two approaches for the evaluation for the TE properties; those based on the actual band structure calculations from first principles, and those based on analytical expressions assuming either parabolic or nonparabolic shape of the bands.

The band structure of  $Mg_2X$  has been investigated with atomistic calculations. Several attempts were made, based on the empirical pseudopotential method (EPM) [117] and density functional theory (DFT) calculations using the local density approximation (LDA) [119,120] or the Korringa-Kohn-Rostoker (KKR) method, taking into account relativistic corrections due to spin-orbit coupling to the valence band [121,122]. Despite the fact that earlier results underestimate the bandgap [123], all calculations agree on the basic features of the band-scheme presented below: The valence band maximum is located at the  $\Gamma$  point in the Brillouin zone, [124] and the conduction band has its minimum at the X point [125]. A schematic representation of the band scheme is shown in Fig. 2.17.11A and B. The valence band shows a Ge-type degeneracy, with two converging bands (VB1 and VB2) with heavy and light holes, with no separation between the bands [126]. A third valence band (VB3), separated by  $\delta E$  arises from spin-orbit interaction [127]. The conduction band consists of two nondegenerate subbands with different effective masses, separated by  $\Delta E = 0.4\text{ eV}$  [5, 6]. The next lowest conduction band minimum is located at the L point and can contribute to multivalley conduction in  $Mg_2Si$  at ultrahigh doping concentrations; however, it has no significant contribution to the electronic properties of  $Mg_2Si$ .

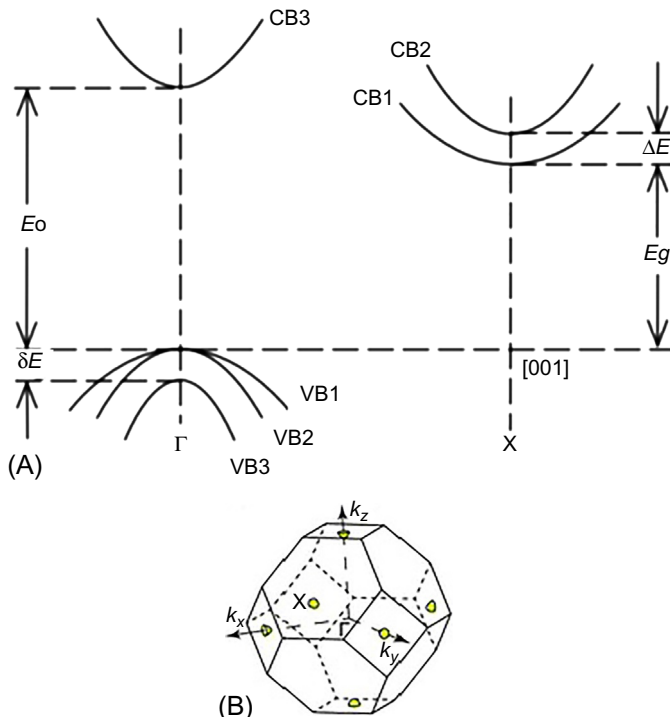


**Fig. 2.17.11** Simplified representation of the band scheme for Mg<sub>2</sub>Si<sub>1-x</sub>Sn<sub>x</sub> solid solutions band structure: (A) Bands arranged at the bottom of the lower conduction band indicating the change of the bandgap ( $E_g$ ) and the band separation ( $\delta E$ ) for the three major phases; (B) The first Brillouin zone showing the threefold degenerated ( $N_v = 3$ ) electron pockets at X.  
 (B) From W. Liu, H. Chi, H. Sun, Q. Zhang, K. Yin, X. Tang, Q. Zhang, C. Uher, Phys. Chem. Chem. Phys. 16 (2014) 6893.

under moderate doping concentrations [122,127]. The band separation between the two X conduction bands remains constant with temperature, while the separation between the valence band edge and the principal conduction band edge constantly decreases with the temperature at a specific rate. In the case of Mg<sub>2</sub>Sn, the band structure is almost similar, but the X1 conduction band edge is lower than that of the X3 band by 0.165 eV. Therefore, in Mg<sub>2</sub>Sn, a forbidden gap occurs between the  $\Gamma$  point valence band edge and the X1 conduction band edge. As with Mg<sub>2</sub>Si, the band gap of Mg<sub>2</sub>Sn also decreases constantly with the temperature at a smaller rate [126].

Kutorasinski et al. [127] have used first-principles calculations combined with the Boltzmann transport approach and have successfully applied both and efficiently modeled the electronic transport for binary as well as for pseudo-ternary systems. Shi and Kioupakis [123] have employed the band-structure calculations based on the many-body perturbation theory and the all-electron GW method including the spin-orbit effect, thus resulting in accurate determination of the bandgaps. The

calculated results are in good agreement with the experimental values. It was found that Sn-rich phase has a higher power factor. In addition, it was shown that the Bi dopant presumably reaches its solubility limit close to 2%, preventing the achievement of the best working concentration. Sn-rich phase falls in the region where band converting occurs.

Analytical expressions for the evaluation of the transport coefficients are based on electron statistics and are expressed in terms of either Fermi or Kane integrals for parabolic or nonparabolic types of the bands [128,129]. Due to the interconnection of transport properties ( $n$ ,  $S$ ,  $\sigma$ ), in a single band model, the power factor is optimized for a given free carrier concentration, and no further enhancement may be obtained. Enhancement for the power factor is achieved by band engineering. In a multiband electronic structure, the electrical conductivity and free carriers are determined by adding the contribution of all bands “ $i$ ” ( $\sigma = \Sigma \sigma_i$  and  $n = \Sigma n_i$ ), while Seebeck coefficient ( $S$ ) and mobility ( $\mu$ ) are determined as the weighted average over conductivity or the band population, respectively, ( $S = \Sigma (\sigma_i S_i) / \sigma$  and  $\mu = \Sigma (n_i \mu_i) / n$ ).

Modeling using analytic expressions has been applied by (i) Satyala and Vashaee [130] in the case of pure Mg<sub>2</sub>Si (either p- or n-type) for arbitrary carrier concentrations, (ii) by Bahk et al. [126] employing two-band model, and (iii) by Zhang et al. [131] employing three-band model. Satyala and Vashaee [130] have employed a non-parabolic band-model, while the other two publications employed a parabolic model. Nonparabolic band (Kane-type) model is usually adopted for the description of the bands in lead chalcogenides, and the reason for that is the strong dependence of the carrier effective mass on free carriers. However, in the case of Mg<sub>2</sub>Si-based compounds, relativistic KKR calculations have shown a weak effect of the effective mass on energy for Mg<sub>2</sub>Si [122]; this result has been experimentally confirmed by Stefanaki et al. [132], who have used Pisarenko plot (Seebeck vs free carriers) combined with IR reflectivity and Hall effect for the determination of the effective mass. The effective mass at the bottom of the first conduction band was found in the range of 0.9–1.0 m<sub>0</sub>, in agreement with the work of Bux et al. [73].

Liu et al. [42] have reported that a single effective mass (i.e., a single band model) cannot describe the Seebeck coefficient vs. carrier concentration data for Sb-doped Mg<sub>2.16</sub>Si<sub>0.4</sub>Sn<sub>0.6</sub> in the entire range of dopant concentration. They have noticed that the Seebeck-free carrier plot (Pisarenko plot) can be described by a set of curves, with different effective mass, which is gradually changing from 1.48 to 2.34 m<sub>0</sub> and samples with higher carrier densities appear to have a larger effective mass; refer to Fig. 2.17.12A. This is an indication of a second band contribution with significantly larger effective mass. Fig. 2.17.12B depicts a compilation of data from various papers for doped Mg<sub>2</sub>Si, Mg<sub>2</sub>Si<sub>0.6</sub>Sn<sub>0.4</sub>, and Mg<sub>2</sub>Si<sub>0.55</sub>Sn<sub>0.4</sub>Ge<sub>0.05</sub> compounds, over an extended range of free carrier concentration. As this latter figure reveals, single-band model (lower curve) may describe the behavior of the Seebeck coefficient versus charge carrier concentration at low carrier densities, up to 10<sup>20</sup> cm<sup>-3</sup>. At higher carrier densities, experimental points diverge from the theoretical single-band model, flatten and finally, decrease again, in absolute values at carrier concentrations higher than

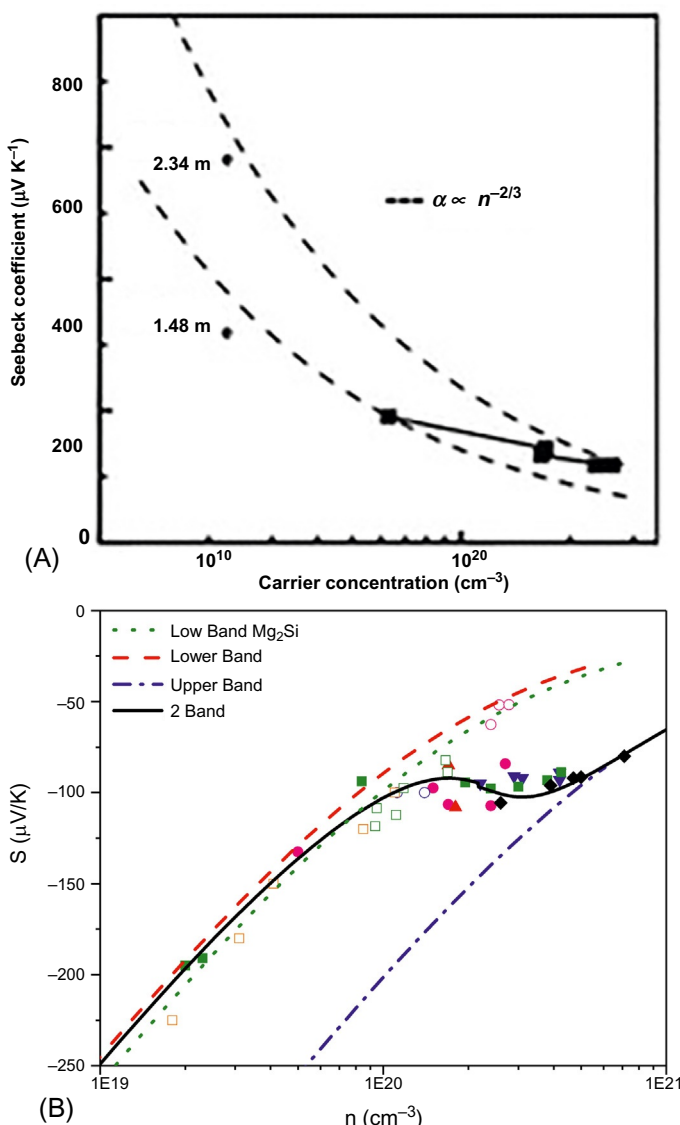


**Fig. 2.17.12** (A) The relationship between the Seebeck coefficient and the carrier concentration for the cases of  $\text{Mg}_{2.16}(\text{Si}_{0.4}\text{Sn}_{0.6})_{1-y}\text{Sb}_y$  ( $0 \leq y \leq 0.025$ ); (B) Two-band model analysis of the Pisarenko plot (open symbols: Mg<sub>2</sub>Si, filled symbols: Mg<sub>2</sub>(Si,Sn) and Mg<sub>2</sub>(Si,Sn,Ge))  
(A) From W. Liu, X. Tang, H. Li, K. Yin, J. Sharp, X. Zhou, C. Uher, *J. Mater. Chem.* 22 (2012) 13653.

$3 \times 10^{20} \text{ cm}^{-3}$ . Carrier redistribution in the two bands causes an increase in Hall coefficient [133] and flattening of the Seebeck coefficient. Energy shift between the two conduction bands is known to decrease when alloying Mg<sub>2</sub>Si with Sn [42,134], and this will cause modifications related to the band pickup.

### 2.17.4.3 The effect of alloying

Alloying is one of the most efficient ways to improve the TE performance of a binary solid. Alloying is known to greatly reduce the lattice thermal conductivity of the pristine binary, with a small sacrifice of the carrier mobility. For materials with multiple bands participating in electron transport, alloying may also help in “band engineering.”

#### 2.17.4.3.1 Band converging due to alloying

The material parameters of  $\text{Mg}_2\text{Si}_{1-x}\text{Sn}_x$  solid solutions depend strongly on the tin content  $x$ . As it was previously stated,  $\text{Mg}_2\text{Si}$  and  $\text{Mg}_2\text{Sn}$  compounds share a similar electronic band structure consisting of two closely lying conduction bands [71,135,136]. While the lower conduction band in  $\text{Mg}_2\text{Si}$  is dominated by the light electron band, the lower conduction band of  $\text{Mg}_2\text{Sn}$  is dominated by the heavy electron band [71,116,137]. This implies that, by forming solid solutions of  $\text{Mg}_2\text{Si}_{1-x}\text{Sn}_x$ , band convergence must take place at some particular value of  $x$  where the band edges of the light and heavy conduction bands attain comparable energy [116]. As shown in Fig. 2.17.13A, the separation of the X1 and X3 conduction bands decreases linearly with increasing Sn content  $x$ , and the complete convergence of the two bands occurs at  $x \sim 0.7$  [5, 6]. Fig. 2.17.13B shows the relative motion of the topmost valence band and the positions of the two conduction bands, being the light and the heavy bands separated in energy by  $\Delta E$ , as the tin content  $x$  increases from  $x=0$  to  $x=1$  [42]. While the heavy band is moving monotonically down in energy with increasing tin content, the light conduction band moves initially down and above  $x=0.3$  up with energy. The two bands thus converge and the theory predicts a crossover at Sn content around 0.65–0.70. As  $\Delta E$  decreases, the heavy band provides a progressively increasing contribution to the electrical properties, resulting in a larger effective mass and an increase in the absolute value of the Seebeck coefficient [138]. When the energy difference between the heavy and the light conduction bands is less than  $2kT$ , the two conduction bands become effectively degenerate, and the number of symmetrically nonequivalent pockets of electrons increases. The merging of these bands enhances the carrier mass and thus the Seebeck coefficient, all without any adverse effect on the carrier mobility [42,134], along with a high power factor. Wang et al. [139] have modeled ZT at 800 K in a two-band system as a function of chemical potential ( $\eta$ ) and band offset  $\Delta E$  and found that the maximum ZT is achieved when the two bands are aligned. Similarly, Kamila et al. [111] have found that for p-type  $\text{Mg}_2\text{Si}_{1-x}\text{Sn}_x$  system, at 500 K the maximum ZT falls in a region close to  $x=0.6$ ; for the Si-rich compositions ( $x \leq 0.4$ ), ZT is lower than that for the Sn-rich compositions ( $x \geq 0.6$ ).

#### 2.17.4.3.2 Carrier mobility and alloying

Electrical conductivity ( $\sigma$ ) is found to increase from binary to ternary compounds. This is partially due to two contradicting effects: the increase in the free carriers on one hand, and the decrease in the carrier mobility ( $\mu$ ) on the other. The decrease of carrier mobility is mainly attributed to alloying [140] though additional scattering

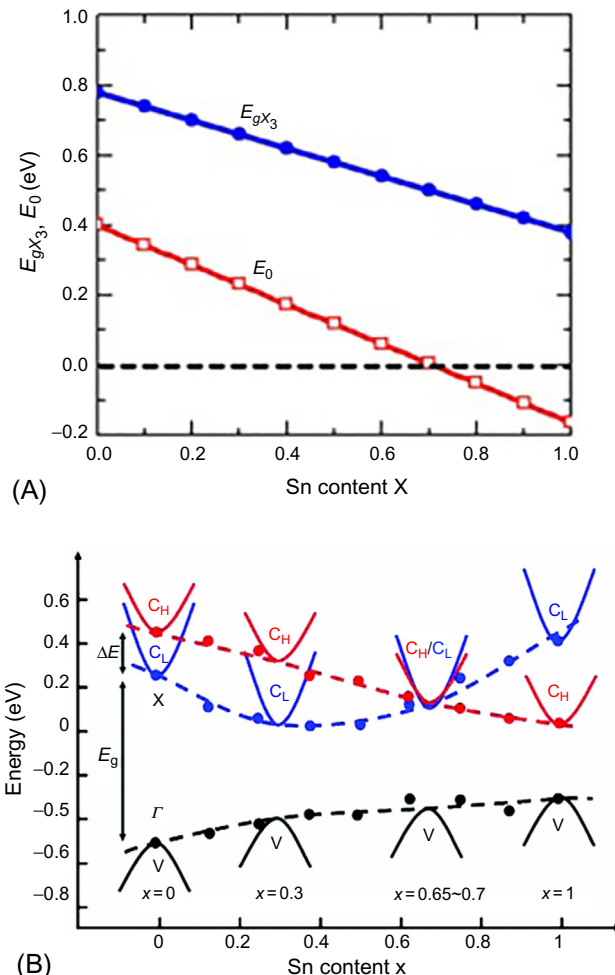


**Fig. 2.17.13** (A) The bandgap between the  $X_3$  conduction band edge and the  $\Gamma$  valence band ( $E_{gX_3}$ ) at 0 K and the separation between the  $X_1$  and  $X_3$  conduction bands, showing the convergence of the two bands for  $x \sim 0.7$ ; (B) Relative positions of the heavy (in red) and light (in blue) conduction bands as well as the topmost valence band (in black) as a function of the tin content for  $Mg_2Si_{1-x}Sn_x$  solid solutions.

(A) From J.-H. Bahk, Z. Bian, A. Shakouri, Phys. Rev. B 89 (2014) 075204. (B) From W. Liu, X. Tang, H. Li, K. Yin, J. Sharp, X. Zhou, C. Uher, J. Mater. Chem. 22 (2012) 13653.

to phase boundaries may not be excluded. In  $Mg_2Si_{1-x}Sn_x$  solid solutions, we should take into account two primary carrier scattering mechanisms including alloy scattering ( $\mu_{AL}$ ) and acoustic phonon scattering ( $\mu_{AC}$ ) [41,141], while the total mobility ( $\mu$ ) is obtained from the Matthiessen's rule ( $\mu^{-1} = \mu_{AC}^{-1} + \mu_{AL}^{-1}$ ) [131]. Both acoustic phonon

scattering and alloying scattering depend on the acoustic deformation potential, which depends quadratically on composition, and the combination of the two results in a decrease in the carrier mobility upon alloying. In addition to the acoustic phonon scattering, Bahk et al. [126] considered the polar optical phonon (POP) scattering and the ionized impurity scattering have been included in the total scattering time, although, as authors state, it turns out that they are still much weaker than the acoustic phonon scattering over the specific temperature range and the doping density range of interest. For complete relations for the various acting carrier scattering mechanisms, reader should refer to the original papers.

#### 2.17.4.3.3 Lattice thermal conductivity and alloying

The thermal conductivity of binary  $\text{Mg}_2\text{Si}$  is quite high, in the range of about  $10 \text{ W m}^{-1} \text{ K}^{-1}$  at room temperature. For the pseudo-binary system  $(\text{Mg}_2\text{Si})_{1-x}(\text{Mg}_2\text{Sn})_x$ , Zaitsev et al. [5, 6] have demonstrated a significant reduction of lattice thermal conductivity, from about  $8 \text{ W m}^{-1} \text{ K}^{-1}$  for  $\text{Mg}_2\text{Si}$  to almost  $1.9 \text{ W m}^{-1} \text{ K}^{-1}$  for  $x=0.4$  in  $\text{Mg}_2\text{Si}_x\text{Sn}_{1-x}$ .

The reduction of lattice thermal conductivity could be discussed in the framework of a phenomenological model. Adachi [142] has used such a phenomenological model to describe the alloying-effect on thermal conductivity on a binary system AB-AC. Thermal resistance ( $w=1/\kappa_L$ ) is modeled by the linear variation of the thermal resistance of the two end members ( $w_{AB}$  and  $w_{AC}$ ) and a bowing factor,  $x(1-x)$ , which accounts for the effect of alloying. A better understanding of the various mechanisms for alloying was introduced by Klemens [143], who proposed an analytical expression between  $\kappa_{L,\text{alloy}}$  and that of the pure compound  $\kappa_{L,\text{pure}}$ , which depends on the Debye temperature, the molar volume, and the velocity of sound. The effect of alloying is expressed by a disorder scaling parameter ( $\Gamma$ ), which depends on mass and strain field fluctuations. Klemens' model assumes that phonon-scattering from interfaces is negligible, as is the case for materials without nanostructuring, and the only existing phonon-scattering mechanism in solid solutions would be the Umklapp and the point defect scattering. Abeles' [144] extended the formula by Klemens, taking into account not only Umklapp and point defect scattering but also phonon scattering by normal process. Zaitsev et al. [5, 6] have used the Abeles' expression for the  $\text{Mg}_2\text{Si}-\text{Mg}_2\text{Sn}$  system and concluded that the lattice thermal conductivity is better described with equal contributions of the Normal and Umklapp processes.

Fig. 2.17.14A shows the dependence of lattice thermal conductivity for the pseudo-binary  $\text{Mg}_2\text{Si}-\text{Mg}_2\text{Sn}$  system (points) top curve as well as the theoretically predicted values, for the three aforementioned models. As can be seen, all models predict the effect of alloying in lattice thermal conductivity however, the Abeles' model (incorporating both Normal and Umklapp process) describes the experimental points better. The lattice thermal conductivity is presented as experimental points in Fig. 2.17.14B, along with the theoretical model (lines) for the three different groups, namely the binary ( $\text{Mg}_2\text{Si}$ ), the pseudo-binary  $(\text{Mg}_2\text{Si})_{1-x}(\text{Mg}_2\text{Sn})_x$ , and the pseudo-ternary  $(\text{Mg}_2\text{Si})_{1-x-y}(\text{Mg}_2\text{Sn})_x(\text{Mg}_2\text{Sn})_y$ . The solid lines in Fig. 2.17.14B stand as the theoretical values that were yielded by the application of the above model. As it becomes

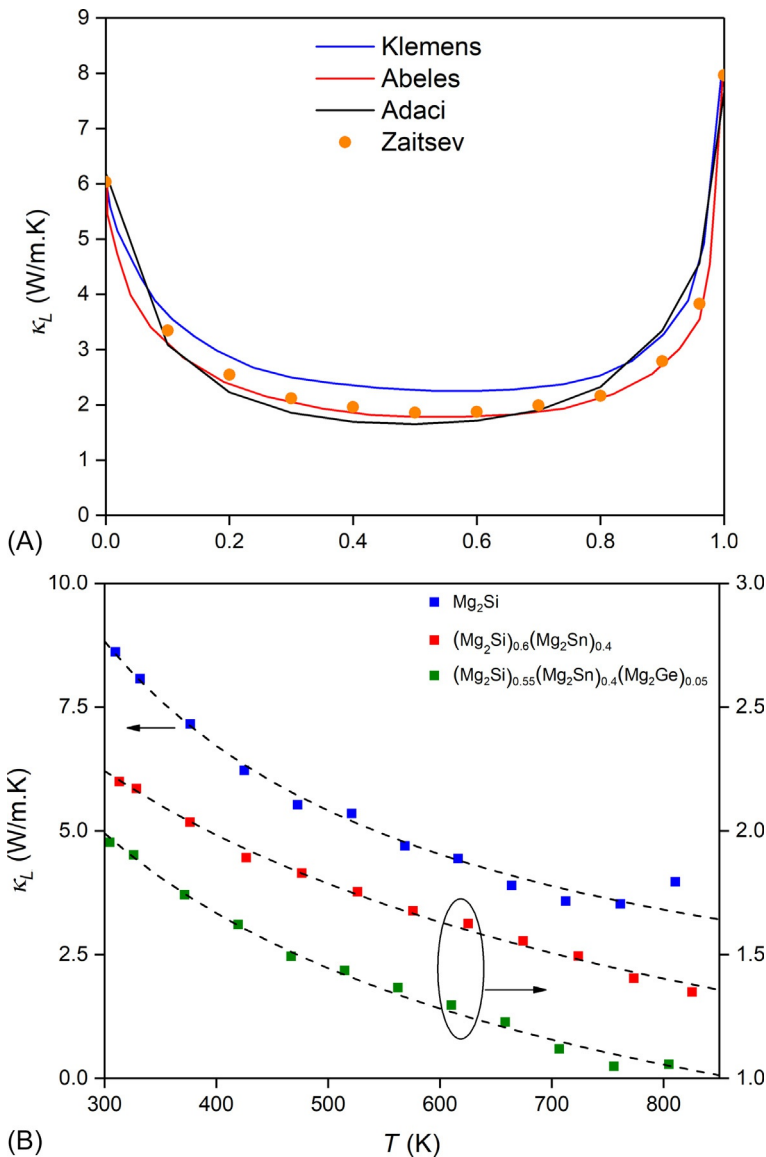


**Fig. 2.17.14** Plot (A) presents the room temperature lattice thermal conductivity as a function of solid solution composition, assuming solid solution. The *solid lines* are calculated according to the models described in the text. Plot (B) presents the lattice contribution to thermal conductivity for three groups of magnesium silicide-based compounds. Note the difference on the vertical axes.

(A) Data from V.K. Zaitsev, M.I. Fedorov, I.S. Eremin, E.A. Gurieva, in: D.M. Rowe (Ed.), Thermoelectric Handbook, Macro to Nano, CRC Press, Boca Raton, FL, 2006.

prominent, the theoretical model describes very well the experimental points. As it was already anticipated, lattice thermal conductivity decreases with temperature. In addition,  $\kappa_L$  decreases from binary to pseudo-binary compounds due to alloying with Sn and is further decreased to pseudo-ternary compounds due to an additional introduction with Ge.

#### **2.17.4.4 Beyond alloying**

In general, the enhancements in the figure of merit achieved in bulk TE materials have resulted from either the reduction in lattice thermal conductivity or the improvement in power factors or both of them. As it was already discussed previously in this chapter, Sn-alloyed Mg<sub>2</sub>Si compounds are structurally characterized by multiple phases (Si-rich, Sn-rich, etc.), which span from nano-meter to milli-meter scale. Alloying introduces an extended network of point defects which scatter mainly the short-wavelength phonons (due to mass difference or due to strain introduced), as it has been shown in the relevant session of this chapter. Medium wavelength phonons are scattered by nanostructuring, while long-wavelength phonons are scattered by millimeter-scale grains. Furthermore, different phases uptake different dopant content. Therefore, both nano- and microstructuring have a dramatic effect in the TE performance of these alloys.

##### **2.17.4.4.1 Thermal conductivity**

In order to understand the mechanisms of phonon scattering, semiclassical theoretical calculation based on the modified Callaway's model [145] is adopted. Callaway's model is an integral expression of the specific heat combined with the phonon relaxation time ( $\tau_C$ ), which accounts for the various phonon-scattering mechanisms summed in the form of Matthiessen's rule. For the complete relations of the various acting phonon-scattering mechanisms, the reader could refer to comprehensive papers by He et al. [146] and Lo et al. [147]. The advantage of the approach based on Callaway's model, over the analytical expression of the model by Klemens is that in the former case one can model the lattice thermal conductivity by modifying each scattering mechanism, including nanostructuring, while the Klemens' model assumes the only phonon-scattering mechanism would be the Umklapp and the point defect scattering.

Very few publications try to model the (lattice) thermal conductivity in Mg<sub>2</sub>Si-based alloys. Satyala and Vashaee [148] have tried to model the effect of nanostructuring in binary p- and n-type Mg<sub>2</sub>Si. They have shown that nanostructuring limits the energy-dependent phonon mean free path in Mg<sub>2</sub>Si, which results in a significant reduction (>50%) in lattice thermal conductivity. However, it was also concluded that nanostructuring in both p-type and n-type Mg<sub>2</sub>Si increases carrier scattering significantly. Due to the loss in carrier mobility, they have estimated a 10% improvement in the maximum ZT for n-type Mg<sub>2</sub>Si and 37% improvement for the p-type. For the pseudo-binary compounds, Bellanger et al.

[81] developed a model, which takes into account the nano and micro (grain) features of Mg<sub>2</sub>Si<sub>0.4</sub>Sn<sub>0.6</sub>, apart from the typical Umklapp and alloying processes to the phonon scattering. The material was nanostructured, consisting of 0.2-μm nano-grains containing a fine distribution of Sn-rich nanoparticles. The total lattice thermal conductivity was greatly reduced due to micro- and nanostructuring (Fig. 2.17.15A). Hatzikraniotis et al. [149] have applied a similar model for evaluating the thermal conductivity in Sb-doped Mg<sub>2</sub>Si<sub>0.6</sub>Sn<sub>0.4</sub>. Fig. 2.17.15B shows the phonon mean free path (MFP) at 500K, as a function of phonon frequency ( $\omega/\omega_D$ ). The various acting mechanisms that are reducing the lattice thermal conductivity are shown in the figure caption. At low frequencies, phonon MFP is limited by the grain boundary (GB) scattering, while at high frequencies by a combination of alloying and Umklapp processes. In the absence of nano-structures, the total phonon MFP is smoothly changing from the GB scattering to an alloy/Umklapp scattering as shown by the orange curve. However, when a nano is encountered (green curve), a considerable amount of mid-range phonons are scattered by nano inclusions (solid black curve). When nano density is increased by a factor of 10, the “nano-curve” (dotted green line) considerably filters out a much larger portion of mid-range phonons, resulting in a significantly lower lattice thermal conductivity.

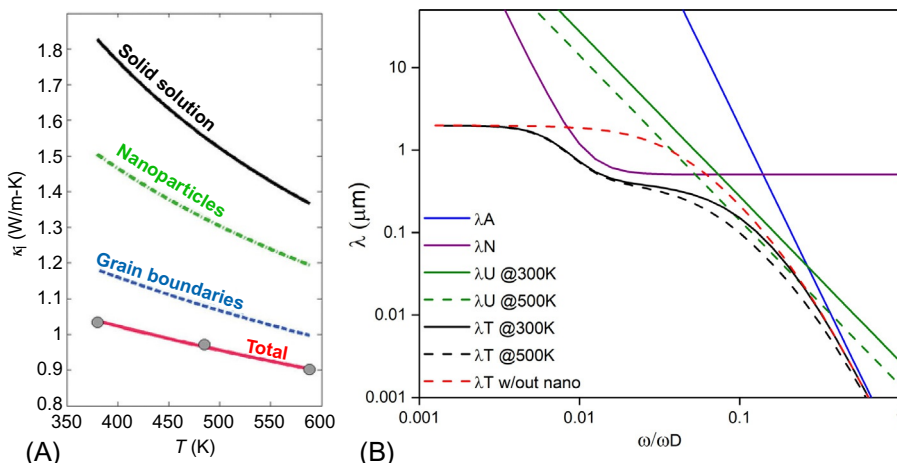


**Fig. 2.17.15** (A): Experimental lattice thermal conductivities (gray circles), obtained by subtracting the electronic contribution to the measured total thermal conductivity, versus temperature of samples synthesized using the SPS technique. Calculated lattice thermal conductivities considering all microstructural parameters are represented by the red line. Individual contributions to the lattice thermal conductivity are represented by the other lines with the following significations: solid solution only (black lines), solid solution with nanoparticles (green dash-dotted lines), and solid solution with grain boundaries (blue dash lines). (B) Phonon means free path for Mg<sub>2</sub>Si<sub>0.55</sub>Sn<sub>0.4</sub>Ge<sub>0.05</sub>. Plot (A) from P. Bellanger, S. Gorsse, G. Bernard-Granger, C. Navone, A. Redjaimia, S. Vivès, Acta Mater. 95 (2015) 102–110.

#### 2.17.4.4.2 The effect of multiple phases

Based on the related and corresponding literature, most of the  $Mg_2Si_{1-x}Sn_x$  compounds yield a group of phases with varying tin content; a tin-rich phase and a silicon-rich one along with a prevalent phase with stoichiometry close to the nominal phase (also termed matrix). For the cases of pseudo-quaternary materials, a Ge-rich phase is also monitored. Therefore, the parameters and the properties of such materials are obtained using effective medium theories. The simplest effective medium theory involves linear interpolations between the end-member's parameters of  $Mg_2Si$  and  $Mg_2Sn$ ; however several other effective medium approaches could be applied. The Si-rich/matrix/Sn-rich phases have different bandgaps and band separation. Furthermore, dopant content is not the same in all phases [62], resulting in a different carrier concentration in each of the phases. The acoustic phonon deformation potential for electrons is modeled as a parabolic function of Sn content  $x$ . Clearly, the multiple phases form hetero-structures, and a common way to represent hetero-structures is by band-alignment at the Fermi level.

An example in band alignment, with respect to Fermi level, is schematically depicted in Fig. 2.17.16. Carrier concentration and the resulting Fermi level were calculated from two-band model taking into account the different band separation of each of the phases. As can be seen, for the case of 2% Bi-doped  $Mg_2Si_{0.55}Sn_{0.4}Ge_{0.05}$ , the Fermi level is located within the lower conduction band in the case of Si-rich phase, touches the upper conduction band, in the case of “matrix” and is well inside the upper conduction band in the case of Sn-rich phase. This means that though the Si-rich phase may be described by a single-band model, the redistribution of carriers in the two conduction bands is evident in the other two major phases, and this redistribution is more profound in the case of Sn-rich phase. Therefore, the presence of the Sn-rich phase plays a crucial role in the enhanced TE properties of Bi-doped solid solution materials.

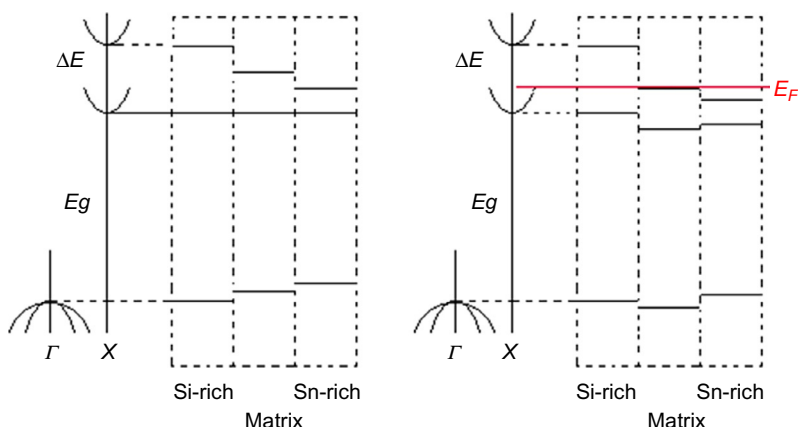


**Fig. 2.17.16** An example of band alignment with respect to the Fermi level for the case of 2% Bi-doped  $Mg_2Si_{0.55}Sn_{0.4}Ge_{0.05}$ . Calculations were performed using the data according to Bahk et al. [126].

Band alignment is a new type of band-offset engineering that takes advantage of the electronic bands of the compositionally alloyed nanostructures. Of great importance become the cases where there are small band offsets between two or more phases, namely small energy differences in the relevant valence or conduction band edges.

## 2.17.5 Summary

The key to a more widespread acceptance of TEs is the development of efficient materials for thermal energy conversion especially using less expensive, more earth-abundant elements, and nontoxic to meet the environmental regulations. Mg<sub>2</sub>Si-based compounds are widely accepted as such promising candidates. Owing to the wide scope of TE materials research, the chapter has reviewed recent progress in high-performance bulk Mg<sub>2</sub>(Si/Sn/Ge) TE materials defining the key approaches for boosting the TE performance.

Different synthesis strategies have been employed, including melting, solid-state or solid-liquid approaches. Evidently, in most of the cases, there is a densification step (i.e., hot pressing, spark plasma sintering, etc.) which is necessary to process the powdery samples. Interestingly, different synthesis methods lead to various microstructural features (nano-features, distribution of grain sizes, secondary phases, etc.) that affect ZT values for materials with same compositions.

Mg<sub>2</sub>Si-based compounds do not form “solid solutions” in the strict meaning of the term. Detailed electron microscopy studies indicate the presence of different phases with varying tin content, besides the main parent matrix family and the magnesium oxide. These phases span from micro-meter scale down to the nanoscale for both pseudo-binary and pseudo-ternary compounds. Furthermore, the dopant is not uniformly distributed in these phases, but exhibits an increasing trend from Si-rich to matrix and finally to Sn-rich phases, which clearly should affect the TE properties.

TE properties can be understood in the frame of doping, alloying, band-converging, nanostructuring, and Sn-rich/Si-rich phases’ architecture. The effort to integrate all of these mechanisms simultaneously and additively, if not synergistically, into a single material is termed the panoscopic approach [150]. The interpretation of transport measurements of multiphase materials is critical for TE optimization and application. Clearly, in the Mg<sub>2</sub>Si<sub>1-x</sub>Sn<sub>x</sub> family of compounds, Si-rich/matrix/Sn-rich phases are formed having different bandgaps and band separation. To the best of our knowledge, there is no effective medium approach in the literature yet. Effective medium theories should be adopted to model the TE properties of the Sn-alloyed Mg<sub>2</sub>Si-based compounds, combining the contribution of each phase in the composite with the microstructure and microstructure engineering in order to design electronically optimized and low lattice thermal conductivity TE materials.

## Acknowledgements

Theodora Kyratsi acknowledges THERMOSS Project funded by EU network M-ERA.NET (KOINA/M-ERA.NET/0316/03)

## References

- [1] R. Santos, S.A. Yamini, S.X. Dou, J. Mater. Chem. A 6 (2018) 3328.
- [2] K. Yin, X. Su, Y. Yan, H. Tang, M.G. Kanatzidis, C. Uher, X. Tang, Scr. Mater. 126 (2017) 1–5.
- [3] S. LeBlanc, S.K. Yee, M.L. Scullin, C. Dames, K.E. Goodson, Renew. Sust. Energ. Rev. 32 (2014) 313–327.
- [4] C.B. Vining, Nat. Mater. 8 (2009) 83–85.
- [5] V.K. Zaitsev, M.I. Fedorov, E.A. Gurieva, I.S. Eremin, P.P. Konstantinov, A. Samunin, M.V. Vedernikov, Phys. Rev. B Condens. Matter 74 (2006), 045207.
- [6] V.K. Zaitsev, M.I. Fedorov, I.S. Eremin, E.A. Gurieva, in: D.M. Rowe (Ed.), Thermoelectric Handbook, Macro to Nano, CRC Press, Boca Raton, FL, 2006.
- [7] L. Wang, X.Y. Qin, Scr. Mater. 49 (2003) 243–248.
- [8] J. de Boor, T. Dasgupta, U. Saparamadu, E. Müller, Z.F. Ren, Mater. Today Energy 4 (2017) 105–121.
- [9] M.W. Gaultois, T.D. Sparks, C.K.H. Borg, R. Seshadri, W.D. Bonificio, D.R. Clarke, Chem. Mater. 25 (2013) 2911–2920.
- [10] S. Bose, H.N. Acharya, H.D. Banerjee, J. Mater. Sci. 28 (1993) 5461.
- [11] E.N. Nikitin, V.G. Bazanov, V.I. Tarasov, Sov. Phys. Solid State 3 (1961) 2648.
- [12] J.-I. Tani, H. Kido, Phys. B 364 (2005) 218–224.
- [13] J.-I. Tani, M. Takahashi, H. Kido, J. Alloys Compd. 488 (2009) 346–349.
- [14] J. Bourgeois, J. Tobola, B. Wiendlöch, L. Chaput, P. Zwolenski, D. Berthebaud, F. Gascoin, Q. Recour, H. Scherrer, Funct. Mater. Lett. 6 (2013) 1340005.
- [15] G. Skomedal, N.R. Kristiansen, M. Engvoll, H. Middleton, J. Electron. Mater. 43 (2013) 1946–1951.
- [16] E.C. Stefanaki, E. Hatzikraniotis, G. Vourlias, K. Chrissafis, G. Kitis, K.M. Paraskevopoulos, G.S. Polymeris, Metall. Mater. Trans. A 47A (2016) 5147.
- [17] H. Inoue, S. Yoneda, M. Kato, I.J. Ohsugi, T. Kobayashi, J. Alloys Compd. 735 (2018) 828–832.
- [18] N. Farahi, C. Stiewe, D.Y. Nhi Truong, J. de Boor, E. Mueller, RSC Adv. 9 (2019) 23021–23028.
- [19] K. Yin, Q. Zhang, Y. Zheng, X. Su, X. Tang, U.C. Ctirad, J. Mater. Chem. C 3 (2015) 10381.
- [20] J.-Y. Jung, I.-H. Kim, J. Electron. Mater. 40 (2011) 1144–1148.
- [21] J.-Y. Jung, K.-H. Park, I.-H. Kim, IOP Conf. Ser. Mater. Sci. Eng. 18 (2011) 142006.
- [22] H.J. Lee, Y.R. Cho, I.-H. Kim, J. Ceram. Process. Res. 12 (2011) 16–20.
- [23] A. Delgado, S. Cordova, I. Lopez, D. Nemir, E. Shafirovich, J. Alloys Compd. 658 (2016) 422–429.
- [24] Q. Zhang, X. Su, Y. Yan, H. Xie, T. Liang, Y. You, X. Tang, C. Uher, ACS Appl. Mater. Interfaces 8 (2016) 3268–3276.
- [25] Q. Zhang, X.B. Zhao, H. Yin, T.J. Zhu, J. Alloys Compd. 464 (2008) 9.
- [26] E. Savary, F. Gascoin, S. Marinel, Dalton Trans. 39 (2010) 11074–11080.
- [27] S. Zhou, C. Bai, Trans. Nonferrous Metals Soc. China 21 (2011) 1785–1789.
- [28] S.C. Zhou, C.G. Bai, C.L. Fu, Adv. Mater. Res. 197–198 (2011) 417–420.
- [29] J. Schilz, M. Riffel, K. Pixius, H.-J. Meyer, Powder Technol. 105 (1999) 149.
- [30] M. Akasaka, T. Iida, T. Nemoto, J. Soga, J. Sato, K. Makino, M. Fukano, Y. Takanashi, J. Cryst. Growth 304 (2007) 196.
- [31] S. Chen, X. Zhang, W. Fan, T. Yi, D.V. Quach, S. Bux, Q. Menga, S.M. Kauzlarich, Z.A. Munird, J. Alloys Compd. 625 (2015) 251–257.

- [32] M. Ito, K. Kawahara, *Mater. Trans.* 56 (2015) 2023–2028.
- [33] Q.S. Meng, L.Q. Wang, B.S. Li, L.Z. Ding, S.P. Chen, *Adv. Mater. Res.* 79–82 (2009) 1639–1642.
- [34] Q.S. Meng, W.H. Fan, R.X. Chen, Z.A. Munir, *J. Alloys Compd.* 509 (2011) 7922–7926.
- [35] R. Yang, S. Chena, W. Fan, X. Gao, Y. Long, W. Wang, Z.A. Munird, *J. Alloys Compd.* 704 (2017) 545–551.
- [36] M. Iida, T. Nakamura, K. Fujimoto, Y. Yamaguchi, R. Tamura, T. Iida, K. Nishio, *MRS Adv.* 1 (60) (2016) 3971–3976.
- [37] M. Ioannou, K. Chrissafis, E. Pavlidou, F. Gascoin, T. Kyrtatsi, *J. Solid State Chem.* 197 (2013) 172–180.
- [38] M. Riffel, J. Schilz, *Scr. Metall. Mater.* 32 (1995) 1951.
- [39] M. Ioannou, E. Hatzikraniotis, C. Lioutas, T. Hassapis, T. Altantzis, K.M. Paraskevopoulos, T. Kyrtatsi, *Powder Technol.* 217 (2012) 523.
- [40] G. Kim, H. Lee, J. Kim, J.W. Roh, I. Lyo, B.-W. Kim, K.-H. Lee, W. Lee, *Scr. Mater.* 128 (2017) 53–56.
- [41] W. Liu, H. Chi, H. Sun, Q. Zhang, K. Yin, X. Tang, Q. Zhang, C. Uher, *Phys. Chem. Chem. Phys.* 16 (2014) 6893.
- [42] W. Liu, X. Tang, H. Li, K. Yin, J. Sharp, X. Zhou, C. Uher, *J. Mater. Chem.* 22 (2012) 13653.
- [43] W. Liu, Q. Zhang, K. Yin, H. Chi, X. Zhou, X. Tang, C. Uher, *J. Solid State Chem.* 203 (2013) 333–339.
- [44] H. Kamila, G.K. Goyal, A. Sankhla, P. Ponnusamy, E. Mueller, T. Dasgupta, J. de Boor, *Mater. Today Phys.* 9 (2019) 100133.
- [45] X. Zhang, H. Liu, Q. Lu, J. Zhang, F. Zhang, *Appl. Phys. Lett.* 103 (2013), 063901.
- [46] A. Sankhla, A. Patil, H. Kamila, M. Yasser, N. Farahi, E. Mueller, J. de Boor, *ACS Appl. Energy Mater.* 1 (2018) 531–542.
- [47] S.-W. You, I.-H. Kim, S.-M. Choi, W.-S. Seo, *J. Nanomater.* 13 (2013) 1–4. Article ID 815925.
- [48] L. Zheng, X. Zhang, H. Liu, S. Li, Z. Zhou, Q. Lu, J. Zhang, F. Zhang, *J. Alloys Compd.* 671 (2016) 452–457.
- [49] J.E. Mahan, A. Vantomme, G. Langouche, J.P. Becker, *Phys. Rev. B Condens. Matter* 54 (1996) 16965–16971.
- [50] Y. Noda, H. Kon, Y. Furukawa, N. Otsuka, I.A. Nishida, K. Masumoto, *Mater. Trans.* 33 (1992) 845–850.
- [51] L.R. Macario, X. Cheng, D. Ramirez, T. Mori, H. Kleinke, *ACS Appl. Mater. Interfaces* 10 (2018) 40585–40591.
- [52] A. Kato, T. Yagi, N. Fukusako, *J. Phys. Condens. Matter* 21 (2009) 205801.
- [53] Y. Imai, Y. Mori, S. Nakamura, K.-I. Takarabe, *J. Alloys Compd.* 664 (2016) 369–377.
- [54] S. Fiameni, S. Battiston, S. Boldrini, A. Famengo, F. Agresti, S. Barison, et al., *J. Solid State Chem.* 193 (2012) 142.
- [55] A.Y. Samunin, V.K. Zaitsev, P.P. Konstantinov, M.I. Fedorov, G.N. Isachenko, A.T. Burkov, S.V. Novikov, E.A. Gurieva, *J. Electron. Mater.* 42 (2013) 1676.
- [56] S.-M. Choi, K.-H. Kim, I.-H. Kim, S.-U. Kim, W.-S. Seo, *Curr. Appl. Phys.* 11 (2011) S388–S391.
- [57] M. Ioannou, G. Polymeris, E. Hatzikraniotis, A.U. Khan, K.M. Paraskevopoulos, T. Kyrtatsi, *J. Electron. Mater.* 42 (2013) 1827.
- [58] T. Sakamoto, T. Iida, A.S. Kurosaki, A. Yano, H. Taguchi, H. Nishio, Y. Takanashi, *J. Electron. Mater.* 40 (2011) 629.

- [59] W. Liu, K. Yin, X. Su, H. Li, Y. Yan, X. Tang, C. Uher, *Intermetallics* 32 (2013) 352–361.
- [60] M. Ioannou, G.S. Polymeris, E. Hatzikraniotis, K.M. Paraskevopoulos, T. Kyrtatsi, *J. Phys. Chem. Solids* 75 (2014) 984.
- [61] Q. Zhang, J. He, X.B. Zhao, S.N. Zhang, T.J. Zhu, H. Yin, T.M. Tritt, *J. Phys. D. Appl. Phys.* 41 (2008) 185103.
- [62] G.S. Polymeris, N. Vlachos, A.U. Khan, E. Hatzikraniotis, C.B. Lioutas, A. Delimitis, E. Pavlidou, K.M. Paraskevopoulos, T. Kyrtatsi, *Acta Mater.* 83 (2015) 285–293.
- [63] G.S. Polymeris, N. Vlachos, E. Symeou, T. Kyrtatsi, *Phys. Status Solidi A* 2018 (2018) 1800136.
- [64] L. Chen, G. Jiang, Y. Chen, Z. Du, X. Zhao, T. Zhu, et al., *J. Mater. Res.* 26 (2011) 3038–3043.
- [65] T. Dasgupta, C. Stiewe, J. de Boor, E. Müller, *Phys. Status Solidi A* 211 (2014) 1250–1254.
- [66] J. de Boor, S. Gupta, H. Kolb, T. Dasgupta, E. Mueller, *J. Mater. Chem. C* 3 (2015) 10467.
- [67] Z. Du, T. Zhu, X. Zhao, *Mater. Lett.* 66 (2012) 76–78.
- [68] P. Gao, X. Lu, I. Berkun, R.D. Schmidt, E.D. Case, T.P. Hogan, *Appl. Phys. Lett.* 105 (2014) 202104.
- [69] J. Jang, B. Ryu, S.-J. Joo, B.-S. Kim, B.-K. Min, H.-W. Lee, S.-D. Park, H.S. Lee, J.E. Lee, *J. Alloys Compd.* 739 (2018) 129–138.
- [70] N. Vlachos, G.S. Polymeris, M. Manoli, E. Hatzikraniotis, A.U. Khan, C.B. Lioutas, E.C. Stefanaki, E. Pavlidou, K.M. Paraskevopoulos, J. Giapintzakis, T. Kyrtatsi, *J. Alloys Compd.* 714 (2017) 502.
- [71] K. Yin, X. Su, Y. Yan, C. Uher, X. Tang, *RSC Adv.* 6 (2016) 16824–16831.
- [72] T.J. Zhu, Y.-Q. Cao, Q. Zhang, X.-B. Zhao, *J. Electron. Mater.* 39 (2010) 1990.
- [73] S.K. Bux, M.T. Yeung, E.S. Toberer, G.J. Snyder, R.B. Kaner, J.-P. Fleurial, *J. Mater. Chem.* 21 (2011) 12259–12266.
- [74] K. Mars, H. Ihou-Mouko, G. Pont, J. Tobola, H. Scherrer, *J. Electron. Mater.* 38 (2009) 1360.
- [75] J. de Boor, T. Dasgupta, H. Kolb, C. Compere, K. Kelm, E. Mueller, *Acta Mater.* 77 (2014) 68–75.
- [76] M. Saleemi, M.S. Toprak, S. Fiameni, S. Boldrini, S. Battiston, A. Famengo, M. Stingaci, M. Johnsson, M. Muhammed, *J. Mater. Sci.* 48 (2013) 1940.
- [77] A.S. Tazebay, S.-I. Yi, J.K. Lee, H. Kim, J.-H. Bahk, S.L. Kim, S.-D. Park, H.S. Lee, A. Shakouri, C. Yu, *ACS Appl. Mater. Interfaces* 8 (2016) 7003–7012.
- [78] N. Farahi, S. Prabhudev, G.A. Botton, J.R. Salvador, H. Kleinke, *ACS Appl. Mater. Interfaces* 8 (2016) 34431–34437.
- [79] A.U. Khan, N.V. Vlachos, E. Hatzikraniotis, G.S. Polymeris, C.B. Lioutas, E.C. Stefanaki, K.M. Paraskevopoulos, I. Giapintzakis, T. Kyrtatsi, *Acta Mater.* 77 (2014) 43–53.
- [80] A.U. Khan, N. Vlachos, T. Kyrtatsi, *Scr. Mater.* 69 (2013) 606–609.
- [81] P. Bellanger, S. Gorsse, G. Bernard-Granger, C. Navone, A. Redjaimia, S. Vivès, *Acta Mater.* 95 (2015) 102–110.
- [82] G. Bernard-Granger, C. Navone, J. Leforestier, M. Boidot, K. Romanjek, J. Carrete, J. Simon, *Acta Mater.* 96 (2015) 437–451.
- [83] G.K. Goyal, S. Mukherjee, R.C. Mallik, S. Vitta, I. Samajdar, T. Dasgupta, *ACS Appl. Energy Mater.* 2 (2019) 2129–2137.

- [84] M. Søndergaard, M. Christensen, K.A. Borup, H. Yin, B.B. Iversen, *Acta Mater.* 60 (2012) 5745–5751.
- [85] Q. Zhang, J. He, T.J. Zhu, S.N. Zhang, X.B. Zhao, T.M. Tritt, *Appl. Phys. Lett.* 93 (2008) 102109.
- [86] N. Farahi, M. VanZant, J. Zhao, J.S. Tse, S. Prabhudev, G.A. Botton, J.R. Salvador, F. Borondics, Z. Liuf, H. Kleinke, *Dalton Trans.* 43 (2014) 14983.
- [87] A. Kozlov, J. Gröbner, R. Schmid-Fetzer, *J. Alloys Compd.* 509 (2011) 3326–3337.
- [88] R. Viennois, C. Colinet, P. Jund, J.-C. Tédenac, *Intermetallics* 31 (2012) 145–151.
- [89] I.-H. Jung, D.-H. Kang, W.-J. Park, N.J. Kim, S. Ahn, *Thermochimica Acta* 466 (2007) 192–200.
- [90] S. Vivès, P. Bellanger, S. Gorsse, C. Wei, Q. Zhang, J.-C. Zhao, *Chem. Mater.* 26 (2014) 4334–4337.
- [91] E. Nikitin, E. Tkalenko, V. Zaitsev, A. Zaslavskii, A. Kuznetsov, *Inorg. Mater.* 4 (1968) 1656–1659.
- [92] S. Muntyanu, E. Sokolov, E. Makarov, *Izv Akad Nauk SSSR Neorg. Mater.* 2 (1966) 870–875.
- [93] A. Sizov, H. Reardon, B.B. Iversen, P. Erhart, A.E.C. Palmqvist, *Cryst. Growth Des.* 19 (2019) 4927–4933.
- [94] M. Yasseri, A. Sankhla, H. Kamila, R. Orenstein, D.Y. Nhi Truong, N. Farahi, J. de Boor, E. Mueller, *Acta Mater.* 185 (2020) 80–88.
- [95] M.-S. Kim, W.-J. Lee, K.-H. Cho, J.-P. Ahn, Y.-M. Sung, *ACS Nano* 10 (2016) 7197–7207.
- [96] W. Liu, Q. Jie, H. Seok Kim, Z. Ren, *Acta Mater.* 87 (2015) 357–376.
- [97] D.A. Porter, K.E. Easterling, M.Y. Sherif, *Phase Transformations in Metals and Alloys*, third ed., CRC Press, Boca Raton, FL, 2009.
- [98] S. Yi, V. Attari, M. Jeong, J. Jian, S. Xue, H. Wang, R. Arroyave, C. Yu, *J. Mater. Chem. A* 6 (2018) 17559.
- [99] P. Zwolenski, J. Tobola, S. Kaprzyk, *J. Electron. Mater.* 40 (2011) 889.
- [100] H. Ihou-Mouko, C. Merciera, J. Tobola, G. Pont, H. Scherrer, *J. Alloy Compd.* 509 (2011) 6503.
- [101] G.S. Polymeris, A. Theodorakatos, K. Mars, E. Godlewska, C. Lioutas, E. Hatzikraniotis, K.M. Paraskevopoulos, *J. Electron. Mater.* 43 (2014) 3876.
- [102] J. Tobola, P. Zwolenski, S. Kaprzyk, *Solid State Phenom.* 196 (2012) 266.
- [103] J. de Boor, U. Saparamadu, J. Mao, K. Dahal, E. Müller, Z.F. Ren, *Acta Mater.* 120 (2016) 273–280.
- [104] J.-I. Tani, H. Kido, *Intermetallics* 16 (2008) 418–423.
- [105] J.-I. Tani, M. Takahashi, H. Kido, *J. Alloys Compd.* 485 (2009) 764–768.
- [106] P. Nieroda, J. Leszczynski, A. Kolezynski, *J. Phys. Chem. Solids* 103 (2017) 147–159.
- [107] D.R. Lide, *CRC Handbook of Chemistry and Physics*, eighty-fourth ed., CRC Press, New York, 2003.
- [108] Y. Isoda, S. Tada, T. Nagai, H. Fujiu, Y. Shinohara, *J. Electron. Mater.* 39 (2010) 1531.
- [109] G. Jiang, J. He, T. Zhu, C. Fu, X. Liu, L. Hu, X. Zhao, *Adv. Funct. Mater.* 24 (2014) 3776–3781.
- [110] G. Kim, H. Lee, H.J. Rim, J. Kim, K. Kim, J.W. Roh, S.-M. Choi, B.-W. Kim, K.H. Lee, W. Lee, *J. Alloys Compd.* 769 (2018) 53–58.
- [111] H. Kamila, P. Sahu, A. Sankhla, M. Yasseri, H.-N. Pham, T. Dasgupta, E. Mueller, J. de Boor, *J. Mater. Chem. A* 7 (2019) 1045.
- [112] M. Søndergaard, M. Christensen, K.A. Borup, H. Yin, B.B. Iversen, *J. Electron. Mater.* 42 (2013) 1417.

- [113] Z. Du, T. Zhu, Y. Chen, J. He, H. Gao, G. Jiang, T.M. Tritt, X. Zhao, *J. Mater. Chem.* 22 (2012) 6838.
- [114] W. Liu, X. Tang, H. Li, J. Sharp, X. Zhou, C. Uher, *Chem. Mater.* 23 (2011) 5256–5263.
- [115] P. Koenig, D.W. Lynch, G.C. Danielson, *J. Phys. Chem. Solids* 20 (1961) 122.
- [116] R.G. Morris, R.D. Redin, G.C. Danielson, *Phys. Rev.* 109 (1958) 1909.
- [117] M.Y. Au-Yang, M.L. Cohen, *Phys. Rev.* 178 (1969) 1358.
- [118] M. Akasaka, T. Iida, A. Matsumoto, K. Yamanaka, Y. Takanashi, T. Imai, N. Hamada, *J. Appl. Phys.* 104 (2008), 013703.
- [119] O. Benhalal, A. Chahed, S. Laksari, B. Abbar, B. Bouhafs, H. Aourag, *Phys. Status Solidi B* 242 (2005) 2022–2032.
- [120] J.L. Corkill, M.L. Cohen, *Phys. Rev. B* 48 (1993) 17138–17144.
- [121] K. Kutorasinski, J. Tobola, S. Kaprzyk, *Phys. Rev. B* 87 (2013) 195205.
- [122] K. Kutorasinski, B. Wiendlocha, J. Tobola, S. Kaprzyk, *Phys. Rev. B* 89 (2014) 115205.
- [123] G. Shi, E. Kioupakis, *J. Appl. Phys.* 123 (2018), 085114.
- [124] C.B. Vining, D.M. Rowe, *Handbook of Thermoelectrics*, CRC Press, New York, 1995.
- [125] F. Aymerich, G. Mula, *Phys. Status Solidi B* 42 (1970) 697.
- [126] J.-H. Bahk, Z. Bian, A. Shakouri, *Phys. Rev. B* 89 (2014), 075204.
- [127] K. Kutorasinski, J. Tobola, S. Kaprzyk, A.U. Khan, T. Kyrtatsi, *J. Electron. Mater.* 43 (2014) 10.
- [128] P.S. Kireev, *Semiconductor Physics*, Mir Publishers, Moscow, 1978.
- [129] H. Wang, Y. Pei, A.D. LaLonde, G.J. Snyder, Material design considerations based on thermoelectric quality factor, in: K. Koumoto, T. Mori (Eds.), *Thermoelectric Nanomaterials*, Springer Series 3 in Materials Science, vol. 182, 2013.
- [130] N. Satyala, D. Vashaee, *J. Electron. Mater.* 41 (2012) 1785.
- [131] L. Zhang, P. Xiao, L. Shi, G. Henkelman, J.B. Goodenough, J. Zhou, *J. Appl. Phys.* 117 (2015) 155103.
- [132] E.C. Stefanaki, G.S. Polymeris, M. Ioannou, E. Pavlidou, E. Hatzikraniotis, T. Kyrtatsi, K.M. Paraskevopoulos, *J. Electron. Mater.* 45 (2016) 1900.
- [133] R.S. Allgaier, *J. Appl. Phys.* 36 (1965) 2429.
- [134] Y. Pei, X. Shi, A. LaLonde, H. Wang, L. Chen, G.J. Snyder, *Nature* 473 (2011) 66–69.
- [135] O. Madelung, *Semiconductors: Data Handbook*, Springer Science & Business Media, Berlin, 2012.
- [136] F. Vazquez, R.A. Forman, M. Cardona, *Phys. Rev.* 176 (1968) 905–908.
- [137] R.D. Redin, R. Morris, *Phys. Rev.* 109 (1958) 1916–1920.
- [138] G.J. Snyder, E.S. Toberer, *Nat. Mater.* 7 (2008) 105–114.
- [139] H. Wang, A.D. LaLonde, Y. Pei, G.J. Snyder, *Adv. Funct. Mater.* 23 (2013) 1586.
- [140] H. Wang, J. Wang, X. Cao, G.J. Snyder, *J. Mater. Chem. A* 2 (2014) 3169.
- [141] X. Liu, T. Zhu, H. Wang, L. Hu, H. Xie, G. Jiang, G.J. Snyder, X. Zhao, *Adv. Energy Mater.* 3 (2013) 1238.
- [142] S. Adachi, *J. Appl. Phys.* 54 (1983) 1844.
- [143] P.G. Klemens, *Phys. Rev.* 119 (1960) 507.
- [144] B. Abeles, *Phys. Rev.* 131 (1963) 1906.
- [145] J. Callaway, *Phys. Rev.* 113 (1959) 1046.
- [146] J. He, S.N. Girard, M.G. Kanatzidis, V.P. Dravid, *Adv. Funct. Mater.* 20 (2010) 764–772.
- [147] S.-H. Lo, J. He, K. Biswas, M.G. Kanatzidis, V.P. Dravid, *Adv. Funct. Mater.* 22 (2012) 5175.
- [148] N. Satyala, D. Vashaee, *J. Appl. Phys.* 112 (2012), 093716.
- [149] E. Hatzikraniotis, G.S. Polymeris, E. Symeou, T. Kyrtatsi, K.M. Paraskevopoulos, *Mater. Today: Proc.* 4 (2017) 12374–12382.
- [150] L.-D. Zhao, V.P. Dravid, M.G. Kanatzidis, *Energy Environ. Sci.* 7 (2014) 251.

# Segmented modules

3.1

Shengqiang Bai<sup>a,b</sup>, Qihao Zhang<sup>a</sup>, and Lidong Chen<sup>a,b</sup>

<sup>a</sup>The State Key Laboratory of High Performance Ceramics and Superfine Microstructure, Shanghai Institute of Ceramics, Chinese Academy of Sciences, Shanghai, China,

<sup>b</sup>Center of Materials Science and Optoelectronics Engineering, University of Chinese Academy of Sciences, Beijing, China

Conversion efficiency and output power of thermoelectric power generation devices are positively correlated with the figure of merit ( $zT$ ) of materials and their operating temperature differences. Therefore, to achieve a more efficient thermal-to-electric conversion, it is desirable to maximize the  $zT$  over a larger temperature range. However, till now there is no one single material that can maintain high thermoelectric performance in its whole service temperature range. Moreover, the maximum  $zT$  values for a certain TE material always goes along within a relatively narrow temperature range (usually 200–300 K). For example, the best working temperature range for n-type  $\text{CoSb}_3$ -based skutterudites is 400–600°C, where the  $zT$  values exceed 1.0 [1]. When the temperature is below 400°C, the  $zT$  value decreases rapidly. Once the temperature is above 600°C, both TE performance and material stability are significantly reduced.

An effective way to promote the average  $zT$  values in a wide temperature range is to construct a segmented thermoelectric device (Fig. 3.1.1), that is, to select thermoelectric materials with different optimal operating temperatures along the direction of temperature gradient and combine them in an electrical series. This segmented structure could make each different TE material work in its own favorable operating temperature range, so as to maximize the average  $zT$  corresponding to the whole temperature range and effectively improve the output performance of devices. The concept to use the segmented design to increase the overall efficiency of thermoelectric devices was originally proposed by Ioffe et al. in the 1940s [2]. Then, in 1962, the segmented thermoelement for generators was patented by Fredrick et al. [3]. Since the 1970s, the radioisotope thermoelectric generators (RTGs) prepared by the Jet Propulsion Laboratory (JPL), use segmented thermoelements (such as TAGS, LAST, etc.) based on  $\text{PbTe}$ -based and  $\text{SiGe}$ -based alloys, with RTG system efficiencies from 3.0% to 7.0%, have been successfully applied in deep space craft (such as Voyager, Galileo, Cassini, Curiosity, etc.) as the power supply sources, providing 40~285 W of electricity [4]. The success of segmented thermoelectric generators in deep space explore application proves the feasibility and effectiveness of the segmented design in energy conversion. Based on the pioneering works, great efforts have been devoted to studying and optimizing the performance of segmented thermoelectric modules, especially in the last few years as the continuously refreshed record of  $zT$  values in both traditional and novel thermoelectric materials bode well for widespread practical

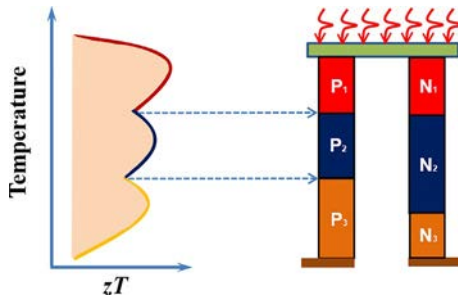


**Fig. 3.1.1** Schematic diagram of a thermoelectric module with segmented structure.

applications of thermoelectric technology. In principle, the number of segments in the n- and p-leg of a segmented thermoelectric module depends on the service temperature range and the  $zT$  values of candidate thermoelectric materials [5]. Meanwhile, the actual conversion efficiency is strongly linked to the rational structure design as well as the parasitic losses resulting from module integration. In this chapter, we present an overview of the recent progress on the design and integration of segmented thermoelectric modules with particular attention on material selection, device topologic structure optimization, interface engineering and bonding technique, as well as on some typical high-performance segmented modules. The future challenges and development strategies concerning segmented thermoelectric devices are also discussed.

### 3.1.1 Selection of TE materials

Segmented thermoelectric modules presented a problem regarding the materials, their properties, and the temperature ranges that should be used. The selection of thermoelectric materials for segmentation was initially based on maximizing the average  $zT$  in service temperature gradient. Early investigations focus on the typical thermoelectric materials including  $\text{Bi}_2\text{Te}_3$ ,  $\text{FeSi}_2$ ,  $\text{PbTe}$ , and  $\text{SiGe}$ . Schilz et al. reported a segmented thermoelectric element consisting of  $\text{Bi}_2\text{Te}_3$ -based materials for the low-temperature part and  $\text{FeSi}_2$  for the high-temperature part [6]. Subsequently, a three-stage segmented thermoelectric element was developed in 1998 by the National Aerospace Laboratory in Japan [7]. The results indicated that the highest calculated efficiency of up to 17% is possible for the three-stage segmented element over a wide range from room temperature to 1073 K, which was constructed by  $\text{Bi}_2\text{Te}_3$ ,  $\text{PbTe}$ , and  $\text{SiGe}$ .

However, researchers in JPL then found that  $\text{SiGe}$  segmented with  $\text{Bi}_2\text{Te}_3$  and/or various skutterudites shows a marked decline in device efficiency [8]. Therefore, in a segmented thermoelectric device, the efficiency depends on more than just the material  $zT$ . The thermoelectric compatibility must also be considered. In the light of understanding the thermodynamics behind segmented thermoelectric devices, Snyder et al. introduced the thermoelectric compatibility factor  $s$ , which is defined as [8]

$$s = \frac{\sqrt{1+zT} - 1}{\alpha T} \quad (3.1.1)$$

According to their reports, the maximum efficiency that a thermoelectric material can provide is only achieved when the relative current density ( $u$ , that is ratio of the electrical current density to the heat flux by conduction:  $u = \frac{J}{\kappa V T}$ ) is equal to  $s$ . In an efficient thermoelectric generator, the  $u$  value is roughly a constant throughout a segmented element (typically  $u$  changes by less than 20%). Thus, the goal is to select high figure of merit thermoelectric materials that have similar compatibility factors. If the compatibility factors differ by a factor of about two or more, a given  $u$  cannot be suitable for both materials and segmentation will not be efficient [8, 9].

Some examples have demonstrated how the material selection can be made rational by considering both material  $zT$  and compatibility factor. For instance, the TAGS material ((AgSbTe<sub>2</sub>)<sub>0.15</sub>(GeTe)<sub>0.85</sub>) must be maintained below 525°C or lower for long-term applications. To achieve a higher efficient thermoelement with a hot-side temperature of 600°C, a segment of another p-type material need be added between 525°C and 600°C [10]. From Fig. 3.1.2A, the p-type PbTe would be a better choice than SnTe between 525°C and 600°C. However, because the compatibility factor (shown in Fig. 3.1.2B) for p-type PbTe is much lower than that of TAGS, the segmentation efficiency of TAGS/PbTe is lower than that of TAGS single-stage thermoelement even though in a wider temperature range (see Table 3.1.1). On the other hand, despite the lower  $zT$  of SnTe, a higher efficiency of 11.09% is obtained for the TAGS/SnTe segmentation due to a close compatibility factor to TAGS. Furthermore, by adopting p-type filled skutterudite of CeFe<sub>4</sub>Sb<sub>12</sub> with both high  $zT$  and similar compatibility factor, the highest efficiency of 11.87% is achieved in the segmented TAGS/CeFe<sub>4</sub>Sb<sub>12</sub> thermoelement.

To evaluate the effect of compatibility factor on the total efficiency of segmented legs containing compatible and noncompatible materials, Hung et al. chose segmentations of n-type leg using doped ZnO as the high-temperature part and Half-Heusler or skutterudites as the low-temperature part [11]. As shown in Fig. 3.1.3A, the  $s$  values

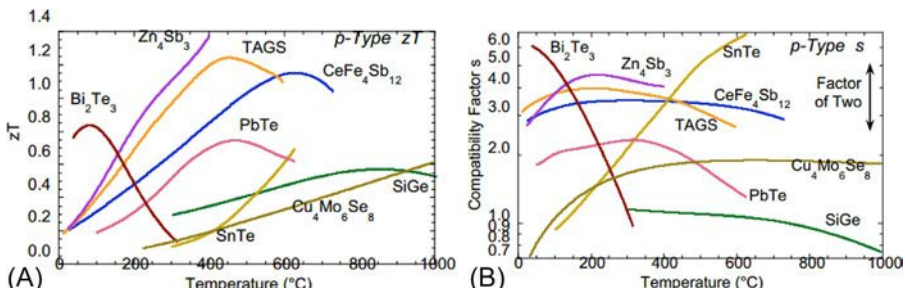


**Fig. 3.1.2** Temperature dependence of (A)  $zT$  and (B) compatibility factor for various *p*-type thermoelectric materials.

Reproduced with permission from G.J. Snyder, T. Caillat, Using the compatibility factor to design high efficiency segmented thermoelectric generators, MRS Proc. 793 (2003) S2.1.

**Table 3.1.1** Maximum single element efficiencies for thermoelectric generators,  $u(T_c)$  is the relative current density that gives the maximum efficiency [10].

Material	Efficiency (%)	$T_c$ (°C)	$T_{\text{Interface}}$ (°C)	$T_h$ (°C)	$u(T_c)$ (V <sup>-1</sup> )
p-TAGS	10.45	100		525	2.97
p-TAGS/PbTe	10.33	100	525	600	2.33
p-TAGS/SnTe	11.09	100	525	600	2.84
p-TAGS/CeFe <sub>4</sub> Sb <sub>12</sub>	11.87	100	525	600	2.94

of multi-filled skutterudite Ba<sub>0.08</sub>La<sub>0.05</sub>Yb<sub>0.04</sub>Co<sub>4</sub>Sb<sub>12</sub> (CoSb for short) are three times larger than that of ZnO, while the difference of  $s$  between Ti<sub>0.6</sub>Hf<sub>0.4</sub>NiSn Half-Heusler (HH for short) and ZnO is less than a factor of 2. The relative current density  $u$  values calculated from the temperature-dependent thermoelectric properties start separating in the high-temperature range for both  $u_{\text{CoSb-ZnO}}$  and  $u_{\text{HH-ZnO}}$ . This is due to the fact that their  $u$  values are different at the hot-side temperature. The actual reduced efficiency and the maximum reduced efficiency at  $u=s$  are shown in Fig. 3.1.3B. The maximum reduced efficiency of CoSb is higher than that of HH due to its higher  $zT$ . However, the actual reduced efficiency of segmented CoSb/ZnO is lower than that of HH/ZnO over the whole temperature range. Eventually, compared with non-segmented CoSb, the maximum total efficiency of the segmented CoSb/ZnO is decreased by 3.5% even under a larger temperature span (Fig. 3.1.3C). Strikingly, the maximum total efficiency of segmented HH/ZnO is increased by 6.3% in comparison with non-segmented ZnO.

In recent years, with remarkable enhancement of thermoelectric properties, there are more and more candidates for constructing the segmented modules from the point of view of  $zT$  value and compatibility. As shown in Fig. 3.1.4A, the candidate n-type thermoelectric materials include filled skutterudites, (Hf,Zr)NiSn-based half-Heusler alloys, Ba<sub>8</sub>Ga<sub>16</sub>Ge<sub>30</sub> clathrates, and rare earth chalcogenides such as La<sub>3</sub>Te<sub>4</sub> [12]. For p-type materials, MgAgSb compound, BiCuSeO oxyselenides, FeNbSb-based half-Heusler alloys, and Zintl antimonide phases such as Yb<sub>14</sub>MnSb<sub>11</sub> are good candidates (Fig. 3.1.4B). Various novel TE materials with high  $zT$  values make it possible to achieve new record efficiencies close to 20%. JPL proposed a new version of a segmented thermoelectric generator utilizing advanced thermoelectric materials with superior thermoelectric figures of merit, which promoted applications in next-generation advanced RTGs. For example, the segmented unicouples incorporating the combination of novel skutterudite, zintls, and La<sub>3-x</sub>Te<sub>4</sub>/composites enable a prediction efficiency of up to 15% [13].

The  $zT$  value and compatibility are most important for segmented devices because the thermoelectric material properties may change dramatically from one segment to another. Actually, other factors may also affect the material selection, such as thermal and chemical stability, heat losses, coefficient of thermal expansion, processing requirements, availability, and cost. For commercial applications, cost is one of the

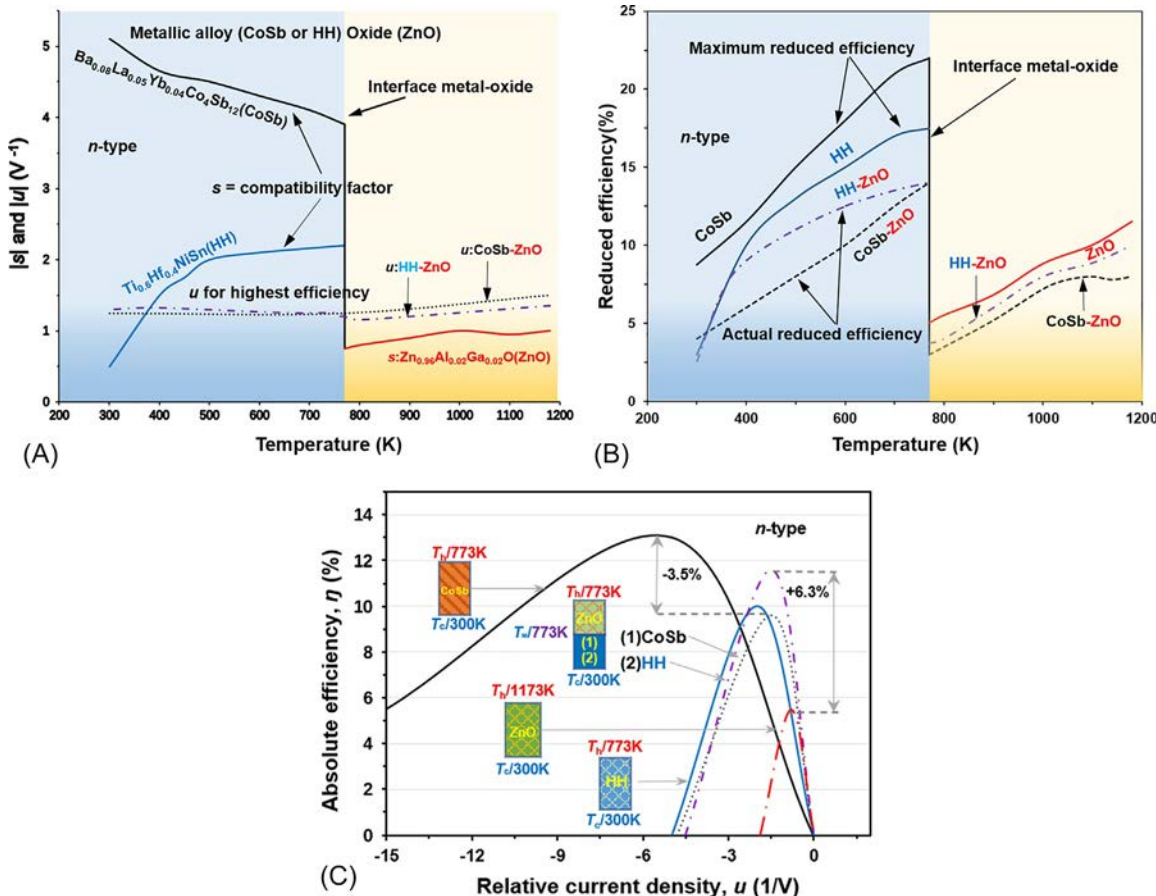


**Fig. 3.1.3** (A) Temperature dependence of the absolute value of compatibility factor  $s$  and relative current density  $u$ . (B) Local and reduced efficiency using the value of  $u$  for the highest efficiency compared to the maximum reduced efficiency for *n*-type segmented CoSb/ZnO and HH/ZnO legs. (C) Total efficiency of single components, incompatible segmented CoSb/ZnO leg, and compatible segmented HH/ZnO leg.  
Reproduced with permission from L.T. Hung, N.V. Nong, S. Linderoth, N. Pryds, Segmentation of low-cost high efficiency oxide-based thermoelectric materials, Phys. Status Solidi A 212 (4) (2015) 767–774.

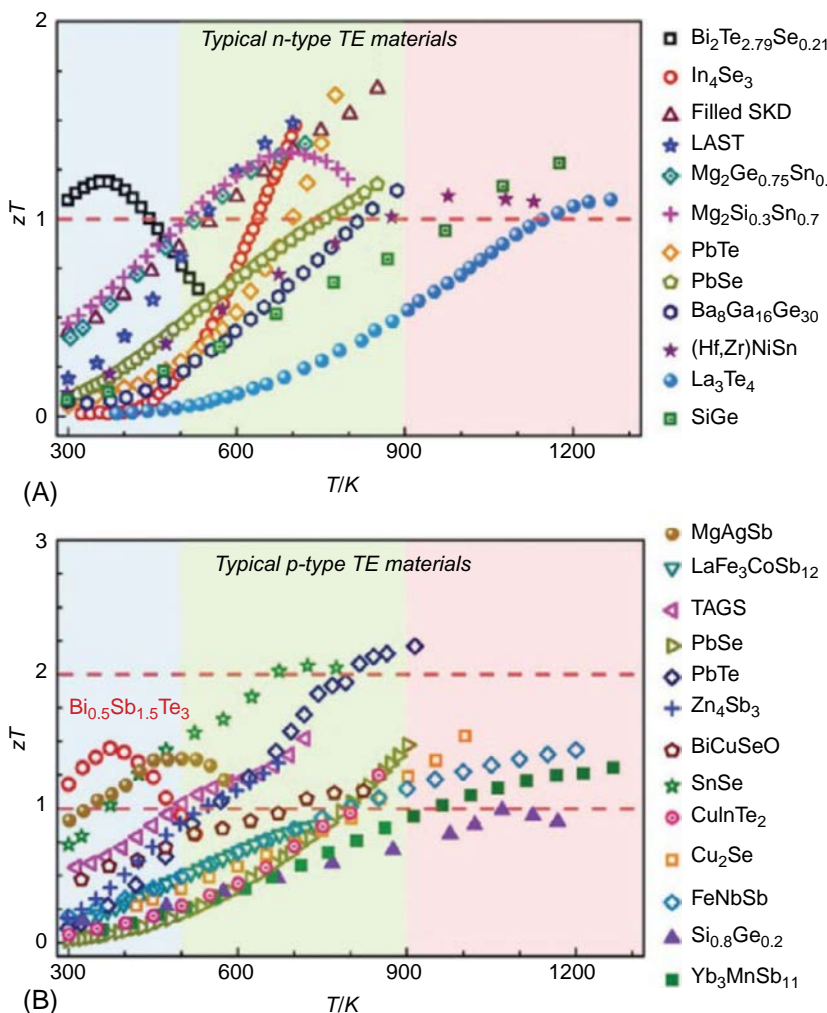


**Fig. 3.1.4** Temperature dependence of  $zT$  values for some typical classes of bulk TE materials: (A) n-type and (B) p-type.

Reproduced with permission from T.J. Zhu, Y.T. Liu, C.G. Fu, J.P. Heremans, J.G. Snyder, X.B. Zhao, Compromise and synergy in high-efficiency thermoelectric materials, *Adv. Mater.* 29 (30) (2017) 1605884.

most important considerations. In order to provide a better comparison of material selection in terms of efficiency and material cost, Hung et al. exploited the efficiency ratio ( $\eta_{\text{ratio}}$ ) to appraise the candidates for high-temperature thermoelectric segments [11]. The  $\eta_{\text{ratio}}$  is expressed as

$$\eta_{\text{ratio}} = \frac{\eta_{\text{leg}}}{M_{\text{cost}}} \quad (3.1.2)$$

where  $\eta_{\text{leg}}$  is the total efficiency of a segmented leg and  $M_{\text{cost}}$  is the cost of the thermoelectric material, which is computed by the sum of the costs of raw materials and processing that need to produce 1 mol of material [11]. As shown in Fig. 3.1.5A, the metallic compounds containing rare earth elements have the highest value of material cost. For example,  $\text{Yb}_{14}\text{MnSb}_{11}$  and  $\text{La}_3\text{Te}_4$  are three or four orders more expensive than oxide materials. Although the peak  $zT$  values of oxide materials are only 60% compared with SiGe or  $\text{Yb}_{14}\text{MnSb}_{11}$ , their efficiency ratios are higher by a factor of five for p-type and 20 for n-type materials (Fig. 3.1.5B). This means that the oxide materials such as doped-ZnO and  $\text{Ca}_3\text{Co}_4\text{O}_9$  nanocomposite can be good candidates for low-cost segments.

### 3.1.2 Topologic structure design

For a segmented thermoelectric module, the structure design includes not only the total leg length, cross-sectional area, and gap between p/n legs, but also the length of each TE material section. In segmented couples, the different materials usually possess different temperature dependences of their thermoelectric parameters (thermal conductivity, electrical conductivity, and Seebeck coefficient). Coupling of material properties and leg geometry directly determine the temperature distribution, heat flux distribution, current density, and its distribution, thereby affecting the conversion efficiency [14]. These issues must be considered very seriously for designing such segmented couples to achieve compatibility through optimization of geometric parameters. Furthermore, the segmented couples possess extra bonding junctions between different segments that inevitably introduce extra electrical and thermal contact resistances, which result in unfavorable temperature drops across the electrodes. These bonded junctions as well as Joule heating at bonded interfaces degraded the conversion efficiency of the TE module.

In the same segmented leg, each section has the same current and heat flow. In order to maintain the desired temperature profile (i.e., keeping the interface temperatures at desired levels), the geometry of each section in the leg must be optimized. Specifically, the relative lengths of each section in a leg must be adjusted, primarily due to the difference in thermal conductivity, to achieve the desired temperature gradient across each material section [15]. A semi-analytical approach to the problem was given by Swanson et al. in 1961 that includes the contributions of Peltier and Thompson effects as well as contact resistance in order to optimize the expected performances of the module [16]. For each section, the average thermoelectric properties over the operation temperature range are used. At each junction (cold side, hot side, or interface between two segments), the relative lengths of the segments are adjusted to ensure heat energy balance at the interface. Without any contact resistance, the efficiency is not affected by the overall length of the module and the relative length of each segment and the optimum cross-sectional area can be optimized.

In 2002, El-Genk et al. developed a one-dimensional analytical model in conjunction with a genetic algorithm for optimizing segmented thermoelectric converters [17, 18]. This model assumes zero side heat losses, but accounts for the temperature

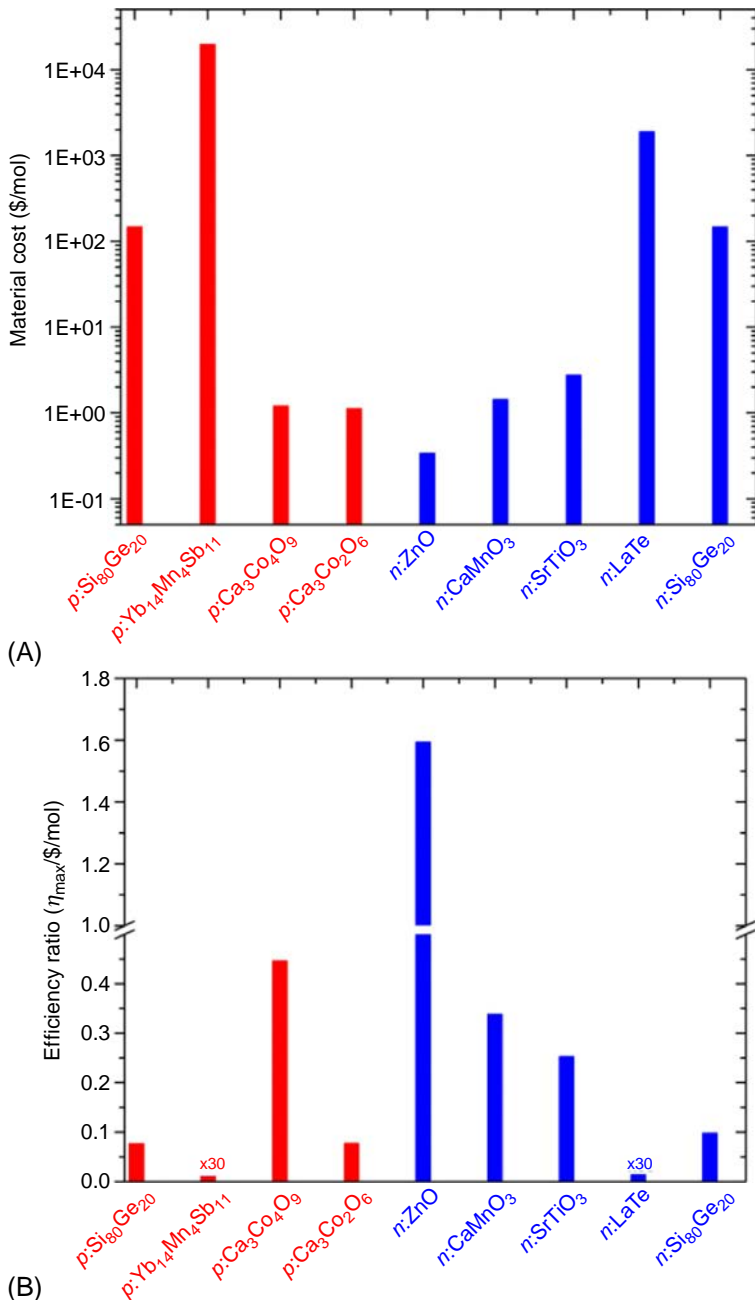


**Fig. 3.1.5** A plot of (A) price in dollars per mole and (B) efficiency ratio for various high-temperature thermoelectric materials.

Reproduced with permission from L.T. Hung, N.V. Nong, S. Linderoth, N. Pryds, Segmentation of low-cost high efficiency oxide-based thermoelectric materials, Phys. Status Solidi A 212 (4) (2015) 767–774.

dependence of material properties. The predictions depend on the specified lengths of the various segments in the  $n$ - and  $p$ -leg or the values of interfacial temperatures. For optimization of module's output properties (efficiency, power density, etc.), the structure parameters include the cross-sectional areas of  $p/n$  legs, the hot-/cold-side temperatures, the various interfacial temperatures, the ratio of load resistance to the module's internal resistance, the total leg length, and each section lengths. When the segmented thermoelectric unicouples are perfectly thermal insulated, the analytical solution of the one-dimensional energy equations could accurately obtain the axial temperature distributions and predict the performance parameters, including the electrical current, load voltage, interfacial temperatures, electrical power, input and rejected thermal powers. Actually, since the surface area to volume ratios of the legs are relatively large, the side heat losses could affect the temperature distributions and, hence, the performance of the modules. In this case, these parameters could not be accurately predicted using the one-dimensional model.

Subsequently, El-Genk et al. further developed a three-dimensional model, which can not only determine the three-dimensional temperature fields in the legs and the spatial distribution of the side heat losses, but also confirm the theoretical performance (potential tapping) of segmented thermoelectric modules [19]. The three-dimensional energy balance equation in each segment is written as

$$\omega C_p \frac{\partial T}{\partial t} = \frac{\partial}{\partial x} \left( k_x(T) \frac{\partial T}{\partial x} \right) + \frac{\partial}{\partial y} \left( k_y(T) \frac{\partial T}{\partial y} \right) + \frac{\partial}{\partial z} \left( k_z(T) \frac{\partial T}{\partial z} \right) - \tau_x(T) J_x \frac{\partial T}{\partial x} + \rho_x(T) J_x^2 \quad (3.1.3)$$

$$T = \hat{T} \text{ on } \Gamma_T \text{ and } \left( -k_x \frac{\partial T}{\partial x} n_x - k_y \frac{\partial T}{\partial y} n_y - k_z \frac{\partial T}{\partial z} n_z \right) = \hat{q} \text{ on } \Gamma_q \quad (3.1.4)$$

$\hat{T}$  and  $\hat{q}$  are specified functions of position on the portions  $\Gamma_T$  and  $\Gamma_q$ , respectively, of the total surface  $\Gamma$  of the segmented thermoelectric unicouples.  $\Gamma_T$  is a portion from the total surface, on which temperature boundary conditions are specified and  $\Gamma_q$  is another portion from the total surface, on which the heat flux, convection, and/or radiation boundary conditions are specified. The sum of the two portions of the surface equals the total surface. Therefore, the model can handle different types of boundary conditions at different portions of the segmented surface of unicouples. In various segmented legs, energy balance equation including Joule, Peltier, and Thomson heating are solved numerically, subject to the prescribed boundary conditions. In the model, the physical and thermoelectric properties of the material in each section can be treated as temperature dependent, either isotropic or orthotropic.

Recently, to realize segmented power generation modules with high conversion efficiencies, Zhang et al. demonstrated a three-dimensional numerical analysis model, which takes into account the temperature-dependent materials' properties and various parasitic losses [20]. Fig. 3.1.6 shows the logical framework for the full-parameter optimization of a thermoelectric power generation module based on the below three-dimensional thermoelectrically coupled field equations.

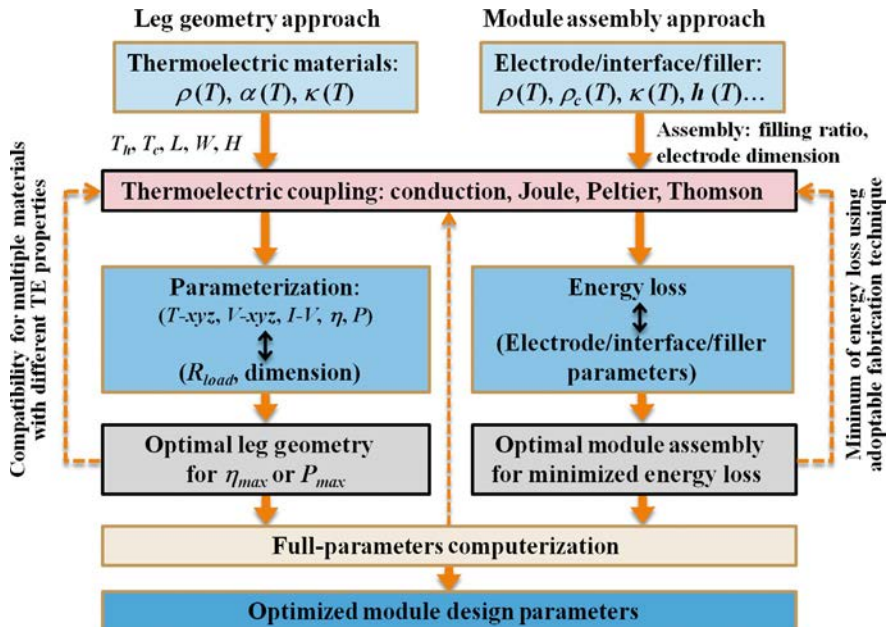


**Fig. 3.1.6** Logical framework for the full-parameter optimization of a thermoelectric power generation module.

Reproduced with permission from Q.H. Zhang, J.C. Liao, Y.S. Tang, M. Gu, C. Ming, P.F. Qiu, S.Q. Bai, X. Shi, C. Uher, L.D. Chen, Realizing a thermoelectric conversion efficiency of 12% in bismuth telluride/skutterudite segmented modules through full-parameter optimization and energy-loss minimized integration, *Energ. Environ. Sci.* 10 (2017) 956–963.

$$\nabla(\kappa\nabla T) + \frac{\mathbf{J}^2}{\sigma} - T\mathbf{J}\cdot\left[\left(\frac{\partial\alpha}{\partial T}\right)\nabla T + (\nabla\alpha)_T\right] = 0 \quad (3.1.5)$$

$$\nabla\cdot\mathbf{J} = 0 \quad (3.1.6)$$

where

$$\mathbf{J} = -\sigma(\nabla V + \alpha\nabla T) \quad (3.1.7)$$

$$\mathbf{q} = \alpha T\mathbf{J} - \kappa\nabla T \quad (3.1.8)$$

In the equations above, vectors  $\mathbf{J}$  and  $\mathbf{q}$  represent the current density and the heat flux in three dimensions, respectively.  $\kappa$  is the thermal conductivity;  $\sigma$  stands for electrical conductivity;  $\alpha$  is the temperature-dependent Seebeck coefficient of materials;  $V$  is the electrostatic potential; and  $T$  is the absolute temperature. The thermal energy is transferred by conduction, Joule effect, Thomson effect, and Peltier effect, which are all considered in the model. Within the full-parameter optimization, the leg geometry

approach is the primary and most essential approach in order to realize the maximum performance of a thermoelectric element (unicouple). It is a complex problem to realize full compatibility among the different thermoelectric parameters in a segmented system containing not only potentially incompatible *p* and *n* legs but also different components in each leg. Numerical simulations take into account the given temperature-dependent thermoelectric properties, initial condition variables that include the temperatures of the hot-side and cold-side electrodes, and dimension variables such as the length, width, and height of each element or each component material. The geometry-dependent maximum conversion efficiency ( $\eta_{\max}$ ) or maximum power output ( $P_{\max}$ ) of a unicouple without considering the energy loss aroused by the module assembly factors can be determined under different temperature drops and different loads for given material properties. By multiparametric combinations, the theoretical maximum conversion efficiency under different temperature conditions for any given thermoelectric material, even with very incompatible transport properties, can be realized by optimizing geometrical dimensions. In addition to the leg geometry factors, module assembly factors, such as electrical and thermal losses at interfaces and thermal radiation and/or convection through the gaps or fillers, are also properly taken into account. Combining the leg geometry approach and the module assembly approach, the full-parameter computer simulation was performed using finite element analysis through the ANSYS-Workbench platform, which yields optimized module parameters with which the maximum power generation performances were implemented.

An example of multiparameter optimization of a segmented thermoelectric module using three-dimensional numerical analysis model is shown in Fig. 3.1.7. Bismuth telluride (BT) and filled skutterudites (SKD) are selected as the low-temperature and high-temperature segments, respectively. As shown in Fig. 3.1.7A, the maximum conversion efficiency ( $\eta_{\max}$ ) initially rises and then falls with the increasing  $H_{p\text{-SKD}}/H_{p\text{-BT}}$  when  $H_{n\text{-SKD}}/H_{n\text{-BT}}$  is fixed, where  $H_{p\text{-SKD}}$ ,  $H_{p\text{-BT}}$ ,  $H_{n\text{-SKD}}$ , and  $H_{n\text{-BT}}$  represent the height of *p*-SKD, *p*-BT, *n*-SKD and *n*-BT segments, respectively. Importantly, the peak value varies with changing the  $H_{n\text{-SKD}}/H_{n\text{-BT}}$ , signifying that the *p*- and *n*-type legs are mutually constrained due to reallocation of the heat flow. Therefore, one must synchronously optimize the height ratio of different sections for both *p*-leg and *n*-leg, rather than treating them individually. Fig. 3.1.7B plots a 3D surface relating  $\eta_{\max}$  with the segment height ratio for  $T_h=530^\circ\text{C}$  and  $T_c=36^\circ\text{C}$ . Apparently, the optimum height ratios of different sections for the *p*-leg and *n*-leg depends on each other. The energy conversion efficiency and the rational geometric parameters should change with temperature conditions. Therefore, under  $T_h=578^\circ\text{C}$  and  $T_c=38^\circ\text{C}$ , the  $\eta_{\max}$  reaches up to 12.28% at the optimized dimensions (Fig. 3.1.7C). Furthermore, due to the asymmetry of thermoelectric properties, the optimum performance of each element is obtained at different current densities, and thus the cross-sectional area ratio of the *p*- and the *n*-type leg ( $A_p/A_n$ ) also need to be optimized (Fig. 3.1.7D). Additionally, segmentation inevitably introduces new interfacial contacts between different materials, where the electrical contact resistance gives rise to an increase in Joule heat, adversely affecting the power-generating performance. The effects of both total contact resistivity (Fig. 3.1.7E) and thermal conductivity of fillers (in the gaps

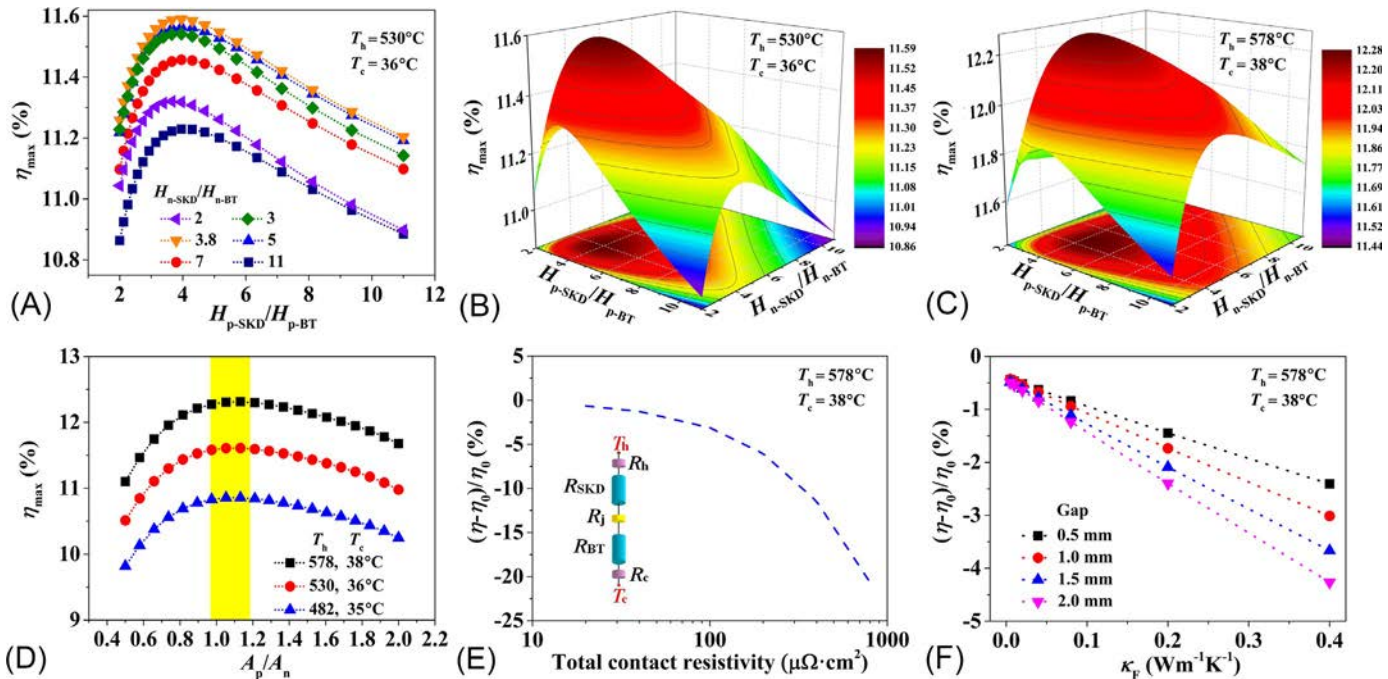


**Fig. 3.1.7** Multiparameter optimization of the BT/SKD segmented unicouple: (A) Maximum conversion efficiency ( $\eta_{\max}$ ) as a function of the segment height ratio  $H_{p\text{-SKD}}/H_{p\text{-BT}}$  at different  $H_{n\text{-SKD}}/H_{n\text{-BT}}$ . (B, C) 3D plots relating  $\eta_{\max}$  with the segment height ratio under different operating temperatures. (D)  $\eta_{\max}$  as a function of the cross-sectional area ratio of  $p$  and  $n$  legs ( $A_p/A_n$ ). The effect of (E) total contact resistivity and (F) thermal conductivity of fillers ( $\kappa_F$ ) on the efficiency loss.

Reproduced with permission from Q.H. Zhang, J.C. Liao, Y.S. Tang, M. Gu, C. Ming, P.F. Qiu, S.Q. Bai, X. Shi, C. Uher, L.D. Chen, Realizing a thermoelectric conversion efficiency of 12% in bismuth telluride/skutterudite segmented modules through full-parameter optimization and energy-loss minimized integration, *Energ. Environ. Sci.* 10 (2017) 956–963.

between different legs) ([Fig. 3.1.7F](#)) on the efficiency loss can be quantitatively assessed in the model.

### 3.1.3 Interfacial materials and bonding technique

For practical segmented thermoelectric element, the interfaces between the different materials play an important role in the transferring of force, heat, and electricity. It is indispensable to note that besides TE materials, module integration including proper interfacial materials and bonding technique must serve the conditions of having low thermal and electrical resistance, weak element diffusion across the junctions as well as good mechanical stability, which is the key issue for module's efficiency and reliability [21]. To reduce interfacial diffusion and enhance bonding strength, diffusion barrier layer usually be introduced at the interface between different materials, such as electrode/TE or different TE materials). Soldering is the common method used in commercial TE cooling module fabrication. For TE power generation module, sintering, welding, brazing, and other bonding techniques are developed in the recent two decades.

Early in 1997, Schilz et al. attempted to form a direct joint by sintering Bi-Te powder to bulk FeSi<sub>2</sub>, but failed [6]. There may be two reasons. One is that no junction was physically or chemically formed possibly due to a thin oxide layer developed on the FeSi<sub>2</sub> that could not be avoided. The other is reason is the thermal expansion coefficient mismatch (CTE) of Bi-Te and that FeSi<sub>2</sub> is serious (CTE =  $19 \times 10^{-6} \text{ K}^{-1}$  for Bi-Te, and  $10 \times 10^{-6} \text{ K}^{-1}$  for FeSi<sub>2</sub>). Later, by using Ni as a suitable common interface material with intermediate CTE which simultaneously acts as a diffusion barrier, all junctions exhibit reliable properties in both electrical and thermal transport.

Muto et al. reported a segmented *p*-type element fabricated using the pulse discharge sintering (PDS) process (see [Fig. 3.1.8A](#)) [22]. The three-layered Bi<sub>0.4</sub>Sb<sub>1.6</sub>Te<sub>3</sub>/Sb<sub>2</sub>Te<sub>3</sub>/AgSbTe<sub>2</sub> are cold compacted between Al electrode in a graphite die and then consolidated by the PDS process. The results show that no reaction layer was observed and no mutual diffusion between Al electrodes and thermoelectric materials ([Fig. 3.1.8B](#)). Without any barrier layer at the interface, mutual diffusion zones of about 500 μm in thickness are observed at the interfaces between thermoelectric materials, which caused high contact resistances.

Hu et al. used In-Ga liquid metal to connect the segments of commercial bismuth tellurides (from Ferrotec Nord) and PbTe-based alloy [23]. Each segment had diffusion barrier layers, such as electroplated nickel for Bi<sub>2</sub>Te<sub>3</sub> and co-sintered Co<sub>0.8</sub>Fe<sub>0.2</sub> for PbTe. Characterization results confirmed the efficiency enhancement in segmented module. But the measured internal resistance and open-circuit heat flow of the segmented modules are obviously larger than the simulated values, which means further improvement of electrical and thermal contacts are necessary.

Interfacial resistance is one issue to evaluate the contact properties of segmented TE modules and to reduce interfacial resistivity is the permanent goal. Interfacial resistivity can be experimentally measured by the four-probe method and the energy loss it costs can also be quantitatively evaluated by the full parameter model

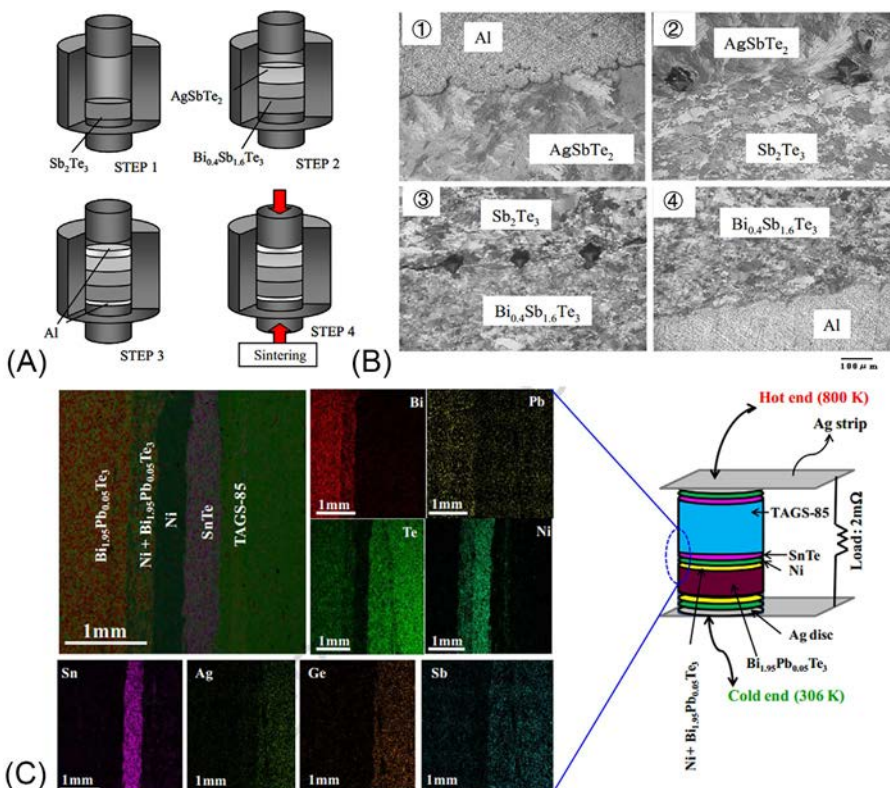


**Fig. 3.1.8** (A) Manufacturing process and (B) micrographs of interfaces of a segmented *p*-type  $\text{Bi}_{0.4}\text{Sb}_{1.6}\text{Te}_3/\text{Sb}_2\text{Te}_3/\text{AgSbTe}_2$  element. (C) Elemental mapping of interfaces of the fabricated segmented TAGS-85/ $\text{Bi}_{1.95}\text{Pb}_{0.05}\text{Te}_3$  thermoelement along with schematic representation of the thermoelectric element.

(A, B) Reproduced with permission from T. Muto, K. Tokuda, T. Itoh, K. Kitagawa, Fabrication of segmented *p*-type  $\text{AgSbTe}_2/\text{Sb}_2\text{Te}_3/\text{Bi}_{0.4}\text{Sb}_{1.6}\text{Te}_3$  thermoelectric module and its performance, 24th International Conference on Thermoelectrics, IEEE (2005). (C) Reproduced with permission from A.K. Bohra, R. Bhatt, A. Singh, S. Bhattacharya, R. Basu, K.N. Meshram, S.K. Sarkar, P. Bhatt, P.K. Patro, D.K. Aswal, K.P. Muthe, S.C. Gadkar, Transition from *n*- to *p*-type conduction concomitant with enhancement of figure-of-merit in Pb doped bismuth telluride: Material to device development, Mater. Des. (2018) <https://doi.org/10.1016/j.matdes.2018.08.035>.

mentioned above. In 2018, a segmented thermoelement of  $\text{Bi}_{1.95}\text{Pb}_{0.05}\text{Te}_3$  and TAGS-85 was reported, fabricated by using hot press with buffer layers of Ag/Ni at  $\text{Bi}_{1.95}\text{Pb}_{0.05}\text{Te}_3$  site and Ag/Ni/SnTe at TAGS-85 end (as shown in the schematic representation of Fig. 3.1.8C) [24]. Sharp interfaces without any diffusion of elements were observed, which yield an average specific contact resistance of  $40 \mu\Omega \text{ cm}^2$ .

Recently, the developed high-performance novel TE materials such as filled skutterudites (SKD) and half-Heusler are selected as candidates for segment modules.

JPL conducted a series of studies by segmenting CoSb<sub>3</sub>-based skutterudites with different thermoelectric materials such as Zn<sub>4</sub>Sb<sub>3</sub> and Bi<sub>2</sub>Te<sub>3</sub> (Fig. 3.1.9A) [15]. Pd was used as the interface material between CoSb<sub>3</sub> and Bi<sub>2</sub>Te<sub>2.7</sub>Se<sub>0.3</sub>, while Zn<sub>4</sub>Sb<sub>3</sub> and CeFe<sub>4</sub>Sb<sub>12</sub> samples were connected using a Pd<sub>70</sub>Ag<sub>30</sub> alloy. The electrical contact resistance measurements showed that both Pd and Pd<sub>70</sub>Ag<sub>30</sub> alloys provided a low electrical contact resistance bonding (Fig. 3.1.9B) with limited cross diffusion. Recently, the Shanghai Institute of Ceramics (SIC) fabricated the segmented Bi<sub>2</sub>Te<sub>3</sub>/SKD elements by the soldering and brazing technique. Each junction possesses low contact resistivity (see Fig. 3.1.9D) and the total contact resistivity for the *p*- and *n*-type segment is about 40  $\mu\Omega \text{ cm}^2$ , which could cause ~2% reduction in maximum conversion efficiency according to the simulated results [20].

Half-Heusler (HH) alloys are very competitive thermoelectric materials suitable for medium-high-temperature ranges of up to about 1000 K [25]. To segment half-Heusler with bismuth telluride, joining between the two segments has certain challenges. This is because bismuth telluride (BiTe) is suitable to work at temperatures upto 523 K and cannot stand temperatures above 773 K due to its volatile constituents, while HH is thermally stable materials with low wettability melting point above 1773 K [26]. According to D'Angelo and Börner et al. [27, 28] in order to directly join the materials, the temperature at their interface should be elevated to the range from 50% to 80% of the lowest melting point. Thus, in principle, HH and BiTe are difficult to be joined directly together due to the large difference in the melting temperature. In 2017, Ngan et al. introduced a two-step process to join HH to BiTe (Fig. 3.1.10A) [29]. Microstructural and chemical element analyses of the joint interfaces showed good contact and no sign of cracks at the junction (Fig. 3.1.10B). However, the diffusion of Sn from the solder into BiTe was observed with a penetration depth of 10  $\mu\text{m}$  (Fig. 3.1.10B). The contact resistivity of the *p*-type Bi<sub>2</sub>Te<sub>3</sub>/Ag<sub>10</sub>Sn<sub>90</sub>/Ag/HH element was measured to be 50  $\mu\Omega\text{cm}^2$  at room temperature and increased to 75  $\mu\Omega\text{cm}^2$  at 523 K (Fig. 3.1.10C). For the *n*-type leg, the contact resistivity was 50  $\mu\Omega\text{cm}^2$  at room temperature and slightly decreased to 35  $\mu\Omega\text{cm}^2$  at 523 K (Fig. 3.1.10C). Recently, Xing et al. used Sn-based solders to weld BiTe and HH [30]. In order to avoid diffusion between the BiTe and HH, an Ni layer with a thickness of about 5  $\mu\text{m}$  was used as a barrier layer. As a result, interfacial resistivities between HH and BiTe were measured to be 5 and 17  $\mu\Omega\text{cm}^2$  for the *n*-type and *p*-type legs, respectively (Fig. 3.1.10D).

In the long-term previous studies, trial and error was used as the only method for interfacial material optimization and it is quite a difficult and time-consuming process. By using the high-throughput strategy, Gu et al. promoted an efficient method for the selection of diffusion barrier layers [31]. By co-sintering the mixture of the TE matrix material and the particles of various diffusion barrier candidates, and then comparing the interfacial diffusion at consequent micro-interfaces at the same time enabled parallel aging and microstructure characterization of different interfaces in the same sample, which makes the screening much more efficient and economical. In 2020, Chu et al. built up an effective criterion for screening barrier layer based on the combination of negative interfacial reaction energy and high activation energy barrier of Sb-migration through the formed interfacial reaction layer for skutterudite

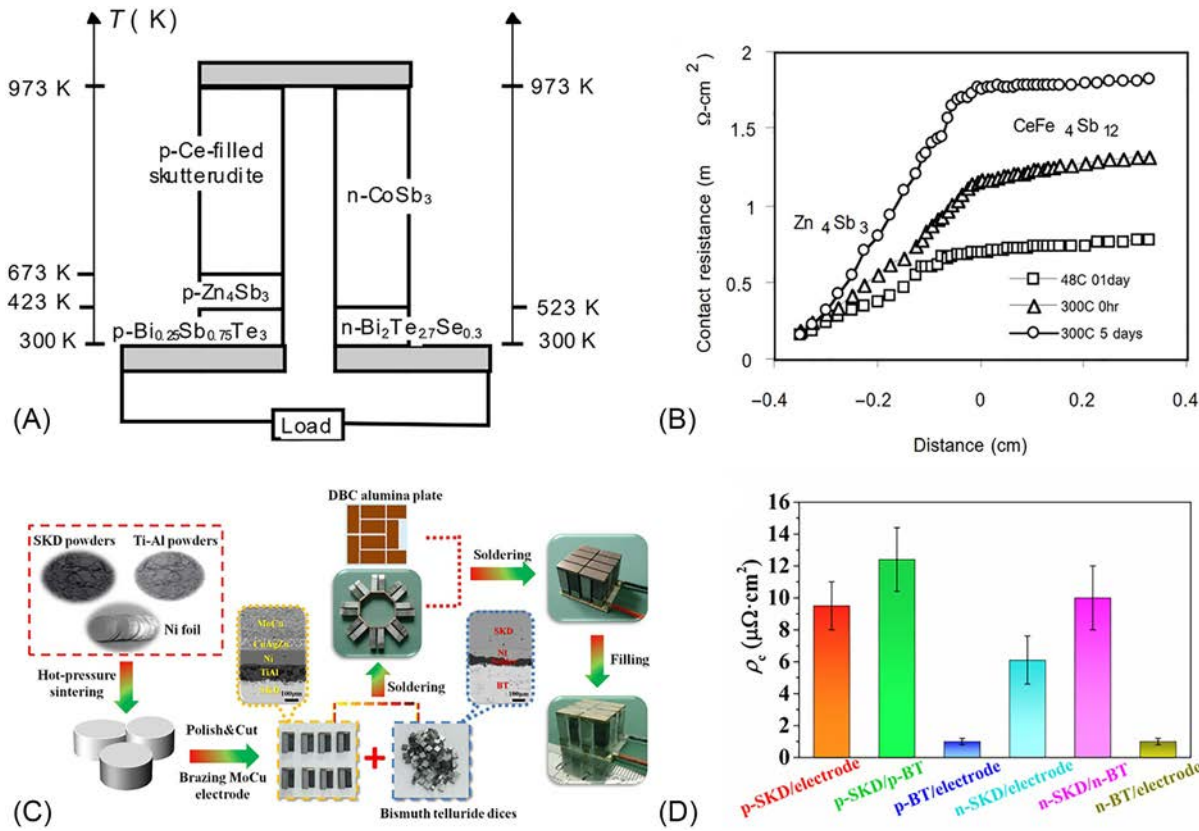


**Fig. 3.1.9** (A) Illustration of the advanced unicouple incorporating new high-performance thermoelectric materials. (B) Electrical contact resistance as a function of distance for a *p*-CeFe<sub>4</sub>Sb<sub>12</sub>/*p*-Zn<sub>4</sub>Sb<sub>3</sub> junction using a Pd<sub>70</sub>Ag<sub>30</sub> alloy interface. The origin corresponds to the interface position. (C) The fabrication flow of BT/SKD segmented modules. (D) The measured contact resistivity  $\rho_c$  between different junctions within the BT/SKD segmented modules.

(A, B) Reproduced with permission from T. Caillat, J.P. Fleuriel, G.J. Snyder, A. Zoltan, D. Zoltan, A. Borshchevsky, A new high efficiency segmented thermoelectric unicouple, 34th Intersociety Energy Conversion Engineering Conference (1999) 2567. (C, D) Reproduced with permission from Q.H. Zhang, J.C. Liao, Y.S. Tang, M. Gu, C. Ming, P.F. Qiu, S.Q. Bai, X. Shi, C. Uher, L.D. Chen, Realizing a thermoelectric conversion efficiency of 12% in bismuth telluride/skutterudite segmented modules through full-parameter optimization and energy-loss minimized integration, Energ. Environ. Sci. 10 (2017) 956–963.

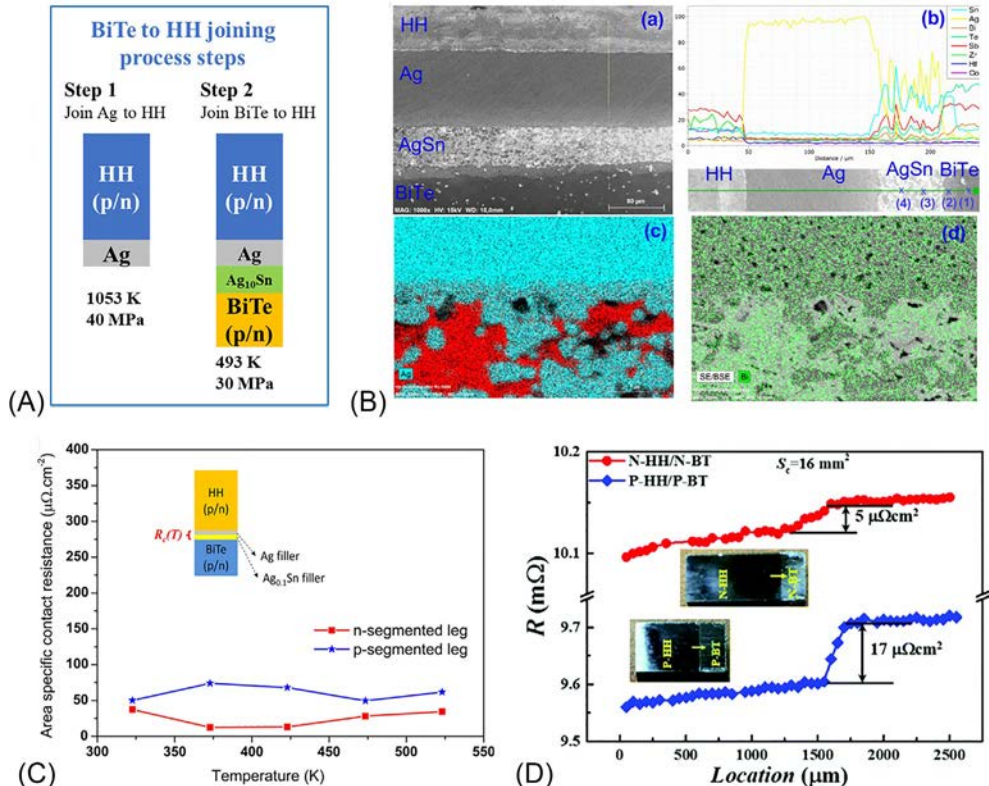


**Fig. 3.1.10** (A) Process to fabricate *p*- and *n*-type HH/BiTe segmented legs. (B) Microstructures and chemical analysis at the joint interface of the *p*-type HH/BiTe segmented leg before heat treatment: (a) SEM image of the interface, (b) EDS line scan across the interface, (c) Zoom-in image of Ag and Sn distributions, and (d) Zoom-in image of Bi distribution. (C) Temperature dependence of area-specific contact resistance of the *p*- and *n*-type HH/BiTe segmented legs. (D) Measured contact resistances of *p*- and *n*-type HH/BiTe interfaces.

(A–C) Reproduced with permission from P.H. Ngan, L. Han, D.V. Christensen, Joining of half-Heusler and bismuth tellurides for segmented thermoelectric generators, *J. Electron. Mater.* 47(1) (2018) 701–710. (D) Reproduced with permission from Y.F. Xing, R.H. Liu, J.C. Liao, Q.H. Zhang, X.G. Xia, C. Wang, H. Huang, J. Chu, M. Gu, T.J. Zhu, C.X. Zhu, F.F. Xu, D.X. Yao, Y.P. Zeng, S.Q. Bai, C. Uher, L.D. Chen, High-efficiency half-Heusler thermoelectric modules enabled by self-propagating synthesis and topologic structure optimization, *Energ. Environ. Sci.* 12 (2019), 3390–3399.

module [32]. This criterion provides an effective guidance on screening barrier layer with bonding-blocking-conducting synergetic functions for TE device integration.

In addition, it is worth to mention that there is another special segmented module using the same kind of TE materials but with different components in different sections, which formed a functionally graded structure. Because the constituent elements in the neighbor section are same, it is quite difficult to restrain the interfacial diffusion between the segments. For the weak possibility in real applications, we do not discuss this type of segmented modules in detail.

### 3.1.4 Samples of high-performance segmented modules

Early in the 1990s, segmented thermoelectric uni-legs and unicouples were fabricated. Their performances were predicted and measured, which present great application potential. Because the voltage of a single leg or couple is too low, the module for practical applications usually consists of a bunch of unicouples wired electrically in series (or partly parallel) and thermally in parallel. Therefore, here we pay attention to the performance of segmented modules. The basic performance measurement of a segmented thermoelectric power generation module includes the power output (or power density) and the conversion efficiency as a function of heat source temperatures and the temperature difference between the hot and cold sides.

In 2002, Matsubara reported a segmented module that was fabricated using the *p* legs of  $\text{YbNi}_{0.4}\text{Fe}_{3.6}\text{Sb}_{12}/\text{Bi}_{0.25}\text{Sb}_{0.75}\text{Te}_3$  and the *n* legs of  $\text{Co}_{0.9}(\text{Pd},\text{Pt})_{0.1}\text{Sb}_3/\text{Bi}_2\text{T}_{e_{2.7}}\text{Se}_{0.3}$  [33]. The module size is  $0.24\text{cm}^2$  in the cross section and of height 0.7 cm. The segmented module with 40 pairs (Fig. 3.1.11A) allows to operate at temperatures of up to  $630^\circ\text{C}$ . The maximum output power of  $\sim 18\text{W}$  was achieved when operating at the hot-side temperature of  $600^\circ\text{C}$  and the cold-side temperature of  $40^\circ\text{C}$ . The conversion efficiency of this module was estimated to be 6%–8%. In 2011, Anatychuk et al. produced a segmented module with  $\text{Bi}_2\text{Te}_3$ -based functionally graded thermoelectric materials [34]. The module has 56 couples with a leg height of 5.6 mm and a leg cross section of  $4.3\text{mm} \times 1.8\text{mm}$ . And it could supply  $6.5\text{W}$  of electricity with an efficiency of 7.8% under a temperature difference of  $220^\circ\text{C}$ . In the same year, D'Angelo et al. reported the 47-couple PbTe-based modules, which was fabricated by Tellurex Corporation using *n*-type  $\text{Bi}_2\text{Te}_{3-x}\text{Se}_x/\text{Ag}_{0.86}\text{Pb}_{19+x}\text{SbTe}_{20}$  and *p*-type  $\text{Bi}_x\text{Sb}_{2-x}\text{Te}_3/\text{Ag}_{0.9}\text{Pb}_{0.9}\text{Sn}_9\text{Sb}_{0.6}\text{Te}_{20}$  segmented legs [35]. Under vacuum and with the hot-/cold-side temperatures of  $400^\circ\text{C}/40^\circ\text{C}$ , an efficiency of 6.56% were obtained.

In 2013, Takabatake reported a segmented module using  $\text{Ba}_8\text{Ga}_{16}\text{Sn}_{30}$  clathrate (Fig. 3.1.11D). The eight-pair module segmented with Bi-Te could output  $0.87\text{W}$  of power at a temperature difference of  $390^\circ\text{C}$  and 7.5% conversion efficiency [36]. Afterwards, Kim et al. designed a segmented module using lightweight thermoelectric alloys of manganese silicide and Bi-Te-based compounds with a high specific power density of  $42.9\text{ W/kg}$  [37]. The two-pair segmented thermoelectric generator achieved the maximum efficiency of 4.6% at  $\Delta T=498^\circ\text{C}$ .

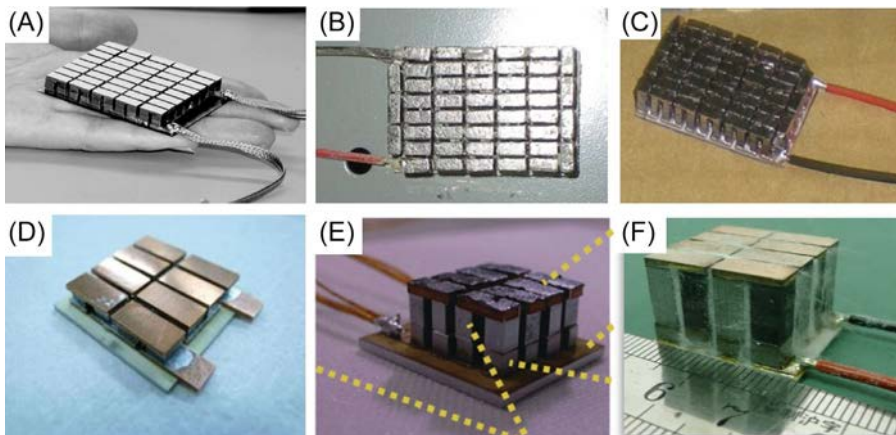


**Fig. 3.1.11** (A) Segmented thermoelectric module fabricated with a *p*-leg of  $\text{Yb}_{0.2}\text{Fe}_{3.6}\text{Ni}_{0.4}\text{Sb}_{12}/\text{Bi}_{0.25}\text{Sb}_{0.75}\text{Te}_3$  and an *n*-leg of  $\text{Co}_{0.9}(\text{Pd},\text{Pt})_{0.1}\text{Sb}_3/\text{Bi}_2\text{Te}_{2.7}\text{Se}_{0.3}$ . (B, C) Examples of two different 47-couple segmented-leg thermoelectric modules consisting of n-type  $\text{Bi}_2\text{Te}_{3-x}\text{Se}_x$  to  $\text{Ag}_{0.86}\text{Pb}_{19+x}\text{Sb}\text{Te}_{20}$  legs and p-type  $\text{Bi}_x\text{Sb}_{2-x}\text{Te}_3$  to  $\text{Ag}_{0.9}\text{Pb}_9\text{Sn}_9\text{Sb}_{0.6}\text{Te}_{20}$  legs fabricated by Tellurex. (D) Thermoelectric module made of eight-pair legs of *p*- and *n*-type  $\text{Ba}_8\text{Ga}_{16}\text{Sn}_{30}$  single crystals. The total dimension is  $28 \times 28 \times 5.4$  mm. (E) Picture of the segmented  $\text{Bi}_2\text{Te}_3$ /nanostructured  $\text{PbTe}$  module. (F) Picture of the segmented  $\text{Bi}_2\text{Te}_3/\text{CoSb}_3$ -based filled skutterudite.

(A) Reproduced with permission from K. Matsubara, The performance of a segmented thermoelectric convertor using Yb-based filled skutterudites and  $\text{Bi}_2\text{Te}_3$ -based materials, MRS Proc. 691 (2001) G9.1.1–G9.1.12, (B, C) Reproduced with permission from J. D'Angelo, E. Case, N. Matchanov, C. Wu, T.P. Hogan, J. Barnard, C. Cauchy, T. Hendricks, M.G. Kanatzidis, Electrical, thermal, and mechanical characterization of novel segmented-leg thermoelectric modules, J. Electron. Mater. 40(10) 2011 2051–2062. (D) Reproduced with permission from T. Takabatake, in Thermoelectric Nanomaterials: Materials Design and Application, ed. K. Koumoto and T. Mori, Springer, Heidelberg, 2013, Chapter 2, pp. 33–49. (E) Reproduced with permission from X.K. Hu, P. Jood, M. Ohta, M. Kunii, K. Nagase, H. Nishiate, M.G. Kanatzidis, A. Yamamoto, Power generation from nanostructured  $\text{PbTe}$ -based thermoelectrics: comprehensive development from materials to modules, Energ. Environ. Sci. 9 (2016) 517–529. (F) Reproduced with permission from Q.H. Zhang, J.C. Liao, Y.S. Tang, M. Gu, C. Ming, P.F. Qiu, S.Q. Bai, X. Shi, C. Uher, L.D. Chen, Realizing a thermoelectric conversion efficiency of 12% in bismuth telluride/skutterudite segmented modules through full-parameter optimization and energy-loss minimized integration, Energ. Environ. Sci. 10 (2017) 956–963.

Owing to the limitations in the thermoelectric performance of materials and the inadequacy of integration techniques, the conversion efficiency cannot break the 10% efficiency in quite a long time. In the recent 5 years, the improvement in the performance of segmented module was accelerated.

In 2015, Hu et al. demonstrated the use of high-performance nanostructured  $\text{PbTe}$ -based materials to achieve high conversion efficiency [23]. Commercial bismuth tellurides and nanostructured  $\text{PbTe}$ -based alloys were used as the low- and high-temperature segments, respectively (Fig. 3.1.11E). A record efficiency of ~11% was achieved (Fig. 3.1.12B) but it was refreshed soon by Zhang et al. in 2017.

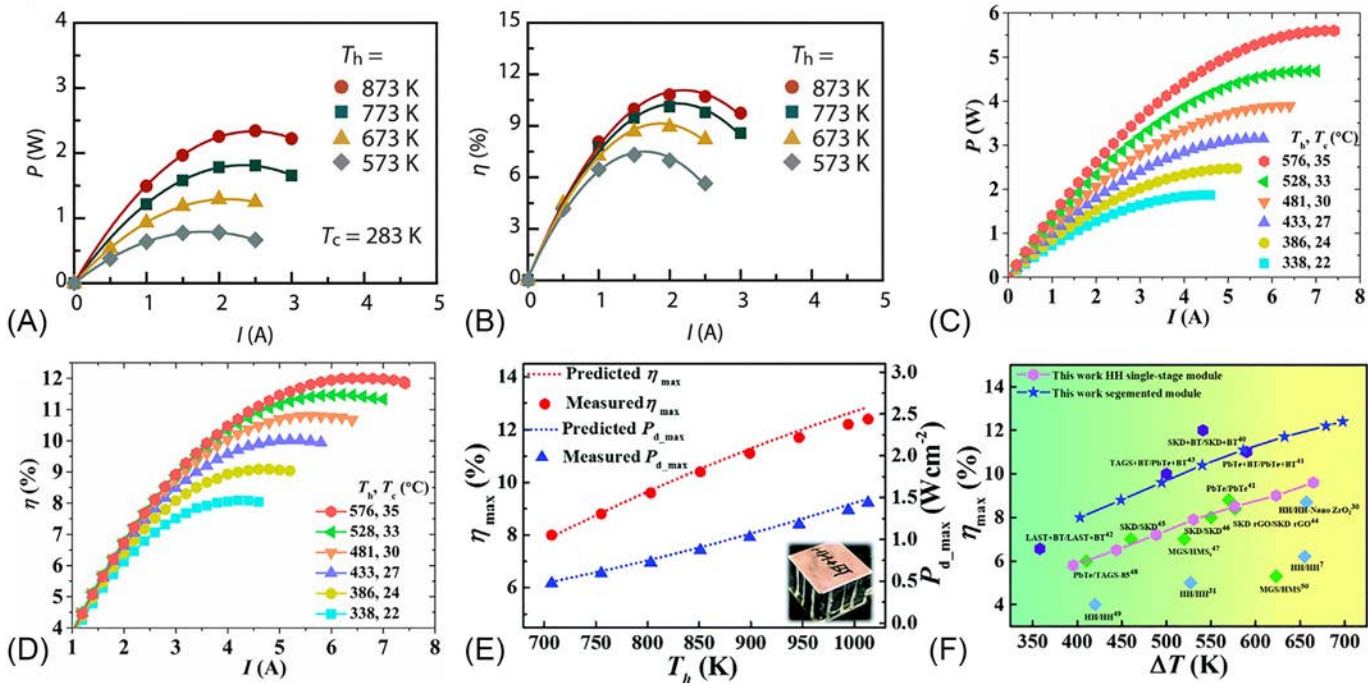


**Fig. 3.1.12** (A) Measured electrical power output ( $P$ ) and (B) conversion efficiency ( $\eta$ ) of the segmented  $\text{Bi}_2\text{Te}_3$ /nanostructured  $\text{PbTe}$  module as a function of electrical current ( $I$ ). (C) Output power and (D) conversion efficiency of the segmented BT/SKD module as a function of current under different operating temperatures. (E) The predicted and experimental maximum power density and maximum conversion efficiency as a function of  $T_h$  for the HH/BT segmented module. (F) Maximum thermoelectric conversion efficiency versus temperature difference for typical thermoelectric modules.

(A, B) Reproduced with permission from X.K. Hu, P. Jood, M. Ohta, M. Kunii, K. Nagase, H. Nishiate, M.G. Kanatzidis, A. Yamamoto, Power generation from nanostructured  $\text{PbTe}$ -based thermoelectrics: comprehensive development from materials to modules, *Energ. Environ. Sci.* 9 (2016) 517–529. (C, D) Reproduced with permission from Q.H. Zhang, J.C. Liao, Y.S. Tang, M. Gu, C. Ming, P.F. Qiu, S.Q. Bai, X. Shi, C. Uher, L.D. Chen, Realizing a thermoelectric conversion efficiency of 12% in bismuth telluride/skutterudite segmented modules through full-parameter optimization and energy-loss minimized integration, *Energ. Environ. Sci.* 10 (2017) 956–963. (E, F) Reproduced with permission from Y.F. Xing, R.H. Liu, J.C. Liao, Q.H. Zhang, X.G. Xia, C. Wang, H. Huang, J. Chu, M. Gu, T.J. Zhu, C.X. Zhu, F.F. Xu, D.X. Yao, Y.P. Zeng, S.Q. Bai, C. Uher, L.D. Chen, High-efficiency half-Heusler thermoelectric modules enabled by self-propagating synthesis and topologic structure optimization, *Energ. Environ. Sci.* 12 (2019), 3390–3399.

Combining full-parameter optimization with energy-loss minimized integration, the segmented modules consisting of  $\text{Bi}_2\text{Te}_3$ -based alloys and  $\text{CoSb}_3$ -based filled skutterudites realized a high conversion efficiency of 12% and high power density of  $1.4 \text{ W cm}^{-2}$  [20]. In 2019, Xing et al. adopted the self-propagating high-temperature synthesis to mass-produce half-Heusler materials in batches of  $0.1 \text{ kg}$  [30]. Furthermore, based on the scaled-up fabrication half-Heusler (HH) and commercial bismuth telluride (BT), they finished the optimization and fabrication of segmented HH/BT modules. The experimental measured conversion efficiency for a eight-pair module reached 12.4% under the temperature difference of  $698^\circ\text{C}$  (Fig. 3.1.12E and F).

It is worth mentioning that the new developed intergration technique included sintering and brazing, which is industrially applicable for the mass production of segmented modules.

### 3.1.5 Future challenges

Thermoelectric conversion has long been recognized as a potentially transformative power generation technology and is now growing rapidly due to its ability to develop cost-effective, pollution-free, solid-state-based conversion of heat into electricity. Recent achievements with segmented thermoelectric devices have expedited the steps to large-scale applications of power generation. This chapter presented an overview on the recent progress of the design and integration of segmented thermoelectric modules. Particular attention was paid to material selection, module topologic structure optimization, interface engineering, and bonding technique for integration. Some typical high-performance segmented modules were summarized.

After years of effort, integration techniques for segmented modules are becoming mature and reliable, developing toward the mass production. The evaluation results indicate that the performance of segmented modules is gradually being improved. However, when it approaches real industrial applications, challenges still lie ahead and much more efforts are required in the future. First of all, conversion efficiency has not reached the ceiling and needs further improvements. Synchronously, module fabrication cost awaits reductions through scaling up and process optimization. Second, a strategy to improve the reliability of the module operating at harsh conditions such as high-temperature and high oxygen environment is required for practical applications. The service behavior (e.g., chemical compatibility, diffusion-driven interface degradation, material degradation performance) under real and complex operation conditions (vibration, oxidation, thermal circling, etc.) should be investigated in detail [38, 39]. Third, the lack of a measurement standard and accurate and reliable measurement instrumentation for evaluation have created another barrier. A systematic method for the prediction of lifetime should be established by combining the service behavior including electrical, mechanical, and thermal performances of materials and modules. All in all, continued efforts from various fields are required to gain a more

thorough understanding of the rational design, cost-effective fabrication, and standard evaluation of segmented thermoelectric modules, which should accelerate the use of thermoelectric technology in a wide range of applications.

## References

- [1] X. Shi, S. Bai, L. Xi, J. Yang, W. Zhang, L. Chen, Realization of high thermoelectric performance in n-type partially filled skutterudites, *J. Mater. Res.* 26 (15) (2011) 1745–1754.
- [2] A.F. IOFFE, Thermoelectric battery, SU author's certificate no. 126158, claimed August 19, 1949, also published in Invention Bulletin no. 4, 1960.
- [3] R.E. Fredrick, W.B. Lake, R.W. Fritts, A. Hills, Thermoelectric devices and thermoelements, Patent US3051767, 1962.
- [4] J.P. Fleural, T. Caillat, B.J. Nesmith, D.F. Woerner, J.F. Mondt, G. Stapfer, High reliability, high temperature thermoelectric power generation materials and technologies, Thermoelectric Applications Workshop, Baltimore, Maryland, 2012. March 21, 2012.
- [5] M.S. El-Genk, H.H. Saber, T. Caillat, Efficient segmented thermoelectric unicouples for space power applications, *Energ. Conver. Manage.* 44 (2003) 1755–1772.
- [6] J. Schilz, L. Helmers, Bismuth-telluride/Iron-disilicide segmented thermoelectric elements: Patterning, preparation and properties, in: 16th International Conference on Thermoelectrics, IEEE, 1997.
- [7] Y.S. Kang, M. Niino, I.A. Nishida, J. Yoshino, Development and evaluation of 3-Stage segmented thermoelectric elements, in: 17th International Conference on Thermoelectrics, IEEE, 1998.
- [8] T.S. Ursell, G.J. Snyder, Compatibility of segmented thermoelectric generators, in: 21st International Conference on Thermoelectrics, IEEE, 2002.
- [9] G.J. Snyder, Design and optimization of compatible, segmented thermoelectric generators, in: 22nd International Conference on Thermoelectrics, IEEE, 2003.
- [10] G.J. Snyder, T. Caillat, Using the compatibility factor to design high efficiency segmented thermoelectric generators, *MRS Proc.* 793 (2003) S2.1.
- [11] L.T. Hung, N.V. Nong, S. Linderoth, N. Pryds, Segmentation of low-cost high efficiency oxide-based thermoelectric materials, *Phys. Status Solidi A* 212 (4) (2015) 767–774.
- [12] T.J. Zhu, Y.T. Liu, C.G. Fu, J.P. Heremans, J.G. Snyder, X.B. Zhao, Compromise and synergy in high-efficiency thermoelectric materials, *Adv. Mater.* 29 (30) (2017) 1605884.
- [13] F. Drymiotis, J.P. Fleural, S. Bux, et al., Development of high efficiency segmented thermoelectric couples for space applications, in: APS March Meeting 2018, American Physical Society, 2018.
- [14] C. Goupil, *Continuum Theory and Modeling of Thermoelectric Elements*, Wiley, 2016 (chapter 3).
- [15] T. Caillat, J.P. Fleural, G.J. Snyder, A. Zoltan, D. Zoltan, A. Borshchevsky, A new high efficiency segmented thermoelectric unicouple, in: 34th Intersociety Energy Conversion Engineering Conference, 1999, p. 2567.
- [16] B.W. Swanson, E.V. Somers, R.R. Heike, Optimization of a sandwiched thermoelectric device, *J. Heat Transfer* (1961) 77–82.
- [17] M.S. El-Genk, H.H. Saber, High efficiency segmented thermoelectric for operation between 973 and 300 K, *Energ. Conver. Manage.* 44 (2003) 1069–1088.
- [18] H.H. Saber, M.S. El-Genk, Optimization of segmented thermoelectric for maximizing conversion efficiency and electric power density, in: 21st International Conference on Thermoelectrics, IEEE, 2002.

- [19] H.H. Saber, M.S. El-Genk, A three-dimensional performance model of segmented thermoelectric converters, in: AIP Space Technology and Applications International Forum-STAF 2002, Albuquerque, New Mexico (USA), 608, 2002, pp. 998–1006.
- [20] Q.H. Zhang, J.C. Liao, Y.S. Tang, M. Gu, C. Ming, P.F. Qiu, S.Q. Bai, X. Shi, C. Uher, L.D. Chen, Realizing a thermoelectric conversion efficiency of 12% in bismuth telluride/skutterudite segmented modules through full-parameter optimization and energy-loss minimized integration, *Energ. Environ. Sci.* 10 (2017) 956–963.
- [21] W.S. Liu, S.Q. Bai, Thermoelectric interface materials: a perspective to the challenge of thermoelectric power generation module, *J. Materomics* 5 (2019) 321–336.
- [22] T. Muto, K. Tokuda, T. Itoh, K. Kitagawa, Fabrication of segmented p-type  $\text{AgSbTe}_2/\text{Sb}_2\text{Te}_3/\text{Bi}_{0.4}\text{Sb}_{1.6}\text{Te}_3$  thermoelectric module and its performance, in: 24th International Conference on Thermoelectrics, IEEE, 2005.
- [23] X.K. Hu, P. Jood, M. Ohta, M. Kunii, K. Nagase, H. Nishiate, M.G. Kanatzidis, A. Yamamoto, Power generation from nanostructured PbTe-based thermoelectrics: comprehensive development from materials to modules, *Energ. Environ. Sci.* 9 (2016) 517–529.
- [24] A.K. Bohra, R. Bhatt, A. Singh, S. Bhattacharya, R. Basu, K.N. Meshram, S.K. Sarkar, P. Bhatt, P.K. Patro, D.K. Aswal, K.P. Muthe, S.C. Gadkar, Transition from n- to p-type conduction concomitant with enhancement of figure-of-merit in Pb doped bismuth telluride: Material to device development, *Mater. Des.* (2018), <https://doi.org/10.1016/j.matdes.2018.08.035>.
- [25] C.G. Fu, S.Q. Bai, Y.T. Liu, Y.S. Tang, L.D. Chen, X.B. Zhao, T.J. Zhu, Realizing high figure of merit in heavy-band p-type half-Heusler thermoelectric materials, *Nat. Commun.* 6 (2015) 8144.
- [26] E. Maciá-Barber, Thermoelectric Materials: Advances and Applications, Pan Stanford, 2015.
- [27] J.J. D'Angelo, E.J. Timm, F. Ren, B.D. Hall, E. Case, H. Schock, M. Kanatzidis, D.Y. Chung, T.P. Hogan, Electrical contact fabrication and measurements of metals and alloys to thermoelectric materials, in: MRS Proceedings 1044, 2008.
- [28] F.D. Boerner, M. Schreier, B. Feng, W. Lippmann, H.P. Martin, A. Michaelis, A. Hurtado, Development of laser-based joining technology for the fabrication of ceramic thermoelectric modules, *J. Mater. Res.* 29 (16) (2014) 1771–1780.
- [29] P.H. Ngan, L. Han, D.V. Christensen, Joining of half-Heusler and bismuth tellurides for segmented thermoelectric generators, *J. Eletron. Mater.* 47 (1) (2018) 701–710.
- [30] Y.F. Xing, R.H. Liu, J.C. Liao, Q.H. Zhang, X.G. Xia, C. Wang, H. Huang, J. Chu, M. Gu, T.J. Zhu, C.X. Zhu, F.F. Xu, D.X. Yao, Y.P. Zeng, S.Q. Bai, C. Uher, L.D. Chen, High-efficiency half-Heusler thermoelectric modules enabled by self-propagating synthesis and topologic structure optimization, *Energ. Environ. Sci.* 12 (2019) 3390–3399.
- [31] M. Gu, S.Q. Bai, J.H. Wu, J.C. Liao, X.G. Xia, R.H. Liu, L.D. Chen, A high-throughput strategy to screen interfacial diffusion barrier materials for thermoelectric modules, *J. Mater. Res.* 34 (7) (2019) 1179–1187.
- [32] J. Chu, J. Huang, R.H. Liu, J.C. Liao, X.G. Xia, Q.H. Zhang, C. Wang, M. Gu, S.Q. Bai, X. Shi, L.D. Chen, Electrode interface optimization advances conversion efficiency and stability of thermoelectric devices, *Nat. Commun.* 11 (2020) 2723, <https://doi.org/10.1038/s41467-020-16508-x>.
- [33] K. Matsubara, The performance of a segmented thermoelectric convertor using Yb-based filled skutterudites and  $\text{Bi}_2\text{Te}_3$ -based materials, *MRS Proc.* 691 (2001) G9.1.1–G9.1.12.
- [34] L.I. Anatychuk, L.N. Vikhor, L.T. Strutynska, I.S. Termena, Segmented generator modules using  $\text{Bi}_2\text{Te}_3$ -based materials, *J. Electron. Mater.* 40 (5) (2011) 957–961.

- [35] J. D'Angelo, E. Case, N. Matchanov, C. Wu, T.P. Hogan, J. Barnard, C. Cauchy, T. Hendricks, M.G. Kanatzidis, Electrical, thermal, and mechanical characterization of novel segmented-leg thermoelectric modules, *J. Electron. Mater.* 40 (10) (2011) 2051–2062.
- [36] T. Takabatake, in: K. Koumoto, T. Mori (Eds.), *Thermoelectric Nanomaterials: Materials Design and Application*, Springer, Heidelberg, 2013, pp. 33–49. Chapter 2.
- [37] H.S. Kim, K. Kikuchi, T. Itoh, T. Iida, M. Taya, Design of segmented thermoelectric generator based on cost-effective and light-weight thermoelectric alloys, *Mater. Sci. Eng. B* 185 (2014) 45–52.
- [38] Q.H. Zhang, X.Y. Huang, S.Q. Bai, X. Shi, C. Uher, L.D. Chen, Thermoelectric devices for power generation: Recent progress and future Challenges, *Adv. Eng. Mater.* 18 (2) (2016) 194–213.
- [39] Next-Generation Radioisotope Thermoelectric Generator Study. <https://rps.nasa.gov/resources/69/next-generation-radioisotope-thermoelectric-generator-presentation/>.

# Power generation performance of Heusler Fe<sub>2</sub>VAI modules

3.2

Masashi Mikami

National Institute of Advanced Industrial Science and Technology, AIST, Nagoya, Japan

## 3.2.1 Introduction

Heusler Fe<sub>2</sub>VAI alloy exhibits large thermoelectric power factor (PF) in the lower temperature range from room temperature to 600 K by virtue of its pseudo-gap electronic band structure [1–3]. Therefore, a thermoelectric module consisting of the Fe<sub>2</sub>VAI alloy is expected to be applied to energy recovery from vast amounts of low-temperature waste heat via thermoelectric power generation. Although the thermoelectric figure of merit (ZT) of the Fe<sub>2</sub>VAI alloy is lower than the high-performance thermoelectric materials, such as the Bi–Te alloy, because of its relatively high thermal conductivity [4], the high mechanical strength and excellent chemical stability of this alloy can gain an advantage in thermoelectric applications with long-term stability in a harsh environment [5, 6]. In addition, the Fe<sub>2</sub>VAI alloy consisting of abundant and inexpensive elements, such as Fe and Al, is also advantageous to producing low-cost thermoelectric devices on a large scale. This section describes the performance of thermoelectric modules consisting of sintered Fe<sub>2</sub>VAI alloys prepared by the powder-metallurgical process.

## 3.2.2 Durable Heusler Fe<sub>2</sub>VAI thermoelectric modules

### 3.2.2.1 Thermoelectric properties of sintered Fe<sub>2</sub>VAI alloys

Electronic band structure of the Heusler Fe<sub>2</sub>VAI alloy is characterized by a steep pseudo-gap around the Fermi level [7–10], which can enhance the Seebeck coefficient (*S*) for both p-type and n-type materials by controlling the valence electron concentration (VEC) [1–4, 11–14]. For instance, the decrease in VEC by the element substitution of Ti for V site leads to an increase in positive *S* value, and the increase of VEC by the substitution of Si for Al site leads to an increase in negative *S* value. This enhancement of *S* by the control of VEC can be well explained by the rigid-band-like shift of the Fermi level [15]. Values of *S* of the element-substituted Fe<sub>2</sub>VAI sintered alloys prepared by the powder-metallurgical process are shown in Fig. 3.2.1. The large *S* around room temperature suggests that this alloy is suitable for the thermoelectric power generation for low-temperature waste heat. In addition, the large *S* for both p-type and n-type enables the construction of thermoelectric module consisting only of the Fe<sub>2</sub>VAI alloy, which is beneficial in relieving thermal stress on thermoelectric

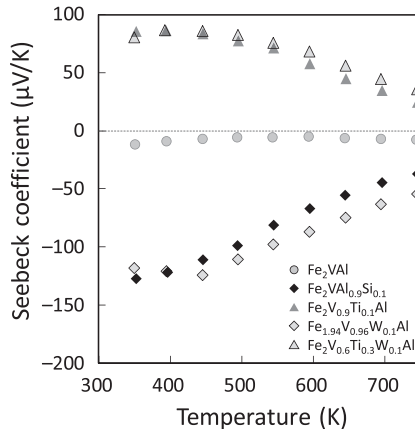


**Fig. 3.2.1** Seebeck coefficient of Heusler  $\text{Fe}_2\text{VAI}$  sintered alloys.

power generation. The narrow pseudo-gap band structure of the  $\text{Fe}_2\text{VAI}$  alloy also promotes electrical conductivity ( $\sigma$ ). As shown in [Fig. 3.2.2](#), while the undoped  $\text{Fe}_2\text{VAI}$  possesses semiconductor-like temperature dependence of  $\sigma$ , the element-substituted  $\text{Fe}_2\text{VAI}$  sintered alloys exhibit high  $\sigma$  with metallic temperature dependence because of sufficient carrier doping. This high  $\sigma$  combined with large  $S$  can provide relatively high PF value, such as  $5.5 \text{ mW/mK}^2$  [1]. In addition, it has been reported that the modification of the electronic band structure by off-stoichiometric compositional control can realize further enhancement of  $S$  and PF, such as  $6.7 \text{ mW/mK}^2$  [16–22], which is higher than conventional thermoelectric materials, such as the Bi-Te alloy.

Contrary to the excellent electronic properties, the highly symmetric crystal structure of  $\text{Fe}_2\text{VAI}$  alloy causes relatively high thermal conductivity ( $\kappa$ ) as a thermoelectric material, such as  $28 \text{ W/mK}$  [4], resulting in poor ZT value. The high

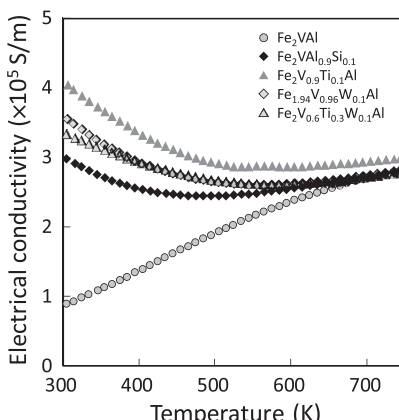


**Fig. 3.2.2** Electrical conductivity of Heusler  $\text{Fe}_2\text{VAI}$  sintered alloys.

$\kappa$  value is also inconvenient to maintain large temperature differences for thermoelectric power generation with realistic leg size in a thermoelectric module with limited amounts of thermal flux from actual heat sources. Therefore, a reduction in  $\kappa$  is indispensable for practical applications of the Fe<sub>2</sub>VAI thermoelectric device. For the reduction of  $\kappa$  in Fe<sub>2</sub>VAI alloy, introduction of phonon scattering effects had been examined, such as the mass fluctuation and the crystal lattice strain effect by heavy-element doping and grain-boundary scattering by grain size reduction [4, 23–29]. Fig. 3.2.3 shows the  $\kappa$  value of sintered Fe<sub>2</sub>VAI alloys prepared by pulsed current sintering (PCS) using powders consisting of nanometer-sized crystallite synthesized by mechanical alloying (MA) [23]. As shown in the inset of Fig. 3.2.3, the sintered Fe<sub>2</sub>VAI alloy consists of submicrometer-sized fine microstructures due to the limited grain growth by the rapid densification of PCS. The increase in phonon scattering at grain boundaries resulting from the reduction in grain size reduced the  $\kappa$  value by almost half compared to that of the arc-melted Fe<sub>2</sub>VAI alloy consisting of submillimeter-sized grains. This microstructure refinement had little effect on the electron transport property presumably because of the relatively short intrinsic electron mean free path of the Fe<sub>2</sub>VAI alloy around 2.4 nm [30], resulting in the improvement in thermoelectric performance of this alloy. For a further reduction of  $\kappa$ , heavy-element doping is effective [24, 25]. For instance, as shown in Fig. 3.2.3, the W substitution for the V site could significantly reduce  $\kappa$ . The temperature-independent  $\kappa$  value of W-substituted Fe<sub>2</sub>VAI sintered alloys suggests that the phonon transport is strongly suppressed by the mass fluctuation and the crystal lattice strain induced by the element substitution. The heavy-element doping also had little effect on the electronic properties of Fe<sub>2</sub>VAI alloy, and consequently ZT value was improved, as shown in Fig. 3.2.4. Using these Fe<sub>2</sub>VAI sintered alloys, thermoelectric modules were constructed and evaluated.

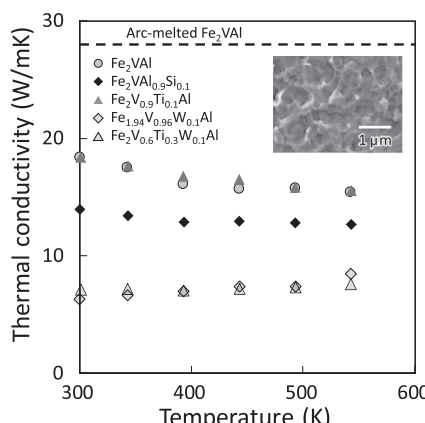


**Fig. 3.2.3** Thermal conductivity of Heusler Fe<sub>2</sub>VAI sintered alloys. Inset is an SEM image of the fracture surface of nonsubstituted Fe<sub>2</sub>VAI sintered alloy.

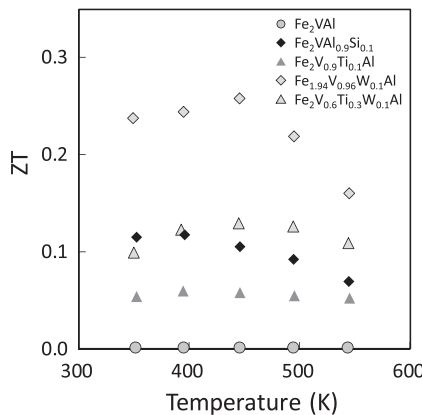


Fig. 3.2.4 ZT of Heusler  $\text{Fe}_2\text{VAI}$  sintered alloys.

### 3.2.2.2 Preparation of thermoelectric module by direct Cu joining

The advantages in the practical use of the  $\text{Fe}_2\text{VAI}$  alloy are its high mechanical strength and excellent oxidation resistance. For example, the  $\text{Fe}_2\text{VAI}$  sintered body composed of submicrometer-sized crystal grains exhibits a high bending strength of 800 MPa and excellent oxidation resistance in air of up to 900 K. In order to take these advantages of  $\text{Fe}_2\text{VAI}$  alloy, a process for producing a thermoelectric module with mechanical durability and heat resistance was required. For the purpose of obtaining an electrode junction with high bonding strength and excellent thermal stability the diffusion joining technique was examined [31]. As shown in Fig. 3.2.5, an electrode joint consisting of a 1- $\mu\text{m}$ -thick diffusion layer without cracking or peeling was obtained by the solid-phase diffusion induced by heating the  $\text{Fe}_2\text{VAI}$  sintered body and the copper electrode under pressure. The bonding strength of the electrode joint evaluated by the shear strength test was about 100 MPa, which is much higher than the solder joint usually used for the Bi-Te thermoelectric module. Consequently, as shown in Fig. 3.2.6,  $\text{Fe}_2\text{VAI}$  thermoelectric modules without a ceramic substrate was constructed and evaluated.

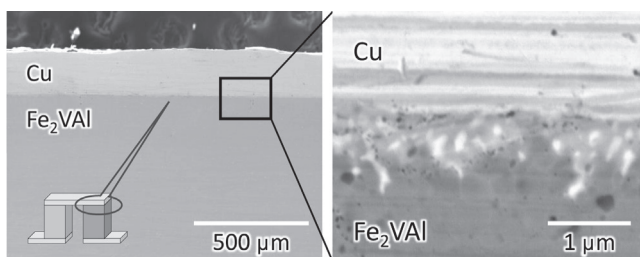
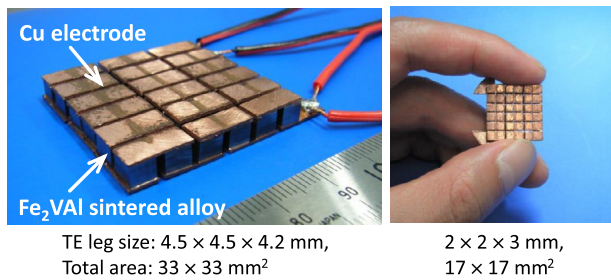


Fig. 3.2.5 Direct joining of  $\text{Fe}_2\text{VAI}$  sintered alloys and Cu electrode.

From M. Mikami, K. Kobayashi, T. Kawada, K. Kubo, N. Uchiyama, Development and evaluation of high-strength  $\text{Fe}_2\text{VAI}$  thermoelectric module, Jpn. J. Appl. Phys. 47 (2008) 1512–1516. Copyright (2008) The Japan Society of Applied Physics.



**Fig. 3.2.6** Heusler Fe<sub>2</sub>VAL thermoelectric module consisting of 18 p-n pairs.

From M. Mikami, K. Kobayashi, T. Kawada, K. Kubo, N. Uchiyama, Development and evaluation of high-strength Fe<sub>2</sub>VAL thermoelectric module, Jpn. J. Appl. Phys. 47 (2008) 1512–1516. Copyright (2008) The Japan Society of Applied Physics.

### 3.2.2.3 Performance and durability of Heusler Fe<sub>2</sub>VAL thermoelectric modules

Power generation tests were conducted on Fe<sub>2</sub>VAL thermoelectric modules consisting of 18 pairs of p-n junctions prepared by direct bonding of Fe<sub>2</sub>VAL sintered bodies and copper electrodes [6]. For comparison, thermoelectric modules consisting of two types of Fe<sub>2</sub>VAL sintered alloys were prepared. One was the sintered alloy with relatively high  $\kappa$ , i.e., the p-type Ti-substituted and n-type Si-substituted Fe<sub>2</sub>VAL sintered alloys, and the other was W-substituted Fe<sub>2</sub>VAL sintered alloys with lower  $\kappa$  values as shown in Fig. 3.2.3. These thermoelectric modules consisting of 4.5 mm<sup>2</sup> TE legs (see Fig. 3.2.6) were mounted between a hot plate set at 573 K and a heat sink cooled by a circulating water of 293 K. As shown in Fig. 3.2.7, the thermoelectric module consisting of the W-substituted Fe<sub>2</sub>VAL alloys exhibited a much larger power generation density of 0.5 W/cm<sup>2</sup> mainly because of the higher output voltage. Apparently, the enlargement of temperature difference at TE legs resulting from the reduction of  $\kappa$  contributed to the enhancement of power generation ability. In addition, Fe<sub>2</sub>VAL

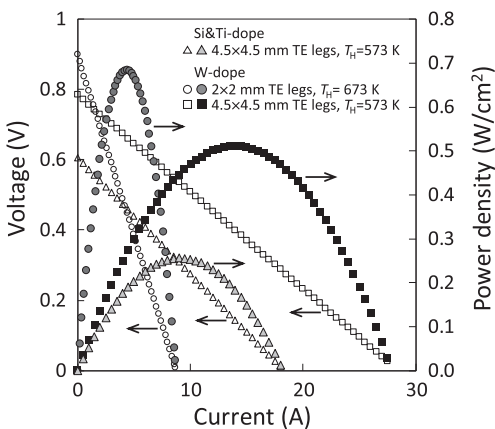
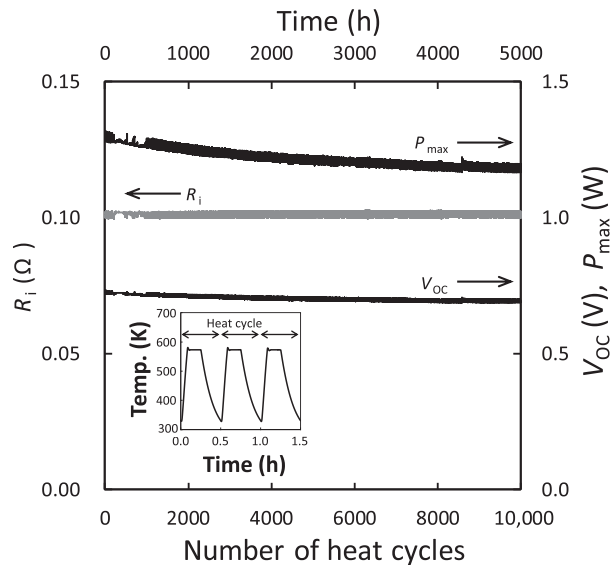


**Fig. 3.2.7** Power generation performance of Heusler Fe<sub>2</sub>VAL thermoelectric module.

thermoelectric modules consisting of  $2.0\text{ mm}^2$  TE legs (see Fig. 3.2.6) placed on a hot plate of 673 K showed larger power density and it reached  $0.7\text{ W/cm}^2$ . It is obvious that these large power density values are mainly due to the high power factor of  $\text{Fe}_2\text{VAl}$  alloys, but the negligibly low electrical resistance at the electrode joint also contributed to minimize the depression of the current flow. For instance, an electrical resistance of  $101.9\text{ m}\Omega$  for the thermoelectric module consisting of  $2.0\text{ mm}^2$  TE legs estimated from the  $I$ - $V$  characteristics of experimental results was almost the same as the theoretical electrical resistance of  $100.4\text{ m}\Omega$  determined from the electrical resistivity of the  $\text{Fe}_2\text{VAl}$  sintered body, which suggested that the electrical resistance at the electrode joint formed by the direct joining was sufficiently low. This result means that the electric power generated in the TE legs can be taken out with insignificant loss.

Long-term durability test of the  $\text{Fe}_2\text{VAl}$  thermoelectric module under thermal cycling was conducted in air, as shown in Fig. 3.2.8. During a cycle of 30 min, the hot side of the thermoelectric module was heated to 573 K in 5 min, held at 573 K for 10 min, and cooled to about 320 K in 15 min (see the inset of Fig. 3.2.8). The cold side was cooled by a circulating water of 293 K. The power generation performance of the thermoelectric module was evaluated during the temperature holding period at 573 K. As indicated in Fig. 3.2.8, the change in internal resistance ( $R_i$ ) of the thermoelectric module was negligible even after 10,000 cycles/5000 h. This result indicates that the  $\text{Fe}_2\text{VAl}$  sintered body and the electrode joint possess high stability against long-term heating and thermal cycles. On the other hand, the open-circuit voltage ( $V_{OC}$ ) and the maximum output power ( $P_{max}$ ) tended to decrease gradually. These decreases in  $V_{OC}$  and  $P_{max}$  were not due to the change of the thermoelectric module itself, but due to the deterioration of the thermal contact between the thermoelectric module and the heat source. In particular, the drying of the thermal grease on the hot

**Fig. 3.2.8** Heat cycling test of Heusler  $\text{Fe}_2\text{VAl}$  thermoelectric module.



side of the thermoelectric module seemed to be the cause of the deterioration in the heat transfer performance. Actually, after the thermal cycling test, the  $V_{OC}$  and  $P_{max}$  could be restored to the same level as the initial performance at the beginning of the thermal cycle test by applying fresh thermal grease. This result suggests that the heat transfer technology to maintain a low thermal contact resistance is also important in improving the performance of the thermoelectric power generation system.

### 3.2.3 Estimation of power generation performance for high-temperature exhaust gases

The high durability of the Fe<sub>2</sub>VAL alloy holds the potential to construct a reliable thermoelectric power generator for automobiles [5]. For this purpose, a thermoelectric power generation unit assuming energy recovery from high-temperature exhaust gases was examined by heat flow calculation and thermoelectric properties of the off-stoichiometric composition controlled Fe<sub>2</sub>V<sub>1-x</sub>Al<sub>1+x</sub> sintered bodies (p-type:  $x=0.10$ , n-type:  $x=-0.10$ ) [29]. For a gas pipe with a diameter of 5 cm and a length of 30 cm, it was assumed that a high-temperature exhaust gas of 873 K and a low temperature gas or liquid of 293 K flowed inside and outside of the gas pipe, respectively. Although the surface area of the gas pipe was about 471 cm<sup>2</sup>, the area for heat transfer from the heat sources to the thermoelectric device was increased to 3111 cm<sup>2</sup> by providing fins for heat transfer promotion. The heat transfer coefficient from the gas to the heat receiving part was empirically set to be 100 W/m<sup>2</sup>K assuming a gas flow rate of about 10 m/s. In the case of water cooling, the heat transfer coefficient was increased to 5000 W/m<sup>2</sup>K. Under these conditions, the maximum output ( $P_{max}$ ), open-circuit voltage ( $V_{OC}$ ), and temperature difference ( $\Delta T$ ) at the thermoelectric legs were calculated as a function of the number of p-n pairs. The results when the size of thermoelectric legs was fixed to a diameter of 3 mm and a height of 5 mm are shown in Fig. 3.2.9.

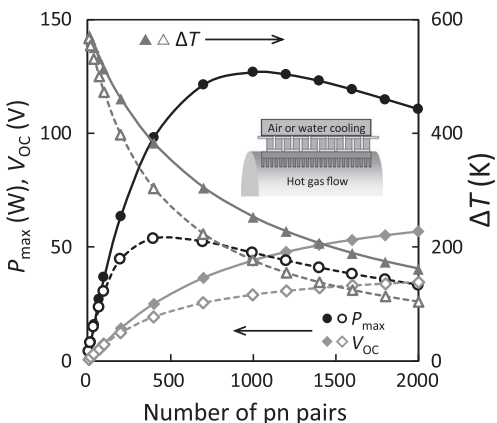


**Fig. 3.2.9** Estimation of performance of a power generation unit consisting of Heusler Fe<sub>2</sub>VAL thermoelectric module for high-temperature gas flow. Solid lines with filled marks and dotted lines with open marks represent results of water cooling and air cooling, respectively.

In both cases of air and water cooling, the  $P_{\max}$  value shows a broad maximum with respect to the number of p-n pairs, which depends on the relationship between the heat-exchange capability from heat sources and the thermal resistance of thermoelectric devices. In the case of the lower number of p-n pairs, which means the thermal resistance is high, a relatively large  $dT$  can be obtained because of a sufficient heat-exchange capacity. However, the total  $P_{\max}$  value is small because of the small number of thermoelectric legs. In this case, it is expected that the most part of thermal energy will be exhausted into the atmosphere without being taken into the thermoelectric device. On the other hand, in the case of the higher number of p-n pairs, although the lowered thermal resistance facilitates the inflow of thermal energy into the thermoelectric device, the  $dT$  becomes small and then the energy conversion efficiency is lowered because of the insufficient heat-exchange capability. Therefore, the enhancement of heat-exchange capacity by water cooling caused a significant increase in the  $P_{\max}$  value and a shifting of its peak position to the higher number of p-n pairs. Although more detailed numerical calculations and experimental verifications are required for precise estimation and design optimization, these results suggest that the 100 W class thermoelectric power generation unit for the recovery of waste heat in the high-temperature exhaust gas could be constructed using the Fe<sub>2</sub>VAL alloy, which has relatively high  $\kappa$  as a thermoelectric material.

### 3.2.4 Summary

In this section, the performance of a thermoelectric module consisting of Heusler Fe<sub>2</sub>VAL sintered alloys prepared by the powder-metallurgical process is briefly discussed. The reduction in thermal conductivity by the microstructure refinement and the heavy-element doping could improve the thermoelectric figure of merit of this alloy. In addition, the reduced thermal conductivity could enhance the power generation ability of the thermoelectric module. The relatively high power density of the Fe<sub>2</sub>VAL thermoelectric module could be achieved by the high power factor value of this alloy by virtue of its pseudo-gap electronic band structure and the direct Cu-electrode bonding with negligibly low electrical contact resistance. Power generation performance for a high-temperature exhaust gas was estimated using the thermoelectric properties of Fe<sub>2</sub>VAL alloys, which is expected to be applied to energy recovery from waste heat of automobiles.

## References

- [1] H. Kato, M. Kato, Y. Nishino, U. Mizutani, S. Asano, Effect of silicon substitution on thermoelectric properties of Heusler-type Fe<sub>2</sub>VAL alloy, *J. Jpn. Inst. Metals* 65 (2001) 652–656.
- [2] H. Matsuura, Y. Nishino, U. Mizutani, S. Asano, Doping effects on thermoelectric properties of the pseudogap Fe<sub>2</sub>VAL system, *J. Jpn. Inst. Metals* 66 (2002) 767–771.
- [3] Y. Nishino, Electronic structure and transport properties of pseudogap system Fe<sub>2</sub>VAL, *Mater. Trans.* 42 (2005) 902–910.

- [4] Y. Nishino, S. Deguchi, U. Mizutani, Thermal and transport properties of the Heusler-type Fe<sub>2</sub>VAL<sub>1-x</sub>Ge<sub>x</sub> ( $0 \leq x \leq 0.20$ ) alloys: effect of doping on lattice thermal conductivity, electrical resistivity, and Seebeck coefficient, Phys. Rev. B Condens. Matter Mater. Phys. 74 (2006) 115115.
- [5] M. Mikami, K. Kobayashi, T. Kawada, K. Kubo, N. Uchiyama, Development of a thermoelectric module using the Heusler alloy Fe<sub>2</sub>VAL, J. Electron. Mater. 38 (2009) 1121–1126.
- [6] M. Mikami, M. Mizoshiri, K. Ozaki, H. Takazawa, A. Yamamoto, Y. Terazawa, T. Takeuchi, Evaluation of the thermoelectric module consisting of W-doped heusler Fe<sub>2</sub>VAL alloy, J. Electron. Mater. 43 (2014) 1922–1926.
- [7] D. Singh, I. Mazin, Electronic structure, local moments, and transport, Phys. Rev. B Condens. Matter Mater. Phys. 57 (1998) 14352–14356.
- [8] R. Weht, W. Pickett, Excitonic correlations in the intermetallic Fe<sub>2</sub>VAL, Phys. Rev. B Condens. Matter Mater. Phys. 58 (1998) 6855–6861.
- [9] M. Weinert, R. Watson, Hybridization-induced band gaps in transition-metal aluminides, Phys. Rev. B Condens. Matter Mater. Phys. 58 (1998) 9732–9740.
- [10] A. Bansil, S. Kaprzyk, P.E. Mijnarends, J. Tobola, Electronic structure and magnetism of Fe<sub>3-x</sub>V<sub>x</sub>X (X=Si, Ga, and Al) alloys by the KKR-CPA method, Phys. Rev. B 60 (1999) 13396–13412.
- [11] F. Kobayashi, N. Ide, Y. Nishino, Effects of Re substitution on thermoelectric properties of pseudogap system Fe<sub>2</sub>VAL, J. Jpn. Inst. Metals 71 (2007) 208–212.
- [12] C.S. Lue, C.F. Chen, J.Y. Lin, Y.T. Yu, Y.K. Kuo, Thermoelectric properties of quaternary Heusler alloys Fe<sub>2</sub>VAL<sub>1-x</sub>Si<sub>x</sub>, Phys. Rev. B Condens. Matter Mater. Phys. 75 (2007) 064204.
- [13] H. Nakayama, N. Ide, Y. Nishino, Thermoelectric properties of P-type Heusler compounds (Fe<sub>2-x</sub>Co<sub>x</sub>)(V<sub>1-y</sub>Ti<sub>y</sub>)Al, Mater. Trans. 49 (2008) 1858–1862.
- [14] W. Lu, W. Zhang, L. Chen, Thermoelectric properties of (Fe<sub>1-x</sub>Co<sub>x</sub>)<sub>2</sub>VAL Heusler-type compounds, J. Alloys Compd. 484 (2009) 812–815.
- [15] Y. Nishino, Development of thermoelectric materials based on Fe<sub>2</sub>VAL Heusler compound for energy harvesting applications, IOP Conf. Ser. Mater. Sci. Eng. 18 (2011) 142001.
- [16] T. Sugiura, Y. Nishino, Doping effects of transition metals on thermoelectric properties of off-stoichiometric Fe<sub>2</sub>VAL alloys, J. Jpn. Inst. Metals 73 (2009) 846–851.
- [17] K. Soda, S. Harada, M. Kato, S. Yagi, M. Inukai, H. Miyazaki, Y. Sandaiji, Y. Tamada, S. Tanaka, T. Sugiura, Y. Nishino, Soft X-ray photoemission study of thermoelectric alloys Fe<sub>2-x-y</sub>Ir<sub>y</sub>V<sub>1+x</sub>Al and Fe<sub>2-x</sub>V<sub>1+x-y</sub>Ti<sub>y</sub>Al, J. Electron Spectrosc. Relat. Phenom. 184 (2011) 236–239.
- [18] H. Miyazaki, K. Renard, M. Inukai, K. Soda, Y. Nishino, Electronic structure of Heusler-type Fe<sub>2</sub>V<sub>1+x</sub>Al<sub>1-x</sub> thermoelectric materials, J. Electron Spectrosc. Relat. Phenom. 195 (2014) 185–188.
- [19] H. Miyazaki, S. Tanaka, N. Ide, K. Soda, Y. Nishino, Thermoelectric properties of Heusler-type off-stoichiometric Fe<sub>2</sub>V<sub>1+x</sub>Al<sub>1-x</sub> alloys, Mater. Res. Express 1 (2014) 015901.
- [20] K. Renard, A. Mori, Y. Yamada, S. Tanaka, H. Miyazaki, Y. Nishino, Thermoelectric properties of the Heusler-type Fe<sub>2</sub>VTa<sub>x</sub>Al<sub>1-x</sub> alloys, J. Appl. Phys. 115 (2014) 033707.
- [21] Y. Nishino, Y. Tamada, Doping effects on thermoelectric properties of the off-stoichiometric Heusler compounds Fe<sub>2-x</sub>V<sub>1+x</sub>Al, J. Appl. Phys. 115 (2014) 123707.
- [22] H. Miyazaki, M. Inukai, Y. Nishino, Effect of Ta substitution on the electronic structure of Heusler-type Fe<sub>2</sub>VAL-based alloy, J. Appl. Phys. 120 (2016) 125106.

- [23] M. Mikami, A. Matsumoto, K. Kobayashi, Synthesis and thermoelectric properties of microstructural Heusler  $\text{Fe}_2\text{VAl}$  alloy, *J. Alloys Compd.* 461 (2008) 423–426.
- [24] M. Mikami, S. Tanaka, K. Kobayashi, Thermoelectric properties of Sb-doped Heusler  $\text{Fe}_2\text{VAl}$  alloy, *J. Alloys Compd.* 484 (2009) 444–448.
- [25] M. Mikami, Y. Kinemuchi, K. Ozaki, Y. Terazawa, T. Takeuchi, Thermoelectric properties of tungsten-substituted Heusler  $\text{Fe}_2\text{VAl}$  alloy, *J. Appl. Phys.* 111 (2012) 093710.
- [26] Y. Terazawa, M. Mikami, T. Itoh, T. Takeuchi, Effects of heavy element substitution on electronic structure and lattice thermal conductivity of  $\text{Fe}_2\text{VAl}$  thermoelectric material, *J. Electron. Mater.* 41 (2012) 1348–1353.
- [27] T. Takeuchi, Y. Terazawa, Y. Furuta, A. Yamamoto, M. Mikami, Effect of heavy element substitution and off-stoichiometric composition on thermoelectric properties of  $\text{Fe}_2\text{VAl}$ -based heusler phase, *J. Electron. Mater.* 42 (2013) 2084–2090.
- [28] M. Mikami, K. Ozaki, H. Takazawa, A. Yamamoto, Y. Terazawa, T. Takeuchi, Effect of Ti substitution on thermoelectric properties of W-doped heusler  $\text{Fe}_2\text{VAl}$  alloy, *J. Electron. Mater.* 42 (2013) 1801–1806.
- [29] M. Mikami, M. Inukai, H. Miyazaki, Y. Nishino, Effect of off-stoichiometry on the thermoelectric properties of Heusler-type  $\text{Fe}_2\text{VAl}$  sintered alloys, *J. Electron. Mater.* 45 (2016) 1284–1289.
- [30] Y. Feng, J.Y. Rhee, T.A. Wiener, D.W. Lynch, B.E. Hubbard, A.J. Sievers, D.L. Schlagel, T.A. Lograsso, L.L. Miller, Physical properties of Heusler-like  $\text{Fe}_2\text{VAl}$ , *Phys. Rev. B Condens. Matter Mater. Phys.* 63 (2001) 165109.
- [31] M. Mikami, K. Kobayashi, T. Kawada, K. Kubo, N. Uchiyama, Development and evaluation of high-strength  $\text{Fe}_2\text{VAl}$  thermoelectric module, *Jpn. J. Appl. Phys.* 47 (2008) 1512–1516.

# Microthermoelectric devices using Si nanowires

3.3

Takanobu Watanabe  
Waseda University, Tokyo, Japan

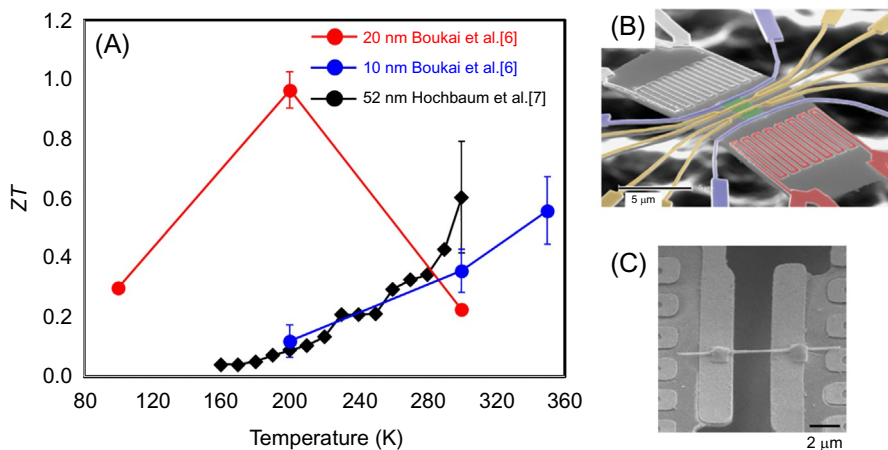
## 3.3.1 Introduction

### 3.3.1.1 Why silicon nanowire?

Si is an excellent platform material for microelectronics. Integration of thermoelectric converters into the Si-based complementary metal-oxide-semiconductor (CMOS) technology has been anticipated to have many significant applications [1, 2]. The future potential of the Internet-of-things (IoT) is now stimulating research in the development of microelectronic thermoelectric generators (TEGs) compatible with the Si-CMOS technology. On-chip cooling by thermoelectric coolers (TECs) is required for efficient heat dissipation from local hot spots in microprocessors [3, 4]. However, Si was considered a material of little interest for thermoelectricity, owing to its low thermoelectric figure of merit,  $ZT$ , of approximately 0.01 at room temperature [5]. Although heavily doped Si can yield a high power factor, the high thermal conductivity of Si lattice has prevented its use in thermoelectric applications.

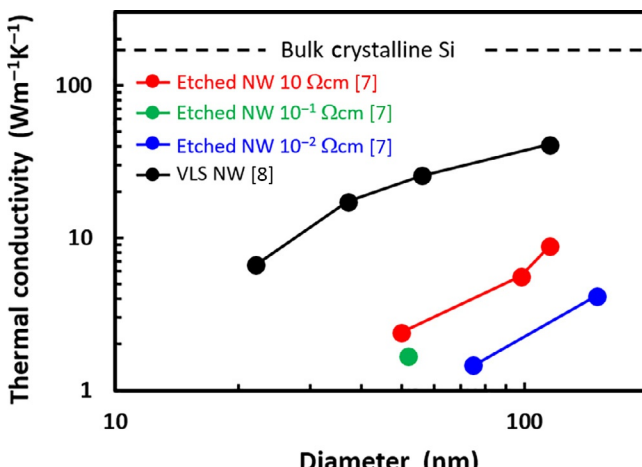
A turning point was reached in 2008 when a superior thermoelectric property of Si nanowires (NW) was discovered by Boukai et al. [6] and Hochbaum et al. [7]. They independently discovered that Si NWs yield  $ZT$  values of 0.3–0.6 at room temperature (see Fig. 3.3.1). This drastic improvement is attributed to the decrease in the lattice thermal conductivity without affecting the Seebeck coefficient and electric conductivity. Boukai et al. further reported that 20-nm-wide Si NWs yielded a peak Seebeck coefficient at 200 K, and an even higher  $ZT$  of about 1.0 was recorded at doping concentrations around  $10^{19} \text{ cm}^{-3}$ .

Fig. 3.3.2 shows the thermal conductivity of Si NWs measured at 300 K as a function of the NW diameter. The reduction is due to an enhancement of the surface scattering of phonons. If the surface is perfectly smooth, the surface scattering is purely specular and does not affect the thermal conductivity. If the surface is coarse, the scattering becomes diffusive, and the thermal conductivity decreases with decreasing characteristic dimension. Fig. 3.3.2 includes two different sets of data: Si NWs etched from wafers using the electroless etching method [7] and Si NWs grown by vapor-liquid-solid (VLS) chemical vapor deposition (CVD) [8]. A typical VLS-CVD-grown Si NW has a smooth surface compared to the electroless etched Si NWs, which produced lower thermal conductivities, indicating that the surface scattering of phonons may have been further enhanced.



**Fig. 3.3.1** (A) Temperature dependence of the thermoelectric figure of merit  $ZT$  for Si NW. (B), (C) Scanning electron micrographs of test devices for the thermoelectric characterization of Si NW.

(B) and (C) are reproduced from A.I. Boukai, Y. Bunimovich, J. Tahir-Kheli, J.K. Yu, W.A. Goddard III, J.R. Heath, Silicon nanowires as efficient thermoelectric materials, *Nature* 451 (2008) 168–171 and A.I. Hochbaum, R. Chen, R.D. Delgado, W. Liang, E.C. Garnett, M. Najarian, A. Majumdar, P. Yang, Enhanced thermoelectric performance of rough silicon nanowires, *Nature* 451 (2008) 163–167, respectively.



**Fig. 3.3.2** Thermal conductivity of Si NW at 300 K as a function of the NW diameter. In Ref. [7], Si NWs were electroless-etched from wafers of different resistivities. In Ref. [8], Si NWs were grown by a vapor–liquid–solid (VLS) chemical vapor deposition method.

Data is taken from A.I. Hochbaum, R. Chen, R.D. Delgado, W. Liang, E.C. Garnett, M. Najarian, A. Majumdar, P. Yang, Enhanced thermoelectric performance of rough silicon nanowires, *Nature* 451 (2008) 163–167 and D. Li, Y. Wu, P. Kim, L. Shi, P. Yang, A. Majumdar, Thermal conductivity of individual silicon nanowires, *Appl. Phys. Lett.* 83 (2003) 2934–2936.

This discovery led to Si-based, CMOS compatible thermoelectric modules with a low environmental load, unlike  $(\text{Bi}, \text{Sb})_2(\text{Se}, \text{Te})_3$  alloys. Many examples of Si-based TEGs have been reported and will be introduced in [Section 3.3.2](#).

### 3.3.1.2 Efficiency or power?

The thermoelectric figure of merit  $ZT$  is an essential factor to determine the conversion efficiency between heat energy and electric energy. A higher  $ZT$  is required to increase the conversion efficiency. However, high  $ZT$  is *not* a necessity for thermoelectric applications. In the case of TEGs, an important factor is the *cost per unit energy*, which is given by [1]

$$C = C_m / (p\Delta t) + C_f / \eta,$$

where  $C_m$  is the fabrication cost per TEG module,  $p$  and  $\Delta t$  are the mean generation output power and the mean lifetime of the TEG module respectively,  $C_f$  is the fuel cost required to generate a unit of electric energy, and  $\eta$  is the conversion efficiency. The conversion efficiency  $\eta$  is proportional to  $ZT$ , i.e., larger  $ZT$  values are required to increase  $\eta$ . When utilizing waste heat, as in the case of vehicles, the enhancement of the energy conversion efficiency  $\eta$  may be the first priority to suppress fuel costs. However, in the case of energy harvesting, or scavenging, from ambient energy sources,  $\eta$  should not necessarily be increased, because the fuel cost  $C_f$  of environmental heat energy is negligible. Thus, suppressing the fabrication cost and increasing the power generation density becomes the most significant endeavors in environmental heat energy harvesting.

The same is true for rapid thermal discharging by TECs. The cooling heat flux,  $Q$ , of a TEC element is given by [9, 10]

$$Q = \alpha IT_c - I^2 R / 2 - \Delta T / R_t,$$

where  $\alpha$  is the Seebeck coefficient,  $I$  is the electric current,  $T_c$  is the temperature of the cold source,  $R$  is the electrical resistance,  $\Delta T$  is the temperature difference created by the TEC element, and  $R_t$  is the thermal resistance of the TEC element. The maximum temperature reduction,  $\Delta T_{max}$ , is  $ZT_c^2/2$ , determined by the thermoelectric figure of merit,  $ZT$ . The maximum cooling heat flux,  $Q_{max}$ , is given by

$$Q_{max} = \alpha^2 T_c / 2R,$$

which can be achieved as  $\Delta T$  tends to 0. Therefore, the power factor holds greater significance over  $ZT$ , regarding rapid thermal discharge. From this perspective, bulk Si is already a promising material for TEC applications because heavily doped bulk Si has a high power factor. The superior performance of bulk silicon for on-chip hot spot cooling was demonstrated experimentally [10] and analyzed numerically [11].

### 3.3.1.3 Basic structures

Most examples of thermoelectric modules have the same structure, with the typical  $\pi$ -like thermoelectric module; n-type and p-type semiconductors, termed *thermoelements* or *legs*, connected electrically in series and thermally in parallel. This is called the *bileg* structure, as seen in Fig. 3.3.3A. The *unileg* structure is simpler and consists only of n-type (or p-type) thermoelements connected thermally in parallel, as shown in Fig. 3.3.3B. The output voltage (open-circuit voltage  $V_{oc}$ ) of the module can be increased by utilizing a multiple-stage connection of the bileg or unileg units. However, in doing so, the conversion efficiency of the unileg module is diminished, owing to an unavoidable heat leakage through the electrical wirings.

Previously demonstrated Si-based microthermoelectric modules can be classified into two groups: *horizontal* and *vertical* structures. In the horizontal structure, Si thermoelements are suspended horizontally between hot and cold reservoirs, relative to the substrate surface, or directly laid on the substrate surface. Upon power generation, they are driven by an in-plane temperature gradient along the substrate surface. In the vertical structure, Si thermoelements stand vertically on the substrate surfaces and are driven by a temperature gradient applied between the front and back substrate surfaces.

### 3.3.1.4 Specific power generation capacity

To compare the power generation of different microthermoelectric modules, it is convenient to use the *specific power generation capacity* (SPGC)  $\phi$ , defined as

$$\phi = p / (A\Delta T^2),$$

where  $p$  is the output power of the TEG module,  $A$  is the footprint area on a chip, and  $\Delta T$  is the externally applied temperature difference across the TEG module. Typically, the horizontal structure is at a disadvantage as the horizontally lying thermoelements require a larger footprint  $A$ , compared to that of vertically standing

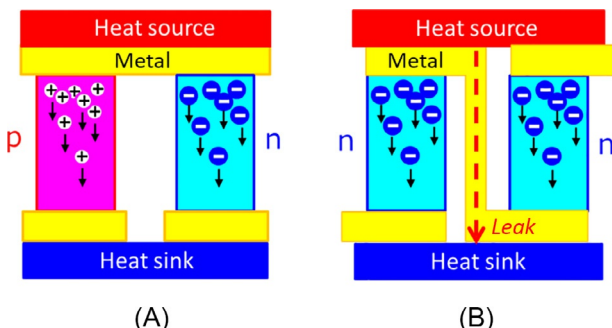


Fig. 3.3.3 Bileg (A) and unileg (B) structure of thermoelectric module.

thermoelements. However, many examples of horizontal modules have been demonstrated for Si-based micro TEGs, owing to their ease of fabrication.

### 3.3.2 Si-based microthermoelectric generator modules

This section describes various examples of TEG modules that use Si NWs, or low-dimensional fine Si structures of a submicrometer scale.

#### 3.3.2.1 Horizontal architectures

Before the discovery of the superior thermoelectric property of Si NWs, Strasser et al. demonstrated a miniaturized TEG with a horizontal structure using poly-Si and poly-SiGe thermoelements [12]. The TEG was fabricated in a CMOS production facility, making it suitable for low-cost applications. A schematic representation of the TEG cell is illustrated in Fig. 3.3.4A. The thick oxide and the cavity together act as a thermal barrier to isolate the hot and cold sides of the thermoelements. The cavity is formed by isotropic dry etching using  $\text{CF}_4$  gas. The test operation was performed at wafer level. The wafer was placed on a heated thermochuck, with Peltier cooler mounted on top. The results in Ref. [13] show that the output power per area (hereinafter called “power density”) of approximately  $6 \mu\text{W cm}^{-2}$  was obtained with a poly-Si-based TEG at a temperature difference of 10 K between the top and bottom of the chip. The reported SPGC  $\phi$  was  $0.06 \mu\text{W cm}^{-2} \text{K}^{-2}$ .

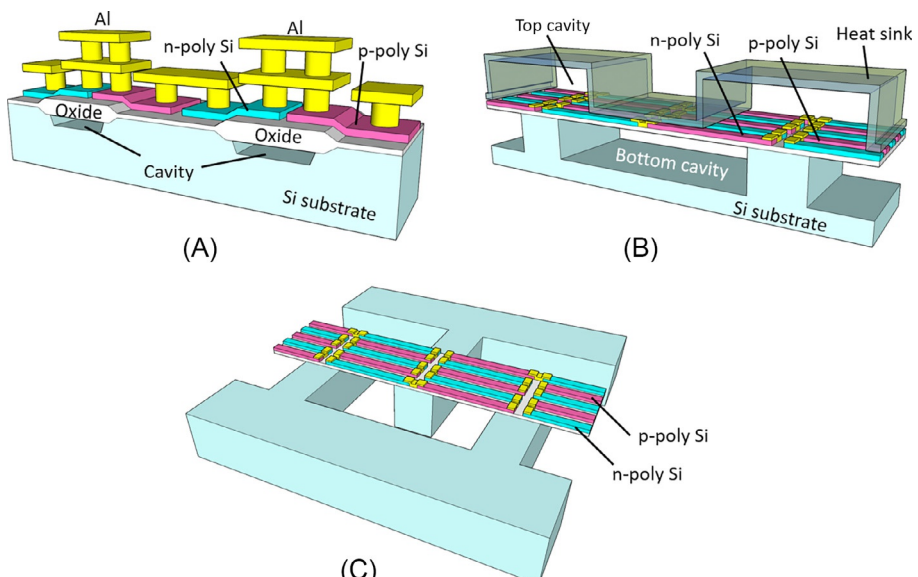


**Fig. 3.3.4** Schematic representation of horizontal poly-Si TEG modules demonstrated by (A) Strasser et al. [12, 13], (B) Xie et al. [14], and (C) Yu et al. [15], respectively.

Xie et al. [14] fabricated a similar horizontal TEG module, in which poly-Si thermoelements were embedded between two microscale vacuum cavities as shown in Fig. 3.3.4B. Power density of approximately  $1.3 \mu\text{W cm}^{-2}$  was obtained when a temperature difference of 5 K is maintained across the two sides of the device. The reported SPGC  $\phi$  was  $0.052 \mu\text{W cm}^{-2} \text{K}^{-2}$ .

Yu et al. [15] fabricated a horizontal TEG module with an improved heat dissipation path. As shown in Fig. 3.3.4C, the substrate was etched into two comb-shaped blocks, which form the hot and cold sides. Poly-Si thermoelements were densely located between the two blocks. The SPGC  $\phi$  was estimated to be  $0.058 \mu\text{W cm}^{-2} \text{K}^{-2}$ .

George et al. demonstrated a horizontal TEG module using single-crystalline Si membranes [16] as shown in Fig. 3.3.5, which was fabricated on a silicon-on-insulator (SOI) wafer by using electron beam lithography and plasma dry etching. To suspend the Si membranes, the oxide layer under the top Si layer was etched with hydrofluoric acid vapor. They reported that the ZT of Si membrane was increased by about 50% by depositing an ultrathin aluminum layer. A power density of  $17.4 \text{nW cm}^{-2}$  was achieved at an external temperature difference of 53 K, applied between the hot plate and the ambient air. The demonstrated SPGC  $\phi$  was  $6.2 \text{ pW cm}^{-2} \text{K}^{-2}$ . It can be improved by forming a heat sink structure as in the study of Xie et al. [14].

Implementation of Si NWs into horizontal TEG was reported by Dávila, Santos, and Fonseca et al. [17–19], merging top-down Si micromachining technology with the bottom-up Si NW growth (Fig. 3.3.6). The Si NWs were grown by VLS chemical vapor deposition using a gold nanoparticle catalyst. Si NWs were suspended on trenches formed by deep reactive ion etching. The TEG performance was characterized by placing it on a hot plate. A heat sink was placed on top of the device, which was cooled to the ambient temperature. Under the condition of natural convection,  $2.2 \text{nW}$  was generated at a hotplate temperature of  $200^\circ\text{C}$ . Under the condition of the air jet forced convection, the output power increased to  $700 \text{nW}$ , which corresponds to  $35 \mu\text{W cm}^{-2}$ , considering the device footprint of  $2 \text{ mm}^2$ . Supposing a temperature difference of 175 K exists, the SPGC  $\phi$  is estimated to be  $1.1 \text{nW cm}^{-2} \text{K}^{-2}$ .

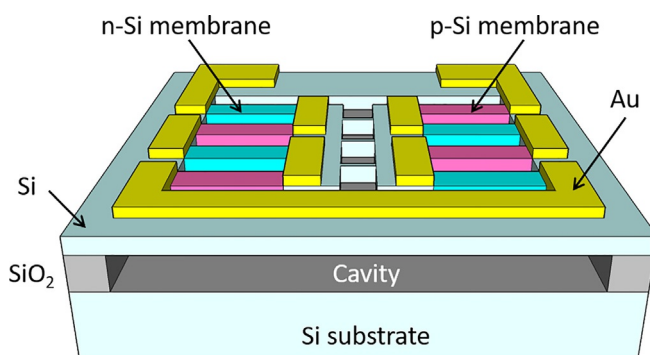


**Fig. 3.3.5** Horizontal TEG module using single-crystalline Si membranes demonstrated by George et al. [16].

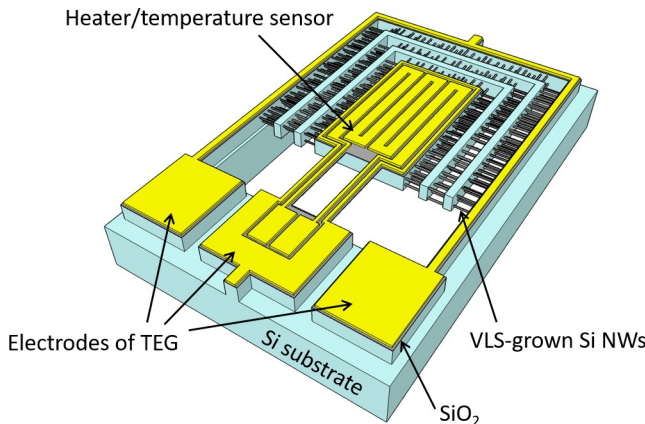


**Fig. 3.3.6** Horizontal TEG using VLS-CVD-grown Si NWs demonstrated by Dávila, Santos, and Fonseca et al. [17–19].

### 3.3.2.2 Vertical architectures

Fabrication of multiple-stage vertical modules is a complicated process because the top and bottom of the vertically standing thermoelement must be alternatively connected to metal wirings. At the time of writing this book, there are only a few reports on vertical type multiple-stage modules.

Norris et al. [20] reported a vertical type TEG using a three-dimensional network of Si NWs formed by a bottom-up approach of plasma-enhanced CVD. A quadruple stack module of p-type Si-NWs was fabricated to demonstrate that  $V_{oc}$  and the maximum output power increase with the number of stacks for a given temperature difference per stack. The output power of 4.7 nW was obtained at a temperature difference of 70 K with a 2 cm<sup>2</sup> area module. The SPGC  $\phi$  was 0.48 pW cm<sup>-2</sup> K<sup>-2</sup>. Although the stack module does not correspond to a multiple-stage TEG module, because the Si NW layers were connected thermally in series, the result clearly demonstrated that the proposed Si NW TEG is both laterally and vertically scalable (Fig. 3.3.7).

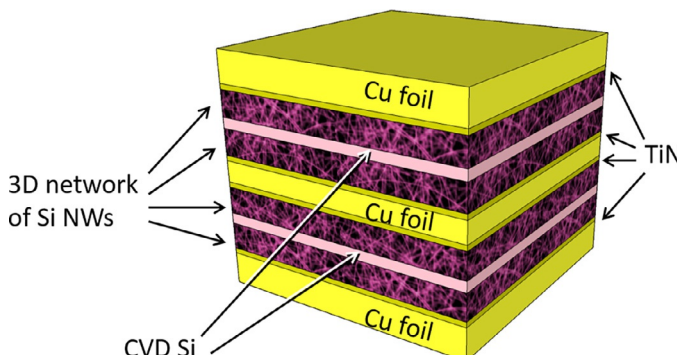


**Fig. 3.3.7** Vertical TEG using three-dimensional network of Si NWs formed by plasma-enhanced CVD demonstrated by Norris et al. [20].

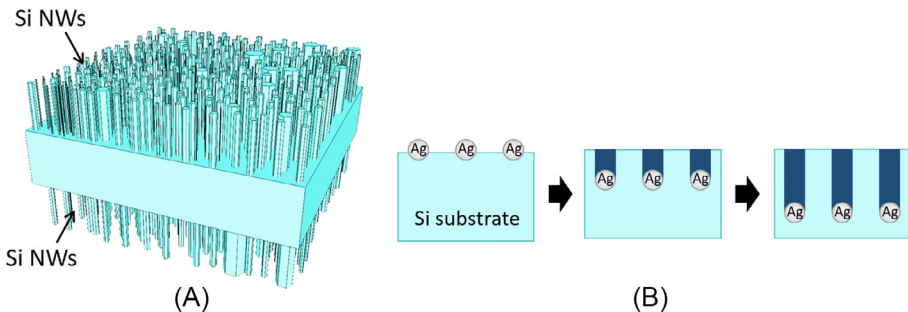


**Fig. 3.3.8** (A) Highly oriented vertical Si NWs fabricated by MACE process [21], and (B) schematic representation of the MACE process.

Highly oriented vertical Si NWs can be fabricated by metal-assisted chemical etching (MACE), where a noble metal catalyst is used to etch bulk silicon in solution as shown in Fig. 3.3.8. For the MACE process, the Si NW array needs to be fabricated from relatively lowly doped bulk, which is a drawback for thermoelectric applications as the power factor would be limited to low values. Xu et al. [21] applied spin-on-doping after the MACE process to improve the power factor of the Si NWs and the contact resistance. For an Si NW/bulk Si/Si NW sandwich structure module with an area of  $25 \text{ mm}^2$ , the maximum output power obtained was  $3.5 \mu\text{W}$  at an external temperature difference of 37 K. The SPGC  $\phi$  was  $0.010 \mu\text{W cm}^{-2} \text{ K}^{-2}$ .

Although the bottom-up approaches are simple and inexpensive to use, with regard to use synthesizing Si NWs, the top-down approach employing lithographic techniques is more feasible from a manufacturing point of view.

Li et al. reported a vertical type multistage bileg TEG module comprising of an n-type and p-type Si NW array, patterned by lithography, on a silicon-on-insulator (SOI) wafer [22, 23]. The diameter and length of the Si NWs were 80 nm and  $\sim 1 \mu\text{m}$ , respectively, and the Si NW array had a pitch of 400 nm. The n-type and p-type Si NW arrays were isolated through a silicon etching process and the bottom electrodes were formed by a nickel silicidation process. The air gap between the pillars was filled with  $\text{SiO}_2$ . By sandwiching the TEG between a heater and a commercial Peltier cooler, a maximum open-circuit voltage of 2.7 mV was measured at a temperature difference of 95 K, which corresponds to a power output of 4.6 nW. Due to the module area being reported as  $25 \text{ mm}^2$ , the SPGC  $\phi$  is estimated to be  $2.0 \text{ pW cm}^{-2} \text{ K}^{-2}$ . By replacing the  $\text{SiO}_2$  filler material with polyimide, the thermal conductivity, of which, is one order of magnitude lower than that of  $\text{SiO}_2$ , the applied temperature difference across the TEG improved (Fig. 3.3.9).

Curtin et al. [24] reported a vertical type, single-stage unileg TEG module comprising of an n-type Si NW array fabricated from highly doped bulk Si wafers by interference lithography. The Si NW arrays were  $1 \mu\text{m}$  tall, with 15% packing density, and the individual NWs had diameters between 80 and 90 nm. Si NW arrays were embedded in spin-on glass (SOG). A resistive heater/insulator/electrical contact stack was formed on the Si NW/SOG composite layer. For the power generation measurement, the TEG module was mounted on a commercial Peltier cooler, and a DC current was

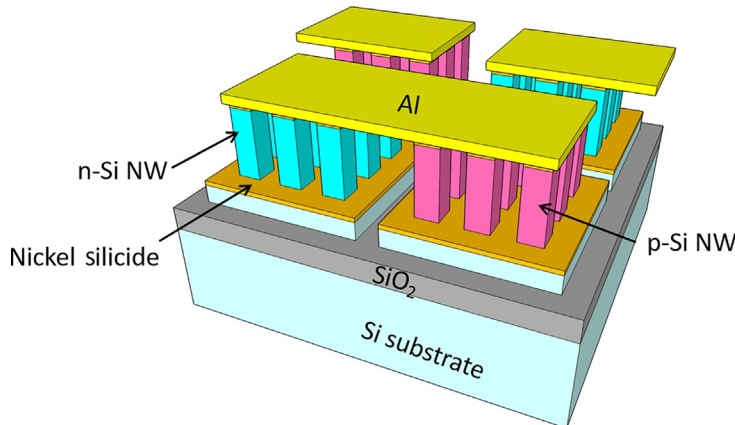


**Fig. 3.3.9** Vertical multistage bileg TEG using an n-type and p-type Si NW array fabricated with a top-down lithographic approach from Li et al. [22, 23].

supplied to the resistive heater fabricated in the module. The maximum generated power was  $29.3 \mu\text{W}$  at a temperature difference of  $56 \text{ K}$  for a  $50 \mu\text{m} \times 50 \mu\text{m}$  device. The SPGC  $\phi$  was estimated to be  $373 \mu\text{W cm}^{-2} \text{ K}^{-2}$ . At the time of writing this book, these were the best-recorded results of Si-based microthermoelectric modules.

Recently, Hu et al. [25] reported a vertical type, single-stage, bileg TEG module using nanostructured Si blades, which was fabricated by industrial standard  $65 \text{ nm}$  technology of Si CMOS processing. Fig. 3.3.10 illustrates a simplified TEG structure. The tops of the Si blades are contacted by tungsten plugs. Metal layers connect the n-type blades and p-type blades. Near the top, a resistive heater, consisting of a thin, serpentine Cu line, is used as both a heater and thermometer. For the thermoelectric measurement, the die of the TEG device was placed on a gold-plated copper chuck.

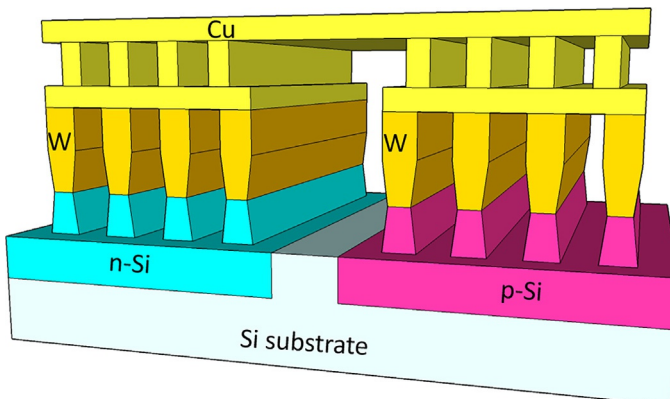


**Fig. 3.3.10** Schematic representation of vertical, single-stage, bileg TEG module using nanostructured Si blades demonstrated by Hu et al. [25].

A platinum resistor thermometer was embedded in the chuck to monitor its temperature. The SPGC  $\phi$  was  $29 \mu\text{W cm}^{-2} \text{K}^{-2}$ .

### 3.3.2.3 Short thermoelements architecture

The abovementioned examples refer to the typical,  $\pi$ -like thermoelectric module, in which the Si thermoelements are connected electrically in series and thermally in parallel. In order to avoid the shortcut of heat flow, the thermoelements are suspended on a cavity or surrounded by low thermal-conductivity materials.

Recently, the present author's group proposed a new planar architecture, shown in Fig. 3.3.11 [26, 27]. The Si NW thermoelements are directly placed on an SOI substrate without forming a cavity space underneath the buried oxide (BOX) layer. The heat current flows perpendicularly to the substrate and the TEG is driven by a steep temperature gradient established around the heat inlet. As the temperature gradient is concentrated in the limited range of a few hundred nm, it is effective in making the Si NW length shorter than or equal to the slope region. The output voltage is increased by alternatively connecting the n-type and p-type Si NWs in series. By injecting the heat into the substrate with a fine pitch, a large number of short Si NWs can be designed to cover the whole surface, and thus, the areal power generation density can be enhanced, i.e., the power density is scalable by decreasing the Si NW length and heat injection pitch.

It was experimentally confirmed that the thermoelectric power was enhanced by shortening the NW and thinning the Si substrate [28–30]. Fig. 3.3.12 shows the fabrication process flow of a test TEG device, which was fabricated on an SOI substrate. Fig. 3.3.13 shows the optical micrograph of the TEG and the scanning electron

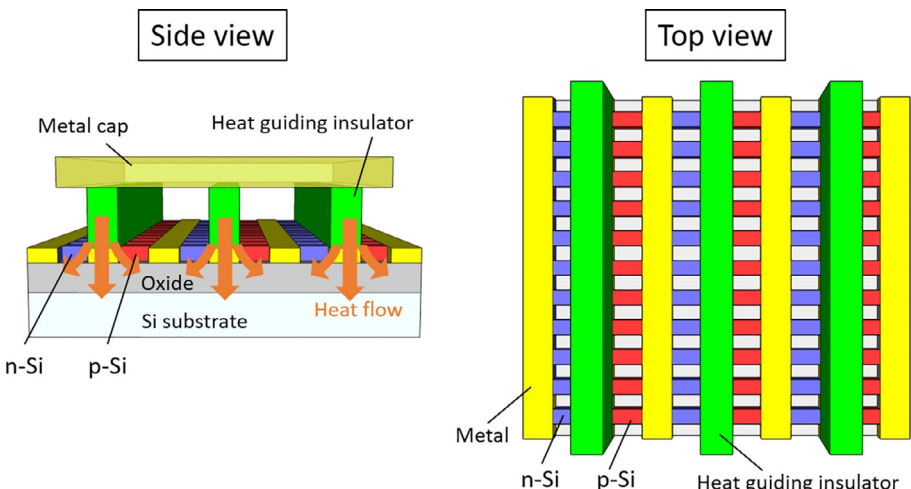


**Fig. 3.3.11** Schematic representation of the planar-type short Si NW TEG structure [26, 27]. It is driven by a steep temperature gradient exuding around the heat flow perpendicular to the substrate.

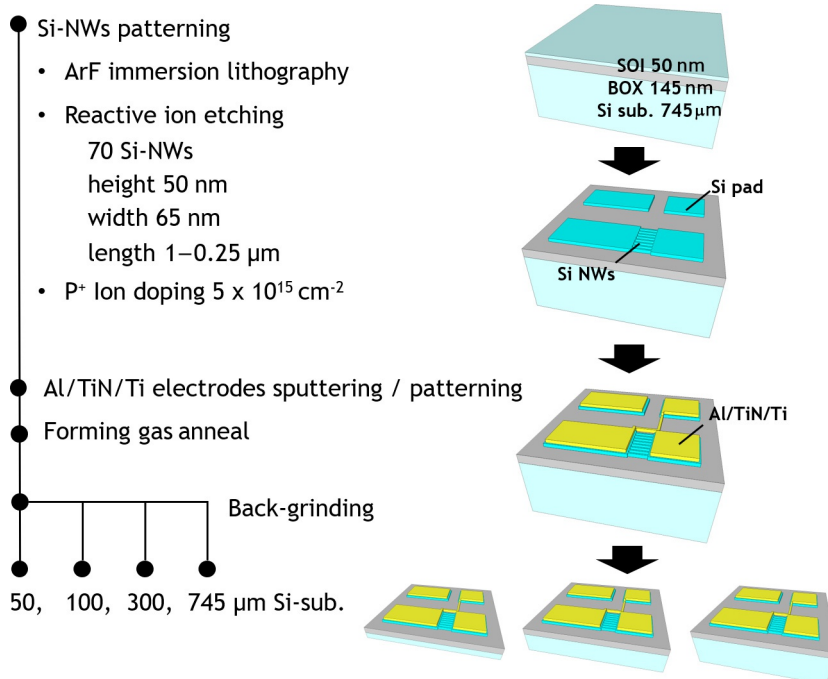


**Fig. 3.3.12** Fabrication process flow of a test device of planar-type short Si NW TEG [29, 30].

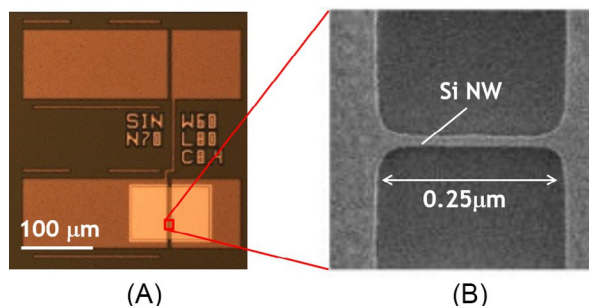


**Fig. 3.3.13** (A) Optical micrograph of the test device of planar-type short Si NW TEG. (B) Scanning electron micrograph of Si NW.

Images are taken from M. Tomita, S. Ohba, Y. Himeda, R. Yamato, K. Shima, T. Kumada, M. Xu, H. Takezawa, K. Mesaki, K. Tsuda, S. Hashimoto, T. Zhan, H. Zhang, Y. Kamakuri, Y. Suzuki, H. Inokawa, H. Ikeda, T. Matsukawa, T. Matsuki, T. Watanabe, 2018 Symposium on VLSI Technology, Digest of Technical Papers, 2018, pp. 93–94 and M. Tomita, S. Ohba, Y. Himeda, R. Yamato, K. Shima, T. Kumada, M. Xu, H. Takezawa, K. Mesaki, K. Tsuda, S. Hashimoto, T. Zhan, H. Zhang, Y. Kamakuri, Y. Suzuki, H. Inokawa, H. Ikeda, T. Matsukawa, T. Matsuki, T. Watanabe, IEEE Trans. Electron Devices 65 (2018) 5180–5188.

micrograph of the Si NW. The top Si layer was patterned into Si NWs via ArF immersion lithography and plasma dry etching. Both ends of Si NW bundle were connected to Si-pads, on which an Al/TiN/Ti electrode was deposited. One side of the electrode was heated by attaching it to a micro-thermostat. The electric contact for the hot-side electrode was separately positioned next to the cold-side electrode. The thickness of the base Si-substrate was thinned by back-grinding and varied from 745 to 50  $\mu\text{m}$ .

**Fig. 3.3.14A** shows the measured thermoelectric power curves under the externally applied temperature difference of 5 K. The maximum power was obtained in the shortest NW device of length 0.25  $\mu\text{m}$ . It should be noted that the open-circuit voltage  $V_{oc}$  increases as the Si NW length decreases. The open-circuit voltage is expressed as  $V_{oc} = \alpha\Delta T$ , and one would assume that the temperature difference  $\Delta T$  across a Si NW must decrease as the Si NW length decreases. For this reason, the  $V_{oc}$  was expected to decrease with the downscaling of the device dimension. The experimental result suggests that the Seebeck coefficient  $\alpha$  is significantly enhanced by shortening the Si NWs.

The thermoelectric power was further enhanced by thinning the Si-substrate. **Fig. 3.3.14B** shows the relation between the power density and the Si-substrate thickness. The power density is calculated by assuming that the pads and the Si NW arrays have the same footprint in an integrated module of the planar TEG. The power density was increased by thinning the Si-substrate, and it reached the maximum value of 12  $\mu\text{W}/\text{cm}^2$  at a thickness of 50  $\mu\text{m}$ . The enhancement can be attributed to the increased temperature difference across the Si NWs by suppression of the series thermal resistance at the Si-substrate. The SPGC  $\phi$  was estimated to be 0.48  $\mu\text{W cm}^{-2}\text{K}^{-2}$ , which is the best performance in the category of horizontal architecture.

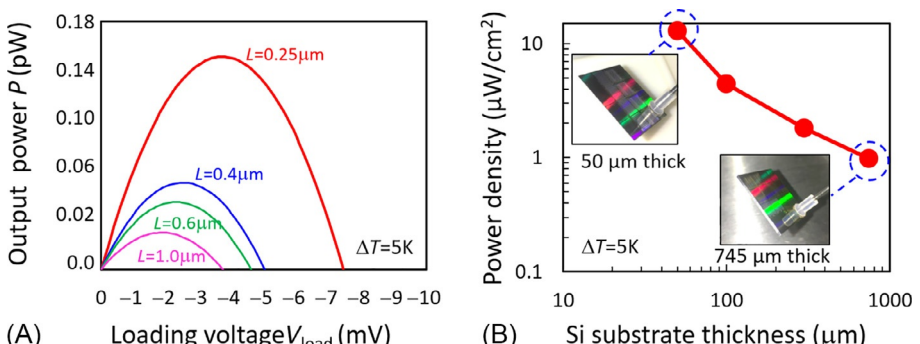


**Fig. 3.3.14** (A) Thermoelectric power curves of planar-type short Si NW TEG measured at an externally applied temperature difference  $\Delta T=5\text{ K}$ . (B) Si-substrate thickness dependency of the maximum power density.

Data is taken from M. Tomita, S. Ohba, Y. Himeda, R. Yamato, K. Shima, T. Kumada, M. Xu, H. Takezawa, K. Mesaki, K. Tsuda, S. Hashimoto, T. Zhan, H. Zhang, Y. Kamakuri, Y. Suzuki, H. Inokawa, H. Ikeda, T. Matsukawa, T. Matsuki, T. Watanabe, 2018 Symposium on VLSI Technology, Digest of Technical Papers, 2018, pp. 93–94 and M. Tomita, S. Ohba, Y. Himeda, R. Yamato, K. Shima, T. Kumada, M. Xu, H. Takezawa, K. Mesaki, K. Tsuda, S. Hashimoto, T. Zhan, H. Zhang, Y. Kamakuri, Y. Suzuki, H. Inokawa, H. Ikeda, T. Matsukawa, T. Matsuki, T. Watanabe, IEEE Trans. Electron Devices 65 (2018) 5180–5188.

### 3.3.3 Characterization

#### 3.3.3.1 Harvesting mode and test mode

The performance of the TEG principally depends on how the measurement was executed. The definition of the applied temperature difference particularly affects the SPGC  $\phi$ . Due to the difficulties with being able to strictly determine the temperatures just at both sides of the TEG module, the temperature difference of heat source and heat sink is used to measure the TEG performance.

The heat sink was typically provided by Peltier chucks, and in some cases, simple air cooling was used. There are two ways of applying a heat source: heating by an external thermostat and by a resistive heater fabricated in the TEG module itself. The former method of measurement is called *harvesting mode*, and the latter is called *test mode* [18].

The harvesting mode measurement is suitable for characterizing TEG under practical usage conditions, but the uncertainty in the contact heat resistance between the external heater and TEG module surface decreases the reproducibility of the measurement. With air cooling, the TE performance depends on whether forced convection is applied or not [17–19].

The test mode measurement can partially improve the reproducibility of thermoelectric performance, due to the fixed heat resistance between the internal resistive heater line and the thermoelectric elements. The test mode measurement is useful in characterizing the intrinsic potential of the TEG module. However, this method frequently overestimates the performance in comparison to the practical operation where the externally applied temperature difference is utilized. Notably high SPGC of  $373 \mu\text{W cm}^{-2} \text{K}^{-2}$  [24] and  $29 \mu\text{W cm}^{-2} \text{K}^{-2}$  [25] were recorded by the test mode measurement.

An example of the harvesting mode measurement set up is shown in Fig. 3.3.15 [29]. The micro-thermostat is used as the heat source. The sample stage is utilized

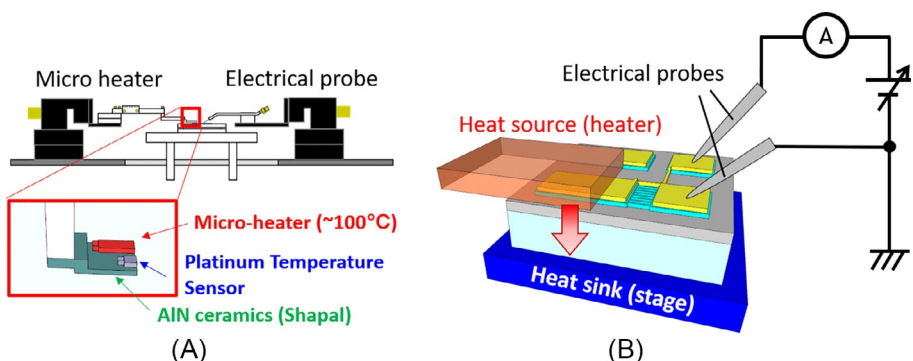


**Fig. 3.3.15** Schematics of the experimental setup for the thermoelectric characteristics measurement [29, 30]. (A) Electrical probe system equipped with a microheater. (B) Setup for TEG device operation.

as a heat sink, the temperature of which was maintained by a water chiller and a Peltier controller.

The thermoelectric performance was evaluated by the typical current-voltage (*I*-*V*) characteristic measurement. The thermoelectric generator was merely a resistive element when not under the application of the temperature difference, so the *I*-*V* relation shows linear ohmic characteristics. By applying a temperature difference to the device, the linear *I*-*V* curve shifts away from the origin and the product of the measured current and loading voltage corresponds to the thermoelectric power. Varying the loading voltage corresponds to varying the load resistance.

### 3.3.3.2 Benchmarking

A benchmark plot of the areal power densities of the Si-based TEGs is shown in Fig. 3.3.16. Most of the plots are in proportion to the square of the temperature difference, showing that the SPGC  $\phi = p/(A \Delta T^2)$  is a useful key performance indicator for miniaturized TEGs.

The best TEG performance was reported by Curtin et al. [24] with a vertical type, single-stage unileg TEG module fabricated by interference lithography. The SPGC was  $373 \mu\text{W cm}^{-2} \text{K}^{-2}$ , however, it should be noted that the performance was measured in test mode using an internally fabricated resistive heater. As mentioned above, the test mode measurement exhibits much higher power than that of the practical operation.

The leading result for the harvesting mode measurement was reported by Tomita et al. [29, 30] with the cavity-free, short thermoelements architecture. The SPGC was  $0.48 \mu\text{W cm}^{-2} \text{K}^{-2}$ , but it was estimated by excluding the area of the peripheral electrode pads of the test device. The highest SPGC of an integrated TEG module was  $0.05\text{--}0.06 \mu\text{W cm}^{-2} \text{K}^{-2}$  [13–15], which was obtained with horizontal TEG modules, fabricated by top-down lithography methods. Bottom-up fabrication did not yield results on par with top-down fabrication. Xu et al. [21] fabricated a vertical Si NW TEG using the MACE process and obtained an SPGC of  $0.010 \mu\text{W cm}^{-2} \text{K}^{-2}$ .

For wireless IoT applications, such as wearable sensor modules in healthcare systems, a  $10 \mu\text{W cm}^{-2}$ -class generator is required [30]. Wireless transmitters, such as Zigbee and Bluetooth, are among the most power-consuming units in an IoT system [31]. They require a few microwatts of the power for retaining their content in RAMs and resistors while in sleep mode. In active mode, they consume  $320 \mu\text{Ws}$  per 32 bits of data transmissions. When the system performs one information sensing operation and 32-bit information transmission per hour, the power consumption would be  $1.4 \text{mWs}$ . Supposing that a chip area of  $1 \text{cm}^2$  is allocated for the generator, the  $10 \mu\text{W/cm}^2$ -class generator would need to store  $36 \text{mWs}$  ( $10 \mu\text{W} \times 1 \text{h}$ ) in the battery per hour at maximum. A  $10 \mu\text{W/cm}^2$ -class generator would, therefore, meet the demand for the energy harvester of intermittent IoT sensors.

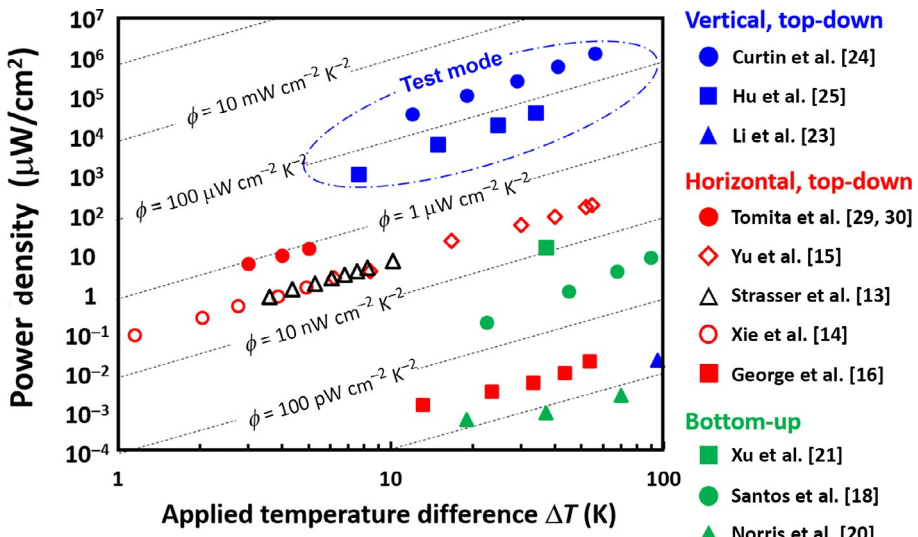


**Fig. 3.3.16** Benchmarking of the areal power densities of the Si-based TEGs.

Data is taken from M. Strasser, R. Aigner, C. Lauterbach, T.F. Sturm, M. Franosch, G. Wachutka, Micromachined CMOS thermoelectric generators as on-chip power supply, Sensors Actuators A 114 (2004) 362–370, J. Xie, C. Lee, H. Feng, Design, fabrication, and characterization of CMOS MEMS-based thermoelectric power generators, J. Microelectromech. Syst. 19 (2010) 317–324, X. Yu, Y. Wang, Y. Liu, T. Li, H. Zhou, X. Gao, F. Feng, T. Roinila, Y. Wang, CMOS MEMS-based thermoelectric generator with an efficient heat dissipation path, J. Micromech. Microeng. 22 (2012) 105011, A. George, R. Yanagisawa, R. Anufriev, J. He, N. Yoshie, N. Tsujii, Q. Guo, T. Mori, S. Volz, M. Nomura, Thermoelectric enhancement of silicon membranes by ultrathin amorphous films, ACS Appl. Mater. Interfaces 11 (2019) 12027–12031, J.D. Santos, M. Salleras, I. Dommez, G. Gadea, C. Calaza, A. Morata, A. Tarancón, L. Fonseca, Power response of a planar thermoelectric microgenerator based on silicon nanowires at different convection regimes, Energy Harvest. Syst. 3 (2016) 335–342, K.J. Norris, M.P. Garrett, J. Zhang, E. Coleman, G.S. Tompa, N.P. Kobayashi, Silicon nanowire networks for multi-stage thermoelectric modules, Energy Convers. Manag. 96 (2015) 100–104, B. Xu, W. Khouri, K. Fobelets, Two-sided silicon nanowire array/bulk thermoelectric power generator, IEEE Electron Device Lett. 35 (2014) 596–598, Y. Li, K. Buddharaju, N. Singh, S.J. Lee, Top-down silicon nanowire-based thermoelectric generator: design and characterization, J. Electron. Mater. 41 (2012) 989–992, B.M. Curtin, E.W. Fang, J. Bowers, Highly ordered vertical silicon nanowire array composite thin films for thermoelectric devices, J. Electron. Mater. 41 (2012) 887–894, G. Hu, H. Edwards, M. Lee, Silicon integrated circuit thermoelectric generators with a high specific power generation capacity, Nat. Electron. 2 (2019) 300–306, and M. Tomita, S. Ohba, Y. Himeda, R. Yamato, K. Shima, T. Kumada, M. Xu, H. Takezawa, K. Mesaki, K. Tsuda, S. Hashimoto, T. Zhan, H. Zhang, Y. Kamakuri, Y. Suzuki, H. Inokawa, H. Ikeda, T. Matsukawa, T. Matsuki, T. Watanabe, 2018 Symposium on VLSI Technology, Digest of Technical Papers, 2018, pp. 93–94 and M. Tomita, S. Ohba, Y. Himeda, R. Yamato, K. Shima, T. Kumada, M. Xu, H. Takezawa, K. Mesaki, K. Tsuda, S. Hashimoto, T. Zhan, H. Zhang, Y. Kamakuri, Y. Suzuki, H. Inokawa, H. Ikeda, T. Matsukawa, T. Matsuki, T. Watanabe, IEEE Trans. Electron Devices 65 (2018) 5180–5188.

### 3.3.4 Summary and conclusion

Recently discovered thermoelectric properties of silicon nanowires initiated development of silicon thermoelectric modules with a low environmental load. In this section, various examples of silicon-based miniaturized thermoelectric modules were reviewed. Previous demonstrations can be classified into horizontal and vertical structures. Most structures follow the typical  $\pi$ -shaped thermoelectric module structure, and the thermoelements are suspended on a cavity or surrounded by low thermal conductivity materials to avoid the shortcut of heat flow. Alternatively, the author's group propose a cavity-free architecture using short thermoelements, which was reviewed in detail. Measurement of thermoelectric performance is not straightforward due to the difficulty in determining the applied temperature difference across thermoelectric devices. Careful consideration is required for comparing different thermoelectric performance data.

## References

- [1] M. Gao, Thermoelectric module design theories, in: D.M. Rowe (Ed.), *Thermoelectrics Handbook*, CRC Press, 2006 (Chapter 11).
- [2] G. Pennelli, Review of nanostructured devices for thermoelectric applications, *Beilstein J. Nanotechnol* 5 (2014) 1268–1284.
- [3] I. Chowdhury, R. Prasher, K. Lofgreen, G. Chrysler, S. Narasimhan, R. Mahajan, D. Koester, R. Alley, R. Venkatasubramanian, On-chip cooling by superlattice-based thin-film thermoelectrics, *Nat. Nanotechnol.* 4 (2009) 235–238.
- [4] G. Li, J.G. Fernandez, D.A.L. Ramos, V. Barati, N. Pérez, I. Soldatov, H. Reith, G. Schierning, K. Nielsch, Integrated microthermoelectric coolers with rapid response time and high device reliability, *Nat. Electron.* 1 (2018) 555–561.
- [5] L. Weber, E. Gmelin, Transport properties of silicon, *Appl. Phys. A* 53 (1991) 136–140.
- [6] A.I. Boukai, Y. Bunimovich, J. Tahir-Kheli, J.K. Yu, W.A. Goddard III, J.R. Heath, Silicon nanowires as efficient thermoelectric materials, *Nature* 451 (2008) 168–171.
- [7] A.I. Hochbaum, R. Chen, R.D. Delgado, W. Liang, E.C. Garnett, M. Najarian, A. Majumdar, P. Yang, Enhanced thermoelectric performance of rough silicon nanowires, *Nature* 451 (2008) 163–167.
- [8] D. Li, Y. Wu, P. Kim, L. Shi, P. Yang, A. Majumdar, Thermal conductivity of individual silicon nanowires, *Appl. Phys. Lett.* 83 (2003) 2934–2936.
- [9] H.J. Goldsmid, *Electronic Refrigeration*, Pion, London, 1986.
- [10] Y. Zhang, A. Shakouri, G. Zeng, High-power-density spot cooling using bulk thermoelectrics, *Appl. Phys. Lett.* 85 (2004) 2977–2979.
- [11] P. Wang, A. Bar-Cohen, On-chip hot spot cooling using silicon thermoelectric micro-coolers, *J. Appl. Phys.* 102 (2007) 034503.
- [12] M. Strasser, R. Aigner, M. Franosch, G. Wachutka, Miniaturized thermoelectric generators based on poly-Si and poly-SiGe surface micromachining, *Sensors Actuators A Phys.* 97–98 (2002) 535–542.
- [13] M. Strasser, R. Aigner, C. Lauterbach, T.F. Sturm, M. Franosch, G. Wachutka, Micromachined CMOS thermoelectric generators as on-chip power supply, *Sensors Actuators A* 114 (2004) 362–370.

- [14] J. Xie, C. Lee, H. Feng, Design, fabrication, and characterization of CMOS MEMS-based thermoelectric power generators, *J. Microelectromech. Syst.* 19 (2010) 317–324.
- [15] X. Yu, Y. Wang, Y. Liu, T. Li, H. Zhou, X. Gao, F. Feng, T. Roinila, Y. Wang, CMOS MEMS-based thermoelectric generator with an efficient heat dissipation path, *J. Micromech. Microeng.* 22 (2012) 105011.
- [16] A. George, R. Yanagisawa, R. Anufriev, J. He, N. Yoshie, N. Tsujii, Q. Guo, T. Mori, S. Volz, M. Nomura, Thermoelectric enhancement of silicon membranes by ultrathin amorphous films, *ACS Appl. Mater. Interfaces* 11 (2019) 12027–12031.
- [17] D. Dávila, A. Tarancón, C. Calaza, M. Salleras, M. Fernández-Regúlez, A.S. Paulo, L. Fonseca, Monolithically integrated thermoelectric energy harvester based on silicon nanowire arrays for powering micro/nanodevices, *Nano Energy* 1 (2012) 812–819.
- [18] J.D. Santos, M. Salleras, I. Donmez, G. Gadea, C. Calaza, A. Morata, A. Tarancón, L. Fonseca, Power response of a planar thermoelectric microgenerator based on silicon nanowires at different convection regimes, *Energy Harvest. Syst.* 3 (2016) 335–342.
- [19] L. Fonseca, J.D. Santos, A. Roncaglia, D. Narducci, C. Calaza, M. Salleras, I. Donmez, A. Tarancón, A. Morata, G. Gadea, L. Belsito, L. Zulian, Smart integration of silicon nanowire arrays in all-silicon thermoelectric micronanogenerators, *Semicond. Sci. Technol.* 31 (2016) 084001.
- [20] K.J. Norris, M.P. Garrett, J. Zhang, E. Coleman, G.S. Tompa, N.P. Kobayashi, Silicon nanowire networks for multi-stage thermoelectric modules, *Energy Convers. Manag.* 96 (2015) 100–104.
- [21] B. Xu, W. Khouri, K. Fobelets, Two-sided silicon nanowire array/bulk thermoelectric power generator, *IEEE Electron Device Lett.* 35 (2014) 596–598.
- [22] Y. Li, K. Buddharaju, N. Singh, G. Lo, S. Lee, Chip-level thermoelectric power generators based on high-density silicon nanowire array prepared with top-down CMOS technology, *IEEE Electron Device Lett.* 32 (2011) 674.
- [23] Y. Li, K. Buddharaju, N. Singh, S.J. Lee, Top-down silicon nanowire-based thermoelectric generator: design and characterization, *J. Electron. Mater.* 41 (2012) 989–992.
- [24] B.M. Curtin, E.W. Fang, J. Bowers, Highly ordered vertical silicon nanowire array composite thin films for thermoelectric devices, *J. Electron. Mater.* 41 (2012) 887–894.
- [25] G. Hu, H. Edwards, M. Lee, Silicon integrated circuit thermoelectric generators with a high specific power generation capacity, *Nat. Electron.* 2 (2019) 300–306.
- [26] T. Watanabe, S. Asada, T. Xu, S. Hashimoto, S. Ohba, Y. Himeda, R. Yamato, H. Zhang, M. Tomita, T. Matsukawa, Y. Kamakura, H. Ikeda, A scalable Si-based micro thermoelectric generator, in: 2017 IEEE Electron Devices Technology and Manufacturing Conference (EDTM) Proceedings of Technical Papers, 2017, , pp. 86–87.
- [27] H. Zhang, T. Xu, S. Hashimoto, T. Watanabe, The possibility of mW/cm<sup>2</sup>-class on-chip power generation using ultrasmall Si nanowire-based thermoelectric generators, *IEEE Trans. Electron Devices* 65 (2018) 2016–2023.
- [28] T. Zhan, R. Yamato, S. Hashimoto, M. Tomita, S. Oba, Y. Himeda, K. Mesaki, H. Takezawa, R. Yokogawa, Y. Xu, T. Matsukawa, A. Ogura, Y. Kamakura, T. Watanabe, Miniaturized planar Sinanowire microthermoelectric generator using exuded thermal field for power generation, *Sci. Technol. Adv. Mater.* 19 (2018) 443–453.
- [29] M. Tomita, S. Ohba, Y. Himeda, R. Yamato, K. Shima, T. Kumada, M. Xu, H. Takezawa, K. Mesaki, K. Tsuda, S. Hashimoto, T. Zhan, H. Zhang, Y. Kamakuri, Y. Suzuki, H. Inokawa, H. Ikeda, T. Matsukawa, T. Matsuki, T. Watanabe, 2018 Symposium on VLSI Technology, Digest of Technical Papers, (2018) pp. 93–94.
- [30] M. Tomita, S. Ohba, Y. Himeda, R. Yamato, K. Shima, T. Kumada, M. Xu, H. Takezawa, K. Mesaki, K. Tsuda, S. Hashimoto, T. Zhan, H. Zhang, Y. Kamakuri, Y. Suzuki,

- H. Inokawa, H. Ikeda, T. Matsukawa, T. Matsuki, T. Watanabe, Modeling, simulation, fabrication, and characterization of a  $10\text{-}\mu\text{W}/\text{cm}^2$  class Si-nanowire thermoelectric generator for IoT applications, *IEEE Trans. Electron Devices* 65 (2018) 5180–5188.
- [31] K. Nair, J. Kulkarni, M. Warde, Z. Dave, V. Rawalgaonkar, G. Gore, J.J. Eduvance, Proceedings of International Conference on Green Computing and Internet of Things, (Oct. 2015) pp. 539–589.

# Measurement techniques of thermoelectric devices and modules

3.4

Hsin Wang<sup>a</sup> and Shengqiang Bai<sup>b</sup>

<sup>a</sup>Oak Ridge National Laboratory, Oak Ridge, TN, United States, <sup>b</sup>The State Key Laboratory of High Performance Ceramics and Superfine Microstructure, Shanghai Institute of Ceramics, Chinese Academy of Sciences, Shanghai, China

## 3.4.1 Introduction

Thermoelectric energy conversion devices based on the Seebeck effect have long been regarded as one of the best solutions to improve the efficiency of energy consumption by turning waste heat directly into electric power. The most attractive features include all solid-state device with no moving parts and easy adaption to generate energy from any heat source. Since 2000, research efforts worldwide have seen steady growth with significant improvement of materials properties. Unlike the fundamental research on thermoelectric materials, device development has been unproportionally lagging behind. Many thermoelectric materials with promising transport properties have been published [1–4] over the past 20 years. Progress reported in quantum dots superlattice [5], quantum well [6], thin films [7], and nanowires [8] have generated lots of interests in research and investment. However, due to the limitation in physical scales and ability to remove heat efficiently, i.e., maintaining large temperature gradient in a small space, there have been no successful energy conversion devices made directly from these low-dimensional materials [9]. Perhaps the most significant contribution of these research efforts has been providing insight into optimizing transport properties and inspiring new microstructure engineering ideas in bulk materials. The only TE material that has been commercially used in both Peltier cooling and power generation using low-grade heat is bismuth telluride. Although the power generating capacity is limited, bismuth telluride devices have seen applications in powering sensors and other low-power devices.

More progress has been made in recent years on materials such as skutterudite [10–13], half-Heusler [14–22], TAGS [23, 24], LAST [25, 26], Zn<sub>3</sub>Sb<sub>4</sub> [27–34], Mg- and Mn-silicides [35–37], oxides [38–43], PbTe [44, 45], SnSe [46], and Cu<sub>2</sub>Se [47, 48]. A few of these materials have been made into small-scale or demonstration modules. However, unlike the bismuth telluride none of the medium- and high-temperature devices is commercially available due to the lack of long-term performance and reliability data, and various issues in device manufacturing and cost. Small-scale productions of the modules are mostly aimed at specific applications. The purpose is usually for demonstration and not for scale-up productions.

It is worth pointing out that the most successful thermoelectric devices that have a proven record in the application are the radioisotope thermoelectric generator (RTG) [49]. SiGe-based general purpose heat source (GPHS) RTG [50] have been powering deep space probes such as the Voyagers and Cassini for 40 years and counting. PbTe-/TAGS-based (Multi-Mission) MMRTG is being used in the latest MARS 2020 rover (Perseverance) with launch date the summer of 2020 [51]. Even these RTG materials have not been used commercially due to its high manufacturing cost and low energy conversion efficiency. In this chapter, thermoelectric devices based on bulk materials will be reviewed. A review of the critical factors that affect device performance is given followed by a discussion on measurement techniques. Detailed device performance evaluation from single couples to standard modules are introduced. Finally, long-term device performance and testing are discussed.

### 3.4.2 Material properties and device performance

#### 3.4.2.1 Transport properties and figure of merit $zT$

Thermoelectric materials are characterized by measuring Seebeck coefficient ( $s$ ), electrical conductivity ( $\sigma$ ) and thermal conductivity ( $\lambda$ ), and a calculated parameter, also known as the figure of merit,  $zT$ , is shown as

$$zT = s\sigma^2 T / \lambda \quad (3.4.1)$$

in which  $T$  is the temperature in Kelvin. Thermal conductivity is usually obtained by measuring thermal diffusivity ( $\alpha$ ), specific heat ( $C_p$ ), and density ( $\rho$ ) and multiplying the three properties using the following equation:

$$\lambda = \alpha \rho \cdot C_p \quad (3.4.2)$$

In the most accurate measurements as a function of temperature, the thickness used to calculate thermal diffusivity and volume to obtain density require an additional measurement of the coefficient of thermal expansion (CTE). In most cases, the change in dimensions within several hundred degrees are negligible. Therefore, a total of five material properties need to be measured. In a 6-year effort organized by the International Energy Agency (IEA) under the implementing agreement for the Advanced Transportation Materials (AMT), three international round-robins have been carried out on bismuth telluride [52, 53] and n-type half-Heusler [54]. Measurement uncertainties on each property and the compounding effect on  $zT$  were shown to be about  $\pm 16\%$ . Round-robin efforts have also been made by the European organization [55] on skutterudite with similar conclusions.

With the knowledge of transport properties,  $zT$ , and operating temperature range, the performance, i.e., ideal energy conversion efficiency,  $\eta_{\max}$ , of a TE device can be calculated using:

$$\eta_{\max} = \frac{T_H - T_C}{T_H} \frac{\sqrt{1+z\bar{T}} - 1}{\sqrt{1+z\bar{T}} + \frac{T_C}{T_H}} \quad (3.4.3)$$

in which  $T_H$  and  $T_C$  are hot side and cold side temperature, respectively,  $\bar{T} = (T_H + T_C)/2$  is the average temperature, and  $z\bar{T}$  is the figure of merit in the same temperature range. The first term is the Carnot efficiency. Eq. (3.4.3) indicates for a very large  $zT$  the second term is close to 1 so conversion efficiency can approach Carnot value. However, most TE materials have average  $zT$  values about 1.  $\eta_{\max}$  is an ideal value based only on transport properties. The actual device efficiency will be smaller because of thermal and electrical interface losses.

Here, it is important to clarify the definitions of various terms used in this chapter:

- *Thermoelectric couple (TEC)*: a single  $\Pi$ -shaped device consists of an n-leg and a p-leg connected in series (it is also called unicouple)
- *Thermoelectric module (TEM)*: multiple TE couples connected in series and parallel on insulating substrates
- *Thermoelectric generator (TEG)*: TE module connected to a heat source via a hot side heat exchanger (or a hot shoe) and a cold side heat sink

The latter two terms sometimes are mixed up. It is important to note a TEG is a system capable of generating power and a TEM is a stand-alone component/device.

As an example, a basic design of bismuth telluride module is demonstrated. Materials properties were obtained using the same materials in the IEA round-robin [52, 53]. Seebeck coefficient, electrical conductivity, and thermal conductivity as a function of temperature were obtained at ORNL and shown in Fig. 3.4.1. These properties are the bases for designing TEM and TEG.

The simplest thermoelectric device is a single TEC shown in Fig. 3.4.2. Assuming the hot side is at 473K and cold side is at 323K, we choose the element size to be 2.0mm  $\times$  2.0mm  $\times$  4.0mm for both n-type and p-type bismuth telluride. Using the 150K temperature gradient and average Seebeck and electrical conductivity values in this temperature range: Seebeck coefficient for p-leg is 210  $\mu\text{V/K}$  and  $-170 \mu\text{V/K}$  for the n-leg; electrical resistivity of p-leg is 2.60 and 2.10 mOhm-cm for n-leg. Therefore, the resistance of n-leg is 21 mOhm and p-leg is 26 mOhm. Under the same 150K temperature difference, the voltage on the p-leg is 42 and 34 mV on n-leg. The calculated short-circuit current through each leg is 1.615 mA for p-leg and 1.619 mA for n-leg. Since the p-leg and n-leg are connected in series, it is the best practice to optimize the current by adjusting the cross-sectional area of one leg to maximize current. In this case, the current values happen to be very close. Here, we are ignoring the resistance of the metal interconnects at both hot and cold sides.

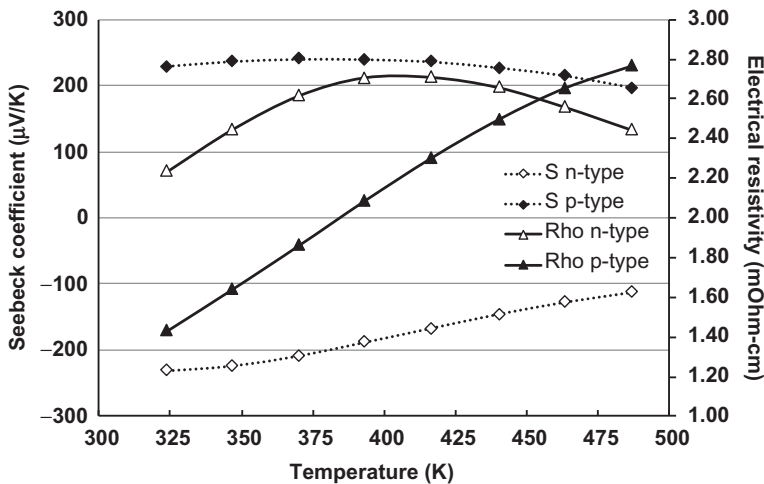


**Fig. 3.4.1** Seebeck coefficient and electrical resistivity of n-type and p-type bismuth telluride as a function of temperature.

The current in the circuit is calculated using:

$$I = \frac{V_p + V_n}{R_p + R_n + R_L} \quad (3.4.4)$$

Typically, when the external load,  $R_L$ , matches the internal resistance of the couple,  $R_p + R_n$ , maximum power is obtained. To build a thermoelectric module (TEM), the number of couples connected in series will add up to the total device voltage and

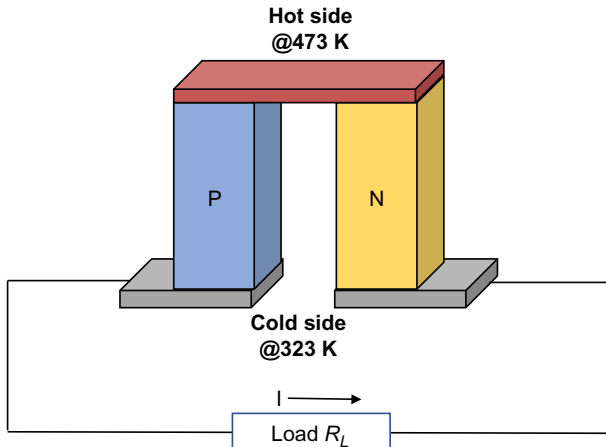


**Fig. 3.4.2** Single bismuth telluride couple and calculation of power with 150-K temperature difference.

device power can be increased by connecting the couples in parallel. In some applications, multiple TEM are connected in series and parallel to achieve the designed voltage and power.

### 3.4.2.2 Effect of interconnect, diffusion barriers, and bonding layers

In the simple bismuth TE module built in the last section, we assume perfect interconnect materials and no electrical loss at the interfaces and connections. In reality, interface resistance must be considered. Fig. 3.4.3 is a modified single couple with interface layers. The top of the hot side is the interconnect material usually an electrically conducting metal such as aluminum, copper, nickel, or molybdenum depending on the maximum temperature. At temperatures about 1000°C (1273K), intermetallic compounds are often used. In a typical design, an electrically insulated heat collector is bonded to the interconnect at the hot side. For low-temperature modules, alumina or AlN substrate are often selected. Commercially available direct bonded aluminum (DBA) or direct bonded copper (DBC) can be used. The interconnect is diffusion bonded to thermoelectric legs at elevated temperature. Soldering or brazing is also used and sometimes a diffusion barrier a few microns in thickness is coated on the thermoelectric legs to prevent elements from diffusing and cross contaminating the TE legs, which is the main cause of degradation. In TEMs, the hot side interface and its long-term stability are the most critical issues. The cold side bonding requirements have fewer restrictions because most materials are stable from ambient

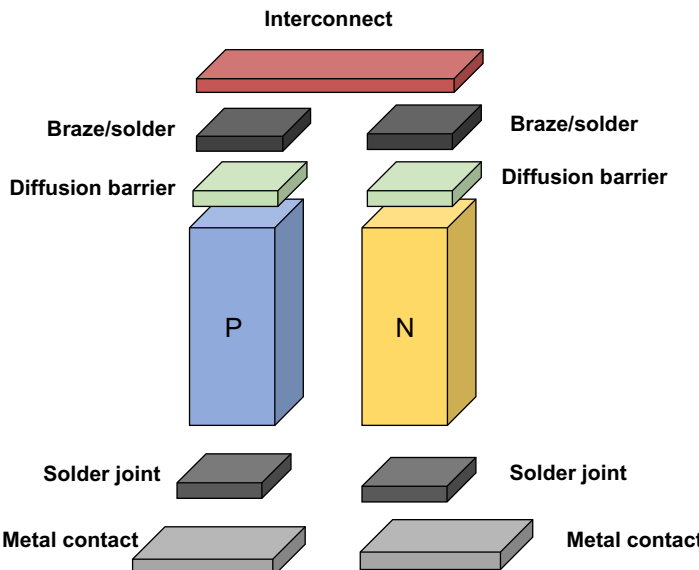


**Fig. 3.4.3** Detailed layers and interfaces in a typical thermoelectric couple (layer thicknesses not to scale).

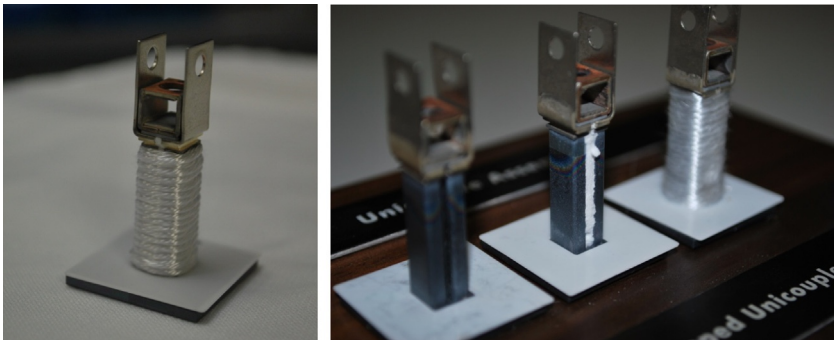


**Fig. 3.4.4** GPHS RTG SiGe unicouples wrapped by quartz fiber insulations.  
Pictures from Jaymon Birch, Idaho National Laboratory.

to 200°C (473 K). Another important factor to consider is the coefficient of thermal expansion (CTE). Mechanical strength of the elements needs to be measured. Thermomechanical analysis, including residual stress and in-gradient thermal stresses, needs to be taken into consideration in the design by matching the CTE of the layers and minimizing stresses.

### **3.4.2.3 Effect of thermal insulations and thermal interfaces**

In thermoelectric module designs utilizing heat sources above 500°C (773 K), there is significant leg spacing described by the filling factor. The power generation exercise in [Section 3.4.2.1](#) assumed constant heat flow and unlimited heat removal capacity at the cold side. However, in a practical device, the heat removal is limited by the cold side heat exchanger design. In order to maintain the constant temperature gradient, thermoelectric element dimensions and thermal conductivity must be used to calculate the heat flux through specific design and filling factor. Since radiation heat transfer can occur between the hot side and cold side through the empty space, thermal insulation is often used to fill the gaps. For the SiGe unicouples used in GPHS RTG, Astroquartz yarn insulation was used to wrap around the legs and fill the space as shown in [Fig. 3.4.4](#). The insulation also helps to prevent or slows down the sublimation of TE materials at the hot side. An alternative thermal insulation is an aerogel [22, 23]. Air-dried aerogel can be poured into the module to fill up space and act as thermal radiation barriers.

## **3.4.3 Thermoelectric device and module testing techniques**

### **3.4.3.1 Heat flux method**

A survey of testing methods showed that most thermoelectric module testing systems were made in-house [56]. Commercial systems from ULVAC-Riko (now Advanced

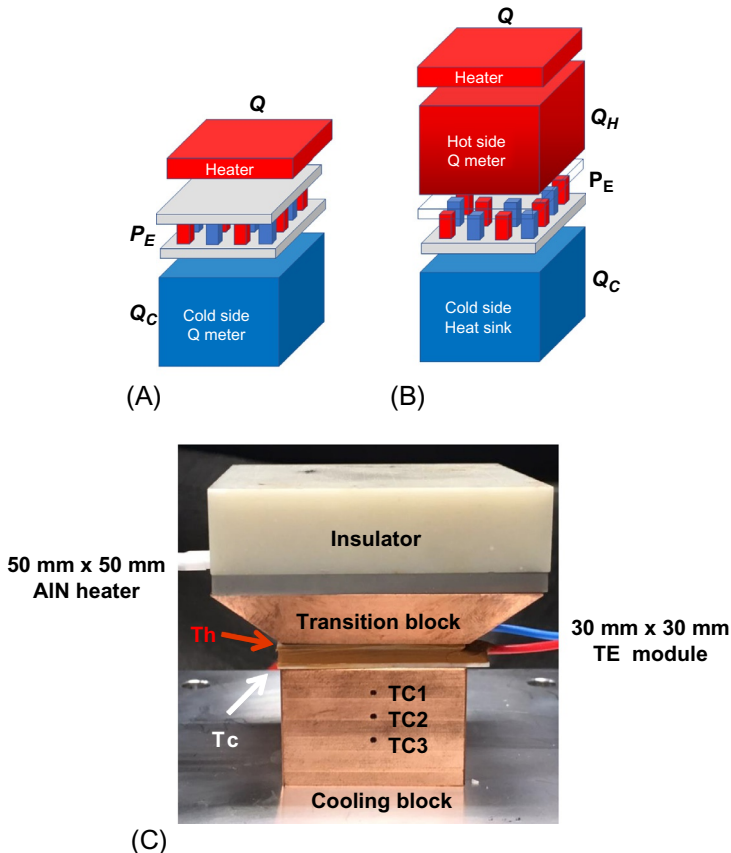


**Fig. 3.4.5** Heat flow method (A) cold side heat flow meter; (B) hot and cold side heat flow meter; and (C) an actual heat flow meter setup.

Riko) have been available recently. Most of the module efficiency testing systems follow the heat flux meter design for thermal conductivity or thermal resistance [57, 58]. Typical test setups are shown in Fig. 3.4.5. Similar to the application of TEM a heat source, e.g., electric heater or a radiation heat collector, is placed at the hot side and a heat sink is attached to the cold side to establish a steady heat flow,  $Q$ , through the TEM.  $P_{\max}$  is the maximum power generator by TEM. In Fig. 3.4.5A, a piece of high thermal conductivity materials, e.g., copper or graphite, is part of the cold side heat sink. The temperature gradient is obtained by measuring at least three temperatures along the thickness with fixed spacing.  $Q_C$  the heat flow is determined from the cross-sectional area and the known thermal conductivity of the material. In Fig. 3.4.5B, a hot side heat flow meter is also used. The material must be stable at high temperatures. Nickle, copper, and graphite are used. Similar to the cold side heat flow meter,  $Q_H$  is obtained. Despite the measured heat flux, Eq. (3.4.5) assumes no heat loss at the interface and TEM. In module efficiency measurements, power can

be determined from I to V curves under varying load resistance. The practical measurement version for device efficiency  $\eta$  of Eq. (3.4.4) becomes

$$\eta = \frac{P_{\max}}{Q_H} = \frac{P_{\max}}{Q_C + P_{\max}} \quad (3.4.5)$$

In a recent international round-robin testing of bismuth telluride modules, the source of measurement error was determined due to the uncertainties of heat flux measurements. In order to carry out the tests, the following key procedures were used in a recent IEA international round-robin testing of TEM:

- Module dimensions were defined at 30 mm × 30 mm
- Test environment was vacuum and nitrogen purge gas
- Specific interface material (graphite sheets) was used in each test at the hot and cold side
- Test pressure was defined at 100 psi (i.e., 62.8 kg load on the 30 mm × 30 mm module)
- Device AC resistance was monitored before and after the tests
- Module cold side was at 50°C, 75°C, 100°C, 125°C, and 150°C and cold side at 20°C

### **3.4.3.2 I-V curves and module testing**

In a typical TEM efficiency test, I-V curves can be measured even at very small temperature gradient. Fig. 3.4.6A shows the I-V power curves under 8.4°C temperature gradient and heater power of 3.3 W using the configuration of Fig. 3.4.5C, which is a quick test of the system setup and readings of various sensors. The heat flow through the transition block to the module is much smaller. Only 4.5 mW power was measured. In high-temperature module tests, a vacuum chamber and vacuum level of  $10^{-2}$ – $10^{-3}$  Torr is achieved with a rotary pump. Higher vacuum requires a second stage turbo-molecular pump or a diffusion pump. In some cases, a cover gas, such as Ar, He or N<sub>2</sub>, flows through the chamber. Fig. 3.4.6B shows the measured temperatures and open-circuit voltages of a five-point efficiency measurements using a ULVAC PEM-2 system. Fig. 3.4.6C shows five sets of I-V curves obtained by the varying external electric load during the measurement. The power curves show a maximum power that is achieved under each set point. Fig. 3.4.6D shows maximum powers reached at load between 1 and 2 Ohms. AC resistance measurement of the module resistance at room temperature is 1.5 Ohm. The PEM-2 system measures Q<sub>C</sub> using a cold-side heat flux meter made of copper. Module efficiency is calculated using Eq. (3.4.5). In most cases, Q<sub>C</sub> is easier to measure than Q<sub>H</sub> because the temperature gradient is smaller at the cold side and the heat flux calculated from material thermal conductivity is more reliable. On the other hand, the hot side temperature gradient is large and not linear. The calculated value depends on the accurate high-temperature thermal conductivity which may not be available, and the effect of heat loss is not taken into account.

### **3.4.3.3 Peltier effect during power generation**

Temperature equilibrium is important in the efficiency measurement. One of the issues that tend to be overlooked is the Peltier effect when the module is connected

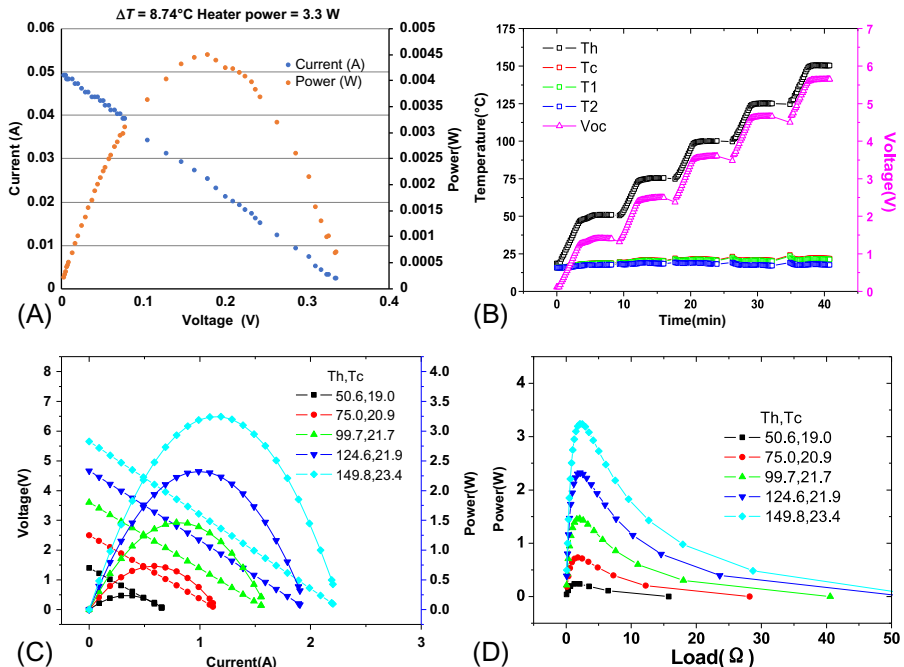


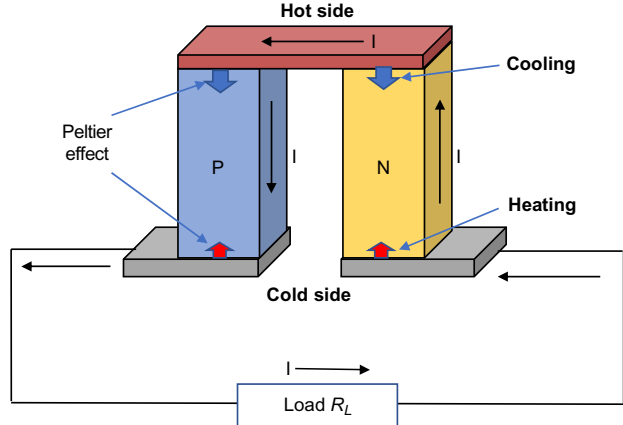
**Fig. 3.4.6** (A) I-V of a module under small temperature gradient, (B) temperatures and open-circuit voltage during a typical efficiency test, (C) I-V curves and power curve at five set points, (D) power vs load curves of five set points.

to an electronic load. When a current flows through the circuit including the TE elements as shown in Fig. 3.4.7A, the TEM also functions as Peltier cooler. It cools at the hot side and heats up at the cold side. As shown in Fig. 3.4.7B, the module was connected to 500 Ohm load that maintained a 26°C temperature gradient, and as soon as the load was switched to 50 mOhm, a larger current going through the module lowered the hot side temperature and increased the cold side temperature. The net effect made the temperature gradient change from 26°C to 23°C in about 20 s.

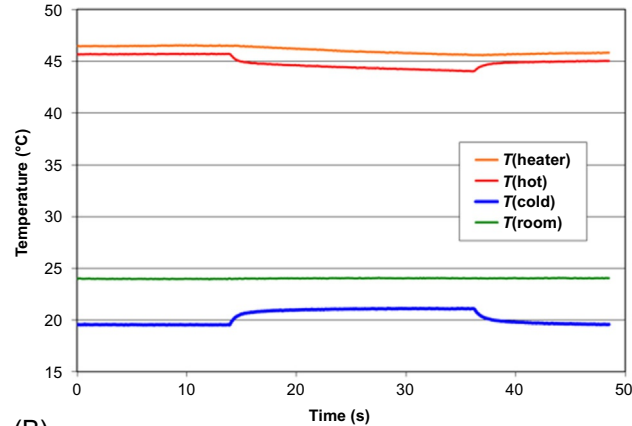
Fig. 3.4.7C and D show close-up temperature changes of the Peltier effect. It is clear the cold side reached equilibrium faster than the hot side. It is usually recommended to wait for at least 30–60 s when the load is changed during the I-V measurement. Since the progressive steps in measurement are not as large as the example, the effect of changing 5–10 mOhm load will be manageable.

### 3.4.3.4 Effect of heat flux sensor

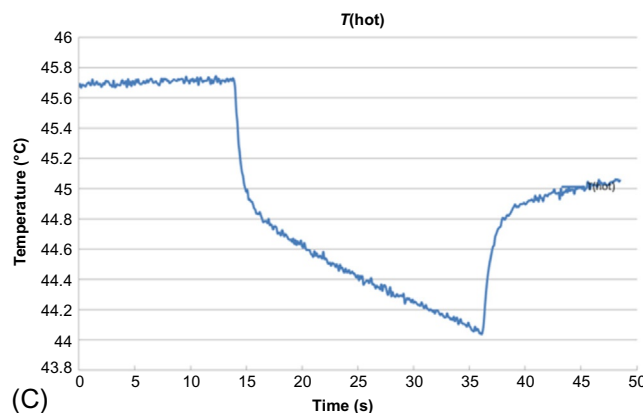
A heat flux sensor is used in the heat flow meter to measure the thermal conductivity of insulation materials. Usually, the required materials are two identical panels 305 cm × 305 cm and a few centimeters in thickness. A heat flux sensor is shown in Fig. 3.4.8. It is a thermocouple pile which will generate a voltage at a given heat flux.



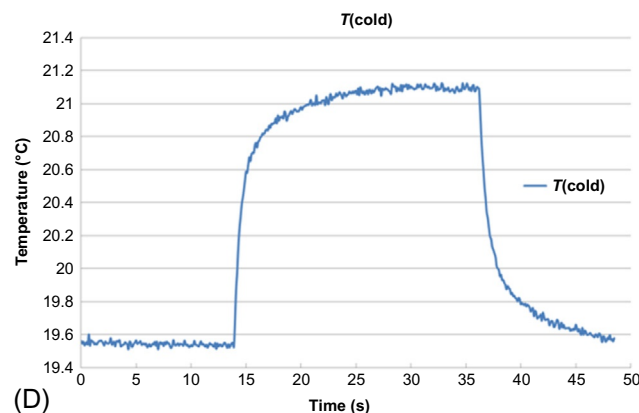
(A)



(B)



(C)



(D)

**Fig. 3.4.7** (A) Peltier effect in power generation mode when a load is applied and current is flowing through, (B) temperature changes when the load is switched from  $500\text{ }\Omega$  to  $50\text{ m}\Omega$ , (C) close-up of hot side cooling, and (D) close-up of cold side heating.

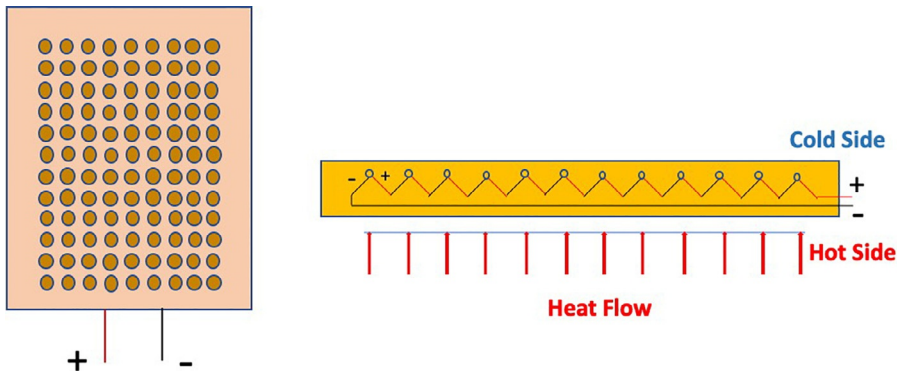


**Fig. 3.4.8** Illustration of a heat flux sensor and layer out.

Therefore, a calibration curve or a constant  $V/(W/cm^2)$  must be used. This method works well when the sample size is large. In a TEM measurement, such heat flux sensor tends to give a larger value and cause the measured efficiency to be lower. This is mainly because the thin heat flux meter adds interface resistance to the heat flow path and its size is too large to be ignored to affect the measurement. The use of a heat flux sensor is not recommended.

### 3.4.3.5 Effect of pressure Macor calibration

As indicated in the previous sections, the most critical parameter in TEM efficiency measurement is the heat going through the module. It is important to minimize the heat losses at the interfaces to the environment from the sides. Contact pressure affects the measured heat flux and TEM power. In order to compare different measurements, it is necessary to specify the type of interface material to use and the applied pressure. Fig. 3.4.9A shows the effect of the applied load on the measured heat flow ( $Q_C$ ) at five set points. The  $Q$  value increases when the applied load changes from 20 to 100 kg. In order to demonstrate the effect of pressure, a piece of MACOR (glass ceramic) was machined to the same size of the TEM (30 mm × 30 mm) and the thickness of 3–4 mm to match the thermal resistance of the TEM. When the TEM is

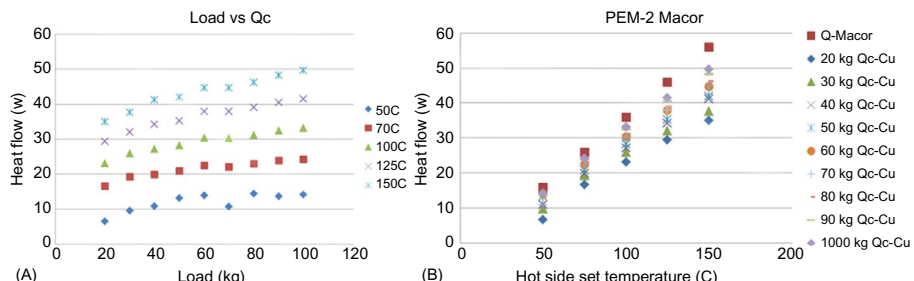


**Fig. 3.4.9** (A) Heat flow as a function of applied load and (B) heat flow of MACOR and Copper ( $Q_C$ ) under increasing load.

replaced by the MACRO block, Eq. (3.4.6) can be used to calculate the thermal conductivity,  $\lambda$ , of MACOR, which has an almost constant value of 1.4 W/mK.  $A$  is the cross-sectional area and  $L$  is the thickness of the block.

$$Q = \lambda A (T_H - T_C)/L \quad (W) \quad (3.4.6)$$

**Fig. 3.4.9B** shows the measured heat flow ( $Q_c$ ) using copper and thermal conductivity of 400 W/mK.  $Q$ -MACOR is the heat flow measured using MACOR thermal conductivity. At 20 kg load, the  $Q_c$  determined at the cold side is much lower. When the pressure increases the  $Q$  value gets close to the MACOR value. At 100 kg load, the lower temperature  $Q$  values are the same indicating the heat loss at the interfaces. For the round-robin specified load of 68 kg, there was some heat loss at high temperatures. However, in order to make sure the module can survive the test and be passed on to the next lab, the moderate load was selected and used consistently. This test showed the importance of maintaining a constant load. A well-designed TEM may not produce predicted power if the interface resistance is not minimized.

### 3.4.3.6 Harman method

Harman method was developed in 1958 [59] utilizing Peltier heating in the TE materials. When a small current is applied to the TE bar with length  $L$  and cross-sectional area  $A$ , a small temperature difference,  $\Delta T$ , is generated between the two ends. The ratio between the Seebeck voltage,  $V_\alpha$ , and Joule (IR) voltage drop,  $V_R$ , and absolute temperature  $T$  gives the figure of merit,  $Z$ :

$$Z = V_\alpha / V_R T \quad (3.4.7)$$

In the thermoelectric module with  $N$  elements, a commercially available  $Z$ -meter has been used to measure AC resistance and  $ZT$  values of the TEMs [60].

$$ZT = \left(1 + \frac{\alpha}{2Nk}\right) \frac{V_\alpha}{V_R} \quad (3.4.8)$$

In a modified version, in which the TE module can be insulated from environmental temperature drift, the same Harman measurements were carried out at various temperatures by putting the TEM in an oven. The module is insulated and allows the  $\Delta T$  due to the Peltier effect to be measured accurately when a small current is passed through the device. The measured  $ZT$  is from the TE legs excluding the hot side and cold side insulation materials (usually ceramic plates) and the test is not affected by the interface conditions and applied pressure. As we have shown previously, the device efficiency measured by the heat flow method depends on interface quality and applied pressure, the  $ZT$  measured by Harman method can be used in Eq. (3.4.3) to calculate an ideal efficiency which should be closer to that calculated from transport properties.

## 3.4.4 Device performance

### 3.4.4.1 Device performance: Single couple

The performance of a TE device is often described using the power produced under a fixed temperature gradient. Single couple or unicouple devices shown in Fig. 3.4.10 are often the first step towards building thermoelectric modules and ultimately TEGs. A single couple includes n-type and p-type legs, hot and cold shoe with interface materials. Measuring efficiency of such a couple is inaccurate and can be misleading. The more practical test is to measure the power produced by the couple and individual legs. After establishing the initial power, the couple is kept under the temperature gradient and simulated environment for a long period of time. Power output is measured in situ. For some applications, thermal cycling is necessary and for applications like the RTG, long-term exposure under a constant gradient is important. Such test usually takes thousands of hours and in some cases, 10–20 thousand hours are needed to generate reliable data on power degradation over time. A degradation model is necessary to predict the available power at the end of design life. For example, the typical requirement for NASA RTG requires 17 years of life prediction including natural nuclear fuel decay and thermoelectric device degradation [61].

### 3.4.4.2 Device performance: Standard module

After the performance of unicouple is established, the next step is to build a thermoelectric module (TEM). The most basic TEM is a  $4 \times 4$  array containing 8 couples connected in series as shown in Fig. 3.4.3. This configuration is considered the “standard” module. It uses the minimum number of couples and the module has all types of elements of any larger module: four corner elements, eight edge elements, and four center elements. It is also important to make the cross-sectional area standard for testing purpose. As shown in Fig. 3.4.11, the four mid-temperature range modules have similar size. But the number of elements, the size of the legs, and cross-sectional area are different. It is beneficial to build the standard module using  $4 \times 4$  configuration and 20 mm  $\times$  20 mm cross-sectional area. Therefore, any laboratory in the world can build standard test rigs for the same geometry. The leg size can be optimized within the given boundary to give maximum power. The temperature gradient depends on the

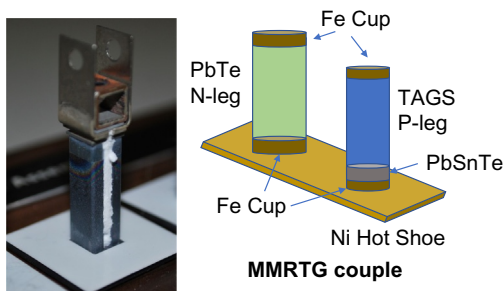


**Fig. 3.4.10** SiGe unicouple for GPHS RTG and illustration of a PbTe/TAGS couple in MMRTG.

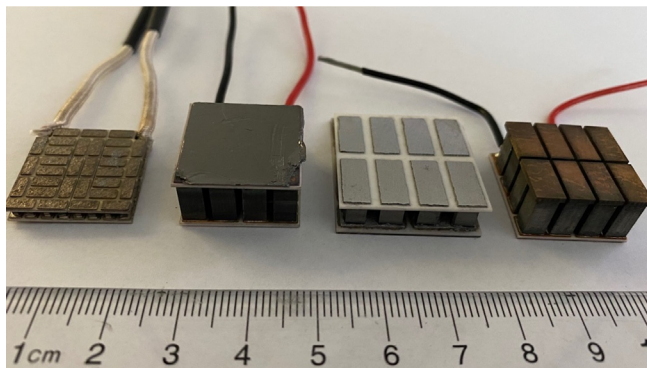


**Fig. 3.4.11** Half-Heusler  $8 \times 8$  (Fraunhofer Institute) and  $4 \times 4$  (SICSAC) modules, PbTe (Marlow Industries) and Skutterudite (SICSAC) modules.

material properties. The teststand should provide sufficient heating and cooling power to maintain the temperature gradient.

The standard module is particularly useful when developing different generations of the same materials. The improvement in power generation can be directly compared and it is easy to utilize the test results to feed into models for large modules and TEG designs. Similar to the unicouples, life testing on standard modules can provide critical reliability data to the design and build of larger TEG.

### 3.4.5 Summary

In summary, thermoelectric module efficiency can be derived from transport properties measurements. Due to interface thermal and electrical resistance losses and device parasitic heat loss, the device efficiency is always smaller and must be measured. Various measurement techniques are reviewed with focus on the heat flow meter method. It was pointed out that unicouple is an important step in device development. However, emphasis should be on power generation and materials performance because an efficiency test on a couple can be misleading. Finally, a suggestion of standard module was made in an effort for thermoelectric modules of different materials and at different temperature ranges to be comparable.

### Acknowledgments

The authors would like to thank the International Energy Agency under the Implementing Agreement for the Advanced Materials for Transportation for supporting the International round-robin studies, the assistant secretary for Energy Efficiency and Renewable Energy of the Department of Energy and the Propulsion Materials program under the Vehicle Technologies program. S.Q. Bai would like to thank the support from the Chinese Academy of Sciences. Oak Ridge National Laboratory is managed by UT-Battelle LLC under contract DE-AC05000OR22725.

## References

- [1] D.M. Rowe (Ed.), CRC Handbook of Thermoelectrics: Macro to Nano, CRC, Boca Raton, FL, 2005.
- [2] G.J. Snyder, E.S. Toberer, Complex thermoelectric materials, *Nat. Mater.* 6 (2008) 105–114.
- [3] G. Chen, M.S. Dresselhaus, G. Dresselhaus, J.P. Fleurial, T. Caillat, Recent developments in thermoelectric materials, *Int. Mater. Rev.* 48 (2003) 45–66.
- [4] T.M. Tritt (Ed.), Recent Trends in Thermoelectric Materials Research, Academic, San Diego, CA, 2001.
- [5] M.S. Dresselhaus, et al., New directions for low-dimensional thermoelectric materials, *Adv. Mater.* 19 (2007) 1043–1053.
- [6] T.C. Harman, P.J. Taylor, M.P. Walsh, B.E. LaForge, Quantum dot superlattice thermoelectric materials and devices, *Science* 297 (5590) (2002) 2229–2232.
- [7] R. Venkatasubramanian, E. Siivola, T. Colpitts, B. O’Quinn, Thin-film thermoelectric devices with high room-temperature figures of merit, *Nature* 413 (2001) 597–602.
- [8] A.I. Hochbaum, R. Chen, R.D. Delgado, W. Liang, E.C. Garnett, M. Najarian, A. Majumdar, P. Yang, Enhanced thermoelectric performance of rough silicon nanowires, *Nature* 451 (2008) 163–167.
- [9] L.D. Hicks, M.S. Dresselhaus, Effect of quantum well structure on thermoelectric figure of merit, *Phys. Rev. B* 47 (19) (1993) 727–731.
- [10] G.S. Nolas, G.A. Slack, S.B. Schujman, *Semicond. Semimet.* 69 (2000) 255.
- [11] B.C. Sales, D. Mandrus, R.K. Williams, *Science* 272 (1996) 1325.
- [12] G.S. Nolas, M. Kaeser, R.T. Littletonand, T.M. Tritt, *Appl. Phys. Lett.* 77 (12) (2000) 1855.
- [13] X. Shi, J. Yang, J.R. Salvador, M. Chi, J.Y. Cho, H. Wang, S. Bai, J. Yang, W. Zhang, L. Chen, Multiple-filled skutterudites: high thermoelectric figure of merit through separately optimizing electrical and thermal transports, *J. Am. Chem. Soc.* 133 (20) (2011) 7837–7846.
- [14] J. Tobola, J. Pierre, S. Kaprzyk, R.V. Skolozdra, M.A. Kouacou, *J. Phys. Condens. Matter* 10 (1998) 1013.
- [15] S. Ogut, K.M. Rabe, *Phys. Rev. B* 51 (1995) 10443.
- [16] W.E. Pickett, J.S. Moodera, *Phys. Today* 54 (2001) 39.
- [17] C. Uher, J. Yang, S. Hu, D.T. Morelli, G.P. Meisner, *Phys. Rev. B* 59 (1999) 8615.
- [18] H. Hohl, A.P. Ramirez, C. Goldmann, G. Ernst, B. Wolfing, E. Bucher, *J. Phys. Condens. Matter* 11 (1999) 1697.
- [19] S. Bhattacharya, A.L. Pope, R.T. Littleton IV, T.M. Tritt, V. Ponnambalam, Y. Xia, S.J. Poon, *Appl. Phys. Lett.* 77 (2000) 2476.
- [20] Y. Xia, S. Bhattacharya, V. Ponnambalam, A.L. Pope, S.J. Poon, T.M. Tritt, *J. Appl. Phys.* 88 (2000) 1952.
- [21] Q. Shen, L. Chen, T. Goto, T. Hirai, J. Yang, G.P. Meisner, C. Uher, *Appl. Phys. Lett.* 79 (2001) 4165.
- [22] S.J. Poon, Recent advances in thermoelectric performance of half-Heusler compounds, *Metals* 8 (2018) 989.
- [23] G.S. Nolas, J. Sharp, H.J. Goldsmid, Thermoelectrics: Basic Principles and New Materials Developments, Springer, New York, 2001.
- [24] E. Skrabeck, D.S. Trimmer, in: D.M. Rowe (Ed.), CRC Handbook of Thermoelectrics, CRC Press, Boca Raton, FL, 1995, p. 267.

- [25] K.F. Hsu, S. Loo, F. Guo, W. Chen, J.S. Dyck, C. Uher, T. Hogan, E.K. Polychroniadis, M.G. Kanatzidis, *Science* 303 (2004) 818.
- [26] E. Quarez, K.F. Hsu, R. Pcionek, N. Frangis, E.K. Polychroniadis, M.G. Kanatzidis, *J. Am. Chem. Soc.* 127 (2005) 9177.
- [27] H.W. Mayer, I. Mikhail, K. Schubert, *J. Less Common Met.* 59 (1978) 43.
- [28] T. Caillat, J.-P. Fleurial, A. Borshchevsky, *J. Phys. Chem. Solids* 58 (1997) 1119.
- [29] V.L. Kuznetsov, D.M. Rowe, *J. Alloys Compd.* 372 (2004) 103.
- [30] S.C. Ur, I.H. Kim, P. Nash, *Mater. Lett.* 58 (2004) 2132.
- [31] K. Ueno, A. Yamamoto, T. Noguchi, T. Inoue, S. Sodeoka, H. Takazawa, C.H. Lee, H. Obara, *J. Alloys Compd.* 385 (2004) 254.
- [32] G.J. Snyder, M. Christensen, E. Nishibori, T. Caillat, B.B. Iversen, *Nat. Mater.* 3 (2004) 458.
- [33] M. Tsutsui, L.T. Zhang, K. Ito, M. Yamaguchi, *Intermetallics* 12 (2004) 809.
- [34] F. Cargnoni, E. Nishibori, P. Rabiller, L. Bertini, G.J. Snyder, M. Christensen, B.B. Iversen, *Chem. Eur. J.* 20 (2004) 3861.
- [35] S.G. Kim, I.I. Mazin, D.J. Singh, *Phys. Rev. B* 57 (1998) 6199.
- [36] V.K. Zaitsev, M.I. Fedorov, E.A. Gurieva, I.S. Eremin, P.P. Konstantinov, A.Y. Samunin, M.V. Vedernikov, *Phys. Rev. B* 74 (2006), 045207.
- [37] M. Fukano, T. Iida, K. Makino, M. Akasaka, Y. Oguni, Y. Takanashi, *MRS Proc.* 1044 (2007), <https://doi.org/10.1557/PROC-1044-U06-13>.
- [38] I. Terasaki, Y. Sasago, K. Uchinokura, *Phys. Rev. B* 56 (1997), R12685.
- [39] R. Funahashi, I. Matsubara, H. Ikuta, T. Takeuchi, U. Mizutani, S. Sodeoka, *Jpn. J. Appl. Phys. Pt. 2* 39 (2000) L1127.
- [40] A.C. Masset, C. Michel, A. Maignan, M. Hervieu, O. Toulemonde, F. Studer, B. Raveau, J. Hejtmanek, *Phys. Rev. B* 62 (2000) 166.
- [41] A. Satake, H. Tanaka, T. Ohkawa, T. Fujii, I. Terasaki, *J. Appl. Phys.* 96 (2004) 931.
- [42] M. Shikano, R. Funahashi, *Appl. Phys. Lett.* 82 (2003) 1851.
- [43] I. Matsubara, R. Funahashi, T. Takeuchi, S. Sodeoka, T. Shimizu, K. Ueno, *Appl. Phys. Lett.* 78 (2001) 362.
- [44] J.P. Heremans, V. Jovovic, E.S. Toberer, A. Saramat, K. Kurosaki, A. Charoenphakdee, S. Yamanaka, G. Jeffrey Snyder, Enhancement of thermoelectric efficiency in PbTe by distortion of the electronic density of states, *Science* 321 (5888) (2008) 554–557.
- [45] Y. Pei, J. Lensch-Falk, E.S. Toberer, D.L. Medlin, G.J. Snyder, High thermoelectric performance in PbTe due to large nanoscale Ag<sub>2</sub>Te precipitates and la doping, *Adv. Funct. Mater.* 21 (2) (2010) 241–249.
- [46] L.D. Zhao, G. Tan, S. Hao, J. He, Y. Pei, H. Chi, H. Wang, S. Gong, H. Xu, V.P. Dravid, C. Uher, G.J. Snyder, C. Wolverton, M.G. Kanatzidis, Ultrahigh power factor and thermoelectric performance in hole-doped single-crystal SnSe, *Science* 351 (6269) (2016) 141–144.
- [47] S. Ballikaya, H. Chi, J.R. Salvador, C. Uher, Thermoelectric properties of Ag-doped Cu<sub>2</sub>Se and Cu<sub>2</sub>Te, *J. Mater. Chem. A* 1 (2013) 12478–12484.
- [48] D.R. Brown, T. Day, T. Caillat, G.J. Snyder, Chemical stability of (Ag,Cu)<sub>2</sub>Se: a historical overview, *J. Electron. Mater.* 42 (2013) 2014–2019.
- [49] D.J. Anderson, J. Sankovic, D. Wilt, R.D. Abelson, J.-P. Fleurial, NASA's advanced radioisotope power conversion technology development status, in: 2007 IEEE Aerospace Conference, Big Sky, MT, 2007, <https://doi.org/10.1109/AERO.2007.352696>.
- [50] C.B. Vining, J.-P. Fleurial, Silicon-germanium: an overview of recent developments, in: Tenth Symposium on Space Nuclear Power and Propulsion, Special Volume Albuquerque, New Mexico, 10–14 January, 1993.

- [51] K.S. Novak, J.G. Kempenaar, M.J. Redmond, P. Bhandari, Preliminary surface thermal design of the Mars 2020 Rover, in: 5th International Conference on Environmental Systems, Bellevue, Washington, July 12-16, 2015.
- [52] H. Wang, W.D. Porter, H. Böttner, J. König, L. Chen, S. Bai, T.M. Tritt, A. Mayolet, J. Senawiratne, C. Smith, F. Harris, P. Gilbert, J.W. Sharp, J. Lo, H. Kleinke, L. Kiss, Transport properties of bulk thermoelectrics—an international round-robin study, part I: seebeck coefficient and electrical resistivity, *J. Electron. Mater.* 42 (4) (2013) 654–664.
- [53] H. Wang, W.D. Porter, H. Böttner, J. König, L. Chen, S. Bai, T.M. Tritt, A. Mayolet, J. Senawiratne, C. Smith, F. Harris, P. Gilbert, J.W. Sharp, J. Lo, H. Kleinke, L. Kiss, Transport properties of bulk thermoelectrics: an international round-robin study, part II: thermal diffusivity, specific heat, and thermal conductivity, *J. Electron. Mater.* 42 (6) (2013) 1073–1084.
- [54] H. Wang, S. Bai, L. Chen, A. Cuenat, G. Joshi, H. Kleinke, J. König, H.W. Lee, J. Martin, M.W. Oh, W.D. Porter, Z. Ren, J. Salvador, J. Sharp, P. Taylor, A.J. Thompson, Y.C. Tseng, International round-robin study of the thermoelectric transport properties of an n-type half-Heusler compound from 300 K to 773 K, *J. Electron. Mater.* 44 (11) (2015) 4482–4491.
- [55] E. Alleno, D. Bérardan, C. By, C. Candolfi, R. Daou, R. Decourt, E. Guilmeau, S. Hébert, J. Hejtmanek, B. Lenoir, P. Masschelein, V. Ohorodnichuk, M. Pollet, S. Populoh, D. Ravot, O. Rouleau, M. Soulier, Invited article: a round robin test of the uncertainty on the measurement of the thermoelectric dimensionless figure of merit of  $\text{Co}_{0.97}\text{Ni}_{0.03}\text{Sb}_3$ , *Rev. Sci. Instrum.* 86 (1) (2015) 011301.
- [56] H. Wang, R. McCarty, J.R. Salvador, A. Yamamoto, J. König, Determination of thermoelectric module efficiency: a survey, *J. Electron. Mater.* 43 (6) (2014) 2274–2286.
- [57] “Standard Test Method for Evaluating the Resistance to Thermal Transmission by the Guarded Heat Flow Meter Technique”, ASTM E1530-19.
- [58] “Standard Test Method for Thermal Transmission Properties of Thermally Conductive Electrical Insulation Materials”, ASTM D5470-17.
- [59] T.C. Harman, J.H. Cahn, M.J. Logan, Measurement of thermal conductivity by utilization of the Peltier effect, *J. Appl. Phys.* 30 (1959) 1351.
- [60] G. Gromov, D. Kondratiev, A. Rogov, L. Yershova, Z-meter: easy-to-use application and theory, in: Proceedings. Sixth European Workshop on Thermoelectricity of the European Thermoelectric Society Freiburg im Breisgau, September 20-21, 2001, pp. 1–8.
- [61] G.L. Bennett, J.J. Lombardo, R.J. Hemler, G. Silverman, C.W. Whitmore, W.R. Amos, E.W. Johnson, A. Schock, R.W. Zocher, T.K. Keenan, J.C. Hagan, R.W. Englehart, Mission of daring: the general-purpose heat source radioisotope thermoelectric generator, in: 4th International Energy Conversion Engineering Conference and Exhibit (IECEC) San Diego, California, 26–29 June, 2006.

# Evaluation method and measurement example of thermoelectric devices and modules

3.5

Satoaki Ikeuchi

ADVANCE RIKO, Inc., Yokohama, Japan

## 3.5.1 Introduction

Thermoelectric materials can convert electricity into heat directly. Their practical use is expected at a point to reuse unused heat. Particularly, in the field of IoT, it attracts attention space-saving, to convert into electricity from heat directly. As the thermoelectric materials carry away electricity, the temperature difference at the both ends of materials is caused by the Peltier effect. However, the temperature difference at the both ends of materials generates voltage due to Seebeck effect. If the resistance is connected with both ends of materials, electricity is generated. On the basis of these theories, various applications are put to practical use. In thermoelectric power generation, the output power and the conversion efficiency in large temperature difference are regarded as important. In this chapter, I discuss a theory and method for the measurement of thermoelectric power generation.

## 3.5.2 Theory

A schematic image is shown in Fig. 3.5.1. There is the thermoelectric module between a hot side and a cold temperature side. The resistance leads to the thermoelectric module. If the temperature difference is given, the voltage difference occurs at the both ends of the thermoelectric module. As there is voltage difference at both the ends of the resistor, the resistance generates electricity. It is defined as the heat flow from the hot side to the thermoelectric module ( $Q_h$  [W]), the heat flow from the thermoelectric module to cold side ( $Q_c$  [W]), and the output power in resistor ( $P$  [W]). The thermoelectric conversion efficiency ( $\eta$  [ ]) is expressed by the following equation:

$$\eta = \frac{P}{Q_h} = \frac{P}{Q_c + P} \quad (3.5.1)$$

To evaluate the maximum output power and conversion efficiency, it is an ideal to perform electrical measurement by changing resistance. In practice, the voltage of

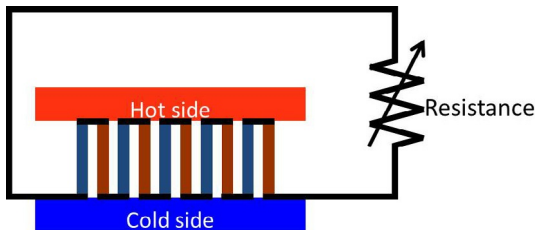


**Fig. 3.5.1** Schematic image in thermoelectric generation.

the module ( $V(I)$  [V]) is measured by changing the load electric current ( $I$  [A]). The current dependence of the output power ( $P(I)$  [W]) is given in the following equation.

$$P(I) = V(I)I = (V(0) - RI)I \quad (3.5.2)$$

where  $V(0)$  (V) and  $R$  ( $\Omega$ ) are the open-circuit voltage of the module and the internal resistance of the module, respectively. The maximum output power ( $P_{\max}$  [W]) is expressed by the following equation.

$$P_{\max} = \frac{V(0)^2}{4R} \quad (3.5.3)$$

However, when the load electric current is added, the heat flow of the low-temperature side ( $Q_c(I)$  [W]) is expressed by the following equation:

$$Q_c(I) = Q_c(0) + \frac{T_c}{T_h - T_c} V(0)I + \frac{1}{2}RI^2 \quad (3.5.4)$$

where  $Q_c(0)$  (W),  $T_h$  (K), and  $T_c$  (K) are the heat flow of low-temperature side when the load electric current is zero, the temperature of the high-temperature side of the module, and the temperature of the low-temperature side of the module, respectively. The contribution of the module is shown on the right-hand side of Eq. (3.5.4). Clause 1 is the contribution of the thermal resistance, and Clause 2 is the contribution of the Peltier effect, and Clause 3 is the contribution of the Joule fever. The conversion efficiency is expressed by the following equation from Eqs. (3.5.1), (3.5.2), and (3.5.4).

$$\eta(I) = \frac{V(0)I - RI^2}{Q_c(0) + \frac{T_h}{T_h - T_c} V(0)I - \frac{1}{2}RI^2} \quad (3.5.5)$$

When it is assumed that the dimensionless figure of merit ( $\bar{\tau}_{\frac{T_h+T_c}{2}}$  []) does not change between  $T_h$  and  $T_c$ , the maximum conversion efficiency is expressed by the following equation:

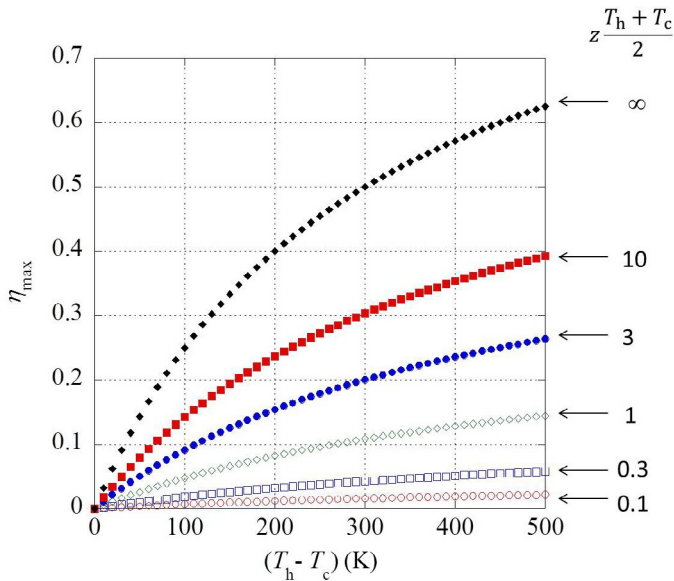


**Fig. 3.5.2** Temperature difference dependence of the conversion efficiency in each dimensionless figure of merit ( $z \frac{T_h + T_c}{2}$ ). It is assumed that  $z \frac{T_h + T_c}{2}$  does not change between  $T_h$  and  $T_c$  and  $T_c$  is 300 K.

$$\eta_{\max} = \frac{T_h - T_c}{T_h} \frac{\sqrt{1 + \frac{1}{2}(T_h + T_c)z} - 1}{\sqrt{1 + \frac{1}{2}(T_h + T_c)z} + \frac{T_c}{T_h}} \quad (3.5.6)$$

The temperature difference dependence of the conversion efficiency is shown in Fig. 3.5.2, in which  $T_c$  is assumed to be 300 K. As the dimensionless figure of merit becomes big, the conversion efficiency becomes big. In the case of  $z \frac{T_h + T_c}{2} \rightarrow \infty$ , the conversion efficiency gets closer to the Carnot efficiency, but cannot exceed it. The thermoelectric conversion obeys the thermodynamic the second law of thermodynamics.

### 3.5.3 Instrument

The schematic image of the evaluation instrument is shown in Fig. 3.5.3. The evaluation instrument of the thermoelectric module consists of the heating block, the heat flow measurement block on the high-temperature side, the sample, the heat flow measurement block on the low-temperature side, the cooling block, and the output power measurement block. In practice, the contact material such as the carbon sheet

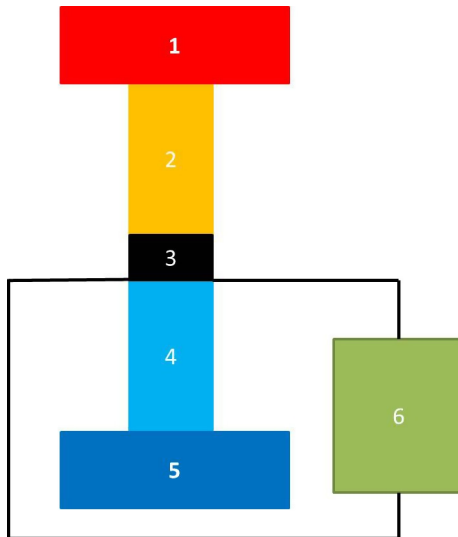


**Fig. 3.5.3** Schematic image in the module evaluation instrument: (1) Heating block, (2) heat flow measurement block to high-temperature side, (3) sample, (4) heat flow measurement block to low-temperature side, (5) cooling block, (6) output power measurement block.

is used to reduce thermal resistance between the sample and the block of the heating (cooling) side. Depending on coverage, the individual constitution differs depending on coverage.

The schematic image of the production instruments (PEM-2, Mini-PEM, F-PEM) is shown in Fig. 3.5.4. The constitution differs depending on use. The high temperature side does not have the heat flow measurement block in all instruments. The reason is that the temperature of the high-temperature side of the sample is hard to rise, and the heat flow measurement is difficult because of thermal radiation on the high-temperature side.

The heat flow measurement method varies depending on the instrument. Fig. 3.5.4A depicts the method where the cooling block becomes different from the heat flow measurement block; however, Fig. 3.5.4B and C shows the method where the cooling block is united with the heat flow measurement block. The constitution shown in Fig. 3.5.4C is almost practical use.

The measured temperatures  $T_1(K)$  and  $T_2(K)$  on the heat flow measurement block is shown in Fig. 3.5.4A. This method is based on the temperature gradient method. If the thermal conductivity ( $\lambda[W\ m^{-1}\ K^{-1}]$ ) and the cross-sectional area ( $A [m^2]$ ) of the heat flow measurement block, and the distance ( $d [m]$ ) between  $T_1$  and  $T_2$  are known, the heat flow can be calculated by Fourier's law.

$$Q_c = \frac{\lambda}{d} \frac{T_1 - T_2}{A} \quad (3.5.7)$$

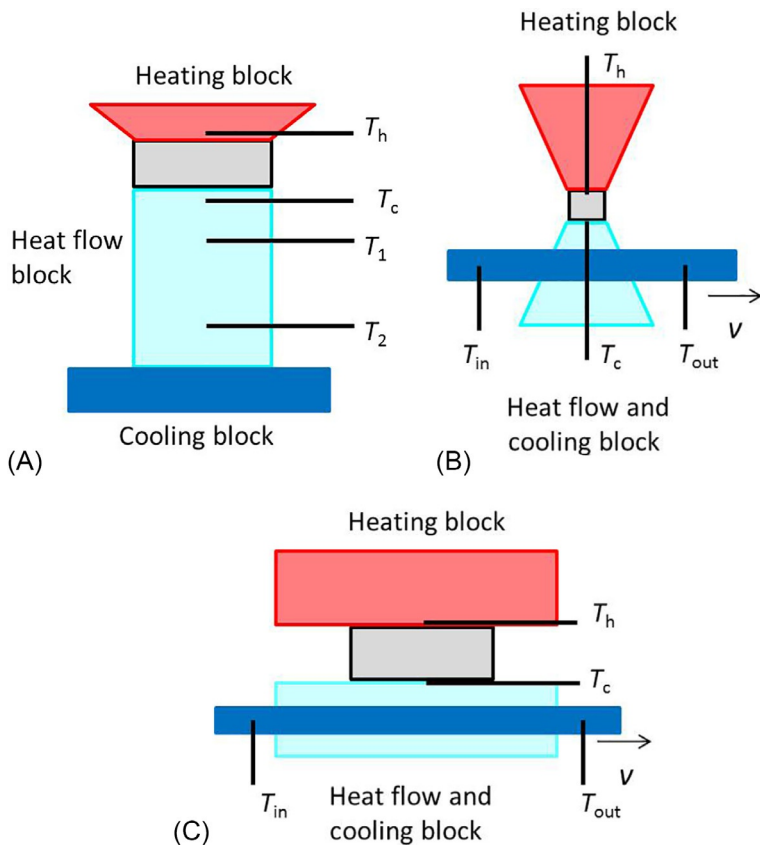


**Fig. 3.5.4** Schematic image in production instruments. (A) PEM-2, (B) Mini-PEM, and (C) F-PEM.

If there is no heat exchange between the heat flow measurement block and the outside world, the heat flow can be evaluated accurately.

The inlet temperature ( $T_{\text{in}}$  [K]) and the outlet temperature ( $T_{\text{out}}$  [K]) of a fluid in the cooling block are shown in Fig. 3.5.4B and C. This method is based on the flow calorimeter. If the flow rate ( $v$  [ $\text{m}^3 \text{s}^{-1}$ ]) and the heat capacity per volume ( $C$  [ $\text{J m}^{-3} \text{K}^{-1}$ ]) of the fluid are known, then the heat flow is expressed by the following equation:

$$Q_c = C v (T_{\text{out}} - T_{\text{in}}) \quad (3.5.8)$$

If we consider the heat exchange between the cooling block and the outside world and measure the changing flow rate, the heat flow can be evaluated accurately [1].

### 3.5.4 Measurement example

The measurement result in a commercial Peltier module of 10mm square by Mini-PEM is shown in Figs. 3.5.5–3.5.7. I measured at 100°C of the high temperature block in vacuum. The time dependence of the temperature of the high-temperature side of the module ( $T_h$ ) and the temperature of the low-temperature side of the module ( $T_c$ ) is shown in Fig. 3.5.5A. The time dependence of the module voltage ( $V_{\text{meas}}$ ) and the load electric current ( $I$ ) is shown in Fig. 3.5.5B. The time dependence of the heat flow of low-temperature side ( $Q_c$  meas) is shown in Fig. 3.5.5C. When the load electric current was added,  $T_h$  decreased but  $T_c$  increased. This depends on the Peltier effect. When the load electric current was added,  $Q_c$  increased. This agrees with a tendency of Eq. (3.5.4). The increased share of  $Q_c$  meas by the electrical contribution agreed with

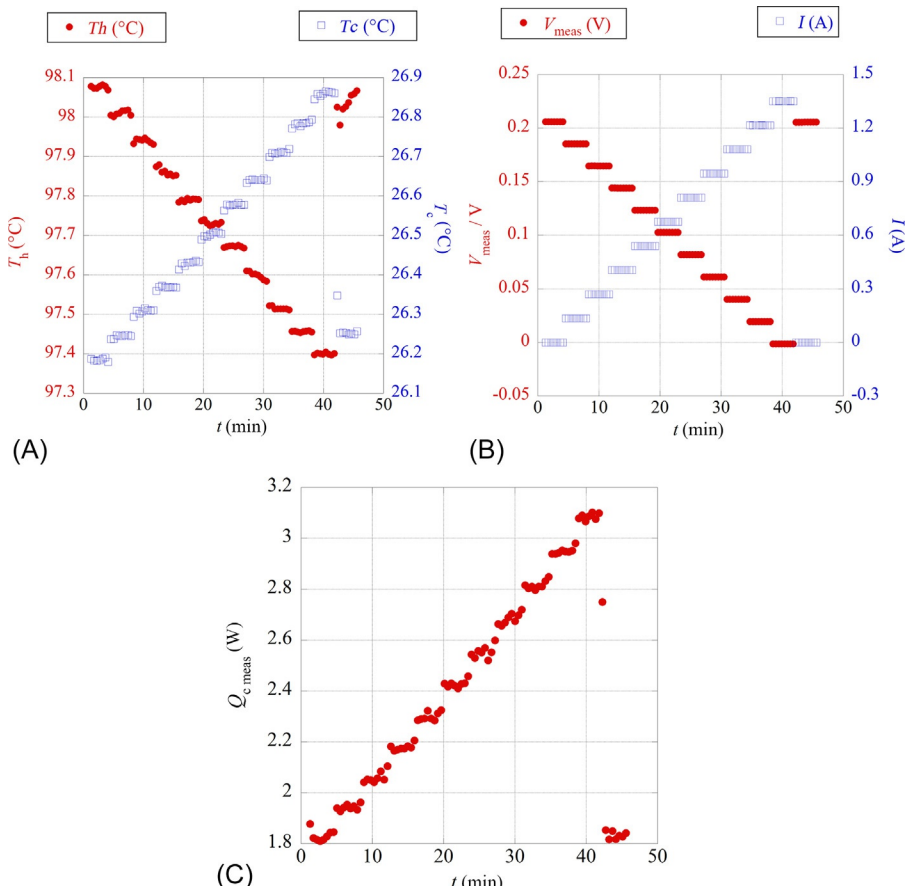


**Fig. 3.5.5** Measurement result by Mini-PEM in a commercial Peltier module of 10mm square. Time dependence of (A)  $T_h$  (closed circle) and  $T_c$  (open square), (B)  $V_{\text{meas}}$  (closed circle) and  $I$  (open square), and (C)  $Q_c$  meas.

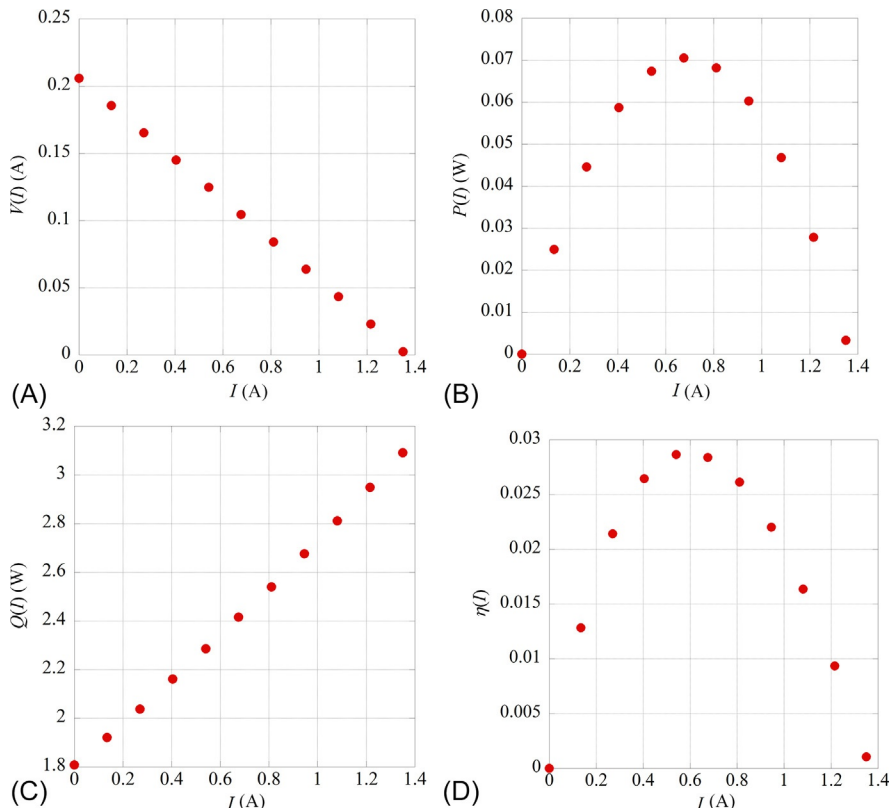


Fig. 3.5.6 Measurement result by Mini-PEM in commercial Peltier module of 10mm square. Current dependence of (A)  $V(I)$ , (B)  $P(I)$ , (C)  $Q(I)$ , and (D)  $\eta(I)$ .

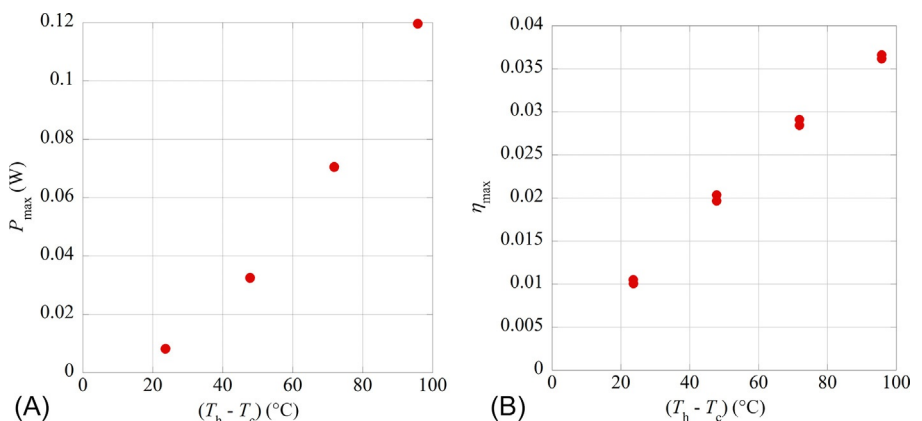
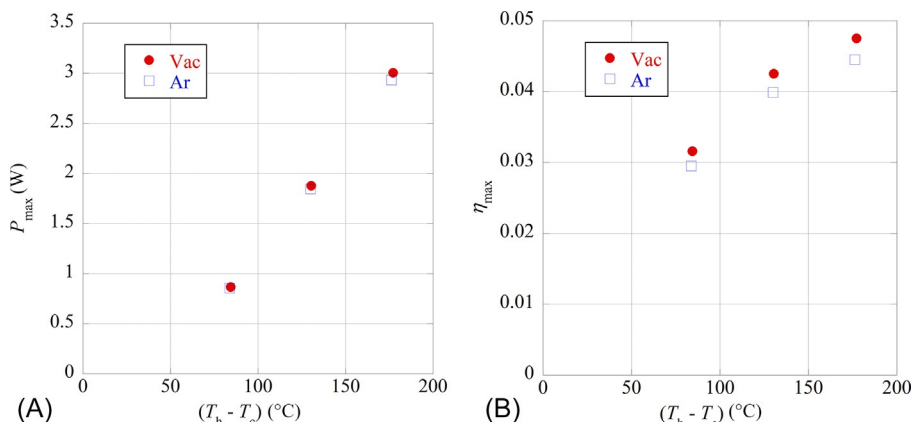


Fig. 3.5.7 Measurement result by Mini-PEM in commercial Peltier module of 10mm square. Temperature difference dependence of (A)  $P_{\max}$  and (B)  $\eta_{\max}$ .

less than 5% of the calculated value based on Eq. (3.5.4) from the electrically measurement result. This measurement result is shown in Fig. 3.5.6 with the current dependence. The current dependence of the sample voltage ( $V(I)$ ) is shown in Fig. 3.5.6A. From this result, the open-circuit voltage ( $V(0)$ ) and the resistance in the module ( $R$ ) can be evaluated. The current dependence of the output power ( $P(I)$ ) is shown in Fig. 3.5.6B. From this result, the maximum output power in the module ( $P_{\max}$ ) can be evaluated. The current dependence of the heat flow of low-temperature side ( $Q(I)$ ) is shown in Fig. 3.5.6C. The current dependence of the conversion efficiency ( $\eta(I)$ ) is shown in Fig. 3.5.6D. From this result, the maximum conversion efficiency in the module ( $\eta_{\max}$ ) can be evaluated. The measurement result of the current dependence has much information. It is necessary to select what you evaluate depending on the purpose. For example, the temperature difference dependence of  $P_{\max}$  is shown in Fig. 3.5.7A, and the temperature difference dependence of  $\eta_{\max}$  is shown in Fig. 3.5.7B.

The measurement result in the commercial Peltier module of 30 mm square by PEM-2 in vacuum and decompression Ar is shown in Fig. 3.5.8. The temperature difference dependence of  $P_{\max}$  is shown in Fig. 3.5.8A, and the temperature difference dependence of  $\eta_{\max}$  is shown in Fig. 3.5.8B.  $P_{\max}$  in vacuum is the same as that in decompression Ar; however,  $\eta_{\max}$  in vacuum is clearly bigger than that in decompression Ar. This shows that  $Q_c(I)$  in vacuum is smaller than that in decompression Ar. This phenomenon shows that the heat reaches the heat flow measurement block by gas conduction in decompression Ar.

For the practical use of the thermoelectric module, it is necessary to perform an endurance test in the atmosphere. I pick up two as an example of the endurance tests. I tried a performance test while changing the temperature of the high temperature side between the low temperature and the high temperature repeatedly. The deterioration situation of the module can be provided from cyclic number of times dependence of the performance. By F-PEM, the result of the cycling test between 500°C and 100°C in



**Fig. 3.5.8** Measurement result by PEM-2 in commercial Peltier module of 30mm square. Temperature difference dependence of (A)  $P_{\max}$  and (B)  $\eta_{\max}$ .

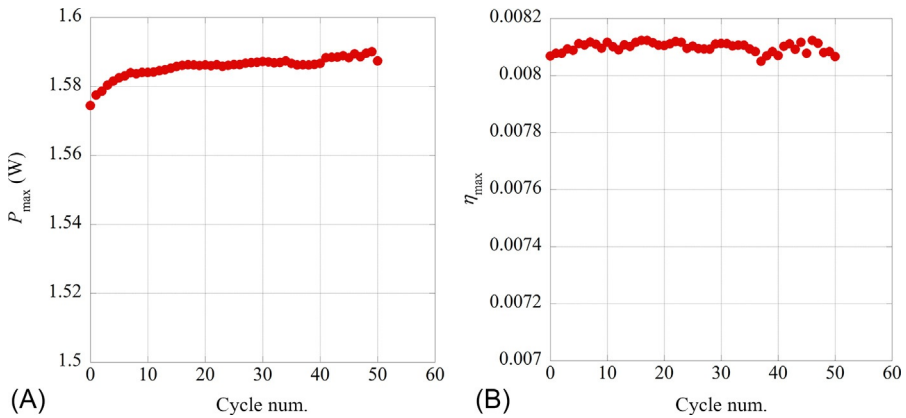


**Fig. 3.5.9** Cyclic test result by F-PEM in oxidation module of 35 mm square in the atmosphere. Cyclic number dependence of (A)  $P_{\max}$  and (B)  $\eta_{\max}$ .

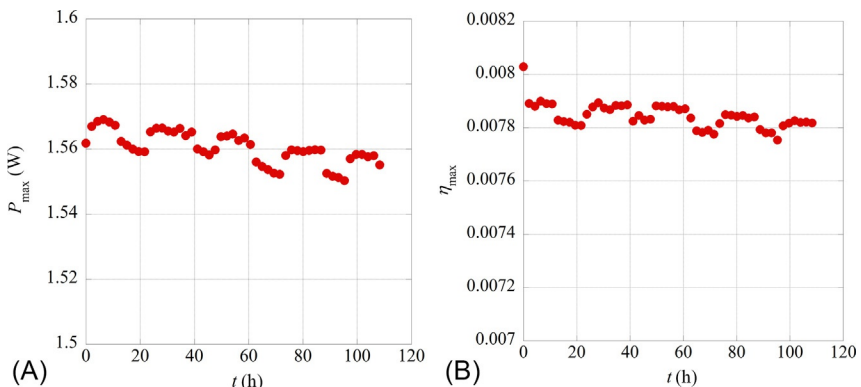


**Fig. 3.5.10** Maintenance test result by F-PEM in oxidation module of 35 mm square in the atmosphere. Maintenance time dependence of (A)  $P_{\max}$  and (B)  $\eta_{\max}$ .

the oxidation module [2] of 35 mm square in the atmosphere is shown in Fig. 3.5.9. The performance test at high temperature is regularly performed in the state that maintains the temperature of the high-temperature side. The deterioration in the module can be confirmed from the long time dependence of the performance. By F-PEM, the result of the maintenance test at 500°C in the oxidation module of 35 mm square in the atmosphere is shown in Fig. 3.5.10. The oxidation module does not deteriorate.

### 3.5.5 Summary

About the evaluation method of the thermoelectric module, I wrote down the measurement principle and example. Many evaluation results were reported in the single device [3], unicouple module [1], and multicouple module [4–6]. Wang et al. have

reported the investigation result of the evaluation of the thermoelectric module [7]. Standardization of the evaluation method of the thermoelectric module is expected. In future, it will be necessary to decide the measurement result and the evaluation quantity, depending on the use of the thermoelectric module.

## References

- [1] X. Hu, K. Nagase, P. Jood, M. Ohta, A. Yamamoto, *J. Electron. Mater.* 44 (2015) 1785–1790.
- [2] R. Funahashi, T. Barbier, E. Combe, *J. Mater. Res.* 30 (2015) 2544–2557.
- [3] R. Cherry, Y. Kikuchi, Y. Bouyrie, P. Jood, A. Yamamoto, K. Suekuni, M. Ohta, *J. Mater. Chem. C* 7 (2019) 5184–5192.
- [4] P. Jood, M. Ohta, A. Yamamoto, M.G. Kanatzidis, *Joule* 2 (2018) 1339–1355.
- [5] C. Fu, S. Bai, Y. Liu, Y. Tang, L. Chen, X. Zhao, T. Zhu, *Nat. Commun.* 6 (2015) 8144.
- [6] R. Funahashi, et. al., to be submitted.
- [7] H. Wang, R. McCarty, J.R. Salvador, A. Yamamoto, J. König, *J. Electron. Mater.* 43 (2014) 2274–2286.

# Thermoelectric air cooling

4.1

Kashif Irshad

Center of Research Excellence in Renewable Energy (CoRE-RE), King Fahd University of Petroleum & Minerals, Dhahran, Saudi Arabia

## 4.1.1 Introduction

The energy crisis and global rise in temperature have become the focus of attention all over the globe. Since past 30 years, this crisis has become worse due to significant increase in world population and gross per capita income [1]. The major contributor to this energy crisis is the increase in high-energy intensive heating ventilation and air conditioning (HVAC) systems in buildings [2]. Recent published report suggests that buildings account for more than 40% of the overall consumption of energy [3]. A significant portion of energy is consumed for providing thermal comfort to the occupants by using HVAC systems [4]. The human beings have become so dependent on artificial thermal comfort system that large developed countries cannot sacrifice thermal comfort and IEQ for energy conservation and consume as much as 30% of total energy consumption in China [5], 40% in the United States [6], and 20%–40% in the rest of the developed countries. HVAC market was dominated by the products based on vapor-compression technologies, but these systems cause irreparable damage to the global environment due to the use of harmful refrigerants. Researchers have proposed phase down of hydrofluorocarbon (HFC) refrigerants for next 20 years to partially shift the issues but for long-term benefits movement of cooling technologies away from vapor-compression technologies is very essential. Thermoelectric cooling come out to be more promising nonvapor-compression technology, with advantages such as light and compact size and weight, requires no moving equipment, high reliability, no operational noise, and more notably is its direct current operation which opens door for direct link between solar photovoltaic system and thermoelectric cooling system.

In this chapter, an overview of various thermoelectric coolers implemented in the building for thermal load reduction is reviewed. The chapter starts by describing the basics of thermoelectric module (TEM) and its dependent parameters, which enhance its performance. Then the integration of thermoelectric cooling technology in the building and its benefits with respect to building energy consumption are presented. In addition, TEM as an alternative to conventional space conditioning technology is reviewed. Finally, literatures focusing on the integration of two systems, i.e., thermoelectric and photovoltaic systems for building applications and potential challenges in the implementation of TEMs as an alternative to conventional HVAC system are also presented.

### 4.1.2 Principles of thermoelectric air cooling

A conventional single-stage TE cooler is made out of N-type and P-type semiconductor intersections that are thermally connected in parallel but electrically connected in series through metallic strips made up of copper. The heat is transferred from one face of thermoelectric cooler (TEC) to other face by applying DC power across the junction as shown in Fig. 4.1.1.

The four basic characteristic equations used to identify every TECs such as  $I_{max}$ ,  $V_{max}$ ,  $\Delta T_{max}$ , and  $Q_{max}$  are defined as follows [7, 8]:

$$S_m = \frac{V_{max}}{T_{hot}} \quad (4.1.1)$$

$$R_m = \frac{(T_{hot} - \Delta T_{max})V_{max}}{T_{hot}I_{max}} \quad (4.1.2)$$

$$K_m = \frac{(T_{hot} - \Delta T_{max})V_{max}I_{max}}{2T_{hot}\Delta T_{max}} \quad (4.1.3)$$

The energy absorbed and dissipated from the hot side and cold side of TEMs can be calculated by applying energy balance equation [7, 8].

$$Q_{cold} = S_m I T_{cold} - \frac{I^2 R_m}{2} - K_m \Delta T \quad (4.1.4)$$

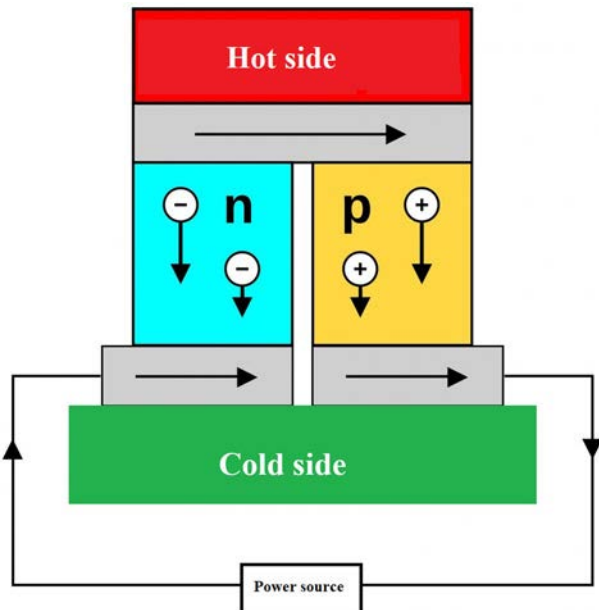


**Fig. 4.1.1** Working diagram of thermoelectric cooler.

$$Q_{hot} = S_m I T_{hot} - \frac{I^2 R_m}{2} - K_m \Delta T \quad (4.1.5)$$

The difference in temperature from both sides of TEMs can be obtained as

$$\Delta T = T_{hot} - T_{cold} \quad (4.1.6)$$

The power consumption by thermoelectric coolers can be obtained by applying the first law of thermodynamics as

$$P_{TEC} = Q_{hot} - Q_{cold} \quad (4.1.7)$$

By putting equations of  $Q_{hot}$  and  $Q_{cold}$  in Eq. (4.1.7) we get

$$P_{TEC} = S_m I \Delta T + I^2 R_m \quad (4.1.8)$$

Now, the heat transfer occurring between TECs and the air inside the air duct system can be calculated as

$$Q_{cold} = \dot{m}_{cold} C_p \Delta T_{cold} (h_{air,in,c} - h_{air,out,c}) \quad (4.1.9)$$

$$Q_{hot} = \dot{m}_{hot} C_p \Delta T_{hot} (T_{air,out,h} - T_{air,in,h}) \quad (4.1.10)$$

By definition the coefficient of performance can be calculated as

$$COP = \frac{Q_{cold}}{P_{TEC}} \quad (4.1.11)$$

This was also suggested from Eqs. (4.1.4) to (4.1.5) that heating and cooling intensity of the TEMs depend on input current. The increase in heat dissipation and absorption capacity of TEMs installed inside an air duct system increases water condensate production. This behavior change is due to the configuration of TEMs, having many pairs of Bismuth Telluride sandwiching between two ceramic layers. The pairs are connected thermally in parallel and electrically in series. Each pair consists of P-type and N-type materials forming a couple having different electron densities at the same time. N-type pairs are made up of materials having excess of electrons while P-type pairs have deficiency of electrons. A new equilibrium establishes inside the materials as direct current starts flowing up and down through the module. The input DC current starts treating P-type pair as hot side wanting to be cooled and the N-type as cold side wanting to be hot. Since the material is at a similar temperature, the outcome is that the hot side ends up being more hot while the cool side ends up colder. The cooling capacity of TECs depends on parameters such as input current  $I$  (Eqs. 4.1.4, 4.1.5), hot and cold side temperatures (Eqs. 4.1.4, 4.1.5), electrical resistance generated due to contact  $R$  (Eq. 4.1.2), P- and N-type thermoelement, and electrical and thermal conductivities ( $\lambda, \sigma$ ).

### 4.1.3 Performance index

The performance index equation of TEC can be derived by substituting  $Q_{cold}$  from Eq. (4.1.4) and power consumption of TEC from Eq. (4.1.8) in Eq. (4.1.11)

$$COP = \frac{S_m IT_{cold} - \frac{I^2 R_m}{2} - K_m \Delta T}{S_m I \Delta T + I^2 R_m} \quad (4.1.12)$$

The optimum current induced by TEC produces optimum COP and is given by

$$I_{opt} = \frac{S_m \Delta T / R}{\sqrt{1 + ZT_m} - 1} \quad (4.1.13)$$

Thus, the optimum COP can be obtained as

$$COP_{max} = \frac{T_c}{T_h - T_c} \frac{\sqrt{1 + ZT_m} - \left(\frac{T_h}{T_c}\right)}{\sqrt{1 + ZT_m} + 1} \quad (4.1.14)$$

The classical COP equation can be written as

$$COP = COP_c \times COP_r \quad (4.1.15)$$

The COP depends on figure of merit  $ZT$  of TEC, which further depends on temperature of the cold and hot side of the module. Eq. (4.1.15) further depends on electrical contact resistance, thermal resistance, material temperature characteristic, and Thomson effect.

Min et al. [9] found that when thermal and electrical contact resistances were neglected, the COP of TEC was not dependent on the length of thermoelement. The figure of merit  $Z$  of TEC based on electrical resistance is given by

$$Z = \frac{zx}{x+n} \quad (4.1.16)$$

The term  $n$  depends on the resistivity of electrical contact between copper stripes and thermoelements and on the thermoelement electrical resistivity. The COP of TEC as presented in Eq. (4.1.15) can be changed by considering electrical contact resistance as

$$COP = COP_c \left( \frac{\sqrt{1 + \left(\frac{zx}{1+n}\right) T_m} - \left(\frac{T_h}{T_c}\right)}{\sqrt{1 + \left(\frac{zx}{1+n}\right) T_m} + 1} \right) \quad (4.1.17)$$

The existing theory is legitimate with long thermoelements, as the COP increases for increasing thermoelement length [10]. However, for thermoelement with shorter length, the contact resistance turns out to be close to the leg resistance, influencing the COP more effectively.

The Thomson effect produces in TEMs when electric current flow through it. Thus heat is absorbed when the electric current flows from the colder region to the hotter region whereas heat is dissipated when electric current flows from the hotter region to the colder region. The heat flux generated from the TEMs is proportional to the product of electric current and thermal gradient and can be defined as

$$Q = -\tau I \nabla T \quad (4.1.18)$$

The constant of proportionality is known as the Thomson coefficient and has a significant effect on the COP of the TEMs.

#### **4.1.4 Application areas of thermoelectric air cooling**

Cooling application areas of TEM are limited because of low COP. Application of TEM is found in the areas where COP is not as essential as energy accessibility, silent operation, such as reliability, electronic hardware, and space missions. However, with the advancement of technology, more new areas of applications are coming out. So, the cooling application of TEM is broadly classified into five categories:

1. Scientific instruments, medical instruments, and laboratory equipment cooling [11, 12].
2. Cooling of small enclosures such as picnic baskets, portable icebox, portable refrigerator, etc. [13, 14]
3. Automobile industry such as heating and cooling of seats [15], mini refrigerators, and air-conditioning [16].
4. Electronic devices and industrial temperature controller [17, 18].
5. Finally, a few researchers are making advancement in thermoelectric household air-conditioning system [19, 20] to compete and to find an alternative to high energy comprising conventional vapor-compression system.

##### **4.1.4.1 Thermoelectric application in buildings**

###### **4.1.4.1.1 Energy recovery system**

The energy recovery system is gaining attention nowadays due to increase in fuel price globally. In buildings different technologies are used for energy recovery such as liquid desiccant [21], heat exchanger and pipe [22], absorption refrigeration [23], and TEC technology [24]. Incorporation of this system into the existing system can minimize energy input and enhance the efficiency of the system. Li et al. [25] examined a novel lab scale model of residential thermoelectric ventilator. Framework is made out of air conduit, two fans, TEMs, aluminum heat exchanger, and heat sinks. The performance of household thermoelectric ventilator framework in both warming and cooling mode was investigated under various working voltages. The optimum COP

of 2.5 was accomplished in both warming and cooling modes at working voltages of 12 V and 8 V, respectively. Moreover, hardly any issues arises in the above framework such as complex pipeline and wet-surface heat exchangers, which result in ashes deposition, increment in thermal resistance, and decrement in quality of air and noise. Han et al. [26] analyzed mathematically the behavior of TE ventilator. The outcomes show that at lower outside air temperature optimum COP of 4.78 was accomplished in summer season while in winter season the optimum COP of 4.16 was accomplished at higher natural air temperature. Zhongbing et al. [27] examined a TE water radiator of capacity 36 L attached to the exhaust of kitchen. The outcome shows that the temperature of water increases from 28°C to 46°C at working voltage of 20V. This framework abbreviates warming time and diminishes 30% of intensity utilization when compared with regular electric water radiators. It was recommended that the COP of the framework could be improved by decreasing the temperature contrast between the hot and the cold side of the TEMs, limiting water temperature and expanding exhaust temperature. Luo et al. [28] experimentally evaluated the performance of thermoelectric water heater system. The outcomes show that at various stream rates water temperature reaches 40°C with 1.45 as energy efficiency ratio, as compared with an electric water radiator with EER of just 0.9. This system reduces 38% more electric energy consumption as compared with conventional one.

Recently, solar PV-driven and TEM-assisted heat recovery system are gaining attention. Liu et al. [29] both experimentally and numerically analyzed the performance of photovoltaic thermal-compound thermoelectric ventilator (PVT-TEV) system. This system provides many benefits such as power generation, shading from sun, recovery of waste heat, and provides fresh air to the buildings. The result shows that as the air volume of fresh air increases from 63 to 153 m<sup>3</sup>/h, electrical efficiency of system increases from 12.03% to 13.31% but COP of the system remain almost unchanged. Further, Liu et al. [30] experimentally investigated the performance of PVT-TEV system for summer and winter climatic condition. The result shows that more heat gain produces more fresh air and during full sunny day thermal efficiency of 26.7% and COP (heating) of 6.4 were achieved. Liu et al. [31] investigated the performance of solar-driven exhaust air thermoelectric heat pump recovery (SDEATHP) system as shown in Fig. 4.1.2. The result shows that average relative heating and cooling coefficient of framework reaches 57.9 and 50.6, respectively.

#### 4.1.4.1.2 Heat ventilation and air-conditioning system

The utilization of TE for air-conditioning purposes is gaining more attention nowadays due to highly reliable operation and no moving parts. Lertsatitthanakorn et al. [32] examined TE cooling unit introduced on the roof. Two heat exchangers, one joined on the evaporator side was utilized to disperse heat generated from the source and other appended on the condenser side, were utilized to dispose of heat to the encompassing environment. The outcome shows that at input current of 3 A, cooling limit of 169 W was accomplished. Nonetheless, in this investigation execution parameters, for example, COP, flow rate of air, Z value of TEMs, were not considered. Maneewan et al. [33] build up a TE cooling framework by executing three TEMs for small area cooling usage. At a working electric current of 1 A, COP of 0.34 and cooling limit

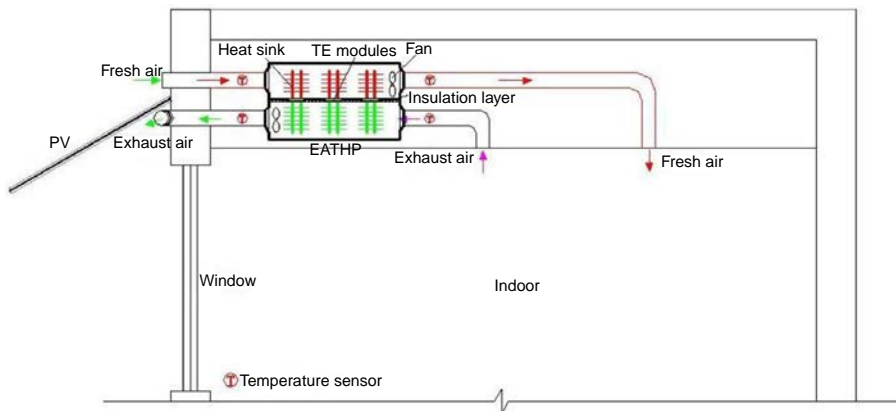


**Fig. 4.1.2** Schematic diagram of solar-driven exhaust air thermoelectric heat pump recovery system [31].

of 29.2 W were accomplished. Gillott et al. [19] explored the impact of TEMs on cooling applications for small-scale buildings. Results show that greatest cooling limit of 220 W and COP of 0.46 were accomplished when TE cooling unit was operated at input electrical flow supply of 4.8 A to every module. The examinations [17, 19, 20] mostly centered around the small-scale research facility model, however the investigation on the heat transfer and performance TEMs in real transient climatic conditions was not revealed. Additionally, techno-economic analysis and thermal comfort analysis of building having TEMs air-cooling systems were not researched. Riffat and Qiu [34] compared performance of vapor compression air-cooling system (VCAS) with TEM air-cooling system. Results demonstrated that the COPs of VCAS ranges between 2.6 and 3.0 while TE air-cooling system was in the range 0.3–0.45. Cosnier et al. [35] examined air warming and cooling limit of TEMs both numerically and experimentally. It was discovered that when the TEM was operated at the input electrical flow supply of 4 A, cooling limit of 50 W for every module, with a temperature distinction of 5°C among hot and cold sides and COP between 1.5 and 2, was accomplished. Lertsatithanakorn et al. [36] changed the normal roof of the test bed having volume 4.5 m<sup>3</sup> with thermoelectric ceiling cooling (TE-CCP) framework and assessed its impact on the cooling execution and comfort. Framework execution was upgraded by appending copper heat exchanger with coursing cooling water on the hot side of TEM and the aluminum roof board on the cold side of TEM. Results show that the TE-CCP framework when worked at 1 A input current produces 201.6 W cooling limit with a COP of 0.82 and normal indoor temperature and air speed of 27°C and 0.8 m/s, respectively. Additionally, over 80% of tenants thermally satisfied and met ASHRAE Standard-55's 80% adequacy criteria. Shen et al. [37] replaced hydronic panel with thermoelectric radiant panel and developed a prototype of thermoelectric radiant air-conditioning (TE-RAC) system. This system was used for dual purposes and obtained optimum performance at input current of 1.2 A. Nonetheless, Hermes and Barbosa [38] presumed that the existing TEMs have just 1% thermodynamic effectiveness when compared with vapor compression and Stirling reciprocating



**Fig. 4.1.3** Working model of thermoelectric air duct cooling system [40].

refrigeration frameworks, which have a 14% thermodynamic efficiency. So to improve execution of the TE cooling framework, Tipsaenporm et al. [39] applied direct evaporative cooling methods that helped with diminishing the temperature of the hot side of TEM by providing cooled air. The cooling intensity of conservative TE forced air system was expanded from 53.0 to 74.5 W. Kashif et al. [40] developed an air duct system by integrating 24 TEMs as shown in Fig. 4.1.3. The result shows that by increasing input current to the thermoelectric air duct (TE-AD) system, COP and cooling capacity of the system increase. The system performance based on occupants comfort criteria was also evaluated [41]. The reduction of 5.3°C temperature was achieved with COP ranging from 0.6 to 1.15.

#### 4.1.4.2 Hybrid systems

Thermoelectric cooling system powered by solar PV system reduces the overall operation cost of the system. Without utilizing any additional equipment, direct electrical current was utilized by TEMs. The application of solar-assisted TE technologies is classified as follows.

##### 4.1.4.2.1 Active building envelope system

By affixing TEMs and PV cell over the surface of the buildings, an active building envelope system (ABE) could be developed which will control cooling and heating load of the buildings. TEC and solar PV system combined are together to form one surface enclosure. The direct electrical current produced by PV cell was used to provide input power to the TEMs for both heating and cooling purposes as per the direction of input current [42]. As shown in Fig. 4.1.4, active building wall (ABW) was established by integrating the TEM and solar PV unit that can control heat flux passing through the wall [44]. The configuration of ABW consists of solar PV panel, then air channel, then layer of TEMs, and finally the wall. Analytical model of ASW was developed by Khire et al. [44] and Van Dessel and Foubert [45]. Experimental study

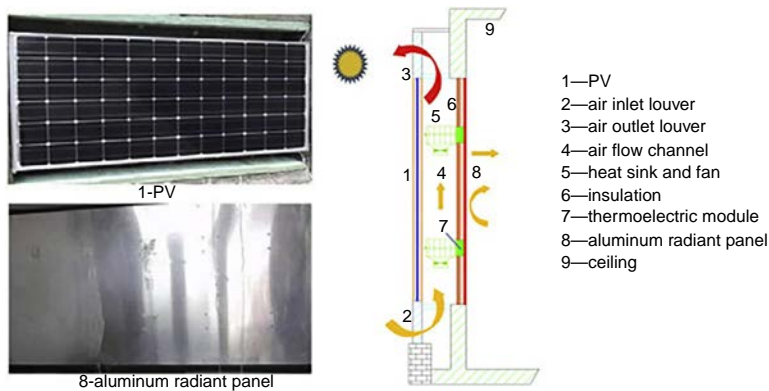


**Fig. 4.1.4** Working model of active wall system [43].

was carried out by Liu et al. [46] and result shows that the solar-assisted thermoelectric radiant wall (ASTRW) not only reduces the thermal load of building but also give cooling comfort to the occupants. Liu et al. [43] further tested ASTRW for winter climatic condition. The result shows that thermal efficiency of 34.2% and COP of 2.3 can be reached at solar insolation of  $325 \text{ W/m}^2$  and heating capacity of  $111 \text{ W/m}^2$ . The PV-integrated TE system was also used in window technology by Xu and Van Dessel [47]. The result shows that eight TEC can decrease indoor temperature by  $2\text{--}6^\circ\text{C}$  with an efficiency of 5% in cooling mode and 13% in heating mode. Lewis et al. [48] controlled the heat input inside the building by using window equipped with active thermal insulator (ATI). This thermal insulator consists of TEMs, semitransparent PV module, and heat sinks. The result shows that ATI system not only developed electrical energy but also reduced heat gain by 67%. The parameters such as window configuration, flow rate of air, placement of window, number of TEMs, and thickness of glazing were not considered in this research. Maneewan et al. [49] numerically analyzed the effect of TEMs on conventional roof solar collector (RSC) for roof heat gain reduction. Results show that the rooftop rate of heat transfer decrease was around  $3\text{--}5 \text{ W/m}^2$  which prompts to yearly electrical energy saving sparing of around 362 kWh. The economic investigation suggested that the payback time of the TE-RSC was 4.36 years. Liu et al. [8] developed solar thermoelectric cooled ceiling combined with displacement ventilation system (STCC-DV) by placing TEMs in place of hydronic pipes for air dehumidification. It was found that major factors influencing the total heat flux and COP of the panel were indoor and outdoor temperature, and input power. The overall heat flux and COP rise to  $60 \text{ W/m}^2$  and 0.9 during cooling phase whereas reach  $110 \text{ W/m}^2$  and 1.9 during heating phase.

#### 4.1.4.2.2 Thermoelectric refrigeration and air conditioners system assisted by solar PV system

The traditional air conditioner system consists of many energy-intensive devices such as condenser, compressor, expansion valve, and evaporator. The refrigerants such as R134a, Freon, etc., used by these air-cooling systems further cause environmental

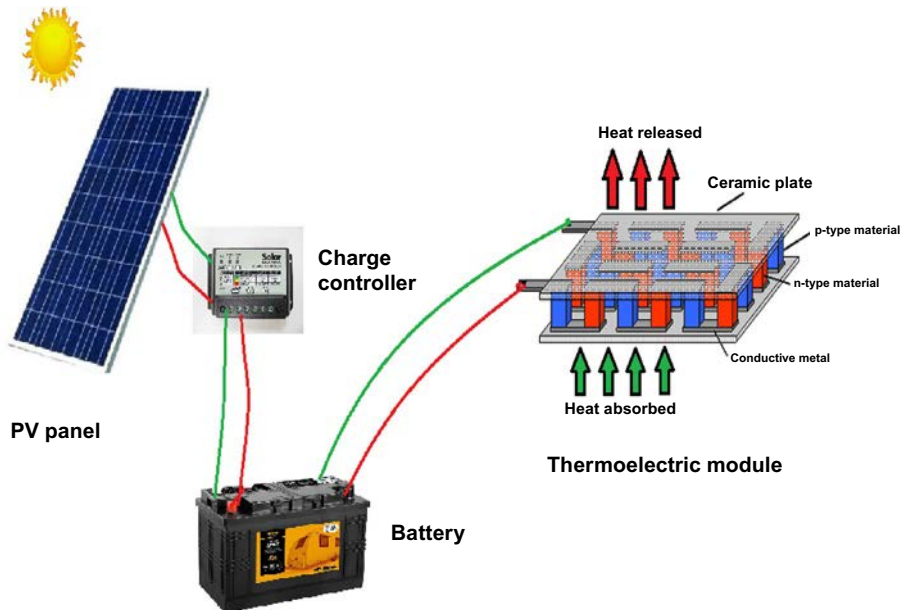


**Fig. 4.1.5** Solar photovoltaic-assisted thermoelectric cooler [24].

hazards. The TEC technology is most promising as it does not involve any of the above energy-intensive mechanical equipment and required direct electrical current for its operation. This benefits provide added advantage to TEC coupling with solar photovoltaic system without using any inverters as shown in Fig. 4.1.5.

Dai et al. [50] tentatively researched solar photovoltaic motorized TE refrigeration framework and acquired the connection between intensity of solar irradiation and COP of a TE cooler. The result shows that temperature contrasts between hot and cold sides of TE module and power of sunlight-based insolation are the two crucial constraints on which execution of TE icebox depends. At refrigerated space, temperature range of 5–10°C and COP of 0.3 were accomplished. Wahab et al. [51] experimentally designed and verified solar powered portable TEC. The outcomes show that in roughly 44 min the refrigeration system temperature diminishes from 27°C to 5°C with a COP of 0.16. In any of the above case study, [43, 46] were completed in small-scale control condition. Further, Atik [52] examined the performance of household fridge furnished with thermoelectric and PV units. Results show that the temperature contrast between within and outside of the cooler was 14.7°C and COP of 0.58. Cheng et al. [20] tried a sun-driven TEMs with a waste warmth recovery unit for green structure applications. For the area of measurement  $30 \times 12 \times 10 \text{ cm}^3$  temperature difference among inside and outside can reach 16.2°C in cooling mode. Warmth vitality disseminated by sun-oriented cell and blistering side of TEMs was consumed by cooling flowing water, in this way builds effectiveness of both sun-oriented cell and TEMs with additional benefit of heating water. Moreover, Cheng's examination does not give any data identified with comfort assessment of inhabitants and financial

advantages of solar-driven TEMs. Mei et al. [53] developed analytical relationship of solar-driven TEC for vehicle applications. Results show that for giving cooling limit of 4 kW at a natural temperature of 38°C, electric intensity of 9.5 kW is required. Melero et al. [54] developed simulation model of solar-assisted air-cooling framework having 48 TEMs fitted in the roof of the fenced in area. Results show that TEMs give adequate temperature decrease expected to fulfill occupant's thermal comfort criteria. Xi et al. [55] looked into the improvement and utilization of sun-oriented TE advancements and reasoned that consolidated TEC and PV cell can be utilized for cooling purpose with less vitality utilization and carbon emission. He et al. [56] investigated the impact of solar-powered TE warming and cooling framework executed in a room of volume 0.125 m<sup>3</sup>. The outcomes show that the COP of 0.45 and least temperature of 17°C were accomplished with warm efficiency of 12.06%. This framework can likewise raise the temperature of water in a tank of capacity 18.5 L by 9°C.

Alomair et al. [57] experimentally and numerically explored sunlight-based TE cooling framework application in remote zones. They found that cooling limit of a sunlight-based TE cooling system relies on limit and the size of TEMs. Liu et al. [58] proposed solar-assisted thermoelectric cooling system with hot water supply (STACHWS) framework. The outcomes show that temperature of water has extraordinary impact on the operation of the STACHWS framework. In space cooling and water warming mode, COP of STACHWS diminishes with the increase in water temperature. The COP in space-cooling and water-warming mode was astoundingly as high as 4.51. When STACHWS framework is operated as a thermoelectric heat pump, COP of 3.01 in warming mode and 2.59 in cooling mode was accomplished.

#### 4.1.5 Recent development in thermoelectric air cooling

Due to increase in popularity of thermoelectric cooling over conventional HVAC system, several researches are going on to increase its COP and material properties. Major factor effecting cooling performance of TEMs is improper thermal management. For this phase change material is used to store thermal energy at constant temperature in the form of latent heat. The heat dissipated from the hot face of the TEC was stored in the PCM which was maintained at constant temperature. Manikandan et al. [59] investigated the effect of PCM on various geometric variables of TEC such as heat sink, input current, and cooling load. The result shows that PCM-assisted TEC have 30% higher COP as compared to normal TEC with temperature reduction of 25–12°C on cold side and 52–30°C on hot side. The flat heat pipe system integrated with PCM and TEMs was investigated by Sun et al. [60]. A combination of TEM and PCM was used to provide heating for longer duration of time. Zhao et al. [61] improved the COP of TEC by using radiative sky cooling technology. The result shows that with the radiative cooling area of 32 m<sup>2</sup>, the yearly cooling by 101 TEC having ZT value of 2.0 can contribute to 45.0% and 55.0% during nighttime and daytime. Further by changing the heat sink configuration performance, improvement of TECs was studied by Naphon et al. [62]. Three different model of heat sink was tested by supplying water at a flow rate of 0.015 kg/s and the result suggests that heat sink configuration has significant effect on coolants

temperature and velocity distribution. Zhou et al. [63] investigated the improvement in performance in evaporative cooling by coupling it with TEMs. Cai et al. [64] investigated the performance of a heat pump system assisted by TEMs. The COP of the system was significantly affected by specific heat and thermal conductance of cold and hot side of heat exchangers. The nanofluid-integrated TECs also play a significant role in thermal management system and are used to enhance the performance of solar still by 81% as stated in Refs. [65, 66].

#### 4.1.6 Challenges

The major challenge of TEM application for air-conditioning purpose is handling huge volatile behavior of ambient conditions, i.e., temperature, relative humidity, wind speed, solar radiations, cloudiness, etc. These parameters adversely affect thermal load of the buildings, due to which most of current research were carried out under international laboratory standards and which may not replicate real conditions. Further, the properties of TEMs such as merit of figure  $ZT = \frac{S^2}{\rho k}T$  significantly changes the thermal performance of TEMs. For practical applications, it was recommended that TEMs with a high peak  $ZT$  value was not adequate owing to low efficiency and high power output density. Other challenges of TEM application in air-conditioning units are poor wettability of layers, metallized contact layer, and occurrence of diffusion between the materials. The TEMs were always equipped with thermal management system such as heat sinks, fans, water cooler, etc. The direct contact of air with the ceramic plate of TEMs causes frost formation. This is due to lower surface temperature of cold side of TEMs, which causes condensation of dew particles present in the air. This formation causes increase in system thermal resistance and blockage in airflow across the TEMs. Thus, for proper dissipation and absorption of thermal energy, different optimization and thermal designs and techniques would be required. These designs will take into consideration parameters such as geometry of heat sink, area for heat transfer, hot and cold side heat transfer coefficient, electrical and thermal contact resistances, and layer configuration. Moreover, when TEM was operated at higher input power, large heat flux was generated due to Joule-Thompson effect which results in the transfer of heat on the hot side back to cold side of TEMs. This was due to insignificant nature of thermal management system such heat sink, fan, etc., in dissipating heat. This causes significant loss in performance of TEMs as air conditioning. Further, high heat flux cooling hot spots are becoming more technical issue for integrated circuit of TEMs. This can be solved by providing uniform thermal heat dissipation which will further require advance designing inputs.

#### 4.1.7 Conclusions

With the depletion of nonrenewable energy source assets combined with increase in global warming, it has gotten progressively important to explore alternative and sustainable sources for cooling. Thermoelectric (TE) coolers are viewed as an option and

environmental friendly alternative for high-energy consuming conventional HVAC technologies. In this chapter, a comprehensive literature review of thermoelectric cooling technologies, their application, performance index, numerical model, and challenges were explained. The increasing researches into TE innovation have prompted a remarkable increment in the estimation of  $ZT$ , making the utilization TEC slightly compatible with existing cooling technologies. But still application of TEC for real climatic condition need more advancement. The examinations have shown the impact of dimensions of the thermoelements on the COP of TEMs. Both COP and cooling limit rely on thermoelement length, and this reliance turns out to be progressively huge with a reduction in thermoelement length. Most economically accessible TEMs have thermoelement length that varies between  $1.0 \cdot 10^{-3}$  and  $2.5 \cdot 10^{-3}$  m. The cooling application of TEMs summarized in [Section 4.1.4](#) is not constrained to these areas. More applications are rising when high-quality TE materials have been created and the TE cooling systems are moving toward better effectiveness. The research also demonstrated that lessening the contact resistance is a basic necessity to accomplish a further improvement in both COP and cooling limit of TEMs. The TEM as a heating and cooling source can be easily incorporated into the building due to its silent and clean operation, low maintenance, and easy integration with solar PV system.

In future, solar PV-integrated TEC system can be used for zero-energy building concepts. Explicit outcomes on the adaptability parts of demand-side management by utilizing TE cooling systems will be accounted. Further research on material side need to explore nanocomposite and resonant level concepts. The nanocomposites could take into consideration higher  $ZT$  values by lessening thermal conductivity while keeping up favorable electronic properties. With new materials with higher effectiveness, the field of collecting waste energy through TEMs would turn out to be progressively predominant.

## References

- [1] B. Mullan, J. Haqq-Misra, Population growth, energy use, and the implications for the search for extraterrestrial intelligence, *Futures* (2019), <https://doi.org/10.1016/j.futures.2018.06.009>.
- [2] S.A. Rashid, Z. Haider, S.M. Chapal Hossain, K. Memon, F. Panhwar, M.K. Mbogba, P. Hu, G. Zhao, Retrofitting low-cost heating ventilation and air-conditioning systems for energy management in buildings, *Appl. Energy* (2019), <https://doi.org/10.1016/j.apenergy.2018.12.020>.
- [3] R. Wang, S. Lu, Q. Li, Multi-criteria comprehensive study on predictive algorithm of hourly heating energy consumption for residential buildings, *Sustain. Cities Soc.* (2019), <https://doi.org/10.1016/j.scs.2019.101623>.
- [4] W.W. Che, C.Y. Tso, L. Sun, D.Y.K. Ip, H. Lee, C.Y.H. Chao, A.K.H. Lau, Energy consumption, indoor thermal comfort and air quality in a commercial office with retrofitted heat, ventilation and air conditioning (HVAC) system, *Energy Build.* (2019), <https://doi.org/10.1016/j.enbuild.2019.06.029>.
- [5] X. Kong, S. Lu, Y. Wu, A review of building energy efficiency in China during “Eleventh Five-Year Plan” period, *Energy Policy* (2012), <https://doi.org/10.1016/j.enpol.2011.11.024>.

- [6] T.A. Nguyen, M. Aiello, Energy intelligent buildings based on user activity: a survey, *Energy Build.* (2013), <https://doi.org/10.1016/j.enbuild.2012.09.005>.
- [7] H. Sadighi Dizaji, S. Jafarmadar, S. Khalilarya, A. Moosavi, An exhaustive experimental study of a novel air-water based thermoelectric cooling unit, *Appl. Energy* 181 (2016) 357–366, <https://doi.org/10.1016/j.apenergy.2016.08.074>.
- [8] Z. Liu, L. Zhang, G. Gong, Experimental evaluation of a solar thermoelectric cooled ceiling combined with displacement ventilation system, *Energy Convers. Manag.* 87 (2014) 559–565, <https://doi.org/10.1016/j.enconman.2014.07.051>.
- [9] G. Min, D.M. Rowe, Improved model for calculating the coefficient of performance of a Peltier module, *Energy Convers. Manag.* (2000), [https://doi.org/10.1016/S0196-8904\(99\)00102-8](https://doi.org/10.1016/S0196-8904(99)00102-8).
- [10] D.M. Rowe, Thermoelectrics Handbook: Macro to Nano, 2005, <https://doi.org/10.1038/kj.2011.318>.
- [11] R. Chein, G. Huang, Thermoelectric cooler application in electronic cooling, *Appl. Therm. Eng.* 24 (2004) 2207–2217, <https://doi.org/10.1016/j.applthermaleng.2004.03.001>.
- [12] H.J. Goldsmid, Introduction to Thermoelectricity, Springer-Verlag, Berlín, 2010. <https://www.springer.com/gp/book/9783642260926>.
- [13] G. Min, D.M. Rowe, Experimental evaluation of prototype thermoelectric domestic-refrigerators, *Appl. Energy* 83 (2006) 133–152, <https://doi.org/10.1016/j.apenergy.2005.01.002>.
- [14] D. Astrain, J.G. Vián, M. Domínguez, Increase of COP in the thermoelectric refrigeration by the optimization of heat dissipation, *Appl. Therm. Eng.* 23 (2003) 2183–2200, [https://doi.org/10.1016/S1359-4311\(03\)00202-3](https://doi.org/10.1016/S1359-4311(03)00202-3).
- [15] H.S. Choi, S. Yun, K.i. Whang, Development of a temperature-controlled car-seat system utilizing thermoelectric device, *Appl. Therm. Eng.* 27 (2007) 2841–2849, <https://doi.org/10.1016/j.applthermaleng.2006.09.004>.
- [16] Á.G. Miranda, T.S. Chen, C.W. Hong, Feasibility study of a green energy powered thermoelectric chip based air conditioner for electric vehicles, *Energy* 59 (2013) 633–641, <https://doi.org/10.1016/j.energy.2013.07.013>.
- [17] Y. Zhou, J. Yu, Design optimization of thermoelectric cooling systems for applications in electronic devices, *Int. J. Refrig.* (2012) 1139–1144, <https://doi.org/10.1016/j.ijrefrig.2011.12.003>.
- [18] P. Naphon, S. Wiriyasart, Liquid cooling in the mini-rectangular fin heat sink with and without thermoelectric for CPU, *Int. Commun. Heat Mass Transfer* 36 (2009) 166–171, <https://doi.org/10.1016/j.icheatmasstransfer.2008.10.002>.
- [19] M. Gillott, L. Jiang, S. Riffat, An investigation of thermoelectric cooling devices for small-scale space conditioning applications in buildings, *Int. J. Energy Res.* 34 (2010) 776–786, <https://doi.org/10.1002/er.1591>.
- [20] T.C. Cheng, C.H. Cheng, Z.Z. Huang, G.C. Liao, Development of an energy-saving module via combination of solar cells and thermoelectric coolers for green building applications, *Energy* 36 (2011) 133–140, <https://doi.org/10.1016/j.energy.2010.10.061>.
- [21] A.E. Kabeel, M.M. Bassuoni, Energy efficient moist free air conditioning system integrated with total heat desiccant solution system, *Int. J. Refrig.* (2019), <https://doi.org/10.1016/j.ijrefrig.2019.02.013>.
- [22] L. Xue, G. Ma, F. Zhou, L. Wang, Operation characteristics of air–air heat pipe inserted plate heat exchanger for heat recovery, *Energy Build.* (2019), <https://doi.org/10.1016/j.enbuild.2018.12.036>.

- [23] P. Cui, M. Yu, Z. Liu, Z. Zhu, S. Yang, Energy, exergy, and economic (3E) analyses and multi-objective optimization of a cascade absorption refrigeration system for low-grade waste heat recovery, *Energy Convers. Manag.* (2019), <https://doi.org/10.1016/j.enconman.2019.01.047>.
- [24] K. Irshad, K. Habib, R. Saidur, M.W. Kareem, B.B. Saha, Study of thermoelectric and photovoltaic facade system for energy efficient building development: a review, *J. Clean. Prod.* 209 (2019) 1376–1395, <https://doi.org/10.1016/j.jclepro.2018.09.245>.
- [25] T. Li, G. Tang, G. Gong, G. Zhang, N. Li, L. Zhang, Investigation of prototype thermoelectric domestic-ventilator, *Appl. Therm. Eng.* 29 (2009) 2016–2021, <https://doi.org/10.1016/j.applthermaleng.2008.10.007>.
- [26] T. Han, G. Gong, Z. Liu, L. Zhang, Optimum design and experimental study of a thermoelectric ventilator, *Appl. Therm. Eng.* 67 (2014) 529–539, <https://doi.org/10.1016/j.applthermaleng.2014.03.073>.
- [27] L. Zhongbing, Z. Ling, X. Min, H. Tianhe, L. Tao, C. Youming, Investigation on a thermoelectric heat pump storage water heater with exhaust heat recovery from kitchens, *Acta Energ. Solaris Sin.* 32 (5) (2011) 650–654.
- [28] Q. Luo, G. Tang, Z. Liu, J. Wang, A novel water heater integrating thermoelectric heat pump with separating thermosiphon, *Appl. Therm. Eng.* 25 (2005) 2193–2203, <https://doi.org/10.1016/j.applthermaleng.2005.01.013>.
- [29] Z. Liu, Y. Zhang, L. Zhang, Y. Luo, Z. Wu, J. Wu, Y. Yin, G. Hou, Modeling and simulation of a photovoltaic thermal-compound thermoelectric ventilator system, *Appl. Energy* 228 (2018) 1887–1900, <https://doi.org/10.1016/j.apenergy.2018.07.006>.
- [30] Z.B. Liu, L. Zhang, Y.Q. Luo, Y.L. Zhang, Z.H. Wu, Performance evaluation of a photovoltaic thermal-compound thermoelectric ventilator system, *Energy Build.* (2018), <https://doi.org/10.1016/j.enbuild.2018.01.058>.
- [31] Z. Liu, W. Li, L. Zhang, Z. Wu, Y. Luo, Experimental study and performance analysis of solar-driven exhaust air thermoelectric heat pump recovery system, *Energy Build.* (2019), <https://doi.org/10.1016/j.enbuild.2019.01.017>.
- [32] C. Lertsatitthanakorn, J. Hirunlabh, J. Khedari, M. Daguenet, Experimental performance of a ceiling-type free convected thermoelectric air conditioner, *Int. J. Ambient Energy* 23 (2) (2002) 173–177.
- [33] S. Maneewan, W. Tipsaenprom, C. Lertsatitthanakorn, Thermal comfort study of a compact thermoelectric air conditioner, *J. Electron. Mater.* 39 (2010) 1659–1664, <https://doi.org/10.1007/s11664-010-1239-8>.
- [34] S.B. Riffat, G. Qiu, Comparative investigation of thermoelectric air-conditioners versus vapour compression and absorption air-conditioners, *Appl. Therm. Eng.* 24 (2004) 1979–1993, <https://doi.org/10.1016/j.applthermaleng.2004.02.010>.
- [35] M. Cosnier, G. Fraisse, L. Luo, An experimental and numerical study of a thermoelectric air-cooling and air-heating system, *Int. J. Refrig.* 31 (2008) 1051–1062, <https://doi.org/10.1016/j.ijrefrig.2007.12.009>.
- [36] C. Lertsatitthanakorn, L. Wiset, Evaluation of the thermal comfort of a thermoelectric ceiling cooling panel (TE-CCP) system, *J. Electron. Mater.* 38 (2009) 1472–1477, <https://doi.org/10.1007/s11664-008-0637-7>.
- [37] L. Shen, F. Xiao, H. Chen, S. Wang, Investigation of a novel thermoelectric radiant air-conditioning system, *Energy Build.* 59 (2013) 123–132, <https://doi.org/10.1016/j.enbuild.2012.12.041>.
- [38] C.J.L. Hermes, J.R. Barbosa, Thermodynamic comparison of Peltier, Stirling, and vapor compression portable coolers, *Appl. Energy* 91 (2012) 51–58, <https://doi.org/10.1016/j.apenergy.2011.08.043>.

- [39] S.S.W. Tipsaenporm, C. Lertsatitthanakorn, B. Bubphachot, M. Rungsiyopas, Improvement of cooling performance of a compact thermoelectric air conditioner using a direct evaporative cooling system, *J. Electron. Mater.* 41 (6) (2012) 1186–1192.
- [40] K. Irshad, K. Habib, N. Thirumalaiswamy, B.B. Saha, Performance analysis of a thermoelectric air duct system for energy-efficient buildings, *Energy* 91 (2015) 1009–1017, <https://doi.org/10.1016/j.energy.2015.08.102>.
- [41] K. Irshad, K. Habib, F. Basrawi, N. Thirumalaiswamy, R. Saidur, B.B. Saha, Thermal comfort study of a building equipped with thermoelectric air duct system for tropical climate, *Appl. Therm. Eng.* 91 (2015) 1141–1155, <https://doi.org/10.1016/j.applthermaleng.2015.08.077>.
- [42] S.B. Sadineni, S. Madala, R.F. Boehm, Passive building energy savings: a review of building envelope components, *Renew. Sust. Energ. Rev.* 15 (2011) 3617–3631, <https://doi.org/10.1016/j.rser.2011.07.014>.
- [43] Z. Liu, L. Zhang, G. Gong, Y. Luo, F. Meng, Evaluation of a prototype active solar thermoelectric radiant wall system in winter conditions, *Appl. Therm. Eng.* 89 (2015) 36–43, <https://doi.org/10.1016/j.applthermaleng.2015.05.076>.
- [44] R.A. Khire, A. Messac, S. Van Dessel, Design of thermoelectric heat pump unit for active building envelope systems, *Int. J. Heat Mass Transf.* 48 (2005) 4028–4040, <https://doi.org/10.1016/j.ijheatmasstransfer.2005.04.028>.
- [45] S. Van Dessel, B. Foubert, Active thermal insulators : finite elements modeling and parametric study of thermoelectric modules integrated into a double pane glazing system, *Energy Build.* 42 (2010) 1156–1164, <https://doi.org/10.1016/j.enbuild.2010.02.007>.
- [46] Z. Liu, L. Zhang, G. Gong, T. Han, Experimental evaluation of an active solar thermoelectric radiant wall system, *Energy Convers. Manag.* 94 (2015) 253–260, <https://doi.org/10.1016/j.enconman.2015.01.077>.
- [47] X. Xu, S. Van Dessel, Evaluation of a prototype active building envelope window-system, *Energy Build.* 40 (2008) 168–174, <https://doi.org/10.1016/j.enbuild.2007.02.027>.
- [48] T. Harren-Lewis, S. Rangavajhala, A. Messac, J. Zhang, Optimization-based feasibility study of an active thermal insulator, *Build. Environ.* 53 (2012) 7–15, <https://doi.org/10.1016/j.buildenv.2012.01.002>.
- [49] S. Maneewan, J. Hirunlabh, J. Khedari, B. Zeghamti, S. Teekasap, Heat gain reduction by means of thermoelectric roof solar collector, *Sol. Energy* 78 (2005) 495–503, <https://doi.org/10.1016/j.solener.2004.08.003>.
- [50] Y.J. Dai, R.Z. Wang, L. Ni, Experimental investigation and analysis on a thermoelectric refrigerator driven by solar cells, *Sol. Energy Mater. Sol. Cells* 77 (2003) 377–391, [https://doi.org/10.1016/S0927-0248\(02\)00357-4](https://doi.org/10.1016/S0927-0248(02)00357-4).
- [51] S.A. Abdul-Wahab, A. Elkamel, A.M. Al-Damkhi, I.A. Al-Habsi, H.S. Al-Rubai'ey', A. K. Al-Battashi, A.R. Al-Tamimi, K.H. Al-Mamari, M.U. Chutani, Design and experimental investigation of portable solar thermoelectric refrigerator, *Renew. Energy* 34 (2009) 30–34, <https://doi.org/10.1016/j.renene.2008.04.026>.
- [52] K. Atik, Y. Yildiz, An experimental investigation of a domestic type solar TE cooler, *Energy Sources A Recover. Util. Environ. Eff.* 34 (2012) 645–653, <https://doi.org/10.1080/15567031003627989>.
- [53] V.C. Mei, F.C. Chen, B. Mathiprakasam, P. Heenan, Study of solar-assisted thermoelectric technology for automobile air conditioning, *J. Sol. Energy Eng.* 115 (1993) 200, <https://doi.org/10.1115/1.2930050>.
- [54] C.C.A. Melero, D. Astrain, J.G. Vian, L. Aldave, J. Albizua, Application of thermoelectricity and photovoltaic energy to air conditioning, thermoelectric, in: 22nd Int. Conf. on—ICT, Spain, 2003, pp. 627–630.

- [55] H. Xi, L. Luo, G. Fraisse, Development and applications of solar-based thermoelectric technologies, *Renew. Sust. Energ. Rev.* 11 (2007) 923–936, <https://doi.org/10.1016/j.rser.2005.06.008>.
- [56] W. He, J. Zhou, J. Hou, C. Chen, J. Ji, Theoretical and experimental investigation on a thermoelectric cooling and heating system driven by solar, *Appl. Energy* 107 (2013) 89–97, <https://doi.org/10.1016/j.apenergy.2013.01.055>.
- [57] M. Alomair, Y. Alomair, S. Mahmud, H.A. Abdullah, Theoretical and experimental investigations of solar-thermoelectric air-conditioning system for remote applications, *J. Therm. Sci. Eng. Appl.* 7 (2015) 021013, <https://doi.org/10.1115/1.4029678>.
- [58] Z.B. Liu, L. Zhang, G. Gong, Y. Luo, F. Meng, Experimental study and performance analysis of a solar thermoelectric air conditioner with hot water supply, *Energy Build.* 86 (2015) 619–625, <https://doi.org/10.1016/j.enbuild.2014.10.053>.
- [59] S. Manikandan, C. Selvam, P.P.S. Praful, R. Lamba, S.C. Kaushik, D. Zhao, R. Yang, A novel technique to enhance thermal performance of a thermoelectric cooler using phase-change materials, *J. Therm. Anal. Calorim.* (2019), <https://doi.org/10.1007/s10973-019-08353-y>.
- [60] H. Sun, B. Lin, Z. Lin, Y. Zhu, Experimental study on a novel flat-heat-pipe heating system integrated with phase change material and thermoelectric unit, *Energy* 189 (2019) 116181, <https://doi.org/10.1016/j.energy.2019.116181>.
- [61] D. Zhao, X. Yin, J. Xu, G. Tan, R. Yang, Radiative sky cooling-assisted thermoelectric cooling system for building applications, *Energy* (2019) 116322, <https://doi.org/10.1016/j.energy.2019.116322>.
- [62] P. Naphon, S. Wiriyasart, C. Hommalee, Experimental and numerical study on thermoelectric liquid cooling module performance with different heat sink configurations, *Heat Mass Transf.* (2019), <https://doi.org/10.1007/s00231-019-02598-x>.
- [63] Y. Zhou, T. Zhang, F. Wang, Y. Yu, Performance analysis of a novel thermoelectric assisted indirect evaporative cooling system, *Energy* (2018), <https://doi.org/10.1016/j.energy.2018.08.013>.
- [64] Y. Cai, D.D. Zhang, D. Liu, F.Y. Zhao, H.Q. Wang, Air source thermoelectric heat pump for simultaneous cold air delivery and hot water supply: full modeling and performance evaluation, *Renew. Energy* (2019), <https://doi.org/10.1016/j.renene.2018.07.007>.
- [65] S. Nazari, H. Safarzadeh, M. Bahiraei, Performance improvement of a single slope solar still by employing thermoelectric cooling channel and copper oxide nanofluid: an experimental study, *J. Clean. Prod.* (2019), <https://doi.org/10.1016/j.jclepro.2018.10.194>.
- [66] S. Nazari, H. Safarzadeh, M. Bahiraei, Experimental and analytical investigations of productivity, energy and exergy efficiency of a single slope solar still enhanced with thermoelectric channel and nanofluid, *Renew. Energy* (2019), <https://doi.org/10.1016/j.renene.2018.12.059>.

# Air-cooled thermoelectric generator

4.2

Ryoji Funahashi, Tomoyuki Urata, Yoko Matsumura,

Hiroyo Murakami, and Hitomi Ikenishi

National Institute of Advanced Industrial Science & Technology, Osaka, Japan

## 4.2.1 Waste heat

The worldwide stream for the decrease in CO<sub>2</sub> emission is getting stronger year by year. The development of sustainable energy systems, such as solar, wind power, geothermal, biomass, and tidal power generation systems, has accelerated. However, the spread of progress in such new methods of power generation is very slow because of low efficiency, high cost, etc. The demand for primary energy in the world was as much as 14,300 million tons of petroleum a year in 2018 [1]. The fossil energies, which are the origin of the CO<sub>2</sub> emission, occupy almost 80% of the total primary energy carriers. The average total energy efficiency in the world is as low as 28% [2]. The major part of the energy loss is exhausted to the air as waste heat. If such large amount of the waste heat can be converted to the electricity, it will have a significant impact on energy efficiency and CO<sub>2</sub> emission. The mechanical conversion systems such as the steam turbine or the Stirling engine are effective for the conversion of heat to the electricity. However, most sources of the waste heat are widely distributed. In this case, thermoelectric conversion using Seebeck effect is significant to generate electricity. Moreover, mechanical conversion systems consume electricity for cooling and circulating water. On the other hand, though high efficiency can be obtained by water cooling in thermoelectric conversion systems, the water is not mandatory. This characteristic makes the air-cooled power generation systems suitable for the thermoelectric conversion.

## 4.2.2 Oxide thermoelectric module

Thermoelectric materials durable against oxidation at high temperature are necessary for air-cooled systems because of high-temperature operation. Oxides are one of the strongest candidates for the recovery of the high-temperature waste heat. The family of the CoO<sub>2</sub> layered materials shows excellent p-type thermoelectric properties at high temperature in air [3–5]. High dimensionless thermoelectric figure of merit (*ZT*) values of the p-type Ca<sub>3</sub>Co<sub>4</sub>O<sub>9</sub> (Co-349) have been reported [4]. Some thermoelectric generation systems have been developed using Co-349 and n-type CaMnO<sub>3</sub> (Mn-113) [6]. The Co-349 phase has a layered structure consisting of CoO<sub>2</sub> sublattice, in which a Co element is surrounded by six oxygen elements, and the Ca<sub>2</sub>CoO<sub>3</sub> sublattice

possesses rock-salt structure. The  $\text{CoO}_2$  sublattice acts as an electrical conducting layer. The single crystal of Co-349 shows  $ZT$  of about 1.1 at 973 K in air [4]. The n-type Mn-113 phase has perovskite structure. Some conductive oxides, such as  $\text{ZnO}$ ,  $\text{TiO}_2$ , or  $\text{SrTiO}_3$ , show n-type conduction. However, these oxides need oxygen defects to possess good electrical conductivity because of the electron doping. This makes it difficult to use these oxides as thermoelectric materials at high temperature in air. In the case of Mn-113, the mixed valence states of  $\text{Mn}^{3+}$  and  $\text{Mn}^{4+}$  are formed to dope the electrons by the elemental substitution at the Ca or Mn sites. The electron-doped Mn-113 shows stable electrical conductivity even at 1073 K in air.

Though the Co-349 phase in form of the single crystalline shows low electrical resistivity in the *ab*-plane because of the two-dimensional structure, the polycrystalline bulks of the Co-349 phase obtain higher electrical resistivity than the single crystals due to the misorientation of the grains and the low bulk density. The uniaxial pressing, especially, a hot pressing process is an appropriate method to improve the  $ZT$  values of the sintered bulks because of good grain orientation and high bulk density [7]. On the other hand, the perovskite Mn-113 phase shows the isotropic electrical conductivity. The electrical resistivity depends on the bulk density. Sintering at temperature higher than 1573 K is effective in enhancing bulk density and lowering electrical resistivity. However, a problem is cracking in the densified Mn-113 bulks because of the brittleness. This could be the reason for the damage of the module during power generation and the suppression of the manufacturing yield of the Mn-113 devices during mass production. The incorporation of the nanosized powder ( $\sim 20$  nm) of the Mn-113 phase can improve the problem of cracking.

The formation of junctions between the thermoelectric materials and electrodes with strong bonding and low electrical contact resistance are essential to obtain high-performance modules. Such good junctions can be formed by developing the silver paste incorporated thermoelectric oxide powders [8].

Thermoelectric modules composed of 14 pairs of p-type  $\text{Ca}_{2.7}\text{Bi}_{0.3}\text{Co}_4\text{O}_9$  (Co-349 phase) and the n-type  $\text{CaMn}_{0.98}\text{Mo}_{0.02}\text{O}_3$  (Mn-113 phase) legs have been produced using silver electrodes and silver paste including the p-type oxide powder (Fig. 4.2.1A). Each pair is composed of two pieces of p- and n-type legs to prevent

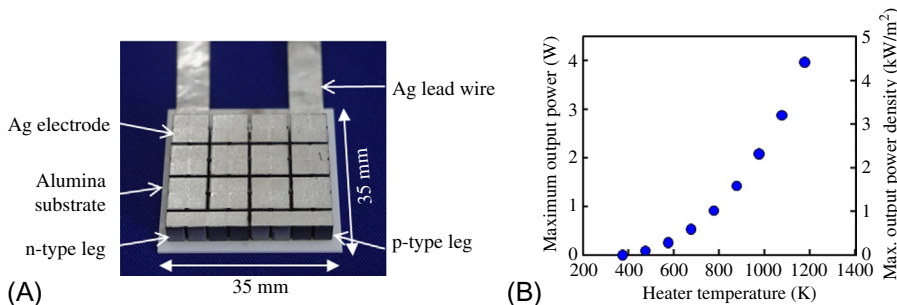


**Fig. 4.2.1** A photograph of the oxide thermoelectric module composed of 14 pairs of p- and n-type legs (A) and temperature dependence of the heater on the maximum output power and the maximum output power density against the surface area of the substrate (B).

electrical cutoff in the module because of the cracks. The maximum output power increases with increase in hot-side temperature of an electrical heater and reaches 4.0 W at 1173 K in air (Fig. 4.2.1B). The maximum power density against the surface area of the substrate is as high as  $4.3 \text{ kW/m}^2$ . The long life and heat cycling tests were carried out at temperature higher than 873 K in air. The obvious degradation of the output power has never been detected in both tests [9].

## 4.2.3 Thermoelectric power unit of oxide module

### 4.2.3.1 Water-cooled unit

Thermoelectric power units were produced using cascaded modules, in which oxide and  $\text{Bi}_2\text{Te}_3$  modules were stacked (Fig. 4.2.2A). Each unit includes four cascaded modules. The four oxide modules were connected in parallel. The four  $\text{Bi}_2\text{Te}_3$  modules were also connected in parallel. The electrical property of the oxide and the  $\text{Bi}_2\text{Te}_3$  module circuits were measured individually. Heat collection fins made of the cast iron are attached to the hot side of the oxide modules. On the other side, namely the cold side of the  $\text{Bi}_2\text{Te}_3$  modules, contacts to a water-cooling jacket for cooling are made of die-cast aluminum alloy (Fig. 4.2.2B). The thermoelectric power units were tested using a pilot incinerator with a natural gas burner (Figs. 4.2.3A and B). The temperatures around the top of the heat collection fins ( $T_{AF}$  and  $T_{BF}$ ) and at the surfaces of the substrate of the oxide module ( $T_{AO}$  and  $T_{BO}$ ) were measured by thermocouples and reached about 1270 and 845 K after the ignition, respectively (Figs. 4.2.3C and D). The temperatures of the hot side of the  $\text{Bi}_2\text{Te}_3$  modules ( $T_{AB}$  and  $T_{BB}$ ) were above 515 K. The temperature of the cooling water was in the range 293–298 K.

The maximum output power of the oxide module circuit in the unit A is 16.3 W at 3.5 h after the ignition (Fig. 4.2.4A). Temperatures around the top of the heat collection fins and at the surfaces of the alumina substrate of the oxide modules are almost same between the units A and B. The maximum output power and the voltage at the maximum output power of the unit A are slightly higher than the unit B. The temperature in the furnace increases with the combustion time. At 15.5 h from the ignition, the maximum output power of the oxide module circuits reaches about 20 W in both units A and B. The internal resistance of the oxide modules increased about

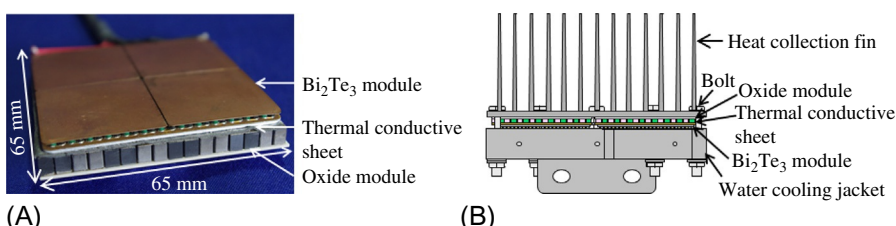
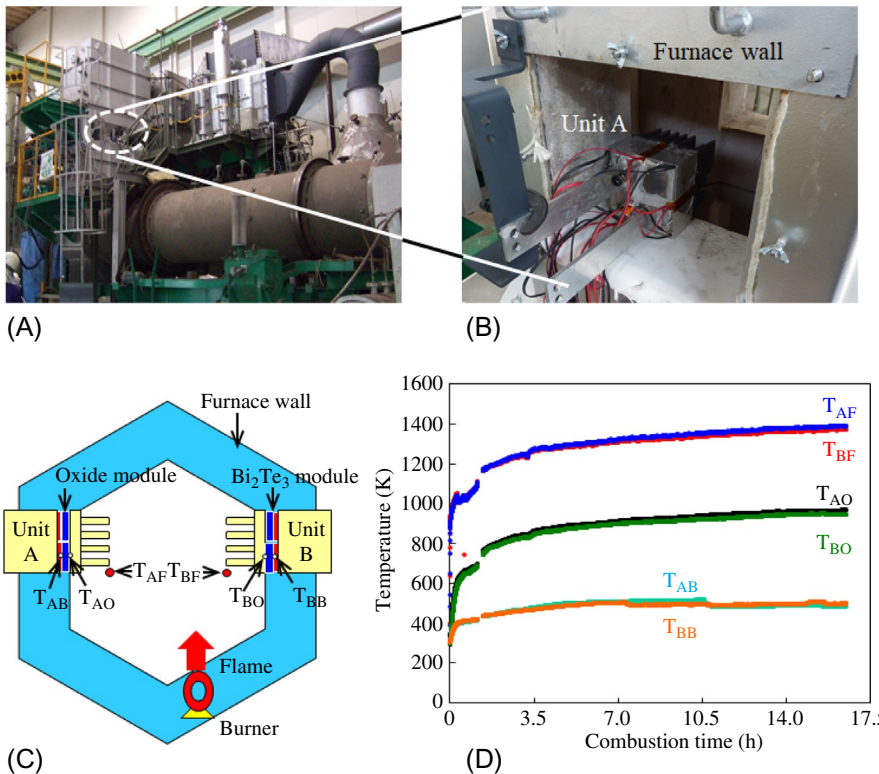
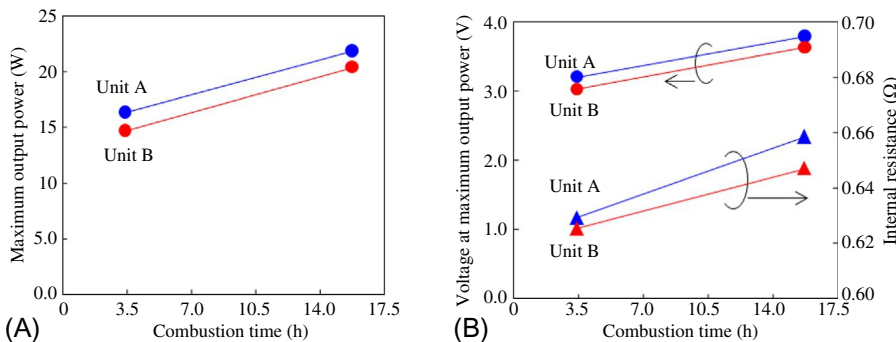


Fig. 4.2.2 A photograph of the oxide/ $\text{Bi}_2\text{Te}_3$  cascaded module (A) and the water-cooled thermoelectric power unit composed of four cascaded modules (B).



**Fig. 4.2.3** Photographs of the pilot incinerator (A) and installation of the thermoelectric unit in the incinerator (B). A schematic drawing of inside of the incinerator viewed downward (C). Changes in temperatures measured by the thermocouples placed around the heat collection fins ( $T_{AF}$  and  $T_{BF}$ ), at the hot side substrates of the oxide ( $T_{AO}$  and  $T_{BO}$ ) and the  $\text{Bi}_2\text{Te}_3$  modules ( $T_{AB}$  and  $T_{BB}$ ) of the units A and B (D).



**Fig. 4.2.4** Maximum output power (A) and voltage at the maximum output power and internal resistance (B) of the oxide module circuits in the units A and B. Four modules are connected in parallel in each unit.

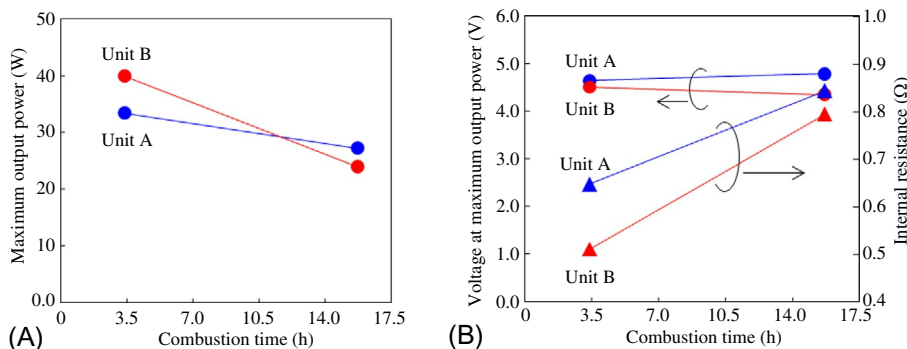


**Fig. 4.2.5** Maximum output power (A) and voltage at the maximum output power and internal resistance (B) of the  $\text{Bi}_2\text{Te}_3$  module circuits in the units A and B. Four modules are connected in parallel in each unit.

3.0%–4.5% with the combustion time (Fig. 4.2.4B). This is not due to any degradation of the oxide modules but due to the rise in the temperature of the hot side of the modules. The internal resistance of the oxide modules increases with increasing temperature.

Although the temperature of the hot side substrate of the  $\text{Bi}_2\text{Te}_3$  modules increases from 470K at 3.5h after the ignition to 500K at 15.5h, the maximum output power decreases in both units A and B (Fig. 4.2.5A). The increase in the internal resistance of the  $\text{Bi}_2\text{Te}_3$  modules is observed in both units (Fig. 4.2.5B). The increase in ratios of the internal resistance is about 30% and 55% for the units A and B, respectively. The degradation of the  $\text{Bi}_2\text{Te}_3$  modules occurs due to heating at temperature higher than 500K. Oxidation of the  $\text{Bi}_2\text{Te}_3$  legs, melting or diffusion of the solder, and exfoliation at the junction can be thought as the reasons for the degradation.

The thermoelectric power systems were built up by 12 and four power units as mentioned previously. The power generation properties of the 12-unit and four-unit systems were measured on an industrial furnace and an incinerator, respectively. The industrial furnace equips burners using the natural gas. The 12-unit system was put on the chimney of the furnace (Fig. 4.2.6). Temperature of the exhaust gas around the heat collection fins of the system was 1283K. The temperature of the water for cooling was about 300K and flow rate 15L/min. The output power generated is 720W at 38V.

The four-unit system was mounted on the incinerator for waste lumbers at a processing plant (Fig. 4.2.7). Since the lumbers are dried completely because of the use for building, the temperature was higher than 1273K in the incinerator. The power system was put between the incinerator and the chimney. The cooling water was flowed at about 6L/min at 298K. The output power reaches 194W at 35V.

The results of both tests of the water-cooled thermoelectric power systems are summarized in Table 4.2.1. The number of the cascaded modules are 48 and 16 in the 12- and 4-unit systems, respectively. In both cases, the temperatures around the heat collection fins are 1273K or higher. In the test using the incinerator, the

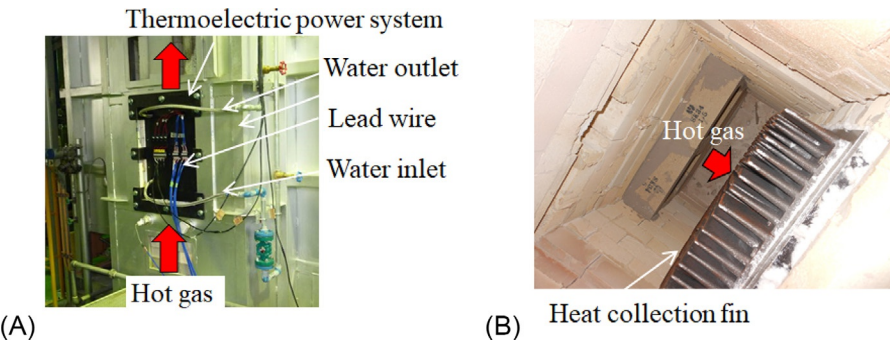


**Fig. 4.2.6** A thermoelectric power system composed of 12 units installed in the industrial furnace: external features (A) and internal features (B). Hot gas rises toward the front side from the backside in (B).

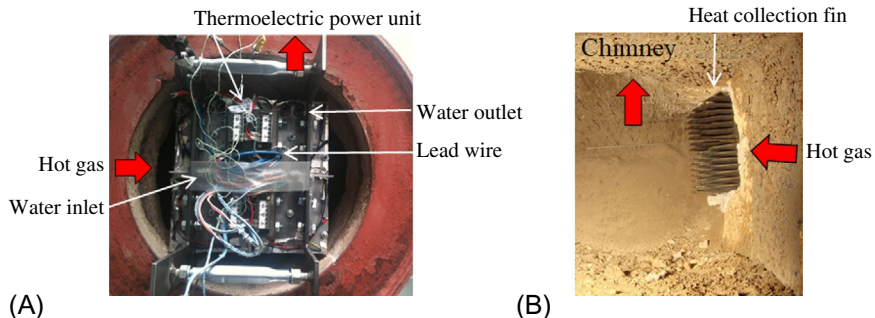


**Fig. 4.2.7** A thermoelectric power system composed of four units installed in the incinerator: external features (A) and internal features (B). Hot gas flows toward the backside from the front side and into the chimney in (B).

**Table 4.2.1** Summary of demonstration tests of the water-cooled thermoelectric power systems on the industrial furnace and the incinerator.

Industrial furnace	Incinerator	
I. Fuel	Natural gas	Waste lumbers
II. Number of units including four cascaded modules	12	4
III. Temperature around heat collection fins (K)	1283	1273
IV. Temperature of water at inlet (K)	—	298
V. Temperature of water at outlet (K)	—	317
VI. Flow rate of water (L/min)	15	6.0
VII. Heat flux into coolant water (W)	—	3567
VIII. Output power (W)	700	194
IX. Conversion efficiency (%)	—	5.2
X. $\text{VIII}/(\text{VII}+\text{VIII}) \times 100$ Power density ( $\text{kW}/\text{m}^2$ )	3.0	2.5
XI. Price of system (mil. JPY/kW)	2.8	3.2
XII. Generation cost by continuous use for 10years (JPY/kWh)	32	37

temperature change of the cooling water between the inlet and the outlet was monitored. The heat flux into the cooling water from the cascaded modules is evaluated as 3.6 kW. The generation efficiency of the system is calculated as 5.2% from the output power and the heat flux into the cooling water. The power density against the area of the outer frame of the systems reaches 2.5–3.0 kW/m<sup>2</sup>. These systems were sold by a startup company of the authors' institute. The price against the output power was about 2.8–3.2 mil. JPY as of 2011. If the systems were operated continuously for 10 years by maximum output power, the cost for the power generation would be 32–37 JPY/kWh. It corresponds to about 0.29–0.34 USD/kWh (1 USD = 110 JPY). The cost could be reduced by the mass production. But currently, the company has stopped production.

#### 4.2.3.2 Air-cooled unit

It has been found through generation tests of the thermoelectric power systems that majority of the users of the incinerators, the industrial furnaces, and instruments exhausting waste heat prefer power generation by air cooling to water cooling. From the point of view of the total energy efficiency, the water-cooled thermoelectric conversion would lead to energy loss because of the low conversion efficiency and high energy consumption to cool the water by the chillers than the generation.

Since the temperature difference would be smaller by air cooling than by water cooling, the output voltage should be low in the air-cooled units. For application on a small scale, which is one of the strongest points of the thermoelectric generation, it is necessary to generate voltage as high as possible to operate electric or electronic devices. One solution is the increase in the number of pairs of the legs. The cross-sectional area of the p- and the n-type leg has to be reduced to produce the module with the same size as of the substrate. Fig. 4.2.8A shows oxide module with 72 pairs

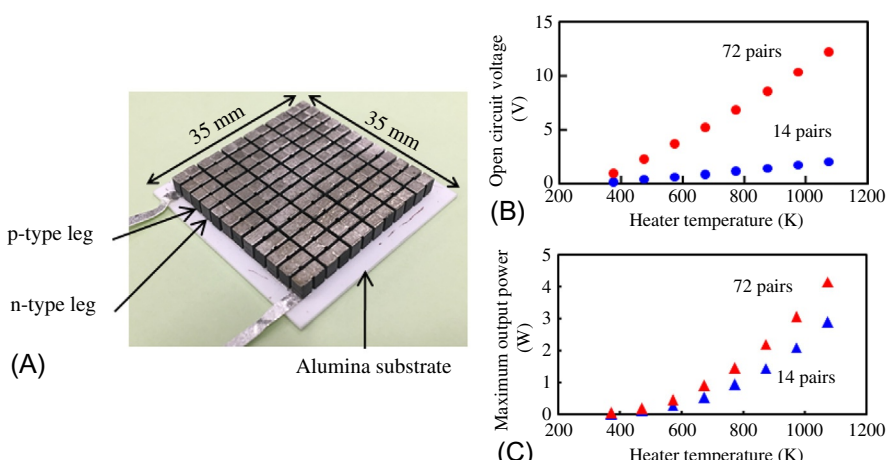


**Fig. 4.2.8** A photograph of the oxide module composed of 72 pairs of the legs (A). Temperature dependence of the heater on the open-circuit voltage (B) and the maximum output power (C) of the oxide modules with 72 and 14 pairs indicated in Fig. 4.2.1A.

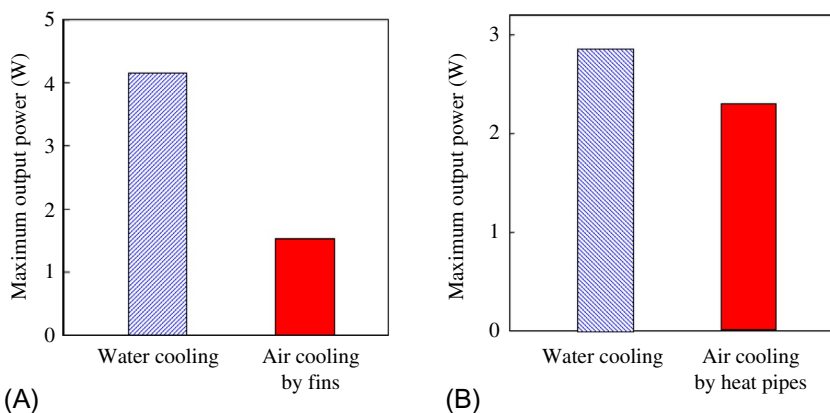


**Fig. 4.2.9** Comparison of the maximum output power of the oxide modules cooled by water and air using the radiation fins (A) and the heat pipes (B). Measurement was carried out in air at 923 K (A) and 773 K (B) of the electrical heater temperature, respectively.

of legs. The open-circuit voltage of this module measured by water cooling is six times higher than the module with 14 pairs with the same substrate size at 1073 K (Fig. 4.2.8B). Due to the reduction in the contact resistance at the junctions, the maximum output power of the 72-pair module is higher than that of the 14-pair one.

It is a major issue to maintain temperature difference by the natural heat radiation from the fins in the air cooling method. The maximum output power for the oxide module, which was measured at 923 K of the electrical heater temperature, is suppressed by 65% in the case of the air cooling (Fig. 4.2.9A). It seems that the use of the latent heat of the coolant (water) is effective to increase the heat flux through the modules, namely, heat pipes are one of the strong tools for the air cooling method. The power generation test was carried out using a commercially available heat pipe device consisting of water in the copper pipes and the radiation fins of the electrical heater temperature at 773 K. The reduction in maximum power stays at 20% by air cooling with the heat pipe device compared to the water cooling (Fig. 4.2.9B). Of course, it is not possible to compare both results without considering the surface area of the heat radiation, thermal contact at the interface between modules and cooling devices, etc. But this result indicates that heat pipe devices are promising to construct thermoelectric power units, the supply of cooling water is undesirable.

An air-cooled thermoelectric power unit has been developed using one piece of the oxide module and heat pipe device (Fig. 4.2.10A). The module is composed of 338 pairs of the oxide thermoelectric legs with alumina substrate of  $65 \text{ mm}^2$  (Fig. 4.2.10B). The output power of the air-cooled unit of the electrical heater reaches 3.1 W at 823 K (Fig. 4.2.11). An electrical fan is put to cool the heat-radiating fins. The electrical power is supplied to the fan from the outside of the thermoelectric unit to measure the net maximum output power.

The air-cooled thermoelectric power unit can light LED lamps (Fig. 4.2.12A) and charge a battery in a smart phone by combustion of firewood (Fig. 4.2.12B).

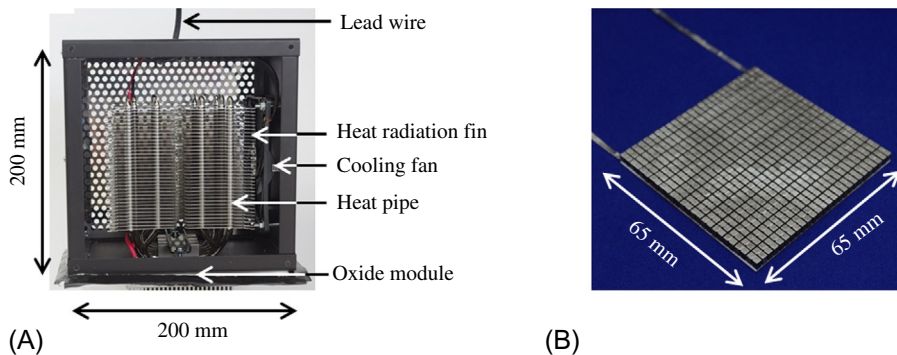


**Fig. 4.2.10** The air-cooled thermoelectric power unit using one piece of oxide module and heat pipe device (A). The oxide module is composed of 338 pairs of p- and n-type legs with the alumina substrate of  $65 \times 65 \text{ mm}^2$  (B).

The electrical power is supplied to the cooling fan from the module in these units, namely, the air-cooled thermoelectric power unit composed of oxide module and heat pipe device can work as a stand-alone system.

A reliability test of an air-cooled thermoelectric power system has been carried out using an industrial furnace for one and half years (Fig. 4.2.13A). The electricity output was used to light the LED lamps. The system includes two sets of the air-cooled power units including the oxide modules and the heat pipe devices. The surface temperature of the conduit of the industrial furnace was about 673 K. The furnace was operated averagely straight for 3 weeks in a month. The maximum power and the internal resistance at room temperature in the shutdown period of the system were measured

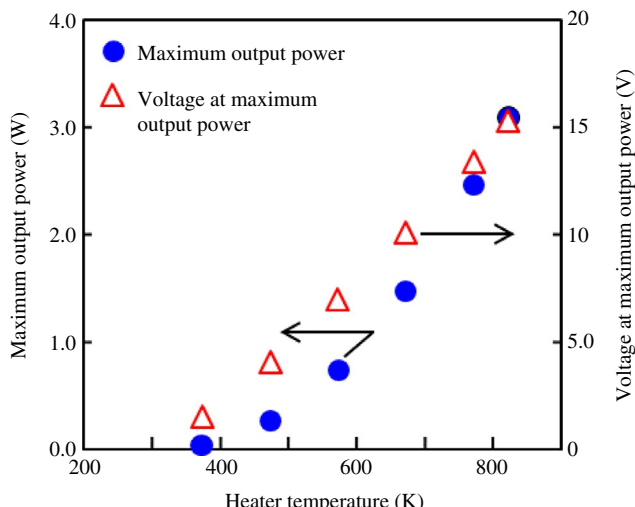


**Fig. 4.2.11** Temperature dependence of electrical heater on maximum output power and voltage.

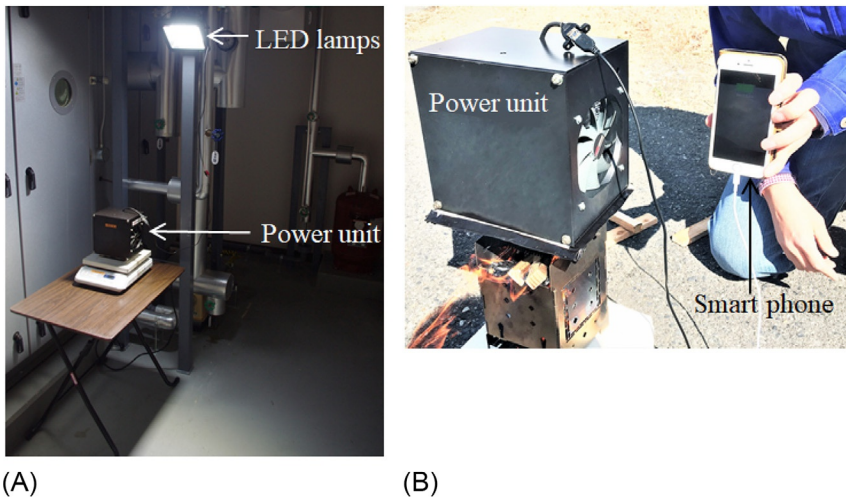


**Fig. 4.2.12** Demonstrations of the air-cooled thermoelectric power unit. LED lighting using the electrical heater (A) and charging a battery in a smart phone by combustion of firewood (B).

irregularly (Fig. 4.2.13B). The degradation of the maximum output power was observed between 10th and 14th cycles. The increases in the internal resistance of the system during and between heating (in the shutdown period) are observed. The reduction in the output power is more significant than the evaluated one from the increase in the internal resistance. The main reason for the decrease in the output

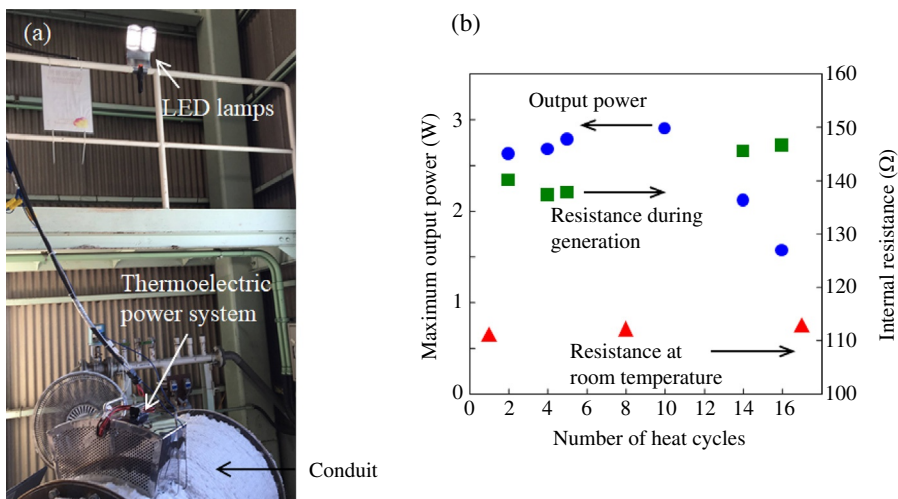


**Fig. 4.2.13** Reliability test of the air-cooled thermoelectric power system on the industrial furnace (A). Surface temperature of the conduit of the furnace attached to the system was 673 K. (B) Change of the maximum output power, the internal resistances during power generation at 673 K and between heating at room temperature during the shutdown period against the number of heat cycles.

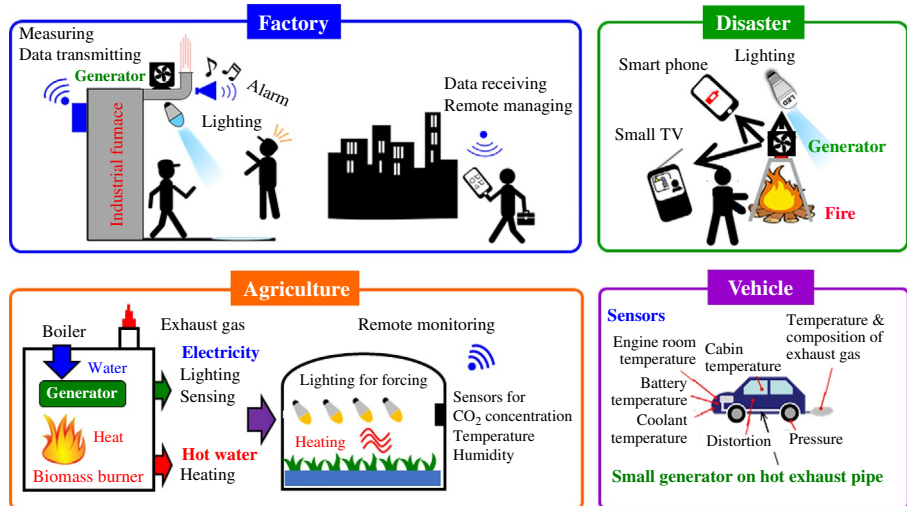


Fig. 4.2.14 Potential applications of thermoelectric power generation systems.

power is the rise in the cold-side temperature of the modules. It is found after the test that the cooling fans have been damaged because of the heat. Absence of moving parts in the systems is one of the strongest points of the thermoelectric generation. It is expected that complete air-cooled thermoelectric power systems will be developed for applications even at high temperature.

Examples of the applications of the thermoelectric power systems are shown in Fig. 4.2.14. In the factories, the waste heat from the industrial furnaces, the reactors, and so on can be converted to the electrical power, which could be used for lighting, sensing, and monitoring facilities. Although the power generation is not effective, the strong points of the oxide modules are good durability, nontoxicity, and cheap production cost. The power density against the surface area of the substrate of the oxide module reaches as high as  $220 \mu\text{W}/\text{cm}^2$  using hot water of 353 K by air cooling. The oxide modules can be used as power sources for microscopic sensors in the IoT society in the near future. Recently, unusual weather caused serious disasters on a global scale. In Japan, not only huge typhoons, but also great earthquakes are significant social issues. The electrical power is indispensable to save the lives, safety, to obtain information, etc. The air-cooled thermoelectric power systems can be applied at the evacuation areas. A large number of sensors will be necessary on the automatic driving cars. Power supplying would be an obstacle to sensing. The waste heat can be used for thermoelectric power generation from the exhaust pipe.

#### 4.2.4 Conclusion

Thermoelectric power units composed of oxide thermoelectric modules, which show excellent durability against high temperature, have been developed and tested. The water-cooled systems including the cascaded modules generated  $2.5\text{--}3.0 \text{kW}/\text{m}^2$  in

the demonstration tests on the industrial furnace and the incinerator. No obvious degradation of the oxide modules was detected by the tests. The conversion efficiency of the water-cooled system was 5.2% against the heat flux through the modules. Although water cooling is effective to generate high output power, the electricity to cool water should be necessarily more than the generated output power. Many potential users of thermoelectric generators prefer air-cooled systems to water-cooled ones. The air-cooled power systems using oxide modules indicate the potentiality for the small power sources. Especially, the application of oxide modules as power sources for IoT devices expects significant market in the near future and requires the air-cooled power generation.

## References

- [1] Global Energy & CO<sub>2</sub> Status Report 2019, International Energy Agency, Paris, 2019. <https://www.iea.org/reports/global-energy-co2-status-report-2019>.
- [2] C. Forman, I.K. Muritala, R. Pardemann, B. Meyer, *Renew. Sust. Energ. Rev.* 57 (2016) 1568–1579.
- [3] I. Terasaki, Y. Sasago, K. Uchinokura, *Phys. Rev. B* 56 (1997) 12685.
- [4] R. Funahashi, I. Matsubara, H. Ikuta, T. Takeuchi, U. Mizutani, S. Sodeoka, *Jpn. J. Appl. Phys.* 39 (2000) L1127.
- [5] R. Funahashi, I. Matsubara, *Appl. Phys. Lett.* 79 (2001) 362.
- [6] D. Flahaut, T. Mihara, R. Funahashi, N. Nabeshima, K. Lee, H. Ohta, K. Koumoto, *J. Appl. Phys.* 100 (2006) 084911.
- [7] R. Funahashi, S. Urata, T. Sano, M. Kitawaki, *J. Mater. Res.* 18 (7) (2003) 1646.
- [8] R. Funahashi, S. Urata, K. Mizuno, T. Kouuchi, M. Mikami, *Appl. Phys. Lett.* 85 (2004) 1036.
- [9] R. Funahashi, in preparation.

# Prospects of TEG application from the thermoelectric cooling market

4.3

*Hirokuni Hachiuma*

Manufacturing Engineering Development Center, Production Division, Komatsu Ltd.,  
Osaka, Japan

## 4.3.1 Introduction

The history of thermoelectric conversion goes back to the dawn of electromagnetism in the 19th century, at the time when Seebeck and Peltier effects were discovered. Since it was a simple method for obtaining electric power, various attempts were made at that time as a technology applicable to power generation.

At present, the device for the thermoelectric conversion is generally known as the Peltier module. It means that it is mainly used for cooling and temperature control technology. The situation began with the research announcement by Goldsmid in 1954 on BiTe material application [1]. After that many research institutes and enterprises promoted its development. Now it has become an indispensable technology, though it is a niche, and its application spreads to the many fields from the consumer to the industry. It took tens of years since the BiTe announcement before the market actually took off, but it is still growing steadily after the 2000s.

The power generation application, which is the inverse effect of cooling, is not yet a big business. But the interest in energy conservation and CO<sub>2</sub> reduction increased after the Kyoto Protocol. Since 2000, waste heat recovery projects of factories or car engines have been carried out in Japan, the United States, and the European Union. After the 2010s, as IoT is beginning to be associated with real industrialization, thermoelectric has been expected as an energy harvesting power source, that is, a technology to obtain electric power from the micro-heat in the environment.

## 4.3.2 History and current situation of thermoelectric application

In the late 19th century, thermoelectric power generation seems to have been practically used as an electricity source of electroplating [2]. However, the system efficiency was less than 1%, and the durability of the material was also low. Even in the 20th century, it was used as a generator for radio using gas in the area without electricity infrastructure. As general power generators and batteries become common, and the infrastructure was improved, low-efficiency thermoelectric power generation was not used except for special applications.

In 1954, Goldsmid announced that BiTe materials produced temperatures below 0°C. People's interest turned to the cooling application after this announcement. At first, products such as refrigerators and room coolers had been developed, but they had not been used practically. Again, efficiency was a problem. Until the early 1960s, many companies and researchers actively worked for the development, but the interest had soon disappeared, and only niche market remained. Since the 1990s, many manufacturers were born in China, the price of the modules lowered, and it came to be widely used.

In recent years, the design of thermoelectric applications has been sophisticated by taking advantage of the features described below, and they realize functions that cannot be replaced by other technologies:

(1) It functions locally.

Both for cooling and power generation, a thermoelectric module functions only on its surface of several millimeters to tens of square millimeters. In addition to the high heat flux, the structure is simple, the heat capacity is small, and the temperature response is agile.

(2) It has less size dependence of performance.

One N and P element pair form a thermoelectric couple. Its performance is proportional to the number of pairs. Unlike mechanical products, performance is less dependent on its size. The structure of the thermoelectric system is simple and miniaturization is easy. The smaller the equipment, the more superior to the substitutional machine.

(3) Both temperature control and power generation function in both directions.

Since both heating and cooling are possible only by switching the current direction, the temperature can be controlled very precisely with feedback control. In some cases, the temperature is controlled with an accuracy of 1/100°C. Generation is possible both hot or cold heat through the direction of the voltage changes depending on the direction of the temperature difference.

(4) It does not use refrigerants and there is no moving part.

There are no rotating or sliding parts like mechanical systems using refrigerants, so there is no noise or vibration. That means there is no abrasion part, and the product has an almost infinite life if used properly. There is no problem of the refrigerant gas sealing or leakage. It can be installed without the influence of gravity.

### **4.3.3 Application of thermoelectric cooling and temperature control**

[Fig. 4.3.1](#) shows the market size of the thermoelectric modules [3]. The market size became twice for 10 years around 2010, and it is estimated that the world market is more than 30 billion yen a year for the sale of the thermoelectric module. The annual

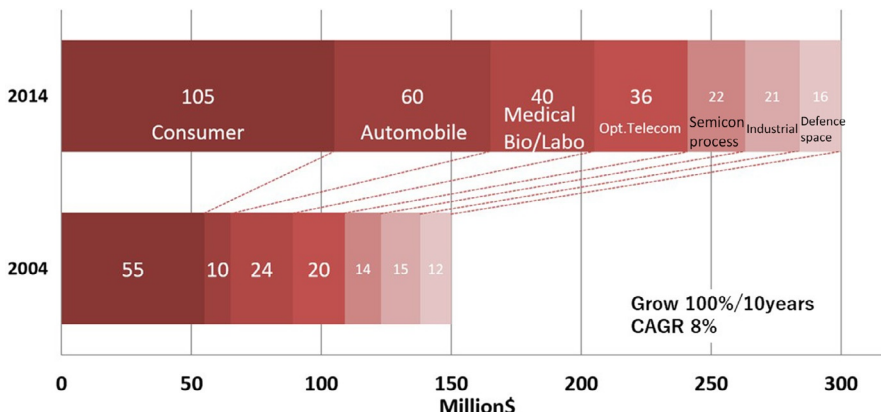


**Fig. 4.3.1** Worldwide market of thermoelectric module.

growth rate is very high, approximately 8%. The advantage of thermoelectric technology is mentioned above. I think the most significant advantage is its “smallness.” In thermoelectric, product design that takes advantage of this “small” feature has made it well known and is growing rapidly.

Examples of thermoelectric applied products and reasons for using it are shown below:

- (1) Consumer products (cold and hot water servers, cooler boxes, refrigerators for hospitals or hotels, wine cellars, mist generators, etc.)

The cooling parts are small and simple. Refrigerators and wine cellars have no noise or vibration as added value.

#### (2) Vehicles

It is used for the seat cooler taking advantage of the speed of the local response until the car air conditioner works.

- (3) Biotechnology, Medicine, Science, and Chemistry (PCR amplifier, circulators, chillers, incubator, blood analyzers, etc.)

It is widely used in this field from general-purpose small temperature control equipment to DNA inspection, because of its smallness and temperature accuracy.

#### (4) Optical communication

The temperature of the laser diode is controlled to stabilize the wavelength. It is characterized by precise temperature control with minimal parts.

#### (5) Semiconductor manufacturing equipment

It is used for temperature control from process chemicals to silicon wafer itself. It is also used for the heat shock inspection as it is small and high-speed heating and cooling are possible.

(6) Industrial (semiconductor laser cooling, infrared sensor cooling, dehumidification, etc.)

Cooling is performed to improve the reliability and performance of optical devices. Condensation and dehumidification by thermoelectric cooling are made before gas analysis. It is small and can cool locally.

(7) Military and space

It is used for cooling infrared night vision sensors.

#### 4.3.4 Prospect of thermoelectric application for power generation

So far, the application of TEG, thermoelectric power generation, is limited to exceptional use like RTG, a radioisotope thermoelectric generator, which uses the decay heat of radioactive materials as a heat source, or anticorrosive protection of pipelines, which use gas or oil for fuel. Both applications are used at an extremely remote area, far away from the power infrastructure. The reliability is the most important, and the cost performance is not so expected.

TEG must improve cost performance so that it is used not only for special but for more general use. At the time of oil shock in the 1970s to 1980s, R&D of TEG was carried out, but the practical application was not realized because of the energy cost decrease. Recently, however, the possibility of TEG is also noticed again, due to the improvement of peripheral technology such as power management or low power technology and the rise of the interest for the global warming countermeasure.

Practical application projects of TEG have been successively carried out in Japan, the United States, and Europe since around 2000. The recovery of industrial waste heat was the central issue of the project in Japan, and automobile waste heat recovery was the central issue in the United States and Europe. Though TEG has not been profitable as a business yet, the development project has got more widely and deeply been done. Several examples are shown below.

[Photo 4.3.1](#) shows a TEG module. The left module has the internal electrodes visible, and the right module has the ceramic plate for electrical insulation mounted on it. As it uses BiTe material, its maximum working temperature is 280°C at the electrode, and the rated working temperature is 250°C. It is the most suitable for waste heat under 400°C.

[Fig. 4.3.2](#) shows a performance curve of this TEG module. The conversion efficiency is proportional to the temperature difference, and the output is proportional to the square of the temperature difference. The conversion efficiency is the ratio of the output to the amount of heat passing through the module. The performance is slightly off the proportional relationship above 200°C. This is because the thermal properties of BiTe materials decrease as the temperature increases in this region. But the fundamental relationship is the same for any size and temperature based on the Carnot efficiency principle. Therefore, the technology of the heat exchanger for

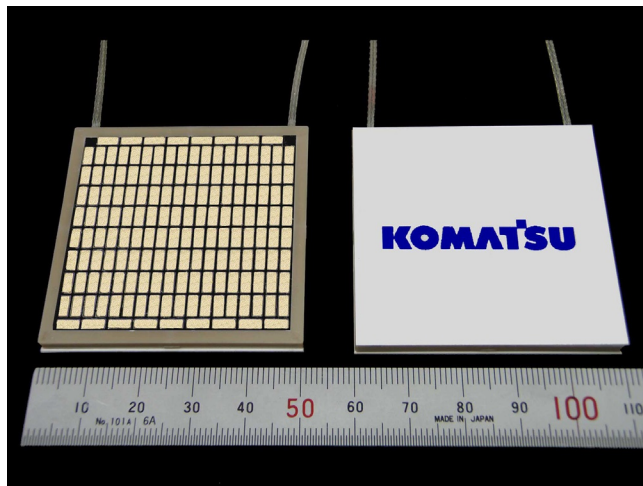


**Photo 4.3.1** Thermoelectric generation module. The left one shows the inside; ceramic insulator is detached.

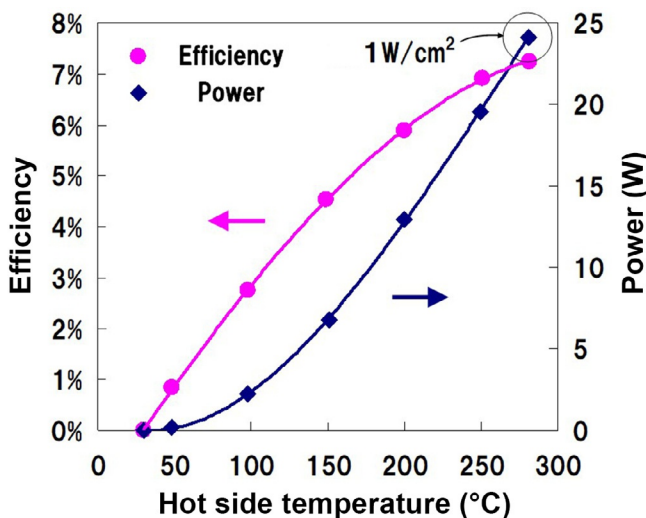


**Fig. 4.3.2** Performance curve of a TEG module.

increasing the temperature difference is one of the most critical in the thermoelectric application.

TEG can be divided mainly into three categories, as shown in Fig. 4.3.3, according to the scale of heat source and purpose of electric power: (1) Energy harvesting applications for sensors, actuators, and transmitters that operate with micro power by capturing little heat flow existing in the environment and converting them into milliwatts

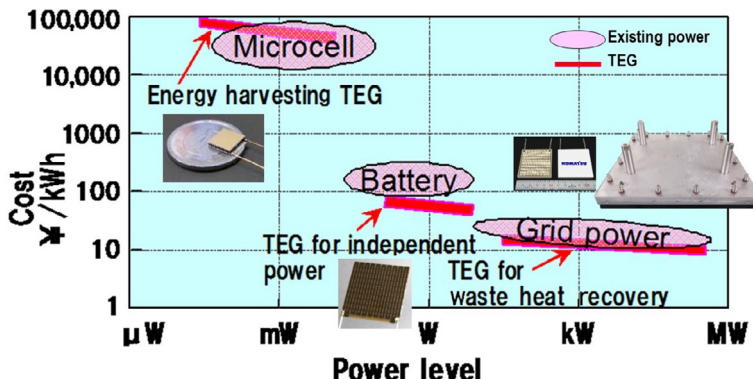


Fig. 4.3.3 Three categories of TEG.

class electric power. (2) Independent power supply applications that convert the heat of a few kilowatts such as open fires and stoves into W class electric power for local use or charging portable equipment. (3) Waste heat recovery application over kilowatts class from industrial waste heat and contributes to energy saving.

As shown in Fig. 4.3.3, there are existing power sources in each category, and thermoelectric power generation is considered to replace them with added value.

From here, some example of an application for each category is shown in the order of “small.”

#### 4.3.4.1 Energy harvesting (EH)

The thermoelectric module for EH, with a size of about 5 mm, can produce  $100\text{ }\mu\text{W}$  only by adding a temperature difference of 2–3°. There are many places where this level of temperature difference occurs temporarily. The machine in operation is where heat flows continuously, and it makes enough temperature difference for TEG. It is the application that best matches the thermoelectric features, “small.” With the recent evolution of power-saving technology, EH is considered as a technology of machine monitoring without a power source. Among the several EH technologies, thermoelectric is the most promising technology around machines.

Generally, when the period of the initial failure passes, the machine part enters the period of the accidental failure, and finally reaches the life. Although the time-based maintenance (TBM) is effective to some extent for the life, the proper maintenance period cannot be set to prevent accidental failure that randomly occurs with each facility. Therefore, condition-based maintenance (CBM) is more and more important in the recent factory management that is becoming increasingly competitive. In CBM, it is necessary to install sensors such as temperature, pressure, vibration, etc. on the monitoring place to get the data continuously. It makes high costs for the sensors (the parts, installation, and wiring), the system for collection and judgment of data, and



**Photo 4.3.2** TEG energy harvesting wireless vibration sensor.

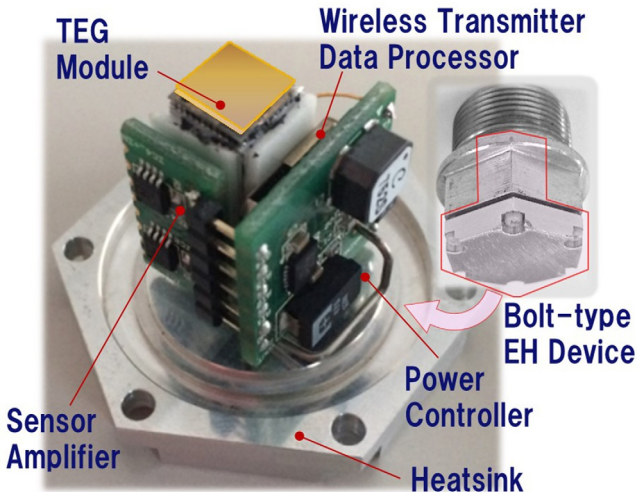


**Photo 4.3.3** Bolt-type TEG energy harvesting device.

maintenance and management. Thus, the CBM operation is limited to some of the steel mills and large plants.

The “thermoelectric EH wireless sensor device” shown in Photos 4.3.2 and 4.3.3 is expected to solve this problem for any type of machine. Since it is wireless and easy to attach and remove, it is possible and suitable to install on the existing machines.

The transmission interval of the EH wireless sensor device depends on the power generation quantity by the micro-TEG. The interval is several seconds to several minutes if the power generation is of several microwatts to tens of microwatts, which is available by the TEG temperature difference of tens of degrees to several degrees. Since the voltage of the thermoelectric module is low at such a small temperature difference, a booster circuit is necessary, and its characteristic matching with TEG is an essential point of the design.

Since a machine generates steady heat during operation, the heat flux through the TEG is also steady, and the power generation quantity is constant even if the ambient changes. That makes the temperature difference between the device's surfaces kept constant even when the temperature fluctuates by almost 10 degrees or even when the temperature suddenly drops due to rain. It means the TEG EH device works with good robustness to the climate, and the sensor data are transmitted at almost constant intervals.

[Photo 4.3.4](#) shows an example of vibration monitoring of a motor outside the factory, and [Photo 4.3.5](#) is monitoring for construction machines. Considering its value as a wireless power source, TEG EH is an important technology for moving machines. The batteryless and wireless features of TEG EH devices are useful in places where wiring is complicated because of moving and where it is difficult to replace batteries such as high place or remote area.

#### 4.3.4.2 Stand-alone power source

The TEG module functions almost permanently as a stand-alone power source without any special wiring only if there is a heat source. With a small amount of flame level thermal energy, it can be a substitute for a battery of several watts to tens of watts. There is no cost of wiring and battery, and also it is cheaper than batteries in terms of energy cost. If the flame can produce electric power while performing functions such as heating and cooking by designing well, the power generation purely added value. It has already been applied to cartridge gas fan heater, stoves, outdoor goods, etc.



**Photo 4.3.4** Vibration monitoring of pump motor.



**Photo 4.3.5** Condition monitoring for construction machine by bolt-type sensor.

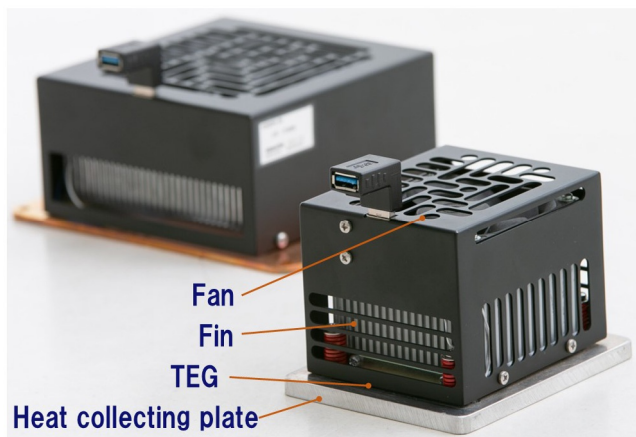


**Photo 4.3.6** Stand-alone TEG unit.

The “stand-alone power unit with TEG” shown in Photo 4.3.6 is a product that assembles a TEG module with a heat receiving plate, a DC-DC converter, a fin, and a fan. The heat receiving side is heated to about 220°C, the heat-dissipating side is cooled by the fan to maintain the temperature difference, and the DC output of several watts is possible.

#### 4.3.4.3 Waste heat recovery

The industrial field uses more than 1/3 of the energy, and the waste heat is large in quantity and quality, namely the temperature is high. Energy saving in the industrial field has been pursued from the viewpoint of economic rationality, and efforts have been made for efficiency improvement. Still, the recovery of waste heat is not made enough. Industrial furnaces, which generate a large amount of waste heat, usually operate continuously for 24 hours, 365 days to prevent heat loss due to starting and stopping and to operate with high efficiency. For the power generation equipment of waste heat recovery, it is a field with the possibility of high operation rate and large power generation.

**Photo 4.3.7** shows the verification test of the “TEG waste heat recovery unit” for the exhaust heat at the detoxifying burner of carburizing furnaces [4]. In this test, the system is connected to the distribution system of the electric utility. The system certified authorization of the Ministry of Economy, Trade, and Industry as a TEG power generation facility for the first time in Japan. The detoxifying burner heat of a general carburizing furnace is about several tens of kilowatts, and it is about several hundred watts when the total power conversion rate is a few percentage. As it is small as a power generation facility, thermoelectric technology seems to be adequate for such an application.

The detoxifying burner flame in carburizing furnaces is generally unstable in shape and vary in quantity during the process. There is temperature distribution on the heat receiving plate, and there is a risk of local degradation. Though the life equivalent to 10 years has been confirmed in the specification temperature of the module itself, the durability in the actual use is one of the most important issues.

**Photo 4.3.8** shows a verification test using radiant heat from a continuous casting machine in steelworks. The iron and steel industry is a high energy-consuming industry which occupies about 10% of the energy consumption of Japan, and about 1/3 of the energy is exhausted and unutilized. Though the steel industry in Japan overwhelms other countries in energy efficiency, there is still waste heat which is not utilized [5].

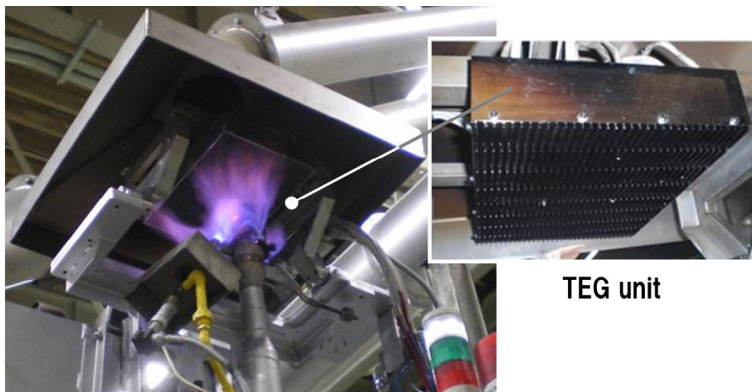


**Photo 4.3.7** TEG waste heat recovery for carburizing furnace.

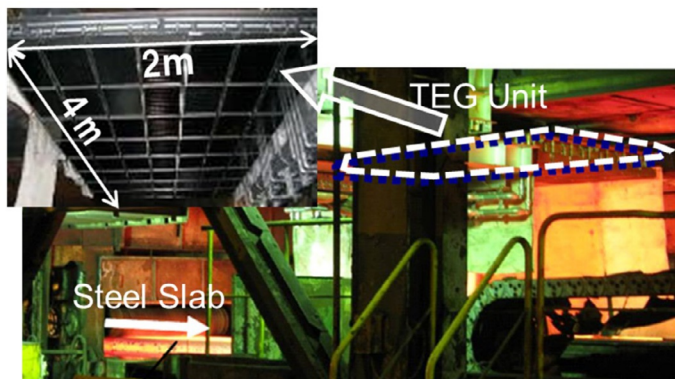


**Photo 4.3.8** TEG waste heat recovery for continuous casting facility.

Since radiant heat is not easy to collect as it diffuses from the site, efficient waste heat recovery is difficult for the generator of a mechanical system. On the other hand, the TEG waste heat recovery unit is advantageous in layout because it can directly generate electricity by receiving radiation heat on the plate. In this verification test, 56 units are set in an area of 2m width and 4m length, and a power generation of 10 kW has been realized [6]. Even in the steel industry where energy saving and waste heat recovery are done almost entirely, thermoelectric technology could be applied for the small but remaining wasted heat.

## References

- [1] H.J. Goldsmid, R.H. Douglas, Br. J. Appl. Phys. 5 (1954) 386.
- [2] A.R. Urbanitzky, Electricity in the Service of Man, Cassell & Co. Ltd., 1886.
- [3] H. Hachiuma, K. Fukuda, Proc. 5th European Conference on Thermoelectrics, ECT2007, 2007.
- [4] H. Kaibe, et al., Komatsu Technical Report, vol. 57 (164), 2011, p. 26.
- [5] T. Kuroki, et al., J. Electr. Mater. 43 (6) (2014) 2405.
- [6] T. Kuroki, et al., J. Electr. Mater. 44 (6) (2015) 2151.

# Thermoelectric applications in passenger vehicles

4.4

Doug Crane  
DTP Thermoelectrics, Altadena, CA, United States

## 4.4.1 Introduction

Thermoelectric (TE) devices are novel in that they can be operated either as solid-state heat pumps or as solid-state power generation devices. Reviews of TE use in automotive applications have been written in the past [1]. This chapter looks to provide an update on previous reviews by looking at how thermoelectrics have been used in passenger vehicles in the past, what has limited their usage, and what can be done to broaden their usage in the future. The chapter is organized into two sections. The first section is focused on heating and cooling and/or thermal management applications of thermoelectrics in automobiles, while the second section is focused on thermoelectrics used for power generation in passenger vehicles.

## 4.4.2 Heating and cooling/thermal management

When in Peltier or heat pumping mode, thermoelectrics have successfully provided thermal management and passenger comfort in passenger vehicles. Their most successful application has been in the provision of more targeted and localized thermal management for passengers and components, but there have also been concepts for the handling of large-scale thermal management issues in the vehicle.

### 4.4.2.1 Seat-based and zonal systems

The largest application of thermoelectrics in passenger vehicles today is in heated and cooled seats. Gentherm introduced the Climate Control Seat in 1996. This system (shown in Fig. 4.4.1) is composed of a thermoelectric subsystem both in the seat bottom and in the seat back. Each TE subsystem is composed of a single TE module with heat transfer fins thermally attached on both sides. A blower then blows air across the fins. When electrical current is applied to the TE device(s), heat is pumped from one side of the module to the other. Depending on the direction of current flow, heat is either pulled out of or pumped into the main flow. The main and waste air flows run parallel to each other. Channels in the seat cushions distribute the conditioned air to the occupant's bottom and back, providing comfort more directly to the passenger than is provided with a full-vehicle HVAC system, which conditions air more centrally in the vehicle. Separate channels help to reject waste flow away from the

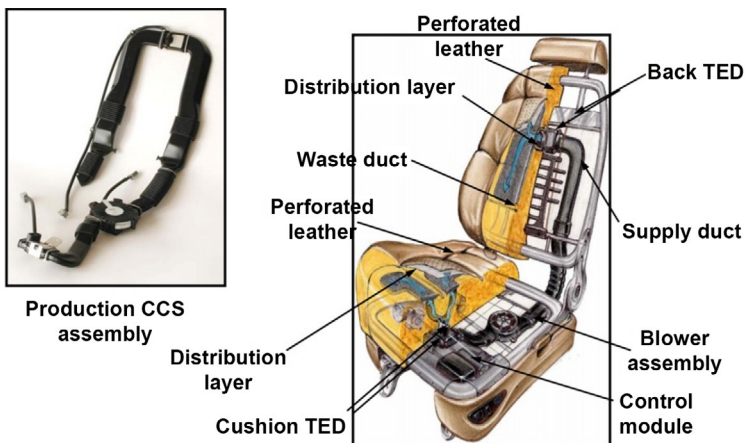


**Fig. 4.4.1** Gentherm Climate Control Seat system [2].

occupants and into the cabin of the vehicle. The TE modules of this system are made with conventional bismuth telluride thermoelectric material.

Each occupant in the vehicle requires approximately 100–200 W of heating or cooling energy to provide comfort. In comparison, a full HVAC system, which conditions all of the interior of the vehicle independent of the number of occupants, can require up to 5 kW of conditioning to provide a similar level of comfort to passengers.

Initially, the seat systems were marketed principally as being able to provide faster and more direct comfort to passengers over other systems. Over the last decade, as more and more attention has turned to improving the energy efficiency of various systems in the vehicle and reducing vehicle emissions, the environmental aspects of the seat system have come under focus. Kreutzer et al. [3] investigated the impact of passenger vehicle seat systems on energy efficiency and CO<sub>2</sub> emissions. The study found that actively cooled seats provided an average reduction of 4.0 g CO<sub>2</sub>/mi. The study also found that use of seat systems saved between 3.5 and 6.6 gal/year of fuel normally attributed to the use of air conditioning in individual passenger vehicles. This is a 10%–20% reduction in comparison to the national vehicle baseline of 30.0 gal/year of fuel use attributed to air conditioning.

While the Climate Control Seat system has been a very successful application of thermoelectrics in passenger vehicles, questions remain as to whether it provides enough thermal comfort under all ambient conditions, which would be necessary in order to be a viable option for full HVAC system replacement. To this point, it has been used as a supplemental system only and, thus, its deployment has been limited to more luxury vehicle applications. Further, under certain environmental conditions, defogging capabilities become necessary. These conditions, which are typically handled by a full HVAC system, have proven to be more difficult to handle with a seat-only system.

In an attempt to resolve these issues, and building on the benefits of the seat systems, two programs were sponsored by the US Department of Energy and the

California Energy Commission to provide zonal heating and cooling in passenger vehicles [4–6]. Ford led one of these programs in partnership with Gentherm, Halla Visteon, and others, while General Motors (GM) led the other zonal program in partnership with Marlow, Delphi, and others. The goal of the zonal HVAC programs was to develop a TE HVAC system capable of both reducing fuel consumption and optimizing passenger comfort [4]. The programs were meant to demonstrate the technical feasibility of the TE HVAC system for light-duty vehicles along with a viable path toward commercialization. The general concept is shown in Fig. 4.4.2.

The Ford project incorporated the Climate Control Seat system with the ability to provide localized comfort for the passenger using additional TE devices throughout the vehicle, such as the headers as shown in Fig. 4.4.2. While device-level coefficient of performance (COP) targets of  $>1.3$  in cooling and  $>2.3$  in heating were achieved, the cost-effectiveness of the system was still a concern.

In the GM program, the constructed system, including the TE device shown in Fig. 4.4.3, achieved a COP of  $>1.4$  in cooling and  $>2.4$  in heating when installed in a conventional vehicle (eAssist Buick LaCrosse) [7]. The system was also tested in a plug-in hybrid electric vehicle (Chevy Volt) where a COP of  $\sim 1$  was measured when used at ambient temperatures  $<0^{\circ}\text{C}$  in steady state, thus, showing a limited COP advantage compared to other systems [7].

Evolving from the zonal concept to a more seat-centric system, GM and Gentherm reported on their latest system design [6], which has many similarities to earlier zonal systems. The objective for their project was a 30% overall reduction in energy to achieve equal or superior occupant comfort typical of today's standard passenger vehicles. The system was installed in the front two seats of a Chevy Bolt electric vehicle and used seat, console, steering wheel, and door arm rest heaters, as well as foot and neck warmers, to provide occupant comfort in cold ambient temperatures. For hot ambient temperatures, the system used climate-controlled seats with cooling provided by thermoelectrics and a mini vapor compression system for additional cooling. The microclimate system, although not nearly as thermoelectric-based as earlier zonal concepts, provided 50% energy savings in heating and 30% energy savings in cooling.

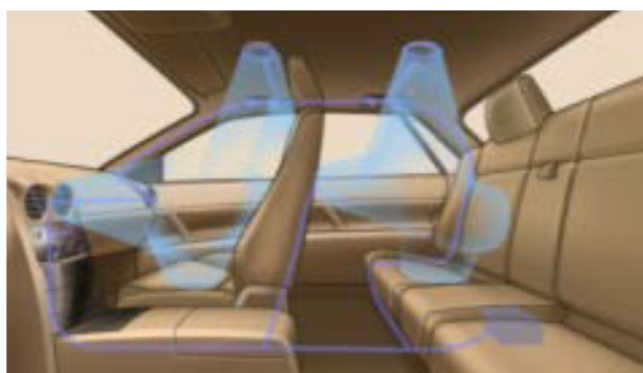


Fig. 4.4.2 Zonal HVAC system concept [4].



**Fig. 4.4.3** Prototype TE device in GM zonal program [7].

This improvement in energy use was reported to cut range degradation in the electric vehicle in half [6].

Cost is still the main factor working against these systems as the cost of the thermoelectric material, bismuth telluride, has remained high while device COPs, which are driven by material figure of merit, ZT, and temperature differences have remained low. The price of tellurium has been as low as \$30/kg and as high as \$450/kg in the past. This instability in cost has made it very difficult for bismuth telluride to see widespread adoption. There are also high assembly costs for TE devices as a result of the high number of parts required. There are typically  $>100$  individual TE legs in a single TE module. The cost of the components, including power electronics, has been a barrier to widespread adoption, as well.

These systems have the potential for widespread adoption if the cost of tellurium can stabilize at a low value and/or if a high-ZT, low-cost, alternative TE material can be identified. The systems would also benefit from system simplification along with a decrease in the cost of the power electronics. If TE material is further integrated into the systems, a potential benefit would be a reduction in the number of system parts and a reduction in parasitic interfacial resistances, which reduce device COP. Manufacturing advances, such as additive manufacturing, could also enable some of these improvements.

#### 4.4.2.2 Battery thermal management

Another application of thermoelectrics in automobiles is in lithium-ion battery thermal management for electric and hybrid electric vehicles. If the operating temperature is too low, the battery impedance increases and if the battery temperature is too high, the battery degrades faster, reducing its life. There have been many academic studies on thermoelectric-based battery thermal management systems for electric vehicles [8]. Barnhart et al. [9] described a battery thermal management system for vehicles with TEs that attach to the battery terminals and provide temperature control. First described in the patent by Kossakovski et al. [10], this concept enables a reduced thermal resistance path to the internals of the battery where the battery heat is generated. Gentherm has gone to production with a TE battery thermal management system [11] that was first launched on the Mercedes S-Class EQ-Boost in 2018 on 48-V lithium-ion batteries. This system uses thermoelectrics as a fully integrated structural component of the battery housing.

The spot cooling nature of TEs has the potential to further enable this application if costs of the system can be reduced. The integration of the thermoelectrics more directly into battery packs, as done with the Gentherm system on the Mercedes S-Class vehicle, has great potential as it helps to keep the cost-effectiveness of the system as high as possible through the elimination of parts and parasitic resistances.

#### 4.4.2.3 Full HVAC system

Use of refrigerants such as R134a, with a global warming potential of 1430, has been greatly restricted in future passenger vehicles [12]. This has caused manufacturers to look for alternatives to traditional vapor compression systems. Since “HVAC is the largest single non-motive consumer of power in a vehicle” [13], there is motivation to look for alternative systems and working fluids. Electric vehicles have the added requirement of providing occupant heating since the waste heat generated as a by-product of internal combustion engine thermal management is not available.

Concepts for full TE HVAC systems have been patented in the past by Gawthrop [14] and Goenka et al. [15]. Wang et al. [16] also documented a TE HVAC prototype design (see Fig. 4.4.4) that was built to have input power ranging from 200 to 3000 W and was tested to have COPs ranging from 0.63 to 1.55 in cooling and 2.15 to 4.60 in heating, depending on the operating conditions. This design utilized the concept of thermal isolation in the direction of flow [17] to boost COP by a factor of two. Other work has included the creation of a TE heat pump system by Mahle [18] and an experimentally validated design for a full automotive HVAC system by Attar et al. [19].

The combination of thermoelectrics with other cycles is a concept that has also been investigated. Okuma et al. [20] looked at adding a TE device in the middle pressure stage of a gas injection cycle. The updated system achieved 1 kW (+19.8%) of additional heating capacity at an ambient temperature of  $-17.8^{\circ}\text{C}$  when compared to a baseline gas injection system. This is of particular benefit in heating for electric

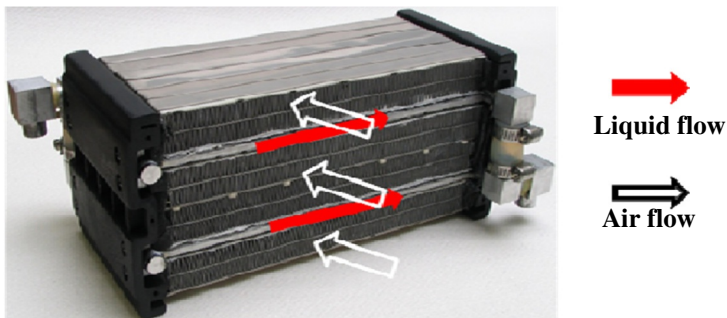


**Fig. 4.4.4** Air/liquid TE device for a full HVAC system [16].

and hybrid electric vehicles, which suffer from significant range degradation in cold ambient temperatures due to insufficient waste heat compared to standard internal combustion engine vehicles.

The refrigerant-free and solid-state nature of thermoelectric systems make them appealing for use in a full HVAC system. However, they are still plagued by the same issues that have been described above for other thermoelectric heating and cooling applications in passenger vehicles. The problems with thermoelectrics are even more severe for the full HVAC application, which needs to provide as much as 5 kW of conditioned air. To this point, this has been too large to provide cost-effectively. Full HVAC systems also do not take advantage of the spot cooling benefits of thermoelectrics and often require larger temperature differences that drive down system COP. The COP of vapor compression cycles is more than four times higher than that of thermoelectrics. Thermal isolation can help to reduce this gap, but it cannot eliminate it entirely.

Higher ZT, lower cost TE materials could further enable this application in the future, as can improved manufacturing methods, which would also help to reduce cost. It will certainly get more attention as more and more systems move away from R134a and look to reduce the amount of power needed to drive these systems.

#### 4.4.2.4 Other heating and cooling applications

In addition to the above applications, thermoelectrics have been used in passenger vehicles in several other ways to provide temperature control for occupant benefit. The thermoelectric cupholder, which is intended to help keep a beverage hot or cold while driving, is one such application [21]. Here, the ability of the TE device to provide heating or cooling to the cupholder is simply a matter of switching electrical current direction.

TEs have also been used to control steering wheel temperature [22]. This type of application can be part of a zonal system, as described earlier, or can be independent from a larger system.

### 4.4.3 Power generation/waste heat recovery

The rule of thumb for the energy flow for a typical gasoline-powered automobile is that one-third of the energy goes toward vehicle propulsion, one-third of the energy goes to the exhaust system and out the tailpipe, and one-third of the energy goes to the radiator or cooling system. It is estimated that over 60% of the total fuel energy used in a vehicle is wasted. As a result of this inefficiency, there has been tremendous pressure to develop methods to reduce and/or reuse some of this wasted energy. Since a reduction in vehicle emissions goes hand in hand with a reduction in fuel consumption, there is double the motivation for improved energy usage methods. One such method is vehicle waste heat recovery which seeks to reduce emissions and fuel consumption as much as possible by cost-effectively recovering waste heat and converting it to electricity.

With about 30% of fuel energy lost to a vehicle's cooling system, the radiator is an attractive location for waste heat recovery. Kim et al. [23] built and integrated a TEG into the radiator of an automobile. At 80 km/h, the TEG generated ~75 W of power at only ~0.3% overall efficiency. In a study by Crane and Jackson [23,24], waste heat recovery from the cooling system was investigated, as well. They found the low temperatures (around 100°C) in the cooling system to be too low for efficient power generation without significant TE-material ZT improvements to boost efficiency.

Waste heat can also be recovered from the engine exhaust system, where temperatures are higher than in the cooling system. Several studies have focused on waste heat recovery from exhaust systems over the past several decades. For example, Birkholz et al. [24] investigated using FeSi<sub>2</sub> to recover waste heat from the exhaust of a Porsche 944 engine. At full engine power, 58 W of power was generated at a temperature difference of 527°C between source and sink. Matsubara [25] investigated the use of segmented TE materials with skutterudites and bismuth telluride to recover waste heat, while Ikoma et al. [26] designed a TEG with SiGe TE devices. This TEG was estimated to have a heat exchanger efficiency of 11% of primary exhaust gas energy flux with generated power at 0.9% of the heat flux from the exhaust gas to the coolant. Unfortunately, the maximum electric power out of this module was only 1.2 W at a hot-cold side temperature differential of 290°C. Each of these studies suffered from poor thermoelectric performance (low ZT) and poor heat transfer. It is critical to the success of a thermoelectric generator to have good heat transfer into and out of the device.

Thacher et al. [27], in partnership with Delphi and Clarkson University, reported on a TEG installation into a 1999 GMC Sierra pickup truck. The TEG generated power up to 255 W with a reported fuel consumption improvement on the order of 1%–2%, depending on speed. Mori et al. [28] from Honda reported on a validated modeling study which saw a 3% improvement in fuel economy through the integration of a TEG into a series hybrid vehicle. Aixala [29] and the Volvo/Renault team developed a TEG made of Mg<sub>2</sub>Si TE materials for a 2 L diesel passenger vehicle that had a measured power output of ~250 W. Liebl et al. [30] described BMW's TEG program (see Fig. 4.4.5), which included TEGs that produced 200, 300, and >600 W when installed in vehicles.

Numerous prototypes have been built, cumulating in the 600W X6 demonstrator.

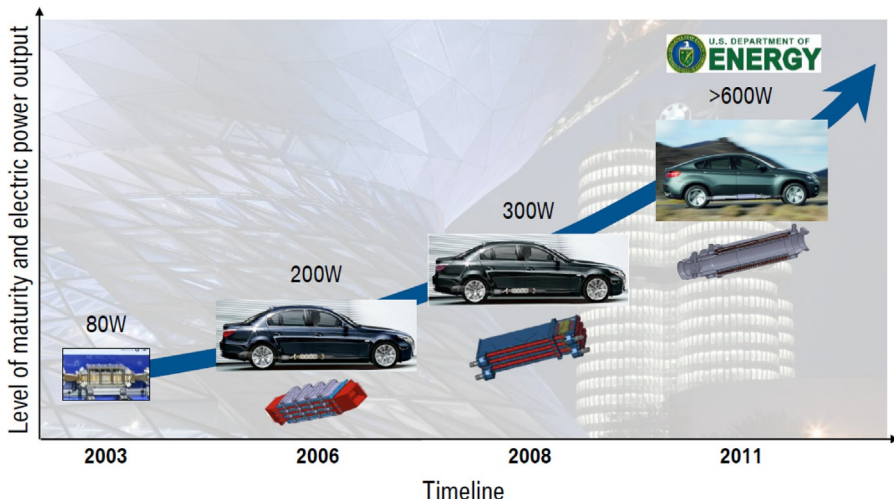


**Fig. 4.4.5** TEGs in BMW vehicles [31].

Gentherm integrated thermoelectric material more directly into the heat exchangers in order to reduce parasitic losses from thermal resistances, increase the power density of the TEG, and reduce cost. Reducing parasitic losses improves the efficiency of the device while increasing the power density of the TEG minimizes size and weight while maximizing power output. Increasing power density also reduces the amount of TE material needed in the TEG, reducing cost. However, increased power density with high temperature differences across the TE legs, increases the thermally induced mechanical stress on the TEG device caused by thermal expansion mismatch between different materials. Gentherm designed a cylindrical TEG (see Fig. 4.4.6) that takes advantage of the thermal expansion of the hot internal heat exchanger into the hot TE connectors (rings that surround the cylinder) to eliminate the need to apply external pressure to the device [33,34]. This helped to reduce the thermally induced stress on the component, increase its robustness, and reduce the cost of providing a means of external pressure.

Two cylindrical TEGs made of segmented TE elements comprising Half Heusler and bismuth telluride TE material were made for a BMW (see Fig. 4.4.5) and a Ford vehicle. A maximum power output of 712 W was achieved for these TEGs on the test bench, Fig. 4.4.7 shows engine dynamometer test results [35]. One of the TEGs was integrated into a BMW X6 35i xDrive test vehicle (see Fig. 4.4.8) with test results shown in Fig. 4.4.9 [35]. A maximum power output of 605 W was measured from the TEG. At 110 km/h, a maximum fuel efficiency improvement of >1.2% was achieved.

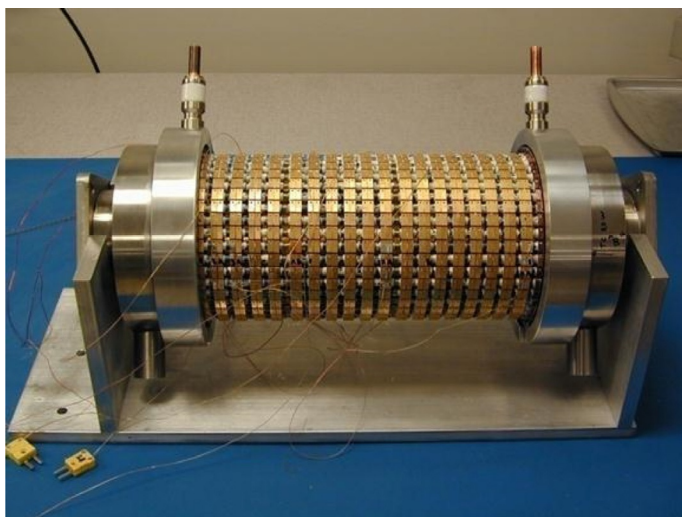


**Fig. 4.4.6** Cylindrical TEG [32].

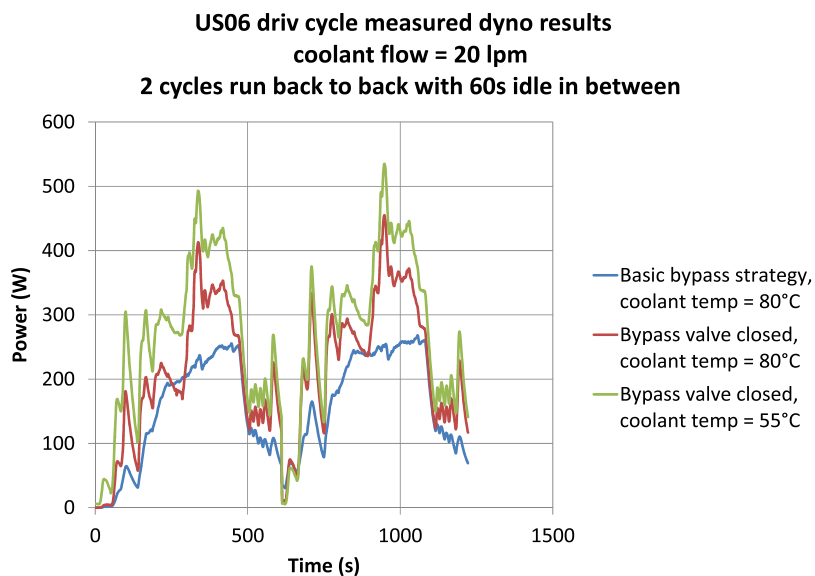


**Fig. 4.4.7** TEG power output over the US06 drive cycle [32].



**Fig. 4.4.8** TEG integration into BMW X6 [32].

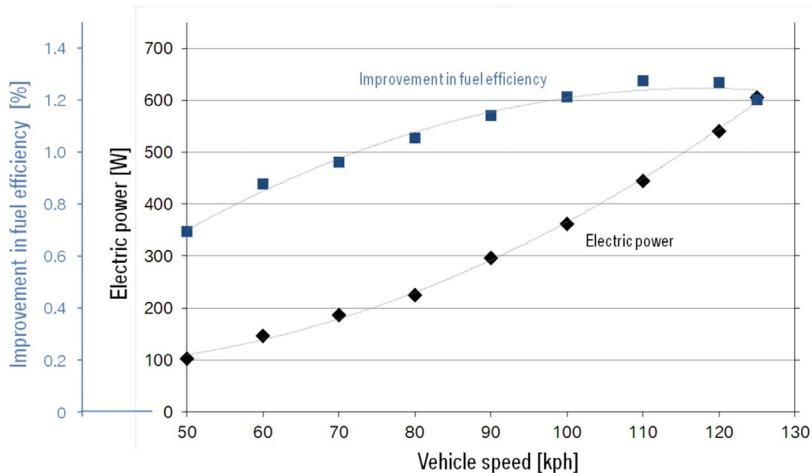


**Fig. 4.4.9** Power output and fuel efficiency improvement vs vehicle speed for TEG integration in BMW X6 [32].

A TEG was also integrated into a 2011 Lincoln MKT (see Fig. 4.4.10) with test data shown in Fig. 4.4.11 [35].

Building on the success of the cylindrical TEG, a smaller, cylindrical TEG subcomponent was developed called the cartridge, which is presented in Fig. 4.4.12 [37]. This design provided a more modular and cost-effective approach that greatly increased scalability of the TEG design. The cartridge was an individually finned tube heat exchanger with TE material sandwiched between the gas and coolant sides. Each cartridge was composed of multiple hot shunt assemblies, as shown in Fig. 4.4.12, connected electrically in series and thermally in parallel. The cartridges were made of different TE materials, including bismuth telluride, Half Heusler, and skutterudite. The TEG design was completed with multiple cartridges assembled in a shell and tube configuration (Fig. 4.4.13).

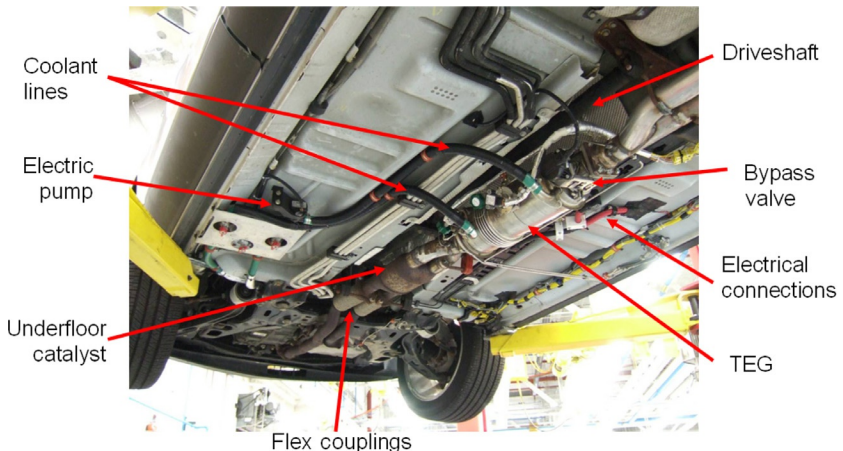


**Fig. 4.4.10** TEG integrated into a 2011 Lincoln MKT [32].

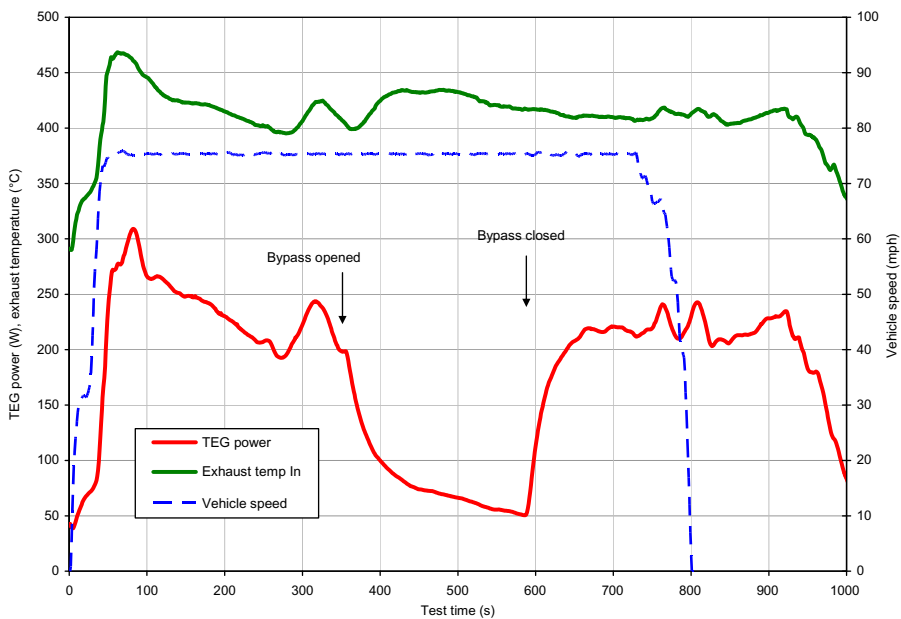


**Fig. 4.4.11** TEG test data showing highway cruise performance at 75 mph [32].

A cartridge-based TEG was installed on a BMW X3 with a “neutral” benefit to fuel economy. The TEG was also installed on a Ford F350 truck and tested over the US06 drive cycle. In this test, power was generated at over 1.1 kW with a fuel economy improvement of 1.2% and an emissions reduction of more than 9 g CO<sub>2</sub>/mi [37].

Building on earlier work with the goal of improving the cost-effectiveness of TEG for passenger vehicles, Alphabet Energy designed a low-cost TEG integrated into a



**Fig. 4.4.12** Modular TEG subcomponent and the hot shunt subassemblies that comprise it [36].

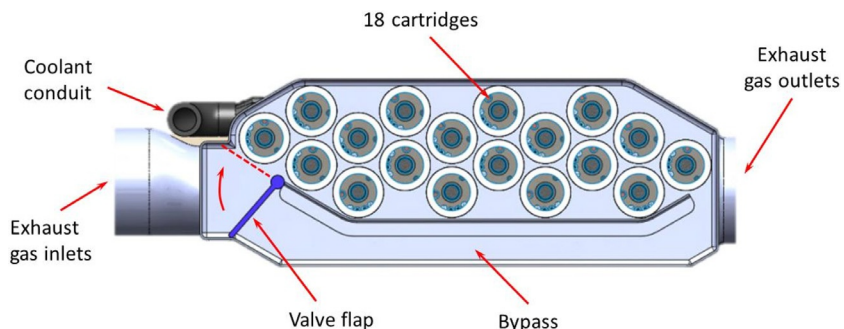


**Fig. 4.4.13** TEG concept using the cartridge subcomponent [36].

light-duty truck that was made with light-element TE materials tetrahedrite ( $\text{Cu}_{12}\text{Sb}_4\text{S}_{13}$ ) and magnesium silicide ( $\text{Mg}_2\text{Si}$ ) [38]. The raw material cost of these TE materials are a fraction of the cost of the TE materials, such as bismuth telluride, Half Heusler, and SiGe, used in previous programs. The TEG was installed on both a 5.3-L Suburban and a 6-L Silverado (Fig. 4.4.14). For the Suburban, 49 W of average power was generated, and 0.9% fuel economy benefit was measured for the combined city-highway drive cycle. For the Silverado, 91 W of average power was measured for the combined cycle. Electrical power for these tests was connected to the vehicle battery by a DC/DC converter [38].



**Fig. 4.4.14** Alphabet Energy TEG installed on 5.3L Chevy Silverado [38].

While many of the above-referenced programs have successfully demonstrated many of the technical aspects of TEG required for commercial success, they have not provided a path to a commercially cost-effective solution. The TEG in current passenger vehicles remains too large, with too many parts, and with efficiencies too low to be cost-effective. Higher ZT materials that can improve TE efficiency would help with these problems. Scalable, low-cost TE materials, along with improved manufacturing methods such as additive manufacturing, would also help to make TEG systems more cost-effective. Power electronics and other components of the TEG system also need to come down in cost. The good news is that overcoming these obstacles is possible in the future and is being worked on today. The bad news for passenger vehicles, however, is that, as vehicles become more electrified, there may not be enough high-temperature waste heat onboard to keep TE waste heat recovery viable.

#### 4.4.4 Conclusion and future outlook

Thermoelectrics have played a successful role in the past in passenger vehicles, including in heated and cooled seats, and will likely have opportunities to play additional roles in the future as cost-effectiveness increases. Currently, however, cost-effectiveness continues to limit the number of applications of TE devices. Further, as passenger vehicles become more and more electrified in the future, the potential application of TEs in waste heat recovery may fade. The internal combustion engine, which provides higher grade (higher temperature) heat, makes efficient thermoelectric energy conversion possible. That said, significant amounts of waste heat will still be generated on tomorrow's passenger vehicles, as a result of ultrafast battery charging and increased power electronics for autonomous driving, which may provide potential for thermoelectric waste heat recovery. Ultrafast charging electric vehicles could

require 15–18kW of heat dissipation [39], while LiDAR required for fully autonomous driving could require 3kW [40].

While vehicle electrification may challenge thermoelectric prospects in waste heat recovery, they increase thermoelectric opportunities in thermal management. Electric vehicles require new solutions for battery thermal management and HVAC, as well as thermal management for ultrafast charging and LiDAR, that were not required for more conventional vehicles. The future is bright for thermoelectric opportunities in the passenger vehicles.

## Acknowledgment

The author thanks Lon Bell for his overall consultation and inspiration, without which this work could not have been completed.

## References

- [1] J. Yang, F.R. Stabler, Automotive applications of thermoelectric materials, in: D.M. Rowe (Ed.), *Thermoelectrics and Its Energy Harvesting: Modules, Systems, and Applications in Thermoelectrics*, CRC Press, 2012.
- [2] J.W. Fairbanks, Thermoelectric developments for vehicular applications, in: DEER Conference, Detroit, MI, 2006.
- [3] C. Kreutzer, et al., Impact of active climate control seats on energy use, fuel use, and CO<sub>2</sub> emissions, in: SAE 2017 Thermal Management Systems Symposium, Plymouth, Michigan, 2017.
- [4] C.W. Maranville, Thermoelectric HVAC and thermal comfort enablers for light-duty vehicle applications, in: 2013 DOE Vehicle Technologies Annual Merit Review, 2013.
- [5] Automotive Thermoelectric HVAC Development and Demonstration Project, 2016.
- [6] T. Gordon, et al., Microclimate comfort system: solution for increasing driving range of electric vehicles, in: 2019 SAE Thermal Management Systems Symposium, Plymouth, Michigan, 2019.
- [7] J. Bozeman, Energy efficient HVAC system for distributed cooling/heating with thermoelectric devices, 2013, in: DOE Vehicle Technologies Annual Merit Review, Office of Energy Efficiency and Renewable Energy, 2013.
- [8] A.R.M. Siddique, S. Mahmud, B.V. Heyst, A comprehensive review on a passive (phase change materials) and an active (thermoelectric cooler) battery thermal management system and their limitations, *J. Power Sources* 401 (2018) 224–237.
- [9] T. Barnhart, et al., Distributed battery thermal management using thermoelectric, in: Thermal Management Systems Symposium, 2013.
- [10] D. Kossakovski, T. Barnhart, A. Piggott, Thermoelectric-Based Thermal Management of Electrical Devices, 2014.
- [11] Gentherm, Gentherm's Thermoelectric Battery Thermal Management System Wins 2019 Automotive News PACE Award, 2019.
- [12] <https://www.epa.gov/mvac/refrigerant-transition-environmental-impacts>.
- [13] C. Maranville, Thermoelectric opportunities for light-duty vehicles, in: 3rd Thermoelectric Applications Workshop, Baltimore, MD, 2012.
- [14] P.R. Gawthrop, Climate Control System for Hybrid Vehicles Using Thermoelectric Devices, 2008.

- [15] L.N. Goenka, D.T. Crane, L.E. Bell, Thermoelectric-Based Heating and Cooling System, 2010.
- [16] D. Wang, D. Crane, J. LaGrandeur, Design and analysis of a thermoelectric HVAC system for passenger vehicles, in: SAE World Congress, 2010.
- [17] L.E. Bell, Use of thermal isolation to improve thermoelectric system operating efficiency, in: 21st International Conference on Thermoelectrics, IEEE, Long Beach, CA, 2002.
- [18] 2019. <https://www.meet.mahle.com/meet/en/thermoelectric-heat-pump/>.
- [19] A. Attar, H. Lee, S. Weera, Experimental validation of the optimum design of an automotive air-to-air thermoelectric air conditioner (TEAC), *J. Electron. Mater.* 44 (6) (2015) 2177–2185.
- [20] T. Okuma, R. Radermacher, Y. Hwang, A novel application of thermoelectric modules in an HVAC system under cold climate operation, *J. Electron. Mater.* 41 (6) (2012) 1749–1758.
- [21] Energy Balance of Automotive Thermoelectric Cup Holder, [www.amstechnologies.com/solutions/solution-single-news/article/energy-balance-of-automotive-thermoelectric-cup-holder/](http://www.amstechnologies.com/solutions/solution-single-news/article/energy-balance-of-automotive-thermoelectric-cup-holder/).
- [22] C. Maranville, J.V. Wiemeersch, J. Cikalo, Heated/Cooled Thermoelectric Steering Wheel, 2013.
- [23] S. Kim, et al., A thermoelectric generator using engine coolant for light-duty internal combustion engine-powered vehicles, *J. Electron. Mater.* 40 (5) (2011) 812–816.
- [24] U. Birkholz, et al., Conversion of waste exhaust heat in automobiles using FeSi<sub>2</sub>-thermoelements, in: 7th International Conference on Thermoelectric Energy Conversion, University of Texas at Arlington, 1988.
- [25] K. Matsubara, Development of a high efficient thermoelectric stack for a waste exhaust heat recovery of vehicles, in: 21st International Conference on Thermoelectrics, IEEE, Long Beach, CA, 2002.
- [26] K. Ikoma, et al., Thermoelectric module and generator for gasoline engine vehicle, in: 17th International Conference on Thermoelectrics, IEEE, Nagoya, Jpn, 1998.
- [27] E.F. Thacher, et al., Testing of an automobile exhaust thermoelectric generator in a light truck, *Proc. Inst. Mech. Eng. D J. Automob. Eng.* 221 (2007) 95–107.
- [28] M. Mori, et al., Simulation of fuel economy effectiveness of exhaust heat recovery system using thermoelectric generator in a series hybrid, *SAE Int. J. Mater. Manuf.* 4 (1) (2011) 1268–1276.
- [29] L. Aixala, RENOTER project, in: TE Applications Workshop, Baltimore, MD, 2012.
- [30] J. Liebl, et al., The thermoelectric generator from BMW is making use of waste heat, *MTZ worldwide* 70 (2009) 4–11.
- [31] B. Mazar, State of the art prototype vehicle with a thermoelectric generator, in: TE Application Workshop, Baltimore, MD, 2012.
- [32] D. Crane, Automotive waste heat recovery using a thermoelectric generator, in: T. Kajikawa (Ed.), *Thermoelectric Power Generation System Technology*, 2013. <http://www.stbook.co.jp/>.
- [33] L.E. Bell, D.T. Crane, Vehicle waste heat recovery system design and characterization, in: International Thermoelectric Conference, Freiburg, Germany, 2009.
- [34] L.E. Bell, J.W. LaGrandeur, D.T. Crane, Progress report on vehicular waste heat recovery using a cylindrical thermoelectric generator, in: Thermoelectrics Goes Automotive, Berlin, Germany, 2010.
- [35] D.T. Crane, et al., TEG on-vehicle performance & model validation & what it means for further TEG development, in: International Conference on Thermoelectrics, Aalborg, Denmark, 2012.

- [36] D. Crane, Thermoelectric Waste Heat Recovery Program for Passenger Vehicles, 2013.
- [37] V. Jovovic, Thermoelectric Waste Heat Recovery Program for Passenger Vehicles, 2016.
- [38] A. Lorimer, et al., Thermoelectric exhaust heat recovery—demonstration of power generation and fuel economy benefits on light duty trucks, in: SAE Thermal Management Systems Symposium, 2016.
- [39] C. Rouaud, Battery thermal management systems development and vehicle integration for conventional and ultra-fast charging, in: Thermal Management Systems Symposium, Plymouth, MI, 2019.
- [40] S.R. Charmer, Thermal management for future powertrains, in: Thermal Management Systems Symposium, Plymouth, MI, 2019.

# Thermoelectric generators for full-sized trucks and sports utility vehicles

4.5

*James R Salvador*

Chemical and Materials Systems Laboratory, GM Global Research and Development Center,  
Warren, MI, United States

## 4.5.1 Introduction

The thermal efficiency of a gasoline internal combustion engine ranges between 30% and 40% depending on torque load and engine speed [1, 2]. The vast majority of the heating value of the fuel is lost to waste heat which is rejected in nearly equal proportion to the engine coolant and into the exhaust gas. Engine coolant is, by its nature, limited to an upper temperature of 120°C and if we use ambient air to reject the heat via the radiator the result is a temperature gradient of less than 150°C and typically closer to 100°C. While abundant, this waste heat is of low quality. Exhaust gas from a gasoline engine, by contrast, can reach 800–900°C as it exits the cylinder resulting in a much higher quality heat source, potentially providing a temperature difference of 400–800°C between exhaust gas and coolant [3]. The exhaust gas is, therefore, far more attractive from a thermodynamic cycle potential standpoint and it is for this reason that a variety of waste heat recovery techniques have been developed to recuperate exhaust gas energy. The most common waste heat recovery systems are electrical and mechanical compounding turbos which convert exhaust gas heat to torque [4]. In the case of mechanical compounding, the torque from the turbo is reintroduced to the drivetrain [5]. In electrical-turbo compounding systems, the turbo converts thermal to mechanical energy and then to electrical energy [6]. Organic Rankine Cycle (ORC) [7] and sterling engines [8] use liquid- to gas-phase transitions of working fluid with an expansion step to convert heat to mechanical energy and then a secondary turbine converts the mechanical energy to electrical energy. In the three cases, the electrical energy produced is supplied to the vehicle to satisfy load requirements without the need to expend fuel energy to produce it via an alternator. Finally, there are more passive approaches such as exhaust gas heat recovery (EGHR) systems [9], which are also found in passenger vehicles, and these are gas-to-liquid heat exchangers that transmit heat from exhaust to coolant for accelerated warm-up of engine oil and transmission fluid. This improves fuel economy by reducing powertrain frictional losses and can reduce the use of electrical heaters for the passenger cabin.

Thermoelectrics are widely used for passenger comfort applications in the automotive industry, particularly heated and cooled seats [10] as well as active heated and

cooled cupholders [11]. Recently, thermoelectrics have been introduced for advance thermal management of battery packs for 48-V electrical systems in hybrids electric vehicles [12]. All these applications utilize  $\text{Bi}_2\text{Te}_3$ -based materials designed to work at room temperatures and in these applications, the modules operate not to convert waste heat to electrical energy but use electricity to enact temperature gradients for thermal management.

The implementation of high-temperature thermoelectric materials for waste heat recovery systems in automobiles has been a long-standing goal of the TE community. It seemingly represents one of the few waste heat recovery applications where its ability to scale to sub 1 kW power output levels without reductions in conversion efficiency makes it advantageous to other approaches [13]. This cannot be said for systems like ORC, and even turbos systems which can only be miniaturized so far before machining tolerances and other limiting factors result in poor performance [14]. Additionally, since thermoelectric generators (TEGs) have no moving parts, noise vibration and harshness (NVH) is less of a concern compared to ORC or electrical or turbo compounding. Finally, TEGs are far less complex with fewer subsystems when compared to ORC or Sterling engines and are easier to pack in passenger vehicles and are generally lighter. TE's power rating scalability and reduced complexity, therefore, compensate for their poor thermal to electrical energy conversion efficiency.

Here we describe the development of a compact thermoelectric generator comprised of skutterudite thermoelectric materials ( $M_xFe_yCo_{1-y}Sb_3$  M=rare earth or alkali earth, with  $y=0$  for n-type  $y>0$  for p-type materials) and also describe the thermal and mechanical design considerations for the TEG and highlight its unique materials and structural features. We detail the vehicle integration approach that allows us to take advantage of both the electrical power generation and the enhanced thermal management approach to achieve maximum fuel economy benefits. Finally, we will highlight the on-vehicle testing results and describe the business case for adopting this and similar fuel economy improvement technologies.

### 4.5.2 Vehicle selection criteria

Several factors were weighed when selecting a vehicle platform for TEG development. Practical considerations included: sufficient packaging space close to the catalytic converters to accommodate the new components, large amounts of high-quality (high exergy) exhaust gas to facilitate the production of sufficient electricity to have a meaningful impact on fuel economy, and excess engine cooling capacity to dissipate the added thermal energy introduced by the TEG's rejected heat. The additional thermal load needs to be managed without introducing parasitic losses such as higher radiator fan duty cycles or having to increase the radiator size which negatively impacts aerodynamics. The added mass from the TEG should not contribute significantly to the vehicle mass and should not interfere with driving dynamics including acceleration and handling. All these considerations point to a large vehicle with an accompanying large, naturally aspirated engine (no turbocharging) such as a full-size truck or sport utility vehicle (SUV). We also undertook a feasibility study for incorporating

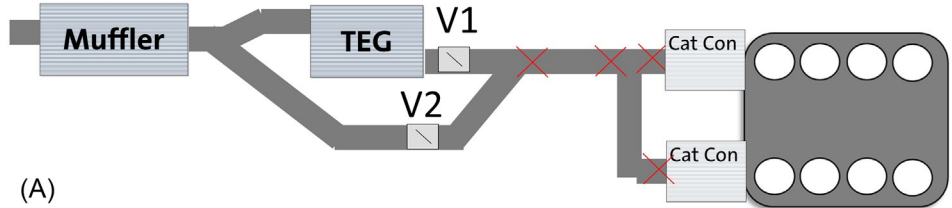
thermoelectric materials into the exhaust gas recirculating cooler (EGR cooler) in heavy-duty diesel engines. Given the low flow rates of the exhaust gas through the EGR cooler under most load conditions found on testing cycles, we concluded that the amount of electrical energy produced and thermal energy recovered to the engine coolant would not make a meaningful impact on fuel economy.

From a business case perspective, we considered vehicle volumes (number of vehicles produced and sold annually) impact to corporate average fuel economy (CAFE), availability, and size of off-cycle credits from the US environmental protection agency (US-EPA), and overall percentage reduction in CO<sub>2</sub> emissions. All of these factors lead us to select full-size trucks and large SUVs with 5.3-L V-8 engines as the best choice for development efforts. From the EGR cooler analysis, it was also clear that full exhaust gas flow was required to generate a meaningful amount of electrical power and so we opted for a traditional approach of integrating a stand-alone TEG system in the exhaust with heat rejection provided by the vehicle's normal cooling system.

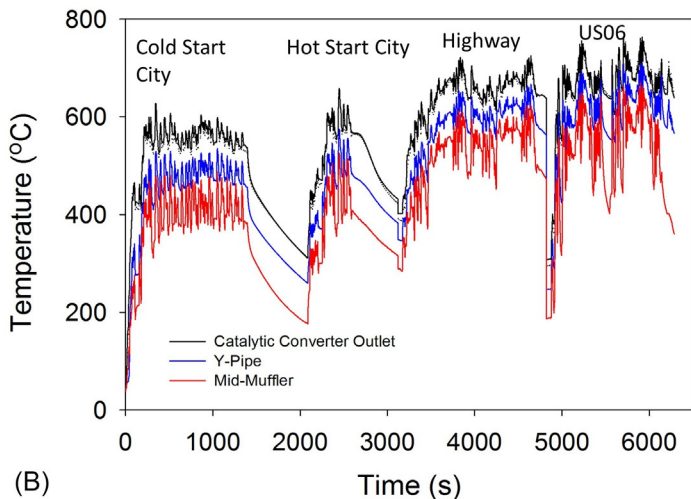
### 4.5.3 Thermal design and system sizing

Having selected the vehicle platform, we began baseline assessment including measurements of coolant and exhaust gas flow rates, and temperatures at several proposed integration locations including at the outlets of the catalytic converters, directly at the joint where the dual take-down manifolds from each bank of the V-8 are jointed as single exhaust pipe (y-pipe), and at the mid-muffler location approximately 1 foot downstream of the y-pipe. As expected the exhaust gas temperature decreased as it traversed the exhaust system, the location with the hottest exhaust gas was directly out of the catalytic converters due to the exothermic nature of the reactions which take place within them. Fig. 4.5.1 shows the locations where the temperatures were measured in the exhaust system as well as time versus temperature traces for several US EPA test cycles including the cold start city Bag 1 and Bag 2 portions, Bag 3 which is a hot start repeat of Bag 1, Highway and US06. The city cycles have the lowest vehicle speeds and accelerations and therefore lower exhaust gas flow rates and temperatures. There is also a larger drop in the temperatures along the exhaust system for the city cycle as compared to the highway and US06 cycles and is likely due to the lower flow velocity that allows for more heat transfer from the gas to the exhaust pipe. The city and highway cycle are part of the standard fuel economy, while the US06 is a supplemental test for assessing the FE under more aggressive accelerations and high-speed driving conditions.

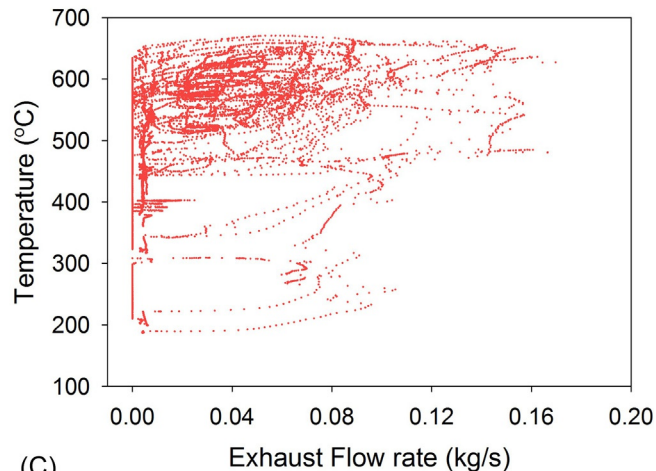
Fig. 4.5.1C shows the distribution of the gas temperature and flow rates for the US 06 and such clustering of data points helps to establish design criteria for the heat exchanger, specifically what flow rates and temperature are the most common. These common flow and temperature conditions can be used as steady-state heat flow conditions to co-optimize the heat exchanger and thermoelectric circuits. In this part of the thermal design exercise, the power output for a particular circuit layout and thermal resistance of the heat exchangers are maximized at several points in the map.



(A)



(B)



(C)

**Fig. 4.5.1** (A) Schematic representation of the engine and exhaust system showing the proposed installation position of the TEG and the red X's showing locations of thermocouples to measure exhaust gas temperatures. (B) Exhaust gas temperatures as measured at the outlet of the catalytic converter (black) at the y-pipe (blue) and just upstream of the mid-muffler region. Temperatures for three test cycles of increasing vehicle speed are shown. (C) Plot of the exhaust gas temperatures vs flow rates. Each point is a corresponding temperature and flowrate for the US06 cycle.

Dynamic simulations run over several drive cycles to assess the power output. Other considerations that fed into the thermal and mechanical design was the imposition of back pressure and what effect that would have over the course of the drive cycle. The effect on tailpipe acoustics, for example, if the TEG removed enough energy from the exhaust gas it may be possible to decontent the muffler, reducing backpressure from this component results in a minimal change in the overall exhaust system restriction. Minimization of TE materials and TE element and module manufacturing considerations, oxidation suppression measures, along with TE materials' thermomechanical behavior response to various stresses imposed by differential thermal expansions, rapid temperature changes, and vibrations were also part of the design process. Finally, there were the considerations of how to interconnect the TE elements in such a way that there was good overlap in the V-I and P-I characteristics such that power could be extracted from all rows of TE elements despite each row operating at different junction temperatures.

Despite choosing the V-8 platform for development, we still wanted the system design to be flexible enough to adopt across a wide variety of vehicle platforms and engine sizes and this consideration along with electrical interconnect topology for the TE elements led to a modular design, such that a certain number of hot/cold side heat exchanger and TE element arrays collectively termed a "TEG subunit" could be grouped into a system. The subunits are designed using the guidelines described above and then the number of such units are chosen according to flow rates and optimization for the cost to benefit ratios.

Thermal modeling quantifies what is intuitive, which is, fewer subunits will result in higher average TE material junction temperatures which will lead to higher power output for each subunit. The fewer the subunits the lower the overall power particularly under high flow conditions. These are rare in real world driving conditions and so the average power output over city and highway cycles needs to be weighed against maximum power output during one phase of the US06 cycles. We find that the average power output under less aggressive driving conditions yields a curve of cycle average power vs subunit count that is rather flat above five subunits for the V-8 platform. Meaning that having more than five subunits, while beneficial to peak power, does not greatly increase the cycle average power for city and highway cycles. We, therefore, concluded that five subunits would be suitable for this engine size. Each subunit was composed of 520 TE elements on each side of the plate and fin style hot side heat exchanger. There are 20 TE elements (10 P-N pairs in each isothermal row, and 26 such rows that run the length of the heat exchanger. The TE elements were optimized to  $1.8 \times 1.8$  mm in cross-sectional area and 2.0 mm in height with a nearly 50% fill fraction.

The final portion of the thermal and electrical design was to determine how to interconnect the TE elements. Connecting all elements in series maximizes voltage but not power. Extracting power from such a circuit results in the elements in the cooler section of the TE circuit being far away from their maximum power point in the P-I curve. Further, such an arrangement can lead to failure of the entire 520 TE element array by the loss in connection of one element. Connecting portions of the circuit in parallel and then connecting these parallel portions in series allows for greater topological

redundancy such that if two isothermal rows are connected electrically in parallel then two or three elements need to be lost in a single P-N, P-N parallel junction in order to lose connectivity in the entire circuit. Further, connecting some rows in parallel results in a wider P-I curve allowing for a higher percentage of power to be drawn from a TE circuit that is subjected to a significant temperature gradient. After several design iterations, we selected to connect the first 20 rows in 10 groups of parallel connections such that rows 1 and 2 are connected in parallel and then connected in series with rows 3 and 4 which are in parallel and then continuing this pattern out to row 20. The final six rows were formed into two groups of three parallel rows to allow for more efficient power extraction despite having much lower junction temperature differentials. A more detailed discussion of the TEG thermal design and TE element interconnection study can be found in Ref. [15].

#### 4.5.4 Thermoelectric generator design and assembly

One of the main focus areas of this program was the development of skutterudite thermoelectric materials for mid- to high-temperature waste heat recovery applications. Thermoelectric Skutterudites are the Sb containing structural analogs of the mineral  $\text{CoAs}_3$  which goes by the same name. The crystal structure is composed of corner-sharing Co-Sb octahedra that pack to form large voids that can accommodate a wide variety of cations from the alkali, alkaline earth, rare-earth groups, and some main group elements [16]. In the base  $\text{CoSb}_3$  structure, the incorporation of these so-called filler cations effect both the electrical and thermal transport properties in a synergistically positive manner. The fillers provide electrons to the  $\text{CoSb}_3$  bonding network making the  $\text{M}_x\text{CoSb}_3$  product an n-type conductor whose carrier concentration can be controlled by amount M incorporated. Concurrently, the filler species also reduces the lattice thermal conductivity substantially to improve the overall  $zT$  ( $zT = (S^2/\rho\kappa)T$  where  $S$ ,  $\rho$ , and  $\kappa$  are the materials Seebeck coefficient, electrical resistivity, and thermal conductivity, respectively, and  $T$  is the absolute temperature in K). The materials can be doped p-type by substituting Fe for Co. This combined with cation filling of the voids also improves the p-type's  $zT$  [16]. The materials development efforts focused on improving  $zT$  of P-type materials and the development of high-volume, low-cost production methods for the skutterudite materials, metallized (diffusion barriers and low contact resistance terminal surfaces) elements and modules [15].

The thermal design work, described above, concluded that TE elements with cross-sectional dimensions of  $1.8 \times 1.8$  mm and a length of 2.0 mm and their accompanying filling fraction would be well matched to the thermal resistance of the heat exchangers while keeping the amount of materials required for the TEG system close to 260 g thus limiting a significant system cost driver. Thermal insulation requirements necessitated that the total element height be  $\sim 4$  mm and so CTE matched Cu-W standoff layers  $\sim 1.0$  mm thick were applied to the metallized skutterudite. The Cu-W layers act as thermal and electrical shorts and, as we will show below, do not contribute appreciably to the thermal or electrical resistance of the TE circuit. The Cu-W terminal faces also hold the advantage of being compatible with a wider variety of joining methods.

The TE materials for the prototype generator build were ultimately made by a combination of melt casting of the constituent elements followed by melt spinning the cast ingot to form ribbons. These ribbons could be briefly heat treated to obtain phase pure and highly homogenous N and P-type skutterudite TE materials. These heat-treated ribbons were subsequently consolidated to full density while concurrently pressing the metallization layer onto the TE materials to form a low contact resistance diffusion barrier/metallization layer. These pucks are polished to a parallel faced disc of uniform height, then the Cu-W layer is applied by hot pressing with subsequent polishing for uniform height [15]. Fig. 4.5.2A shows a photograph of the elements after dicing, and (B) shows a scanning electron micrograph cross section highlighting the metallization layer and the CuW standoff layer.

After completing the thermal layout analysis of the TEG subunits and determining the number of subunits that would be incorporated into the full system a mechanical design study of the respective components was initiated. The thermal layout established the flow path length of the hot side heat exchangers, the fin density for optimal heat transfer from gas to solid, and the thermal resistance of the hot and cold side heat exchangers. This determined the aspect ratio of the TE elements and the number required to achieve the desired fill factor (cross section of TE materials/active heat exchanger area). To reduce system weight, volume, complexity, and cost over previous TEG designs that used standalone thermoelectric modules requiring careful and uniform clamping between the hot and cold side heat exchangers [15], we pursued a more integrated design approach. We incorporated the hot side dielectric and metal interconnects into coatings that were applied directly to the hot side heat exchanger surfaces. We used a commercially available ceramic oxide coating that is screen printed and fired to provide a highly electrically insulative layer with breakdown

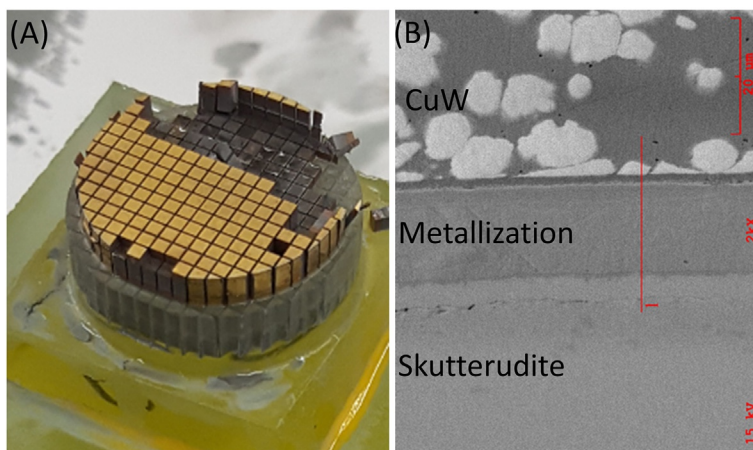


**Fig. 4.5.2** (A) Photograph of diced P-type skutterudite materials after the application of the metallization layer and the CuW standoff. (B) Micrograph of the interface between the skutterudite, metallization, and the CuW standoff layer demonstrating the intimate contact achieved through hot press processing.

voltages in the range of tens of kV-cm. The coating is compatible with a silver paste that can be subsequently layered on the dielectric. Screen printing and firing form the hot side anchoring points for the current carrying interconnects and TE elements. The coating materials, application, and firing techniques are already used in the automotive industry for the manufacture of heated fuel injector housings and therefore should meet stringent durability requirements. Fig. 4.5.3(A) shows a hot side heat exchanger section coated with the dielectric and (B) shows the silver thick films after firing.

Several of these coated coupons were subjected to thermal up-shock and down-shock stress testing by placing the sections in an oven set to 850°C holding for 10min then water quenching, the process was repeated 20 times. We observed no cracking or delamination during thermal shock testing indicating good adhesion of both the dielectric and metal film layers.

Concurrently, we developed silver sintering methodologies for attaching interconnects (metal current carriers for the hot side of the TE circuit) and TE elements to the printed silver thick films. Silver sintering uses a combination of pressure and temperature to activate and consolidate a thin layer of fine silver powder dispersed between the joining surfaces in a carrier paste, resin, or oil [17]. This joining method is finding wider applications in the automotive industry for making low loss interconnects in power electronic systems for hybrid and fully electric vehicles. We joined the TE elements to the silver thick films printed on the hot side heat exchanger surface with silver foils coated with a thin layer of silver sintering material. The preform foils end up being the structure that carries the majority of electrical current between the TE elements. Optimized pressure and temperature conditions achieved a mechanically robust joint with both low thermal and electrical contact resistance at the interface between the TE elements and foil and the foil and the printed silver film. The cold

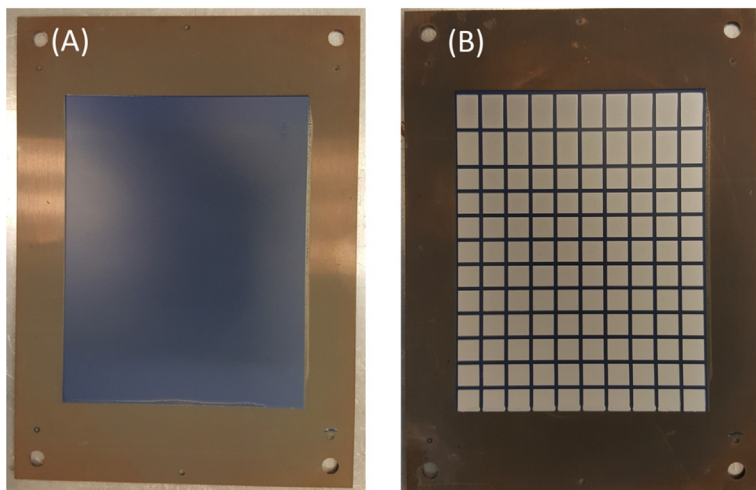
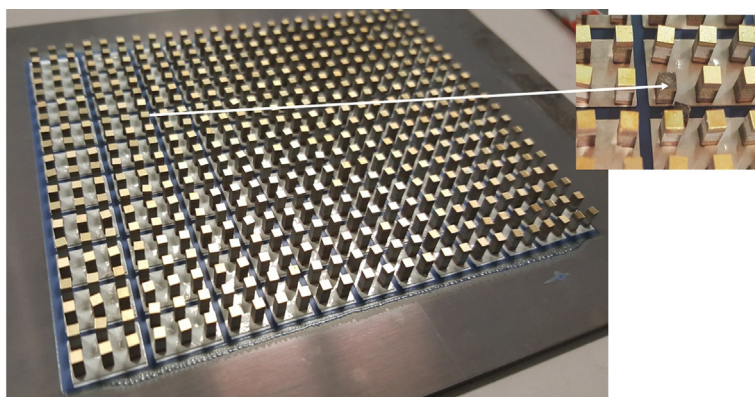


**Fig. 4.5.3** (A) Hot side heat exchanger section after printing and firing the dielectric coating.  
(B) The same section after printing the silver thick films.

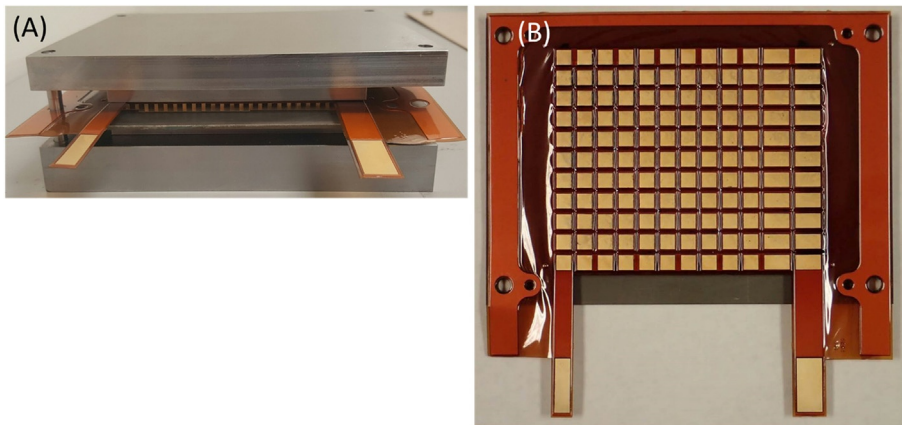
side circuit interconnects are copper foil pads embedded in a polyimide carrier sheet. Silver sintering paste, dispensed on the CuW surface of the elements, combined with similar sintering conditions, were used to form an equally high-quality joint between the CuW layer and copper circuit. Confocal scanning acoustic microscopy (CSAM) and X-ray tomography verified the quality of the sintered joints [15]. Skutterudite and surrogate copper elements of comparable dimension were used to produce small scale test modules. Shear stress testing and AC resistance measurements showed they could withstand an average of 80 MPa tensile stress at the sintering joint interface [18], with an electrical contact resistance of  $2 \mu\Omega \cdot \text{cm}^2$  or lower. The dielectric and metal film coating, and silver sinter joining proved scalable to the large surface area of the TEG subunit heat exchangers. Fig. 4.5.4 shows a heat exchanger populated with 520 TE elements after sintering them in place using a heated platen press, but prior to the cold side circuit attachment. The advantage of silver sintering is that TE elements can be joined to interconnect on the hot and cold side, in a single sintering operation at temperatures ( $250^\circ\text{C}$  was used here) well below where skutterudite materials begin to oxidize in an ambient atmosphere ( $300^\circ\text{C}$ ) [19]. This eliminates the need for high-temperature brazing operations in inert atmospheres or vacuum and should reduce manufacturing costs.

Fig. 4.5.5A shows a full-sized (520 element) array in a sintering fixture with the cold side circuit in place before the sintering operation. Fig. 4.5.5B shows the fully sintered array with cold side carrier sheet attached. The residual resistance attributable to the contact resistance interconnects, and CuW standoffs combine for  $\sim 10\%$  to the overall resistance of the array. This is based on summing the measured room temperature resistance values of just the TE materials and comparing it to the measured AC resistance values of the array.

To alleviate stress associated with differential thermal expansion of the hot side heat exchanger imposed by the temperature drop along the flow path and difference in the hot and cold side heat exchangers expansion, the polymer carrier sheet can be



**Fig. 4.5.4** Picture showing a steel heat exchanger plate after deposition of the dielectric and silver thick film and sintering of 520 TE elements the inset show cracked skutterudite elements that broke due to alignment fixture binding.



**Fig. 4.5.5** (A) A photo of a full-sized heat exchanger section with skutterudite TE materials sintered to the hot side surface, and the cold side circuit placed for sintering. Array is being held in a sintering fixture which aligns the hot and cold side TE circuits with the TEM elements. (B) A photo of the same array after the sintering operation.

cut so that each of the four elements joined to it behave as independently floating entities thereby reducing sheer stress imparted to them. The flexible cold side interconnect also helps alleviate stresses imposed by differential thermal expansion between the n- and p-type skutterudites.

The three final issues of the subunit design that needed addressing were how to apply a compressive force on the TE elements, a method to protect the TE materials from oxidation, and to provide cold side heat rejection. The solution comes from forming a hermetic seal around the TE array using a thin gauge (to minimize thermal shunt paths) stamped steel shield laser welded to the hot side heat exchanger surface around the perimeter of the dielectric coating. The cold side heat exchanger, composed of similarly thin stamped steel sheets were brazed together to form an envelope for coolant flow as shown in [Fig. 4.5.6](#). It is then laser welded to the top of the shield and epoxy is used to form an air-tight seal around the TE circuit's electrical leads. For oxidation protection, a vacuum is drawn in the sealed space containing the TE elements and interconnects and a compressive load (equal to the atmospheric pressure of 100kPa) helps alleviate tensile stresses in the TE materials and encourages good thermal contact between the cold side circuit and the cold side heat exchanger.

The TEG subunits were assembled in the following manner. First, the hot and cold side heat exchangers were formed using standard brazing techniques. The hot side heat exchanger is a standard plate and fin style and the cold side is formed by brazing two opposing stamped formed sheets together along with coolant inlet and outlet tubes. After heat exchanger fabrication, the dielectric and silver thick film is applied to the hot side heat exchanger surface as shown in [Fig. 4.5.7A](#). Next, the silver preforms are affixed to the silver thick film using a volatile adhesive, followed by placement of the skutterudite elements on both surfaces of the heat exchanger using an element alignment fixture. The subsequent sintering operation, using a heated platen

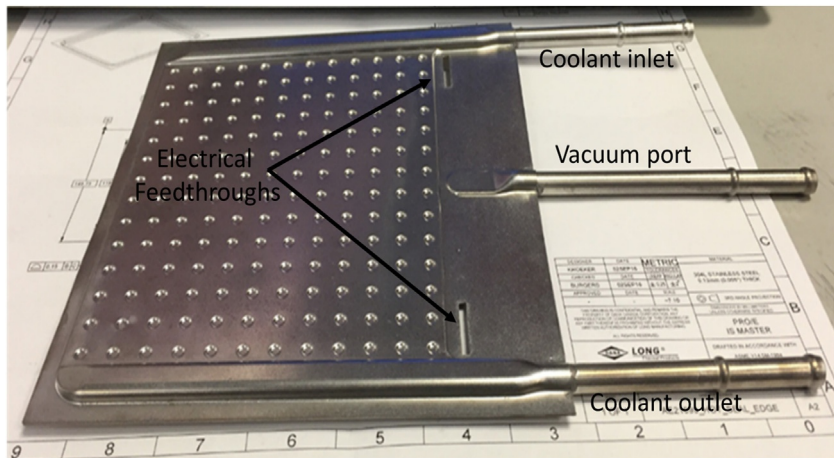


**Fig. 4.5.6** A photograph of a cold side heat exchanger unit after brazing operations. Annotated for clarity are the coolant inlet and outlet ports, the electrical feedthrough slots for the cold side circuit leads, and a port used for drawing a vacuum.

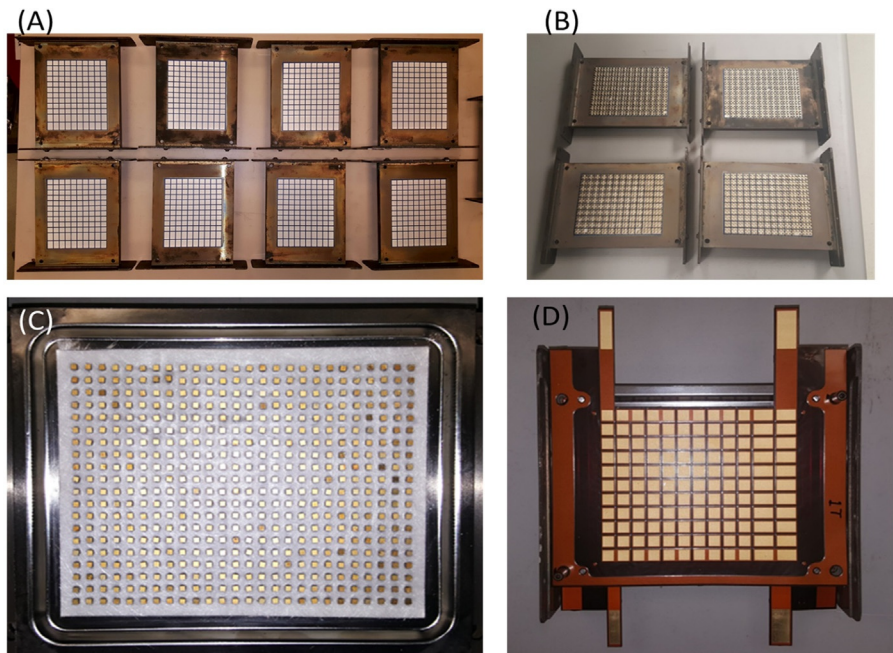


**Fig. 4.5.7** (A) Hot side heat exchangers after printing and firing of the dielectric and silver films. (B) Four heat exchangers with skutterudite elements sintered in place. (C) Photograph after the peripheral shield has been welded to the hot side heat exchanger surface and application of thermal insulation that minimizes parasitic heat transfer from the hot side to the cold side heat exchangers. (D) Photo of a subunit after attachment of cold side circuit.

hot press, joins the TE elements to the silver preforms and the preforms to the printed silver thick film. Four subunits with skutterudite TE elements sintered to the hot side heat exchanger are shown in Fig. 4.5.7B. The peripheral steel shield is then laser welded to the hot side heat exchanger. Subsequently, fiberglass insulation is placed in the void space between the TE elements to limit heat flow around the TE elements (Fig. 4.5.7C), then the cold side circuit is sintered in place using the same conditions used to attach the elements to the hot side heat exchanger (Fig. 4.5.7D). Thermally conductive and electrically insulating thermal interface materials are applied to the copper interconnects opposite the TE materials, and the cold side heat exchanger is slid into place and laser welded to the peripheral shield. Finally, the gap between the electrical leads on the cold side circuit and the cold side heat exchanger is sealed with a high-temperature stable epoxy. After curing the volume confined by the hot and cold side heat exchanger surfaces and the peripheral steel shield are evacuated to  $\sim 5$  mTorr, the leak is checked, and if they pass, they are sealed for use. Each subunit was functionally tested for AC resistance and open-circuit voltage as a function of gas inlet temperature conditions with constant coolant temperature. The assembled subunits can be seen in Fig. 4.5.8.

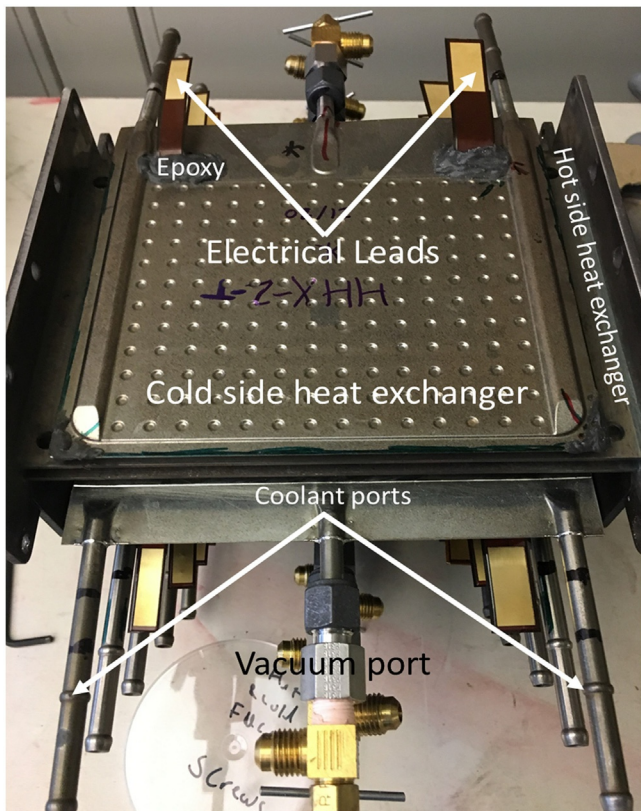
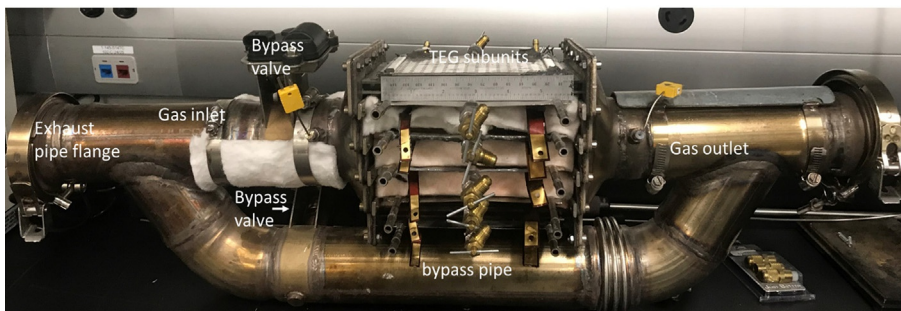


Fig. 4.5.8 Photograph of five fully assembled subunits.

The overall system design study commenced after the TEG subunit design was frozen. This included the overall mechanical layout to accommodate five of the sub-units described above, and layout of other required system components so that the entire system would fit within the packaging envelope. Other system components that were designed during this phase were the exhaust gas inlet and outlet cones, coolant manifolds, exhaust gas bypass routing, and bypass valve placement. The inlet and outlet cones were designed using computational fluid dynamics to ensure that each of the five channels received a nearly equal proportion of the gas flow under a variety of mass flow and temperature conditions. Finite element analysis was used to look for areas of stress in the structure that could lead to inelastic strains in the metal structures causing fatigue or failure. This analysis was performed by computing the accumulated stresses that build up during the repeated application of a thermal gradient of 300°C (650°C system inlet pipe temperature and 300°C outlet pipe temperature) across the system. In the first design iterations several such points were identified near the inlet cone location and in the y-shaped pipe that joins the inlet cone under the maximum predicted operating temperature. These stresses on the inlet cones were induced by differential thermal expansion between the TEG subunits and the bypass pipe. Those in the y-shaped pipes were caused by temperature gradient across the entire TEG subunit. The stresses in the inlet cone were alleviated by adding a bellowed pipe region in the bypass leg and by machining in slotted holes for the bolts that held the inlet and outlet cones to the heat exchanger faces. These slotted holes allowed a small amount of slippage between the cone and hot side heat exchanger faces and the bellow allowed the bypass leg to stretch along with the subunits. The stresses in the y-pipe were not alleviated and instead the area of concern was structurally reinforced to mitigate fatigue. Fig. 4.5.9 shows the fully assembled TEG system prior to integration and testing, and Fig. 4.5.10 shows a close-up view of the TEG subunits and how they are incorporated into the overall system. There is a 6-in ruler in both figures to provide scale.



**Fig. 4.5.9** Annotated photograph of the fully assembled TEG system. Note the 6" ruler on the top TEG subunit that provides scale.



**Fig. 4.5.10** Close-up photo of the five TEG subunits integrated into the rest of the system. The photo highlights exhaust gas inlet and outlet cones.

#### 4.5.5 Vehicle integration and testing

During TEG assembly the test vehicle's exhaust, powertrain cooling, and electrical systems were modified for integration and testing of the device. It was assumed that electrical power production was going to be minimal during the city cycle due to the low flow rate and temperatures of the exhaust, and so every effort was made to harness the exhaust gas heat, transfer it to the coolant, and use it to accelerate the warm-up of the engine oil and transmission fluid as a means of improving fuel economy. Accelerated warm-up of powertrain fluids like engine and transmission oil reduce parasitic friction losses. [Fig. 4.5.11](#) shows a schematic representation of the coolant circuit along with the CAD layout of the hardware. Three new components were added to the base cooling system and include a 60-W booster pump for coolant, a liquid to liquid heat exchanger to transfer heat from the coolant to the transmission oil and a three-way valve to control the flow of engine coolant to the transmission oil loop. The booster pump and valve required control algorithms to maximize their effectiveness and minimize their parasitic effects; the auxiliary water pump control was based on feedback from the measured flowrate of coolant out of the TEG such that if the flow fell below certain threshold values the pump would turn on to boost flow through cold side coolant loop. The three-way pump was controlled by feedback from the transmission oil temperature and once the transmission oil reached its specified operating temperature then the TEG outlet coolant flow would be diverted away from the liquid to the liquid heat exchanger and directed back to the coolant reservoir by way of the radiator.

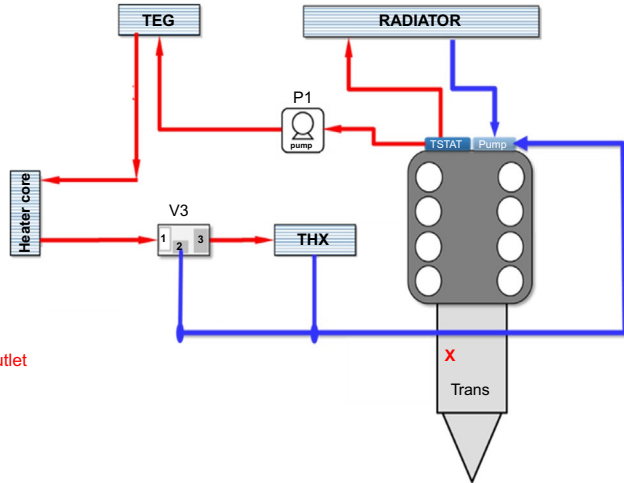
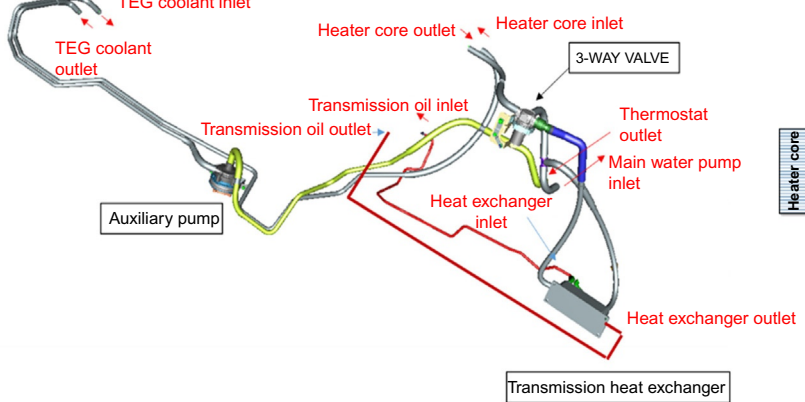


**Fig. 4.5.11** The left image shows CAD of the modified coolant layout. Annotation with text enclosed in a box indicates components added to the base vehicle's cooling system and the red text indicates coolant and transmission oil flow paths. The right image is a schematic representation of the modified cooling system for clarity.

The integration of the TEG's electrical power into the vehicle was straight forward. Base controls for the electrical system comprehend auxiliary power supplies and any additional power supplied to the battery results in the reduction of electrical power generated by the alternator. The reduction in electrical power demand will reduce the required torque from the engine to generate electricity and will reduce fuel consumption proportionally. Early experiments looking at the upper limit of fuel economy improvement for this vehicle found that fully supplementing the electrical requirements using waste heat recuperation would reduce CO<sub>2</sub> emissions by nearly 10 g CO<sub>2</sub>/mile. The output voltage of the TEG varies with the junction temperatures of the TE elements which are influenced by the exhaust gas and coolant temperatures. For the vehicle's electrical system to accept power from the TEG and to electrically load the TEG so that power can be extracted at or near the maximum power point, the TEG voltage needs to be conditioned. For the purposes of this development project, we chose to use off the shelf boost/buck DC-DC converters with maximum point tracking capability. These converters are normally used for solar panel power conditioning but adequately serve as a means of taking the highly variable voltage of the TEG either boosting it up to- or bucking it down to 12 V. Some limitations of the converters we chose to use was rather high minimum turn-on threshold of nearly 6 V, a maximum input voltage of 20 V, and power output rating of 200W. We chose to connect each subunit to its own DC-DC converter for the highway and US06 cycles since we expected that each subunit would generate sufficient voltage to require it. Since the expected voltages for the city cycle for each subunit were expected to be lower than the minimum turn on voltage for much of the cycle, a switching box was inserted that put two to three subunits in series and then these groups were fed to one DC-DC converter. The series connections increased the circuit voltage in order to keep the converters operational thereby delivering power to the vehicle for a longer portion of the cycle. The outputs of the converters were connected in parallel with the positive leads feeding the positive terminal of the truck's lead-acid battery and the negative leads attached to the chassis (grounded). The DC-DC converters were measured to be ~90%+ efficient over the highway and US-06 cycles but even with switching from parallel to series inputs, the DC-DC converters took nearly 200s to activate after the start of the test cycle (see the testing section below). Should TEGs be brought into a more advanced development program, further optimization of the DC-DC converters with better maximum power point tracking will need to be done.

Finally, the TEG needed to be installed into the vehicle's exhaust system. The underfloor catalytic converter was removed with the understanding that future full-sized truck and SUV models would have split volume converters that would have both functionalities incorporated into a can that is packaged where the primary catalytic converters currently reside. Fig. 4.5.12 shows schematic placement of the TEG into the underfloor of the vehicle. Several hangers were required to support the TEG to maintain ground clearance and prevent sagging and excess sway. The other required feature were two exhaust gas bypass valves. One was placed right before the inlet to the TEG and other on the bypass leg. Two valves were required with the current design to ensure that gas flowed exclusively into or around the TEG. This provided vehicle performance comparisons between TEG active and TEG bypass modes. Developed

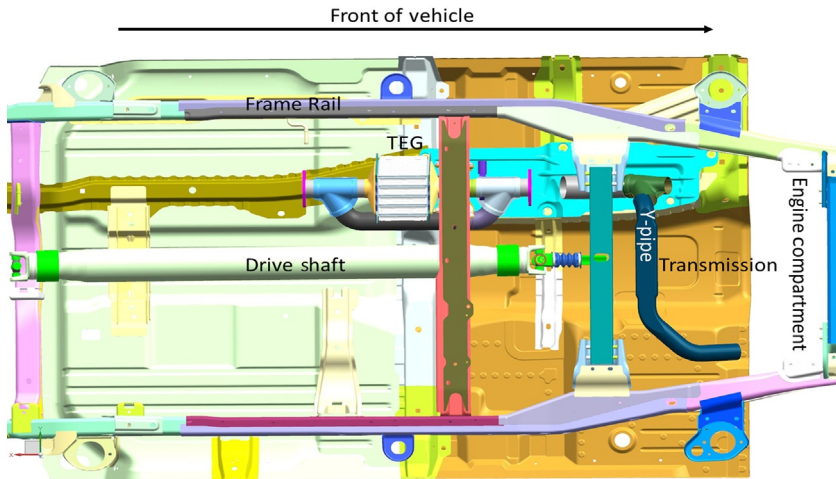


**Fig. 4.5.12** CAD drawing of the underside of the integration vehicle showing the final placement and fitting of the TEG system.

valve controls were based on feedback from several sensor inputs including TEG inlet temperature, pressure drop across the TEG, and the temperature of the coolant exiting the TEG. Exhaust gas would be diverted around the TEG under the following conditions: inlet gas temperature exceeds 850°C for 30 s (to prevent TEG component degradation), the pressure drop across the TEG exceeds 30 mbar for 10 s (to prevent negative fuel economy and horsepower impacts by the imposition of excessive back pressure), and coolant outlet temperature greater than 120°C for 20 s (to prevent excessive heat rejection by the engine cooling system which can also negatively impact fuel economy). The latency inherent in the pulse width modulation (PWM) controller would switch the TEG back to harvesting conditions 10 s after all by-pass conditions were eliminated.

Analog signals from thermocouples, pressure transducers and flow meters, TEG and DC-DC converter voltage taps, and current shunts were logged at 10Hz. The exhaust gas and coolant temperatures, pressure drop, and coolant flow were fed into a LIN controller box and power supply for actuating the bypass valves in the exhaust, three-way valve for transmission oil heat up and a booster pump for increasing TEG coolant flow. All of these were powered by the vehicle's electrical system, so their parasitic contributions were accounted for in the testing. Powertrain signals such as fuel flow rate, air to fuel ratio, engine speed, etc. were collected using a Neovi CAN bus data logger. These signals will provide valuable test data to better understand the TEG's effects on the powertrain and can be used for future controls development requiring little to no temperature, flowrate, or pressure drop data, and thus reducing integration cost associated with controls and on-board diagnostics.

The TEG integration vehicle was tested on a specialized high-resolution chassis dynamometer. The test facility used four independent dynamometers which were bolted directly to each wheel hub to eliminate tire slippage and the test cycles were driven

using a robotic controller to reduce the test to test variability and both led to higher resolution and repeatability.

Two cold start city tests were run in a TEG active mode and one in a TEG bypass mode to test the reproducibility of any fuel consumption changes we observed. The vehicle is required to soak at room temperature overnight to be considered a true cold start test. This reduced the number of tests of this type that could be run. A total of 10 highway cycles, five in bypass and five with TEG active, and the same number of US06 were also part of the testing.

As was expected very limited electrical power was generated during the cold start city cycle. Fig. 4.5.13 shows the power that was delivered to the vehicle as calculated from the product of the voltage and current on the output side of the DC-DC converters. As can be seen, no power is generated for the first 200s of the cycle due to the TEG voltage being below the minimum turn on value and therefore it remains open circuit. The cycle average power was correspondingly low at  $\sim 13\text{ W}$  and therefore we do not expect that reduction in alternator load will make a measurable change in FE. However, the rejected heat was found to make a significant difference in the coolant and transmission oil temperatures, indicating that the coolant system modifications and the introduction of the harvested exhaust heat from the TEG are effective in accelerating the warm-up of powertrain components. This added heat should have a measurable impact on vehicle FE. Fig. 4.5.14A shows a comparison of the coolant temperature vs time for the TEG active and TEG bypassed cold start test, and Fig. 4.5.14B shows the corresponding data for the transmission oil. A further advantage of accelerated coolant warm-up is that during cold weather ( $10^\circ\text{C}$  or below), during cold start electrical heaters are needed for windshield defrost and passenger comfort. Faster warm-up of engine coolant will accelerate the warm-up of the heater core which will reduce electrical loads and provide the heat required for defrosting and passenger comfort quickly.

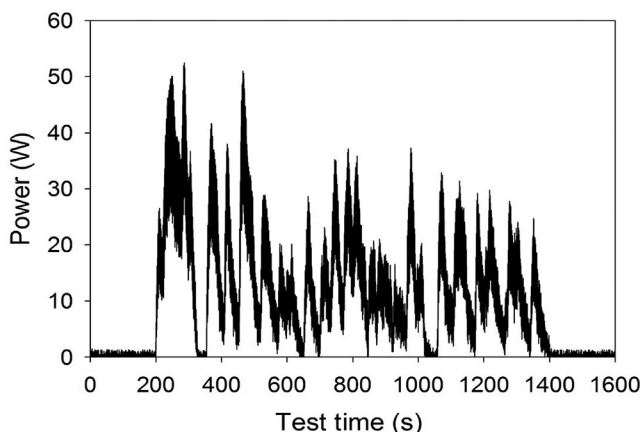


**Fig. 4.5.13** TEG power output as a function of time for the cold start federal test procedure city cycle. Lack of power production in the first 200s is due to TEG voltage being lower than the minimum threshold. Heat for accelerated warm-up is being harvested continuously.

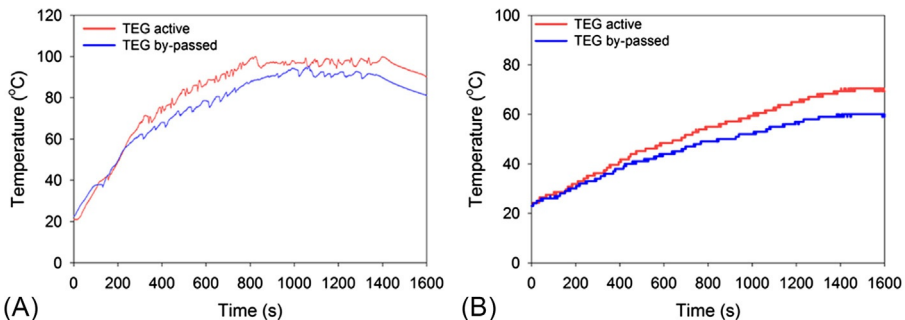


**Fig. 4.5.14** (A) Coolant temperature as it exits the heater core (downstream TEG) as a function of the time for the cold start city cycle *blue* shows the coolant warm-up curve when the TEG is bypassed and the *red* is TEG active. (B) The temperature of the transmission oil in the sump (in the transmission component) during the same period.

The next set of test cycles performed were the FTP highway sections. Here the flow rates and temperatures of the exhaust gas were both higher and we anticipated concomitantly higher power production. Fig. 4.5.15A shows the TEG power output as a function of time for two back to back highway cycles. The first is a preparatory cycle to ensure full vehicle warm-up. The second is the test cycle where FE is measured. The boundary between these two phases is demarcated by the vertical red line in Fig. 4.5.15A. Since it was anticipated that the TEG subunit voltages were going to be higher with higher speed conditions, and to improve power extraction efficiency by eliminating subunit V-I imbalances two TE circuits (1 subunit) were loaded to a single DC-DC converter. Disappointingly only four of the DC-DC converters turned-on and so the power output shown in Fig. 4.5.15A does not represent the full potential. It is apparent from the rapid jumps in TEG power output (now taken as the sum of the products output voltage and current) that the four working DC-DC converters turn on at different times, this can be seen in test cycle at 1100s, where the steep increase in power is attributed to two additional converters turning on and the output electrical power. Despite one TEG subunit being open circuit, as shown in Fig. 4.5.15B, the alternator output current drops significantly and proportionally to the amount of outpower from the TEG. During the testing period when four TEG subunits deliver power to the battery, the alternator current drops to nearly half of its nominal value (22–24 Amps) Fig. 4.5.15B.

Next, we performed several US06 cycles tests. As indicated earlier, this is the most aggressive test cycle and will result in the highest flow rates and exhaust gas temperature that yields the highest power outputs. As expected these conditions resulted in significantly more power production as compared to the previous tests. Fig. 4.5.16A shows conditioned power output from the TEG (power after DC-DC converters), and Fig. 4.5.16B shows the alternator current response in comparison to the same driving conditions with the TEG bypassed. Similar to the highway cycle case, as the TEG power increases the alternator current decreases. In a couple of portions of the test cycle, the alternator is fully idled, while the TEG provides sufficient electrical power to meet all non-accessory demands. Again only four of the five DC-DC converters

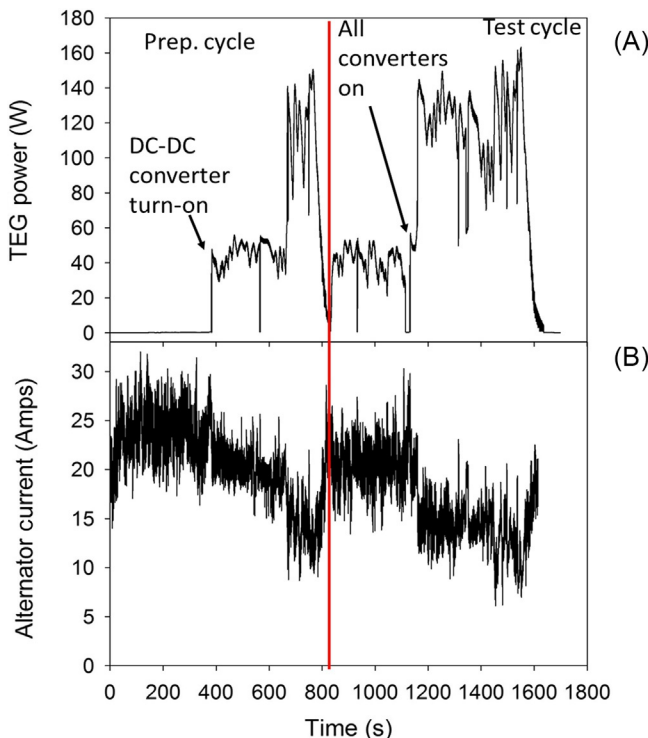


**Fig. 4.5.15** (A) TEG power output during a preparatory (first 800s) and test (final 800s) highway cycle. (B) The alternator response to the introduction of auxiliary power from the TEG.

delivered power to the vehicle pinning one subunit at open circuit and so we can expect significantly more power out of a fully functioning TEG allowing it to meet the full electrical demand for a larger portion of the cycle. One potential drawback with harvesting waste heat under such high load conditions is the fact that the rejected energy in the coolant loop still needs to be rejected to the environment. It was noted that after US06 tests were run in TEG active mode that the engine cooling fan and coolant auxiliary pump ran for a longer period of time and at higher speeds as compared to the bypassed tests. These loads will not necessarily show up during the test, but they also cannot be ignored as they are a source of battery depletion if the fans and pumps run for prolonged periods after the vehicle has been shut off. Another issue of high load driving followed by engine shutdown is the possibility of coolant boiling in the TEG cold side heat exchangers causing system damage. To prevent damage to the system during our testing, we ran the vehicle at idle with TEG bypassed until the coolant temperature at the TEG inlet and outlet were nearly equal. This took up to 3 min in some cases. This is an important control and integration issue that will need to be resolved.

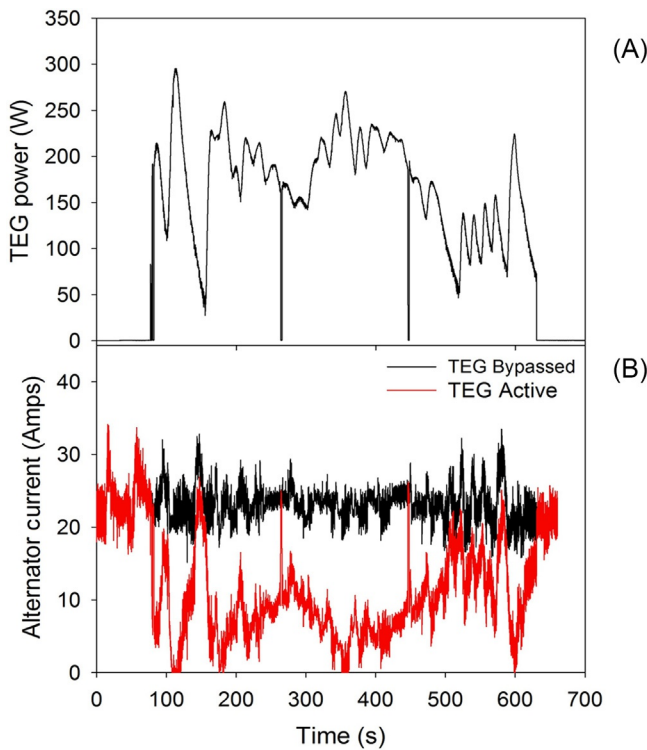


**Fig. 4.5.16** (A) TEG power output during a US06 cycle. (B) The alternator response to the introduction of auxiliary power from the TEG.

**Table 4.5.1** summarizes the measured fuel economy of the test vehicle in the test cycles described above. For the cold start city tests sections known as Bags 1, 2, and 3 the measured FE improvements are based on two TEG active cycles and 1 TEG bypassed. As can be seen, there is little FE benefit in the Bag 1 near the beginning of the test and this is expected as neither electrical power generation had commenced during most of this phase nor had there been the opportunity to deliver a significant

**Table 4.5.1** List of the testing segments and their corresponding measured average fuel economy ratings for test conditions with the TEG active and bypassed.

Test cycle	Average FE TEG active	Average FE TEG bypass
Cold Start City Bag 1	16.535	16.543
Cold Start City Bag 2	18.806	18.477
Cold Start City Bag 3	20.204	19.949
Highway	28.346	27.913
Composite	18.632	18.416
US06	18.118	18.289

amount of heat to the coolant system to assist in accelerated powertrain warm up. By the end of Bag 2 we can see a significant difference in the fluid temperature between TEG active and bypass modes and as seen below this seemingly translates into FE improvement. This result is carried over into Bag 3 but the delta in FE is more modest. Interestingly, we also see a significant FE benefit from the TEG during the highway cycle. This can be attributed to both electrical power generation and active warm-up, particularly of the transmission oil (data not shown above) which takes a considerable amount of time to reach its optimal operating temperature. Finally, we see that for the US06 the TEG is equivocal or detrimental to FE when comparing the active and bypassed modes. There are several possible reasons for this and they include increased loads on the belt-driven coolant pump and excessive exhaust gas backpressure. The composite FE improvement, which is a weighted average of the three city sections and the highway portion of the testing was 0.20 MPG which translates into a CO<sub>2</sub> emissions reduction of nearly 6 g CO<sub>2</sub>/mile.

#### 4.5.6 Cost/benefit analysis

Fuel economy improvement technologies are generally ranked, in the United States, by a cost-benefit metric with units of US\$ per g CO<sub>2</sub>/mile. This metric comprehends total component costs, integration costs (prices for additional hardware or controls), penalties for additional mass, and off-cycle credits for the incorporation of specific technologies whose real-world FE benefits are recognized but may not be adequately measured using standard certification tests. For reference, many near term technologies for FE improvement have cost/benefits metrics in the range of \$10–\$20 per CO<sub>2</sub>/mile [20].

As shown in the previous section, we have demonstrated that the TEG can deliver an on-cycle CO<sub>2</sub> emissions reduction of 6 g CO<sub>2</sub>/mile. Additionally, there are several off-cycles credits for which the TEG potentially qualifies. For example, there is a TEG-specific off-cycle credit for electrical power generation that is worth 0.7 g CO<sub>2</sub>/mile for every 100 W of rated electrical power which is taken as the maximum power the TEG can deliver on any test cycle. If we extrapolate the TEG's full power capacity in the US06 cycle this credit could be worth an additional 2–3 g CO<sub>2</sub>/mile. Finally, there are credits for the active thermal warm-up of powertrain fluids, specifically engine and transmission oil, which are worth 1.5 g CO<sub>2</sub>/mile for each fluid in passenger cars and 3.2 g CO<sub>2</sub>/mile for each fluid in full-sized trucks [21]. Taking a conservative approach and claiming only one active warm-up credit for the truck, from the TEG-specific off-cycle credit and measured on-cycle benefit, we get a total of 11–12 g CO<sub>2</sub>/mile, and this increases to 14–15 g CO<sub>2</sub>/mile if both credits are claimable by the implementation of the TEG. Finally, there is a cost penalty associated with adding to the vehicle mass. All these considerations would set a piece and integration cost target between \$160 and \$240 for a 6-kg system (mass estimate of production TEG) to be cost-competitive with more mature technology options.

## 4.5.7 Summary and conclusions

Here we have described the development of a highly integrated TEG system, that is compact and significantly lighter than many previous prototype systems. Vehicle integration and testing demonstrated an on-cycle composite FE improvement of 0.2 miles per gallon or 6 g CO<sub>2</sub>/mile. FE benefits are mainly due to the active warm-up feature of the TEG with minimal benefit gleaned from offsetting the electrical load. For higher road load conditions, a substantial amount of electrical power was generated but there was a significant added burden to the cooling system due to the rejection of heat not converted into electrical power. These factors would indicate that comparable fuel economy improvements and off-cycle credit qualification could come from a simple EGHR system which is far less complex and much lower cost.

Only with significant improvement in the TE materials conversion efficiency can commercialization of TEGs for automotive applications proceed. As these test results show when energy harvesting conditions where the vehicle's coolant capacity is not over-burdened, very little electrical energy can be produced and under conditions where there is significant potential electrical power, the amount of heat rejected creates controls issues around how to protect the powertrain and TEG from overheating after high road load driving and engine key-off. Given these issues, the cost modeling estimates, low level of technology readiness and complexity of controls development, and vehicle integration, it was determined undesirable to pursue further development efforts at this time.

## Acknowledgments

Funding from the US DOE's NETL and VTO directorates are gratefully acknowledged. None of this would have been possible without excellent technical contributions from John Burgers, Matthew Birkett From Dana, Jean-Pierre Fleuriel, and Terry Hendricks from Jet Propulsions Laboratory, Scott Brandenburg, Ray Fairchild and David Ihms of Delphi automotive, Lakshmikanth Meda from Eberspaecher NA and Jeff Sharp and Alan Thompson from II to IV. JRS would like to thank Dan Mung for all the help he provided in leading the installation of the TEG into the demonstration. His work along with the support of others at the R&D garage at MPG was integral in making this work possible. Finally, Doug Dickson and Lawrence Ziehr are acknowledged for the coolant, electrical and exhaust gas integration and controls development, and Sam Scime for RLS vehicle testing.

## ***Disclaimer***

This report was prepared as an account of work sponsored by an agency of the US Government. Neither the US Government nor any agency thereof, nor any of their employees, makes any warranty, express or implied, or assumes any legal liability or responsibility for the accuracy, completeness, or usefulness of any information, apparatus, product, or process disclosed, or represents that its use would not infringe privately owned rights. Reference herein to any specific commercial product, process, or service by trade name, trademark, manufacturer, or otherwise does not necessarily constitute or imply its endorsement, recommendation, or favoring by the

US Government or any agency thereof. The views and opinions of authors expressed herein do not necessarily state or reflect those of the US Government or any agency thereof.

## References

- [1] [https://www.energy.gov/sites/prod/files/2014/03/f8/deer11\\_edwards.pdf](https://www.energy.gov/sites/prod/files/2014/03/f8/deer11_edwards.pdf).
- [2] [https://www.energy.gov/sites/prod/files/2017/08/f36/fy16\\_adv\\_comb\\_report\\_print.pdf](https://www.energy.gov/sites/prod/files/2017/08/f36/fy16_adv_comb_report_print.pdf).
- [3] <https://www.osti.gov/servlets/purl/1337561>.
- [4] A.M. Noor, R.C. Puteh, S. Rajoo, *J. Modern Sci. Technol.* 2 (2014) 108–119.
- [5] <https://www.greencarcongress.com/2017/07/20170717-volvod13tc.html>.
- [6] [https://www1.eere.energy.gov/vehiclesandfuels/pdfs/deer\\_2006/session6/2006\\_deer\\_vuk.pdf](https://www1.eere.energy.gov/vehiclesandfuels/pdfs/deer_2006/session6/2006_deer_vuk.pdf).
- [7] F. Zhou, E. Dede, S. Joshi, *SAE Int.* (2016), <https://doi.org/10.4271/2016-01-0178>.
- [8] M. Gueven, H. Bedir, G. Anlas, *Energy Convers. Manag.* 180 (2019) 411–424.
- [9] S. Karagoz, M. Karaer, N.A. Dasdemir, *SAE Int.* (2016), <https://doi.org/10.4271/2016-01-0235>.
- [10] <https://www.gentherm.com/en/solutions/automotive/seat-comfort>.
- [11] <http://www.amstechnologies.com/solutions/solution-single-news/article/energy-balance-of-automotive-thermoelectric-cup-holder/>.
- [12] Y. Lyu, A.R.M. Siddique, S.H. Majid, M. Biglardegian, S.A. Gadsden, S. Mahmud, *Energy Rep.* 5 (2019) 822–827.
- [13] L. Bell, *Science* 321 (2008) 1457–1461.
- [14] M. Imran, M. Usman, B.S. Park, D.H. Lee, *Renew. Sust. Energ. Rev.* 57 (2016) 1090–1109.
- [15] <https://www.osti.gov/servlets/purl/1414341>.
- [16] G. Rogl, P. Rogl, *Curr. Opin. Green Sustain. Chem.* 4 (2017) 50–57.
- [17] P. Peng, A. Hu, A.P. Gerlich, G. Zou, L. Liu, Y.N. Zhou, *Appl. Mater. Interfaces* 7 (2015) 12597–12618.
- [18] <https://www.osti.gov/servlets/purl/1423116>.
- [19] Y.S. Park, T. Thompson, Y.S. Kim, J.R. Salvador, J.S. Sakamoto, *J. Mater. Sci.* 50 (2015) 1500–1512.
- [20] National Research Council, *Assessment of Fuel Economy Technologies for Light-Duty Vehicles*, The National Academies Press, Washington, DC, 2011, <https://doi.org/10.17226/12924>.
- [21] <https://www.epa.gov/sites/production/files/2017-06/documents/itb-thermal-mngmt-2017-epa-2017-04-27.pdf>.

# Thermoelectric generation using solar energy

4.6

Sajjad Mahmoudinezhad and Alireza Rezaniakolaei

Department of Energy Technology, Aalborg University, Aalborg, Denmark

## 4.6.1 Solar thermoelectric generators (STEGs)

In this section, the fundamental concept of utilizing the STEG systems is presented, and different components of an inclusive STEG system is introduced. The overall efficiency of the STEGs depending on different parameters is defined. In addition, by using the energy conservation law, a time-dependent numerical model is proposed, which is confirmed by experimental results considering the transient response of the STEG system to variation in the solar concentration. In the last part of this section, the impact of using different thermoelectric materials on the STEG module and geometrical optimization of the STEG system are investigated.

### 4.6.1.1 STEG, components, and state of the art

A simple STEG system composes of a TEG placed between a heat sink and a solar absorber. However, in order to achieve high efficiency, other components need to be added to the system. Fig. 4.6.1 displays a comprehensive STEG module comprising five main components [1].

1. *Optical collector*, which concentrates the solar irradiation and collects the photons receiving from the Sun. Generally, flat plate, parabolic troughs, Fresnel lenses, and parabolic dishes, shown in Fig. 4.6.2, have been used as the solar collector in STEG systems.
2. *Thermal absorber*, which converts photons into heat and conducts the heat to the TEG. In order to minimize the heat losses and enhance the absorbed heat, thermal absorber should have a high thermal conductivity and low emittance material. Usually, a proper solar selective absorber, deposited on a metallic layer, is used as the thermal absorber in STEG systems. Fig. 4.6.3 illustrates the incident solar energy ( $q_{inc}$ ) that is either absorbed ( $q_{abs}$ ) or reflected ( $q_{ref}$ ). A fraction of the absorbed energy is also re-radiated to the ambient ( $q_{rad}$ ) and the rest of the thermal energy ( $q_{TE}$ ) conducts to the TEG.
3. *Thermoelectric generator*, which is the essential element in a STEG system and converts the incident solar energy into the useful electricity.
4. *Heat sink*, which dissipates heat at the cold side of the TEG, utilizes a high-performance cooling system, and is a very crucial component in the STEG system. Using a highly efficient heat sink can enhance the power generation by the STEG system, maximizing the temperature gradient across the TEG.
5. *Vacuum encapsulation*. An evacuated encapsulation is needed to drive heat to the TEG and reduce the thermal convective and conductive losses to the ambient air. The thermoelectric module and thermal absorber are encapsulated in the vacuum enclosure.

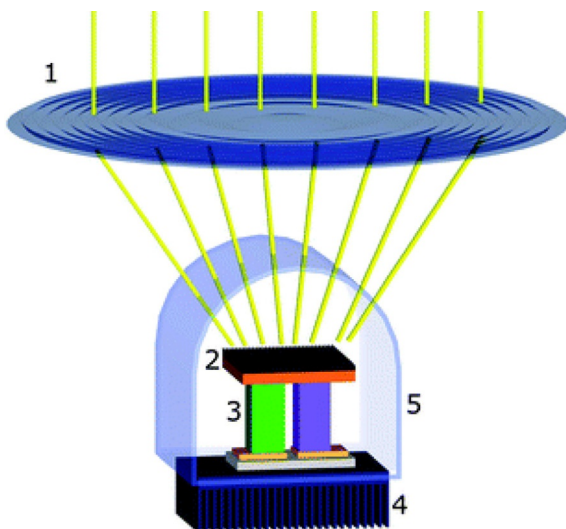


**Fig. 4.6.1** STEG system [2].

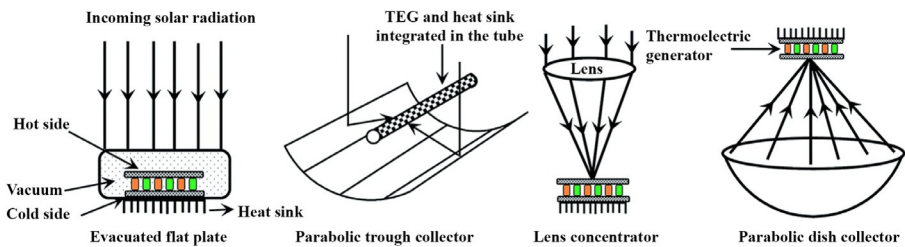


**Fig. 4.6.2** Different types of the optical collectors [3].

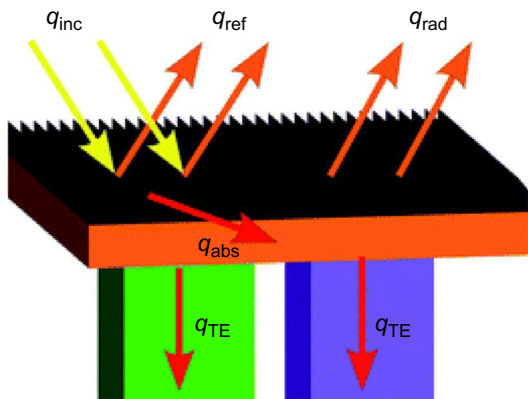


**Fig. 4.6.3** Energy balance of schematic representation on the STEG [2].

The idea of utilizing TEGs to harvest solar energy is referred to around one century ago. The earliest STEG system was designed by Coblenz [4] in 1922. Due to its low efficiency (less than 0.01%), investigation of the proposed STEG concept was ceased. With the emergence of new thermoelectric materials, a significant improvement in the efficiency of the STEGs was reported by Telkes [5] in 1954. It was illustrated that the efficiency of the presented STEG system was 0.63% and 3.35% for 1 sun and 50 suns, respectively, which was a high efficiency and could be competitive with the other solar energy harvesting devices [6]. After this remarkable achievement, STEG systems were mostly studied to be applied in the space uses [7–10] with insignificant progress for terrestrial applications. There are many studies on different STEG systems considering different materials and configurations [11–18] but no remarkable improvements until the last decade.

In 2010, Amatya and Ram [19] reported an efficiency of 3% for the solar concentration of 66 suns and predicted that, by using new thermoelectric materials, the efficiency of 5.6% can be achieved under 120 suns. Urbiola and Vorobiev [20] presented a STEG with 5% electrical efficiency obtained under 52 suns. A substantial improvement in the efficiency of the STEG systems under standard illumination condition (one sun) was reported in 2011. Kraemer et al. [21] demonstrated a promising STEG system with high thermal concentration and the peak efficiency of 4.6% under standard illumination condition. In another investigation by Kraemer et al. [22] for a STEG system under an optical concentration ratio of 211 suns, the peak efficiency of 9.6% was achieved. Baranowski et al. [2] developed a numerical approach to predict the maximum theoretical efficiency of the STEGs. It was found that with the present materials ( $zT=1$ ) and the temperature difference of 1000°C, and under optical concentration of 100 suns, the efficiency of 15.9% can be achieved. It was indicated that this competitive value of the efficiency can be improved up to 23.5% with sensible advances in the thermoelectric materials at  $zT=2$ .

#### **4.6.1.2 Efficiency of STEGs**

The conversion efficiency of a STEG system can simply be calculated as the ratio of the generated power to the input energy. In order to acquire higher efficiencies, thermal and optical concentration systems are utilized in the STEG systems. Since the elements of the STEG are connected thermally in series (see Fig. 4.6.1), the efficiency of the STEG is the product of the efficiencies of the optical collector, thermal absorber, and the TEG [1].

$$\eta_{STEG} = \eta_{ta}\eta_{TEG}\eta_{opt}\eta_{HS} \quad (4.6.1)$$

In this equation, the efficiency of the thermal absorber,  $\eta_{ta}$ , and TEG,  $\eta_{TEG}$ , are the most effective quantities on the conversion efficiency of the STEG. The efficiency of both the thermal absorber and TEG efficiencies strongly depends on temperature. On the other side, the efficiency of the optical collector,  $\eta_{opt}$ , is not dependent on the temperature. The efficiency of the cooling system,  $\eta_{HS}$ , is influenced by the type of the cooling technology selected, which can be passive or active.

#### 4.6.1.3 Transient response of STEGs

Most of the studies in the field of STEG systems have focused on the material and efficiency improvement under steady-state condition, while in real applications, the solar irradiance may fluctuate during the day, especially in partly cloudy climates. In this section, an experimental approach is considered in order to study the STEG performance under concentrated light. Then, a time-dependent numerical model is presented to study the behavior of the STEG under variable solar concentrations. The proposed model is then used to expand the results from the experiments and to optimize the STEG. Lastly, the performance of the STEG using different materials is investigated under various operating conditions.

##### 4.6.1.3.1 Conceptual model

[Fig. 4.6.4](#) shows the two-dimensional physical model of the STEG system. In this model, a simple STEG system is composed of an optical concentrator, a TEG, and a heat sink. A graphite sheet, which acts as the thermal absorber is attached to the hot surface of the TEG in order to absorb a higher amount of the simulated irradiation. Different elements of the TEG are also displayed in [Fig. 4.6.4](#). In the proposed method, properties of the thermoelectric materials such as Seebeck coefficient, thermal and electrical conductivities and, as a result, the figure of the merit were considered temperature-dependent.

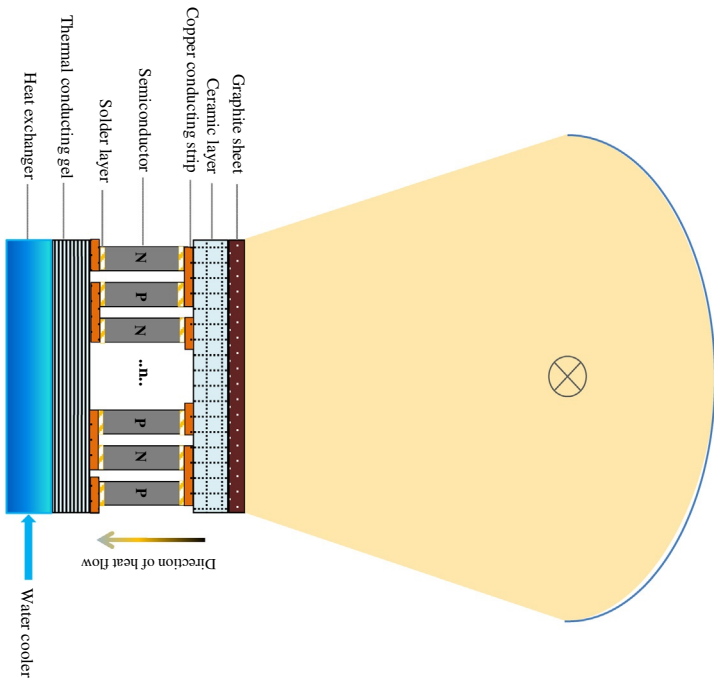


**Fig. 4.6.4** Two-dimensional physical model of the STEG system [23].

#### 4.6.1.3.2 Numerical model

In order to consider the optimization of the STEG, a one-dimensional and time-dependent heat transfer model was developed. First, the energy conservation law was used to obtain the governing equations for each contact surface, and then finite volume method [24] was used to discretize the governing equations and to represent the equations in the form of algebraic equations. Since the TEG device is a nonlinear system with various elements and effective parameters, some reasonable simplifications are considered to keep the focus on the critical performance parameters of the STEG. The main simplifying assumptions are as follows:

1. The TEG is well thermal insulated, therefore except the radiative heat loss from the top surface of the TEG, heat transfer from the TEG side walls to the ambient is assumed to be zero.
2. The heat losses between the TE elements including both radiative and convective heat losses are neglected.
3. The TEG is well connected to the heat sink; so that contact resistances are taken negligible.

**Fig. 4.6.5** illustrates the one-dimensional heat transfer physical model of the STEG module.

In order to achieve the efficiency and power generation by the STEG, the temperature profile across the module was obtained first. The coupled nonlinear equations obtained for different contact surfaces using the energy conservation law are listed as follows:

On the top surface (CS1) of the graphite sheet (Gr) the boundary condition can be written as [23]

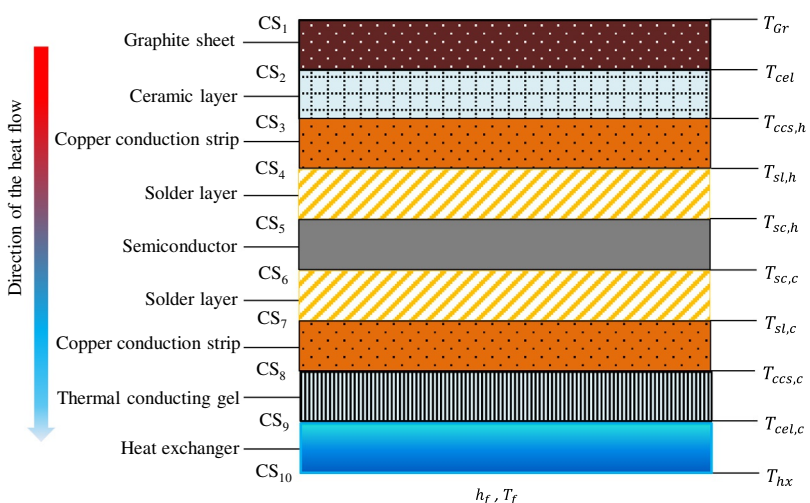


**Fig. 4.6.5** One-dimensional heat transfer physical model of the STEG [23].

**Table 4.6.1** Corresponding coefficients for various contact surfaces in Eq. (4.6.4).

<b><i>i</i></b>	<b><i>C<sub>1</sub></i></b>	<b><i>C<sub>2</sub></i></b>	<b><i>C<sub>3</sub></i></b>	<b><i>C<sub>4</sub></i></b>	<b><i>C<sub>5</sub></i></b>	<b><i>C<sub>6</sub></i></b>
2	1	0	1	0	0	0
3	1	0	1	0	1	0
4	1	1	1	0	1	0
5	1	1	1	1	1	1

$$\rho_{Gr} c_{Gr} V_{Gr} \frac{\partial T_{Gr}}{\partial t} = \alpha \times SC \times G \times A_{Gr} - Q_{rad} + KA \left( \frac{\partial T}{\partial x} \right) \Big|_{x=CS_i^b} \quad (4.6.2)$$

where  $Q_{rad}$  is the radiative heat loss from the surface of the STEG given by the following equation:

$$Q_{rad} = \epsilon \sigma A_{Gr} (T_{Gr}^4 - T_{sky}^4) \quad (4.6.3)$$

In Eq. (4.6.3), the sky temperature,  $T_{sky}$ , is a function of the ambient temperature [25] and  $\sigma = 5.67 \times 10^{-8} \text{ W/m}^2 \text{ K}^4$  is the Stefan-Boltzmann constant.

For the contact surfaces, 2–5, Eq. (4.6.4) is used. For each layer, the corresponding coefficients are presented in Table 4.6.1.

$$\begin{aligned} \rho_i c_i V_i \frac{\partial T_i}{\partial t} &= C_1 k_{(i-1)} n_{(i-1)} A_{(i-1)} \left( \frac{\partial T}{\partial x} \right) \Big|_{x=CS_i^t} - C_2 \frac{n_{(i-1)} I^2 r_{(i-1)}}{2} - C_3 k_i n_i A_i \left( \frac{\partial T}{\partial x} \right) \Big|_{x=CS_i^b} \\ &+ C_4 n_i S_{i,h} I T_{i,h} - C_5 \frac{n_i I^2 r_{i,l}}{2} - C_6 \frac{n_i \tau_l I (T_{i,h} - T_{i,2})}{2} \end{aligned} \quad (4.6.4)$$

Eq. (4.6.5) with the corresponding coefficients presented in Table 4.6.2 is used for the contact surfaces 6–9.

$$\begin{aligned} \rho_i c_i V_i \frac{\partial T_i}{\partial t} &= C_7 k_i n_i A_i \left( \frac{\partial T}{\partial x} \right) \Big|_{x=CS_i^b} - C_8 n_i S_{i,h} I T_{i,h} - C_9 \frac{n_i I^2 r_{i,m}}{2} - C_{10} \frac{n_i \tau_m I (T_{i,m} - T_{i,c})}{2} \\ &- C_{11} k_{(i+1)} n_{(i+1)} A_{(i+1)} \left( \frac{\partial T}{\partial x} \right) \Big|_{x=CS_i^t} + C_{12} \frac{n_{(i+1)} I^2 r_{(i+1)}}{2} \end{aligned} \quad (4.6.5)$$

**Table 4.6.2** Corresponding coefficients for various contact surfaces in the Eq. (4.6.5).

<b><i>i</i></b>	<b><i>C<sub>7</sub></i></b>	<b><i>C<sub>8</sub></i></b>	<b><i>C<sub>9</sub></i></b>	<b><i>C<sub>10</sub></i></b>	<b><i>C<sub>11</sub></i></b>	<b><i>C<sub>12</sub></i></b>
6	1	1	1	1	1	1
7	1	0	1	0	1	-1
8	1	0	1	0	1	0
9	1	0	0	0	1	0

On the contact surface between the working fluid the heat exchanger base (CS10):

$$\rho_{hx}c_{hx}V_{hx}\frac{\partial T_{hx}}{\partial t} = k_{hx}A_{hx}\left(\frac{\partial T}{\partial x}\right)\Big|_{x=CS'_{10}} + h_f A_f(T_{hx,2} - T_f) \quad (4.6.6)$$

Variation of the temperature of each contact surface in the STEG module is achieved by solving the abovementioned thermally coupled equations. The electromotive force (EMF) of the TEG can be obtained by considering different TE effects and the impact of the Thomson effect:

$$EMF = n_{sc} \left[ S_{sc,h}T_{sc,h} - S_{sc,c}T_{sc,c} - \sum_{i=1}^{m-1} \tau_i(T_i - T_{i+1}) \right] \quad (4.6.7)$$

The internal electrical resistance of the TEG is calculated by

$$R_i = \left( n_{ccs}r_{ccs} + n_{sl}r_{sl} + n_{sc} \sum_{i=1}^m r_{sc,i} \right) \quad (4.6.8)$$

By using Eqs. (4.6.7), (4.6.8), the generated power by the TEG can be obtained by

$$P_{TEG} = (E/(R_i + R_L))^2 R_L \quad (4.6.9)$$

The instantaneous efficiency of the TEG is defined as

$$\eta_{TEG} = P_{TEG}/(\alpha \times SC \times G \times A - Q_{rad}) \quad (4.6.10)$$

#### 4.6.1.3.3 Experimental setup

An experimental work has been carried out in order to investigate the performance of the STEG under concentrated light. In order to provide a uniform and precise solar concentration over the STEG system, a solar simulator is used in the experiment (see Fig. 4.6.6). Pressurized water is used to cool down the solar simulator that comprises 10 xenon arc lamps and can simulate up to 11,000 suns (11,000 kW/m<sup>2</sup>) on a focal point [26,27].

The schematic representation of the experimental setup is also shown in Fig. 4.6.4. Active cooling system is used in the experiments in order to provide constant temperature on the cold side of the STEG and to maximize the temperature gradient across the module. The heat sink with water as the working fluid and constant volumetric flow rate of 5L/min was located behind the TEG. The *I-V* characteristics and temperatures of the hot and cold sides of the TEG are measured.

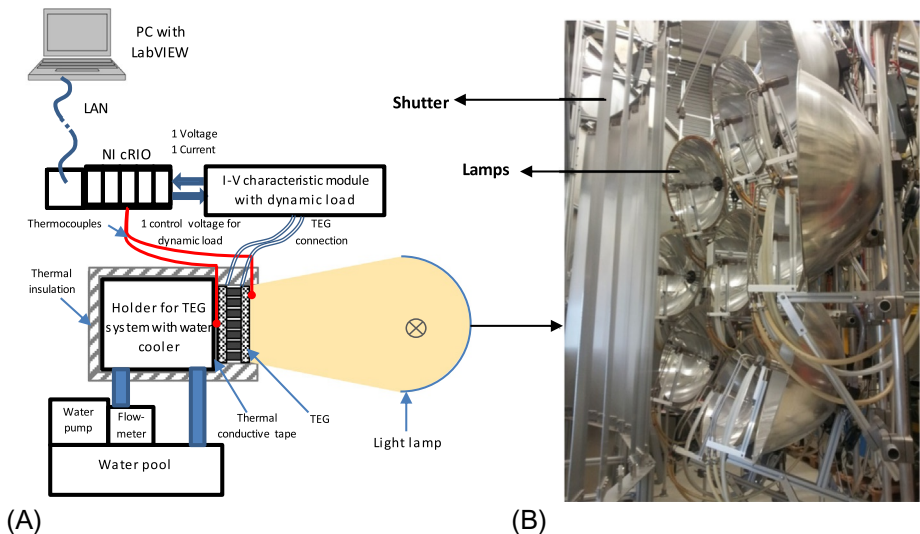


**Fig. 4.6.6** (A) Schematic representation of the experimental setup and (B) solar simulator used in this study [23].

#### 4.6.1.3.4 Results for different thermoelectric materials

The study has been carried out for two types of TEGs. An oxide TEG model CMO-25-42S used in the study, shown in Fig. 4.6.7, is composed of 50 unicouples with the module size of 42 mm × 42 mm. CaMnO<sub>3</sub> (Mn-113) and Ca<sub>3</sub>Co<sub>4</sub>O<sub>3</sub> (Co-349) are used as the N-Type and P-Type materials in the TEG, respectively [28].

In order to evaluate the performance of the STEG system under variant solar concentrations, an arbitrary pattern for the solar concentration was applied to the STEG system using the solar simulator, shown in Fig. 4.6.6. Fig. 4.6.8 illustrates the applied

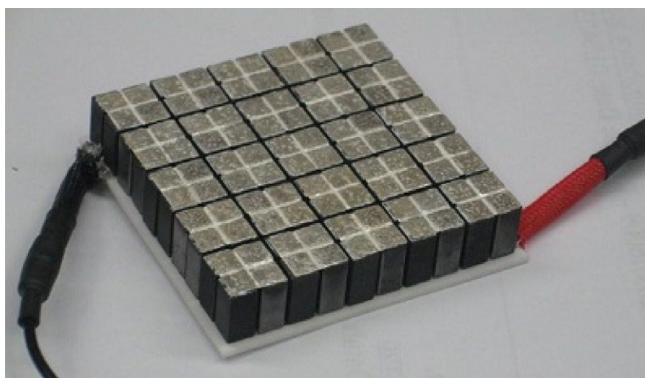


**Fig. 4.6.7** Oxide TEGs used in experiments [28].

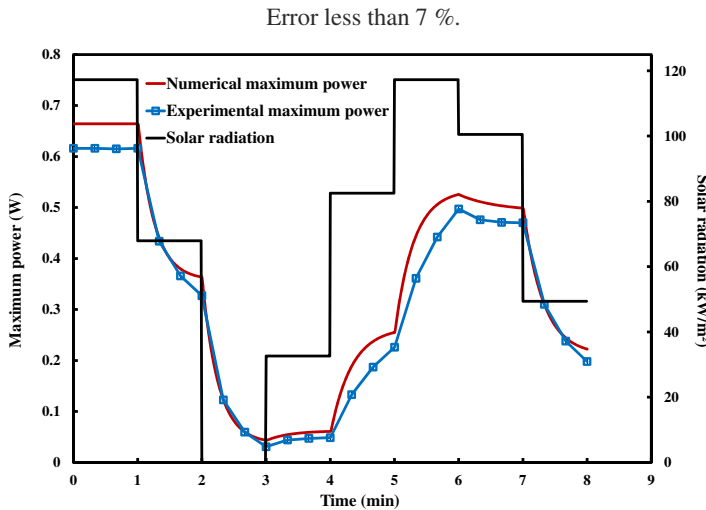


**Fig. 4.6.8** Numerical and experimental results of the maximum power versus time for the oxide-based STEG system.

solar concentration pattern and the variation of the maximum electric powers obtained from the numerical model and experimental work.

The numerical model can trace the temperature and power fluctuations of the STEG system for every variation of the solar concentrations. Fig. 4.6.8 indicates that the experimental and numerical results are in a close agreement with the average error of less than 7%.

Another oxide-based STEG system also was studied by Tomeš et al. [29]. It was found that for the temperatures up to 900°C, the efficiency of their oxide-based STEG system was less than 1%, however, the maximum theoretical efficiency of a Si<sub>80</sub>Ge<sub>20</sub>-based STEG system studied by Pereira et al. [30] was 1.8%. Increasing the solar concentration causes increment on the temperature of the TEG. By using the numerical model, a higher range of temperatures can be considered. In Fig. 4.6.9, the maximum temperature for the oxide-based TEG is limited to 950°C. It displays the efficiency and output power by the oxide-based STEG system, for various solar concentrations. Power generation by the STEG system enhances from 0.62 to 6.97 W and the efficiency of the STEG system increases from 0.3% to 1.2%, for solar concentrations of 117 and 329 kW/m<sup>2</sup>, respectively.

The same numerical model was used in order to evaluate the performance of a Bi<sub>2</sub>Te<sub>3</sub>-based STEG and a Zn<sub>4</sub>Sb<sub>3</sub> STEG system under variant solar concentrations. The same pattern was applied for both of the STEGs. Fig. 4.6.10 illustrates that in the applied range of the solar concentration, both of the STEGs have the same trend of variation, but the value of the generated power by the Bi<sub>2</sub>Te<sub>3</sub>-based STEG is higher than the Zn<sub>4</sub>Sb<sub>3</sub> STEG.

In the applied range of the solar concentration, the value of the figure of merit of the Bi<sub>2</sub>Te<sub>3</sub> is more than the Zn<sub>4</sub>Sb<sub>3</sub>. Therefore, the value of the generated power is higher

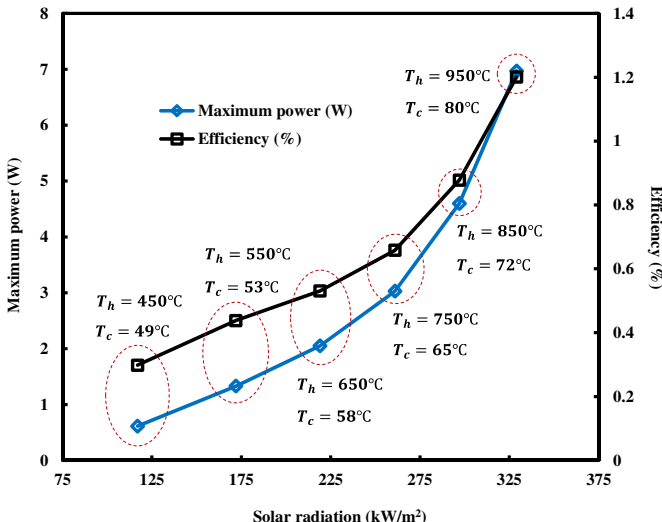


**Fig. 4.6.9** Maximum power and efficiency of the oxide-based STEG system versus solar radiation.

as well. The value of the figure of merit and the temperature difference across the TEG changes when the solar concentration changes. Fig. 4.6.11 shows the variation of these two key parameters for both of the  $\text{Bi}_2\text{Te}_3$ -based and  $\text{Zn}_4\text{Sb}_3$ -based STEGs, and for different values of the solar concentrations. As can be observed, for both of the STEGs, the efficiency and generated powers are increased by enhancement of the solar concentrations. The maximum value of the figure of merit of the  $\text{Bi}_2\text{Te}_3$  TEG is at 380K [31], while by increasing the temperature, the figure of merit drops. As can be seen,  $\text{Zn}_4\text{Sb}_3$  TEG has an opposite manner and by enhancement of the solar concentration, the value of the figure of merit also increases [32].

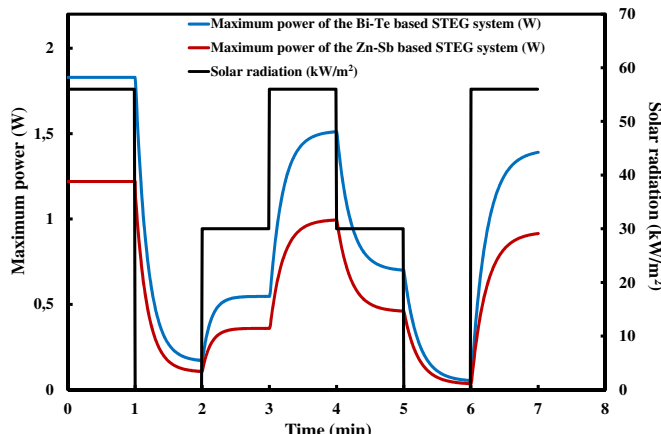


**Fig. 4.6.10** Maximum power versus time for the  $\text{Bi}_2\text{Te}_3$ -based and  $\text{Zn}_4\text{Sb}_3$ -based STEG systems.

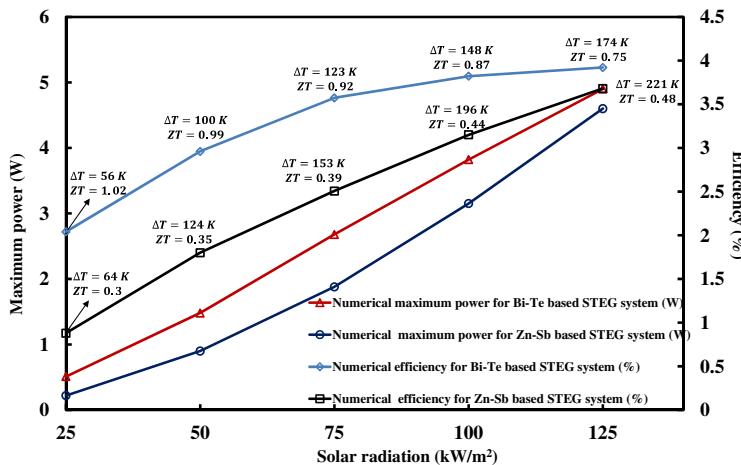


Fig. 4.6.11 Maximum powers and efficiencies of the STEG systems versus concentrated solar radiation.

## 4.6.2 Integration of thermoelectric generators with solar photovoltaic cells

In a STEG system, the TEGs are the energy harvester element. This element can be used along with photovoltaic (PV) cells to create a hybrid energy harvesting system. A significant development in the PV technologies has occurred in recent years, but in order to enhance the utilization of the solar energy, efficiency of the PV cells still needs to be improved. Less than half of the solar energy can be converted into useful electrical energy by the most efficient existing multi-junction (MJ) PV cells. Consequently, more than half of the input solar energy is dissipated as heat. Since TEGs are highly reliable and solid-state device, and are easy to integrate with PV cells, this technology is appropriate for harvesting this waste heat and converting a fraction of it into electricity.

Various configurations with different types of PV cells and thermoelectric materials have been investigated by different studies. The studies in this field can be generally categorized to the hybrid systems either under standard illumination condition or concentrated light. Based on the type of the PV cell and configuration of the hybrid system, they can be classified in the following categories.

### 4.6.2.1 PV-TEG hybrid system under standard illumination condition

Conventional PV cells that are currently used in a very large amount all around the world have less than 20% conversion efficiency, and more than 80% of the input solar energy is wasted. Many studies have been carried out on using TEGs for harvesting this waste heat in the standard illumination condition. The most common configuration is

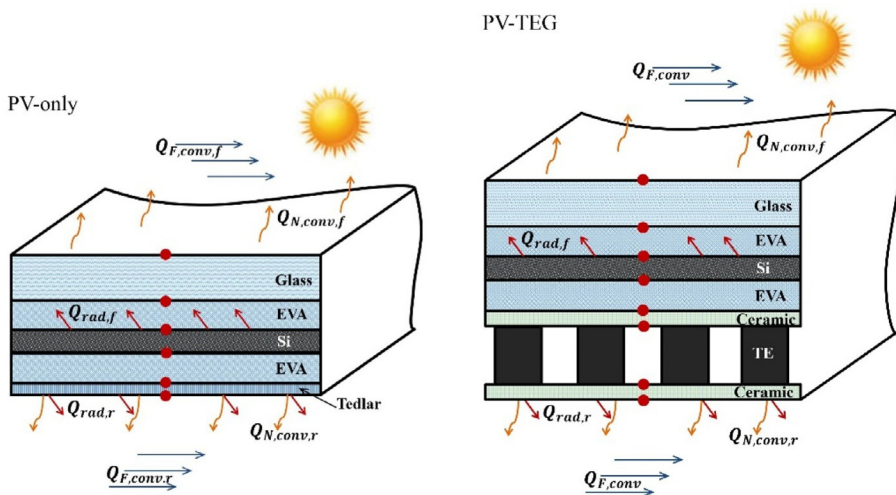


**Fig. 4.6.12** PV and PV-TEG hybrid system studied by Rezania et al. [33].

to locate TEGs underneath the PV cells. A PV-only and a PV-TEG hybrid system, shown in Fig. 4.6.12, was studied by Rezania et al. [33]. It was found that the amount of the generated power by the TEG using the current thermoelectric materials is insignificant compared to the PV cell, however, results of an investigation by Dallan et al. [34] indicated that, for the same thermal boundary conditions, the power generation by a PV cell in the hybrid PV-TEG module was 39% more than the power generation by the PV-only module.

Feasibility of using hybrid PV-TEG systems in different applications also has been extensively studied. A theoretical investigation was carried out by Kwan and Wu [35] in order to evaluate the performance of the hybrid PV-TEG system in space applications. The results showed that, by optimization of the TEG design, the power generation by the TEG can have a considerable contribution to the overall power generation by the hybrid system. van Sark [36] developed a numerical model for the hybrid PV-TEG system applicable for different PV cells and TEGs. The results indicated that depending on the application and the use of PV and TEG, the efficiency of the hybrid system can be enhanced from 8% to 23%. Both experimental and theoretical approaches were used by Kossyvakis et al. [37] in order to investigate PV-TEG hybrid systems with Dye-sensitized and poly-Si-based solar cells. The impact of the length of the TEG's thermoelectric elements, as a key parameter, was investigated indicating that the hybrid PV-TEG system has a better performance by decreasing the length of the elements. Kraemer et al. [38] also proposed an optimization approach in order to maximize the utilization of the solar energy by the hybrid PV-TEG system. It is been proved by Urbiola et al. [39] that more efficient materials are needed for the hybrid PV-TEG system in order to be used in real applications in the future.

#### **4.6.2.2 PV-TEG hybrid system under concentrated solar radiations**

Different types of optical collectors can be used (see Fig. 4.6.2) in order to increase the incident sun over the hybrid system and generate more power by the concentrated PV/CPV-TEG system. Various techniques have been used in different studies to enhance the efficiency and performance of hybrid systems. Yin et al. [40] proposed a thermal resistance analysis to optimize the design and to improve the conversion efficiency of the CPV-TEG system. It was indicated that various PV cells have different behaviors under concentrated lights, whereas in their study, amorphous silicon and polymer PV cells were the best options. Kil et al. [41] examined a hybrid module composed of a GaAs-based PV cell and a commercial TEG under concentrated light up to 50 suns. The results showed 3% increment in the efficiency of the CPV-TEG system than CPV-only system for the concentration ratio of 50 suns. A three-dimensional model of the CPV-TEG hybrid system was developed by Kiflemariam et al. [42] using COMSOL Multiphysics, and the effect of the thermal resistance on the performance of the system was evaluated. The results showed a significant impact of the thermal resistance on the hybrid system performance. Zhang and Xuan [43] also developed a three-dimensional model and confirmed the impact of the thermal resistance on the performance of a hybrid system.

Due to the thermal resistance created by the TEG components between the PV cell and heat sink, using the same heat sink with identical cooling efficiency leads to a higher temperature in the PV cell in the hybrid system in comparison with the PV-only system. Consequently, the generated power by the PV in a PV-only system is higher than the power generation by the PV cell in a PV-TEG system. Xu et al. [44] established a three-dimensional model using COMSOL Multiphysics and approved this crucial point. Material properties and thermoelectric effects including the Seebeck, Thomson, Joule, and Fourier heat conduction effects also have a substantial impact on the performance of the hybrid systems. Lamba and Kaushik [45] developed a thermodynamic model considering all the thermoelectric effects and showed that the efficiency of the PV-only system is 13.37% less than CPV-TEG hybrid system. Although the thermoelectric material properties play an important role in the power generation by the hybrid system, enhancement of the figure of merit, Z, will not necessarily increase the overall conversion efficiency of the system [46].

Performance and efficiency of a hybrid system are functions of different parameters such as geometry and material properties of the PV cell and TEG, thermal resistance between different components of the hybrid system, cooling effectivity of the heat sink, solar concentration, etc. All of these parameters are important critical factors, which affect the temperature profile across the device and the power generation and efficiency of both of the PV cell and TEG. There is a contradiction between the response of the PV cell and TEG to the variation of the temperature. A lower temperature is more appropriate for the PV cells, while a higher temperature gradient across a TEG generates higher power. Therefore, all the affecting parameters should be considered carefully in the design of the hybrid system in a way that the overall generated power by the hybrid system stays maximized. In general, it is proved that, by emerging

new materials, the CPV-TEG hybrid systems can make substantial growth in renewable technologies [3].

#### **4.6.2.3 MJ-TEG hybrid system under concentrated solar radiations**

Multi-junction (MJ) solar cells are more efficient than the conventional single-junction PV cells. Dissimilar semiconductor materials are used for different layers of the MJ cell in order to harvest a broader range of wavelength of the light. Fewer studies have been done on the MJ-TEGs in comparison with the conventional PV-TEGs. TEGs are able to harvest a fraction of the waste heat from the MJ cell and convert it into the useful electricity. The contribution of the power generation by the TEG enhances with increasing the operating temperature [47] and solar concentration [48,49]. Operating under unmatched load resistance, where the external electrical load is far from the internal electrical resistance of the TEG, leads to a considerable reduction in the power output by the TEG [50]. Results of the study by Sweet et al. [51,52] indicated that the lifetime and power generation by the MJ-TEG hybrid system can be enhanced while the energy cost decreases.

The same numerical approach and experimental setup, as used for the STEG systems in [Section 4.6.1.3.2](#), is applied to evaluate the performance of a concentrated triple junction (CTJ)-TEG hybrid system under both transient and steady-state conditions. A commercially available CTJ photovoltaic cell with the surface dimensions of  $10.075 \text{ mm} \times 10.68 \text{ mm}$  [53] and a Bi-Te-based TEG with the area of  $8.7 \text{ mm} \times 8.7 \text{ mm}$  [54] were connected to form the CTJ-TEG hybrid system ([Fig. 4.6.13](#)).

In comparison with the STEG, the hybrid module includes two more layers. By using the energy conservation law, we have the following equation on the top of the CTJ cell [55]:

$$\rho_{CTJ} c_{CTJ} V_{CTJ} \frac{\partial T_{CTJ}}{\partial t} = SC \times G \times A_{CTJ} - Q_{rad} + KA \left( \frac{\partial T}{\partial x} \right) \Big|_{x=CS_1^b} - P_{CTJ} \quad (4.6.11)$$

In Eq. (4.6.11),  $P_{CTJ}$  is the output power by the CTJ cell and is defined as [55]

$$P_{CTJ} = SC \times G \times A_{CTJ} \times \eta_{CTJ} \quad (4.6.12)$$

$\eta_{CTJ}$  is the efficiency of the CTJ that is given as [56]

$$\eta_{CTJ} = \eta_{T_{ref}} [1 - \beta_{ref} (T_{CTJ} - T_{ref})] \quad (4.6.13)$$

where  $\eta_{T_{ref}}$  is the efficiency of the CTJ cell at the reference temperature ( $T_{ref}=25^\circ\text{C}$ ) and reference solar radiation ( $G_{ref}=1000 \text{ W/m}^2$ ) [57].  $\beta_{ref}$ , which is offered by the manufacturer, is the temperature coefficient of the CTJ cell at the reference temperature. It is considered  $-0.1\%/\text{K}$  [58] in this framework.

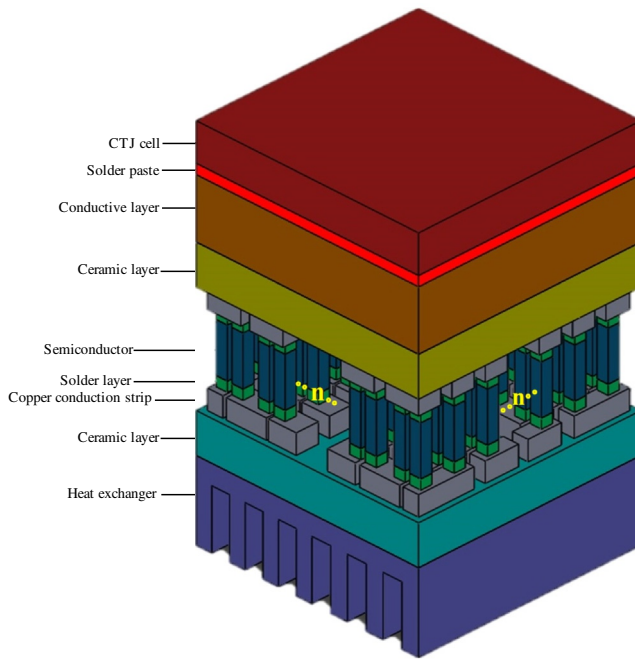


**Fig. 4.6.13** Physical model of the CTJ-TEG hybrid system [55].

For the contact surface between the CTJ cell and solder paste ( $CS_2$ ):

$$\rho_{sp}c_{sp}V_{sp}\frac{\partial T_{sp}}{\partial t} = k_{CTJ}A_{CTJ}\left(\frac{\partial T}{\partial x}\right)\Big|_{x=CS_2^t} - k_{sp}A_{sp}\left(\frac{\partial T}{\partial x}\right)\Big|_{x=CS_2^b} \quad (4.6.14)$$

For the contact surface between the solder paste and conductive layer ( $CS_3$ ), we have

$$\rho_{col}c_{col}V_{col}\frac{\partial T_{col}}{\partial t} = k_{sp}A_{sp}\left(\frac{\partial T}{\partial x}\right)\Big|_{x=CS_3^t} - k_{col}A_{col}\left(\frac{\partial T}{\partial x}\right)\Big|_{x=CS_3^b} \quad (4.6.15)$$

For the other contact surfaces in the hybrid system, the same equations as used for the STEG system in [Section 4.6.1.3.2](#) can be applied.

An arbitrary pattern for the solar concentration was applied to the hybrid system to show transient behavior of the system under transient condition. [Fig. 4.6.14](#) shows the applied solar concentration pattern and the temperatures of the CTJ cell and the hot and cold sides of the TEG obtained in the experiments. Although with different slopes, all the temperatures fluctuation followed a variation of the solar concentration. It is worth noticing that the input solar concentration must be selected in a way that the temperature of the CTJ stays less than the critical temperature to prevent the system from the overheating [59].

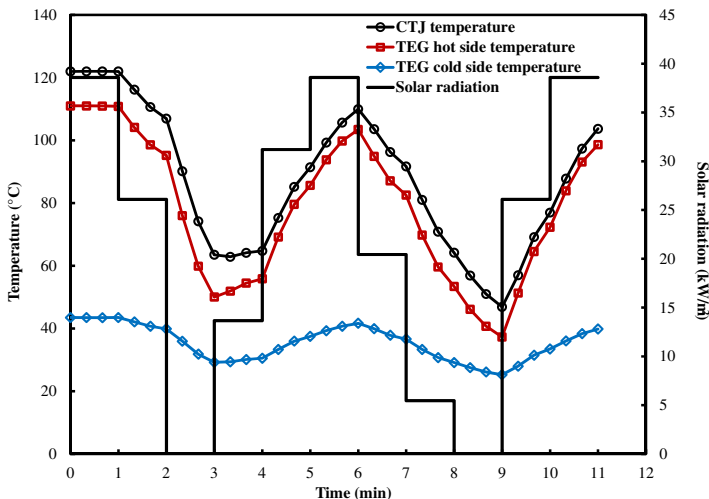


**Fig. 4.6.14** Variation of the solar radiation and the temperatures of the CTJ and hot and cold sides of the TEG [60].

The experimental and numerical results for the generated power by the CTJ and TEG are shown in Fig. 4.6.15. The variation of the power generation by the CTJ is very fast and similar to the applied pattern of the solar concentration. Therefore, the solar concentration is the most affective parameter on the power generation by the CTJ cell. The temperature of the CTJ is another parameter with less effect on power. The impact of the temperature can be observed in the area (1) and (2). When the solar concentration and consequently the temperature decreases, a small enhancement in maximum power happens, see area (1) in Fig. 4.6.15A. The opposite variation can be seen in the area (2) indicating that by enhancement of the solar concentration and, consequently, the CTJ temperature, the power generation decreases slightly.

The figure of merit and the temperature difference across the TEG are the most important parameters in power generation by the TEG. In the experimented range of the temperature, shown in Fig. 4.6.14, the variation of the figure of merit is insignificant [54]. Therefore, the temperature gradient across the TEG is the most dominant parameter in the power generation by the TEG. In addition, due to the higher heat capacity and thermal resistance of the TEG than the CTJ, the fluctuation of the generated power by the TEG is not stepwise like CTJ and it almost follows the variation of the temperatures.

Noticing areas (1) and (2) in Figs. 4.6.15A and B, shows the reverse variation of the power generation by the CTJ and TEG. It illustrates that the TEG can compensate a portion of the waste heat by the CTJ. This value can enhance using more efficient thermoelectric materials and geometrical optimization [61].

In order to study the steady-state behavior of the CTJ-TEG hybrid system, the variation of the temperature with the time,  $\frac{\partial T}{\partial t} = 0$  should be considered zero in the

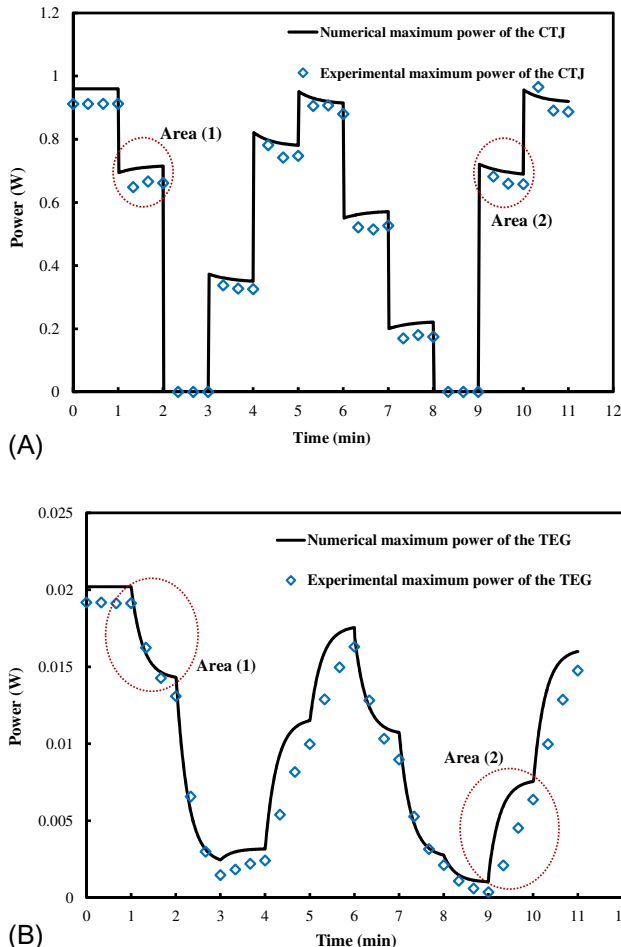


**Fig. 4.6.15** Experimental and numerical maximum output power by (A) the CTJ cell and (B) TEG module versus time [60].

obtained governing Eqs. A single-diode model [62] is applied to evaluate the performance and efficiency of the CTJ. In this model, shown in Fig. 4.6.16, the CTJ cell current is defined as a function of the CTJ cell voltage as

$$I = I_{PH} - \frac{V + IR_S}{R_{SH}} - I_0 \left[ \exp \left( \frac{V + IR_S}{nV_T} \right) - 1 \right] \quad (4.6.16)$$

where  $I_{PH}$  is the light-generated current in the cell,  $I_0$  is defined as the diode reverse saturation current,  $V_T = kT/q$  is the thermal voltage, and  $n$  is the diode ideality factor that is equal to 1 for an ideal diode.

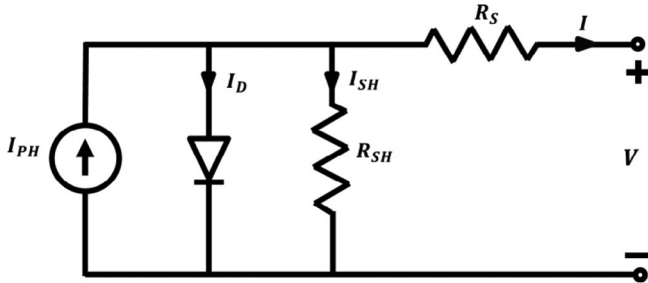


**Fig. 4.6.16** The equivalent circuit of the CTJ module with a single-diode system [63].

Eq. (4.6.16) can be rewritten using Lambert W function [63–65] as follows:

$$I = \frac{(I_{PH} + I_0) - \frac{V}{R_{SH}}}{1 + \frac{R_S}{R_{SH}}} - \frac{nV_T}{R_S} W \left( \frac{I_0 R_S}{nV_T \left( 1 + \frac{R_S}{R_{SH}} \right)} \exp \left( \frac{V}{nV_T} \left( 1 - \frac{R_S}{R_S + R_{SH}} \right) + \frac{(I_{PH} + I_0) R_S}{nV_T \left( 1 + \frac{R_S}{R_{SH}} \right)} \right) \right) \quad (4.6.17)$$

and the voltage of the CTJ cell can be obtained as

$$V = (I_{PH} + I_0) R_{SH} - I(R_S + R_{SH}) - nV_T W \left( \frac{I_0 R_{SH}}{nV_T} \exp \left( \frac{(I_{PH} + I_0 - I) R_{SH}}{nV_T} \right) \right) \quad (4.6.18)$$

Clearly, the output power by the CTJ cell is given as

$$P_{CTJ} = VI \quad (4.6.19)$$

Furthermore, the efficiency of the CTJ cell can be defined as

$$\eta_{CTJ} = \frac{P_{CTJ}}{SC \times G \times A_{CTJ}} \quad (4.6.20)$$

**Fig. 4.6.17** shows the variation of the power generation by the CTJ and TEG for different solar concentrations. Newton-Raphson algorithm [66] is applied to obtain the best-fitted curve for the experimental results. For both the CTJ cell and TEG module, the output power enhances by increasing the solar concentration, though a higher solar concentration decreases the CTJ efficiency due to increment in the cell temperature. The obtained maximum powers by the CTJ are 0.283 and 0.852 W for the concentration ratios 8 and 37 suns, respectively. These values for the TEG module are 2.43 and 24.1 mW.

The contribution of the TEG in the overall power generation by the hybrid system enhances by increasing the solar concentration. The ratio of the maximum output power by the TEG module to the maximum generated power by the CTJ cell is shown in **Fig. 4.6.18A**. The ratio, which is 0.86% and 2.83% for the solar concentrations 8 and 37 suns, respectively, shows the enhancing contribution of the TEG on the power generation at higher sun concentrations. According to studies [60], the ratio increases due to geometrical and material optimization.

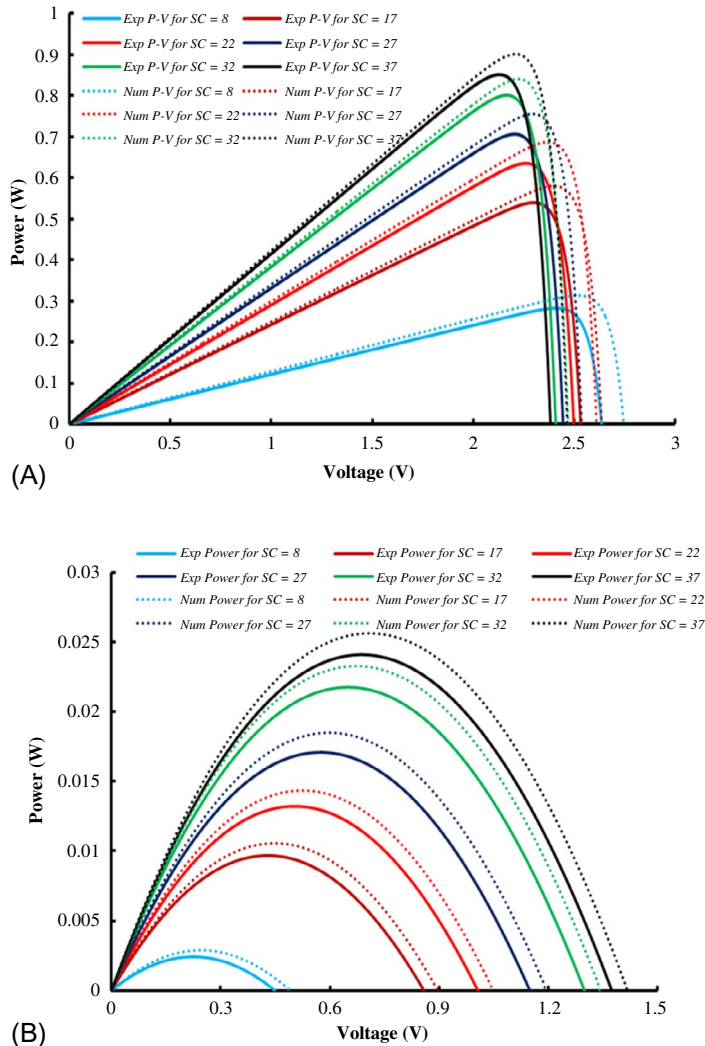


**Fig. 4.6.17** The  $P$ - $V$  curves for the (A) CTJ cell and (B) TEG module, and for different solar concentrations [67].

Variations of the efficiencies of each component in the hybrid CTJ-TEG system are displayed in Fig. 4.6.18B. By increasing the solar concentration and, accordingly, the temperature of the CTJ cell and the temperature difference across the TEG, the efficiency of the CTJ drops while the efficiency of the TEG increases. The results of the experimental study show that conversation efficiency of 23.02% and 35.33% can be obtained by the CTJ cell under solar concentrations of 37 and 8 suns, respectively, while the conversion efficiency of the TEG becomes double as the solar concentration increases from 8 to 37 suns. The developed one-dimensional numerical model and the simplifying assumptions in this study can be a source of overestimation of the numerical results in comparison with the experimental data.

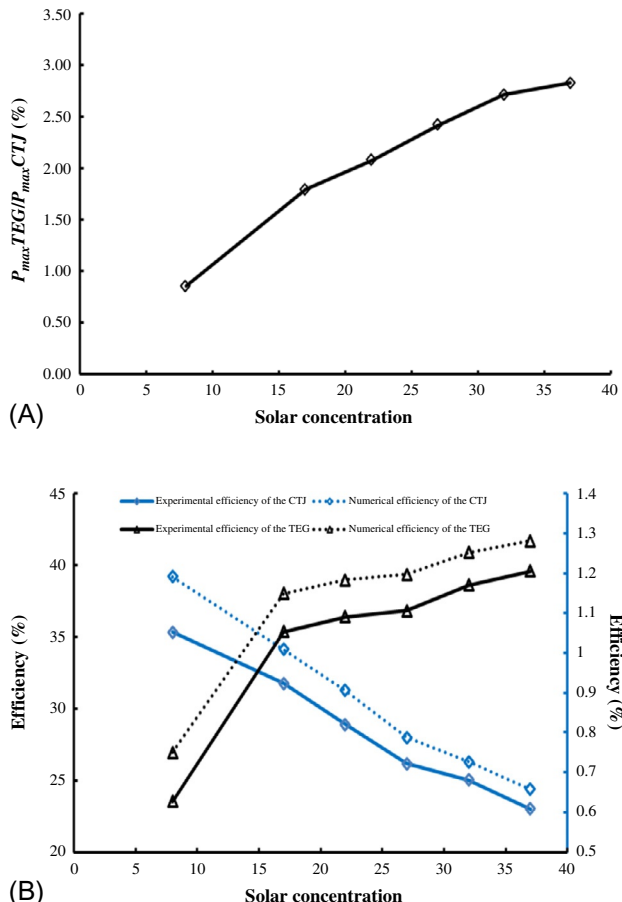


**Fig. 4.6.18** (A) Ratio of the maximum power of the TEG to the CTJ versus the solar concentration and (B) variation of the efficiencies of the CTJ and the TEG versus the solar concentration [67].

### 4.6.3 Other techniques to enhance performance of hybrid systems

#### 4.6.3.1 Energy storage

Solar radiation has an intermittent nature and considerably fluctuates during the day. Therefore, using an energy storage unit is sometimes required to smooth the power delivery by the system especially in areas with semi-cloudy weather conditions. Phase change materials (PCMs) are able to store and release a large amount of thermal energy when the phase of the material changes. PCMs can be used to absorb heat at the high solar radiations and release it when the solar radiation is low. Consequently, in addition to the possibility of the energy storage, the system's working

temperature will be more stable. This is the main advantage of using PCM material in the hybrid systems [68,69].

The performance of the PV panels can be improved using smart cooling systems composed of PCM and TEG module [70]. Therefore, a PV-TEG-PCM hybrid system is more efficient than the PV-TEG hybrid system. Depending on the operating condition, different PCMs with different melting points can be used in the hybrid system [71]. Considering different configurations [72] for the PV-TEG-PCM hybrid systems shows great potential for using such hybrid systems in different applications. In order to make use of these hybrid systems, more efficient with a higher figure of merits is needed [73]. In addition to the material properties and configuration of the hybrid system, different parameters such as cooling efficiency of the heat sink, sunlight intensity, and the uniformity of the light spot affect the stability of the output power and efficiency of the hybrid system [74]. In order to maximize the utilization of the solar energy, the optimal operating condition that depends on the PV cell and the TEG used in the hybrid system, needs to be obtained. It is also worth noting that the thermal contact resistance has a remarkable impact on the performance of the hybrid system [75]. While there are different advantages such as enhancement and stabilizing the power output by using PCM in the hybrid system, the additional cost also has to be considered and a trade-off must be made in relation with the extra cost of such optimization.

#### **4.6.3.2 Spectral beam splitting technology**

In the spectrum splitting method, a splitter reflects the solar radiation at a specific wavelength (cut-off wavelength). The separated radiations can be used by the PV and TEG for the energy conversion. Since the PV cells and TEGs convert different ranges of the solar spectrum into the electricity, using the beam splitter can enhance the utilization of the solar energy and as a specific required range of the solar spectrum, it can be converted into electricity by the PV. The spectral beam splitter is an optical device that splits an incident light beam into two or more beams (see Fig. 4.6.19). PV cells can convert the ultraviolet and visible regions (200–800 nm) of the solar spectrum into the electricity while the infrared region (800–3000 nm) of the solar spectrum can be converted into electricity by the TEG [76]. In this configuration of the hybrid system, PV and TEG work independently having no impact on each other.

The spectrum splitting hybrid system is composed of a concentrator, a PV cell, a TEG, a beam splitter device, and a cooling system. Two key parameters affecting the performance of the system are the solar concentration and the efficiency of the cooling system. Furthermore, compared to the PV-only system, the spectrum splitting hybrid system is more suitable to be used under higher solar concentrations [77]. The material properties and the geometry of the TEG affect the optimal temperature distribution in the TEG while the optimized cut-off wavelength of the hybrid system is determined by the solar cell's bandgap. The thermoelectric figure of merit and spectral splitter optimum cut-off wavelength have opposite relationship [78]. It is proven that the increment of the efficiency of the hybrid system without concentration is limited [79]. Although using such hybrid system can improve the conversion efficiency of the

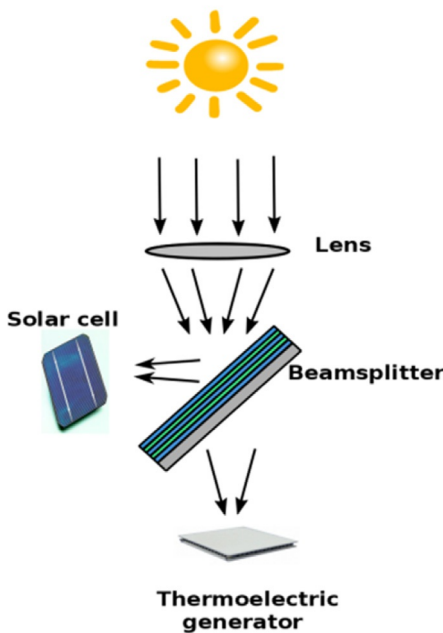


**Fig. 4.6.19** PV-TEG spectrum splitting hybrid system.

system compared to the PV-only system [80], an economical evaluation is needed to be accomplished. Furthermore, different optimization methods can be used in order to enhance the performance of the hybrid system. For instance, a cascaded thermoelectric generator configuration can be used to convert higher wavelength radiation (infra-red region) into electricity [81].

#### 4.6.4 Summary

In this chapter, the solar applications of the TEGs are investigated. The focus was on two different systems called STEG systems and hybrid PV-TEG systems. The performance of both systems was evaluated under the steady-state and transient conditions using both numerical and experimental approaches. Different components of the STEG and hybrid PV-TEG systems were introduced, and the literature and the state of the art of such systems were presented. Moreover, a numerical approach was proposed to investigate the behavior of the considered systems under transient and steady-state conditions. The governing equations were obtained using the energy conservation law and solved by means of the finite volume method. In the experimental work, a solar simulator was used to provide uniform and precise solar radiation over the setup. Finally, some methods were suggested and discussed briefly for thermal management of the systems.

## References

- [1] D. Narducci, P. Bermel, B. Lorenzi, N. Wang, K. Yazawa, Hybrid and Fully Thermoelectric Solar Harvesting, vol. 268, Springer Series in Materials Science, 2018.
- [2] L.L. Baranowski, G. Jeffrey Snyder, E.S. Toberer, Concentrated solar thermoelectric generators, *Energy Environ. Sci.* 5 (2012) 9055–9067.
- [3] P. Sundarraj, D. Maity, S.S. Roy, R.A. Taylor, Recent advances in thermoelectric materials and solar thermoelectric generators – a critical review, *RSC Adv.* 4 (87) (2014) 46860–46874.
- [4] W.W. Coblenz, Harnessing heat from the sun, *Sci. Am.* 324 (127) (1922).
- [5] M. Telkes, Solar thermoelectric generators, *J. Appl. Phys.* 25 (6) (1954) 765–777.
- [6] D.M. Chapin, C.S. Fuller, G.L. Pearson, A new silicon p-n junction photocell for converting solar radiation into electrical power, *J. Appl. Phys.* 25 (5) (1954) 676–677.
- [7] N. Fuschillo, R. Gibson, Solar thermoelectric generators for missions toward the sun, *IEEE Trans. Aerosp. Electr. Syst. AES-2* (4) (1966) 93–102.
- [8] M. Swerdlng, V. Raag, Solar thermoelectric power generation for mercury orbiter missions, *J. Energy* 3 (5) (1979) 291–298.
- [9] G.W. Glassburn, Flat plate solar thermoelectric generator orbital experiment, *IEEE Trans. Aerosp.* 1 (2) (1963) 1396–1403.
- [10] N. Fuschillo, et al., Flat plate solar thermoelectric generator for near-earth orbits, *Adv. Energy Convers.* 6 (2) (1966) 103–125.
- [11] D.M. Rowe, A high performance solar powered thermoelectric generator, *Appl. Energy* 8 (4) (1981) 269–273.
- [12] H.J. Goldsmid, J.E. Giutronich, M.M. Kaila, Solar thermoelectric generation using bismuth telluride alloys, *Solar Energy* 24 (5) (1980) 435–440.
- [13] C.L. Dent, M.H. Cobble, A solar thermoelectric generator experiments and analysis, in: 4th International Conference on Thermoelectric Energy Conversion, 1982.
- [14] T. Durst, L.B. Harris, H.J. Goldsmid, Studies of a thermoelectric generator operating from tubular solar collectors, *Solar Energy* 31 (4) (1983) 421–425.
- [15] S.A. Omer, D.G. Infield, Design optimization of thermoelectric devices for solar power generation, *Solar Energy Mater. Solar Cells* 53 (1–2) (1998) 67–82.
- [16] N. Vatcharasathien, et al., Design and analysis of solar thermoelectric power generation system, *Int. J. Sustain. Energy* 24 (3) (2005) 115–127.
- [17] A. Weidenkaff, et al., Development of thermoelectric oxides for renewable energy conversion technologies, *Renew. Energy* 33 (2) (2008) 342–347.
- [18] P. Tomeš, et al., Direct conversion of simulated solar radiation into electrical energy by a perovskite thermoelectric oxide module (TOM), in: 2008 MS&T Conference Proceedings, 2009.
- [19] R. Amatya, R.J. Ram, Solar thermoelectric generator for micropower applications, *J. Electr. Mater.* 39 (9) (2010) 1735–1740.
- [20] C. Urbiola, E. Arturo, Y. Vorobiev, Investigation of solar hybrid electric/thermal system with radiation concentrator and thermoelectric generator, *Int. J. Photoenergy* 2013 (2013) (2013).
- [21] D. Kraemer, et al., High-performance flat-panel solar thermoelectric generators with high thermal concentration, *Nature Mater.* 10 (7) (2011) 532.
- [22] D. Kraemer, et al., Concentrating solar thermoelectric generators with a peak efficiency of 7.4%, *Nat. Energy* 1 (11) (2016) 1–8.
- [23] S. Mahmoudinezhad, A. Rezania, P.A. Cotfas, D.T. Cotfas, L.A. Rosendahl, Transient behavior of concentrated solar oxide thermoelectric generator, *Energy* 168 (2019) 823–832.

- [24] S.V. Patankar, Numerical Heat Transfer and Fluid Flow (Series in Computation and Physical Processes in Mechanics and Thermal Sciences), Taylor & Francis, London, 1980.
- [25] H. Nowak, The sky temperature in net radiant heat loss calculations from low-sloped roofs, *Infrared Phys.* 29 (2–4) (1989) 231–232.
- [26] Petrasch, JÅkrg, et al., A novel 50kW 11,000 suns high-flux solar simulator based on an array of xenon arc lamps, *J. Solar Energy Eng.* 129 (4) (2007) 405–411.
- [27] I. Alxneit, H. Schmit, Spectral characterization of PSI's high-flux solar simulator, *J. Solar Energy Eng.* 134 (1) (2012). 011013-1-5.
- [28] <http://espressomilkcooler.com/wp-content/uploads/2014/06/CMO-25-42S-OXIDE-NEW.pdf> (Online, Cited: 29 September 2019).
- [29] P. Tomeš, M. Trottmann, C. Suter, M.H. Aguirre, A. Steinfeld, P. Haueter, A. Weidenkaff, Thermoelectric oxide modules (TOMs) for the direct conversion of simulated solar radiation into electrical energy, *Materials* 3 (2010) 2801–2814.
- [30] A. Pereira, T. Caroff, G. Lorin, T. Baffie, K. Romanjek, S. Vesin, K. Kusiaku, H. Duchemin, V. Salvador, N. Miloud-Ali, L. Aixala, J. Simon, High temperature solar thermoelectric generator-indoor characterization method and modeling, *Energy* 84 (2015) 485–492.
- [31] <http://thermoelectric-generator.com/wp-content/uploads/2014/07/Ingot-Raw-Material-BiTe-N-and-P.pdf> (Online, Cited: 29 September 2019).
- [32] T. Dasgupta, et al., Thermoelectric studies in  $\beta$ -Zn<sub>4</sub>Sb<sub>3</sub>—the complex interdependence between thermal stability, thermoelectric transport, and zinc content, *J. Appl. Phys.* 113 (10) (2013). 103708-1-9.
- [33] A. Rezania, D. Sera, L.A. Rosendahl, Coupled thermal model of photovoltaic-thermoelectric hybrid panel for sample cities in Europe, *Renew. Energy* 99 (2016) 127–135.
- [34] B.S. Dallan, J. Schumann, J.L. Frédéric, Performance evaluation of a photoelectric–thermoelectric cogeneration hybrid system, *Sol. Energy* 118 (2015) 276–285.
- [35] T.H. Kwan, X. Wu, Power and mass optimization of the hybrid solar panel and thermoelectric generators, *Appl. Energy* 165 (2016) 297–307.
- [36] W.G.J.H.M. van Sark, Feasibility of photovoltaic – thermoelectric hybrid modules, *Appl. Energy* 88 (2011) 2785–2790.
- [37] D.N. Kossyvakis, G.D. Voutsinas, E.V. Hristoforou, Experimental analysis and performance evaluation of a tandem photovoltaic-thermoelectric hybrid system, *Energy Convers. Manag.* 117 (2016) 490–500.
- [38] D. Kraemer, L. Hu, A. Muto, X. Chen, G. Chen, M. Chiesa, Photovoltaic-thermoelectric hybrid systems: a general optimization methodology, *Appl. Phys. Lett.* 92 (2008). 243503-1.
- [39] E.A.C. Urbiola, Y.V. Vorobiev, L.P. Bulat, Solar hybrid systems with thermoelectric generators, *Solar Energy* 86 (1) (2012) 369–378.
- [40] E. Yin, Q. Li, Y. Xuan, Thermal resistance analysis and optimization of photovoltaic-thermoelectric hybrid system, *Energy Convers. Manag.* 143 (2017) 188–202.
- [41] T.-H. Kil, S. Kim, D.-H. Jeong, D.-M. Geum, S. Lee, S.-J. Jung, S. Kim, C. Park, J.-S. Kim, J.M. Baik, K.-S. Lee, C.Z. Kim, W.J. Choi, S.-H. Baek, A highly-efficient, concentrating photovoltaic/thermoelectric hybrid generator, *Nano Energy* 37 (2017) 242–247.
- [42] R. KifleMariam, M. Almas, C. Lin, Modeling integrated thermoelectric generator-photovoltaic thermal (TEG-PVT) system, in: Excerpt from the Proceedings of the 2014 COMSOL Conference in Boston, 2014.
- [43] J. Zhang, Y. Xuan, Investigation on the effect of thermal resistances on a highly concentrated photovoltaic-thermoelectric hybrid system, *Energy Convers. Manag.* 129 (2016) 1–10.

- [44] X. Xu, S. Zhou, M.M. Meyers, B.G. Sammakia, B.T. Murray, Performance analysis of a combination system of concentrating photovoltaic/thermal collector and thermoelectric generators, *J. Electron. Packag.* 136 (2014) 0410041–0410047.
- [45] L. Ravita, S.C. Kaushik, Modeling and performance analysis of a concentrated photovoltaic–thermoelectric hybrid power generation system, *Energy Convers. Manag.* 115 (2016) 288–298.
- [46] Y.Y. Wu, S.Y. Wu, L. Xiao, Performance analysis of photovoltaic–thermoelectric hybrid system with and without glass cover, *Energy Convers. Manag.* 93 (2015) 151–159.
- [47] R. Tamaki, T. Toyoda, Y. Tamura, A. Matoba, T. Minamikawa, M. Tokuda, M. Masui, Y. Okada, Hybrid photovoltaic and thermoelectric module for high concentration solar system, in: *AIP Conference Proceedings* 1881, 2017, p. 100002.
- [48] O. Beeri, O. Rotem, E. Hazan, E.A. Katz, A. Braun, Y. Gelbstein, Hybrid photovoltaic–thermoelectric system for concentrated solar energy conversion, experimental realization and modeling, *J. Appl. Phys.* 118 (11) (2015). 115104-1-8.
- [49] A. Rezania, L.A. Rosendahl, Feasibility and parametric evaluation of hybrid concentrated photovoltaic–thermoelectric system, *Appl. Energy* 187 (2017) 380–389.
- [50] D.T. Cotfas, P.A. Cotfas, L. Floroian, D.I. Floroian, Study of combined photovoltaic cell/thermoelectric element/solar collector in medium concentrated light, in: *Optimization of Electrical and Electronic Equipment (OPTIM) & 2017 Intl Aegean Conference on Electrical Machines and Power Electronics (ACEMP), 2017 International Conference on Date of Conference*, Brasov, Romania, 25–27 May, 2017.
- [51] T.K.N. Sweet, M.H. Rolley, M.J. Prest, G. Min, Novel hybrid III: V concentrator photovoltaic–thermoelectric receiver designs, in: *AIP Conference Proceedings* 1881, 2017, p. 080009.
- [52] T.K.N. Sweet, M.H. Rolley, W. Li, M.C. Paul, M. Gao, A.R. Knox, Experimental characterization and multi-physics simulation of a triple-junction cell in a novel hybrid III: V concentrator photovoltaic–thermoelectric receiver design with secondary optical element, *Energy Procedia* 142 (2017) 809–814.
- [53] SolAero Technologies, <https://solaerotech.com/wp-content/uploads/2018/03/CTJ-Datasheet.pdf> (Online). SolAero Technologies Corp. (Cited: 21 September 2019).
- [54] www.Tecteg.com, <http://thermoelectric-generator.com/wp-content/uploads/2014/07/Ingot-Raw-Material-BiTe-N-and-P.pdf> (Online, Cited: 21 September 2019).
- [55] S. Mahmoudinezhad, A. Rezania, L.A. Rosendahl, Behavior of hybrid concentrated photovoltaic–thermoelectric generator under variable solar radiation, *Energy Convers. Manag.* 164 (2018) 443–452.
- [56] D.L. Evans, Simplified method for predicting photovoltaic array output, *Solar Energy* 27 (6) (1981) 555–560.
- [57] G. Notton, C. Cristofari, M. Mattei, P. Poggi, Modelling of a double-glass photovoltaic module using finite differences, *Appl. Thermal Eng.* 25 (17–18) (2005) 2854–2877.
- [58] <http://www.azurspace.com>, [http://www.azurspace.com/images/pdfs/DB\\_3877-00-00\\_3C42\\_AzurDesign\\_10x10\\_20140226.pdf](http://www.azurspace.com/images/pdfs/DB_3877-00-00_3C42_AzurDesign_10x10_20140226.pdf) (Online). AZUR SPACE Solar Power GmbH (Cited: 21 September 2019).
- [59] P. Espinet-González, C. Algorta, N. Núñez, V. Orlando, M. Vázquez, J. Bautista, K. Araki, Evaluation of the reliability of commercial concentrator triple-junction solar cells by means of accelerated life tests (ALT), in: *AIP Conference Proceedings* 1556, 2013, p. 222.
- [60] S. Mahmoudinezhad, S. Ahmadi Atouei, P.A. Cotfas, D.T. Cotfas, L.A. Rosendahl, A. Rezania, Experimental and numerical study on the transient behavior of multijunction

- solar cell-thermoelectric generator hybrid system, *Energy Convers. Manag.* 184 (2019) 448–455.
- [61] S. Mahmoudinezhad, A. Rezania, L.A. Rosendahl, Numerical parametric study on the performance of CPV-TEG hybrid system, *Energy Procedia* 158 (2019) 453–458.
  - [62] E.I. Batzelis, S.A. Papathanassiou, A method for the analytical extraction of the single-diode PV model parameters, *IEEE Trans. Sustain. Energy* 7 (2) (2016).
  - [63] M. Tripathy, K. Manish, P.K. Sadhu, Photovoltaic system using Lambert W function-based technique, *Sol. Energy* 158 (2017) 432–439.
  - [64] J. Appelbaum, A. Peled, Parameters extraction of solar cells – a comparative examination of three methods, *Sol. Energy Mater. Sol. Cells* 122 (2014) 164–173.
  - [65] H. Fathabadi, Lambert W function-based technique for tracking the maximum power point of PV modules connected in various configurations, *Renew. Energy* 74 (2015) 214–226.
  - [66] W. Xiao, M.G.J. Lind, W.G. Dunford, A. Capel, Real-time identification of optimal operating points in photovoltaic power systems, *IEEE Trans. Ind. Electr.* 53 (4) (2006).
  - [67] S. Mahmoudinezhad, A. Rezania, D.T. Cotfas, P.A. Cotfas, L.A. Rosendahl, Experimental and numerical investigation of hybrid concentrated photovoltaic–thermoelectric module under low solar concentration, *Energy* 159 (2018) 1123–1131.
  - [68] Z. Qi, A. Agbossou, Z. Feng, M. Cosnier, Solar micro-energy harvesting based on thermoelectric and latent heat effects. Part II: experimental analysis, *Sensors Actuators A Phys.* 163 (1) (2010) 284–290.
  - [69] M.L. Olsen, J. Rea, G.C. Glatzmaier, C. Hardin, C. Oshman, J. Vaughn, T. Roark, et al., Solar thermoelectricity via advanced latent heat storage, in: AIP Conference Proceedings, vol. 1734 (1), 2016, p. 050035.
  - [70] Q. Zhang, A. Agbossou, A smart PV cooler based on solar thermoelectric generator with phase change material, *Adv. Mater. Res.* 986–987 (2014) 1163–1168.
  - [71] P. Motiei, M. Yaghoubi, E. GoshtasbiRad, Transient simulation of a hybrid photovoltaic-thermoelectric system using a phase change material, *Sustain. Energy Technol. Assess.* 34 (2019) 200–213.
  - [72] J. Zhang, Y. Xuan, Performance improvement of a photovoltaic – thermoelectric hybrid system subjecting to fluctuant solar radiation, *Renew. Energy* 113 (2017) 1551–1558.
  - [73] T. Cui, Y. Xuan, E. Yin, Q. Li, D. Li, Experimental investigation on potential of a concentrated photovoltaic-thermoelectric system with phase change materials, *Energy* 122 (2017) 94–102.
  - [74] D. Li, Y. Xuan, E. Yin, Q. Li, Conversion efficiency gain for concentrated triple-junction solar cell system through thermal management, *Renew. Energy* 126 (2018) 960–968.
  - [75] T. Cui, Y. Xuan, Q. Li, Design of a novel concentrating photovoltaic–thermoelectric system incorporated with phase change materials, *Energy Convers. Manag.* 112 (2016) 49–60.
  - [76] T.M. Tritt, H. Böttner, L. Chen, Thermoelectrics: direct solar thermal energy conversion, *Harnessing Mater Energy* 33 (4) (2008) 366–368.
  - [77] X. Ju, Z. Wang, G. Flamant, P. Li, W. Zhao, Numerical analysis and optimization of a spectrum splitting concentration photovoltaic-thermoelectric hybrid system, *Solar Energy* 86 (6) (2012) 1941–1954.
  - [78] E. Yin, Q. Li, Y. Xuan, A novel optimal design method for concentration spectrum splitting photovoltaicthermoelectric hybrid system, *Energy* 163 (2018) 519–532.
  - [79] R. Bjørk, K.K. Nielsen, The maximum theoretical performance of unconcentrated solar photovoltaic and thermoelectric generator systems, *Energy Convers. Manag.* 156 (2018) 264–268.

- [80] Z. Yang, W. Li, X. Chen, S. Su, G. Lin, J. Chen, Maximum efficiency and parametric optimum selection of a concentrated solar spectrum splitting photovoltaic cell thermoelectric generator system, *Energy Convers. Manag.* 174 (2018) 65–71.
- [81] D. Liang, Q. Luo, P. Li, Y. Fu, L. Cai, P. Zhai, Optimization and experimentation of concentrating photovoltaic/cascaded thermoelectric generators hybrid system using spectral beam splitting technology, in: IOP Conference Series, Earth and Environmental Science, 2018.

# Development and demonstration of outdoor-applicable thermoelectric generators for IoT applications

4.7

Kanae Nakagawa<sup>a,\*</sup> and Takashi Suzuki<sup>a,†</sup>

<sup>a</sup>Fujitsu Laboratories LTD., Kawasaki, Japan

## 4.7.1 Introduction

The use of a wireless sensor network in which sensor nodes can be installed anywhere with a wireless connection makes it possible to easily collect a wide range of sensor data. As such, a wireless network can provide measurements and control for applications that are otherwise difficult by the conventional wired method. However, it can be difficult to secure a power source when taking advantage of the high degree of freedom with respect to installation. For this reason, various attempts have been made to apply energy harvesting technology as a power source for sensor nodes at the end of a network. In this chapter, we explain the development of a thermoelectric generator (TEG) module with a single thermoelectric device that can supply the power required for sensing and wireless transmission, which utilizes only the 1-day-cycle temperature change of outdoor objects.

Possible applications for wireless sensor networks include factories, buildings, and outdoor facilities. Examples of outdoor applications currently include environmental monitoring (temperature/humidity/illuminance/rainfall) and disaster prevention monitoring, and a wider range of applications is anticipated. In this study, we developed a real-time water-level monitoring system for sewers and rivers, which is categorized as environmental monitoring.

By monitoring sewer water levels, we can detect floods from inland water, which has been increasing in recent years, and the monitoring of sewer flow can detect bottlenecks, which makes it easier to establish sewer-network maintenance plans. Since sensors and wireless devices are installed in manholes, it is very difficult to secure a corresponding power source. Alternatively, thermoelectric power generated by utilizing the heat of a manhole cover can generate power semipermanently, and there is no need for replacement. We developed a power generator for water-level sensing and wireless transmission, and it was adopted as a power supply [1, 2]. A sewer

\* Current affiliation: Sony LSI Design Inc., Atsugi-shi, Japan

† Current affiliation: KYOCERA Corporation, Yokohama-shi, Japan

water-level monitoring system using our generator was commercialized in December 2016 and introduced in the city of Koriyama in June 2017 [3].

Another application is river water-level monitoring. In Japan, attempts to measure water-levels upstream have facilitated the early detection of river flooding. Because water-level measurement devices are likely to be installed at remote and rarely visited locations, they must be maintenance-free. A solar cell can be considered for use as a power source, but because the exposed power generation area might become covered with plants, bird droppings, or mud, the amount of power generated could drastically decrease over time. Therefore, as a power source available over the long term, we investigated the potential application of thermoelectric power generation.

A practical TEG module was developed using the following procedure:

- |     |  |
|-----|--|
| I   | Calculation of required power generation           |
| II  | Simulation of annual power generation              |
|     | (1) Simulation of heat source temperature          |
|     | (2) Simulation of power generation                 |
| III | Thermoelectric generator design                    |
| IV  | Demonstration experiment and simulation validation |

These steps are described in the sequence below.

#### 4.7.2 Thermoelectric generation as a power source for wireless sensor networks

We developed the system for real-time sewer water-level monitoring [4, 5]. Figs. 4.7.1 and 4.7.2 show schematic designs of our system, which consists of multiple sensor nodes, a gateway, and a cloud system. The sensor node, which is placed in a manhole, consists of a water-level sensor, a wireless transmission module, and a TEG module. The water-level sensor, which is a commercially obtained sensor that calculates the water level from pressure, is set at the bottom of a manhole and is connected to a wireless transmission module that is attached to the bottom of the manhole cover.

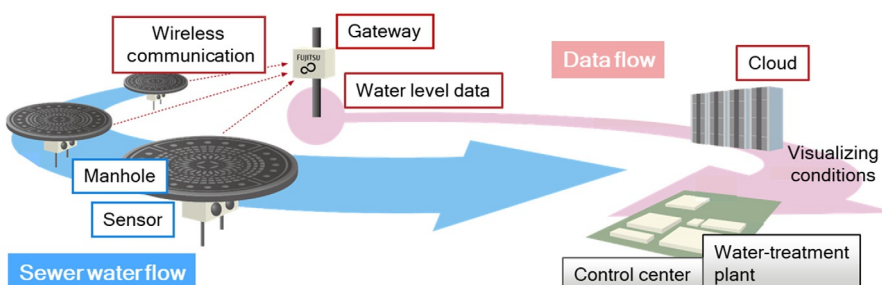


**Fig. 4.7.1** Real-time sewer monitoring system using ICT.

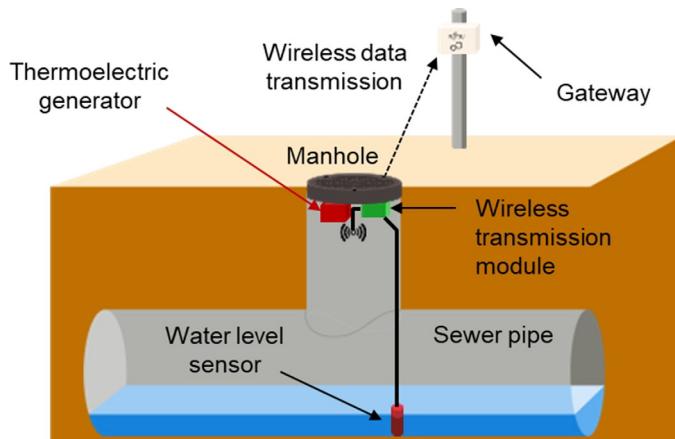


**Fig. 4.7.2** Schematic design of the system attached to a manhole.

The wireless transmission module transfers measured data to the cloud system via the gateway. The gateway is placed near the manhole on a pole. The wireless frequency from the wireless module to the gateway is 920 MHz, and carrier communication networks transmit the signal from the gateway to the cloud. Therefore, it is possible to reduce both the power consumed by the wireless transmission module and the communication expense by transmitting data from many sensor nodes to one gateway. The data obtained by the cloud system can then be observed and easily understood by users of a website both in real time and after a flood has occurred. Therefore, the staff at the control centers of water-treatment plants and pumping stations can use this system.

The generated energy can also be used effectively by the adoption of adaptive sensing, which is a power-control sensor technology that adjusts to circumstances, as shown in Fig. 4.7.3 [4]. This technology can predict changes in water levels based on past measurements and it can automatically adjust the measurement and transmission intervals based on the circumstances of the sensors at any given time. The measurement interval is changed based on widely broadcast weather information. These intervals are set automatically, for example, to every 10 min when the weather is clear and every 5 min when there is a downpour. A threshold established as a certain difference between measured and predicted water level changes the transmission interval. Predicted water levels are calculated by the least-squares method using the 10 most recent data points on both the sensor node and gateway. Only when the difference between the measured and predicted data exceeds the threshold, the sensor node transmits this data to the cloud via the gateway. If the difference is lower than the threshold, the sensor node transmits no data and the gateway transmits the predicted data to the cloud. Using this technology, it is possible to economize by limiting the required sensor power and thereby operate for long periods of time.

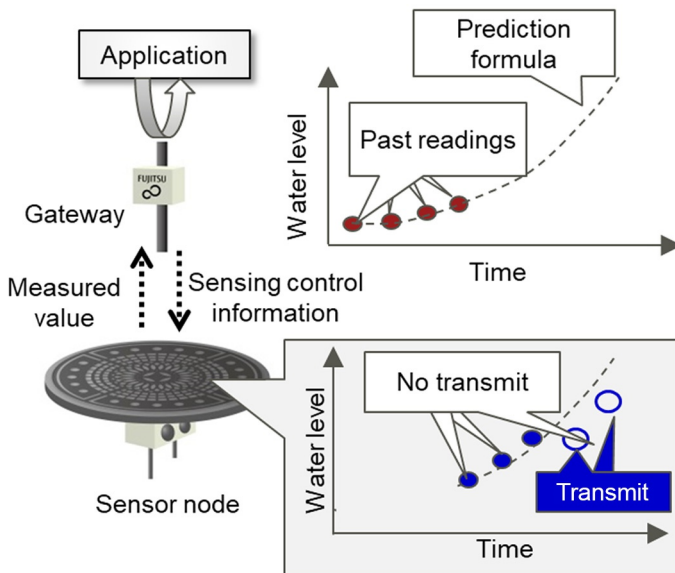


**Fig. 4.7.3** Adaptive sensing technology that adjusts to circumstances.

#### 4.7.2.1 Power supply design based on the energy balance calculation

In the design of the TEG module, it is essential to estimate the power required for wireless transmission and sensing.

The communication parameters for this study were as follows: the periodic measurement interval was once every 10 min in clear weather and once every 5 min during rain, the communication rate was 200 kbps, and the data size was 100 bytes. The sensing parameters were as follows: the periodic measurement interval was once every hour during fine weather and once every 5 min during rain, and the sensing time required was 1 s. Based on past weather data in Japan, we set the annual rainfall duration to 2000 h. The power consumption  $P_{total}$  (J/day) per day is described as shown in Eq. (4.7.1):

$$\begin{aligned}
 P_{total} = & \frac{24 \times 365 - 2000}{24 \times 365} (P_{tr}^{nor} + P_{sta}^{nor} + P_{sen}^{nor}) \\
 & + \frac{2000}{24 \times 365} (P_{tr}^{re} + P_{sta}^{re} + P_{sec}^{re}) + P_{con}
 \end{aligned} \quad (4.7.1)$$

where  $P_{tr}$  is the communication transmit and receive power,  $P_{sta}$  is the standby power,  $P_{sen}$  is the sensing power, and  $P_{con}$  is the power-control-unit power.

Each of these indicates the power consumption per day. The superscript "nor" indicates steady power consumption and "re" indicates rainy weather.

The communication power per day is described as shown in Eq. (4.7.2):

$$P_{tr} = \frac{24 \times 60}{10} \times T_{tr} \times P_s \times P_r \quad (4.7.2)$$

where  $T_{tr}$  is the communication time,  $P_s$  is the transmitted power, and  $P_r$  is the received power.

When it rains, the communication interval is halved, which means the communication power per day becomes  $P_{tr} \times 2$ . The standby power and sensing power consumed during normal (clear or cloudy) and rainy weather are calculated based on the communication conditions.

The target value is set so that the annual average power generation per day exceeds  $P_{total}$ .

The energy management system includes a circuit, battery, rechargeable battery, and TEG. The generated power is stored in the rechargeable battery and is consumed as the main power source for sensing and wireless transmission. The battery is switched only when the rechargeable battery is depleted due to long-term lack of sunlight. We performed a detailed calculation of the energy balance based on the past weather conditions at the installation site and determined that the required amount of power to be generated was 38 J/day.

#### 4.7.2.2 Simulation

When operating IoT systems, such as sensing and wireless transmission using systems that harvest energy harvesting and whose power generation depends on environmental conditions, a reliable power design is vital to ensure the provision of the required power to the system. In the case of thermoelectric power generation, when the waste heat of indoor equipment is used, such as that in a factory, the temperatures of the equipment and the environment can be predicted annually and estimating the amount of power generated is often easy. However, when using outdoor structures or objects that are mainly heated by sunlight, the power generated varies greatly depending on the season, weather conditions, and time zone. Therefore, it is necessary to estimate the temperature changes of the heat source to predict the annual power generation. Two approaches can be used to calculate the temperature change of the heat source.

The first calculation approach uses a heat balance model in which meteorological data are used as variables and the shape, material, and other structural parameters of the heat source are used as input. The other calculation approach is to measure the temperature of the heat source over a certain number of days (a minimum of 1 week), obtain an approximate relational equation based on the meteorological data during that time, and calculate the temperature change using this equation.

The annual power generation is then calculated using the simulated heat source temperature. At this time, since the amount of power generated varies greatly depending on the cooling method used, it is necessary to select a cooling method based on the temperature characteristics of the heat source.

In addition, we used a DC/DC converter to boost the generated voltage to a practical level. However, to estimate the available power, we must consider both the input voltage at which boosting occurs and the conversion efficiency. In this section, we describe the simulation methods we used.

#### 4.7.2.2.1 Heat source temperature

##### (a) Simulation method

###### (i) Heat balance model

The annual temperature of a steel bridge deck can be calculated using a bridge heat balance model [6–8].

[Fig. 4.7.4](#) shows a conceptual diagram of a heat balance model of a bridge. The heat balance of the upper surface of the bridge is described by Eqs. (4.7.3), (4.7.4).

$$Q_u = \sigma T_U^4 + H_U + E_u + G \quad (4.7.3)$$

$$H_U = S(1 - \alpha_u) + L_U \quad (4.7.4)$$

where  $T_U$  is the temperature of the upper side of the bridge,  $H_U$  is the convection heat transfer quantity,  $E_u$  is the quantity of latent heat (LH) transferred by evaporation or condensation,  $G$  is the heat-storage quantity of the bridge,  $\sigma$  is a Stefan-Boltzmann constant,  $S$  is the solar radiation quantity,  $\alpha_u$  is the reflectance of the upper side of the bridge, and  $L_U$  is the net quantity of atmospheric radiation. The subscript  $U$  indicates the upper side of the bridge. Each of the terms in Eqs. (4.7.3), (4.7.4) are calculated by input meteorological data and the shape and materials of the heat source structure [9].

###### (ii) Approximate equation

A temperature simulation method that uses an approximate expression can be explained by considering the calculation of the temperature of a manhole cover as

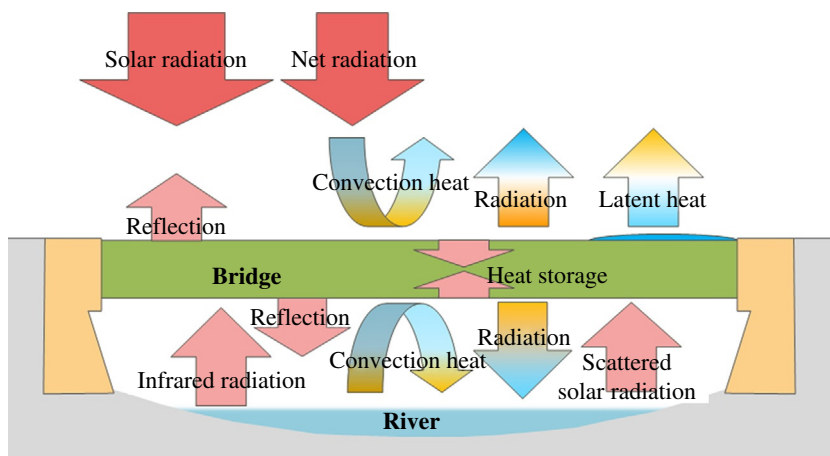


**Fig. 4.7.4** Heat balance model in a bridge.

an example. In this procedure, we first measure the temperature inside the cover of the manhole and obtain the approximate relational equation from the temperature, amount of solar radiation, and other variables of the meteorological data. The temperature inside the manhole is measured as the ambient temperature around our TEG module because the TEG module is installed underneath the cover. The cover temperature was measured in Koriyama where the practical demonstration was performed. The weather data for Koriyama was obtained from the Japan Meteorological Agency website. Of all the meteorological data, the temperature and total solar radiation were strongly correlated with the measured manhole-cover temperature, with little correlation between precipitation, wind speed, and cloud cover. Therefore, we obtained an approximation equation using temperature and total solar radiation.

#### (b) Simulated result

The bridge-temperature calculation period of the bridge temperature was from April 2017 to March 2018, and that for the manhole cover was from April 2015 to March 2016. Since the amount of solar radiation is data every hour, it is divided proportionately at 10-min intervals according to the temperature, which is data every 10 min.

[Fig. 4.7.5](#) shows the calculation results of the annual temperature changes of the bridge and manhole cover. [Fig. 4.7.6](#) shows the calculation results and actual measurements of the temperatures of the bridge and manhole cover, and the actual measurements of the ambient temperature. For both the bridge and manhole cover, the calculation results nearly follow

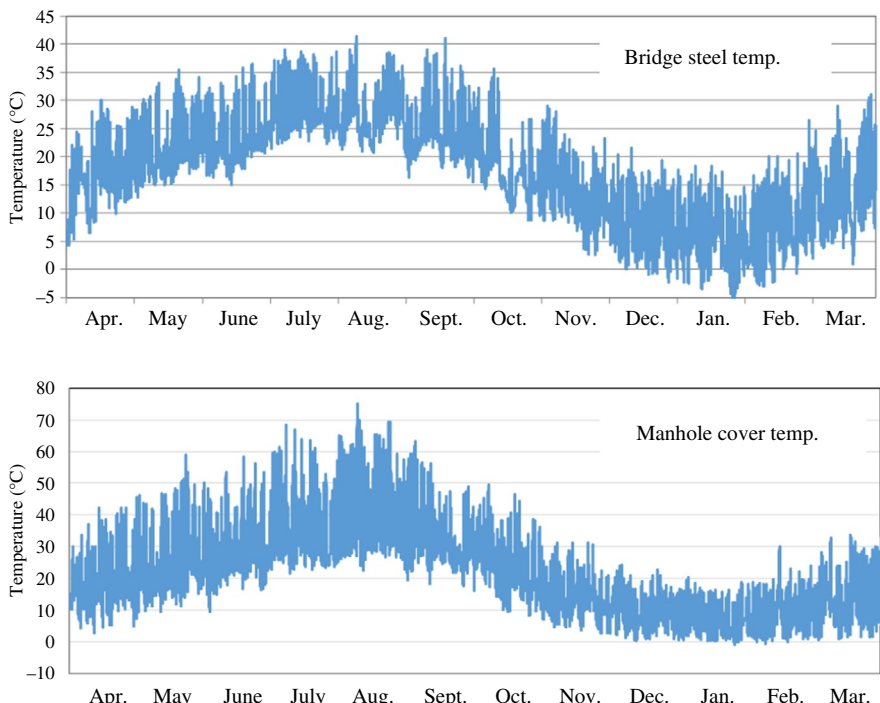


**Fig. 4.7.5** Simulated result of the annual temperature change of the bridge steel and manhole cover.

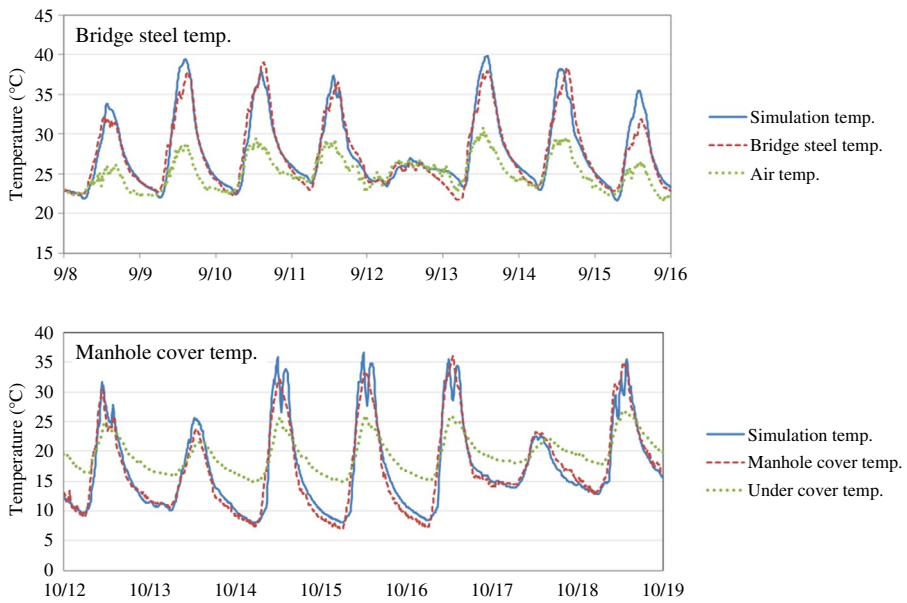


**Fig. 4.7.6** Simulated result and the actual temperature of the bridge steel and manhole cover.

the actual measurements. Some of the data did not fit because the data divided into 10-min intervals differed from the actual data.

Both bridge and manhole cover were found to experience changes in temperature in the same daily cycles due to changes in the solar radiation and temperature, with some significant differences.

- (1) In summer, the maximum manhole-cover temperature exceeded 60°C, and the 1-day temperature difference was around 30°C, whereas the maximum temperature of the bridge was around 40°C, and the temperature difference was around 15°C. This difference is likely because the thermal capacity of the bridge is much greater than that of the manhole, so the temperature increase is gradual and it is more difficult for the bridge temperature to drop at night.
- (2) In winter, the manhole-cover temperature was about half that during the summer, with a daily temperature difference of about 15°C, but that of the bridge was greater than that in summer. This is thought to be because the temperature of the manhole cover does not decrease as much at night due to the temperature inside the manhole, which is higher than the air temperature in winter, whereas the temperature of the bridge suddenly decreases at night and falls below the air temperature.

#### 4.7.2.2.2 Cooling method

The main cooling method for the thermoelectric power generation is natural air cooling using a radiating fin. However, this method is not optimal for outdoor structures or objects that are heated primarily by sunlight.

As shown in Fig. 4.7.6, there is a limited time during which there is a sufficient difference between the heat source temperature and ambient temperature, which changes throughout the daily cycle. Considering that the temperature difference across a TEG is even smaller, there is concern that the amount of generated power required per year will be insufficient. Instead of natural air cooling, it is possible to generate power more efficiently by utilizing a heat-storage material on the cooling side [2]. There are two types of heat-storage materials, one of which utilizes sensible heat (SH) and the other LH. LH storage materials utilize the phase change of a liquid-solid and is also called a phase-change material (PCM). There have been many studies on thermoelectric generation using PCM [10–14]. However, scant research has been conducted on the utilization of SH storage. In the next section, we explain our simulation for designing a TEG module that can generate the required power.

#### 4.7.2.2.3 Amount of power generation

The temperature change of the heat-storage material is calculated using the heat source temperature, as calculated in Section 4.7.2.2.1, followed by calculating the open circuit voltage ( $V_{OC}$ ) from the temperature difference between the temperatures of the heat source and the heat-storage material, to obtain the amount of power generated.

(a) Simulation method

(i) Open circuit voltage

While the amount of LH must be equal to or greater than the heat input amount, the volume of the LH storage material must be reduced as much as possible to reduce the size of the generator.

The required amount of LH storage material is calculated using the simulated bridge temperature. The heat transfer amount  $Q(t)$  flowing into the heat-storage material at time  $t$  is described as follows:

$$Q(t) = \frac{T_B(t) - T_{ST}(t)}{\theta_{TEG} + \theta_{other}} \quad (4.7.5)$$

where  $T_B(t)$  is a time variation of 1-day bridge temperature and  $T_{ST}(t)$  is that of the heat-storage-material temperature,  $\theta_{TEG}$  is the thermal resistance of the TEG, and  $\theta_{Other}$  is the sum of the thermal resistance of other parts. In SH storage, the temperature increase in the heat-storage material is described as follows:

$$dT_{ST}(t) = \frac{dQ(t)}{C} = \frac{dQ(t)}{mc_p} \quad (4.7.6)$$

where  $C$  is the heat capacity,  $c_p$  is the specific heat capacity, and  $m$  is the mass of the heat-storage material.

In LH storage, the temperature of PCM is described as follows:

$$T_{ST}(t) = T_{MP} \quad (4.7.7)$$

$$\int Q(t)dt = \int \frac{T_B(t) - T_{MP}}{\theta_{TEG} - \theta_{other}} dt \leq H_L \quad (4.7.8)$$

where  $T_{MP}$  is the melting point and  $H_L$  is the amount of LH in the PCM. During the period when Eq. (4.7.8) holds (i.e., when LH is utilized), the PCM temperature is constant at the melting point (Eq. 4.7.7). Except for this period, the PCM temperature is obtained by Eqs. (4.7.5), (4.7.6).

We determined the type and amount of PCM used in the simulation, and selected paraffin as the PCM because it has a melting point within the temperature range of outdoor objects and a relatively large LH. To maximize the use of LH, we used paraffin that has a melting point that nearly coincides with the annual average temperature of the heat source. Table 4.7.1 shows the physical properties of the paraffin used in the TEG module (Model TS7, TSAC20: JXTG Nippon Oil & Energy Co.). The required amounts of LH and  $H_L$  are described as follows:

$$H_L = \int_{t1}^{t2} \frac{T'_B(t) - T_{B\_AVE}}{\theta_{TEG} + \theta_{other}} dt \quad (4.7.9)$$

where  $T'_B(t)$  is the time variation of 1-day bridge temperature for which the average,  $T_{B\_AVE}$ , is equal to the melting point of the PCM and  $t1$  and  $t2$  are the times when the bridge temperature coincides with its average temperature in 1 day. We used a metal heat transfer fin for heat exchange between the TEG and PCM. Since the melting/solidification of paraffin starts at the surface of the fin, there is a problem that the melting/solidifying paraffin becomes thermal resistance, which makes it impossible to utilize all the LH obtained by the calculation. Although more LH can be utilized using narrowly spaced fins, the amount used is still only 50%–60% of the full amount of LH [2]. Therefore, the required weight of paraffin,  $M_L$ , is given by

$$M_L = \frac{1}{0.5} \times \frac{H_L}{h_L} \quad (4.7.10)$$

**Table 4.7.1** Physical properties of paraffin (JX Nippon Oil & Energy Co. Ltd).

Model	Melting point (°C)	Latent heat (kJ/kg)	Thermal conductivity (W/m K)	Specific heat (15°C) (kJ/kg K)	Density (15°C) (g/cm³)
TS7	19.6	165	0.143	1.99	0.797
TSAC20	19.1	174	0.143	1.99	0.797

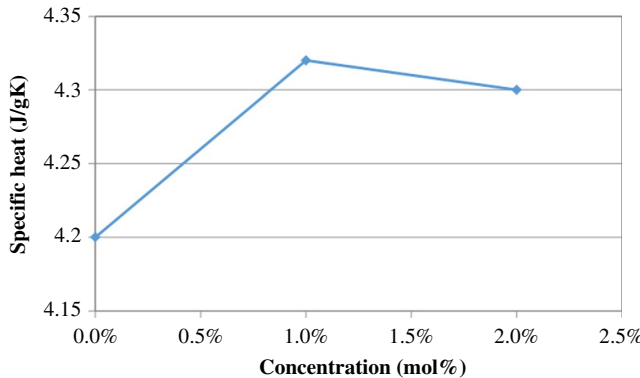


**Fig. 4.7.7** Specific heat as a function of the TBA concentration.

where  $h_L$  is the LH of the paraffin. As a SH storage material, water is suitable as it has a maximum specific heat  $c_p$  at room temperature as a single substance. However, in the case of bridges, the calculation results in Section 4.7.2.2.1 reveal that in winter the bridge temperature becomes lower than the freezing point. Therefore, to prevent freezing in winter, we mixed in *tert*-butyl alcohol (TBA), which has high water solubility. Although the freezing point decreases as the alcohol concentration increases, the specific heat also decreases. Fig. 4.7.7 shows the change in specific heat with TBA concentration. With TBA concentration of 3.5 mol%, the melting point is  $-9^\circ\text{C}$ , which is less than that of water, whereas the specific heat is 4.31 J/g K, which is slightly greater than the 4.18 J/g K of water. There is a certain concentration of an ethanol solution that also increases the specific heat [15], however, the ethanol solution will corrode aluminum [16]. Therefore, we used a TBA solution. Table 4.7.2 shows the physical properties of a 3.5 mol% TBA solution. The weight of the TBA solution is 1.0 kg, the same as that of the paraffin. Next, we performed simulations and experiments.

After calculating the temperature of the heat-storage material, the temperature difference  $\Delta T$  across a TEG can be described as follows:

$$\Delta T = \theta_{TEG} \times \frac{T_B(t) - T_{ST}(t)}{\theta_{TEG} + \theta_{other}} \quad (4.7.11)$$

The  $V_{OC}$  is described as

$$V_{OC} = \Delta T \times Z \quad (4.7.12)$$

**Table 4.7.2** Physical properties of the TBA solution.

Concentration (mol%)	Melting point ( $^\circ\text{C}$ )	Specific heat (20 $^\circ\text{C}$ ) (kJ/kg K)	Density (20 $^\circ\text{C}$ ) (g/cm $^3$ )
3.5	-9.0	4.31	0.96

where  $Z$  is the Seebeck coefficient of the TEG.

**(ii) Power generation amount**

The amount of power generated  $P$  is calculated based on the output voltage boosted by a DC/DC converter. According to the maximum power transfer theorem, the maximum power  $P$  that can be used in a load circuit is determined as follows:

$$P = \frac{(0.5V_{OC})^2}{R_{TEG}} \times \eta_b \quad (4.7.13)$$

where  $R_{TEG}$  is the internal resistance of the TEG and  $\eta_b$  is the conversion efficiency of the DC/DC converter. The amount of power generated is calculated in units of 1 day. All of the power generation amounts described below were obtained using Eq. (4.7.13) multiplied by the number of seconds in a day.

When the load resistance  $r$  is connected and the current  $I$  flows, heat flows across the TEG due to the Peltier effect  $Z \times \Delta T \times I$ , which generates Joule heat  $R_{TEG} \times I^2$ . Therefore, in the calculation of the power generation, when the output power is very high, it is necessary to consider these heat values. However, these values are far smaller than the amount of heat transferred from the heat source when using outdoor objects (for example, manhole covers) heated by solar radiation as the heat source.

As shown in Eq. (4.7.13), the power generated greatly depends on the efficiency of the DC/DC converter and the resistance of the TEG. When using a heat-storage material with a constant volume, to generate the maximum amount of power, a TEG with a large Seebeck coefficient, high thermal resistance, low internal resistance, and a highly efficient converter may be selected. However, a TEG with a large Seebeck coefficient often has a low thermal resistance and a high resistance value. In addition, since a high-efficiency converter has a relatively high boost threshold, it is important to select the appropriate TEG and converter. Here, we used two types of TEGs and DC/DC converters for the simulation.

Table 4.7.3 shows the characteristics of the TEGs used in this study (Model TEG254-200-12, Model TEG127-150-26:Thermalforce Co. Ltd). The TEG254-200-12 model has a large Seebeck coefficient but high resistance, whereas the Seebeck coefficient of the TEG127-150-26 model is about half that of TEG254-200-12 with 1/4 the resistance. The DC/DC converters used for the booster circuit are model LTC3019 (Linear Technology Co.) and model BQ25505 (Texas

**Table 4.7.3** Electrical characteristics of TEG (Thermalforce. de Co. Ltd).

Model	Dimensions (mm)	Thickness (mm)	Seebeck effect (V/K)	Electrical resistance ( $\Omega$ )	Thermal resistance (K/W)
TEG254-200-12	40 × 40	4.8	0.103	13.0	2.8
TEG127-150-26	30 × 30	3.6	0.054	3.4	3.2

Instruments Inc.). The LTC3019 model has a low boost threshold of  $\pm 55\text{ mV}$ , but a maximum efficiency of about 35%, whereas the BQ25505 model has a boost threshold of  $+0.2\text{ V}$  and does not boost from the negative electromotive force, but its efficiency is as high as 70% at an input voltage of  $0.2\text{ V}$  and is 80% at  $0.4\text{ V}$ .

### (b) Simulated result

#### (i) Manhole cover heat source

In the calculation of the power generated when the manhole cover is used as the heat source, we used the TEG127-150-26 as the TEG and LTC3019 as the DC/DC converter. From the annual change in the manhole-cover temperature shown in Fig. 4.7.5, we can see that primarily during spring and summer, the cover temperature becomes hot during the day and the temperature difference increases, although this difference is small in winter. Therefore, as the DC/DC converter, we used the LTC3019, which has a small boost threshold and boosts from a negative electromotive force. As the TEG, we used TEG 127-150-26, which has a small electrical resistance value.

We used TS7 as the PCM and Eq. (4.7.10) to determine  $0.74\text{ kg}$  as the required amount, based on data for the beginning of October when the average annual cover temperature and the average daily cover temperature are almost the same. For the alcohol solution, which is a SH storage material, we used the same weight.

Fig. 4.7.8 shows the annual change in the power generated per day by each heat-storage material. With the PCM, the annual average is  $50.4\text{ J/day}$ , and with the alcohol solution, it is  $60\text{ J/day}$ . Therefore, both can secure the required power generation. The power generation amount per day with the PCM exceeded that with the alcohol solution in October and March, but during other periods the alcohol solution generated larger amounts of power.

There are two possible reasons for this. One is the four seasons of Japan. To utilize LH most efficiently, the LH storage material requires the average temperature of the heat source to be the same temperature as its melting point. However, because Japan has four seasons, the average daily manhole-cover temperature varies greatly throughout the year. Therefore, the period in the year during which LH can be utilized is short. The other reason is the specific heat of the heat-storage material. Because the specific heat of paraffin is less than half that of the alcohol solution, the temperature difference from this heat source is smaller than that of the alcohol solution during the majority of the time when LH is not utilized.

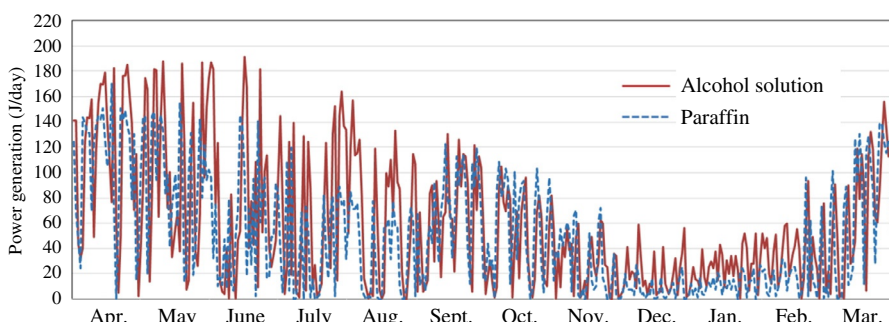
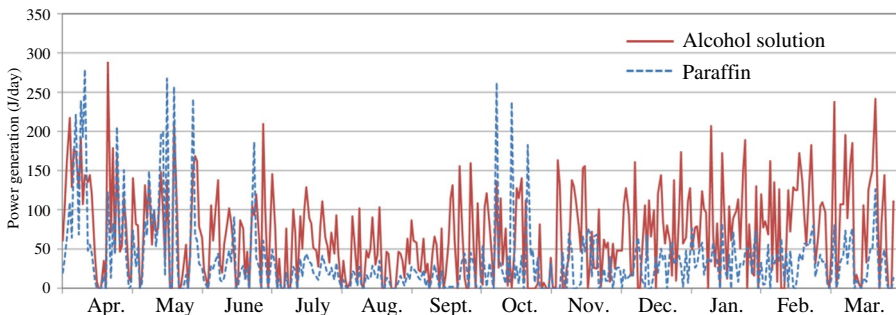


Fig. 4.7.8 Simulated result of the annual transition of power generation (The manhole cover).



**Fig. 4.7.9** Simulated result of the annual transition of power generation (The steel bridge deck).

#### (ii) Steel bridge deke heat source

To calculate the power generated when using the steel bridge deck as the heat source, we used TEG127-150-26 as the TEG and LTC3019 as the DC/DC converter. From the annual change in the bridge temperature shown in Fig. 4.7.5, we can see that the daily temperature difference is smaller than that of the manhole-cover temperature except in winter and its annual change is small too. Therefore, we used TEG254-200-12, which has a large Seebeck coefficient and can generate a large electromotive force from a slight temperature change. In addition, when the LTC3019 is used as a DC/DC converter, the TEG254-200-12 has a high resistance value of  $13.3\Omega$ , so only a very small output can be obtained. Therefore the BQ25505 was used. We used the TSAC20 as the PCM. Using Eq. (4.7.10), we calculated the required amount to be 1.05 kg, based on mid-October data where the average annual bridge temperature and the average daily temperature are almost the same. For the alcohol solution, which is a SH storage material, we used the same weight.

Fig. 4.7.9 shows the simulation result of the annual transition of the power generation amount per day by each heat-storage material from April 1, 2017 to March 31, 2018. The average amount of power generated by SH storage, 69.3 J/day, was nearly twice that generated by LH storage, 35.3 J/day, and paraffin did not meet the power generation requirement. The reason why a larger amount of power can be generated using the SH storage material is almost the same as the explanation for the manhole cover, but when the bridge is used as a heat source, the difference due to the heat-storage material used is even greater. According to the bridge-temperature simulation result, the 1-day temperature difference averaged only  $12.6^\circ\text{C}$  over the year. Therefore, even during the period when LH is available, the average temperature departed significantly from the melting point depending on the weather conditions, so there are more days when it cannot be utilized than is true for manhole covers.

There is a significant difference in the annual change in power generated when using a manhole cover or bridge as the heat source. This finding is consistent with the temperature of each heat source shown in Fig. 4.7.5, which indicates that the 1-day temperature difference directly affects the amount of power generated.

#### 4.7.2.3 Design

Fig. 4.7.10 shows a schematic of our generator with the heat-storage. This generator consists of one TEG, a heat transfer pillar that transmits heat from the heat source to

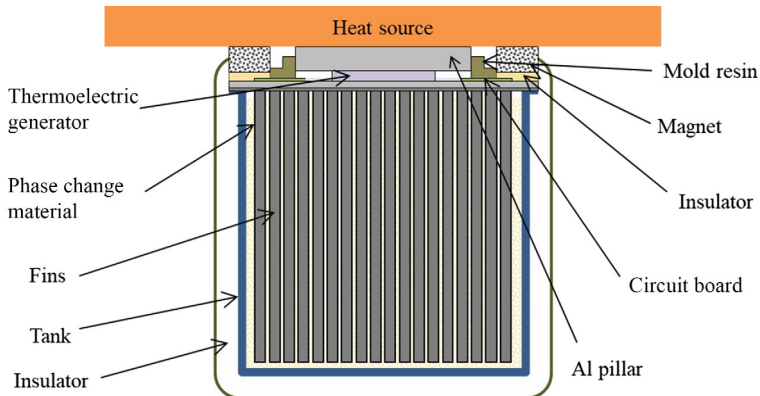


Fig. 4.7.10 Schematic design of the TEG module.

the TEG, a heat-storage material and heat transfer fins as a heat exchanger, a heat-storage material case, a heat-storage material, and a heat-insulation material. Of these components, the shape of the heat transfer fins differs depending on the type of the heat-storage material used. In the case of paraffin, to increase the LH utilization efficiency, we used heat transfer fins with a narrow pitch and high fin density [2]. In the case of the alcohol solution, we used a pin type that does not hinder convection of the heat-storage material. The heat transfer pillar and the fins are made of aluminum with high thermal conductivity. Parts other than the TEG are fixed with screws and other fittings and heat transfer grease is applied to each interface. To fix our module to the steel deck of the bridge or the manhole cover, we used four neodymium magnets. Fig. 4.7.11 shows a photograph of the module we used with the manhole cover.

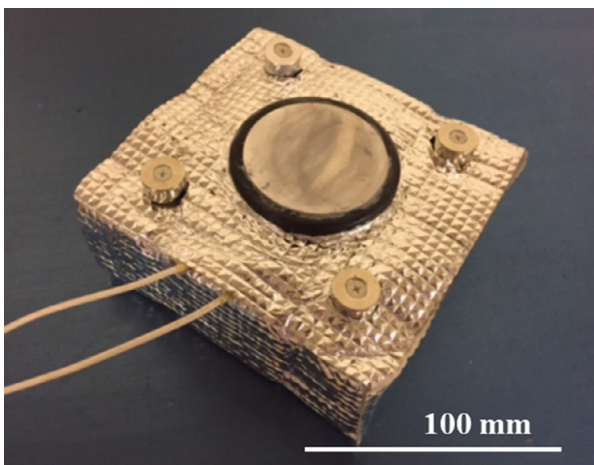


Fig. 4.7.11 Photograph of the TEG module.

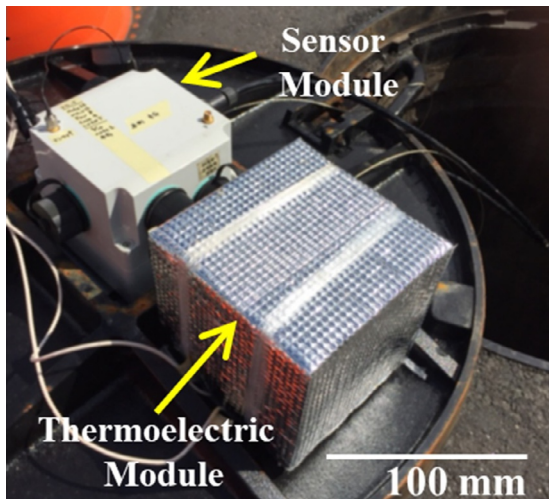
## 4.7.3 Practical implementation

### 4.7.3.1 Latent-heat-storage-type TEG module

We conducted demonstration experiments in Koriyama from 2015 to 2016 to measure the amount of power generated by our TEG module with LH storage and monitor the sewer water level. Fig 4.7.12 shows a photograph of the generator after installation/attachment to the cover. For comparison, we also installed an air-cooled fin-type TEG module (fin size 10cm × 10cm × 4 cm) of the same plane size. The voltage data, manhole-cover temperature data, and water-level data were transmitted from the wireless node to the cloud via the gateway. Fig. 4.7.13 shows the changes in power generation per day from October 19 to 25, 2015 for which we calculated the amount of power generated using Eqs. (4.7.5)–(4.7.8), (4.7.11)–(4.7.13) based on weather information obtained during the same period and the average daily temperature. The average power generated during this period obtained by actual measurement was 53.3 J/day and that obtained by calculation was 56.6 J/day, with an error of less than 10%, but the power generated per day does not always match. Before and after the average daily temperature reaches the melting point of the PCM, the amount of change in the calculated value is larger than the actual measurement. The calculation assumes that the temperature does not change until the entire PCM melts or solidifies and that it uses up the available amount of LH. However, in actuality, since the PCM that is in direct contact with the fins melts or solidifies sequentially, the utilization of LH storage is changed to the utilization of SH storage around the fins earlier than expected.

The manhole-cover temperature in October was almost equal to that of the annual average, and the actual power generated exceeded that required, as determined in the simulation. Therefore, we can conclude that the TEG module using the LH storage material can secure the required amount of annual power generation.

**Fig. 4.7.12** TEG module installed under the manhole cover.



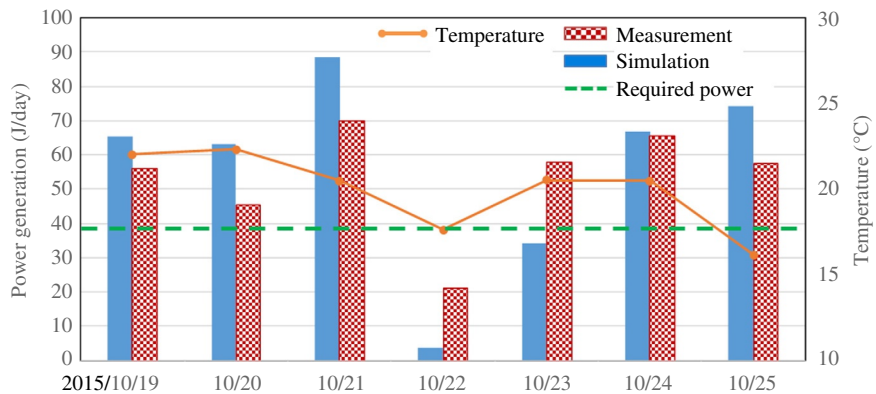


**Fig. 4.7.13** Measurement and simulation of power generation per day.

Furthermore, Fig. 4.7.14 shows the measurement results of the heat-storage-type and the fin-type power generators during the same period. The generated power of the heat-storage type is about seven times that of the air-cooled fin-type (average 7.8 J/day), which proves that the heat-storage-material type that uses the temperature change of the heat source can definitely secure the temperature difference across the TEG and thus yield greater power generation than the fin-type.

#### 4.7.3.2 Sensible-heat-storage-type TEG module

We conducted a demonstration experiment to measure the amount of power generated by our TEG module with SH storage from September 2017 to March 2018 on a bridge in the Kanto area. The bridge temperature and voltage data were stored by a wireless data logger. Fig. 4.7.15 shows the generator installed/attached to the bridge. The generator was placed on the northeastern side of the bridge on a surface that receives little direct sunlight during the daytime. Therefore, the heat supplied to the generator is only the heat transferred from the upper surface of the bridge that has been heated by sunlight. Fig. 4.7.16 shows the transition of the power generated per day during the

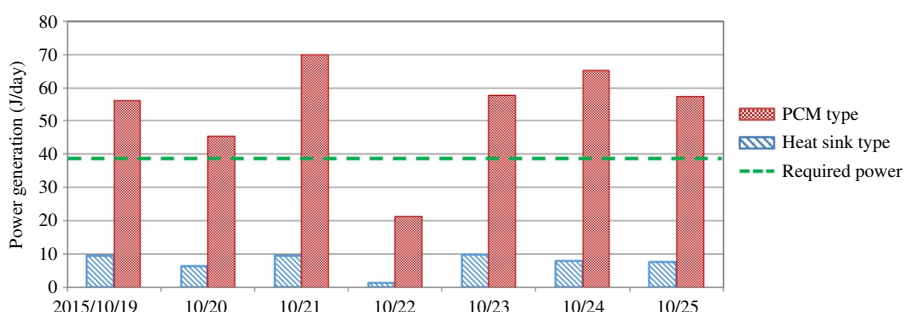


**Fig. 4.7.14** Power generation per day. Comparison between heat storage and natural air-cooling.

**Fig. 4.7.15** TEG module installed on the bridge.



demonstration. The average power generated during this period was 57.3 J/day, which greatly exceeds the required power generation of 38 J/day.

As predicted by the simulation results, when a steel bridge deck is used as the heat source, the bridge temperature and the power generated do not necessarily correlate. The average power generated was 53.2 J/day in September, 81.5 J/day in March, and 76.4 J/day in December. Despite having the shortest daylight hours in the year, the amount of power generated did not decrease in December. The average value of the 1-day temperature difference  $\Delta T_b$  in each period was 12.7°C in September, 17.0°C in March, and 14.6°C in December, which agree with the trends in the amount of power generated. Given that  $\Delta T_b$  is the same, we can conclude that it is possible to generate power stably regardless of the season.

Fig. 4.7.17 shows the changes in power generated per day from October 30 to November 12, 2017, and the amount of power generated calculated using Eqs. (4.7.5)–(4.7.8), (4.7.11)–(4.7.13) based on the weather information obtained for the same period. The average power generated actually measured during this

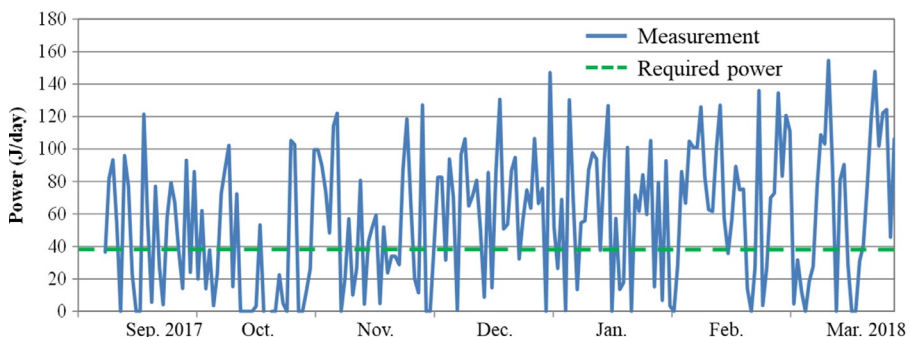


**Fig 4.7.16** Power generation amount per day during the demonstration.

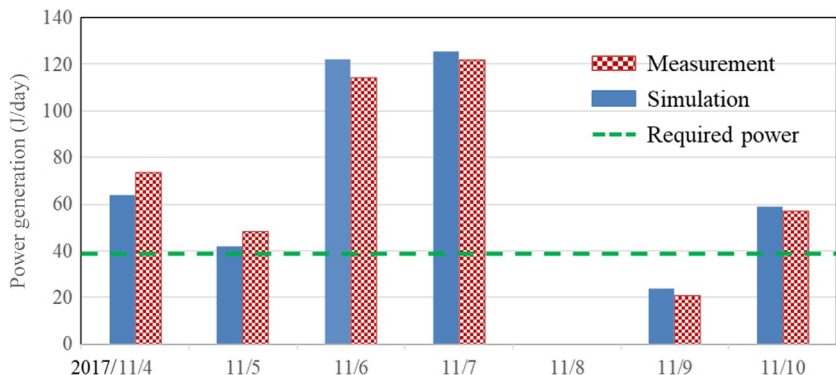


**Fig. 4.7.17** Measurement and simulation of power generation per day.

period was 57.1 J/day and that calculated was 58.6 J/day, for an error of only 2.5%, The average error rate per day is about 15%, which is not large. In the case of power generation using SH, it is possible to predict the amount of power generated with high accuracy by simulation.

In the case of thermoelectric power generation that uses an object whose temperature changes with the season and the day, the TEG module can effectively utilize SH storage when using a material with large specific heat. As a result, a single TEG can supply a sufficient amount of power to stably operate an IoT sensing system.

#### 4.7.4 IoT application

As an example of an IoT application using our TEG module, here, we present sewer water-level monitoring results in real time. The water-level sensor, signal processing, and wireless circuit were operated by the electric power provided by our TEG module.

[Fig. 4.7.18A](#) shows a photograph of the location of the demonstration experiment, where the sensor was installed in a manhole near a station in Koriyama where traffic is heavy. Also shown is the gateway box that received radio waves from the manhole and was installed on the streetlight pole on the opposite side of the road. The obtained measurement data were aggregated in the cloud from the gateway through the mobile line.

The sewer pipe, which was a combined sewer mainline, had a diameter of 1.8 m, which enabled stable water-level measurement. The graph in [Fig. 4.7.18B](#) shows an example of successful water-level monitoring in localized torrential rain that occurred on August 2, 2016 during the demonstration period. In about 10 min, the water level had surged nearly 2 m, and it was observed in real time that the sewer pipe capacity had been exceeded.

Real-time monitoring of the sewer water levels is expected to speed up the dispatch of staff to flood sites, emergency responses, and the distribution of evacuation information. In addition, we expect that inundation damage will be reduced by the use of

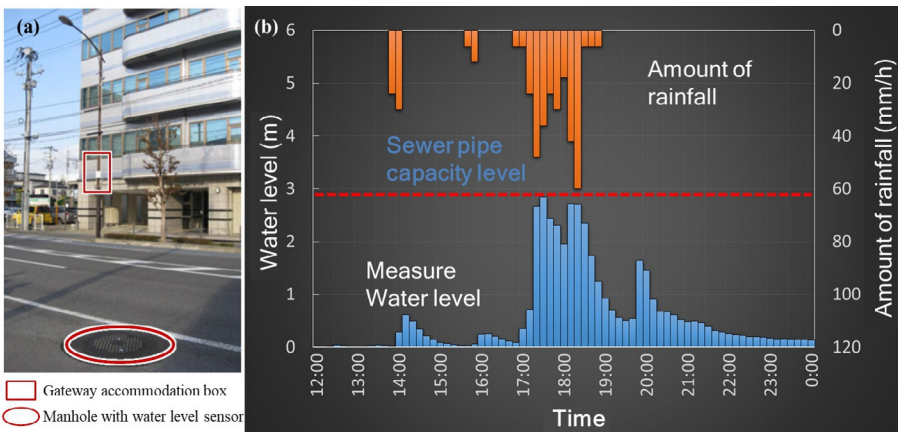


**Fig. 4.7.18** (A) External view of manhole and gateway with thermoelectric conversion module installed. (B) Changes in rainfall during torrential downpours and changes in sewer water level detected in real time on August 11, 2015.

data obtained for the formulation of future rainwater countermeasure plans. Furthermore, the use of TEG modules in dangerous places such as roadways can lead to improved worker safety and reduced maintenance costs.

## 4.7.5 Conclusion

We developed a TEG module that uses heat-storage materials and conducted a demonstration experiment of its use as an IoT application in a real-time water-level monitoring system. As heat sources, we used a manhole cover and a steel bridge deck whose temperatures change in a daily cycle depending on the amount of solar radiation and temperature. To design a TEG module that can secure the required power generation, we first simulated the annual heat source temperature and then the annual power generation. Next, we conducted a demonstration experiment to measure the amount of power generated when using a manhole cover and bridge as heat sources and to use the generated power to monitor the sewer water level in real time. As heat-storage materials, we used paraffin as a PCM to utilize LH and a TBA solution to utilize SH. The following conclusions can be drawn:

- (1) A comparison of the calculated values of annual average power generation by sensible and LH utilizations reveals that if the heat source is a manhole cover, the required amount of power generation can be secured with either type of heat-storage material. However, if using a bridge, only the use of SH can secure the required power generation. Furthermore, with both heat sources, the amount of power generated was greater when SH was used.
- (2) We demonstrated the practicality of performing sewer water-level monitoring using our LH-storage-type TEG module in Koriyama. Our measurements indicate that this system can generate the amount of power required for water-level sensing, signal processing, and wireless transmission. However, there was a difference between the simulated and

- actual measurement values when utilizing LH. This seems to be because the total amount of LH utilized in the calculation cannot actually be utilized in practical settings.
- (3) We conducted a demonstration experiment using a steel bridge deck as a heat source to measure the amount of power generated by our SH-storage-type TEG module and the measurements indicated that the power generated is equivalent to that obtained by simulation and can supply the power required for water-level sensing and wireless transmission.

## References

- [1] <http://www.fujitsu.com/global/about/resources/news/press-releases/2016/0815-01.html>.
- [2] K. Nakagawa, T. Suzuki, Procedia Eng. 168 (2016) 1630–1633.
- [3] <http://www.fujitsu.com/ca/en/about/environment/society/sustainability/sdgs-case-studies/sdgs-03/>.
- [4] <http://www.fujitsu.com/global/about/resources/news/press-releases/2015/0210-03.html>.
- [5] <http://www.fujitsu.com/global/about/resources/news/press-releases/2015/0723-01.html>.
- [6] S. Miyamoto, S. Okumura, Proceeding of 9th Symposium, November, 2016, pp. 149–154.
- [7] S. Miyamoto, Proceedings of the Civil Engineering Society, 595/VI-39, 1998, pp. 117–125.
- [8] N. Takahashi, R. Tokunaga, M. Asano, N. Ishikawa, Monthly Report of Ceri, No. 643, December, 2006, pp. 40–48.
- [9] K. Nakagawa, T. Suzuki, J. Electron. Mater. 48 (4) (2019) 1939–1950.
- [10] M.E. Kiziroglou, A. Elefsiniotis, S.W. Wright, T.T. Toh, P.D. Mitcheson, T. Becker, E.M. Yeatman, Appl. Phys. Lett. 103 (2013) 193902.
- [11] A. Elefsiniotisa, N. Kokorakisa, T. Beckera, U. Schmid, Sensor Actuat A-Phys. 206 (2014) 159–164.
- [12] A. Agbossou, Q. Zhang, G. Sebald, D. Guyomar, Sensor Actuat A-Phys. 163 (2010) 277–283.
- [13] L. Tan, R. Singh, A. Date, A. Akbarzadeh, Front. Heat Pipes (FHP) 2 (2011) 043001.
- [14] M.K. Altstedde, F. Rinderknecht, H. Friedrich, J. Electron. Mater. 43 (2014) 6.
- [15] F. Blacet, P. Leighton, E. Bartlett, J. Phys. Chem. 35 (1931) 1935–1943. <https://pubs.acs.org/doi/pdf/10.1021/j150325a005>.
- [16] G.L. Song, M. Liu, Corros. Sci. 72 (2013) 73–81.

# Index

Note: Page numbers followed by *f* indicate figures, and *t* indicate tables.

## A

- AB<sub>2</sub>X<sub>2</sub> composition, 162–165, 164*f*
- Active building envelope (ABE) system, 558–559
- Active building wall (ABW), 558–559
- Active thermal insulator (ATI), 558–559
- ACu<sub>3</sub>Ru<sub>4</sub>O<sub>12</sub> quadruple perovskites, 7–8, 8*f*
- Adaptive sensing technology, 663, 664*f*
- AgBiSe<sub>2</sub>, 233–235
- AgCrSe<sub>2</sub>, 236
- AgSbSe<sub>2</sub>, 232–233, 234*f*
- Air-cooled power generation system, 569
- Air-cooled thermoelectric generator
  - oxide thermoelectric module, 569–571
  - thermoelectric power unit of oxide module
    - air-cooled unit, 575–579
    - water-cooled unit, 571–575
  - waste heat, 569
- Air-cooled unit, 575–579
- Air/liquid TE device, 597, 598*f*
- Akhiezer damping, 26–27
- All-electron GW method, 451–452
- All-molten synthesis, 390, 390*f*, 395–396
- Alloying
  - band converging, 454, 455*f*
  - carrier mobility, 454–456
  - effect of, 454–458
  - lattice thermal conductivity, 456–458, 457*f*
- Alphabet Energy Inc., 200
- A<sub>2</sub>MPn<sub>2</sub> compounds, 168–170
- A<sub>11</sub>M<sub>6</sub>Pn<sub>12</sub> composition, 171–172
- A<sub>14</sub>MPn<sub>11</sub> composition, 165–168, 165–166*f*
- Anharmonic bonding, 224
- Anharmonic scattering magnitude, 28
- Anisotropic thermal and electrical transport, organic semiconductors, 341–342, 342–343*f*
- Apparent Fermi liquid (AFL) model, 5
- APt<sub>4</sub>Ge<sub>12</sub> skutterudites, 76
- ArF immersion lithography, 512–514

## A-site deficient perovskites, 314

- A-site deficient SrTiO<sub>3</sub>, 313
- Atomistic Green's function (AGF) method, 29–30

## B

- Band convergence, lead telluride, 253–256, 253*f*
  - bipolar thermal conductivity, 256
  - heavy-mass hole contribution, 254
  - phonon and carrier scattering, 254–256
  - Pisarenko plot, 254, 255*f*
- Band converging due to alloying, 454, 455*f*, 461
- Band engineering, 135, 452
- Band features and modeling, 450–453, 451*f*, 453*f*
- Bandgaps and band separation, 460, 460*f*
- Band theory, 15
- Ba<sub>x</sub>Ru<sub>8</sub>O<sub>16</sub>, 9, 10*f*
- Battery thermal management, 597
- Bending test on single-edge notched beam (SENB) specimen, 404–405
- β-CuAgSe, 235–236
- BiCuSeO, 236–239, 237*f*
- Bileg structure, 506, 506*f*
- Binary copper sulfides, 189–190
- Binary metal selenides
  - Cu<sub>2</sub>Se, 225–227, 226*f*
  - GeSe, 230–231, 230*f*
  - In<sub>4</sub>Se<sub>3</sub>, 227–229
  - SnSe, 222–225, 222*f*
- Binary skutterudites
  - electronic energy bands, 81–83, 81*f*
  - electronic transport, 87–90, 88–90*f*
  - pnictogen ring structure, 70–71
  - thermal conductivity of, 95–96, 96*f*
  - unit cell of, 69–70, 70*f*
- BiSe, 232
- Bismuth strontium cobaltite, 304–305
- Bismuth sulfide, 186–187

- Bismuth telluride ( $\text{Bi}_2\text{Te}_3$ ), 51–62, 184, 186*f*, 479–481, 480*f*, 487–489  
 band structure of, 45–46, 47*f*  
 $(\text{Bi},\text{Sb})_2\text{Te}_3$  and  $\text{Bi}_2(\text{Te},\text{Se})_3$   
 $\text{Bi}_{0.5}\text{Sb}_{1.5}\text{Te}_3$  band convergence, 55–57  
 doping mechanism in, 54–55  
 microstructure engineering, 57–62,  
   58–61*f*  
 n-type  $\text{Bi}_2(\text{Te},\text{Se})$ , 53–54  
 crystal structure of, 45, 46*f*  
 fine-grained  
   mechanical strength of, 51, 52*f*  
   point defect chemistry, 49–51, 50*f*  
   reducing thermal conductivity, 49  
 material application, 581  
 module, 523  
 nanocomposites, 62, 63*f*  
 physical and thermoelectric properties of,  
   46–48, 48*t*  
 STEG, 641, 642*f*
- Bismuth Triborate (BIBO), 31–32
- Bolt-type TEG energy harvesting device, 587,  
   587*f*
- Boltzmann transport equation, 25–26,  
   451–452
- Bonding technique, 481–486
- Bornite, 192, 197–198
- Bose-Einstein distribution, 25, 28–30
- Bragg scattering, 25
- Bridgman methods, 48
- Brillouin zone (BZ), 25, 45–46
- C**
- $\text{Ca}_{14}\text{AlSb}_{11}$  structure type, 167–168
- $\text{CaAl}_2\text{Si}_2$  ( $\text{AB}_2\text{X}_2$ ) structure, 162–163, 164*f*
- Calcium cobaltite, 304
- Calcium cobalt oxide ( $\text{Ca}_3\text{Co}_4\text{O}_9$ ), 283–286,  
   285*f*  
 alkali-earth elements, 285–286  
 doping of, 285  
 effects of transition elements, 286  
 free-edge cold pressing, 284  
 microstructure, 284, 285*f*  
 rare-earth elements, 285  
 Seebeck coefficient, 286  
 sintering, oxygen atmosphere, 285
- Calcium manganite ( $\text{CaMnO}_3$ ), 281, 282*f*,  
   307
- Callaway's model, 458
- Carbon nanotubes (CNT), thermal and  
 thermoelectric properties, 367–372
- Carnot efficiency principle, 584–585
- Carrier mobility and alloying, 454–456
- Cartridge-based TEG, 603
- $\text{CeCu}_6$ , heavy-fermion compounds, 20–21
- Chalcocite, 197–198
- Chalcopyrite, 190–191
- Charge-balanced Zintl phases, 170
- Charge density wave (CDW), 227–228
- Charge transport in organic thermoelectric  
 materials, 347–348
- Climate Control Seat, 593–594
- $\text{CO}_2$  emission, 569
- $\text{CO}_2$  reduction, 581
- Cobalt oxides, 21
- Coefficient of performance, 553
- Coefficient of thermal expansion (CTE), 522,  
   525–526
- Cold high-pressure pressing, 284
- Cold side heat exchanger unit, 618, 619*f*
- Colusites ( $\text{Cu}_{26}\text{V}_2\text{M}_6\text{S}_{32}$ )  
   composition, 203  
   crystal structure, 203, 204*f*  
   Cu–S network and the electronic  
    properties, 206–207  
   electronic properties, 203, 204*f*  
   first-principles electronic-structure  
    calculations, 204  
   phonon scatterers, 206  
   sintering temperature, 205–206, 206*f*  
   thermoelectric properties, 204–205,  
    205*f*  
   thermoelectric single elements, 207–208,  
    207*f*
- Compact tension (CT) specimen, 404
- Complementary metal-oxide-semiconductor  
 (CMOS), 503
- Composite skutterudites  
   extrinsic, 79  
   intrinsic, 78–79
- Concentrated triple junction (CTJ)-TEG  
 hybrid system, 646
- Condition-based maintenance (CBM),  
   586–587
- Conduction band, HMS, 379–380
- Contact resistance measurement for  $\text{Mg}_2\text{Si}$ ,  
   395–396, 395–396*f*

- Conversion efficiency, 469, 486–489, 488/*f*, 539
- Cooling capacity, 553
- Cooling method, 668–669
- Copper aluminate ( $\text{CuAlO}_2$ ), 305–307
- Corporate average fuel economy (CAFE), 611
- Cost per unit energy, 505
- Coulomb repulsion, 15–16
- Coupled harmonic oscillators, 28
- CTJ cell voltage, 648–649
- $\text{Cu}_2\text{Se}$ , 189, 225–227, 226/*f*
- $\text{Cu}_5\text{FeS}_4$ , 192–193
- $\text{Cu}_{12}\text{As}_4\text{S}_{13}$ , 198–199, 202
- $\text{Cu}_{12}\text{Sb}_4\text{S}_{13}$ , 198–200, 202, 203/*f*
- $\text{Cu}_{26}\text{Nb}_2\text{Ge}_6\text{S}_{32}$ , 207–208, 207/*f*
- Cu–S-based minerals, 197–198
- D**
- De-doping process
- carrier concentration, 349–353
  - solid-state photoinduced charge-transfer reaction, 335
- de Haas-van Alphen measurements, 46
- Density-functional theory (DFT), 411–412 calculations, 127, 450–451
- Density of states (DOS)
- for  $\text{Fe}_2\text{VAl}$ , 144
  - $\text{Mg}_2\text{S}$ , 412–413, 412/*f*
- Device-scale preparation, 431
- Dichalcogenides, 184
- Digenite, 189–190, 197–198
- Direct bonded aluminum (DBA), 525–526
- Direct Cu joining, 496
- Directed bonded copper (DBC), 525–526
- Domain separation, HMS, 384–385, 384/*f*
- Donor-doped  $\text{SrTiO}_3$ , 312–313
- Dopant-stimulated phase separation, 440–447
- Doped poly(3,4-ethylenedioxythiophene) (PEDOT) synthesis, 334
- anisotropicity and stability, 342
  - carrier density, 335
  - chemical structure of, 334, 334/*f*
  - coating, stable dispersion, 335
  - de-doping of, 335
  - in situ polymerized PEDOT films, 334–335
  - PEDOT:PSS films
    - carrier density in, 335
    - electromotive force, 335, 337/*f*
- thermoelectric power enhancement, 335, 336/*f*
- during polymerization, thermoelectric properties, 334–336
- self-doped PEDOT (S-PEDOT) polymer, 335
- thermoelectric performance, 335
- Doping
- of calcium cobalt oxide, 285
  - carrier concentration, 349–353
  - mobility, optimizing the morphology, 353–354
  - of zinc oxide, 272–275
- Dulong-Petit heat capacity value, 236
- Durable Heusler  $\text{Fe}_2\text{VAl}$  thermoelectric modules
- direct Cu joining, 496
  - performance and durability of, 497–499
  - thermoelectric properties, 493–495
- E**
- Effective medium theory (EMT), 440–443
- Elastic modulus, 399–404, 400–401/*t*
- Electrical conductivity, 454–456, 522
- of conducting polymers, 349
- Electrochemical method, oxidation level of PEDOT, 350–352, 351/*f*
- Electrode formation method with low contact resistance, 392–397
- Electron beam lithography, 508
- Electron correlation
- heavy-fermion compounds, 19–21, 20/*f*
  - Hubbard model, 15–16
  - layered cobalt oxides, 18–19
  - Mott insulator, 15–16
  - thermopower enhanced, 16–18
- Electron-doped manganese oxides, 3–4
- Electronic band dispersion, 412–414, 412/*f*
- Electronic energy bands, skutterudites
- binary skutterudites, 81–83, 81/*f*
  - electronegative fillers, 84–86, 86/*f*
  - filled skutterudites, 84, 85/*f*
  - [ $\text{Pt}_4\text{Ge}_{12}$ ] framework, 84, 86/*f*
  - ternary skutterudites, 83
- Electropositive fillers, 72–76, 73/*t*
- Empirical pseudopotential method (EPM), 450–451
- Energy conservation, 581

- Energy-dispersive X-ray (EDX) analysis, 153  
 Energy harvesting (EH), 586–588  
     applications, 585–586  
 Energy recovery system, 555–556  
 Energy storage, 652–653  
 Environmental monitoring, 661  
 $\text{Eu}_2\text{ZnSb}_2$  crystallization, 168–170  
 $\text{Eu}_{11}\text{Cd}_6\text{Sb}_{12}$ , 171–172  
 Evaluation instrument, 541–542, 542*f*  
 Exhaust gas heat recovery (EGHR) systems, 609  
 Extrinsic composite skutterudites, 79  
 Extrinsic scatterings, 26
- F**
- Fast-sintering technique, 49  
 Fe-based Heusler compounds, 146  
 Fermi level, 143–148, 460–461  
 Fermi’s golden rules, 28  
 Fermi surfaces of  $\text{Bi}_2\text{Se}_3$ , 46  
 $\text{Fe}_2\text{V}_{1+x}\text{Al}_{1-x}$  alloys, 150–152, 151*f*  
 $\text{Fe}_2\text{VAl}$ -based thermoelectric Heusler  
     compounds  
 Fe/V off-stoichiometric effect, 146–148  
 high-pressure torsion processing, 152–153,  
     153–154*f*  
 pseudogap engineering of, 144–146, 144–145*f*  
 single-phase intermetallic compound, 143  
 synergistic effect of off-stoichiometry and  
     Ta doping, 150–152, 151*f*  
 Fe/V off-stoichiometric effect, 146–150,  
     149–150*f*  
 Figure of merit, 74–75, 78–79, 87, 91–94,  
     97–100, 103–104, 106–107, 192–193,  
     522–525  
 Filled skutterudites (SKD), 479–483, 480*f*  
     electronegative fillers, 76–78  
     electronic energy bands, 84, 85*f*  
     electronic transport in, 90–95, 92–93*f*  
     electropositive fillers, 72–76, 73*f*  
     thermal conductivity, 96–97, 98*f*  
 Fine-grained sintered materials, 50–51, 60–61  
 First law of thermodynamics, 553  
 Flow calorimeter, 543  
 Fourier’s law, 23–24, 542–543  
 Four-phonon scattering, 27  
 Fracture toughness, 429  
     of TE materials, 404–405, 407–409, 408*f*
- Free-edge SPS (SPT), 284  
 Fuel economy, 630  
 Full-Heusler (FH) structure, 126–127, 126*f*  
 Full HVAC system, 597–598  
 Full-sized trucks and sports utility vehicles  
     (SUVs)  
     cost/benefit analysis, 630  
     engine coolant, 609  
     exhaust gas, 609  
     exhaust gas heat recovery, 609  
     organic Rankine cycle, 609  
     sterling engines, 609  
     thermal design and system sizing, 611–614  
     thermoelectric generator design and  
         assembly, 609–610, 614–621  
     vehicle integration and testing, 622–630  
     vehicle selection criteria, 610–611  
     waste heat recovery, 609
- G**
- Gas treatment method, 349  
 Gentherm Climate Control Seat system,  
     593–594, 594*f*  
 Ge-rich phase, 460  
 Germanite-derivative, 197–198  
 $\text{GeSe}$ , 230–231, 230*f*  
     GeSe-alloyed  $\text{PbSe}$ , 220  
 Gibbs-Duhem equation, 17  
 Goldfieldite, 198–199  
 Grain boundary (GB) scattering, 458–459  
 Graphene(oxide)-based materials,  
     thermoelectrics, 311–314, 311*t*  
     A-site deficient, 313  
     composites, thermoelectrics, 313–314  
     donor-doped, 312–313  
 Grüneisen parameter, 46–48, 236–238
- H**
- Half-Heuslers (HHs) thermoelectrics  
     alloys, 471–472, 482–483  
     band modeling, 127  
     DFT, 127  
     18-electron rule, 126–127  
     electronic parameters, 127, 128*t*  
     Hall measurements, 127  
     new n-type compositions, 137–138  
     new p-types, 135–137, 136*f*  
     n-type  $\text{TiNiSn}$  system, 126–127

- XNiSn and XCoSb, 129–134  
zincblende (YZ)<sup>n-</sup> network, 126, 126f  
Hall measurements, 46–48, 127  
Hamilton's equation of motion, 29  
Harman method, 532  
Harvesting mode, 515–516  
Heat balance model, 666  
Heat current, 25  
Heat flow, 539  
    measurement method, 542  
Heat flux method, 526–528  
Heat flux sensor, 529–531  
Heating and cooling/thermal management,  
    passenger vehicles  
    applications, 598  
    battery thermal management, 597  
    full HVAC system, 597–598  
    seat-based and zonal systems, 593–596  
Heating ventilation and air conditioning  
    (HVAC), 551  
Heat pipe, 576, 576f  
Heat sink, 633  
Heat source temperature, 666–668  
Heat ventilation and air-conditioning system,  
    556–558  
Heavy-fermion compounds, 19–21, 20f  
Heikes formula, 5–6  
Heusler compound Fe<sub>2</sub>VAL  
    Fe/V off-stoichiometric effect, 146–148  
    high-pressure torsion processing, 152–153,  
        153–154f  
    high-temperature exhaust gases, 499–500  
    performance and durability, 497–499  
    preparation by direct Cu joining, 496  
    pseudogap engineering of, 144–146,  
        144–145f  
    single-phase intermetallic compound, 143  
    synergistic effect of off-stoichiometry and  
        Ta doping, 150–152, 151f  
    thermoelectric properties, 493–495  
    V/Al off-stoichiometric effect, 148–150,  
        149–150f  
HgSe-alloyed PbSe, 218–220  
HHs thermoelectrics. *See* Half-Heuslers  
    (HHs) thermoelectrics  
Hierarchical structuring, lead telluride,  
    249–253  
    alkaline earth elements, 250  
    band alignment, 250–253  
decoupling of the charge carrier, 250–253  
heat-carrying phonons, 250  
phonon transport processes, 250–253  
power generation characteristics, 258  
second phase through precipitation  
    processes, 250, 251f  
spinodal decomposition, 250  
spontaneous nucleation and growth, 250  
Higher manganese silicide (HMS), 375–376  
    conduction band, 379–380  
    crystal structure of, 375–376, 376f, 385  
    dissipation of MnSi striations, 377–379,  
        379f  
    domain separation, 384–385, 384f  
    electronic structure and density of states,  
        379–380, 380f  
HMS-based solid solutions  
    formation of, 381  
    thermoelectric performance of, 381–384  
low lattice thermal conductivity, 380–381  
Mn–Si binary system, high-temperature  
    X-ray diffraction, 377, 378f  
phonon and lattice dynamics, 380–381  
superspace symmetry, 380  
temperature evolution of lattice  
    parameters, 376–377, 377f  
unusual thermal expansion and striation  
    problem, 376–377, 378f  
valence band, 379–380  
valence electron counts per number of  
    transition elements, 380  
Highly oriented vertical Si NWs, 510  
High-performance thermoelectrics  
    of metal selenides (*see* Metal selenides)  
    sulfide (*see* Sulfide thermoelectric  
        materials)  
High-pressure torsion processing, 152–153,  
    153–154f  
High-temperature exhaust gases, 499–500  
HMS-based solid solutions  
    formation of, 381  
    thermoelectric performance of, 381–384  
HMS-matrix/electrode interface adhesion,  
    396, 397f  
Hollandites, 9–12  
Hot pressing (HP), 284, 399  
Hot side heat exchanger section, 615–616,  
    616f  
Hubbard model, 15–16

Hund coupling, 5

Hydrofluorocarbon (HFC) refrigerants, 551

## I

Impurity doping and thermal durability,

$\text{Mg}_2\text{Si}$ , 389–392

electronic and thermoelectric properties,  
412–414

lattice constants and formation energies,  
416–417, 417*f*

parameters, variable-cell relaxation  
calculations, 414–416, 416*t*

screening of, 414–418, 415*f*, 416*t*

$\text{In}_2\text{O}_3$  bixbyites, 3–4

$\text{In}_4\text{Se}_3$ , 227–229

Incommensurate crystal structure of  $\text{MnSi}$ ,  
375–376, 376*f*, 385

Indentation fracture (IF) technique, 404–405

Indentation test, 399

Independent power supply applications,  
585–586

Induction melting, spark plasma sintering,  
431

Instruments, 541–543

Integration techniques for segmented  
modules, 487, 489–490

Interface interdiffusion, speculative model,  
393–395, 394*f*

Interface scatterings, 26, 28

Interfacial materials and bonding technique,  
481–486

Interference lithography, 510–511

Internet of things (IoT), 367

Intrinsic composite skutterudites, 78–79

Intrinsic scatterings, 26

Inverse skutterudites, 84–85

Isocubanite, 197–198

I-V curves and module testing, 528

## K

Kadowaki-Woods ratio, 7–8

$\text{KAlSb}_4$  structure type, 172–174, 173*f*

Kelvin formula, 17, 20–21

Kesterite, 197–198

Klemens' model, 456, 458

$\text{K}_2\text{MnS}_2$  structure type, 168–170, 169*f*

Kondo interaction, 21

Korringa-Kohn-Rostoker (KKR) method,

450–451

$\text{KRu}_4\text{O}_8$  hollandites, 9

Kyoto Protocol, 581

## L

$\text{LaCoO}_3$  (LCO), 305

Latent-heat-storage-type TEG module, 676–677

Lattice dynamics, 28

Lattice thermal conductivity and alloying,  
456–458, 457*f*

Layered cobaltites, p-type oxides

Bismuth strontium cobaltite, 304–305

calcium cobaltite, 304

sodium cobaltite, 304

Layered cobalt oxides, 18–19, 281–286

Layered perovskite oxides, 314–316

Lead-antimony-silver-tellurium (LAST)  
compound, 405

Lead-antimony-silver-tellurium-Tin  
(LAST-T) compound, 405

Lead telluride ( $\text{PbTe}$ )

band convergence, 253–256

band engineering, 247

based materials, 218

developmental stages, 247, 248–249*t*

nanostructuring and hierarchical  
structuring, 247, 249–253

power generation module, 256–261

in power generation technologies, 247

radioisotope thermoelectric generators, 247

thermoelectric waste heat recovery, 249

Leg geometry approach, 478–479

$\text{Li}_x\text{CoO}_2$ , 3

Linear elastic fracture mechanics (LEFM)  
approach, 407–408

Linearized augmented-plane-wave (LAPW)  
method, 81–82

Lithography, 510

Load electric current, 539–540

Local-density approximation (LDA), 81–82,  
450–451

Low-dimensional sulfides

bismuth sulfide, 186–187

layered materials, 184–186, 185–186*f*

pseudo-two-dimensional shandite  
structure, 187–188, 188*f*

Low-temperature side, 540

**M**

Magneli phases, 309–310

Magnesium silicide

anti-oxidation passivation coating,  
390–392

mechanical properties, 398–411  
at elevated temperatures and long-term  
durability, 406–407

fracture toughness, 404–405

grain refinement, 407–410

instability of p-type conductivity,  
418–419

modulus and hardness, 399–404,  
400–401<sup>t</sup>

simultaneous enhancement of toughness  
and ZT, 409–410

strength of TE materials, 405

TE materials toughening, 407–409

Magnesium silicide ( $Mg_2Si$ )-based

thermoelectric materials

backscattered scanning electron  
microscopy, 434–436

chemical instability, 432

crystallite size distribution, 440, 444<sup>f</sup>

device-scale preparation, 431

high-angle annular dark-field, 438, 441<sup>f</sup>

high-resolution TEM combined with EDS  
studies and mapping, 438–440,  
442–443<sup>f</sup>

induction melting followed by spark  
plasma sintering, 431

interstitial defects, 431–432

mechanical alloying, 431

mechanical-assisted alloying synthesis

combined with sintering, 431

melting or solid-state or solid-liquid  
approaches, 430

microstructure, 431–438

mixing of all commercially available  
elements, 431

module fabrication, 431

nanostructure, 438–440

nonparabolic band (Kane-type) model, 452

phase purity, 431–432

phase separation phenomena, 446–447

powder/solid-state techniques, 431

pseudo-binary solid solutions, 431, 438

pseudo-ternary materials, 432–434

pseudo-ternary solid solutions, 431

Seebeck coefficient vs. carrier  
concentration data, 452–453

short time ball milling and annealing for  
solid-state reaction, 431

Sn-rich group of phases with Sn:Si ratio,  
444

solid-state reaction combined with spark  
plasma sintering, 431

structural properties and alloying, 431–447

synthetic strategies, 430

transmission electron microscopy, 438,  
439–440<sup>f</sup>

transport coefficients, electron statistics,  
452

volatilization and oxidation, 431

Magnetism, 5, 9–10

Manganese silicide

mechanical properties, 398–411  
at elevated temperatures and long-term  
durability, 406–407

fracture toughness, 404–405

grain refinement, 407–410

instability of p-type conductivity,  
418–419

modulus and hardness, 399–404,  
400–401<sup>t</sup>

simultaneous enhancement of toughness  
and ZT, 409–410

strength of TE materials, 405

TE materials toughening, 407–409

Manhole cover heat source, 673

Many-body perturbation theory, 451–452

Material properties and device performance

interconnect, diffusion barriers, and

bonding layers effect, 525–526

thermal insulations and thermal

interfaces, 526

transport properties and figure of merit,  
522–525

Matthiessen's rule, 26, 458

Mean free path (MFP), 23, 26

Measurement techniques of thermoelectric  
devices and modules

device performance

single couple, 533

standard module, 533–534

material properties and device performance

- Measurement techniques of thermoelectric devices and modules (*Continued*)  
 interconnect, diffusion barriers, and bonding layers effect, 525–526  
 thermal insulations and thermal interfaces, 526  
 transport properties and figure of merit, 522–525
- thermoelectric device and module testing techniques  
 Harman method, 532  
 heat flux method, 526–528  
 heat flux sensor, 529–531  
 I-V curves and module testing, 528  
 Peltier effect, 528–529  
 pressure Macor calibration, 531–532
- Mechanical alloying, 431  
 synthesis combined with sintering, 431
- Mechanical properties of Mg- and Mn-based silicides, 398–411  
 at elevated temperatures and long-term durability, 406–407  
 fracture toughness, 404–405  
 grain refinement, 407–410  
 instability of p-type conductivity, 418–419  
 modulus and hardness, 399–404, 400–401t  
 simultaneous enhancement of toughness and ZT, 409–410  
 strength of TE materials, 405  
 TE materials toughening, 407–409
- Mechanical stress, vibrations and temperature cycling, 429
- Melting or solid-state approaches, 430
- Metal-assisted chemical etching (MACE), 510, 510f
- Metal chalcogenide semiconductors, 217–218
- Metallic oxides, 5
- Metal oxides  
 conversion, 270  
 emission control, 270  
 energy generation, 270  
 storage, 270
- Metal selenide  
 binary  
 $\text{In}_4\text{Se}_3$ , 227–229  
 $\text{BiSe}$ , 232  
 $\text{Cu}_2\text{Se}$ , 225–227, 226f  
 $\text{GeSe}$ , 230–231, 230f  
 $\text{PbSe}$ , 218–221, 219f, 222f  
 $\text{SnSe}$ , 222–225, 222f  
 oxy-selenides, 236–239, 237f  
 ternary  
 $\text{AgBiSe}_2$ , 233–235  
 $\text{AgCrSe}_2$ , 236  
 $\text{AgSbSe}_2$ , 232–233, 234f  
 $\text{CuAgSe}$ , 235–236
- Metal-type electronic SWCNTs, 370
- Microstructure engineering, 57–62, 58–61f
- Microthermoelectric devices  
 basic structures, 506  
 characterization  
 benchmarking, 516–517  
 harvesting mode and test mode, 515–516  
 efficiency or power, 505  
 Si-based microthermoelectric generator modules  
 horizontal architectures, 507–508  
 short thermoelements architecture, 512–514  
 vertical architectures, 509–512  
 silicon nanowire, 503–505  
 specific power generation capacity, 506–507
- Mini-PEM, 542
- Miscibility gap of compounds, 440–447
- MnSi striations dissipation, 377–379, 379f
- Module assembly approach, 478–479
- Module fabrication, 431
- Module integration, 481
- Mohite, 197–198
- Molecular dynamics, 29
- Monte Carlo ray tracing (MCRT) for phonons, 30
- Mott insulators, 15–17
- Multi-junction (MJ) solar cells, 646
- Multi-junction-thermoelectric generator (MJ-TEG) hybrid system under concentrated solar radiations, 646–651
- Multiple inversion boundaries (IBs), 274
- N**
- $\text{Na}_x\text{CoO}_2$ , 3–4, 18, 19f
- Nanostructures  
 interface softening, 36–37  
 phonon coherent effect, 34f, 35–36  
 phonon confinement, 38, 39f

- Nanostructuring and hierarchical structuring, lead telluride, 249–253  
alkaline earth elements, 250  
band alignment, 250–253  
decoupling of the charge carrier, 250–253  
heat-carrying phonons, 250  
phonon transport processes, 250–253  
power generation characteristics, 258  
second phase through precipitation processes, 250, 251*f*  
spinodal decomposition, 250  
spontaneous nucleation and growth, 250
- Nanowires, 521
- Natural superlattice interfaces (IBs) on charge and heat transport, 274
- NbCoSb, 137–138
- NbCoSn-based compositions, 137
- 19 valence electron systems, 137–138
- Nonparabolic band (Kane-type) model, 452
- N-type bismuth telluride, 51–55, 54*f*, 57, 60–62, 523
- N-type CaMnO<sub>3</sub>, 569–570
- N-type organic thermoelectric materials, 338–340
- N-type oxides, thermoelectrics, 3–4  
A-site deficient perovskites, 314  
calcium manganite, 307  
layered perovskite oxides, 314–316  
Perovskite-type thermoelectric materials, 275–281
- SrTiO<sub>3</sub>-based materials, 311–314, 311*t*  
titanium oxides of the Magneli phases, 308–310  
transition-metal oxides, 272–275
- Tungsten bronze structured materials, 310
- ZnO-based materials, 307–308
- N-type zintl phases, 172
- O**
- Off-stoichiometry, 150–152, 151*f*
- One-dimensional heat transfer physical model, 637, 637*f*
- Open circuit voltage, 539, 669
- Optical collector, 633
- Organic electrochemical transistor (OECT) configuration, 359, 360*f*
- Organic Rankine Cycle (ORC), 609
- Organic semiconductors, 333–334  
anisotropic thermal and electrical transport, 341–342, 342–343*f*  
with controlled molecular doping, 337–338, 339–340*f*
- Organic thermoelectric devices, 359–363, 362*f*
- Organic thermoelectric materials  
charge transport in conducting polymers, 347–348  
crystallinity and morphology, 347  
low TE performance, 347  
nonflat heat sources, 347  
nonpercolated carbon nanotubes, 347–348  
polymer nanocomposites, 356–359  
polymers and small molecules, 349–356  
portable and wearable applications, 347–348  
Seebeck coefficient, 347–348  
transport mechanisms, 347–348
- Outdoor-applicable thermoelectric generators  
IoT application, 679–680  
latent-heat-storage-type module, 676–677  
sensible-heat-storage-type module, 677–679  
wireless sensor networks  
amount of power generation, 669–674  
cooling method, 668–669  
heat source temperature, 666–668  
power supply design, 664–665
- Oxide-based STEG system, 640–641, 641*f*
- Oxide/Bi<sub>2</sub>Te<sub>3</sub> cascaded module, 571, 571*f*
- Oxide TEGs, 640, 640*f*
- Oxide thermoelectrics, 18, 303  
applications, 316, 317*f*  
chalogenides, 270–271  
ecological technologies, 269–270  
electronics, 269–270  
energetics, 269–270  
energy-filtering effect, 286–287  
environmental and economic criteria, 269  
grain boundaries, 286–287  
high-temperature applications, 269  
module, 569–571  
n-type oxide, 272–281, 307–316  
point defects, crystal lattice, 286–287  
polycrystalline volume ceramics, 271–272  
power densities of, 316, 317*f*  
p-type oxides, 281–286, 303–307  
research and development, 286–287

- Oxide thermoelectrics (*Continued*)  
 scutterudites, 270–271  
 segregation of fine nano-precipitates, 286–287  
 spark plasma sintering, 286–287  
 structural and microstructural features, 287  
 tetrahedrites, 270–271  
 thermoelectric performance of, 286–287
- Oxoruthenates, 12, 12*f*
- Oxy-selenides, 236–239, 237*f*
- P**
- Pair distribution function (PDF) analysis, 218–220
- Paraffin, 670–671, 670*t*
- Passenger vehicles  
 heating and cooling/thermal management applications, 598  
 battery thermal management, 597  
 full HVAC system, 597–598  
 seat-based and zonal systems, 593–596
- power generation/waste heat recovery, 599–605
- Pauli metallic ruthenates, 8–9
- Pauli-type magnetism, 9–10
- PbSe  
 Al doping, 220–221  
 band convergence, 218–220  
 Cu<sub>2</sub>Se-doped, 221  
 electronic structure of, 218  
 GeSe-alloyed, 220  
 HgSe alloyed, 218–220, 219*f*  
 Na and Cd co-doped, 221  
 pair distribution function, 218–220  
 rock-salt type cubic structure, 218  
 Seebeck coefficient, 218, 220–221  
 zT, 221
- PbTe-/TAGS based (multipurpose)  
 MMRTG, 522
- Peierls instability, 227–228
- Peltier cooling applications, 45
- Peltier effect, 528–529
- Peltier module, 581
- Performance index, 554–555
- Perovskite-type thermoelectric materials, 275–281  
 calcium manganite, 281  
 strontium titanate, 277–281
- Phase change materials (PCMs), 652–653, 669
- Phase segregation, 125, 129
- Phonon and lattice dynamics, HMS, 380–381
- Phonon coherent effect, 34*f*, 35–36
- Phonon dispersion relations, 30–31
- Phonon gas model, 25
- Phonon-glass electron-crystal (PGEC), 69, 235–236
- Phononic crystals (PnCs), 35–36
- Phonon mean free path (MFP), 458–459
- Phonon relaxation time, 26, 28, 31, 34*f*
- Phonon-scattering mechanisms, 458
- Phonon transport  
 thermal conductivity of  
 binary skutterudites, 95–96, 96*f*  
 filled skutterudites, 96–97, 98*f*  
 to thermoelectrics (*see* Phonon transport to thermoelectrics)
- Phonon transport to thermoelectrics  
 benefits of, 23
- Boltzmann transport equation, 25–26  
 in computational methods  
 atomistic Green's function, 29–30  
 lattice dynamics, 28  
 molecular dynamics, 29  
 Monte Carlo ray-tracing method, 30
- industrial applications, 23
- inelastic neutron scattering, dispersion and scattering rate, 30–31
- nanostructures  
 interface softening, 36–37  
 phonon coherent effect, 34*f*, 35–36  
 phonon confinement, 38, 39*f*
- scattering mechanisms, 26–28
- thermal conductivity (*see* Thermal conductivity)
- Phosphide skutterudites, 72
- Photovoltaic thermal-compound  
 thermoelectric ventilator (PVT-TEV) system, 556
- Photovoltaic-thermoelectric generator (PV-TEG) hybrid system  
 under concentrated solar radiations, 645–646  
 under standard illumination condition, 643–644
- Plasma-assisted sintering (PAS) method, 389–393

- Plasma dry etching, 508  
Plastic deformation, 429  
Pnicogen atom, 69–71  
Point defect scattering, 456  
Polarized beam splitter (PBS), 31–32  
Polymer nanocomposites, 356–359  
  composite structures for high TE performances, 358–359, 359–361*f*  
  decoupling electrical conductivity and Seebeck coefficient, 356–357, 357*f*  
  and thermal conductivity, 357, 358*f*
- Polymers  
  doping  
    carrier concentration, 349–353  
    mobility, optimizing the morphology, 353–354  
  thermoelectric materials, 349–354
- Poly-SiGe thermoelements, 507
- Poly-Si thermoelements, 507
- Powder metallurgy methods, 440
- Powder/solid-state techniques, 431
- Power density, 507
- Power generation module, nanostructured lead telluride, 256–261, 259*f*, 260*t*
- Power generation/waste heat recovery, passenger vehicles, 599–605
- Power supply design, energy balance calculation, 664–665
- Pressure Macor calibration, 531–532
- Primary oxidation doping method, 352
- Pseudo-binary solid solutions, 431
- Pseudogap engineering, 144–146, 144–145*f*
- Pseudo-ternary solid solutions, 431
- Pseudo-two-dimensional shandite structure, 187–188, 188*f*
- P-type bismuth telluride, 49, 51–55, 54*f*, 57–58, 62, 523
- P-type  $\text{Ca}_3\text{Co}_4\text{O}_9$ , 569–570
- P-type oxides, thermoelectrics, 3–4, 303–307  
  calcium cobalt oxide, 283–286, 285*f*  
   $\text{CuAlO}_2$ , 305–307  
   $\text{LaCoO}_3$  (LCO), 305  
  layered cobaltites, 303–305  
  layered cobalt oxides, 281–286
- P-type skutterudite materials, 614–615, 615*f*
- Pudding-mold model, 5
- Pulsed current sintering (PCS), 494–495, 495*f*
- Pulse-echo method, 399
- Q**
- Q-MACOR, 532
- Quadruple perovskites, 7–8, 8*f*
- Quantum dots superlattice, 521
- Quantum well, 521
- R**
- R134a refrigerant, 597
- Radioisotope thermoelectric generator (RTG), 522, 584
- Real-time sewer monitoring system, 662–663, 662*f*
- Real-time water-level monitoring system, 661
- Resistive heater/insulator/electrical contact stack, 510–511
- Resonance ultrasound spectroscopy (RUS), 399
- Rietveld analyses, 150–151
- River water-level monitoring, 662
- $\text{RPt}_4\text{Ge}_{12}$  skutterudites, 76–78
- $\text{RT}_4\text{X}_{12}$  skutterudites, 76–78
- Ru-based Heusler compounds, 146
- $\text{RuO}_6$  corner-shared octahedra, 7
- Ruthenates, 5–12
- Ruthenium hollandites, 9–10
- S**
- Scattering mechanisms of phonons  
  Akhiezer damping, 27  
  four-phonon scattering, 27  
  interface scattering, 28  
  rate, 30–31  
  surface scattering, 27  
  three-phonon scattering, 27
- Seat-based and zonal systems, 593–596
- Secondary doping, 352
- Seebeck coefficient, 493–494, 494*f*, 522  
  acoustic phonon scattering, 127  
  of  $\text{BiCuSeO}$ , 5, 236–238  
   $\text{Bi}_2\text{Te}_3$ , 46–48  
  vs. carrier concentration data, 452–453  
  of  $\text{CuAgSe}$ , 235–236  
   $\text{Eu}_{11}\text{Cd}_6\text{Sb}_{12}$ , 171–172  
   $\text{Fe}_2\text{VAl}$ -based compounds, 145–146, 145*f*  
   $\text{Fe}_{2-x}\text{V}_{1+x}\text{Al}$  alloys, 146–150, 147*f*, 149*f*  
  of  $\text{In}_4\text{Se}_3$ , 227–228  
   $\text{KAlSb}_4$  parent compound, 172  
  in  $\text{NaxCoO}_2$ , 12–13

- Seebeck coefficient (*Continued*)  
 oxoruthenates, 12, 12*f*  
 of PbSe, 218, 220–221  
 skutterudite, 72–74, 78, 81–83, 87–93, 102  
 of SnSe, 223–224  
 of SrRuO<sub>3</sub>, 5–7, 6*f*  
 Yb<sub>14</sub>MnSb<sub>11</sub>, 166–167  
 Zr<sub>3</sub>Ni<sub>3</sub>Sb<sub>4</sub> compound, 176
- Seebeck effect, 23
- Segmented thermoelectric modules, 469–470, 470*f*  
 applications, 489–490  
 availability, and cost, 472–475  
 bulk TE materials, 472, 474*f*  
 coefficient of thermal expansion, 472–475  
 compatibility factor, 471  
 compatible and noncompatible materials, 471–472  
 CoSb<sub>3</sub>-based skutterudites, 482–483  
 heat losses, 472–475  
 high-performance segmented modules, 486–489, 487*f*  
 interfacial materials and bonding technique, 481–486  
 material selection, 470–475  
 metallic compounds containing rare earth elements, 472–475, 476*f*  
 processing requirements, 472–475  
 single element efficiencies, 471, 472*t*  
 temperature dependence, 471, 471*f*  
 temperature span, 471–472, 473*f*  
 thermal and chemical stability, 472–475  
 topologic structure design, 475–481  
 zT value and compatibility, 472–475
- Segment-type and cascade-type modules, nanostructured lead telluride, 258
- Semiconductor thermoelectrics, 23
- Sensible heat (SH), 669
- Sensible-heat-storage-type TEG module, 677–679
- Sewer water-level monitoring system, 661–662
- Shandite mineral, 187–188, 188*f*
- Short thermoelements architecture, 512–514
- Short time ball milling and annealing for solid-state reaction, 431
- Si-based microthermoelectric generator modules  
 horizontal architectures, 507–508
- short thermoelements architecture, 512–514  
 vertical architectures, 509–512
- SiGe-based general purpose heat source RTG, 522
- Silicide materials, mechanical properties, 398–411
- Silicon nanowire, 503–505
- Silicon-on-insulator (SOI) wafer, 508, 510
- Silicon-rich manganese silicide. *See* Higher manganese silicide (HMS)
- Si nanocrystalline (SiNC), 38, 39*f*
- Single couple, 533
- Single-edge notched beam (SENB) specimen, 404
- Single parabolic band (SPB) model, 127, 137, 220–221, 410
- Single-walled carbon nanotubes (SWCNTs)  
 characteristics of, 367  
 chemical doping, 369  
 dispersant effects, chemical doping uniformity, 370–371, 370*f*
- Seebeck effect, 369  
 as thermoelectric materials, 367–369
- Sintered Fe<sub>2</sub>VAL alloys, 493–495
- Skutterudites, 614  
 electronic energy bands (*see* Electronic energy bands)  
 electronic transport properties, 87–95  
 mechanical properties of, 100–102  
 phonon transport, 95–97  
 power-generating applications, 69  
 structural forms of  
   binary, 69–71, 70*f*  
   composite (*see* Composite skutterudites)  
   filled with electronegative fillers, 76–78  
   filled with electropositive fillers, 72–76, 73*t*  
   [Pt<sub>4</sub>Ge<sub>12</sub>] framework, 76, 77*t*  
   ternary, 71–72  
 synthesis of, 79–81  
 thermal stability of, 102–103  
 thermoelectric modules based, 103–107, 106–107*f*
- thermoelectric performance, 97–100, 99*f*
- Small molecules, thermoelectric materials, 354–356, 355–356*f*
- Sodium cobaltite, 304

- Solar-assisted thermoelectric cooling system with hot water supply (STACHWS) framework, 561
- Solar-driven exhaust air thermoelectric heat pump recovery (SDEATHP) system, 556
- Solar photovoltaic-assisted thermoelectric cooler, 559–560, 560*f*
- Solar PV-driven and TEM-assisted heat recovery system, 556
- Solar PV system, 559–561
- Solar thermoelectric generators (STEGs) components, and state of the art, 633–635 efficiency of, 635 energy storage, 652–653 multi-junction-thermoelectric generator hybrid system under concentrated radiations, 646–651 photovoltaic-thermoelectric generator hybrid system under concentrated solar radiations, 645–646 under standard illumination condition, 643–644 spectral beam splitting technology, 653–654 transient response conceptual model, 636 experimental setup, 639 numerical model, 637–639 results for different thermoelectric materials, 640–642
- Soldering method, TE cooling module fabrication, 481
- Solid-state reaction combined with spark plasma sintering, 431 short time ball milling and annealing, 431
- Sommerfeld coefficients, 7–8
- Soret effect, 352–353
- Spark-plasma sintering (SPS) technique, 49, 61–62, 185, 284, 399, 402–403*t*
- Specific heat, 670–671, 671*f*
- Specific power generation capacity (SPGC), 506–507
- Spectral beam splitting technology, 653–654
- Spin-orbit coupling (SOC), 5
- Sports utility vehicles (SUVs), full-sized trucks cost/benefit analysis, 630
- engine coolant, 609
- exhaust gas, 609
- exhaust gas heat recovery, 609
- organic Rankine cycle, 609
- sterling engines, 609
- thermal design and system sizing, 611–614
- thermoelectric generators, 609–610, 614–621
- vehicle integration and testing, 622–630
- vehicle selection criteria, 610–611
- waste heat recovery, 609
- $\text{Sr}_{11}\text{Cd}_6\text{Sb}_{12}$  structure type, 171–172, 171*f*
- $\text{SrRuO}_3$  perovskite, 5
- $\text{SrTiO}_3$ -based composites, thermoelectrics, 313–314
- $\text{SrTiO}_3$ -based materials, thermoelectrics, 311–314, 311*t* A-site deficient, 313 donor-doped, 312–313
- $\text{SrTiO}_3$  perovskites, 3–4
- $\text{Sr}_2\text{ZnP}_2$  structure type, 168–170, 169*f*
- Stand-alone power source, 588–589
- Standard module, 533–534
- Stanoidite, 197–198
- Steel bridge deke heat source, 674
- Stefan-Boltzmann constant, 638
- STEGs. *See* Solar thermoelectric generators (STEGs)
- Stirling reciprocating refrigeration, 556–558
- Strongly correlated electrons, 15
- Strontium titanate ( $\text{SrTiO}_3$ ) charge-carrier concentration, 277–278 electrical conductivity, 277–278 Fermi energy, 277 isotropic cubic perovskite structure, 277 La-substitution, A-site vacancies, 277–278, 279*f*
- microstructural enhancement, thermoelectric characteristics, 279–280
- Seebeck coefficient, 277–278
- Sulfide thermoelectric materials low-dimensional sulfides bismuth sulfide, 186–187 layered materials, 184–186, 185–186*f* pseudo-two-dimensional shandite structure, 187–188, 188*f*
- phonon-liquid electron crystal and related materials

- Sulfide thermoelectric materials (*Continued*)  
 binary copper sulfides and derivatives, 189–190  
 ternary copper sulfides, 190–193
- Surface scatterings, 26–27
- Sustainable energy systems, 569
- Synthetic metals, 349
- T**
- Ta doping, 150–152, 151*f*  
 TaFeSb composition, 135  
 Tellurium, 197–198  
 Templated grain growth, 284  
 Ternary copper sulfides, 190–193  
 Ternary metal selenides  
   AgBiSe<sub>2</sub>, 233–235  
   AgCrSe<sub>2</sub>, 236  
   AgSbSe<sub>2</sub>, 232–233, 234*f*  
   CuAgSe, 235–236
- Ternary skutterudites  
   band structure of, 83  
   isoelectronic substitutions, 71–72
- Tert*-butyl alcohol (TBA), 670–671, 671*t*
- Test mode, 515–516
- Tetrahedrites (Cu<sub>12-x</sub>Tr<sub>x</sub>Sb<sub>4</sub>S<sub>13</sub>)  
   band-engineering strategy, 202  
   compositions, 198  
   contact and diffusion barrier metal layers, 200  
   Cu<sub>12-x</sub>Tr<sub>x</sub>As<sub>4</sub>S<sub>13</sub> tennantites, 200, 201*f*, 202  
   elemental combinations, 198–199, 199*f*  
   first-principles electronic-structure calculations, 199–200  
   inelastic neutron scattering intensity map, 202, 203*f*  
   p-type, 200  
   structural traits and lattice dynamics, 202  
   thermal ellipsoids of Cu(2), 198, 199*f*  
   thermoelectric properties, 200
- ThCr<sub>2</sub>Si<sub>2</sub> structure, 163–165
- Thermal absorber, 633
- Thermal and electrical resistance, 481
- Thermal boundary conductance (TBC) of phonons, 30
- Thermal conductivity, 522  
   of binary skutterudites, 95–96, 96*f*  
   definition, 23–24  
   of filled skutterudites, 96–97, 98*f*
- one-dimensional (1D) atom chain, 24–25, 24*f*
- 3w method, 32–34
- time-domain thermal reflectance for, 31–32
- Thermal design and system sizing, 611–614
- Thermal durability, Mg<sub>2</sub>Si, 389–392  
   electronic and thermoelectric properties, 412–414
- lattice constants and formation energies, 416–417, 417*f*
- parameters, variable-cell relaxation calculations, 414–416, 416*t*  
   screening of, 414–418, 415*f*, 416*t*
- Thermal energy conversion, 429
- Thermal expansion coefficient mismatch (CTE), 481
- Thermal insulations and thermal interfaces, 526
- Thermal neutrons, 30–31
- Thermodynamics of phase separation, 440–447
- Thermoelectric air cooling  
   in buildings  
     energy recovery system, 555–556  
     heat ventilation and air-conditioning system, 556–558  
   challenges, 562  
   hybrid systems  
     active building envelope system, 558–559  
     solar PV system, 559–561  
     performance index, 554–555  
     principles of, 552–553  
     recent development in, 561–562
- Thermoelectric air duct (TE-AD) system, 556–558
- Thermoelectric ceiling cooling (TE-CCP) framework, 556–558
- Thermoelectric characteristics  
   electrode formation with low contact resistance, 392–397  
   improvement strategies, 420  
   by impurity doping and thermal durability, 389–392  
   sizable supercells, impurities and/or defects, 421
- Thermoelectric conversion efficiency, 539
- Thermoelectric coolers, 503, 552, 552*f*

- Thermoelectric cooling and temperature control, 582–584
- Thermoelectric couple (TEC), 523
- Thermoelectric device and module testing techniques
- Harman method, 532
  - heat flux method, 526–528
  - heat flux sensor, 529–531
  - instrument, 541–543
  - I-V curves and module testing, 528
  - measurement example, 544–547
  - Peltier effect, 528–529
  - pressure Macor calibration, 531–532
  - theory, 539–541
- Thermoelectric EH wireless sensor device, 587, 587*f*
- Thermoelectric generators (TEGs), 503, 523, 633
- in BMW vehicles, 599, 600*f*
  - design and assembly, 614–621
  - energy harvesting wireless vibration sensor, 587, 587*f*
  - subunit, 613
  - waste heat recovery unit, 590, 590*f*
- Thermoelectric materials and devices,
- carbon nanotubes
  - doping, 370–371
  - structure-property relationship, 369
- Thermoelectric module (TEM), 523, 551, 582–583, 583*f*
- Harman method, 532
  - heat flux method, 526–528
  - heat flux sensor, 529–531
  - instrument, 541–543
  - I-V curves and module testing, 528
  - measurement example, 544–547
  - Peltier effect, 528–529
  - pressure Macor calibration, 531–532
  - theory, 539–541
- Thermoelectric oxides, 3
- Thermoelectric power factor (PF), 493
- Thermoelectric (TE) power generation, 493
- colusites (*see* Colusites ( $\text{Cu}_{26}\text{V}_2\text{M}_6\text{S}_{32}$ ))
  - devices, 469
  - output power, 469
  - tetrahedrites (*see* Tetrahedrites ( $\text{Cu}_{12-x}\text{Tr}_x\text{Sb}_4\text{S}_{13}$ )))
- Thermoelectric power generation (TEG) market
- application of thermoelectric cooling and temperature control, 582–584
- history and current situation, 581–582
- prospect of thermoelectric application for power generation
- energy harvesting, 586–588
  - stand-alone power source, 588–589
  - waste heat recovery, 590–591
- Thermoelectric power unit of oxide module
- air-cooled unit, 575–579
  - water-cooled unit, 571–575
- Thermoelectric radiant air-conditioning (TE-RAC) system, 556–558
- Thermoelectrics (TEs)
- alloying, effect of, 454–458
  - automotive waste heat recovery and aeronautics, 430
  - band features and modeling, 450–453, 451*f*, 453*f*
  - of Cu–S-based materials, 198
  - experimentally achieved  $ZT_{\max}$  values and doping, 447–450, 449*f*
  - organic, 333–334
  - anisotropic thermal and electrical transport, 341–342, 342–343*f*
  - with controlled molecular doping, 337–338, 339–340*f*
  - phonon transport (*see* Phonon transport to thermoelectrics)
  - of p-type oxides, 4–5
  - of skutterudites (*see* Skutterudites)
- Thermoelements/legs, 506
- Thermopower
- electron correlation, 16–18
  - $\text{Na}_x\text{CoO}_2$ , 3, 19
  - of  $\text{Sr}_2\text{RuO}_4$ , 5–7
- Thin films, 521
- Thomson coefficient, 555
- Thomson effect, 555
- 3D modulation doping, 238–239
- Three-phonon scattering, 26–28
- Time-based maintenance (TBM), 586–587
- Time domain thermoreflectance technique (TDTR), 31, 32*f*
- TiNiSn-system, 132, 134*f*
- Tin(II) selenide (SnSe)
- anisotropic thermoelectric performance of, 224–225

- Tin(II) selenide (SnSe) (*Continued*)  
 crystal structure of, 222–223  
 high temperature phase transition, 222–223  
 indirect bandgap semiconductor, 223–224  
 layered and corrugated crystal structure of,  
   222–223, 222f  
 polycrystals, 224–225  
 p-type, 225  
 Seebeck coefficient of, 223–224  
 temperature variation, 222–223, 222f  
 thermoelectric figure of merit, 222–223,  
   222f  
 2D nanoplates, 224–225  
 ultralow lattice thermal conductivity, 224
- TiS<sub>2</sub>, 184–185, 185f
- Titanium oxides, 308–309
- Top-down Si micromachining technology,  
 508
- Topologic structure design, segmented TE  
 modules, 475–481  
 finite element analysis, ANSYS-  
   Workbench platform, 478–479  
 genetic algorithm, converters, 475–477  
 geometry-dependent maximum conversion  
   efficiency, 478–479  
 Joule heating, 475  
 multiparameter optimization, 479–481,  
   480f  
 one-dimensional energy equations, 475–477  
 power generation modules with high  
   conversion efficiencies, 477–478,  
   478f  
 Seebeck coefficient of materials, 478–479  
 semi-analytical approach, 475  
 three-dimensional energy balance  
   equation, 477  
 zero side heat losses, 475–477
- Transition-metal oxides, 272–275  
 zinc oxide (ZnO), 272–275
- Transition metal Zintl phases, 157–159
- Transport properties, 522–525
- Trial and error method, 483–486
- Tungsten bronze structured materials, 310
- Two-band system, 454
- U**
- UBe<sub>13</sub>, heavy-fermion compounds, 20–21
- ULVAC PEM-2 system, 528
- Undoped conducting polymers, 349–350
- Unileg structure, 506, 506f
- US06 cycles tests, 627–628
- V**
- Vacuum encapsulation, 633
- Valence electron concentration (VEC),  
 145–147, 145f, 147f, 161, 493–494
- V/Al off-stoichiometric effect, 148–150,  
 149–150f
- Vapor compression air-cooling system  
 (VCAS), 556–558
- Vapor-liquid-solid (VLS) chemical vapor  
 deposition, 503
- VCoSb, 137–138
- Vehicle selection criteria, 610–611
- Vertical type multistage bileg TEG module,  
 510, 511f
- Voltage of module, 539–540
- W**
- Waste heat, 569  
 recovery, 493, 500, 590–591, 599–605  
 application, 585–586
- Water-cooled thermoelectric power systems,  
 573–575, 574f
- Water-cooled unit, 571–575
- Water-level sensing and wireless  
 transmission, 661–662
- Wireless sensor networks  
 amount of power generation, 669–674  
 cooling method, 668–669  
 heat source temperature, 666–668  
 power supply design, 664–665
- X**
- ZNiSn-based systems, 125, 129–134
- Y**
- Yb<sub>2</sub>CdSb<sub>2</sub> structure type, 168–170, 169f
- Yb<sub>14</sub>MnSb<sub>11</sub>, 166–167, 167f
- Yttrium iron garnet Y<sub>3</sub>Fe<sub>5</sub>O<sub>12</sub> (YIG), 13
- Z**
- Zinc oxide (ZnO), 272–275, 307–308  
 donor dopants, 273–274  
 electrical properties, 273  
 internal diffusion mechanism, 275

- resonant scattering of phonons, 274–275  
technological applications for overvoltage protection, 272  
transparent conducting oxide, 272  
 $\text{ZnO}$ -based dilute magnetic semiconductors, 273  
Zintl-Klemm concept, 157, 170  
Zintl phases  
     $\text{AB}_2\text{X}_2$  composition, 162–165, 164*f*  
    alkali or alkaline earth cations, 157–159  
     $\text{A}_2\text{MPn}_2$  compounds, 168–170  
     $\text{A}_{11}\text{M}_6\text{Pn}_{12}$  composition, 171–172  
     $\text{A}_{14}\text{MPn}_{11}$  composition, 165–168, 165–166*f*  
     $\text{Ba}_4\text{GeAs}_4$ , 161  
     $\text{Ca}_{14}\text{AlSb}_{11}$  structure type, 157–159  
    chemical intuition, 161–162  
    Clathrates, 157–159  
    history of, 159–161  
    intermetallic compounds, 157  
    isovalent substitution, 161–162  
     $\text{KAlSb}_4$  structure type, 172–174, 173–174*f*  
     $\text{Mg}_3\text{Sb}_2$ , 159–161, 160*f*  
     $\text{NaTl}$ , 159–161  
    n-type, 172  
    publications vs. year, 157–159, 158*f*  
    rational design, 161–162  
    skutterudites, 157–159  
    structural and bonding complexity, 157  
    thermoelectrics, 157–159, 162, 163*f*  
    transition metal, 157–159  
    valence electron concentration, 161  
     $\text{Zr}_3\text{Ni}_3\text{Sb}_4$  structure type, 175–176, 175*f*, 177*f*  
ZnO-based materials  
    homologous compounds, 308  
    zinc oxide, 307–308  
 $\text{Zn}_4\text{Sb}_3$ -based STEG, 641, 642*f*  
 $\text{Zr}_3\text{Ni}_3\text{Sb}_4$  structure type, 175–176, 175*f*, 177*f*